CONF-970317--

Fourth International Reservoir Characterization Technical Conference

Proceedings

Sponsored by
Department of Energy,
BDM-Oklahoma, Inc.,
and
American Association of Petroleum Geologists

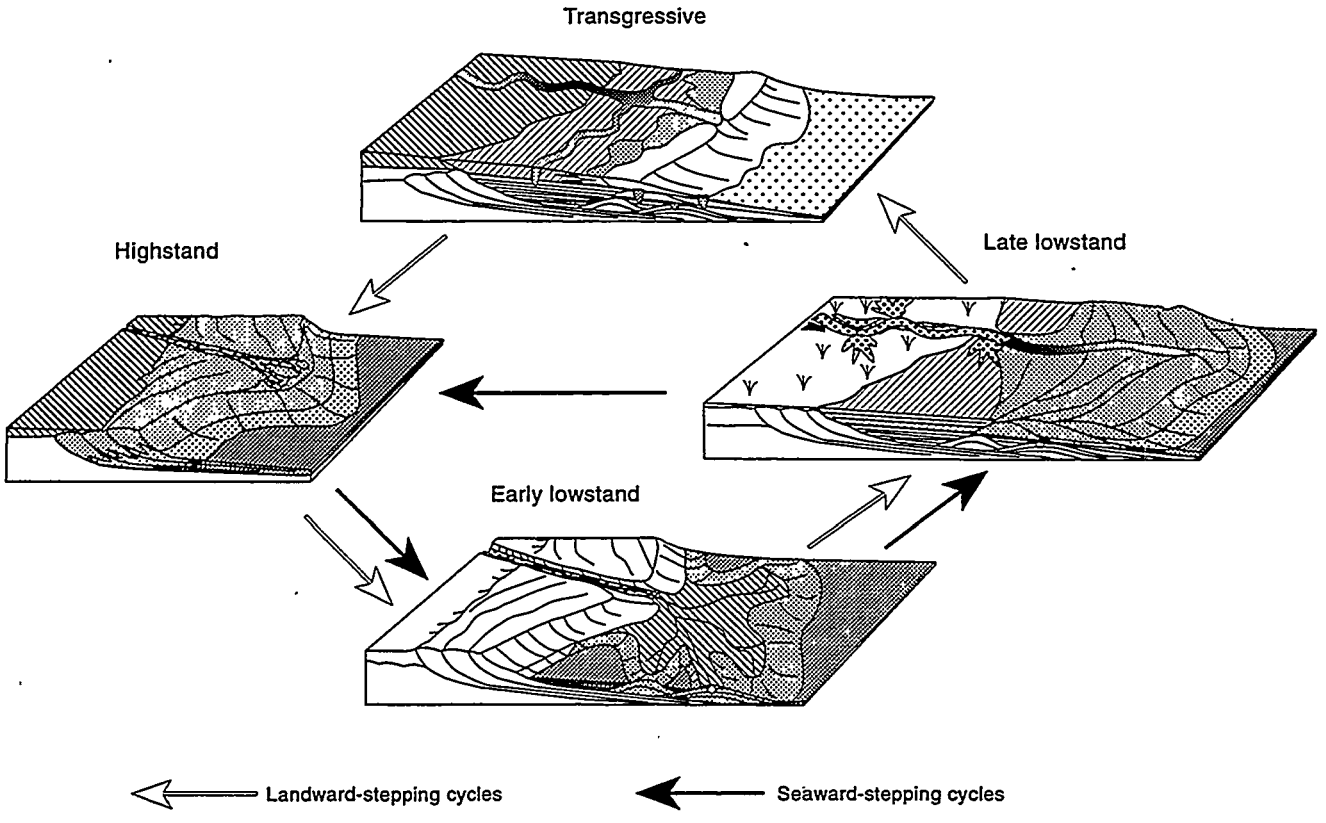

Wyndham Greenspoint Hotel
Houston, Texas • March 2 - 4, 1997

Cover figure is from Paul R. Knox and Mark D. Barton,
Bureau of Economic Geology, University of Texas at Austin
(see paper beginning on page 411)

Fourth International Reservoir Characterization Technical Conference

Proceedings

Sponsored by
Department of Energy,
BDM-Oklahoma, Inc.,
and
American Association of Petroleum Geologists

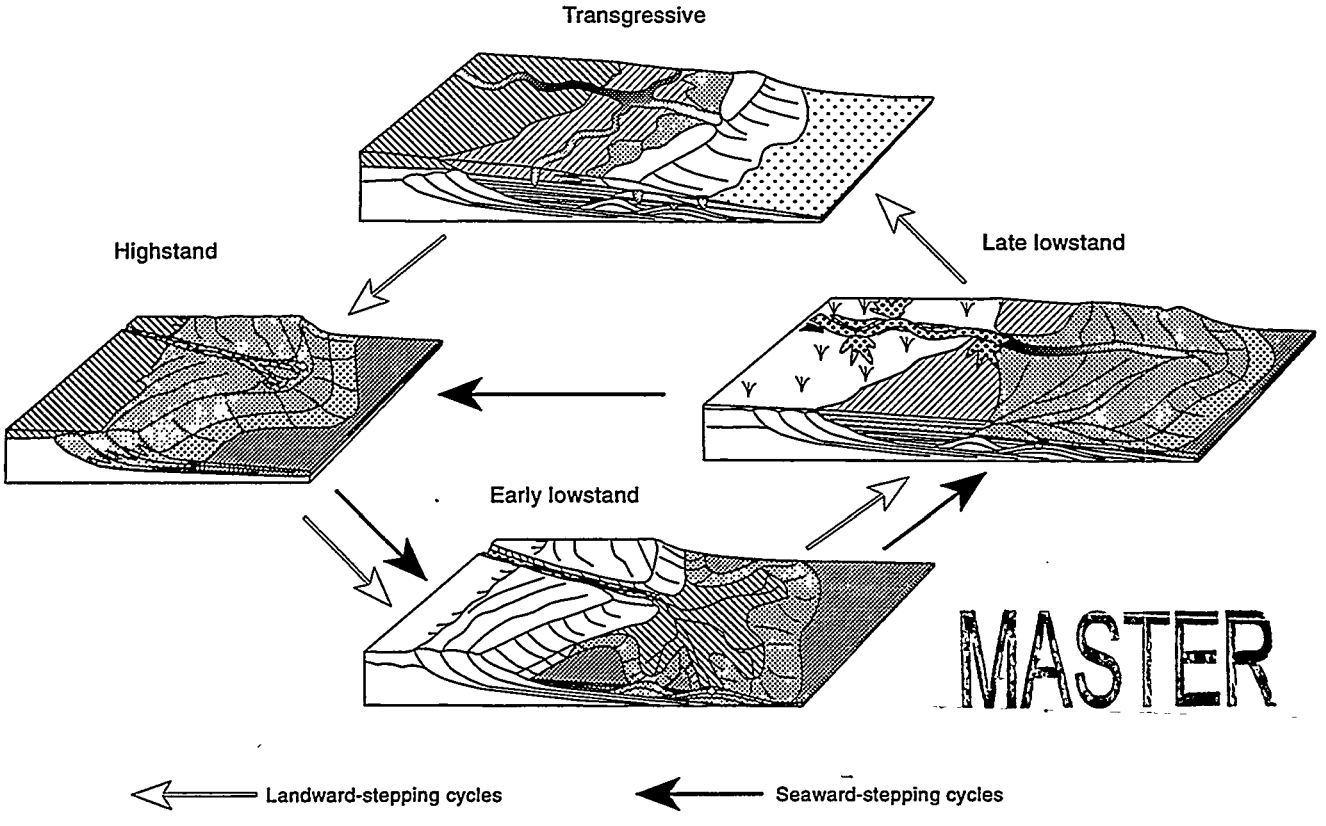

Wyndham Greenspoint Hotel
Houston, Texas • March 2 - 4, 1997

4th International Reservoir Characterization Conference Proceedings

ERRATA SHEET

1. Figure 3 in the paper by Parra, Collier, and Angstman was inadvertently omitted. It is inserted between pages 12 and 13.

2. Pages 699–700 purposely omitted

3. Omit p. 714

4. Omit p. 726

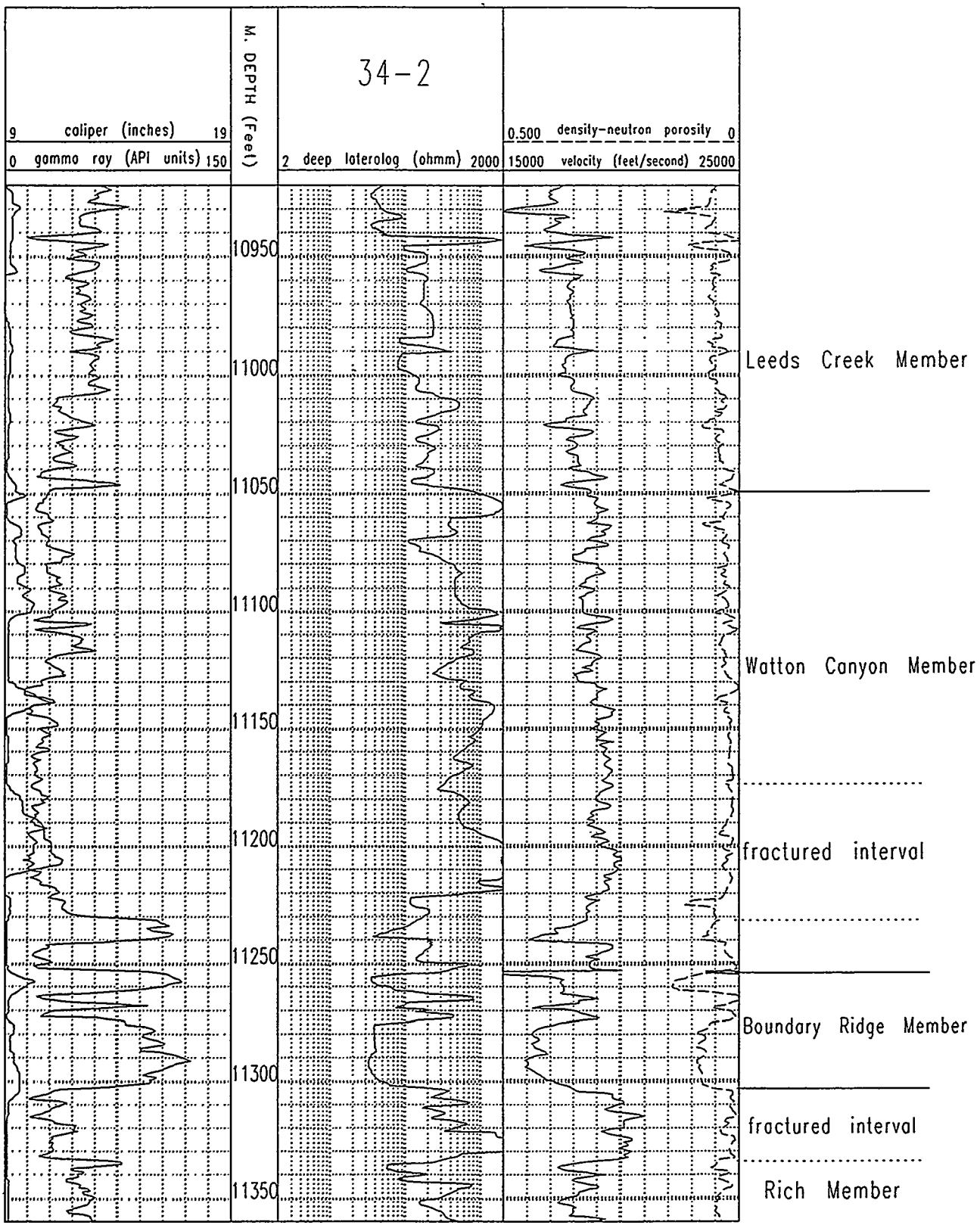

Figure 3. Well log display for well 34-2 Judd including gamma ray, deep lateral log, compressional wave velocity and density-neutron porosity.

CONTENTS

PREFACE

This volume contains the Proceedings of the Fourth International Reservoir Characterization Technical Conference held March 2-4, 1997 at the Wyndham Greenspoint Hotel, Houston, Texas. The Department of Energy Bartlesville Project Office (DOE/BPO), BDM-Oklahoma, Inc., and the American Association of Petroleum Geologists (AAPG) were co-sponsors of the event. The theme for the conference was Advances in Reservoir Characterization for Effective Reservoir Management. Thomas C. Wesson, DOE/BPO, and Thomas E. Burchfield of BDM-Oklahoma, Inc., were Conference Co-Chairmen. The opening address was given by Dr. Olivier Guillon, Deputy Director of Research and Development, Elf Aquaitaine Production. Luncheon speakers included Dr. Mark McElroy, Division Manager of E&P, Phillips Petroleum Company and Dr. Leif Hinderaker, Senior Advisor for Reservoir Technology at the Norwegian Petroleum Directorate (NPD). On Sunday, March 2, 1997, the DOE Class Workshop kicked off with tutorials by Dr. Steve Begg (BP Exploration) and Dr. Ganesh Thakur (Chevron). Tutorial presentations are not included in these Proceedings but may be available from the authors.

The conference consisted of four half-day sessions with each session consisting of 6 presentations and an alternate. Poster sessions were presented on the evenings of Monday, March 3, and Tuesday, March 4. Session Topics and co-chairs were as follows:

Data Acquisition--Co-Chairs: Eve Sprunt, Mobil Oil Corporation, and Jack Caldwell, Geco-Prakla

Reservoir Modeling--Co-Chairs: Robert Finley, Bureau of Economic Geology, and Mohan Kelkar, University of Tulsa

Scaling Reservoir Properties--Co-Chairs: Steve Begg, BP Exploration, and Jerry Jensen, Heriot-Watt University

Managing Uncertainty--Co-Chairs: Michael Fowler, BDM Petroleum Technologies, and Ganesh Thakur, Chevron Petroleum Technology Company

Poster Session--Co-Chairs: Lifu Chu, University of Tulsa, and Dominique Guerillot, IFP

Susan Jackson and Michael Fowler co-chaired the DOE Class Workshop that consisted of six poster and oral sessions. Proceedings of the DOE Class Workshop are available in a separate volume.

We sincerely thank Phillips Petroleum Company for sponsoring the social hour on Sunday, March 2, 1997. Thanks also go to AAPG for their financial assistance with the registration process. A particular thanks goes to Susan Hayden, conference secretary. No conference can be a success without a dedicated Steering Committee. Ours consisted of the following:

Steve Begg
BP Exploration

Tom Burchfield
BDM-Oklahoma, Inc.

Jack Caldwell
Geco-Prakla

Lifu Chu
University of Tulsa

Robert Finley
Bureau of Economic Geology, University of Texas

Dominique Guerillot
IFP

Neil Humphreys
Mobil Oil Corporation

Susan Jackson
BDM-Oklahoma, Inc.

Jerry Jensen
Heriot-Watt University

Mohan Kelkar
University of Tulsa

Bob Lemmon
DOE/BPO

Charles Mankin
Oklahoma Geological Survey

Yi Nan Qiu
RIPED

Rick Schatzinger
BDM Petroleum Technologies

Eve Sprunt
Mobil Oil Corporation

Ray Sulak
Phillips Petroleum Company

Ganesh Thakur
Chevron Petroleum Technology Company

Min Tham
BDM-Oklahoma, Inc.

Lynn Watney
Kansas Geological Survey

Paul Worthington
Gaffney, Cline & Associates

David Zornes
Phillips Petroleum Company

Rick Schatzinger
Steering Committee Chairman
BDM Petroleum Technologies

Seismic Signatures of the Lodgepole Fractured Reservoir in Utah-Wyoming Overthrust Belt

by

Jorge Parra, Southwest Research Institute
Hughbert Collier, Tarleton University
Burke Angstman, Union Pacific Resource

ABSTRACT

In low porosity, low permeability zones, natural fractures are the primary source of permeability which affect both production and injection of fluids. The open fractures do not contribute much to porosity, but they provide an increased drainage network to any porosity. An important approach to characterizing the fracture orientation and fracture permeability of reservoir formations is one based upon the effects of such conditions on the propagation of acoustic and seismic waves in the rock.

We present the feasibility of using seismic measurement techniques to map the fracture zones between wells spaced 2400 ft at depths of about 1000 ft. For this purpose we constructed computer models (which include azimuthal anisotropy) using Lodgepole reservoir parameters to predict seismic signatures recorded at the borehole scale, crosswell scale, and 3D seismic scale. We have integrated well logs with existing 2D surfaces seismic to produce petrophysical and geological cross sections to determine the reservoir parameters and geometry for the computer models. In particular, the model responses are used to evaluate if surface seismic and crosswell seismic measurements can capture the anisotropy due to vertical fractures. Preliminary results suggested that seismic waves transmitted between two wells will propagate in carbonate fracture reservoirs, and the signal can be received above the noise level at the distance of 2400 ft. In addition, the large velocities contrast

between the main fracture zone and the underlying unfractured Boundary Ridge Member, suggested that borehole reflection imaging may be appropriate to map the fracture zone thickness variation and fracture distributions in the reservoir.

Introduction

Lodgepole field is the southernmost in a series of oilfields in the Overthrust Belt of southwestern Wyoming and neighboring Utah producing from the Jurassic Twin creek Formation. Union Pacific Resources (UPRC) has three fields in the play in Summit County, Utah: Lodgepole, Elkhorn, and Pineview. These three fields are shown in the overthrust field map of Utah and Wyoming in Figure 1.

Six horizontal and twelve vertical boreholes have been drilled in Lodgepole field. The field has produced 1,132 MBO. It is a depletion drive reservoir, but most of the wells have significant water production. The well location map (see Figure 2) shows the vertical and horizontal well paths. In particular, the map is showing the horizontal well path for the 34-1H Judd well and the seismic line CREA-25k that is used in the integration analysis.

Lodgepole was selected as the type field for this study because:

1. UPRC is continuing to drill horizontal wells in the field and they are interested in further characterizing the field.
2. An extensive database is available.
    a. Over 20 2D seismic lines are available. The lines are both parallel and perpendicular to the fracture orientation.
    b. UPRC recently ran a 4D seismic survey southwest of Lodgepole field. A small part of the survey overlaps the southwest edge of Lodgepole.

c. UPRC conducted an outcrop study of the fracture orientation in the Twin Creek formation.

d. Resistivity density, neutron, sonic, caliper, and gamma ray logs are available for almost all the vertical wells. As an example Figure 3 shows a suite of logs from vertical well 34-2. MWD gamma ray logs are available for every horizontal well and formation microscanner (FMS) logs have been run in three of them (35-2H, 4-2H and 34-1H).

e. A velocity survey and synthetic seismogram are available for the 35-1.

f. Cuttings are available for most wells, but no cores were taken in the field.

Stratigraphy

The Twin Creek Formation is approximately 1,500 feet thick in Lodgepole Field and is divided into seven members. The following descriptions of each member, beginning with the basal member, are taken from Bruce (1988):

Gypsum Springs. Approximately 50 feet of sabkha evaporites, red beds, and minor carbonates. In most places it serves as a barrier to hydrocarbon migration between the underlying Nugget Formation and the Twin Creek. Note: some workers given the Gypsum Springs formation status.

Sliderock. Approximately 90 feet of micritic limestone with thin beds of oolitic grainstone and thin shaly zones. No primary porosity has been preserved, but calcite-filled fractures are present.

Rich. Approximately 250 feet of argillaceous limestone that cleans upward. The upper 20 to 50 feet has some intergranular porosity and may be dolomitized.

Boundary Ridge. Approximately 50 feet of red siltstones and claystones with a sabkha character. It serves as a good marker bed in the Twin Creek Formation.

Watton Canyon. Approximately 250 feet of limestone with thin, tightly cemented oolitic zones. The limestones of the Watton Canyon are thinner bedded and more terrigeneous than the Rich Member.

Leeds Creek. Approximately 300 feet of interbedded argillaceous and relatively clean limestones. A highly radioactive unit near the top of the member is devitrified tuff.

Giraffe creek. Approximately 450 feet of micritic and oolitic carbonates. It becomes sandy toward the top.

The Twin Creek Formation represents a major marine transgression over the underlying Nugget Formation, which is eolain sandstones. The Nugget is one of the primary hydrocarbon producing reservoirs in the Overthrust Belt.

The Basan Preuss Silt, a 30 to 100 foot interval of tightly cemented quartz siltstone, overlies the Twin Creek Formation. The Preuss Salt overlies the siltstone. It varies from 20 to 300 feet in thickness.

Geologic Controls on Hydrocarbon Production

Virtually all the effective porosity in the Twin Creek Formation is from fractures. Existing vertical production comes from five members of the Twin Creek. The Gypsum Springs and Giraffe creek Members do not produce and production from the Leeds Creek Member has been limited. However, horizontal wells produce from fractured intervals in only the Rich and Watton Canyon members. In the Rich the upper 30 feet is the fractured interval.

The Watton Canyon is the most prolific hydrocarbon-producing member of the Twin Creek and it is also the most intensely fractured. The clean, shale-free section approximately 100 feet thick in the lower part of the Watton Canyon contains fractures. The main fractured zone is the lower 30-50 feet of this clean interval. An interval approximately 20 feet thick near the base of the Watton canyon is the primary target for most of UPRC's horizontal wells, including the 34-1H in Section 34.

Based on outcrop studies, FMS logs, and production data, the fractures run NW-SE. Fracturing was produced by faulting and tight folding of the hanging wall of the Absaroka Thrust sheet (Bruce, 1988). The Gypsum Springs Member served as a detachment surface between the Nugget and Twin creek in the thrusting process. The trapping mechanisms is structural closure on asymmetrical anticlines in the hanging wall. The geometry of the Watton canyon member of the Twin Creek Formation is given by the structural map and the structural cross-section shown in Figures 4 and 5.

Study Area

Lodgepole field extends over six sections. Section 34 in the center of the field was chosen as the initial study area for this project. The section contains three vertical and two horizontal well, with all of the data types listed above.

Structural cross sections were constructed with the logs from the vertical wells in Section 34. The cross sections center on the Watton Canyon and Boundary Ridge Members, which contain the fractured intervals in the Twin Creek Formation. The cross sections include the acoustic velocity, bulk density, gamma ray, and caliper curves. These cross-sections are given in Figures 6 and 7.

In the fractured interval within the Watton Canyon sonic velocity ranges from 18,500-20,000 feet/second and bulk density ranges from 2.6 to 2.75 g/cm^3. The upper boundary does not appear

to have a significant change in sonic velocity and the lower boundary is a shale with a sonic velocity of 16,000-17,000 feet/second.

For most of the fractured interval in the Rich, sonic velocities range from 18,800 to 21,000 feet/second and bulk density ranges from 2.65 to 2.8 g/cm^3. The interval is bounded above by a shale with a sonic velocity of 16,000 feet/second and below by a shaly limestone with a velocity of approximately 18,000 feet/second. The fractured interval is relatively clean (i.e. shale-free). The upper 15 feet of the fractured interval appears to be dolomite, which accounts for the corresponding higher bulk densities and may also explain, at least in part, the higher sonic velocities. The fractured interval in the Rich has ore shale than the fractured interval in the Watton Canyon.

Future Petrophysical Analysis

A petrophysical analysis of the logs and a petrographic analysis of the cuttings in selected wells in Section 34 will be conducted in order to ascertain the factors controlling horizontal and vertical distribution of fractures, relationships between petrophysical properties an fracture density and distribution, and the extent to which matrix porosity contributes to hydrocarbon production. Lateral fracture distribution is being quantified with the FMS log of horizontal well 34-1H. Petrographic analysis of the cuttings from the same well are being analyzed in order to ascertain the factors controlling fracture distribution. These data will be correlated with lateral variations observed on the 2D seismic lines.

Preliminary Integration of Seismic and Well Log Data

The seismic line CREA-25k was selected because follow the horizontal path of well 34-1H Judd. This well and well 34-2 are plotted in the migrated seismic section given in Figure 6. A synthetic seismogram was produced using the compressional wave velocity log and the density log

from well 34-2. The synthetic was superimposed on the migrated seismic line together with the geological boundaries defined by the well logs in Figure 7. Both Figures 6 and 7 show the horizontal path of well 34-1H in the Watton Canyon intercepting the fractured zone define in cross-section shown in Figure 3. The Watton Canyon is the most important geological unit which upper and lower boundaries correlate with the sonic, density and gamma logs, and seismic events in the seismic section of Figures 6 and 7. In fact, the synthetic seismogram fit reasonably well at the well position 34-1H Judd in " time-depth" on the seismic section. For example the top of the Watton Canyon is at 1600 ms and the top of the Rich Member is at 1640 ms.

In general the petrophysical boundaries defined by the well logs correlate with the seismic events in the seismic section. The seismic signatures associated with the Watton Canyon suggests lateral velocity changes between wells 34-1H and 34-2. There is an small change in thickness of the Watton Canyon up to about 27 traces from well 34-2 to well 34-1H. Following this event a different signature having similar characteristics is observed below the horizontal path which is approaching the vertical position of well 34-2. This event is associated the petrophysical characteristics of the Rich Member in the region below the Watton Canyon .

The fractured zones are located in the bottom part of the Watton Canyon Member and in the top of the Rich Member, where these fractured zones are intercepted by well 34-2. Both fractured zones are associated with low gamma ray counts. The top fractured zone in the Watton Canyon is separated from the bottom fractured zone by the a 50-foot Boundary Ridge Member formed by siltstones and claystones. A reflection event associated with this boundary is observed in the seismic sections of Figures 6 and 7 and is below the horizontal path of well 34-1H. This analysis suggests that the Watton Canyon in the region between both wells under consideration are associates with the

"trough"- reflection response ,which may be caused by the presence of the fractured zone containing vertical fractures. This fractured zone is intercepted by the horizontal well in the bottom part of the Watton Canyon. The FMS logs recorded in the horizontal well intercepted vertical fractures having a variable fracture density distribution.

Computer Models

In order to confirm the above interpretation , computer models will be produced for the geological units intercepted by well 34-2 and the fracture zones of interest. The fractures will be modeled assuming the axis of anisotropy perpendicular to the fractures. Synthetic seismograms will be produced considering the geometry of the formations and the rock physical properties determined from well logs. As a comparison synthetic seismograms will be produced for a model containing only the geological boundaries without the fractures. This modeling effort will determine if fractures zones can be detect using surface seismic in the Lodgepole field. This will be done by comparing both synthetic seismograms with the observed migrated seismic data.

In addition the fractured model based on the above geometry will be used to calculate synthetic interwell seismic response by assuming a seismic source in well 34-1H and three-component detectors in well 34-2. This modeling effort will determine the feasibility of transmitting and detecting interwell seismic waves in the Lodgepole formation. Also we will determine if fractures or fracture zones can be delineated using interwell seismic methods. In particular, we expect that small target zones can be image by using cross well methods of measurements. Several models will be produced to analyze the seismic signature characteristics associated with the vertical fractures that will be modeled assuming azimuthal anisotropy. To analyze the seismic waves time-frequency will be applied to the data to separate signatures of fractured zone from others associated with the different

geological units. This seismic analysis will be applied to the observed and calculated surface seismic data as well.

Conclusions

Correlation between the lithology and the well logs and the migrated seismic data from Lodgepole field served to identify seismic events associated with geological units of interest. A fractured zone in the Watton Canyon correlates with seismic signatures observed in the seismic section. Computer models including the fracture zones are proposed to confirm the qualitative interpretation at the Lodgepole field. In addition, computer models will be produced to determine the feasibility of detecting fracture zones using interwell seismic measurement techniques between wells at the Lodgepole field.

References

Bruce, C.L., 1988, Jurassic Twin Creek Formation: a fractured limestone reservoir in the Overthrust Belt, Wyoming and Utah: Rocky Mountain Association of Geologists, pp. 105-120.

Parra, J.O., 1995, A feasibility study of high-resolution reverse VSP and interwell seismic methods for hydrocarbon reservoir characterization: The Log Analysts, May-June, pp. 64-81.

Parra, J.O., Zook, B.J., and Collier, H.A., 1996, Interwell seismic logging for formation continuity at the Gypsy test site, Oklahoma: Journal of Applied Geophysics. v. 35, pp. 45-62.

Parra, J.O., 1996, Characterization of fracture reservoirs using static and dynamic data: from sonic and 3D seismic to permeability distribution: September Quarterly Report, U.S. Department of Energy, Contract No. DE-AC22-94PCp1008; SwRI Project 15-7939.

Captions

Figure 1. Regional map showing location of Overthrust Field.

Figure 2. Location map showing horizontal well path for the 35-1H Judd and seismic line CREA-25k.

Figure 3. Well log display for well 34-2 Judd including gamma ray, deep lateral log, compressional wave velocity and density-neutron porosity.

Figure 4. Structural map on top of Watton Canyon member of the Twin Creek Formation.

Figure 5. Structural cross-section along traverse AA'.

Figure 6. A structural cross-section through the Wells 34-2 and 34-1 at the Lodgepole field.

Figure 7. A structural cross-section through the wells 34-2 and 34-3 at the Lodgepole field.

Figure 8. Migrated seismic section CREA-25k along horizontal well path of well 34-1H Judd.

Figure 9. Migrated seismic section CREA-25k of Figure 8 with synthetic seismogram inserted at well location 34-2 Judd.

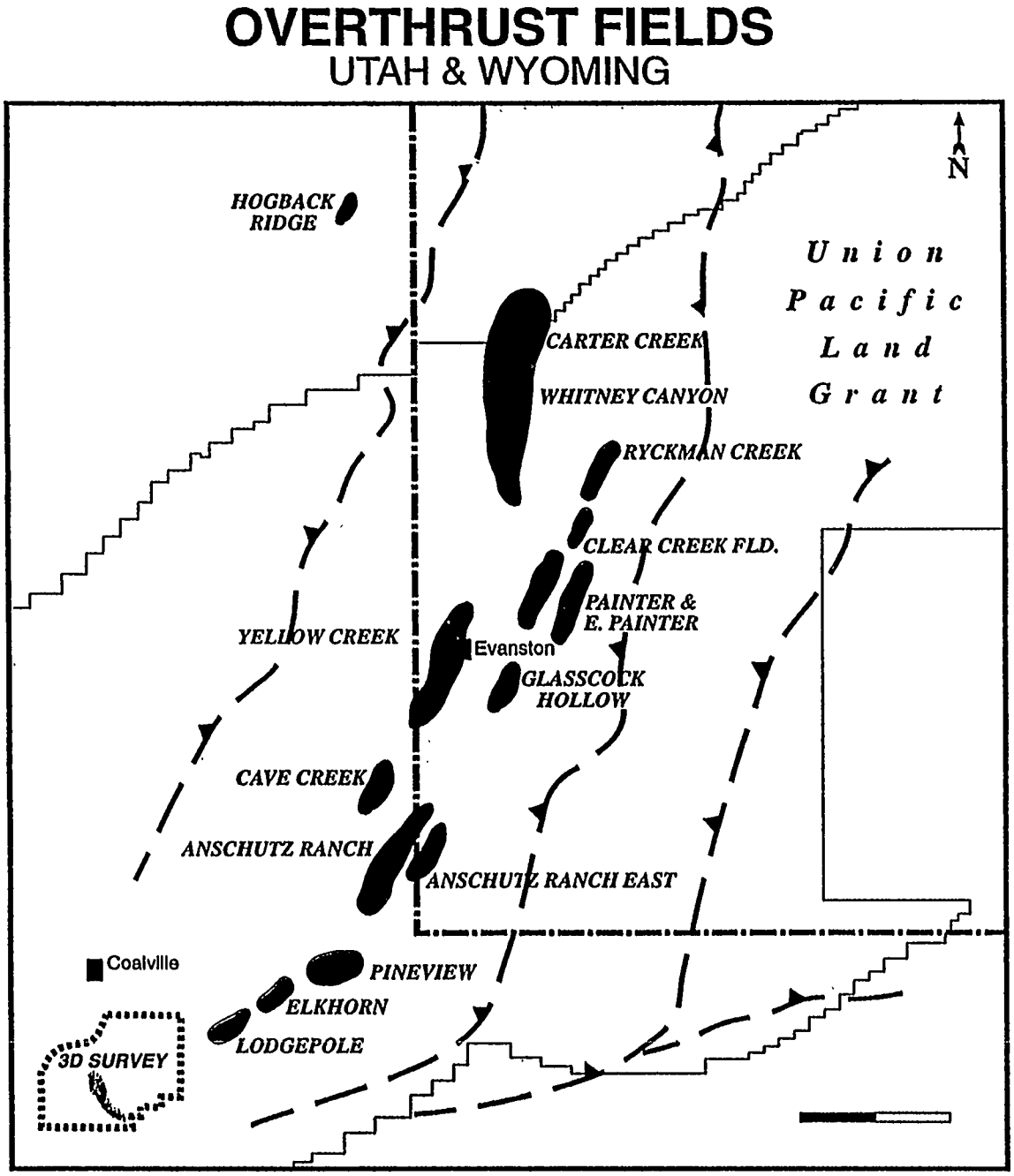

Figure 1. Regional map showing location of Overthrust Field.

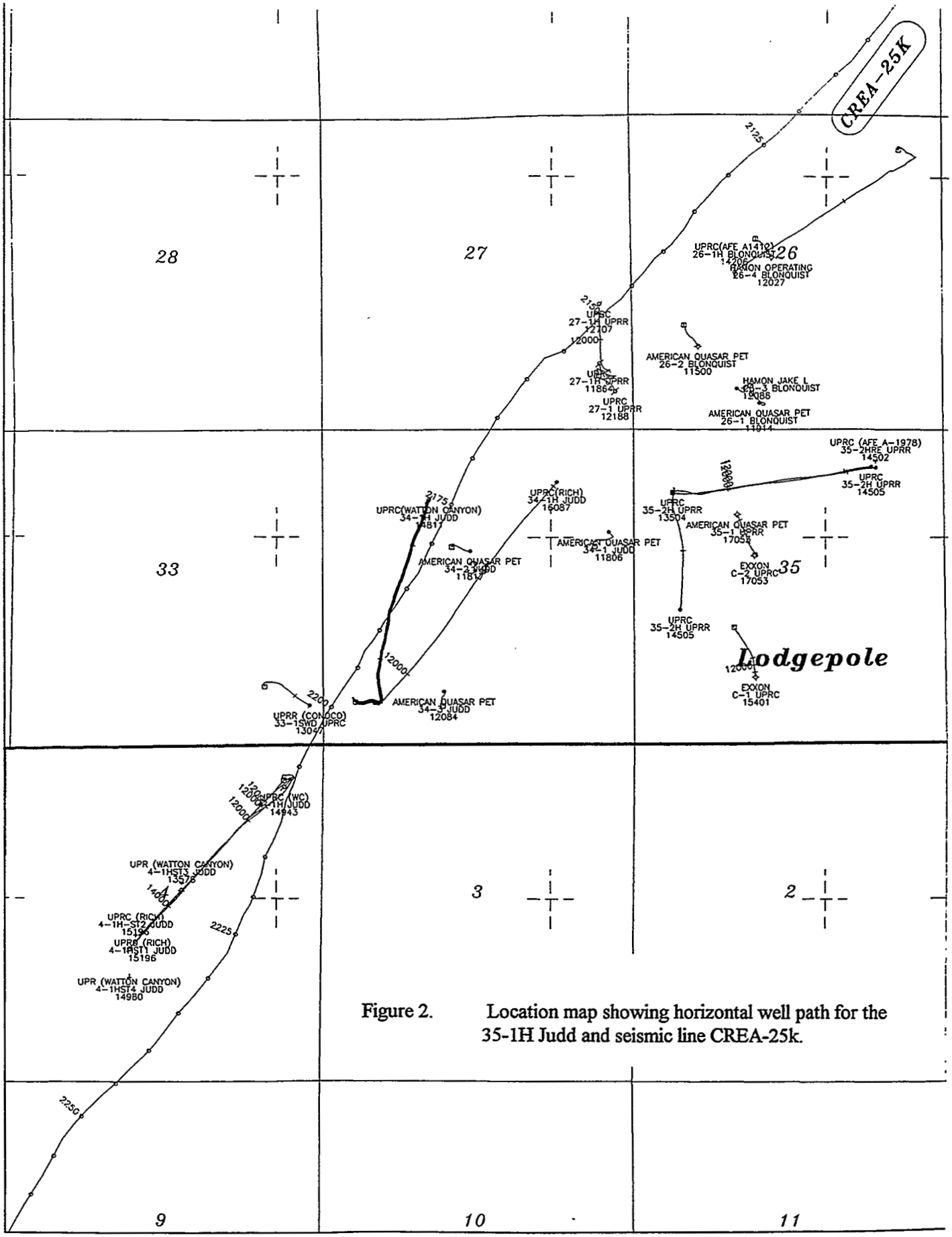

Figure 2. Location map showing horizontal well path for the 35-1H Judd and seismic line CREA-25k.

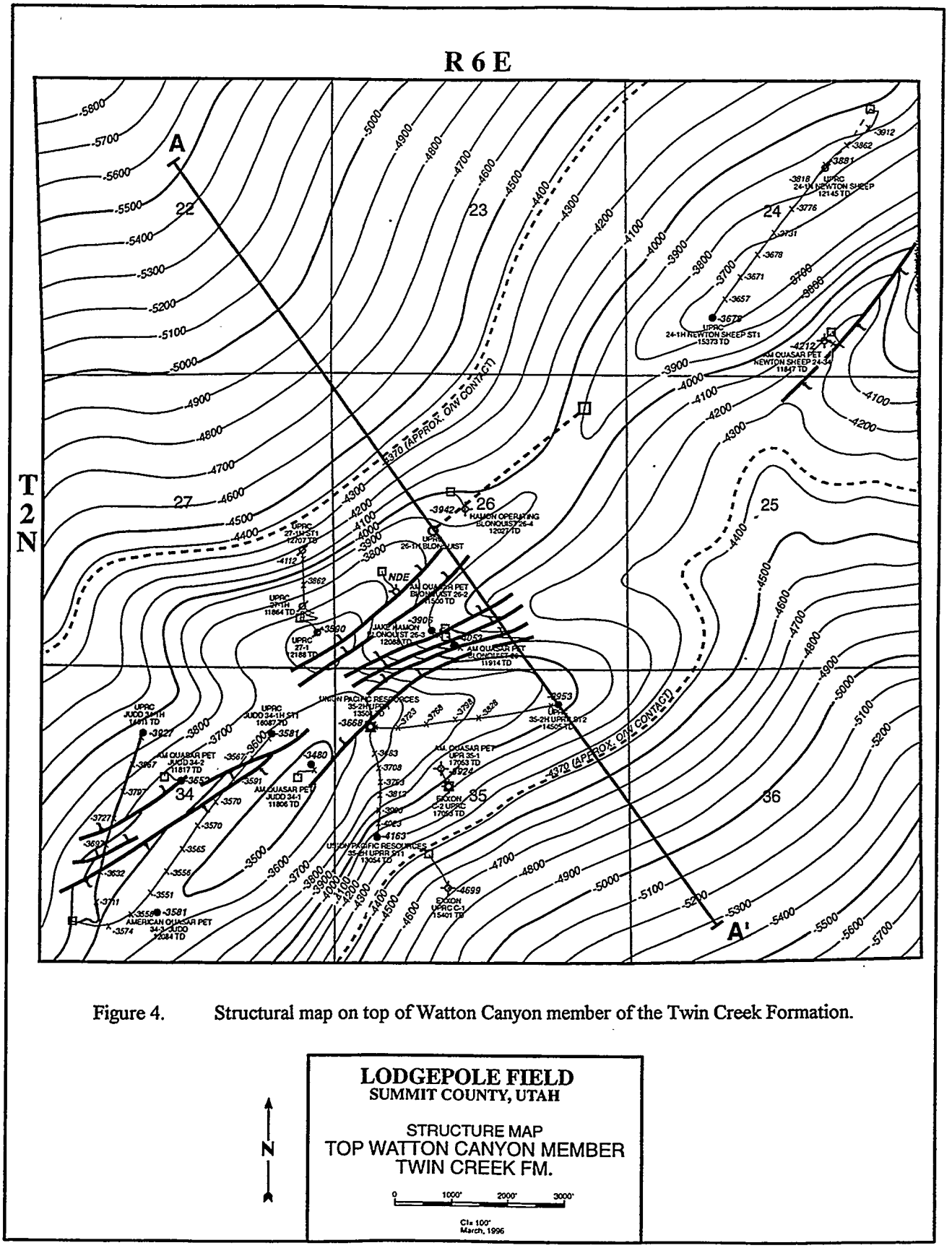

Figure 4. Structural map on top of Watton Canyon member of the Twin Creek Formation.

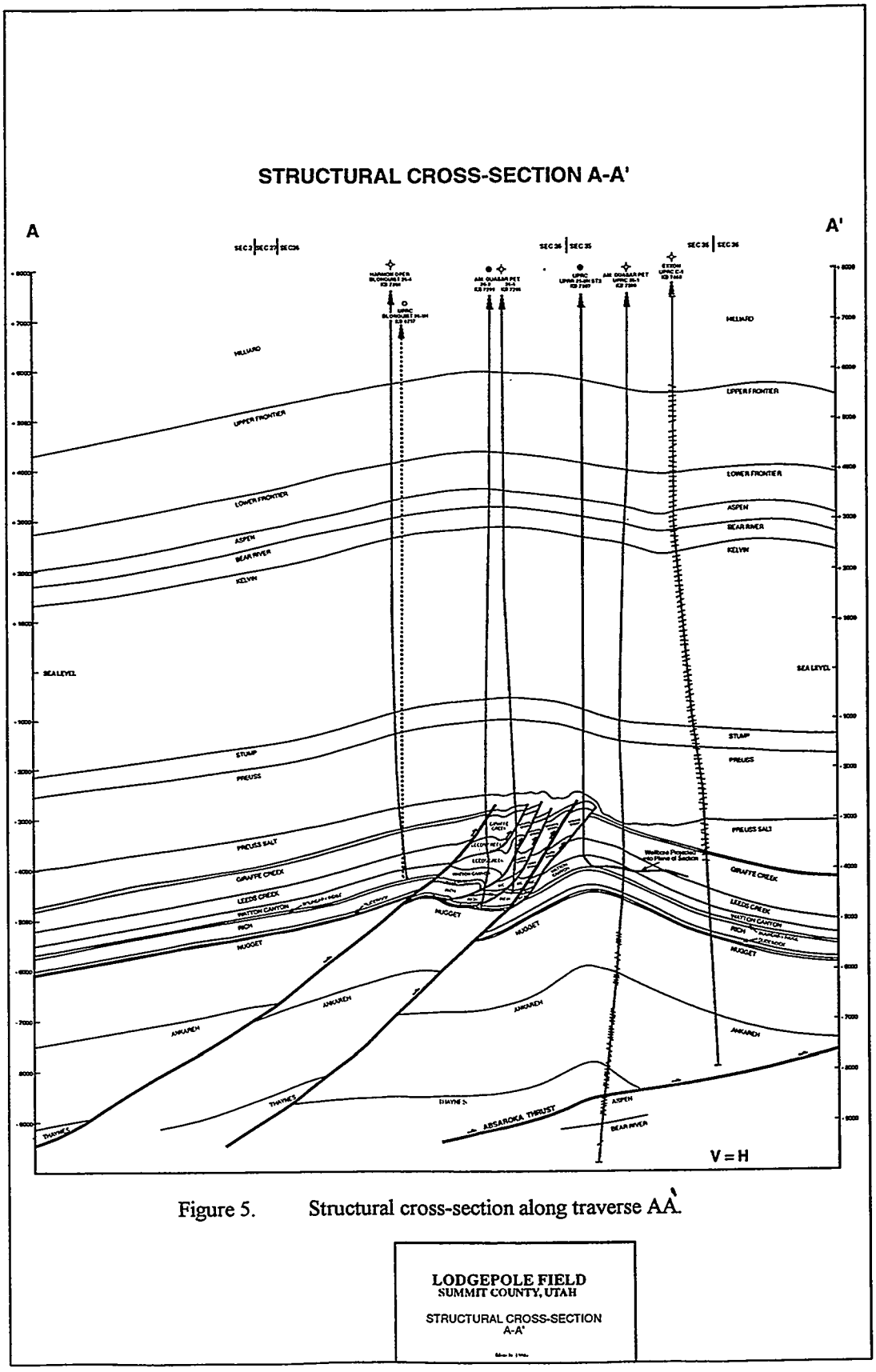

Figure 5. Structural cross-section along traverse AA'.

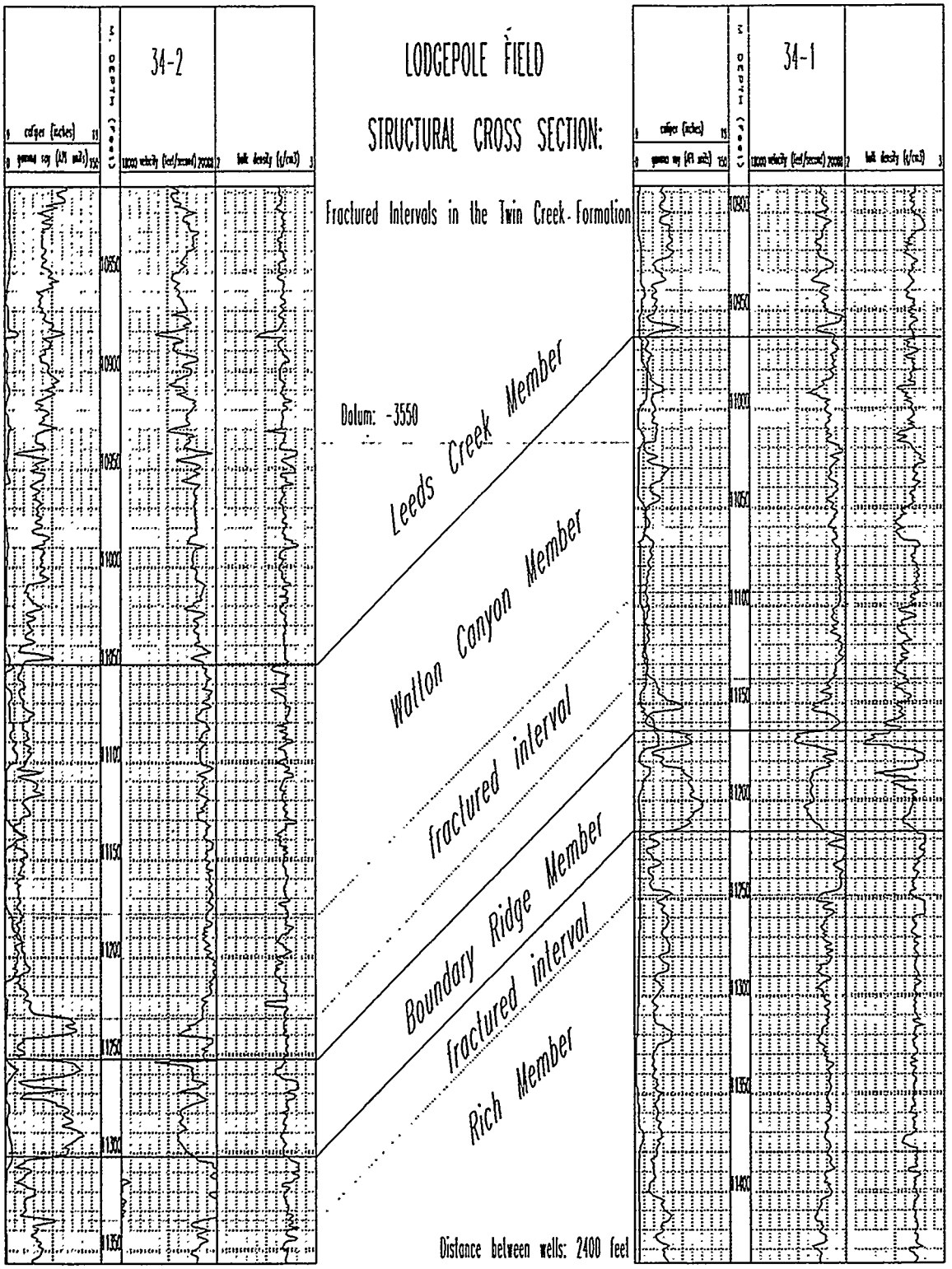

Figure 6. A structural cross-section through the Wells 34-2 and 34-1 at the Lodgepole field.

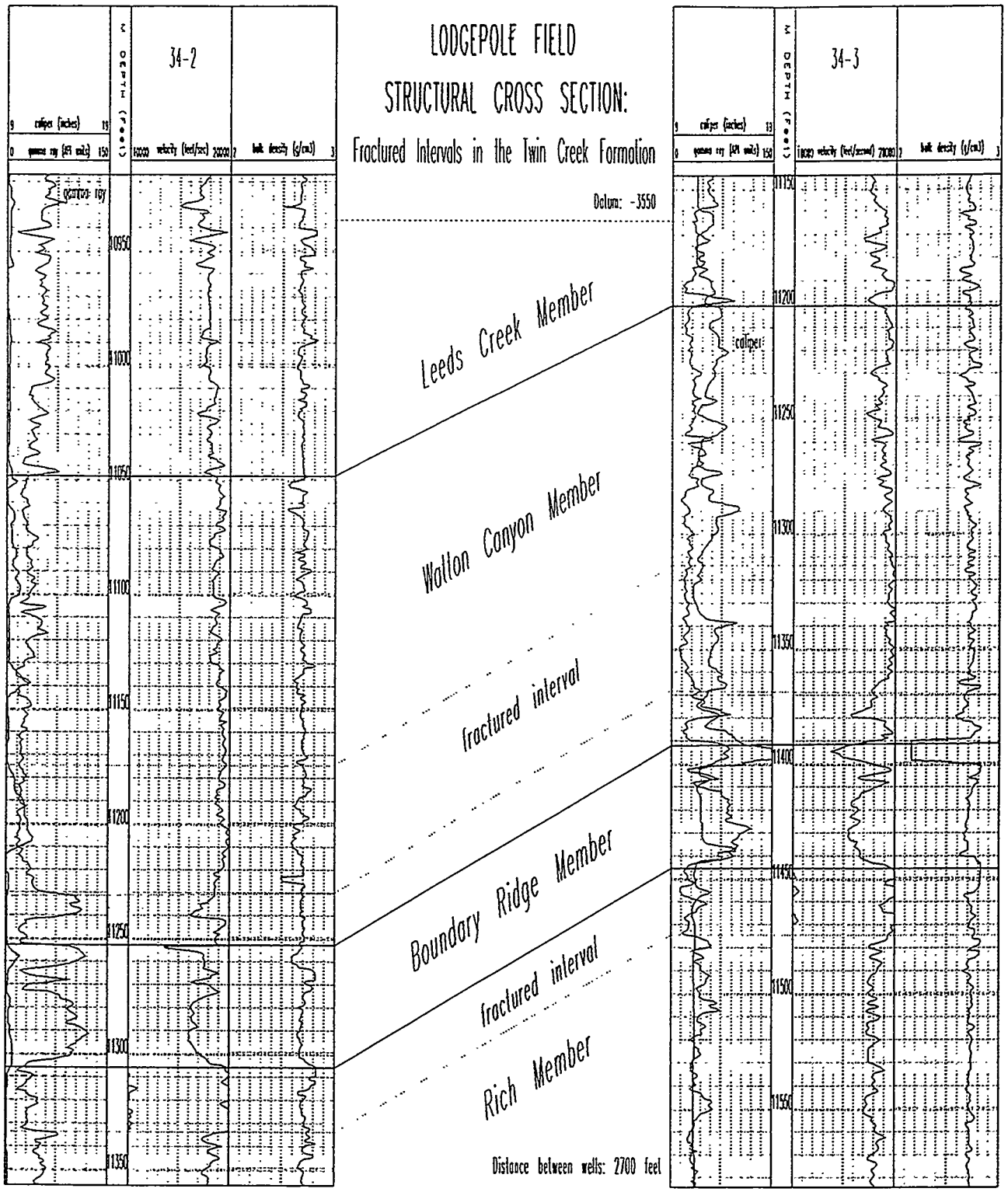

Figure 7. A structural cross-section through the wells 34-2 and 34-3 at the Lodgepole field.

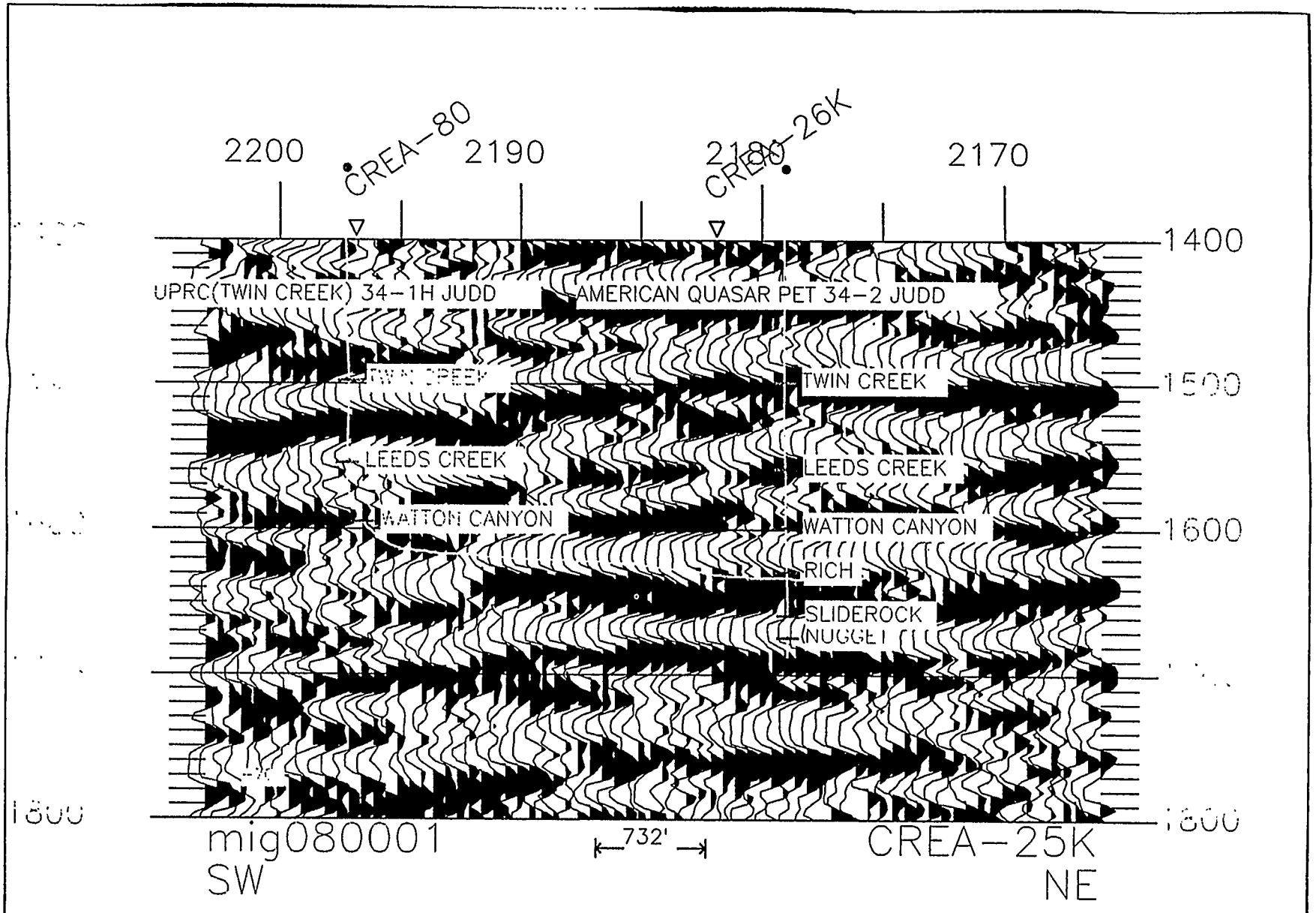

Figure 8. Migrated seismic section CREA-25k along horizontal well path of well 34-1H Judd.

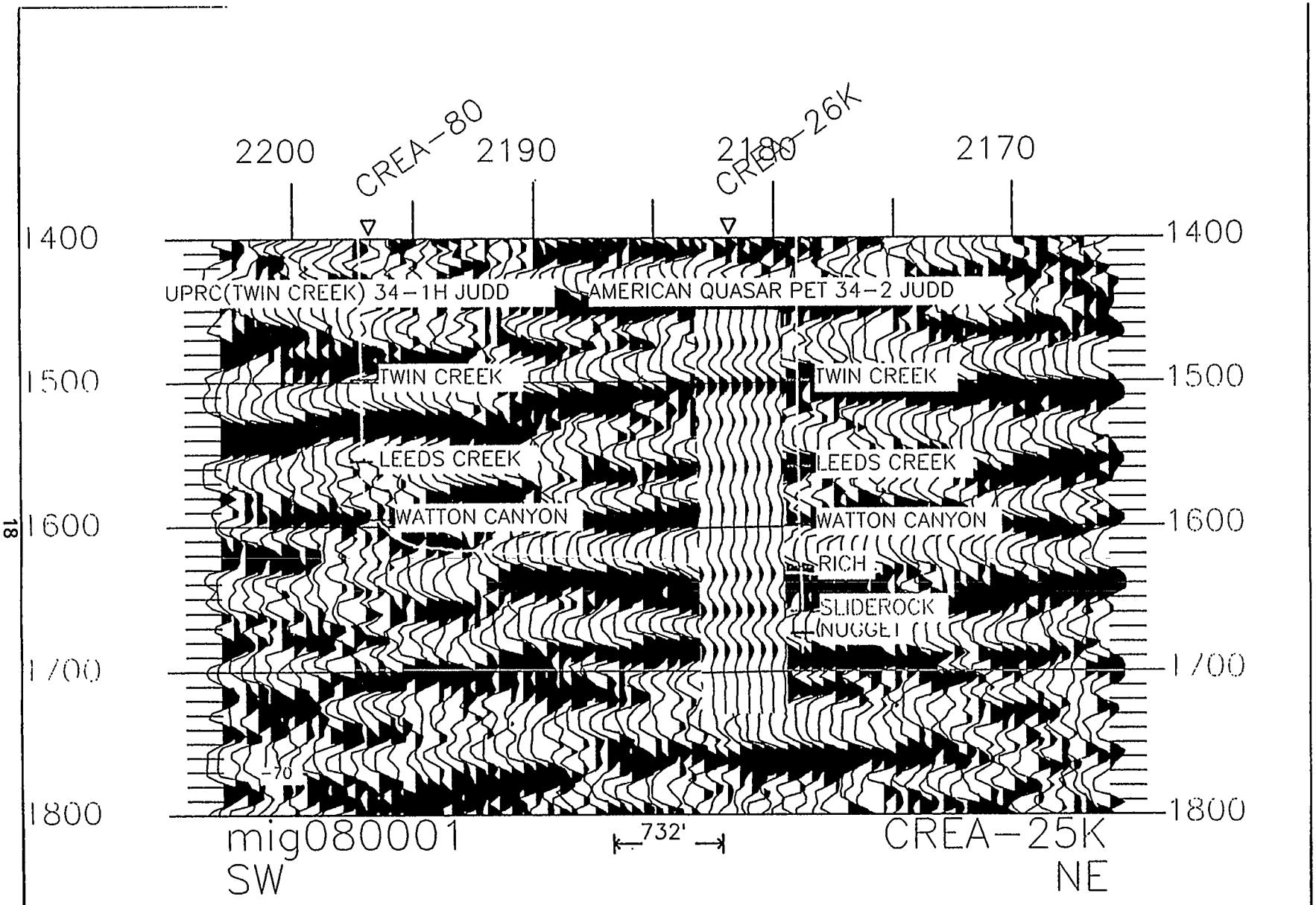

Figure 9. Migrated seismic section CREA-25k of Figure 8 with synthetic seismogram inserted at well location 34-2 Judd.

Putting Integrated Reservoir Characterization into Practice — In House Training

Dr. F. M. Wright, Jr., D. A. Best; R. T. Clarke
Mobile Exploration and Producing Technical Center
P.O. Box 819047
Dallas, TX 75381

ABSTRACT

The need for even more efficient reservoir characterization and management has forced a change in the way Mobil Oil provides technical support to its production operations. We've learned that to be successful, a good understanding of the reservoir is essential. This includes an understanding of the **technical** and **business** significance of reservoir heterogeneities at different stages of field development. A multi-disciplinary understanding of the business of integrated reservoir characterization is essential and to facilitate this understanding, Mobil has developed a highly successful "Reservoir Characterization Field Seminar". Through specific team based case studies that incorporate outcrop examples and data the program provides participants the opportunity to explore historic and alternative approaches to reservoir description, characterization and management. We explore appropriate levels and timing of data gathering, technology applications, risk assessment and management practices at different stages of field development. The case studies presented throughout the course are a unique element of the program which combine real life and hypothetical problem sets that explore how different technical disciplines interact, the approaches to a problem solving they use, the assumptions and uncertainties contained in their contributions and the impact those conclusions may have on other disciplines involved in the overall reservoir management process. The team building aspect of the course was an added bonus.

Study on Detailed Geological Modelling for Fluvial Sandstone Reservoir in Daqing Oil field

Zhao Hanqing; Fu Zhiguo; Lu Xiaoguang
Institute of Petroleum Exploration and Development
Daqing, China 163712

ABSTRACT

Guided by the sedimentation theory and knowledge of modern and ancient fluvial deposition and utilizing the abundant information of sedimentary series, microfacies type and petrophysical parameters from well logging curves of close spaced thousands of wells located in a large area. A new method for establishing detailed sedimentation and permeability distribution models for fluvial reservoirs have been developed successfully. This study aimed at the geometry and internal architecture of sandbodies, in accordance to their hierarchical levels of heterogeneity and building up sedimentation and permeability distribution models of fluvial reservoirs, describing the reservoir heterogeneity on the light of the river sedimentary rules. The results and methods obtained in outcrop and modern sedimentation studies have successfully supported the study.

Taking advantage of this method, the major producing layers (PI_{1-2}), which have been considered as heterogeneous and thick fluvial reservoirs extending widely in lateral are researched in detail. These layers are subdivided into single sedimentary units vertically and the microfacies are identified horizontally. Furthermore, a complex system is recognized according to their hierarchical levels from large to small, meander belt, single channel sandbody, meander scroll, point bar, and lateral accretion bodies of point bar.

The achieved results improved the description of areal distribution of point bar sandbodies, provide an accurate and detailed framework model for establishing high resolution predicting model. By using geostatistic technique, it also plays an important role in searching for enriched zone of residual oil distribution.

Application of Fractal Theory in Refined Reservoir Description for EOR Pilot Area

Yue Li Xin Jiang Petroleum Institute , P.R. China , Yonggang Duan and Yun Li
Southwest Petroleum Institute . P.R. China , Yuan Lu Xin Jiang Petroleum Institute , P.R. China

Acknowledgments

I would like to thank Xin jiang petroleum exportation and development research institute to support this project. I would also like to thank Dr. Di Jiao and yi-li Kang for exchanging idea to writing this paper.

Abstract

A reliable reservoir description is essential to investigate scenarios for successful EOR pilot test. Reservoir characterization includes formation composition, permeability, porosity, reservoir fluids and other petrophysical parameters. In this study, various new tools have been applied to characterize Kilamayi conglomerate formation. This paper examines the merits of various statistical methods for recognizing rock property correlation in vertical columns and gives out methods to determine fractal dimension including R/S analysis and power spectral analysis. The paper also demonstrates that there is obvious fractal characteristics in conglomerate reservoirs of Kilamayi oil fields . Well log data in EOR pilot area are used to get distribution profile of parameters including permeability, porosity, water saturation and shale content .

Introduction

Three dimensions geologic modeling of a reservoir requires the ability to detect the short and long range correlation of properties. Fractal provide a method for implementation of specific conceptual models to address the problem of heterogeneity mapping in geologic structure. While many natural entities have been demonstrated to follow fractal models, the universal application to all phenomena has not been established yet[1] . Efforts have been underway to synthesize various observations related to geologic system and to examine the applicability of fractal models[2],[3].

As pointed out by Hewett[1] , because of the inverse relationship between the variance and the lag , the R/S methodology is the best suited to long-range correlation estimation . As shown by Mandelbrot[4], fractal dimension D is related to Hurst exponent by D=2-H for fBM signals. Many studies have been published describing porosity well logs as fGn[5][6][7][8] . All of these authors used the R/S analysis, and several used many more of the tools. The discovery that well logs often have a fGn character was made by Hewett[1] He reported an H value of 0.855 . Aasum et al [8] analyzed 18 wells from a single unit. They used both R/S and variogram analysis . They found fGn with H varying between 0.70 and 0.94 for logs of both porosity and

the logarithm of permeability . Crane and Tubman [6] analyzed three horizontal wells and four vertical wells in a carbonate formation . They found all the logs to be fGn. H ranges between 0.88 and 0.89 for the vertical wells and between 0.85 and 0.93 for the horizontal wells . Taggart[7] analyzed a well from the Bowen/Surat Basin, a well from the Hutton Sandstone in the Jackson Field, and two wells from in Windalia Sandstone, Barrow Island. He found H values of 0.82, 0.82, and 0.8 .

This paper will review some of the important results of the statistical theories of reservoir properties and discuss their implications for modeling the influence of reservoir heterogeneity. Thirteen vertical wells are analyzed , the properties of fractal distributions is shown in conglomerate reservoirs at first time . This paper also gives out a fractal interpolation method for both internals and for the plane . Fractal distribution of reservoir heterogeneity can be gained from EOR pilot area in Kilamayi oil field .

Basic Characterization of EOR Pilot Area

EOR pilot wellblock located Er Zhong area on north of Ki~Wu structure and south of north black oil mountain, distance from this area to Kilamayi is about ten kilometers(Fig .1). EOR pilot area has four units with five-spot well pattern and , total well number is 13 including 9 producer wells and 4 injection wells. Well spacing from injection to producer is 50 meters.

Well depth in this area is from 599 to 678 meters. Total thickness of the formation is about 65 meters, and glutenite thickness of pay zones is about 20 meters. The formation form bottom to top divided into five layers , that is s_7^4 , s_7^3 , s_7^2 , s_7^1 and s_6^4, s_7^4 , s_7^3 and s_7^2 are main production layers . In the study, main work targets are s_7^4 , s_7^3 layers in EOR pilot area .

The effective permeability of glutenite zone is average ($150\sim450\times10^{-3}\mu m^2$) (Table1), and the average effective porosity is 17%~21% . Permeability between wells is from $100\sim3000\times10^{-3}\mu m^2$. Table 1 shows that heotergenous distribution of permeability is serious and complicated .

Since formation conditions are very complicated, reservoir engineers can not exactly describe the physical properties of interwells using traditional geological and statistical method. At present , a better way of disposing random changing of reservoir parameters between wells is by fractal geometry method .

Methodologies

Details about the correlation methods examined in this studies are well documented in the literature's . The following is a very brief description of the various techniques .

R/S Analysis Method (R/S)

As introduced by Hurst[9] ,[10] and later on improved by Mandelbrot and Wallis[11],[12], the appropriate statistic for evaluating long-range statistical dependence is the rescaled range $R(x,\ell)/S(x,\ell)$, where $R(x,\ell)$ is the cumulated or "graded" range of a process between positions x+1 and $x+\ell$ after removal of the sample average and $S^2(x,\ell)$ is the corresponding sample variance. For any function Z(x) with equal sample spacing normalized to unity, with Zg(x), defined as the graded sequence[1]:

$$Zg(x)= \sum_{u=1}^{x} Z(u) \qquad (1)$$

and given any lag $\ell>1$, $R(x,\ell)$ and $S^2(x,\ell)$ are defined as

$$R(x,\ell)= \mathrm{Max}_{0\le u\le \ell}\{Zg(x+u)-Zg(x)-(u/\ell)[Zg(x+\ell)-Zg(x)]\}$$
$$-\mathrm{Min}_{0\le u\le \ell}\{Zg(x+u)-Zg(x)-(u/\ell)[Zg(x+\ell)-Zg(x)\} \qquad (2)$$

This is the maximum range of deviations of the graded function from its trend over the lag interval . the sample variance is

$$S^2(x,\ell)=1/\ell[\sum_{u=1}^{\ell} Z^2(x+u)]-[^1/_\ell \sum_{u=1}^{\ell} Z(x+u)]^2 \qquad (3)$$

The sequential range of fBM asymptotically obeys an ℓ^H scaling law . For process of fractional Gaussian noise Z(x) , the corresponding Zg(x) is fBM:

$$\lim_{\ell\to\infty}\ell^H R(x,\ell)/S(x,\ell)=\mathrm{Const} \qquad (4)$$

The H coefficient can be obtained from a plot of $R(x,\ell)/S(x,\ell)$ vs. ℓ (Fig.2) .

Power Spectral Density Analysis (PSD)[14]

Applying a Fourier transform of finite samples

$$Z(f,\ell)=1/L\int_0^L z(x)e^{2\pi i f x}dx \qquad (5)$$

Spectral density is defined: $S_Z(f)=L|Z(f,L)|^2$ for large L .

Further , we can express $S_Z(f)=C_H\frac{1}{f\beta}$. From fast Fourier transform we obtain S(f) , and f=(1:N/2)/N . β is obtained from the plot of log Sz~log f . As indicated by Hewett[1] and Barnsley et al [15] , for power law scaling distribution the grading of a sequence raises the β by 2 to β+2 . For an fGn signal β=2H-1 and for fBM signal , β=2H+1. For ideal data sets we can use β to judge the nature of the original

The Fractal Interpolation Method Between Wells in Section

In this paper, are employed to describe fractal distribution of heotergenous parameters between wells. The method shows as follow and in Fig.4 .

The first iterated step of interpolation is:

$$\sigma_1=\sigma_0/2^H \tag{7}$$

$$Z_{1,1}=Z_{1,0}+\sigma_1 \cdot R_{1,1} \tag{8}$$

$$Z_{2,1}=Z_{2,0}+\sigma_1 \cdot R_{2,1} \tag{9}$$

$$Z_{3,1}=[(Z_{1,0}+Z_{2,0})/2]+\sigma_1 \cdot R_{3,1} \tag{10}$$

The second iterated step is :

$$\sigma_2=\sigma_1/2^H \tag{11}$$

$$Z_{1,2}=Z_{1,1}+\sigma_2 \cdot R_{1,2} \tag{12}$$

$$Z_{2,2}=Z_{2,1}+\sigma_2 \cdot R_{2,2} \tag{13}$$

$$Z_{3,2}=Z_{3,1}+\sigma_2 \cdot R_{3,2} \tag{14}$$

$$Z_{4,2}=[(Z_{1,1}+Z_{3,1})/2]+\sigma_2 \cdot R_{4,2} \tag{15}$$

$$Z_{5,2}=[(Z_{2,1}+Z_{3,1})/2]+\sigma_2 \cdot R_{5,2} \tag{16}$$

. . . . . .

repeat above step

where:

$Z_{1,0}$、 $Z_{2,0}$ — the initial iterated values determined by log data ;

H— Hurst exponent , the slope of lnR/S ~ lnτ curve ;

i— section location ;

j— the number of iterated ;

$Z_{i,j}$— well log data in ith location and jth iteration;

σ_0^2— inital variance, obtained by all data point of well log ;

$R_{i,j}$ — a random number of obeying distributions of N(0,1), it must be randomly generated at position of difference and iteration times of difference .

Fractal Interpolation Method for a Unit with Five-spot Well in Plane

Specific operation adopted Pyramid method , as Figure 5 shown , first defined a value of certain number point in the figure, included value of four top point a 、 b 、 c and d , then conducted random factal

interpolation for other point in figure, value of middle point e was defined by a and b, the same as defining value of i point by four points of e、f、g and h, interpolation function follows as describing above, as continue weight interpolation until there are value of all point of having put up grey degree can not conduct interpolation.

Example: Analysis OF Well Log Data

Calculation Hurst Exponent (H)

In geological column, because of sequencing of various lithologies, establishment of long rang correlation requires a composite model incorporating various sections of a particular lithology To test the validity of these methods, a series of numerical experiments are conducted R/S method is used to calculate fractal dimension of single well, well log curves of 13 wells from EOR pilot area in Kalamyi conglomerate reservoirs are collected. Curves include eight kinds of well log, such as AC, DEN, RXO, CAL, CNL, GR, SP. Through comparing and analyzing, we select proximity log curve to calculate Hurst exponent (H). These samples are taken at intervals of 0.125 m from proximity log curve which depth is from 650~680 meters for each well. Figure 1 is shown the behavior of the rescaled range for this sequence, along with a least squares fit of the values for ℓ>20 and a reference line with a slope of 1/2. Clearly, this sequence exhibits long-run interdependence and shows no sign of "breaking" to an $\ell^{1/2}$ behavior for large ℓ. The least square method is used to determine Hurst exponent (H) in the R/S analysis. Table 2 shows that values of Hurst exponent (H) are ranged from 0.8428 to 0.955, average value is 0.8936. Although Hurst exponent is different from 13 wells, difference value for Hurst exponent is not very large. Permeability of EOR pilot area for $s_7^4 \sim s_7^3$ layers forms at the same condition. Table 3 not only shows that pertophyiscal properties and from process of EOR pilot area for $s_7^4 \sim s_7^3$ are the same ,but also changing frequency for well of composition and permeability. The larger value of Hurst exponent, the more serious permeability changing and heotergenous of pay zone.

Selecting and Treating Data for Interwells Profile Distribution

Based on the same reason as calculating Hurst exponent, well log curves are selected. Well log curves must be the same interval and 8 points per meter. Fractal interpolation can be processed between wells. After fractal interpolation of each point between two wells are processed, obtaining new interpolation points will be covered whole well profiles. Fig.5 to Fig.8 show the distributed results of ptrophysical

parameters , these parameters include permeability, porosity, shale content, water saturation. In the Fig 5, fractal interpolation results of permeability in section show that permeability of conglomerate formation distributes characteristic of skip changing compound rhyme.

Selecting and Treating Data for Plane Distribution

Because of selecting pyramid random interpolation methods, every zone of each wells only use one data. Therefore, data must be treated for each layer . The method as follow:

(1) At the first, for well intervals of 650~680 meters, we divided it into four intervals from top to bottom according to s_7^{3-1}, s_7^{3-2}, s_7^{3-3}, s_7^{4-1}.

(2) In each intervals, mean and mean square deviation of corresponding parameters were obtained by arithmetic average method for all well logs interpretation results of this interval .

(3) Hurst exponent , mean and mean square deviation of parameters will be input computer program for selecting mine zones of five wells in plane area and data is shown in table 3. Plane distribution graph of heterogeneous parameters can be carried out for this layer. Fig.9 to Fig 12 shows distributing results of petrophysical parameters. Fig.9 shows that permeability distribution characteristic of fractal interpolation is the same as the well performance analysis results. Fig.5 also shows more detail characteristic of changing permeability than traditional geology analysis methods.

Conclusion

1. The self-similar statistics of random fractal provide a good tool for reservoir property distributions.

2. Through R/S method , this sequence exhibits long-run interdependence and fractal characteristics for EOR pilot area in conglomerate reservoirs of Kilamayi oil fields .

3. In EOR pilot area, Hurst exponent (H) ranges from 0.8428 to 0.955. H is higher than sandstone reservoirs ,this result show that there is very serious heotergenous for conglomerate formation.

4. Random fractal property distributions can be processed with fractal interpolation both in section and in plane.

5. Through fractal property distributions , results from fractal interpolation is the same as geology and well performance analysis results. Because shale content is lower , it is not obvious that shale content affects formation heotergenous. It is very obvious that water saturation affects formation heotergenous.

Reference

[1] Hewett, T.A., " Fractal Distributions of Reservoir Heterogeneity and Their Influence on Fluid Transport " , SPE 15386, 61th Ann . Tech . Con . of SPA , New Orleans , Oct . 5-8 , 1986

[2] Goggin, D.J., Chandler, M.A., Kocurek, G. and Lake, L.W., Permeability Transects of Eolian Sands and Their Use in Generating Random Permeability Fields , SPE Formation Evaluation, March 1992

[3] Perez, G. and Chopra, A.K., Evaluation of Fractal Model to Describe Reservoir Heterogeneity and Performance, SPE 22694, 66th Ann. Tech. Conf. of SPE, Dallas, Oct..6-9,91

[4] Mandelbrot, B.B., The Fractal Geometry of Nature , Freeman, New York, 1983.

[5] H . H . Hardy , SPE Paper 23968 , presented at SPE Permian Basin Oil and Gas Recovery Conf, Midland , Texas(1992)

[6] S.E . Crane and K . M . Tubman , SPE Paper 20606 , SPE Ann . Tech . Conf . , New Orleans (1990)

[7] I.J. Taggart and H.A.Salisch , APEA Journal 31 (1991) 377-385

[8] Y.Aasum, M.G.Kelkar, and S.Gupta, SPE Formation Evaluation. 6 (1991) 11-19

[9] Hurst, H.E., Long-Term Storage Capacity of Reservoirs , Trans. Am. Soc. Civil Engrs., 116, 770-808, 1951

[10] Hurst, H.E. , Methods of Using Long-Term Storage in Reservoirs , Proc.Inst. Civil Engrs., Part I

[11] M andelbrot, B.B. and Wallis, J.R., Computer Experiments with Fractional Gaussian Noises Part I , Part II and Part III , Water Res., Vol.5 , No. 1 , 228-267, Feb. 1969

[12] M andelbrot, B.B. and Wallis, J.R., Some Long-Run Properties of Geophysical Records , Water Res., Vol. 5, No.2, 321-340, April, 1969

[13] M andelbrot, B.B. and Wallis, J.R., Robustness of the Rescaled Range R/S in the Measurement of Nobcyclic Long Run Statisatical Dependence, Water Res., Vol.5 , No. 5 , 967-988, Oct. 1969

[14] Chanson Du and Ira . Ershaghi , " A Critical Evalution of Short and Long Range Correlation Methods for Heterogeneous Rocks " , SPE 26422

[15] Barnsley, M.F. AND dEVANEY, r.., Mandelbrot, B.B., Peitgen, H.O., Dietmar,S. and Voss, R.F., The Science of Fractal Images, Editors: Peitgen, H.O.and Dietmar,S., Springer-Verlag, New York, 1988

[16] H . H . Hardy Richard A . Beier , " Fractals in Reservoir Engineering " , 1994, World Scientific Publishing Co. . Ltd

[17] H . H . Hardy , in Reservior Characterization III , ed . B. Linvile (Penn Well, Tulsa, Oklahoma, 1993) pp. 787-797

[18] James R . Wallis and Nicholas C . Matalas , " Small Sample Peroperties of H and K — Estimation of Hurst Coefficient H " , Water Resources Research , vol . 6 , No .6 , December 1970 , P 1583 ~ 1594

[19] T.A. Hewett and R . A . Behrens , " Conditional Simulation of Reservoir Heterogeneity with Fractals " , SPE Formation Evaluation , September 1990

[20] A.S. Emanuel,G.K. Alameda , R.A.Behrens and T.A. Hewett . , "Reservior Performance Prediction Methods Based on Fractal Geostatistic " , SPE 16971

[21] K. Aasum ,et al ., " An Application to Geostatistics and Fractal Geometry for Reservoir Characterization " , SPE/DOE 202578

Table 1 Statistical Permeability Data in layers

layer	K_{max} (md)	K_{min} (md)	K average (md)	K_{max}/K_{min}	K_{max}/K average
S^{3-1}_7	3851.39	14.66	775.78	262.71	4.96
S^{3-2}_7	2667.77	41.98	474.36	63.55	5.62
S^{3-13}_7	3035.29	35.02	979.51	86.67	3.10
S^{4-1a}_7	3327.18	14.83	890.29	224.36	3.74
S^{4-1b}_7	1165.19	2.01	251.18	579.70	4.66

Table 2 Results of calculating for each well

Well Number	Hurst Exponent (H)	Fractal dimension D=2-H
ES2001	0.8953	1.1047
ES2002	0.8503	1.1497
ES2003	0.8428	1.1572
ES2004	0.9550	1.0450
ES2005	0.8661	1.1339
ES2006	0.9277	1.0723
ES2007	0.9490	1.051
ES2008	0.8476	1.1524
ES2009	0.9301	1.0699
ES2010	0.8452	1.1548
ES2011	0.8732	1.1268
ES2012	0.9036	1.0964
ES2013	0.9309	1.0691
Average	0.8936	1.1064

Table 3 Data of plane interoplation for 13 wells

Well No.	κ	σ	ϕ	σ	Sn	σ	Sw	σ	Layer
ES2001	269.0277	16.0840	18.8357	2.2043	7.0938	3.1639	60.7047	1.8226	s73-1
	——	——	——	——	——	——	——	——	s73-2
H=0.8953	379.5630	123.9028	18.1250	2.2850	6.8388	2.3954	63.2433	2.8687	s73-3
	337.7500	197.4371	23.5940	2.8359	6.0593	3.2880	55.8657	4.5594	s74
ES2002	277.9311	155.3707	18.1070	2.6570	7.5611	2.2240	60.5276	7.5490	s73-1
	111.8500	80.0004	18.5262	1.7391	8.3887	1.4209	63.4625	1.4336	s73-2
H=0.8503	89.7618	66.9357	16.1527	1.4546	8.3769	1.3781	68.6300	2.2408	s73-3
	256.4025	121.1720	15.1800	1.9456	6.3004	2.0822	68.1691	4.9847	s74

Well No.	κ	σ	ϕ	σ	Sn	σ	Sw	σ	Layer
ES2003	401.7933	205.0750	14.9244	1.9780	7.8533	1.0982	67.6688	5.2185	s_7^{3-1}
	364.1133	39.2511	16.7800	1.6347	8.2659	1.2387	69.3683	2.5875	s_7^{3-2}
H=0.8428	513.2025	52.4408	15.2025	1.1165	8.0833	0.2101	66.3683	2.3350	s_7^{3-3}
	363.0382	95.6365	16.4000	1.5114	6.6847	2.3359	62.4582	3.9765	s_7^{4}
ES2004	240.4241	224.1621	17.8166	4.6464	10.082	0.7315	63.6591	2.9919	s_7^{3-1}
	232.7564	128.7264	16.2005	2.6450	9.3105	1.3458	59.0422	2.9482	s_7^{3-2}
H=0.9550	430.5052	163.0341	18.4817	1.9726	8.0311	1.7758	60.5005	4.6405	s_7^{3-3}
	350.1173	59.8491	18.3873	1.8235	8.6986	0.6811	59.0680	2.5969	s_7^{4}
ES2005	276.5617	303.2599	14.9733	4.0234	8.0195	1.2777	64.1576	8.0810	s_7^{3-1}
	73.2700	14.3116	14.6000	0.6001	8.5320	0.4465	74.1300	0.9735	s_7^{3-2}
H=0.8661	319.5375	39.9016	16.4618	1.0671	8.6381	0.1809	63.6162	1.5753	s_7^{3-3}
	354.6451	93.0542	14.5268	2.4211	6.9644	2.0437	66.8641	4.4036	s_7^{4}
ES2006	373.1433	87.4120	21.1841	1.9759	5.3091	3.0340	52.9091	4.4289	s_7^{3-1}
	191.6018	103.8214	17.9018	1.8527	9.8031	0.9499	61.1412	4.4076	s_7^{3-2}
H=0.9277	347.6300	91.7451	18.5693	1.1643	7.5081	1.2105	60.3812	3.4665	s_7^{3-3}
	338.3848	123.0444	16.6417	2.2949	8.1374	1.6112	65.1780	3.3291	s_7^{4}
ES2007	241.2969	78.4363	21.2015	0.8185	9.5023	2.2037	59.6584	3.0625	s_7^{3-1}
	294.9906	10.5557	17.4480	0.8666	6.5500	0.9521	62.2520	1.9783	s_7^{3-2}
H=0.9490	302.6016	51.4266	15.9444	1.8574	7.1583	1.1563	65.3777	1.4307	s_7^{3-3}
	272.2869	202.7579	16.9736	1.2289	7.4877	1.2691	63.4594	2.6126	s_7^{4}
ES2008	362.4566	80.3914	14.8133	0.8418	5.6655	1.7598	66.4966	2.1858	s_7^{3-1}
	246.2661	70.1039	14.1046	0.8728	9.8307	2.1065	70.8800	3.3861	s_7^{3-2}
H=0.8476	341.4429	209.7518	15.1917	0.9774	8.7700	2.2245	67.6188	1.3355	s_7^{3-3}
	424.9042	138.6820	15.1442	0.5102	8.1431	2.1724	64.2147	3.8748	s_7^{4}
ES2009	159.9045	88.3213	18.1263	0.4320	7.0754	1.5391	62.8990	2.1110	s_7^{3-1}
	210.6360	76.6998	18.0440	0.3359	6.3200	0.9258	62.3600	1.4753	s_7^{3-2}
H=0.9301	440.1980	138.5119	14.6726	1.2875	7.4380	2.6987	66.0300	2.1406	s_7^{3-3}
	349.9820	115.7455	17.4580	0.4565	8.5140	0.6725	62.7593	1.4034	s_7^{4}
ES2010	51.8114	81.2770	17.9900	0.5009	5.2285	1.2827	63.7357	0.5675	s_7^{3-1}
	152.5252	31.1206	15.1331	2.7413	9.2163	0.4109	71.5694	4.1118	s_7^{3-2}
H=0.8452	229.2321	140.6519	17.9704	1.4953	7.7965	1.5078	63.7960	2.9686	s_7^{3-3}
	296.2800	124.6636	16.8632	1.5563	7.2123	2.2676	64.4830	3.0813	s_7^{4}
ES2011	207.6220	42.5704	18.0140	1.2001	10.908	1.1445	61.4140	2.9999	s_7^{3-1}
	This layer is no data								s_7^{3-2}
H=0.8732	282.3596	103.8016	20.0914	0.6859	7.8151	2.4490	58.0870	3.1349	s_7^{3-3}
	362.6090	75.2518	18.9676	1.3420	8.5985	1.3425	59.3961	3.0466	s_7^{4}
ES2012	423.1691	100.2563	15.5666	1.4665	8.3466	1.4813	65.0941	3.4369	s_7^{3-1}
	354.1805	50.7182	18.0060	1.8815	8.8438	1.0248	61.9327	2.0129	s_7^{3-2}
H=0.9036	357.3427	47.1262	16.3772	1.0617	8.6354	0.6461	62.9845	3.2771	s_7^{3-3}
	345.3111	67.0954	16.5222	0.8015	7.0357	2.1377	61.0971	4.0414	s_7^{4}
ES2013	250.7463	53.0052	18.0000	2.1690	10.028	0.6488	57.7900	6.1884	s_7^{3-1}
	64.1075	13.8398	17.3246	1.3631	9.8246	0.9649	68.0766	1.8972	s_7^{3-2}
H=0.9309	217.8220	42.9408	18.7375	1.8279	7.8476	0.7523	55.9892	1.6721	s_7^{3-3}
	242.1605	67.2135	18.0922	1.0426	6.6966	2.5572	57.1694	3.1952	s_7^{4}

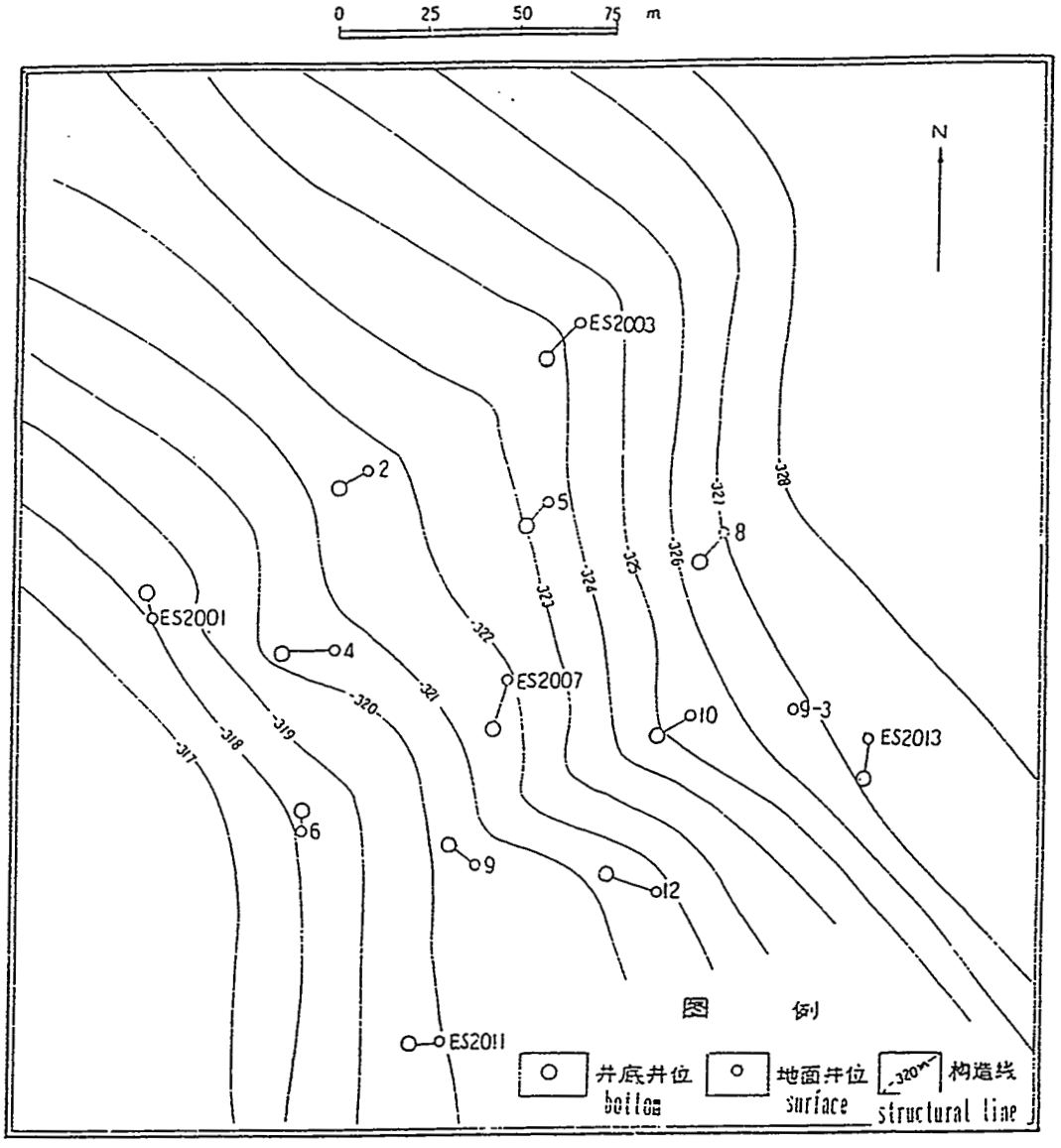

Fig 1: Top of structure contour line graph

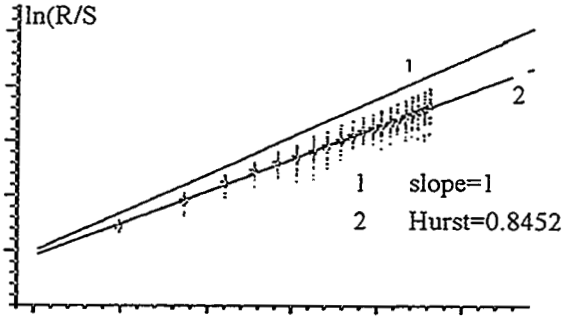

Fig 2: R/S analysis of normalized sequence for ES 2010 well

Fig 3. Schematic figure of random fractal interwells
(a) The rough shape of mountain before interpolation
(b) The final shape of mountain after interpolation

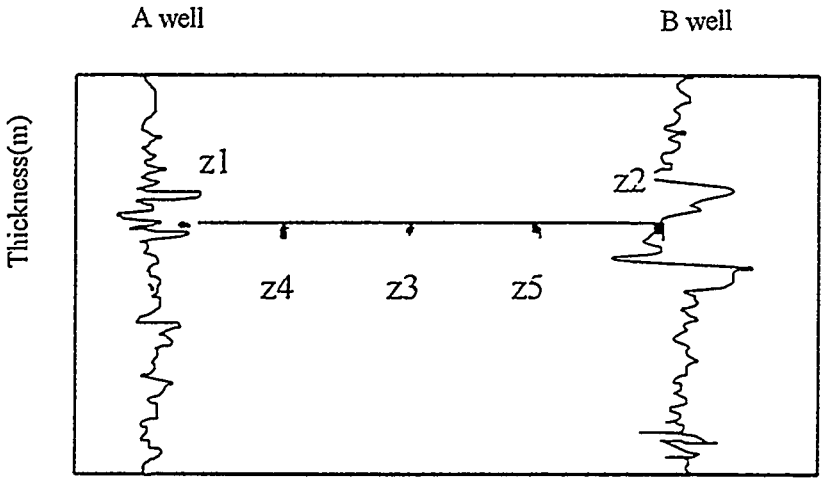

Fig 4. Random fractal interpolation of interwells in section

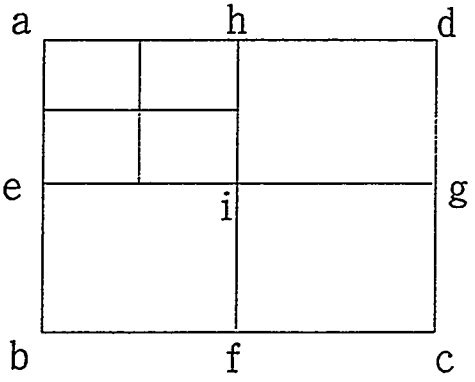

Fig 5. Random fractal interpolation of Pyramid in plane

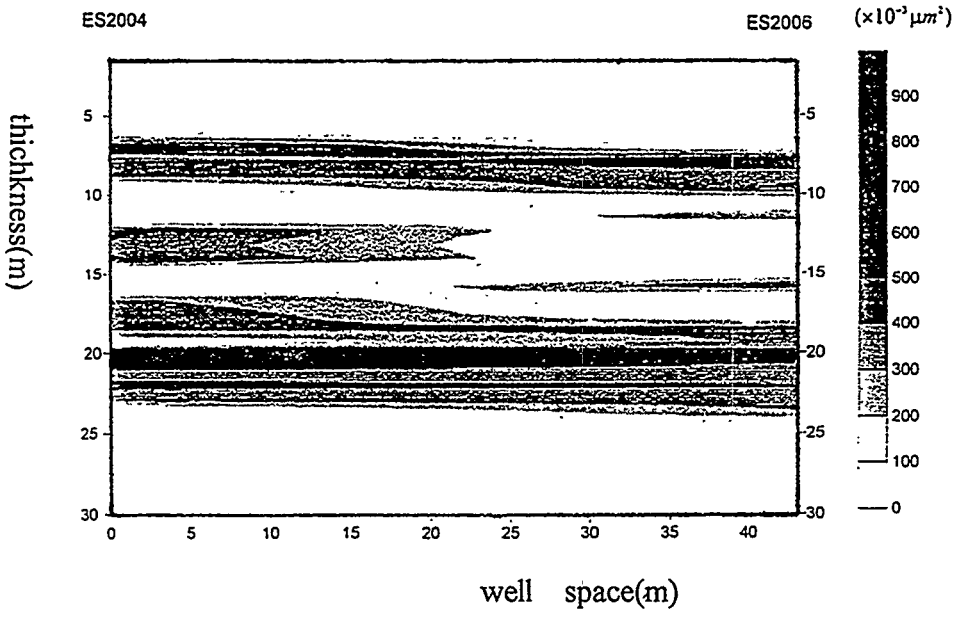

Fig. 6 Permeability distribution of between wells(ES2006~ES2004)

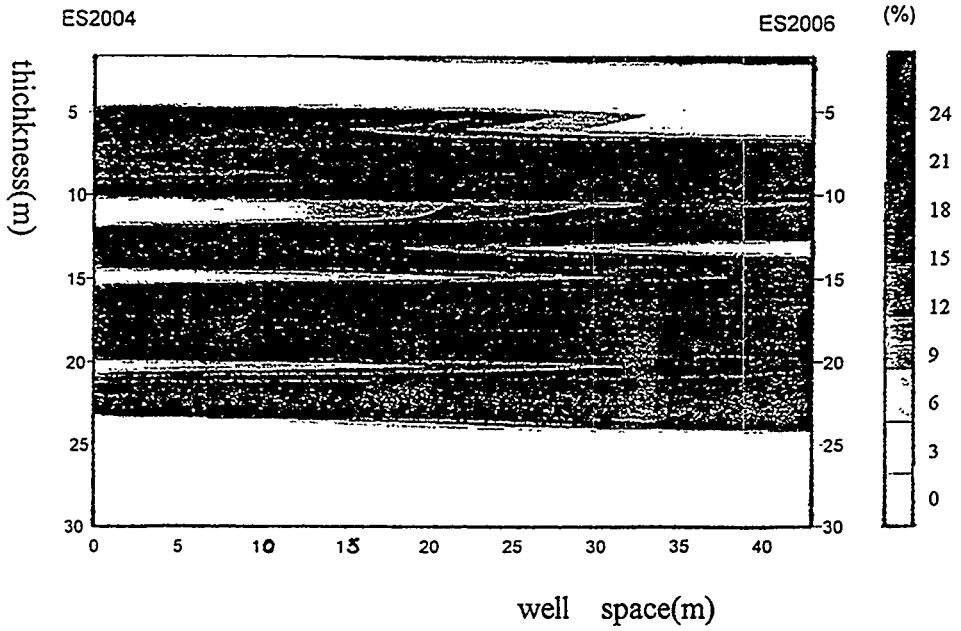

Fig .7 Porosity distribution of between wells(ES2006~ES2004)

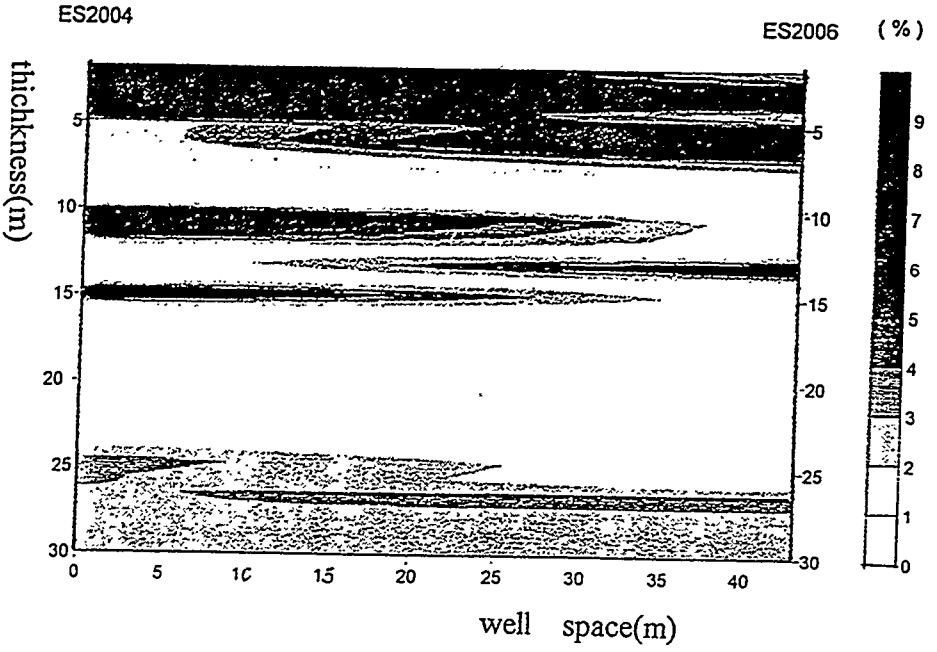

Fig. 8 Shale content distribution of between wells(ES2006~ES2004)

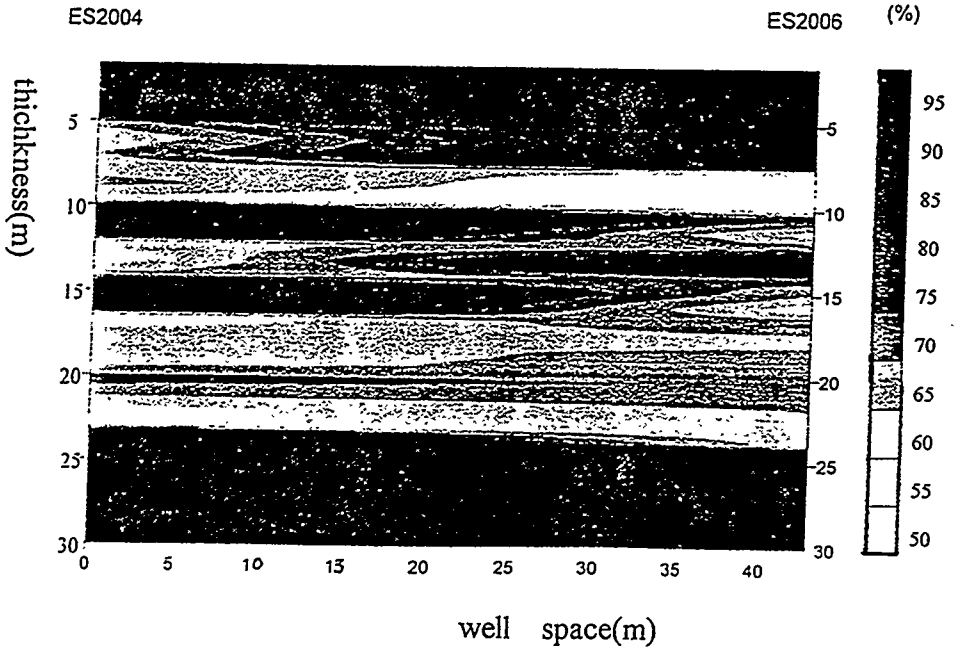

Fig. 9 Water saturation distribution of two well(ES2006~ES2004)

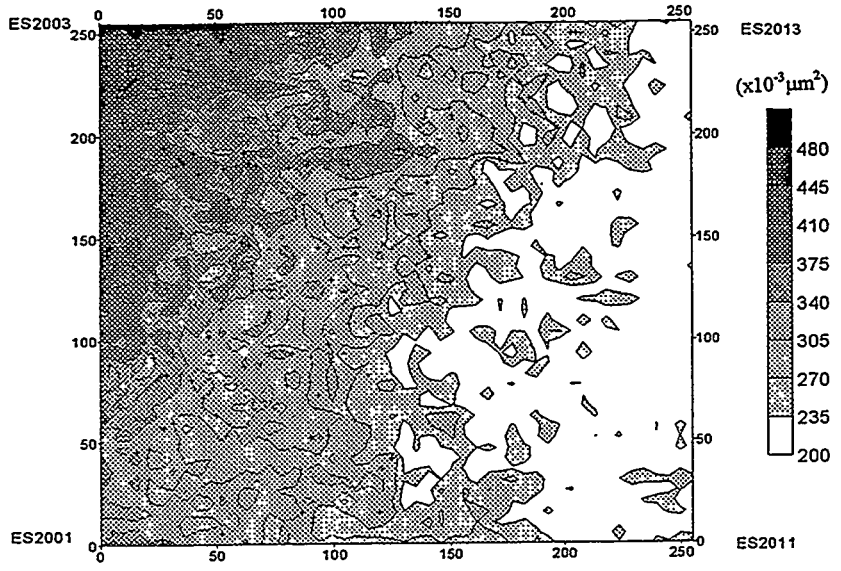

Fig . 10 Permeability distribution of plane for one unit(S_7^{3-3})

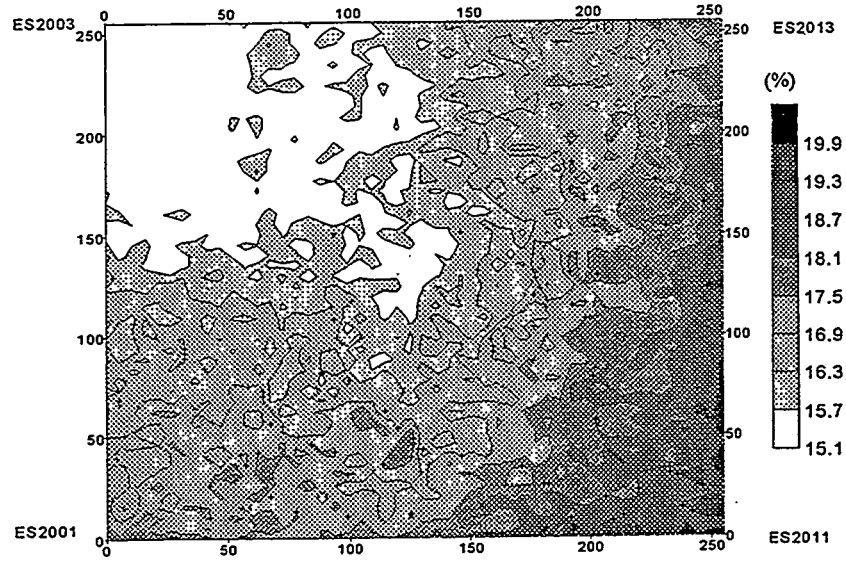

Fig . 11 Porosity distribution of plane for one unit (S_7^{3-3})

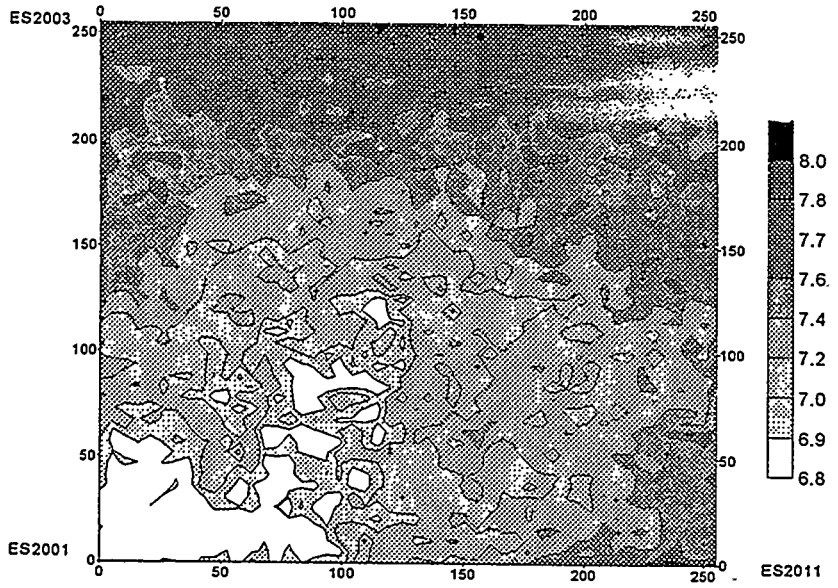

Fig . 12 Shale content distribution of plane for one unit (S_7^{3-3})

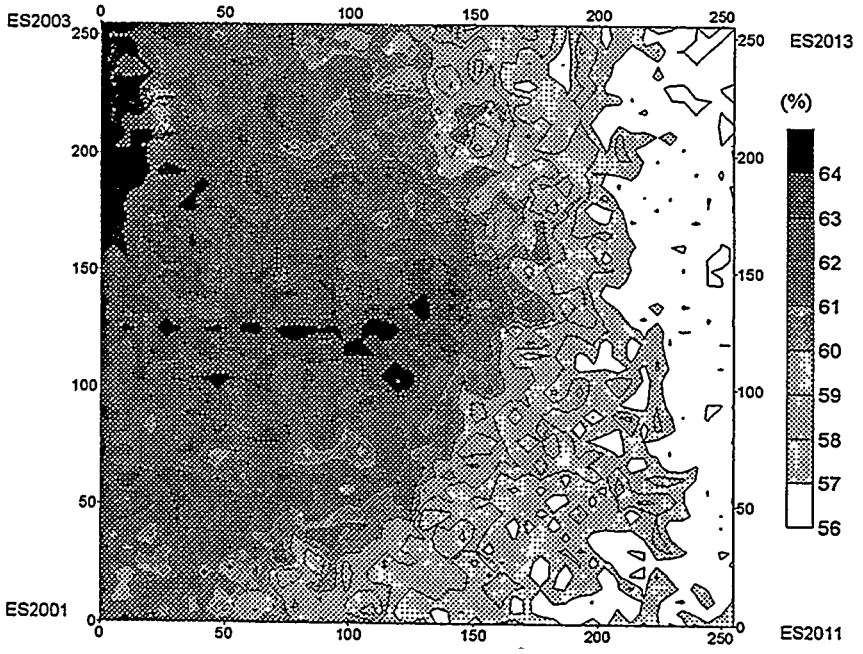

Fig. 13 Saturation distribution of plane for one unit (S_7^{3-3})

3-D Description of Fracture Surfaces and Stress-Sensitivity Analysis for Naturally Fractured Reservoirs

S.Q. Zhang, D. Jiao, Y.F. Meng, Southwest Petroleum Institute, China, and
Y. Fan, U. of Tulsa at NIPER

Acknowledgments

The authors acknowledge State Key Laboratory of Oil and Gas Reservoir Geology and Exploitation, China, for funding this research. Special thanks go to Profs. Su Wangyong and Li Lusen for their experimental plan and valuable discussion.

Abstract

Three kinds of reservoir cores (limestone, sandstone, and shale with natural fractures) were used to study the effect of morphology of fracture surfaces on stress sensitivity. The cores, obtained from the reservoirs with depths of 2170 to 2300 m, have fractures which are mated on a large scale, but unmated on a fine scale. A specially designed photoelectric scanner with a computer was used to describe the topography of the fracture surfaces. Then, theoretical analysis of the fracture closure was carried out based on the fracture topography generated. The scanning results show that the asperity has almost normal distributions for all three types of samples. For the tested samples, the fracture closure predicted by the elastic-contact theory is different from the laboratory measurements because plastic deformation of the asperities plays an important role under the testing range of normal stresses. In this work, the traditionally used elastic-contact theory has been modified to better predict the stress sensitivity of reservoir fractures. Analysis shows that the standard deviation of the probability density function of asperity distribution has a great effect on the fracture closure rate.

Introduction

The term "dual-porosity reservoir" often refers to a naturally fractured formation which has two distinct porosity types: matrix porosity and fracture porosity. The matrix has low permeability but relatively large storage capacity, whereas the fracture has high permeability with small storage capacity. In such naturally fractured reservoirs, many petrophysical properties, such as permeability and compressibility, are controlled by the fracture closure stress. Since fractures are major channels of

hydrocarbon flow, the fracture aperture determines the transport capability of hydrocarbons. Clearly, understanding fracture closure and its changes under different normal stresses is indispensable in characterizing fractured reservoirs. It is also important for controlling formation damages during drilling and well completion, because mud invasion can be effectively controlled by adding some appropriate fiber particles to the drilling and completion fluids if the fracture aperture under reservoir conditions is known.

Historically, studies on wells in dual-porosity reservoirs have considered two kinds of models for the matrix-fracture fluid transfer: the pseudo steady-state flow (Warren and Root, 1963) and the transient matrix flow (de Swaan, 1976. Kasemi, 1969). These models have been in wide use for well production performance and well treatment interpretations (Ehlig-Economides et al., 1994). However, the description of the fractures using assumption of parallel planes is not sufficient to study the fracture closure under normal stresses. In reality, a fracture has rough surfaces with some tortuosity. The surface roughness is dependent on formation deposition environment and history. Initially, some contacts of asperities on the fracture surfaces exist. The stress sensitivity is governed by the density and distribution of asperities on the fracture surface. In order to understand fracture closure under normal stress, topography of the fracture surface must be analyzed in detail.

Study of a fracture closure under the normal stresses is based on Hertz's elastic-contact theory. Using the assumption that asperities on fracture surfaces are spheres and the contacts between the asperities are elastic, Yamada et al. (1978a, 1978b) proposed a mathematical equation that describes the relation between the applied stress and the fracture closure:

$$p_n = \frac{16\pi}{15} n_1 n_2 E' \sqrt{R_1 R_2 R_t} \int_0^{Z_a} \int_0^{Z_a - Z_1} \left(Z_a - Z_1 - Z_2\right)^{5/2} \varphi(Z_1)\varphi(Z_2) dZ_1 dZ_2 \quad \text{.....(1)}$$

where

$$\frac{1}{E'} = \frac{1-\gamma_1^2}{E_1} + \frac{1-\gamma^2{}_2}{E_2}$$

$$R_t = R_1 + R_2$$

p_n = applied stress

E_1, E_2 = Young's modulus

γ_1, γ_2 = Poisson's ratio

R_1, R_2 = radius of curvature asperities

n_1, n_2 = number of asperities per unit area

Z_a = overlapped distance between two surfaces

$\varphi(Z_1), \varphi(Z_2)$ = probability density function

Brown and Scholtz (1985, 1986) measured surface profiles of both contact sides, and composed them into a composite profile. Then, the composite surface was intersected with a plane to investigate the fracture closure. Surface topographical parameters were obtained from the composite profiles by a random process. Figure 1 shows the principle of a composite surface. According to Brown and Scholtz's theory, the contacts between the composite surface and the plane are in elastic range. Therefore, Eq. (2) can be used to compute the fracture closure at the applied normal stress.

$$p = \frac{4n}{3} \Psi E' \sqrt{\beta} \int_{d_0 - \delta}^{\infty} (Z - d_0 + \delta)^{3/2} \varphi(Z) dZ \quad \text{.....(2)}$$

where

p = normal stress

n = total number of asperities per unit area

Ψ = mean value of tangential stress correction factor (≈ 1)

E' = mean value of elastic constant

$\sqrt{\beta}$ = mean value of square root of curvature term

δ = joint closure

$\varphi(Z)$ = probability density function

d_0 = distance between reference planes at $p = 0$

In this study, a specially designed photoelectric scanner with a computer, as shown in Fig. 2, was used to generate 3-D topographic pictures of fracture surfaces. We regard a data point on the composite surface as a summit when that point is higher than the surrounding four points. Then, the initial aperture of the surface, asperity distribution, and mean curvature of the asperities are calculated. Elastic-contact

theory was adapted to predict the fracture closure under the normal stress. Compressing fracture closure tests were made to verify the numerical results. Eq. (2) was used to perform theoretical analysis.

Experiments and Results

For the samples tested, fracture surfaces are mated on a large scale, but unmated on a fine scale. The relative position of both surfaces is very important. Before experiments, both fracture surfaces were twisted in order to get the maximum mate. Three kinds of cores (limestone, sandstone, and shale with natural fractures) were analyzed. The tested cores have a diameter of 105 mm, and their detailed physical properties are presented in Table 1.

Fig. 3 shows a scanning result of the sandstone fracture surfaces. One of them has been turned 180° and overlapped with another to produce a composite surface. From this composite surface, the description of the 3-D distribution of a fracture surface morphology, density of the asperity, mean radius of curvature of asperities, and probability density function of the asperity distribution can be obtained. Eq.(2) is then used to predict fracture closures.

In order to verify the theoretical predictions, experimental measurements of the fracture closure with the same cores under applied normal stresses were conducted. Fig. 4 shows a schematic of the compressing tests. During the measurements, the extensometer was placed between the fractures. Normal stresses applied to the formation cores were gradually increased at a constant rate, and the displacement was recorded until the stress reaches the designed value. Then, the stresses were gradually reduced, and the displacement is recorded again. Such tests were repeated for two or three cycles. In the same way, the extensometer was used to measure the displacement of the rock matrix under the same normal stress for nonfractured cores. Consequently, the fracture closure can be obtained by subtracting the rock matrix displacement from the fractured displacement. Figs. 5 to 8 present the results of measured fracture closure curves for the different core samples. In this study, the shale sample broke at 3 MPa; therefore, no detailed data were analyzed.

Discussion

All three experimental results (Figs. 5 to 8) have indicated hysteresis effects in the fracture closure when loading and unloading applied stresses. In the first cycle of tests, the rock deformation is the largest, possibly due to further mating of the two surfaces, and causing plastic deformation of surface asperities. Once the normal stress is applied, the fracture surfaces cannot be separated easily. In the

second and the third cycles of the tests, smaller hysteresis effects were observed. The data measured in the second or third cycles were compared with those predicted by the model. Figs. 9 and 11 show the comparison of experimental and theoretical results. The model predictions cannot match the experimental measurements, especially in the low normal stress range. These computations are based on input of the 3-D composite surface before loading tests. However, after the loading experiments, the parameters obtained from scanning fracture surfaces changed significantly. For instance, the mean square root of the asperity summits can differ by a factor of 2 to 3 before and after loading tests. Such differences are directly caused by the plastic deformation of the asperities. The core samples used contain 5 to 8% clays, which are soft and therefore easily deform plastically, even under relatively low stresses.

Figs. 12 to 14 show measurements of fracture closure and the model predictions using the parameters obtained after the loading tests. (Table 2 presents the parameters after loading tests.) The model predictions are in good agreement with the experimental measurements. It appears that the plastic deformation of the asperities is an important factor in predicting the fracture closure.

The model proposed by Brown and Scholtz (1985) assumes that the contact among the asperities is purely elastic. This may be true for hard materials such as quartz and granite, but reservoir rocks contain clays which easily deform permanently. Even at low applied stress, the local stress may exceed the elastic limit, and results in plastic deformation. For the samples tested, Eq. (2) is not valid because the contribution of the plastic deformation is significant. However, after the permanent deformations, Eq. (2) can accurately predict fracture closures for reservoir rocks. Ironically, in terms of reservoir engineering, the initial fracture apertures, which are determined by the original morphology of the fracture surfaces under the reservoir conditions, are most interested in determining fracture closure. Therefore, Eq. (2) needs to be modified to properly predict fracture closure.

Figs. 15 to 17 show that closure and normal stress have the following empirical relationship:

$$\delta = A + B \ln p \quad \text{.....(3)}$$

where A is a correlation constant that is related to the initial aperture of a fracture (at $p = 0$). B is also a constant related to deviation of the asperity distribution. Generally, smaller values of B mean the composite surface is relatively less rough or the asperities height is more uniform and more asperities contact each other at a given normal stress. As a result, the resistance to fracture closure is larger than

that with a higher value of B. In Figs. 15, 16 and 17, the means of curvatures are 26 μm, 5 μm and 8 μm, respectively. For Fig. 15, the closure is more sensitive to the normal stress than the others. Therefore, the deviation of the probability density function of the composite topography has a larger effect on fracture closure. Eq. (3) also implies that for a given composite surface, the closure should be more rapid at lower values of the applied stress, and should be gradually slowed down with an increase in the applied stress, because more and more asperities come into contact and the resistance to closure increases.

Conclusions

1. A photoelectric scanner designed to investigate fracture surfaces is an effective tool to characterize the morphology of fracture surfaces. With the scanner combined with a computer imaging technique, the asperity density, mean radius of curvature, and probability density function can be accurately determined for reservoir formations.
2. Because clays in the formation rock are easily deformed permanently, even at a relatively low normal stress, the fracture closure predicted by the model using elastic-contact theory differs from laboratory measurements. The permanent deformation of the asperities changes the topography of the fracture surfaces significantly. Elastoplastic contact theory should be used to predict the fracture closure for reservoir formations.
3. The deviation of probability density function of the asperity distribution has a significant effect on the fracture closure rate. Larger values of deviation causes more rapid fracture closure.

References Cited

Brown, S. R. and Scholtz, C. H., 1985, "The Closure of Random Elastic Surfaces in Contact", *Journal of Geophysical Research*, v. 90, p 5531-5545.

Brown, S. R. and Scholtz, C. H., 1986, "Closure of Rock Joints", *Journal of Geophysical Research*, v. 91, p 4939-4948.

De Swaan, O.A., 1976, "Analytic Solutions for Determining Naturally Fractured Reservoir Properties by Well Testing" *SPEJ*, p 117-122.

Ehlig-Economides, C.A., Fan, Y. and Economides, M.J., 1994, "Interpretation of Fracture calibration Tests in Naturally Fractured Reservoirs", paper SPE 28690 presented at the SPE International Petroleum Conference of Mexico held in Veracruz, Mexico, 10-13 October, 1994.

Kasemi, H., 1969, "Pressure Transient Analysis of Naturally Fractured Reservoirs With Uniform Fracture Distribution", *SPEJ*, p 451-458.

Warren, J.E. and Root, P.J., 1963, "The Behavior of Naturally Fractured Reservoirs", *SPEJ*, p245-255.

Yamada, K., Takeda, N., Kagami, J., and Naoi, T., 1978a, "Surface Density of Asperities and Real Distribution of Asperity Heights on Rubbed Surface", *Wear*, v. 47, p5-20.

Yamada, K., Takeda, N., Kagami, J., and Naoi, T., 1978b, "Mechanisms of Elastic Contact and Friction between Rough Surfaces", *Wear*, v. 48, p15-34.

Table 1— Mechanical Properties and Topographical Data of Composite Surfaces Before Loading Experiments.

Samples	Rock Type	Young's Modulus E (10^4 MPa)	Poisson's Ratio γ	Asperity Density n (10^{-8}/mm^{-2})	Mean Square Root, $\sqrt{\beta}$ ($\sqrt{\mu m}$)	Standard Deviation σ (μm)	Initial Aperture d_0 (μm)
A	Limestone	6.1	0.33	323	240	81	243
B	Shale	1.5	0.15	32	781	196	
C	Sandstone	3.2	0.2	4.1	2300	202	606
D	Limestone	6.8	0.31	263	203	92	276

Table 2— Mechanical Properties and Topographical Data of Composite Surfaces After Loading Experiments.

Samples	Rock Type	Young's Modulus E (10^4 MPa)	Poisson's Ratio γ	Asperity Density n (10^{-8}/mm^{-2})	Mean Square Root, $\sqrt{\beta}$ ($\sqrt{\mu m}$)	Standard Deviation σ (μm)	Initial Aperture d_0 (μm)
A	Limestone	6.1	0.33	367	73	20	60
C	Sandstone	3.2	0.2	52	411	91	273
D	Limestone	6.8	0.31	213	86	26	78

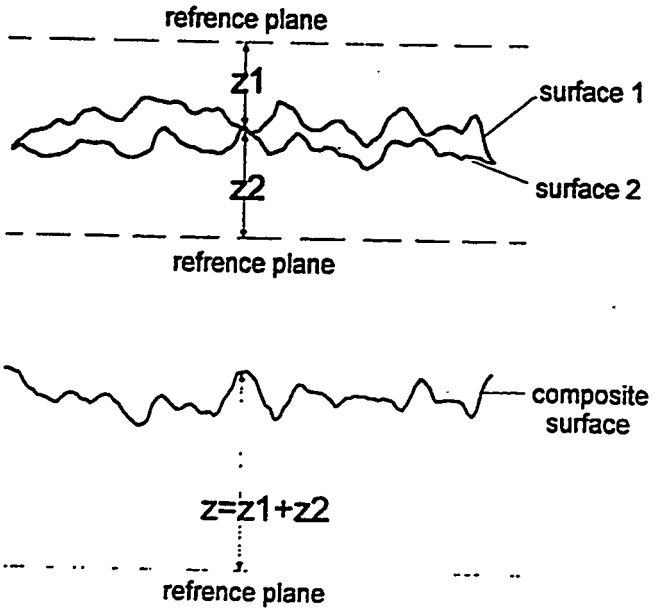

Fig. 1—Schematic of a composite surface profile.

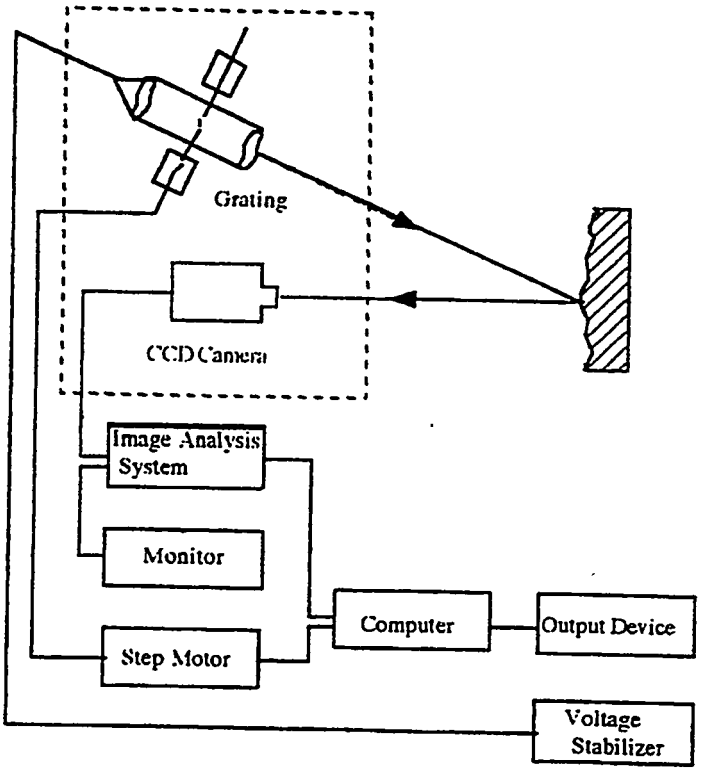

Fig. 2—Schematic of photoelectric scanning system.

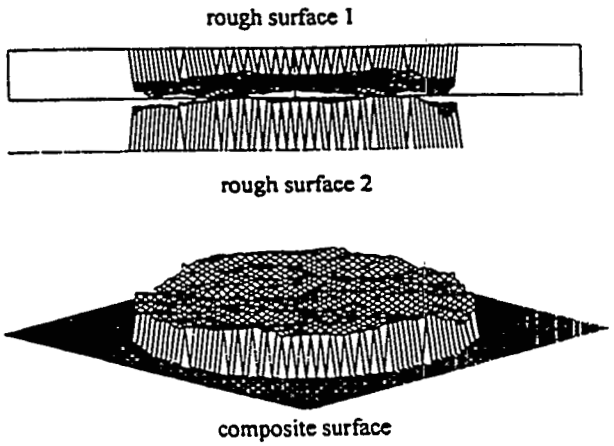

Fig. 3—Photoeletic scanning results of sandstone fracture.

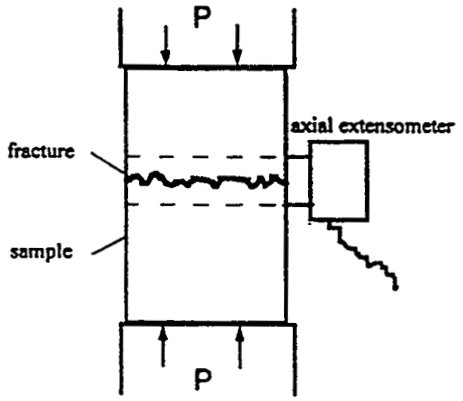

Fig. 4—Schematic of the compressing test.

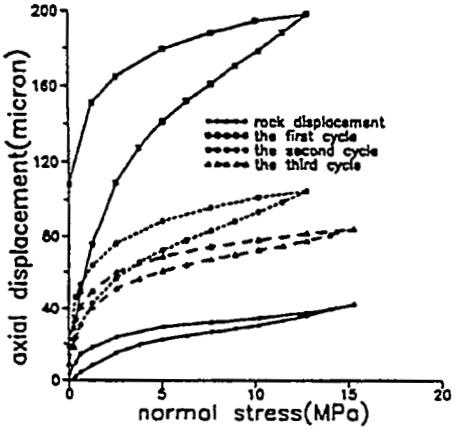

Fig. 5—Fracture closure curves of sample A (limestone).

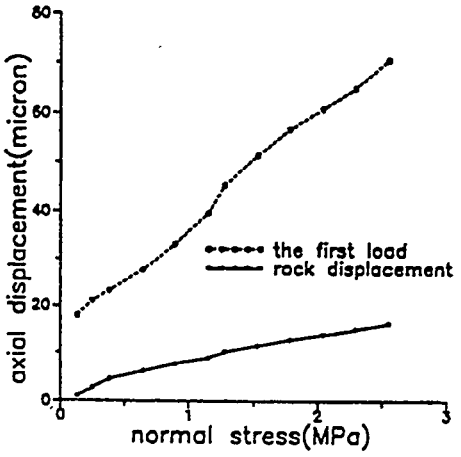

Fig. 6—Fracture closure curves of sample B (shale).

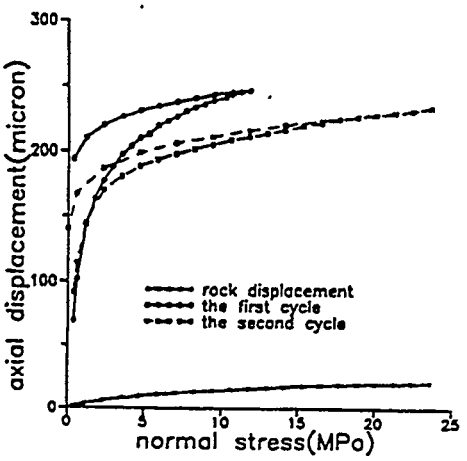

Fig. 7—Fracture closure curves of sample C (sandstone).

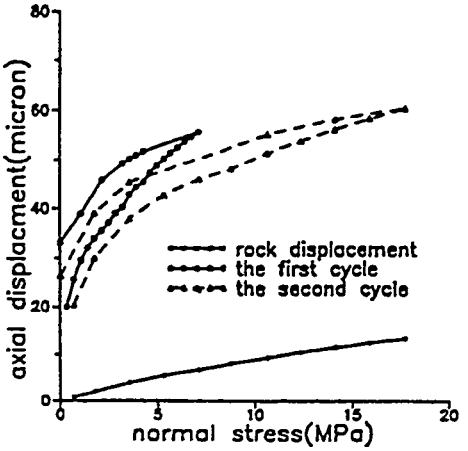

Fig. 8—Fracture closure curves of sample D (limestone).

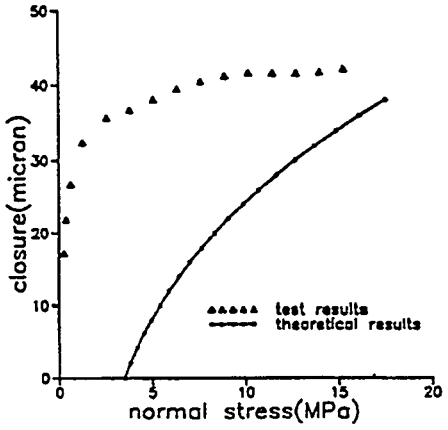

Fig. 9—Comparison of tests and theoretical results for sample A (surface parameters obtained before loading).

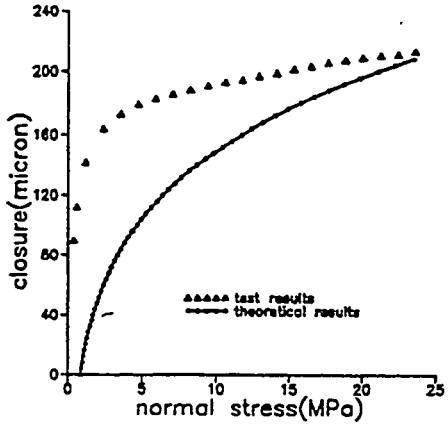

Fig. 10—Comparison of test and theoretical results for sample C (surface parameters obtained before loading).

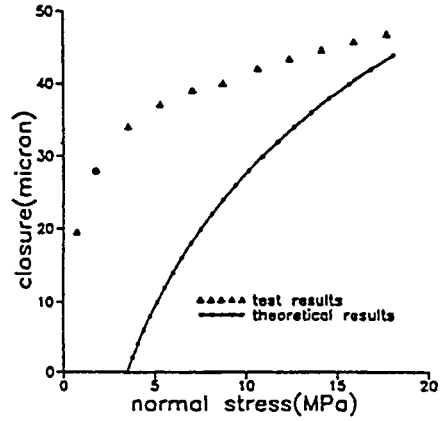

Fig. 11—Comparison of test and theoretical results for sample D (surface parameters obtained before loading).

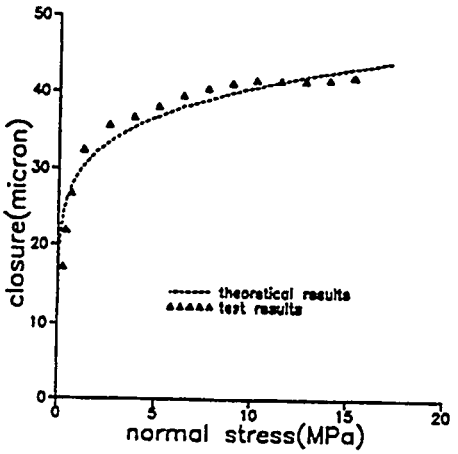

Fig. 12—Comparison of test and theoretical results for sample A (surface parameters obtained after loading).

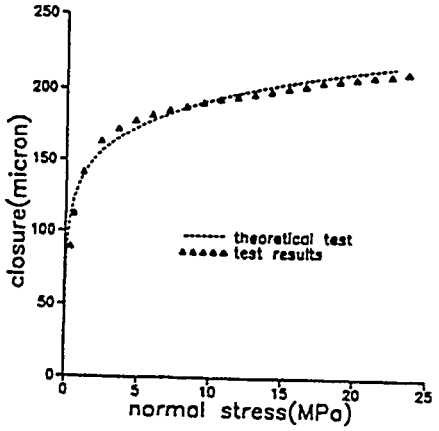

Fig. 13—Comparison of test and theoretical results for sample C (surface parameters obtained after loading).

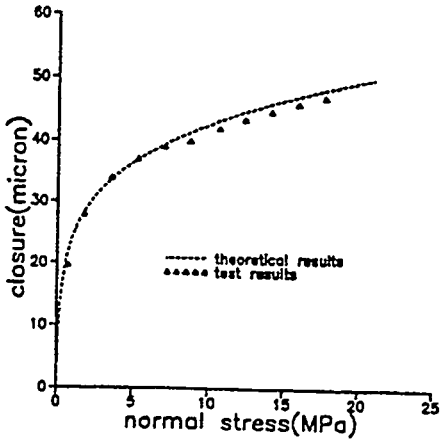

Fig. 14—Comparison of test and theoretical results for sample D (surface parameters obtained after loading).

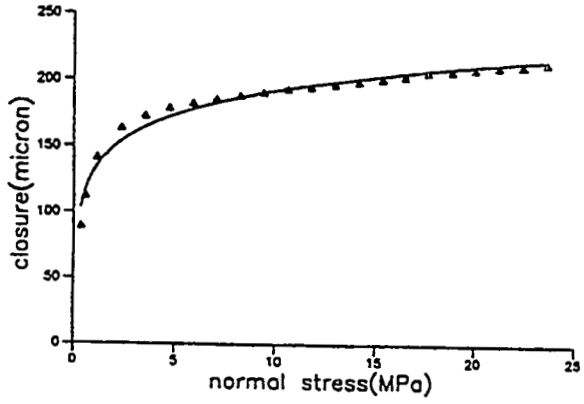

Fig. 15—Curve fitting of fracture closure for sample C $(\delta = 131 + 26\ln p)$.

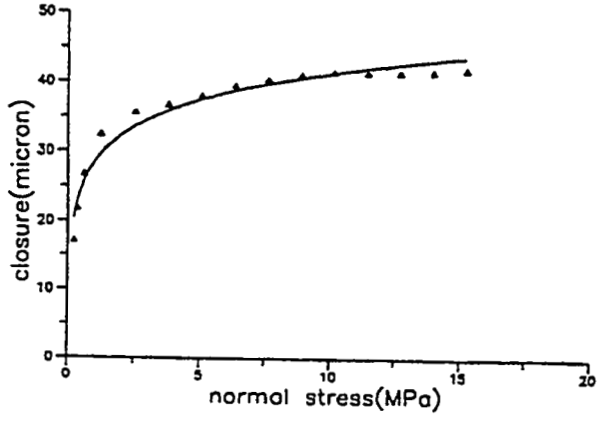

Fig. 16—Curve fitting of fracture closure for sample A $(\delta = 28 + 5\ln p)$.

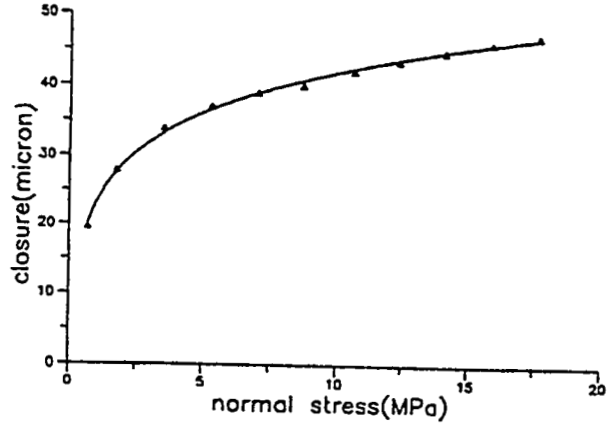

Fig. 17—Curve fitting of fracture closure for sample D $(\delta = 23 + 8\ln p)$.

Fig. 1—Schematic of a composite surface profile.

Fig. 2—Schematic of photoelectric scanning system.

Fig. 3—Photoeletic scanning results of sandstone fracture.

Fig. 4—Schematic of the compressing test.

Fig. 5—Fracture closure curves of sample A (limestone).

Fig. 6—Fracture closure curves of sample B (shale).

Fig. 7—Fracture closure curves of sample C (sandstone).

Fig. 8—Fracture closure curves of sample D (limestone).

Fig. 9—Comparison of tests and theoretical results for sample A (surface parameters obtained before loading).

Fig. 10—Comparison of test and theoretical results for sample C (surface parameters obtained before loading).

Fig. 11—Comparison of test and theoretical results for sample D (surface parameters obtained before loading).

Fig. 12—Comparison of test and theoretical results for sample A (surface parameters obtained after loading).

Fig. 13—Comparison of test and theoretical results for sample C (surface parameters obtained after loading).

Fig. 14—Comparison of test and theoretical results for sample D (surface parameters obtained after loading).

Fig. 15—Curve fitting of fracture closure for sample C ($\delta = 131 + 26\ln p$).

Fig. 16—Curve fitting of fracture closure for sample A ($\delta = 28 + 5\ln p$).

Fig. 17—Curve fitting of fracture closure for sample D ($\delta = 23 + 8\ln p$).

Integrated reservoir characterization: Improvement in heterogeneities stochastic modelling by integration of additional external constraints.

B.Doligez(*), H.Beucher(**), F.Geffroy(**), R.Eschard(*) & Heresim group (*) (**)
(*) Institut Francais du Pétrole, 1&4 av. de Bois Préau, BP311 -92506- Rueil Malmaison -France
(**) Centre de Géostatistique, 35 rue Saint Honoré -77305- Fontainebleau Cédex- France

Abstract:

The classical approach to construct reservoir models is to start with a fine scale geological model which is informed with petrophysical properties. Then scaling-up techniques allow to obtain a reservoir model which is compatible with the fluid flow simulators.

Geostatistical modelling techniques are widely used to build the geological models before scaling-up. These methods provide equiprobable images of the area under investigation, which honour the well data, and which variability is the same than the variability computed from the data. At an appraisal phase, when few data are available, or when the wells are insufficient to describe all the heterogeneities and the behaviour of the field, additional constraints are needed to obtain a more realistic geological model. For example, seismic data or stratigraphic models can provide average reservoir information with an excellent areal coverage, but with a poor vertical resolution.

New advances in modelisation techniques allow now to integrate this type of additional external information in order to constrain the simulations. In particular, 2D or 3D seismic derived information grids, or sand-shale ratios maps coming from stratigraphic models can be used as external drifts to compute the geological image of the reservoir at the fine scale.

Examples are presented to illustrate the use of these new tools, their impact on the final reservoir model, and their sensitivity to some key parameters.

1 - Introduction

Reservoir characterization techniques involve more and more geosciences integration for a better recovery of hydrocarbons. However, in such reservoir integrated studies, the available data are of different kinds. Generaly, qualitative structural and sedimentological models are constructed, in order to give the general framework of the reservoir layering, using methods as sequence stratigraphy or regional geology synthesis, and only provide soft informations and global trends.

Quantitative data are also of different kinds and resolution scales. They could be splitted into different categories:

- the well data, which are 1D, with a high resolution along the vertical, but a very sparse lateral density generaly integrate a lot of parameters, . One problem is to synthetize all this information in a suitable database,

- the seismic data are generaly lateraly continuous and good for mapping. On the other hand, they have only a poor vertical resolution, and are difficult to be interpreted in terms of geological parameters. Moreover, at a reservoir scale, the precision of the picking is of primary importance for the construction of the reservoir layering. New methods based on the interpretation of seismic parameters in terms of reservoir properties using multivariate statistics can give some keys to merge these different sources of information. In favourable cases, seismic can also provide informations on lithological, petrophysical or fluid variations between the wells.

- other geological "soft" data as qualitative geological interpretations can help to introduce some rules or constraints in the models. Also, the stratigraphic modelling provides trends of lateral facies evolution and of their lithological components in a studied area.

Geostatistical modelling techniques are widely used to build the geological models at the fine scale within predefined sedimentary units. Geostatistic tools are also well adapted to deal with data of various resolution scale, and seem to be efficient for their integration.

Heresim is such a geostatistical tool, developed by IFP and CG which algorithm is based on the truncated gaussian method (Matheron et al., 1987, Ravenne et al., 1990). New advances in modelling techniques allow now to integrate average geological parameters grids, derived from seismic data or from stratigraphic models, to build 3D matrices of proportions which are used in the non stationary conditional simulations.

Some examples will illustrate these new methods, and point out the influence of these additional external constraints on the petrophysical properties distribution in the final reservoir grid.

2 - Principles of the methodology

2-1 - Some preliminary recalls

The methodology implemented into Heresim has already been presented in other papers (Ravenne et Beucher, 1988, de Fouquet et al., 1988, Galli et al., 1990, Eschard et al 1991, Doligez et al., 1992...). The main purpose is to provide to the reservoir engineers several equiprobable images of a reservoir which may be used for fluid flow simulations. Heresim is both a methodology and a geostatistical tool for reservoir characterization. The underlaying philosophy is that the description of the petrophysical heterogeneities of a reservoir is directly linked to the description of the lithofacies heterogeneities. The main steps of the method, illustrated on figure1, are the following:

1/ a database compilation, and the construction of a conceptual geological model,

2/ the lithofacies reservoir simulations in a high resolution grid

3/ the petrophysical properties attribution on these fine-scaled images

4/ the scaling-up of petrophysical properties in a coarser grid which will be the input for fluid flow simulators.

The sedimentological interpretation of the well data and concepts from sequence stratigraphy allow to define the main sedimentary units of the studied reservoir, their geometries, and the chronostratigraphic horizons which can be used as reference level for a flattening. In some cases, the units may also be defined as proportional, when the beds are concordant with the limits of the units, in case of differential subsidence for example.

For each unit, which are simulated independantly, the proportion curves and variograms are first computed, to characterize qualitatively and quantitatively the spatial variability of the sedimentary facies. In particular, the vertical proportion curve represents a cumulated histogram of the proportions of the lithofacies present on the discretized wells, computed at each stratigraphic level, parallely to the reference level of the considered unit, as illustrated in figure 2. It characterizes the vertical distribution of the lithotypes in the reservoir unit. The horizontal proportion curve is a projection of the cumulated proportions of each facies computed well by well and projected on an horizontal line. It allows to appreciate the degree of lateral variability of the facies within the studied unit.

The lithofacies simulation are made using a stationary simulation of a gaussian random function which is truncated level by level using thresholds, which are directly linked to the proportions of the lithofacies on each level. The equiprobable simulations honour the well data, and the global variograms and proportion curves computed from the simulated blocks are the same than those computed from the well data.

Originally, Heresim worked with an horizontal stationarity hypothesis for the lithofacies distribution, which means that the geological lateral variations are averaged across the field. In that case, the simulation algorithm uses constant thresholds, level by level, to truncate the gaussian function which is generated, as illustrated on figure 3.a. In this process, the thresholds are directly linked to the lithotypes proportions given by the vertical proportion curves.

Depending on the values of the gaussian function, compared to the different thresholds, it is possible to attribute a lithofacies value in each space location.

This horizontal stationarity hypothesis may be valid in some cases, when the facies distribution does not show any major trend in the simulated area. But this hypothesis is often not geologicaly satisfactory, especially when few well controls are available, or when the wells cannot be considered to be representative of the field behaviour. For these reasons, a non-stationary version of the software has been developed which allows to take into account in the simulations not only the vertical but also the horizontal trends of the facies repartition. Instead of defining only one vertical proportion curve, which represents the main vertical facies sequences in the unit, and which is used to define the truncation thresholds of the gaussian function level by level, the method deals in that case with a 3D proportion function which represents the mean spatial variations of the facies. The truncation thresholds of the gaussian function are then varying through space, as illustrated on figure 3.b, and the corresponding lithofacies values follow these variations.

2-2 - Building a 3D block of proportions

Different ways are possible to estimate the 3D functions of proportions, in a regular block support, from well data and possibly additional external data which may be qualitative or quantitative. A first approach is to divide the reservoir into several zones to each of which a representative vertical proportion curve is attributed, or where the mean proportions of lithofacies are estimated from initial vertical proportion curves.

The partition of the reservoir may be based on geological criteria, or on qualitative seismic interpretation using seismic facies analysis techniques. This methodology mainly uses pattern recognition techniques and statistical tools to rely each seismic trace of the field to a class, itself linked to a group of wells and thus to a vertical proportion curve (Johann et al, 1996, Fournier and Derain 1995, Fournier 1995). The result of such an analysis is a zonation of the studied field,

with an associated probability of assignment of the traces to the different classes. In other cases, this zonation may also be defined using a conceptual geological model which allows to recognize different depositional environments in different areas of the field, and their lateral extension, again associated to an uncertainty coefficient.

In other cases, the 3D block of proportions can be computed directly from the well data, if the wells are considered to be representative of the behaviour of the reservoir, or from initial vertical proportion curves (computed from the wells or imported from analogue examples). The principle remains to compute smooth or mosaic 3D functions of lithofacies proportions on block support, using more or less refined geostatistical methods, as illustrated on the next diagram:

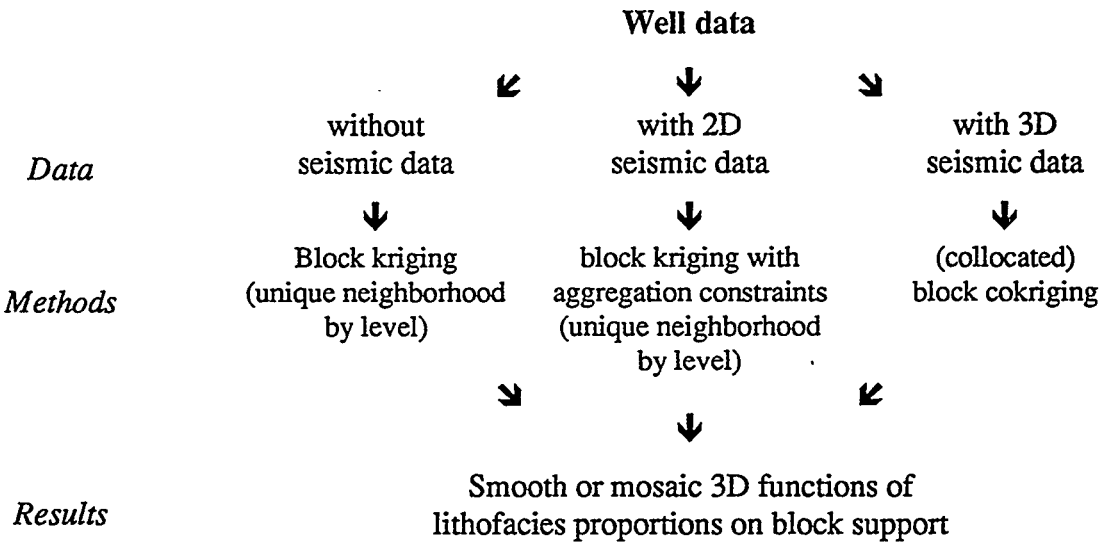

The estimation of the proportions from the well data or from initial vertical proportion curves may be done using an ordinary kriging method. If an additional information is available, derived from seismic or from a geological model, the kriging system is written with an additional constraint on the sum of the proportions of the facies in each cell of the 3D proportions block. Moreover, stratigraphic modelling techniques provide some quantitative maps of mean

lithofacies thicknesses which may be used as external drift for the proportions estimations (Joseph et al., 1996). In the same way, statistical calibration techniques of seismic attributes allow now in some cases to convert seismic attributes into proportions or thicknesses of lithofacies.

The different techniques may be mixed, and representative vertical proportion curves may be attributed in some zones, and estimated by kriging in other parts, taking into account wells data and these eventual additional external constraints.

The choice of the methodology mainly depends on the available data (Mouliere et al, 1996). The computation by zones is specific to the cases when the information, geological as well as derived from seismic is qualitative, or when the transition between the reservoir zones is very rapid. Generaly, the kriging methods and the use of these 3D functions of lithofacies proportions allow to obtain more realistic results than those obtained with the stationary algorithm. It is to notice that their estimation from initial vertical proportion curves is very flexible, as it allows to introduce some qualitative knowledge on the field, even if it is combined with a quantitative information.

2-3- Simulations

The non stationary algorithm is an extension of the stationary one. In the non stationary case, the thresholds which are used to truncate the gaussian function are now dependant on the location of the considered point of computation. In this option, the transition between lithofacies may vary and does not necessarily follow the sequential order of the facies.

Once the lithofacies grids are built, the process remains the same as in the stationnary case to translate the geological information into petrophysical values, and then to homegeneize these properties into coarser cells which will be the framework for the fluid flow simulations.

Porosities and permeabilities are assigned to the fine scale grid, according to experimental values distributions and regression laws depending on each lithofacies. The last step is to define a reservoir grid and to scale-up the petrophysical properties in this coarser grid, using algebraic and numeric methods, in order to get an adequate grid for fluid flow computations.

It seems obvious that the more the lithofacies simulations will be realistic, the better the petrophysical properties heterogeneities will be constrained, and the impact on the final reservoir grid properties will be important. The following application will illustrate this methodology.

3 - Applications on the Mesa Verde example

3-1- stationary simulations

This case study is extracted from an outcrop database collected in the MesaVerde area in the framework of a joined Elf, GDF, IFP and Total project. The geological interpretation of the 3D outcrop (campanian series of Colorado) in terms of chronostratigraphy and lithostratigraphy allowed to define the main genetic units, their limits and reference levels, and the lithofacies corresponding to three main depositional environments (Eschard et al., 1993, Homewood et al., 1992). For the demonstration purpose, we focussed on a seaward stepping wedge of littoral sediment, which corresponds to an overall progradation punctuated by transgressive events. In such a sequence, the lateral transition between coastal plain, foreshore, shoreface and offshore presents a typical non-stationary configuration. The conceptual seaward stepping stacking pattern model is shown on figure 1.a. After the extraction from the data base of ten representative wells from field sections and geological interpretation, we first used the stationary algorithm to simulate the 3D block, as a single relative unit, named PLO, for Point Lookout Sandstone.

The wells have been described using seven lithofacies, corresponding to two main depositional environments, a marine sequence (offshore, upper and lower shoreface, foreshore) and a

continental sequence (washover, channels and floodplain shales). From this numerical database, the main geostatistical parameters have been quantified, the vertical proportion curve, shown on figure 4, the horizontal and vertical variograms, and the lithofacies simulations performed.

It is to notice that the vertical proportion curve is also a powerful tool which helps to control the geological interpretations and hypotheses. In figure 4 for example, the main geological features of the studied unit may be analysed, with a transition of the sedimentary system from a marine pole to a continental pole.

The display of a lithofacies block diagram on figure 1.b shows that the results may be considered as globally correct, when compared to the conceptual geological model. This is due to overestimated values of the horizontal ranges of the variogram model, in order to recover the main bodies continuities. But in details, the real geometry of the clinoforms and of the shales is smoothed when compared to the real case, and most of the permeability barriers of the reservoir are not simulated, especially in the north-south direction.

Petrophysical values have then been attributed to each cell of this 3D block using a model which has been defined for each lithofacies using core analyses (figure 1.c shows the same block informed with petrophysical values). Then a scaling-up has been computed on a coarser grid as displayed on figure 1.d.

3-2 Comparison between stationary and non stationary simulations

In order to compare both approaches, we performed an other set of simulations, using the non stationary approach, from the same dataset. We computed 3D blocks of proportions as the one displayed on figure 5, using a set of six initial vertical proportion curves, which have been kriged level by level in order to fill the 3D block of proportions. This figure 5 may be described as an horizontal map of the unit PLO, which has been divided into regular blocks, each of them being filled with a vertical and local proportion curve computed using a block kriging with aggregation

constraints method. If we compare on figure 6 the same north-south cross section, obtained using the two algorithms, stationary and non stationary, it appears that the result is now much closer from the conceptual model if we use the non stationary approach than if we use the stationary one, and respects the main facies transitions.

After attribution of the same petrophysical model on both images and scaling-up on a simple reservoir mesh, the comparison of the horizontal permeabilities maps on a chosen layer of the reservoir (layer 7, figure 7.a, from a stationary model, figure 7.b, from a non stationary model) evidences the differences in the final results. This display points out the importance of the initial fine scale model heterogeneities on the reservoir model, and thus on the fluid flow simulations. With the stationary approach, the permeability heterogeneities are scattered throughout the field, whereas with the non stationary simulation, a trend is evidenced from the low permeabilities in the southern part of the field to the higher permeabilities in the north.

4 - Conclusions

New algorithms in geostatistical simulations allow now to better integrate more and more external constraints and data in order to obtain more precise images of a reservoir under investigation. In particular, the use of 3D functions of proportions of lithofacies instead of a single vertical proportion curve allows to take into account and to integrate both qualitative or quantitative informations derived from seismic or geological models.

The use of the non stationary algorithm in the lithofacies simulation of a reservoir becomes very powerful as the heterogeneities are more accurately simulated. The scaling-up process will take into account the petrophysical properties heterogeneities at the fine scale, which are directly linked to the lithofacies ones.

References Cited:

Doligez B., Ravenne C., Lemouzy P., Galli A., 1992: Une méthodologie pour une étude intégrée des réservoirs: des données de puits aux simulations d'écoulement en utilisant des outils géostatistiques. Pétroles et Techniques, n.372, p.43-47.

Eschard R., Doligez B., Rahon D., Ravenne C., Leloch G., and Heresim Group, 1991: A new approach for reservoirs description and simulation using geostatistical methods. In proceedings: Advances in resrvoir technology, characterization, modelling and management, Edinburg.

Eschard R., Tveiten B., Desaubliaux G., Lecomte JC., Van Buchem F., 1993: High resolution sequence stratigraphy and reservoir prediction of the Brent group (Tampen Spur area) using an outcrop analogue (Mesaverde group, Colorado). In: Subsurface reservoir characterization from outcrop observations. R.Eschard, B.Doligez Eds, Editions Technip, Paris, p.35-52.

de Fouquet C., Beucher H., Galli A., Ravenne C., 1988: Conditional simulation of random sets. Application to an argillaceous sandstone reservoir. 3rd International Geostatistics Congress, Avignon. M.Armstrong ed: Geostatistics, v.2, Kluwer, Academic Publishers, Dordrecht, p.517-530.

Fournier F., 1995: Integration of 3D seismic data in reservoir stochastic simulations: a case study. SPE 30564.

Fournier F. and Derain J.F., 1995: A statistical methodology for deriving reservoir properties from seismic data, Geophysics, v.60, n.5, p.1437-1450.

Galli A., Guerillot D., Ravenne C., and Group Heresim., 1990: Combining geology, geostatistics and multiphase flow for 3D reservoir studies. In: 2nd European Conference on the Mathematics of Oil recovery, Arles. D.Guerillot and O.Guillon eds, Editions Technip, p.11-19.

Homewood P., Guillocheau F., Eschard R., Cross T., 1992: Corrélations haute résolution et stratigraphie génétique: une démarche intégrée. Bull. Elf Acquitaine Production, F-31360, Boussens.

Johann P., Fournier F., Souza O., Eschard R., Beucher H., 1996: 3D stochastic modeling constrained by well and seismic data on a turbidite field. SPE 36501.

Joseph P., Eschard R., Doligez B., Granjeon D., 1996: 3D stratigraphic modelling, a new way to constrain geostatistical reservoir simulation. EAEG Amsterdam.

Matheron G., Beucher H., de Fouquet C., Galli A., Ravenne C., 1987: Conditional simulation of the geometry of Fluvio-Deltaic reservoirs. SPE 16753.

Mouliere D., Beucher H., Hu L.Y., Fournier F., Terdich P., Melchiori F., Grifi G., 1996: Integration of seismic derived information in reservoir stochastic modeling using truncated gaussian approach. Geostatistical Congress of Wollongong, Australia.

Ravenne C., Galli A., Beucher H., Eschard R., Guérillot D., and Heresim group, 1990: Outcrop studies and geostatistical modelling of a middle Jurassic Brent analogue. In proceedings of: The European Oil and Gas conference, Altavilla Milicia, Palermo, Sicily, Italia.

Ravenne C. et Beucher H., 1988: Recent development of sedimentary bodies in a fluvio-deltaic reservoir and their 3D conditional simulations. SPE 18310.

Figure captions:

Figure 1: the main steps of the Heresim methodology (stationary simulation)

Figure 2: example of computation of a vertical proportion curve

Figure 3: truncation of a gaussian function. Comparison between stationary and non stationary approach.

Figure 4: experimental vertical proportion curve computed for the PLO unit

Figure 5: 3D proportion block computed for the PLO unit from initial proportion curves

Figure 6: comparison between the stationary and the non stationary approach on a north-south lithological section of the PLO unit.

Figure 7: comparison of scaled-up horizontal permeability maps resulting from the stationary and non stationary approaches.

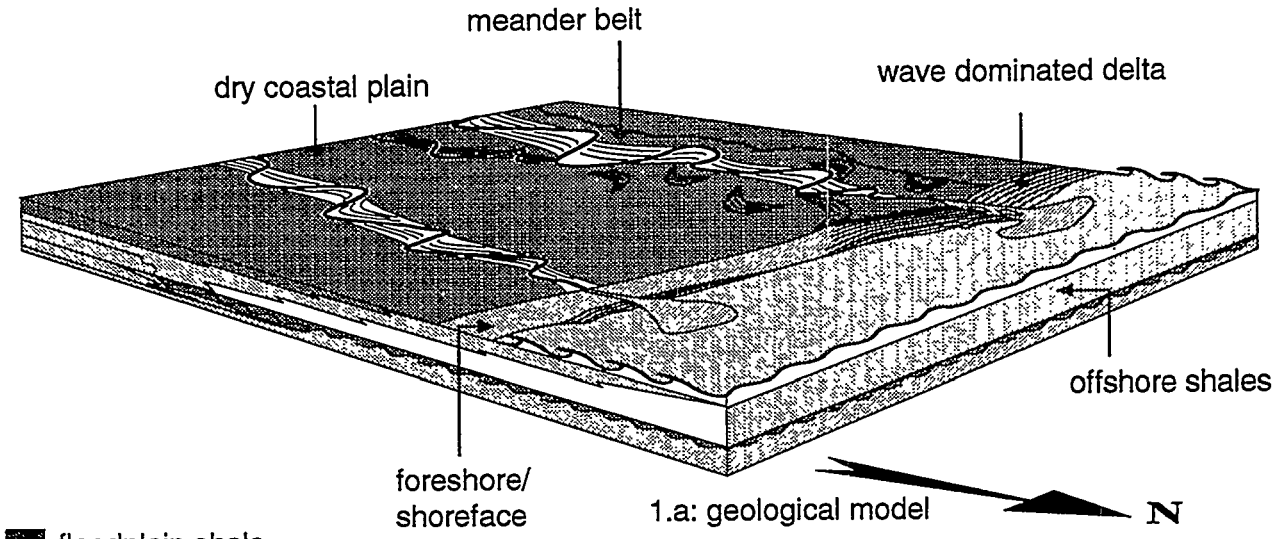

1.a: geological model

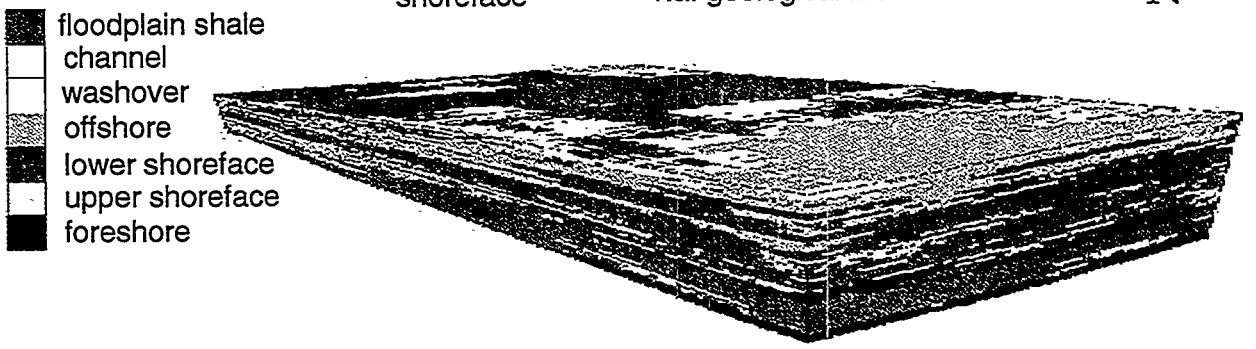

1.b: lithofacies simulation

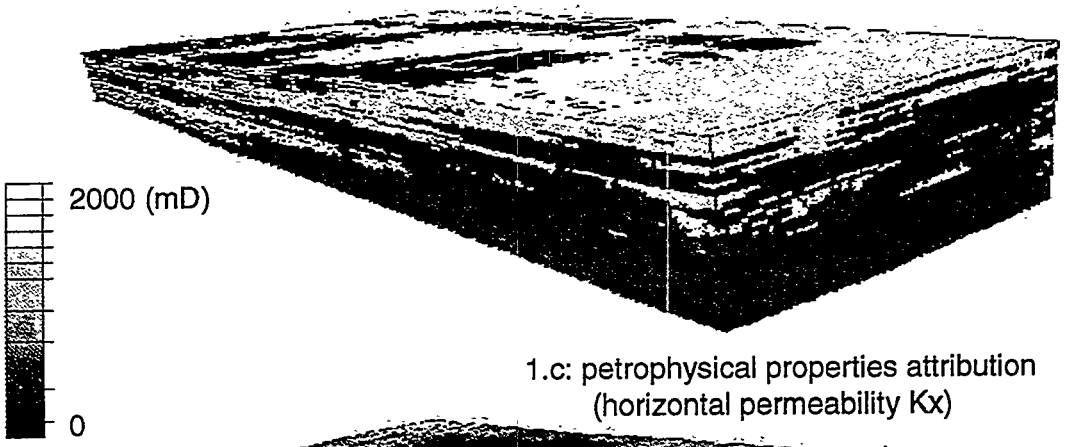

1.c: petrophysical properties attribution
(horizontal permeability Kx)

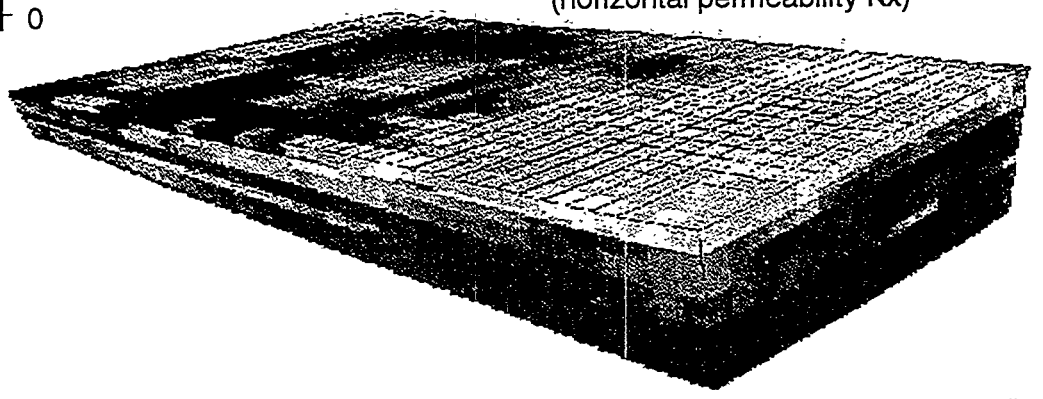

1.d: scaling-up (Kx)

figure 1

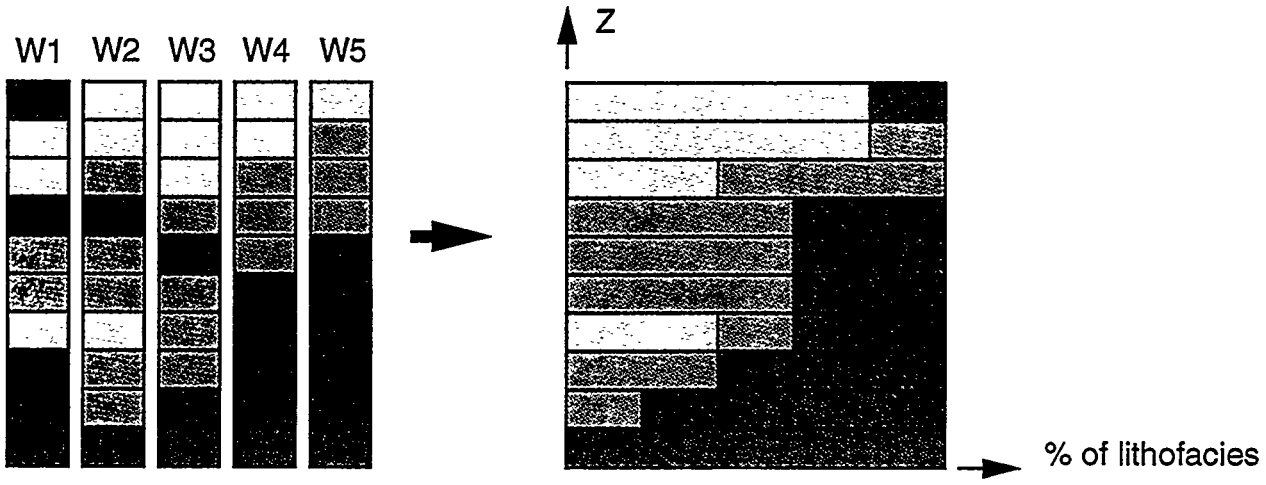

example of computation of a vertical proportion curve from five wells

figure 2

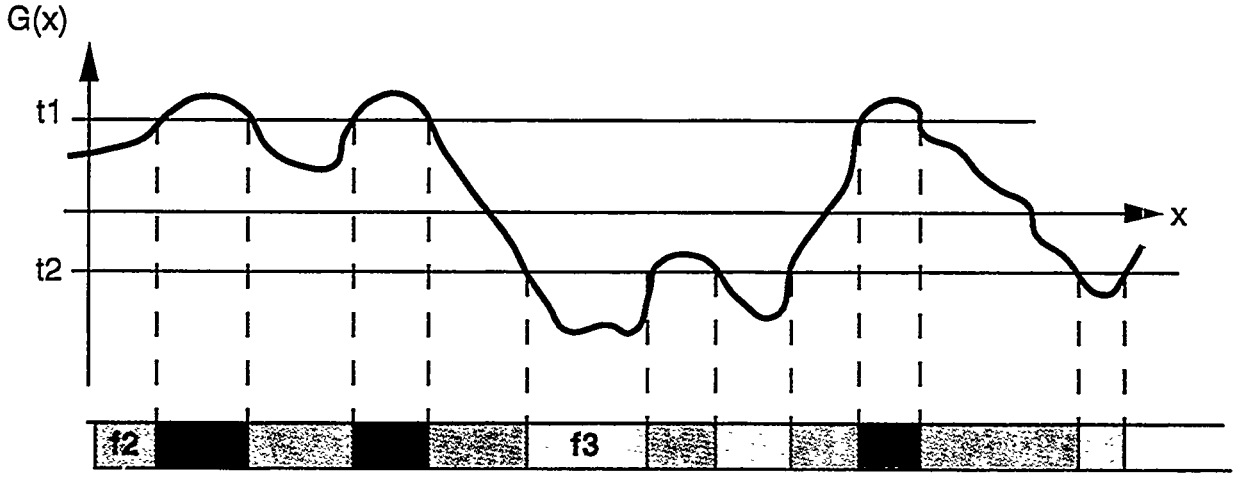

3.a: stationary case-
truncation of a gaussian function by constant thresholds t1 and t2,
and associated lithofacies f1, f2 and f3

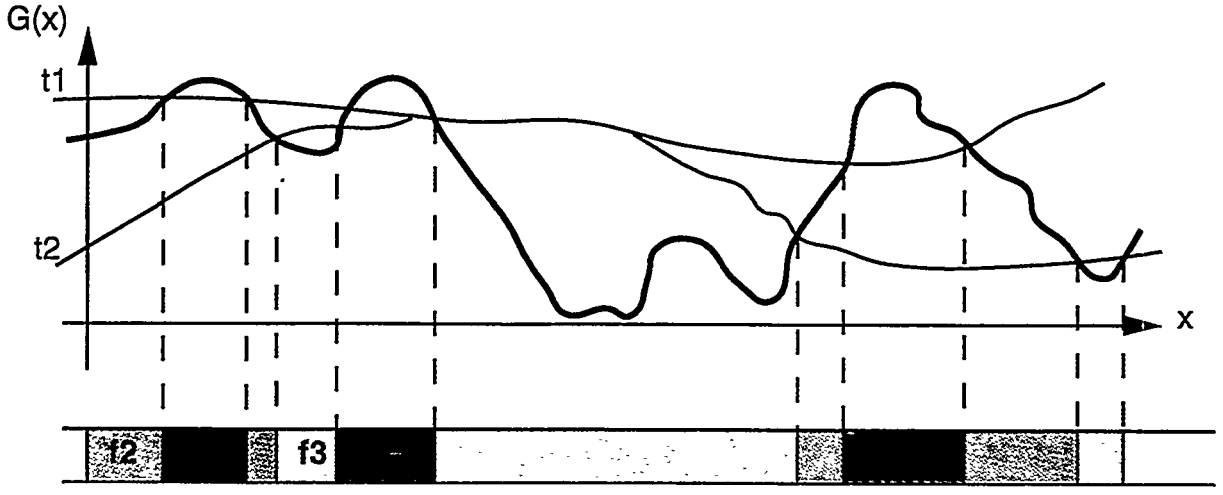

3.b: non stationary case-
truncation of a gaussian functionby thresholds t1(x) and t2(x),
and associated lithofacies f1, f2 and f3

figure 3

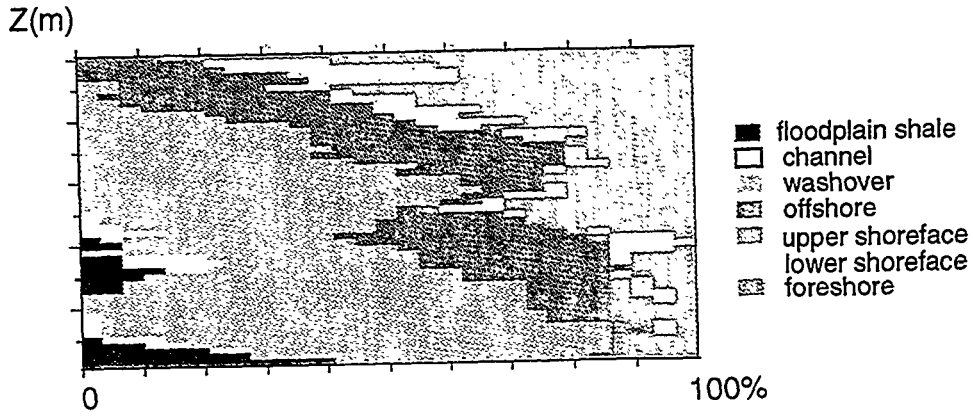

figure 4

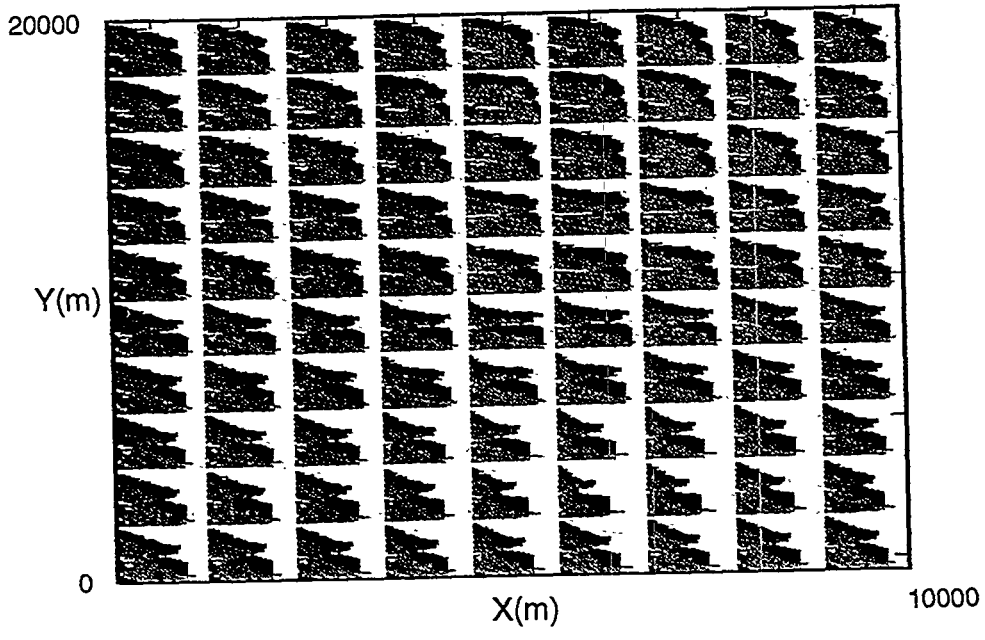

figure 5

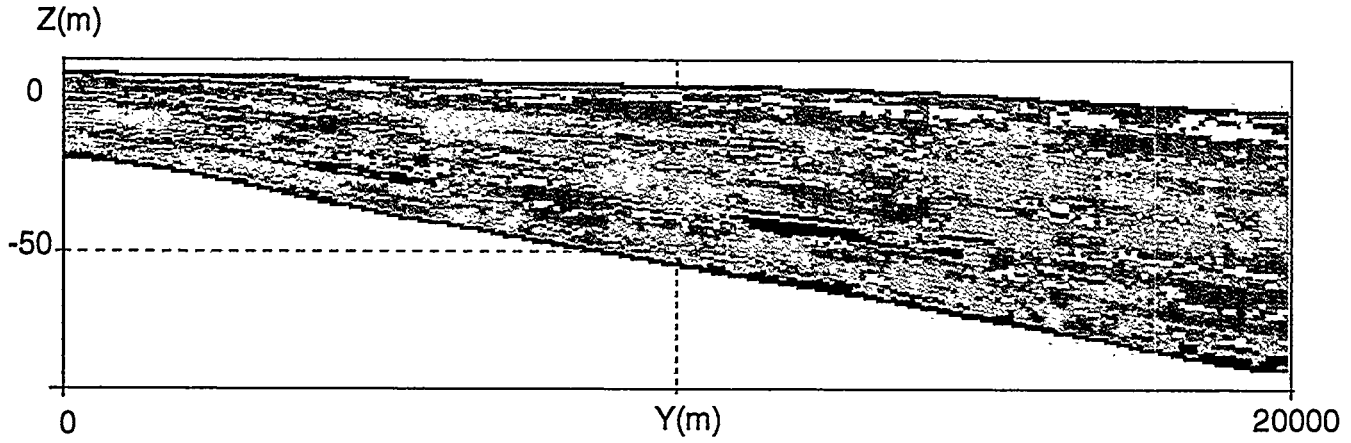

stationary simulation - NS section

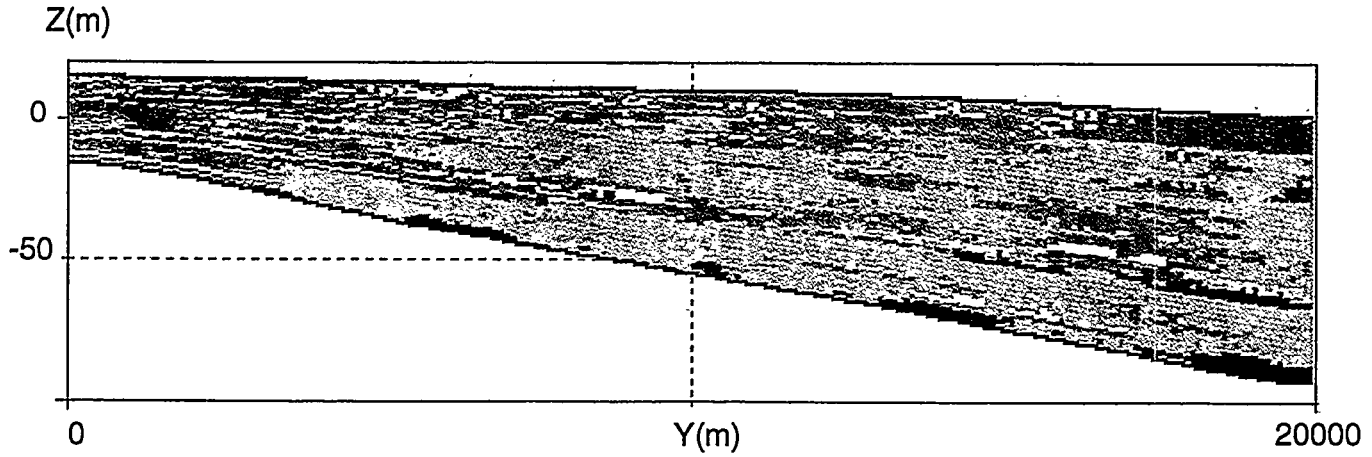

non stationary simulation - NS section

figure 6

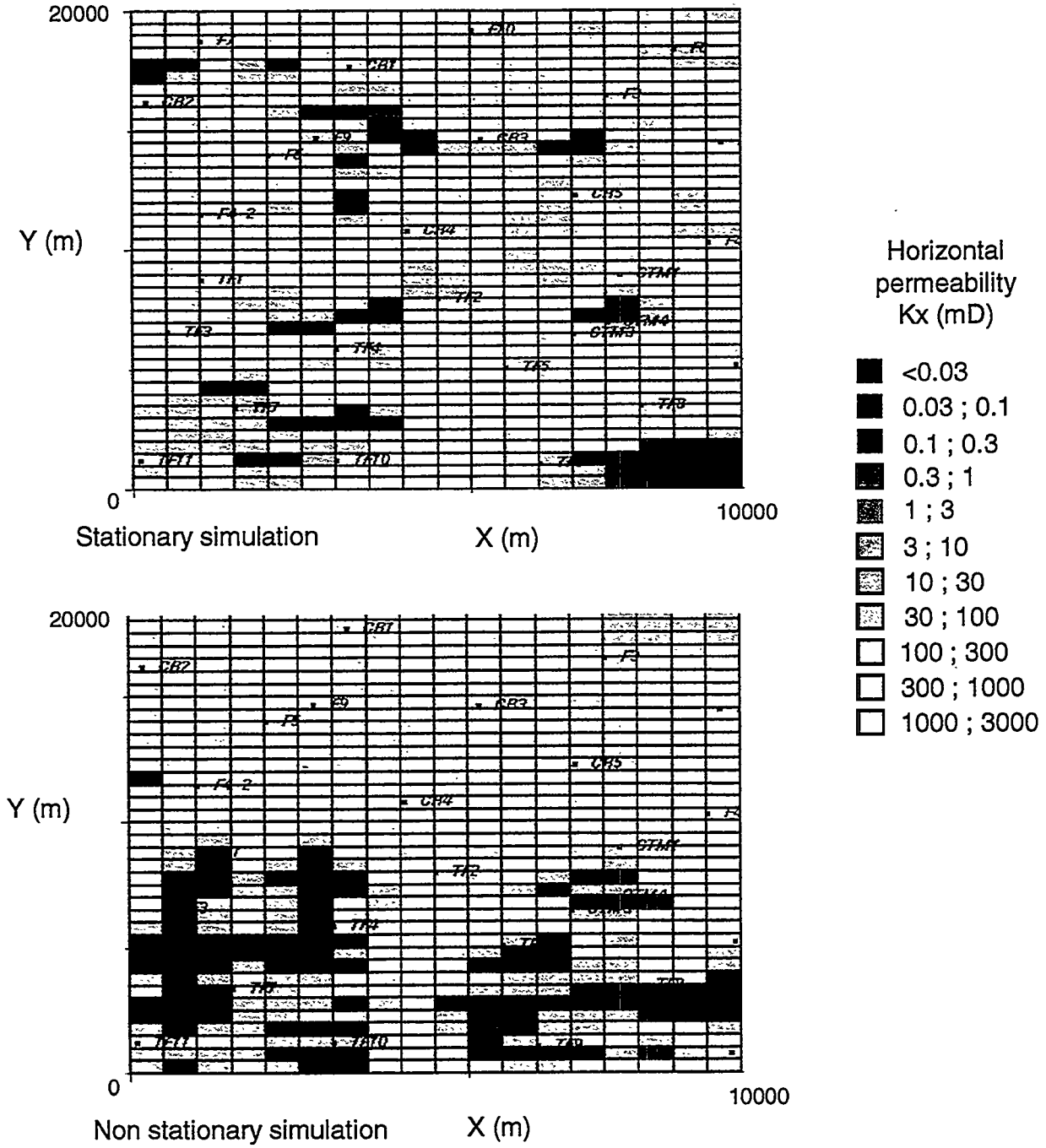

Scaled-up horizontal permeabilities - layer 7

figure 7

Facies Architecture of the Bluejacket Sandstone in the Eufaula Lake Area, Oklahoma: Implications for the Reservoir Characterization of the Bartlesville Sandstone

Liangmiao Ye and Kexian Yang
Department of Geosciences, The University of Tulsa, Tulsa, Oklahoma

Acknowledgments

The results presented here were partially supported by an industry-government partnership funded under US Department of Energy Contract No. DE-FC22-93BC14951 and by the Research Office of The University of Tulsa under Student Research Grant Program. We are grateful to Amoco Production Company Technology Center, Tulsa for allowing access to their microresistivity imaging interpretation facility, and core analysis facilities. We also thank D. Kerr and R. Tillman who provided valuable insights and helpful discussion.

Abstract

Outcrop studies of the Bluejacket Sandstone (Middle Pennsylvanian) provide significant insights to reservoir architecture of the subsurface equivalent Bartlesville Sandstone. Quarry walls and road cuts in the Lake Eufaula area offer excellent exposures for detailed facies architectural investigations using high-precision surveying, photo mosaics. Directional minipermeameter measurements are being conducted. Subsurface studies include conventional logs, borehole image log, and core data.

Reservoir architectures are reconstructed in four hierarchical levels: multi-storey sandstone, i.e. discrete genetic intervals; individual discrete genetic interval; facies within a discrete genetic interval; and lateral accretion bar deposits. In both outcrop and subsurface, the Bluejacket (Bartlesville) Sandstone comprises two distinctive architectures: a lower braided fluvial and an upper meandering fluvial.

Braided fluvial deposits are typically 30 to 80 ft thick, and are laterally persistent filling an incised valley wider than the largest producing fields. The lower contact is irregular with local relief of 50 ft. The braided-fluvial deposits consist of 100-400-ft wide, 5-15-ft thick channel-fill elements. Each channel-fill interval is limited laterally by an erosional contact or overbank deposits, and is separated vertically by discontinuous mudstones or highly concentrated mudstone interclast lag conglomerates. Low-angle parallel-stratified or trough cross-stratified medium- to coarse-grained sandstones volumetrically dominate. This section has a blocky well log profile.

Meandering fluvial deposits are typically 100 to 150 ft thick and comprise multiple discrete genetic intervals. Channel-fill facies width/thickness ratio for a given discrete genetic interval is from 30 to 60. Channel-fill facies successions include: a basal trough cross-stratified, medium-grained sandstone; a medial epsilon cross-stratified fine-grained sandstones with numerous mudstone drapes; an upper mudstone. Well log profile is typically a serrated bell shape. Splay facies is up to 20 ft thick and consists of ripple-stratified and lesser trough cross-stratified, medium-grained sandstones separated by laterally persistent thin mudstones. Floodplain mudstones laterally and vertically segment, with the exception of very limited areas, channel-fill and splay sandstones into reservoir compartments.

Introduction

The Middle Pennsylvanian Bartlesville (Bluejacket) Sandstone extends from southeastern Kansas across the northeastern Oklahoma platform and into the Arkoma foreland basin. The Bartlesville Sandstone has been a major oil producer in Oklahoma for more than 90 years, producing more than 2 billion bbl oil since the discovery of a number of fields back to the early 1900's. However, estimates of recovery of OOIP are as low as 20% for many Bartlesville-producing fields/reservoirs, despite post-primary recovery attempts (Welch, 1989).

The reason for poor recoveries is clearly attributed to complex reservoir architecture, which is very difficult to properly characterize with conventional subsurface information only. Static and dynamic data obtained from analogous outcrop is critical to reconstructing reliable reservoir models and developing effective reservoir management strategies.

This study offers detailed description of Bluejacket Sandstone road cuts and quarry walls in the Eufaula Lake area and characterization of selected reservoir units in Glenn Pool field, Oklahoma. The intent is to illustrate the usefulness of outcrop information to proper subsurface reservoir modeling.

A. Regional Depositional Framework

This section highlights key points regarding the regional depositional framework in both earlier view and our new interpretation, serving as background information for understanding the detailed study.

Extensive previous geological studies on the Bartlesville Sandstone have been conducted since late in the last century. Most recent systematic study of the depositional origin and framework was completed in late 1960's (Saitta, 1968; Saitta and Visher, 1968; Phares, 1969; Visher and Saitta and Phares, 1971), which concluded that the Bartlesville/Bluejacket Sandstone is part of a large fluvial-deltaic complex deposited in essential as a single regressive interval (figure 1).

However, regional scale to reservoir scale investigation in both outcrop and subsurface in a area over 2000 square miles in northeastern Oklahoma reveals that Bartlesville Sandstone is a mainly fluvial incised valley-fill deposited in a transgressive manner from a lower braided fluvial to an upper tidal-influenced meandering fluvial. Sequence stratigraphic analysis illustrates that the whole Bartlesville Sandstone incised valley-fill section consists of two sequence stratigraphic architectural elements: 1) the lower lowstand system tract, 40-150 ft, composed of braided fluvial deposits and distal lowstand delta; 2) the upper transgressive system tract, 70-100 ft, composed of meandering fluvial, estuarine tidal, and shallow marine deposits. The regional Inola Limestone marker, capping the Bartlesville Sandstone interval, is equivalent to a condensed section which represents maximum flooding (figure 2).

This new interpretation is supported by following observations:

1. Outcrop survey illustrates that a type-1 sequence boundary exists at the base of Bartlesville Sandstone, indicated by subaerial erosion of underlying Savanna Shale and basinward facies shift from pure marine shale below to braided fluvial deposits above. Core facies and log facies interpretation validate the facies shift.

2. Well log correlation shows Bartlesville Sandstone thickens at the expense of the Savanna Shale. The incised valley extends from north to south over 120 miles within Oklahoma, and is 4-5 miles wide in

Washington County to over 40 miles wide in the Eufaula Lake area. The thickness of Bartlesville Sandstone interval varies from 120-250 ft within the valley to less than 30 ft outside the valley.

3. Well log analysis observes a usually very sharp base, a interval with blocky log response at the lower part, and a fining-upward sequence at the upper part of Bartlesville Sandstone throughout the study area. Core and outcrop facies interpretation indicates that sedimentary facies transition upwards from braided fluvial, to meandering, to tidal-influenced meandering, to tidal estuarine and shallow marine deposits (figure 2). Same sequence of facies variation may be observed horizontally from north to south. This pattern of facies association clearly indicates that Bartlesville Sandstone is deposited in a transgressive manner. The regional Inola Limestone marker, capping the Bartlesville Sandstone interval, represents maximum flooding.

B. Study Areas

Self Unit

Self Unit is a 160 acre tract in southern part of Glenn Pool oil field, which was discovered in 1905 about 20 miles south of Tulsa, Oklahoma (The Bartlesville Sandstone here is therefore called Glenn Sand, Kuykendall and Matson, 1992). The Self Unit has been developed with 82 wells drilled to date. Data available includes: 41 conventional logs, 1 microresistivity borehole image log, 1 whole core, and porosity and permeability measurements from 9 cores.

Glenn Sand in Self Unit is about 130 ft thick. Detailed well log correlation resulted in the division of Glenn Sand into 6 discrete genetic intervals (explained later) descending from A to F. Core and log facies interpretation shows that DGI A through E are meandering fluvial channel-fill and crevasse splay sandstones and floodplain mudstones, and F braided fluvial sandstones.

Tract 7 and Adjacent Area

Tract 7 and adjacent area, located about one mile north of Self Unit, covers about 1000 acres. About 300 wells have been drilled. However, only 119 logs are available for study. As what was done in the Self Unit, the Glenn Sandstone is divided into 7 DGIs descending from A to G. DGI G is absent in the Self Unit because of the base relief of the incised valley. Log facies analysis indicates that DGI A through E again are meandering fluvial channel-fill and crevasse splay sandstones and floodplain mudstones. DGI F and G are braided fluvial sandstones.

Figure 3 shows the location of Glenn Pool field, Self Unit, and Tract 7 and adjacent areas.

Checotah Road Cut

This is a road cut surface on the Oklahoma Highway 266, 6.5 miles east of Checotah. The road cut extends 680 ft east-west, and is about 50 ft tall. Being normal to the general paleo-current direction (north to south), the road cut exposes a transverse cross section. With the dip of 50-60 degree, the road cut is mostly accessible for detailed investigation. Detailed facies interpretation was performed based on observations on the lithology, physical structures, and current orientations. Spatial configuration of facies element boundaries were measured using an infra-based precision survey system.

Comparative study of outcrop and subsurface equivalent leads to a believe that this road cut is sedimentologically analogous to middle-upper part of the Glenn Sand.

Eufaula Dam Cliff

This is a vertical cliff at the north end of Eufaula Dam. The cliff includes two segments--west leg, extending northwest-southeast, 70 ft tall and 850 ft long; and east leg, extending approximately southwest-northeast, 60-70 ft tall and 400 ft long. Both legs are oblique to general north-south flow direction. For this road cut, detailed observations can be done only for the lower part of the section because of limited accessibility. However, architectural element boundaries down to level of single channel-fill facies can be identified and surveyed precisely from distance.

This section, composed of braided fluvial deposits, is believed to be sedimentologically analogous to lower (DGI F and G) Glenn Sand reservoirs. Location of these two outcrops is shown on figure 1.

Reconstruction of Reservoir Architectures

One important concept in modern reservoir characterization is that reservoir architectures are of hierarchical features (Miall, 1985; Jordan and Pryor, 1992). A fluvial pay zone like Bartlesville Sandstone usually consists of multiple DGIs, one DGI is composed of several different facies, and one facies is made up of different subfacies and/or facies elements, and so on. Proper documentation of heterogeneity at each level of reservoir architectures is critical to better management planning for mature reservoirs.

A. Facies Architecture Hierarchy

Level 1: Multi-Storey Sandstone- Discrete Genetic Intervals

DGI (discrete genetic interval) is defined as a collection of contiguous facies that were deposited in a brief discrete increment of time (Kerr and Jirik, 1990). For the case of fluvial Glenn Sand, one DGI is equivalent to one fluvial rhythmic sequence which consists of all channel-fill and associated facies deposited in the same time period.

First level of hierarchical reservoir architectures deals with the stacking pattern of multiple discrete genetic intervals. Figure 4 (a) shows the vertical relationship of different DGIs surveyed from Checotah road cut. Eight DGIs are present here. One DGI basically represents one channel sequence and its equivalent deposits. For most of the DGIs, the upper part (i.e. upper channel subfacies and floodplain mudstone) has been eroded by overlying DGIs. Middle channel subfacies are mostly preserved except for DGI 5 and 6. Horizontally, DGI 8 is truncated by DGI 7, and DGI 4, 5, 6 are truncated by DGI 3. Top of DGI 7 is partially eroded by DGI 3. All these indicate that different discrete genetic intervals are not well separated vertically. Even though the rip-up clast shale, mud pebbles common on the bottom of channel-fill may function as flow barrier/baffles between different DGIs.

In comparison, vertical separation of different DGIs are much more evident in the subsurface. Figure 4 (b) is a cross section cut in the middle of Self Unit to illustrate that at most cases, different DGIs of Glenn Sand are separated by 1-5 ft floodplain mudstones. However, one DGI cutting into the other is observed in the subsurface too.

Other important observation in this level of hierarchical architectures is that the thickness of each DGI is decreasing upwards for both outcrop and subsurface, as shown in figure 5. For Glenn Sand reservoirs in Self Unit, maximum thickness of one DGI decreases upwards from 33 ft of DGI E to 22 ft of DGI A. For Checotah road cut, thickness of a individual DGI decreases upwards from 23 ft (DGI 8) to 7 ft (DGI 1). Thinning upward in both outcrop and subsurface implies one aspect of their similarities and also supports the interpretation that Bartlesville Sandstone is deposited in a transgressive manner.

Level 2: Individual Discrete Genetic Interval

As stated earlier, DGI (discrete genetic interval) is defined as a collection of contiguous facies that were deposited in a brief discrete increment of time (Kerr and Jirik, 1990). From sedimentological point of view, one DGI represents a brief episode of sedimentation which deposited a genetically related 3-D volume of sedimentary rocks. From oil development point of view, DGI represents the smallest subsurface mappable unit. DGI concept is critical for detailed and accurate reservoir characterization.

For the fluvial Bartlesville Sandstone, one DGI is commonly made of three facies: channel-fill sandstone, splay sandstone, and floodplain mudstone. These three facies are identified in all meandering DGIs recognized in the subsurface (figure 6 & 7). In the outcrop (figure 4-a), splay deposits only appear in DGI 2 and 6, floodplain mudstone is recognized in DGI 5 only. The lower presence of floodplain mudstone and splay sandstone in outcrop is probably due to the 2-D nature of the road cut, and their low volume percentages.

The relationship between these three facies elements are better shown in the facies map constructed for the Glenn Sand reservoirs. As shown in these maps (figure 6, 7), channel fill facies constitutes the main framework of the system. Channels extend generally from north to south, which is consistent to regional paleo-current direction. Channels may bifurcate or merge as they proceed. Splay is deposited as a result of bank-breaking during flooding, thus develops on the margin of channels and spreads outward in a fan-like shape. Floodplain mudstone occurs between channels and/or splays, or on top of channels. Therefore floodplain mudstones laterally and vertically segment channel-fill and splay sandstones into reservoir compartments.

Level 3: Facies Within a Discrete Genetic Interval

Third level of hierarchical reservoir architectures deals with individual channel-fill, splay and floodplain facies. Figure 8 are the first-hand description of these facies on both outcrop and cores of Glenn Sandstone.

1. Meandering Channel-Fill Facies

Checotah road cut and upper part of Glenn Sand are mainly composed of meandering channel-fill deposits, which are characterized by: a general fining-upward texture; upward decrease in scale of physical sedimentary structures; upward increase in proportion of mudstone interbeds. In the core and outcrop, channel-fill facies were subdivided into:

Lower channel-fill subfacies: well to moderately sorted, medium-grained sandstone with medium-scale (2 to 8 inch) cross stratification. Mudstone drapes common on cross strata. Rip-up clast shale and mud pebbles commonly occur on the bottom part.

Middle channel-fill subfacies: moderately sorted, lower medium-grained to poorly sorted, silty fine-grained sandstones with horizontal to low-angle parallel stratification and ripple lamination. Medium- to very thin-bedded (1 to 6 inch) mudstones to silty mudstones drape lateral accretion surfaces. Dip direction of lateral accretion surfaces rotate progressively upwards in response to the migration of lateral accretion bars.

Upper channel-fill subfacies: mudstone to silty claystone.

2. Splay Facies

Coarsening-upward texture from fine-grained to medium-grained sandstone. Upward increase in stratal thickness in lower levels only; otherwise, irregular vertical stacking of thick to thin beds (3 to 25 inch). Ripple lamination and low-angle parallel bedding dominate; medium-scale cross stratification and contorted bedding less common. Thin bedded (1 to 3 inch) mudstones interstratified with sandstones throughout.

3. Floodplain Facies

Deposited in floodplain area are usually clays, mudstone, silts, in corresponding to the relative quiet environment which characterize the floodplain environments. These lithologies usually functions as impermeable barriers to fluid flow in the reservoir.

4. Braided Channel-Fill Facies

DGI F of Self 82 core of Glenn Sand are interpreted as braided fluvial channel-fill deposits characterized by moderately to well sorted, generally structureless (but less commonly parallel-bedded), upper medium- to lower coarse-grained sandstone. In Glenn Pool field, thickness of braided fluvial deposits varies from 30 to 80 ft depending on local relief of the base contact, i.e. base of the incised valley. This section has a blocky well log profile and is laterally persistent filling the incised valley. Figure 6, 7 shows thickness pattern of DGI F and G braided sandstone in the Self Unit. Internal architectures could not be reconstructed through well log analysis because of its excellent vertical and horizontal continuity and lack of continuous mudstones or shales.

Interpretation of this massive DGI F sandstone as braided fluvial deposits was really assured by outcrop study. Similar thick-bedded, structureless rocks have been observed in the lower part of Bluejacket Sandstone outcrops in the Eufaula Dam area. These "massive" thick sandstones laterally transition to well cross-stratified and/or parallel-bedded thick sandstone in short distance; they are highly channelized, showing unidirectional paleoflow and vary greatly in thickness according to the position relative to the channel thalwegs. Figure 9 displays a outcrop section of the braided fluvial deposits. The figure indicates that braided fluvial deposits are actually made of many individual channels which are stacked together and cross-cutting each other horizontally and vertically, resulting in a widespread distribution. Each channel-fill is characterized by relatively uniform lithology and sedimentary structures.

may actually be amalgamation of more than one DGIs which can be clearly identified in outcrop but hard to be differentiated in the subsurface conditions.

3. Minipermeameter measurements of permeability are quite reliable in comparison with lab plug measurements. Its reliability, convenience and low cost allow description of very detailed level of permeability changes. Outcrop could offer excellent place for developing a database of three dimensional permeability variations.

References Cited

Jordan, D. W., and W. A. Pryor, 1992, Hierarchical levels of heterogeneity in a Mississippi river meander belt and application to reservoir systems, AAPG bulletin, V76, N10, p1601-1624.

Kerr, D., and L. A. Jirik, 1990, Fluvial architecture and reservoir compartmentalization in the Oligocene Middle Frio formation, South Texas, Gulf Coast Association of Geological Societies, V XL, 8p.

Kuykendall, M. D. and T. E. Matson, 1992, Glenn Pool field, Northeast Oklahoma platform, AAPG treatise of petroleum geology--atlas of oil and gas fields, (stratigraphic traps III), p155-188.

Leeder, M. R., 1973, Fluviatile finning-upwards cycles and the magnitude of palaeochannels", Geology Magazine, V 110, N 3, p 265-276.

Miall, A.D., 1985, Architectural-element analysis: a new method of facies analysis applied to fluvial deposits, Earth Science Review, N22, p261-308.

Phares, R. S., 1969, Depositional framework of the Bartlesville sandstone in northeastern Oklahoma, M.S. thesis, 56p, university of Tulsa.

Saitta, S., 1968, Bluejacket Formation-A subsurface study in northeastern Oklahoma: M. S. Thesis, The University of Tulsa, Tulsa, OK, 142 p.

Schumm, S. A., 1963, Sinuosity of alluvial rivers on the Great Plains, GSA Bulletin, V 74, p 1089-1099.

Saita., S., and G. S. Visher, 1968, Subsurface of the southern portion of the Bluejacket delta, A guidebook to the Bluejacket-Bartlesville sandstone, Oklahoma City Geological Society, 72p, 1968.

Visher, G. S., S. B. Saitta, and R. S. Phares, 1971, Pennsylvanian delta patterns and petroleum occurrence in eastern Oklahoma. AAPG Bulletin, V55, No.8 , p 1206-1230.

Welch, R. A., 1989, Berryhill Glenn Sand Unit, ARCO Reservoir Engineering Report.

Ye, L. and D. Kerr, 1995, Use of microresistivity image logs in the detailed reservoir architecture reconstruction of Glenn Sandstone, Glenn Pool field, northeastern Oklahoma: Transactions of the 1995 AAPG Mid-Continent Section Meeting, Tulsa, OK, Tulsa Geological Society, p 203-213.

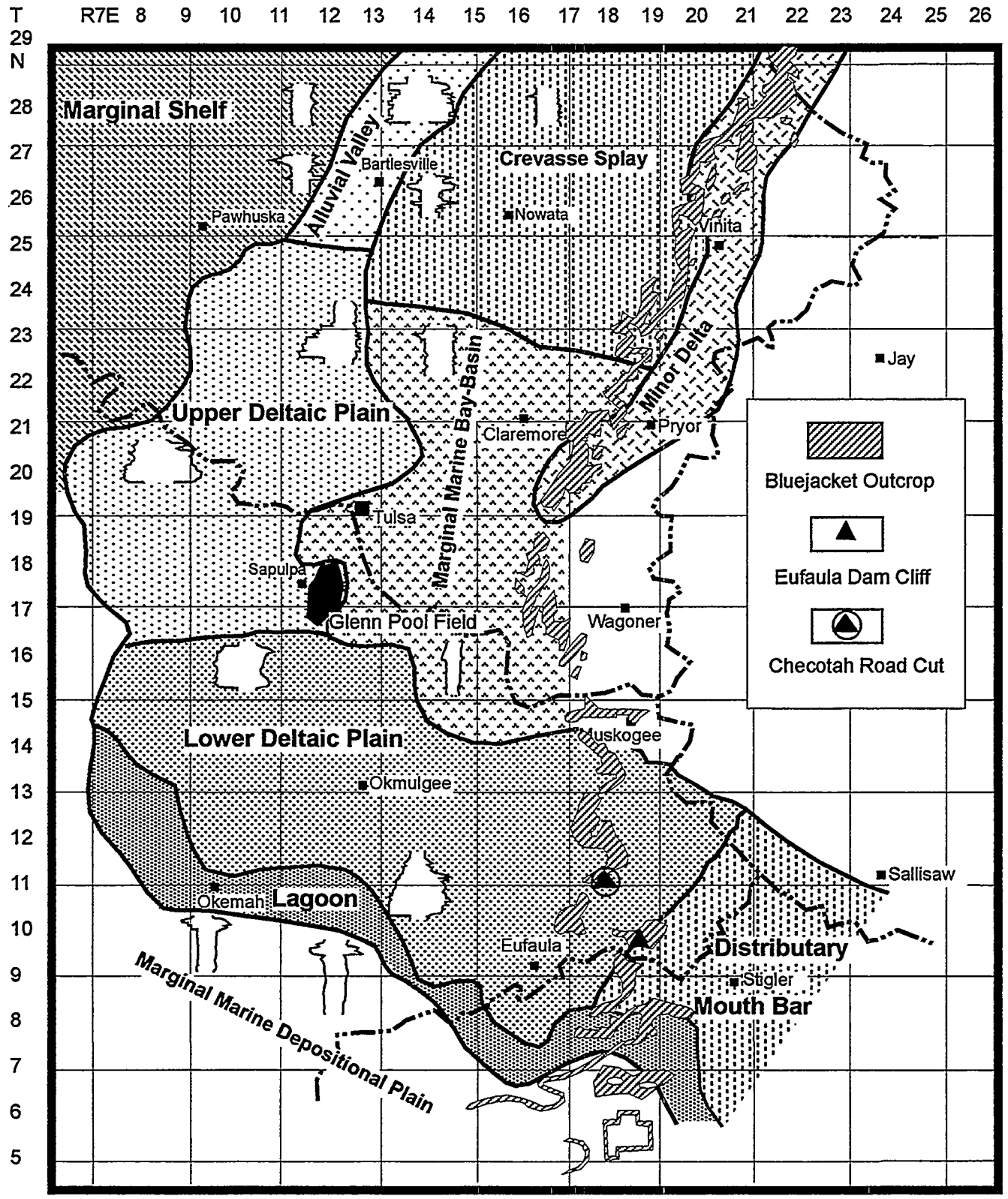

Figure 1 Well Log Patterns and Environmental Reconstruction

(modified from Visher, et al., 1971)

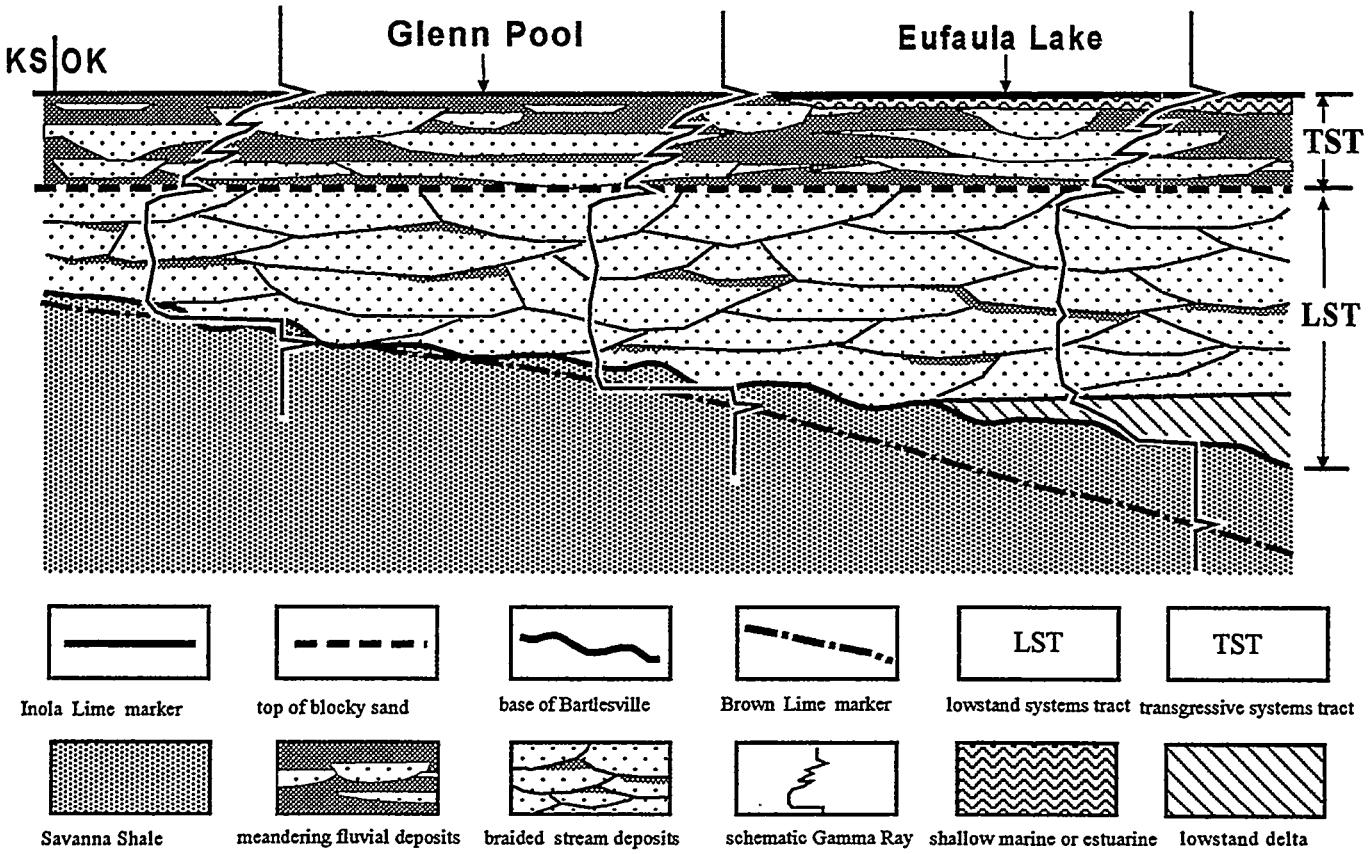

Figure 2 Regional Sequence Stratigraphic Architecture of Bartlesville Sandstone Expressed in Schematic Longitudinal Cross Section

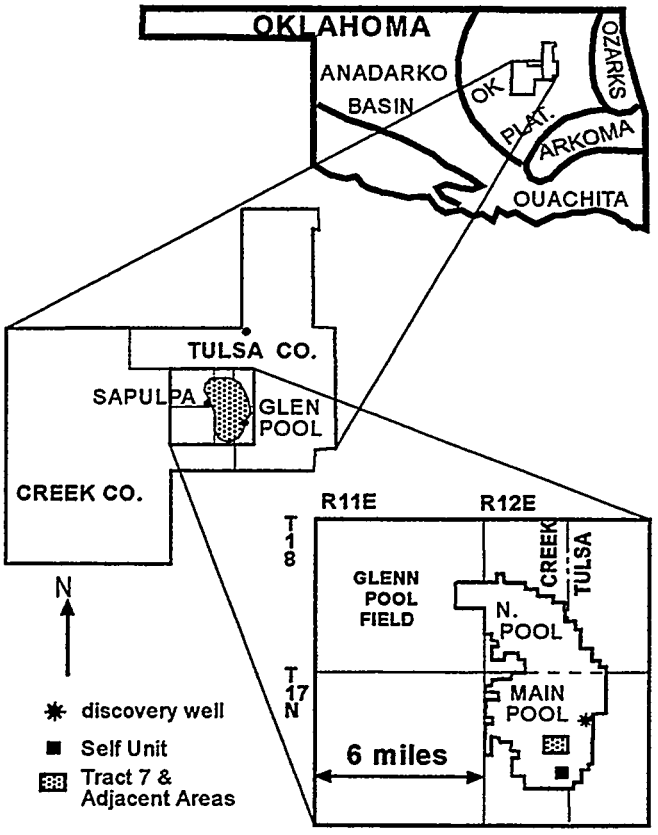

Figure 3 Geographic Location of Glenn Pool field, Self Unit, and Tract 7 and Adjacent Areas

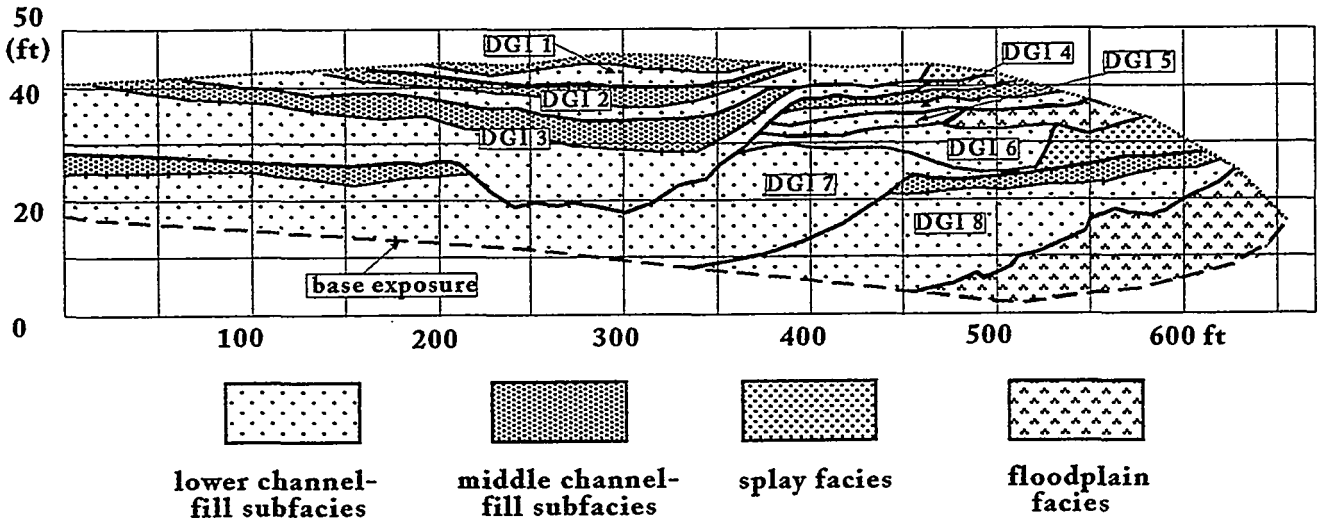

Figure 4 (a) Facies Architecture and Geometry Surveyed on Checotah Road Cut

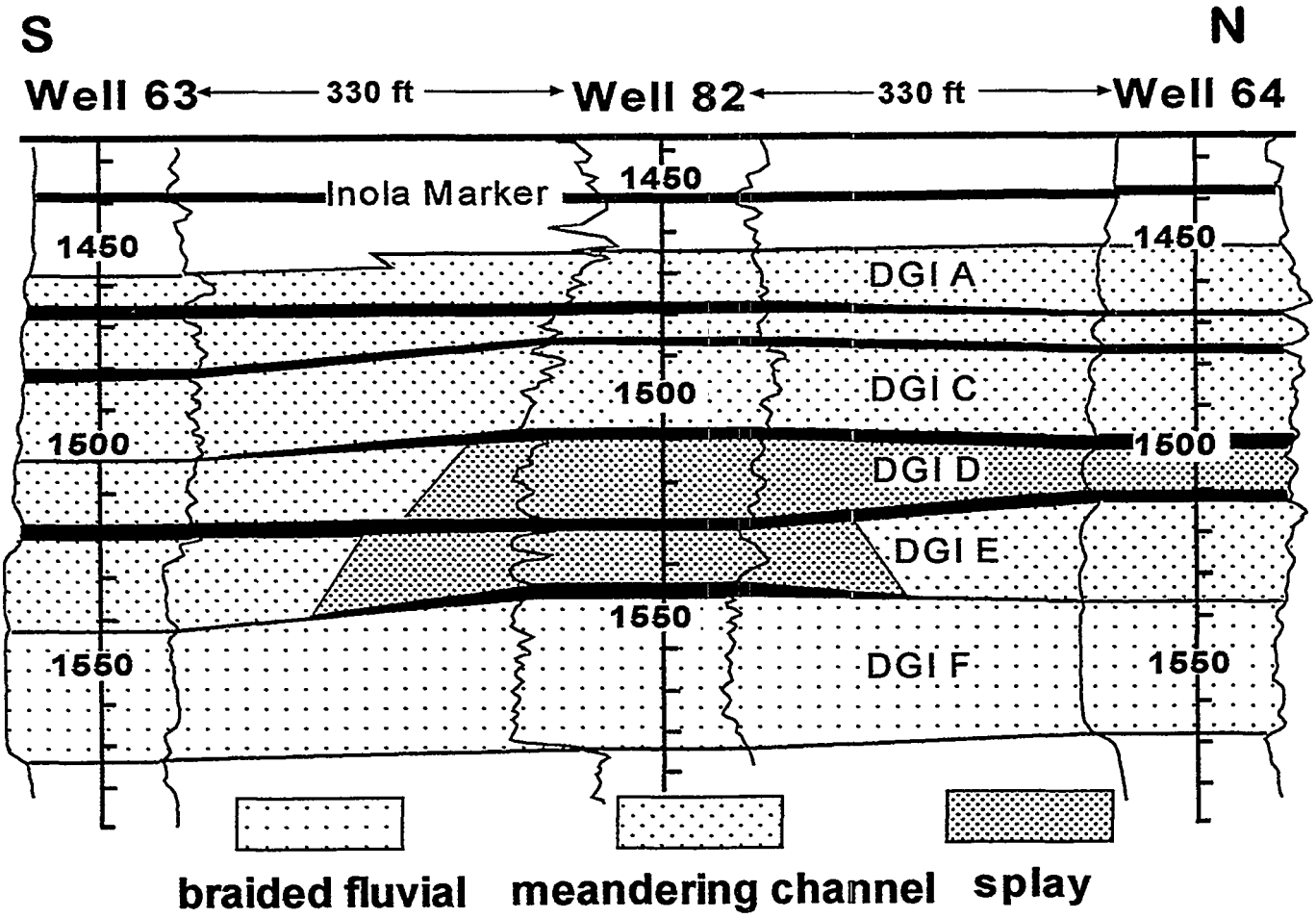

Figure 4 (b) A N-S Cross Section Cut in the Middle of Self Unit Showing DGIs and Facies Distribution

Figure 5 Thinning-Upward Sequence of Meandering Fluvial Deposits
Shown by Upward-Decrease of Maximum Thickness for Each DGI

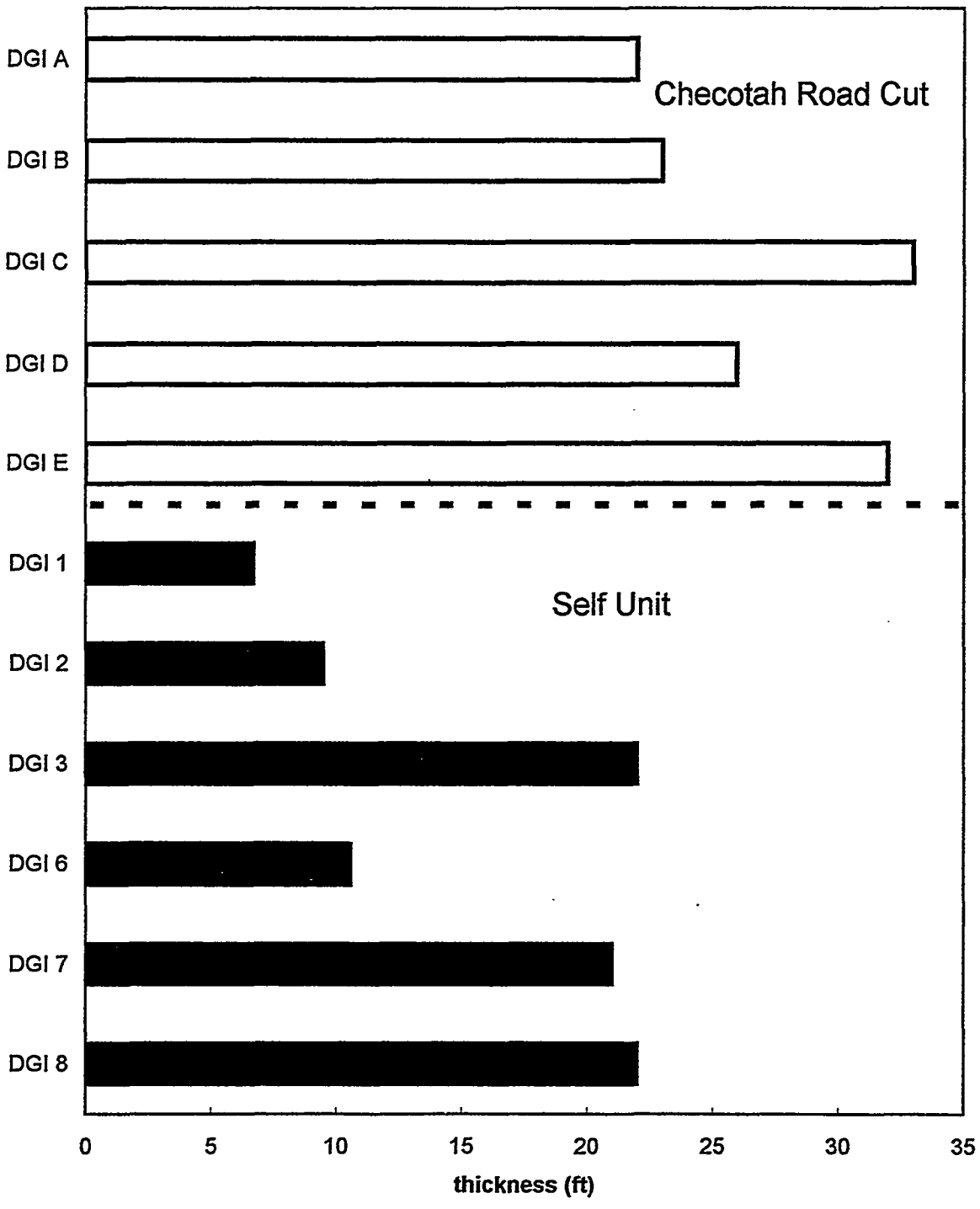

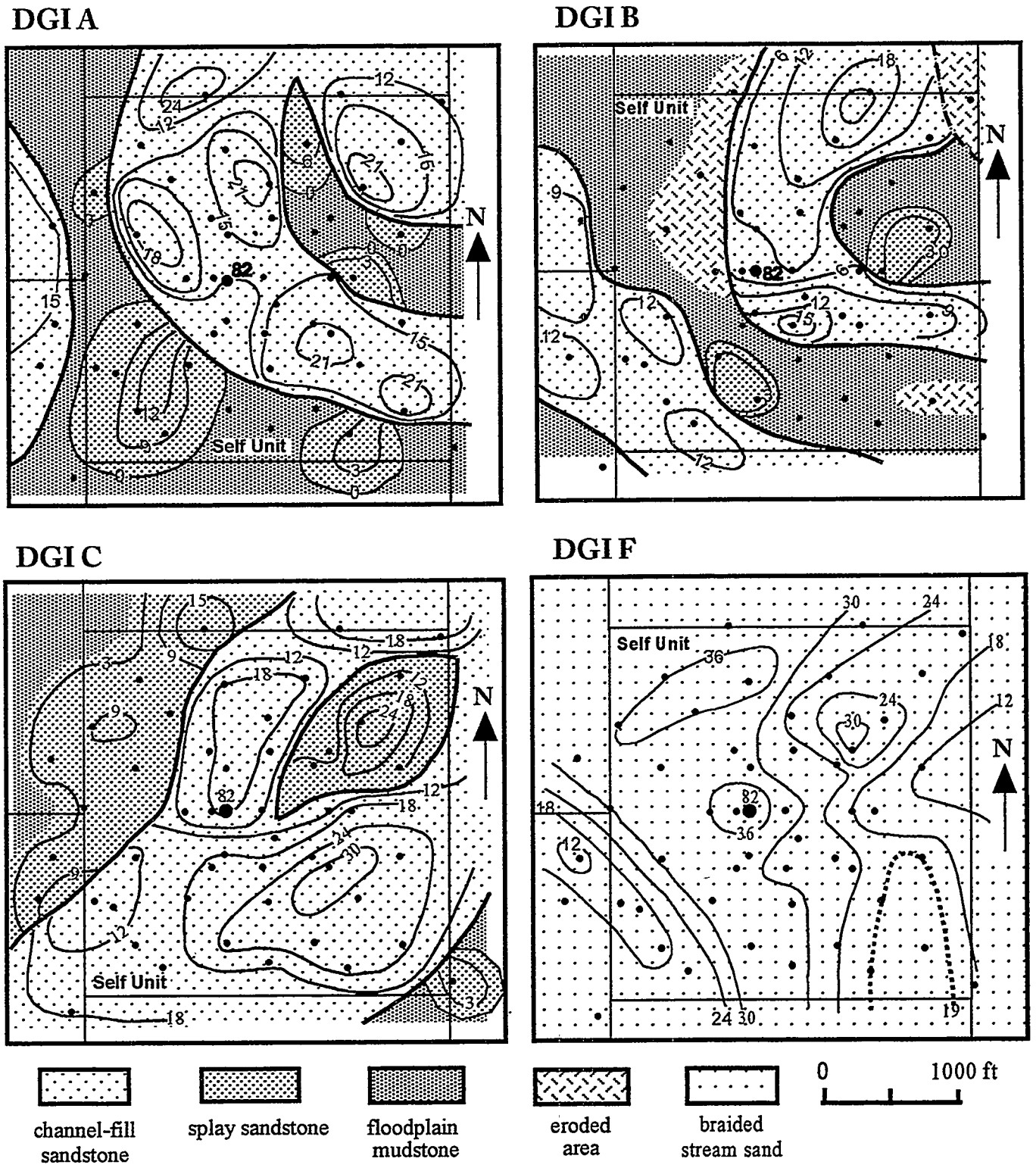

Figure 6 Net Sand Isopach and Facies Map, Self Unit

(thickness in ft)

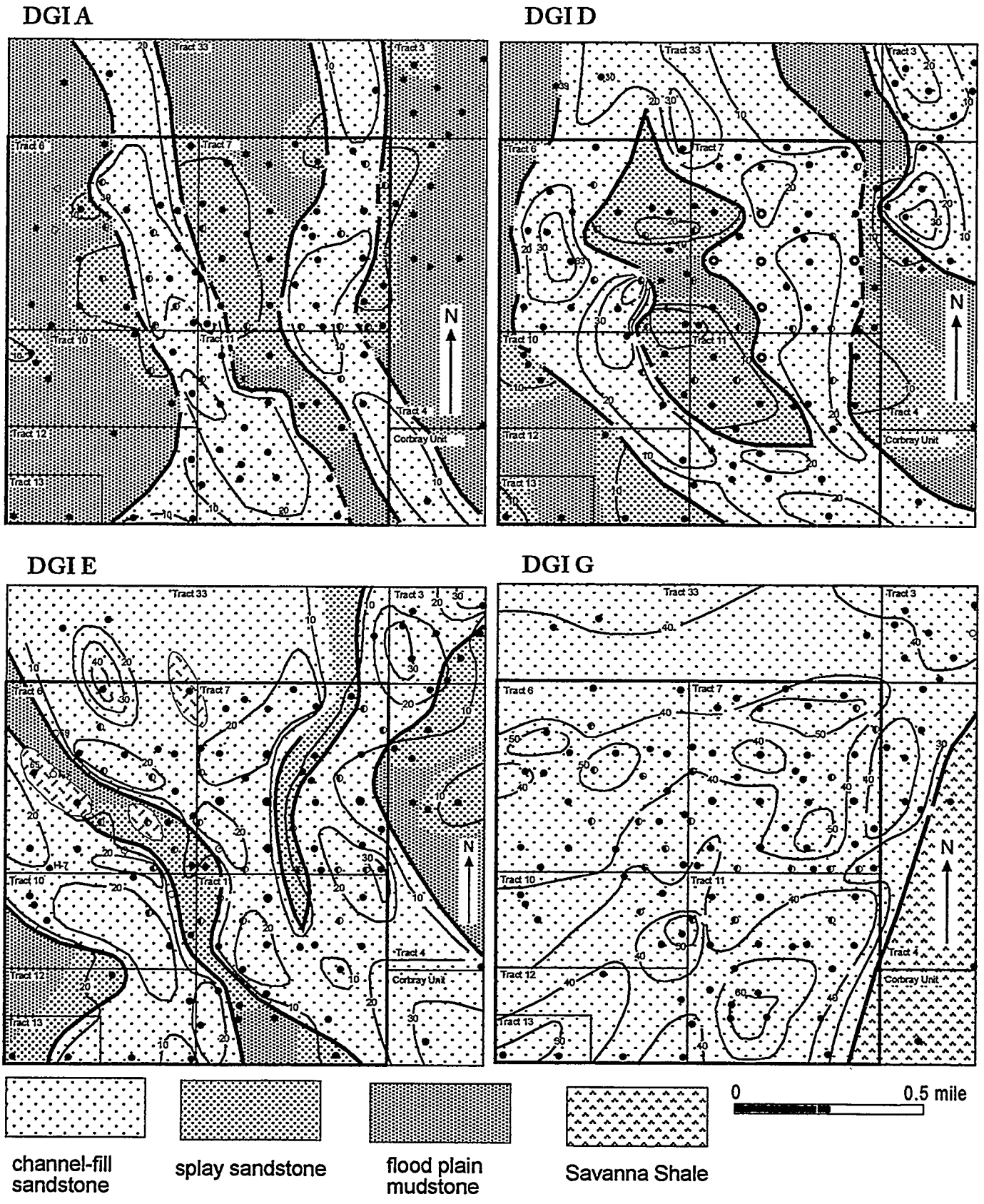

Figure 7 Net Sand Isopach and Facies Map, Tract 7 & Adjacent Areas (thickness in ft)

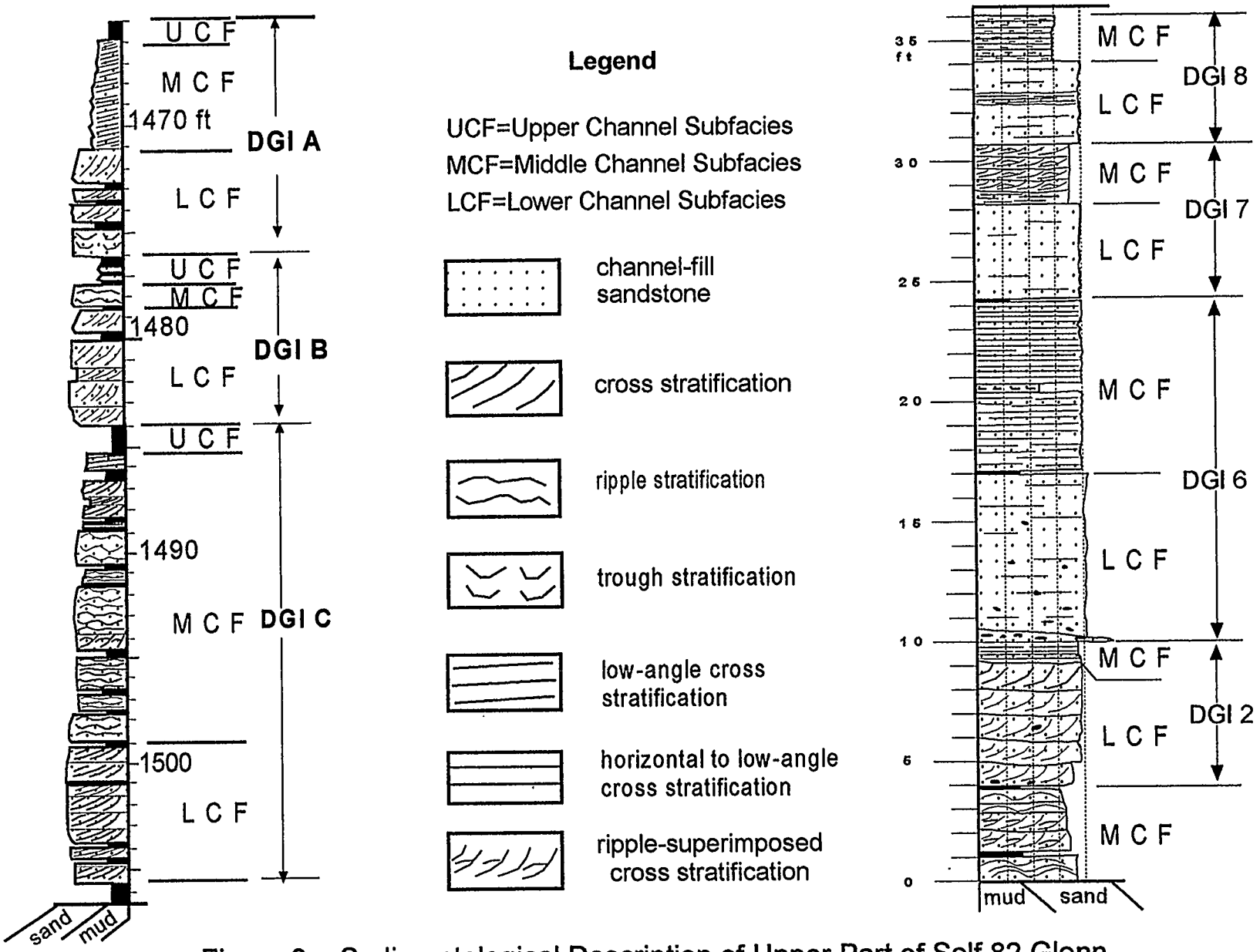

Figure 8 Sedimentological Description of Upper Part of Self 82 Glenn Sand (left) and Checotah Bluejacket Sandstone Road Cut (right)

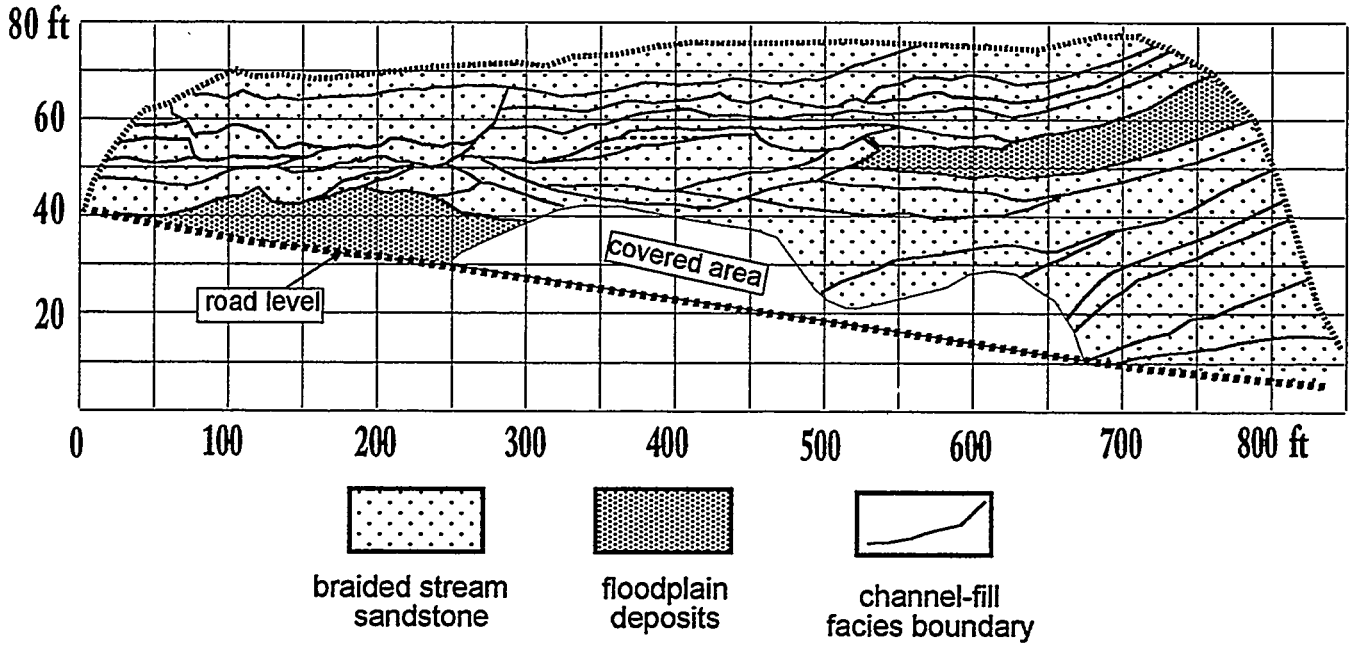

Figure 9 Distribution & Stacking Pattern of Braided Channel Deposits Surveyed on the West Leg of Eufaula Dam Cliff

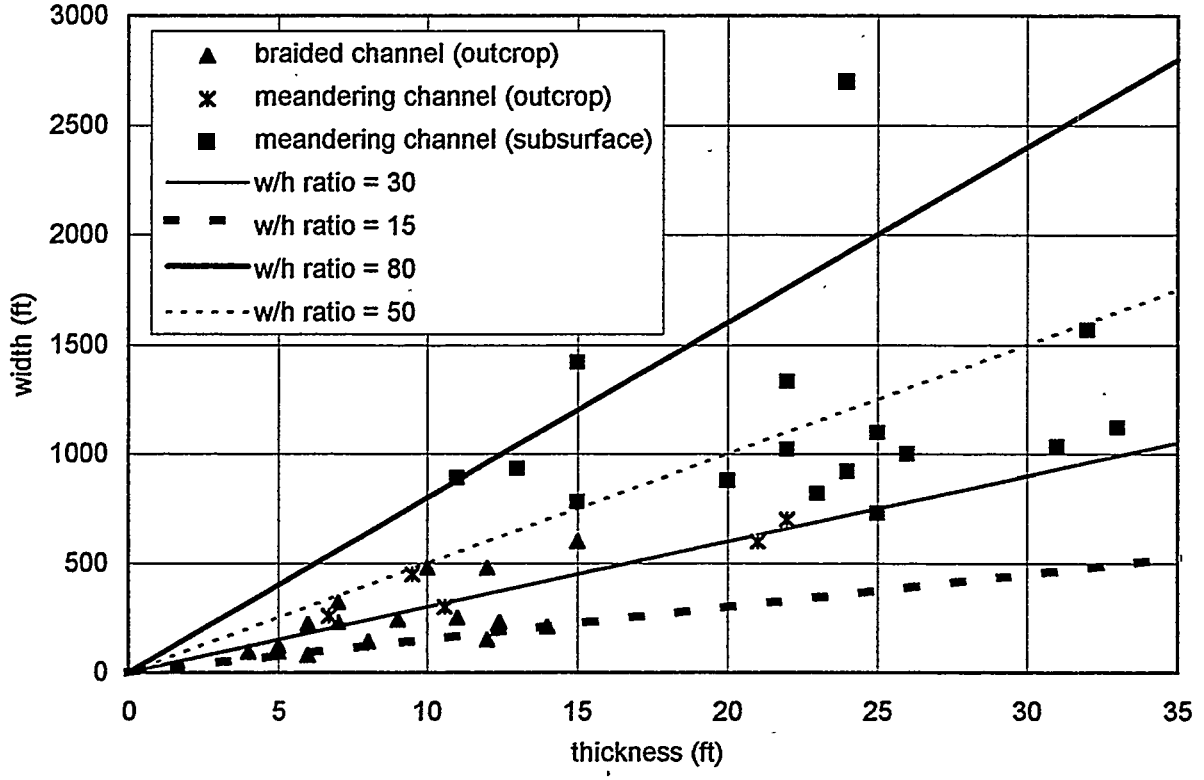

Figure 10 Channel-Fill Thickness vs. Width

Figure 11 Self 82 Core Porosity and Permeability Profile

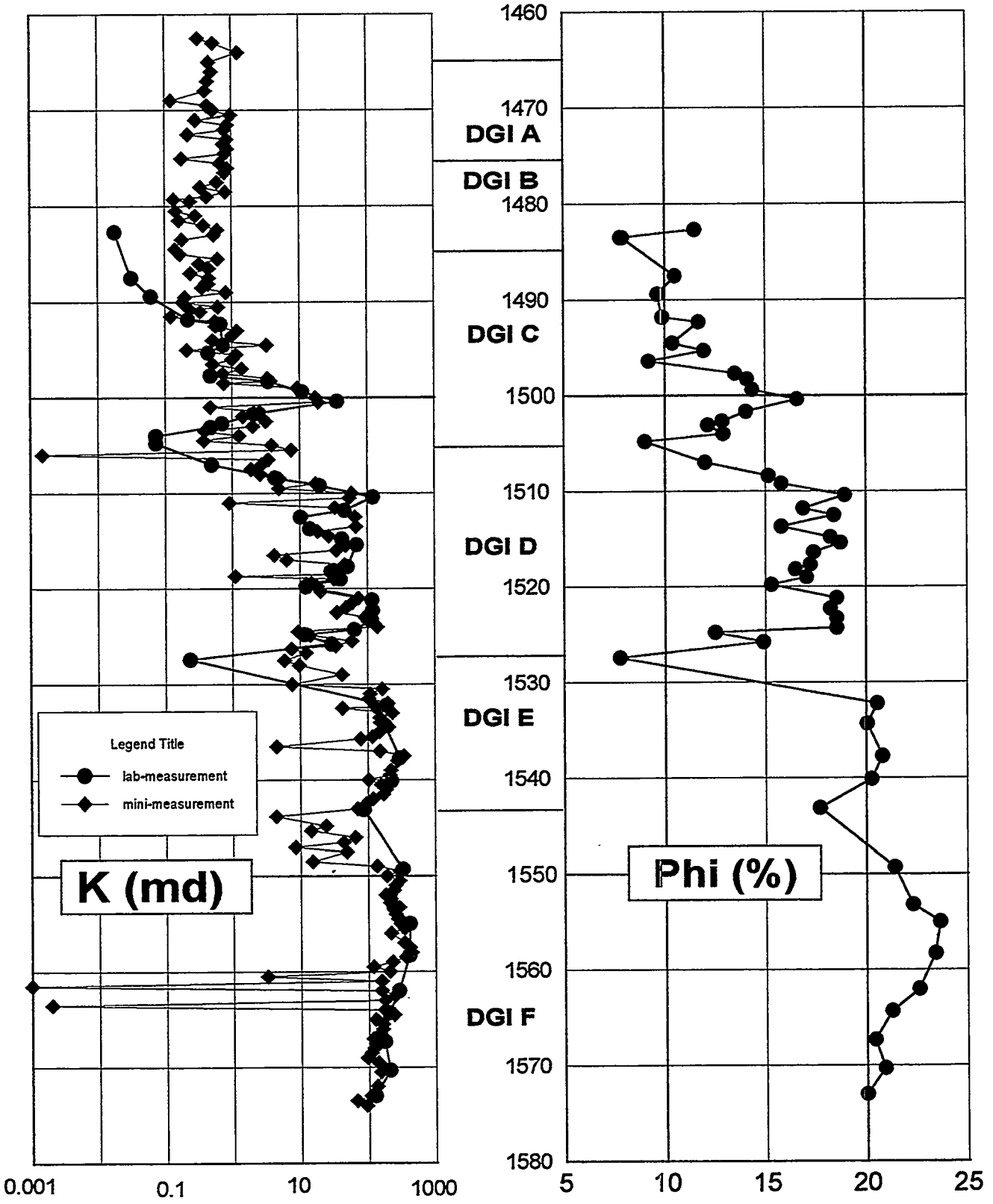

Figure 12 Kh vs. Kv for different DGIs and Facies

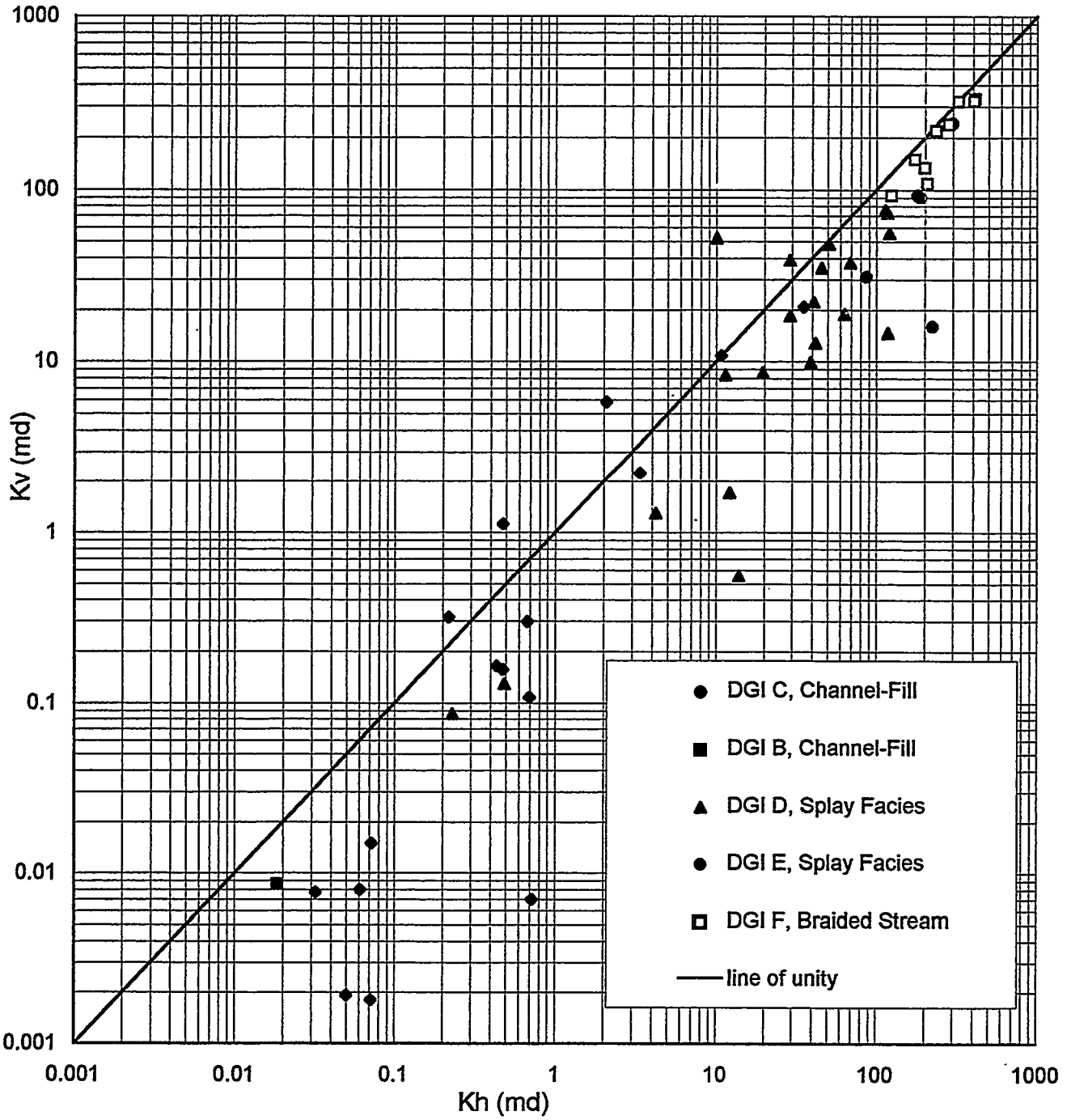

RESERVOIR COMPARTMENTALIZATION AND MANAGEMENT STRATEGIES: LESSONS LEARNED IN THE ILLINOIS BASIN

J. P. Grube, J. E. Crockett, B. G. Huff, H. E. Leetaru,
D. G Morse, B. Seyler, and E. O. Udegbunam

A research project jointly sponsored by the U.S. Department of Energy and the Illinois State Geological Survey focused on the Cypress and Aux Vases Formations (Mississippian), major clastic reservoirs in the Illinois Basin. Results from the research showed that understanding the nature and distribution of reservoir compartments, and using effective reservoir management strategies, can significantly improve recovery efficiencies from oil fields in this mature basin. Compartments can be most effectively drained where they are geologically well defined and reservoir management practices are coordinated through unified, compartment-wide, development programs.

Our studies showed that the Cypress and Aux Vases reservoirs contain lateral and vertical permeability barriers forming compartments that range in size from isolated, interlaminated sandstone and shale beds to sandstone bodies tens of feet in thickness and more than a mile in length. Stacked or shingled, genetically similar sandstone bodies are commonly separated by thin impermeable intervals that can be difficult to distinguish on logs and can, therefore, cause correlation problems, even between wells drilled on spacing of less than ten acres. Lateral separation of sandstone bodies causes similar problems. Reservoir compartmentalization reduces primary and particularly secondary recovery by trapping pockets of by-passed or banked oil. Compartments can be detected by comparing recovery factors of genetically similar sandstone bodies within a field; using packers to separate commingled intervals and analyzing fluid recoveries and pressures; making detailed core-to-log calibrations that identify compartment boundaries; and analyzing pressure data from waterflood programs.

Petrofacies Analysis - The petrophysical tool for geologic/engineering reservoir characterization

Watney, W.L., W.J. Guy, J.H. Doveton, S. Bhattacharya, P. M. Gerlach, G. C. Bohling, T. R. Carr
Kansas Geological Survey, 1930 Constant Avenue - Campus West, Lawrence, Kansas 66047

Acknowledgments

Several grants that have supported the petrofacies project and utilized its developments over the past few years including the "Petrofacies Analysis Project" with the Kansas Technology Enterprise Corporation and industrial consortium, "Development and Demonstration of An Enhanced, Integrated Spreadsheet-based Well Log Analysis Software," Subcontract No. G4S60821 with BDM-Oklahoma and industry consortium, "Shaben Field -- Class II Field Demonstration Project, " Contract No. DE-FC22-94PC14987, and "Digital Petroleum Atlas," Contract No. DE-FG22-95BC14817, both supported by the Department of Energy.

Abstract

Petrofacies analysis is defined as the characterization and classification of pore types and fluid saturations as revealed by petrophysical measures of a reservoir. The word "petrofacies" makes an explicit link between petroleum engineers' concerns with pore characteristics as arbiters of production performance, and the facies paradigm of geologists as a methodology for genetic understanding and prediction. In petrofacies analysis, the porosity and resistivity axes of the classical Pickett plot are used to map water saturation, bulk volume water, and estimated permeability, as well as capillary pressure information, where it is available. When data points are connected in order of depth within a reservoir, the characteristic patterns reflect reservoir rock character and its interplay with the hydrocarbon column. A third variable can be presented at each point on the crossplot by assigning a color scale that is based on other well logs, often gamma ray or photoelectric effect, or other derived variables. Contrasts between reservoir pore types and fluid saturations will be reflected in changing patterns on the crossplot and can help discriminate and characterize reservoir heterogeneity.

Many hundreds of analyses of well logs facilitated by spreadsheet and object-oriented programming have provided the means to distinguish patterns typical of certain complex pore types (size and connectedness) for sandstones and carbonate reservoirs, occurrences of irreducible water saturation, and presence of transition zones. The result has been an improved means to evaluate potential production such as bypassed pay behind pipe and in old exploration holes, or to assess zonation and continuity of the reservoir.

Petrofacies analysis is applied in this example to distinguishing flow units including discrimination of

pore type as an assessment of reservoir conformance and continuity. The analysis is facilitated through the use of color cross sections and cluster analysis.

Introduction

Reservoir characterization and modeling are ongoing procedures utilized as the reservoir is developed. Well log data and occasional cores provide the fundamental stratigraphic information critical to delineating flow units, a primary objective of reservoir characterization. Flow units are correlatable and mapable regions in the reservoir that control fluid flow. Their distinction is usually centered on comparing permeability and porosity information. This classification is refined as fluid recovery, pressure data or chemical fingerprinting become available. Often times, particularly in older fields, production is commingled and cannot be used to substantiate flow units. Moreover, the costs of extensive fluid and pressure testing are not economic. The question examined here is whether the traditional definition of flow units can be modified to include additional information obtained from basic suites of well logs. An approach referred to as petrofacies analysis is described that extends the use of well logs to maximize information that relates to pore type and fluid flow. In particular, the utility of distinguishing vertical and lateral trends and patterns of irreducible bulk volume water, water saturation, and porosity is evaluated as a tool to improve the definition of flow units using well logs. Petrofacies are defined as portions of the reservoir that exhibit distinctive geological facies and petrophysical attributes.

Selecting flow units from core and log data is subjective due to judging whether reservoir conformance (interconnection) and lateral continuity exist without actual fluid flow information (Willhite, 1986). Consistent, explicitly defined steps must be developed between wells to ensure that the procedure is robust and can be repeated and improved as more information becomes available.

The initial task is correlating the reservoir interval and establishing stratigraphic subdivisions and lithofacies. Next, the correlated stratigraphic intervals are mapped with the subsurface control to test coherency of the data. At this stage, porosity and permeability data are integrated with stratigraphic units and lithofacies to define porous and permeable flow units. This information is then compared with the production and test data to check for consistency and correlations.

An intermediate step proposed here is to extract further information about pore types and fluid saturations utilizing petrofacies analysis. The analysis is based on the Pickett plot and delineation of depth-based trends and patterns in porosity, resistivity, water saturation, and bulk volume water (BVW). Thousands of analyzes of this type have demonstrated a well know fact, that porosity varies considerably due to varying pore

type and capillarity. Furthermore, the use of "rules of thumb" values for effective porosity and saturation cutoffs are inadequate to address today's needs to improve oil recovery from existing fields.

While porosity may vary little, saturations and productivity can be considerably different when pore types change. Alternatively, changes in water saturation and BVW may vary closely with elevation of the reservoir, suggesting fluid continuity and reservoir conformance as well as serving as an additional tool in evaluating lateral reservoir continuity. Added information on pore types, vertical reservoir conformance, and fluid/reservoir continuity provided by petrofacies analysis is important in assessing flow units and ensuring robust reservoir modeling.

Petrofacies analysis is used in this example to extend an initial stratigraphic analysis of a sandstone reservoir in an attempt to define flow units. The ultimate objective of this reservoir characterization will be to conduct a reservoir simulation of the field to help evaluate future production options.

Study Area

Petrofacies analysis was applied to a Lower Morrow (Lower Pennsylvanian) sandstone reservoir in Arroyo Field, Stanton County, Kansas (Township 29 South - Range 41 West)(Figure 1). Arroyo Field, operated by J.M. Huber Corporation, is a prolific field, discovered in 1992 through application of subsurface methods. Cumulative production exceeds 651,000 barrels of oil and 21 billion cubic feet of natural gas. Arroyo Field is a combination structural stratigraphic trap, currently containing 6,240 proven productive acres with 24 oil and gas wells and 3 dry holes. The field contains two reservoirs, the Lower Morrow sandstone and the St. Louis Limestone (oolite). The Lower Morrow sandstone is located at approximately 1715 m (5,400 ft) below the surface. The sandstone ranges from 0 to 19 m (0 to 60 ft) thick and is lenticular throughout the field (Figure 2). The porosity of the sandstone ranges up to 20% and averages 14%. All positions of the sandstone have been perforated in the field, some wells reported as only gross intervals. Initial reservoir pressure was 1,434 psi.

The upper portion of the sandstone has produced only natural gas and the lowest portion has produced significant amounts of both oil and gas. No water has been produced in any of the wells. Also, no oil:water contact has been recognized. The reservoir drive appears to be gas expansion.

A considerable amount of supporting data on Arroyo Field including digital well logs, completion reports, and interpretive maps, cross sections, and synthetic seismograms are included in a digital publication of this field on the Kansas Geological Survey's Digital Petroleum Atlas located on the Survey's Internet Home Page (URL=http://crude2.kgs.ukans.edu/DPA/Arroyo/arroyoMain.html).

The lenticular Lower Morrow sandstone is comprised of a series of upward-coarsening shoreface deposits that are mostly confined to within one-half mile wide meandering valley, up to 48 m (150 ft) deep (Figure 1). The sandstone was previously correlated and subdivided into five separate sandstone-dominated genetic units (1, 3, 5, 9, 11) using gamma ray, porosity, and resistivity logs and one spectral gamma ray log. Each genetic unit is delineated by bounding surfaces usually characterized by abrupt changes in lithofacies. Each genetic unit is believed to represent temporally distinct episodes deposition, i.e., a genetic unit. Only several of the genetic units are developed at any particular location in the field (Figure 2).

The sandstones were deposited in a meandering valley system. Maps of each genetic unit record episodes of infilling of this valley, each unit with varying geometries and sand abundance and quality. The lowest sandstones are more limited in distribution, filling only the lowest (deepest) portions of the valley, while the higher sandstones locally extend beyond the confines of the valley. For these reasons, the stratigraphic distribution was believed to be a controlling factor on flow unit definition.

Methodology

Volumetric properties of pore space and fluid saturation can be calculated from porosity logs (density, neutron, or sonic) and resistivity logs using the standard Archie equations. When plotted on a double-logarithmic plot of porosity versus resistivity (a "Pickett plot"), additional information on pore size and fluid producibility may be deduced by the use of pattern recognition informed by basic reservoir engineering principles. A "template" Pickett plot is shown in Figure 3 for the Upper Morrow in the Arroyo Field. A "water line" (Ro) expresses the theoretical resistivity-porosity coordinates of all zones that are completely saturated with water. The water line is established by the first Archie equation that links the "formation factor". F (the ratio of the resistivity of the completely water-saturated rock, Ro, to the resistivity of the formation water, Rw) to the porosity of the rock:

$$F = R_o/R_w = a/phi^m$$

using an Arroyo Field formation water resistivity, Rw, of 0.04 ohm-m and Archie parameter values of a=1 and m=1.8, which express pore geometry in the Morrow sandstone. Contours for different values of water saturation parallel the water line, with a spacing determined by the saturation exponent, n (generally with a value of about 2 in water-wet rocks) in the second Archie equation:

$$I = R_t/R_o = 1/Sw^n$$

where I is the "resistivity index" and Rt is the actual resistivity of the rock. Lines can also be drawn on the plot that are contours of bulk volume water (BVW), where water content is expressed as a proportion of the total rock, rather than in terms of the pore space as is the case with saturation.

The disposition of crossplotted zones with respect to the log axes of resistivity-porosity and the computed reference axes of water saturation and bulk volume water (BVW) gives useful clues on both pore type and producibility. These properties can be seen when relating Pickett plots to production histories (Figure 3) from some example wells in the Arroyo Field. Notice how overall well performance is determined to a large extent by higher porosities and lower water saturations. However, the location of the data-cloud with respect to the BVW contours reflects the pore size and likely water-cut. Lower values of BVW are matched with coarser pores; higher values of BVW are linked with either finer pores and/or zones with coarse pores and producible water. In terms of data-cloud shape, a classic reservoir profile would show zones high in the reservoir at "irreducible" water saturation and relatively low BVWs with a progressive increase in bulk volume water with increasing depth and descent into the transition zone. Some aspects of this ideal character are shown in the plots in Figure 4, where the four wells have been arranged from most productive at the top to least productive at the bottom. Notice that the bottom example was not completed for production, but abandoned because a DST yielded nothing but salt water. The associated Pickett plot shows a rather ragged scatter of mostly low-porosity zones with high water saturations that probably reflect residual hydrocarbon saturations. This pattern is common at the margins of fields as is this well and contrasts with an idealized situation far away from fields where zones are completely water-saturated and form a trend on a Pickett plot that conforms closely to the water line(Ro).

The Pickett (porosity-resistivity) cross plots are the fundamental components in the petrofacies analysis. The connection of data points by depth and the ability to annotate the data points with a third variable help establish relationships between the petrophysical response and the geology -- lithologies, stratigraphic units, and structure, i.e., the petrofacies. Template lines identify minimum BVW and associated water saturations and porosities on the Pickett plot. This, in turn, helps to correlate the geology to fluid-related parameters and delineate specific changes in fluids and variations in the pores between the different wells.

The definition of flow units might be refined to include regions of similar/related BVW and pore type using the petrofacies analysis. Often, permeability data are either lacking or are limited to averaging from core-log porosity and permeability correlations. In these cases, assessment of pore type using petrofacies analysis may help to provide novel constraints to flow units, lacking other substantial data. Of course, production and transient test data and geochemical tests are necessary to more definitively constrain the definition of flow units.

A west-to-east cross section was chosen to further characterize the sandstone reservoir using the petrofacies analysis approach (Figure 2). The cross section crosses the valley in two places, separated by a intervening high area.

The questions addressed in this analysis include 1) Is additional evidence available to confirm or reject the continuity of sandstones across the intervening high region residing between the valleys? 2) What is the evidence of vertical conformance and lateral continuity? 3) How do properties of the sandstones compare on either side of the valley? 4) Can the definition of flow units be improved? 5) How do the flow units compare with the detailed stratigraphic subdivisions?

In addition to the stratigraphic analysis, the procedure included three operations 1) construct Pickett plots for each of the wells on the cross section, 2) perform a cluster analysis of basic petrophysical data to independently define similar reservoir properties, 3) prepare a series of color cross sections of selected petrophysical variables with datums on sea level elevation and a stratigraphic marker (Middle Morrow limestone located above the sandstone), and 4) integrate this information to define flow units -- compare with stratigraphic zonation, Pickett plots, color log cross sections, cluster analysis, and well productivities.

Results

The digital data from five well logs comprising an west-to-east cross section in Arroyo Field were examined utilizing petrofacies analysis. The standard well log cross section was shown earlier in Figure 2. The objective was to compare well data on the cross section to test for evidence of lateral continuity. The cross section would suggest that some of the units are continuous. Units that are not shown as continuous may also be connected from outside of the plane of the cross section.

Pickett plots

LAS (log ascii standard) digital well log files were read into an Excel-Visual Basic program called PfEFFER to generate the Pickett cross plots. The initial Pickett cross plots provide a visual differentiation of the variation in the porosity, resistivity, water saturation, and bulk volume water. Permeability lines are annotated on the crossplots, estimated using empirical relationship between water saturation and porosity developed by Timur. The relationship holds for clean sandstones when water saturations are at irreducible values. We believe that to be the case here.

The crossplot with points annotated with gamma ray values indicate that points with higher gamma ray

values are located on the left side of the crossplot at BVWs in excess of 0.06 (Figure 5). This location presumably represents more shaly and finer pores. The permeability lines are not applicable to these points.

The reservoir has no water leg and no water has been produced. The points are annotated by stratigraphic interval and form rather tight clusters or bands for each stratigraphic unit (Figure 6). The clustering of points in distinct stratigraphic intervals and accompanying lower water saturations suggest that these zones are near their respective minimum BVWs. Also, the bands of points closely correspond to particular stratigraphic zones. Also, the bands parallel water saturation lines. This pattern is ascribed to changing minimum BVW and pore size within a zone. These relationships have implications to fluid flow. If any portions of the reservoir were in a gas or oil:water transition zone, the bands of points may have more likely paralleled porosity lines, if the pore type was not changing. However, this is not seen and no wells have experienced any water-cut oil or gas production.

The interwell comparison of the clusters and bands for each stratigraphic interval easily illustrate changes and similarities. The variations suggest possible changes in pore type and evidence for reservoir continuity or lack thereof.

Cluster Analysis

Some the boundaries between stratigraphic units involve sand on sand and may not present barriers to flow, but changes in transmissibility. Also, the internal variability in sandstone units may present further heterogeneity that can retard fluid flow. Cluster analysis was used to examine the similarity among petrophysical data. The method provides a consistent automated treatment of the data to aid in comparing considerable amounts of data among the zones and wells. Ward's Method was selected as the clustering technique. The method consists of a series of clustering steps that begins with "t" clusters each containing one object. The clustering ends with one cluster containing all objects. At each step, a merger of two clusters is made that results in the smallest increase in the variance (Romesburg, 1984).

The petrophysical variables included in the cluster analysis are gamma ray, deep induction resistivity, Pe, water saturation, BVW, and apparent permeability using the Timur equation,

$$ka = 1x10^4 * phi^{4.5}/Sw^2.$$

This apparent permeability is a minimum estimate when Sw is greater than irreducible Sw. Phi (porosity) and Sw are fractional values in this equation. Shaly intervals were assigned to zero permeability (removing depth intervals where gamma ray exceeded 60 API units and neutron minus density porosity was

greater than one). Depth was also included within the cluster analysis as an adjacency constraint to enhance spatial continuity.

Six separate agglomeration of points were selected from the cluster analysis of each well. Several criteria were used to determine this number. First, the number is not large so as to produce too many groups and thus probably complicate reservoir modeling. Second, the cluster dendrogram for each well show good separation of groups at this level. Third, the number is comparable to the stratigraphic divisions and might show useful groupings and comparison.

The assigned groupings derived from cluster analysis were first compared by depth with the petrophysical data and stratigraphic zonation. The boundaries between the stratigraphic intervals and the cluster assigned groupings generally coincide. The clustering identified a moderate amount of smaller scale heterogeneity within each stratigraphic interval (Figure 7). However, the general finding is that each stratigraphic interval is dominated by only one or two assigned cluster groupings.

The posting of assigned cluster groups as an attribute on the Pickett plot further indicates a close correspondence between stratigraphic units and assigned cluster grouping, e.g., Figure 8. The cluster analysis can be adapted in the spreadsheet environment to help facilitate consistent, rapid assignment of cluster groups and further aid in flow unit assessment.

Color Cross Sections

Flow units are assigned to zones in the reservoir with similar permeability and porosity and which also exhibit some degree of lateral continuity. Flow units are inferred to control fluid flow and confirmation is sought to substantiate these units. Petrophysical variation within individual well profiles has been described up to this point, focused on vertical conformance. The question remains as to the extent of lateral continuity. Flow units may not be everywhere present, but are anticipated to be correlatable in the field to some degree. This continuity is ultimately established using petrophysical data, fluid recovery, pressure and fluid chemistry. The suites of petrophysical variables including BVW can be used to evaluate laterally continuity. Continuous trends or constancy of properties of the sandstone and correlations with structural elevation suggest possible fluid continuity in the reservoir.

Computer-assisted generation of color cross sections based on original digital well log sampling of 0.16 m (0.5 ft) provides the means to observe and evaluate detailed subtle changes in reservoir character and substantially assist in assessing continuity and assigning flow units. The cross sections are generated with a

elevation (subsea) or stratigraphic datum.

Cross sections for key petrophysical parameters were generated including gamma ray, permeability calculated with the Timur equation (apparent permeability filtered on gamma ray and neutron-density shale indicators), Pe (photoelectric effect) from the Lithodensity log, porosity, water saturation, BVW, and deep induction resistivity. Each petrophysical variable is presented as a structural and stratigraphic cross section placed side by side, the later with a datum at the top of the Middle Morrow limestone. Stratigraphic units are identified and correlated. Perforated intervals are shown alongside each well profile.

The five wells in the cross section are perforated in two distinct intervals, a lower interval restricted to stratigraphic unit #1 in the Lauman 28-1 and Kendrick 22-1. Also, the lowest part of unit #3 in the Santa Fe 2-21 is suggested to be part of the lower interval and may possibly be recorrelated with unit #1.

The lower interval produces significant amounts of oil and gas. The upper perforated interval includes stratigraphic units #3, #5, #9, and #11. The upper interval produces natural gas and minor amounts of oil from the Santa Fe 2-11 and Santa Fe 2-22. This difference suggests that the reservoirs are separate. The lower and upper sandstones are isolated by a prominent shaly interval according to the gamma ray and photoelectric logs (Figure 9).

On closer inspection of the gamma ray cross section, the stratigraphic units can be distinguished with the help of the correlation lines. However, there is considerable variation in the internal properties of the stratigraphic units (Figure 9). This variation persists in the other parameters. The stratigraphic units generally appear to delineate most of the petrophysical variation except for several possible re-correlations. These recorrelations are based on further analysis.

Porosity varies from 15 to 20% in the Lauman well to 0-8% in the Kendrick (Figure 10). Apparent permeability calculated from the Timur equation and filtered on gamma ray and neutron shale indicators shows considerable changes on the cross section (Figure 11). The permeability and porosity are both higher on the west. Permeability ranges between 10 and 100 millidarcies (md) in the Lauman 28-1 on the west side to 0.1 to 1 md in the Kendrick 22-1 on the east side.

High permeability and porosity correlate well with a trend of increased natural gas production and decreased oil production in the Lauman 28-1 with 2.5 billion cubic feet of gas and 75,000 barrels of oil. In comparison, the Kendrick 22-1 well on the east and lowest side of the cross section recovered less gas, one billion cubic feet, but more oil, over 120,000 barrels. Permeability varies considerably in thin streaks near the base of the Kendrick 22-1 well. Unit #1 is separated from the overlying sandstones by a thicker shaly interval.

Unit #3 is also thick in the paleovalleys on either side of a central high. Santa Fe #2-21 is perforated in the basal part of a thin sandstone that is in close proximity to the lower interval, unit #1. This zone in Santa Fe 2-21 has produced 12.7 million m^3 (450 million ft^3) of gas and nearly 50,000 barrels of oil. Production values are less than Lauman and Kendrick, but the mixed production is similar to the recoveries noted in unit #1, suggesting that they are a common reservoir in the deeper portions of the paleovalleys.

Production from perforations in the upper interval in Santa Fe 21-1 and Santa Fe 22-2 are notably different. Santa Fe 21-1 has realized 16.1 million m^3 (570 million ft^3) of gas from the upper zone and has been declining relatively rapidly to 1 million cubic feet per month. In contrast, the Santa Fe 22-2 well has produced nearly three times more gas at 1.8 billion cubic feet and its production has declined to only 0.51 million m^3 (18 million ft^3) per month. Both wells have produced for nearly 3 years at the time the production figures were reported.

Conclusions

The stratigraphic units serve as adequate means to classify flow units in this reservoir with added refinements using petrofacies analysis. Petrofacies analysis utilizes Pickett plots to decipher reservoir properties of each stratigraphic unit. Cluster analysis provide as consistent means to further delineate reservoir properties. The boundaries of the clustered groups are commonly those of the stratigraphic units. The clustered groups provide further subdivisions of the reservoir rock that could be used to classify finer-scale flow units. Color cross sections further substantiate the use of the stratigraphic divisions as basic templates for distinguishing flow units. The color cross sections are a representative of the original digitized well log data and provide the means to precisely subdivide the stratigraphic units. The petrofacies analysis should be useful in future considerations when evaluating improved petroleum recovery options.

References Cited

Romesburg, H.C., 1984, Cluster Analysis for Researchers: Belmont, California, Lifetime Learning Publications, 334 p.

Willhite, G.P., 1986, Waterflooding: SPE Textbook Series Volume 3: Richardson, Texas, Society of Petroleum Engineers, Richardson, 326 p.

Figure Captions

Figure 1. Index map of Arroyo Field identifying cross section (Figure 2). Map include (a) with well names and (b) an isopachous map of the Lower Morrow interval (top Middle Morrow limestone to top Mississippian).

Figure 2. West-to-east stratigraphic well log cross section through Arroyo Field containing Lauman 28-1, Santa Fe 21-1, Santa Fe 22-1, Santa Fe 22-2, and Kendrick 22-1. Datum of section is Middle Morrow limestone. Correlated stratigraphic intervals are correlated through the Lower Morrow sandstone interval. Line of cross section is shown on Figure 1.

Figure 3. A "template" Pickett plot for the Upper Morrow sandstone in Arroyo Field.

Figure 4. Pickett plots and corresponding production histories for the Upper Morrow sandstone in Arroyo Field.

Figure 5. Pickett plot of Lower Morrow sandstone in the Santa Fe 22-1 annotated with gamma ray.

Figure 6. Pickett plot of Lower Morrow sandstone in the Santa Fe 22-1 annotated with stratigraphic units shown in type log in Figure 2.

Figure 7. Display of well log suite from the Santa Fe 22-1 well accompanied by derived information including water saturation (SW), bulk volume water (BVW), permeability derived from Timur equation (Timur k), stratigraphic units, and amalgamation groups from cluster analysis.

Figure 8. Pickett plot of Lower Morrow sandstone in the Santa Fe 22-1 annotated with amalgamation groups from cluster analysis.

Figure 9. East-to-west gray-level versions of color cross section depicting gamma ray variation across Arroyo Field. The section includes same wells as Figure 2, except direction is reversed. Left cross section is a structural version with a sea-level datum and right cross section is a stratigraphic cross section with a datum on the top of the Middle Morrow limestone overlying the Lower Morrow sandstone.

Figure 10. East-to-west gray-level versions of a color cross section depicting porosity variation across Arroyo Field. The section includes same wells as Figure 2, except direction is reversed. Left cross section is a structural version with a sea-level datum and right cross section is a stratigraphic cross section with a datum on the top of the Middle Morrow limestone overlying the Lower Morrow sandstone.

Figure 11. East-to-west gray-level versions of a color cross section depicting permeability variation across Arroyo Field. The section includes same wells as Figure 2, except direction is reversed. Left cross section is a structural version with a sea-level datum and right cross section is a stratigraphic cross section with a datum on the top of the Middle Morrow limestone overlying the Lower Morrow sandstone.

Fig. 1

a)

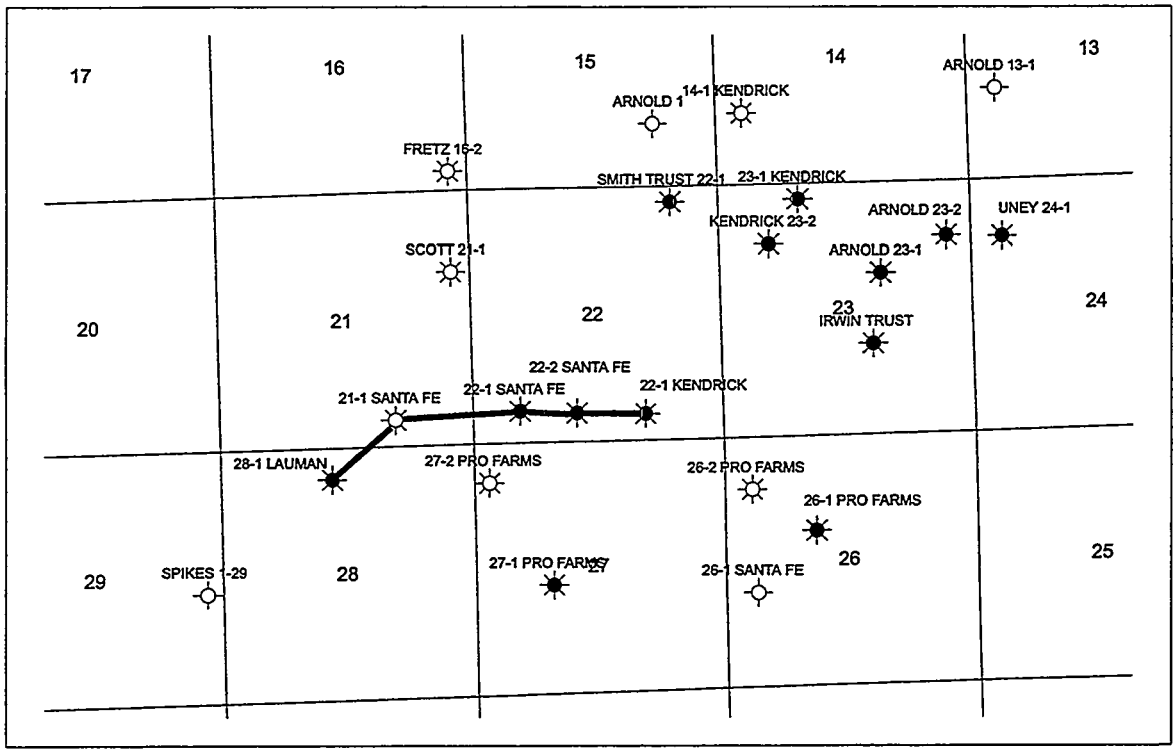
17
16
15
14
13
ARNOLD 13-1
ARNOLD 1
14-1 KENDRICK
FRETZ 16-2
SMITH TRUST 22-1
23-1 KENDRICK
KENDRICK 23-2
ARNOLD 23-2
UNEY 24-1
SCOTT 21-1
ARNOLD 23-1
20
21
22
23
IRWIN TRUST
24
22-2 SANTA FE
21-1 SANTA FE
22-1 SANTA FE
22-1 KENDRICK
28-1 LAUMAN
27-2 PRO FARMS
26-2 PRO FARMS
26-1 PRO FARMS
29
SPIKES 1-29
28
27-1 PRO FARMS
26-1 SANTA FE
26
25

b)

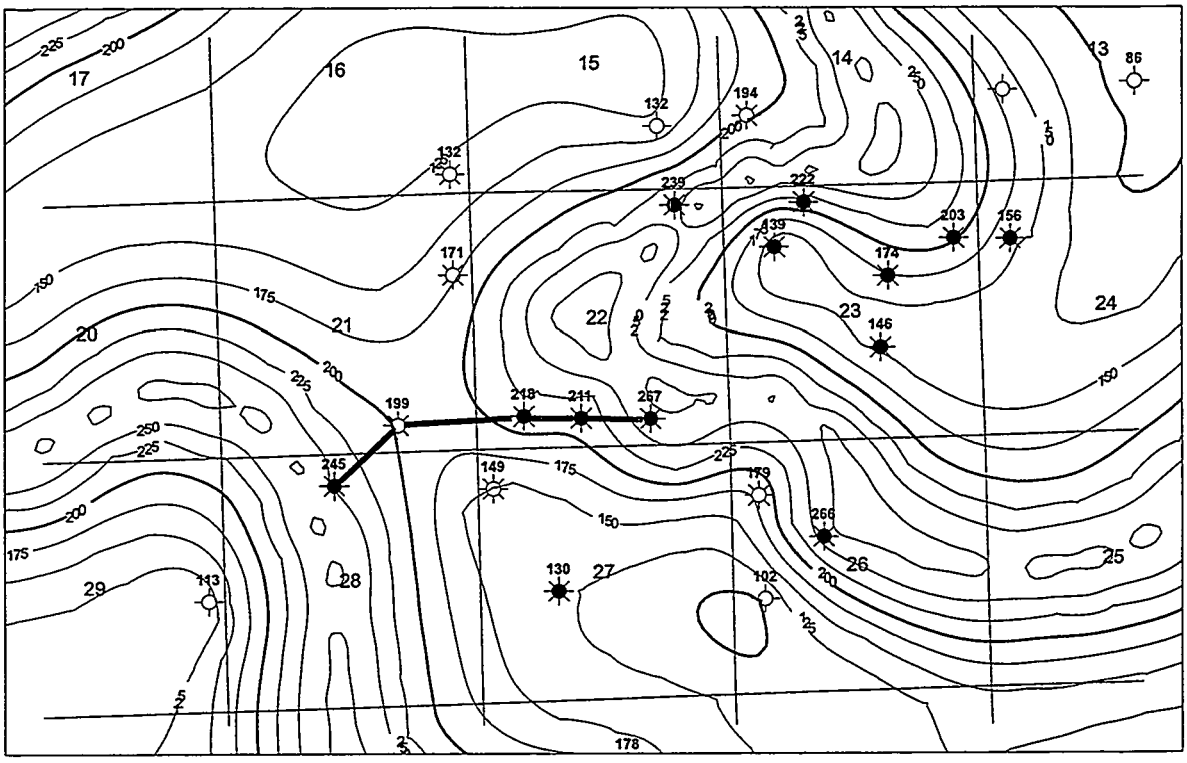
17
16
15
14
13
86
132
194
132
239
222
439
203
156
171
174
20
21
22
23
146
24
199
218
211
267
245
149
179
266
29
113
28
27
130
102
26
25
178

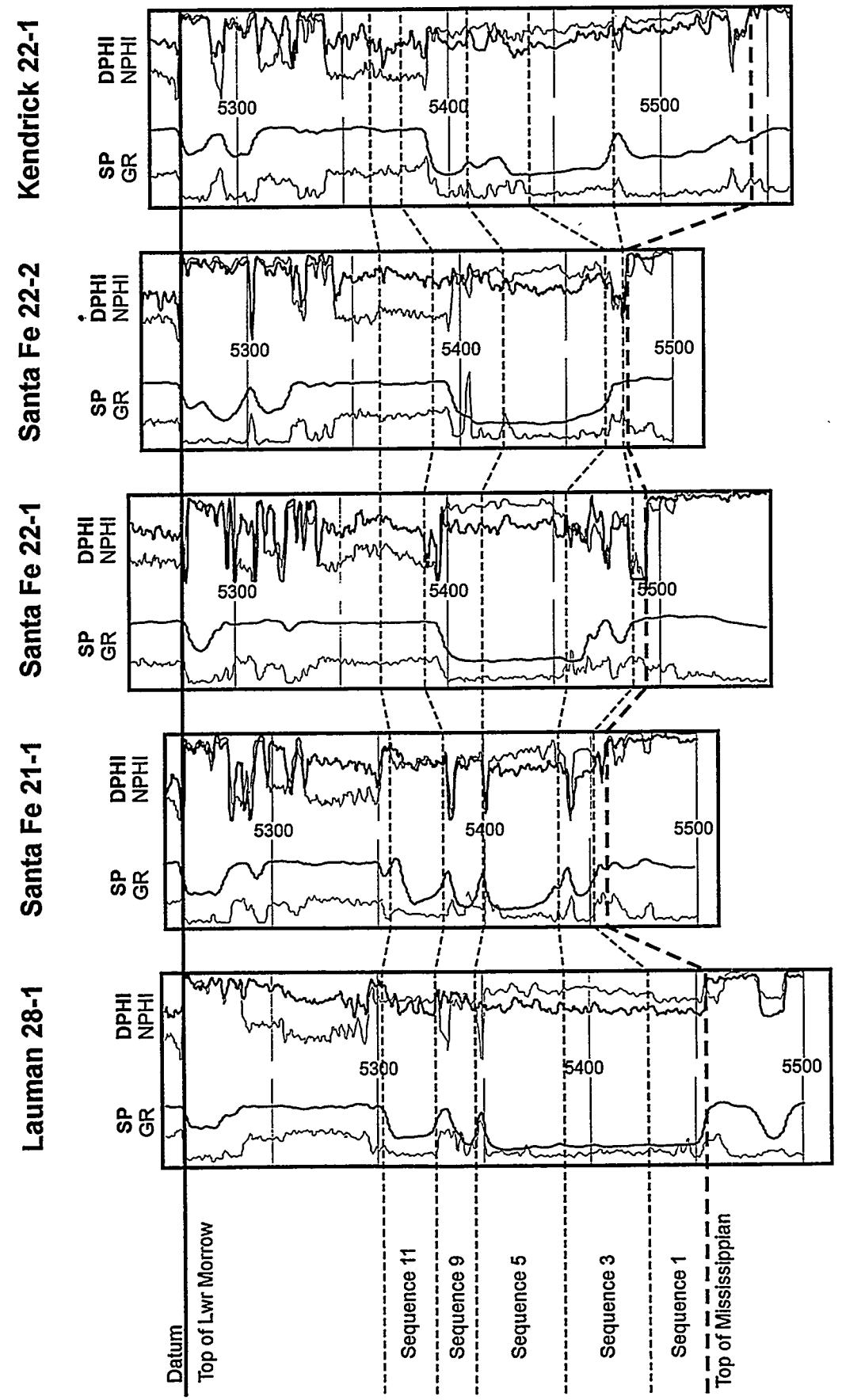
Kendrick 22-1
Santa Fe 22-2
Santa Fe 22-1
Santa Fe 21-1
Lauman 28-1
DPHI
NPHI
SP
GR
5300
5400
5500
Datum
Top of Lwr Morrow
Sequence 11
Sequence 9
Sequence 5
Sequence 3
Sequence 1
Top of Mississippian

Fig. 2

Fig. 3

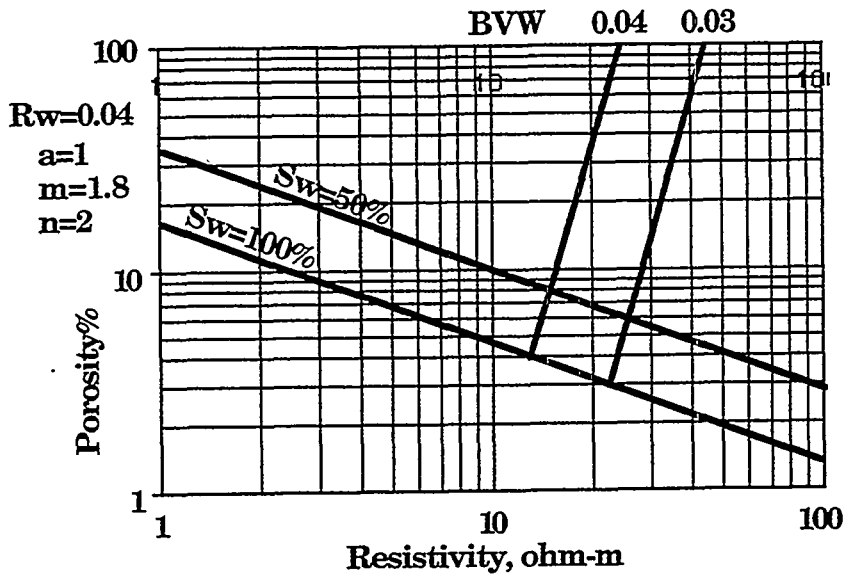
BVW
0.04
0.03
100
Rw=0.04
a=1
m=1.8
n=2
Sw=50%
Sw=100%
10
1
Porosity%
1
10
100
Resistivity, ohm-m

Fig. 4

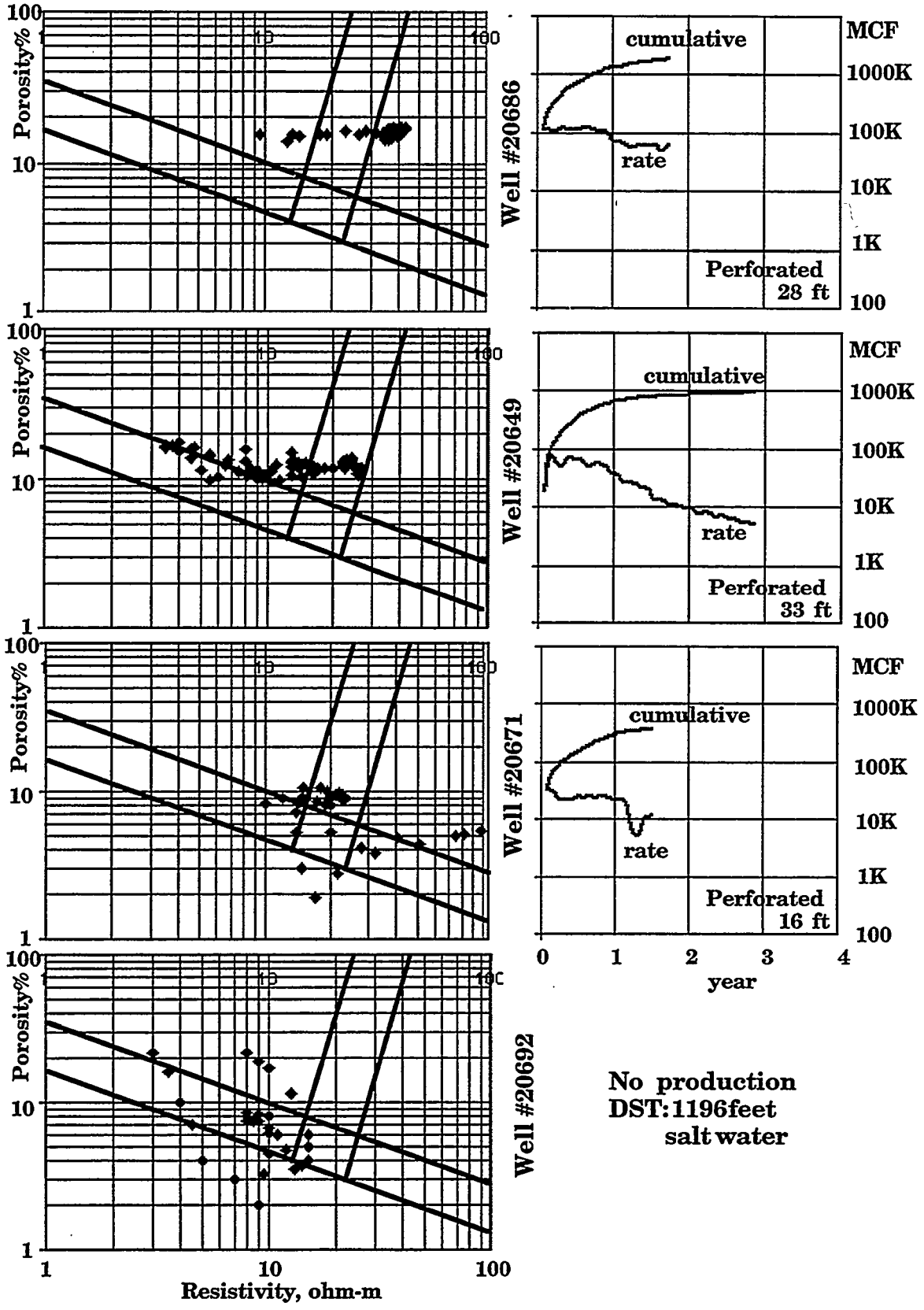
Porosity%
100
10
1
1
10
100
Resistivity, ohm-m
Well #20686
Well #20649
Well #20671
Well #20692
cumulative
rate
MCF
1000K
100K
10K
1K
100
Perforated
28 ft
Perforated
33 ft
Perforated
16 ft
0
1
2
3
4
year
No production
DST:1196feet
salt water

Fig. 5 & 6

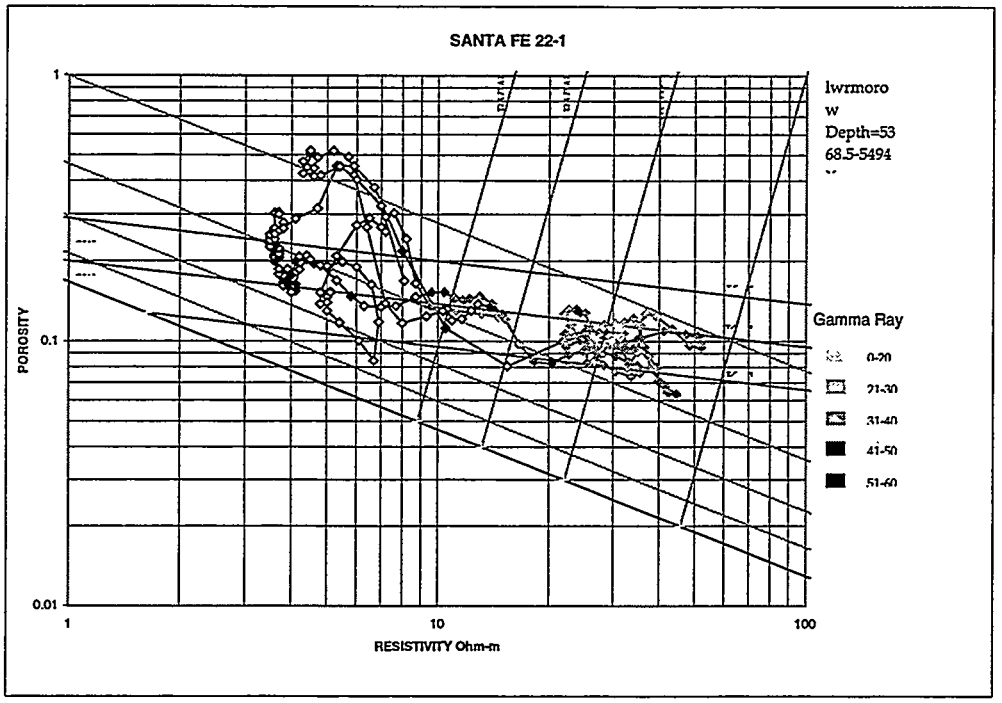
SANTA FE 22-1
POROSITY
1
0.1
0.01
1
10
100
RESISTIVITY Ohm-m
lwrmoro
w
Depth=53
68.5-5494
Gamma Ray
0-20
21-30
31-40
41-50
51-60

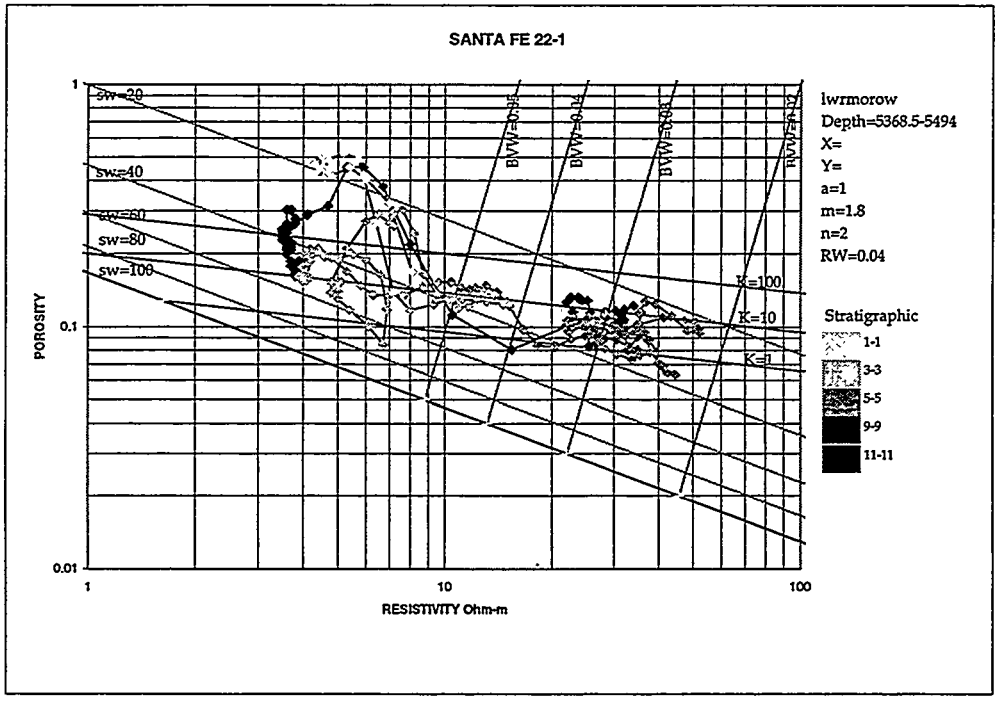
SANTA FE 22-1
POROSITY
1
0.1
0.01
1
10
100
RESISTIVITY Ohm-m
sw=20
sw=40
sw=60
sw=80
sw=100
BVW=0.08
BVW=0.04
BVW=0.02
BVW=0.01
K=100
K=10
K=1
lwrmorow
Depth=5368.5-5494
X=
Y=
a=1
m=1.8
n=2
RW=0.04
Stratigraphic
1-1
3-3
5-5
9-9
11-11

Fig. 7 & 8

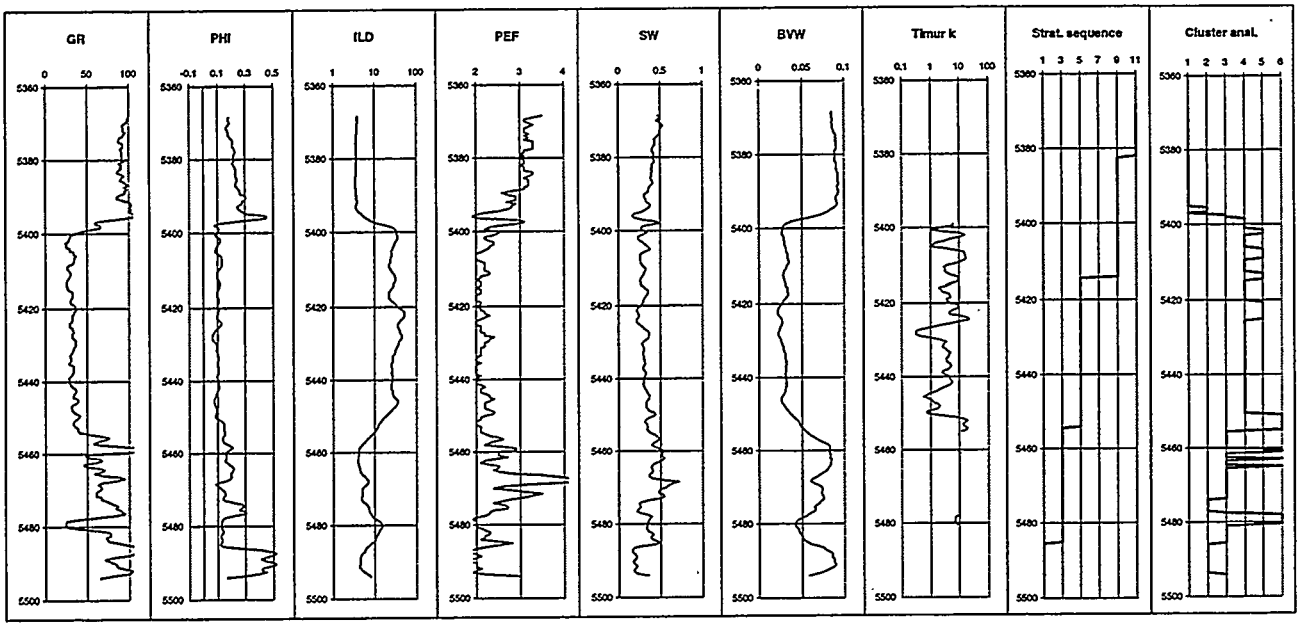
WELL: SANTA FE 22-1
FILE: D:\PFEFFER2\ARROYO\CROSSS-1\22-1SANT\20640-B.TXT
GR
PHI
ILD
PEF
SW
BVW
Timur k
Strat. sequence
Cluster anal.

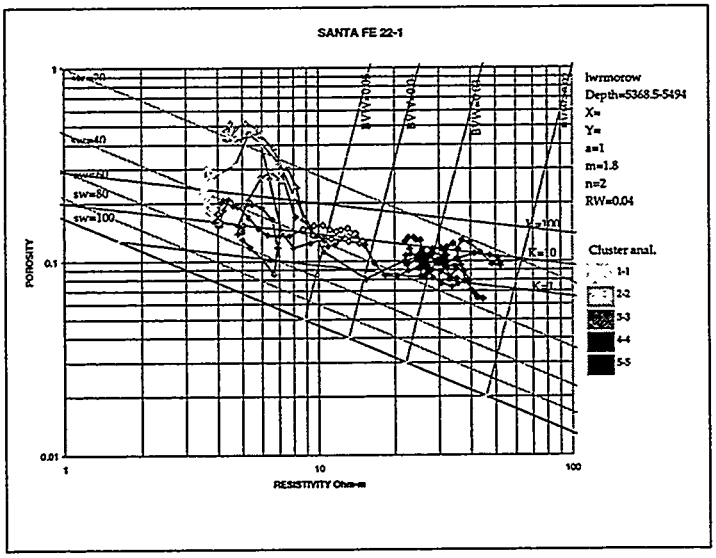
SANTA FE 22-1
POROSITY
RESISTIVITY Ohm-m
lwrmorow
Depth=5368.5-5494
X=
Y=
a=1
m=1.8
n=2
RW=0.04
Cluster anal.
1-1
2-2
3-3
4-4
5-5

Fig. 9

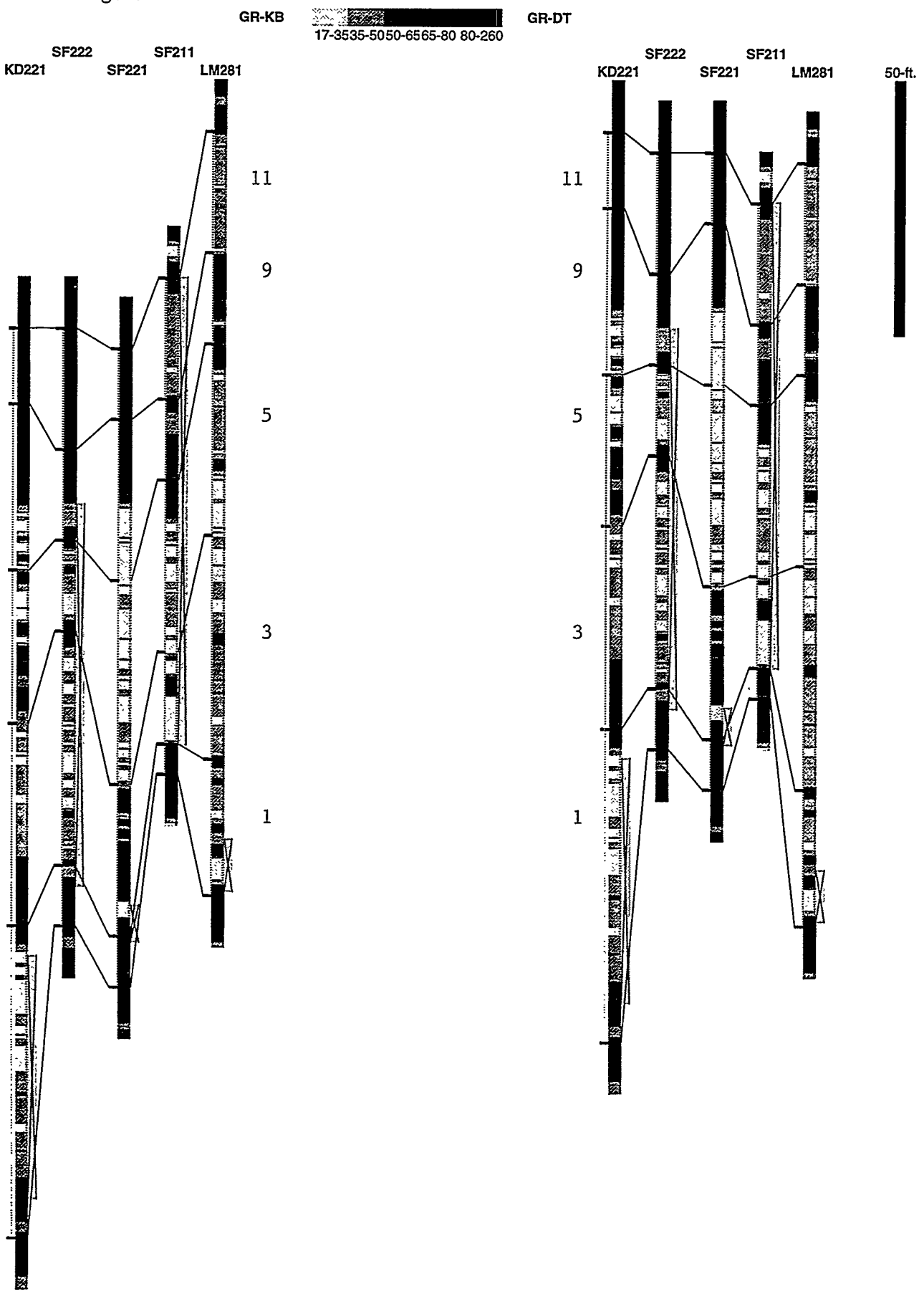
GR-KB
17-3535-5050-6565-80 80-260
GR-DT
KD221
SF222
SF221
SF211
LM281
11
9
5
3
1
KD221
SF222
SF221
SF211
LM281
50-ft.
11
9
5
3
1

Fig. 10

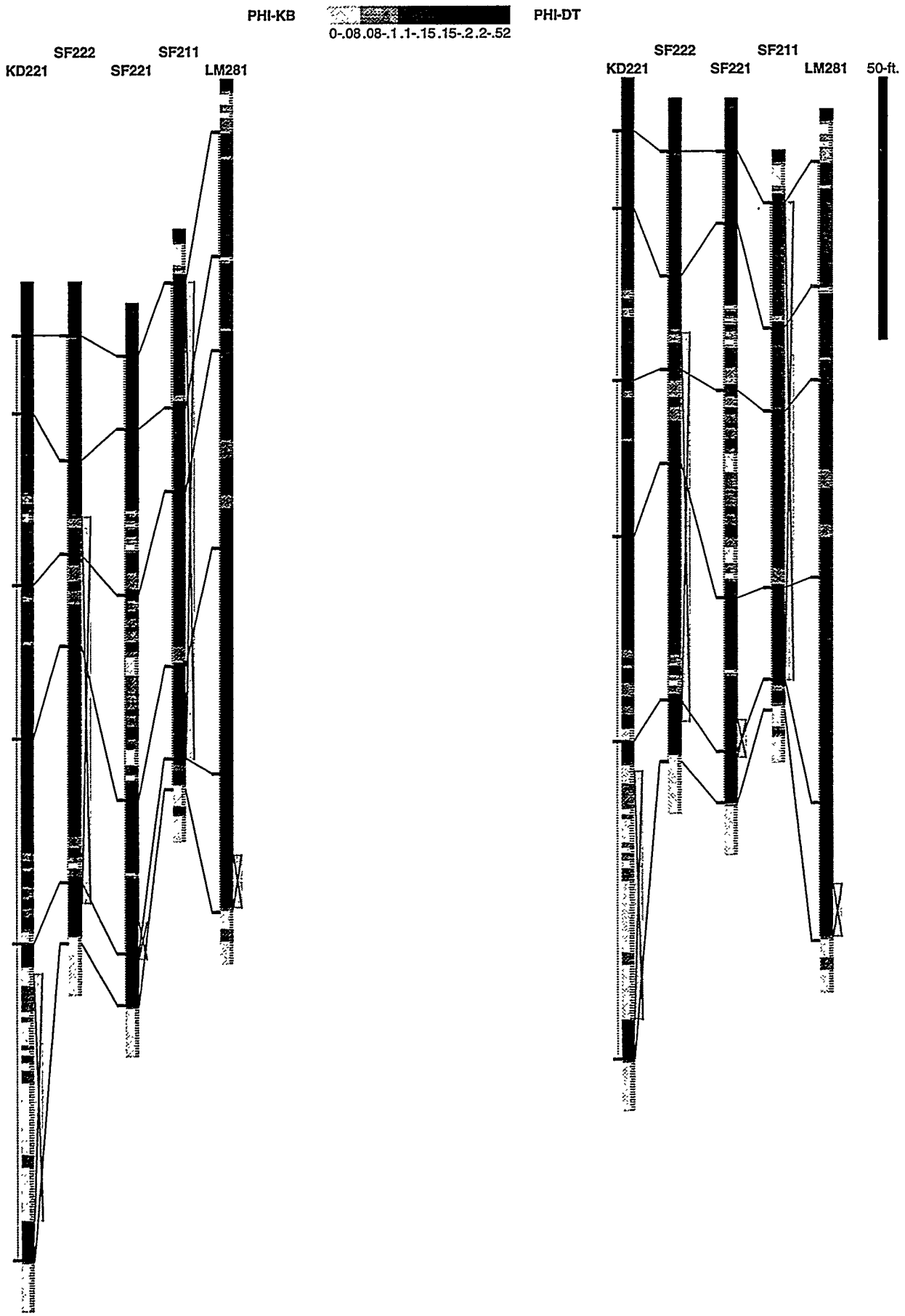
PHI-KB
0-.08.08-.1.1-.15.15-.2.2-.52
PHI-DT
KD221
SF222
SF221
SF211
LM281
KD221
SF222
SF221
SF211
LM281
50-ft.

Fig. 11

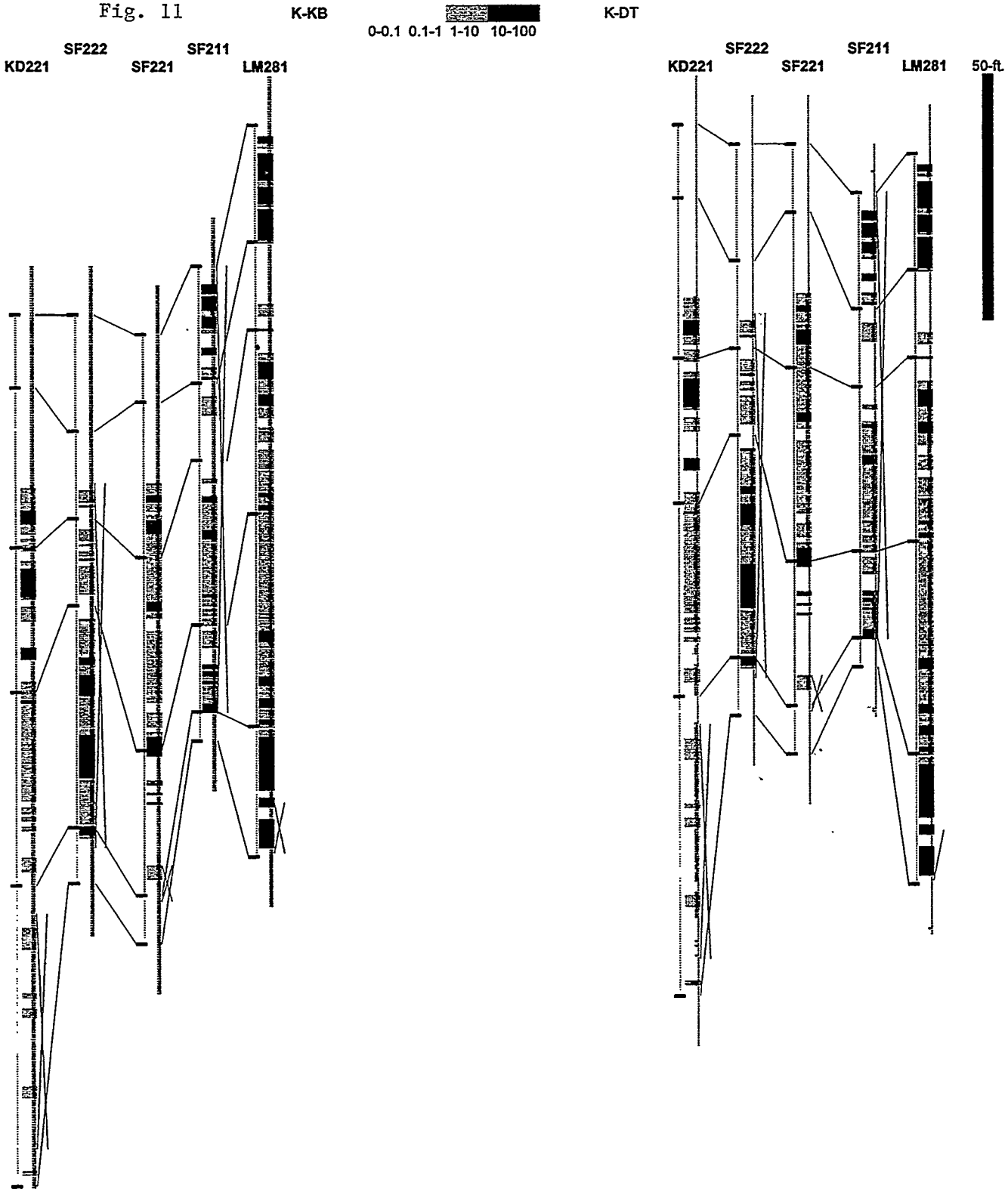
K-KB
0-0.1 0.1-1 1-10 10-100
K-DT
KD221
SF222
SF221
SF211
LM281
KD221
SF222
SF221
SF211
LM281
50-ft.

Compartmentalization Analysis using Discrete Fracture Network Models

Paul R. La Pointe*, Thorsten Eiben*, William Dershowitz*, Eugene Wadleigh+

* Golder Associates Inc., 4104 - 148th Ave. N.E., Redmond, WA, 98052

+ Marathon Oil Company, Mid-Continent Region Production U.S., P.O. Box 552, Midland, TX 79702

ACKNOWLEDGMENTS

This research is supported by the U.S. Department of Energy, National Institute for Petroleum and Energy Research (DOE/NIPER) under contract number #G4S51728.

ABSTRACT

This paper illustrates how Discrete Fracture Network (DFN) technology can serve as a basis for the calculation of reservoir engineering parameters for the development of fractured reservoirs. It describes the development of quantitative techniques for defining the geometry and volume of structurally controlled compartments. These techniques are based on a combination of stochastic geometry, computational geometry, and graph theory. The parameters addressed are compartment size, matrix block size and tributary drainage volume. The concept of DFN models is explained and methodologies to compute these parameters are demonstrated.

1. INTRODUCTION

In fractured reservoirs, the low permeability rock matrix holds the storage for the hydrocarbons while the high permeability fracture system provides the pathways to produce them. The amount of hydrocarbon that can be produced therefore is a function of the fracture network connectivity and geometry.

For fractured reservoirs the quantity and rate of fluid movement between the rock mass and a well often significantly departs from what a porous continuum model of the system might indicate (La Pointe and Dershowitz 1994). High initial production (IP) rates may drop dramatically over the first months of production. Estimates of recoverable hydrocarbons based upon dynamic and mass balance calculations may differ substantially. A key parameter in this context is reservoir compartmentalization, i.e. the division of the reservoir in not or only poorly connected regions. A petroleum reservoir that is compartmentalized either increases the cost of production or reduces the quantity of oil that is ultimately recovered. This economic cost has spawned renewed interest in understanding reservoir compartmentalization and methods to engineer compartmentalized reservoirs (e.g. Ortoleva, 1994).

Compartmentalization may arise due to a variety of structural and depositional geological processes (Ortoleva, 1994). One process which has not been well-studied but occurs widely is compartmentalization due to the finite extent of poorly connected fracture networks. One reason that this compartmentalization process has not been studied more thoroughly is that tools have only recently become available.

Recently, a new method to study flow and transport in fractured rock has evolved to the point that it provides a useful way to study fractured reservoir compartmentalization. This method is based upon Discrete Fracture Network (DFN) models. DFN models are three-dimensional stochastic or combined stochastic/deterministic realizations of the fractures in a rock mass. Fracture properties such as orientation, size, intensity, location and transmissivity can be conditioned to match either observed fracture statistics or structural models related to folding, faulting or in-situ stress.

The DOE/NIPER research project *"Fractured Reservoir Discrete Fracture Network Technologies"*, undertaken by Golder Associates, Marathon Oil Co. and The Massachusetts Institute of Technology, will develop and demonstrate technologies for improving recovery from fractured oil reservoirs. The project focuses on applying DFN-technology to tertiary recovery processes. The research is designed to use information gathered during a field trial of Thermally-Assisted-Gravity-Segregation (TAGS) at the Yates field in West Texas.

This paper presents some preliminary results of this research showing how DFN models might be used for the analysis of reservoir compartmentalization.

2. DFN MODELS

DFN models, like all models, idealize the fracturing in a reservoir. While conventional dual-continuum models simplify fracture geometry in order to better model transient multiphase flow behavior, DFN models focus on realistic fracture geometries while simplifying the flow physics (Figure 1).

Each type of modeling strategy has its strengths and weaknesses, and there is some useful overlap in these modeling approaches. However, when fracture networks dominate rock mass permeability, DFN models will significantly out-perform conventional models based on effective continuum properties (La Pointe et al., 1996b). This is because network geometry and the connectivity structures that result control the scale at which wells can communicate with each other, how much matrix can be accessed by a well, and the rate of advective flow, mass transport and heat conduction. The effects of multiphase flow or other physical processes, though also important, are second-order effects for these applications.

DFN models are stochastic or a combination of deterministic and stochastic fractures. Large-scale faults are easily identified from seismic profiles, geological mapping, lineament analyses and well logs/core. These large-scale faults are either significant flow conduits or act as barriers due to stratigraphic offset or mineralization. Since large-scale

faults are known and because they are important, they are treated as deterministic features. This means that the DFN model will have each large- scale fault represented in the location that it occurs, and with the geometry and fluid flow characteristics that have been measured or inferred. Every stochastic realization of the entire DFN model will have these deterministic features whose properties will remain unchanged throughout all of the realizations.

However, there are many medium- and small-scale faults and joints that are not detected by seismic or remote sensing imagery, or encountered in wells. Yet these faults and large joints form important flow conduits through the rock mass. It is possible to derive statistical distributions necessary for the construction of DFN models for these smaller faults and joints, as detailed for example in Dershowitz et al. (1996). These fractures constitute the stochastic portion of the DFN model, since their locations, orientations, etc. are assigned as a random sample from the statistical distributions for each realization.

The statistical distributions of fracture properties may vary in different regions. Structural models abound that relate fracture intensity, orientation, permeability and location according to the structural geology of folds, faults or in-situ stress fields thought to have produced the fractures (e.g. Stearns 1971, Stearns and Friedman 1972, Suppe 1983, Mitra 1993). Advanced DFN modeling software (Dershowitz et al., 1996) incorporates this type of conditioning.

Because the resulting DFN models contain a stochastic component, it is possible to generate multiple statistical realizations of the faults and joints. These realizations can then be used to calculate the statistics for any parameter, such as compartment size and shape, and also to carry out sensitivity studies to determine what factors control compartment size. This makes the DFN approach particularly useful for economic decision analysis.

3. METHODOLOGIES FOR CALCULATING RESERVOIR ENGINEERING PARAMETERS FROM DISCRETE FRACTURE NETWORKS

Once a DFN realization has been created, the calculation of practical reservoir engineering parameters is a straightforward, although numerically sophisticated, process. First, it is necessary to determine which fractures intersect to form networks, and to determine whether these networks intersect a well. Elementary graph theory algorithms can be used to identify completely isolated fracture networks or networks that are weakly connected to other networks. This intersection information can be stored as either an *adjacency matrix* or an *adjacency list* (Sedgewick, 1990).

Based on the intersection information various parameters can be computed. In the current stage of the project there are three parameters calculated from the DFN model:

Compartment size is defined only by the fracture network geometry. It gives the oil in place which is associated with a connected fracture system. In combination with a recovery factor it can serve as a rough quantitative measure of how much oil or gas can be produced by a well.

Matrix block shape and size also is a purely geometrical parameter. It gives a measure of the typical undisturbed volume of rock matrix in a fractured reservoir. Fluid flow within such a block will be purely dependent upon the matrix properties.

Drainage volume is a more precise quantity and important for the ultimate recovery of hydrocarbon from a producing well and for the rate of movement and shape of the heat front during steam injection. It describes the estimated volume of matrix that a fracture system intersected by a well can access. The drainage volume therefore is related to both compartmentalization and matrix block size.

4. COMPARTMENT SIZE

4.1 EFFECT OF COMPARTMENTALIZATION ON FIELD DEVELOPMENT PLANNING

The "size" of a compartment formed by a fracture network may be defined in different ways, depending upon the reservoir engineering application. For example, the horizontal cross-section of each compartment relates to how efficient a particular well pattern will be in accessing potentially recoverable oil. The number of wells, representing an economic cost, needs to be balanced against the estimated ultimate recovery (EUR) that can be produced from those wells. If many compartments are missed by a proposed well pattern, then potentially recoverable hydrocarbons are being left in the ground. Alternatively, a well pattern that already produces from most of the reservoir compartments will not benefit from an infill drilling program.

Compartmentalization as it relates to economically efficient well patterns can be assessed by computing the horizontal dimensions and area of all of the fracture compartments in a series of DFN realizations. From these Monte Carlo realizations of a model, it is possible to compute a cumulative probability graph for compartment cross-sectional area. Such a graph provides an estimate of the mean acreage of the reservoir which a well could access. This acreage provides an indication whether a particular well pattern spacing will probably miss intersecting a number of compartments, whether each compartment is typically intersected by numerous wells (and thus may be economically inefficient), or whether the number of wells balances compartment access with drilling costs.

While it is usually possible to identify large-scale fault-bounded reservoir compartments from seismic or production histories, it is far more difficult to assess the compartmentalization due to joint network geometry and connectivity, for which seismic information is of little use. Joint network compartmentalization is often suspected when static and dynamic calculations of recoverable oil or gas do not agree, and there is no evidence for fault-offset or other types of fault-related compartmentalization.

Figures 2 and 3 illustrate the effect compartmentalization has on the connectivity within a reservoir. Figure 2 shows the DFN of a compartmentalized and intensively fractured rock mass. By looking at the figure one would expect all areas of the reservoir to be well connected. Figure 3, however, displays the same fracture network but only shows that portion of the network which is connected directly or indirectly to one of the 5 wells.

4.2 COMPARTMENTALIZATION ANALYSIS

The computation of the volume and horizontal extent of joint network compartments is a three-step process:

Step 1. Identify individual fracture networks within the DFN model

Step 2. Compute the bounding surface for each identified network

Step 3. Calculate the volume within the bounding surface and the horizontal extent of the network

While it would be possible to compute the "bounding box" for a network, and use this box volume and horizontal cross-section as surrogates for compartment volume and horizontal extent, this would lead to an overestimation in most cases of both volume and cross-section. This in turn would produce overestimates of the ultimate recovery from wells, and suggest greater well spacings and recovery efficiencies than would actually be the case. To reduce the potential for overestimates, it is necessary to calculate a bounding surface that better approximates the outer limits of the network. A convex hull meets these requirements.

A convex hull is essentially a bounding surface with certain advantageous mathematical properties. For points with three-dimensional spatial coordinates, the convex hull is a convex polyhedron, which has the minimum volume of all possible convex polyhedra that bound the point set. Figure 4 shows such a three-dimensional convex hull calculated using the QuickHull algorithm and the Qhull software package (Barber et al., 1995) for the central well shown in Figure 3. In Figure 5, the horizontal projection of the hull is

shown. The resulting data can easily be used to compute the volume and cross-sectional area of each hull.

5. MATRIX BLOCK SIZE

The fracture surface area of matrix blocks within a simulation grid cell influences the rate and quantity of fluids that can move between the matrix and the fracture system. The Z-dimension of matrix blocks influences gravity drainage mechanisms. The shape of the matrix blocks influences the choice of sugar cube, matchstick or slab idealization. A realistic description of block size and shape in a way that can be implemented in existing dual porosity simulators will benefit not only the thermal simulation TAGS processes, but also non-thermal simulations of injection or production in fractured reservoirs.

5.1 BLOCK SIZE ANALYSIS

Two DFN algorithms have been developed to compute matrix block shape and size that are :

1. Based on geologically realistic three-dimensional fracture systems, and
2. Provide output in the form required by conventional dual-porosity simulators.

The first algorithm is a fast computational method to compute blocks based upon fracture spacing distributions in several directions. Its main advantage is that the calculation is computationally fast. Its disadvantage is that it assumes that block x, y and z dimensions are uncorrelated. This algorithm is referred to as the *multidirectional spacing distribution algorithm* (Figure 6).

For each realization of the discrete fracture model, a series of randomly-located lines in selected directions are generated. The location of fractures intersected by each line is recorded. This leads to a spacing frequency distribution in several directions. Typically, the directions include the vertical direction, in order to calculate the vertical dimension of blocks for gravity drainage considerations, and in two or three orthogonal directions that relate to simulator grid layering geometry and the fracture system.

The spacing probability distributions are multiplied together using Monte Carlo sampling techniques to produce a frequency distribution of block volumes and surface areas. This is carried out by selecting X, Y and Z spacing values at random with selection probability proportional to their frequency, and multiplying them together to create a prismatic block volume.

The second algorithm is based upon graph theory and, again, uses convex hulls. This algorithm is therefore referred to as the *convex hull algorithm.* It is based upon computing the convex hull of points lying on fractures bounding or partially bounding a matrix block.

The convex hull algorithm is more computationally intensive, but measures the actual dimensions of the blocks, rather than reconstructing blocks stochastically from spacing frequencies. Thus, any correlation among block dimensions or non-prismatic block shapes are considered appropriately. The algorithm's accuracy is governed by two factors: whether in fact the matrix blocks are convex; and how many points are required to accurately characterize the convex block. The algorithm as implemented allows the user to specify the number of points for characterizing the convex block.

Test cases (La Pointe et al., 1996b) suggest that both the multi directional spacing (MDS) and convex hull (CH) algorithms provide reliable and consistent estimates of fracture surface area, at least for simple fracture geometries. The CH algorithm appears to provide better estimates of the mean volume of matrix blocks when block dimensions are partially correlated. Since jointing in many sedimentary rocks is characterized by pseudo-periodic spacings (e.g., La Pointe and Hudson, 1985), it may be preferable to use the CH algorithm to estimate block volumes. On the other hand, the geometric construction of a convex hull from a sparse data set creates hulls with slightly greater average Z-dimensions than the MDS algorithm. In both test cases 1 and 2, the MDS algorithm provided more accurate estimates of the Z-dimension. Thus, both algorithms have proven useful and necessary to provide estimates of matrix block parameters, and neither alone is completely satisfactory.

6. DRAINAGE VOLUME

The tributary drainage volume for a well is that volume of the matrix that can be drained by the fracture network connected to a well or heated up by steam injection. The drainage volume takes into account both the geometry of the fracture network and the physical processes of advective flow, transport, diffusion and heat conduction. Tributary drainage volume is related to both block size and compartmentalization.

6.1 DRAINAGE VOLUME ANALYSIS

The algorithm developed to compute the tributary drainage volume is divided into two steps:

Step 1. Identify the fracture networks connected to the well or perforated zone of interest

Step 2. Estimate the volume of matrix within the network that could be produced

While the procedure for step 1 is the same as for the compartmentalization analysis, step 2 can become extremely complex. The task is to predict which portion of the matrix volume is close enough to a fracture, given the pressure drawdown within the matrix block, to be able to contribute to production.

Different ways could be used to accomplish step 2. If the fracture network is very dense, then the volume of the matrix accessed by the fracture network will be closely approximated by the volume of the convex hull enclosing the network. In essence, this means that the tributary drainage volume is equal to the compartment volume. The same conclusion applies if the matrix permeability is sufficiently large to allow production to take place from all of the matrix volume.

In less dense fracture networks where the typical matrix block size is large, some or maybe most of the volume inside the convex hull will be too far from any of the fractures to be easily produced. For these cases, the user can specify an average drainage percentage. It is possible to compute this percentage with the help of the blocksize information

derived earlier. The average drainage percentage is then used to reduce the convex hull volume.

Another approach to exclude matrix that might not be efficiently produced through pressure depletion drainage is to surround each fracture in the network with a polygon that is calculated from the area of the fracture and the distance away from the fracture over which drainage might be effective (Figure 7). This leads to a prism that encloses the fracture. For pressure depletion mechanisms, the fracture forms the midplane of the prism. An obvious problem with this algorithm is to avoid double-counting the volume where there is overlap between the prisms. Calculations based upon solid geometry to compute the volume while accounting for the overlap are highly time-consuming for the number of fractures that might commonly be encountered in a fracture network. A simpler method has been devised which is much more efficient, though not as numerically exact (La Pointe et al. 1996b).

Computing the drainage volume is a critical reservoir engineering parameter. For computing the ultimate recovery, it is necessary to combine the static parameters like compartment volume and block size with the dynamics involved in the flow of fluids from the matrix into the fracture system. Because of the time dependent pressure distribution within a matrix block the drainage volume will also be time dependent. This corresponds to the step from volumetric oil in place estimation to dynamic ultimate recovery calculation using reservoir simulation.

Nonetheless, the measures described above will provide an estimate of the recoverable reserves from a reservoir. They offer an advantage, however, that a large number of realizations can be run, and so the uncertainty relating to simplification can be quantified in a clear and straightforward manner. The alternative of carrying out hundreds of numerical fluid flow simulations requires substantially greater, and perhaps prohibitive, computing times.

7. SUMMARY AND OUTLOOK

The ongoing DOE/NIPER research project "*Fractured Reservoir Discrete Fracture Network Technologies*" is developing technologies for improving recovery from fractured oil reservoirs. This paper illustrates some preliminary results of this effort. The work thus far has concentrated on the development of methodologies and algorithms which can be used to extract valuable parameters from fracture network information for the use in reservoir engineering tasks. It has been shown how Discrete Fracture Network models can be used to calculate parameters like compartment size, matrix block size and tributary drainage volume.

At the time of the submission of this paper, the methods described are undergoing an intense verification process (La Pointe et al. 1996b). In the next step, the methods will be used on field data from the Yates field.

8. REFERENCES

Barber, C. B., D.P. Dobkin, and H.T. Huhdanpaa, 1995. The Quickhull Algorithm for Convex Hulls. ACM Transactions on Mathematical Software.

Dershowitz, W., G. Lee, J. Geier, T. Foxford, P. La Pointe and A. Thomas, 1996. FracMan Interactive Discrete Feature Data Analysis, Geometric Modeling, and Exploration Simulation: User Documentation Version 2.5. Golder Associates Inc., Redmond, WA.

La Pointe, P.R., and J. Hudson, 1985. Characterization and Interpretation of Rock Joint Patterns. GSA Special Paper 199. GSA, Denver.

La Pointe, P.R., and Dershowitz, W.S., 1994. Discrete Fracture Approaches for Oil and Gas Applications. Proceedings: 1st North American Rock Mechanics Symposium, The University of Texas at Austin, June 1-3, 1994, p. 19-30.

La Pointe, P.R., Wallmann, P.C., and Follin, S., 1996a. Continuum Modeling of Fractured Rock Masses: Is it useful? Proceedings: Prediction and Performance in Rock Mechanics and Rock Engineering (EUROCK '96), Torino, Italy, September 2-5, 1996, p. 343-350.

La Pointe, P.R., Eiben, Th., and Dershowitz, W.S., 1996b. Fractured Reservoir Discrete Fracture Network Technologies. Research Report Reservoir Compartmentalization. Golder Assoc. Inc., Redmond, WA.

Mitra, S., 1993. Geometry and kinematic evolution of inversion structures. Bulletin American Association of Petroleum Geologists, Vol 77, p. 1159-1191.

Ortoleva, P.J.(ed), 1994. Basin Compartments and Seals. AAPG Memoir 61, American Assoc. of Petroleum Geologists, Tulsa.

Sedgewick, R., 1990. Algorithms in C. Addison-Wesley Pub. Co., Reading, MA.

Stearns, D. W. 1971. Mechanisms of drape folding in the Wyoming Province. Wyoming Geol. Assoc. Guidebook. Twenty-third Field Conference, p. 125-143.

Stearns, D. W. and Friedman, M. 1972. Reservoirs in fractured rock. Memoir 16, American Association of Petroleum Geologists, p. 82-106.

Suppe, J. 1983. Geometry and kinematics of fault-bend folding. American Journal of Science, Vol 283, p. 684-721.

LIST OF FIGURES

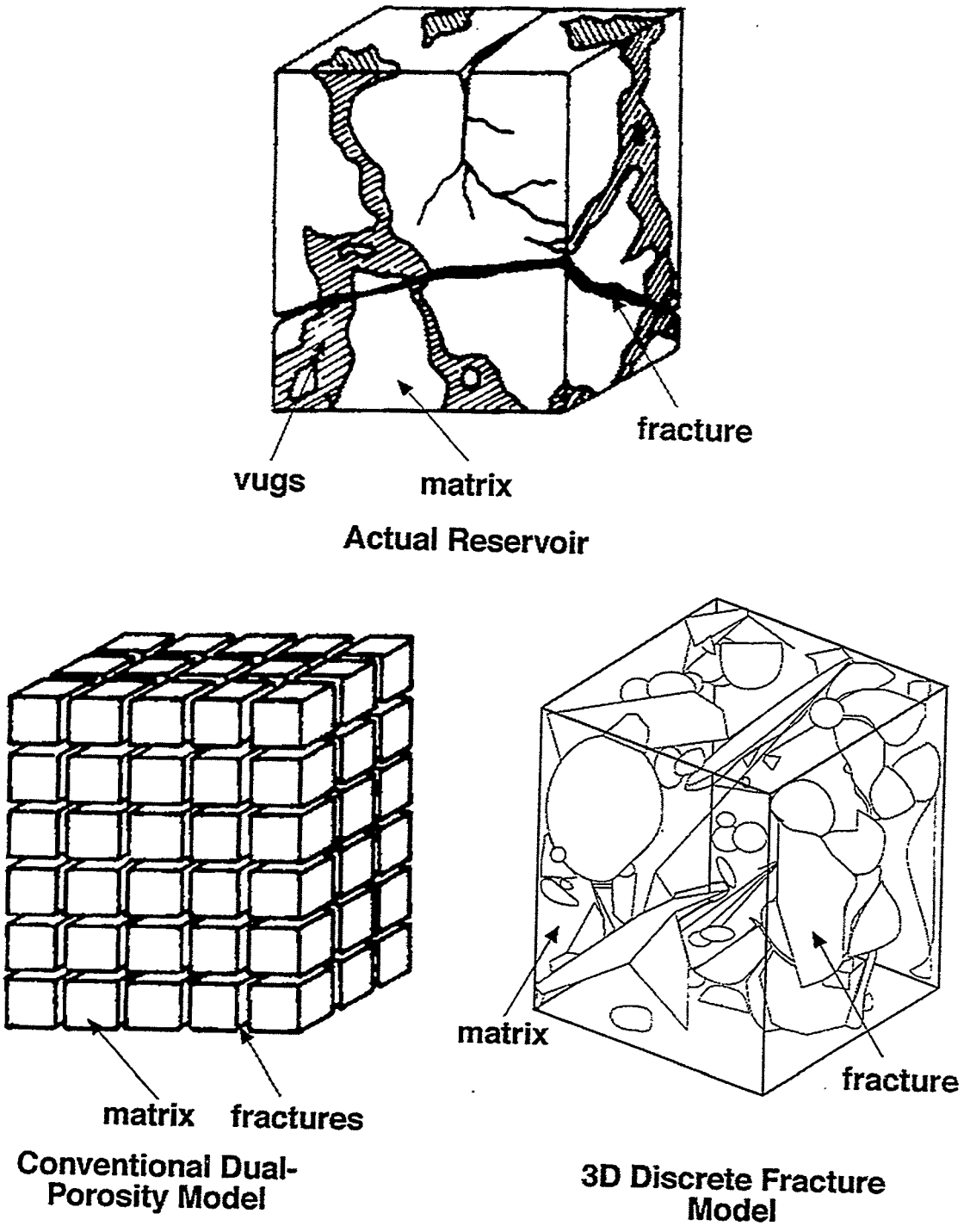

Fig. 1: Discrete Fracture Network model approach for a fractured rock mass

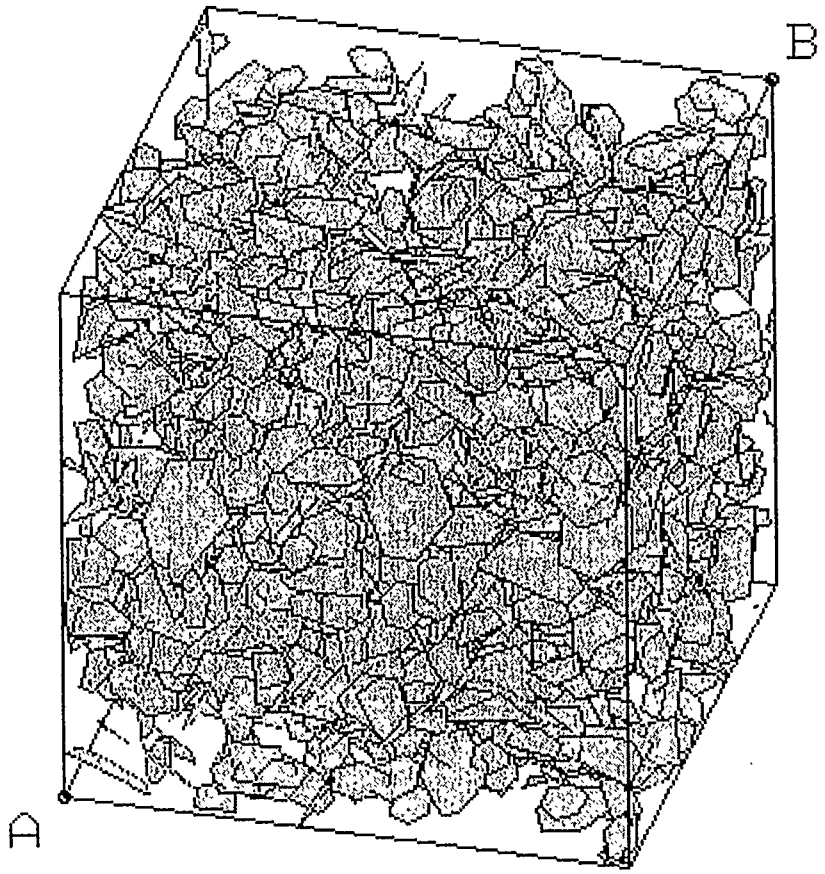

Fig. 2: DFN model of compartmentalized intensively fractured rock mass

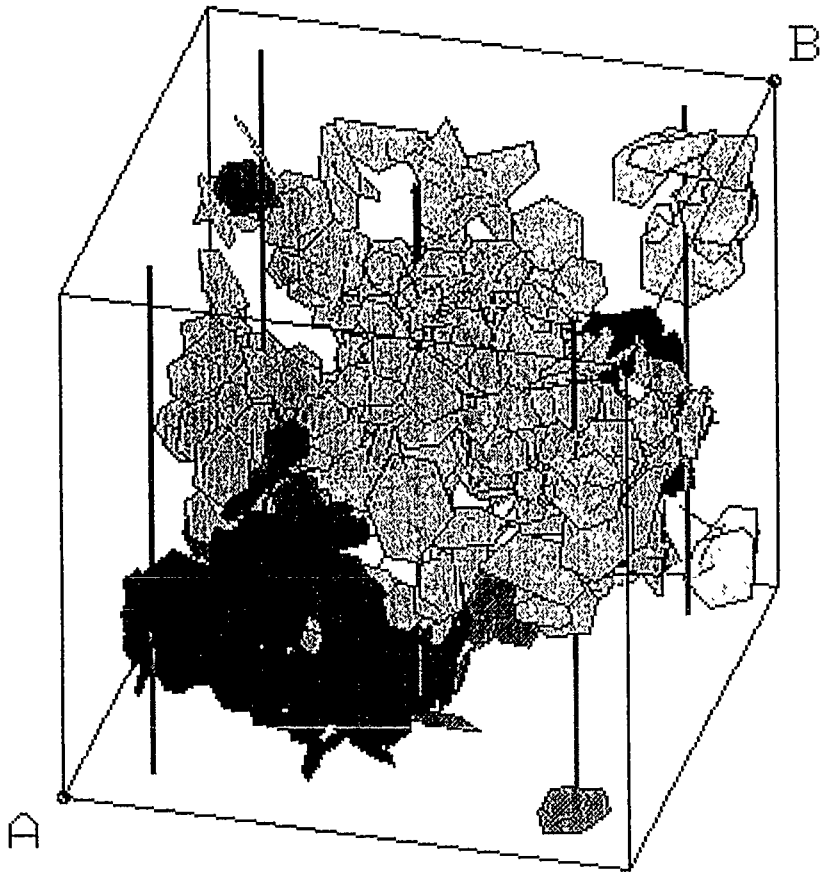

Fig. 3: Production from compartmentalized intensively fractured reservoir

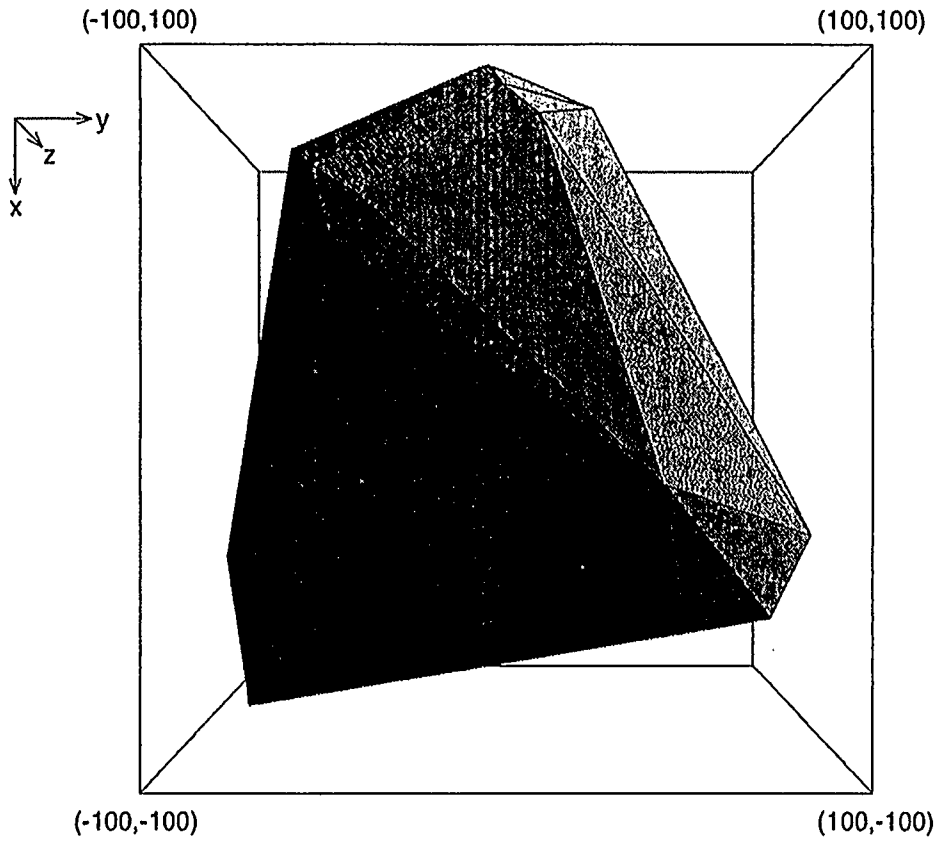

Fig. 4: Convex hull of fracture network connected to center well

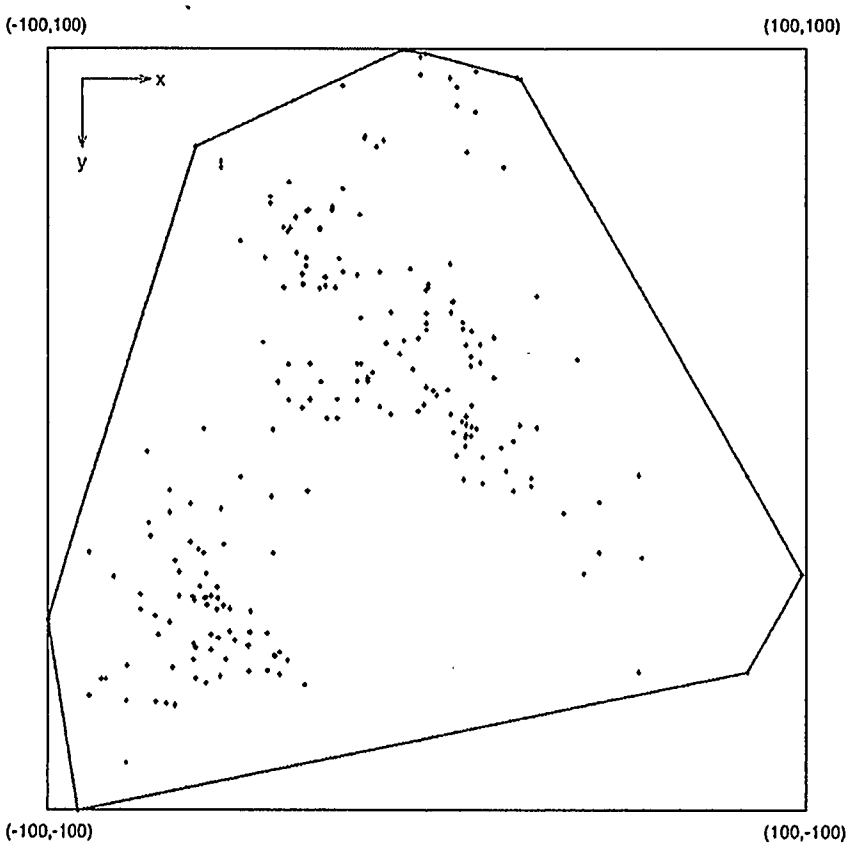

Fig. 5: Horizontal projection of convex hull connected to center well

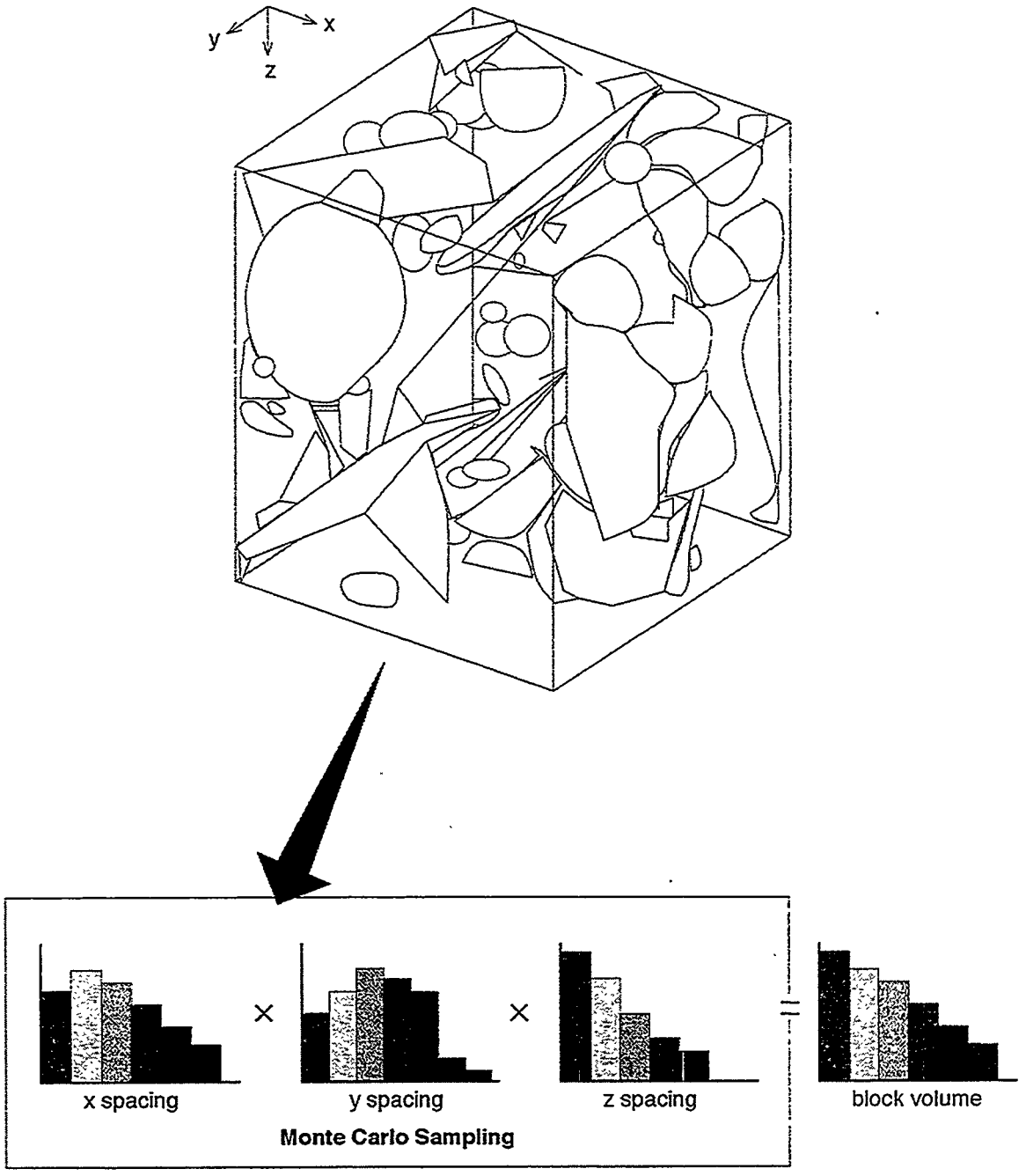

Fig. 6: Multi-Directional Spacing Algorithm

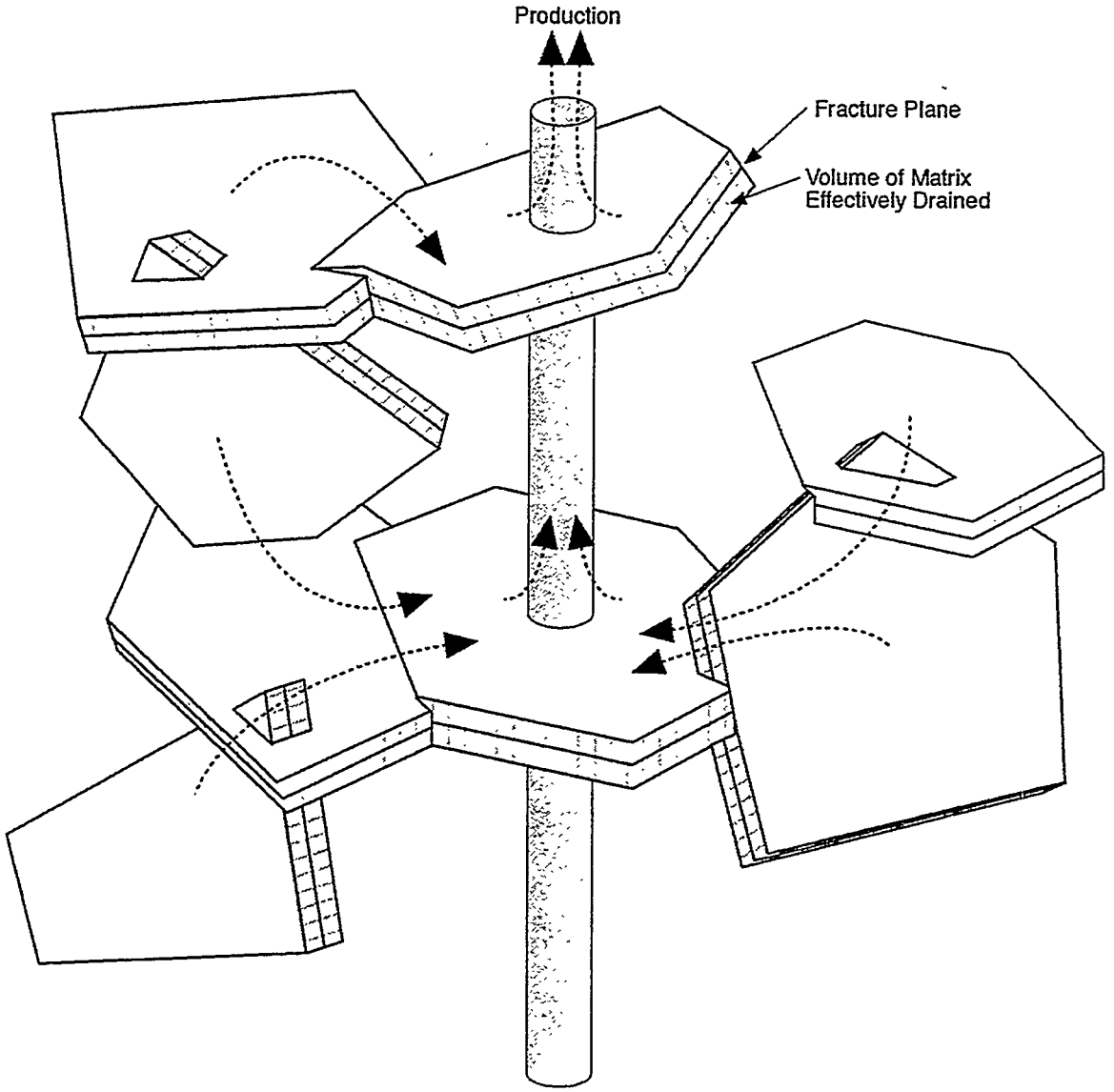

Fig. 7: Tributary Drainage Volume

Characterization of Dynamic Change of Fan-delta Reservoir Properties in Water-drive Development

Wu Shenghe; Xiong Qihua; Liu Yuhong
Department of Geosciences
University of Petroleum
Changping, Beijing P.R. China

ABSTRACT

Fan-delta reservoir in Huzhuangji oil field of east China, is a typical highly heterogeneous reservoir. The oil field has been developed by water-drive for 10 years, but the oil recovery is less than 12%, and water cut is over 90%, resulting from high heterogeneity and serious dynamic change of reservoir properties. This paper aims at the study of dynamic change of reservoir properties in water-drive development.

Through quantitative imaging analysis and mercury injection analysis of cores from inspection wells, the dynamic change of reservoir pore structure in water-drive development was studied. The results show that the "large pore channels" develop in distributary channel sandstone and become larger in water-drive development, resulting in more serious pore heterogeneity.

Through reservoir sensitivity experiments, the rock-fluid reaction in water-drive development is studied. The results show the permeability of some distal bar sandstone and deserted channel sandstone becomes lower due to swelling of I/S clay minerals in pore throats. On the other hand, the permeability of distributary channel and mouth bar sandstone become larger because the authigenic Koalinites in pore throats are flushed away with the increase of flow rate of injection water.

Well-logging analysis of flooded reservoirs are used to study the dynamic change of reservoir properties in various flow units. The distribution of remaining oil is closely related to the types and distribution of flow units.

Calculation of Large Scale Relative Permeabilities from Stochastic Properties of the Permeability Field and Fluid Properties

Roland Lenormand; Marco R. Thiele (Stanford University)
Institut Français du Pétrole
1 et 4 Avenue de Bois-Priau - B.P. 311
Rueil Malmaison 92506
Cedex, France

ABSTRACT

The paper describes the method and presents preliminary results for the calculation of homogenized relative permeabilities <Kr> using stochastic properties of the permeability field.

In heterogeneous media, the spreading of an injected fluid is mainly sue to the permeability heterogeneity and viscosity fingering. At large scale, when the heterogeneous medium is replaced by a homogeneous one, we need to introduce a homogenized (or pseudo) relative permeability <Kr> to obtain the same spreading. Generally, <Kr> is derived by using fine-grid numerical simulations (Kyte and Berry). However, this operation is time consuming and cannot be performed for all the meshes of the reservoir. We propose an alternate method which uses the information given by the stochastic properties of the field without any numerical simulation.

The method is based on recent developments on homogenized transport equations (the "MHD" equation, Lenormand SPE 30797). The MHD equation accounts for the three basic mechanisms of spreading of the injected fluid:

1) Dispersive spreading due to small scale randomness, characterized by a macrodispersion coefficient D.
2) Convective spreading due to large scale heterogeneities (layers) characterized by a heterogeneity factor H
3) Viscous fingering characterized by an apparent viscosity ration M

In the paper, we first derive the parameters D and H as functions of variance and correlation length of the permeability field. The results are shown to be in good agreement with fine-grid simulations. The <Kr> are then derived a function of D, H and M. The main result is that this approach lead to a time dependent <Kr>. Finally, the calculated <Kr> are compared to the values derived by history matching using fine-grid numerical simulations.

Statistical Analysis of Surface Lineaments and Fractures for Characterizing Naturally Fractured Reservoirs

Genliang Guo and Stephen A. George, BDM Petroleum Technologies, and Rhonda P. Lindsey, DOE Bartlesville Project Office

Abstract

Thirty-six sets of surface lineaments and fractures mapped from satellite images and/or aerial photos from parts of the Mid-continent and Colorado Plateau regions were collected, digitized, and statistically analyzed in order to obtain the probability distribution functions of natural fractures for characterizing naturally fractured reservoirs. The orientations and lengths of the surface linear features were calculated using the digitized coordinates of the two end points of each individual linear feature. The spacing data of the surface linear features within an individual set were obtained using a new analytical sampling technique. Statistical analyses were then performed to find the best-fit probability distribution functions for the orientation, length, and spacing of each data set. Twenty-five hypothesized probability distribution functions were used to fit each data set. A chi-square goodness-of-fit test was used to rank the significance of each fit. A distribution which provides the lowest chi-square goodness-of-fit value was considered the best-fit distribution.

The orientations of surface linear features were best-fitted by triangular, normal, or logistic distributions; the lengths were best-fitted by PearsonVI, PearsonV, lognormal2, or extreme-value distributions; and the spacing data were best-fitted by lognormal2, PearsonVI, or lognormal distributions. These probability functions can be used to stochastically characterize naturally fractured reservoirs.

Introduction

The characterization of naturally fractured reservoirs has challenged geologists and engineers for decades. From a reservoir engineering point of view, the objective of characterizing a naturally fractured reservoir is to estimate the flow and storage capacity, both of which require a quantitative description of natural fracture characteristics. Unfortunately, subsurface natural fracture data are rarely available and very expensive to obtain. The scarcity of subsurface natural fracture data and our inability to cost-effectively acquire sufficient amount of them have prevented us from obtaining a realistic and quantitative description of subsurface fracture systems.

One technique for characterizing a naturally fractured reservoir, which may overcome the limitation in the availability of subsurface natural fracture data, is to stochastically simulate the subsurface fracture systems and numerically calculate their permeability tensor distributions (Guo et al. 1994). The reliability of this technique, however, rests on the validity of the probability distribution functions of natural fracture characteristics used in the stochastic simulations. Many attempts have been made to use surface fracture data mapped from outcrop studies to derive the probability distributions of natural fracture characteristics.

Studies show that natural fracture orientations have a normal or Arnold's hemispherical normal distribution for two-dimensional data and a Fisher-Von Mises distribution for three-dimensional data (Long et al. 1982, Cacas et al. 1990, Dverstorp et al. 1989, Belfield et al. 1995). Fracture lengths have been found by various investigators to have a lognormal, exponential, or power law distribution (Long et al. 1982, Cacas et al. 1990, Dverstorp et al. 1989, Baecher et al. 1977, Baecher 1983, Roulean et al. 1985, Heffer et al. 1990). The distribution functions which provide best fits to many fracture aperture data include normal and lognormal distributions (Long et al. 1982, Belfield et al. 1995, Snow 1970). As the most extensively investigated characteristic of natural fractures, fracture spacing is found to have an exponential, lognormal, Weibull, Gamma, or power law distribution (Long et al. 1982, Belfield et al. 1995, Baecher et al. 1977, Baecher 1983, Roulean et al. 1985, Heffer et al. 1990, Lorentz et al. 1991, Loosveld et al. 1992). These distribution functions were usually identified by best-fitting measured data to a few hypothesized distributions.

In this paper, we present the results of a statistical analysis of natural fracture characteristics using a large number of surface lineaments and fractures in the Mid-continent and Colorado Plateau regions collected and digitized from previous studies reported in the literature. Twenty-five different probability distribution functions (see the Appendix) are used to best fit the orientation, length, and spacing of each of the 36 fracture and/or lineament sets identified. A chi-square goodness-of-fit test is employed to identify the best fits. The abundance of surface lineaments and fractures and the list of 25 hypothesized distribution functions used in the statistical analysis will inevitably result in more reliable probability distributions for describing natural fracture characteristics.

Statistical Analysis Procedure

The basic data used in this study were obtained by digitizing the two end points of the surface linear features mapped from

satellite images and/or aerial photos of various parts of the Mid-continent and Colorado Plateau regions. Due to the nature of the data, only orientation, length, and spacing were analyzed. No data were available for aperture analysis. The following procedure was used for the statistical analysis of surface lineament and fracture characteristics:

- A rose diagram analysis for identifying the number of subsets in a surface lineament and/or fracture system.
- A filtering analysis for partitioning a surface-fracture system into subsets.
- A sampling analysis for collecting surface-fracture spacing data using a new analytical technique.
- A best-fit analysis for obtaining distribution functions for surface lineament and fracture orientation, length, and spacing.

In the following discussion, the surface fractures in Osage County, Oklahoma, are used to demonstrate the procedure for statistical analysis of surface-fracture characteristics.

Shown in Fig. 1 are the surface fractures in Osage County. They were mapped from satellite images and aerial photos (Guo et al. 1995). A rose diagram for these surface fractures was generated (see Fig. 2). This rose diagram shows that the surface fractures primarily consist of two sets trending northeast and northwest. Figs. 3 and 4 show the northeast- and northwest-trending surface fractures, after they are separated through a filtering analysis based on their orientations.

Within each subset, the orientation and length data are calculated using the digitized coordinates of the two end points for each surface fracture. The spacing data are obtained using an analytical sampling technique. The technique involves overlapping a set of uniform imaginary scanlines on top of an individual fracture set (see Figs. 5 and 6). The scanlines are oriented perpendicular to the average orientation of the fracture set. The intersection points along each imaginary scanline are then identified and sorted. The spacing data are obtained by calculating the distance between two adjacent intersection points along a scanline. After orientation, length, and spacing data are obtained for each fracture set, they are fitted to 25 hypothesized probability distributions. A chi-square goodness-of-fit test is used to identify the best-fit distributions.

Fig. 7 shows the histogram and best-fit orientation distribution of the northeast-trending surface fractures. A total of 2,046 data points were used in the analysis. A triangular distribution, TRIANG(-1.47, 37.38, 95.63), appears to provide the best fit to the data, although a normal distribution, NORMAL(43.59, 19.80), also fits the data closely. Similarly, Fig. 8 shows the histogram and best-fit orientation distribution of the northwest-trending surface fractures. There are 1,322 surface fractures in this set. The orientations of this set of surface fractures were best-fitted by a logistic distribution, LOGISTIC(128, 12.01).

As shown in Fig. 9, the length data of the northeast-trending surface fractures, were best-fitted by a PearsonVI distribution, PearsonVI(11.35, 4.54, 1480). Fig. 10 shows the histogram and best-fit length distribution for the northwest-trending surface fractures. A PearsonVI distribution, PearsonVI(8.95, 3.95, 1500), provides the best fit, but a lognormal2 distribution, LOGNORM2(8.20, 0.60), also fits the data very well.

The spacing data of the northeast-trending surface fractures, were best-fitted by a lognormal2 distribution, LOGNORM2(8.21, 1.11). The histogram, best-fit distribution, and statistical parameters of the northeast-trending surface-fracture spacing data are shown in Fig. 11. Similar results were also obtained for the spacing data of the northwest-trending surface fractures, as shown in Fig. 12. A lognormal2 distribution, LOGNORM2(8.64, 1.18), is the best-fit distribution.

Statistical Analysis of Surface Lineaments and Fractures in Northeastern Arizona

A photogeological interpretation study was conducted in the Cameron and the Black Mesa Basin areas in northeastern Arizona (Guo et al. 1995). Over 50,000 surface fractures were mapped from aerial photos and subsequently digitized. In addition, large-scale surface lineaments were collected and digitized in the general northeastern quarter of Arizona (Lepley 1977). Using the statistical analysis procedure discussed in the previous section, the characteristics of the surface lineaments and fractures in northeastern Arizona were statistically analyzed.

Surface Lineaments in Northeastern Arizona. Fig. 13 is a rose diagram for the surface lineaments in northeastern Arizona. The surface lineaments apparently can be partitioned into four subsets, including two major sets trending northeast and northwest and two minor sets trending east and north. Figs. 14 to 17 show the histograms, best-fit orientation distributions, and sample data statistics for the four sets of the surface lineaments. A normal distribution provides the best fit to the orientation data of the east-trending surface lineaments; whereas those of the northeast-, north-, and northwest-trending surface lineaments were best-fitted by three triangular distributions.

The results of a statistical analysis on the corresponding length data are given in Figs. 18 to 21. The length data of the east- and north-trending surface lineaments were best-fitted by two PearsonV distributions; those of the northeast- and northwest-trending surface lineaments were best-fitted by two PearsonVI distributions.

Similarly, the results of a statistical analysis on the corresponding spacing data are given in Figs. 22 to 25. The spacing data of the east-trending surface lineaments were best-fitted by a PearsonVI distribution; those of the northeast-, north-, and northwest-trending surface lineaments were best-fitted by three lognomal2 distributions.

Surface Fractures in the Cameron Area in Northeastern Arizona. Over 6,100 surface fractures were mapped from aerial photos in the Cameron area in northeastern Arizona (Guo et al. 1995). Fig. 26 is a rose diagram for those surface fractures. From this rose diagram, three subsets were identified, including two major sets trending northeast and north-northeast and a minor set trending east. The histograms, best-fit orientation distributions, and sample data statistics for the

three sets of the surface fractures are shown in Figs. 27 to 29. The orientation data of the northeast-trending surface fracture set were best-fitted by a normal distribution, whereas those of the other two fracture sets were best-fitted by two triangular distributions.

Figs. 30 to 32 show the results of a statistical analysis on the corresponding three sets of surface fracture length data in the Cameron area. A PearsonVI distribution appears to provide the best fit to the length data of the east-trending fracture set; two loglogistic distributions provide the best fits to the other two fracture sets.

Similarly, Figs. 33 to 35 show the histograms, best-fit distributions, and sample data statistics for the spacing data of the three sets of surface fractures in the Cameron area. A lognormal distribution provides the best fit to the spacing data of the east-trending surface fracture set. Those of the northeast- and north-northeast-trending surface fractures were best fitted by two lognormal2 distributions.

Surface Fractures in the Black Mesa Basin Area in Northeastern Arizona. Over 44,000 surface fractures were mapped from aerial photos of the Black Mesa Basin area in northeastern Arizona (Guo et al. 1995). Fig. 36 shows a rose diagram of these surface fractures. Four subsets were identified from Fig. 36 trending east, northeast, north-northeast, and northwest. A statistical analysis was performed on the orientations of these four sets of surface fractures. The results are given in Figs. 37 to 40. The orientation data of the east- and northeast-trending fractures were best-fitted by two normal distributions. Those of the north-northwest-trending fractures were best fitted by a triangular distribution, whereas those of the northwest-trending fractures were best-fitted by a chi-square distribution.

Similarly, the length data of the four sets of surface fractures were also statistically analyzed. The results are shown in Figs. 41 to 44. It appears that the length data of the east- and northwest-trending surface fractures in this area were best-fitted by two PearsonVI distributions. Those of the northeast-trending surface fractures were best-fitted by an extreme-value distribution, whereas those of the north-northwest-trending surface fractures were best-fitted by a lognormal2 distribution.

Figs. 45 to 48 show the results of a statistical analysis on the spacing data of the four sets of surface fractures in the Black Mesa Basin area. A lognormal distribution appears to provide the best fit to the spacing data of the northwest-trending surface fractures, but those of the other three sets were best-fitted by lognormal2 distributions.

Statistical Analysis of Surface Lineaments and Fractures in the Mid-continent Region

A large number of surface lineaments and fractures were also collected and digitized from many previous studies of various parts of the Mid-continent region (Guo et al. 1996). Using the procedure discussed earlier, best-fit statistical distribution functions were obtained for the surface lineament and fracture characteristics in this region through extensive best-fitting analyses.

Surface Lineaments in Northeastern Oklahoma. Fig. 49 is a rose diagram for the surface lineaments in northeastern Oklahoma (Burchett et al. 1983). From this rose diagram, one can see that the surface lineaments in this area can be partitioned into five subsets oriented east-northeast, north-northeast, north, north-northwest, and northwest. Figs. 50 to 54 show the histograms, best-fit distributions, and sample data statistics for the five sets of the surface lineament orientation data. The orientations of the east-northeast-, north-northeast-, and north-northwest-trending surface lineaments in this area were best-fitted by normal distributions. Those of the north- and northwest-trending surface lineaments were best-fitted by triangular distributions.

The histograms, best-fit distributions, and sample data statistics of the corresponding lengths for the five sets of surface lineaments in the northeastern Oklahoma are shown in Figs. 55 to 59. It appears that PearsonV or PearsonVI distributions provide the best fits to the five sets of the lineament length data.

The spacing data for the surface lineaments in northeastern Oklahoma were also analyzed. The results are shown in Figs. 60 to 64. Inverse Gaussian, lognormal, lognormal2, and PearsonVI distributions appear to provide best fits to the five sets of the spacing data.

Surface Lineaments in Eastern Kansas. Fig. 65 shows a rose diagram of the surface lineaments in eastern Kansas (Burchett et al. 1983). Three major subsets can be identified from this diagram. They are oriented in the northeast, north-northwest, and northwest directions. Figs. 66 to 68 show the histograms, best-fit distributions, and sample data statistics of the orientation data. A triangular, a normal, and a chi-square distribution provide the best-fit probability distribution functions for the orientation data of the surface lineaments in eastern Kansas.

The corresponding length data were also analyzed. The results are shown in Figs. 69 to 71. One can see that the lengths of the surface lineaments in eastern Kansas are best-fitted by lognormal, PearsonVI, and PearsonV distributions.

The results of a statistical analysis on the corresponding spacing data are shown in Figs. 72 to 74. Lognormal2 and PearsonVI distributions were found to provide the best fits to the three sets of spacing data for the surface lineaments.

Surface Lineaments in Eastern Nebraska and Western Iowa. Fig. 75 is a rose diagram of the surface lineaments in eastern Nebraska and western Iowa (Burchett et al. 1983). Clearly, the lineaments can be partitioned into three sets, oriented in northeast, north and northwest. A statistical analysis of the lineament orientations shows that triangular distributions provide the best fits to the three sets of surface lineaments in the area. Figs. 76 to 78 show the histograms, best-fit distributions, and sample data statistics.

Similarly, a statistical analysis was also performed on the corresponding three sets of length and spacing data. The results for the length data analysis are given in Figs. 79 to 81. PearsonVI distributions appear to provide the best fits to the length data. The results for the spacing data analysis are shown in Figs. 82 to 84. An inverse Gaussian, a PearsonVI, and a lognormal distribution are the best-fitted spacing distributions for the surface lineaments in eastern Nebraska and western Iowa.

Surface Lineaments and Fractures in Western Oklahoma. Fig. 85 shows a rose diagram of the surface lineaments and fractures in western Oklahoma (Collins et al. 1974). From this figure, the surface lineaments and fractures can apparently be partitioned into three subsets trending in northeast, north, and northwest. Figs. 86 to 88 show the histograms, best-fit distributions, and sample data statistics for the three sets of the orientation data. A logistic, a normal, and a triangular distribution provide the best fits to the orientation data.

The results of a statistical analysis on the three sets of length data are given in Figs. 89 to 91. A lognormal, a lognormal2, and a PearsonV distribution appear to provide the best fits to the length data. The corresponding three sets of spacing data were sampled and statistically analyzed. The results are shown in Figs. 92 to 94. The spacing data were best-fitted by three lognormal2 distributions.

Surface Lineaments and Fractures in Western Kansas. Fig. 95 shows a rose diagram of the surface lineaments and fractures in western Kansas (Cooley 1984). The surface linear features in this area can be divided into two subsets trending northeast and northwest, although there appears an insignificant set trending north. Upon being partitioned into two sets, the orientation data were statistically analyzed. The best-fitted distributions are a triangular distribution for the northeast-trending set and a logistic distribution for the northwest-trending set. The histograms, best-fit distributions, and sample data statistics for the orientation data are shown in Figs. 96 and 97.

Similarly, the corresponding length and spacing data are also analyzed. The results for the two sets of the length data are shown in Figs. 98 and 99. PearsonVI distributions appear to provide the best fits to the length data. The results for the spacing data are shown in Figs. 100 and 101. The spacing data are also best-fitted by PearsonVI distributions.

Surface Lineaments and Fractures in the Hugoton Gas Field. Fig. 102 is a rose diagram of the surface lineaments and fractures in the western Hugoton Gas Field in southwestern Kansas and the Oklahoma Panhandle (Swanson et al. 1990). It is clear from this rose diagram that the surface linear features in this area can be partitioned into two subsets trending northeast and northwest. Figs. 103 and 104 show the histograms, best-fit distributions, and sample data statistics for the two sets of orientation data. A logistic and a triangular distribution appear to provide the best fits to the orientation data.

Similar analyses were also performed on the corresponding length and spacing data. The results for the length data are given in Figs. 105 and 106. A lognormal2 and a PearsonVI distributions were found to provide the best fits to the two sets of length data. The results for the spacing data are shown in Figs. 107 and 108. The best-fitted distributions are a lognormal2 distribution for the spacing data of the northeast-trending linear features, and a Weibull distribution for the spacing data of the northwest-trending linear features.

Surface Fractures in the Northern Forest City Basin. Fig. 109 shows a rose diagram of the surface fractures in northern Forest City Basin in southwestern Iowa (Herman et al. 1986). The surface fractures in this area appear to consist of two subsets trending east and north-northeast. The results of a statistical analysis on the orientation data are given in Figs. 110 and 111. A triangular and a normal distribution provide the best fits to the two sets of orientation data.

Figs. 112 and 113 show the histograms, best-fit distributions, and sample data statistics for the corresponding length data. A logistic and an extreme-value distribution give the best fits to the two sets of length data.

Similarly, the results for an analysis of the corresponding spacing data are shown in Figs. 114 and 115. The best-fitted distributions for the two sets of spacing data are an exponential distribution for the east-trending surface fractures and a lognormal2 distribution for the north-northeast-trending surface fractures.

Surface Lineaments and Fractures in Northeastern Iowa. Fig. 116 shows a rose diagram of the surface lineaments and fractures in northeastern Iowa (Chen 1992). Three subsets can be identified trending east, northeast, and northwest. Figs. 117 to 119 show the histograms, the best-fit distributions, and the sample data statistics for the three sets of orientation data. A PearsonV and two triangular distributions provide the best fits to the three sets of orientation data.

Similarly, Figs. 120 to 122 show the results of a statistical analysis on the corresponding length data. The best-fitted distributions are a triangular distribution for the lengths of the east-trending linear features, a PearsonV distribution for the lengths of the northeast-trending linear features, and an extreme-value distribution for the lengths of the northwest-trending linear features.

The results of a statistical analysis on the corresponding spacing data are shown in Figs. 123 to 125. A Weibull, a PearsonV, and a PearsonVI distribution provide the best fits to the three sets of spacing data for the surface lineaments and fractures in northeastern Iowa.

Discussions on the Statistical Distributions of Surface Lineaments and Fractures

The surface lineaments and fractures mapped from nine areas in the Mid-continent region and three areas in the northeastern Arizona were collected, digitized, and statistically analyzed in this paper. In all, 36 sets were identified based on their orientations. The best-fit distributions were obtained for the orientation, length, and spacing of each set.

Fig. 126 shows the best-fit distributions and their frequencies for the orientations of the 36 sets of surface lineaments and fractures. Triangular, normal, and logistic distributions provided the best fits to 33 of the 36 sets of the orientation data. The best-fit distributions and their frequencies for the corresponding 36 sets of the length data are shown in Figure 127. PearsonVI, PearsonV, lognormal, and extreme-value distributions provided the best fits to 30 of the 36 sets of length data. Similarly, the best-fit distributions and their frequencies for the corresponding 36 sets of spacing data are given in Fig. 128. Lognormal2, PearsonVI, and lognormal distributions provided the best fits to 30 of the 36 sets of spacing data.

Comparing the results of this study to those of the previous studies reviewed earlier in this paper, one can notice both consistency to a certain degree and significant discrepancies between them. Many probability distribution functions identified in the previous studies, such as normal distribution for orientation data, lognormal distribution for length data, and lognormal and Weibull distributions for spacing data, also provided best fits to some of the 36 sets of surface lineaments and fractures. However, these distribution functions only fitted a few of the 36 sets of data. Different from previous studies, this study shows triangular distributions are the most significant type of probability functions for describing natural fracture orientation data, followed by normal and logistic distributions (see Fig.126). PearsonVI distributions are the most significant type of probability functions for describing natural fracture length data, followed by PearsonV, lognormal2, and extreme-value distributions (see Fig. 127). Natural fracture spacing data, as shown in Fig. 128, appear to be best characterized by lognormal2 distribution, followed by PearsonVI and lognormal distributions.

The probability distribution functions identified in this study for describing natural fracture characteristics were obtained through an extensive statistical analysis of a large number of surface lineaments and fractures, and using 25 different hypothesized probability functions during best fitting. We believe they provide realistic descriptions of natural fracture orientation, length, and spacing. However, these distribution functions must be conditioned using any available subsurface fracture data before they can be used for stochastic simulations of natural fractures in a naturally fractured reservoir.

Conclusions

In this paper, we presented the results of an extensive statistical analysis of natural fracture characteristics using a huge number of surface lineaments and fractures mapped in the Mid-continent and Colorado Plateau regions. The following conclusions are obtained:

Natural fracture orientations are best described by triangular and normal distributions, followed by logistic, chi-square, and PearsonV distributions. Triangular and normal distributions are, by far, the most significant distributions for characterizing natural fracture orientation data.

Natural fracture lengths are best described by PearsonVI and PearsonV distributions. Other favorable distribution functions for characterizing natural fracture length data include extreme-value, lognormal2, lognormal, loglogistic, logistic, and triangular distributions.

Natural fracture spacing data are best described statistically by lognormal2 and PearsonVI distributions followed by lognormal, inverse Gaussian, Weibull, exponential, and PearsonV distributions.

The probability distribution functions identified for characterizing natural fracture characteristics using surface lineaments and fractures must be calibrated using any available subsurface fracture data before they can be used for stochastic simulations of subsurface natural fracture systems in a naturally fractured reservoir.

References

1. Baecher, G.B., Lanney, N.A., and Einstein, H.H. 1977. "Statistical Description of Rock Properties and Sampling," presented at the 18th U.S. Symp. on Rock Mechanics, Energy Resources and Excavation Technology, 1977, 5C1-1.
2. Baecher, G.B., 1983. "Statistical Analysis of Rock Mass Fracturing," *Math. Geol.* (Vol. 15, No. 2, 1983) 329.
3. Belfield, W.C., and Sovich, J.P. 1995. "Fracture Statistics from Horizontal Wellbores," *JCPT* (Vol. 34, No. 6, June 1995) 47.
4. Burchett, R.R., Luza, K.V., Van Eck, O.J., and Wilson, F.W. 1983. *Seismicity and Tectonic Relationships of the Nemaha Uplift and Midcontinent Geophysical Anomaly*, Division of Health, Siting and Waste Management, Office of Nuclear Regulatory Commission.
5. Cacas, M.C., *et al.*,1990. "Modeling Fracture Flow with a Stochastic Discrete Fracture Network: Calibration and Validation 1. The Flow Model," *Water Resources Research* (Vol. 26, No. 3, March 1990) 479.
6. Chen X. 1992. "Applications of Remote Sensing and GIS Techniques for Environmental Geologic Investigation, Northeastern Iowa," PhD thesis, University of Iowa.
7. Collins, R.J., McCown, F.P., Stonis, L.P., Petzel, G.J., Everett, J.R. 1974. *An Evaluation of ERTS Data for the Purposes of Petroleum Exploration*, final report prepared for Goddard Space Flight Center.
8. Cooley, M.E. 1984. *Linear Features Determined from Landsat Imagery in Western Kansas*, U.S. Geological Survey Open-File Report 84-241.
9. Dverstorp, B., and Andersson, J. 1989. "Application of the Discrete Fracture Network Concept with Field Data: Possibilities of Model Calibration and Validation," *Water Resources Research* (Vol. 25, No. 3, March 1989) 540.

10. Guo, G., and Carroll, H.B. 1995. *A New Methodology for Oil and Gas Exploration Using Remote Sensing Data and Surface Fracture Analysis*, NIPER/BDM-0163, Aug. 1995.
11. Guo, G., and George, S.A. 1996. *An Analysis of Surface and Subsurface Lineaments and Fractures for Oil and Gas Exploration in the Midcontinent Region*, NIPER/BDM-0223, March 1996.
12. Guo, G., and Evans, R.D., 1994. "Geologic and Stochastic Characterization of Naturally Fractured Reservoirs," SPE 27025 presented at the 1994 SPE III Latin American & Caribbean Petroleum Engineering Conference, Buenos Aires, Argentina, April 27-29.
13. Heffer, K.J., and Bevan, T.G. 1990. "Scaling Relationships in Natural Fractures: Data, Theory, and Application," SPE 20981 presented at the 1990 European Petroleum Conference held in Hague, Netherlands, Oct. 22-24.
14. Herman, J., Etzler, P.J., Wilson, M.L., and Vincent, R.K. 1986. "Remote Sensing Study of the Mid-continent Geophysical Anomaly in Iowa," Paper presented at the Society of Mining Engineers Fall Meeting, St. Louis, Missouri, Sep. 7-10, 1986.
15. Lepley, L.K. 1977. *Landsat Lineament Map of Arizona with Emphasis on Quaternary Fractures*. University of Arizona Bureau of Geology and Mineral Technology Open-File Report 77-2.
16. Long, J.C.S., Remer, J.S., Wilson, C.R., and Witherspoon, P.A. 1982. "Porous Media Equivalents for Networks of Discontinuous Fractures," *Water Resources Research* (Vol. 18, No. 3, June 1982) 645.
17. Loosveld, R. J. H., and Franssen, R.C.M.W. 1992. "Extensional vs. Shear Fractures: Implications for Reservoir Characterization," SPE 25017 presented at the 1992 SPE European Petroleum Conference held in Cannes, France, Nov. 16-18.
18. Lorentz, J.C., and Hill, R.E. 1991. "Subsurface Fracture Spacing: Comparison of Inferences from Slant/Horizontal Core and Vertical Core in Mesaverde Reservoirs," SPE 21877 presented at the 1991 Rocky Mountain Regional Meeting and Low-Permeability Reservoirs Symposium held in Denver, April 15-17.
19. Rouleau, A., and Gale, J.E. 1985. "Statistical Characterization of the Fracture System in the Stripa Granite, Sweden," *Int. J. Rock Mech. Min. Sci. & Geomech.* Abstr. (Vol. 22, No. 6, 1985) 353.
20. Snow, D.T., 1970. "The Frequency and Apertures of Fractures in Rock," *Int. J. Rock Mech. Min. Sci.* (Vol. 7, 1970) 23.
21. Swanson, D.C., and Shannon, P.J. 1990. "Landsat Interpretation Useful in Hugoton Gas Field," *World Oil* (January 1990) 108.

Appendix. Probability Density Functions

$BETA(\alpha_1,\alpha_2)$: $f(x)=\dfrac{x^{\alpha_1-1}(1-x)^{\alpha_2-1}}{B(\alpha_1,\alpha_2)}$

where $B(x_1,x_2)=\int_0^1 t^{x_1-1}(1-t)^{x_2-1}dt$

$BINOMIAL(n,p)$: $f(x)=\binom{n}{x}p^x(1-p)^{n-x}$

$CHISQ(v)$: $f(x)=\dfrac{x^{\frac{v}{2}-1}e^{\frac{-x}{2}}}{2^{\frac{v}{2}}\Gamma\left(\frac{v}{2}\right)}$

$ERF(h)$: $f(x)=\dfrac{h}{\sqrt{\pi}}e^{-h^2x^2}$

$ERLANG(m,\beta)$: $f(x)=\dfrac{\beta^{-m}x^{m-1}e^{\frac{-x}{\beta}}}{\Gamma(m)}$

$EXPON(\beta)$: $f(x)=\dfrac{e^{\frac{-x}{\beta}}}{\beta}$

$ExtremeValue(a,b)$:

$$f(x)=\left(\frac{1}{b}\right)\exp\left(-\frac{x-a}{b}\right)\exp\left[-\exp\left(-\frac{x-a}{b}\right)\right]$$

$GAMMA(\alpha,\beta)$: $f(x)=\dfrac{\beta^{-\alpha}x^{\alpha-1}e^{\frac{-x}{\beta}}}{\Gamma(\alpha)}$

$GEOMET(p)$: $f(x)=p(1-p)^x$

$HYPERGEO(n,D,M)$: $f(x)=\dfrac{\binom{D}{x}\binom{M-D}{n-x}}{\binom{M}{n}}$

$InverseGaussian(\lambda,\mu)$: $f(x)=\left(\dfrac{\lambda}{2\pi x^3}\right)^{\frac{1}{2}}\exp\left(\dfrac{-\lambda(x-\mu)^2}{2\mu^2x}\right)$

$LOGISTIC(\alpha,\beta)$: $f(x)=\dfrac{z}{\beta(1+z)^2}$

where $z=\exp\left[\dfrac{-(x-\alpha)}{\beta}\right]$

$LOGLOGISTIC(\alpha,\beta,\gamma)$: $f(x)=\dfrac{\alpha\left(\frac{x-\gamma}{\beta}\right)^{\alpha-1}}{\beta\left[1+\left(\frac{x-\gamma}{\beta}\right)^{-\alpha}\right]^2}$

$LOGNORM(\mu,\sigma)$: $f(x)=\dfrac{1}{x\sqrt{2\pi\sigma_1^2}}\exp\dfrac{-(\ln x-\mu_1)^2}{2\sigma_1^2}$

where $\mu_1=\ln\left(\dfrac{\mu^2}{\sqrt{\sigma^2+\mu^2}}\right)$ and $\sigma_1=\sqrt{\ln\left(\dfrac{\sigma^2+\mu^2}{\mu^2}\right)}$

$LOGNORM2(\mu,\sigma)$: $f(x)=\dfrac{1}{x\sqrt{2\pi\sigma^2}}\exp\dfrac{-(\ln x-\mu)^2}{2\sigma^2}$

$NEGBIN(s,p)$: $f(x)=\binom{s+x-1}{x}p^s(1-p)^x$

$$NORMAL(\mu,\sigma): \quad f(x)=\frac{1}{\sqrt{2\pi\sigma^2}}e^{\frac{-(x-\mu)^2}{2\sigma^2}}$$

$$PARETO(\theta,a): \quad f(x)=\frac{\theta a^{\theta}}{x^{\theta+1}}$$

$$PearsonV(\alpha,\beta): \quad f(x)=\frac{x^{-(\alpha+1)}\exp\left(-\frac{\beta}{x}\right)}{\beta^{-\alpha}\Gamma(\alpha)}$$

$$PearsonVI(\alpha_1,\alpha_2,\beta): \quad f(x)=\frac{\left(\frac{x}{\beta}\right)^{\alpha_1-1}}{\beta B(\alpha_1,\alpha_2)\left(1+\frac{x}{\beta}\right)^{\alpha_1+\alpha_2}}$$

$$POISSON(\lambda): \quad f(x)=\frac{e^{-\lambda}\lambda^{x}}{x!}$$

$$RAYLEIGH(b): \quad f(x)=\frac{x}{b^2}\exp\left(-\frac{x^2}{2b^2}\right)$$

$$Student'sT(\upsilon): \quad f(x)=\frac{\Gamma\left(\frac{\upsilon+1}{2}\right)}{(\pi\upsilon)^{\frac{1}{2}}\Gamma\left(\frac{\upsilon}{2}\right)\left[1+\frac{x^2}{\upsilon}\right]^{\frac{\upsilon+1}{2}}}$$

$$TRIANG(a,b,c): \quad f(x)=\begin{cases}\dfrac{2(x-a)}{(b-a)(c-a)} & \text{if } a\le x\le b\\ \dfrac{2(c-x)}{(c-a)(c-b)} & \text{if } b\le x\le c\end{cases}$$

$$WEIBULL(\alpha,\beta): \quad f(x)=\alpha\beta^{-\alpha}x^{\alpha-1}e^{-(x/\beta)^{\alpha}}$$

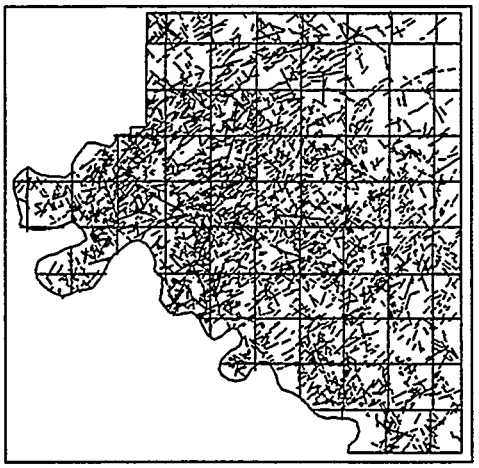

Fig. 1—Surface fractures in Osage County, Oklahoma.

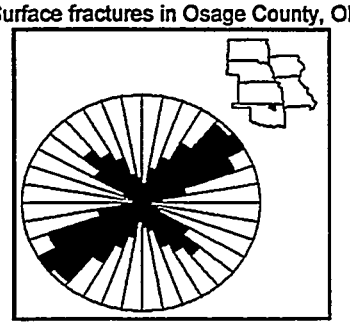

Fig. 2—A rose diagram of the surface fractures in Osage County, Oklahoma.

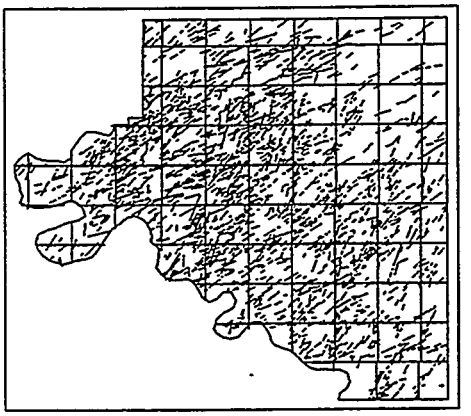

Fig. 3—Northeast-trending surface fractures in Osage County, Oklahoma.

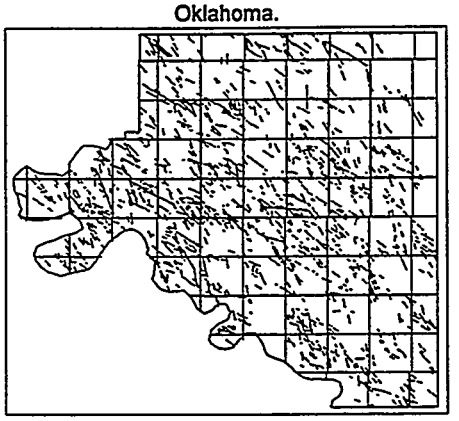

Fig. 4—Northwest-trending surface fractures in Osage County, Oklahoma.

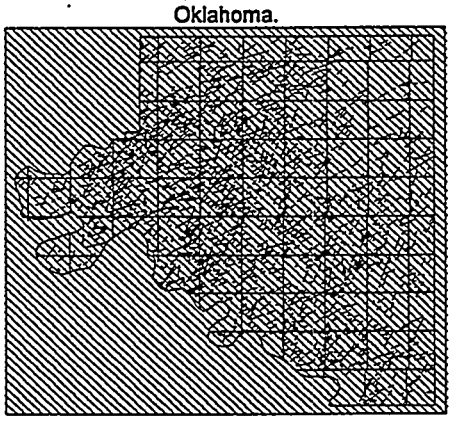

Fig. 5—The northeast-trending surface fractures and a set of imaginary scanlines in Osage County, Oklahoma.

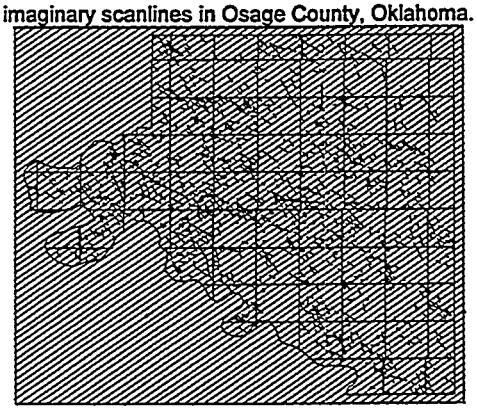

Fig. 6—The northwest-trending surface fractures and a set of imaginary scanlines in Osage County, Oklahoma.

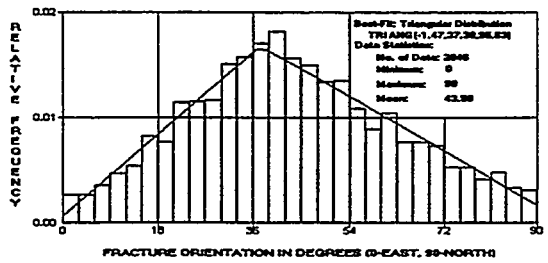

Fig. 7—The histogram and best-fit orientation distribution of the northeast-trending surface fractures in Osage County, Oklahoma.

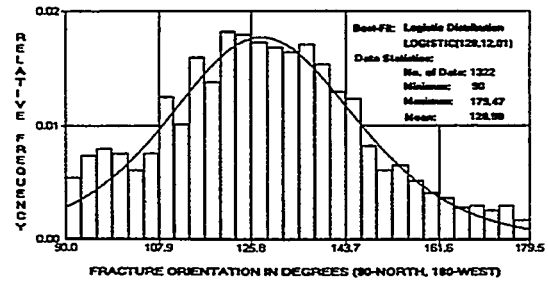

Fig. 8—The histogram and best-fit orientation distribution of the northwest-trending surface fractures in Osage County, Oklahoma.

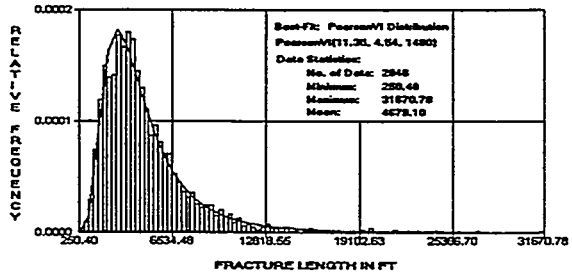

Fig. 9—The histogram and best-fit length distribution of the northeast-trending surface fractures in Osage County, Oklahoma.

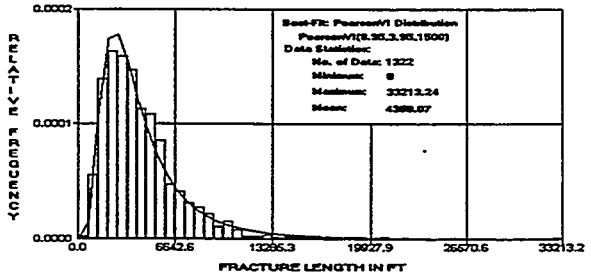

Fig. 10—The histogram and best-fit length distribution of the northwest-trending surface fractures in Osage County, Oklahoma.

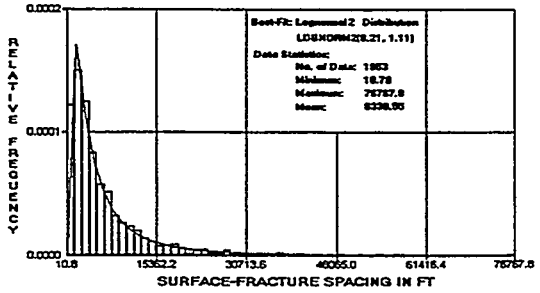

Fig. 11—The histogram and best-fit spacing distribution of the northeast-trending surface fractures in Osage County, Oklahoma.

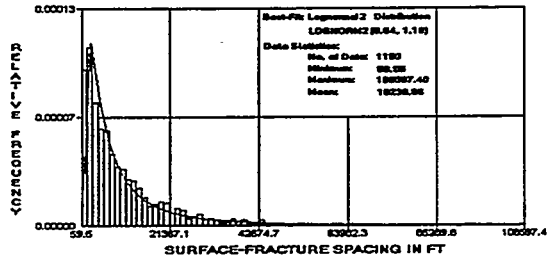

Fig. 12—The histogram and best-fit spacing distribution of the northwest-trending surface fractures in Osage County, Oklahoma.

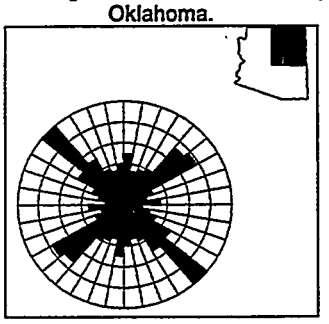

Fig. 13—A rose diagram of the surface lineaments in northeastern Arizona.

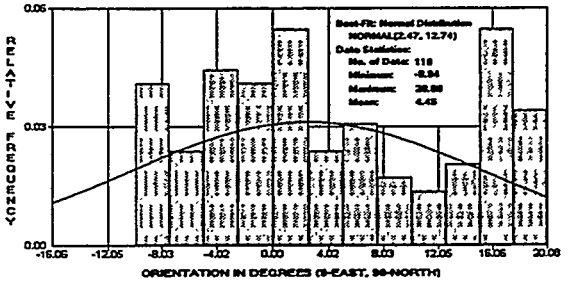

Fig. 14—The histogram and best-fit orientation distribution of the east-trending surface lineaments in northeastern Arizona.

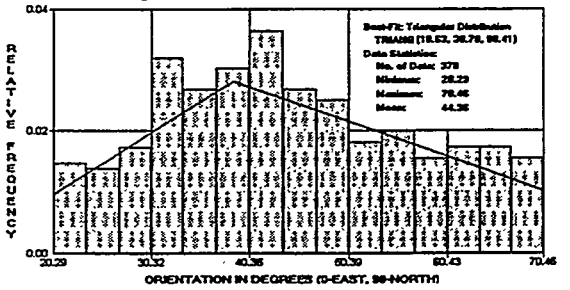

Fig. 15—The histogram and best-fit orientation distribution of the northeast-trending surface lineaments in northeastern Arizona.

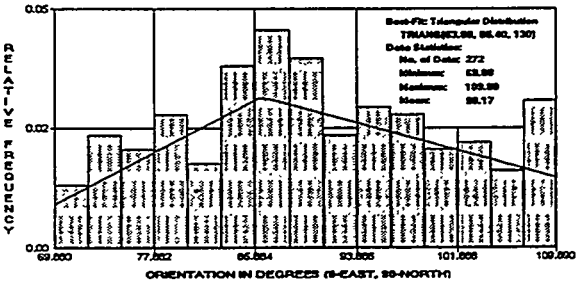

Fig. 16—The histogram and best-fit orientation distribution of the north-trending surface lineaments in northeastern Arizona.

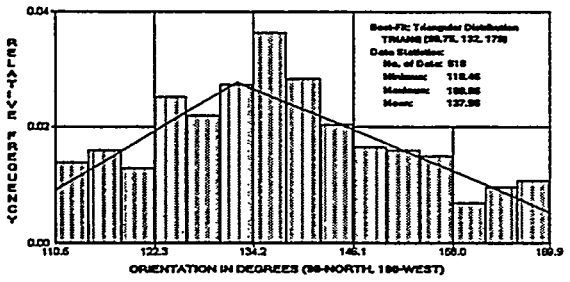

Fig. 17—The histogram and best-fit orientation distribution of the northwest-trending surface lineaments in northeastern Arizona.

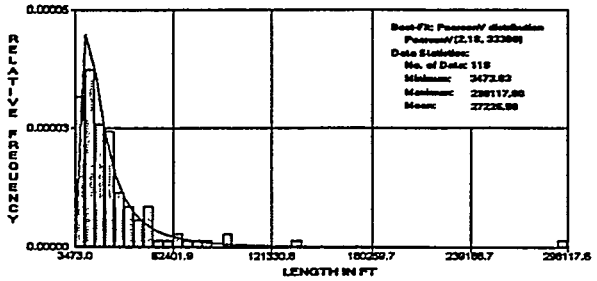

Fig. 18—The histogram and best-fit length distribution of the east-trending surface lineaments in northeastern Arizona.

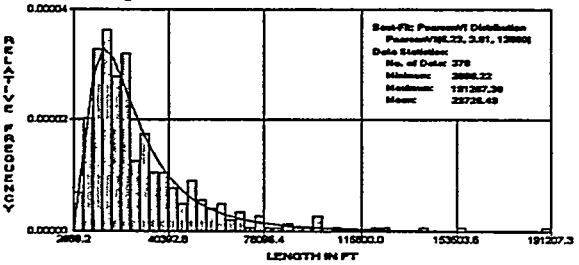

Fig. 19—The histogram and best-fit length distribution of the northeast-trending surface lineaments in northeastern Arizona.

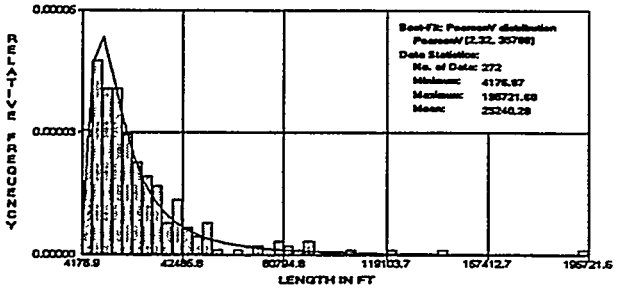

Fig. 20—The histogram and best-fit length distribution of the north-trending surface lineaments in northeastern Arizona.

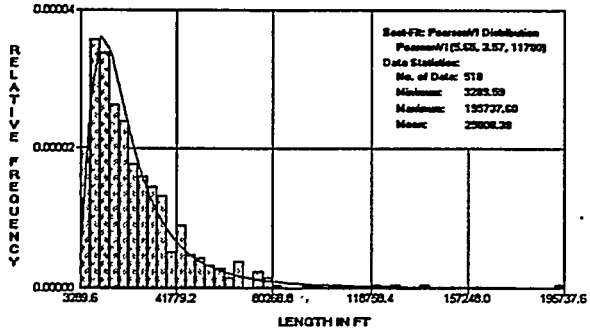

Fig. 21—The histogram and best-fit length distribution of the northwest-trending surface lineaments in northeastern Arizona.

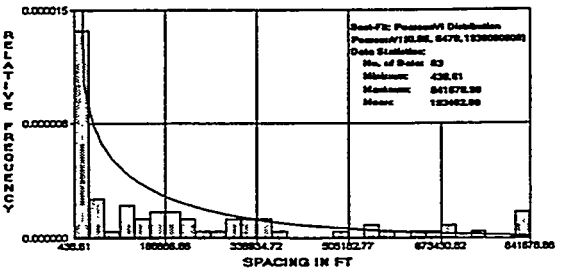

Fig. 22—The histogram and best-fit spacing distribution of the east-trending surface lineaments in northeastern Arizona.

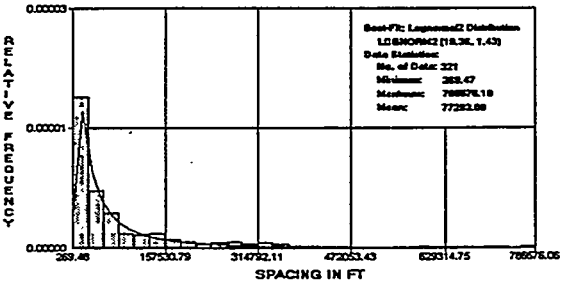

Fig. 23—The histogram and best-fit spacing distribution of the northeast-trending surface lineaments in northeastern Arizona.

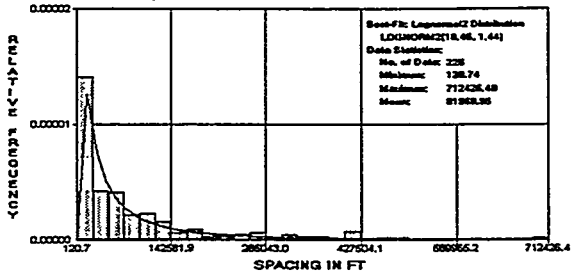

Fig. 24—The histogram and best-fit spacing distribution of the north-trending surface lineaments in northeastern Arizona.

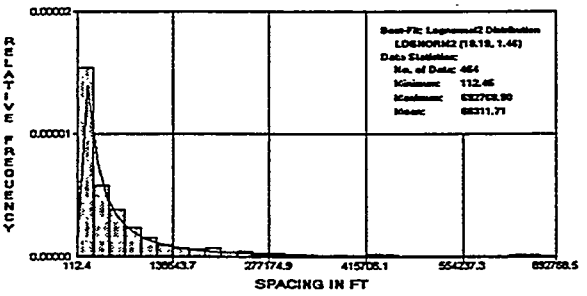

Fig. 25—The histogram and best-fit spacing distribution of the northwest-trending surface lineaments in northeastern Arizona.

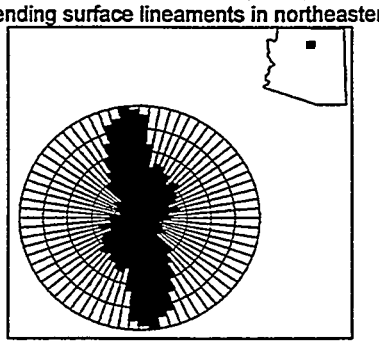

Fig. 26—A rose diagram of the surface fractures in the Cameron area in northeastern Arizona.

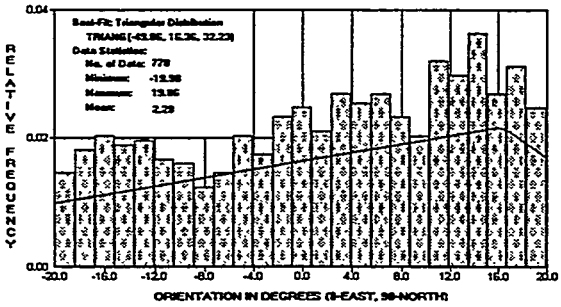

Fig. 27—The histogram and best-fit orientation distribution of the east-trending surface fractures in the Cameron area.

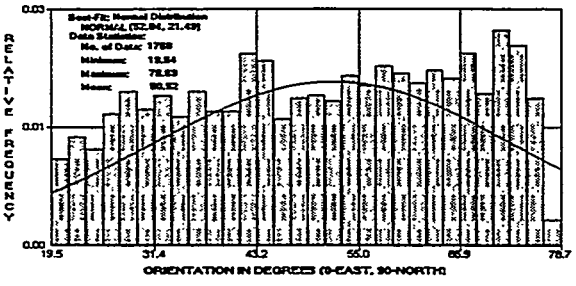

Fig. 28—The histogram and best-fit orientation distribution of the northeast-trending surface fractures in the Cameron area.

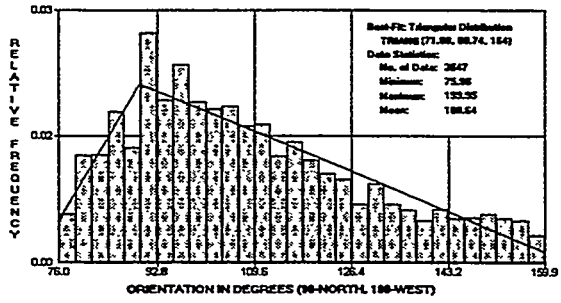

Fig. 29—The histogram and best-fit orientation distribution of the north-northwest-trending surface fractures in the Cameron area.

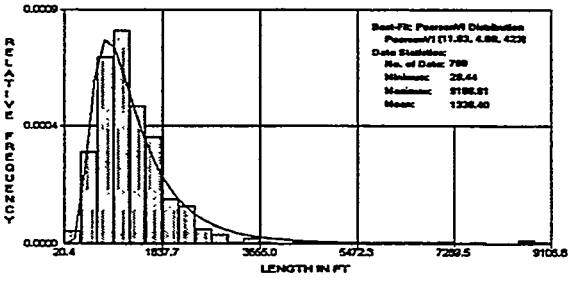

Fig. 30—The histogram and best-fit length distribution of the east-trending surface fractures in the Cameron area.

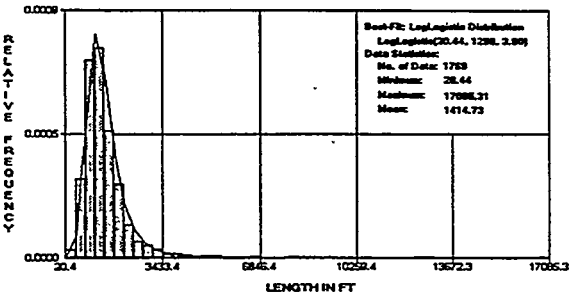

Fig. 31—The histogram and best-fit length distribution of the northeast-trending surface fractures in the Cameron area.

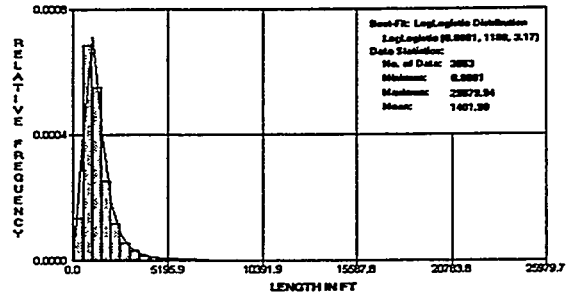

Fig. 32—The histogram and best-fit length distribution of the north-northwest-trending surface fractures in the Cameron area.

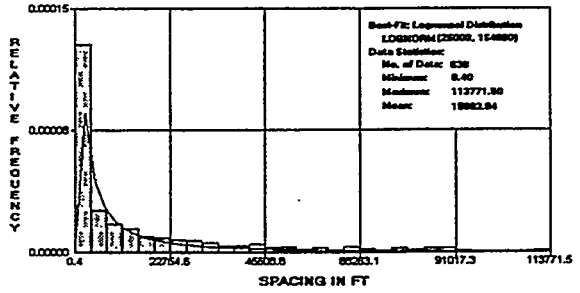

Fig. 33—The histogram and best-fit spacing distribution of the east-trending surface fractures in the Cameron area.

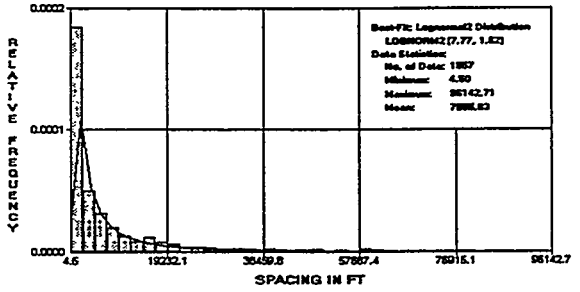

Fig. 34—The histogram and best-fit spacing distribution of the northeast-trending surface fractures in the Cameron area.

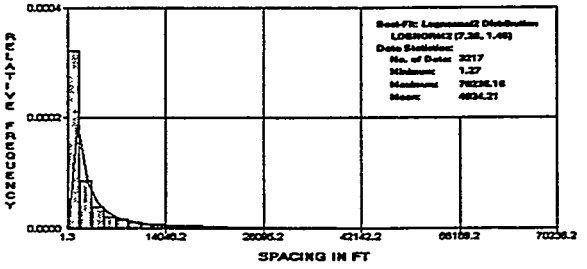

Fig. 35—The histogram and best-fit spacing distribution of the northwest-trending surface fractures in the Cameron area.

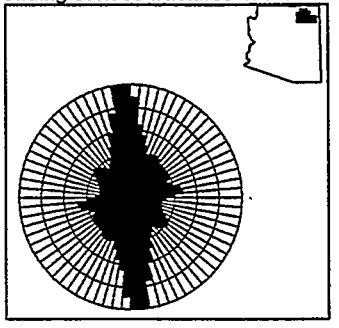

Fig. 36—A rose diagram of the surface fractures in the Black Mesa Basin area in northeastern Arizona.

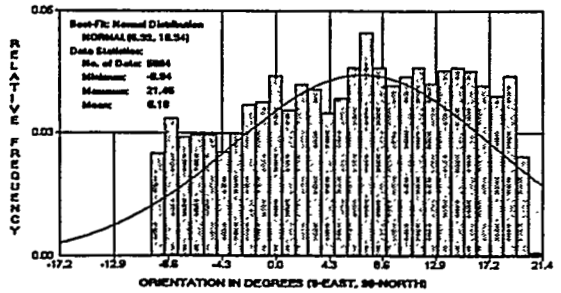

Fig. 37—The histogram and best-fit orientation distribution of the east-trending surface fractures in the Black Mesa Basin area.

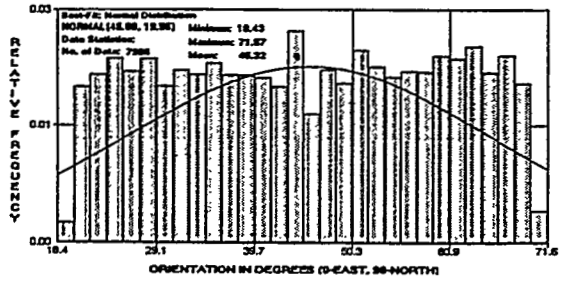

Fig. 38—The histogram and best-fit orientation distribution of the northeast-trending surface fractures in the Black Mesa Basin area.

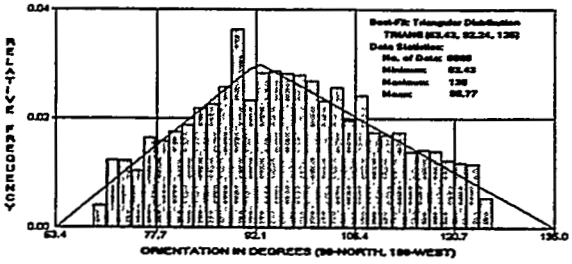

Fig. 39—The histogram and best-fit orientation distribution of the north-northwest-trending surface fractures in the Black Mesa Basin area.

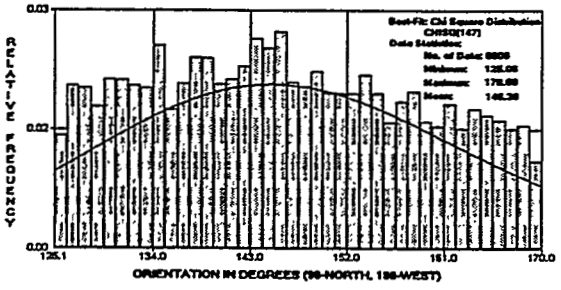

Fig. 40—The histogram and best-fit orientation distribution of the northwest-trending surface fractures in the Black Mesa Basin area.

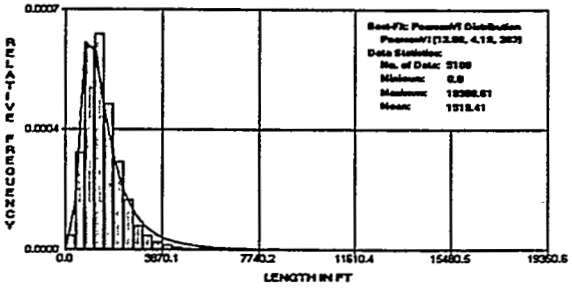

Fig. 41—The histogram and best-fit length distribution of the east-trending surface fractures in the Black Mesa Basin area.

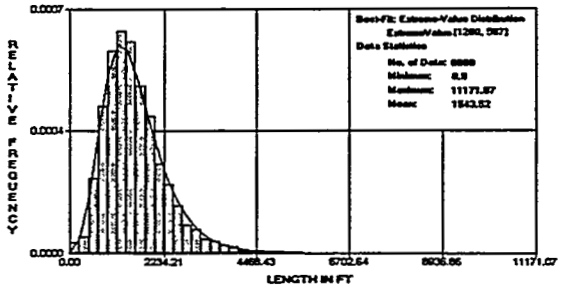

Fig. 42—The histogram and best-fit length distribution of the northeast-trending surface fractures in the Black Mesa Basin area.

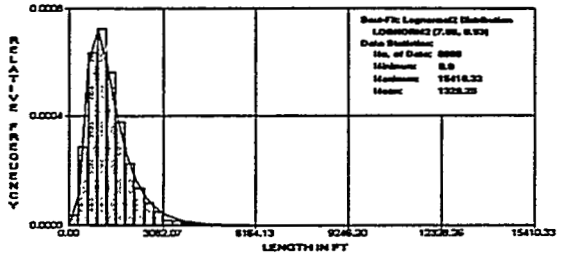

Fig. 43—The histogram and best-fit length distribution of the north-northwest-trending surface fractures in the Black Mesa Basin area.

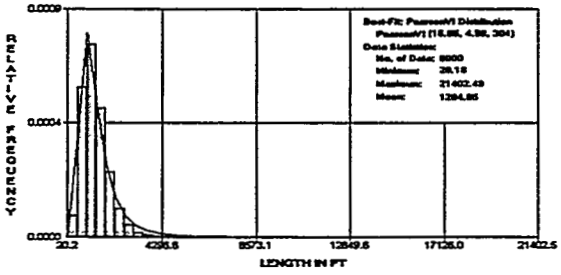

Fig. 44—The histogram and best-fit length distribution of the northwest-trending surface fractures in the Black Mesa Basin area.

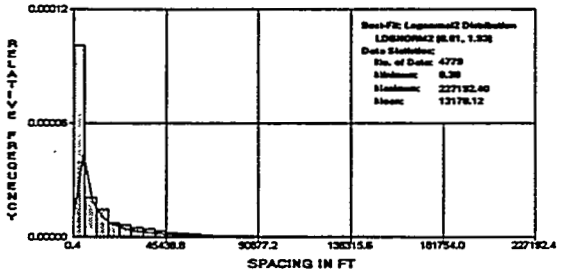

Fig. 45—The histogram and best-fit spacing distribution of the east-trending surface fractures in the Black Mesa Basin area.

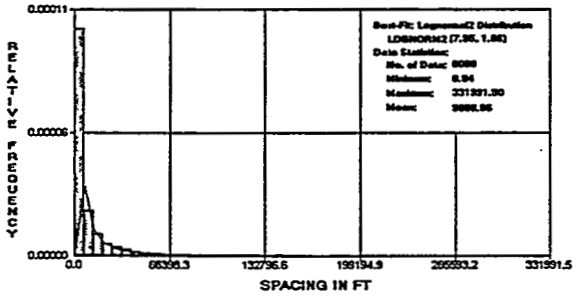

Fig. 46—The histogram and best-fit spacing distribution of the northeast-trending surface fractures in the Black Mesa Basin area.

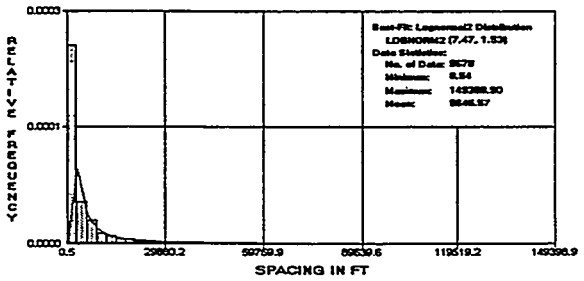

Fig. 47—The histogram and best-fit spacing distribution of the north-northwest-trending surface fractures in the Black Mesa Basin area.

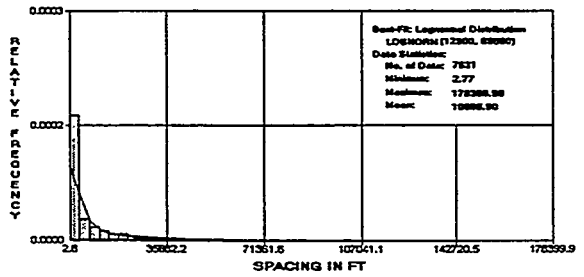

Fig. 48—The histogram and best-fit spacing distribution of the northwest-trending surface fractures in the Black Mesa Basin area.

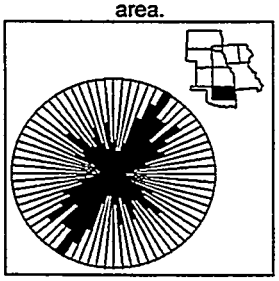

Fig. 49—A rose diagram of the surface lineaments in northeastern Oklahoma.

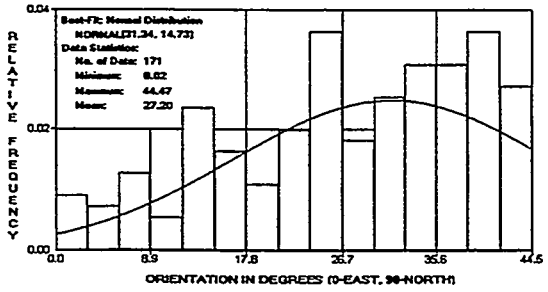

Fig. 50—The histogram and best-fit orientation distribution of the east-northeast-trending surface lineaments in northeastern Oklahoma.

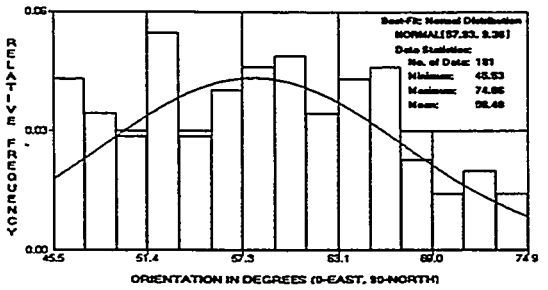

Fig. 51—The histogram and best-fit orientation distribution of the north-northeast-trending surface lineaments in northeastern Oklahoma.

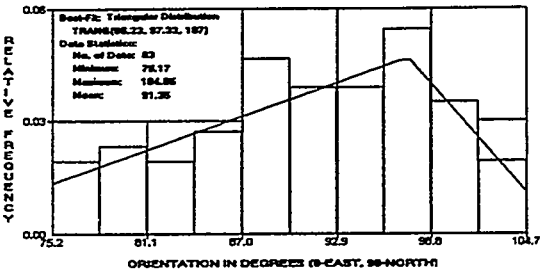

Fig. 52—the histogram and best-fit orientation distribution of the north-trending surface lineaments in northeastern Oklahoma.

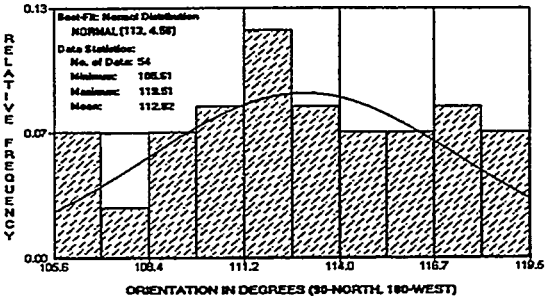

Fig. 53—The histogram and best-fit orientation distribution of the north-nothwest-trending surface lineaments in northeastern Oklahoma.

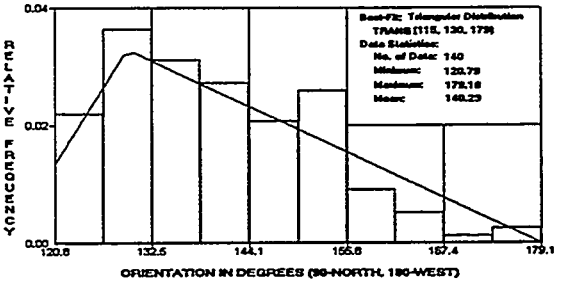

Fig. 54—The histogram and best-fit orientation distribution of the northwest-trending surface lineaments in northeastern Oklahoma.

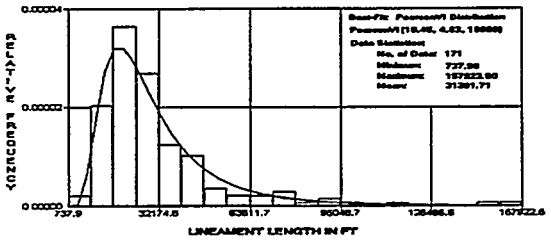

Fig. 55—The histogram and best-fit length distribution of the east-northeast-trending surface lineaments in northeastern Oklahoma.

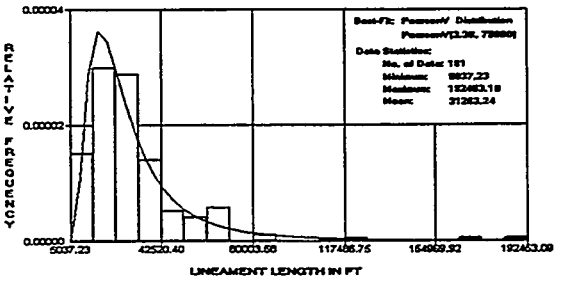

Fig. 56—The histogram and best-fit length distribution of the north-northeast-trending surface lineaments in northeastern Oklahoma.

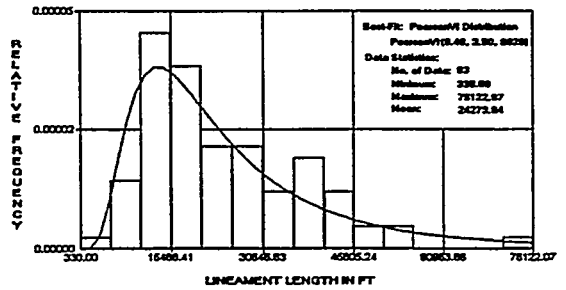

Fig. 57—The histogram and best-fit length distribution of the north-trending surface lineaments in northeastern Oklahoma.

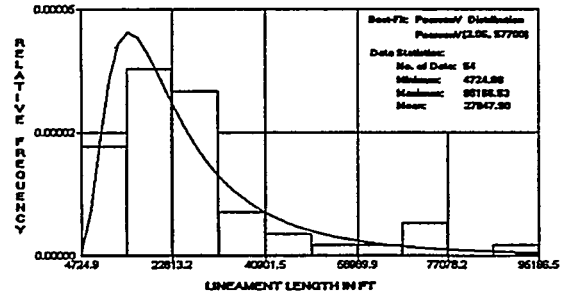

Fig. 58—The histogram and best-fit length distribution of the north-northwest-Trending Surface Lineaments in Northeastern Oklahoma.

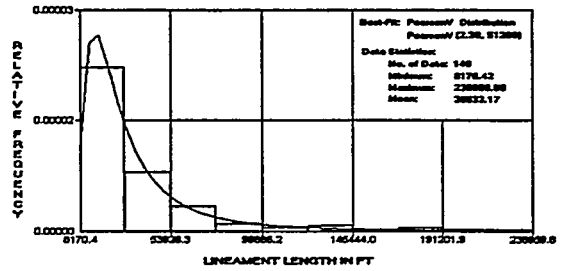

Fig. 59—The histogram and best-fit length distribution of the northwest-trending surface lineaments in northeastern Oklahoma.

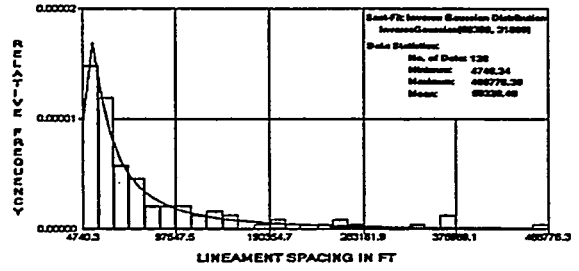

Fig. 60—The histogram and best-fit spacing distribution of the east-northeast-trending surface lineaments in northeastern Oklahoma.

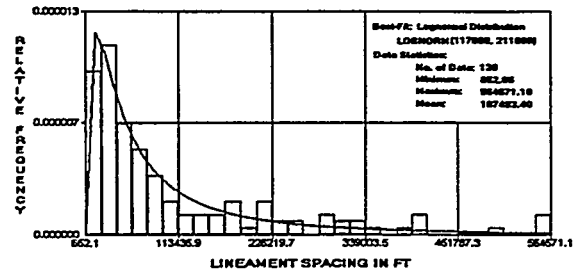

Fig. 61—The histogram and best-fit spacing distribution of the north-northeast-trending surface lineaments in northeastern Oklahoma.

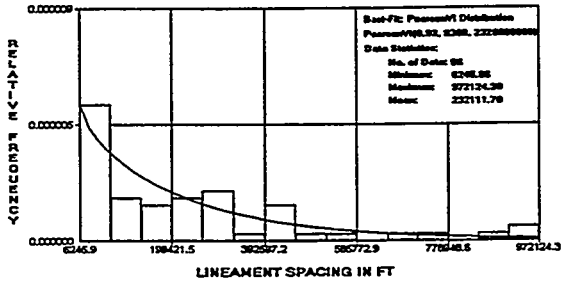

Fig. 62—The histogram and best-fit spacing distribution of the north-trending surface lineaments in northeastern Oklahoma.

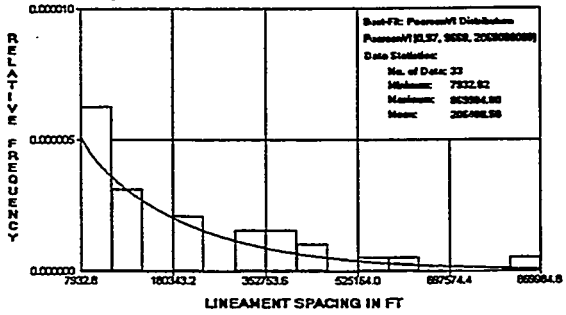

Fig. 63—The histogram and best-fit spacing distribution of the north-northwest-trending surface lineaments in northeastern Oklahoma.

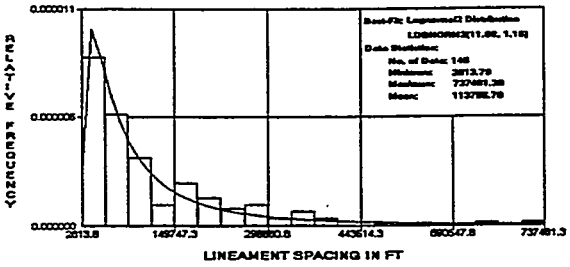

Fig. 64—The histogram and best-fit spacing distribution of the northwest-trending surface lineaments in northeastern Oklahoma.

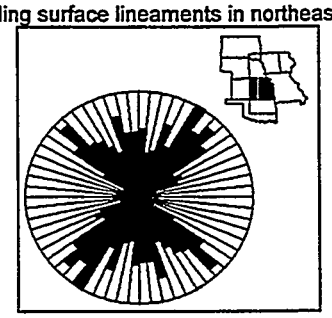

Fig. 65—A rose diagram of the surface lineaments in eastern Kansas.

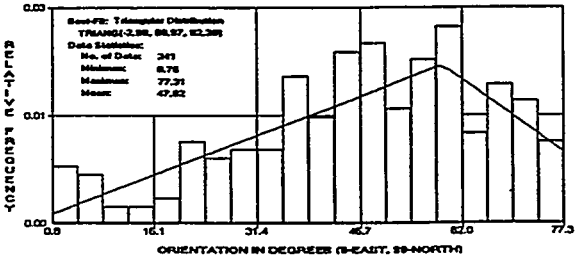

Fig. 66—The histogram and best-fit orientation distribution of the northeast-trending surface lineaments in eastern Kansas.

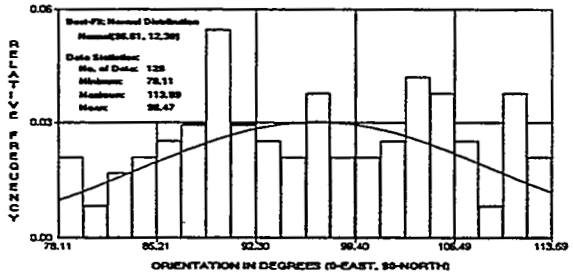

Fig. 67—The histogram and best-fit orientation distribution of the north-northwest-trending surface lineaments in eastern Kansas.

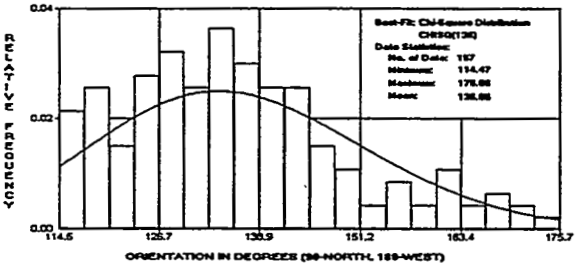

Fig. 68—The histogram and best-fit orientation distribution of the northwest-trending surface lineaments in eastern Kansas.

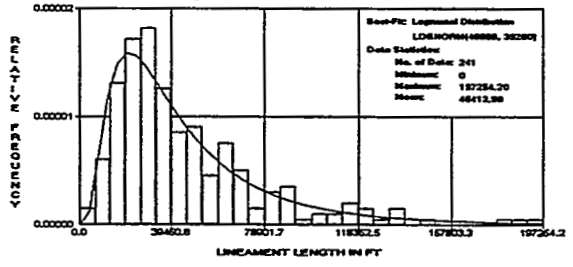

Fig. 69—The histogram and best-fit length distribution of the northeast-trending surface lineaments in eastern Kansas.

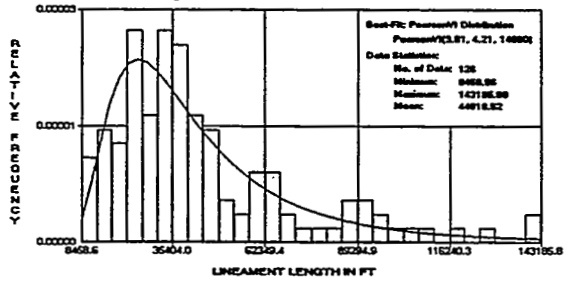

Fig. 70—The histogram and best-fit length distribution of the north-northwest-trending surface lineaments in eastern Kansas.

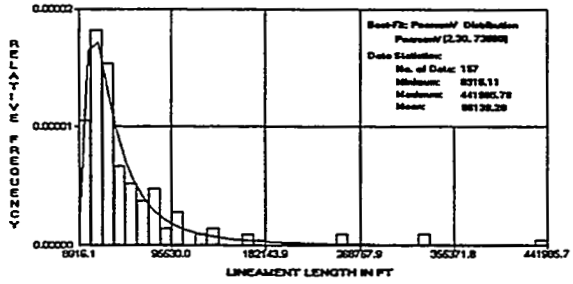

Fig. 71—The histogram and best-fit length distribution of the northwest-trending surface lineaments in eastern Kansas.

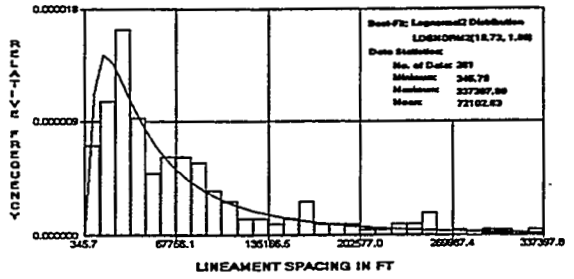

Fig. 72—The histogram and best-fit spacing distribution of the northeast-trending surface lineaments in eastern Kansas.

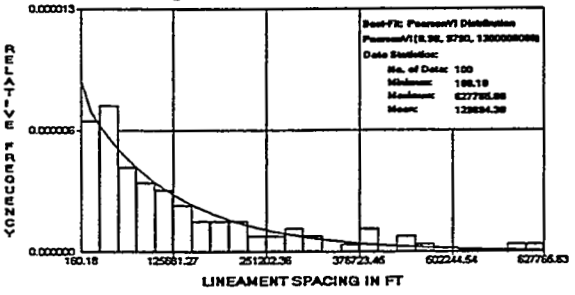

Fig. 73—The histogram and best-fit spacing distribution of the north-northwest-trending surface lineaments in eastern Kansas.

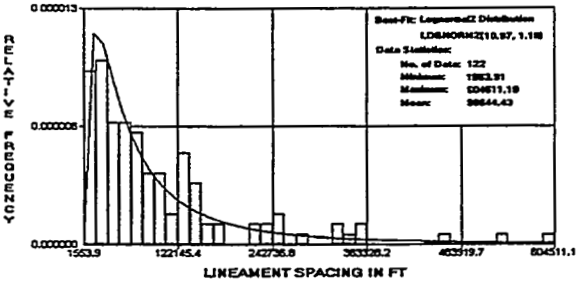

Fig. 74—The histogram and best-fit spacing distribution of the northwest-trending surface lineaments in eastern Kansas.

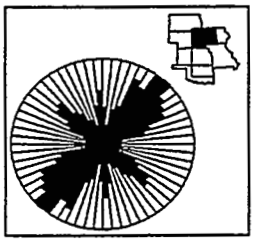

Fig. 75—A rose diagram of the surface lineaments in eastern Nebraska and western Iowa.

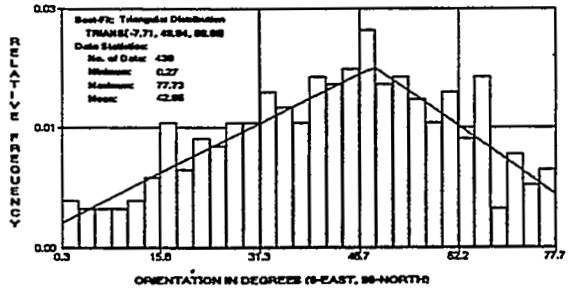

Fig.76—The histogram and best-fit orientation distribution of the northeast-trending surface lineaments in eastern Nebraska and western Iowa.

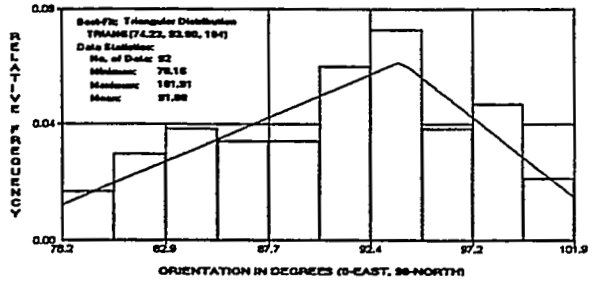

Fig. 77—The histogram and best-fit orientation distribution of the north-trending surface lineaments in eastern Nebraska and western Iowa.

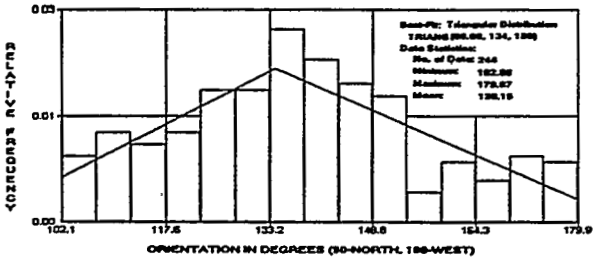

Fig. 78—The histogram and best-fit orientation distribution of the northwest-trending surface lineaments in eastern Nebraska and western Iowa.

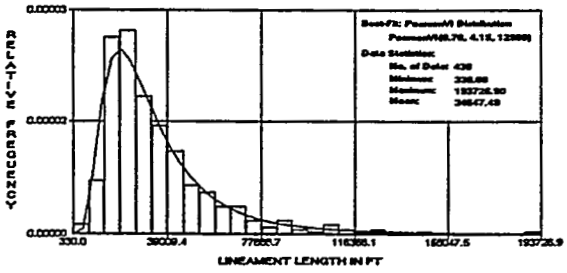

Fig. 79—The histogram and best-fit length distribution of the northeast-trending surface lineaments in eastern Nebraska and western Iowa.

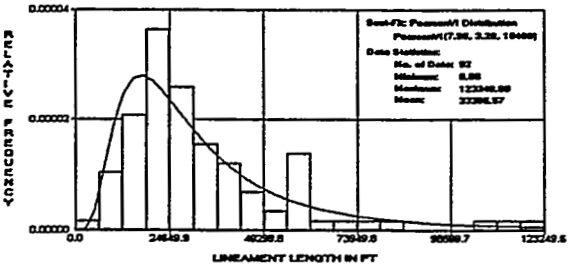

Fig. 80—The histogram and best-fit length distribution of the north-trending surface lineaments in eastern Nebraska and western Iowa.

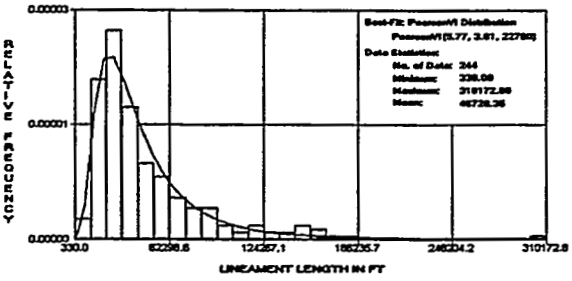

Fig. 81—The histogram and best-fit length distribution of the northwest-trending surface lineaments in eastern Nebraska and western Iowa.

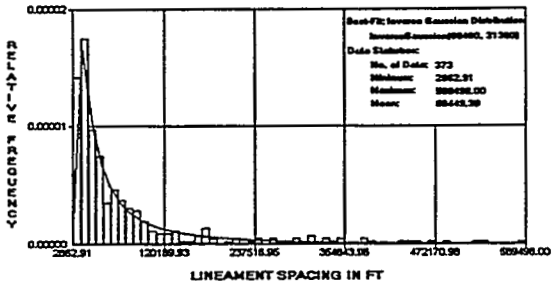

Fig. 82—The histogram and best-fit spacing distribution of the northeast-trending surface lineaments in eastern Nebraska and western Iowa.

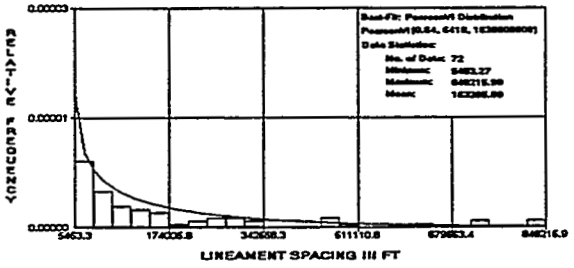

Fig. 83—The histogram and best-fit spacing distribution of the north-trending surface lineaments in eastern Nebraska and western Iowa.

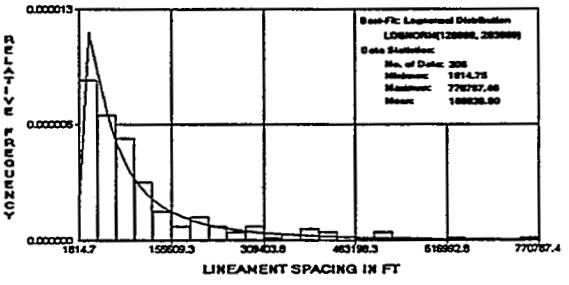

Fig. 84—The histogram and best-fit spacing distribution of the northwest-trending surface lineaments in eastern Nebraska and western Iowa.

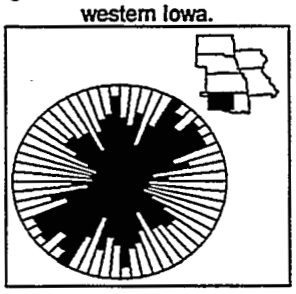

Fig. 85—A rose diagram of the surface lineaments and fractures in western Oklahoma.

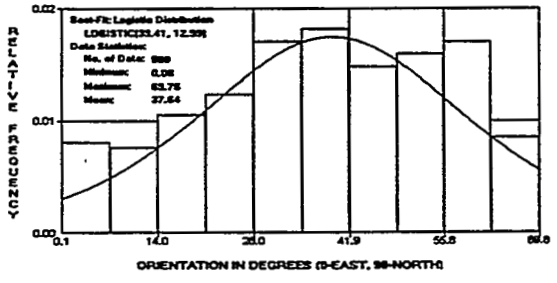

Fig. 86—The histogram and best-fit orientation distribution of the northeast-trending surface lineaments and fractures in western Oklahoma.

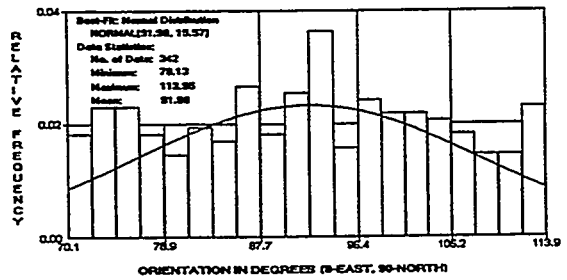

Fig. 87—The histogram and best-fit orientation distribution of the north-trending surface lineaments and fractures in western Oklahoma.

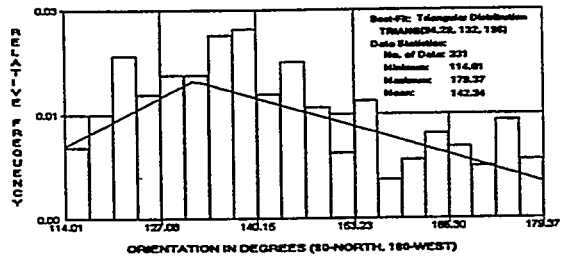

Fig. 88—The histogram and best-fit orientation distribution of the northwest-trending surface lineaments and fractures in western Oklahoma.

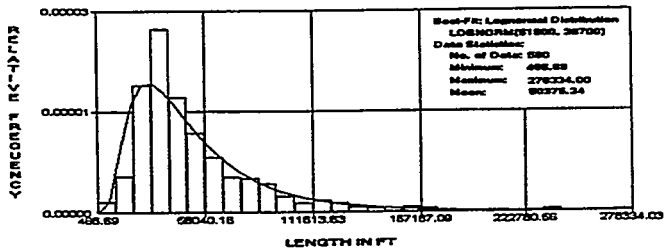

Fig. 89—The histogram and best-fit length distribution of the northeast-trending surface lineaments and fractures in western Oklahoma.

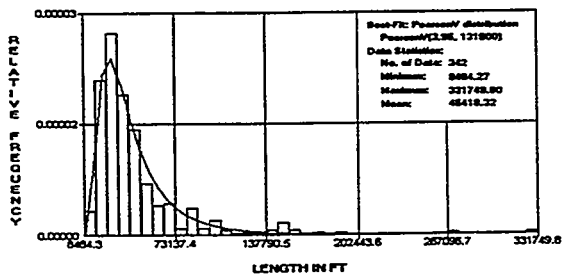

Fig. 90—The histogram and best-fit length distribution of the north-trending surface lineaments and fractures in western Oklahoma.

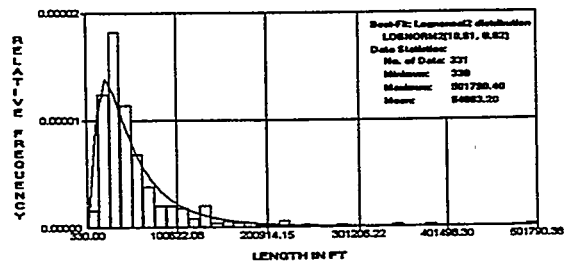

Fig. 91—The histogram and best-fit length distribution of the northwest-trending surface lineaments and fractures in western Oklahoma.

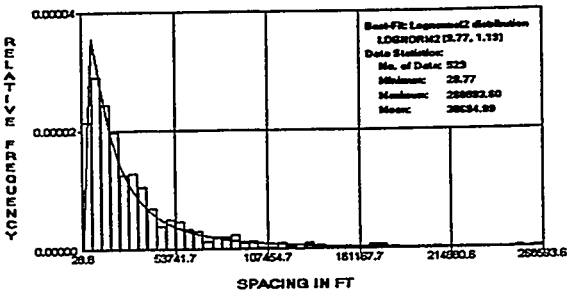

Fig. 92—The histogram and best-fit spacing distribution of the northeast-trending surface lineaments and fractures in western Oklahoma.

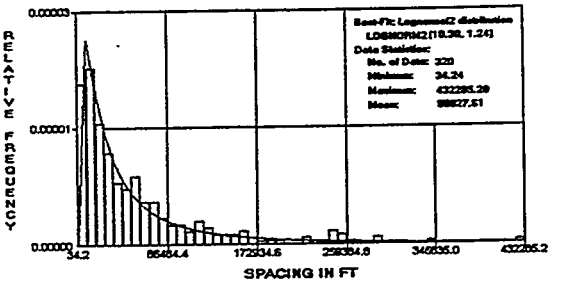

Fig. 93—The histogram and best-fit spacing distribution of the north-trending surface lineaments and fractures in western Oklahoma.

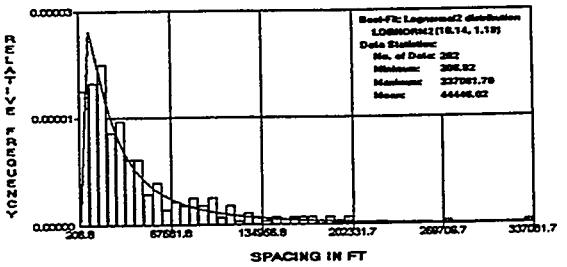

Fig. 94—The histogram and best-fit spacing distribution of the northwest-trending surface lineaments and fractures in western Oklahoma.

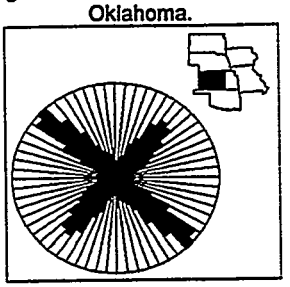

Fig. 95—A rose diagram of the surface lineaments and fractures in western Kansas.

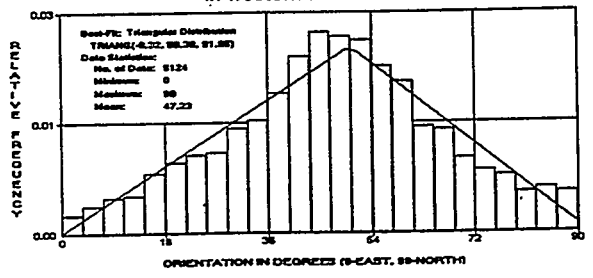

Fig. 96—The histogram and best-fit orientation distribution of the northeast-trending surface lineaments and fractures in western Kansas.

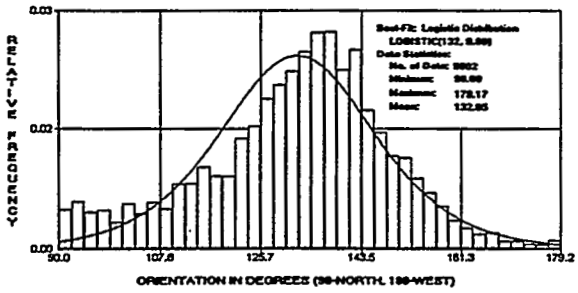

Fig. 97—The histogram and best-fit orientation distribution of the northwest-trending surface lineaments and fractures in western Kansas.

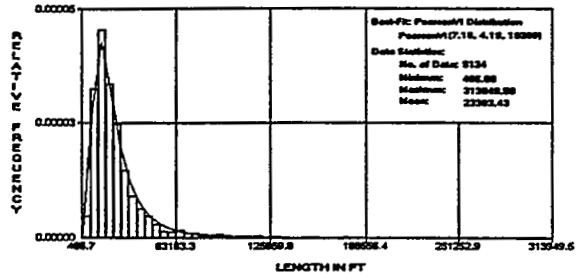

Fig. 98—The histogram and best-fit length distribution of the northeast-trending surface lineaments and fractures in western Kansas.

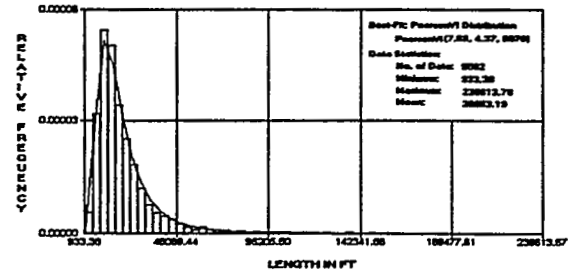

Fig. 99—The histogram and best-fit length distribution of the northwest-trending surface lineaments and fractures in western Kansas.

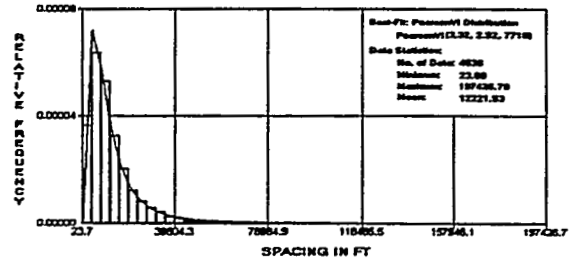

Fig. 100—The histogram and best-fit spacing distribution of the northeast-trending surface lineaments and fractures in western Kansas.

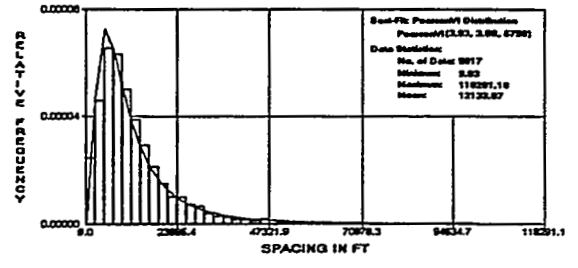

Fig. 101—The histogram and best-fit spacing distribution of the northeast-trending surface lineaments and fractures in western Kansas.

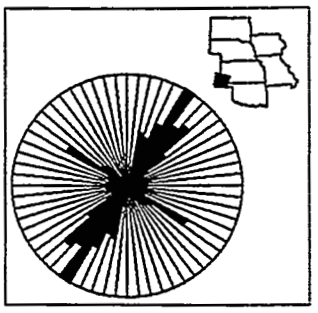

Fig. 102—A rose diagram of the surface lineaments and fractures in the western Hugoton Gas Field.

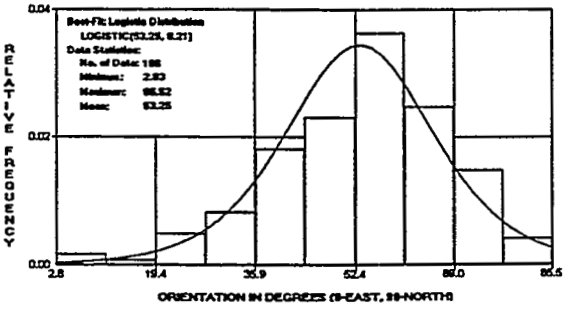

Fig. 103—The histogram and best-fit orientation distribution of the northeast-trending surface lineaments and fractures in the western Hugoton Gas Field.

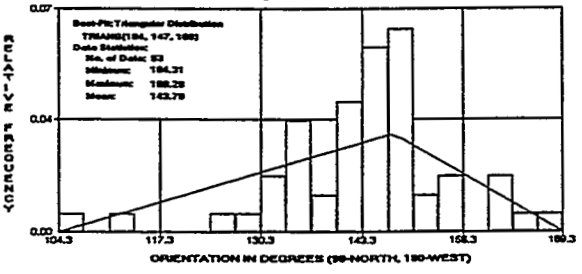

Fig. 104—The histogram and best-fit orientation distribution of the northwest-trending surface lineaments and fractures in the western Hugoton Gas Field

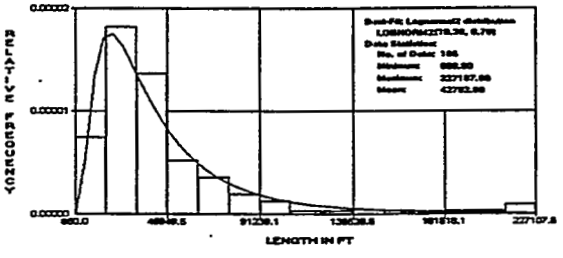

Fig. 105—The histogram and best-fit length distribution of the northeast-trending surface lineaments and fractures in the western Hugoton Gas Field.

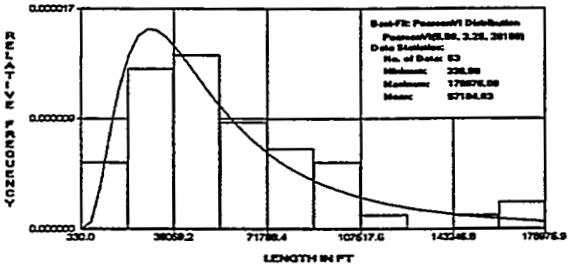

Fig. 106—The histogram and best-fit length distribution of the northwest-trending surface lineaments and fractures in the western Hugoton Gas Field.

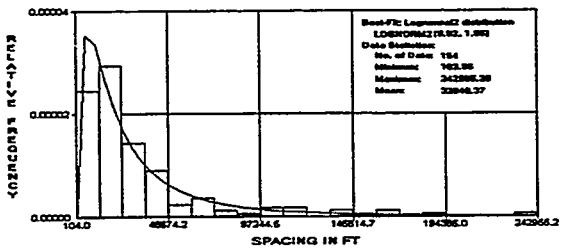

Fig. 107—The histogram and best-fit spacing distribution of the northeast-trending surface lineaments and fractures in the western Hugoton Gas Field.

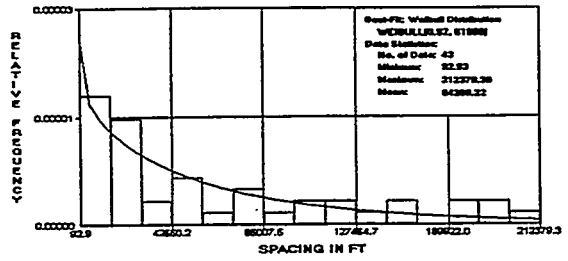

Fig. 108—The histogram and best-fit spacing distribution of the northwest-trending surface lineaments and fractures in the western Hugoton Gas Field.

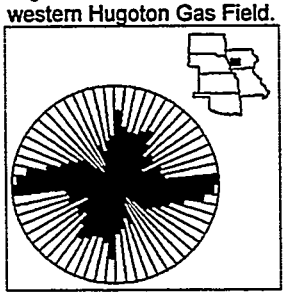

Fig. 109—A rose diagram of the surface fractures in northern Forest City Basin.

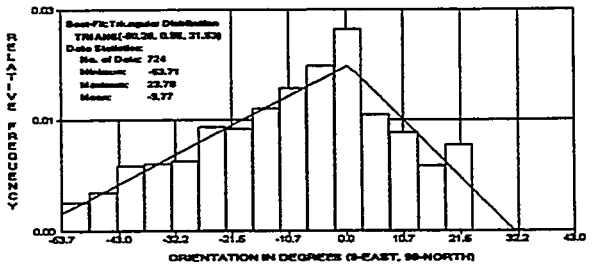

Fig. 110—The histogram and best-fit orientation distribution of the east-trending surface fractures in northern Forest City Basin.

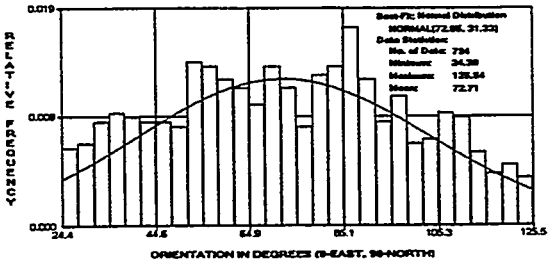

Fig. 111—The histogram and best-fit orientation distribution of the north-northeast-trending surface fractures in northern Forest City Basin.

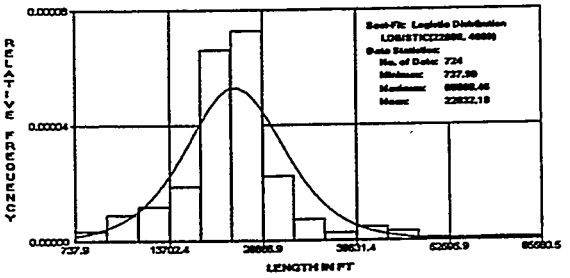

Fig. 112—The histogram and best-fit length distribution of the east-trending surface fractures in northern Forest City Basin.

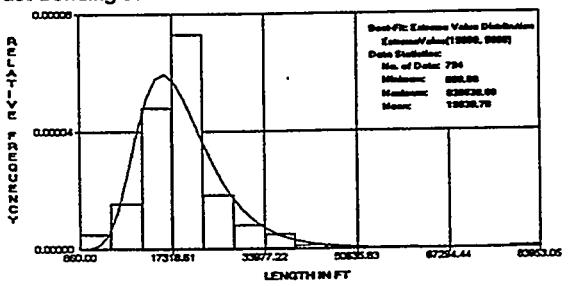

Fig. 113—The histogram and best-fit length distribution of the north-northeast-trending surface fractures in northern Forest City Basin.

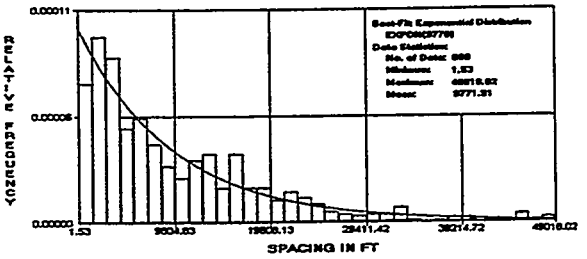

Fig. 114—The histogram and best-fit spacing distribution of the east-trending surface fractures in northern Forest City Basin.

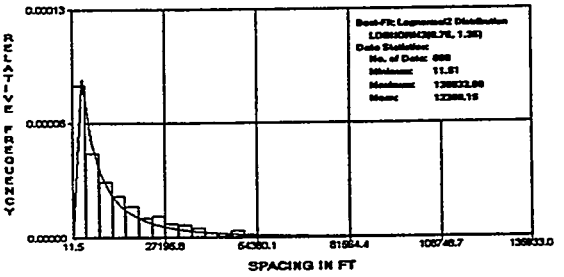

Fig. 115—The histogram and best-fit spacing distribution of the north-northeast-trending surface fractures in northern Forest City Basin.

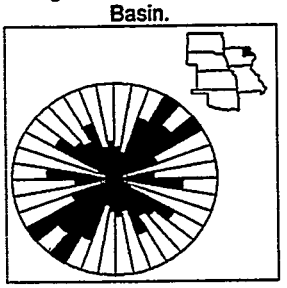

Fig. 116—A rose diagram of the surface fractures in northeastern Iowa.

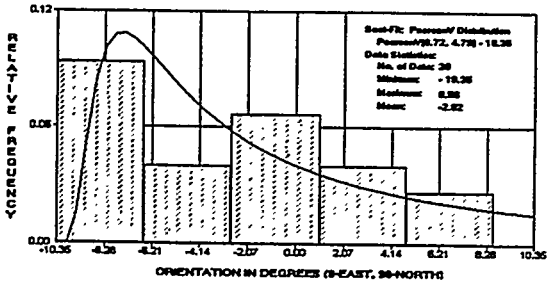

Fig. 117—The histogram and best-fit orientation distribution of the east-trending surface fractures in northeastern Iowa.

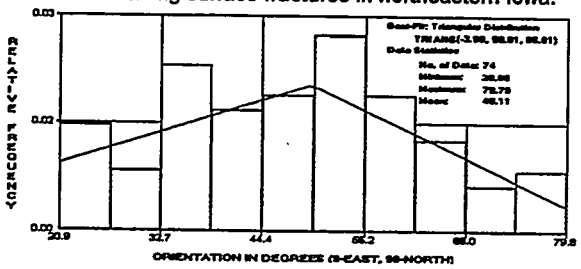

Fig. 118—The histogram and best-fit orientation distribution of the northeast-trending surface fractures in northeastern Iowa.

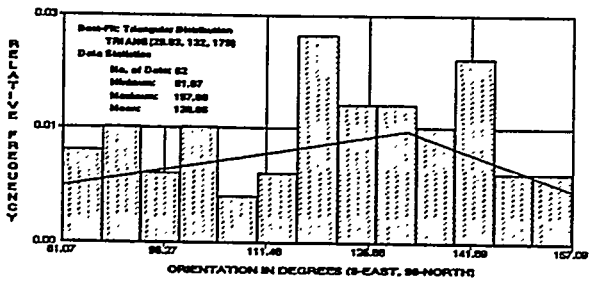

Fig. 119—The histogram and best-fit orientation distribution of the northwest-trending surface fractures in northeastern Iowa.

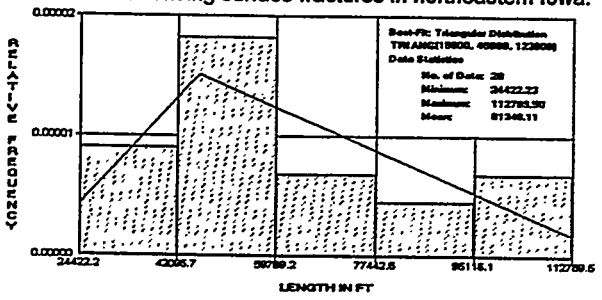

Fig. 120—The histogram and best-fit length distribution of the east-trending surface fractures in northeastern Iowa.

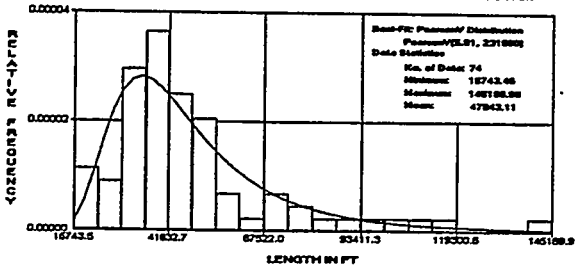

Fig. 121—The histogram and best-fit length distribution of the northeast-trending surface fractures in northeastern Iowa.

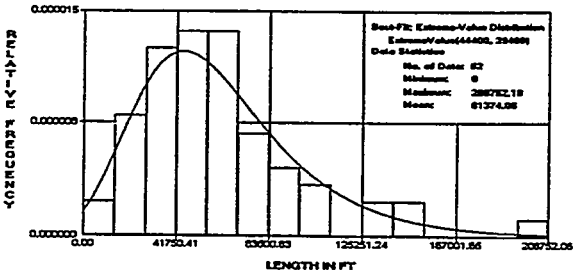

Fig. 122—The histogram and best-fit length distribution of the northwest-trending surface fractures in northeastern Iowa.

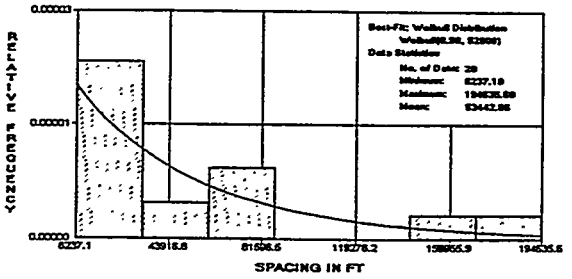

Fig. 123—The histogram and best-fit spacing distribution of the east-trending surface fractures in northeastern Iowa.

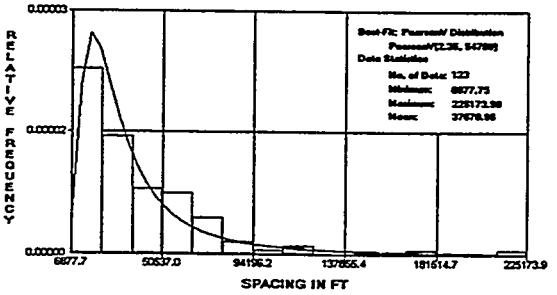

Fig. 124—The histogram and best-fit spacing distribution of the northeast-trending surface fractures in northeastern Iowa.

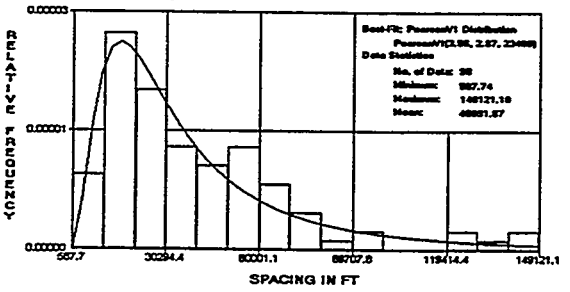

Fig. 125—The histogram and best-fit spacing distribution of the northwest-trending surface fractures in northeastern Iowa.

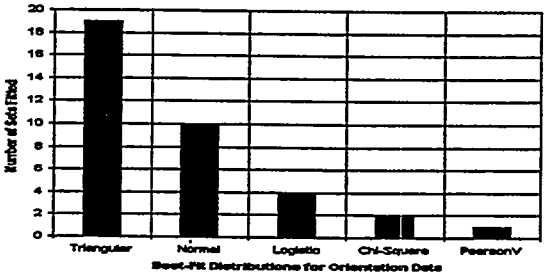

Fig. 126—The best-fit distributions for the orientations of 36 sets of surface lineaments and fractures based on chi-square goodness-of-fit tests.

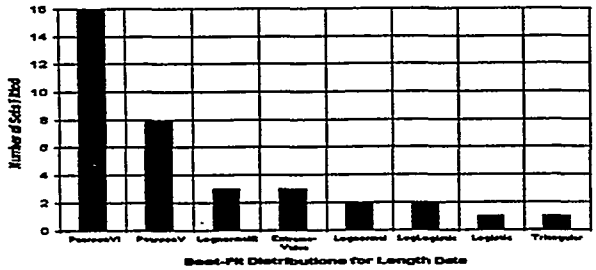

Fig. 127—The best-fit distributions for the lengths of 36 sets of surface lineaments and fractures based on chi-square goodness-of-fit tests.

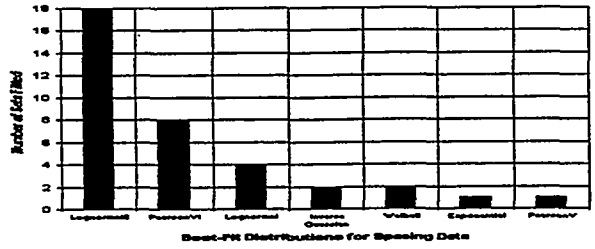

Fig. 128—The best-fit distributions for the spacing of 36 sets of surface lineaments and fractures based on chi-square goodness-of-fit tests.

TRANSIENT PRODUCTIVITY INDEX FOR NUMERICAL WELL TEST SIMULATIONS

G. BLANC
D.Y. DING
A. ENE
T. ESTEBENET
D. RAHON

INSTITUT FRANÇAIS DU PÉTROLE
PAU, FRANCE

ACKNOWLEDGEMENTS

This work has been done within the framework of an ARTEP project sponsored by ELF, the Institut Français du Pétrole and TOTAL. The authors would like to thank both ARTEP and the Institut Français du Pétrole for their permission to publish this work. They would also like to thank L. Piacentino for his help.

ABSTRACT

The most difficult aspect of numerical simulation of well tests is the treatment of the Bottom Hole Flowing (BHF) Pressure. In full field simulations, this pressure is derived from the Well-block Pressure (WBP) using a numerical productivity index which accounts for the grid size and permeability, and for the well completion. This productivity index is calculated assuming a pseudo-steady state flow regime in the vicinity of the well and is therefore constant during the well production period.

Such a pseudo-steady state assumption is no longer valid for the early time of a well test simulation as long as the pressure perturbation has not reached several grid-blocks around the well. This paper offers two different solutions to this problem :

- The first one is based on the derivation of a Numerical Transient Productivity Index (NTPI) to be applied to Cartesian grids ;
- The second one is based on the use of a Corrected Transmissibility and Accumulation Term (CTAT) in the flow equation.

The representation of the pressure behavior given by both solutions is far more accurate than the conventional one as shown by several validation examples which are presented in the following pages.

INTRODUCTION

Need for better numerical Well Test simulation

Analytical well test solutions have been extensively used for a long time by reservoir engineers to interpret their well tests results. In the field of hydrogeology, C. V. Theis (1935), offered one of the first solutions to the problem of the lowering of the piezometric surface under the effect of the rate and duration of a discharge well. Theis' solution was based on the use of the Exponential Integral or Ei function and is still being used by petroleum engineers. Hundreds of papers have been published since that date to account for more complex reservoir models, well completion and test designs. An SPE monograph has summarized the practical aspects of pressure transients (Volume 5 by Earlougher Jr. R. C). Two SPE Reprint Series have been also published (Volume No. 9, *Pressure Analysis Methods*, Volume No. 14, *Pressure Transient Testing Methods*). Published more recently, R. Horne's book gives the status of the knowledge in the 90's.

Despite this abundance of solutions, there are many cases where the analytical solutions no longer apply. Heterogeneous reservoirs with complex in boundaries and complex well geometry are examples where numerical model simulation is the only way to compute the pressure transient. Geostatistical modeling, which is now widely used by geoscience engineers to fill in reservoir simulation grids, also requires numerical reservoir simulation (Blanc G., 1995 and 1996).

In the meantime the well testing technology has been improved allowing bottom hole shut down and early time pressure recording. This is where the need for more and more precise numerical BHF Pressure simulation becomes evident.

Numerical simulation of Well Tests

The pressure behavior of a single-phase flow in a 3D reservoir is governed by the following equation:

$$\frac{\partial}{\partial x_i}\left(\frac{k_i}{\mu}\frac{\partial(P+\rho g z)}{\partial x_i}\right)=\phi c_t\frac{\partial P}{\partial t}+q \quad \text{..... (1)}$$

where :

P	is the pressure
i	is the axis index
x_i	coordinates (x_1, x_2, x_3, stands for x, y, z)
k_i	is the directional permeability
μ	is the fluid viscosity
ρ	is the fluid density
g	is the gravity
ϕ	is the porosity
c_t	is the total rock and fluid compressibility
q	is a sink term

SIMTESTW is the IFP numerical well test simulation program that uses the 7-point finite-difference scheme of Equation (1). The grid-block system is Cartesian irregular and dead cells are used to simulate complex shapes.

Discretization of Equation (1) in space and time, for a grid-block i and at time step n, is:

$$\sum_j \frac{T_{ij}}{\mu}\left[\left(P_j^n-P_i^n\right)+\rho g\left(z_j-z_i\right)\right]=\phi c_t Vi\frac{P_i^n-P_i^{n-1}}{t^n-t^{n-1}}+\delta_{ip}Q_p \quad \text{..... (2)}$$

where:

j is the index of all neighbors of grid-block i

$\Delta x_i, \Delta y_i$ and Δz_i are the size of the rectangular grid-block i

T_{jj} is the transmissibility between grid-blocks i and j (harmonic average of $\Delta z_i \times k_i$ products)

V_i is the volume of grid-block $i = \Delta x_i \times \Delta y_i \times \Delta z_i$

Q_p is the rate of the well p

δ_{ip} is equal to 1 when grid-block i contains the well p and 0 elsewhere

P^n, is then the solution vector of the following matrix equation:

$$A^n \times P^n = B^n \quad (3)$$

where:

A^n is the 7-band matrix of the system of discretized equations at time n

P^n is the vector of the pressure map at time n

B^n is the vector column of the right-hand side of the system of discretized equations at time n

This program can handle vertical, horizontal or complex wells operated at an imposed rate or at an imposed BHF Pressure. The management of the well completion is flexible enough to allow the user to open or close any grid-block to the flow during the simulation time.

Previous Works - PEACEMAN Numerical Productivity Index (NPI)

Steady State flow

The problem of getting the BHF Pressure from the well grid-block pressure has been addressed by Peaceman D. W. (1978).

Peaceman has shown that the steady state grid-block pressure P_b at the well location, computed using a square grid-block system ($\Delta x_i = \Delta y_i = \Delta L$) in a homogeneous, isotropic and infinite reservoir (permeability = k, porosity = ϕ, compressibility c_t) produced at constant flow rate by a vertical well, is the same as would be observed at a dummy well of radius ro given by :

$$r_0 = 0.198 \times \Delta L \quad (4)$$

When these conditions apply, the BHF Pressure can be obtained using a Numerical Productivity Index (NPI), which relates the grid-block pressure P_0 to the BHF Pressure P_{wf} according to:

$$P_{wf} = P_0 - \frac{Q_b}{NPI} \quad (5)$$

NPI can be computed using the steady state radial flow equation between ro and rw :

$$NPI = \frac{2\pi \times \Delta z_i k}{\mu \ln(\frac{r_w \times e^{-S}}{r_o})} \quad (6)$$

where :

rw is the well radius

S is the well skin

Each well can then be assigned a well bore storage C which relates the well rate Q to the sand face rate Q_{sf} applied to the reservoir as follows:

$$Q_{sf} = Q + C \times \frac{\Delta P_{wf}}{\Delta t} \quad (7)$$

where :

ΔP_{wf} is the pressure drop within the well during the time step Δt

Unsteady State Flow

Peaceman (1978) has also shown that, for unsteady state flow, and when a pseudo steady state flow regime is reached near the well, *ro* can be derived from the following equation :

$$r_0 = \Delta L\left[4t_D \exp(-\gamma - 4\pi p_{Db})\right] \quad \text{..... (8)}$$

where :

γ is the Euler's constant

$t_D = \dfrac{k}{\phi\mu c_t \Delta L^2} \times t$ is the dimensionless time related to ΔL ..... (9)

$p_D = \dfrac{kh}{Q\mu} \times p$ is the dimensionless pressure, p_{Db} rely to rate Q_b..... (10)

Peaceman (1978) concluded that when t_D>1, *ro* computed from equation (4) is close enough to the value given by relation (4), and that equation can therefore be applied in most full field simulation cases.

Previous Works - IFP Transmissibility Correction Multiplier (TCM)

Peaceman's work has been extended to many more complex conditions by the author himself (1983,1990 and 1994) and by several others. All these works are based on the derivation of a better NPI or on the evaluation of numerical pseudo skin to be used with relations (5) and (6).

Recently a new method has been proposed by Ding Y. et al (1993 & 1995a) for improving the well modeling in non standard configurations such as non-uniform Cartesian grids, flexible grids and off-center wells. The principle of this method is to improve the flow representation around the well by modifying the transmissibility in the near well region. This approach, referred to as the Transmissibility Correction Multiplier (TCM) approach, is particularly suited to 3D well modeling as shown by Ding (1995b).

Within this approach the pressure p_0 corresponding to a radius r_0 is obtained using equivalent transmissibility T_{eq} which links p_0 to the pressure of adjacent grid-blocks through equivalent distances (Figure 1). The following transmissibilities must be used instead of the conventional harmonic average ones :

$$T_{eq,i} = k\Delta z_i \frac{\Delta y_0}{L_{eq,i}} \text{ and with } L_{eq,i} = \Delta y_0 \frac{\ln\left(\frac{\Delta x_0 + \Delta x_i}{r_0}\right)}{\phi_i} \text{ for i=1 and 3 ..... (11)}$$

$$T_{eq,i} = k\Delta z_i \frac{\Delta x_0}{L_{eq,i}} \text{ and with } L_{eq,i} = \Delta x_0 \frac{\ln\left(\frac{\Delta y_0 + \Delta y_i}{r_0}\right)}{\phi_i} \text{ for i=2 and 4 ..... (12)}$$

The radius r_0 can be chosen by the user and the BHF Pressure is obtained using relation (6).

This method can be easily implemented in conventional numerical simulators, provided that they allow transmissibility multipliers.

TRANSIENT NUMERICAL PRODUCTIVITY INDEX (TNPI)

Generalities

In order to investigate how the Peaceman approach behaves at early time we simulated a pumping test on a vertical well producing a homogeneous "infinite" reservoir using a regular square (10m×10m) grid system. Table 1 shows all the properties of the test, referred to as Reference Case 1.

Figure 2 is a semi-log plot of the results showing the grid-block pressure p_o, the BHF Pressure p_{wf} derived from relation (5) and (6), and the Ei analytical solution. This figure points out the following facts :

- At late time of the test, the Peaceman approach provides a very good BHF Pressure (less than 1% of error).
- At early time, the pressure perturbation has not yet reached the neighbor blocks and all the produced fluid comes from the well-block capacity. The well-block draw-down pressure is negligible compared to the r_o-r_w steady state correction and then the corresponding BHP Pressure is higher than the analytical one.
- In between these two periods, the neighbor blocks start providing an increasing part of the well rate, and the BHF Pressure is lower than the analytical one to compensate for the delay at early time.

The second question addressed concerns the influence of the grid-block size on the BHF Pressure and on its derivative. To do so, the previous draw-down test was simulated using a set of different grid sizes ΔL : 20m×20m, 10m×10m, 5m×5m and 1m×1m. Figure 3, which represents a log-log plot of the BHF Pressure and its derivative versus the time, shows all the results together with the Ei analytical solution. This Figure shows that :

- Decreasing the mesh size leads, as expected, to better results at earlier time.
- An equivalent "well bore storage effect" appears at early time when nearly all the produced fluid comes from the well-block capacity.

This phenomena leads two more questions :

- Is there any rule to calculate the maximum mesh size to be used in order to get clean results from any given pressure recording time ?
  Figure 4, which gathers results calculated using various grid-block size and reservoir permeability, is a log-log plot of dimensionless BHF Pressure and its derivative versus dimensionless time computed using Δx^2 (relations (9) and (10)). This figure shows that for $t_D > 2.6$ the derivative is flat, as expected by the analytical solution of the fluid flow equation. This time, which was determined as the one from which the apparent well-block storage ends, leads to the relation :

$$t \geq 2.6\Delta L^2 \times \frac{\phi \mu c_t}{k} \quad \text{..... (13)}$$

- Is it possible to use the mesh storage to simulate well bore storage whenever the numerical simulation program does not account for such a condition ?
  Figure 5 is the derivative plot of the PIE well test interpretation program which has been used to interpret the results of the ΔL=20 m grid-block simulation. For such a grid the well-block capacity is equal to $\Delta x \times \Delta y \times \Delta z \times \phi \times c_t$ that is 0.8 m^3/bar, and the interpretation leads to a close 0.737 m^3/bar. However the shape of the pressure derivative shows a huge discrepancy between the behavior of a true well bore storage (solid line) and the apparent well block storage (dash line), pointing out that the latter can be used to simulate the former.

Derivation of the Transient Numerical Productivity Index

Three different attempts have been made to correct the early time problem coming from the use of the NPI steady state grid-block correction. Reference Case 1 (described in Table 1) has been used to check for their validity. A one-layer system made of square (20m×20m) grid-blocks has been selected for all numerical simulations. The well bore storage and skin are both equal to 0.

The Peaceman_Ei correction

The first attempt was to use a unsteady state radial flow equation between *ro* and *rw* to compute the *NPI* as follows :

$$NPI = \frac{4\pi \times \Delta z_i k}{Ei\left(-\frac{r_0^2}{4kt}\right) - Ei\left(-\frac{r_w^2}{4kt}\right)} \quad \text{with} \quad r_0 = 0.198 \times \Delta L \quad \text{..... (14)}$$

The corresponding BHF Pressure and its derivative which are shown in Figure 7 are far better than the conventional ones. The pressure is relatively correct compared to the analytical Ei solution. The early part of the apparent well-block storage was removed from the derivative which still shows a "wave" before the stabilization.

The Peaceman Explicit Transient correction

The main drawback of the first attempt seems to come from the use of a constant equivalent radius r_o. We then extended the Peaceman transient analysis of r_0, using relation (8), far more toward the early time than Peaceman did. Figure 6 shows that the ratio $r_0/\Delta x$ first grows rapidly up to a maximum of 0.3 for t_D=0.01 and then decreases down to the 0.198 limit value.

The corresponding BHF Pressure and its derivative are referred to as $r_{0(t)}$_explicit in Figure 7. Compared to the analytical Ei solution, the pressure is not as good as that achieved by the Peaceman_Ei, the derivative being far better than the previous one.

The full TNPI correction

The previous correction is based on a pseudo-steady state approximation of the transient flow equation corresponding to a pseudo-steady state flow regime around the well. The approximation allows the explicit derivation of r_0.

To be more accurate we used the full transient Ei solution. The r_0 radius was obtained using a Newton method of solution. Figure 6 shows that the corresponding radius is close to the previous one when the dimensionless time t_D becomes greater than 0.2. Earlier than 0.2, the two radii are slightly different. The BHF pressure and derivative computed using this new radius are referred to as NTPI in Figure 7. They both correspond well with the analytical solution.

Validation of the NTPI correction

Three different Reference Cases (Tables 3 to 5) were used to check for the validity of the full NTPI proposed correction.

The first validation was used to check for the accuracy of the proposed NTPI correction in the case of partial well penetration in a homogeneous reservoir. The last two validations were devoted to multiple rate tests such as Drill Stem Tests (DST) and build-up tests. As demonstrated earlier, the correction works properly when the well rate is constant, but it vanishes when the well is shut-down as

does the conventional Peaceman approach. To by-pass this limitation we used a constant rate simulation to derive a « kernel» pressure which was then used as the reference pressure response for a superposition (rate convolution) program. By doing so, any kind of multiple rate test can be simulated, even if it includes shut-down periods. This method can only be applied when the permeability, the porosity and the compressibility are not pressure or fluid saturation dependent, i.e. when the equation (1) is linear (necessary validity condition of the superposition theorem).

Reference Case3 - Homogeneous Reservoir - Draw-down test - Partial penetration

A 10 m thick homogeneous reservoir is produced at constant rate by a well that is perforated in the top 2 m. The grid-block system is made of square (20m×20m) grids 2m thick, the numerical model is made of 10 layers. Table 3 shows all the characteristics of this reference case.

Figure 8 gives the results of the simulation. The computed BHF Pressure as well as its derivative are close to the analytical one computed by the analytical well test interpretation program PIE down to 0.2 s. The derivative is far better than the one computed with the conventional Peaceman correction.

Reference Cases 4 - Three-layer reservoir - DST - Partial penetration

Reference Case 4 is a 3-layer reservoir for which the characteristics are shown in Table 4. There are 3 layers in the numerical model (one per reservoir layer) which are made of square grid-blocks (20m×20m×2m). The purpose of this case was to check for the validity of the superposition method proposed to simulate build-up flow periods of a DST. The simulated DST is made of three flow periods of 7 hours followed by a build-up of more than 100 hours (Table 4). The well is only perforated in the middle layer of the reservoir. The results of the simulated build-up, which are represented in Figure 9, correspond well with those given by the analytical program. The improvement of the conventional Peaceman correction is very significant in the 10^3 first seconds of the build-up.

Reference Case 5 - Three- layer reservoir - DST - Full penetration

Reference Case 5 is also a 3-layer reservoir for which the characteristics are shown in Table 5. The grid-block system is the same as the one used in Reference Case 4. The purpose of this case was to check for the validity of the superposition method with and without the presence of a well bore storage for a full penetration well. The two simulated build-ups are represented in Figures 10 and 11. They both correspond well with the analytical program results. When there is no well bore storage the improvement of the proposed correction is also very significant, as previously observed with Reference Case 4.

TRANSMISSIBILITY and ACCUMULATION Correction Multipliers (TACM)

Derivation of the Transmisibility and Accumulation Correction Multiplier

The Transmissibility Correction Multiplier which is based on a steady state flow regime was also improved to account for the short time period when the well flow rate is essentially produced from the well-block by the « volume storage », that is, by the term :

$$c_t \phi \int_{V_0} \frac{\partial p}{\partial t} dV \quad \text{..... (15)}$$

However, as p_0 is expected to be the pressure corresponding to the radius r_0, the « volume storage » variation will be approximated by :

$$c_t\phi V_0\frac{\partial p_0}{\partial t} = -c_t\phi V_0\frac{q\mu}{4\pi kh}\frac{e^{-\frac{r_0^2}{4kt}}}{t} \quad \text{..... (16)}$$

where the well block pressure is assumed to be equal to :

$$p_0 = p_i + \frac{q\mu}{4\pi hk}Ei\left(-\frac{r_0^2}{4kt}\right) \quad \text{..... (17)}$$

so that the derivative :

$$\frac{\partial p_0}{\partial t} = -\frac{q\mu}{4\pi kh}\frac{e^{-\frac{r_0^2}{4kt}}}{t} \quad \text{..... (18)}$$

is independent of the integration variables on V_0. This approximation is not accurate enough for short time period. To improve this calculation, we introduce the Accumulation Correction coefficient for volume storage by determining the coefficient β such that :

$$\begin{aligned} -\beta c_t\phi V_0\frac{q\mu}{4\pi kh}\frac{e^{-\frac{r_0^2}{4kt}}}{t} &= c_t\phi\int_{V_0}\frac{\partial p}{\partial t}dV \\ &= -c_t\phi\frac{q\mu}{4\pi kh}\int_{V_0}\frac{e^{-\frac{r^2}{4kt}}}{t}dr \end{aligned} \quad \text{..... (19)}$$

The result is as follows :

$$\beta = \frac{1}{V_0}\int_{V_0} e^{-\frac{(r^2-r_0^2)}{4kt}}dr \quad \text{..... (20)}$$

Validation of the TACM correction

Reference Case2 - Homogeneous Limited Reservoir - Draw-down test - Full penetration

The validity of the full TACM correction was first checked with the Reference Case 2 (this case is the same as the Reference Case 1 but for a limited reservoir, as shown on Tables 1 and 2). Figure 12 shows that, while the early time improvement obtained with the TACM correction is not as good as the full NTPI one, it is still better than the pure Peaceman_Ei correction and it is close to the one obtained with the Peaceman Explicit Transient correction.

Reference Case3 - Homogeneous Reservoir - Draw-down test - Partial penetration

Reference Case 3 simulation confirms the previous conclusions for early time as illustrated on Figure 12: NTPI gives better results than TACM. On the contrary, the TACM correction works better than the NTPI one for late times. This is the result of the use of the transmissivity multipliers which have proven to be more accurate than the conventional Peaceman approach in steady state flow conditions (i.e. for late test times) as demonstrated by DING Y. (1994).

CONCLUSIONS

The main conclusions from this work are the following :

The Peaceman approach can be used for numerical well test simulation as long as the following relation between the petrophysical properties, the time and the grid-block size is fulfilled :

$$t \geq 2.6\Delta L^2 \times \frac{\phi \mu c_t}{k}$$

This relation is true if and only if the well is located at the center of a local 5x5 square grid system within which the reservoir is isotropic and homogeneous.

For the simulation of early time two approaches have been proposed :

- The Numerical Transient Productivity Index correction which has been validated on several reference case and has proven to give far better results than the conventional Peaceman approach.

- The Transmissibility and Accumulation Correction Multipliers is not as good as the previous one but is still far better than the conventional Peaceman approach. However, the use of transmissibility multipliers gives a better simulation of late time.

For both approaches, the simulation of multiple rate and build up tests, must be done using the rate convolution of a constant rate simulation. This approach is only valid when the permeability, the porosity and the compressibility are not pressure or fluid saturation dependent.

This work indicates that the combination of the NTPI approach and the transmissibility multipliers would probably give both better early and late times than the previous approaches for the numerical simulation of well tests.

Nomenclature

c_t = total compressibility, Lt^2/m, 1/bars
C = well bore storage, , m^3/bar
$\Delta x, \Delta y, \Delta z$ = grid-block dimension, L,m
h = reservoir thickness, L, m
k = permeability, L^2, mD
NPI = numerical productivity index, L^4t/m
P = pressure, $m/L\ t^2$, bar
q = sink term, L^3/t
Q = well flow rate, L^3/t, m^3/d
r_w = well radius, L, cm
r = Peaceman equivalent radius, L, cm
S = well skin
t = time, t
T = transmissibitity,L^2/t
V_i = grid block volume, L^3, m^3
β = accumulation multiplier
ϕ = porosity, fraction
μ = fluid viscosity, m/Lt, cp
ρ = fluid density, m/L^3, g/cm^3

REFERENCES

BLANC, G. *et al.*, Numerical Well Tests Simulations in Heterogeneous Reservoirs. Poster presented at AAPG, Nice 95.

BLANC, G. & al, 1996, Building Geostatistical Models Constrained by Dynamic Data". SPE 35478 presented at the SPE/NPF European Conference held in Stavanger, Norway, 16-17 April 1996.

DING Y., RENARD, G. and WEILL, L., Representation of Wells in Numerical Reservoir Simulation, paper SPE 29123, presented at the 13 th SPE Symposium on Reservoir Simulation, San Antonio, Feb. 12-15, 1995.

DING Y., and RENARD, G., A New Representation of Wells in Numerical Reservoir Simulation SPERE, May 1994, p. 140.

DING Y., A Generalized 3D Well Model for Reservoir Simulation, paper SPE 30724, presented at the SPE Annual Technical Conference help in Dallas, USA, Oct. 22-25, 1995.

EARLOUGHER, LR. C. Jr., 1977. Advances in Well Test Analysis. Monograph Volume 5 of the Henry L. Doherty Series. Published by Society of Petroleum Engineers of AIME , New York , Dallas.

LEE, John, 1982. Well Testing. SPE Textbook Series, vol. 1. Published by Society of Petroleum Engineers of AIME , New York , Dallas.

PEACEMAN, D. W., 1978, Interpretation of Well-block Pressures in Numerical Reservoir Simulation: in Transactions of AIME, 1978, p253.

PEACEMAN, D. W., 1983, Interpretation of Well-block Pressures in Numerical Reservoir Simulation with Non Square Grid-Blocks and Anisotropic Permeability. SPEJ (June), p531.

PEACEMAN, D. W., 1990, Interpretation of Well-block Pressures in Numerical Reservoir Simulation, part 3 - Off Center and Multiple Wells Within a Well Block, SPERE, May 1990, p.1990.

PEACEMAN, D. W., 1995, A New Method for Representing Multiple Wells with Arbitrary Rates in Numerical Reservoir Simulation, paper SPE 29120, presented at the 13 th SPE Symposium on Reservoir Simulation, San Antonio, Feb. 12-15, 1995.

PIE - Well Test Analysis, User's Manual, S.M.C. limited, June 1994.

SPE Reprint Series N° 9, 1967, Pressure Analysis Methods. Published by Society of Petroleum Engineers, Dallas, Texas.

SPE Reprint Series N° 14, 1980, Pressure Transient Testing Methods. Published by Society of Petroleum Engineers, Dallas, Texas.

THEIS, C. V. , 1935, The relationship Between the Lowering of the Piezometric Surface and the Rate and Duration of Discharge Well Using Ground-Water Storage. Trans. Amer. Geophysical Union, vol. 16, pages 515-524.

FIGURES

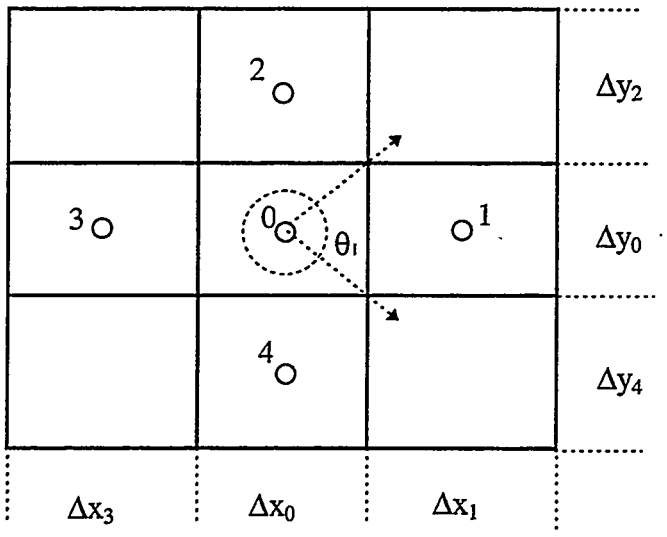

Figure 1 - Well-block pressure calculation - TCT method

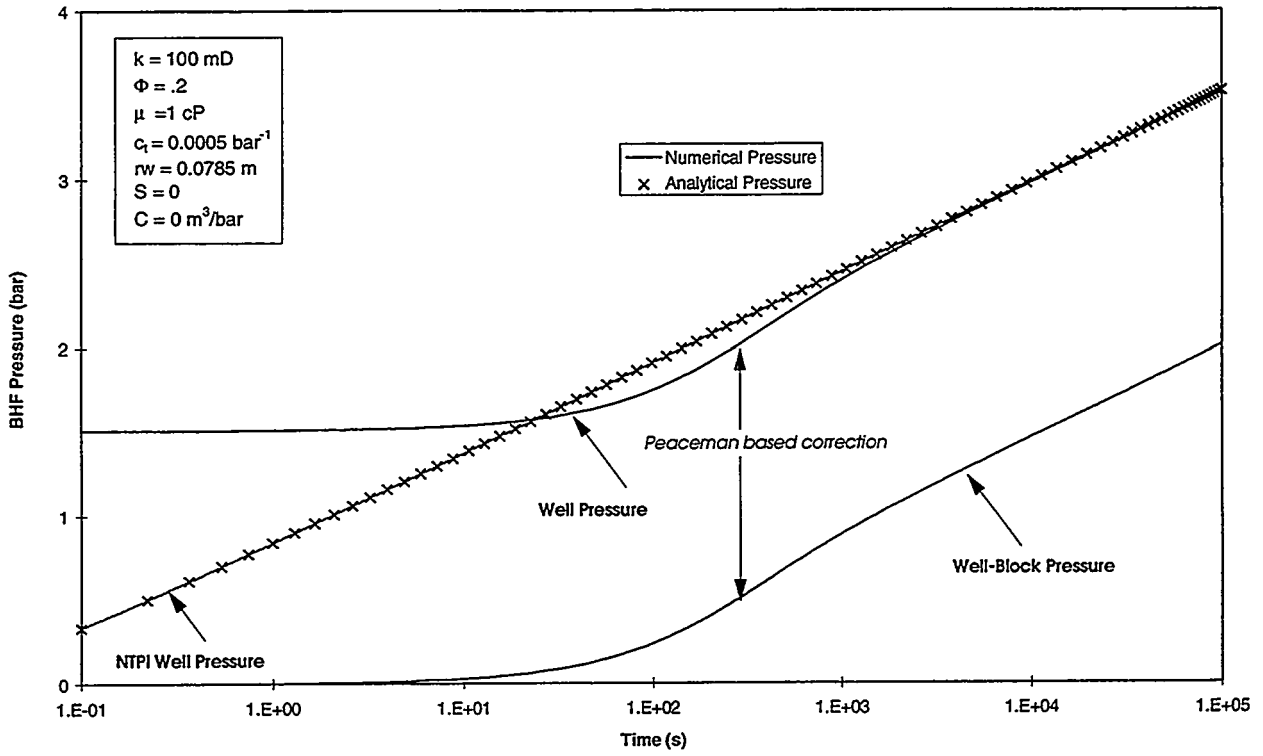

Figure 2 - Conventional BHF Pressure computation (Reference Case 1- 10m×10m grid-blocks)

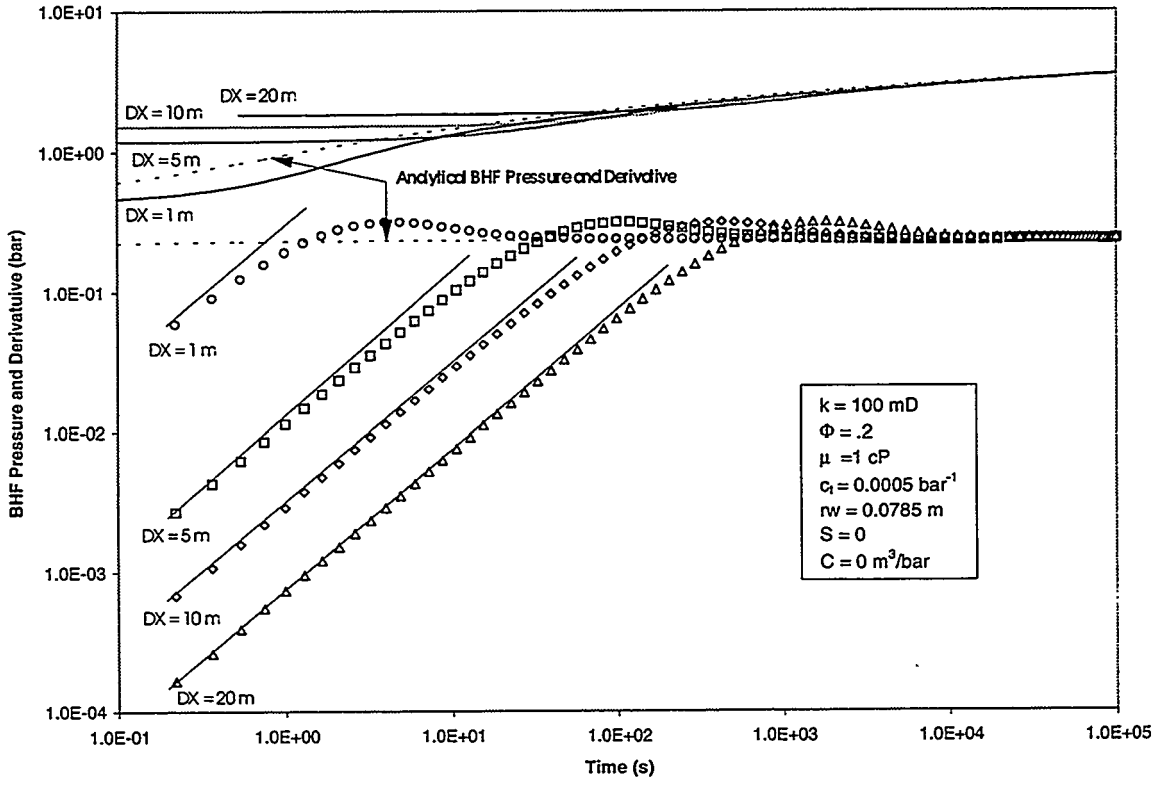

Figure 3 - Conventional BHF Pressure and Derivative Plot computation (Reference Case 1)

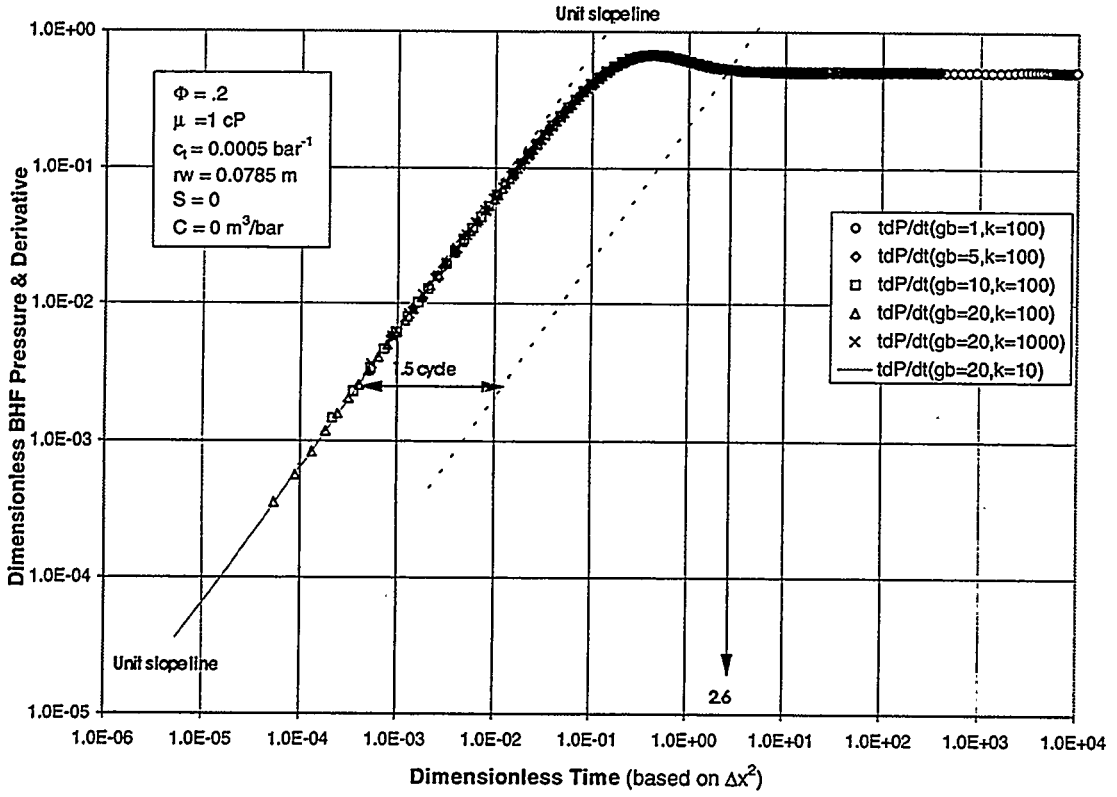

Figure 4- Well-block size effects on Conventional BHF Derivative computation (Reference Case 1)

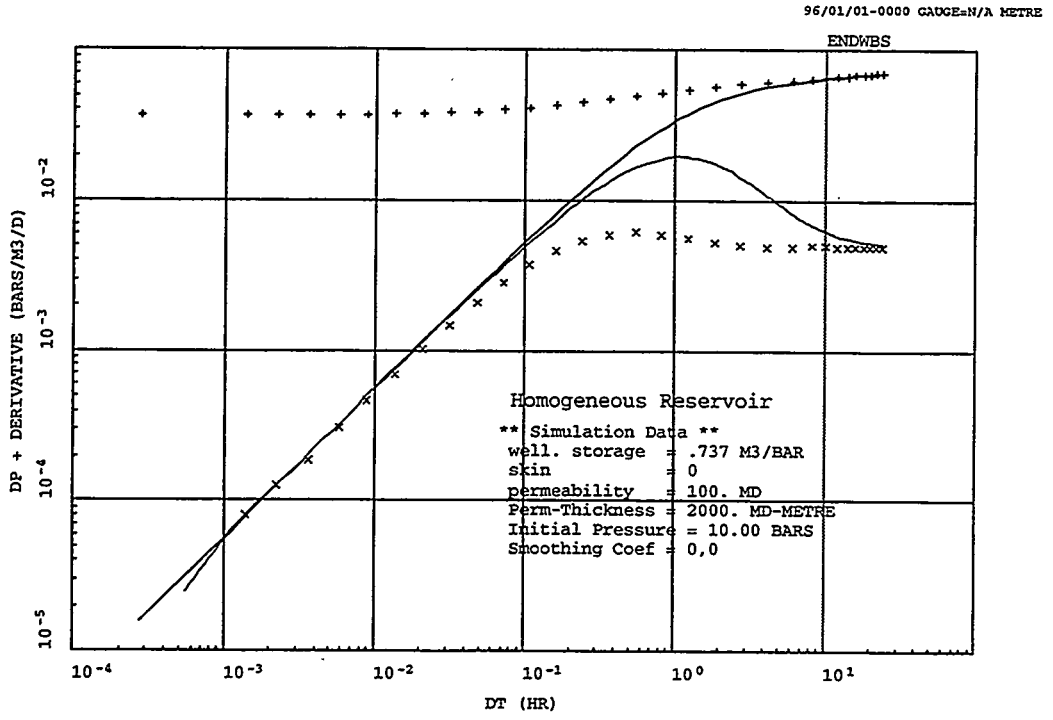

Figure 5 - Apparent Well-Block storage (Reference Case 1- 20m×20m grid-blocks)

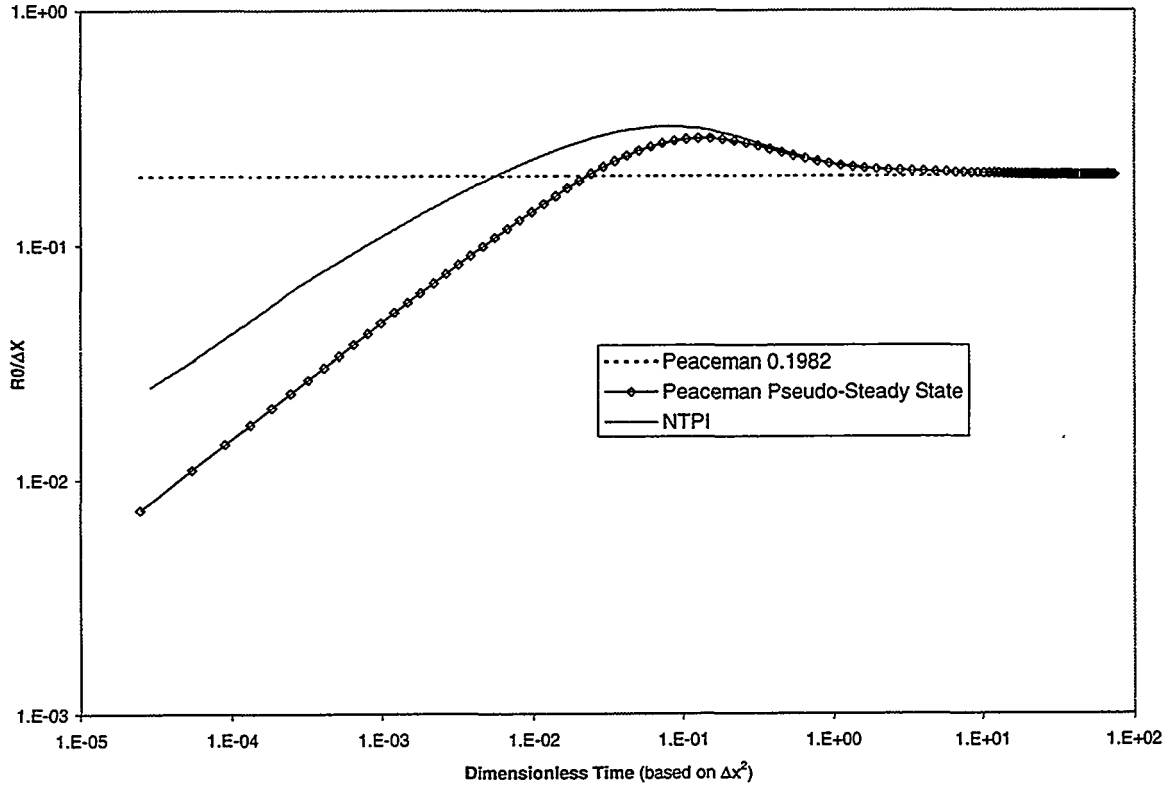

Figure 6 - Equivalent Well-block radius versus time

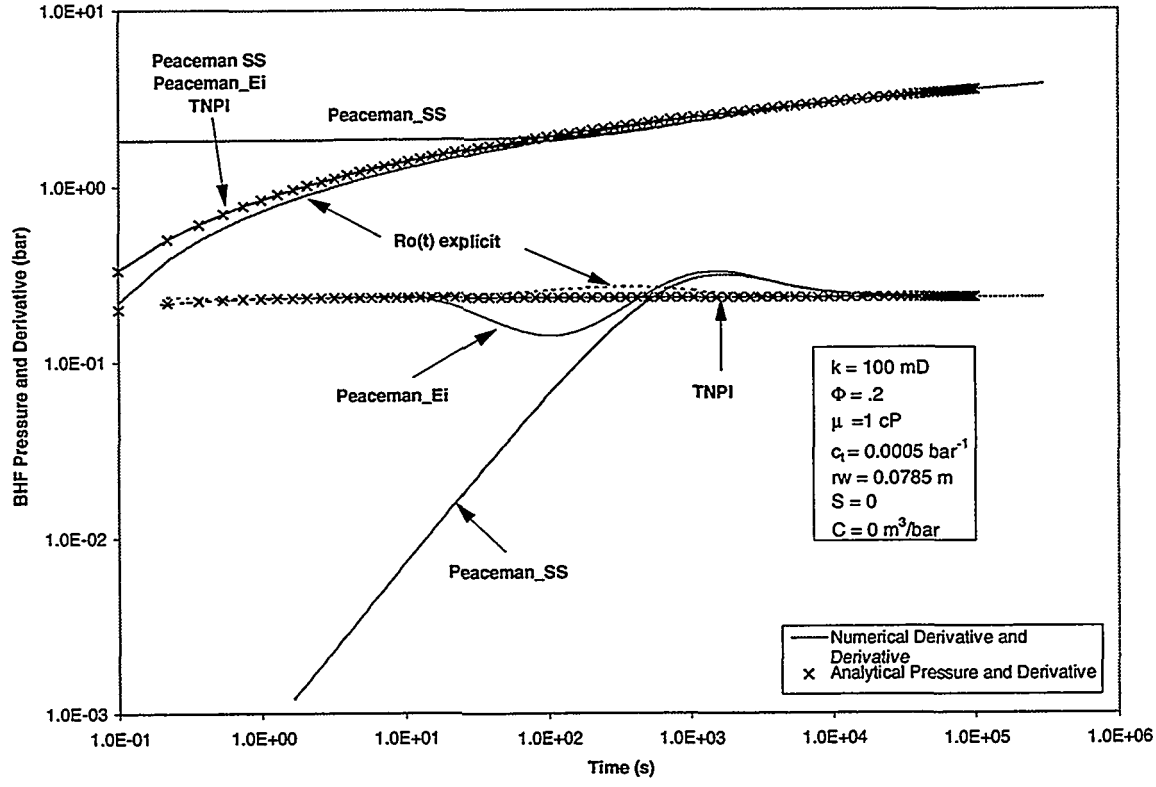

Figure 7 - Summary of NPI transient corrections (Reference Case 1 - 10m×10m grid-blocks)

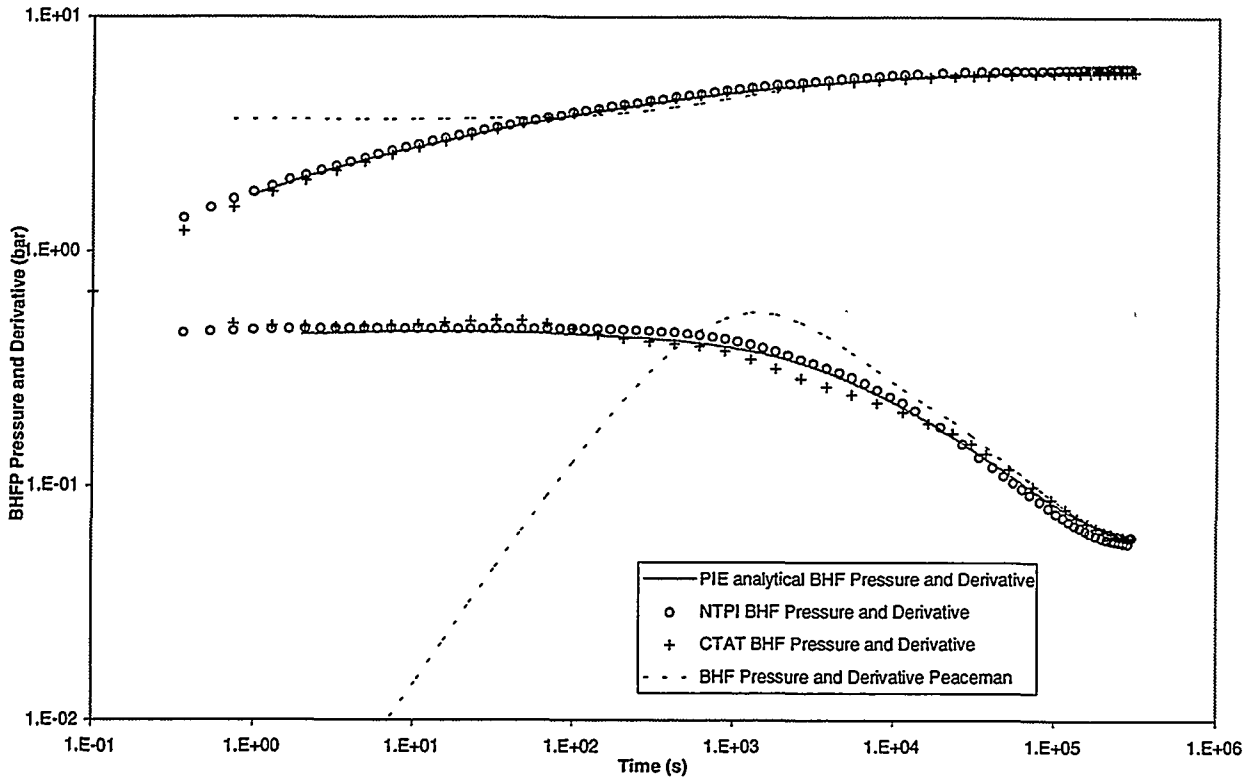

Figure 8 - Homogeneous reservoir - Partial penetration (Reference Case 3- 20m×20m grid-blocks)

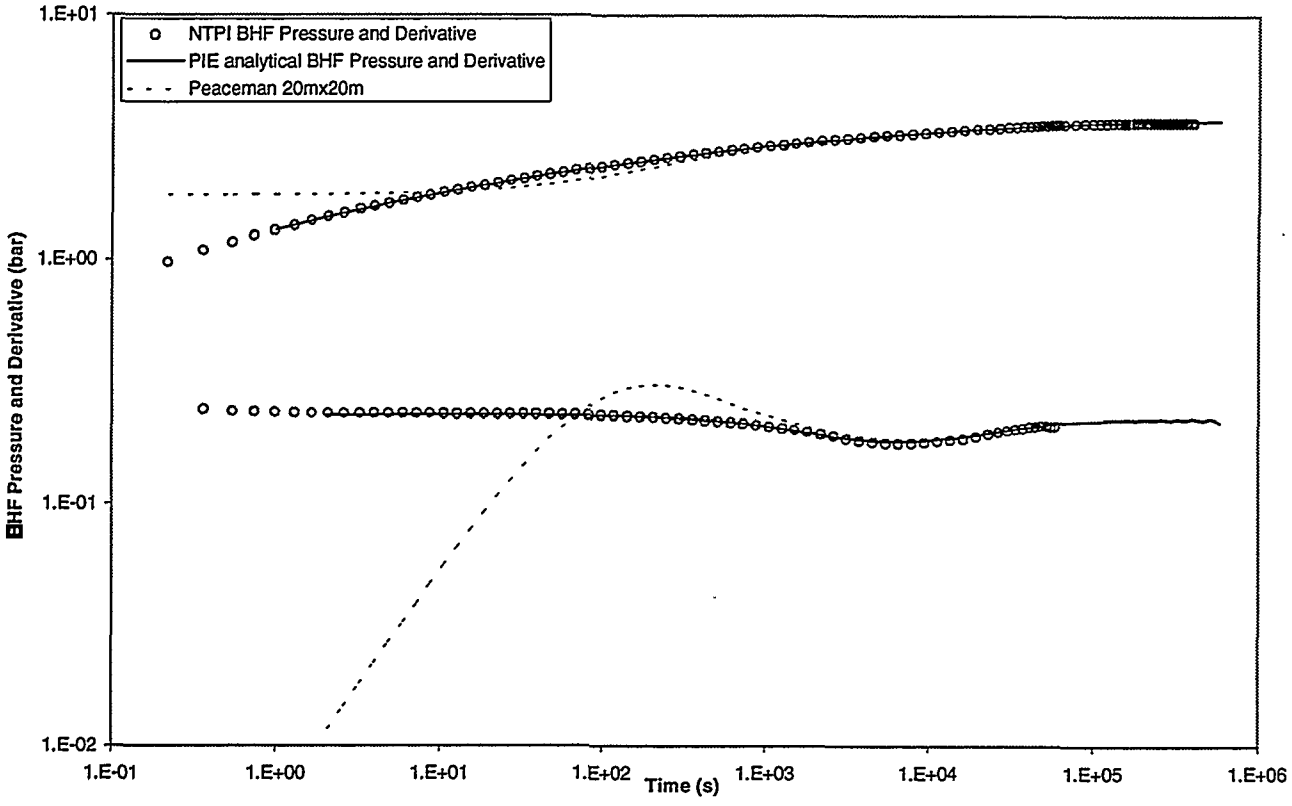

Figure 9 - 3 Layers - Partial penetration (Reference Case 4 - 20m×20m grid-blocks)

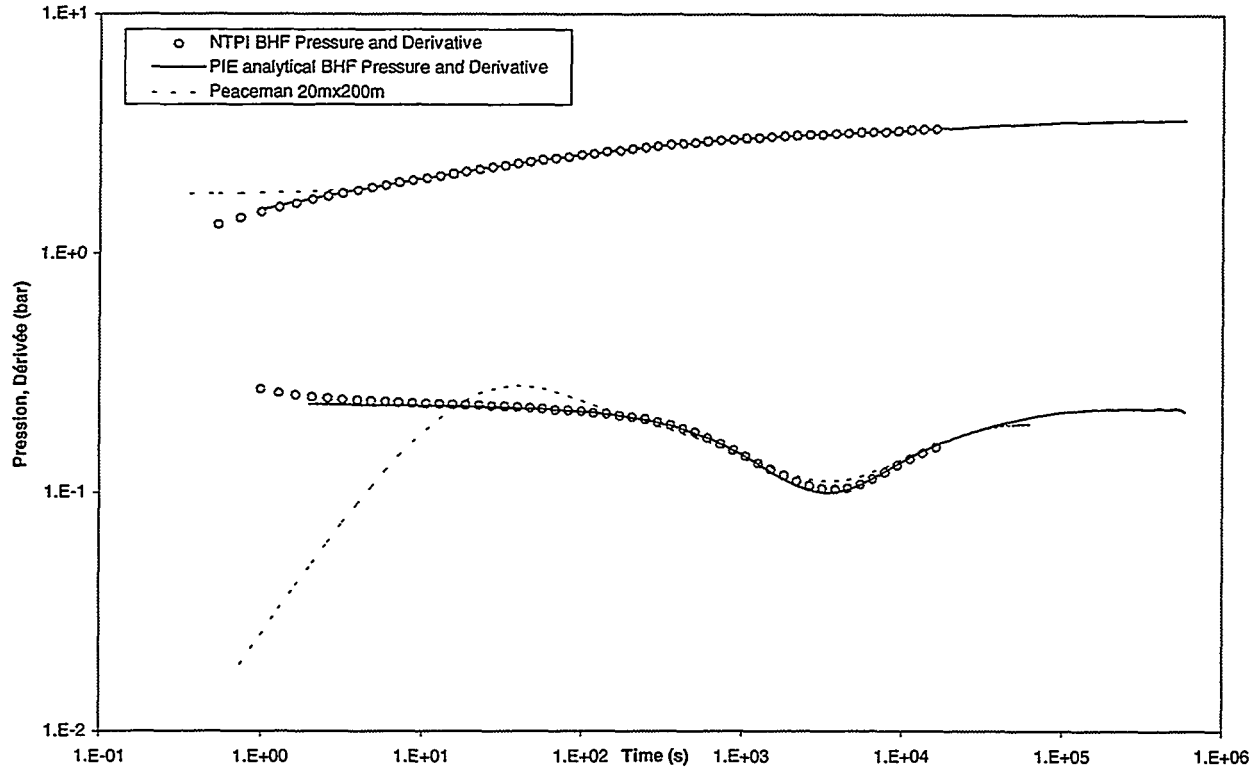

Figure 10 - 3 Layers - Full penetration - no WBS (Reference Case 5 - 20m×20m grid-blocks)

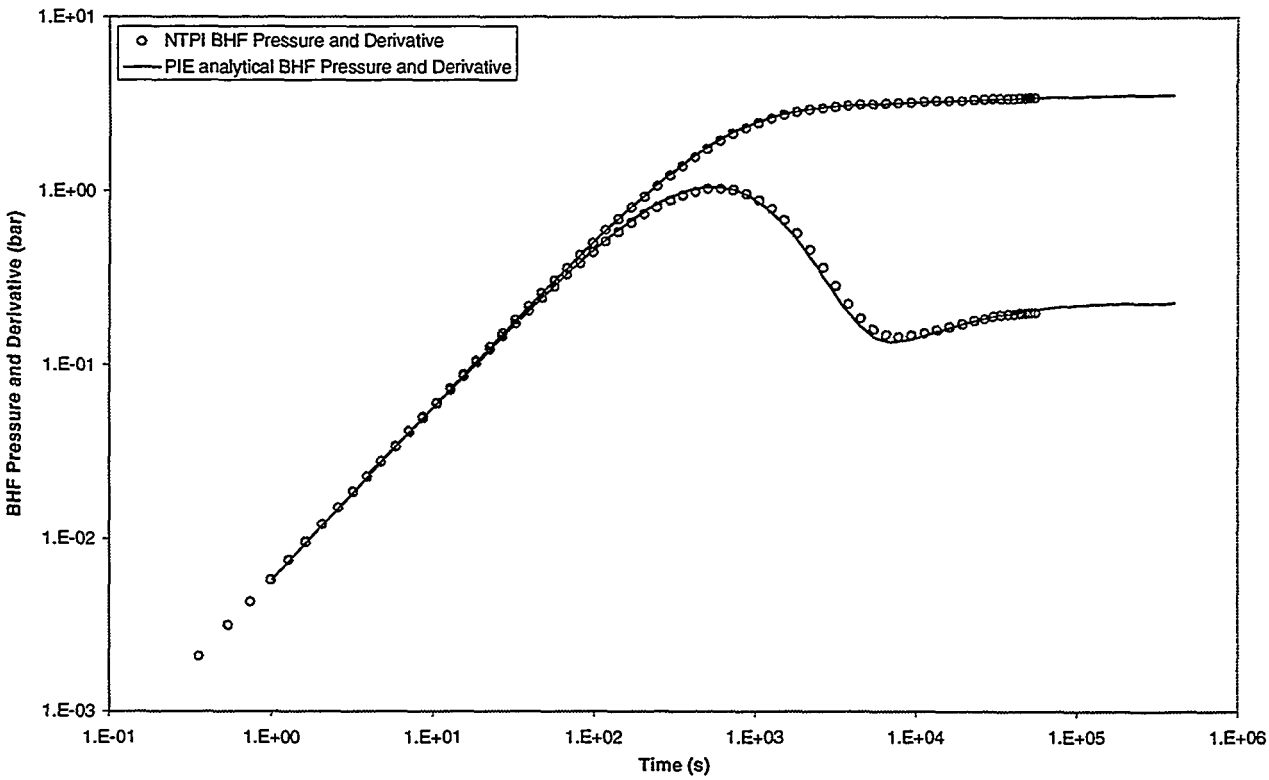

Figure 11 - 3 Layers - Full penetration - WBS (Reference Case 5 - 20m×20m grid-blocks)

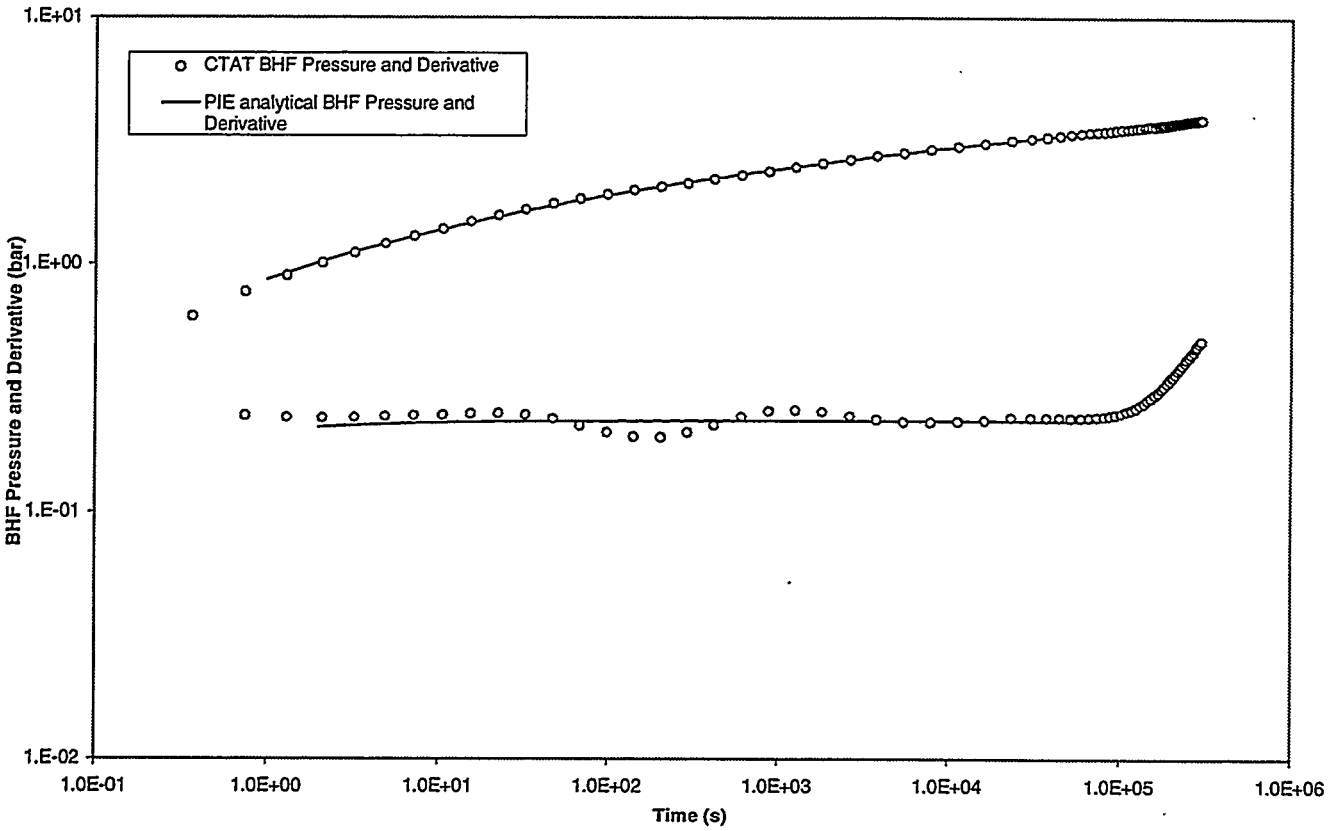

Figure 12 - Homogeneous reservoir - CTAT Correction (Reference Case 2 - 20m×20m grid-blocks)

TABLES

Table 1 - Reference Case 1 - Characteristics

(corresponding to figures 2,3,4,5 and 7)

Reservoir - one layer - infinite	k (mD)	ϕ (fraction)	c_t (1/bar)	h (m)
	100	.20	$5\ 10^{-4}$	20

Fluids	μ (cPo)	ρ (g/cm³)	Bo (m^3/m^3)
	1	1	1

Well	rw (m)	S	C (m^3/bar)
	0.0785	0	0

Test	type	duration (s)	rate (m^3/d)
	Pumping test	10^5	50

Table 2 - Reference Case 2 - Characteristics

(corresponding to figure 12)
Same as Table 1 but Reservoir limited 1020mx1020m

Table 3 - Reference Case 3 - Characteristics

(corresponding to figure 8)

Reservoir - 8 layers - infinite	k_h (mD)	k_v (mD)	ϕ (fract.)	c_t (1/bar)	h (m)
all layers	100	10	.20	$5\ 10^{-4}$	10

Fluids	μ (cPo)	ρ (g/cm³)	Bo (m^3/m^3)
	1	1	1

Well	skin	rw = 0.0785 m
layer 1	0	S = 0
layer 2 to 8	closed	C = 0 m^3/bar

Test	Type	duration (s)	rate (m^3/d)
	pumping test	$5\ 10^5$	50

Table 4 - Reference Case 4 - Characteristics

(corresponding to figures 9)

Reservoir - 3 layers - infinite - c_t=5 10^{-4} bar	k_h (mD)	k_v (mD)	ϕ (fraction)	h (m)
layer 1	10	.1	.08	2
layer 2	1000	1	.25	2
layer 3	30	.3	.12	2

Fluids	μ (cPo)	ρ (g/cm³)	Bo (m^3/m^3)
	1	1	1

Well	skin	
layer 1	closed	rw = 0.0785 m
layer 2	0	S = 0
layer 3	closed	C = 0 m^3/bar

Test	duration (h)	rate (m^3/d)
flow period 1	7	10
flow period 2	7	30
flow period 3	7	50
flow period 4	112	0 build up

Table 5- Reference Case 5 - Characteristics

(corresponding to figures 10 and 11)

Reservoir - 3 layers - infinite - c_t=5 10^{-4} bar	k_h (mD)	k_v (mD)	ϕ (fraction)	h (m)
layer 1	10	.1	.20	2
layer 2	1000	1	.05	2
layer 3	30	.3	.20	2

Fluids	μ (cPo)	ρ (g/cm³)	Bo (m^3/m^3)
	1	1	1

Well	skin	rw = 0.0785 m
layer 1	0	S = 0
layer 2	0	C= 0 m^3/bar - fig 10
layer 3	0	C = 0.1 m^3/bar - fig 11

Test	Same as Reference case 4

Approaches to Identifying Reservoir Heterogeneity and Reserve Growth Opportunities from Subsurface Data: The Oficina Formation, Budare Field, Venezuela

D. S. Hamilton; S. K. Raeuchle; M. H. Holtz, M. Uzcategui; T. Jimenez
Bureau of Economic Geology
10100 Burnet Road
Austin, TX 78758

ABSTRACT

We applied an integrated geologic, geophysical, and engineering approach devise to identify heterogeneities in the subsurface that might lead to reserve growth opportunities in our analysis of the Oficina Formation at Budare field, Venezuela. The approach involves 4 key steps: 1) Determine geologic reservoir architecture; 2) Investigate trends in reservoir fluid flow; 3) Integrated fluid flow trends with reservoir architecture; and 4) Estimate original oil-in-place, residual oil saturation, and remaining mobile oil, to identify opportunities for reserve growth.

There are three main oil-producing reservoirs in the Oficina Formation that were deposited in a bed-load fluvial system, an incised valley-fill, and a barrier-strandplain system. Reservoir continuity is complex because, in addition to lateral facies variability, the major Oficina depositional systems were internally subdivided by high-frequency stratigraphic surfaces. These surfaces define times of intermittent lacustrine and marine flooding events that punctuated the fluvial and marginal marine sedimentation, respectively. Syn and post depositional faulting further disrupted reservoir continuity. Trends in fluid flow established from initial fluid levels, response to recompletion workovers, and pressure depletion data demonstrated barriers to lateral and vertical fluid flow caused by a combination of reservoir facies pinchout, flooding shale markers, and the faults.

Considerable reserve growth potential exists at Budare field because the reservoir units are highly compartment by the depositioinal heterogeneity and structural complexity. Numerous reserve growth opportunities were identified in attics updip of existing production, in untapped or incompletely drained compartments, and in field extensions.

Characterization of Oil and Gas Reservoirs and Recovery Technology Deployment on Texas State Lands

Roger Tyler; R. P. Major; M. H. Holtz; H. Scott Hamlin; S. P. Dutton
University of Texas
University Station, Box X
Austin, TX

ABSTRACT

Texas State Lands oil and gas resources are estimated at 1.6 BSTB of remaining mobile oil, 2.1 BSTB or residual oil, and nearly 10 Tcf of remaining gas. An integrated, detailed geologic and engineering characterization of Texas State Lands has created quantitative descriptions of the oil and gas reservoirs, resulting in delineation of untapped, bypassed compartments and zones of remaining oil and gas. On Texas State Lands, the knowledge gained from such interpretative, quantitative reservoir descriptions has been the basis for designing optimized recovery strategies, including well deepening, recompletions, workovers, targeted infill drilling, injection profile modification, and waterflood optimization. The State of Texas Advanced Resource Recovery program is currently evaluating oil and gas fields along the Gulf Coast (South Copano Bay and Umbrella Point fields) and in the Permian Basin (Keystone East, Ozona, Geraldine Ford and Ford West fields). The program is grounded in advanced reservoir characterization techniques that define the residence of unrecovered oil and gas remaining in select State Land reservoirs. Integral to the program is collaboration with operators in order to deploy advanced reservoir exploitation and management plans. These plans are made on the basis of a thorough understanding of internal reservoir architecture and its controls on remaining oil and gas distribution. Continued accurate, detailed Texas State Lands reservoir description and characterization will ensure deployment of the most current and economically viable recovery technologies and strategies available.

High Resolution Reservoir Geological Modelling Using Outcrop Information

Zhang Changmin; Lin Kexiang; Liu Huaibo; Qiu Yinan
Department of Geology
Jianghan Petroleum Institute
Jingsha, Hubei, China 434102

ABSTRACT

This is China's first case study of high resolution reservoir geological modelling using outcrop information. The key of the modelling process is to build a proto-type model and using the model as a geological knowledge bank. Outcrop information used in geological modelling including seven aspects: 1) Determining the reservoir framework pattern by sedimentary depositional system and facies analysis; 2) Horizontal correlation based on the lower and higher stand duration of the paleo-lake level; 3) Determining the model's direction based on the paleo-current statistics; 4) Estimating the sandbody communication by photomosaic and profiles; 6) Estimating reservoir properties distribution within sandbody by lithofacies analysis; 7) Building the reservoir model in sandbody scale by architectural element analysis and 3-D sampling. A high resolution reservoir geological model of Youshashan oil field has been built by using this method.

Characterization and Estimation of Permeability Correlation Structure from Performance Data

I. Ershaghi; M. Al-Qahtani
University of Southern California
Petroleum and Engineering Program
Los Angeles, CA 90089

ABSTRACT

In this study, the influence of permeability structure and correlation length on the system effective permeability and recovery factors of 2-D cross-sectional reservoir models, under waterflood, is investigated. Reservoirs with identical statistical representation of permeability attributes are shown to exhibit different system effective permeability and production characteristics which can be expressed by a mean and variance. The mean and variance are shown to be significantly influenced by the correlation length. Detailed quantification of the influence of horizontal and vertical correlation lengths for different permeability distributions is presented.

The effect of capillary pressure, P_{c1} on the production characteristics and saturation profiles at different correlation lengths is also investigated. It is observed that neglecting P_c causes considerable error at large horizontal and short vertical correlation lengths. The effect of using constant as opposed to variable relative permeability attributes is also investigated at different correlation lengths.

Next we studied the influence of correlation anisotropy in 2-D reservoir models. For a reservoir under five-spot waterflood pattern, it is shown that the ratios of breakthrough times and recovery factors of the wells in each direction of correlation are greatly influenced by the degree of anisotropy. In fully developed fields, performance data can aid in the recognition of reservoir anisotropy.

Finally, a procedure for estimating the spatial correlation length from performance data is presented. Both the production performance data and the system's effective permeability are required in estimating the correlation length.

2D X-RAY SCANNER AND ITS USES IN LABORATORY RESERVOIR CHARACTERIZATION MEASUREMENTS

by Dan Maloney and Kevin Doggett

BDM Petroleum Technologies

ABSTRACT

X-ray techniques are used in petroleum laboratories for a variety of reservoir characterization measurements. This paper describes the configuration of a 2D X-ray scanner and many of the ways in which it simplifies and improves accuracy's of laboratory measurements.

Linear X-ray scanners are most often used to provide descriptions of fluid saturations within core plugs during flow tests. We configured our linear scanner for both horizontal and vertical movement. Samples can be scanned horizontally, vertically, or according to horizontal and vertical grids. X-ray measurements are fast, allowing measurements of two- and three-phase fluid saturations during both steady- and unsteady-state flow processes. Rock samples can be scanned while they are subjected to stress, pore pressure, and temperature conditions simulating those of a petroleum reservoir.

Many types of measurements are possible by selecting appropriate X-ray power settings, dopes, filters, and collimator configurations. The scanner has been used for a variety of applications besides fluid saturation measurements. It is useful for measuring porosity distributions in rocks, concentrations of X-ray dopes within flow streams during tracer tests, gap widths in fracture flow cells, fluid interface levels in PVT cells and fluid separators, and other features and phenomena.

HARDWARE

Many have used X-rays to determine two- and three-phase fluid saturations in rocks.[1-11] The system used by the authors is based primarily on systems described by Oak, Potter, and others,[7-11] except that scans can be taken in both horizontal and vertical directions. Figure 1 is a general schematic of the X-ray scanner used by BDM Petroleum Technologies.[12,13] The figure shows the relative position of a sample with respect to the X-ray source and detector.

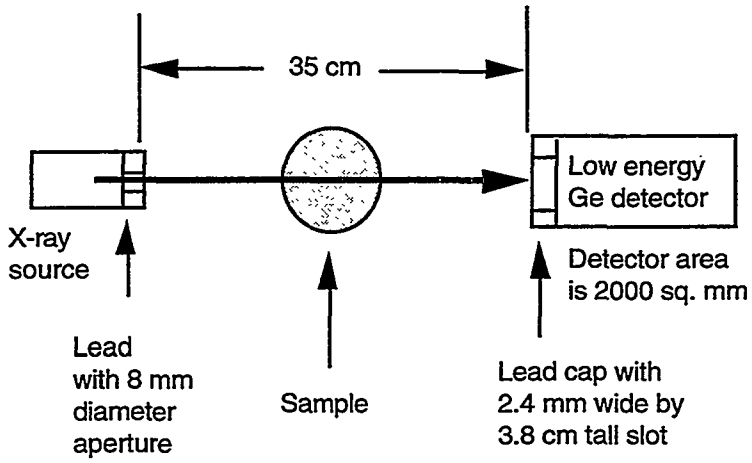

Figure 1 General schematic of the X-ray source and detector.

The X-ray source is a Philips PW2184/00 tungsten target XRF tube. The tube is rated for 3 kW at 100 kV, although normal operating conditions include voltages from 25 to 60 kVp and currents to 80 mA. The tube is normally operated with peak voltages close to but above the k-emission energies of X-ray dopes contained in test fluids. This yields maximum contrast between X-ray absorption characteristics of the test fluids. The tube is powered by a Philips XRG 3100 X-ray generator.

The portion of the tube that emits X-rays is housed within a thick, lead-lined stainless steel turret that has several collimation ports of different lengths. A lead shutter within the turret is normally closed unless a scan is taking place. The ends of the collimation ports are machined to accept cuvettes containing doped fluid solutions for beam conditioning.

A chiller is required to protect the tube from heat damage. The chiller used with this X-ray device was made by the Haskris Co.

The X-ray detector is a Canberra low energy germanium detector, which has a 2000 sq. mm area, 20 mm thickness, 0.5 mm Beryllium window, and the following resolution characteristics: FWHM at 5.9 keV of 400 eV and FWHM at 122 keV of 700 eV. The detector has an RC preamplifier. The detector electronics are cooled by liquid nitrogen using a 15 liter, horizontal integral cryostat. The 15 liter capacity provides about 10 days of operation before the cryostat must be refilled with liquid nitrogen. To prevent damage to the detector from a low liquid nitrogen condition, the preamplifier has a high-temperature inhibitor. Damage can also occur if full power is

suddenly applied to the deenergized detector. To protect against this occurrence, power to the detector passes through a pull-down switch that protects against sudden off-and-on power cycles during storms. An integrated signal processor, slave board, and software are used for multichannel data acquisition and analysis. These reside within a Gateway 486 computer.

The detector is surrounded by a lead shield. A thick lead cap was installed into the end of the detector shield between the detector and sample. The lead cap contains a slit that limits X-rays that reach the detector to only those which pass through the test sample. The slit is used to gain better resolution of position-specific X-ray intensities during linear X-ray scans. For scans on horizontal samples, the slit is positioned vertically. For scans on vertical samples, the slit is positioned horizontally. For samples in which X-ray scans are taken in 2 dimensions (vertical and horizontal), another lead cover with a 2 mm aperture is placed in front of the detector.

The X-ray tube and detector are mounted on an inverted U-shaped frame. The horizontal and vertical positions of this frame are controlled by drive screws and motors. Parker Compumotor indexers and motors along with other hardware are used to control horizontal and vertical movement of the scanning platform. The Compumotor indexers controlling the horizontal and vertical stages of the X-ray scanner are daisy-chained so that commands to change the scanner horizontal and vertical positions are sent through a single communication channel. The laboratory PC computer communicates with the indexers during X-ray scans. As a sample is scanned, the X-ray tube and detector move with respect to the stationary samples.

As previously stated, the laboratory computer is used for data acquisition and X-ray scanner control. The system uses LabVIEW, a software product by National Instruments, for these functions. The computer also controls pumps and other laboratory hardware, collects data from instruments, and performs calculations using measured data.

GENERAL X-RAY SCANNER OPERATION

Samples to be scanned are mounted within the scanning region of the X-ray device. The horizontal scan range is approximately 3 meters while the vertical scan range is approximately 0.6 m. An X-ray scan consists of a number of X-ray intensity measurements taken at discrete positions along the length and height of a sample. For small rock samples, scan increments of 0.1 to 0.5 cm

are often employed. A scanning pattern is determined for a sample during the initial stages of experimentation. Scan parameters are entered into the computer program. Thereafter, scans can be automatically programmed for specific time intervals.

When a scan is initiated, the X-ray device moves to the first measurement position. Upon reaching the first position, the scanner stops moving. The lead shutter opens, emitting X-rays. The intensities of X-rays that pass through the sample are measured by the detector. After the predefined count interval, which is usually about 5 seconds, the X-ray device moves to the next position. Intensities are measured at the second position, then the scanner moves again. This process continues until measurements have been recorded at each scan position. Upon completing the final measurement, the lead shutter closes. Scanning an 8 cm long sample at 15 positions takes about 2 minutes. Faster scans are also possible, making the device useful for determining changing saturations during unsteady-state tests.

The first sets of X-ray scans taken of a sample are used to correlate X-ray intensities to fluid contents or in situ rock fluid saturations. Once these correlations are established, they are entered into the scanning program. For subsequent scans, the correlation equations are used to calculate fluid saturations as soon as X-ray intensities are measured. Results are plotted on the computer's screen, providing a real-time image of the saturation conditions within the sample. Several experiments on different samples are often conducted at the same time. The only restriction here is that scan times have to be scheduled in a manner that avoids conflicts.

X-RAY TERMINOLOGY AND BASIC CALCULATIONS

X-ray measurements described in following sections of this report are for various X-ray tube voltage and current settings. Because the X-ray source is polychromatic, X-rays with a range of photon energies are emitted from the X-ray tube for particular X-ray generator settings. For this reason, the X-rays which pass through the sample and reach the detector also are over a range of photon energies.

Figure 2 shows intensities of X-ray photons that passed through a coreholder for various tube voltage and current settings.[12] A fairly broad band of X-rays pass through a sample during a typical X-ray scan. For example, for scans of figure 2 with the X-ray generator set to 55 kV, intense X-rays were within a range from about 40 keV to 60 keV with greatest intensity at around 55 keV.

Increasing the tube voltage shifts the region of greatest intensity to a higher photon energy and increases the relative intensities of the photons which emerge from the coreholder. Increasing the tube current while keeping the voltage constant generally increases the amplitude of the photon intensity distribution plot. Another way to increase intensities at the detector is to increase the area of the collimator, allowing greater numbers of photons to reach the detector. Decreasing the collimator area decreases the intensities of detected photons, but provides a better measure of the photons which pass through a specific region of the sample.

The X-ray detector is used to count the number of photons which emerge from the coreholder over a specified live-time interval (part of the total detector time is dead-time). Intensities are calculated by dividing the number of counts by the live-time interval in seconds.

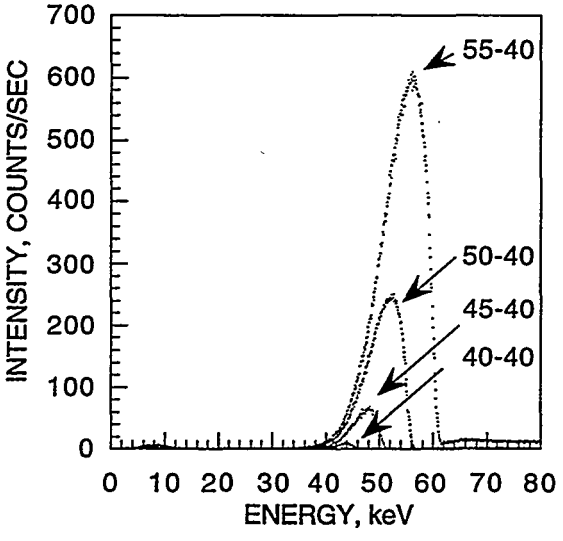

Figure 2 **X-ray results from scans through an aluminum coreholder of a Bluejacket sandstone plug. X-ray generator kV and mA settings (kV-mA) are shown from scans with different tube voltages.**

Lambert's Law is often cited[14,15] to relate intensities of X-rays which emerge from a sample to intensities of X-rays which are incident to the sample:

$$I = I_0 e^{(-kx)} \quad (1)$$

where I is the emergent intensity, I_0 is the incident intensity, k is the linear absorption coefficient of the sample, and x is the sample thickness. Taking natural logs of both sides of equation 1 and manipulating the result yields:

$$Ln(I) = -kx + Ln(Io) \quad (2)$$

When more than one absorber is in the X-ray beam path, the equation is:

$$I=Ioe(-k1x1 - k2x2 - ...) \quad (3)$$

For typical rock fluid saturation measurements, I_O, the X-ray absorption characteristics of the specific rock and coreholder assembly, and the X-ray path length are constants so that changes in Ln(I) result from changes in rock fluid saturations. As long as incident X-ray intensities remain constant throughout a particular flow experiment in which X-ray absorption techniques are used for fluid saturation measurements, a value for the incident intensity is not specifically required. However, knowledge of incident X-ray intensities are important when predicting X-ray absorption characteristics of experimental fixtures that have never been scanned before. X-ray scan results from this laboratory are usually described using natural logs of emergent X-ray intensities because this is the variable predominantly used for rock fluid saturation calculations.

X-Ray Calibrations

For tests in which two different fluids exist within the sample, one of the fluids is typically doped with an X-ray absorber, such as sodium iodide in the brine phase or bromodecane in the oil phase.

Figure 3 shows X-ray data from scans of a particular position within a rock sample when it was completely saturated with air, then oil, and finally with a doped brine.[16] The absorption characteristics of the sample change significantly with changes in fluid content. Figure 4 shows the result of taking the natural log of the integrated intensities under each curve to construct two-phase saturation calibrations. The figure shows correlations for air-brine and oil-brine fluid systems. Using these types of calibrations for each scan position within the rock, two-phase fluid saturations within rock samples can be easily determined from X-ray measurements. Figure 5 shows a typical result from a coreflood experiment. The saturation gradient toward the outlet end of the sample is probably indicative of a capillary end-effect.

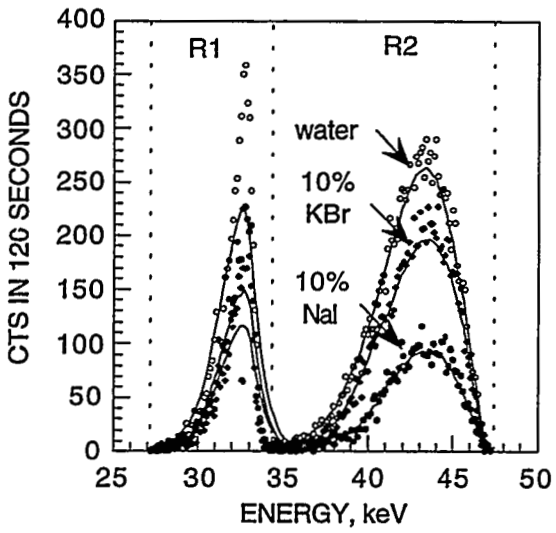

Figure 3 **X-ray scan data for one scan position with different saturating fluids.**

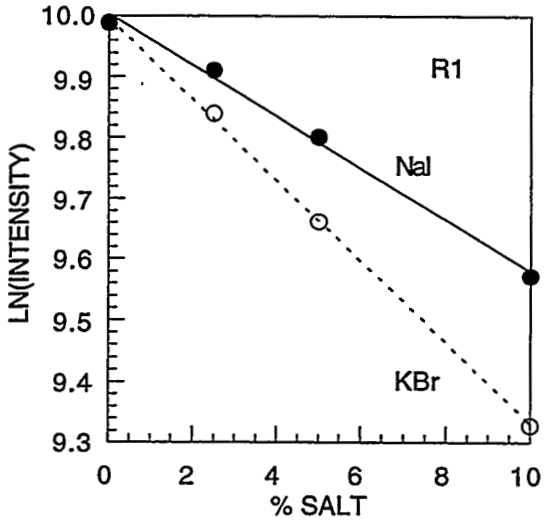

Figure 4 **Resulting X-ray correlations to fluid saturations.**

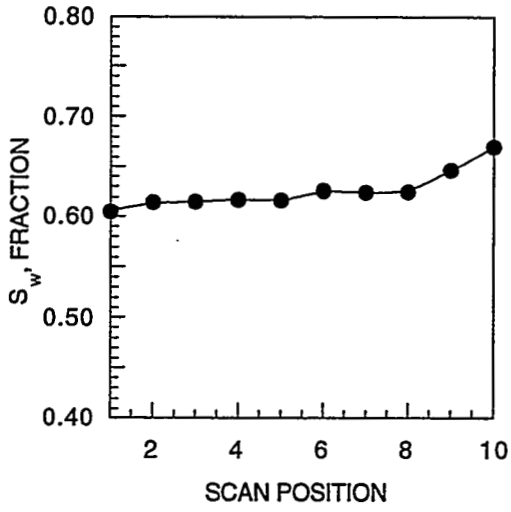

Figure 5 **Typical scan results showing an end-effect.**

For tests with three fluid phases, two of the fluids are doped with absorbers that have X-ray absorption edges at different energies. Additionally, the incident X-ray beam is filtered by passing it through an absorber that splits the distribution of intensities into two distinct regions. Figure 6 provides an example in which containers filled with water, water doped with potassium bromide, and water doped with sodium iodide were scanned using a filtered X-ray beam.[16] As shown, the dopes yield different absorption characteristics for each fluid on each side of the split. Figures 7 and 8 show how taking the natural log of the integrated intensities under each curve

provide sets of equations that can be used to determine three phase saturations from a single X-ray scan. Figure 9 graphically shows how these results are used to calculate three phase saturations. The beauty of this "dual energy" technique is that saturations for each of the three fluid phases are calculated from data measured during a single X-ray scan.

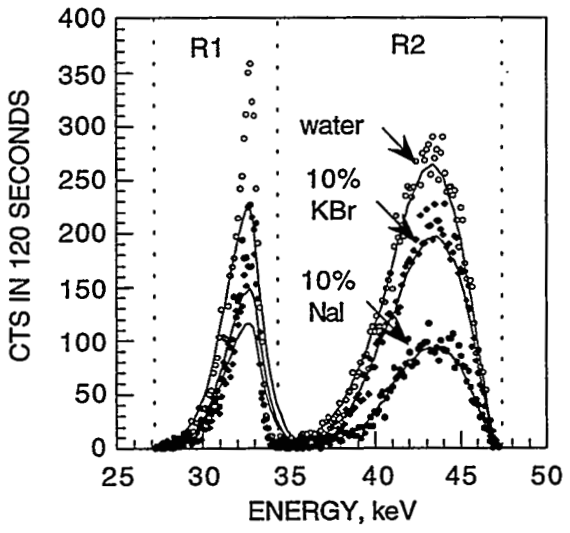

Figure 6 **Intensities from "dual energy" measurements.**

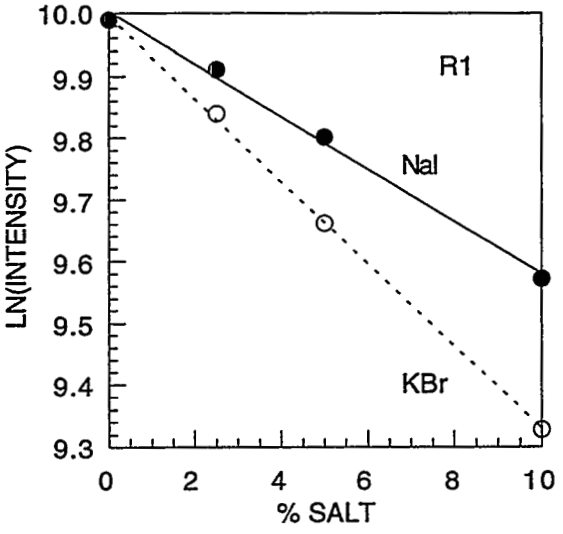

Figure 7 **Resulting X-ray range 1 correlations to saturations.**

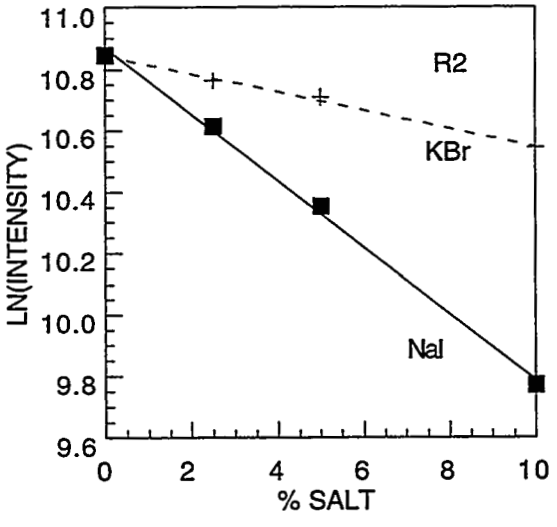

Figure 8 **Resulting X-ray range 2 correlations to saturations.**

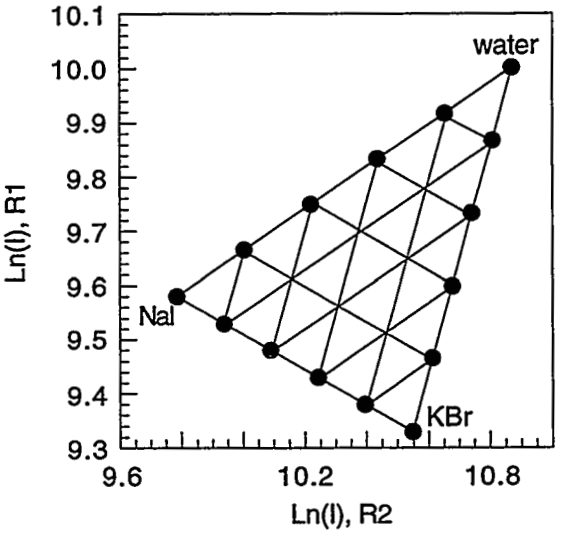

Figure 9 **Determination of three-phase saturations from range 1 and range 2 X-ray measurements.**

X-RAY SCANNER APPLICATIONS

The following lists some of the more novel measurements that have been performed using the scanner.

Corefloods

The X-ray scanner is commonly used for two and three-phase steady- and unsteady-state relative permeability tests and corefloods. Figure 10 shows a simple schematic of a closed-loop flow system that was used for three-phase measurements during a reservoir condition coreflood. Rock fluid saturations were determined by X-ray scanning the core plug through the coreholder. Produced fluid volumes were determined by vertically scanning the fluid separator.

As shown by figure 11, fluid interface levels within the separator are easily determined from X-ray results. The interface levels can be clearly defined from step-changes in X-ray intensities. The X-ray technique for measuring fluid volumes within a separator is effective even when the fluids mix or form emulsions. Scans of fluids within the separator can be used to determine linear X-ray absorption coefficients for the fluids "on the fly" so that X-ray calibrations can be adjusted for changes in fluid properties.[16] This type of X-ray technique is also applicable for PVT measurements and provides an added advantage in that windowless cells can be employed.

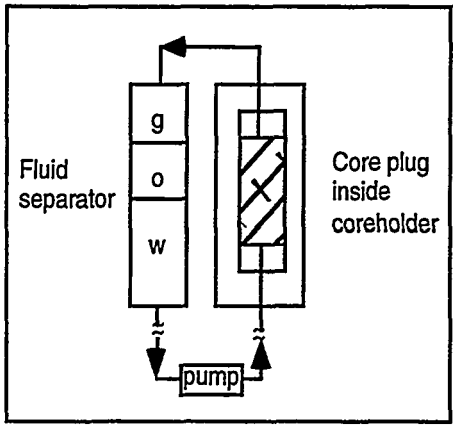

Figure 10 **Simple schematic of a closed-loop flow system.**

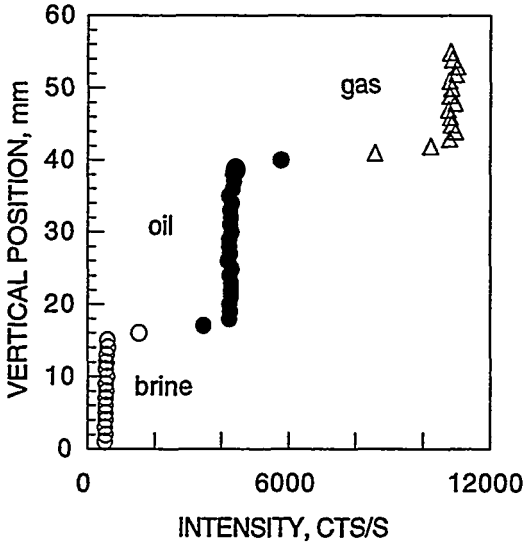

Figure 11 **Fluid interface level measurements from a separator scan.**

Porosity Distribution Imaging

Rock porosity distributions can be calculated from X-ray intensity measurements.[9] Software can be used to create images from the 2-D X-ray data. Figure 12 shows results for a 10 x 10 x 3 cm sandstone block.[17] The block was X-ray scanned while dry and then after it was saturated with brine. Intensity measurements were recorded at about 1000 horizontal and vertical positions. Differences in X-ray intensities for the dry and brine saturated sample and the total porosity were used to calculate porosity distributions. Permeabilities measured along the lower face of the dry sample by a probe permeameter are overlaid on the porosity map. This information simplified interpretations of results from subsequent spontaneous imbibition measurements.[17]

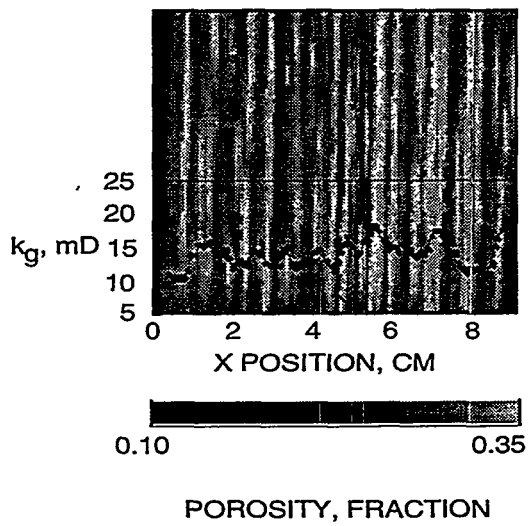

Figure 12 Characteristics of a Berea Sandstone slab. Porosities were calculated from X-ray measurements of the dry and brine-saturated rock. Permeabilities were from probe minipermeameter measurements.

Determination of Fluid Saturations Within Fracture Models

X-rays techniques are also particularly well suited for measurements of fluid flow properties in fractures or cracks. Figure 13 is a schematic of a plastic fracture model that was used for multiphase fluid flow measurements in fractures.[17,18] The fracture gap width within the cell was 790 μm. Flow properties and saturation distributions were measured as oil and brine flowed

upward through the cell. In addition to measurements of fluid saturations, the X-ray device was also found to be an effective tool for measuring the width of the open fracture. Fracture widths were measured with resolution to about 5 μm.

Figure 14 shows saturation profiles that were measured by the X-ray scanner during this steady-state relative permeability test. For each steady-state flow condition in this particular test, the oil flowed through a narrow stream in the center of the fracture. Contrary to what some might expect, the brine saturation was considerably different than the brine fractional flow.

Figures 15 and 16 provide comparisons of fracture relative permeabilities for two different fracture widths with vertical upward flow. As shown, relative permeabilities are considerably different for wide and narrow fractures. Differences in fluid densities and the direction of fluid flow had pronounced effects on results for the wide fracture. As shown by these results, the 2-D X-ray scanner was a useful tool for fracture relative permeability measurements. This X-ray application should help to resolve some of the questions concerning multiphase flow in fractures.

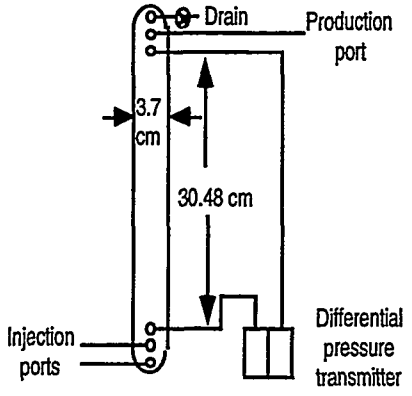

Figure 13 Simple fracture cell schematic.

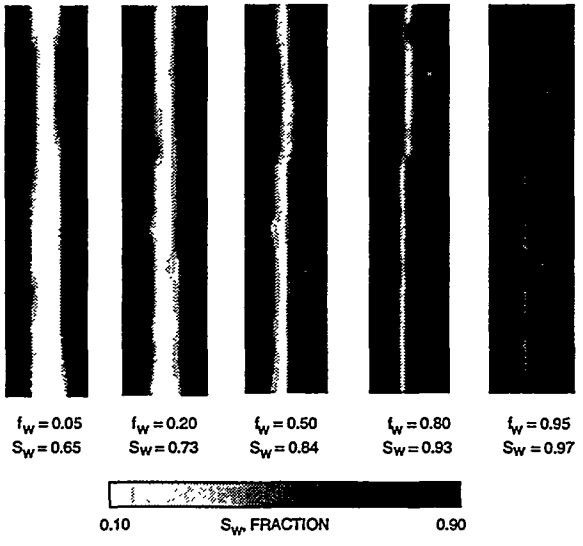

Figure 14 Two-phase oil-brine saturation profiles within a 790 μm wide fracture. Flow was vertically upward.

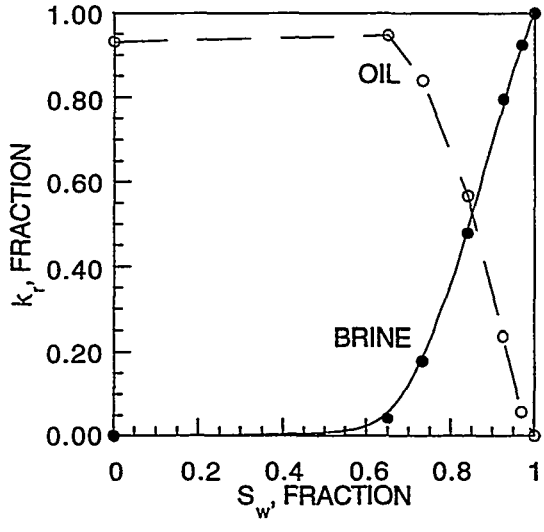

Figure 15 Oil-brine relative permeability results, 790 μm fracture. The flow direction was upward.

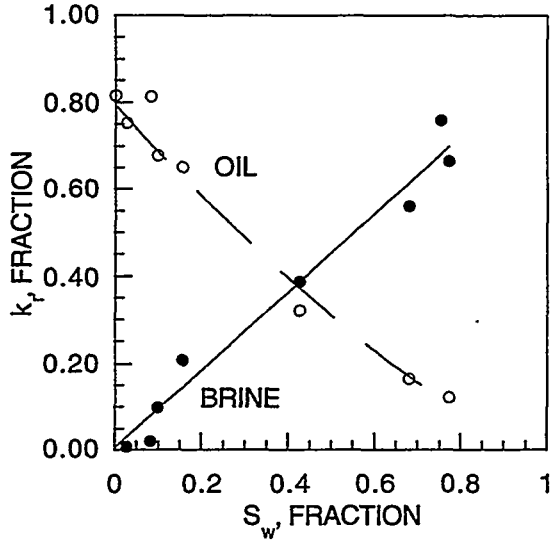

Figure 16 Oil brine relative results, permeability results, 50 μm fracture. The flow direction was upward.

Tracer Tests

The X-ray scanner is also useful during tracer tests to evaluate changes in in-situ rock fluid saturations as well as tracer concentrations in the effluent. With the X-ray generator set at its lowest tube power settings of 25 kV and 1 mA, X-ray scans of fluid-filled tubes were used to identify changes in salt concentrations in a brine.[16] Adding salt to the brine increased the X-ray attenuation appreciably, much like what happens when an X-ray absorber is added to a test fluid with higher tube power settings. This application provides flexibility for tracer tests when dopes or other unnatural compounds cannot be added to the rock fluids.

CONCLUSIONS

In conclusion, many types of rock and fluid characterization measurements are possible using a 2-D X-ray scanning device and appropriate X-ray power settings, dopes, filters, and collimator configurations. While linear scanners have traditionally been used for measuring fluid saturations in rocks, X-ray data from the scanner can also be used to create images of rock and fluid distribution characteristics. The scanner is useful for measuring porosity distributions in rocks, concentrations of X-ray dopes within flow streams during tracer tests, gap widths in fracture

flow cells, fluid interface levels in PVT cells and fluid separators, and other features and phenomena. In essence, X-ray scanners are powerful tools for a variety of applications in petroleum laboratories.

ACKNOWLEDGMENTS

The authors express appreciation to U.S. Department of Energy for supporting the preparation and publication of this paper. Many of the X-ray applications reported in this paper were developed during the performance of Department of Energy funded projects. We thank the management of BDM Petroleum Technologies for giving permission to publish this work.

REFERENCES

1. Boyer, R., F. Morgan and M. Muskat: A New Method for Measurement of Oil Saturation in Cores. Trans. AIME, vol. 170, 1947, pp. 15-33.
2. Morgan, F., J. McDowell, and E. Doty: Improvements in the X-ray Saturation Technique of Studying Fluid Flow. Petroleum Transactions, AIME, vol. 189, 1950, pp. 183-194.
3. Laird, A. and J. Putnam: Fluid Saturation in Porous Media by X-ray Technique. Petroleum Transactions, AIME, vol. 192, 1952, pp. 275-284.
4. Laird, A. and J. Putnam: Three Component Saturation in Porous Media by X-Ray Techniques. Petroleum Transactions, AIME, v. 216, 1959, pp. 216-220.
5. Schneider, F. and W. Owens: Sandstone and Carbonate Two- and Three-Phase Relative Permeability Characteristics. Soc. of Petr. Eng. Journal, March 1970, pp. 75-84.
6. Schneider, F. and W. Owens: Steady-state Measurements of Relative Permeability for Polymer/Oil Systems. Soc. of Petr. Eng. Journal, February 1982, pp. 79-86.
7. Oak, M. and R. Ehrlich: A New X-Ray Absorption Method for Measurement of Three-Phase Relative Permeability. Paper SPE 14420 presented at the 60th Annual Technical Conference and Exhibition of the Society of Petroleum Engineers, Las Vegas, NV, Sept. 22-25, 1985.
8. Oak, M., L. Baker, and D. Thomas: Three-Phase Relative Permeability of Berea Sandstone. Paper SPE/DOE 17370 presented at the 1988 SPE/DOE Symposium on Enhanced Oil Recovery, Tulsa, OK, April 17-20.
9. Potter, G. and D. Groves: Displacements, Saturations, and Porosity Profiles from Steady-State Permeability Measurements. Paper SPE 19679 presented at the 64th Annual Technical Conference and Exhibition of the Society of Petroleum Engineers, San Antonio, TX, Oct. 8-11, 1989.
10. Oak, M.: Three-Phase Relative Permeability of Water-Wet Berea. Paper SPE/DOE 20183 presented at the 1990 SPE/DOE Symposium on Enhanced Oil Recovery, Tulsa, OK, April 22-25.

11. Oak, M.: Three-Phase Relative Permeability of Intermediate-Wet Berea Sandstone. Paper SPE 22599 presented at the 66th Annual Technical Conference and Exhibition of the Society of Petroleum Engineers, Dallas, TX, Oct. 6-9, 1991.
12. Maloney, D. and K. Doggett: Advances in Steady- and Unsteady-State Relative Permeability Measurements and Correlations FY 1995. Report NIPER/BDM-0160 prepared under DOE contract DE-AC22-94PC91008, July 1995, pp. 21-28.
13. Maloney, D. and L. Tomutsa: Use of X-ray Scanners in Petroleum Research. Paper HD 31D-03 presented at the 1995 Fall Meeting of the American Geophysical Union, San Francisco, CA, Dec. 11-15, 1995.
14. Sproull, W.: X-rays in Practice. McGraw Hill, New York, 1946.
15. Bertin, E.: Principles and Practice of X-ray Spectrometric Analysis. Plenum Press, New York, 1970.
16. Maloney, D. and K. Doggett: Relative Permeability Research FY 1994. Report NIPER/BDM-0067 prepared under DOE contract DE-AC22-94PC91008, Sept. 1994, pp. 23-29.
17. Chang, M. and D. Maloney: Analytical Solutions and Experiments to Two-Phase Flow Problems of Naturally Fractured Reservoirs, Imbibition Transfer Function. Report NIPER/BDM-0171 prepared under DOE contract DE-AC22-94PC91008, Sept. 1995, p. 124.
18. Maloney, D., K. Doggett, and A. Sarkar: Laboratory Characterization of Oil Production Mechanisms in Fractured Rock. Report NIPER/BDM-0274 prepared under DOE contract DE-AC22-94PC91008, Sept. 1996, pp. 9-21.

Multiscale Heterogeneity Characterization of Tidal Channel, Tidal Delta and Foreshore Facies, Almond Formation Outcrops, Rock Springs Uplift, Wyoming

By
Richard A. Schatzinger and Liviu Tomutsa
BDM Petroleum Technologies
Bartlesville, Oklahoma

ABSTRACT

In order to accurately predict fluid flow within a reservoir, variability in the rock properties at all scales relevant to the specific depositional environment needs to be taken into account. The present work describes rock variability at scales from hundreds of meters (facies level) to millimeters (laminae) based on outcrop studies of the Almond Formation. Tidal channel, tidal delta and foreshore facies were sampled on the eastern flank of the Rock Springs uplift, southeast of Rock Springs, Wyoming. The Almond Fm. was deposited as part of a mesotidal Upper Cretaceous transgressive systems tract within the greater Green River Basin.

Bedding style, lithology, lateral extent of beds of bedsets, bed thickness, amount and distribution of depositional clay matrix, bioturbation and grain sorting provide controls on sandstone properties that may vary more than an order of magnitude within and between depositional facies in outcrops of the Almond Formation. These features can be mapped on the scale of an outcrop. The products of diagenesis such as the relative timing of carbonate cement, scale of cemented zones, continuity of cemented zones, selectively leached framework grains, lateral variability of compaction of sedimentary rock fragments, and the resultant pore structure play an equally important, although less predictable role in determining rock property heterogeneity. A knowledge of the spatial distribution of the products of diagenesis such as calcite cement or compaction is critical to modeling variation even within a single facies in the Almond Fm. because diagenesis can enhance or reduce primary (depositional) rock property heterogeneity. Application of outcrop heterogeneity models to the subsurface is greatly hindered by differences in diagenesis between the two settings.

The measurements upon which this study is based were performed both on drilled outcrop plugs and on blocks. One inch diameter plugs were taken at lateral spacing from 6 inches (15 cm) to 50 feet (16.5 meters) and vertical spacing from 3 inches (8 cm) to 5 feet (1.5 meters) to capture hierarchically stacked patterns of variations on the scale of meters to hundreds of meters. Probe permeameter permeability and x-ray CT porosity from outcrop blocks captured variations at the scale of a few mm to a few hundred mm. Conventional gas porosity and permeability measurements were performed on the plugs and were integral to mapping the distribution of petrophysical properties at the scale of the facies (tens to hundreds of meters). Microscopic scale heterogeneities such as grain size, pore distribution, authigenic cement content, and paragenetic stages were recorded using thin section point count methods and semi-automated petrographic image analysis.

INTRODUCTION

The Upper Cretaceous Almond Formation was deposited as a dominantly transgressive shoreline along the western margin of the North American Cretaceous Western Interior Seaway. It marks the uppermost phase of Mesaverde Group sedimentation (Fig. 1). In the area of the Rock Springs Uplift and eastward in the Washakie Basin the Almond Formation has typically been informally divided into lower (dominantly estuarine) and upper (dominantly marine) units (e.g. Van Horn, 1979). Almond sedimentation was markedly cyclical, particularly within the lower, estuarine section. Even within the upper marine section multiple periods of eastward regression of the shoreline can be mapped into the Washakie Basin (Krystinik and Mead, 1996). Within the greater Green River Basin area, especially the Washakie Basin, these sands comprise important gas and oil reservoirs (see Table 1 of Martinsen and Christensen, 1992). Rapid fluctuations of relative shoreline positions are typical in the upper Almond. Each regression was terminated by a rapid flooding event as the western margin of the Lewis Shale transgressed farther to the west. Regressive fluvial to alluvial plain deposits of the Ericson Sandstone lie immediately beneath the

Almond Formation in the study area (Fig. 2) where the Ericson's upper portion records the earliest phases of the overall shoreline retreat that occurred during late Cretaceous (Campanian) time.

The study area from which the samples for this report were collected is located on the eastern flank of the Rock Springs Uplift in southwestern Wyoming (Fig. 2). Excellent outcrops of Almond Formation that exhibit the lateral relationship between depositional facies are located immediately north of highway 430 in the SE 1/4 of the SW 1/4 of section 33, T. 16 N., R. 102 W, approximately 32 miles southeast of Rock Springs Wyoming. This area was called "outcrop G" in a detailed study of Almond coals and depositional environments by Roehler (1988). The paleogeography of the area during Almond deposition was that of an embayed shoreline created by progradation of deltas north and south of the area. Tidal forces were amplified within the Rock Springs Embayment so that the Almond in this area was deposited under mesotidal conditions (Roehler, 1988; Schatzinger, and others, 1992; and Van Horn 1979).

ROCK PROPERTY VARIATIONS AT VARIOUS SCALES

Outcrop Stratigraphic Cross Section

The coarsest scale of heterogeneity within the Almond Formation was evaluated by mapping the facies relationships at "Outcrop G". At this location 8 detailed geological profiles were measured over the lateral distance of more than 1,000 ft. Outcrop gamma ray profiles were collected at and between geologically described profiles and all of the profiles were correlated to produce a cross section that approximates the distance between wells with a 40 acre spacing. Photo mosaics were made to help trace out facies architecture and critical contacts were "walked out" on the outcrop. The critical southern half of this work is reproduced here as a stratigraphic cross section (Fig. 3). The lower portion of this cross section illustrates the northward pinchout of a major tidal inlet containing reservoir quality sands that are nearly 20 ft thick. The inlet channel overlies and cuts into adjacent foreshore sands (beach and welded swash bar). Just above the Pintail coal bed is a 30 ft thick section of non-reservoir marsh/lagoonal shales and thin, silty tidal creek deposits that contains a horizon with laterally extensive reservoir quality tidal channel sands.

Note that the architecture of this "horizon" consists of discontinuous tidal channels. In the strike parallel cross section presented here (Fig. 3) tidal channel units have geometries with average lateral extents of only 300-350 ft. In reality, tidal channels are often sinuous and highly elongate. If the three-dimensionality of the channels could be accounted for, they might be expected to have a greater extent than 300 ft, however, the meander loops of smaller backbarrier tidal channels are frequently cut off and abandoned at which time they fill in with clay plugs. If this geometry were present in a reservoir, log correlations for wells with as little as 10 acre spacing would almost certainly erroneously indicate a continuous reservoir unit. However, as can be seen in the stratigraphic cross section (Fig. 3) the discontinuity of tidal channels in the plane of this cross section creates a scale of heterogeneity that could lead to significant bypassed oil if a simple layercake model were used. One would clearly expect little sweep of this zone if an "injection well" was placed at the southernmost limit of this cross section. At the inter-facies scale, additional complexity to modeling fluid flow is created by the Oyster Marker Bed which is tightly cemented by calcite. Calcite cement supplied by the abundant oyster shells filled virtually all pore space in this bed very early in its diagenetic history creating a field-to-regional scale impermeable barrier to vertical flow of fluids (except along fractures). Although several reservoir quality sands are present in the stratigraphic cross section, the facies architecture illustrated at this outcrop would lead one to expect poor sweep and little cross flow with sands higher in the formation because of the marsh/lagoon shales and the calcite cemented Oyster Marker Bed deposits.

Petrophysical Properties from Plugs

The measurements upon which this study is based were performed both on drilled outcrop plugs from 9 depositional facies and on blocks collected from the Almond Formation at "locality G". One inch diameter plugs were taken at lateral spacing from 6 inches (15 cm) to 50 feet (16.5 meters) and vertical spacing from 3 inches (8 cm) to 5 feet (1.5 meters) to capture hierarchically stacked patterns of variations on the scale of meters to hundreds of meters. Plugs were subjected

to standard core analysis do determine porosity and permeability and to aid in mapping petrophysical property distribution within depositional facies.

When porosity and permeability for the various depositional facies was analyzed it was recognized that, in terms of reservoir quality sandstones, there were only two groups of facies: tidal delta sandstones and all other facies combined. A representative chart (Fig. 4) comparing the porosity and permeability of tidal delta, tidal channel and foreshore facies (beach and beach-welded swash bar) illustrates the significantly higher values for the tidal delta compared to the other facies which all have similar petrophysical properties. The plug data indicate average values of just greater than 1 darcy permeability and 31.5% porosity for the tidal delta compared to 226 md and 25.6% for tidal channels, 422 md and 27.3% for the beach, and 219 md and 25.3% for the beach-welded swash bar.

The structure of the porosity and permeability distribution (lamination, bedding, bedsets), however, is different in each of the facies. In this case the structure or geometry of the petrophysical property distribution rather than the scale of the heterogeneity would cause each of the major reservoir quality facies to react differently to fluid flow.

Semi-variograms were constructed from tidal delta, tidal channel, and foreshore (spit/swash bar) facies plug permeability data in order to investigate the structure of the petrophysical properties:

Beach semi-variograms: Permeability semi-variograms of plug data from the foreshore (beach) facies (not including the beach-welded swash bar) indicate horizontal correlation lengths of less than 1 ft and 7-8 feet. The data was collected essentially parallel to depositional strike. In an unmodified fore-beach the lateral correlation lengths would be expected to be much greater than 8 ft. It is believed that the Almond data indicate shorter lateral correlation lengths because the flat lying semi-parallel laminations are not well preserved and that some degree of diagenetic compartmentalization has occurred. Clay cement variations (related to partial leaching of skeletal sand grains) and relative differences in compaction are currently being investigated as primary causes of the 7-8 ft scale heterogeneity. Lateral correlation lengths of less than one foot

are believed to be due to grouping of laminae with similar permeability values, but may have to do with the minimal horizontal sample distance.

Beach-welded tidal swash bar semi-variograms: Permeability semi-variograms of data taken exclusively from the beach-welded tidal swash bar indicate a horizontal correlation length of approximately 7 ft. Planar-tabular foreset cross bedding with millimeter thick laminae are well preserved within this sub-facies. It is believed that the horizontal correlation length for the beach-welded swash bars correlates to the width of individual sand waves that were washed shoreward across the swash platform just downdrift of a tidal inlet to become welded onto the beachface.

Tidal channel semi-variograms: Permeability semi-variograms for the tidal channel facies indicate a vertical correlation length at approximately 4 ft and two lateral correlation lengths at approximately 2 feet and 10 ft. It is interesting, but probably accidental that the 4 ft vertical correlation length is twice the *thickness* of major bedsets within the measured tidal channels. It is likely that the 2 ft lateral correlation length reflects the scale of poorly-preserved foreset bedding within major bedsets. Well-preserved large scale lateral accretion surfaces mark the significant bedset boundaries within the tidal channel facies (illustrated below). Bedding within major tidal channel bedsets is poorly preserved, however, there is evidence from the photo-mosaics that the 10 ft. correlation length may represent the distance that bedding (ripple to dune-size sand waves) can be traced laterally within bedsets. Large, compacted clay clasts, clay-rich laminae, thin clay and carbonate cemented laminae and beds as well as imprints or organic material such as plant stems and other vegetation are abundant at the base of the tidal inlet channel where it cuts into laminated, white beach sands. Oysters and other molluscan remains are not abundant in the base of the inlet channel that was studied.

Tidal delta semi-variograms: Permeability semi-variograms of data from the tidal delta facies show a wide scatter, however, in both lateral and vertical directions, a correlation length of approximately 5 ft is found. additional samples are necessary to better resolve the variogram range. Raw permeability data taken along a single bedset boundary where lateral

spacing of samples was 5 ft over a distance of 450 ft indicates a well developed 20 ft cyclicity. This scale of cyclicity is only a fraction of the lateral extent of mapped major bedsets in the tidal delta facies. It is believed that the 20 ft cyclicity seen on raw permeability data reflects the frequency of beds (i.e. dune size sandwaves) within the major bedsets.

Bi-directional lamination between major beds and bedsets is moderately to well preserved. Broad, low angle festoon bedding is well preserved at major bedset surfaces. Iron oxide cements accentuate bedset boundaries and form concretionary layers that extend laterally for distances up to 50 ft.

Based on the permeability distribution of plug data and process driven geological interpretations the differences in permeability structure between depositional facies, therefore, is primarily related to the differing bedding styles present and enhancement of these heterogeneities by diagenetic processes.

Mapping Bedsets and Permeability Distribution

Tidal delta facies: Mapped bedsets within the tidal delta facies tend to extend laterally for 100 to more than 300 ft (Fig. 5) and are up to 3 ft thick. Permeability within bedsets follows the "grain" of the primary bedding direction and often exhibits significant differences across bedset surfaces (Fig 6). It was found that the permeability trend within major bedsets of this facies and others could not be properly interpreted based on widely spaced plugs (5 ft to 50 ft spacing) without first understanding the location of the bedset boundaries and the bedding direciton within the bedsets.

Thin sections indicate that the bedset boundaries, which are well preserved and very obvious on the outcrop, are enhanced by iron oxide and kaolinite cements, tighter packing with more long grain contacts, and have smaller pores than the sandstone beds on either side of the surface. The beds away from the bedset surfaces tend to have larger, clean pores that appear well connected, better grain and pore size sorting, and only local "clumps" of compacted rock fragments or partly clay-filled interparticle porosity.

Figure 7 displays X-ray CT and probe permeameter surface views from a block containing a tidal delta bedset boundary. The CT image was reconstructed from sections taken at 5 mm spacing. The probe permeameter measurements were performed on a grid 4 mm along laminations and 2 mm across laminations using a 3 mm ID and 6 mm OD tip. The X-ray attenuation values are consistent with the relatively high porosity values determined by plug measurements. They indicate a small porosity contrast between the bedset boundary and the rest of the rock, with the bedset boundary displaying the lower porosity. The probe permeameter measurements indicate a small permeability contrast between the bedset boundary and the rest of the rock with the bedset boundary displaying the lower permeability.

Tidal channel facies: Laterally accreting major bedsets within the tidal channel facies have average lateral dimensions (parallel to depositional strike) of approximately 150 ft (Fig.8).

Thin sections from the basal portion of a tidal inlet channel that cutinto an adjacent beach deposit exhibit very poor grain size sorting, widespread cm-thick layers containing iron oxide cements, finely crystalline calcite and siderite, and small, dirty appearing pores. The "dirty" appearance of the pores is caused by the presence of disseminated clays of two origins. Detrital clay-size particles within interparticle pore space originated from partly leached framework grains and compacted rock fragments. Authigenic kaolinite is also present within the pores, further reducing the permeability. Multiple layers of cm-thick channel fill were noted at the base of the inlet channel and all were poorl- to very poorly-sorted.

Figure 9 displays X-ray CT and probe permeameter surface views from a block containing a tidal channel/beach facies contact. The CT image was reconstructed from 4 mm thick sections taken at 5 mm spacing. The probe minipermeameter measurements were performed on a 5mm x 5mm grid using a 3 mm ID and 6 mm OD tip The X-ray attenuations are higher than in figure 7 indicating a lower average porosity and greater content of minerals with increased CT densities (such as iron oxide cement). The higher attenuations for to the tidal channel correspond to both a lower average porosity and more CT-dense mineralization while the beach displays a higher porosity and less diagenetic alteration. The probe permeameter measurements indicate a large

permeability contrast between the tidal channel and the beach facies, with the beach displaying permeabilities in the 150-500 mD range and the tidal chanel displaying permeabilities in the 20-150 mD range.

Foreshore facies: Bedsets were not recognized within the beach facies. However, within the 1 ft thick beach-welded swash bar closely spaced samples allowed us to map the permeability distribution (Fig. 10). Once again a primary knowledge of the bedding style (planar-tabular foreset cross bedding) was necessary to contour the permeability map correctly. Although the bedding within this unit is technically laminations (mm scale), several laminations with similar permeability values seem to be group together providing permeability layers that dip in the same direction as the bedding but less steeply.

Thin sections from the tidal swash bar facies show great variations in grain size, a relatively clean pore system with only minor amounts of interparticle clay cement, but an abundance of partly compacted soft rock fragments that tend to block pore throats.

CONCLUSIONS

Permeability distribution based on 1 inch diameter plugs collected within and between depositional facies corresponds to process driven geological explanations for the differences in permeability. The differences in petrophysical properties between bedsets and as well as between facies is primarily related to the differing bedding styles present and enhancement of these heterogeneities by diagenetic processes.

Distribution of petrophysical properties interpreted from reservoir quality sandstone blocks using CT and mini-permeameter analysis can be mapped at a scale approximately two orders of magnitude finer than that mapped using plugs. The CT and mini-permeameter data distribution can be explained through petrographic analysis. Both the large scale plug data and the detailed minipermeameter maps of sandstone blocks show similar ranges of permeability for the equivalent depositional facies based on our study of outcropping Almond Formaion barrier island sandstones. This correspondence implies that, for this system, if one correctly identifies the depositional facies and has an understanding of the facies architecture, then small sized samples are not a major hinderance to modeling the reservoir at a larger scale. Thus it is possible to provide a good approximation of scaled fluid flow*within this system* from cuttings, thin sections, or core plugs.

For our study we found that permeability dropped from approximately 1 darcy ("matrix" values) to 400-500 mD across tidal delta bedset boundaries. Matrix permeability for the tidal channel and foreshore (beach and beach-welded swash bar) are both on the order of 200-500 md. The drop in permeability across the facies contact between a tidal inlet channel deposit and the adjacent beach sandstones is 1-2 orders of magnitude.

REFERENCES

Krystinik, L .F., and R. H. Mead, 1996, Sequence stratigraphic and synsedimentary tectonic controls on reservoir compartmentalization in a transgressive sequence set: Almond Formation, southwest Wyoming: AAPG Annual Convention, Program with Abstracts, p. A79.

Martinsen, R. S., and G. Christensen, 1992, A stratigraphic and environmental study of the Almond Formation, Mesaverde Group, Greater Green River Basin, Wyoming, *in* C. E. Mullen, ed., Wyoming Geological Association Guidebook, Forty-Third Field Conference, p. 171-190.

Roehler, H., 1988, The Pintail coal bed and barrier bar G- A model for coal of barrier bar-lagoonal origin, Upper Cretaceous Almond Formation, Rock Springs Coal Field, Wyoming: USGS Professional Paper 1398, 60 p.

Schatzinger, R. A., M. J. Szpakiewicz, S. R. Jackson, M. M. Chang, B. Sharma, and M. K. Tham, 1992, Integrated geological-engineering model of Patrick Draw field and examples of similarities and differences among various shoreline barrier systems: DOE Report NIPER-575, 146 p.

Van Horn, M., 1979, Stratigraphic relationships and depositional environments of the Almond and associated formations east-central Flank of the Rock Springs Uplift, *in* Rocky Mountain Section SEPM Field Trip, Cretaceous of the Rock Springs Uplift, Wyoming, Sept. 21-23, p. 51-63.

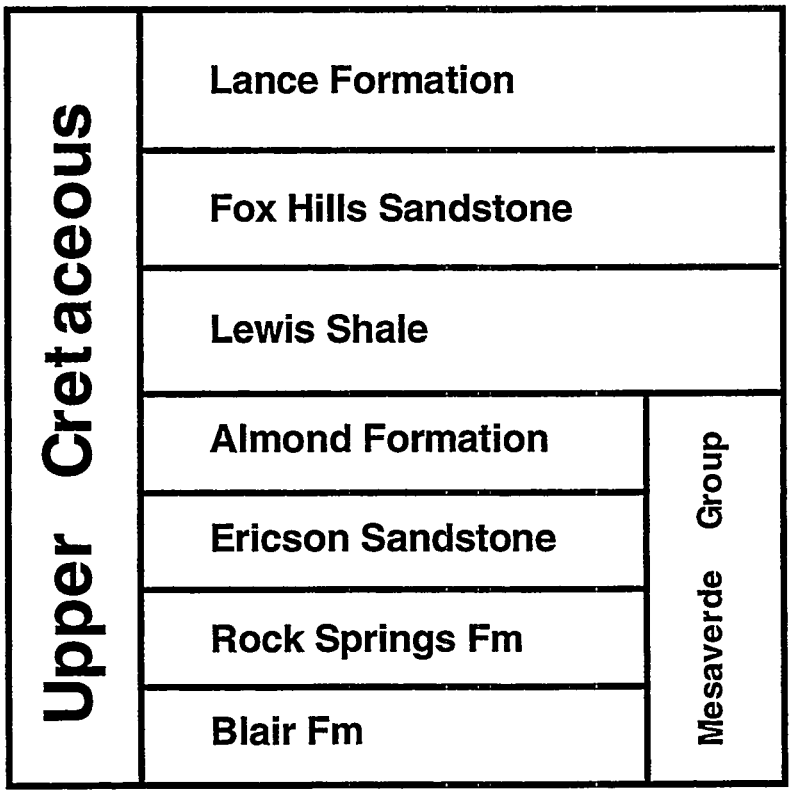

Figure 1. Stratigraphic column for outcropping Upper Cretaceous units in the study area.

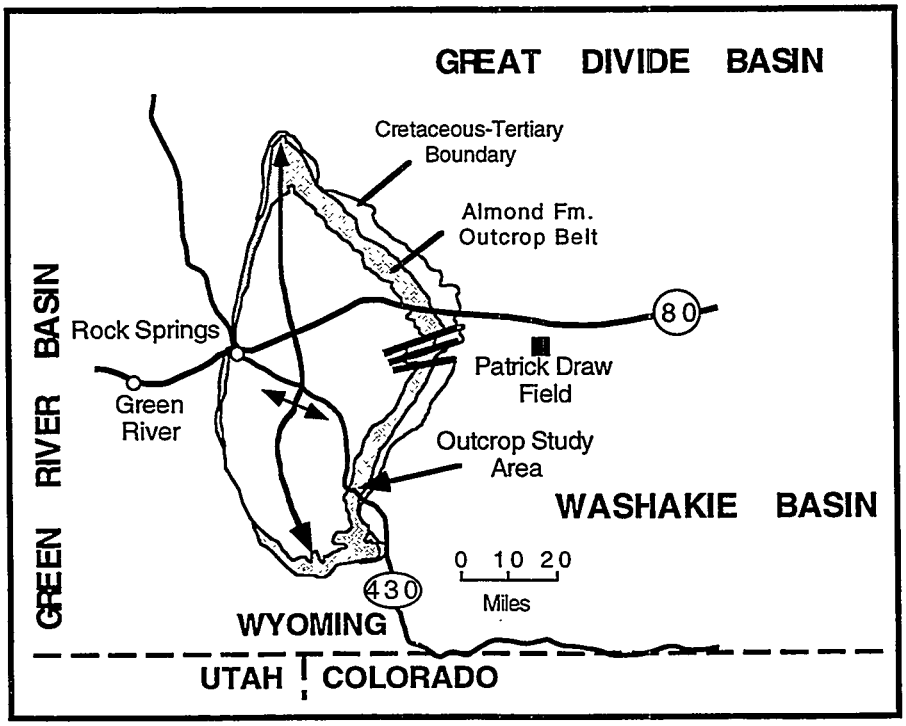

Figure 2. Location map of the study area on the eastern flank of the Rock Springs Uplift, southwestern Wyoming.

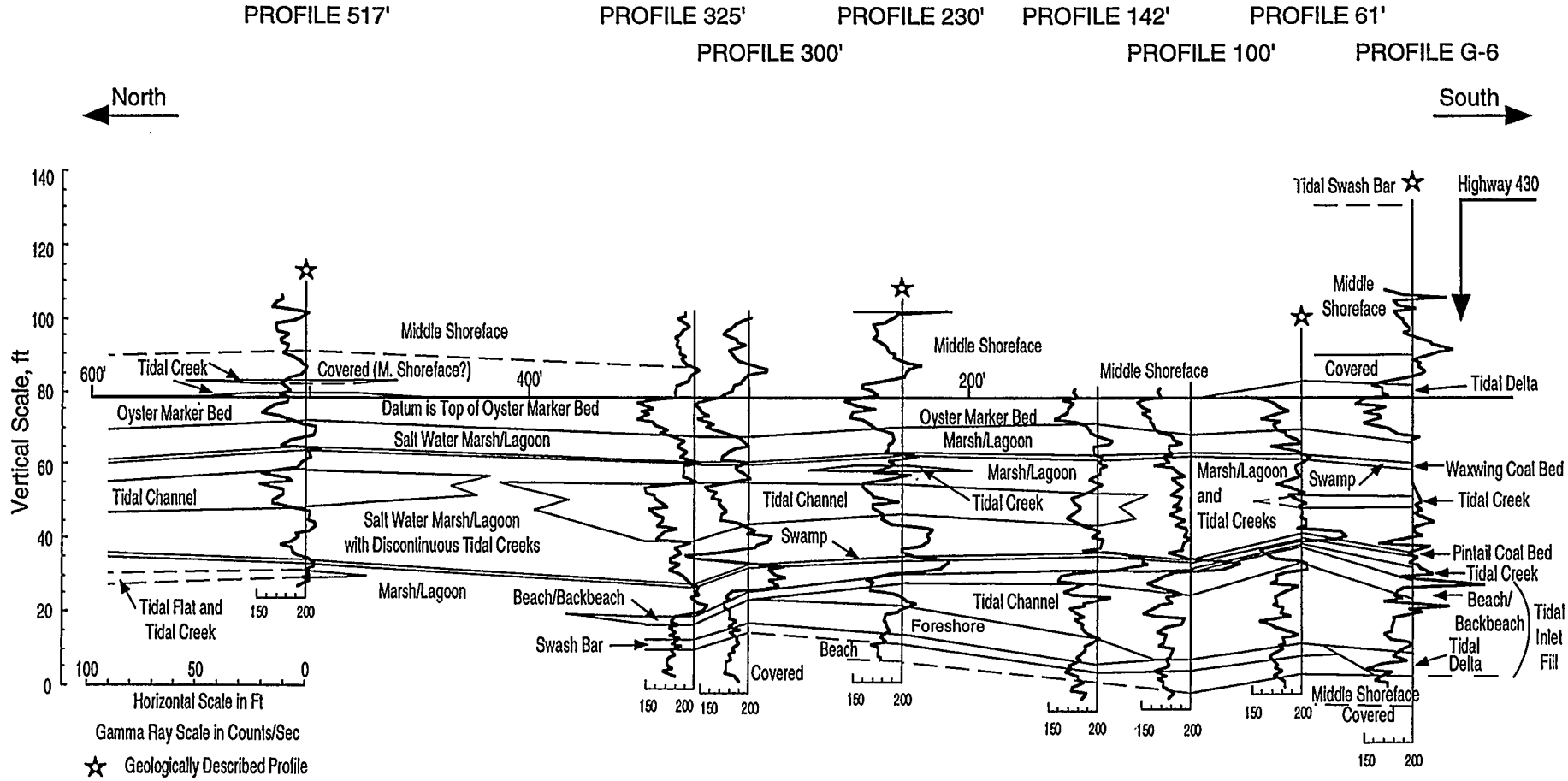

Figure 3. Outcrop stratigraphic cross section is nearly parallel to depositional strike. Note the breaks in tidal channel facies and the complexity of tidal inlet fill that can be found between distances much less than that of 40 acre well spacings.

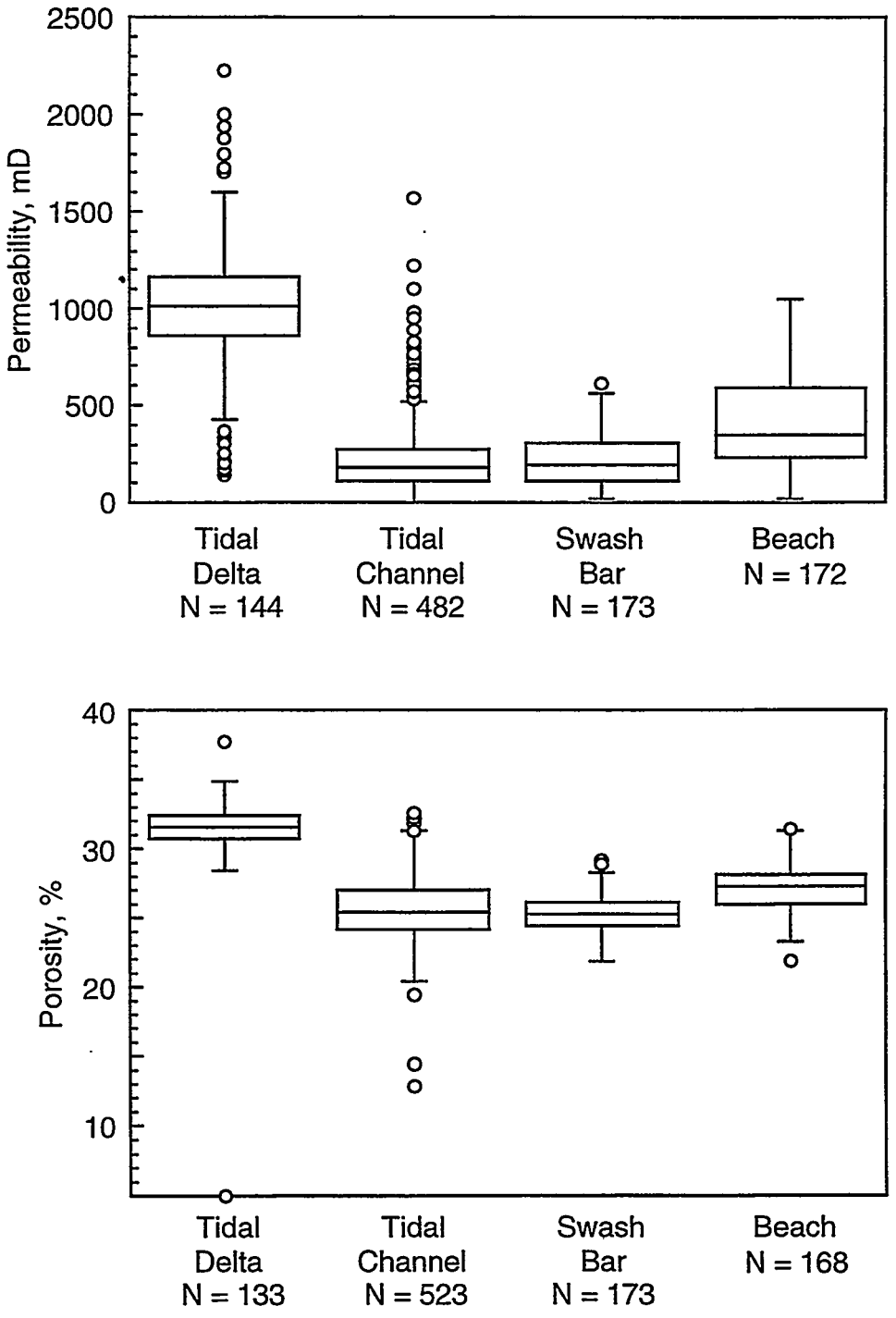

Figure 4. Comparison of porosity and permeability for outcrop facies samples. Box encloses 50% of the data centered about the median value. Lines extend to 95% value. Outliers beyond these ranges are indicated by circles. N = number of samples analysed.

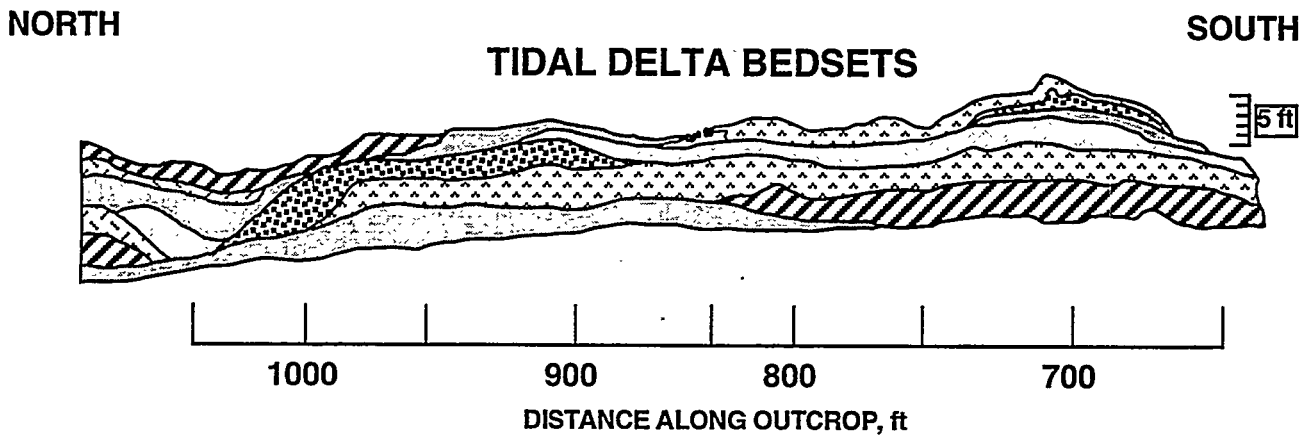

Figure 5. The lateral distribution of major bedsets within the tidal delta facies. Note that the lateral extent of bedsets is less typically less than 300 ft. Uneven horizontal scale is due to construction of cross section from photomosaic.

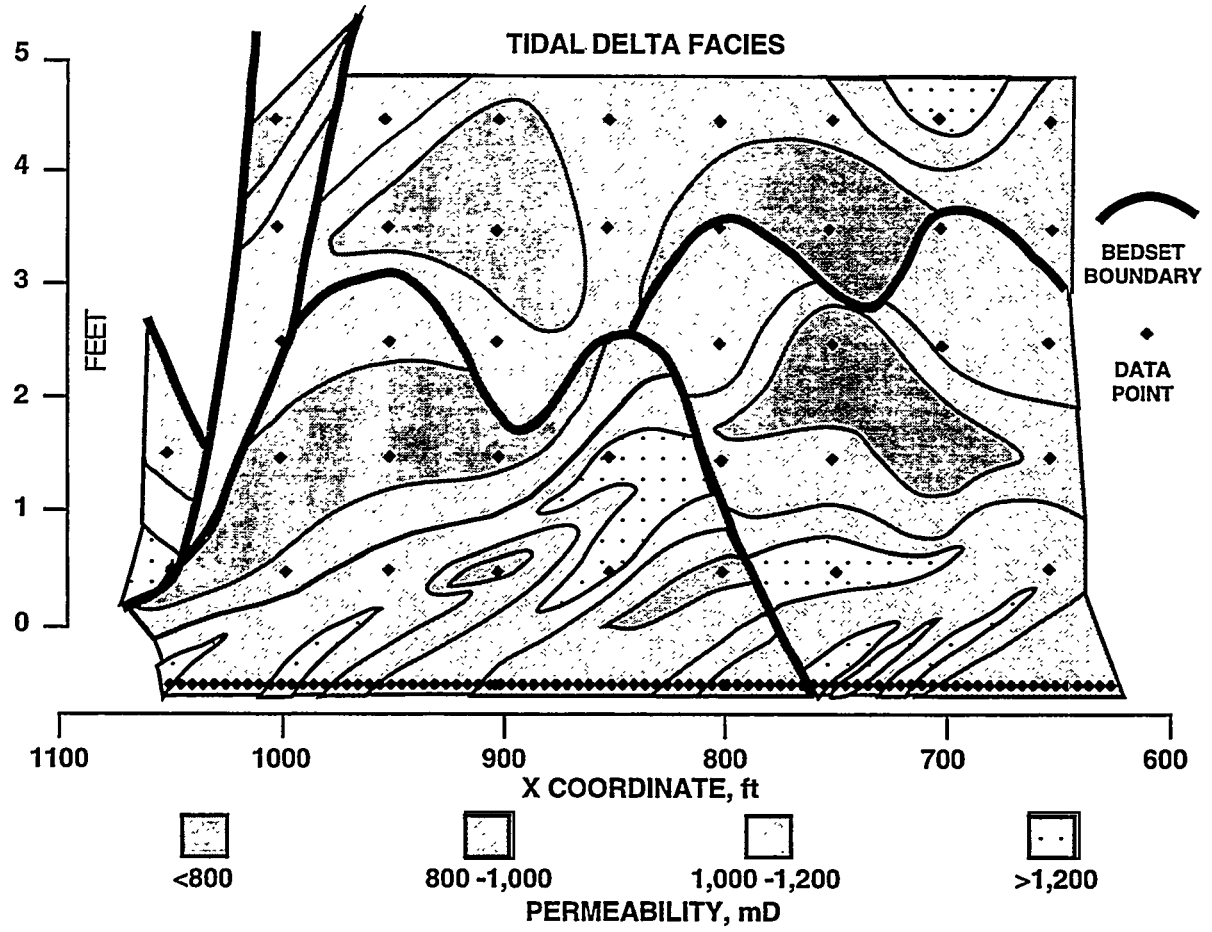

Figure 6. Distribution of permeability within major bedsets comprising the tidal delta facies.

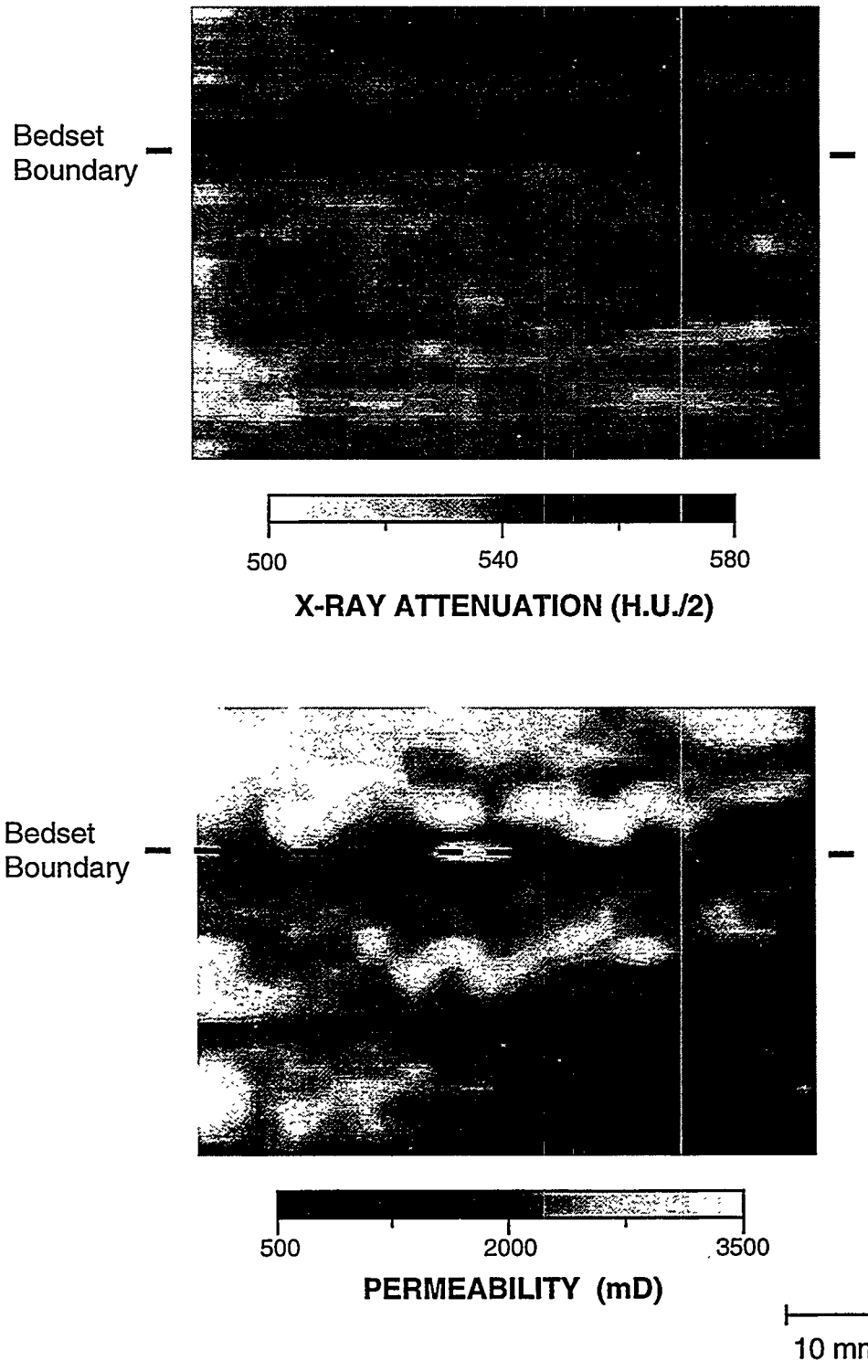

Figure 7. X-ray CT and Probe permeameter maps of a tidal delta bedset boundary. The CT image was reconstructed from sections taken at 5 mm spacing. The probe mini-permeameter measurements were performed on a grid 4 mm along laminations and 2 mm across laminations using a 3 mm ID tip.

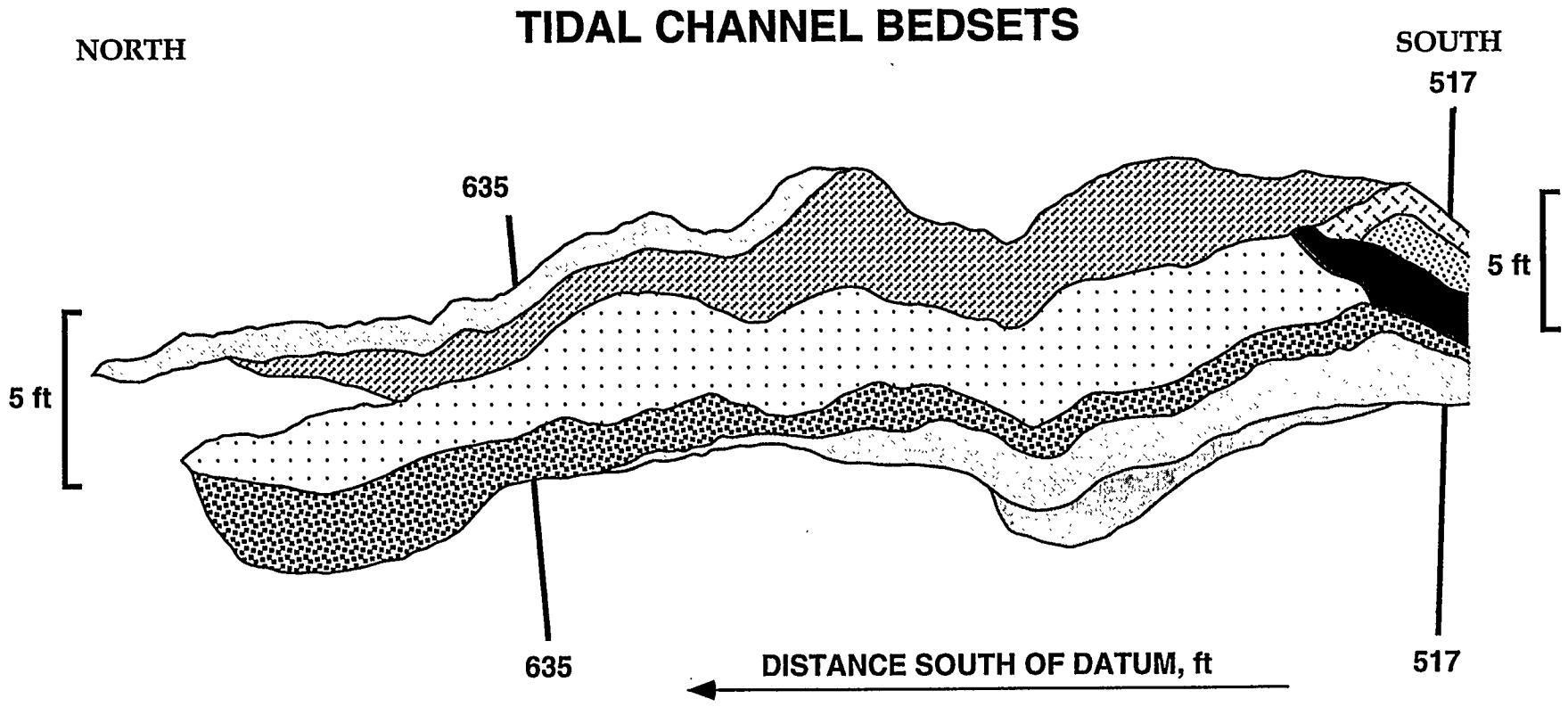

Figure 8. Distribution of laterally accreting major bedsets within the tidal channel facies. Note that fluids moving laterally through this facies would have to pass through more than one bedset boundary.

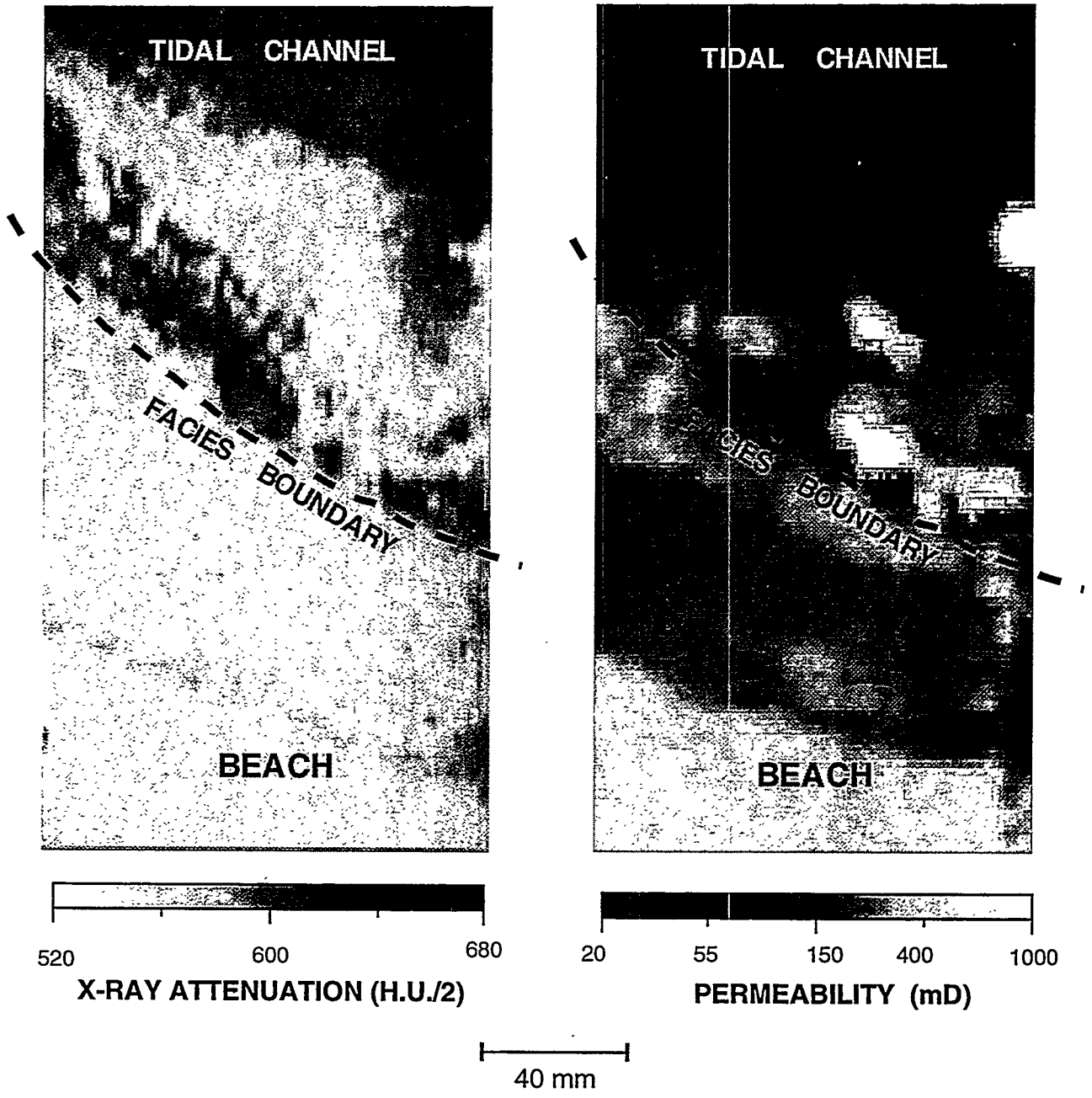

Figure 9. X-ray CT and Probe permeameter maps of a tidal channel/beach facies contact. The CT image was reconstructed from sections taken at 5 mm spacing. The probe mini-permeameter measurements were performed on a 5 mm by 5 mm grid, using a 3 mm ID tip.

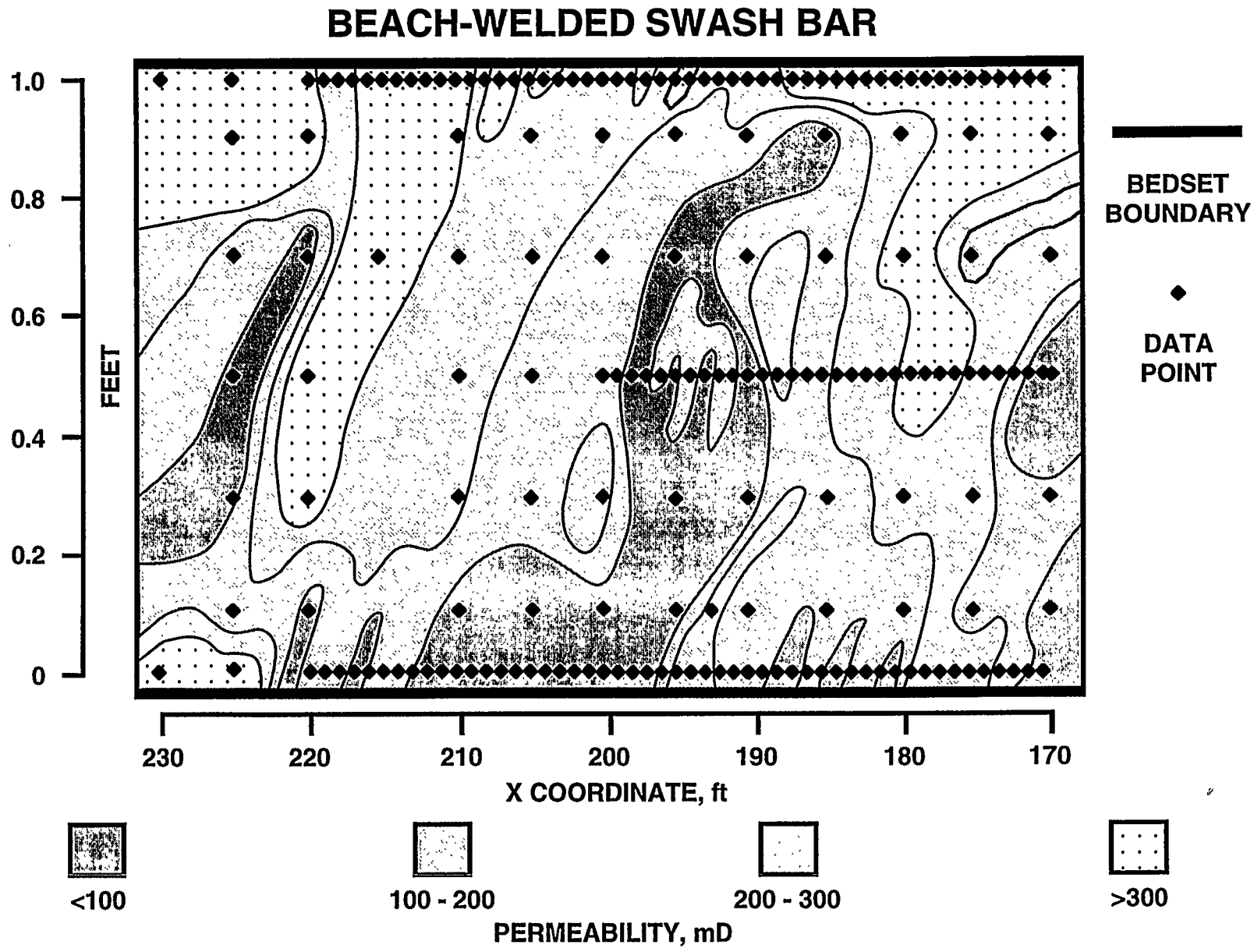

Figure 10. Map of the distribution of permeability within the tidal swash bar based on closely spaced one inch diameter outcrop plugs. Note northward dip (to the left) of permeability trend is in the same direction as the planar tabular cross bedding.

Well Test Imaging - A New Method for Determination of Boundaries From Well Test Data

Bruce A. Slevinsky, SPE, M. Sc., P. Eng.
Senior Reservoir Engineering Advisor
Petro-Canada

Acknowlegments
I would like to thank Petro-Canada for permission to publish this paper, and particularly Mike Danyluk and Duncan Robertson for their support in the development of the technique as Managers of the Technology Improvement Group. As well, I wish to thank all of my colleagues at Petro-Canada for their patience and willingness to share their well tests, geological and geophysical data, and scarce time to make the Well Test Imaging process so much better than it would be otherwise.

Abstract

A new method has been developed for analysis of well test data, which allows the direct calculation of the location of arbitrary reservoir boundaries which are detected during a well test. The method is based on elements of ray tracing and information theory, and is centred on the calculation of an instantaneous 'angle of view' of the reservoir boundaries. In the absence of other information, the relative reservoir shape and boundary distances are retrievable in the form of a Diagnostic Image. If other reservoir information, such as 3-D seismic, is available; the full shape and orientation of arbitrary (non-straight line or circular arc) boundaries can be determined in the form of a Reservoir Image. The well test imaging method can be used to greatly enhance the information available from well tests and other geological data, and provides a method to integrate data from multiple disciplines to improve reservoir characterization. This paper covers the derivation of the analytical technique of well test imaging and shows examples of application of the technique to a number of reservoirs.

Introduction

Conventional well test analysis methods determine the distance to boundaries using either a simplified technique outlined by Earlougher [2] or by regression on distance parameters in a mechanistic model of well test response as described by Gringarten [3]. The analytical technique for calculating distance for a single linear sealing fault involves the estimation of an intersection time, t_x, calculated from the intersection point of the two straight line segments of the Horner plot for the pressure buildup as illustrated in Figure 1. This intersection time is then substituted into equation 1 (from Earlougher [2])

$$L=0.01217(kt_x/(phi*mu*c_t))^{.5} \qquad \text{eq. 1}$$

This represents approximately 42 percent of the equivalent radius of investigation at that particular

point in time,

$$Rinv=.029(kt/(phi*mu*c_t))^{.5} \qquad \text{eq. 2}$$

Multiple boundaries in the vicinity of a well can cause many different transient-test behaviours depending on the number, type, and orientation of the boundaries. Few general rules are given in the literature to resolve these differences. A simple example may show some of the difficulties:

1) two linear boundaries intersecting at right angles serve to produce three straight line segments showing slope doubling, and two intersection points on the Horner plot which can be interpreted to give the distances to the two boundaries, Figure 2,

while

2) two linear boundaries arranged parallel to each other produce a continuously increasing Horner plot characteristic of linear flow which cannot be readily interpreted to give the distances to the two boundaries using the technique described above, Figure 3.

In the computer-aided well test analysis technique based on mathematical models and regression analysis of the model parameters; the analyst selects an overall model based on near wellbore, reservoir flow character, and reservoir boundary parameters which are then 'solved' to fit the observed behaviour. The mathematical models usually involve solutions in Laplace space and inversions to real space, using multiple regression passes to converge to values which attempt to characterize the whole system of equations and effects. The mathematical background is complex, the numerical difficulty is significant, and the traditional handling of reservoir boundaries has been simplistic, involving linear bounding elements arranged as wedges or elements of a rectangle. Because the reservoir boundary effects usually occur late in time, the numerical approach above is dominated by near wellbore and reservoir character parameters, and there is usually significant uncertainty in the choice of the reservoir boundary model and the accuracy of the predicted boundary parameters. The development of well test imaging was targeted at increasing the understanding of boundary effects, removing limitations imposed by arbitrary linear boundary systems, and increasing the ease with which boundary data can be interfaced to other forms of data to increase the confidence in boundary distances and orientations.

Well Test Imaging - Theoretical Development

A) Information Theory and Boundary Type Curve Development

The development of well test imaging began with the use of a conventional well test analysis program, in its test design mode, to produce theoretical well test responses for simple boundary systems to deduce the behaviour of the boundary signal. The first case was a single linear boundary system under a variety of conditions of near wellbore, reservoir flow character, and boundary distance. The models were constructed in pairs

with and without the boundary effects to get a visual presentation of the impact of a boundary. A typical simple model with wellbore storage and skin, and a uniform homogeneous reservoir produces the log-log type curve responses of Figures 4 and 5. The boundary effects show up most clearly in the difference in the Bourdet derivative curves at the bottoms of these Figures.

Information theory indicates that we should attempt to isolate the effect of any input parameter by filtering out all of the extraneous information in a signal so that we can concentrate solely on the response to the input. In the case of the pairs of well test designs above, a simple way of removing the near wellbore and reservoir character effects was found by dividing the Bourdet derivative response of the case with boundary effects by the Bourdet derivative of the case without boundaries. This produces a very simple 'Boundary Ratio Type Curve' which has a value of 1.0 up to the point at which boundary interactions take place and a shift upward in response to boundary interactions, as shown on Figure 6, which was derived from Figures 4 and 5. When many well test designs are processed in this way it can be seen by inspection that the curves are all similar, Figure 7, and can be condensed into one curve, Figure 8, by a shift in the time scale. This implies geometric similarity for the single boundary problem with the time, t_0, being representative of the time for the boundary interaction to be perceived at the test well.

A similar set of well test designs was done for the case of two boundaries in the form of a wedge. The Boundary Ratio Type Curves for the case of a 60 degree wedge with the well on the centre-line are shown onFigure 9. The Boundary Ratio Type Curve was found to have a geometric similarity relationship similar to that seen in the single boundary case, Figure 10. For all of the wedge angle cases, the Boundary Ratio Type Curve approached an asymptotic limit value equal to,

$$\text{Wedge Boundary Ratio Limit} = \frac{360}{\text{Wedge included angle}} \qquad \text{eq. 3}$$

as shown on Figure 11.

The final set of well test designs studied was the set of two parallel boundary 'channel flow' cases, shown on Figure 12. It was found again that only the short time behaviour showed differences which could be characterized by the position of the well between the two boundaries, but that all cases approached a linear, half slope on the log-log plot, limit behaviour. For a common ratio of distances to the two boundaries, a normalized type curve could be developed for each case as on Figure 13.

The strong geometric similarity behaviour of the sets of cases studied argues strongly that there is an underlying linkage in the physics of how the information about a boundary is sensed by the well test, and that this is linked to the flow and pressure transient behaviour of the reservoir. In particular, it can be concluded that the magnitude of the response seen on the Boundary Ratio Type Curve was independent of distance to the boundary, and represents a measure of the geometric properties of the boundary. The distance to the boundary appears to be related to the time scaling of the

boundary response.

B) Ray Tracing and Interpretation of Boundary Effects

A set of visualization experiments of a drawdown or buildup well test with a single boundary was conducted using a simple computer program which plotted the position of the radius of investigation as a function of time, under the assumption that the well test could be treated as a non-linear transient wave phenomenon. A composite sequence of these images is shown on Figure 14, illustrating that the effective wave position is dependent on the square root of the test time. The information about the first contact with the boundary (t=100) reaches the well at a time equal to 4 times the contact time (t=400). All of the information about the boundary, however, does not reach the test well at one time as seen on the type curves generated in the previous section. In order to determine just how all of the information reaches the well, the overall wave front was broken down into a number of rays or packets. In order for information on the boundary contact to propagate back to the test well it was necessary to assume that the boundary behaved in a manner similar to an elastic absorbtion and re-radiation rather than as a reflection, similar to the concepts used in interpreting seismic data. These subsequently re-radiated rays which pass information back to the source well, illustrated on Figure 15, have wave fronts that combine to form the overall front of Figure 14. Information is carried back to the test well along a straight line path, from the contact point to the test well, which arrive back at the test well at 4 times the contact time for each ray. Considering just the array of rays carrying information back to the test well over time as in Figures 16 and 17, it was observed that the rays passing through the test well formed an 'angle of view' of the boundary which asymptotically approached 180 degrees. Going back to equation 3 this also predicts the asymptotic Boundary Ratio Type Curve value for the single linear boundary.

If we assume that the instantaneous 'angle of view' of the boundary, AOV(t), is directly related to the Boundary Ratio Type Curve value through,

$$BRTC(t) = 360/(360-AOV(t)) \qquad \text{eq. 4}$$

it is possible to calculate a theoretical type curve for the single linear boundary case. This is accomplished by following the logic of Figure 18, which shows a ray with Rinv(t) just contacting the boundary. The value of the angle of view of the boundary is 2*theta which can be expressed through relationships with the radius of investigation with time

$$Rinv(t) = d_c*(t/t_c)^{\wedge}.5 \qquad \text{eq. 5}$$

as

$$AOV(t) = 0 \quad \text{for } t<=4*t_c \qquad \text{eq. 6 a}$$

where t_c is the time to first contact with the boundary at which time $Rinv=d_c$

and therefore,

$$AOV(t) = 2*theta \quad \text{for } t>4*t_c \qquad \text{eq. 6 b}$$

$$= 2*\arccos(2*d_c/Rinv(t))$$

$$= 2*\arccos((4*t_c/t)^{\wedge}.5) \qquad \text{eq. 6c}$$

Therefore, an equation for the BRTC(t) for a single linear boundary can be expressed as,

$$BRTC(t) = 360/(360-2*\arccos((4*t_c/t)^{\wedge}.5)) \quad \text{for } t>4*t_c \qquad \text{eq. 7}$$

If we normalize this curve at $t_0=4*t_c$ then the resulting normalized type curve plot is shown on Figure 19, which can be compared with the normalized linear boundary ratio plot of Figure 8, derived from the well test design exercises which began the process. The approximate answer of equation 7 is a very close match to Figure 8, and has several desirable characteristics:

1) it is easy to evaluate
2) it has a clear physical interpretation
3) it is easily inverted

This same construction process can be used on the 60 degree wedge example and the parallel channel boundary to reconstruct approximations of those type curves as well, as shown on Figures 20, and 21.

Any arbitrary reservoir boundary system whether it is composed of straight lines or curves can be evaluated using the ray tracing methodology, to construct a Boundary Ratio Type Curve for that boundary system. Combined with any base line near wellbore and reservoir flow characteristic log-log type curve, this technique can generate an overall type curve for that reservoir and boundary system. Yeung et al [4] proposed a method to analyze the transient pressure behaviour of an arbitrarily shaped reservoir using a superposition in time approach which is much more time consuming and difficult than the method proposed above.

Inversion of a Well Test Response - Calculation of a Well Test Image

As useful as being able to construct a type curve for a given geometry may be, the bigger problem in well test analysis is the interpretation of the actual test response to determine the distance to and orientation of the boundaries observed in a well test. The simple form of equation 6 allows simple inversion; that is, for a given well test response, a picture of the boundary system can be created. The process starts by conducting a conventional analysis to produce the best possible match to the early time data to properly calibrate the near wellbore and reservoir flow characteristics. At this point we either do not match the boundary affected portion of the test or turn off the boundary effects once the best conventional match is achieved. The resulting difference between the model log-log type curve and the actual data represents the information or signal of the boundary. By dividing the actual reservoir response by the non-boundary predicted response we create the Boundary Ratio Type Curve as a function of time. As well, with most programs, the analysis method without boundaries will predict a radius of investigation for the whole test (i.e. $Rinv(t_{max})$) which will be used to calibrate distances for the calculations.

Given the Boundary Ratio Type Curve as a function of time, BRTC(t), the Angle of View of

the boundary as a function of time and radius of investigation can be determined by inverting equation 4,

$$AOV(t) = 360 - 360/BRTC(t) \qquad \text{eq. 8}$$

Given the Angle of View of the reservoir boundary system as a function of time, the distance to the reservoir boundary is determined as a function of the Radius of Investigation as a function of time. The distance to a reservoir boundary which will affect a given well test at a given time is exactly half of the radius of investigation at that point (since the information must travel back to the source well covering twice the distance)

$$Rinf(t) = Rinv(t)/2 \qquad \text{eq. 9}$$

This distance is called the Radius of Information in the terminology of this paper. Given $Rinv(t_{max})$, the Rinf(t) is calculated at each point from,

$$Rinf(t) = 0.5*Rinv(t_{max})*(t/t_{max})^{.5} \qquad \text{eq. 10}$$

With Rinf(t) and the AOV(t), a picture of the reservoir surrounding a well can be drawn in the following manner. Beginning at the last point where the BRTC(t) is less than or equal to 1.0 ($t=t_0$), draw a circular arc at a radius equal to

$$Rinf(t_0)=0.5*Rinv(t_{max})*(t_0/t_{max})^{.5} \qquad \text{eq. 11}$$

This represents the maximum radius of reservoir behaviour without boundary influences. At each point $t>t_0$, draw an arc of radius Rinf(t) from equation 10, through an angle of 360-AOV(t) showing the non-boundary containing reservoir as a function of time. Continue to draw these arcs until $t=t_{max}$ is reached. The resulting diagram, similar to a sonar display, will be an image or realization of the reservoir and, by difference, the boundary system. A Well Test Image drawn at this stage is called a Diagnostic Image, in that it can give you a general reservoir shape and distance to a boundary, but the picture may not be realistic or recognizable in terms of geological features which you might be able to recognize in other data. In order to make this picture more understandable in terms of our usual visualization processes and to help distinguish more complex systems when more than one boundary may be present, three standardized interpretation models have been devised:

a) Angular Model. Draw a tangent line to the circle at $Rinf(t_0)$, and draw all remaining arcs with one end placed on the tangent line.

b) Balanced Model. Draw a radial line from the centre of the circle of radius $Rinf(t_0)$ and centre all of the remaining arcs on this line.

c) Channel Model. Draw a tangent line to the circle at $Rinf(t_0)$ and a radial line perpendicular to it through the test well. Begin to draw arcs centred on the perpendicular line until the remaining arc ends fail to cross or contact the tangent line. At this point split the arc in half and place the two original ends on

the initial tangent line on opposite sides of the well and predict the position of the other boundary by tracing out the position of the newly cut arc ends.

The model descriptions above can be expressed mathematically, calculated, and displayed directly from the well test analysis. In many cases, all three models may produce results which are valid and need to be tested against other geological information. This merely illustrates that the well test data (and the information returned by a well test alone) may be insufficient to provide a unique answer to the question of boundary configuration.

Well Test Imaging - Examples

There are few examples in the literature with enough data to allow comparison of conventional and well test imaging approaches to the prediction of reservoir boundaries. One exception is the paper by Clark [1] on the Oseberg reservoir which shows the application of conventional techniques to predict two boundaries at right angles around well 30/6-13, Figure 22. Application of well test imaging to the raw data from the paper produces the log-log type curve of Figure 23, the BRTC(t) of Figure 24, and the well test image (Diagnostic Image) of Figure 25. The key difference is that the boundaries are found to be neither at right angles nor precisely linear and the distances to the boundaries are slightly different than those predicted conventionally. These differences could be significant in terms of interpretation of the alignment of the boundaries with known seismic or geological anomalies and illustrate how our dependence on fixed models of reservoir boundaries could alter our perception of the boundary system.

Another example of the application of the approach is taken from a Petro-Canada operated well in the Fireweed pool in northeastern British Colombia. This pool is a fractured and dolomitized carbonate reservoir containing gas, where reservoir quality and continuity are an issue. The well test log-log type curve for an initial well in a new area of the pool is shown on Figure 26. The Boundary Ratio type curve of Figure 27 shows some significant variations which were difficult to fit with conventional techniques (predicting two boundaries at right angles, but leaving a high residual error in the match). The Diagnostic Image of the test, Figure 28, shows a system with several 'steps' in the boundary system. We believe that these variations depict the underlying fracturing fabric of the reservoir and a conjugate set of lineaments which both create the reservoir and simultaneously set up internal reservoir boundaries. These considerations have influenced our application of horizontal well technology to develop the field using our knowledge of local tectonic history to orient the well test images in the preferred fracturing directions and to orient the horizontal wells along axes which allow the maximum number of lineaments to be contacted.

Well Test Image Enhancement - Integration of Geological and Geophysical Data

The problem of well test image solution uniqueness can be addressed in many ways, including:

a) fitting together of well test images of neighbouring wells which may image parts of the same boundary system, much like solving a jig-saw puzzle.

b) observing a well test at offsetting wells and interpreting the interference data to determine boundary orientations. The ray tracing methodology proposed above can be used to interpret the offset well response.

c) incorporating geological or geophysical information from other sources to fit against the well test images, to provide information on orientation of lineaments or depositional directions.

The experience of the last few years with well test imaging indicates that the integration with geological and geophysical data offers the most potential for significant improvement in the quality of the images. As well, it can lead to an improvement in the understanding of the characteristics of the boundaries in terms of their expression in the other data types.

Geological maps and 3-D seismic data represent excellent sources of information which can be integrated with well test imaging. As an example, an attribute of the 3-D seismic data (amplitude of a reflector, depth of a surface, slope of a surface), is contoured in the form of a 2-D map. The well location is marked on the map, and the well test image is superimposed at the same scale. As a first approximation, the whole image can be rotated and positioned so that the circular boundary of the radial flow reservoir region just contacts a likely lineament. This represents identification of the most likely boundary forming element in the region surrounding the well. The image is then rotated until the boundary image tangent to the radial region parallels the mapped lineament. Then the individual arc segments can be rotated to exactly contact the mapped boundary, because in most instances it is not perfectly linear. In many instances several mapped lineaments or potential boundary elements can be made to fit simultaneously, adding to the potential that a more unique match has been determined.

As an example of the application of the process, consider the well test shown on Figure 29, which has been modeled as well as possible to match the early time data. The difference between the match curve and the actual well test was used to create the Diagnostic Image shown on Figure 30. The angular model indicates a generally open-ended rectangular model with three no-flow boundaries. The slope of a surface near the level of this test was derived from 3-D seismic and is shown of Figure 31. Combining the Diagnostic Image and the 2-D map of the surface slope produced the Reservoir Image shown on Figure 32. This image very clearly identified the boundary forming critical slope of .12 to .20 m/m which is characteristic of fault boundaries in this field, and fit two prominent lineaments simultaneously. While the perception of the general character of the well test boundaries did not change, the additional work did allow the precise orientation of the open end of the system to be deduced and aided in the placement of a potential waterflood

support well. This same image can then be superimposed on other data representations; in the case of Figure 33 on the structure top of the zone derived from seismic, and presented in a 3-D mesh perspective to allow visualization of the effective reservoir around the well.

Other Uses of Well Test Images

The digital nature of the well test imaging process, allows a number of calculations to be carried out using the Rinf(t) and AOV(t) data generated by the analysis that would otherwise not be possible:

1) it is possible to integrate the area and volume swept by the test to show the area over which information was generated. This leads to a better descriptor of the volume affected by a well test than the Radius of Investigation. This can be used to develop an estimate of 'proved' reserves due to the test.

2) by constructing a line joining nearest neighbour ends of the concentric arcs of the well test a picture of the boundary alone can be generated.

3) an automated procedure for generation of simulation model grids with realistic boundaries can be set up since the region of reservoir around the well is known.

4) When multiple tests of several zones are conducted in a single well which shows fault boundaries, the images of each test can be stacked to provide a 3-D representation of the fault surfaces, as shown on Figure 34.

All of these applications are new to the field of well test analysis, and allow significant input to be provided to 3-D seismic and geological interpretations. Well test imaging provides a natural integrating mechanism for well test data which spans the gamut of reservoir characterization from 3-D seismic to reservoir simulation.

Conclusions

1) A new type curve, the Boundary Ratio Type Curve, is proposed as a way to characterize boundary influences and to measure the boundary signal in a well test.

2) Based on observation of the Boundary Ratio Type Curve characteristics, the magnitude of the response is concluded to be due to the geometric shape of the boundary which is characterized by the 'Angle of View' (AOV(t)) of the boundary; while the distances to the boundary contacts are represented by the time scaling of the response through the 'Radius of Information' (Rinf(t)).

3) The accuracy of the boundary calculations is limited only by the accuracy with which the underlying time and pressure measurements are made, and with modern gauges this can be down to the order of meters.

4) The well test images derived directly from AOV(t) and Rinf(t) with perhaps an analytical

model as a guide, Diagnostic Images, are non-unique.

5) Integration of the Well Test Image with geological or geophysical information can lead to enhanced images (Reservoir Images) which can resolve the uniqueness problem, and increase the quality of the interpretation overall.

6) Well Test Imaging can help to extract more information from well test data, enabling better quality interpretations and enhanced reservoir characterization that are unconstrained by simplistic straight-line boundary models.

7) Well Test Imaging provides a key element in the integration of well test data with geological and geophysical analyses, and reservoir engineering simulation in the reservoir characterization process.

Nomenclature

AOV = angle of view
arccos = inverse cosine ($\cos^{-1}$)
BRTC = boundary ratio type curve value
ct = total system compressibility [1/psi or 1/kPa]
k = permeability [md]
L = distance to a boundary
mu = oil viscosity [cp or mPa.s]
phi = porosity [frac]
Rinf = radius of information
Rinv = radius of investigation
t = time
t_c = time for radius of investigation to first contact with a boundary
t_0 = time for first boundary interaction to be sensed or measured at the test well
t_x = intersection time, calculated from intersection of straight-line segments on Horner plot.
t_{max} = maximum test time (shut-in or drawdown)
theta = angle between the shortest distance between a well and a surface and the current ray contact with the surface

References Cited

1) Clark , D. G., Van Golf-Racht, Pressure-Derivative Approach to Transient Test Analysis: A High-Permeability North Sea Reservoir Example, SPE 12959, 1985

2) Earlougher, R. C. Jr., Advances in Well Test Analysis, SPE Monograph Vol. 5, pp. 124-125, 1977

3) Gringarten, A. C., Computer-Aided Well Test Analysis, SPE 14099, 1986

4) Yeung, Kacheong and Chakrabarty, Chayan; An Algorithm for Transient Pressure Analysis in Arbitrarily Shaped Reservoirs, Computers and Geosciences, Vol. 19, No. 3, pp 391-397, 1993

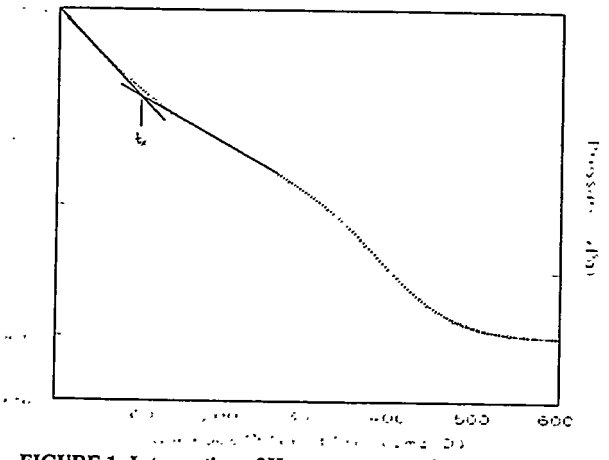

FIGURE 1: Intersection of Horner curve straight-line segments

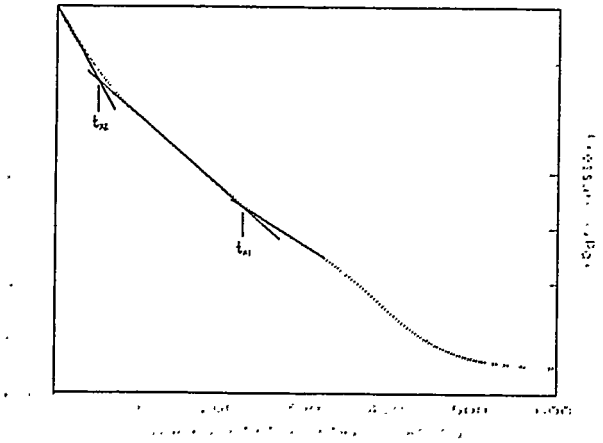

FIGURE 2: Horner curve for 2 boundaries at right angles

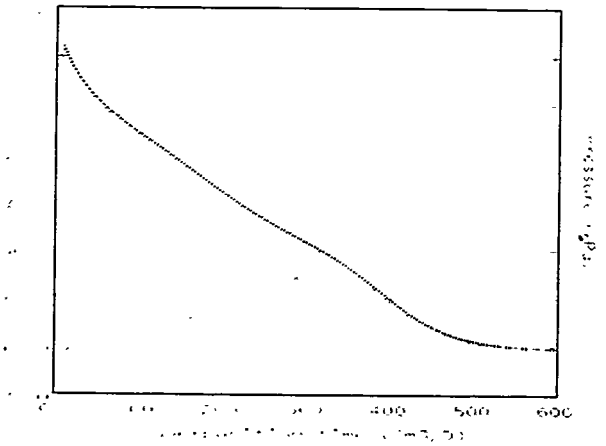

FIGURE 3: Horner curve for 2 parallel boundaries

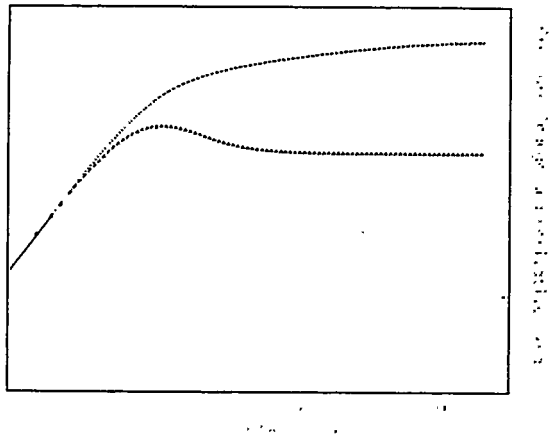

FIGURE 4: Log-log type curve for homogeneous reservoir

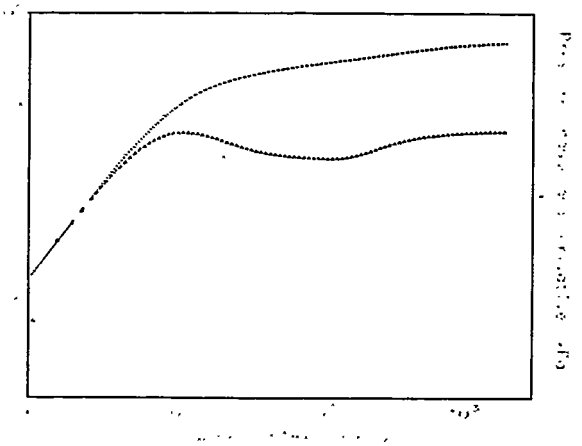

FIGURE 5: Log-log type curve for homogeneous reservoir with a single linear boundary

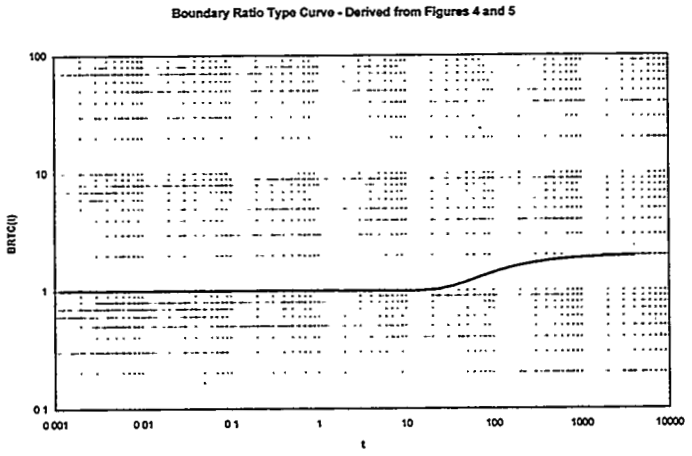

FIGURE 6: Boundary Ratio Type Curve for a single linear boundary

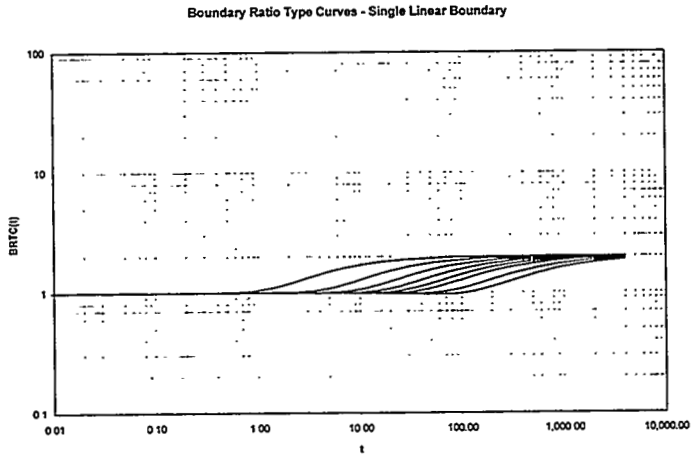

FIGURE 7: Boundary Ratio Type Curves for single linear boundary cases

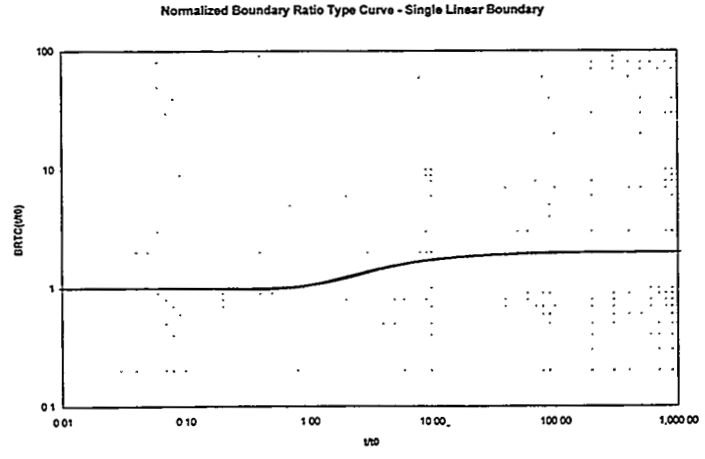

FIGURE 8: Normalized Boundary Ratio Type Curve - Single Linear Boundary

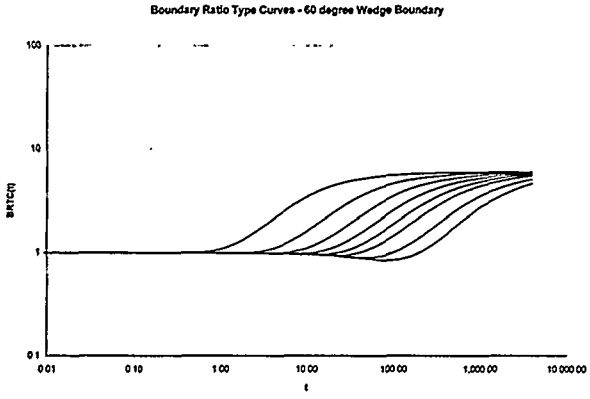

FIGURE 9: Boundary Ratio Type Curves - 60 degree Wedge Boundary

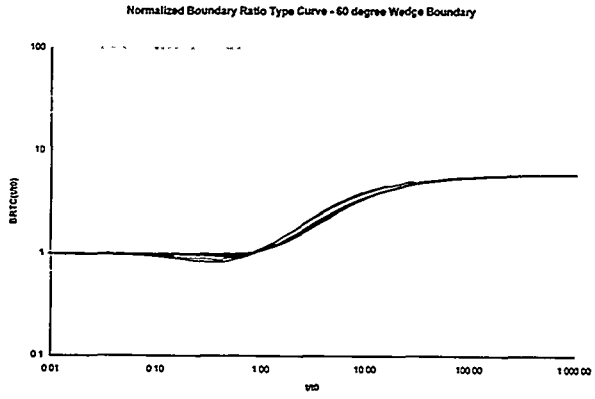

FIGURE 10: Normalized Boundary Ratio Type Curve - 60 degree Wedge Boundary

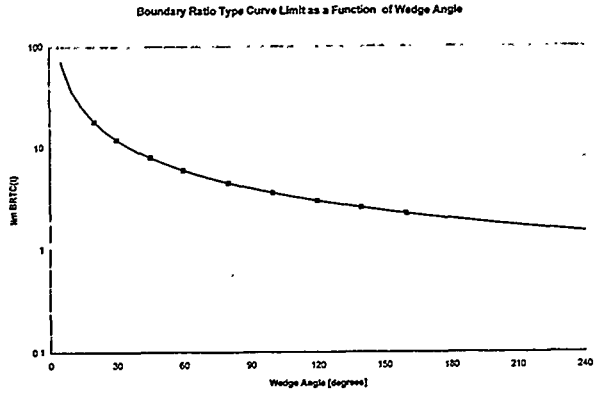

FIGURE 11: Boundary Ratio Type Curve Limit as a Function of Wedge Angle

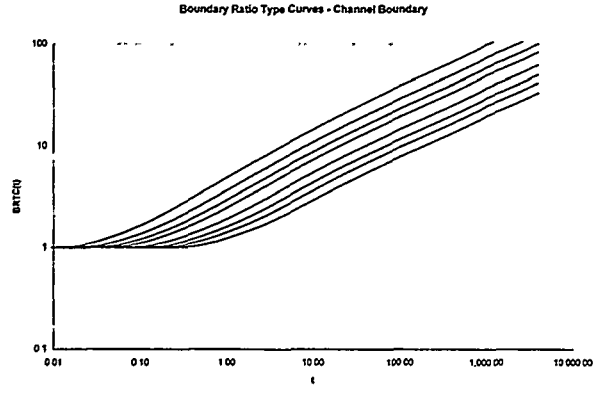

FIGURE 12: Boundary Ratio Type Curves - 2:1 Parallel Boundaries

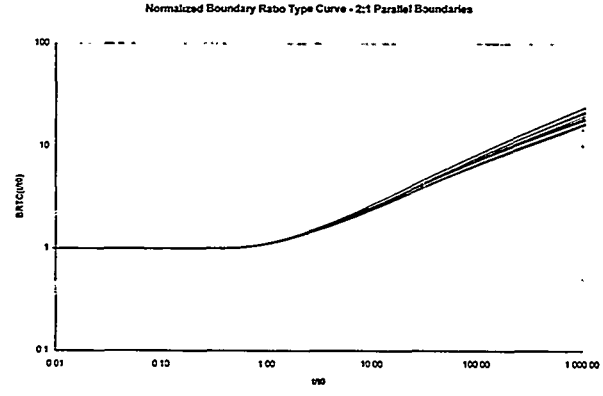

FIGURE 13: Normalized Boundary Ratio Type Curve - 2:1 Parallel Boundaries

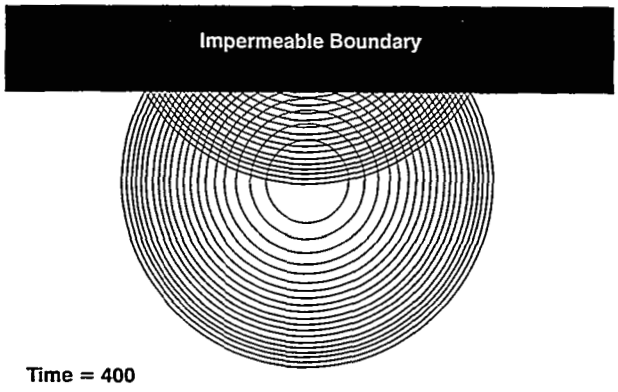

FIGURE 14: Composite Images of Rinv as a Function of Time

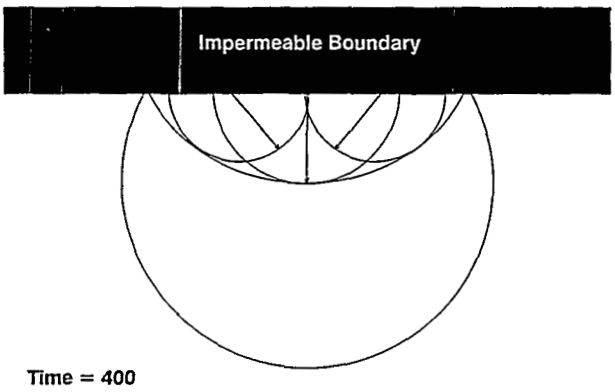

FIGURE 15: Assumed Boundary Interaction Wave Fronts

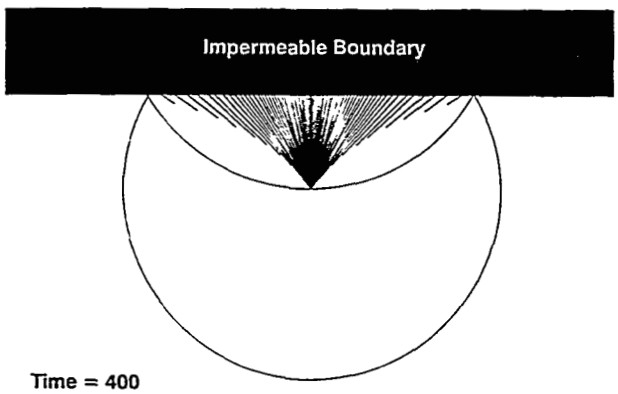

FIGURE 16: Rays Showing Boundary Interactions at Time t_0

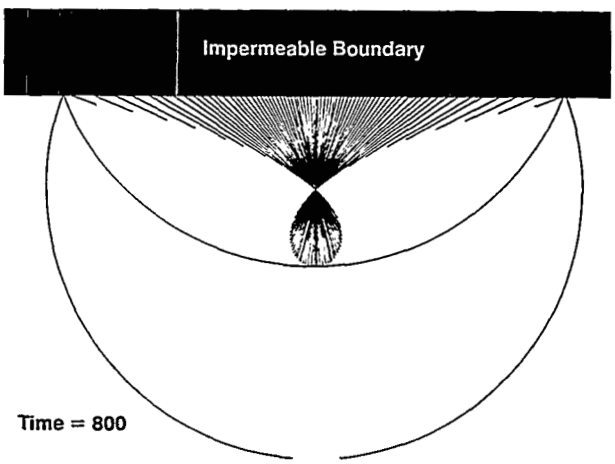

FIGURE 17: Rays Showing Boundary Interactions at Time $t>t_0$

Well Test Imaging - Elemental Boundary Contact

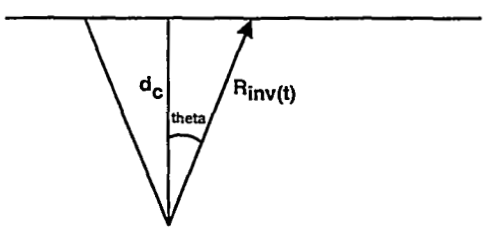

theta = arc cos ($d_c/R_{inv(t)}$)

FIGURE 18: Diagram of Ray Interaction With Boundary at Time $t>t_c$

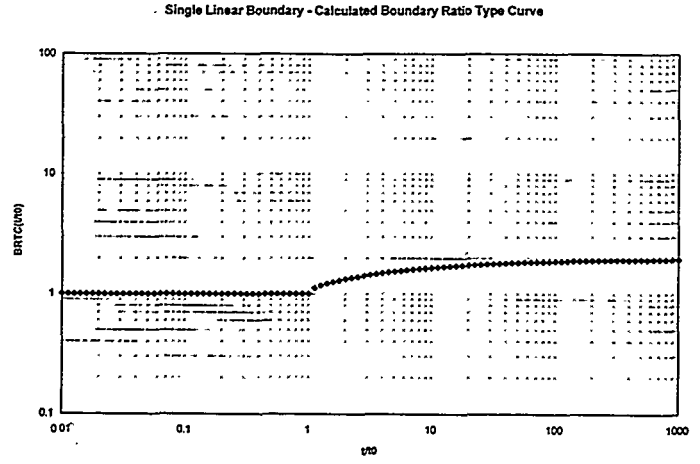

FIGURE 19: Calculated Normalized Boundary Ratio Type Curve for Single Linear Boundary

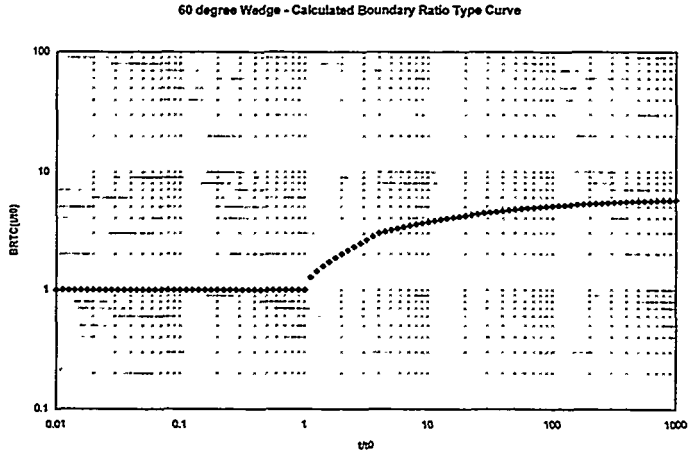

FIGURE 20: Calculated Normalized Boundary Ratio Type Curve for 60 degree Wedge Boundary

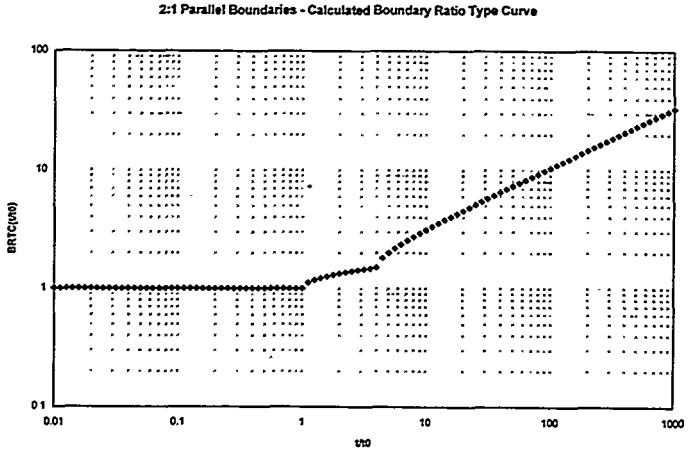

FIGURE 21: Calculated Normalized Boundary Ratio Type Curve for 2:1 Parallel Boundaries

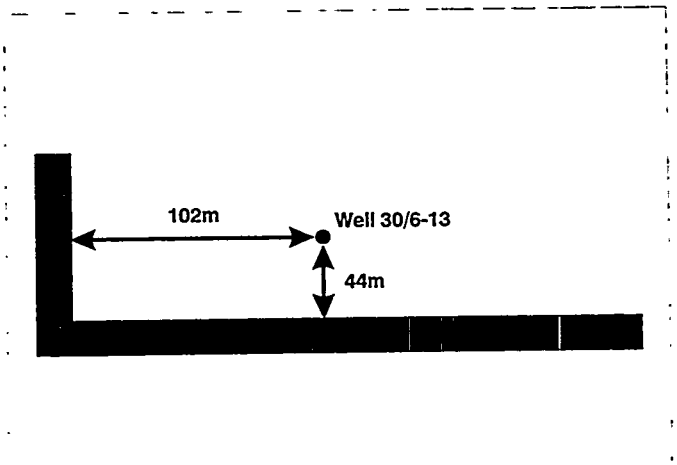

FIGURE 22: Conventional Boundary Prediction - Oseberg 30/6-13 after Clark et al

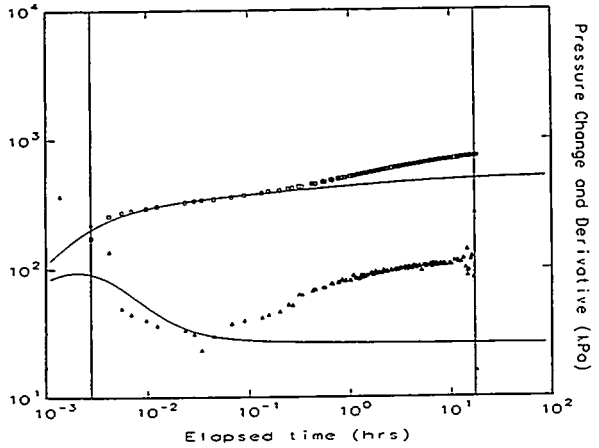

FIGURE 23: Oseberg 30/6-13 - Log-log Type Curve of Test B after Clark et al

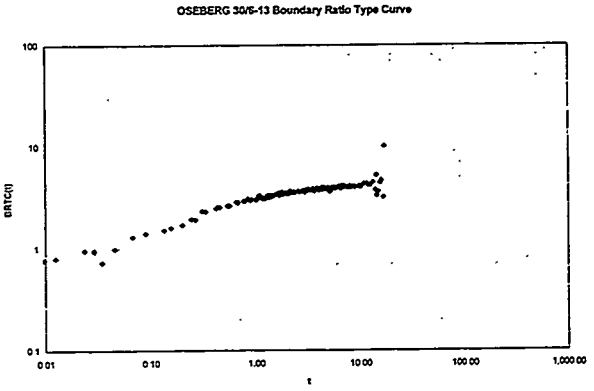

FIGURE 24: Oseberg 30/6-13 - Boundary Ratio Type Curve

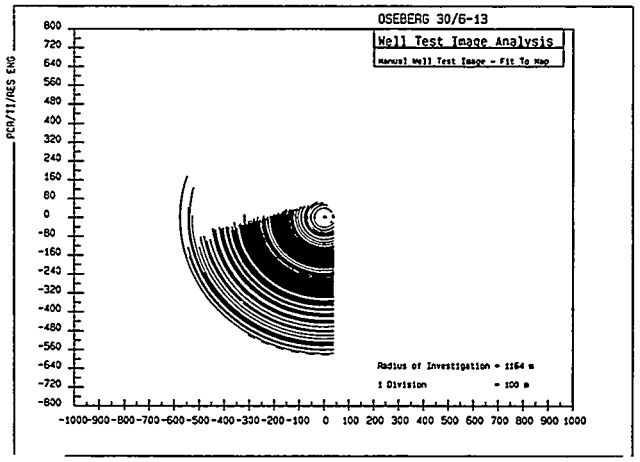

FIGURE 25: Oseberg 30/6-13 - Diagnostic Well Test Image

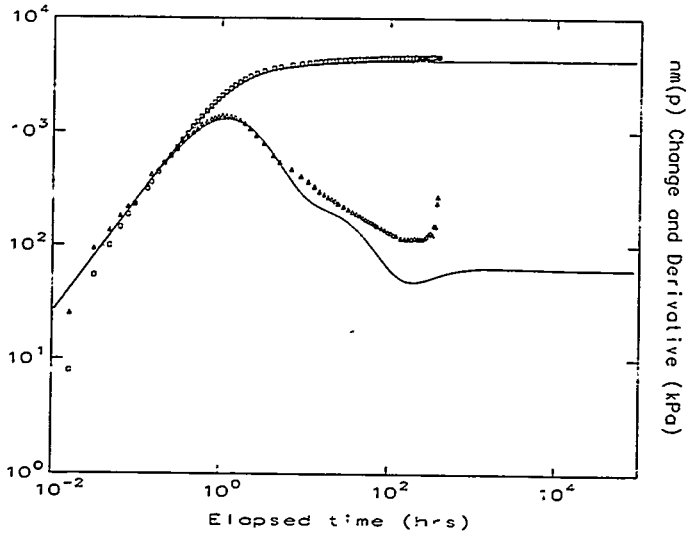

FIGURE 26: Fireweed b-6-A - Log-log Type Curve

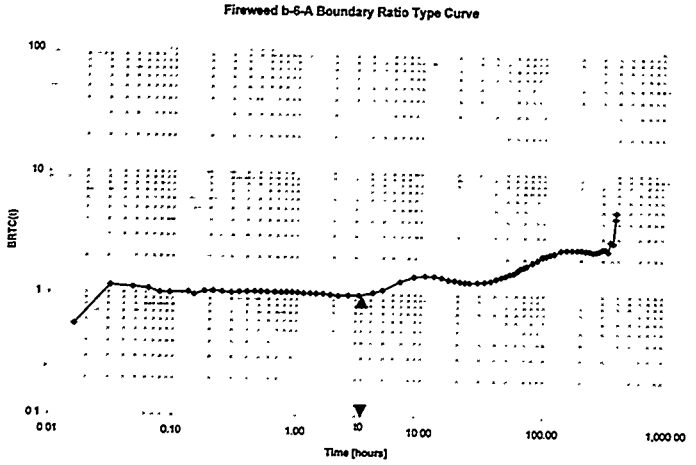

FIGURE 27: Fireweed b-6-A - Boundary Ratio Type Curve

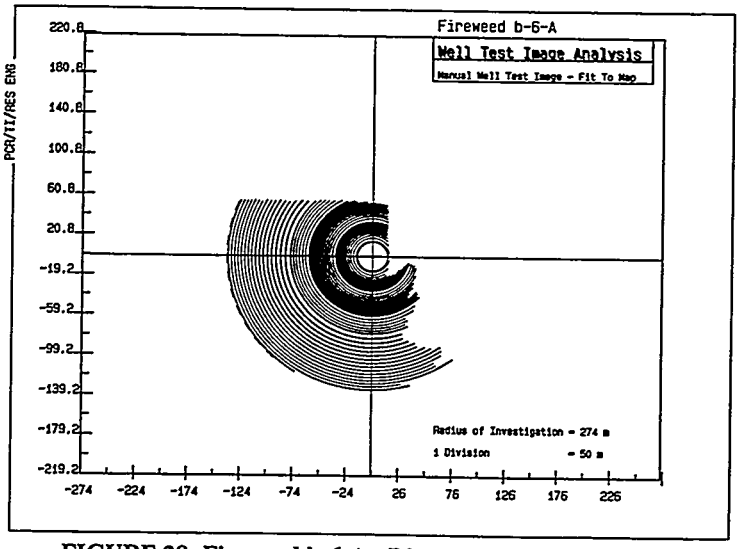

FIGURE 28: Fireweed b-6-A - Diagnostic Well Test Image

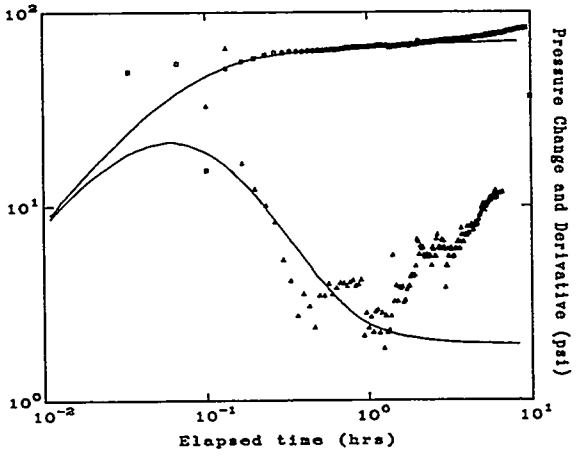

FIGURE 29: Example Well - Log-log Type Curve

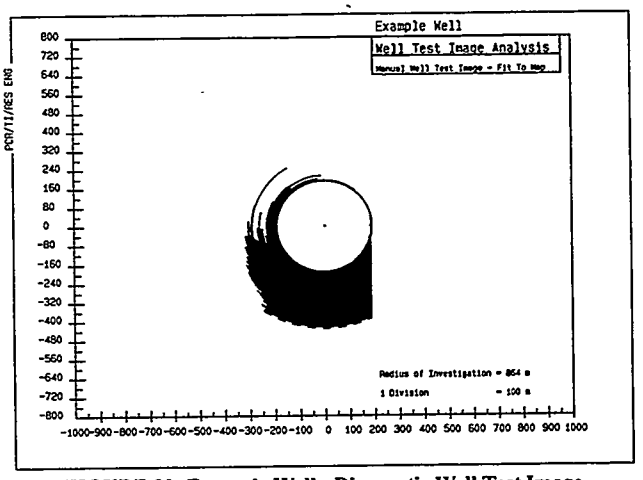

FIGURE 30: Example Well - Diagnostic Well Test Image

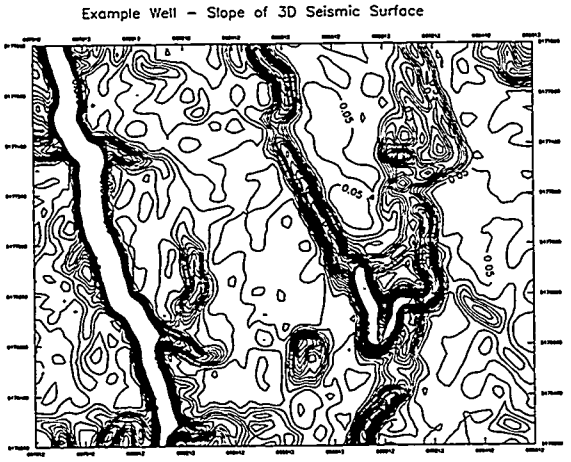

FIGURE 31: Example Well - First Derivative of 3-D Seismic Structure

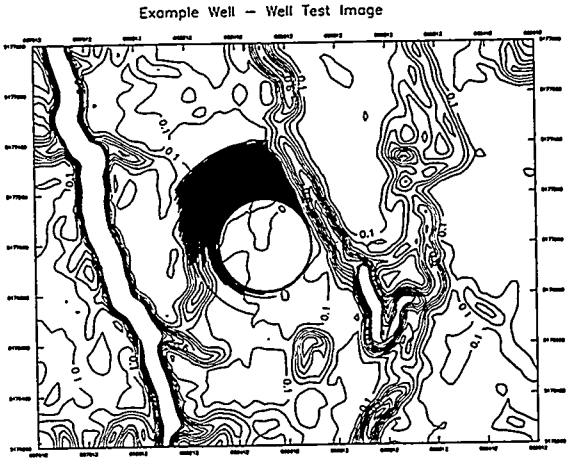

FIGURE 32: Example Well - Reservoir Image

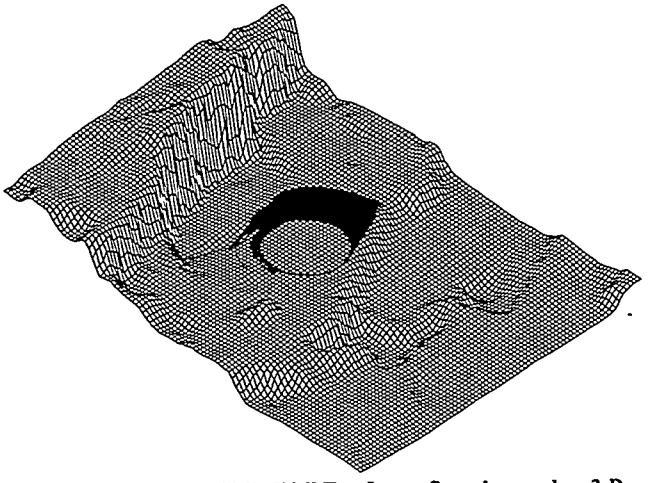

FIGURE 33: Example Well - Well Test Image Superimposed on 3-D Seismic Structure

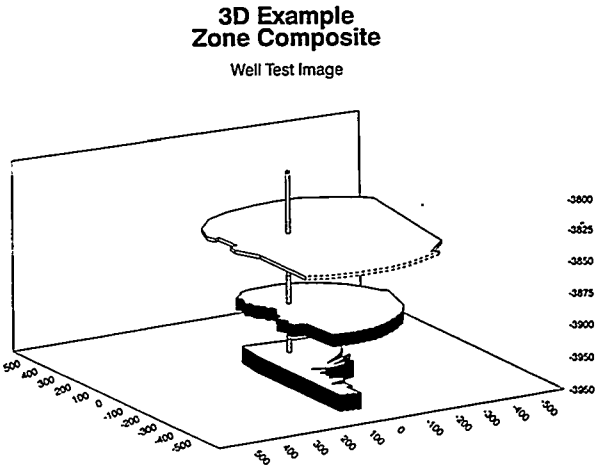

FIGURE 34: Example Well - 3-D Representation of Multiple Tests

An Efficient Permeability Scaling-up Technique Applied to the Discretized Flow Equations

Denise Urgelli
Yu Ding

Institut Français du Pétrole
Rueil Malmaison, France

Abstract

Grid-block permeability scaling-up for numerical reservoir simulations has been discussed for a long time in the literature. It is now recognized that a full permeability tensor is needed to get an accurate reservoir description at large scale. However, two major difficulties are encountered: 1) grid-block permeability cannot be properly defined because it depends on boundary conditions; 2) discretization of flow equations with a full permeability tensor is not straightforward and little work has been done on this subject.

In this paper, we propose a new method, which allows us to get around both difficulties. As the two major problems are closely related, a global approach will preserve the accuracy. So, in the proposed method, the permeability up-scaling technique is integrated in the discretized numerical scheme for flow simulation. The permeability is scaled-up via the transmissibility term, in accordance with the fluid flow calculation in the numerical scheme. A finite-volume scheme is particularly studied, and the transmissibility scaling-up technique for this scheme is presented.

Some numerical examples are tested for flow simulation. This new method is compared with some published numerical schemes for full permeability tensor discretization where the full permeability tensor is scaled-up through various techniques. Comparing the results with fine grid simulations shows that the new method is more accurate and more efficient.

I. Introduction

Reservoir heterogeneity can be described using geostatistical models. But these models generate the heterogeneity on million fine grid blocks, which leads to prohibitive computational costs for reservoir simulations. In order to reduce the number of grid blocks, averaging techniques are needed to scale-up the fine scale permeabilities to the larger scales appropriate for flow simulations and engineering calculations.

Generally, when the principal flow direction is not parallel to the grid-block axes, the effective permeability must be represented as a full tensor to capture the flow properties of the system. But this scaling-up procedure leads to two difficulties: 1) grid-block permeability cannot be properly defined because it depends on boundary conditions; 2) discretization of flow equations with a full permeability tensor is not straightforward. One of the solution is using a global approach to improve the accuracy.

Nowadays, more and more authors recommend the use of internodal permeabilities calculated at the center of the interface and not at the center of block. This calculation is equivalent to the calculation of transmissibilities, once the numerical scheme is fixed. Scaling-up of the transmissibility is more accurate than scaling-up of the permeability because the transmissibility is calculated directly with the fine scale permeability. Furthermore, reservoir simulators are incorporating as input the transmissibilities from each block to each of its neighbours.

The purpose of this paper is to present a new procedure for computing the equivalent transmissibility in the discretized flow equations. An application of this technique to a finite-volume type numerical scheme is detailed. In Section II, we give a non exhaustive review of scaling-up of full permeability tensor and discuss the different methods for the computation of transmissibilities. Then we present a new procedure to scale-up the transmissibility for a finite-volume scheme in Section III. Finally, we compare the results of the transmissibility scaling-up and the permeability scaling-up by two examples.

II. Review of scaling-up technique for single phase flow

II.1 Permeability scaling-up

The determination of the effective permeability in grid blocks has been discussed for a long time in the literature (*Warren and Price,* 1961). It is now recognized that a full block permeability tensor (*Bamberger*, 1977; *Durlofsky*, 1991; *Gautier and Noetinger*, 1994; *Guerillot et al.*, 1989; *Guerillot*, 1988; *Pickup and Sorbie*, 1994; *Samier*, 1990; *Wang et al.*) is needed to get an accurate reservoir description. In this section, several methods currently used are reviewed, and the advantages and disadvantages of these methods are analyzed.

Bamberger (1977) proposed to define the equivalent block permeability using an energy criterion. The equivalent permeability is determined using a bilinear form of the variational formula associated to the elliptic operator: $A = -div[k\nabla]$ and the bilinear form associated to the elliptic operator: $\tilde{A} = -div[K_{eq}\nabla]$. This method is based on the fact that the work realized by the viscous force in the heterogeneous media and in the equivalent homogeneous media must be equal. The energy criterion presents an immediate physical sense. This method is also studied by *Njifenjou* (1993, 1994).

Another numerical approach to obtain a full tensor consists of using linear boundary conditions (*Guerillot,* 1988, 1989). A pressure gradient is imposed in the flow direction and a linear pressure in the two other opposite faces. This method allows to construct a non-symmetrical permeability tensor. This type of condition is equivalent to putting the block in a uniform large scale flow. This method takes into account the cross flow term, but it may lead to overestimating the grid-block permeability in some cases (*Galli et al.,* 1996).

The most successful approach to the computation of equivalent permeability tensor consists of using a periodic boundary condition (*Durlofsky* 1991). The permeability tensor is determined using a pressure gradient in the x-direction to obtain K_{eq}^{xx} and K_{eq}^{xy} and a pressure gradient in the y-direction to obtain K_{eq}^{yx} and K_{eq}^{yy}. This method is exact for infinitely repeated permeability structures. Periodic boundary conditions were also adopted by *Pickup and Sorbie* (1994) for their studies.

The periodic boundary condition was also applied by *Gautier and Noetinger* (1994) to the renormalization scaling-up technique (tensorial renormalization). The renormalization method was introduced by *King* (1989). The scaled-up permeability is calculated by a series of successive aggregations. *King* computes the permeability of an elementary cell of four meshes (in 2-D) with a finite difference approximation and with standard no flow boundary conditions. This method can be improved by the simplified renormalization where the general idea is to group the cells only two by two and to calculate the permeability of the cell pairs by applying the harmonic mean if the cells are in series, or the arithmetic mean if the cells are in parallel (*Le Loc'h,* 1987; *Kruel Romeu,* 1994). But the effective permeability is diagonal. If the non-diagonal terms are necessary, it is important to use the tensorial renormalization.

II. 2. Transmissibility scaling-up

The scaled-up block permeability will be integrated in the transmissibility terms in a numerical scheme for flow simulation on coarse grid blocks. However, it is difficult to determine accurately the transmissibility from the block permeability. Usually, the harmonic average of the block permeability is used for the transmissibility calculation (*Kruel Romeu and Noetinger,* 1995), but using the harmonic average might cause a loss of precision for 2-D problem. So, several authors proposed to directly scale-up the transmissibility from the fine grid heterogeneity (*White and Horne* , 1987; *Palagi,* 1992, 1993; *Kruel Romeu and Noetinger,* 1995; *Peaceman,* 1996).

White and Horne (1987) seem to be the first authors who considered the scaling-up of transmissibilities between grid blocks rather than the equivalent permeabilities of a grid block. They scaled-up the transmissibility on a global domain, which included all the fine grid blocks. Several boundary conditions are imposed on the whole domain to evaluate the transmissibility tensor between the connected blocks. The well conditions are particularly considered as one of the boundary conditions. Then the pressures and fluxes from fine scale simulations were

averaged and summed to obtain pressures and fluxes on a coarse scale. Using this pressures and fluxes on a coarse scale and the least square method, they determined macro transmissibilities. As the whole simulation domain is considered with different boundary conditions, the linear system will be solved several times on fine grid scale with all grid blocks, which might be very expensive in terms of computing time.

Palagi (1992) and *Palagi et al.* (1993) presented a scaling-up procedure for the permeability at the interface of Voronoi grid blocks. They used the power law average to calculate the homogenized permeability. The optimum value for the power law coefficient ω obtained by the minimum between the fine grid results and coarse grid results for various value of ω.

Kruel Romeu and Noetinger (1995) presented a numerical method with impermeable boundary conditions on rectangular grid blocks. The impermeable conditions consist of imposing a pressure drop between two opposite faces and no flow boundary on the remaining two faces. The *Kruel Romeu and Noetinger*'s method is equivalent to the calculation of the permeability in a block placed between the two blocks where the transmissibility are calculated.

More recently, *Peaceman* (1996) proposed a transmissibility scaling-up method on corner point geometry. For each coarse blocks, six half block transmissibilities are scaled-up. In a first step, *Peaceman* represents each half block as a rectangular block. To calculate the transmissibility on this rectangular block, he proposed a direct method which consist to use the impermeable boundary conditions and to calculate the flow through the block by solving sets of difference equations for the pressure. Then, he compares this direct method with the renormalization. He found that the renormalization is less accurate and less easy to implement than the direct method.

It is clear that using transmissibility scaling-up can give more accurate results than using permeability scaling-up. However, the *White and Horne*'s method needs to consider a global domain, which is CPU consuming. The other methods, which calculate locally the transmissibility, are limited to finite-difference type numerical scheme and do not fully incorporate the full tensor property. In this paper, we will present a transmissibility scaling-up technique related only to the local grid block for a finite-volume type method with a full tensor discretization.

III. Scaling-up of Transmissibility for a Finite-Volume Scheme

III.1 Finite-Volume Scheme

Consider a two-phase flow problem in 2-D:

$$\frac{\partial}{\partial t}\left(\frac{\Phi S_l}{B_l}\right) = \nabla(\lambda_l k \nabla p) - Q_l$$

where $l = w$ or o indicates the phase, λ is the mobility, and k is a full permeability tensor given by $k = \begin{pmatrix} k^{xx} & k^{xy} \\ k^{yx} & k^{yy} \end{pmatrix}$.

One of the difficulty for the numerical method is the discretization of the elliptic operator $\nabla(\lambda k \nabla p)$ with a full permeability tensor. We present a finite-volume type method for the discretization of this operator. Integrating on a considered grid block *(i,j)* and applying the Gauss divergence theorem (Figure 1), we have:

$$\int_{\Omega} \nabla(\lambda k \nabla p) d\Omega = -\sum_{m=1}^{4} \int_{\Gamma_m} \lambda k \nabla \bar{p}.\bar{n} d\gamma$$

Without loss of generality, we will study the fluid flow calculation through the interface Γ_1:

$$F_1 = \int_{\Gamma_1} \lambda k \nabla \bar{p}.\bar{n} d\gamma = \lambda_{i+1/2,j} \int_{Y_1}^{Y_2} (k^{xx} \frac{\partial p}{\partial x} + k^{xy} \frac{\partial p}{\partial y}) dy$$
$$= \lambda_{i+1/2,j} (F_{1a} + F_{1b})$$

where $F_{1a} = \int_{Y_1}^{Y_2} k^{xx} \frac{\partial p}{\partial x} dy$ represents the fluid flow through the interface Γ_1 by a force in x-direction and $F_{1b} = \int_{Y_1}^{Y_2} k^{xy} \frac{\partial p}{\partial y} dy$ represents the fluid flow through this interface by a force in y-direction. The last one is also called the cross flow for an uniform grid that $\Delta x = Cte$ and $\Delta y = Cte$. These two terms can be approximated by:

$$F_{1a} = \frac{\Delta y}{\Delta x} k^{xx}_{i+1/2,j} (p_{i+1,j} - p_{i,j})$$

and

$$F_{1b} = \frac{1}{4} k^{xy}_{i+1/2,j} (p_{i,j+1} + p_{i+1,j+1} - p_{i,j-1} - p_{i+1,j-1})$$

Finally, the fluid flow through the interface Γ_1 is calculated by:

$$F_1 = \lambda_{i+1/2,j} (T^{xx}_{i+1/2,j} (p_{i+1,j} - p_{i,j}) + \frac{1}{4} T^{xy}_{i+1/2,j} (p_{i,j+1} + p_{i+1,j+1} - p_{i,j-1} - p_{i+1,j-1}))$$

From this discretization, we observe that $T^{xx}_{i+1/2,j} = \frac{\Delta y}{\Delta x} k^{xx}_{i+1/2,j}$ represents the transmissibility (permeability) between the blocks *(i,j)* and *(i+1,j)* and $T^{xy}_{i+1/2,j} = k^{xy}_{i+1/2,j}$ represents the cross transmissibility (permeability) between these two blocks. However, one of the difficulty is the determination of the transmissibility (permeability) at the interface, if the permeability is known on the grid block. In homogeneous media, these terms are well defined. But, in heterogeneous media, the interface permeability $k^{xx}_{i+1/2,j}$ or $k^{xy}_{i+1/2,j}$ are usually

unknown. To get an accurate transmissibility formula, one of the possibility is to calculate these terms directly from the scaling-up procedure.
For the fluid flow at the interface Γ_2, it can be calculated by:

$$F_2 = \lambda_{i,j+1/2}(T^{yy}_{i,j+1/2}(p_{i,j+1} - p_{i,j}) + \frac{1}{4}T^{yx}_{i,j+1/2}(p_{i+1,j} + p_{i+1,j+1} - p_{i-1,j+1} - p_{i-1,j}))$$

where $T^{yy}_{i,j+1/2}$ represents the transmissibility between the blocks *(i,j)* and *(i,j+1)* and $T^{yx}_{i,j+1/2}$ represents the cross transmissibility between these two blocks.
A complete discretization formula is given in Appendix 1.

III. 2 Transmissibility Scaling-up on a shifted block

A transmissibility scaling-up method was proposed by *White and Horne* (1987) for this kind of scheme. But their method needs to solve several linear systems in the whole domain with millions of fine grid blocks. So, it is very time consuming. In this section, we propose to scale-up the transmissibility which depends only on the local heterogeneity. The principle of the proposed technique is similar to the calculation of a full block permeability tensor, but the considered block is not the coarse grid block. The block is shifted. To calculate the transmissibility related to the flow in the *x*-direction, a shifted block is used as shown in Figure 2a. With a given scaling-up procedure, a permeability tensor $k_{i+1/2,j} = \begin{pmatrix} k^{xx}_{i+1/2,j} & k^{xy}_{i+1/2,j} \\ k^{yx}_{i+1/2,j} & k^{yy}_{i+1/2,j} \end{pmatrix}$ can be determined on this block, where $k^{xx}_{i+1/2,j}$ represents the permeability on the *x*-direction, and $k^{xy}_{i+1/2,j}$ represents the cross permeability on this direction. From this formula, we can determine the transmissibility terms for the flow in the *x*-direction for the finite-volume scheme with $T^{xx}_{i+1/2,j} = \frac{\Delta y}{\Delta x}k^{xx}_{i+1/2,j}$ and $T^{xy}_{i+1/2,j} = k^{xy}_{i+1/2,j}$.

In the same way, we can determine the transmissibility terms related to the flow in the *y*-direction. Calculating the permeability tensor $k_{i,j+1/2} = \begin{pmatrix} k^{xx}_{i,j+1/2} & k^{xy}_{i,j+1/2} \\ k^{yx}_{i,j+1/2} & k^{yy}_{i,j+1/2} \end{pmatrix}$ on the shifted block in the *y*-direction (Figure 2b), the transmissibility terms are $T^{yy}_{i,j+1/2} = \frac{\Delta x}{\Delta y}k^{yy}_{i,j+1/2}$ and $T^{yx}_{i,j+1/2} = k^{yx}_{i,j+1/2}$.

In the examples presented below, we use, for the transmissibility scaling-up procedure, the periodic boundary conditions which was successfully used for block permeability scaling-up. In fact, on the shifted block which can be refined by the user for a good affectation of fine scale heterogeneities, a pressure gradient is imposed on the faces perpendicular to the flow direction and the flow rates in the same direction are equal. On the other faces, pressures and

flow rates on opposite boundaries are equal. This can be expressed as follows (Figure 1) for pressure gradient in x-direction:

$$\begin{cases} p(x, y=0) = p(x, y=L) \text{ on } \Gamma_2 \text{ and } \Gamma_4 \\ q(x, y=0) = q(x, y=L) \text{ on } \Gamma_2 \text{ and } \Gamma_4 \\ p(x=0, y) = p(x=L, y) - Cte \text{ on } \Gamma_3 \text{ and } \Gamma_1 \\ q(x=0, y) = q(x=L, y) \text{ on } \Gamma_3 \text{ and } \Gamma_1 \end{cases}$$

Thus, the pressure and consequently the flow rate on each refined blocks are calculated using a 5-point scheme and an iterative solver. Imposing a pressure gradient Δp_x in the x-direction for a shifted block as shown in Figure 2a, the transmissibility (permeability) $T^{xx}_{i+1/2,j}$ can be determined by:

$$k^{xx}_{i+1/2,j} = \frac{Nx_r \Delta x_r \sum_{i_1=1}^{Nx_r} \sum_{j_1=1}^{Ny_r} q^{xx}_{i_1,j_1}}{\Delta p Ny_r \Delta y_r}.$$

Imposing a pressure gradient Δp_y in the y-direction for the same block, we can determine the cross transmissivity (permeability) term $T^{xy}_{i+1/2,j}$:

$$k^{xy}_{i+1/2,j} = \frac{Nx_r \Delta x_r \sum_{i_1=1}^{Nx_r} \sum_{j_1=1}^{Ny_r} q^{yy}_{i_1,j_1}}{\Delta p Ny_r \Delta y_r}$$

where Nx_r, Ny_r= number of the refined blocks in the x-, y-direction, respectively,

Δx_r, Δy_r= size of the refined blocks in the x-, y-direction, respectively.

To calculate $k^{yy}_{i,j+1/2}$ and $k^{yx}_{i,j+1/2}$, we use the same procedure for the shifted block as shown in Figure 2b.

It must be mentioned that the scaled-up transmissibility might strongly depend on the boundary condition as in the case of scaling-up the block permeability. But the transmissibility scaling-up can be considered as an improvement with respect to the block permeability scaling-up, since the transmissibility will not be determined again from the scaled-up block permeability. Moreover, we think that the effect of boundary condition might be less sensitive at the field scale and the flow simulation at the reservoir scale might be approximated by considering two kinds of flow pattern, as discussed by *Ding* (1995).

IV. Numerical Results

Two numerical examples are presented to compare this new transmissibility scaling-up method and several published permeability scaling-up methods. For the transmissibility scaling-up procedure, we use the periodic boundary condition (*Durlofsky*, 1991). For

permeability scaling-up, we use the periodic boundary condition (*Durlofsky*, 1991) and the optimized linear boundary condition (*Bamberger*, 1977). For the permeability scaling-up, the transmissibilities are calculated using an harmonic average for block permeability as presented in Appendix 1.

The general data is given in Table 1. To validate the proposed method, the flow is simulated using the fine scale isotropic permeability distribution. The fine scale simulation results are assumed to be the reference solution.

Example 1

The permeability distribution is given in Figure 3. This heterogeneity field is well-known and was studied by several authors (*Samier* 1990, *White and Horne* 1987, *Wang et al.*). They showed the necessary of using a full permeability tensor. Here, we will compare the transmissibility scaling-up method and some permeability scaling-up methods.

Two wells, one injector and one producer are placed at the corner of this field. Water is injected into the oil reservoir with a fixed flow rate. The results of water-cut curves are presented in Figure 4 and the results of saturation distribution are presented in Figure 5. All the coarse grid simulation results are very similar. But, we can observe that scaling-up of transmissibility, which uses periodic boundary conditions, gives slightly better results than the scaling-up of permeability. In this case, the improvement using transmissibility scaling-up is not significant. But, it proves that scaling-up of transmissibility is a good initiative.

Example 2

A field with parallel barriers of permeability is used as shown in Figure 6 with a strong permeability contrast. The fine grid has 99x99 grid blocks, and the coarse grid has 11x11 grid blocks. Water is injected into an oil reservoir. In this example, we have one injector and three producers. For the fine grid simulation, it is clear that the #3 producer produces the most because it is connected to the injector by a permeable layer, and the #2 producer produces less because it is separated by several "impermeable" zones. For coarse grid simulation, if the permeability is scaled-up on grid blocks, the phenomenon resulting from anisotropy might be homogenized in the transmissibility calculation. Figure 7 shows the water-cut. Even though using the transmissibility scaling-up gives the results far from the fine grid simulation, they are much better than using the permeability scaling-up method. Figure 8 and Figure 9 represent the saturation distribution and the pressure distribution, respectively for the fine grid and the coarse grid simulations with different scaling-up methods. It is clear that using transmissibility scaling-up gives the best result, which represents the same trend as fine grid simulation. The improvement of using transmissibility scaling-up is significant.

V. Conclusion

The scaling-up of transmissibility and permeability are discussed. Scaling-up of transmissibility is more accurate than scaling-up of permeability. A new transmissibility scaling-up procedure, which uses shifted blocks to calculate locally the transmissibility, is proposed for a finite-volume type numerical scheme with a full permeability tensor.

Some numerical examples are presented. The results show that using the transmissibility scaling-up improves the coarse grid simulation accuracy. In some cases, like a stratified field, this improvement is significant.

Appendix 1. Discretization of Elliptic Operator with a Full Permeability Tensor

According to the discussion in the section III.1, the elliptic operator can be discretized as:

$$\begin{aligned}\Delta x\Delta y\, div(k\nabla p) = {} & \lambda_{i+1/2,j}\Big(T^{xx}_{i+1/2,j}(p_{i+1,j}-p_{i,j})+ \\ & \qquad \tfrac{1}{4}T^{xy}_{i+1/2,j}(p_{i,j+1}+p_{i+1,j+1}-p_{i,j-1}-p_{i+1,j-1})\Big) \\ & +\lambda_{i,j+1/2}\Big(T^{yy}_{i,j+1/2}(p_{i,j+1}-p_{i,j})+ \\ & \qquad \tfrac{1}{4}T^{yx}_{i,j+1/2}(p_{i+1,j}+p_{i+1,j+1}-p_{i-1,j+1}-p_{i-1,j})\Big) \\ & +\lambda_{i-1/2,j}\Big(T^{xx}_{i-1/2,j}(p_{i-1,j}-p_{i,j})- \\ & \qquad \tfrac{1}{4}T^{xy}_{i-1/2,j}(p_{i,j+1}+p_{i-1,j+1}-p_{i,j-1}-p_{i-1,j-1})\Big) \\ & +\lambda_{i,j-1/2}\Big(T^{yy}_{i,j-1/2}(p_{i,j-1}-p_{i,j})- \\ & \qquad \tfrac{1}{4}T^{yx}_{i,j-1/2}(p_{i+1,j}+p_{i+1,j-1}-p_{i-1,j-1}-p_{i-1,j})\Big)\end{aligned}$$

In this formula, λ represents the mobility. It takes an upstream value according to the flow direction at the interface. For example,

$$\lambda_{i+1/2,j}=\begin{cases}\lambda_{i+1,j} & If\ \delta_{i+1/2,j}>0\\ \lambda_{i,j} & If\ \delta_{i+1/2,j}\le 0\end{cases}$$

with $\delta_{i+1/2,j}=T^{xx}_{i+1/2,j}(p_{i+1,j}-p_{i,j})+\frac{1}{4}T^{xy}_{i+1/2,j}(p_{i,j+1}+p_{i+1,j+1}-p_{i,j-1}-p_{i+1,j-1})$

This scheme is conservative, because the fluid flux through an interface is always the same for the discretization of the block in both sides ($\delta_{i+1/2,j}=\delta_{i\to i+1,j}=\delta_{i+1\to i,j}$).

In section III, we present a scaling-up procedure to calculate these transmissibility terms. However, if the block permeability is scaled-up, these transmissibility terms should be calculated depending on the block permeability value. For this case, we propose to use the harmonic average for the calculation, which is calculated by:

$$T^{xx}_{i+1/2,j}=\frac{\Delta y}{\Delta x}\frac{2k^{xx}_{i+1,j}k^{xx}_{i,j}}{k^{xx}_{i,j}+k^{xx}_{i+1,j}}$$

for the cross term $T^{xy}_{i+1/2,j}$ is calculated by:

$$T^{xy}_{i+1/2,j} = \frac{1}{2}\left[\frac{4k^{xy}_{i,j+1}k^{xy}_{i,j-1}k^{xy}_{i,j}}{k^{xy}_{i,j+1}k^{xy}_{i,j} + k^{xy}_{i,j+1}k^{xy}_{i,j-1} + k^{xy}_{i,j}k^{xy}_{i,j-1}} + \frac{4k^{xy}_{i+1,j+1}k^{xy}_{i+1,j-1}k^{xy}_{i+1,j}}{k^{xy}_{i+1,j+1}k^{xy}_{i+1,j} + k^{xy}_{i+1,j+1}k^{xy}_{i+1,j-1} + k^{xy}_{i+1,j}k^{xy}_{i+1,j-1}}\right]$$

This formula is used in the examples for the comparison with the block permeability scaling-up.

It cannot be written in the general standard nine-point scheme form (*Yanosik and McCracken*, 1979). However, for the single-phase flow modelling, the discretization formula can be written in a standard form, but it is a non-symmetrical scheme:

$$\begin{aligned}
-\int_{\partial\Gamma} k\nabla\vec{p}.\vec{n}.d\gamma \approx & \left[T^{xx}_{i+1/2,j} + \frac{T^{yx}_{i,j+1/2}}{4} - \frac{T^{yx}_{i,j-1/2}}{4}\right]\left(p_{i+1,j} - p_{i,j}\right) \\
& + \left[T^{xx}_{i-1/2,j} - \frac{T^{yx}_{i,j+1/2}}{4} + \frac{T^{yx}_{i,j-1/2}}{4}\right]\left(p_{i-1,j} - p_{i,j}\right) \\
& + \left[T^{yy}_{i,j+1/2} + \frac{T^{xy}_{i+1/2,j}}{4} - \frac{T^{xy}_{i-1/2,j}}{4}\right]\left(p_{i,j+1} - p_{i,j}\right) \\
& + \left[T^{yy}_{i,j-1/2} - \frac{T^{xy}_{i+1/2,j}}{4} + \frac{T^{xy}_{i-1/2,j}}{4}\right]\left(p_{i,j-1} - p_{i,j}\right) \\
& + \left[\frac{T^{xy}_{i+1/2,j}}{4} + \frac{T^{yx}_{i,j+1/2}}{4}\right]\left(p_{i+1,j+1} - p_{i,j}\right) \\
& + \left[-\frac{T^{xy}_{i+1/2,j}}{4} - \frac{T^{yx}_{i,j-1/2}}{4}\right]\left(p_{i+1,j-1} - p_{i,j}\right) \\
& + \left[-\frac{T^{xy}_{i-1/2,j}}{4} - \frac{T^{yx}_{i,j+1/2}}{4}\right]\left(p_{i-1,j+1} - p_{i,j}\right) \\
& + \left[\frac{T^{xy}_{i-1/2,j}}{4} + \frac{T^{yx}_{i,j-1/2}}{4}\right]\left(p_{i-1,j-1} - p_{i,j}\right)
\end{aligned}$$

Nomenclature

A = elliptic operator,

B = formation volume factor,

F = flow term,

K_{eq} = effective permeability tensor,

L = length of the shifted block,

Nx_r, Ny_r = number of the refined blocks in the x-,y-direction, respectively,

T = internodal transmissibility,

k = permeability tensor of fine grid block,

n = normal direction,

p = pressure,

Q = well flow rate,

u = Darcy filtration velocity,

Δx, Δy = size of the coarse grid block,

Δx_r, Δy_r = size of the refined block,

μ = fluid viscosity,

λ = mobility,

Φ = porosity,

δ = fluid flux,

Ω = domain,

$\partial\Omega = \Gamma$ = domain boundary,

ω = power law coefficient.

Subscript

i,j = indice of blocks in x-, y- direction, respectively,

o = oil phase,

w = water phase,

x,y = spatial directions.

Acknowledgements

We would like to thank P. Lemonnier and E. Delamaide for their encouragement and critical comment during the writing of this paper.

References

Bamberger, A., 1977, "Approximation des coefficients d'opérateurs elliptiques stables pour la G-convergence", rapport du Centre de Mathématiques Appliquées, École Polytechnique.

Ding, Y., 1995, "Scaling-up in the Vicinity of Wells in Heterogeneous Field", SPE n°29137 presented at the 13th SPE Symposium on Reservoir Simulation, 12-15 Feb., San Antonio, Texas.

Durlofsky, L.J., 1991, "Numerical calculation of equivalent grid block permeability tensors for heterogeneous porous media", Water Ressources Research, v. 27 (5), p. 699-708.

Galli, A., Goblet, P., Griffin, D., Ledoux, E., Le Loc'h, G., Mackay, R., Renard, P., 1996, "Quick upscaling of flow and transport related parameters", Technical Report.

Gautier, Y., Noetinger, B., 1994, "Preferential flow paths detection for heterogeneous reservoirs using a new renormalization technique", 4th European Conference on the Mathematics of Oil Recovery, 7-10 June, Roros, Norway.

Guerillot, D., 1988, "Composition des perméabilités absolues aux échelles intermédiaires pour les gisements d'hydrocarbures hétérogènes; application à un affleurement du Yorkshire; rapport d'avancement, IFP report n°36738.

Guerillot, D., Rudkiewicz, J. L., Ravenne, Ch., Renard, G. ,Galli, A., 1989, "An integrated model for computer aided reservoir description: from outcrop study to fluid flow simulations", presented at the IOR Symposium, Budapest, Hungary.

King, P.R., 1989, "The use of renormalization for calculating effective permeability", Transport in Porous Media, v. 4, p. 37-58.

Kruel Romeu, R., 1994, "Écoulement en milieux hétérogènes : prise de moyenne de perméabilités en régimes permanent et transitoire", PhD thesis, Université Paris VI, France.

Kruel Romeu, R., Noetinger, B., 1995, "Calculation of internodal transmissivities in finite difference models of flow in heterogeneous media", Water Ressources Research, v. 31, p. 943-959.

Le Loc'h, G., 1987, "Etude de la decomposition des perméabilités par des méthodes variationnelles", PhD thesis, Ecole Normale Superieure des Mines de Paris, France.

Njifenjou, A., 1993, "Éléments finis mixtes hybrides duaux et homogénéisation des paramètres pétrophysiques; application à l'étude numérique de l'écoulement en milieux poreux", PhD thesis, Université Paris VI, France.

Njifenjou, A., 1994, "Expression en termes d'énergié pour la perméabilité absolue effective", IFP review, v. 49 (4), p. 345-358.

Palagi, C., 1992, "Generation and application of Voronoi grid to model flow in heterogeneous reservoirs", PhD thesis, Stanford University, California.

Palagi, C. L., Ballin, P. R., Aziz, K., 1993, "The modelling of flow in the heterogeneous reservoirs with Voronoi grid", SPE n°25259 presented at the SPE Symposium on Reservoir Simulation, 28 Feb.-3 March, New Orleans, Louisiana.

Peaceman, D.W., 1996, "Effective transmissibilities of a gridblock by upscaling; why use renormalization?", SPE n°36722 presented at the SPE Annual Technical Conference and Exhibition, 6-9 Oct., Denver, Colorado.

Pickup, G. E., Sorbie, K. S.,1994, "Development and application of a new two phase scale up method based on tensor permeabilities", SPE n°28586 presented at the SPE Annual Technical Conference and Exhibition, 25-28 Sept., New Orleans, Louisiana.

Pickup, G. E., Sorbie, K. S.,1994, "The scale-up of two phase flow using permeability tensors", 4th European Conference on the Mathematics of Oil Recovery, 7-10 June, Roros, Norway.

Samier, P., 1990, "A finite element method for calculating transmissibilities in N-point difference equations using a non diagonal permeability tensor", 2nd European Conference on the Mathematics of Oil Recovery, 11-14 Sept., Arles, France.

Wang, J. T., Daltaban, T. S., Archer, J. S., "The use of permeability tensor in modelling heterogeneous and fractured flow media", SPE n°24503.

Warren, J.E., Price, H.S., 1961 : "Flow in heterogeneous porous media", SPEJ Sept., p. 153-169

White, C. D., Horne, R. N., 1987, Computing absolute transmissibility in the presence of fine scale heterogeneity", SPE n°16011 presented at 9th Symposium on Reservoir Simulation, 1-4 Feb., San Antonio, Texas.

Yanosik, J.L., McCracken, T.A., 1979 : "A nine-point finite difference reservoir simulator for realistic prediction of adverse mobility ratio displacements", SPEJ Agu., p. 253-262.

Figure captions:

Figure 1. Finite-volume scheme (on coarse grid block)

Figure 2. Transmissibility upscaling on shifted blocks

Figure 3. Heterogeneous field in example 1

Figure 4. Water cut for the production well in example 1

Figure 5. Water saturation distribution for example 1

Figure 6. Heterogeneous field in example 2

Figure 7. Water cut curves in example 2

Figure 8. Water saturation distribution for example 2

Figure 9. Pressure distribution for example 2

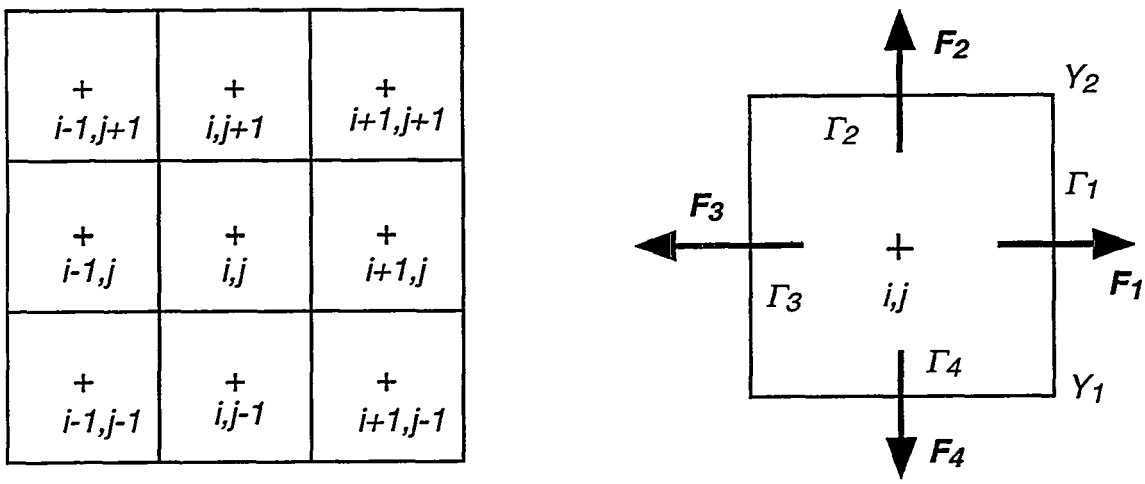

Figure 1. Finite-volume scheme (on coarse grid block)

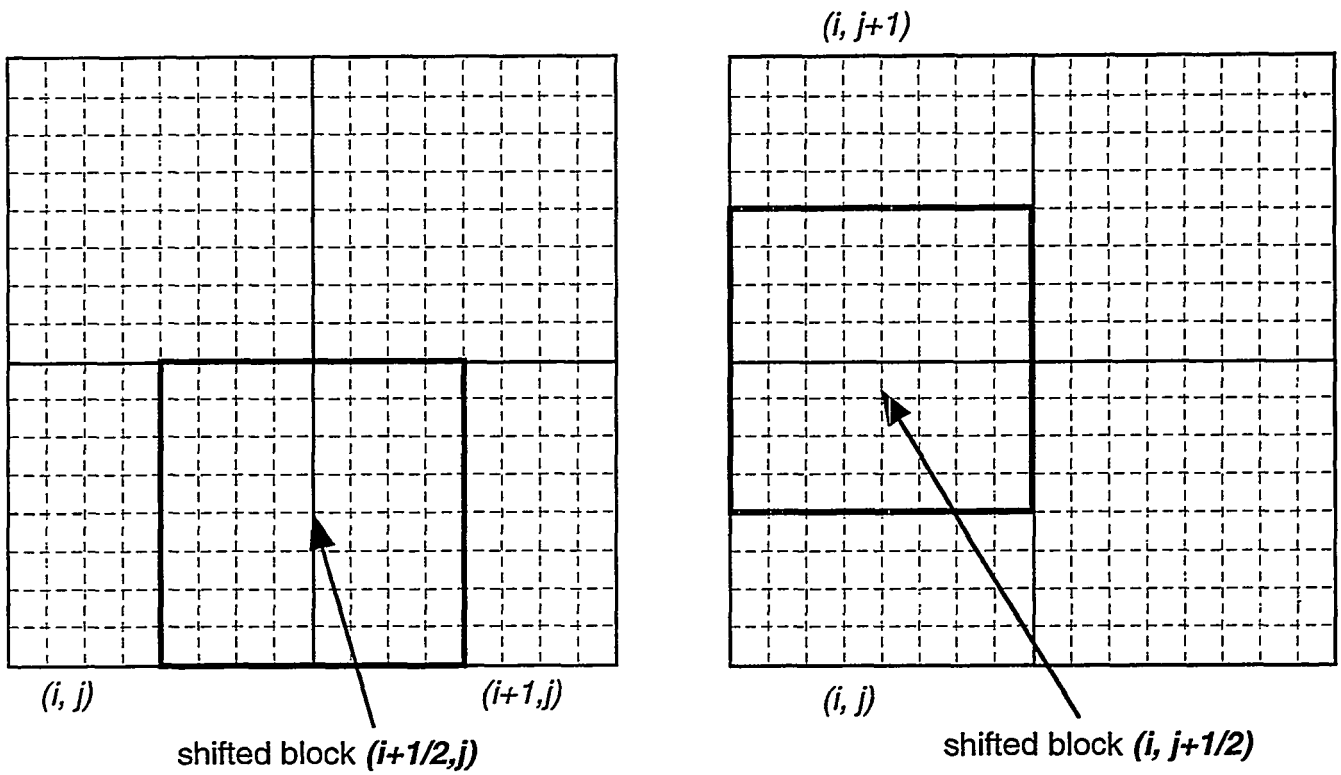

a). Scaling-up in *x*-direction

b). Scaling-up in *y*-direction

Figure 2. Transmissibility scaling-up on shifted blocks

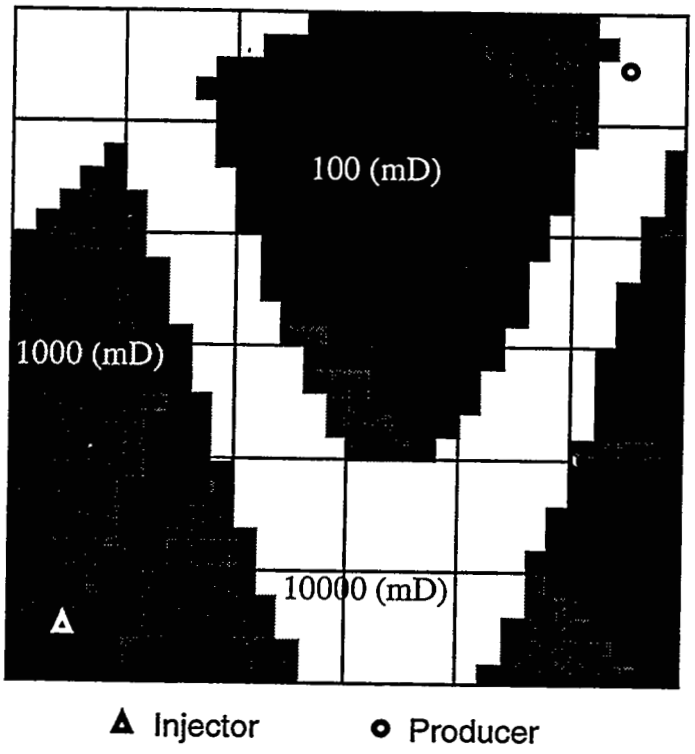

Figure 3. Heterogeneous field in example 1.

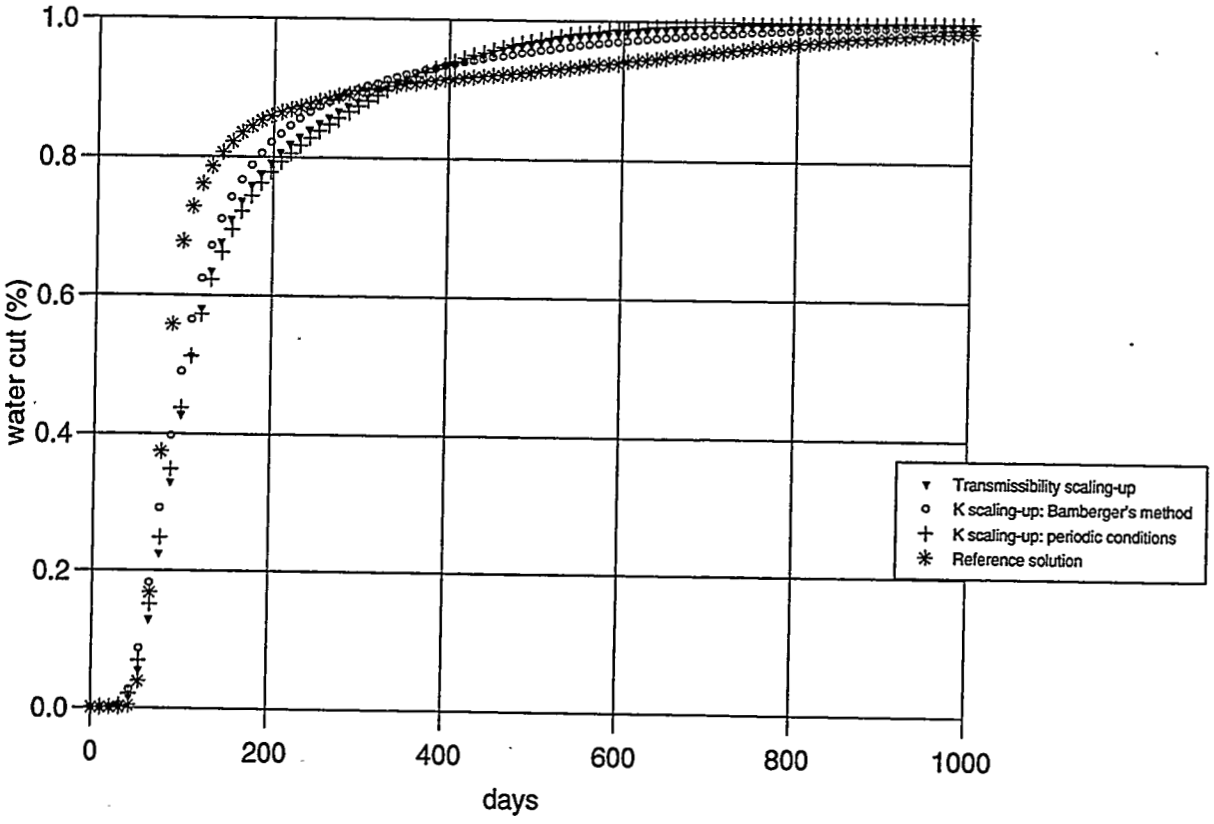

Figure 4. Water cut for production well in example 1.

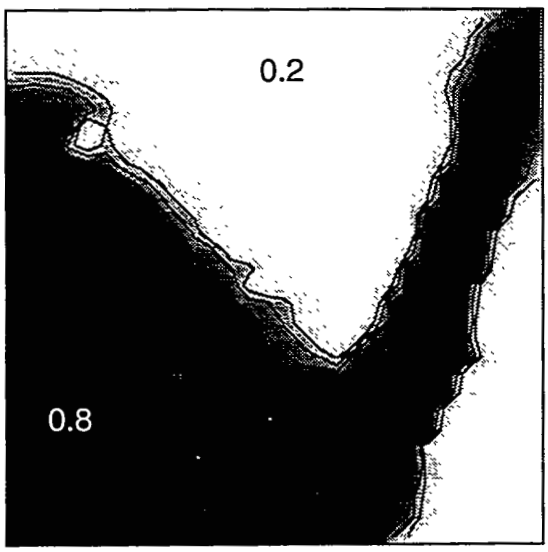

5a). Fine grid simulation

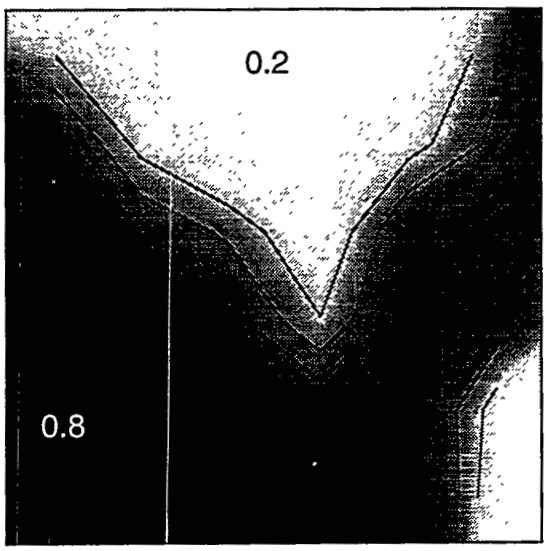

5b). Coarse grid simulation with transmissibility scaling-up

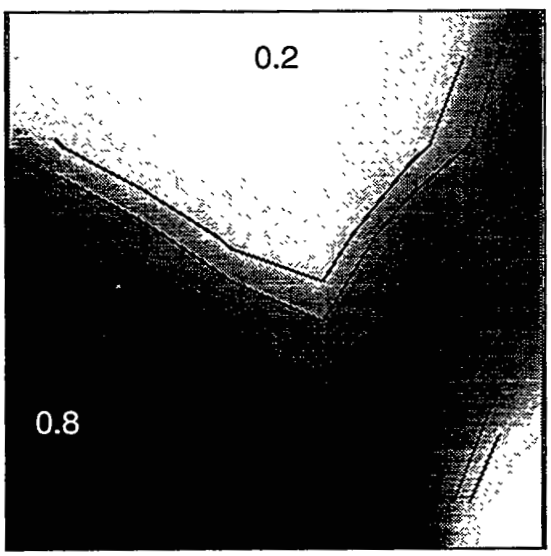

5c). Coarse grid simulation with permeability scaling-up using Bamberger's method

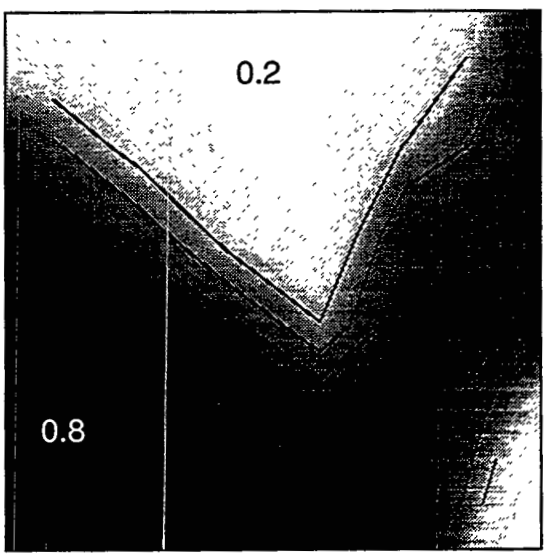

5d). Coarse grid simulation with permeability scaling-up using periodic boundary conditions

Figure 5. Water saturation distribution for example 1

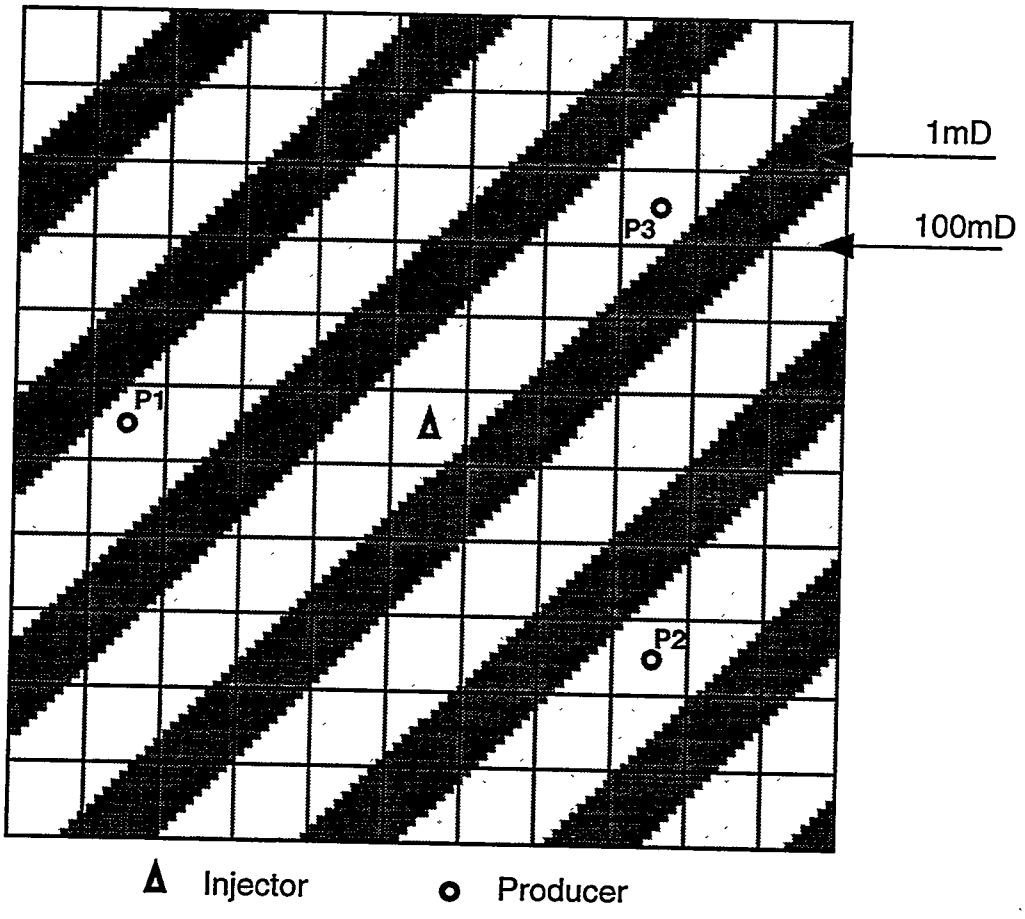

Figure 6. Heterogeneous field in example 2

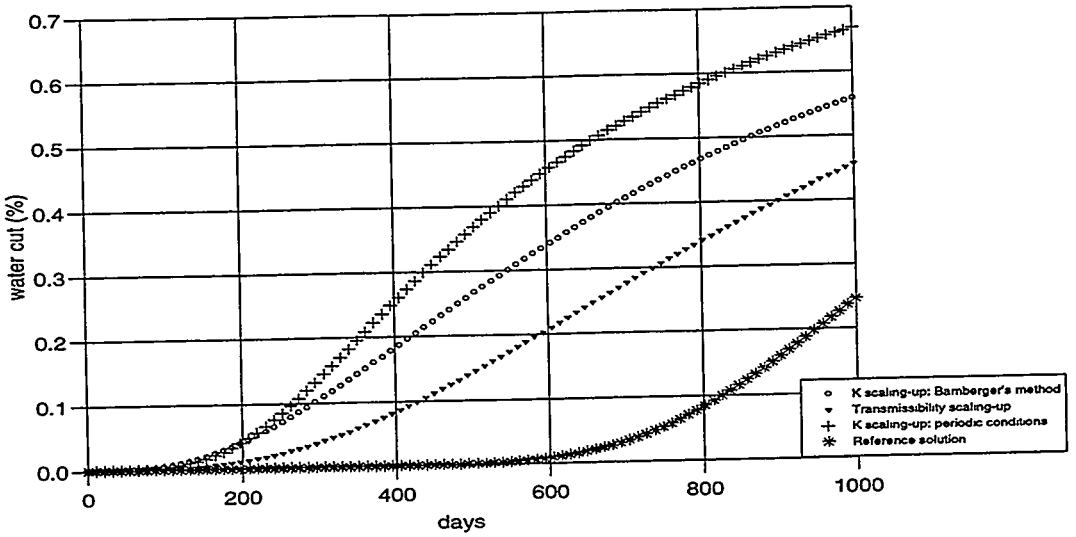

7a). Water cut for the production well P1

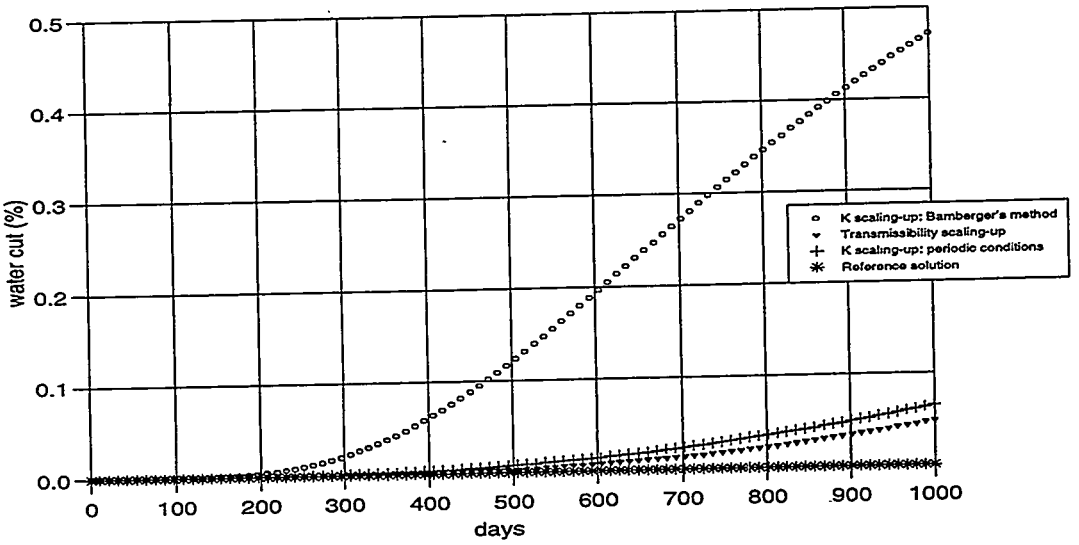

7b). Water cut for the production well P2

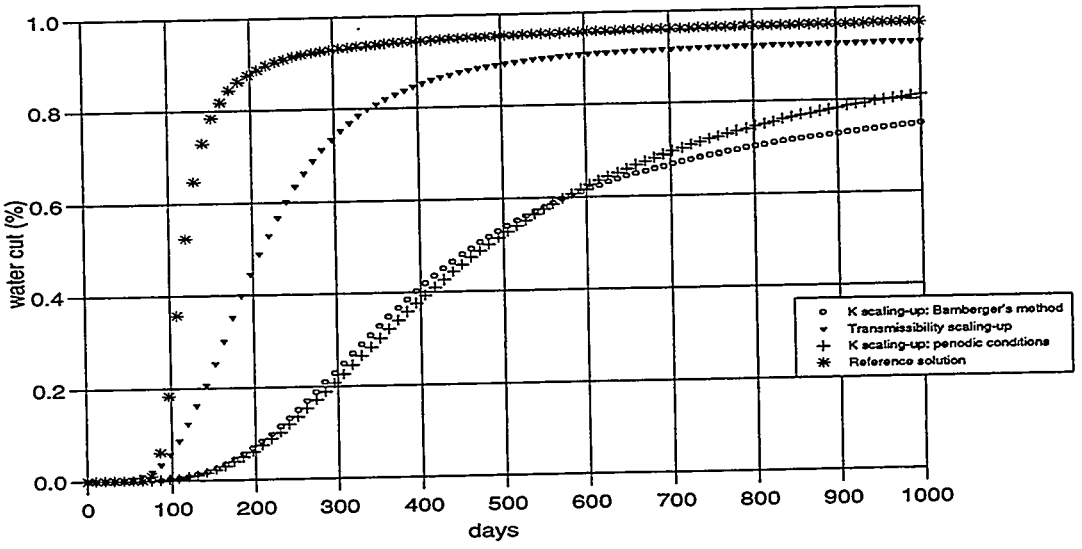

7c). Water cut for the production well P3

Figure 7. Water cut curves in example 2

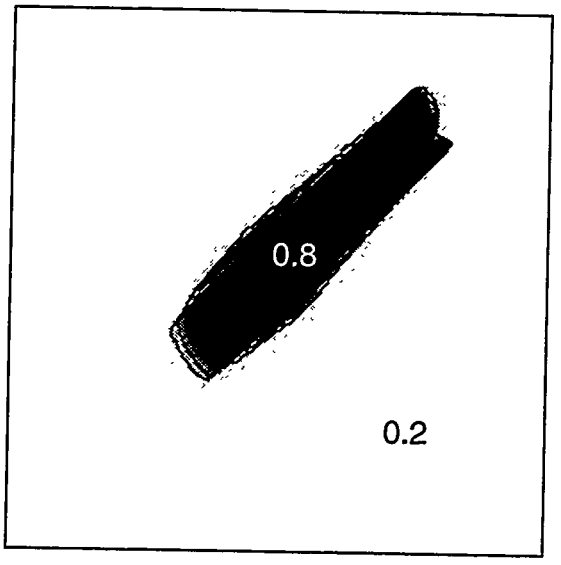

8a). Fine grid simulation

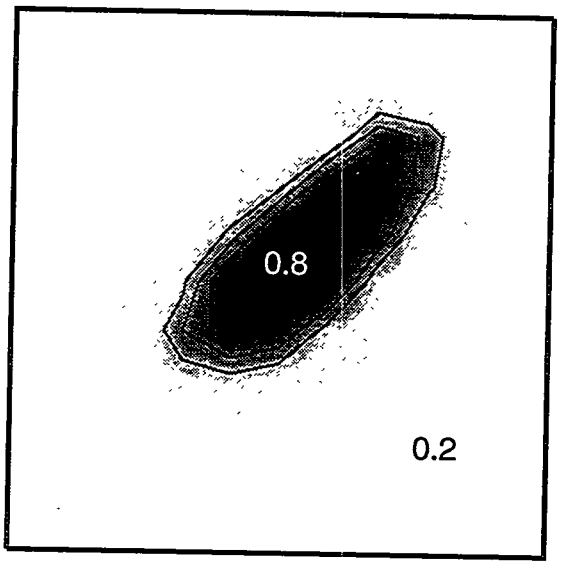

8b). Coarse grid simulation
with transmissibility scaling-up

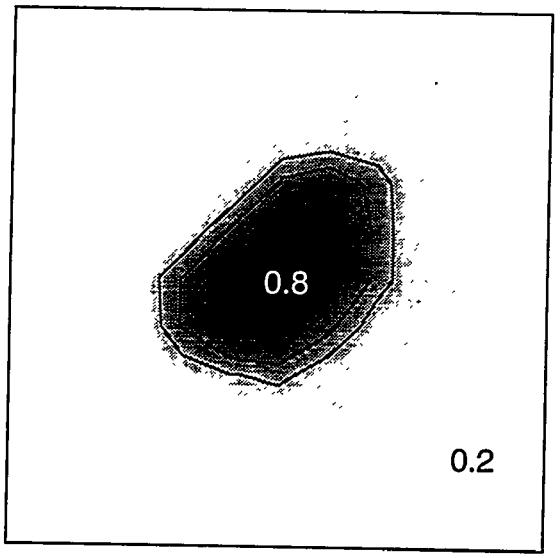

8c). Coarse grid simulation with permeability scaling-up using Bamberger's method

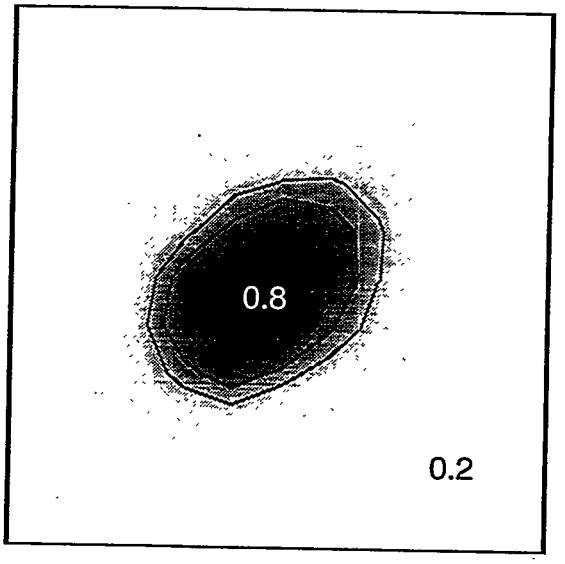

8d). Coarse grid simulation with permeability scaling-up using periodic boundary conditions

Figure 8. Water saturation distribution for example 2

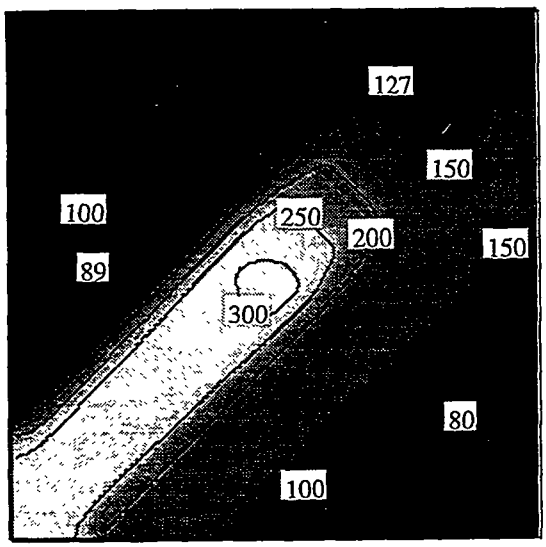

9a). Fine grid simulation

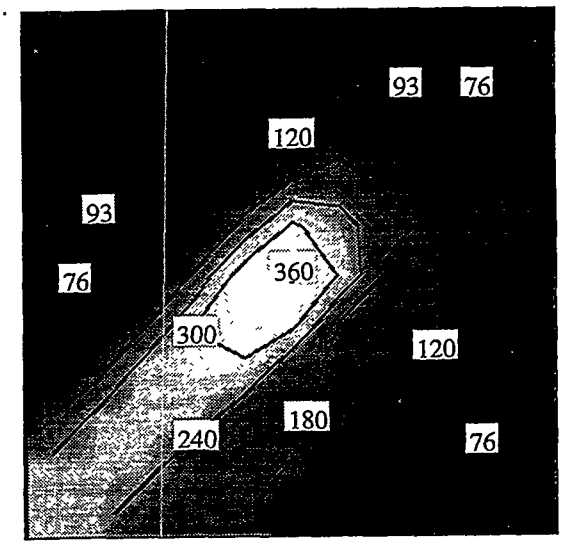

9b). Coarse grid simulation with transmissibility scaling-up

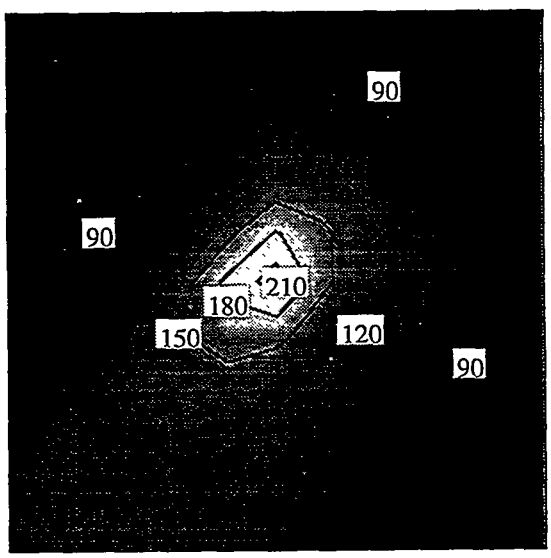

9c). Coarse grid simulation with permeability scaling-up using Bamberger's method

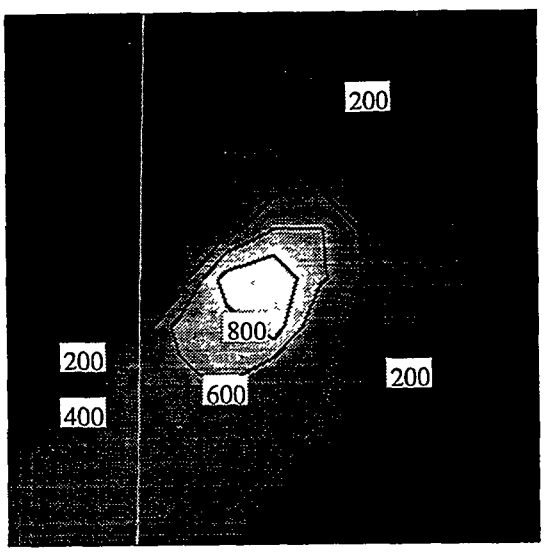

9d). Coarse grid simulation with permeability scaling-up using periodic boundary conditions

Figure 9. Pressure distribution for example 2

Parameter	Input data (S.I. unit)
Injection rate	0.00081 m^3/s
Production well pressure	$7x10^6$ Pa
Oil viscosity	0.001 Pa.s
Water viscosity	0.001 Pa.s
Initial/irreducible water saturation	0.2
Residual oil saturation	0.2
Porosity	0.2
Thickness	1 m
Areal Dimensions	300 m by 300 m for example 1 990 m by 990 m for example 2
Initial pressure	$85x10^5$ Pa

Table 1. Simulation input data

A SIMPLE METHOD TO ESTIMATE INTERWELL AUTOCORRELATION

Jorge O. S. Pizarro
Larry W. Lake
Department of Petroleum and Geosystems Engineering
The University of Texas at Austin

ABSTRACT

The estimation of autocorrelation in the lateral or interwell direction is important when performing reservoir characterization studies using stochastic modeling. This paper presents a new method to estimate the interwell autocorrelation based on parameters, such as the vertical range and the variance, that can be estimated with commonly available data.

We used synthetic fields that were generated from stochastic simulations to provide data to construct the estimation charts. These charts relate the ratio of areal to vertical variance and the autocorrelation range (expressed variously) in two directions. Three different semivariogram models were considered: spherical, exponential and truncated fractal.

The overall procedure is demonstrated using field data. We find that the approach gives the most self-consistent results when it is applied to previously identified facies. Moreover, the autocorrelation trends follow the depositional pattern of the reservoir, which gives confidence in the validity of the approach.

INTRODUCTION

The importance of reservoir characterization methods has been established in the last decade by reservoir studies that are based on stochastic models that account for the heterogeneity of the porous media.

A reliable study depends on prior quantification of the heterogeneity of the reservoir (Srivastava, 1994). The geostatistical approach describes the heterogeneity through averages, variances and autocorrelation. Although it has several advantages, when compared with

deterministic approaches, the confidence in geostatistical modeling will be a strong function of how well the input data represent reality. The horizontal autocorrelation, especially, is among the most critical of the parameters to be estimated; we propose a new procedure to estimate it in this paper. The method uses serial data from several vertical wells, as would exist from wells in mature projects.

MOTIVATION

There are in the literature several works stressing that the estimation of horizontal autocorrelation is important in achieving a good reservoir description. Lucia and Fogg (1990) stated that the principal difficulty in reservoir characterization is estimating the spatial distribution of petrophysical properties between vertical wellbores. These points have also been highlighted by Hewett (1986), Lemouzy *et al.* (1995) and Jensen *et al.*(1996).

Lambert (1981) calculated and tabulated Dykstra-Parsons coefficients (measures of heterogeneity) in both the horizontal and vertical directions from 689 wells in 22 fields. In 90 % of the cases, the ratio of the coefficients in the horizontal and vertical directions was less than one. This result, governed by the depositional trends observed in petroleum reservoirs, indicates a spatial dependence among these variables.

Figures 1 and 2 illustrate this idea in more detail. The figures show an idealized cross-section (x,z) that is being penetrated by several vertical cored wells. We can calculate two types of variances for the cross section. The *vertical* variance is the arithmetic average of the variances for each individual well; the *areal* variance is the variance of the well averages. A cross section that is strongly autocorrelated in the x direction will have a small areal variance; strong autocorrelation in the z direction will lead to a small vertical variance. The ratio of these two is a measure of the extent of autocorrelation in the respective directions.

If we quantify the relationship between the autocorrelation and the variances, in both directions, we will be able to estimate one parameter from the others. Therefore, the main idea behind our method is that the horizontal autocorrelation must depend on the ratio of the areal-to-vertical variances and the autocorrelation in the vertical direction. With a chart that expresses this relationship, one can estimate autocorrelation in the horizontal direction.

METHOD OF STUDY

This section states the approach used to estimate autocorrelation in the interwell region of a reservoir. In the following derivation, we focus on the estimation of horizontal autocorrelation

since, in most cases, vertical wells can provide information on autocorrelation in the vertical direction. We also restrict attention to the estimation of horizontal autocorrelation in permeability.

The autocorrelation will be a function of the type of model chosen to represent it. Three different theoretical semivariogram models were tested: spherical, exponential and truncated fractal (power-law). The fractal model usually does not have a finite autocorrelation, but we will truncate at some upper cutoff; hence, the use of *truncated* fractal.

The way we express autocorrelation depends on the model being used for it. For the spherical semivariogram model,

$$\gamma(h) = \mathrm{Cov}(0) \begin{cases} \frac{3}{2}\left(\frac{h}{a}\right) - \frac{1}{2}\left(\frac{h}{a}\right)^3 & 0 \le h \le a \\ 1 & h \ge a \end{cases} \qquad (1)$$

autocorrelation is expressed by the range a. For the vertical direction $a = \lambda_z$; for the horizontal, $a = \lambda_x$. For the exponential model,

$$\gamma(h) = \mathrm{Cov}(0)\, e^{-\frac{h}{\lambda}} \qquad (2)$$

we use the autocorrelation length. As before, for the vertical direction $\lambda = \lambda_z$; for the horizontal, $\lambda = \lambda_x$. For the truncated fractal fBm model,

$$\gamma(h) = \mathrm{Cov}(0) \begin{cases} h^{2H} & 0 \le h \le a \\ 1 & h \ge a \end{cases} \qquad (3)$$

we use the cut-off length, a. For the vertical direction $a = \lambda_z$; for the horizontal, $a = \lambda_x$. We use the word *range* to generically express all three autocorrelation measures. Since a log-normal distribution is assumed for the permeability, all variances and averages are calculated on the logarithm of the permeability (ln k). In the above equations, Cov(0) stands for the sill, h the lag distance, and H the Hurst coefficient.

Formally, the vertical variance is the expectation of the conditional variances of $Y(x,z) = \ln(k(x,z))$:

$$\sigma^2_{vert} = E(\mathrm{Var}(Y(x_0, z)) \qquad (4)$$

where $\mathrm{Var}(Y(x_0, z)$ indicates a z-direction variance conditioned to a fixed location x_0. As suggested in Fig. 2, σ^2_{vert} is estimated as

$$s^2_{vert} = \frac{1}{N_w} \sum_{i=1}^{N_w} Var(Y(i,j)) \qquad j = 1, ..., N_l \tag{5}$$

where i and j are the indices on the x and z directions, respectively. The areal variance is the variance of the conditional expectation of Y:

$$\sigma^2_{areal} = Var(E(Y(x_0, z)) \tag{6}$$

It is estimated as

$$s^2_{areal} = Var\left(\frac{1}{N_l} \sum_{j=1}^{N_l} Y(i,j) \right) \qquad i = 1, ..., N_w \tag{7}$$

See Jensen *et al.* (1996) for details on conditional variances and expectations.

Our approach consists of the generation of synthetic, equiprobable permeability fields using stochastic simulation and a statistical treatment of the obtained data.

There are several methods that can generate stochastic reservoir images (Srivastava, 1994). One is the matrix decomposition method (MDM). This method is an averaging technique based on the decomposition of the autocovariance matrix. The present study uses a program developed by Yang (1990) that performs simulations based on MDM.

The MDM can generate permeability fields for reservoir modeling, but several statistics must be known as input data. In this step, it is essential to quantify the geologic knowledge in terms of a few parameters that can characterize the static properties of the reservoir. In doing this some assumptions were necessary; we considered that the permeability distribution can be represented by a single log-normal distribution that obeys second-order stationarity. The log-normal assumption was corroborated by the work of several authors, which results are summarized in a paper by Jensen *et al.* (1987).

The generation of synthetic permeability fields provided the necessary data to describe the relation among all investigated parameters. Averaging results from several realizations will provide a good estimate for the actual value of λ_x.

TYPE-CURVE PROCEDURE

To perform the numerical experiments, we established the following procedure. First, we chose a rectangular cross section with 4,000 blocks, 200 blocks in the x direction and 20 in the z direction. The sampling procedure represents a reservoir with 11 vertical wells aligned in one

direction having a constant spacing between them. We later concluded that the difference in results caused by staggered wells is small (Pizarro, 1996). Therefore, the analysis can be used for irregularly spaced wells, provided the average spacing is used as the reference distance.

The ranges input to MDM were converted to dimensionless form to provide more generality to the results. The dimensionless horizontal autocorrelation was normalized by the interwell spacing; the total thickness (H) is the reference distance in the vertical direction. We sample the generated fields at a constant interval to generate the estimated variances.

In the stochastic simulations, the dimensionless ranges were varied between 0.1 and 100 in the x direction and from 0.1 to 2.0 in the z direction. This range is believed to describe the autocorrelation existing in most petroleum reservoirs.

To make the results accurately represent the expectations in Eqs. 5 and 7, several realizations were performed. For each realization, Y values in each well were collected in a table in which there were 11 columns in the horizontal direction (each corresponding to one well) and 20 lines in the vertical direction, representing layer values. For each well the arithmetic average of Y was calculated in the vertical direction as well as the variance in the vertical direction.

Once both areal and vertical variances are known, the calculation of the ratio between them is straightforward. Since all of the semivariances used in Eqs. 5 and 7 are directly proportional to the variance, the ratio will be a function only of λ_{x_D}, λ_{z_D} and the semivariogram model. Therefore, if s^2_{areal} and s^2_{vert} are calculated and λ_{z_D} is estimated from fitting a specific semivariogram model to the vertical data, λ_{x_D} can be estimated.

RESULTS

Here we present the simulation results used to build the type-curve charts. The procedure stated above was implemented and several simulations performed.

All fields were generated for $\sigma^2 = 1$, which is equivalent to $V_{DP} = 0.63$. Since both areal and vertical variances are derived from the autocovariance, their ratio is independent of σ^2 (Pizarro, 1996). We used the minimal number of realizations (N_R) that would provide stable results, $N_R = 50$ (Pizarro, 1996).

The results obtained are expressed in Figs. 3 to 5 for the spherical, exponential and truncated fractal semivariogram models, respectively. Each figure is a plot of s^2_{areal}/s^2_{vert} versus λ_{z_D} with λ_{x_D} as a parameter. The truncated fractal fBm plot uses a Hurst coefficient of 0.25, since this seems to fit various types of field data (Neumann, 1994). Each figure contains results from 3,500 MDM simulations, since we calculate the average of 50 realizations.

Validation The overall procedure cannot be validated since we only have analytical expressions for some limiting cases. We would need an extraordinary amount of field data to cover all the possible situations aside from the limiting cases. However, some insight into the results can be given by analyzing the available solutions.

The first result that can be compared is for the case when we have no autocorrelation in either the horizontal or vertical directions. This means that the permeability values are completely random with no spatial correlation. The central limit theorem states that no matter what distribution a group of independent random variables are from, the sample mean of these variables is approximately normally distributed. So, if $Y_1, Y_2, Y_3, \ldots, Y_N$ denote independent random variables each having the same mean, μ, and variance, σ^2, and $\overline{Y}$ equals the mean of N of these random variables, we will obtain

$$\overline{Y} = \frac{Y_1}{N} + \frac{Y_2}{N} + \cdots \frac{Y_N}{N} = \frac{1}{N} \sum_{i=1}^{N} Y_i \tag{8}$$

Applying the property that the variance of a sum of independent variables will be equal to the sum of the variance of each one, we obtain

$$\mathrm{Var}(\overline{Y}) = \frac{\sigma^2}{N} \tag{9}$$

According to this procedure, the variance of the mean can be approximated by the areal variance (s^2_{areal}). Hence, the above relation states that, for the case of an uncorrelated field ($\lambda_{x_D} = \lambda_{z_D} = 0$), the areal variance should be equal to

$$\sigma^2_{areal} = \frac{\sigma^2}{N_l} \tag{10}$$

When the number of layers (N_l) equals 20, the above expression gives $\sigma^2_{areal} = 0.050$. In the numerical experiments with MDM we obtained $s^2_{areal} = 0.047$, a good approximation.

Another way to validate the results is to make use of an analytic expression that describes the relationship between variances of properties measured at different scales. Several authors, including Neuman (1994), Lasseter *et al.* (1986) and Haldorsen (1986), have reported the effect of the scale on the measurement of heterogeneity. One of the strong points of geostatistics is its ability to represent this behavior. For instance, the permeability of a well can be measured from a series of core measurements representing blocks of a certain size, shape and orientation. As the

size of these blocks increases, the variance of the mean value within the blocks get smaller although they may have the same mean.

Krige's relationship (Journel and Huijbregts, 1978) can be adapted to the present application. If a mining deposit (D) is split up into blocks (V), the variance of the properties of these blocks will be called the block variance and be denoted by $\sigma^2_{(V/D)}$. The variance of point grades (O) within a block is expressed by $\sigma^2_{(O/V)}$. This relationship states that these variances can be related to the variance of point grades within a deposit ($\sigma^2_{(O/D)}$)

$$\sigma^2_{(V/D)} = \sigma^2_{(O/D)} - \sigma^2_{(O/V)} \tag{11}$$

In our application the block represents a well, the point grades will be core samples within each well, and the deposit will correspond to the reservoir. With this analogy, Krige's relationship will be

$$s^2_{areal} + s^2_{vert} = \sigma^2 \tag{12}$$

Figure 6 illustrates how each variance behaves with λ_{x_D} increasing from 0.1 to 100, when σ^2 equals 1, an exponential model is used, and $\lambda_{z_D} = 0.8$. The sum of s^2_{areal} and s^2_{vert} is constant and equals the value expected from Krige's relationship for all values of λ_{x_D}. The agreement between Eq. 12 and the numerical response is very good. The good agreement between analytical and numerical solutions indicates that the dependence on sample number is small.

The chart in Fig. 6 reveals, also, how both s^2_{areal} and s^2_{vert} behave with increasing λ_{x_D}. As described above, for small λ_{x_D}, s^2_{areal} reaches a maximum and s^2_{vert} a minimum. As λ_{x_D} becomes greater than one, s^2_{areal} declines while s^2_{vert} rises. For very large values of λ_{x_D}, the horizontal autocorrelation is so large that s^2_{areal} tends to zero while s^2_{vert} approaches the population variance (σ^2).

Krige's equation also provides an alternative way to develop the relationships expressed in the charts of Figs. 3 to 5. Knudsen and Kim (1978) showed that, using the definition of the autocovariogram (Cov(h)), the areal variance could be calculated by

$$\sigma^2_{(V/D)} = \frac{1}{V^2} \int_V \int_V \mathrm{Cov(h)dvdv} \tag{13}$$

where h stands for the distance between any two points in the volume V, and the above integrals represent an integration over a volume. However, the amount of effort to be spent in these integrations is excessive, which motivated us to adopt the numerical approach using MDM.

Discussion Here we discuss the results and interpret some features of the type charts. The differences in results among the three semivariogram models are related with the degree of autocorrelation that each model incorporates. As s^2_{areal}/s^2_{vert} represents a ratio between two variances, the effect of the autocorrelation model will depend on which of the variances controls the final result. One way to illustrate this effect is by plotting the dependence of $\sigma^2_{areal}/\sigma^2_{vert}$ on the Hurst coefficient for the truncated fractal model. This parameter represents the degree of autocorrelation among data.

Figure 7 shows how s^2_{areal}/s^2_{vert} can vary with H and λ_{x_D}, for $\lambda_{z_D} = 1$. For instance, considering a reservoir strongly autocorrelated in the horizontal direction ($\lambda_{x_D} = 100$), the larger the H, the smaller will be s^2_{areal}/s^2_{vert}. However, when dealing with smaller values of λ_{x_D}, the behavior of the vertical variance will control the ratio s^2_{areal}/s^2_{vert}. Therefore, as H increases, s^2_{areal}/s^2_{vert} also increases.

The charts in Figs. 3 to 5 also show that s^2_{areal}/s^2_{vert} increases when λ_{z_D} is greater than 0.1. However, in the horizontal direction, s^2_{areal}/s^2_{vert} decreases very slowly with the vertical autocorrelation until λ_{x_D} reaches 1.0. This behavior is the same for all three semivariogram models and shows that a field with $\lambda_{x_D} = 1$ will behave similarly to an uncorrelated field in this direction. This result is a consequence of the fact that s^2_{areal} depends strongly on horizontal autocorrelation only for ranges greater than the interwell spacing. Ranges smaller than one have only a slight effect on s^2_{areal}. This observation also illustrates that, as expected, it is impossible to estimate ranges smaller than the well spacing ($\lambda_{x_D} < 1$).

One limitation of this method is the variability of s^2_{areal}/s^2_{vert} among the 50 realizations. Figure 8 expresses how the results for $\lambda_{z_D} = 0.1$ and 0.5, obtained from the exponential model, vary with λ_{x_D}. The figure shows the average of 50 realizations and also curves representing plus or minus one standard deviation about the mean. The estimate of λ_{x_D} is more precise when it is large.

APPLICATION

We chose data from a particular field to demonstrate how the procedure works. The results represent an illustration of the method rather than a comprehensive analysis of the reservoir. A complete analysis requires additional effort and integration among geologists and reservoir engineers to interpret the results in the light of all the knowledge about the field.

We applied the procedure to the El Mar field, located in the Delaware Basin of West Texas and New Mexico (Fig. 9). This unit is currently operated by Burlington Resources Co.

The El Mar This field is located 30 km north of Mentone, Texas. The entire field covers approximately 40 km^2 with two-thirds of the field located in the western portion of Loving County, Texas, and the remainder in southwest Lea County, New Mexico. In this study, we investigated only the data from the El Mar (Delaware) Unit, which covers an area of 5 by 8 km and contains 175 wells.

The primary producing horizon is the Ramsey sand, which is composed of an upper "A" sand and a lower "B" sand separated by a shale laminae. These sandstones were deposited in deep water, probably by submarine-fan complexes formed by turbidity-current deposition during lowstands of sea level. Dutton *et al.* (1996) discuss this and other alternative models of Delaware sandstone deposition. The Ramsey formation lies at an average producing depth of 1500 m and the formation's weighted average porosity and permeability are, respectively, 23 % and 22 md. A description of other petrophysical properties of the Delaware Formation can be found in Jenkins (1961).

The difficulty in estimating the water saturation caused a large number of cored wells to be taken. This made it possible to find several cored wells aligned in the orthogonal directions of the field, leaving it in a favorable condition to perform the present analysis. We selected six wells aligned in the north-south direction and two more in the east-west, totaling three in this direction.

We selected the data from the eight wells and built a vertical semivariogram of Y for each. Most of the data analyzed were from Unit A because of the predominance of this unit in this part of the field. Our approach was to separate the data from both units, because they seem to have different petrophysical properties. We performed the analysis only for Ramsey A, since the amount of data for Ramsey B was less; only two wells, 1814 and 1824, have data that include core samples from both Units A and B. We later comment on the difference in the results if data from both units were grouped together for the analysis.

The goal here was simply a practical demonstration of the method. Therefore, we assumed that there were no problems concerning data acquisition and the further analysis was based on the semivariograms constructed with primary data. We also did not consider the possibility of nugget effects in the semivariogram fitting.

The procedure outlined above was performed to calculate the average values and the s^2_{areal} and s^2_{vert} for each set of data. To calculate λ_z, the experimental semivariograms must be fitted by a theoretical model. The difficulties and the importance of this step are well described in the literature by several authors, including Journel and Huijbregts (1978), Isaaks and Srivastava (1989), and Olea (1994).

Estimating λ_{z_D} We tested three different semivariogram models, trying to find the one that best described the experimental data.

The spherical semivariogram fit was considered poor. The second model tested was the truncated fBm fractal or power-law model. For the fitting, a value of H = 0.15 gave a better adjustment than the value of H = 0.25. Therefore, a new set of curves for the fractal model, analogous to the ones in Fig. 5, was generated for H = 0.15. The final result was better than the spherical fitting for most wells. The exponential model gave a fit close to that obtained with the fractal for most wells and reproduced a similar response for the ones in which the spherical model worked better. The results are summarized in Table 1 for the East-West (EW) section and in Table 2 for the North-South (NS) section. The average ranges in the vertical direction calculated with the spherical, exponential and fractal models were, respectively, 0.19, 0.08 and 0.32 for the EW direction, and 0.22, 0.10 and 0.33 for the NS direction.

Estimating λ_{x_D} Using these results and the ratio s^2_{areal}/s^2_{vert} for each direction, we enter the charts and interpolate λ_{x_D}, as shown in Fig. 10. The results shown in Table 3 for the spherical, exponential and fractal are, respectively, $\lambda_{x_D}\big|_{EW}$ = 1.2, 1 and 3, and $\lambda_{x_D}\big|_{NS}$ = 4, 2 and 6.

The results show anisotropy in the autocorrelation pattern of the El Mar field, at least along the directions indicated. The permeability range in the NS direction is at least twice that in the EW direction. This behavior roughly coincides with the depositional characteristic of the field, since the major axis of the turbidite channel is aligned with the northeast-southwest direction (Fig. 9).

A less rigorous approach would be to group the data from both units A and B together, instead of performing the analysis only for Unit A. Additional data from two wells (1814 and 1824) need to be considered. Since the wells in the EW section do not contain the Ramsey B sand only results from the NS section will change. The main difference is that the value of s^2_{areal} changes from 0.23 to 0.36, making s^2_{areal}/s^2_{vert} = 0.18 instead of 0.12. This change would led to the conclusion that the ranges were similar in both directions, in conflict with the depositional

pattern. This illustrates the importance of prior geological analysis of the data to be used in making the estimation.

Final Remarks The autocorrelation analysis of the El Mar field shows that answers obtained by using different semivariogram models can be different. These results were expected, since each model uses a different approach. Even when using the same model, different interpretations of the semivariogram data can lead to different values of horizontal autocorrelation. Although this seems a little strange at first, it may not have a great effect on a simulated flow response. Indeed, Fogg *et al.* (1991) referred to a study in which two ranges of 120 and 390 m caused significantly different permeability patterns but practically identical cumulative oil recoveries and water-oil rates, when used in simulation.

When calculating the data to construct the charts in Figs 3 to 5 we also derived a chart to correct the vertical variance, measured at the wells, to the value that should be used in conditional simulation studies. Recall that the vertical variance measured at the wells will be equal to the population variance only when there is no autocorrelation. Figure 11 shows how s^2_{vert}/σ^2 varies with λ_{z_D} and λ_{x_D}. The more vertically autocorrelated the permeability field is, the more the s^2_{vert} is different from σ^2.

Figure 12 shows an analogous result but expressed as the Dykstra-Parsons coefficient instead of the variance. To express the variance in terms of the V_{DP}, the chart is no longer general and depends on the population V_{DP}. Figure 12 considered a $V_{DP\,pop}$ of 0.9.

These charts can be used to correct data for input into stochastic simulation. For instance, from Fig.12, we can conclude that a sample V_{DP} of 0.85 ($s^2_{vert} = 3.6$) calculated from a reservoir with $\lambda_{z_D} = 0.3$ and $\lambda_{x_D} = 1.0$, given by the exponential model, will have a population $V_{DP\,pop} = 0.9$ ($\sigma^2 = 5.3$).

SUMMARY AND CONCLUSIONS

We developed a set of charts for estimating autocorrelation in the horizontal direction based on the ratio of areal-to-vertical variances, the vertical autocorrelation and the type of semivariogram model used.

The procedure was partially validated through a comparison of results; analytical solutions were available for some limiting situations. A field case was analyzed to demonstrate how the method can be applied. Data from eight wells in the El Mar field, Ramsey A sand, were used to estimate horizontal autocorrelation for two directions of the field.

Results from the El Mar analysis point out the anisotropy in the permeability distribution of this field. The autocorrelation ranges in the vertical direction were found to be between 0.1 and 0.3 of the sampled interval, depending on the type of model used. The horizontal range in the north-south direction varied between 2 and 6 times the mean well spacing, being at least twice the autocorrelation in the east-west direction. These results can be used in conditional simulations to generate the expected permeability pattern of this field.

The present approach seems to be an effective tool to be used, along with the geological knowledge of the facies continuity, for estimating the autocorrelation for the interwell region between vertical wells.

NOMENCLATURE

a	=	semivariogram range
Cov	=	covariance
D	=	mining deposit
E	=	expectation value
h	=	distance lag
H	=	Hurst coefficient
	=	reservoir thickness
k	=	permeability
N_l	=	number of layers
N_R	=	number of realizations
N_w	=	number of wells
O	=	point grades
s^2	=	estimation of the variance
V	=	volume of a block
V_{DP}	=	Dykstra-Parsons coefficient
Var	=	variance
Y	=	natural logarithmic of the permeability
λ	=	autocorrelation range (general)
	=	range (spherical model)
	=	correlation length (exponential model)
	=	truncated upper cutoff (fractal model)
μ	=	population mean

σ = population standard deviation

σ^2 = population variance

σ^2_{areal} = areal variance

σ^2_{vert} = vertical variance

Subscripts

D = dimensionless variable

EW = east-west direction

NS = north-south direction

O/D = point grades within a mining deposit

O/V = points grades within a block

pop = population values

V/D = blocks within a mining deposit

x,y,z = Cartesian coordinate directions

ACKNOWLEDGEMENTS

This work was supported, in part, by the Enhanced Oil Recovery Research Program of the Center for Petroleum and Geosystems Engineering at The University of Texas. Jorge Pizarro's support is provided by Petrobrás S.A.. Larry W. Lake holds the W.A. (Tex) Moncrief Centennial Chair. We thank Dr. I.H. Silberberg for his editorial comments and John Barnes with Burlington Resources for supplying the core data on the El Mar (Delaware) Unit.

REFERENCES

Dutton, S. P., Hovorka, S. D. and Cole, A. G.: "Application of Advanced Reservoir Characterization, Simulation, and Production Optimization Strategies to Maximize Recovery in Slope and Basin Clastic Reservoirs, West Texas (Delaware Basin)," Bureau of Economic Geology, The University of Texas at Austin (1996).

Fogg, G.E., Lucia, F.J. and Senger, R.K.: "Stochastic Simulation of Interwell-Scale Heterogeneity for Improved Prediction of Sweep Efficiency in a Carbonate Reservoir," *Reservoir Characterization II*, L. W. Lake, H. E. Carroll and T. C. Wesson (eds.), Academic Press, New York (1991).

Haldorsen, H.H.: "Simulation Parameter Assignment and the Problem of Scale in Reservoir Engineering," *Reservoir Characterization*, L. W. Lake and H. E. Carroll (eds.), Academic Press, New York (1986)

Hewett. T. A., "Fractal Distributions of Reservoir Heterogeneity and Their Influence on Fluid Transport," paper SPE 15386 presented at the 1986 Soc. Pet. Eng. Annual Tech. Conf. and Exhibition, New Orleans, LA, Oct. 5-8.

Isaaks, E. H. and Srivastava, R. M.: *Applied Geostatistics*, Oxford University Press, New York 1989.

Jenkins, R.E.: "Characteristics of the Delaware Formation," *J. Pet. Tech.* (Dec. 1961), 1230-1236.

Jensen, J.L., Hinkley, D.V. and Lake, L.W.: "A Statistical Study of Reservoir Permeability: Distributions, Correlations, and Averages," *SPE Formation Evaluation* (1987) **2** 461-468.

Jensen, J.L., Lake, L.W., Corbett, P.M.W. and Goggin, D.J.: *Statistics for Petroleum Engineers and Geoscientists*, PTR Prentice Hall, Englewood Cliffs, New Jersey (1996).

Journel, A. G. and Huijbregts, CH. J.: *Mining Geostatistics*, Academic Press, New York (1978).

Knudsen, H. P. and Young C. Kim. : "A Short Course on Geostatistical Ore Reserve Estimation," Department of Mining and Geological Engineering, College of Mines, The University of Arizona, Tucson, AZ (1978).

Lambert, M.E.: "A Statistical Study of Reservoir Heterogeneity," M.S. thesis, The U. of Texas at Austin (1981).

Lasseter, T. J., Waggoner, J. R., Lake, L. W.: "Reservoir Heterogeneities and Their Influence on Ultimate Recovery," *Reservoir Characterization* , L. W. Lake and H. E. Carroll (eds.), Academic Press, New York (1986)

Lemouzy, P. M., Parpant, J., Eschard, R., Bachiana, C., Morelon, I., Smart, B.: "Successful History Matching of Chaunoy Field Reservoir Behavior Using Geostatistical Modeling," paper SPE 30707 presented at the 1995 Soc. Pet. Eng. Annual Tech. Conf. and Exhibition, Dallas, TX, Oct. 22-25.

Lucia, F.J. and Fogg, G.E.: "Geologic/Stochastic Mapping of Heterogeneity in a Carbonate Reservoir," paper SPE 19597 presented at the 1989 Soc. Pet. Eng. Annual Tech. Conf. and Exhibition, San Antonio, TX, Oct. 8-11.

Neuman, S. P.: "Generalized Scaling of Permeabilities: Validation and Effect of Support Scale," *Geophysical Research Letters* (March 1994), **21**, 5, 349-352.

Olea, R. A.: " Fundamentals of Semivariogram Estimation, Modeling, and Usage," *Stochastic Modeling and Geostatistics*, J. M. Yarus and R. L. Chambers (eds.), AAPG (1994).

Pizarro, J. O. S.: Ph.D. dissertation in progress, The University of Texas at Austin (1996).

Srivastava, R. M.: "An Overview of Stochastic Methods for Reservoir Characterization," *Stochastic Modeling and Geostatistics*, J. M. Yarus and R. L. Chambers (eds.), AAPG (1994).

Yang, A. P.: "Stochastic Heterogeneity and Dispersion," Ph.D. dissertation, The U. of Texas at Austin (1990).

Table 1. Summary of results for the East-West cross section of the El Mar field.

	WELLS			
	1514	1513	1512	AVERAGE
Average of Ln (k) in vertical direction	1.15	2.25	2.17	1.86
Variance of Ln (k) in vertical direction	1.96	2.44	2.81	2.40
Vertical correlation range with spherical model	0.21	0.18	0.17	0.19
Vertical correlation length with exponential model	0.09	0.07	0.08	0.08
Vertical truncated upper cutoff with fractal model (H=0.15).	0.35	0.26	0.34	0.32

Table 2. Summary of results for the North-South cross section of the El Mar field.

	WELLS						AVERAGE
	1514	1524	1534	1532	1814	1824	
Average of Ln (k) in vertical direction	1.15	1.89	2.37	2.40	1.85	1.58	1.87
Variance of Ln (k) in vertical direction	1.96	1.47	0.46	2.09	4.00	1.71	1.95
Vertical correlation range with spherical model	0.21	0.20	0.23	0.20	0.22	0.24	0.22
Vertical correlation length with exponential model	0.09	0.08	0.12	0.09	0.11	0.11	0.10
Vertical truncated upper cutoff with fractal model (H=0.15)	0.35	0.28	0.30	0.34	0.42	0.30	0.33

Table 3. Summary of the results from autocorrelation analysis of the El Mar field.

SUMMARY	NORTH-SOUTH	EAST-WEST
Areal variance	0.23	0.37
V_{DP} areal	0.46	0.46
Vertical variance	1.95	2.40
V_{DP} vertical	0.75	0.79
Ratio areal/vertical variances	0.12	0.15
λ_{x_D} (Spherical model)	4	1.2
λ_{x_D} (Exponential model)	2	1
λ_{x_D} (Fractal model)	6	3

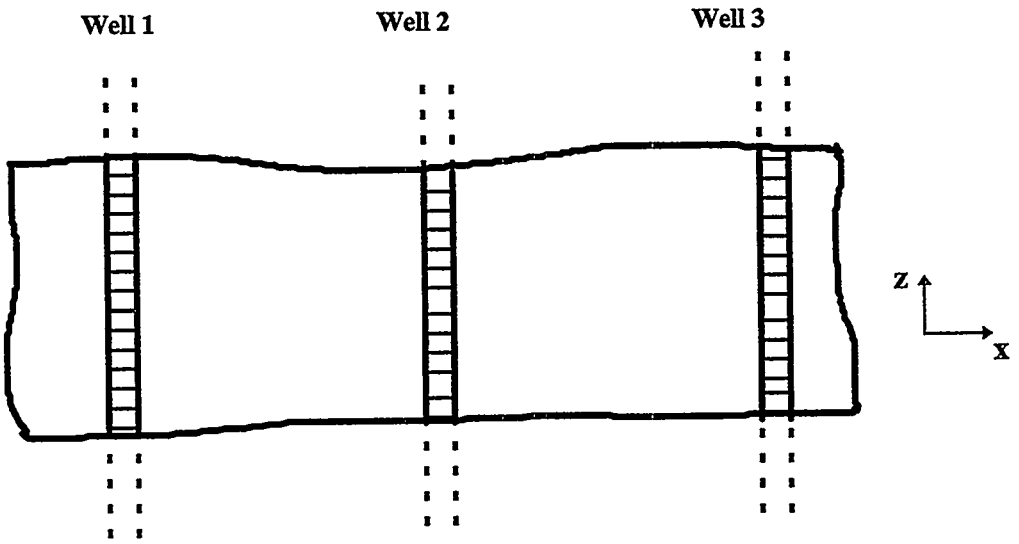

Figure 1. An idealized cross section (x,z) penetrated by vertical wells.

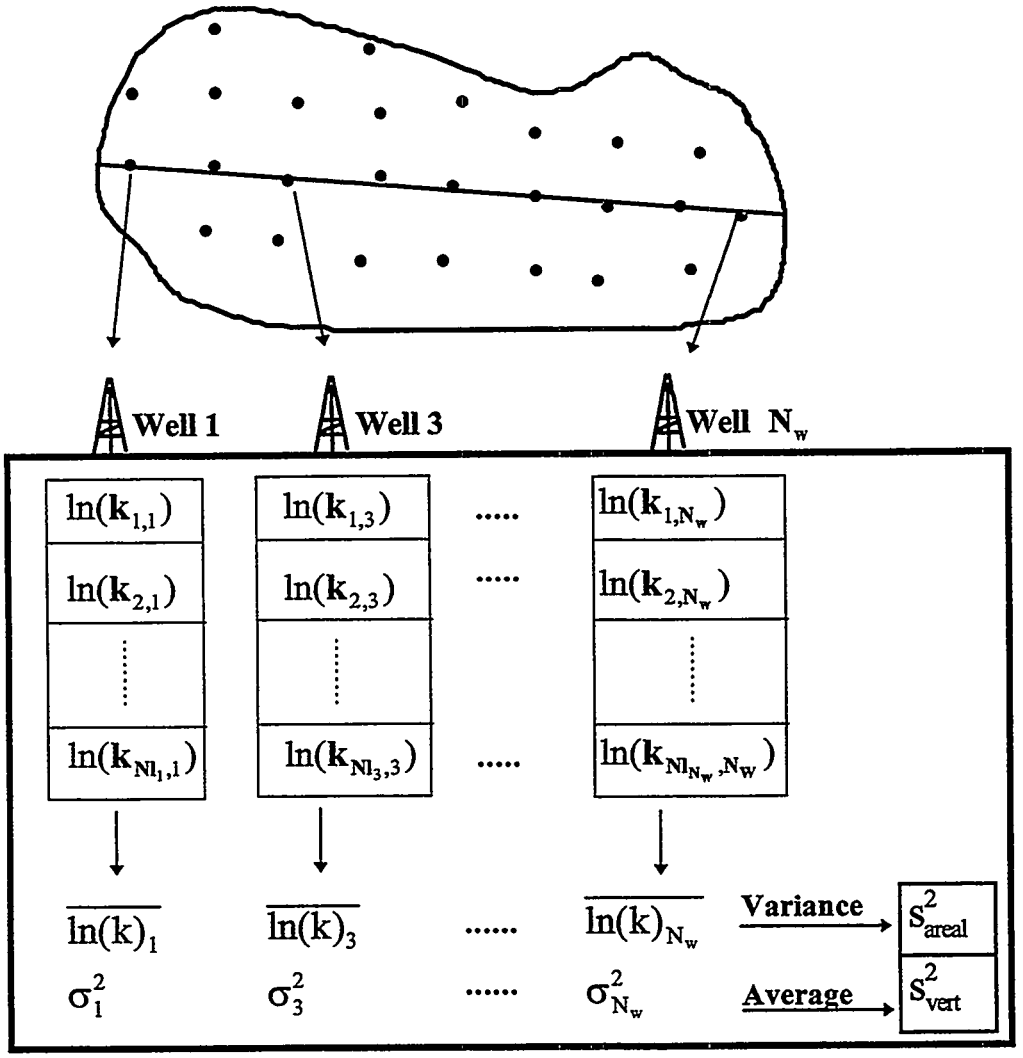

Figure 2. Schematic of the procedure to calculate the areal and vertical variances.

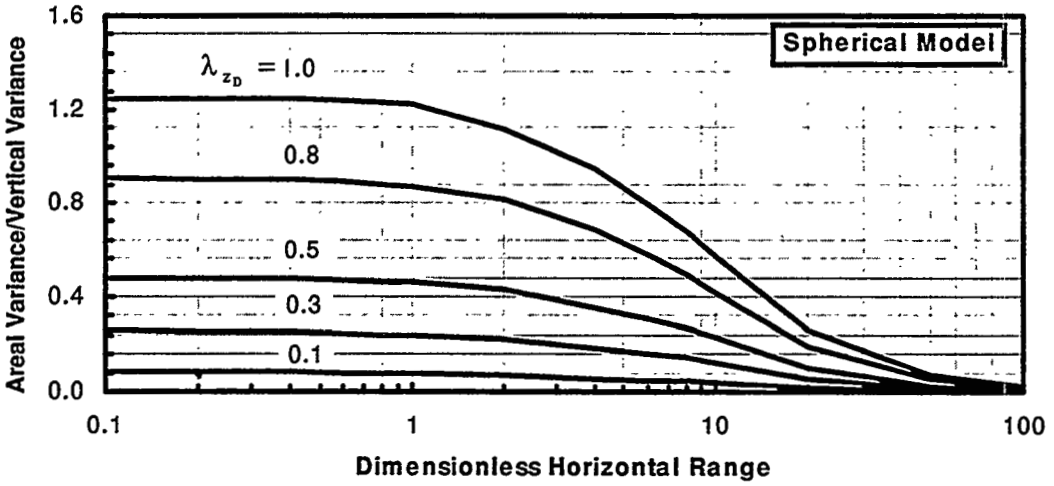

Figure 3. Autocorrelation chart for spherical semivariogram model obtained from 50 realizations.

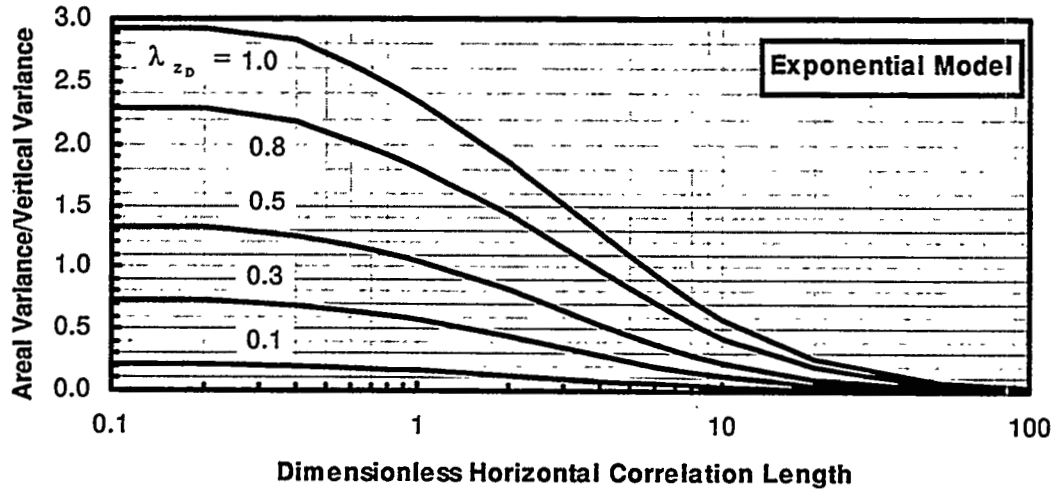

Figure 4. Autocorrelation chart for exponential semivariogram model from 50 realizations.

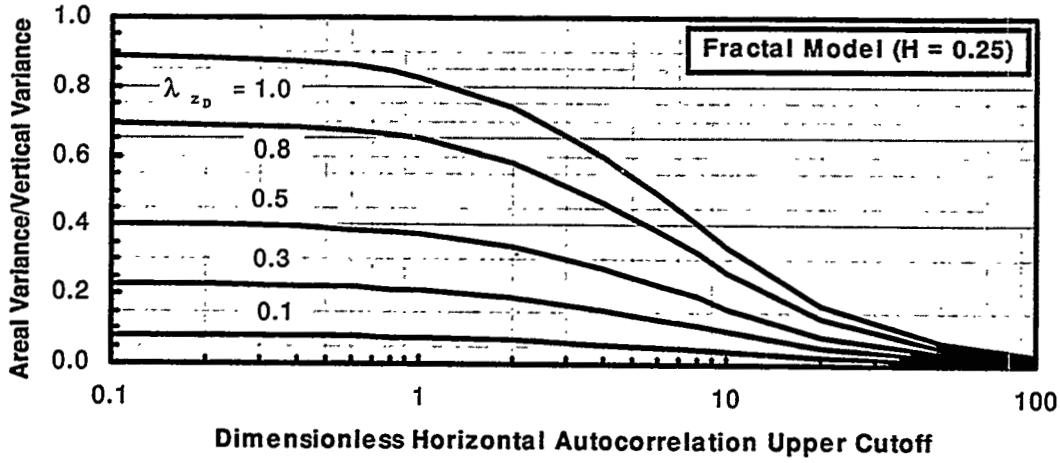

Figure 5. Autocorrelation chart for fractal semivariogram model obtained from 50 realizations.

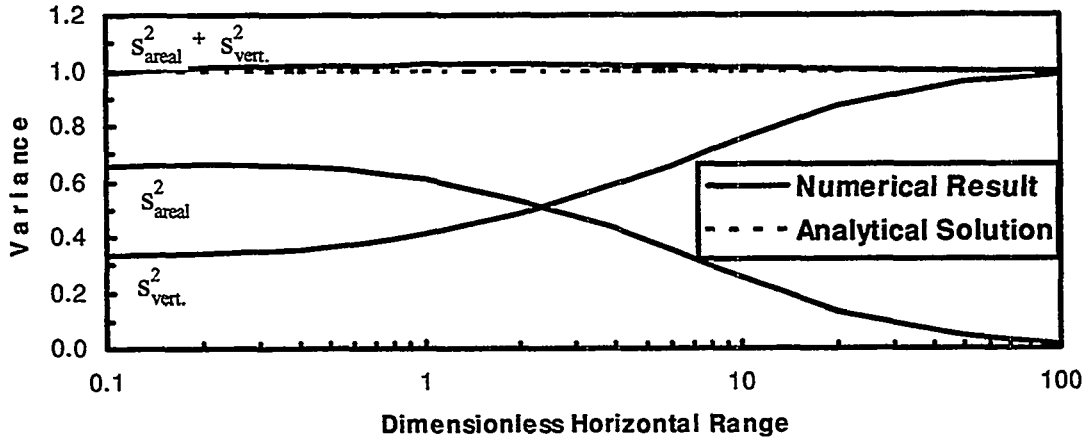

Figure 6. Analytical validation (exponential model, $\lambda_{z_D} = 0.8$, and 50 realizations).

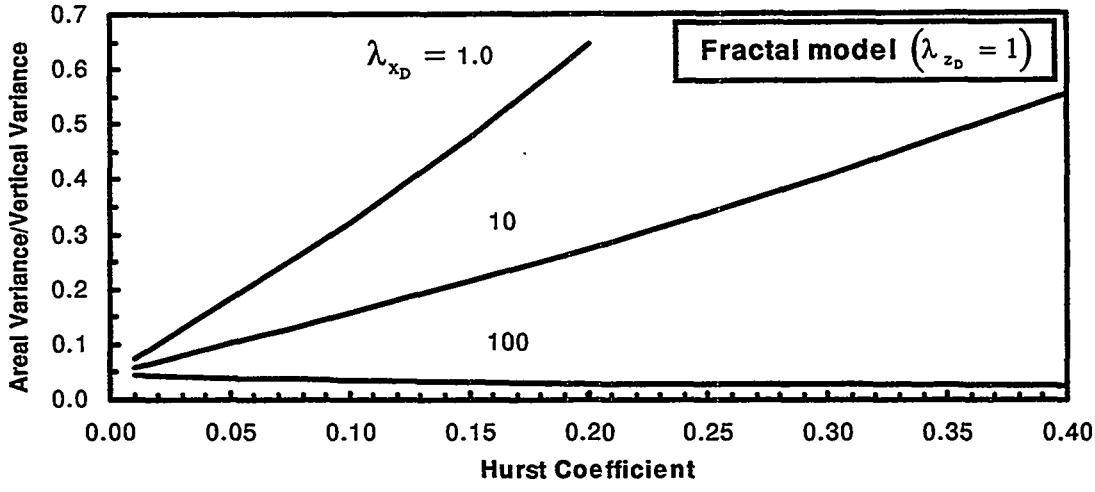

Figure 7. Estimation of s^2_{areal} / s^2_{vert} sensitivity to the Hurst coefficient for different truncated ranges.

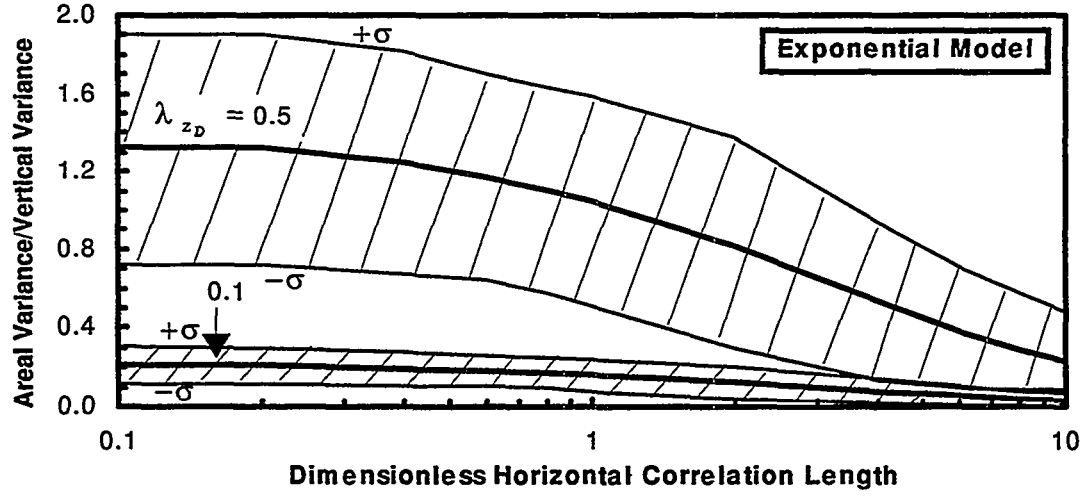

Figure 8. Variability (expressed as ± 1 standard deviation) of s^2_{areal} / s^2_{vert} among the 50 realizations.

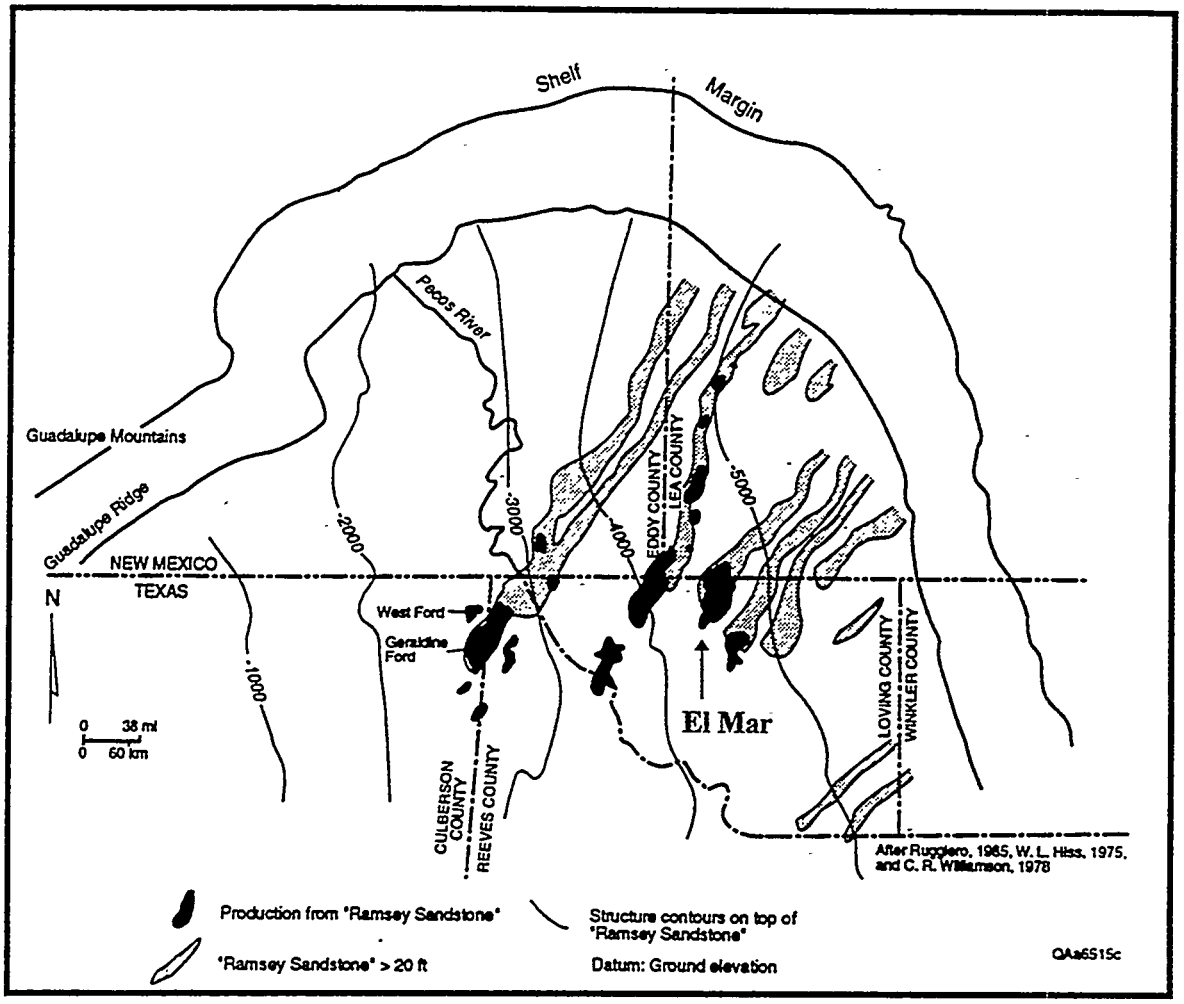

Figure 9. Map of the Delaware basin (from Dutton *et al.* (1996)).

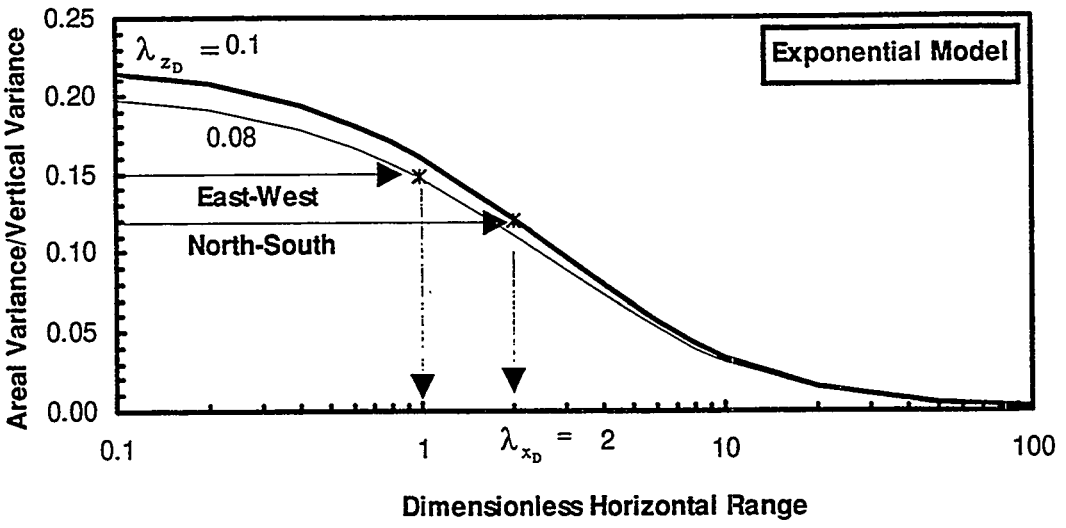

Figure 10. Determining λ_{x_D} for the North-South and the East-West sections of El Mar field.

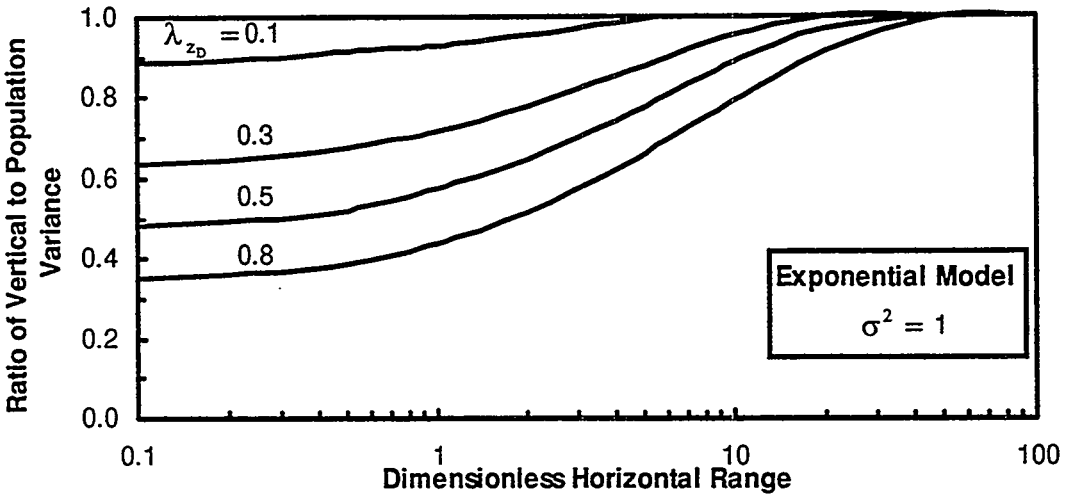

Figure 11. Differences between the vertical (sample) and population variance caused by autocorrelation.

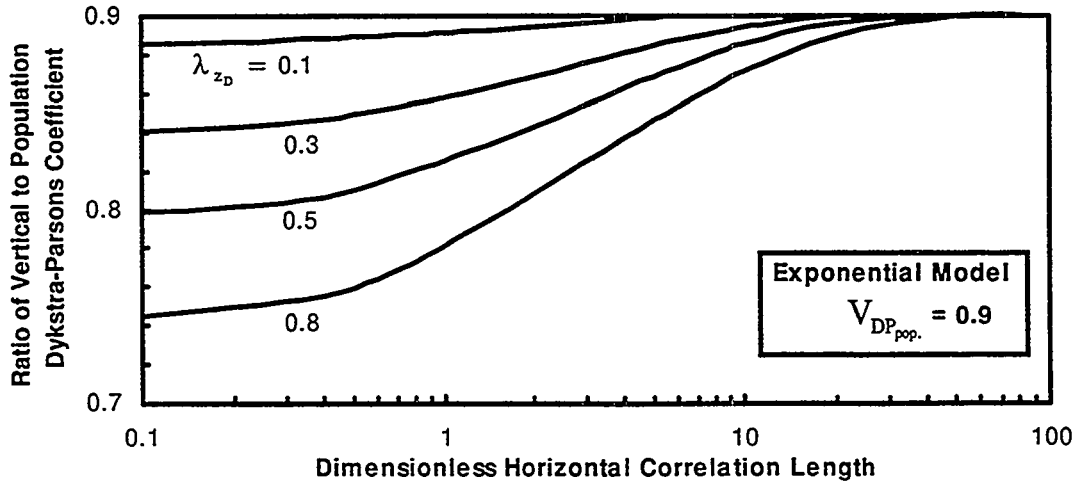

Figure 12. Differences between the vertical (sample) and population V_{DP} caused by autocorrelation

EXTRACTING MAXIMUM PETROPHYSICAL AND GEOLOGICAL INFORMATION FROM A LIMITED RESERVOIR DATABASE

Maqsood Ali, Adwait Chawathé, Ahmed Ouenes, Martha Cather, and William. W. Weiss

New Mexico Petroleum Recovery Research Center
New Mexico Institute of Mining and Technology
Socorro, New Mexico

ACKNOWLEDGMENTS

This research was funded by the Department of Energy (contract no. DE-AC22-93BC14893), State of New Mexico, Landmark Graphics Corporation (Halliburton), Texaco and Yates Petroleum. The authors greatly appreciate the financial support.

ABSTRACT

The characterization of old fields lacking sufficient core and log data is a challenging task. This paper describes a methodology that uses new and conventional tools to build a reliable reservoir model for the Sulimar Queen field. At the fine scale, permeability measured on a fine grid with a minipermeameter was used in conjunction with the petrographic data collected on multiple thin sections. The use of regression analysis and a newly developed fuzzy logic algorithm led to the identification of key petrographic elements which control permeability. At the log scale, old gamma ray logs were first rescaled/calibrated throughout the entire field for consistency and reliability using only four modern logs. Using data from one cored well and the rescaled gamma ray logs, correlations between core porosity, permeability, total water content and gamma ray were developed to complete the small scale characterization. At the reservoir scale, outcrop data and the rescaled gamma logs were used to define the reservoir structure over an area of ten square miles where only 36 wells were available. Given the structure, the rescaled gamma ray logs were used to build the reservoir volume by identifying the flow units and their continuity. Finally, history-matching results constrained to the primary production were used to estimate the dynamic reservoir properties such as relative permeabilities to complete the characterization. The obtained reservoir model was tested by forecasting the waterflood performance and which was in good agreement with the actual performance.

INTRODUCTION

In an ideal situation, the data required for detailed reservoir characterization range from regional to field-scale to small-scale, and consist of lithological description, petrophysical properties, fluid properties, well-test, production, and pressure data. Optimal data density is also crucial in addition to the variety and quality of data, and is governed by the type and scales of heterogeneity. Adequate data density is needed so that statistically significant conclusions can be drawn. However, in actual reservoir characterization problems neither all types of data nor the appropriate data density may be available.

A large number of oil and gas fields developed prior to 1970's lack modern logs as well as sufficient core material. The economic constraints and risks involved prohibit both small and large operators from spending large sums of money on drilling new wells, coring, logging, and running special well test operations in these old

fields. The characterization of such fields using available information is a challenging task, and no proven methodology is available in the industry. Also, the production data available from these fields are sometimes not reliable. Under these circumstances the simulation/history-matching process may result in petrophysical properties (porosity, permeability, relative permeabilities, etc.) far removed from reality.

This paper describes the methodology employed for the reservoir characterization of an old field - the Sulimar Queen. This field is deficient in core material, modern logs, and complete production data. The Sulimar Queen field is located in the Chaves County, southeast New Mexico (Figure 1). The reservoir is present in the upper Queen Formation called the "Shattuck Member". The Shattuck member was deposited in mixed lagoonal-sabkha-eolian environment, is internally complex and can only be successfully exploited if the distribution of individual porosity and permeability units within the reservoir is clearly understood.

For the characterization of the field, the only control points available consisted of *one core, core reports from two wells, and modern log suites from four wells.* From the rest of the field only *old gamma ray and neutron logs* were available. Neutron logs, because of their wide scale ranges and anomalous high and low porosity values, were discarded and were not used in this study (Ali et al., 1996). Two additional cores were obtained from the adjacent fields, and additional outcrop studies were conducted to supplement the database (Figure 1). Cores and logs from the adjacent fields were collected to capture the regional trend, so that the relationships developed in the Sulimar Queen field could be verified.

SMALL-SCALE HETEROGENEITY STUDY

The first objective was to analyze the scale of heterogeneity in the vertical direction from the available cores. Permeability measurements were made using a computer controlled minipermeameter (Suboor and Heller., 1995), and approximately 5,000 permeability measurements were made. Permeability measurements were made on a square grid with an interval of 12.5 mm, which created five vertical permeability profiles along the length of the core. The average of the five profiles for the three cores are shown in Figure 2 (also refer to Figure 3). The permeability varied from less than 0.1 md to 500 md, and the scale of permeability heterogeneity was the same for three cores (Figure 2). This similarity suggested that the vertical permeability heterogeneity in the Sulimar Queen and adjacent fields may be caused by the same depositional and diagenetic events. This regional trend provided the first confirmation of the assumption that the data from the adjacent fields may be used.

The producing zone of the Shattuck member consists of greenish brown, greenish gray, gray, brown, red, very fine-grained sandstone. It is bounded at the top and the bottom by anhydrite (Figure 2). The permeability heterogeneity is caused by minor changes in the depositional environment. Minor changes in the lithology are evident from the changes in the permeability (Figure 2). Permeability measurements made on a smaller-scale also improved the lithologic description of the core. On the basis of permeability distribution, the reservoir was divided into two separate layers, an upper high permeability layer (zone 1) with one low permeability subzone (subzone A) and a lower tighter layer (zone 2) as illustrated in Figure 2.

Improving the quantity and quality of petrographic data:

The problem was to collect enough samples for the petrographic analysis, so that the control of petrographic elements such as porosity types, pore morphologies, mineralogy, textures, and type, amount, and distribution of clay and cement in creating permeability heterogeneity can be determined. Conventionally,

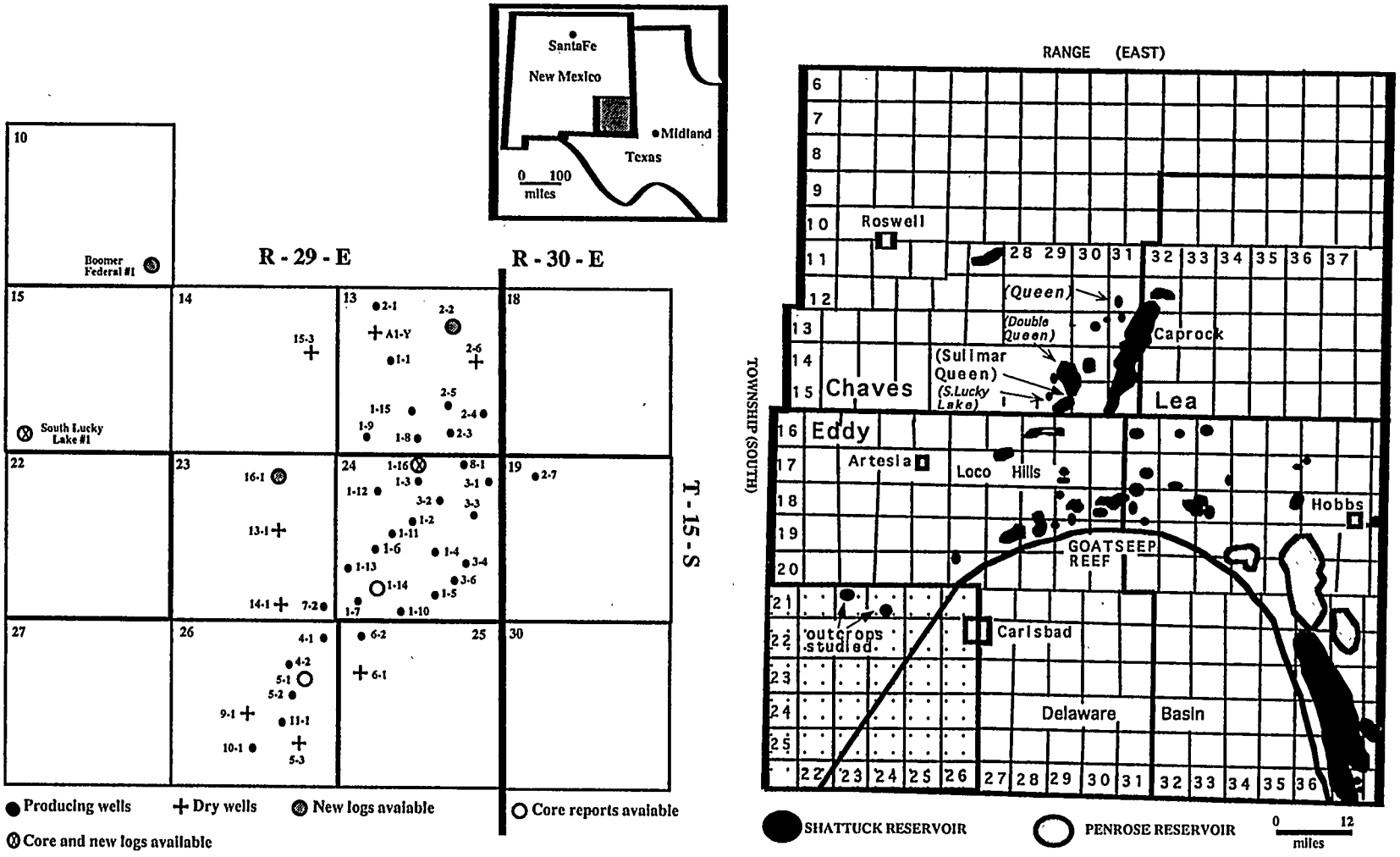

Figure 1: Showing the locations of the Sulimar Queen, South Lucky lake, Queen, and other Queen fields field and the outcrops relative to Goat Seep Reef. Distribution of the wells in the Suliamr Queen field is also shown.

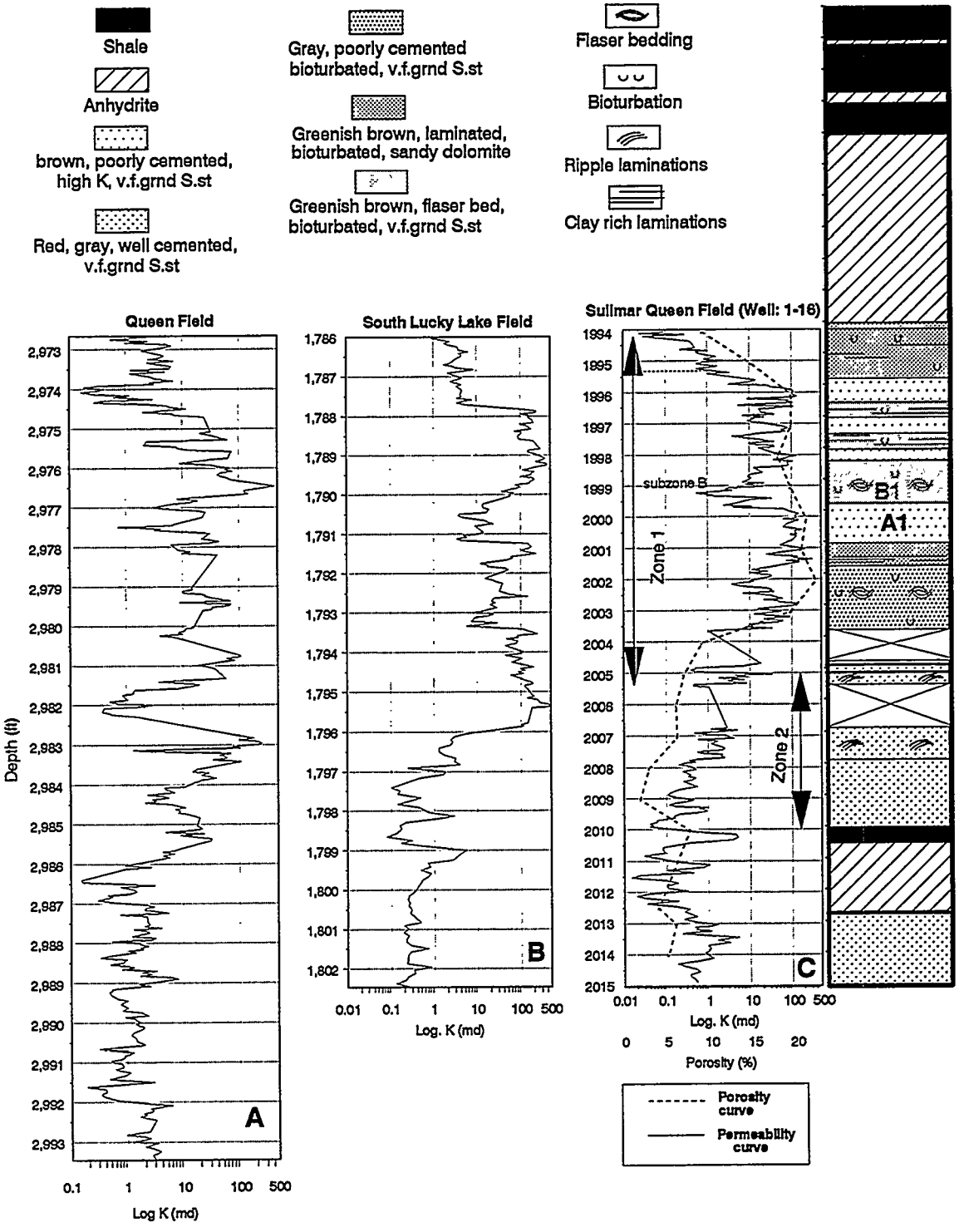

Figure 2: Permeability distribution in the cores from Queen (A), South Lucky Lake (B), and Sulimar Queen field (C). Core description from the Sulimar Queen field is also shown along side the permeability distribution. Note the similar permeability distribution especially between South Lucky Lake (B) and Sulimar Queen field (C).

relationships between permeability and petrographic elements are determined by using core plugs and thin sections, but there is a large difference in their respective volumes of investigation. Permeability varies from point to point within most core plugs. Therefore, a thin section prepared from the edge of that core plug may not contain the petrographic elements that are representative of the core plug's permeability. Consequently, such correlations may be misleading. Because of the destructive nature and the size, core plug analysis also restricts the detailed investigation of permeability heterogeneities on small-scale, especially in sedimentary structures with dimensions less than 2.5 cm. In the Shattuck member, permeability heterogeneities exist on a small-scale (Figure 2) and the whole range of permeability distribution cannot be sampled using core plugs. A new methodology was developed by utilizing a fine scale grid (on which permeability measurements were made with a minipermeameter) based on the premises that: (1) the area of investigation of minipermeameter is very small and can be examined in thin sections, and (2) each thin section contains many permeability points (Figure 3). The advantage of collecting a large set of data points is that detailed statistical analyses can be done and the effects of each petrographic element on permeability can be determined. This, also, helps assess the effects of diagenesis and porosity evolution on permeability more accurately.

According to Goggin et al. (1988), the effective radius and depth of investigation of a minipermeameter probe tip is four times the internal radius of the probe tip. However, it was found during the calibration and permeability measurements with the minipermeameter, the area immediately under and around a probe tip exerts the main control over the permeability. After careful examination, it was decided that, for a probe tip with inner radius of 0.125 inches (3.125 mm), the area of the thin section to be analyzed should have a diameter of 0.4 inches (10 mm). Depending on the number of permeability points located on each thin section, the thin section was divided into that many equal parts and petrographic data was collected from each part separately (Figure 3). With this new method, data equivalent to 7 thin sections on the average, were collected from one thin section which would not have been possible using the conventional core plugs. The minipermeameter, in addition to providing large amount of permeability data and resolving small-scale heterogeneity, also provided the opportunity to collect more petrographic data using few thin sections. Because of the similarity of the areas of investigation of both, the thin sections and the minipermeameter, the correlations established between permeability and petrographic elements were also more accurate than the correlations obtained from conventional core plugs.

Petrographic Analysis:

Thirty-eight thin sections were made from the cores and total of 267 data points were obtained. The petrographic elements collected for each permeability point were: total porosity, total secondary porosity, secondary intergranular porosity, microporosity, intraconstituent porosity, moldic porosity, microfractures, quartz, feldspar, rock fragments, anhydrite, dolomite, detrital clay, dead oil, pore size, grain size, grain sorting, pore sorting, and pore interconnection. Detailed petrographic analysis also helped determine the paragenetic sequence, porosity evolution, and the depositional environment. A generalized paragenetic sequence is shown in Figure 4. Petrographic analysis was done to establish the ranking of each petrographic element in controlling the permeability. In addition to simple regression analysis, a newly developed fuzzy logic algorithm was also used to determine the importance (ranking) of each petrographic elements in controlling the permeability (Table II and Figure 5). Depending on the ranking, the permeability may be estimated by

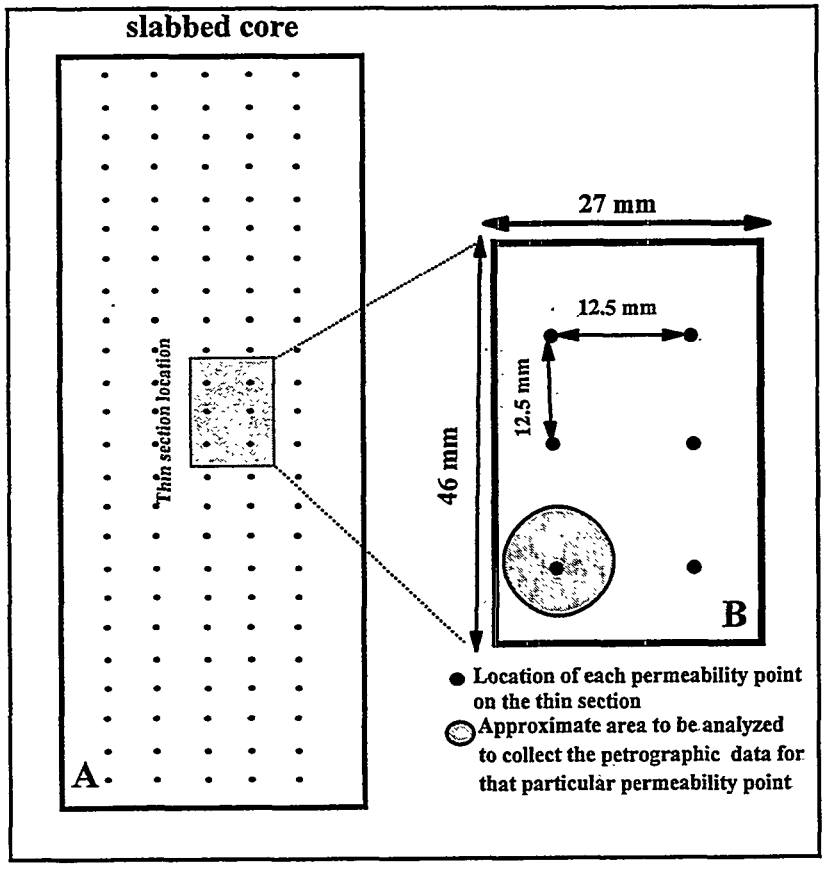

Figure 3: (A) Grid on which permeability measurements were made. Five vertical profiles were generated by this grid. The average of the five profiles is shown in Figure 2. Thin section location is also shown. (B) Distribution of permeability points on the thin section.

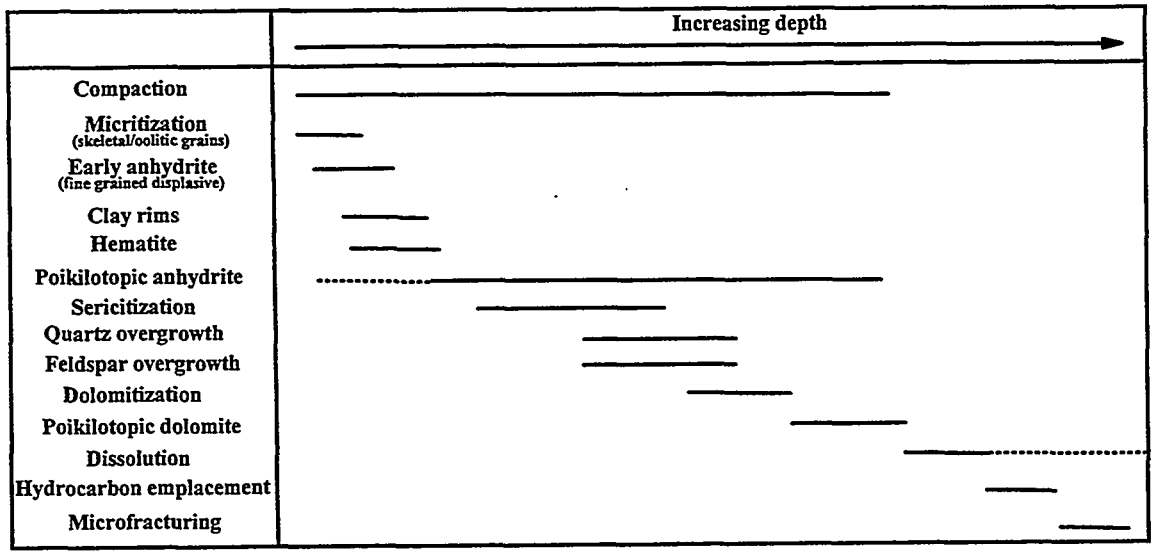

Figure 4: Generalized paragenetic sequence for the Shattuck member, Sulimar Queen Field.

using only the most important petrographic elements. In old fields, where the samples are scarce or not suited for making permeability measurements, thin section analysis may be used to estimate the permeability. The results of the fuzzy logic algorithm were in excellent agreement with conventional regression analysis. The advantage of using this new algorithm lies in the speed of analysis.

The petrographic analysis also indicated that quartz and feldspars are the dominant detrital grains, whereas, anhydrite and dolomite are the dominant cements. Both quartz and feldspar overgrowths are ubiquitous throughout the reservoir but never exceeded 2%. Most of the feldspar grains are altered (sericitized) and majority of the intraconstituent porosity is present among the partially dissolved feldspar grains especially in zone 1. Quartz and feldspar grains are also coated with clay and hematite. These clay rims consist of authigenic chlorite (Haynes, 1978). Hematite is more conspicuous in the low permeability part (zone 2), where it coats the grain and also stains the anhydrite (poikilotopic) cement. Both quartz and feldspar ranked in the middle with respect to controlling the permeability based on the fact that as their percentage increases, the percentage of anhydrite and dolomite cement decreases. The rock fragments consist of clay, dolomite (dolomicrite), and metamorphic rock fragments (zone 1). Rock fragments do not exert much control over the permeability because of their low percentage and fine sand size. Only when clay fragments form the pseudomatrix as they get squeezed between the harder grains, both porosity and permeability are reduced. Detrital clay may have originally been carbonate clay which was diagenetically altered to dolomicrite. Detrital clay (now dolomicrite) could be easily identified due to its exclusive presence in the primary pores. Detrital clays are present in substantial amounts only in the thinly laminated poorly sorted silty sandstone zones not thicker than 2 inches (zone 1). This is the reason why clay does not affect the permeability and is close to the bottom of the conventional ranking (Table I). Cement is present in the form of anhydrite and dolomite. Anhydrite is present in three morphologies: (1) fine crystalline nodules, mainly in the upper silty-shaly zone at the top of the Shattuck Member and in small amounts in zone 2 (Figure 2), (2) coarse, pore filling crystals, and (3) large patches of poikilotopic crystals surrounding several grains. It is the poikilotopic morphology which has affected the permeability especially in zone 2. Dolomite is present in two morphologies: (1) micritic dolomite, probably formed by the dolomitization of the carbonate mud, and (2) large poikilotopic patches. The presence of the inclusions of dolomicrite and anhydrite in the poikilotopic dolomite suggest that poikilotopic dolomite post-dates both of them. Dolomite and anhydrite are distributed in the form of irregular patches (2 - 4 mm in diameter) throughout the reservoir zone. This patchy distribution is probably due to the heterogeneous dissolution pattern. Both dolomite and anhydrite have also replaced the detrital grains. Although, based on the correlation coefficient and fuzzy logic, dolomite seems to more important than anhydrite in controlling permeability, it should be the opposite. This inverse ranking of dolomite and anhydrite is due to a 1.5 ft. thick low porosity and permeability layer of clastic dolomite at the top of the Shattuck Member which contains as much as 50% dolomite. In the rest of the reservoir zone, the amount of dolomite never exceeded 15 %. Because of this biased distribution, dolomite seems to have more control over permeability (Figure 5E). The dead oil present reduced the porosity and the interconnection between the pores and, therefore, its effect on the permeability was also acknowledged.

Among the porosities, the secondary intergranular porosity is the most dominant type and exerts the most influence on the permeability (Table I and Figure 5K). As the dissolution increases, the secondary intergranular porosity increases and the interconnection between the pores becomes good.

Petrographic elements	Amount (Ranges)	Correlation (R^2) with permeability	Correlation (R^2) with total ϕ	Ranking based on the R^2 with permeability
Secondary intergranular ϕ	0 - 27%	0.75	0.91	1
Total Secondary ϕ	0 - 27%	0.71	0.97	2
Total ϕ	0 - 27%	0.70	-	3
Pore size (microns)	0 - 70 μm	0.70	0.81	4
Quartz	0 - 75%	0.47	0.37	5
Feldspar	0 -26%	0.43	0.33	6
Dolomite	0 - 55%	-0.36	-0.26	7
Grain size (microns)	0 - 120 μm	0.30	0.25	8
Intraconstituent ϕ	0 - 3.5%	0.21	0.36	9
Primary ϕ	0 - 4%	0.17	0.20	10
Moldic ϕ	0 - 3%	0.13	0.14	11
Anhydrite	0 - 40%	-0.12	-0.07	12
Dead oil	0 - 11%	0.11	0.09	13
Micro- ϕ	0 - 5.5%	-0.10	-0.03	14
Clay	0 - 21%	-0.06	-0.13	15
Rock Fragments	0 - 9%	0.01	-0.06	16

Table I: Summary of the petrographic elements and their relationship (R^2) with permeability and total porosity. The ranking shows the importance of that petrographic element in controlling the permeability as determined by the conventional regression analysis.

As the amount of secondary porosity increases, so does the pore size. This explains why the pore size is very important in controlling the permeability (Figure 5M). The relationship between the grain size and permeability is not very good (Table I and Figure 5N). The larger size grains are present among the well-sorted part of the reservoir (zone 2) were affected by early anhydrite cementation and almost all the original porosity was lost. The moderately-sorted lagoonal sandstones (zone 1) were not affected by early cementation and enough primary porosity was available for the fluids responsible for dissolution to move freely through the system and produce secondary porosity.

The Fuzzy Logic Algorithm:

As indicated earlier, a new fuzzy logic algorithm was applied to determine the ranking of the petrographic elements with respect to permeability. The following paragraphs briefly describe the application of the fuzzy logic algorithm, and Table II shows the comparison between the conventional ranking and the fuzzy logic ranking.

All the petrophysical attributes examined under the thin section contribute to permeability. Although, this is true we are also aware that each attribute alters permeability in a unique manner. It is difficult to accurately

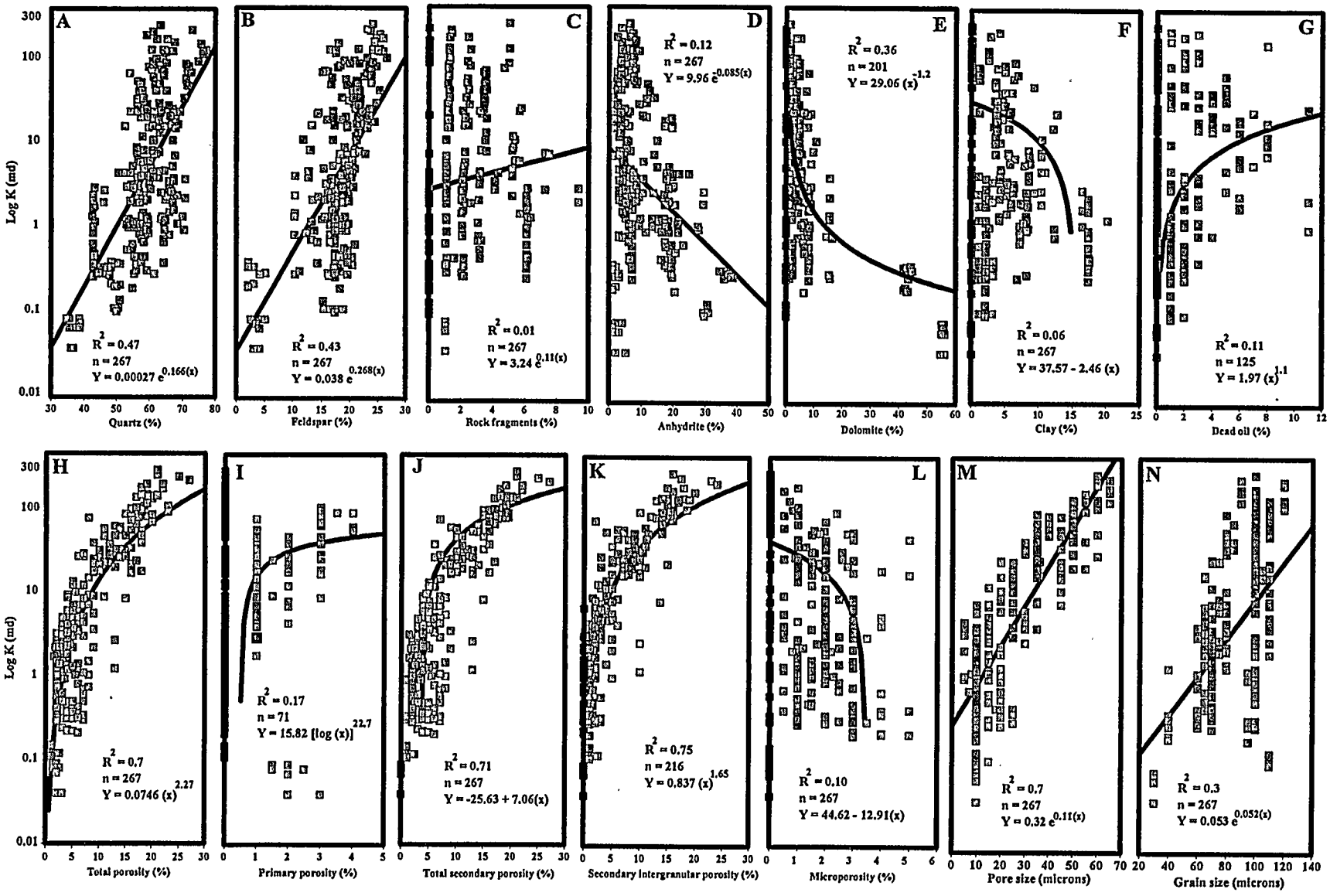

Figure 5: Relationships between permeability and different petrographic elements in the Shattuck Member, Sulimar Queen and South Lucky Lake fields.

quantify the non-linear interaction between each of the petrophysical parameters with permeability. The fact that permeability is affected differently by each attribute brings out the question of orthogonality of the petrophysical attributes with respect to each other. Truly dependent attributes should alter permeability in a similar fashion.

Facing the dilemma of not knowing the explicit relationship between the petrophysical attributes and permeability, the question of the most significant attributes that contribute to permeability was resolved using the fuzzy logic algorithm. This data-directed algorithm compares the effect of each individual input parameter (the petrophysical measurement) on the output (the minipermeameter permeability). Briefly, the algorithm achieves this comparison by building fuzzy membership functions for each of the input parameter. The fuzzy membership functions are then defuzzified using the centroid defuzzification rule to plot fuzzy curves. The range of each of these fuzzy curves on the ordinate reflects the effect of each input parameter on the output (Figure 6). Details of the fuzzy logic algorithm are beyond the scope of this paper and the interested reader is referred to Lin (1994). Our objective in this study was to rank the petrophysical attributes in a descending order of their influence on the permeability of the sample.

Figure 6 shows the fuzzy curves resulting from the Fuzzy Logic method. The first row, represents the petrophysical parameters which have the largest influence on the permeability. This is evident from the range of each fuzzy curve on the corresponding ordinate. For example, the fuzzy curve for total porosity exhibits a range of approximately 160, whereas, feldspar and anhydrite exhibit ranges of approximately 90 and 45 respectively. Here, total porosity has greater influence than feldspar which, in turn, affects permeability more than anhydrite.

Prior to generating the fuzzy curves for these petrophysical attributes, histograms were plotted for each attribute. The histograms ensure that the data have approximately gaussian distribution. Heavily skewed data result in erroneous results from the fuzzy logic algorithm. Histograms for moldic porosity and intraconstituent porosity were skewed even after normalization and hence the fuzzy logic results pertaining to these parameters were considered inconclusive. These parameters were eliminated from analysis. Table II compares the ranking obtained from the fuzzy logic algorithm with conventional regression analysis. It is evident from Table II that the most important petrographic elements (ranking 1 to 5) controlling permeability are accurately predicted by the new algorithm. From Table II, we can also see that the fuzzy logic algorithm ranked microporosity in the 6th place. From conventional ranking, we see that microporosity was ranked 8th. In the case of Sulimar Queen, we know that microporosity should affect permeability more than dolomite which appears to be in agreement in the fuzzy logic prediction.

It is important to realize that the conventional ranking technique compares the best regression models for different petrographic parameters. These regression models do not have the same polynomial order and hence the comparison is not entirely equitable. The fuzzy logic algorithm compares all the parameters on the same basis and hence is more superior in that aspect.

From the petrographic analysis, we concluded that zone 1 is the main reservoir since it was not affected by anhydrite cementation. Zone 1 also indicated the effects of dissolution and thus has the highest porosity and permeability. This detailed petrographic analysis also helped to understand the subtle changes in the depositional environment and the development of the depositional model.

Petrographic elements	Ranking due to regression	Ranking due to fuzzy logic
Secondary intergranular ϕ	1	1
Total secondary ϕ	2	2
Total ϕ	3	3
Quartz	4	4
Feldspar	5	5
Dolomite	6	7
Anhydrite	7	9
Microporosity	8	6
Clay	9	8
Rock fragments	10	10

Table II: Comparison of conventional and fuzzy logic based ranking of petrographic elements.

LOG ANALYSIS

As mentioned previously, only four modern log suites were available, and the rest of the field contained only old gamma ray and neutron logs. Due to the absence of other logs (e.g., resistivity, sonic, density, etc.) and the unreliability of the old neutron logs; correlations between core porosity, permeability, water saturation, and petrographic elements had to be made with gamma ray logs in order to predict these properties in the uncored wells. Both, the old and new logs, were digitized on 0.5 feet interval.

Developing relationships between gamma ray and porosity, total water content, and permeability:

In the Sulimar Queen and adjacent fields, a negative correlation was observed between old gamma ray (API) and neutron (API) values. This correlation implied that porosity increases with the increase in gamma (Ali et al., 1996). Although, old neutron and gamma ray logs were not reliable, this behavior still helped to understand the overall relationship between gamma ray values and porosity. A positive correlation was also observed between core porosity and gamma ray in the Sulimar Queen field (Figure 7A) as well as in the Queen field (Figure 7B) which is located 20 miles northeast of Sulimar Queen field. Similar relationships between gamma ray and porosity in the Sulimar Queen and adjacent fields suggested a possible regional trend. This increased our confidence in using the correlation between core porosity and gamma ray, developed in one well (Well 1-16) to be used for predicting porosity throughout the field (Figure 7A). The correlation may be expressed as:

$$\phi = 0.334\, e^{0.0526(\gamma)} \qquad (1)$$

where "ϕ" is the porosity in percent and "γ" represents the gamma ray value in the API units.

This relationship was only good for the *sand portion of the Shattuck member* as determined from the core description. In the Shattuck zone, the gamma ray values were not be controlled by the amount of clay but

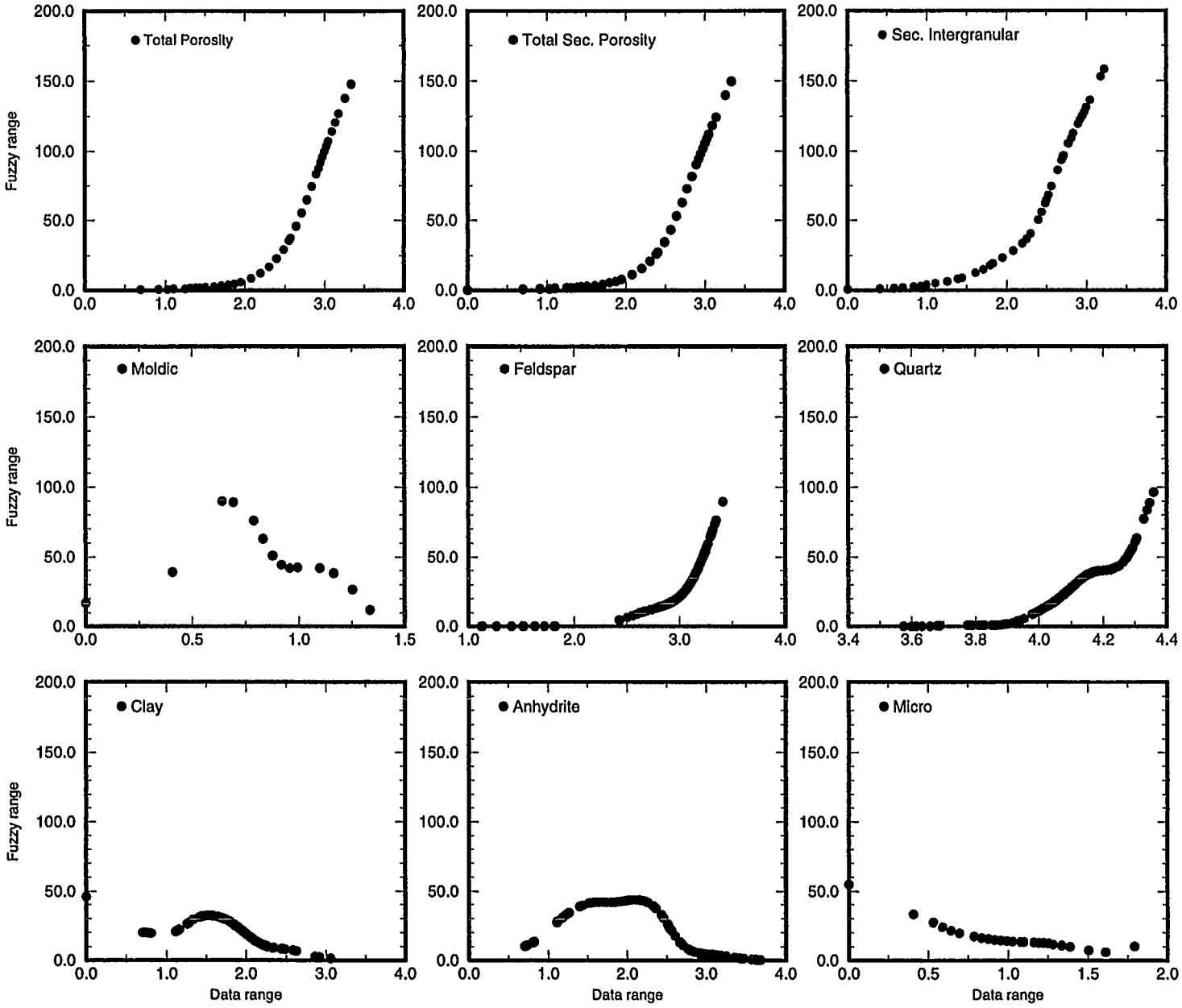

Figure 6: Fuzzy curves for various petrographic elements. The importance of each element is decided by the range of its fuzzy curve.

by the amount of potassium feldspar (confirmed by petrographic and XRD analysis) and uranium (confirmed by the spectral gamma ray log from one well in the Queen field) (Figure 8A). Unfortunately, the spectral gamma ray log was not available from well 1-16 in which core porosity, water saturation, and permeability data were available (Figure 8C). This uranium was assumed to be present in the formation water since gamma ray values are proportional to the total water content (W_{TC}) (Figure 9A). Similar relationships were also observed in the Queen (Figure 9B) and adjacent fields, again implying a regional trend. These trends emphasized that the relationship developed in only one well could be applied with reasonable confidence throughout the field (Ali et al., 1996).

The total water content represents the percentage of the total rock volume occupied by the water. The conventional way of representing the water saturation (S_w) as the percentage of porosity occupied by water was not used because of its inadequacy in conveying the amount of water present. For example, a 5% porosity rock with water saturation of 90% contains less volume of water than 20% porosity rock with only 35% water saturation. If we use the conventional representation of the water saturation the relationship between gamma ray response and volume of water could not be identified correctly. We suggest using total water content (W_{TC}) instead of conventional water saturation (S_w) in order to understand the relationship between the gamma ray response and the control of radioactive dissolved species in the water. The following relationship developed in well 1-16 was then used with caution to predict the total water content (W_{TC}) (Figure 9A):

$$W_{TC} = 4.6\ 10^{-5}\ \gamma^{2.9} \qquad (2)$$

Here, "W_{TC}" is the total water content in percentage, and "γ" the gamma ray value in API units. Once the total water content is calculated, then water saturation for particular a porosity can be calculated using:

$$S_W = [W_{TC}/\phi]\ X\ 100 \qquad (3)$$

Improving the reliability of old gamma ray logs:

The old gamma ray logs had varying scale ranges, therefore, a comparison of gamma ray API values from different wells was meaningless (Ali et al., 1996). Also, porosity and total water content obtained from the *unscaled* old gamma ray logs using the relationships developed in well 1-16 (Equations 1 & 2) were erroneous. Because of the different scale ranges of the old gamma ray logs, the extrapolation beyond the range of original data values (Well 1-16) yielded wrong results. In order to make old gamma ray logs useful and reliable, they had to be rescaled to the same datum so that the information provided by each well became comparable.

The old gamma ray logs were rescaled using the methodology proposed by Barrett (1994). In this methodology, modern logs are needed to determine the representative value ranges and the average high and low values in the zone of interest in that area. The average high and low gamma ray values were determined from the four modern logs available in the field. These values were 80.5 API and 12 API units (Ali et al., 1996) respectively. Using these average values, all the old gamma ray logs were rescaled. Example of the rescaled logs from well 1-14 and 5-1 are shown in Figure 10. The increase in the reliability of the old gamma ray logs after rescaling is also evident from the improved correlation coefficient between the core porosity and

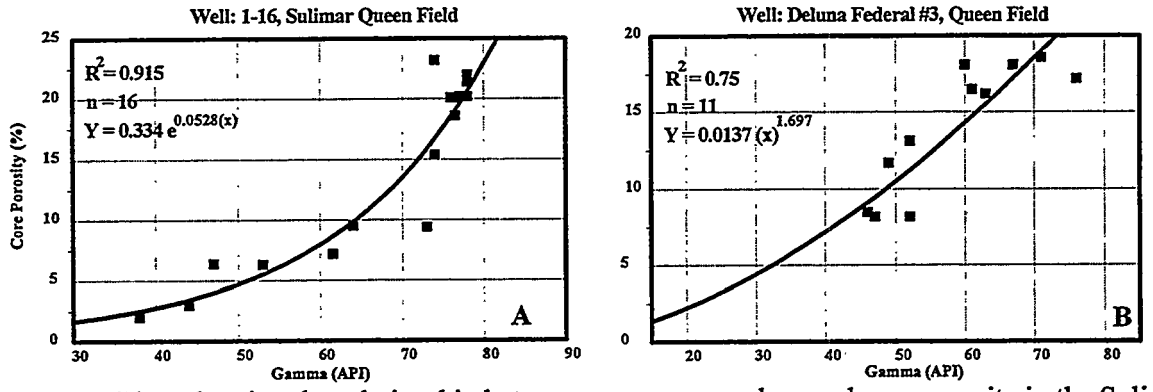

Figure 7: Plots showing the relationship between gamma ray values and core porosity in the Sulimar Queen (A) and the Queen field (B).

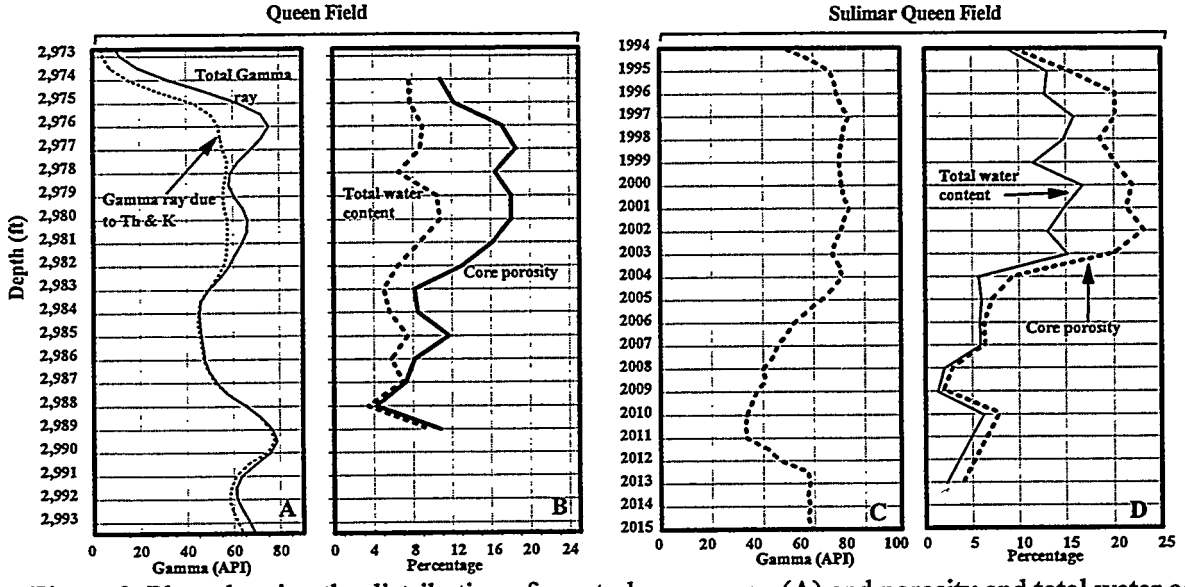

Figure 8: Plots showing the distribution of spectral gamma ray (A) and porosity and total water content (B) in the Queen field. Also shown is the gamma ray log (C) and porosity and total water content (D) in the Sulimar Queen field. As the porosity and total water content increases so does the gamma ray value.

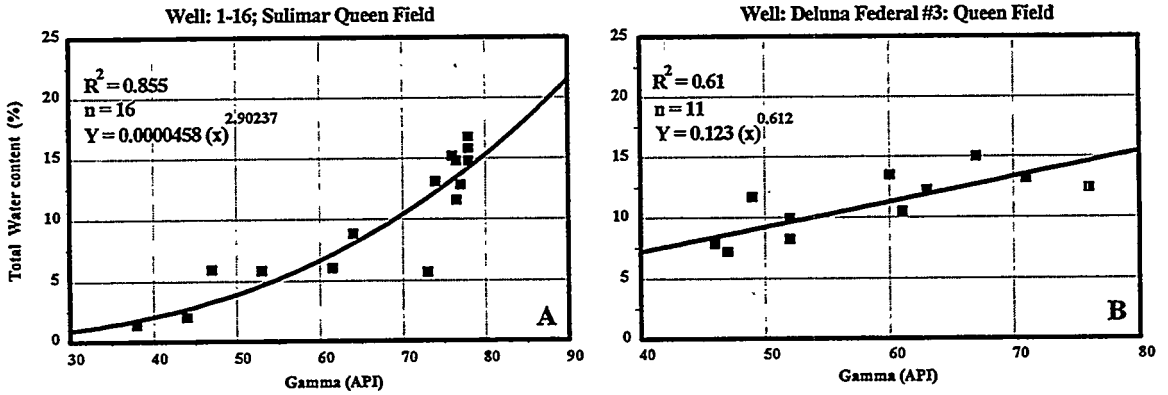

Figure 9: Plots showing the relationship between total water content and gamma ray values in the Sulimar Queen (A) and the Queen field (B).

the gamma ray values (Figure 11). The gamma ray derived porosity and total water content using Equations 1 and 2 were compared with the core porosities and total water content in wells 1-14 and 5-1 for reliability (Figures 12 and 13). Porosity calculated from the rescaled gamma ray logs also captured the presence of individual high and low porosity zones which were not distinguishable in the porosities obtained from unscaled gamma ray logs (Figure 14).

Air permeability and porosity also indicated a positive relationship in the Sulimar Queen field (Figure 15A). Similar relationships were also observed in the adjacent fields (Ali et al., 1996). A positive correlation was also observed between gamma derived porosity and permeability (Figure 15B). The relationship between gamma ray derived porosity and permeability is more useful (Figure 15B) because it can predict the whole range of original permeability distribution as opposed to one obtained from cores (Figure 15A). The whole range of permeability values could not be predicted using the gamma ray values because the maximum gamma ray reading was 80 API. This corresponds to a permeability of approximately 40 md while the maximum core permeability 116 md.

DEPOSITIONAL ENVIRONMENT

Two opposing interpretations for the deposition of the Queen Formation are available in the literature. Boyd (1958), Pray (1977), and Sarg (1977) proposed an aqueous "all wet" depositional model. They attribute the deposition in a subsiding lagoon based on the lack of evidence for extensive subaerial exposure in the Queen or the adjacent formations in the Guadalupe Mountains in Texas and New Mexico. On the other hand, Silver and Todd (1969), Mazzullo (1984) (1985), and Malicse and Mazzullo (1990) suggested an eolian/continental environment. During Guadalupian time, the northwest shelf was a flat, slowly subsiding platform to the north of the Delaware Basin (Figure 1). During Queen deposition, a broad lagoon was present between carbonate sand shoals and the land - sea margin (Ball, 1971).

Our depositional model was constructed after assimilating all the information from the cores, petrographic analysis, logs, lithologic description of the cores and chip analysis (Haynes, 1978), and the outcrop data. In the Sulimar Queen and the South Lucky Lake fields, the Shattuck Member was deposited in a mix of coastal sabkha, shallow lagoon (with variable energy and depth), and eolian (dry eolian sand sheets of Mazzullo, 1990) (Figure 16). These environments were established based on the variations in grain size and sorting, poorly developed sedimentary features (flaser bedding, ripple laminations, cross laminations, bioturbation, and haloturbation), and the distribution of overlying and underlying anhydrite (Figure 16).

Coastal Sabkha is the deflation flat present behind the lagoon. Well-sorted sandstone underlying the bottom anhydrite was deposited in the sabkha and exhibits haloturbation due to the growth of the displasive anhydrite nodules. This coastal sabkha is overlain by lagoonal deposit comprising of anhydrite, shaly-siltstone, and well-sorted, structureless red sandstones. These sandstones were probably deposited when sand was blown into the lagoon as the desert (sand sheet) environment encroached onto the lagoon. In the case of zone 2, these sandstones are well cemented by the anhydrites and have the lowest porosity and permeability. They also do not indicate effects of haloturbation. Another important observation which suggests a lagoonal deposition is the regional extent of this anhydrite. Overlying is a three feet sequence of well sorted eolian sandstones with weakly developed cross-stratifications and asymmetric wind ripples. Both lagoonal and eolian sandstones are very well cemented by anhydrite and have very low clay content and porosity. The combined distribution of

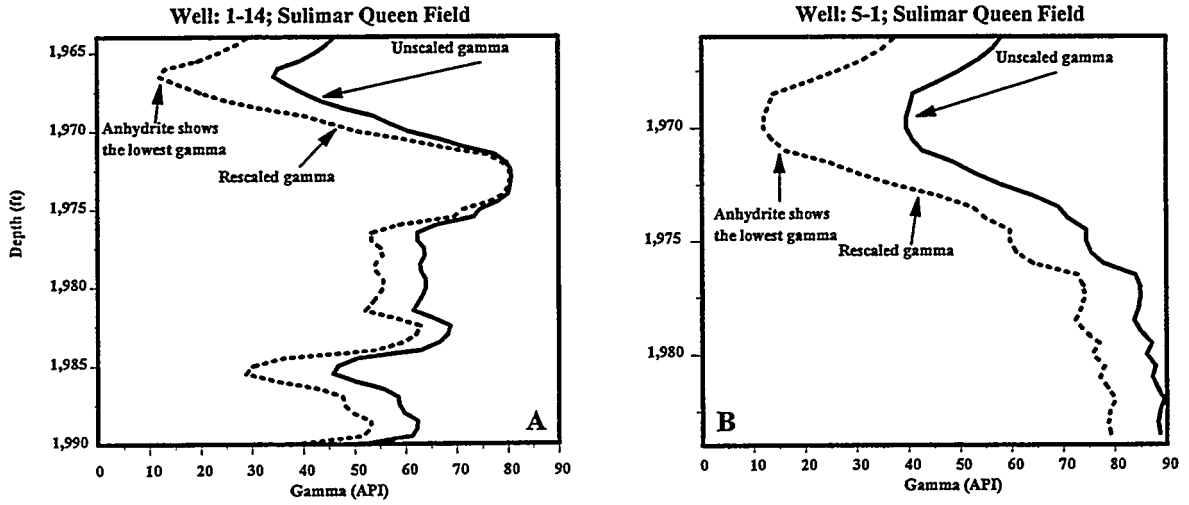

Figure 10: Comparison of unscaled and rescaled gamma ray logs. The rescaled logs have the minimum of 12 API and maximum of 80 API values. Note the presence of anhydritic portion in the rescaled gamma ray logs which were not easily identifiable in unscaled logs.

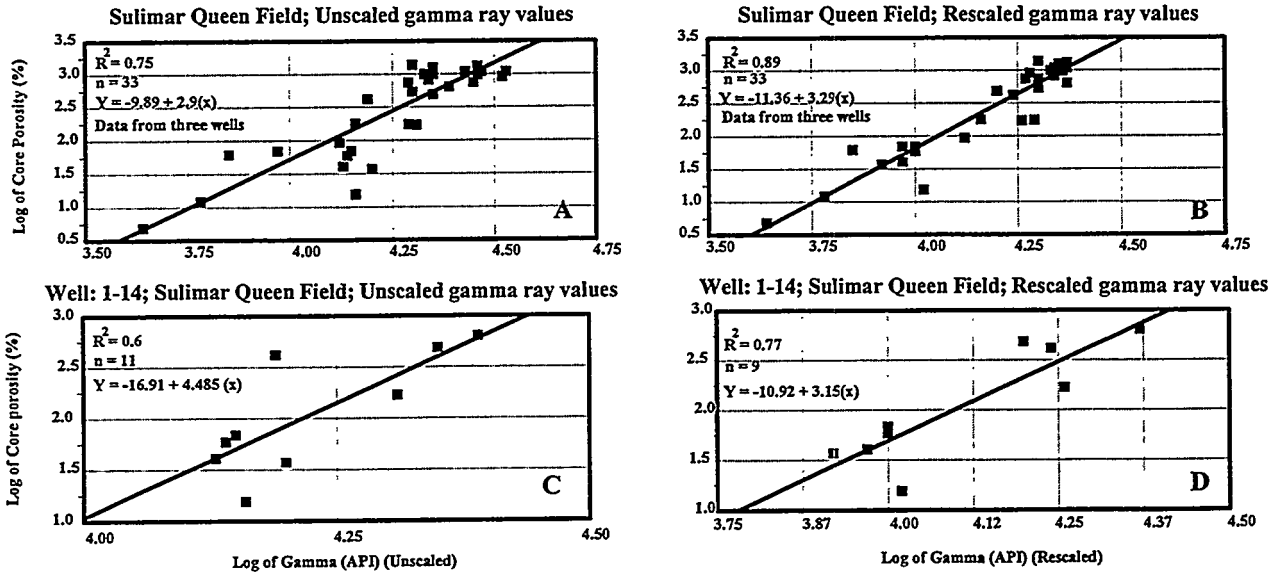

Figure 11: Plots showing the effects of rescaling on the correlations between core porosity and gamma ray values. Note the improvement of correlation from (A) to (B) and (C) to (D).

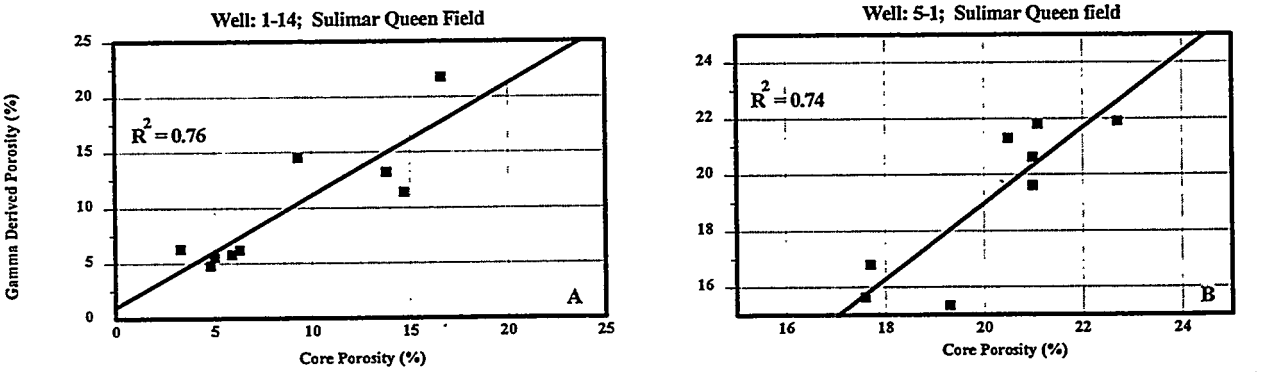

Figure 12: Comparison of core porosity and the porosity predicted using rescaled gamma ray logs in the Sulimar Queen Field.

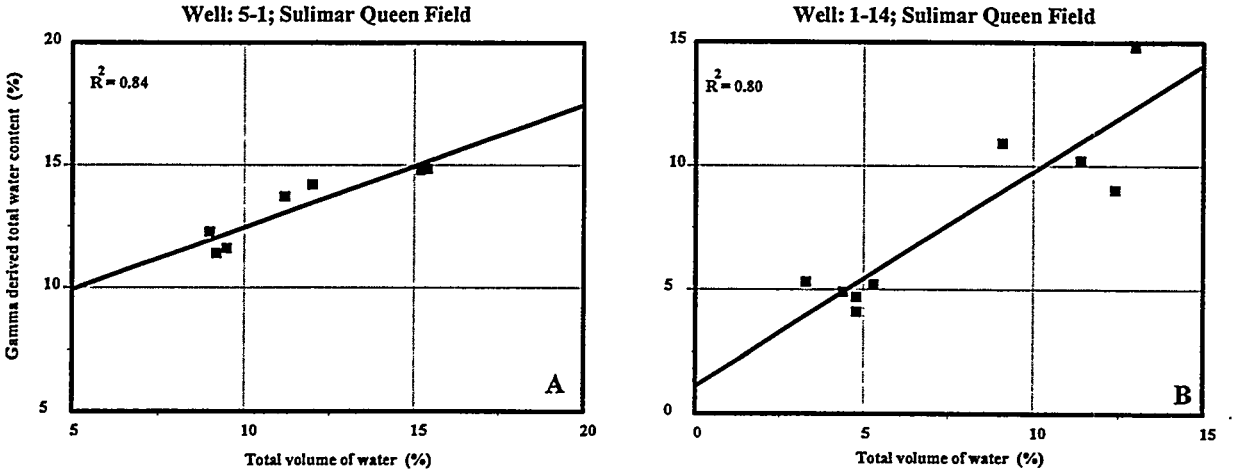

Figure 13: Comparison of core derived and rescaled gamma ray logs derived total water content. Note a strong correlation in both wells.

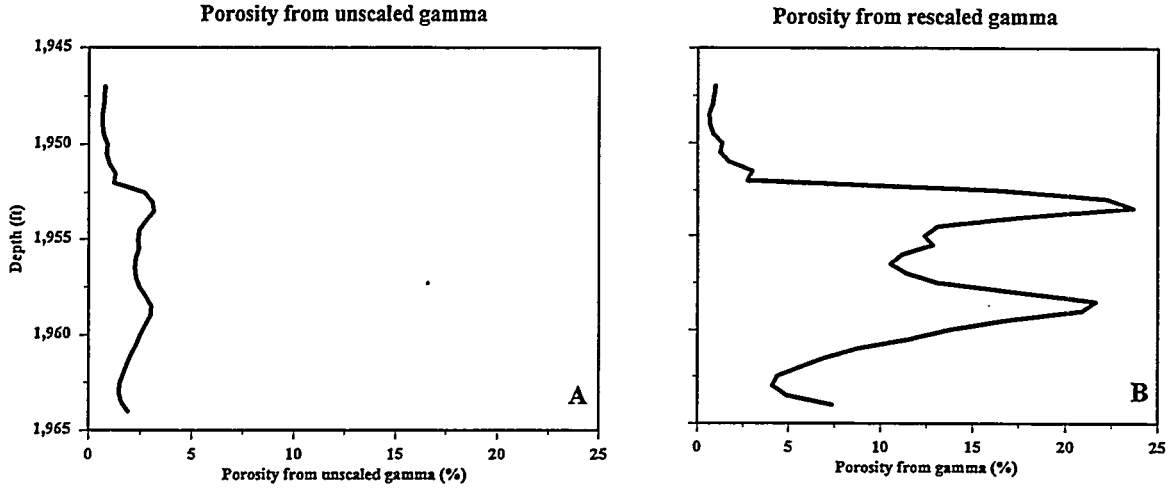

Figure 14: Comparison of porosity distribution as calculated from unscaled (A) and rescaled (B) gamma ray logs in well 5-2. High and low porosity zones are clearly visible in the porosity derived from rescaled gamma ray log (B).

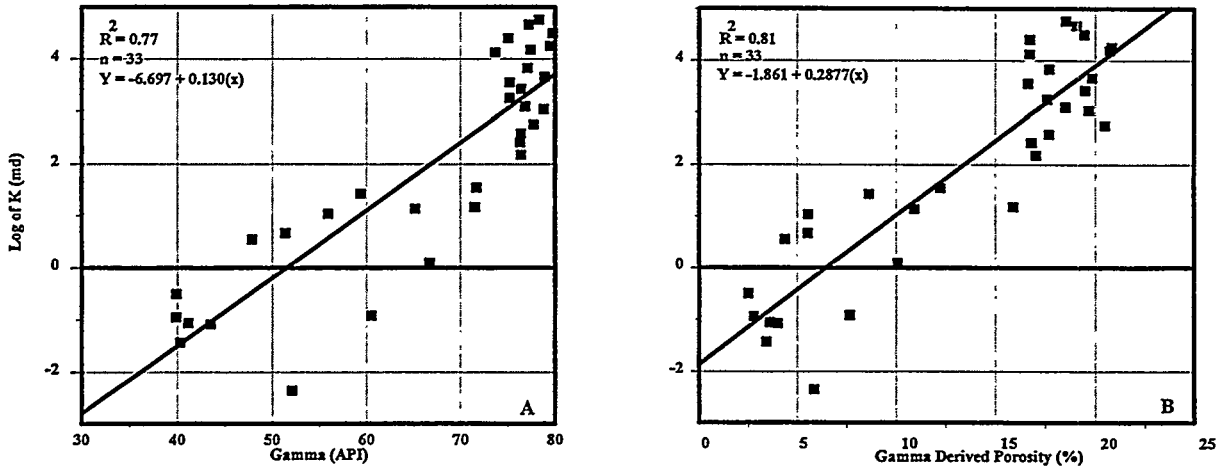

Figure 15: Plots showing the positive correlation between Gamma (API) values and permeability (A), and gamma ray derived porosity and permeability (B) in well 1-16 in the Sulimar Queen field.

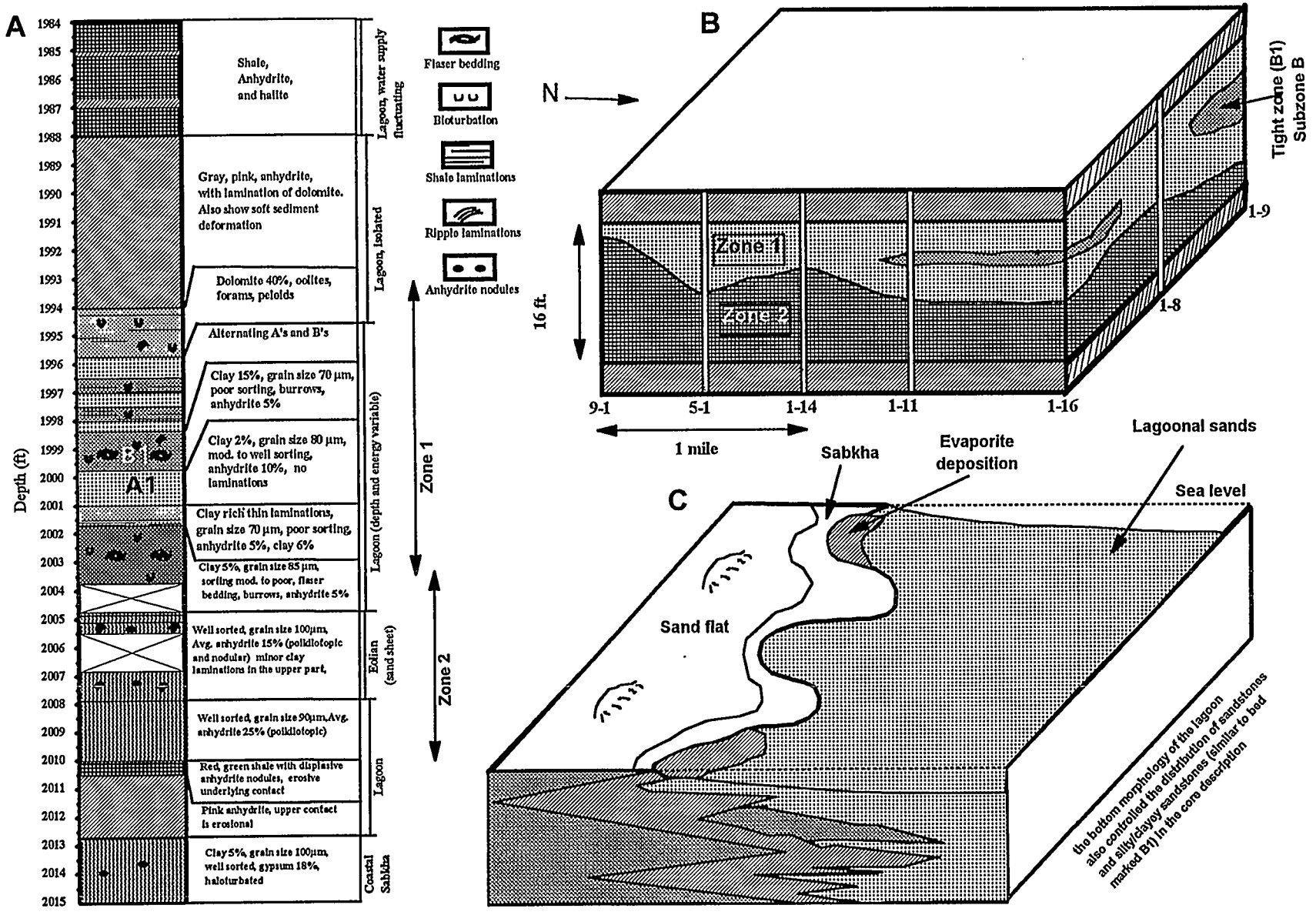

Figure 16: (A) Core description along with inferred depositional environments. (B) Block diagram of the Sulimar Queen field showing the distribution of the zone 1, zone 2, and low permeability subzone B1 within zone 1. (C) Generalized depositional model for the Shattuck zone in the Sulimar and adjacent fields. The interfingring of different environments created the present distribution of the Shattuck Member.

the bottom lagoonal and overlying eolian sandstones (zone 2, Figure 16) can be traced throughout the field because of their low gamma ray values (API). These sandstones thicken and completely replace the overlying lagoonal reservoir facies forming a trap in the western part of the field.

Zone 1 was deposited in a shallow lagoon with variable depth and energy level and displays moderate-sorting. This zone also has the highest porosity and permeability and forms the main pay. This zone probably escaped the early pervasive cementation by anhydrite and later porosity enhanced by dissolution. Zone 1 (Figure 16) lacks evidence of subaerial exposure and sedimentary structures typical of sabkha, fluvial, or eolian environments. The absence of curled clay flakes, clay pebbles, mud cracks with sandy infills, cross stratification, channel or flood plain deposits supports its deposition in a lagoon. Also, the eolian sands interbedded with beds of aquatic origins should show effects of fluvial erosion and wind deflation, which are also absent in zone 1. The alternating clay rich beds (B1) (Figure 16) containing thin laminations of clayey-silty sandstone with the featureless moderately-sorted sandstone beds (A1) (Figure 16) suggest a minor fluctuation in the energy of the lagoon. Zone 1 grades upward through sandy dolomite into anhydrites that precipitated in the lagoon. This transition was observed in the cores from Sulimar Queen as well as the adjacent fields. This regional extent of anhydrite points towards the deposition in a lagoon instead of local ponds or salinas. The absence of fossils suggest the conditions were hypersaline.

The Shattuck Member in the Sulimar Queen and adjacent fields was deposited in a mixed lagoonal-sabkha-eolian environment. The Sulimar Queen and adjacent fields were formed due to combining affects of lagoon bottom morphology, migration of different depositional environments in response to minor sea level fluctuations, the distribution of lagoonal anhydrite and anhydrite cemented lagoonal and eolian sandstone, minor structural features, and most importantly the development of secondary porosity.

NUMERICAL SIMULATION OF THE SULIMAR QUEEN

The overall objective of this project was to characterize the Sulimar Queen from a limited dataset. The confirmation of successful characterization is accomplished through a reliable reservoir model which honors most static (petrophysics and geology) and dynamic (production and pressure) data, and results in a reasonably accurate forecast of the reservoir performance.

The following paragraphs explain the stages of data integration which resulted in successful reservoir characterization. The old gamma ray and neutron logs (unscaled) were only useful for detecting the radioactive Shattuck sand, and were treated as perforating logs. Rescaling the logs provided improved correlations to predict porosities in the pay zone. The process of rescaling also improved the log signatures for detecting the anhydrite sequences bounding the pay sand which helped in delineating the sand thickness and the top of the structure for the 36 wells present in the field. Once the top of the structure was accurately identified in all the wells, a simple geostatistical mapping algorithm was applied to obtain a smooth fieldwide top of the structure. Using geologic input, this structure was modified manually (Figure 17). The initial porosity field distribution was also estimated using the same geostatistical mapping technique. The permeability control points in the field were obtained from inverse DST tests which were performed at many wells. Using an analytical k-ϕ relationship for each layer, derived from well 1-16, the initial permeability map was obtained.

The rescaling of the logs indicated the presence of a thin, tight zone which separated zones 1 and 2. The outcrop histograms also suggested three distinct lithological units (DOE Report). The proposed geologic model

and some of the well logs indicated that this zone may not be continuous throughout the field. Since the tight zone was thin and assumed to be discontinuous, the final simulation model comprised two layers only. The upper simulation flow layer representing the zone with high permeability and the lower flow layer for the low permeability zone. The thin, tight zone was combined with the lower layer.

The PVT analysis performed on oil samples collected from an adjacent field was used as initial PVT data in the simulator. This PVT data was unable to explain the large gas production in the initial producing life of the field. This is because the reservoir was initially assumed to be undersaturated. Careful analysis of the structure and production (GOR) profile indicated the presence of a gas cap. This was later confirmed independently (Lemay, 1996). Since, the only accurate measurement in the field was the oil production, this was used as an inner boundary condition constraint in an automatic history matching algorithm developed at the Petroleum Recovery Research Center. Based on this constraint, a good history-match was obtained for the primary production. The waterflood forecast obtained by using the reservoir model derived after primary production history-match is shown in Figure 18.

We considered the Sulimar Queen to be successfully characterized based on the detecting and locating the previously unconfirmed gas cap, combined with a consistent geologic description and reasonable simulation forecasts.

CONCLUSIONS:

In this study, new techniques were applied for improving the quantity and quality of data for better reservoir characterization of old fields.

1. The minipermeameter is useful in capturing the small-scale heterogeneities. Permeability measurements made on fine grids also improve the lithologic description of the cores.
2. Combination of minipermeameter and petrographic analysis allows the collection of large amount of petrographic data using fewer thin sections. The control of different petrographic elements on permeability can be easily and accurately determined. Correlations developed between the permeability and petrographic elements are also reliable.
3. The newly developed fuzzy logic algorithm is a fast, unbiased and reliable method for establishing the importance of each petrographic element on permeability.
4. Rescaling of the old logs improves their reliability. In the Shattuck Member, porosity, permeability, and water saturations could be estimated using the gamma ray logs.
5. Maximum geological and petrophysical information was gathered from the limited database by combining small-, medium-, and large-scale data obtained from minipermeameter, cores, petrographic analysis, and logs. The distribution of the different zones was mapped successfully in the field and a depositional model was developed.
6. Using this data, a successful characterization of the Sulimar Queen was obtained and confirmed through a good history-match of the primary production and a reasonably accurate forecast of the waterflood performance.

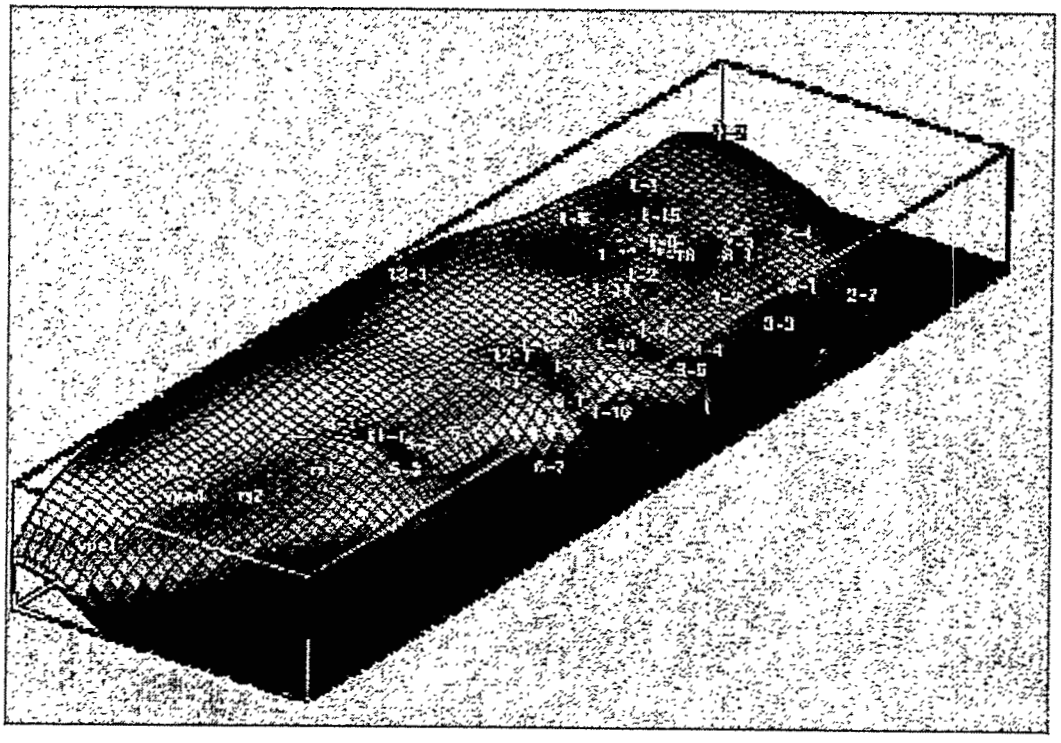

Figure 17: Top of the Sulimar Queen structure predicted using a simple geostatistical method and manually adjusted to geologic input.

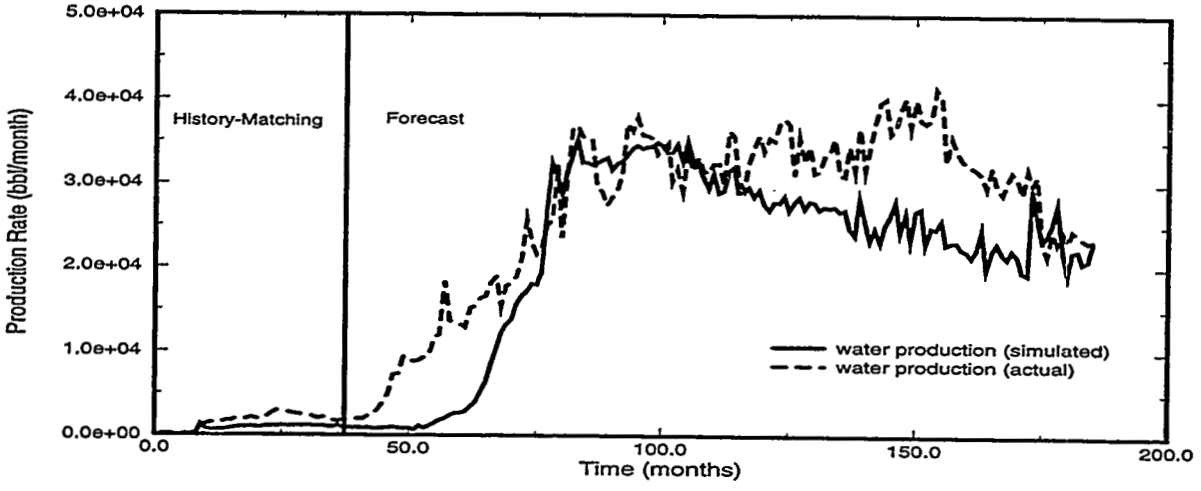

Figure 18: Waterflood history–match and forecast.

REFERENCES CITED

Ali, M., Chawathé, A., Ouenes, A., Weiss, W.,1996, Improved log analysis for the characterization of the Sulimar Queen field, southeast New Mexico: PRRC Report No. 96-33, pp. 32.

Balls, S. M., Roberts, J. W., Norton, J. A., and Pollard, W. D., 1971, Queen Formation (Guadalupian, Permian) outcrops of Eddy County, New Mexico, and their bearing on recently proposed depositional models: American Association of Petroleum geologists Bulletin, v. 55, p. 1348 - 1355.

Boyd, D. W., 1958, Permian sedimentary facies, central Guadalupe Mountains, New Mexico, New Mexico Bureau of Mines and Mineral Resources bulletin. 40, pp. 100.

Barrett, G. D., 1994, Use of computers to perform old log analysis: SPE Computer Applications, August, p. 9 - 12.

Goggin, D. J., Thrasher, R. L., and Lake, L. W., 1988, A theoretical and experimental analysis of minipermeameter response including gas slippage and high velocity flow effects: In Situ, v. 12 (1&2), p. 79 - 116.

Haynes, L. Cynthia, 1978, Sandstone diagenesis and development of secondary porosity, Shattuck Member, Queen Formation, Chaves County, New Mexico: M.A., Thesis, The University of Texas at Austin, pp.148.

Lemay, William, 1996, Personal Communication

Lin, Yinghua., 1994, Input identification of Modeling with fuzzy and neural systems: Ph.D., Dissertation, New Mexico Institute of mining and Technology, Socorro, New Mexico, pp. 89.

Martin, D. F., Buckley, J., Weiss, W. W. and Ouenes, A., 1996, Integration of advanced geoscience and engineering techniques to quantify interwell heterogeneity, Quarterly Technical Report submitted to DOE under contract no. DE-AC22-93BC14893.

Mazzullo, J. M., Williams, M., and Mazzullo, S. J., 1984, The Queen formation of Millard Field, Pecos county, Texas: Its lithologic characteristics, environment of deposition, and reservoir petrophysics: Transactions southwest section American Association of Petroleum Geologists, publication 84-78, p. 103 - 110.

Mazzullo, S. J., and Hendrick, C. L., 1985, Road log and locality guide, lithofacies, stratigraphy, and depositional models of the back-reef Guadalupian section (Queen, Seven Rivers, Yates, and Tansill Formations), SEPM Field Guidebook, p. 1 - 30.

Pray, L. C., 1977, The all wet, constant sea level hypothesis of Upper Guadalupian, shelf and shelf edge strata, Guadalupe Mountains, New Mexico and Texas: West Texas Geological Society, Special Publication 77 - 16.

Sarg, J. F., 1977, Sedimentology of the carbonate-evaporite facies transition of the Seven Rivers formation (Guadalupian, Permian) in southeast New Mexico: SEPM Permian basin section, special publication, 77 - 16, p. 451 - 478.

Silver, B. A., and Todd, R. G., 1969, Permian cyclic strata, northern Midland and Delaware Basins, west Texas, and southeastern New Mexico: American Association of Petroleum Geologists bulletin, v. 53, p. 2223 - 2251.

Suboor, M. A., and Heller, J. P., 1995, Minipermeameter characteristics critical to its use: In Situ, v. 19 (3), p. 225 - 248.

Towards an Integrated Petrophysical Tool for Multiphase Flow Properties of Core Samples

Roland LENORMAND

Institut Français du Pétrole
Rueil Malmaison 92852 cedex FRANCE
e-mail: roland.lenormand@ifp.fr

Abstract

This paper describes the first use of an Integrated Petrophysical Tool (IPT) on reservoir rock samples. The IPT simultaneously measures the following petrophysical properties:

- Complete capillary pressure cycle: primary drainage, spontaneous and forced imbibitions, secondary drainage (the cycle leads to the wettability of the core by using the USBM index);
- End-points and parts of the relative permeability curves;
- Formation factor and resistivity index.

The IPT is based on the steady-state injection of one fluid through the sample placed in a Hassler cell. The experiment leading to the whole Pc cycle on two reservoir sandstones consists of about 30 steps at various oil or water flow rates. It takes about four weeks and is operated at room conditions..

Relative permeabilities are in line with standard steady-state measurements. Capillary pressures are in accordance with standard centrifuge measurements. There is no comparison for the resistivity index, but the results are in agreement with literature data. However, the accurate determination of saturation remains the main difficulty and some improvements are proposed.

In conclusion, the Integrated Petrophysical Tool is as accurate as standard methods and has the advantage of providing the various parameters on the same sample and during a single experiment. The IPT is easy to use and can be automated. In addition, it can be operated in reservoir conditions.

1. Introduction

The purpose of reservoir models is to simulate fluid displacements in very complicated rock geometry. The flow equations are based on Darcy's law which includes both fluid and rock properties. The basic

equations can be written for two immiscible fluids (1 and 2) flowing in a porous medium with porosity ø and permeability K. At any point x of the medium:

$$u_1 = \frac{K Kr_1}{\mu_1}(\rho_1 g - \frac{dP_1}{dx})$$

$$u_2 = \frac{K Kr_2}{\mu_2}(\rho_2 g - \frac{dP_2}{dx})$$

In these equations, u is the filtration velocity (volume flow rate per unit surface area), μ and ρ the viscosity and density of the fluids, Kr is the relative permeability, g the gravity constant and P the pressure.

For two immiscible fluids that are both in continuous phase, the difference of pressure is equal to the capillary pressure:

$$Pc = P_1 - P_2$$

The monophasic permeability K depends only on the rock structure. In reservoir engineering it is assumed that the capillary pressure (Pc) and the relative permeabilities (Kr) do not depend on fluid viscosities, flow rate and pressure. These petrophysical parameters are only functions of the fluid saturation and displacement history.

The purpose of petrophysical measurement is to determine the capillary pressure (Pc) and relative permeability curves (Kr) as functions of saturation. In addition, electrical properties (formation factor and resistivity index I_R) are determined for the calibration of log data.

The petrophysical measurement methods have been developed over several years. However, there is still on-going research to improve not only the accuracy but also the speed and automation of measurements. One approach is to measure different parameters during the same experiment with the same sample ("integrated measure"). The purpose is not only to reduce cost but also to increase the representativeness by using the same sample.

In this paper, I will first recall the standard and integrated methods for measuring Pc and Kr curves. I will then describe the original method developed for the simultaneous measurement of the three properties : Pc, Kr, I_R. Finally, I will present and discuss the results obtained with two reservoir samples.

2. Measurement of Petrophysical properties

Let us recall the notations which are commonly used in petroleum engineering.

2.1. Definitions

It is now recognized that most reservoirs are not strongly water-wet (Anderson, 1986; Cuiec, 1991). Consequently, the definitions for capillary pressure must be valid for any type of wettability. In core analysis, the following definitions are generally used (Lenormand et al., 1993):

- *Reference fluid.* One of the fluids is arbitrarily chosen as the "reference". The reference fluid is water when oil and water are involved, and the liquid for liquid/gas systems.
- *Capillary pressure* is defined as: Pc=P(non-ref)-P(ref).
- A *drainage* is a displacement where the saturation of the reference fluid is decreasing; an *imbibition* is a displacement where the saturation of the reference fluid is increasing.
- A *Pc(S) curve* is an equilibrium curve obtained by a succession of displacements with small increments of pressure (or flow rate).

We will now take the example of oil and water systems. This set of definitions leads to the different parts of the Pc cycle shown in figure 1.

1) Primary drainage (Pc>0) : oil is displacing water
2) Positive imbibition, also called "spontaneous" imbibition
3) Negative imbibition, also called "forced" imbibition
4) Negative (secondary) drainage
5) Positive (secondary) drainage.

Let us now describe the different methods used for measuring capillary pressures.

2.2. Porous Plate

The capillary pressure is balanced by the *static* pressure difference between the fluids. The fluids are injected through two semipermeable porous plates to measure the positive and negative parts of the capillary pressure curve. The displacements are controlled by the pressure difference between the fluids which is increased step by step during drainage and decreased during imbibition. With the two semipermeable plates, this difference can take any positive or negative values and the whole Pc cycle can be measured (curves 1 to 5, fig. 1). When equilibrium is reached, the saturation is uniform along the sample and its value can be deduced from the effluent production.

Recently, the Porous Plate method has been improved by replacing the porous plates by very thin micropore membranes which are much more permeable (Longeron et al., 1994). The equilibrium time is around 100 times faster. A complete cycle takes only a few weeks instead of several months with the standard porous plates, and with the same accuracy.

2.3. Centrifuge

The capillary pressure is balanced by the pressure difference due to centrifuging (see for instance O'Meara et al, 1988). The pressure profile in each fluid can be related to the rotation speed and to the fluid density. In drainage, for instance, the sample is immersed in oil and Pc is assumed to be zero at the outlet. In any section of the sample, the pressure is known, but the saturation must be calculated from the effluent production by using the general flow equations (Forbes, 1991). Corrections for radial effects have also been proposed (Forbes et al., 1994).

2.4. Semidynamic method

The capillary pressure is balanced by the viscous pressure drop (Lenormand et al., 1993, 1995). The experimental set-up is described in Figure 2. It consists of a standard core-holder with no semipermeable membrane and a separator used to measure the fluid production. The saturations are either measured in different sections of the sample (conductivity, X-ray, γ-ray, etc.) or calculated using a method described in the next section.

For positive capillary pressures, oil is injected through the sample and water only "washes" the outlet face in order to establish the continuity between water inside the sample and the outlet. The first role of this circulation is to maintain the pressure Pw in water at a known and measured value (atmospheric pressure, or any fixed back-pressure). The second role is to allow water to invade the sample when the pressure in oil is decreased (imbibition).

An increase in the oil flow rate displaces water and the level of the meniscus in the fluid separator rises. When the steady state is reached, water is no longer produced, and therefore there is no pressure gradient in the water phase. The water pressure Pw is uniform along the sample, but there is a gradient in the oil that is flowing (Fig. 3). The pressure Po in the oil phase is measured either at the entrance or at any position along the sample. From the values of Pw and Po, we can calculate the capillary pressure defined as Pc=Po-Pw.

The primary drainage curve is obtained by increasing the oil flow rate from zero in a sample initially saturated with water to a maximum value corresponding to the irreducible water saturation (Fig. 3). Imbibition is obtained by decreasing the oil flow rate. During all these displacements, the water flow rate is kept constant at a low level to prevent any disturbance of the flow in the sample (negligible pressure drop) but high enough to wash the oil in the outlet.

The negative part of the Pc curve is obtained by permuting the roles of oil and water. The pressure measured inside the core is then the water pressure.

2.5. Relative permeability measurements

The relative permeabilities (Kr curves) are generally measured separately from capillary pressures using one of these two methods :

- transient displacement. A high flow rate displacement is performed and capillary pressure is neglected for interpretation.
- steady-state displacements. The two fluids are injected together. and generally saturation is assumed to be uniform along the core. More accurate results are obtained by using local saturation measurements (X ray, γ ray, etc. .)

2.6. Simultaneous determination of petrophysical properties

In core analysis, there is a general trend towards the simultaneous determination of relative permeabilities and capillary pressure curves during the same experiment.

A few years ago, several studies (Richmond and Watson, 1988, Chardaire-Rivière, 1992) were devoted to the simultaneous determination of capillary pressure curves (Pc) and relative permeabilities (Kr) by automatic history matching during core flood experiments. It is now recognized that it is more accurate to measure the capillary pressure separately. However, the Kr functions can be derived using the transient of the production. Several papers have been published for the various methods. For the centrifuge method: O'Meara and Crump, 1985; Nordtvedt et al., 1993; Nimmo, 1990 with local saturation measurements using resistivity. For the "porous plate" or "membrane" method: Jennings et al., 1985; Longeron et al., 1994; Christoffersen, 1995. In the membrane method, the transient is often used to estimate the equilibrium saturation (Guo and Hammervold, 1993). However, the method is not accurate due to the high hydraulic resistance of the membrane and the presence of the second fluid

(Lenormand *et al.* 1996). A new method combines the membrane method and a continuous injection (Kokkedee and Boutkan, 1993; Kokkedee, 1994).

With the membrane method, a simultaneous Pc and resistivity index is also available (Fleury and Longeron, 1996).

2.7. Discussion

In order to design an integrated tool that can perform simultaneous measurements of the Pc and Kr curves and the resistivity index, we have looked at the drawbacks and advantages of the various methods:

- the porous plate and membrane methods are not suitable for Kr measurements.
- the centrifuge method cannot measure the positive imbibition and the negative drainage. In addition the method is limited for high pressure and temperature.

Consequently, we preferred use the semidynamic method for an integrated petrophysical tool (IPT).

3. The Integrated Petrophysical Tool (IPT)

3.1. Principle of the IPT

The semidynamic method allows the complete Pc cycle to be determined. During the same experiment, it is also possible to detemine parts of the Kr curves by steady measurement. In addition, resistivity indices are easily measured.

During positive capillary pressure measurements, oil is flowing through the samples. Consequently, there is a direct measurement of permeability to oil provided that saturations are known. If we note S_0 the inversion point (corresponding to Pc=0 during imbibition), Kr(oil) is measured for $S<S_0$ and Kr (water) for $S>S_0$ (Fig. 4).

In this study, we used a cell with 6 pressure taps along the sample (Fig. 5). For electrical measurement, the current is injected through the end-pieces and tensions are measured using the pressure taps. The effluent volume, leading to the average saturation, is measured by an accurate capacitance method in the tube separator.

Local saturation at the entrance is calculated from the average saturation using the following method.

3.2. Calculation of the local saturation

The first version of the semidynamic method had the drawback of requiring saturation measurement at a few points along the sample. For this purpose, we used an ultrasonic technique, which is accurate but impossible to use with gas and difficult to incorporate in an automatic set-up. The problem has been solved by calculating the saturation from the average saturation. This new approach is based on an analytical calculation that only use the entrance pressure and average saturation (Ramakrishnan and Capiello, 1991). The calculation is the following.

Darcy's law is written below for two immiscible phases (fluids 1 and 2) flowing in direction x (without gravity)

$$q_1 = -K\frac{Kr_1}{\mu_1}A\frac{\partial P_1}{\partial x} \qquad q_2 = -K\frac{Kr_2}{\mu_2}A\frac{\partial P_2}{\partial x}$$

q is the volume flow rate, P the pressure, K and Kr are the single-phase and relative permeabilities; μ the viscosity and A the cross section area of the sample. When the steady-state is reached, only fluid 2 (oil, for Pc>0) is flowing at a uniform flow rate q_2 and water is no longer produced (q_1=0). The pressure P_1 in water is then uniform and will be taken as a reference (P_1=0). The relative permeability Kr_2 can be written as a function of the capillary pressure $Pc = P_2-P_1$. Darcy's law is rewritten as:

$$q_2\, dx = -K\frac{Kr_2(Pc)}{\mu_2}A\, dPc$$

and then integrated between the entrance (x=0), where Pc=Pe and outlet (x=L), with Pc(L):

$$q_2\, L = K\frac{A}{\mu_2}\int_{Pc(L)}^{Pe} Kr_2(Pc)\, dPc$$

The originality of Ramakrishnan's calculation is to consider the series of experiments performed at different flow rates. The entrance pressure Pe is then a function of the flow rate q_2. The capillary pressure Pc(L) at the outlet remains constant and equal to zero as in centrifuge experiments (O'Meara *et al.*, 1988). Equation 4 is then differentiated with respect to Pe :

$$\frac{dq_2}{dPe} = \frac{KA}{L\mu_2} Kr_2(Pe)$$

This equation gives the relative permeability of the injected fluid as a function of the derivative of the entrance pressure:

$$Kr_2 = \frac{L\mu_2}{KA} \frac{dPe}{dq_2}$$

The local water saturation S can be derived from the average saturation <S> by using the same technique:

$$L<S> = \int_0^L S\, dx$$

This equation is rewritten by using Pc as the variable instead of x :

$$<S> = \frac{KA}{L\mu_2 q_2} \int_{Pc(L)}^{Pe} S(Pc)\, Kr_2(Pc)\, dPc$$

and by differentiating with respect to the entrance pressure Pe:

$$S(Pe) = \frac{L\mu_2}{KKr_2(Pe)A} \frac{d(<S>q_2)}{dPe}$$

We have simplified this equation by differentiating the product and replacing Kr by its value :

$$S(Pe) = <S> + q_2 \frac{d<S>}{dq_2}$$

For each flow rate, the entrance saturation S(Pe), together with entrance pressure Pe gives a point on the Pc curve (since the pressure in water is taken as reference, Pe=Pc).

For Ramakrishnan and Capiello, the method was applicable mainly for relative permeability, since the average saturation is too difficult to measure experimentally. In this paper we will show that the capillary pressure curve can also be measured. We have tested this method using simulated data as well as real experiments with saturation measurement using a CAT scanner (Lenormand et al., 1995).

4. Results

4.1. Procedure

Sample 1 and 2 are two reservoir sandstone cores of diameter 4 cm and length 8 cm. They are first cleaned with toluene and isopropanol to remove crude oil. Then, the samples are saturated with brine and the displacements are started at room conditions (20 C and exit at atmospheric pressure). The injection flow rates range from 5 to 1000 cm^3/hour. The rate used for washing the outlet is always 20 cm^3/hour. The duration for the whole cycle (primary drainage, positive and negative imbibition, secondary drainage) is about one month.

Table 1 Fluid and rock properties.

Rock samples		sample #1	sample #2
	porosity	0.22	0.22
	solid density (g cm^{-3})	2.65	2.70
	water permeability (m^2)	$0.125\ 10^{-12}$	$1.19\ 10^{-12}$
Paraffinic Oil	viscosity (Pa s)	$1.3\ 10^{-3}$	$1.3\ 10^{-3}$
Brine	viscosity (Pa s)	$1\ 10^{-3}$	$1\ 10^{-3}$
	salinity (g/l)	120	25

4.2. Capillary pressures

Capillary pressure curves are first displayed using the average saturation: pressure difference between the two faces of the sample vs. average saturation (Fig. 6). The maximum capillary pressure is higher for sample #1 which is less permeable.

Then the local saturation at the entrance is calculated using Ramakrishnan's equations. Using a 3rd order polynomial for the average saturation <S> vs. Ln (Q) produces a good fit (Fig. 7). Other methods (spline) lead to similar results. The drainage Pc curve with local saturation is shown in Fig. 8. For both samples, the shape of the "local" curve is not altogether satisfactory. The correction due to the derivative is too large and leads to a non monotonic variation in saturation. This effect had not been observed with the simulated cases. It may be due to an incorrect fluid distribution at the inlet and outlet leading to 2-dimensional flow effects and fluid trapping. For imbibition and second drainage, the local and average curves are very close (Fig. 9).

The shapes of the Pc curves show that both samples are water-wet.

4.3. Electrical Properties

We first measured the formation factor when the samples are saturated with brine.

sample #1 : F_R=18.9; Archie exponent m=1.94

sample #2 : F_R= 17 ; Archie exponent m=1.90

For the resistivity index, we have tried to use the theoretical calculation to derive resistivity at the entrance using the global resistivity. The results are not favorable. In fact, this method corresponds to a "two electrode" measurement with additional contact resistance due to the presence of oil covering the electrodes. It is well established that "four electrodes" are needed to ensure correct measurement (Sprunt et al., 1990; Fleury and Longeron, 1996) This is achieved by measuring the potential along the core. We used both the average saturation (sample 1) and the saturation calculated at the center of the core using a numerical simulator (sample 2). The resistivity index is then close to the results of standard methods with a saturation exponent close to 2 (Fig. 10).

4.4. Relative Permeabilities

The Kr determination using the analytical calculation and the overall pressure drop. is not possible. The cause may be the same as for electrical measurements, i. e, an additional pressure drop at the contact between the end-piece and the sample. We also used the local measurements.

For sample 2, the whole oil Kr curve is determined during drainage and only the end points during imbibition (Fig. 11). The results are very similar to direct measurements by the standard steady state method, using the same set-up (Fig. 11).

For sample 1 (Fig. 12), the oil Kr is accurately determined, but for water there is only one value, since the negative Pc curve is vertical (water-wet sample). The low value for Kr (water) is also consistent with water wet samples.

5. Discussion

The capillary pressure curves were compared to centrifuge measurements. For both samples, the pressure level is the same. However, the residual saturation differs by 0.1 for sample 1. The analysis of our experimental set-up shows a lack of accuracy in saturation measurement. In addition, there is a

difference for the saturations derived from a Karl-Fisher titration at end of experiment. The problem is not due to the capacitance measurement of the effluent volume. The main reasons are the following :

1) some leaks in the fittings, especially at high pressure during negative imbibition,
2) dead volumes in pressure sensors, tubing and fittings,
2) leaks in the piston seals of the syringe pumps,
3) difficulty to measure the sample pore volume in the conditions of the experiment (effect of confining pressure, for instance).

We have studied the different causes of error and proposed improvements for subsequent measurements. For instance, we have designed an "in-situ" gas porosimeter to measure the pore volume.

The design of the groove on the end-piece is still a problem. We used a spiral groove to prevent any fluid trapping. The surface of the groove is not large enough and the flow is not uniform at the entrance and exit of the sample. The addition of a metallic screen may improve the flow but will increase the possibility of trapping .

We have shown that local electrical and pressure measurements along the sample are needed. There is no technical difficulty with these measurements, even at high pressure and temperature. For interpretation of the local measurements, we have shown that the average saturation was close to the local saturation in the center. In the future, it would be more accurate to have a 1-D numerical simulation of the flow and adjust the Kr to have the best fit with local measurements.

6. Conclusion

This paper describes the first use of an Integrated Petrophysical Tool (IPT) on two reservoir rock samples.

The IPT is based on the steady-state injection of one fluid through the sample placed in a Hassler cell. The experiment leading to the whole Pc cycle consists of about 30 steps at various oil or water flow rates. It takes about four weeks to measure the following petrophysical properties:

- Complete capillary pressure cycle: primary drainage, spontaneous and forced imbibitions, secondary drainage
- End-points and parts of the relative permeability curves;
- Formation factor and resistivity index.

Relative permeabilities agree with steady-state measurements. and Capillary pressure with centrifuge measurements. There is no comparison for resistivity index, but the results are in agreement with literature data. For these experiments, special attention must be paid to the precise determination of effluent production. Above all, any fluid leakage must be avoided.

In conclusion, the Integrated Petrophysical Tool is as accurate as standard methods and has the advantage of providing the various parameters on the same sample and during a single experiment. The IPT is easy to use and can be automated. In addition, it can be operated at reservoir condition.

References cited

Anderson, W. G., "Wettability literature survey: Part 2. Wettability measurement", 1986, Journal of Petroleum Technology, p. 1246.

Chardaire-Rivière, C. Chavent, G. , Jaffre J. and Liu J., 1990, Multiscale estimation of relative permeabilities and capillary pressure, SPE 20501.

Christoffersen, K. R., 1995, "Gas/Oil Capillary Pressure of Chalk at Elevated Pressures", SPEFE, sept. , p. 153-159.

Cuiec, L., "Evaluation of Reservoir Wettability and its Effect on Oil Recovery", 1991, Interfacial Phenomena in Petroleum Recovery, Ed. N.R. Morrow, M. Dekker Inc., New-York, p. 319-376.

Fleury, M. and Longeron, D., "Combined resistivity and capillary pressure measurements using micropore membrane technique", 1996, presented at the meeting of Society of Core Analysts, Montpellier, France.

Forbes, P., "Simple and accurate methods for converting centrifuge data into drainage and imbibition capillary-pressure curves", 1991, SCA Conference Paper, 9107.

Guo, Y. and Hammervold, W. L.,1993, "Equilibrium Time and Accuracy of Capillary Pressure Measurements Using Diaphragm Method", paper presented at the SPWLA Annual Symposium, Calgary.

Jennings, J. W., McGregor, D. S. and Morse, R. A., 1985, "Simultaneous Determination of Capillar Pressure and Relative Permeability by History Matching," paper SPE 14418, Las Vegas.

Kokkedee J.A. and Boutkan, V. K., 1993, "Towards measurement of Capillary Pressure and relative Permeability at Representative Wettability", 7th European EOR Symposium, Moscow.

Kokkedee J.A., 1994, "Simultaneous Determination of Capillary Pressure and Relative Permeability of a dispplaced Phase", paper SPE 28827, European Conference, London.

Lenormand R., Eisenzimmer A and Zarcone C., A novel method for the determination of water/oil capillary pressures of mixed wettability samples, paper SCA 9322, 1993.

Lenormand R., Eisenzimmer A. and Delaplace Ph., "Improvements of the Semi-Dynamic Method for Capillary Pressure Measurements", 1995, presented at the meeting of Society of Core Analysts, San Francisco.

Lenormand R., Delaplace Ph. and Schmitz P. "Can we really measurethe relative permeabilities using the micropore membrane method?", 1996, presented at the meeting of Society of Core Analysts, Montpellier, France.

Longeron, D.G., Hammervold, W.L., and Skjaeveland, S.M.: "Water-Oil Capillary Pressure and Wettability Measurements Using Micropore Membrane Technique", SCA 9426 in Proceedings of the 1994 International Symposium of the Society of Core Analysts, Stavanger, Norway, Sept.

Nimmo, J. R., 1990, "Experimental testings of transient Unsaturated Flow Theory at Low Water Content in a Centrifugal Field", Water Resources Research, Vol. 26, N° 9, p. 1951-1960.

Nordtvedt, J. E., Gerardo Mejia, Pin-Huel Yang and A. T. Watson, 1993, "Estimation of Capillary Pressure and Relative Permeability Functions from Centrifuge Experiments", SPERE, p. 292-298.

O'Meara D. J., Hirasaki G. J and Rohan J. A.: "Centrifuge Measurements of Capillary Pressure", 1988, SPE paper 18296.

O'Meara, D. J. and Crump, J. G., 1985, "Measuring Capillary Pressure and Relative Permeability in a Single Centrifuge Experiment", SPE 14419.

Ramakrishnan T.S. and Capiello A. , A new technique to measure static and dynamic properties of a partially saturated porous medium, Chem. Eng. Sci., 1991, p. 1157-1163.

Richmond P.C. and Watson A. T., Estimation of multiphase flow functions from displacement experiments, SPERE, 1990, 121-127.

Sprunt, E. S., Maute, R. E. and Rackers, C. L., "An interpretation of the SCA electrical resistivity study", the Log Analyst, pp. 76-88, 1990.

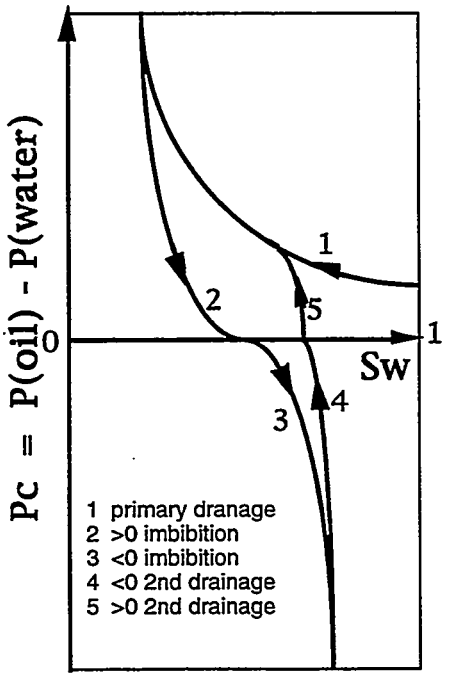

Fig. 1 - Definition of the various capillary pressure curves

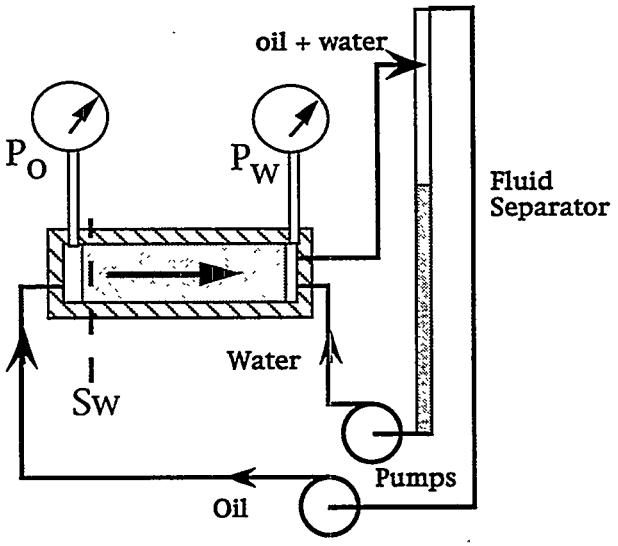

Fig. 2 - Principle of the experimental set-up for measurements using the semidynamic method.

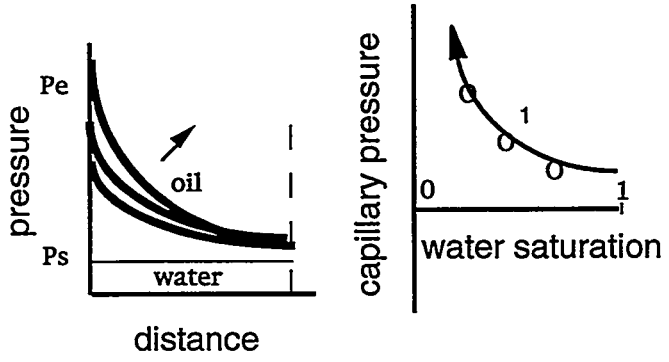

Fig. 3 - Pressure profiles and corresponding points on the Pc curves during an IPT measurement.

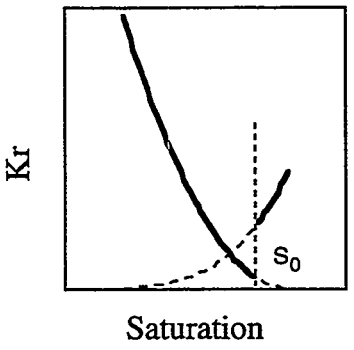

Fig. 4 - Parts of the Kr curves determined during an IPT measurement.

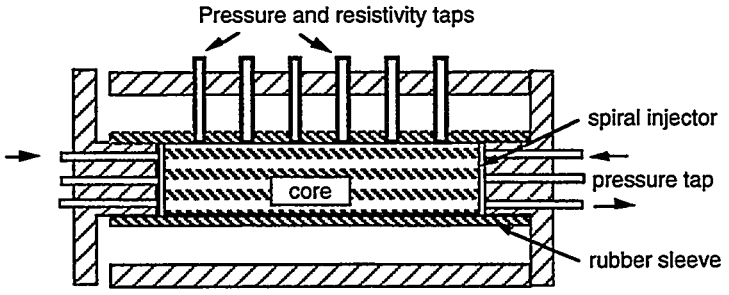

Fig 5 - Core-holder for the Integrated Petrophysical Tool

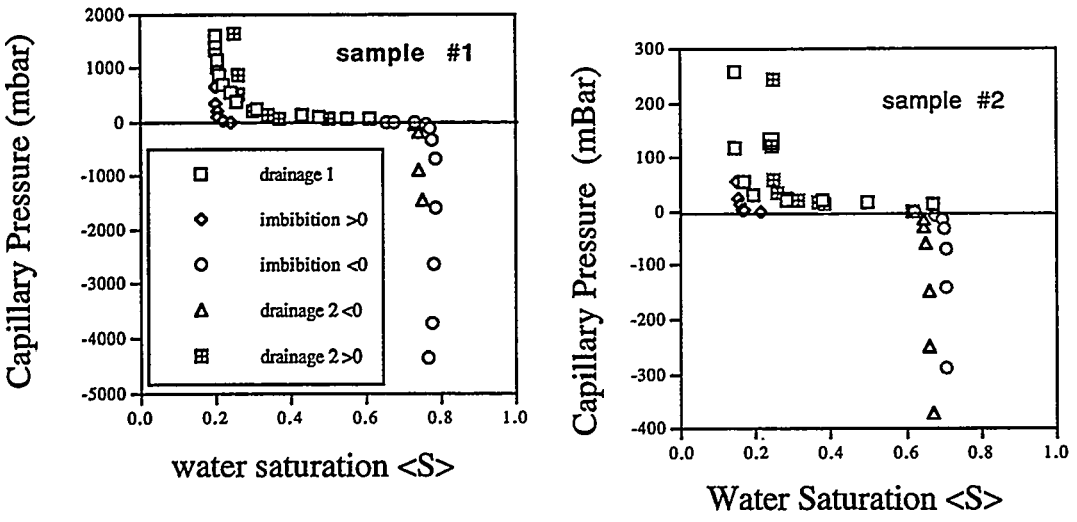

Fig. 6 - Capillary pressure cycles with average saturation.

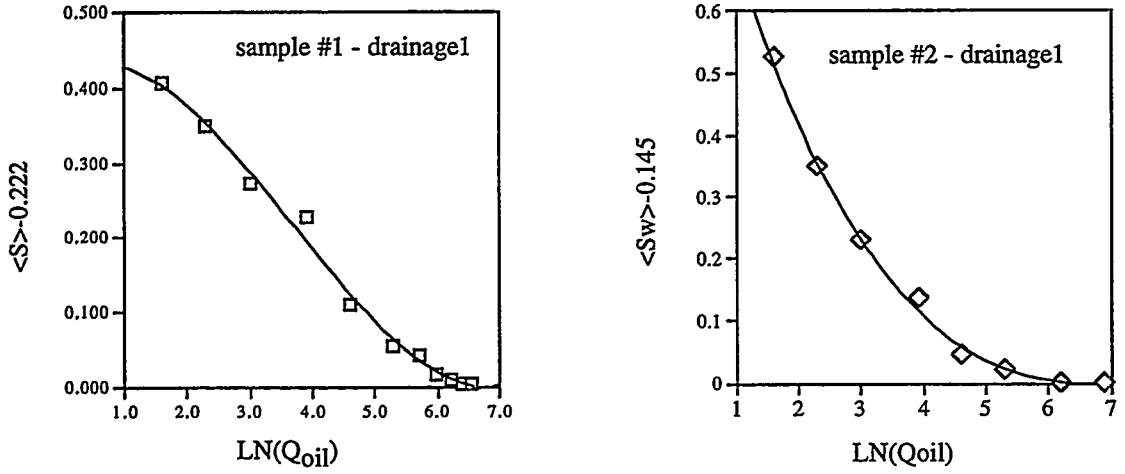

Fig. 7 - Calculation of the local saturation: approximation of <Sw> vs LN (Q) by a 3rd order polynomial.

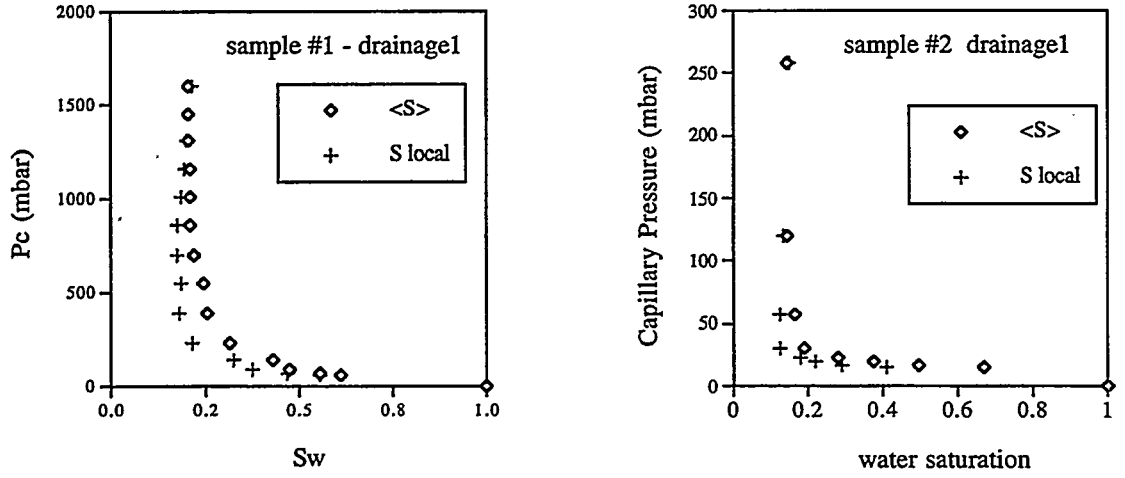

Fig. 8 - Primary drainage Pc curves: Average and local saturation

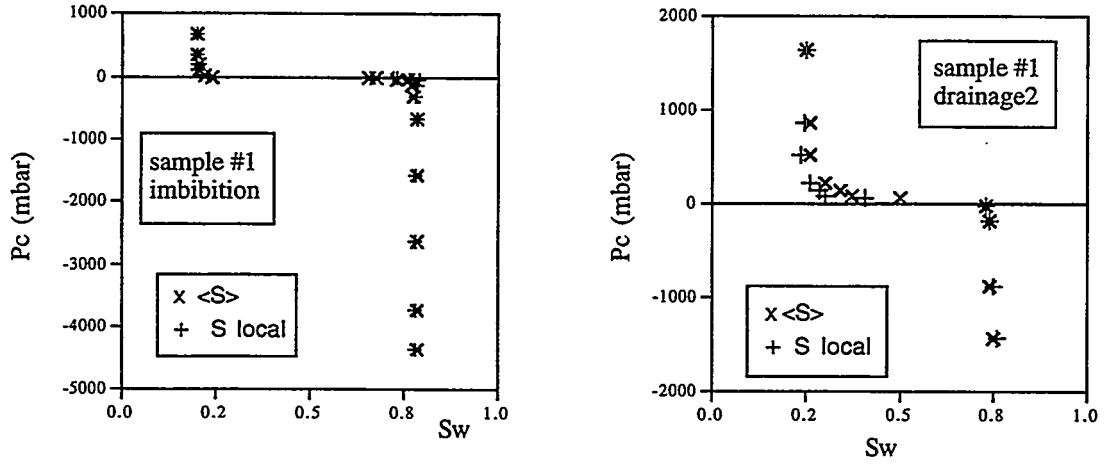

Fig. 9 - Capillary pressure with local saturation for imbibition and second drainage (sample #1).

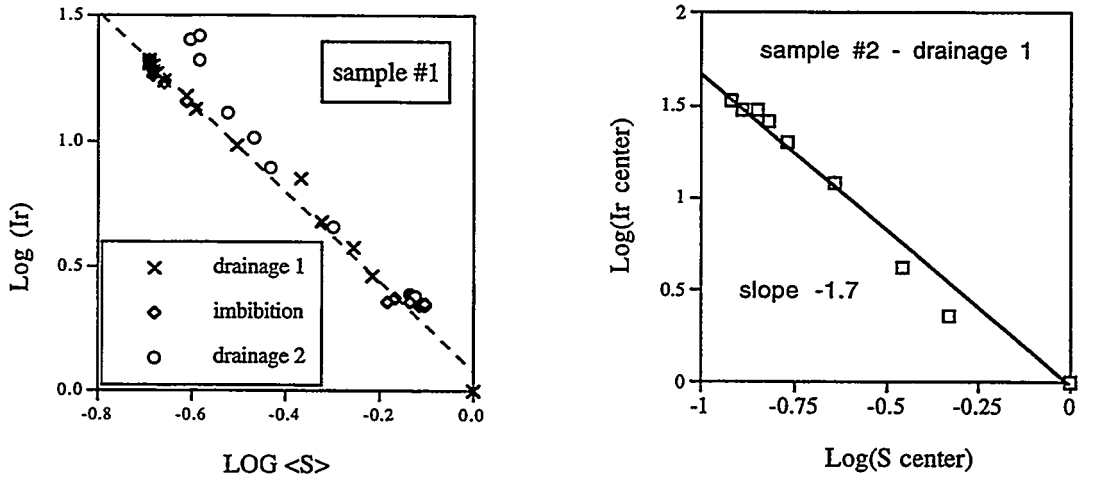

Fig. 10 - Resistivity index measurements.

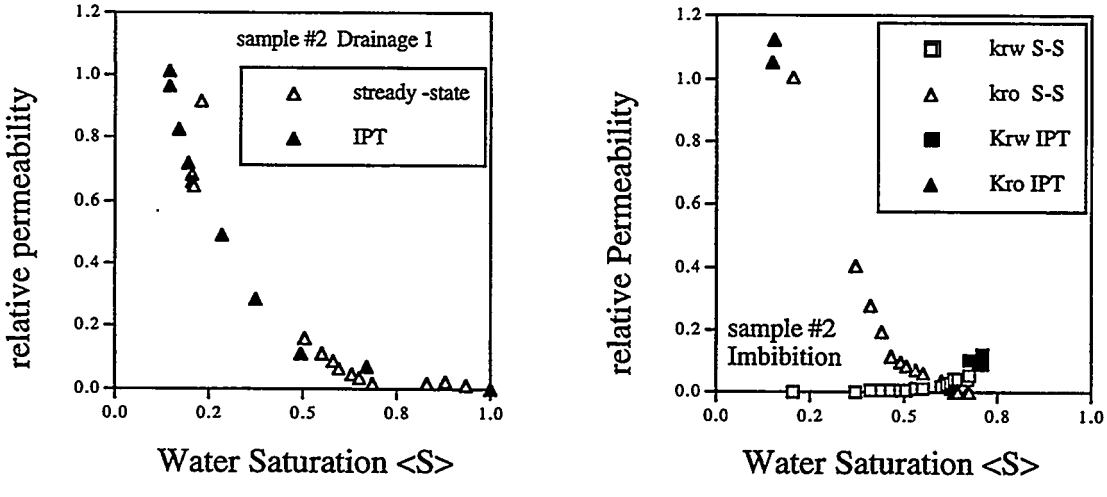

Fig. 11 - Relative permeability. Comparison between steady-state (S-S) and IPT measurements.

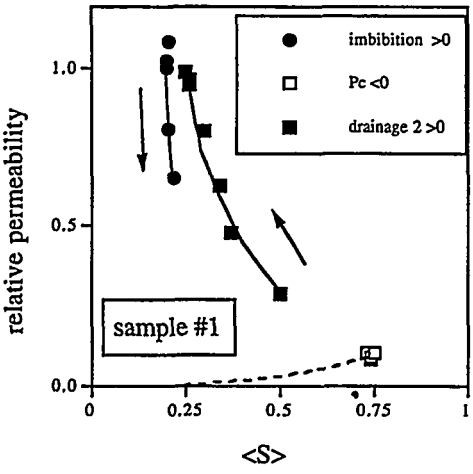

Fig. 12 - Relative permeability measurements for sample #1 (IPT)

FLOW UNITS FROM INTEGRATED WFT AND NMR DATA

E. Kasap, M. Altunbay and D. Georgi

Western Atlas Logging Services

ABSTRACT:

Reliable and continuous permeability profiles are vital as both hard and soft data required for delineating reservoir architecture. They can improve the vertical resolution of seismic data, well-to-well stratigraphic correlations, and kriging between the well locations. In conditional simulations, permeability profiles are imposed as the conditioning data. Variograms, covariance functions and other geostatistical indicators are more reliable when based on good quality permeability data.

Nuclear Magnetic Resonance (NMR) logging and Wireline Formation Tests (WFT) separately generate a wealth of information, and their synthesis extends the value of this information further by providing continuous and accurate permeability profiles without increasing the cost. NMR and WFT data present a unique combination because WFTs provide discrete, in situ permeability based on fluid-flow, whilst NMR responds to the fluids in the pore space and yields effective porosity, pore-size distribution, bound and moveable fluid saturations, and permeability. The NMR permeability is derived from the T_2-distribution data. Several equations have been proposed to transform T_2 data to permeability. Regardless of the transform model used, the NMR-derived permeabilities depend on interpretation parameters that may be rock specific.

The objective of this study is to integrate WFT permeabilities with NMR-derived, T_2 distribution-based permeabilities and thereby arrive at core quality, continuously measured permeability profiles. We outlined the procedures to integrate NMR and WFT data and applied the procedure to a field case. Finally, this study advocates the use of hydraulic unit concepts to extend the WFT-NMR derived, core quality permeabilities to uncored intervals or uncored wells.

INTRODUCTION

Over the years traditional reservoir characterization techniques have evolved into a multi-disciplinary process. Geostatistical techniques provide a framework for integrating all available engineering and geoscience data over multiple scales while honoring the petrophysical well data and geological and sedimentological models.

Well logs provide direct measures of reservoir formation properties and are a vital source for hard and soft data required for delineating reservoir architecture. They are used to improve the vertical resolution of seismic data[1-5], well-to-well stratigraphic correlations[6-7], and kriging between the well locations. In conditional simulations, well log porosity profiles are imposed as the conditioning data and the sand-to-shale ratios from well logs are maintained throughout the relevant vertical cross-sections. Well-log measured heterogeneity in a vertical cross-section is used to generate variograms, covariance functions and other geostatistical indicators within a single well or between well pairs. Corbett, et al.[8] incorporated wireline formation pressure test data into a reservoir characterization study to identify connectivity between the adjacent zones.

Recently, great effort has been dedicated to the integration of well logs into seismic data.[1-5] Conventionally seismic data has been used to delineate reservoir structure (lateral extent), but its vertical resolution is limited. Yang, C. T. et al.[2] pointed out that generally it is difficult to identify beds thinner than 25 ft from 3-D seismic signals. Although seismic data is routinely and effectively used to estimate the structure of the reservoir bodies, it typically plays no role in the essential task of estimating rock properties, which are measured or computed from well logs. In the presence of 3-D seismic surveys and logged wells, the simultaneous analysis of seismic-attribute data and borehole data often leads to better estimates of property distributions in comparison with estimates generated from either seismic or well data alone.[1-8]

Porosity and permeability are the key reservoir properties needed for proper reservoir description and simulation. Porosity is routinely available from wireline log data and, in conjunction with 3-D seismic data, can be used to generate excellent reservoir porosity models. Until recently, cores were the only source of permeability data measured on a

small enough scale to provide critical reservoir heterogeneity data. Usually permeability is derived from core based permeability-porosity cross-plots. However, such an approach is flawed as the porosity-permeability correlations are often poor and core data may be sparse and expensive to obtain.

Newly developed Nuclear Magnetic Resonance (NMR) logging techniques do provide vertically continuous pore-size distributions, but do not measure permeability directly. Transient pressure tests are the only direct, in situ measurement that can yield formation permeability. Well tests assess the largest possible scale and average all vertical variations in permeability. Wireline Formation Tests (WFT) access a limited volume of the reservoir and are well suited for characterizing reservoir heterogeneities. They also measure on a scale that closely matches the measurement scale of NMR logs.

The objective of this study is to integrate WFT-calculated permeabilities with NMR-derived permeabilities and, thereby, arrive at core quality, continuously measured permeability profiles, without increasing the cost. NMR and WFT data present a unique combination because WFTs provide discrete, in situ permeability measured through fluid-flow and NMR logs provide continuous T2 distributions. This study outlines a procedure to integrate NMR and WFT data and illustrates its application to a field study. The study extends the Hydraulic Unit concepts of Amaefule et al.[9] to the WFT-NMR derived, core quality permeabilities to uncored intervals or uncored wells.

WIRELINE FORMATION TESTS

When a WFT probe is set against the formation and a measured volume of fluid is withdrawn, a wireline formation test is initiated. Pressure changes are continuously recorded throughout the test. Decreasing pressure is sometimes followed by a stabilized flow period when the drawdown period is extended and permeability of the formation is high enough to supply fluid at a rate equal to that required by the pump withdrawal. The buildup period starts when the fluid withdrawal stops and ends when the system pressure reaches the formation fluid pressure.

Figure 1 shows a WFT test repeated three-times. This particular test was performed at a depth of 8775 ft. Approximately thirty tests at ten depths were performed. Permeability, undisturbed formation pressure (P*) and fluid compressibility can be extracted from transient-measured pressures and drawdown rates. Shown in Fig. 2 are the calculated P*s at ten vertical depths, which shows an excellent correlation between the depth and formation pressure indicating a constant pressure gradient. The calculated slope of -3.62 translates to an in situ API gravity of 90.8 which may be indicative of solution gas in the oil under the reservoir conditions. Alternatively the reservoir oil might also contain large quantities of light hydrocarbon components.

In addition to P*, WFTs can provide a direct measure of near wellbore permeability. Although WFTs are short (seconds to a minute), tests cannot feasibly be conducted continuously, because the time to set the tool and the time for the pressure to stabilize before ending the test are too long to permit "continuous" permeability profiling. Figure 3 shows ten permeability values calculated at ten vertical depths. The figure indicates that ten measurements of permeability are not sufficient to delineate reservoir heterogeneity, although 10 pressure values are quite satisfactory for calculating reservoir fluid pressure gradient and in situ API gravity. However, even though WFT-measured permeabilities are too sparse to produce a continuous profile, they are curretnly the most reliable in situ measured permeability obtainable on a small enough scale to permit the identification of local heterogeneity.

In the following section, we discuss the calculation of P* and permeability from WFTs. New concepts and analysis techniques, combined with 3-D numerical studies, have recently been reported in the literature.[10-15] 3-D numerical simulations have also contributed to the diagnosis of WFT-related problems and the improved analysis of WFT data. We first review, the Formation Rate Analysis Technique (FRAT), a new technique that combines drawdown and buildup data analysis.

Formation Rate Analysis

Kasap et al.[10-11] proposed FRAT for the entire WFT to obtain permeability and P*. FRAT combines the drawdown and buildup data into a single plot where both the drawdown and buildup periods are well represented by straight lines with identical slopes. The geometric factor (G_O) concept[16] is the foundation of FRAT, from which we obtain both P^* and permeability. G_O is calculated for modified hemispherical-flow geometry, which does nor require a cavity in the formation, nor a probe seal of infinite extent. In Darcy's equation with this modified hemispherical geometry for isothermal, steady-state

flow of a liquid, the dimensionless G_O replaces the factor 2π that would apply for true semi-infinite, hemispherical-flow geometry.

During the drawdown period, fluid will be withdrawn at a rate of q_{dd}. The accumulation rate, q_{ac}, is the difference between the formation flowrate, q_f, expressed with Darcy's equation, and drawdown rate of the pump. The pressure-transient theory for slightly compressible liquids can be derived from the definition of isothermal compressibility:

$$q_{ac} = C_t V_{sys} \frac{\partial P(t)}{\partial t}. \quad (1)$$

The rate q_{ac} for all practical purposes, is equal to the difference between q_f, the volumetric rate flowing through the rock adjacent to the packer probe (Darcy flux), and q_{dd}, the drawdown rate of the pump. Thus, we can rewrite the Darcy equation and account for the WFT drawdown, stabilized flow and buildup data:

$$P(t) = P^* - \left(\frac{\mu}{kG_o r_i}\right)\left(C_t V_{sys} \frac{\partial P(t)}{\partial t} + q_{dd}\right) \quad (2)$$

Note that the terms within the last parentheses in Eq. 2 correspond to the accumulation and drawdown rates, respectively. The two terms act against each other, and their difference, in essence, is the flowrate from the formation. Eq. 2 provides a means to estimate formation permeability and P^* from drawdown or/and buildup data. A plot of $P(t)$ vs. Formation Rate, which is given in Eq. 2 as

$$q_f = \left(C_t V_{sys} \frac{\partial P(t)}{\partial t} + q_{dd}\right) \quad (3)$$

should approach to a straight line with a negative slope and intercept P^* at the P(t) axis. The absolute value of the slope, m, is

$$m = \frac{\mu}{kG_o r_i},$$

and permeability is calculated from

$$k = \frac{\mu}{G_o r_i m}. \quad (4)$$

We note that Eq. 2 does not require a constant drawdown rate as long as q_{dd} is continuously recorded.

Theoretically, both drawdown and buildup should have the same slope and should go through the same straight line. However, during the early stages of the drawdown period when the flow is being established and during the early stages of the buildup period when the flow is adjusting to the changing flow conditions, the actual pressure vs. formation rate plot may deviate from the assumed pseudo-steady state solution.

Field Tests

We illustrated FRAT with two field examples collected with the Reservoir Characterization Instrument (RCI[SM])[17]. Test A6-4 was chosen because it shows a stabilized flow during the drawdown period and test A7-2 was chosen because it is representative of many wireline formation tests.

Figure 4 shows pressure versus formation rate and its best-fit straight line. The slope of the straight line is directly related to permeability and the intercept with the vertical axis is P*. When the probe radius of 2.25 cm, a viscosity of 0.75 cp and G_o of 4.27 are used a permeability of 70.1 mD is calculated.

This calculation can be performed in real time with every new pressure value measured by using weighted averages of formation rate. A plot of such a calculation is shown in Fig. 5. Figure 5 indicates that calculated permeability stabilizes within a very short period of time and remains constant for the drawdown and buildup periods at around 69.5 mD. Figure 5 also shows the corresponding formation rate, calculated by using Eq. 2, and indicates that during the test formation rate nearly stabilizes due to high permeability and low drawdown rate.

Formation rate analysis is also applied to A7-2 test, (the first repeat test, Fig. 1). The FRAT plot, shown in Fig. 6 indicates very little scatter in the data. Using the same viscosity, probe radius and G_o as in the A6-4 test, the calculated permeability and P*, based on the best-fit straight line, are 10.1 mD and 4627.7 psi, respectively. For the formation rate calculations a system volume of 267 cc and fluid compressibility of $6.8 \cdot 10^{-4}$/psi were used. Figure 7 shows the continuously calculated permeability and flow rate. The figure indicates that for this test the formation rate did not stabilize; nevertheless, the calculated permeability is not affected and reaches a constant value immediately after the start of the test and remains constant at that value throughout the drawdown and buildup periods.

Numerical Simulations

In this section, we use numerical simulations to verify the FRAT results. A 3-D finite-element scheme applied to the diffusivity equation in Cartesian coordinates is used to calculate transient pressures due to the flow in the near-wellbore region of the formation. The details of the simulator are given in previous publications.[10-13]

Figure 8 shows the comparison of pressure versus time plot from the field data, and the numerical simulation data for the A6-4 test. We used measured drawdown rates at the pump and the information given in Table 1 for this simulation. The figure shows that the permeability of 69.5 mD used in the simulation (FRAT permeability is 70.1 mD) satisfactorily matches the pressure response of the formation. The match between the field data and the numerical simulation data is excellent.

Numerical simulations were also conducted for the A7-2 test (Fig. 1, the first repeat test) by using the FRAT-obtained permeability and the continuously measured drawdown pump rate. Simulation results and field data are compared in Fig. 9. The results indicate that the simulation run with the FRAT permeability match well the field data.

These field test studies confirm that FRAT analysis correctly predicts formation permeability and undisturbed formation pressure. WFTs can very accurately provide fluid type, density and location and formation permeability and pressure.

Table 1- Numerical Simulation Parameters

	Value
Flow Line Volume (cm^3)	267.1
Wellbore Radius (cm)	15
Outer Boundary, r_e (cm)	230
Probe Radius (cm)	1.27
Pay Thickness (cm)	242.25
Duration of Drawdown (s)	5
Porosity	0.15
Fluid Viscosity (cp)	0.75
Reservoir Pressure, P* (atm)	315.116
Total Compressibility (/atm)	$1.x10^{-4}$

NMR LOGGING

The earliest industry workers[18-20] recognized the potential for NMR measurements to provide porosity, pore-size distribution and permeability. Initial attempts to make downhole NMR measurements proved cumbersome. However, in the early 1990's a new magnet configuration[21] greatly simplified the measurement and significantly increased the data quality. Today in many areas of the world NMR logs are run routinely as part of the open hole formation evaluation suite.

NMR logs provide the petrophysicist two types of data:

- mineralogy independent porosity
- T2 distributions

The NMR measurement essentially counts the number of hydrogen protons aligned with an external magnetic field, and then monitors the dephasing of the protons' spins with time. The number of protons initially aligned with the external magnetic field is proportional to the porosity, while the change in amplitude of subsequent echoes, known as the transverse relaxation, is characterized by a quasi-exponential decay with a characteristic time, T2 (Fig. 10). The initial NMR signal amplitude only depends on the hydrogen proton density in the pore space, as the measurement is insensitive to the hydrogen in the rock matrix (e.g., OH^- groups in clays) and is, thus, a mineralogy independent measure of porosity.

To measure T2-decay, a series of evenly spaced radio frequency, (RF) pulses are used to rephase the transverse magnetization. These RF pulses essentially recall the NMR signal, which is then referred to as an echo. In a gradient-magnetic field or in a heterogeneous magnetic field the apparent T2-decay rate depends on the inter-echo spacing (TE). However, for liquids, diffusion effects are minimal for commonly used inter-echo times (e.g., 0.6 and 1.2 ms.); however, they can be important for very light hydrocarbon liquids and gasses.[22]

The dominant factor on the T2-relaxation process is controlled by nuclear magnetic interactions occurring on the pore wall. Including diffusion effects, the T2 relaxation is well described by:

$$\frac{1}{T2} = \frac{1}{T2_{bulk}} + \frac{\lambda}{T2_{surf.}}\frac{S}{V} + \frac{1}{T2_D} \qquad (5)$$

where:

$T2_{bulk}$ = relaxation time of the bulk fluids in the pore space

$T2_{surf.}$ = relaxation time of the fluid in a few molecular layers next to the pore surface

λ = thickness of the surface fluid layer

S, V = pore surface and pore volume, respectively

$T2_D$ = relaxation time due to diffusion

If diffusion effects are negligible, and because the bulk T2 for water is of the order of seconds while the observed T2 is only a few hundred milliseconds or less, then the above can be approximated by:

$$\frac{1}{T2} = \rho_s \frac{S}{V} \qquad (6)$$

where:

ρ_s = surface relaxivity (0.003 - 0.03 cm/s) - clastics

= surface relaxivity (< 0.003 cm/s) - carbonates

In water filled pore systems, T2 is a measure of the S/V ratio. Large pores will have a small surface-area-to-pore-volume ratio and long T2's, while small pores will have a large surface-area-to-pore-volume ratio and will exhibit short T2's. Rocks with a spectrum of pore sizes give rise to a corresponding spectrum of T2 relaxation times (Fig. 11).

The NMR echo data from the logging tool are converted to a T2 spectrum that is closely related to the pore-size distribution for a single-phase fluid. The T2 spectrum derived from the echo data, measures the porosity fraction associated with each T2. The integral of the T2 spectrum, (the sum of the porosities at each T2), is the NMR porosity. However, the real benefit from NMR logging derives not just from the NMR porosity, but from the partitioning of the T2 spectrum into fast decaying fluids (bound and irreducible water) and free fluids.[23] Generally, clay bound water relaxes in a few milliseconds or less,[24] and, thus, if we log with a short enough TE (~0.6 ms) and faithfully record the early echoes, the integral from 0 to 4 ms will be a measure of the clay bound water. For clastics, the integral of the T2 spectrum from 4 to ~32 ms is a measure of the irreducible water and the remainder, e.g. 32 ms to ∞, is the moveable fluid fraction. The T2-time separating the moveable and irreducible fluids is referred to as the T2-cutoff time.

In clastic systems, the NMR T2 data has been used successfully to estimate permeability.[25] Several models are currently used to derive permeability from T2 spectra. Timur[19] (1968) recognized the relationship between moveable fluids and permeability.

$$k = 0.136 \frac{\phi^{4.4}}{S_{wir}^{\ 2}} \qquad (7)$$

Kenyon[26] and others have related permeability to the mean T2. This approach is formulated as:

$$k_{NMR} = C \cdot T2_{gm}^{\ 2} \cdot \phi^{4} \qquad (8)$$

The constant C may need to be adjusted for different reservoirs and formations.

Coates[27] put forward a permeability model which incorporates both the moveable and bound fluid fractions and does not explicitly depend on the mean T2.

$$k = \left(\frac{100\phi}{C}\right)^4 \left(\frac{S_{moveable}}{S_{wir}}\right)^2 \qquad (9)$$

where:

$S_{moveable}$ = Movable fluid saturation = $(1-S_{wir})$

S_{wir} = Bulk volume irreducible fluid saturation

C = Formation specific constant

This is particularly advantageous in the presence of hydrocarbons. In a water wet system, if liquid hydrocarbons are present then Eq. 5 does not simplify to Eq. 6, because the hydrocarbons are shielded from the rock surface and do not undergo surface relaxation. If a rock contains both water and oil, the pore space occupied by hydrocarbons will no longer exhibit the T2 relaxation associated with the S/V ratio of these pores and the mean T2 will be anomalously large compared to the mean T2 for a water saturated rock. Thus, Eq. 8 will over estimate the permeability in hydrocarbon zones whilst permeability calculated with the Coates' equation, Eq. 9, will be relatively unaffected by hydrocarbons.

RCI CALIBRATION OF NMR PERMEABILITY

The NMR signal is obtained from the fluids in the pores of a porous media. To interpret this signal a good understanding of the relationship between the signal, the rock matrix and the fluids is required. An accurate interpretation of the NMR data also requires calibration of the processing parameters (e.g. T2-cutoff

time, coefficients and exponents in the permeability model). Where available, core data are the natural source for the calibration data. However, advancements in logging technology, specifically in WFT tool-design, has moderated this requirement, and provided an alternative solution to interpretation calibration for most fields where cores are unavailable or too expensive to obtain.

In this study, RCI generated permeability values are used to calibrate the coefficient in the Coates' equation. Plotted in Fig. 12 are the RCI permeabilities and the MRIL® permeabilities for different values of C. To determine the best Coates constant, we have summed the absolute value of the difference between the RCI and MRIL permeabilities and plotted the sum versus the C-value (Fig. 13). The optimum C for this formation is obtained from the minimum at 14.5. Calibration of the coefficient in Coates bound-water permeability model via RCI data makes it possible to translate the NMR log responses into an accurate permeability profile for the formation despite the lack of core data.

DETERMINATION OF FLOW UNITS

"A flow unit is a volume of reservoir rock within which geological and petrophysical properties that affect the fluid flow are internally consistent and predictably different from properties of surrounding rock volumes".[28] Flow units are extensively used in reservoir characterization studies and in numerical simulations for performance predictions and reserve estimations. Two key elements for deriving the flow-unit profiles are accurate permeability and effective porosity profiles. RCI-calibrated MRIL permeability and MRIL porosity meet this requirement, and, hence, enable the flow unitization process.

Permeability and porosity data from a control well or interval are processed to determine RQI, the Reservoir Quality Index[9] (Figs 14a and b).

$$RQI = 0.0314\sqrt{\frac{k}{\phi}} \qquad (10)$$

Then a transformation of RQI to hydraulic units is performed by employing the hydraulic unitization technique as outlined below.

Traditional plots of permeability versus porosity (Fig. 14a) have little petrophysical and no mathematical justification. Usually, log-normally distributed permeability is plotted against normally-distributed porosity in a semi-logarithmic format to reduce the scatter. The underlying assumption for this plot is the capillary-tube model from which the Kozeny-Carman equation stems.

$$k = \frac{1}{8}\phi\frac{r^2}{\tau^2} \qquad (11)$$

When capillary-tube geometry is assumed, the r^2 term is replaced with an expression for the specific surface area, S_{gv}:

$$k = \frac{\phi_e^{\,3}}{(1-\phi_e)^2}\frac{1}{F_s\tau^2 S_{gv}^2} \qquad (12)$$

where:

k	=	RCI calibrated MRIL permeability, cm^2
ϕ_e	=	effective Porosity (MRIL MPHI)
τ	=	tortuosity
F_s	=	shape factor
S_{gv}	=	specific surface area, cm^{-1}

This equation can be rewritten as:

$$k = \frac{\phi_z}{K_z S_{gv}^2} \qquad (13)$$

where:

ϕ_z	=	normalized ϕ ratio, $\phi^2/(1-\phi)^2$
K_z	=	Kozeny-Carman Constant, $F_S\,\tau^2$

In reality, tortuosity and shape factor vary from one sample to another reflecting formation heterogeneity; therefore, the traditional permeability versus porosity cross-plots show scatter, even in semi-logarithmic space. Therefore, any transform equation derived from this approach (via statistical best fit-line) is prone to have unacceptable error. Assuming that the Kozeny-Carman constant is a single "universal" constant has proven unacceptable. The hydraulic unitization concept assigns a different constant for each hydraulic (flow) unit to account for variations in the pore-space attributes. To apply the hydraulic unitization methodology, we apply the following steps:

1. Algebraic manipulation of the Kozeny-Carman equation yields the following when both sides of the original equation are divided by porosity and raised to the power of 0.5 :

$$\sqrt{\frac{k}{\phi_e}} = \frac{1}{S_{gv}\,K_z^{0.5}}\frac{\phi_e}{(1-\phi_e)} \qquad (14)$$

2. Taking logarithms of both sides of the above equation results in a ***straight-line relationship***:

$$\log\left[\sqrt{\frac{k}{\phi_e}}\right] = \log\left[\frac{1}{S_{gv}\ K_z^{0.5}}\right] + \log\left[\frac{\phi_e}{(1-\phi_e)}\right]$$

$$y = b + mx \qquad (15)$$

3. The left-hand side of the above equation (with the proper conversion factor for permeability - cm^2 to $microns^2$) yields the RQI (Fig. 14b).

The relationship of K_z and S_{gv} to permeability and porosity remains constant for data points with similar pore-space attributes. Therefore, when RQI is plotted versus normalized porosity in logarithmic space, data fall on a straight-line with a 45° slope. Where this straight line intersects the y-axis (x =1) the intercept is equal to $\log(1/SgvK_z^{0.5})$. This intercept is called the Flow Zone Indicator (FZI). Samples with similar pore space attributes exhibit similar y-intercepts. They remain within a confidence envelope (set by the required data accuracy) around a 45° straight-line. Pore-space attributes control intrinsic flow properties; samples with similar y-intercepts belong to the same hydraulic unit. Any large deviation from this straight line indicates the existence of a separate hydraulic unit for which the relationship between K_z, S_{gv}, porosity and permeability is different.

To identify the correct number of hydraulic units (i.e. to draw the correct number of straight-lines with the prescribed 45° slope through the data), cluster analysis is used (Fig. 15). The analysis is based on deciding the optimum center for each data cloud and isolating that set of data with a cluster identification tag. The clustering algorithm used for the RCI-calibrated-MRIL data maximizes the between-cluster distance and minimizes the within-cluster variations. It should be noted that cluster analysis introduces a bias to the determination because the number of clusters should be known prior to clustering. This bias is later eliminated from the determination of flow units via sensitivity analysis.

Sensitivity Analysis

Independent input variables used in the flow-unit formulation have associated uncertainties and known inaccuracies. Because of these uncertainties adjoining hydraulic units may not be statistically independent. If the computed uncertainties for adjoining hydraulic units overlap, the two units are merged.

In this study, error margins are calculated for RQI and FZI based on the rms (root mean square) equation and recommended API practices for permeability and porosity determinations. The following rms equation applies, if:

$$y = f(x_1, x_2, x_3, \ldots, x_n)$$

then, the error in y-function can be calculated:

$$\Delta Y = \pm\left(\begin{array}{l}\left(\left(\partial Y / \partial x_1\right)\Delta x_1\right)^2 + \ldots. \\ +\left(\left(\partial Y / \partial x_n\right)\Delta x_n\right)^2\end{array}\right)^{0.5} \qquad (16)$$

where:

$\partial Y / \partial x_i$ are partial derivatives of the function with respect to its independent variables. Δx_i are uncertainties associated with independent variables.

With the above equation, an error margin is calculated for each cluster. These margins are used to establish whether clusters are truly independent. Then clusters with similar means are merged into one unique flow unit (Figs 16 and 17). Redundant clusters are eliminated. Clusters with more than 20 % variation are isolated and then reanalyzed to refine the clustering. Thus, the bias introduced initially into the analysis is eliminated. At this stage of unitization, flow units are plotted in depth format with available wireline logs (Fig. 18).

Further study is planned for deriving permeability and MBVI transform equations by using the flow unit profiles generated from RCI-calibrated MRIL permeability and conventional logs. This hopefully will permit us to derive MRIL equivalent irreducible water saturation and permeability profiles for adjoining cased wells from conventional log data.

CONCLUSIONS

In this study, we used RCI pressure transient permeabilities to calibrate MRIL derived permeabilities. The constant in the Coates equation was changed from a generic 10 to the reservoir specific 14.5. We then used the hydraulic units concept to classify the reservoir into six distinct flow units based on the MRIL effective porosity and RCI calibrated MRIL permeabilities

We conclude from this work, that

1. WFT data analyzed with FRAT simultaneously provides excellent pressure data for fluid identification and permeabilities.
2. WFT permeabilities are ideally suited for calibrating NMR permeabilities.
3. WFT-calibrated, NMR-permeability profiles are an excellent source of reservoir heterogeneity data.
4. MRIL effective porosity and RCI-calibrated MRIL-permeability data can provide core-quality in situ data in reservoir flow unit studies.

NOMENCLATURE

C_t	compressibility factor, *1/psi*
F_s	shape factor
G_o	geometric factor
k	permeability, *mD*
K_z	Kozeny-Carman Constant
P	pressure, *psi*
q	volumetric flowrate, cm^3/s
r_i	packer-probe radius, *cm*
S	pore surface area, cm^2
S_{gv}	specific surface area, cm^{-1}
t	time, *s*
$T2_{bulk}$	bulk fluid relaxation time, *ms*
$T2_{surf.}$	Surface relaxation time, *ms*
$T2_D$	relaxation time due to diffusion, *ms*
V	pore volume, cm^3
V_{sys}	system volume, cm^3
ϕ	porosity, *fraction*
ϕ_e	effective porosity, *fraction*
ϕ_z	normalized ϕ ratio
λ	thickness of the surface fluid layer
μ	viscosity of fluid, *cp*
ρ_s	surface relaxivity, *cm/s*
τ	tortuosity

Subscripts

ac	accumulation
dd	drawdown
f	formation

ACKNOWLEDGMENTS

We gratefully acknowledge the assistance of J. Michaels and M. Moody with data collection and preparation, and D. Oliver and T. Jbeili for editorial assistance. Finally, we thank Western Atlas Logging Services for permission to publish this paper.

REFERENCES

1. Araktingi, U. G., Bashore, W. M.,Tran, T. T. B., and Hewett, T. A., " Integration of Seismic and Well Log Data in Reservoir Modeling," Reservoir Characterization III, Edited by B. Linville, T. E. Burchfield and T. C. Wesson, PennWell Publishing Co., 1993, p515-554.
2. Yang, C. T., Chopra, A. K., J. Chu, Huang, X., and Kelkar, M. G.,"Integrated Geostatistical Reservoir Description Using Petrophysical, Geological and Seismic Data for Yachheng 13-1 Gas Field," SPE 30566, presented at the SPE Annual Technical Conference and Exhibition, 22-25 October, Dallas, Texas, 1995.
3. Yang, A-P. and Gao, Y.,"Reservoir Characterization by Integrating Well Data and Seismic Attributes," SPE 30563, presented at the SPE Annual Technical Conference and Exhibition, 22-25 October, Dallas, Texas, 1995.
4. Schultz, P.S., Ronen, S., Hattori, M., Mantran, P., Hoskins, J., and Crobett, J., "Seismic-Guided Estimation of Reservoir Properties," SPE 28386, presented at the SPE Annual Technical Conference and Exhibition, 25-28 September, New Orleans, LA, 1994.
5. Hand, J. L., Moritz, A.L., Jr., Yang, C-T., Chopra, A. K., "Geostatistical Integration of Geological, Petrophysical, and Outcrop Data for Evaluation of Gravity Drainage Infill Drilling at Prudhoe Bay," SPE 28396, presented at the SPE Annual Technical Conference and Exhibition, 25-28 September, New Orleans, LA, 1994.
6. Johann, P., Fournier, F., Souza, O., Eschard, R. and Beucher, H. "3-D Stochastic Reservoir Modeling Constrained by Well and Seismic Data on a Turbidite Field," SPE 36501, presented at the SPE Annual Technical Conference and Exhibition, 6-9 October, Denver, CO, 1996.
7. Reedy, G. K., and Pepper, C. F.; "Analysis of Finely Laminated Deep Marine Turbidites: Integration of Core and Log Data Yields a Novel Interpretation Model," SPE 36506, presented at the SPE Annual Technical Conference and Exhibition, 6-9 October, Denver, CO, 1996.
8. Corbett, C., Solomon, G. J., Kartikay, S., Ujang, S. and Ariffin, T.; " Application of Seismic-Guided Reservoir Property Mapping to the Dulang West Field, Offshore Peninsula Malaysia," SPE 30568, presented at the SPE Annual Technical Conference and Exhibition, 22-25 October, Dallas, Texas, 1995.
9. Amaefule, J. O., Altunbay, M., Tiab, D., Kersey, D. G., Keelan, D. K.; "Enhanced Reservoir Description: Using Core and Log Data to Identify

Hydraulic (Flow) Units and Predict Permeability in Uncored Intervals/Wells", SPE 26436, 68th Annual SPE Conference, Oct. 1993.

10. Kasap, E., Huang, K., Shwe, T. and Georgi D.; "Robust and Simple Graphical Solution for Wireline Formation Tests: Combined Drawdown and Buildup Analysis," SPE paper 36525, presented at the SPE Annual Technical Conference and Exhibition, Denver, Colorado, 6-9, 1996, Vol. Ω, p343-357.

11. Kasap, E., and Georgi, D., Micheals J., and Shwe, T.; "A New Simplified, Unified Technique for the Analyses of Wireline Formation Test Data," paper presented at the 1996 SPWLA Annual Logging Symposium, New Orleans, LA, June 16-19.

12. Huang, K., Samaha, A., and Kasap, E.; "Dimensionless Parameters for Interpretation of WFT Data: Simulations and Experiments," paper presented at the 1996 SPWLA Annual Logging Symposium, New Orleans, LA, June 16-19.

13. Samaha, A., Huang, K., Kasap, E., Shwe, T., and Georgi, D.; "Near Wellbore Permeability and Damage Measurements: Experiments and Numerical Simulations for Interpretation of WFT Data," SPE 35150 presented at the SPE 1996 International Symposium on Formation Damage Control in Lafayette, Louisiana, U.S.A. 14-15 February.

14. Waid, M. C., Proett, M.A., Chen, C.C., and Ford, W.T.: "Improved Models for Interpreting the Pressure Response of Formation Testers," paper SPE 22754 presented at the 1991 SPE Annual Technical Conference and Exhibition, Dallas, TX, Oct. 6-9.

15. Proett, M. A. and Chin, W. C.,; "Supercharge Pressure Compensation Using a New Wireline Testing Method and Newly Developed Early Time Spherical Flow Model," paper SPE 36524 presented at the 1996 SPE Annual Technical Conference and Exhibition, Denver, CO, Oct. 6-9.

16. Goggin, D. J., Trasher, R. L., and Lake, L. W.; "A Theoretical and Experimental Analysis of Minipermeameter Response Including Gas Slippage and High Velocity Flow Effects," In Situ 12, No. 1 and 2 (1988) 79-116.

17. Micheals, J., Moody, M. and Shwe, T.; "Wireline Fluid Sampling," paper SPE 30610, presented at the SPE Annual Technical Conference and Exhibition, Dallas, TX, October 22-25, 1995.

18. Brown, R.J.S., Gamson, B.W.; "Nuclear Magnetism Logging", SPE 1305-G, Dallas, Tx, October 4-7, 1959

19. Timur, A.; "Pulsed Nuclear Magnetic Resonance Studies of Porosity, Movable Fluid, and Permeability of Sandstones", Trans. AIME, v. 246, p. 775, 1969

20. Seevers, D.O.; "A Nuclear magnetic Method for Determining the Permeability of Sandstones", Trans. SPWLA, v.6, Sec. L, 1966

21. Miller, M.N., Paltiel, M.E., Gillen, J. Granot and J.C. Bouton; "Spin Echo Magnetic Resonance Logging: Porosity and Free Fluid Index Determination", SPE 20561, 65 th Annual Tech. Conf., New Orleans, Sep 23-26, 19990

22. Akkurt, R., Vinegar, H.J., Tutunjian, P.N., and Guillory, A.J.; "NMR Logging of Natural Gas Reservoirs", Paper N, Presented at the 36th Annual Logging Symposium, SPWLA, Paris, France, 1995.

23. Starley, C., Morris, C. E., Kenyon, W. E. and Howard, J. J.; "NMR in Partially Saturated Rocks: Laboratory Insights on Free Fluid Index and Comparison With Borehole Logs," paper CC, presented at the 32nd Annual Logging Symposium, SPWLA, Midland, TX, June 16-19, 1991.

24. Prammer, M. G., Drack, E. D., Bouton, J. C., Gardner, J. S. and Coates, G. R., "Measurements of Clay-Bound Water and Total Porosity by Magnetic Resonance Logging; " SPE 36522, presented at the SPE Annual Technical Conference and Exhibition, 6-9 October, Denver, CO, 1996.

25. Kubica,P.; "Statistical Tests of Permeability Estimates Based on NMR Measurements", SPWLA 36 th Annual Logging Convention, Paper VVV, June 26-29, 1995.

26. Kenyon, W.E., Day, P.I., Straley, C., Willemsen, J.F.; "A Three-Part Study of NMR Longitudinal Relaxation Properties of Water-Saturated Sandstones", SPE Formation Evaluation, September 1988.

27. Coates, G.R., Miller, M., Gillen, M., Henderson, G.; "An Investigation of a New Magnetic Resonance Imaging Log", SPWLA Convention in Midland, Tx, June 18, 1991.

28. Ebanks, W. J., Jr.; "Flow Unit Concept-Integrated proach to Reservoir Description for Engineering Projects", ARCO Oil and Gas Company, Plano, TX.

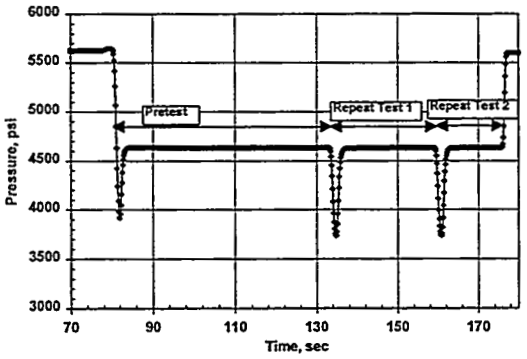

Figure 1. Pressure versus time from a WFT showing a pretest and two repeated tests.

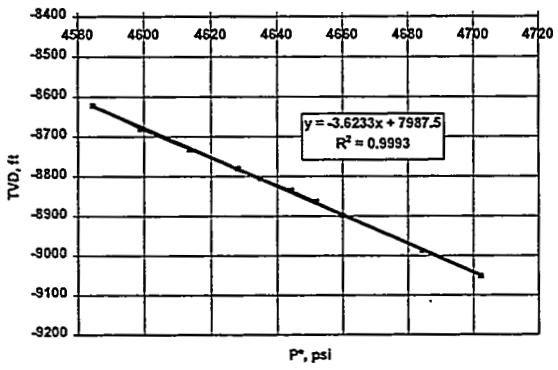

Figure 2. Depth versus formation pressure obtained from a WFT. The calculated pressure gradient corresponds to 90.8 API gravity formation fluid.

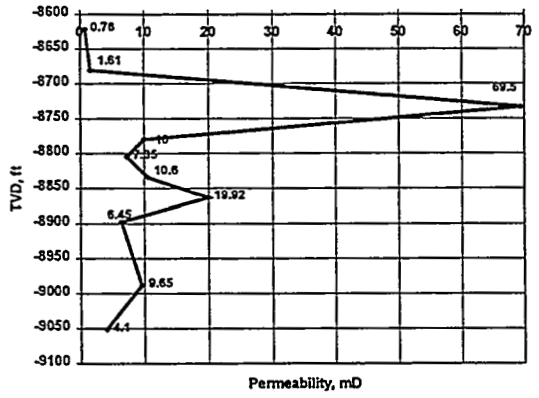

Figure 3. Permeability profile at Well A, obtained with RCI.

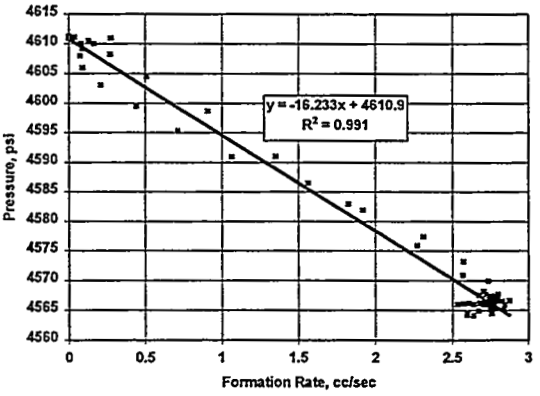

Figure 4. Pressure versus formation rate plot for Test A6-4 and its best fit straight line. A permeability of 70.1mD is calculated from the slope.

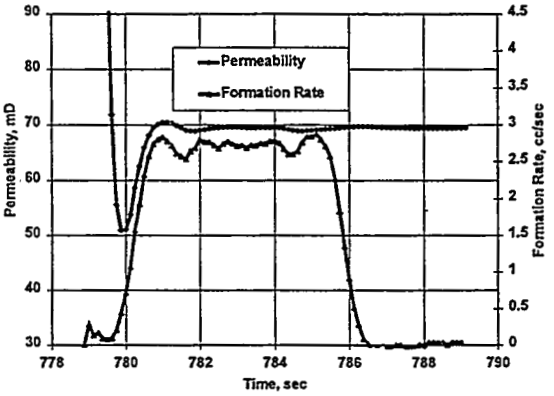

Figure 5. Continuously calculated formation rate and permeability from FRAT (Test A6-4).

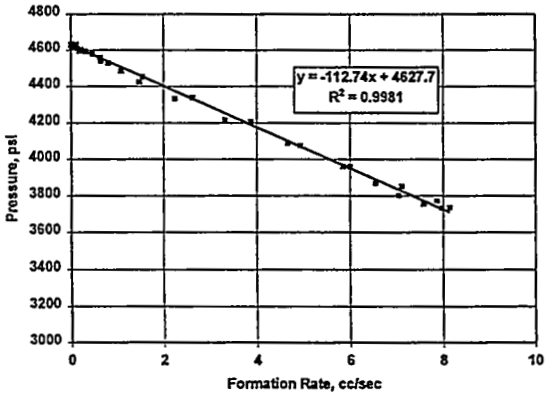

Figure 6. Pressure versus formation rate for Test A7-2 and its best-fit straight line. A permeability of 10.1mD is calculated from the slope.

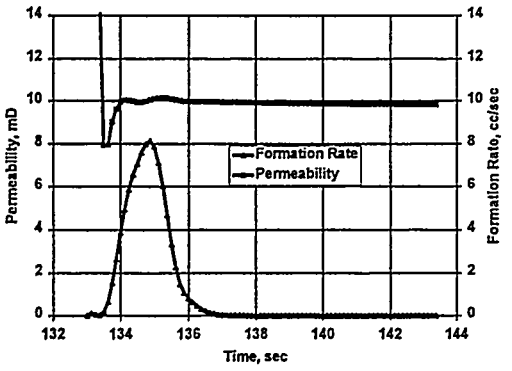

Figure 7. Continuously calculated formation rate and permeability from FRAT (Test A6-4).

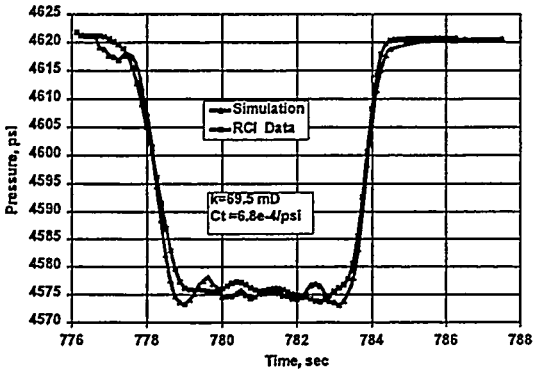

Figure 8. Comparison of transient pressures from RCI with the pressures from numerical simulation for Test A6-4.

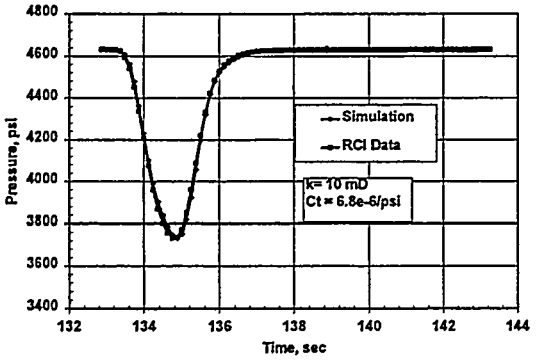

Figure 9. Comparison of transient pressures from RCI with the pressures from numerical simulation for Test A7-2.

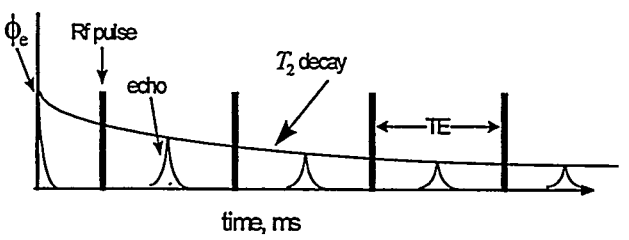

Figure 10a. Schematic of NMR data acquisition.

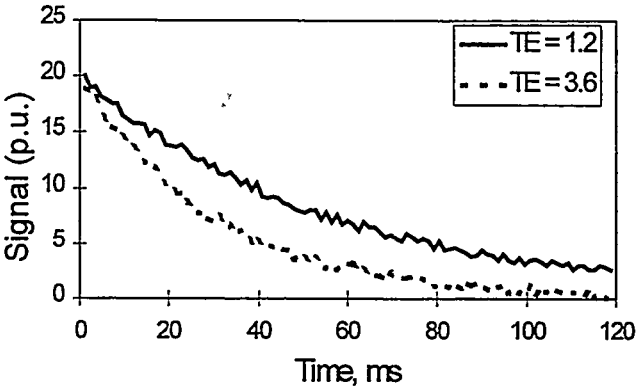

Figure 10b. Typical NMR echo data.

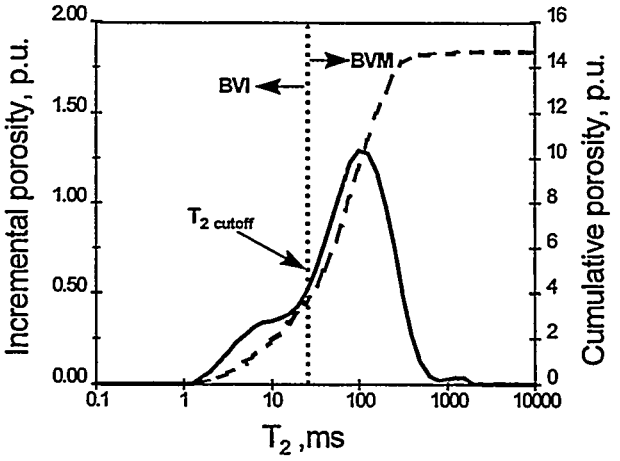

Figure 11. T2 spectrum with indicated T2 cutoff.

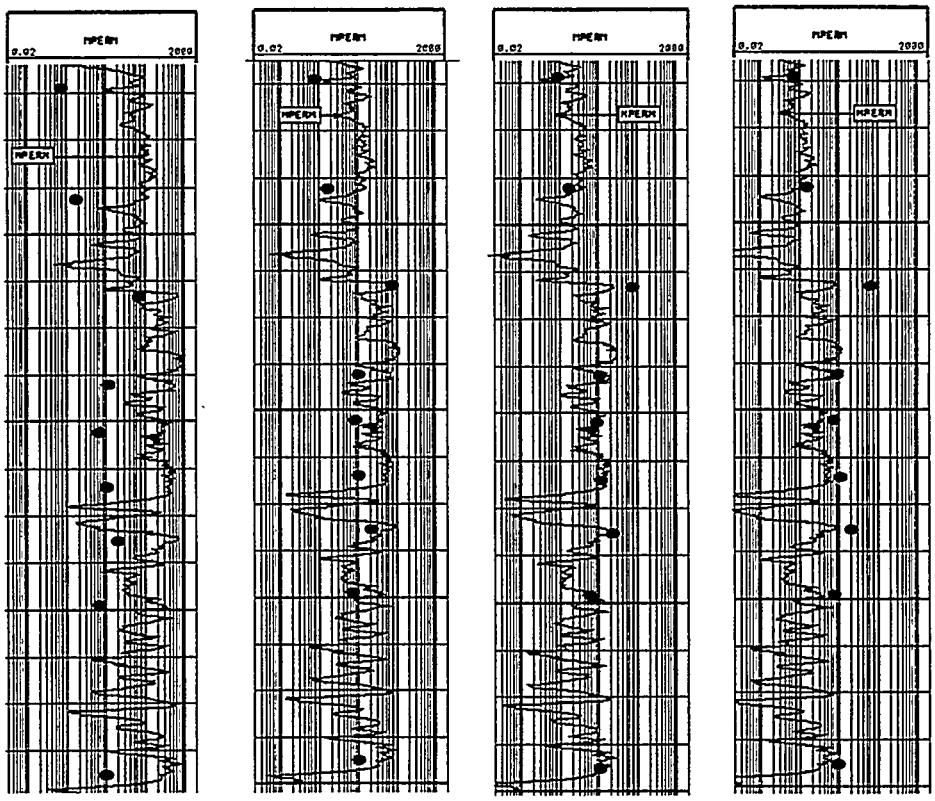

Figure 13. Calibration of C based on RCI permeabilities.

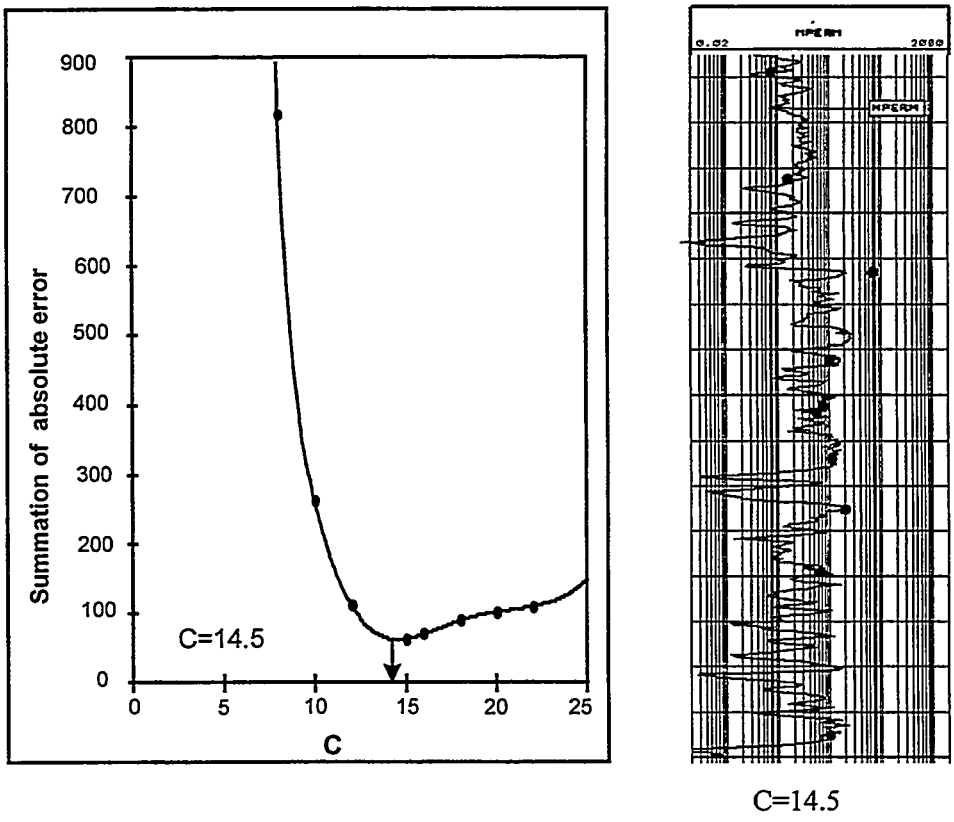

Figure 14. Proper selection of C minimizes error for permeability estimation

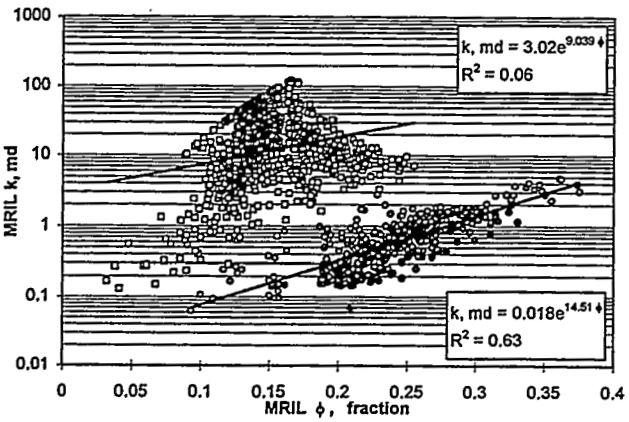

Figure 14a. Permeability versus porosity relationship.

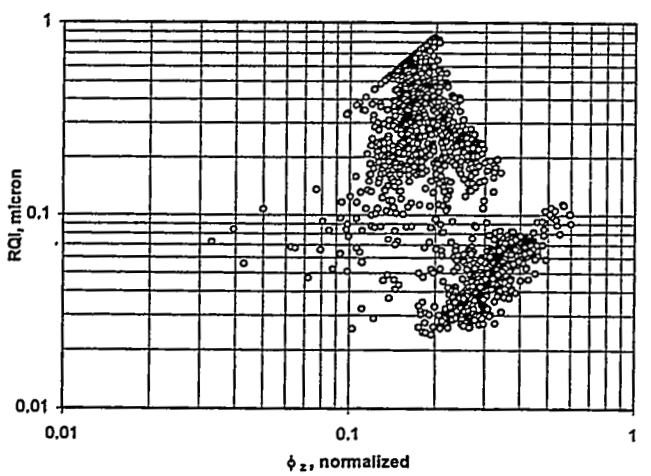

Figure 14b. Reservoir Quality Index versus normalized porosity.

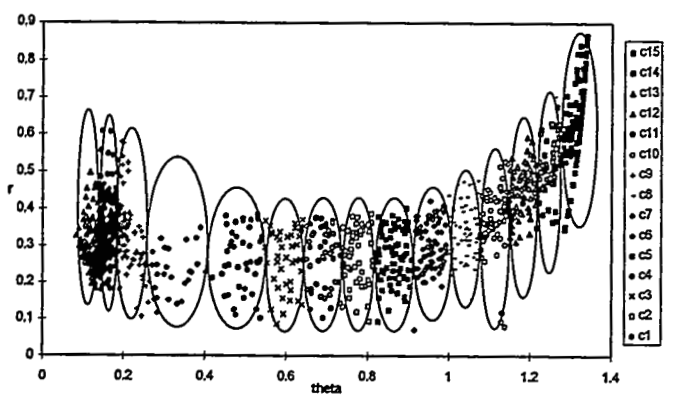

Figure 15. Cluster analysis maximizes between-cluster distance and minimizes within cluster variations.

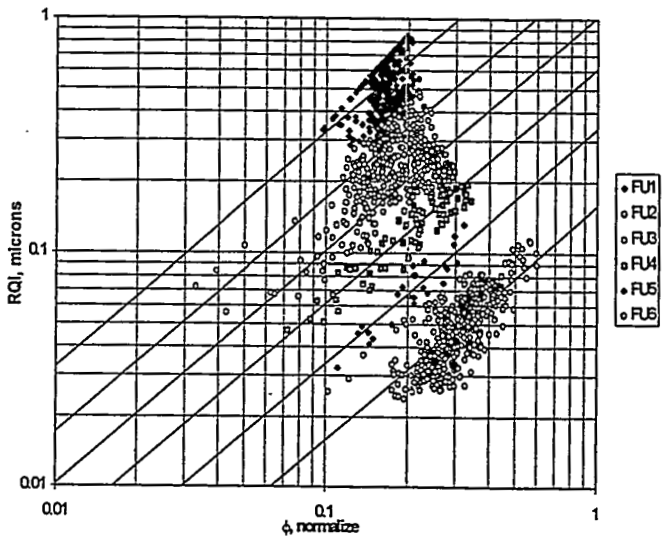

Figure 16. Sensitivity analysis of the clustering-results produce the unique classification of flow (hydraulic) units.

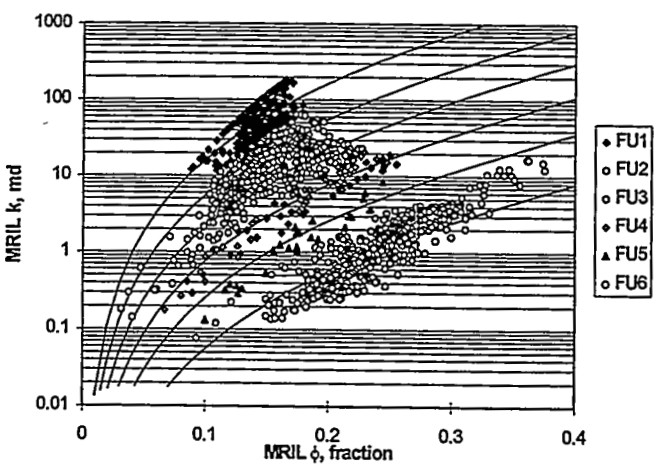

Figure 17. Traditional permeability versus porosity plot for the six unique flow units.

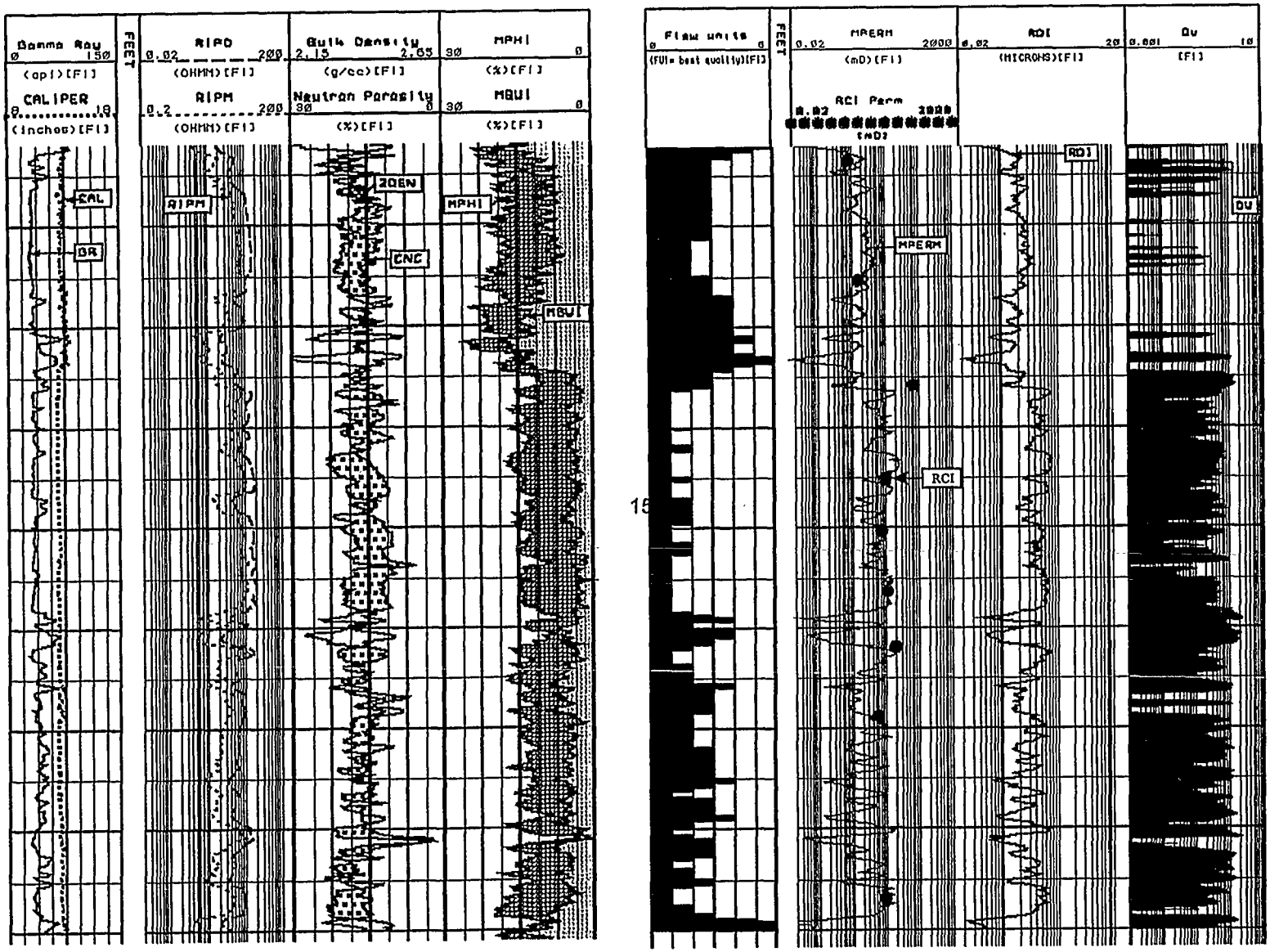

Figure 18. RCI-calibrated MRIL permeability and hydraulic unitization with conventional log data enable the derivation of permeability transform equations for the neighbouring cased-wells.

New Developments in High Resolution Borehole Seismology and their Application to Reservoir Development and Management

Björn N.P. Paulsson

Chevron Petroleum Technology Company
1300 Beach Blvd., La Habra, CA 90631-6374

Abstract

Single-well seismology, Reverse Vertical Seismic Profiles (VSP's) and Crosswell seismology are three new seismic techniques that we jointly refer to as borehole seismology. Borehole seismic techniques are of great interest because they can obtain much higher resolution images of oil and gas reservoirs than what is obtainable with currently used seismic techniques. The quality of oil and gas reservoir management decisions depend on the knowledge of both the large and the fine scale features in the reservoirs. Borehole seismology is capable of mapping reservoirs with an order of magnitude improvement in resolution compared with currently used technology. In borehole seismology we use a high frequency seismic source in an oil or gas well and record the signal in the same well, in other wells, or on the surface of the earth.

Introduction

Borehole Seismology has been regarded as a promising technique for reservoir imaging. In Figure 1 the resolution and measurement length are given for a number of seismic techniques including borehole seismic techniques. The combination of large measurement

lengths and high resolution is the reason for the current interest in Borehole seismology. In the first quarter of 1997 we are deploying a new, powerful, yet non-destructive borehole seismic source, and a new receiver system, the combination of which has a projected capability of handling source-receiver spacing of more than 2,000 meters and well depths as great as 6,100 meters.

This advanced borehole seismic data acquisition system consists of a powerful, clamped, swept-frequency, vibratory source which is non-destructive, a multi-level (up to 100 levels) receiver string of clamped, three-component geophones, and an acquisition system for Reverse VSP's. The downhole vibrator produces high quality *S*-waves, with controlled polarization, as well as *P*-wave direct arrivals and reflections. The radiation pattern of the two different actuators which will be part of the three component source are shown in Figure 2 and the measured force from both the prototype and the new actuators together with the modeled force of the new actuator are shown in Figure 3.

An early prototype of the clamped hydraulic downhole vibrator produced wide bandwidth (10 - 640 Hz) seismic data in the crosswell mode (Paulsson *et al.,* 1994), Figure 4. The data from this prototype source routinely contained high quality transmitted *P*-waves and *S*-wave arrivals as well as *P*- and *S*-wave reflections. This source was used to produce cross well seismic images which contained high resolution information about the reservoir as seen in Figure 5.

The new advanced borehole seismic source will be significantly more powerful, controllable, and deployable than the early prototype. The source in a Single well configuration is shown in Figure 6 and in a Reverse VSP/Cross well configuration in Figure 7.

We anticipate that borehole seismology will soon be used in management of both new and mature reservoirs. There are two different classes of applications for the borehole seismic techniques. The first is monitoring and evaluation of improved or enhanced oil recovery efforts such as water, steam or CO_2 floods using time-lapse methods. The process of injecting steam, water or CO2 into a rock formation will change both measured P and S wave velocities and can therefore be monitored using borehole seismology. A second application is reservoir characterization, whereby we determine with much greater resolution the architecture of the reservoir, including the continuity of bedding, the direction of fractures and fault planes, and the lateral variability of porosity. This will allow for the accurate positioning of directional or in-fill wells.

Development and Production Seismology

The primary task of the emerging field of high resolution development and production seismology is to map fine-scale geological heterogeneities to lower the risk of proper placement of new wells, re-drilling of existing wells and to improve the recovery of the hydrocarbon resources. Improved understanding and delineation of reservoirs lowers the economic risk, allowing for the operation of smaller, more marginal fields and the

identification of bypassed pockets of oil and gas in larger fields. In most producing reservoirs, an improved description is needed to manage production effectively. In many cases it is desirable to have greater resolution than 3-D surface seismic data can provide, and/or larger area coverage than well-logging techniques provide. Borehole seismology fills the resolution and coverage gap between 3-D seismology and well logging techniques, which makes it complementary to these proven methods. Furthermore, borehole seismology can provide accurate formation velocity information for improved processing of 3-D seismic data and for determining petrophysical parameters. One particularly important application for borehole seismic data is in areas where reliable surface seismic data can not be collected.

Surface seismic data account for the most of the worldwide geophysical activity in oil fields. However, higher resolution of the reservoir can be achieved by placing the seismic source and the receivers in boreholes near the reservoir. This has been demonstrated over the last twenty years with experimental crosswell seismology, the most tested of the three new borehole seismic techniques. The primary reasons for the superior performance of these borehole methods are:

- The avoidance of a near-surface weathering layer allows the use of seismic frequencies more than an order of magnitude higher than is possible using surface techniques.
- The avoidance of the near-surface weathering layer makes it possible to record high quality *S*-wave data routinely.

- The recording environment is very quiet.
- The transducers are closer to the targets.

The resolution of various seismic methods and their corresponding measurement lengths are shown in the Table. The measurement length is the distance over which the seismic energy propagates in a particular method and is a partial indication of how much of the reservoir is actually sampled by this technique.

Seismic Technique (Hz)	Measurement Length (m)	Resolution (m)
Ultra sonic on core (10^5-10^6)	.01 - 0.1	.001 - .01
Sonic logs (1,000 - 10,000)	0.1 - 3	.01 - 0.1
Crosswell seismology (10-2,000)	10 - 2,000	1 - 5
Single-well seismology (10-1,000)	10 - 1,000	1 - 5
Reverse VSP (10 - 500)	100 - 3,000	2 - 10
VSP (10 -100)	100 - 5,000	10 - 50
Surface Seismology (10 - 100)	100 - 10,000	20 - 50

When using the single-well acquisition geometry, the seismic source and the receiver array are placed in the same vertical or deviated well shown in Figure 8. This technique is suitable for mapping features at depth which are parallel or sub-parallel to the well used for the survey. Application examples include, for vertical wells, salt dome flanks or fault surfaces, and for deviated wells, horizontal or near horizontal lithology boundaries.

Single well seismic methods will provide a new type of high frequency seismic data which have previously been unavailable. The technology for deploying well logging tools in horizontal wells has been developed over the last few years and includes the use of coiled tubing, regular tubing, and newly developed well tractors. The same technology will be used for the single-well seismic system. Figure 9 shows a cross section through the Bayou Choctaw Salt Dome Site where a consortium of companies are testing and evaluating single well seismic imaging.

For Reverse VSP's, Figure 8, seismic energy is transmitted from the borehole to an array of geophones on the surface of the earth or on the sea floor, in the case of offshore wells. We have observed that considerably higher seismic frequencies can be recorded in the Reverse VSP configuration compared with the conventional VSP technique. This is most likely due to the better coupling of a seismic source in a well compared to the surface where the source coupling is a major issue. It is also likely that it will be more cost effective in many situations to deploy an array of receivers at the surface for reverse VSP's, than it will be to establish multiple shot points on the surface in the case of a conventional walkaway VSP.

For the third borehole seismic technique, crosswell seismology, Figure 8, we can construct two-dimensional velocity images for the region between pairs of wells using travel time tomography, and two dimensional reflection images using migration techniques. The combination of these two image types can be a very powerful tool in key areas of the reservoir and it offers resolution on the scale of 1 to 2 meters.

We believe that borehole seismology will eventually be an integrated part of the oil and gas reservoir production process and that it will fundamentally change the way we are using seismic methods. Much of the processing will be done in the field to provide fast results. We will compute velocity tomograms and eventually, the reflection images in the field. This is a departure from the processing approach of surface seismic data used for development purposes. In this sense, borehole seismology will be more like well logging, where the preliminary results are delivered in the field. Client reservoir engineers and geologists will be able to change the direction and the scope of the survey based upon initial results. This will make the borehole seismic imaging of oil and gas reservoirs a dynamic, client driven process.

Summary

We have developed a downhole seismic source which has the potential to make borehole seismology into an economic and widely used technique for oil and gas reservoir characterization. The new tool has an effective force output which will allow it to be used in large well spacing and in reservoirs with highly attenuating sediments. It also has a very broad seismic bandwidth, which allows us to achieve both long range and high resolution using the same source tool. Since the source is clamped, the tool can also be used in gas-filled wells. This feature also helps to minimize tube waves during single-well seismic surveys. The source system design includes 3-component motion providing for multi-component data. The advanced borehole seismic system is also the first system

in the oil and gas industry where both the source and the receivers operate on fiber optic wirelines. Data examples from the new system will be presented in 1997.

References

The Steepbank Crosswell Seismic Project: Reservoir Definition and Evaluation of Steamflood Technology in Alberta Tar Sands, Paulsson, B.N.P., Fairborn, J.W., Meredith, J.A., Wang, Z., Geophysics: The Leading Edge of Exploration, July 1994.

Acknowledgment

The following individuals are acknowledged for contributing substantially to the development of the downhole seismic vibrator: Robert Heming and Frank McCaffery with Chevron, Marion Scott, Bob Cutler and Chad Harding with Sandia National Laboratories, Frank Bernhard and Glen Kirkendall with E-Systems, Sen Chen with Exxon Production Research Company, Tim Fasnacht with Gas Research Institute, John Giles and Kim Mitchell with Pelton Company, Henry Tan with Amoco, Dale Cox with Conoco and Jack Cole with University of Arkansas.

Figure captions

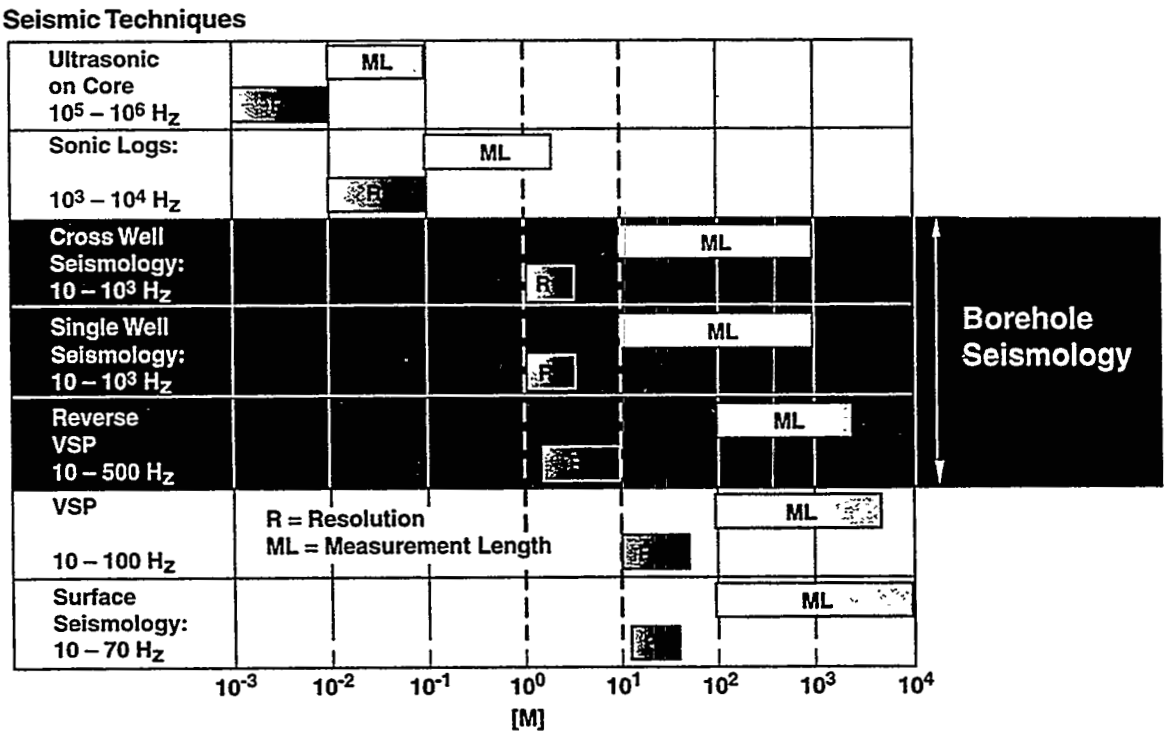

Figure 1. Resolution and Measurement Length for Different Seismic Techniques

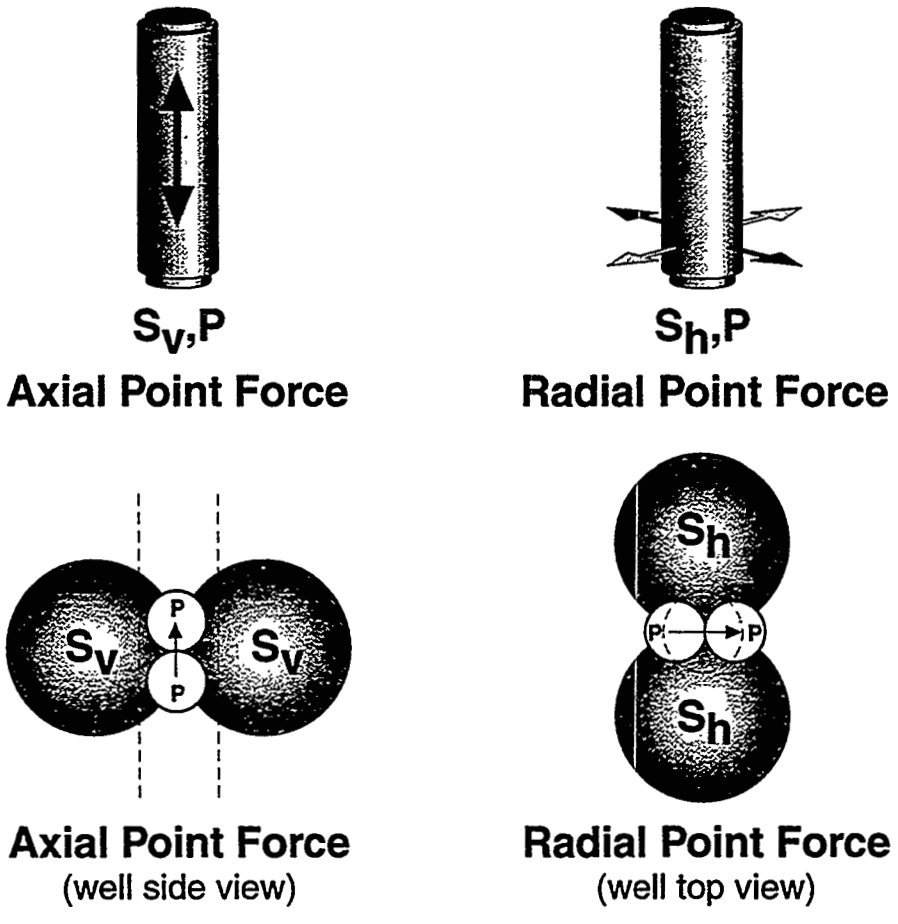

Figure 2. Radiation Patterns for Different Actuators

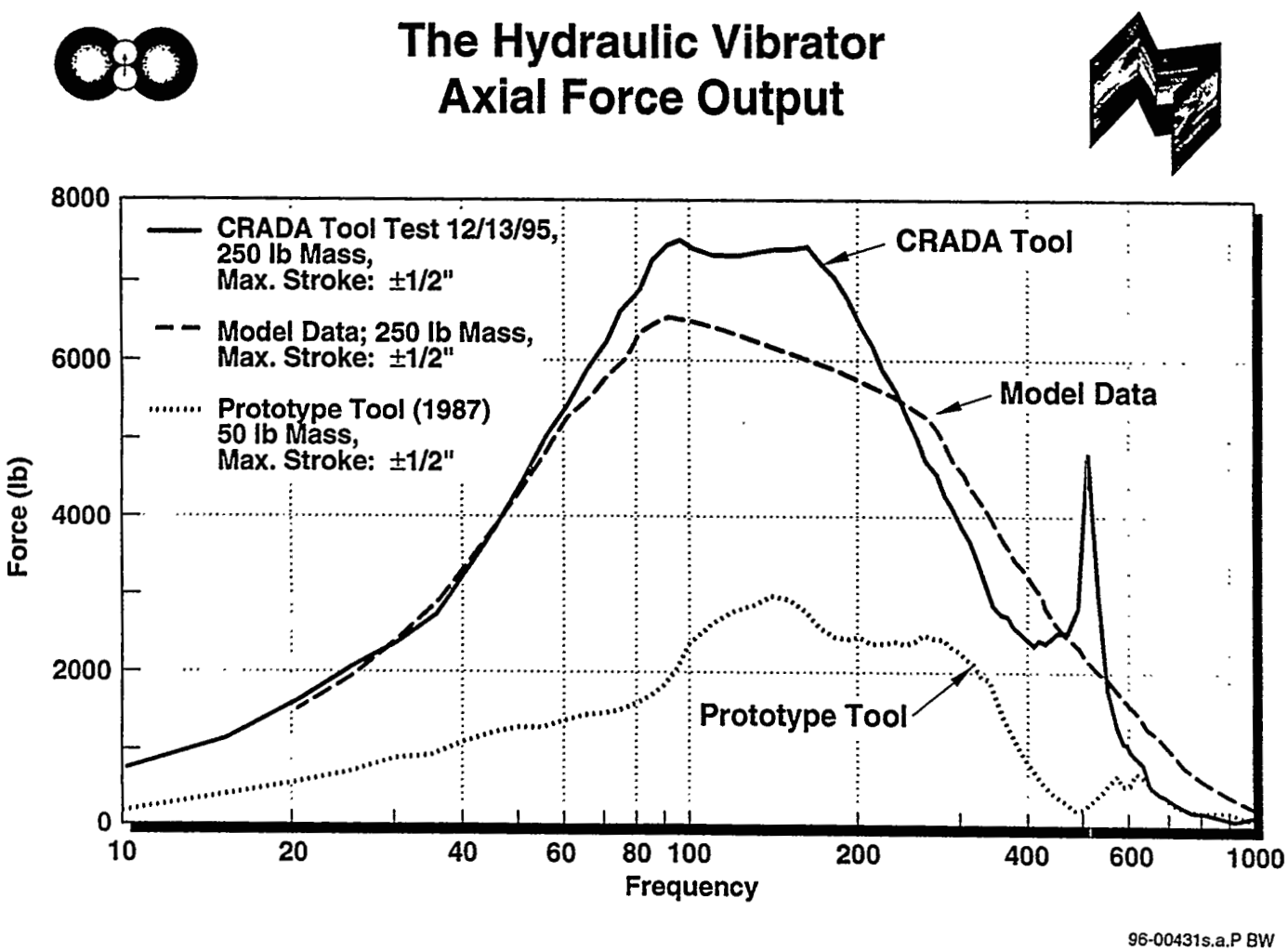

Figure 3. The Hydraulic Vibrator Axial Force Output

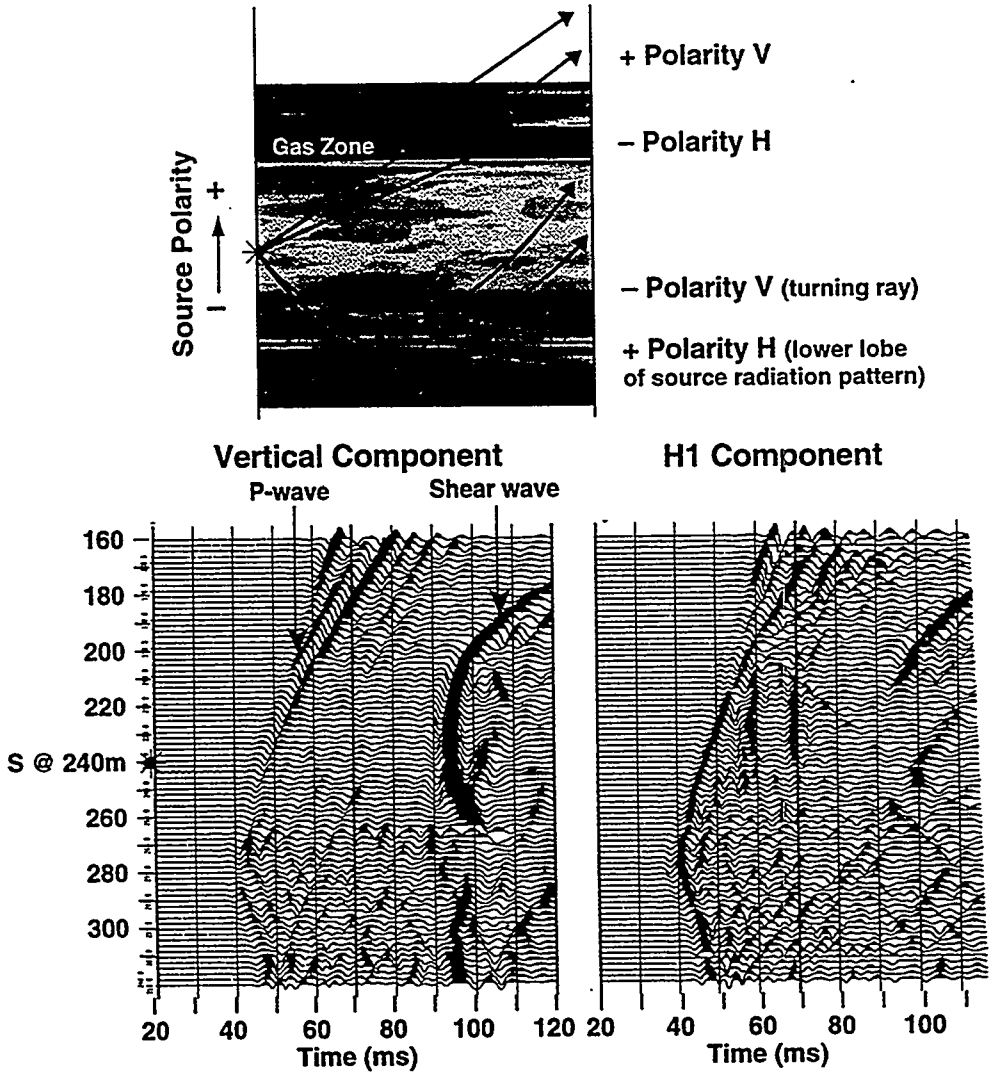

Figure 4. Steepbank Cross Well Seismic Data

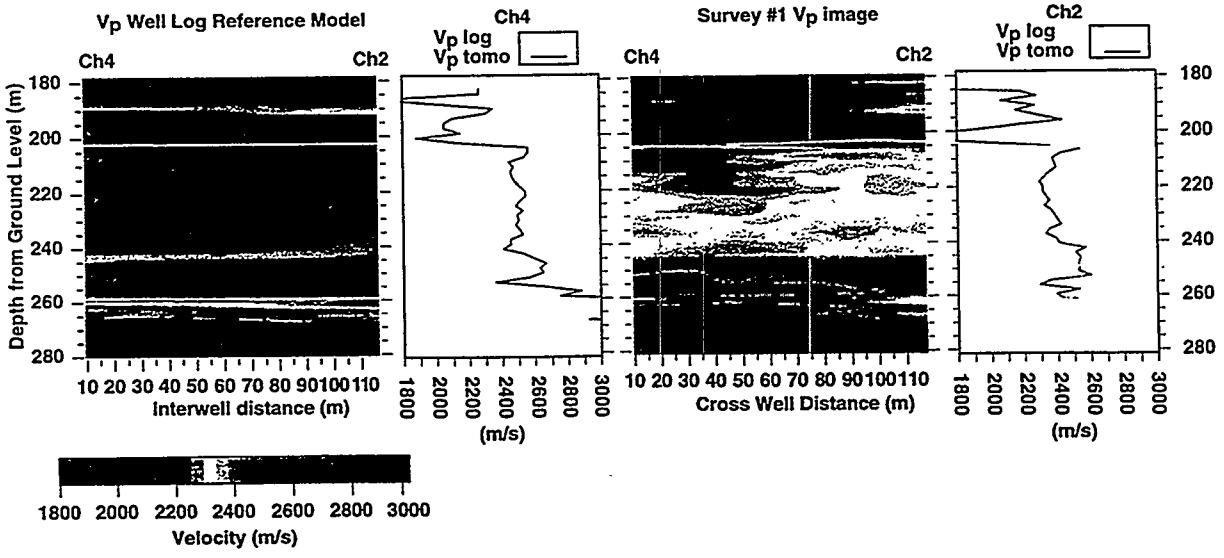

Figure 5. Steepbank Cross Well Seismic Tomograms

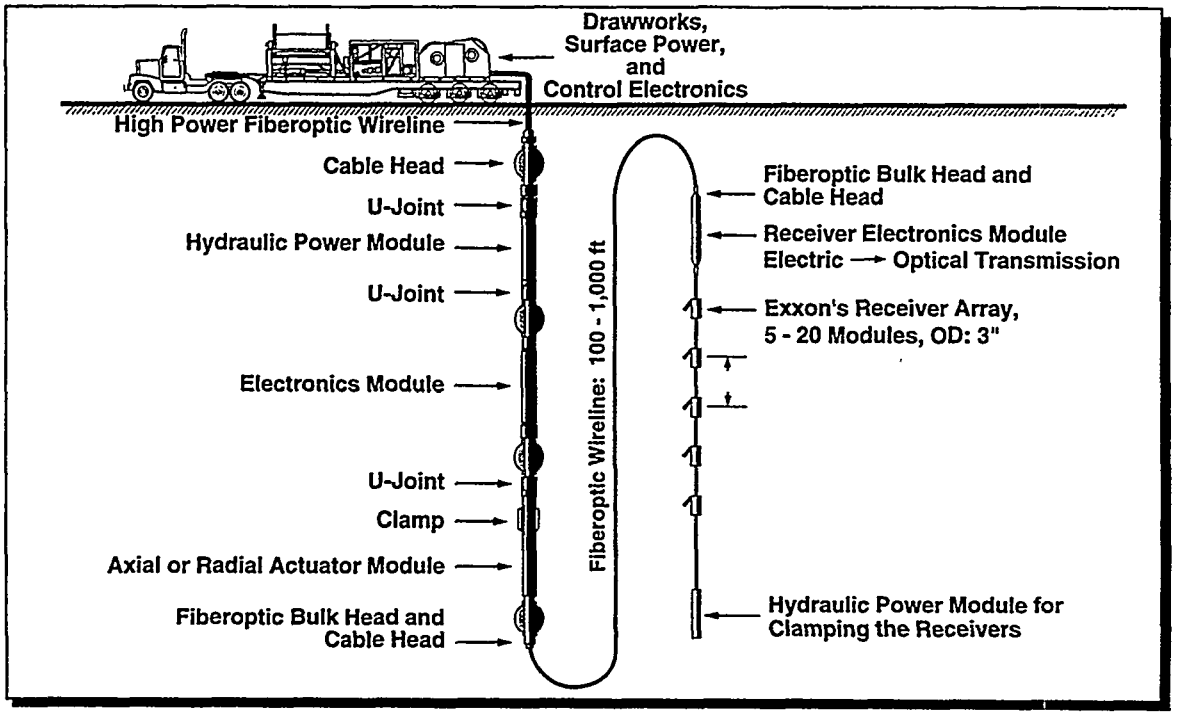

Figure 6. Single Well Configuration of the Downhole Seismic Vibrator

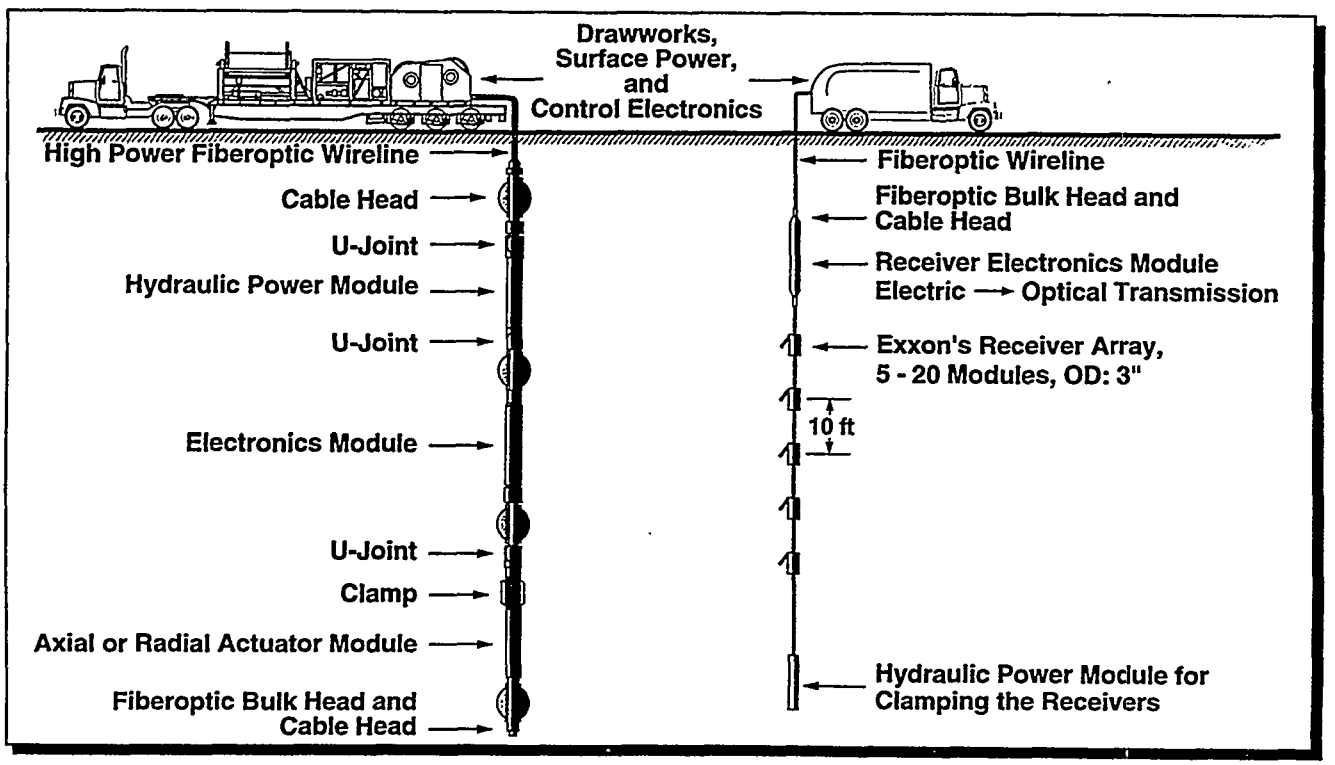

Figure 7. Reverse VSP/Cross Well Seismic Configuration of the Downhole Seismic Vibrator

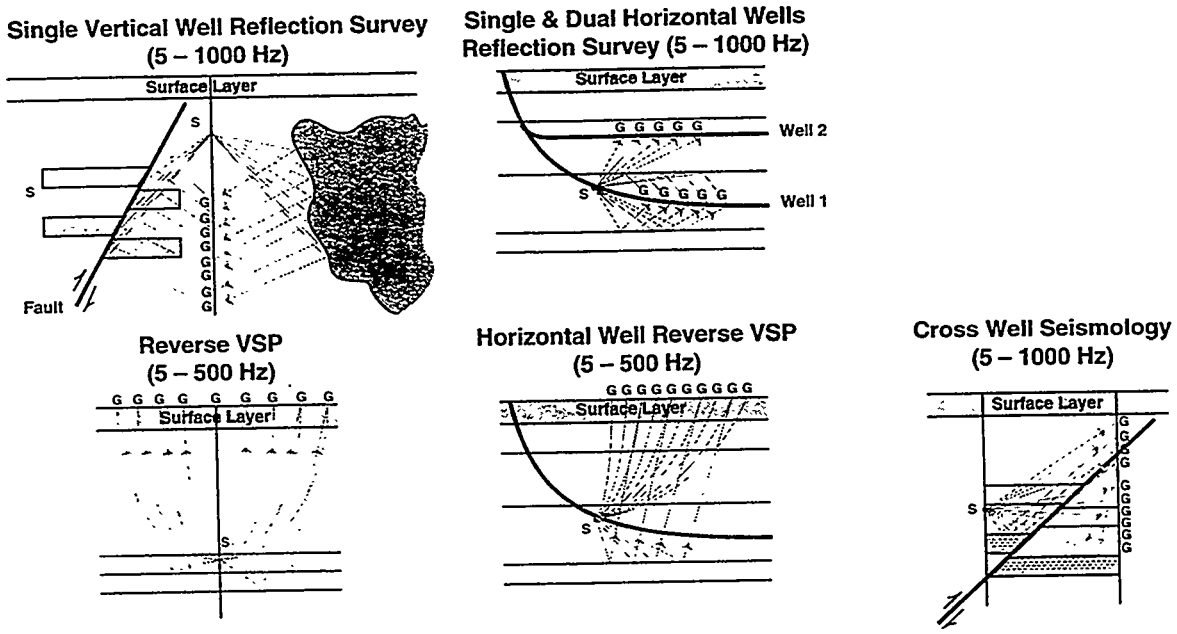

Figure 8. Borehole Seismology

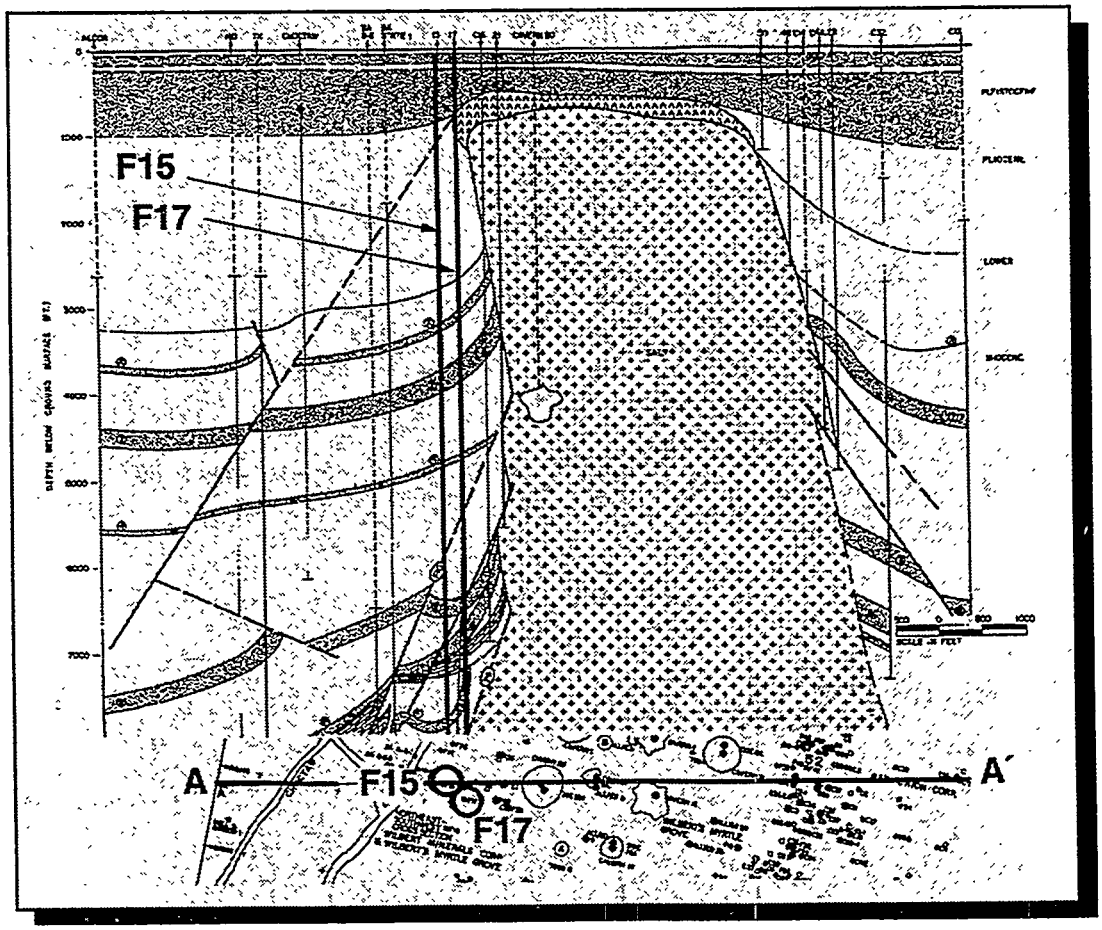

Figure 9. The Bayou Choctaw Salt Dome Site

A Direct Method For Determining Complete Positive And Negative Capillary Pressure Curves For Reservoir Rock Using The Centrifuge

E. A. Spinler - Phillips Petroleum Co., Bartlesville, OK

B. A. Baldwin - Phillips Petroleum Co., Bartlesville, OK

Acknowledgments

The authors thank Phillips Petroleum Co. for permission to publish this extended abstract and thank D. M. Chancellor for his mechanical assistance in building equipment for this work, J. C. Stevens for performing the centrifuging and R. L. King for assistance with magnetic resonance imaging.

Abstract

A method is being developed for direct experimental determination of capillary pressure curves from saturation distributions produced during centrifuging fluids in a rock plug. A free water level is positioned along the length of the plugs to enable simultaneous determination of both positive and negative capillary pressures. Octadecane as the oil phase is solidified by temperature reduction while centrifuging to prevent fluid redistribution upon removal from the centrifuge. The water saturation is then measured via magnetic resonance imaging. The saturation profile within the plug and the calculation of pressures for each point of the saturation profile allows for a complete capillary pressure curve to be determined from one experiment. Centrifuging under oil with a free water level into a 100 percent water saturated plug results in the development of a primary drainage capillary pressure curve. Centrifuging similarly at an initial water saturation in the plug results in the development of an imbibition capillary pressure curve. Examples of these measurements are

presented for berea sandstone and chalk rocks.

Background

Knowledge of capillary pressure for each specific rock/oil/water combination is important for predicting potential hydrocarbon recovery from a reservoir. Capillary pressure is a measure of the interaction between fluids and the rock pore surface. The strength of the interaction varies with the fluid saturations, the interfacial tension between the fluids, the pore structure and the wettability of the pore surfaces. A measure of the capillary pressure can be calculated from the force exerted by the density difference between retained fluids at each height above or below the free water level. Knowing the fluid saturations as a function of the height above and below the free water level permits the determination of a capillary pressure curve for any given reservoir rock/fluid system. However, in practice this has been difficult, of uncertain accuracy, or very time consuming to experimentally determine.

Capillary pressure curves are typically determined by either mercury intrusion, porous plate/membrane or centrifuge methods. Mercury intrusion, although rapid, provides questionable results due to the use of mercury in a vacuum to mimic water/oil behavior. It's methodology limits the technique to primary drainage and possible positive imbibition capillary pressures. Porous plate/membrane methods can generate all the capillary pressure curves, but to reach an apparent equilibrium saturation can take days to months per pressure point for 5 to 8 data points. This delays the availability of the results and limits the number of tests which can be made. The lengthy experimental time also increases the chance for mechanical failure. The centrifuge method is normally only used to determine drainage or negative imbibition curves. It takes days to months to complete a test. The limitation of most centrifuge methods is that they only provide an indirect, or assumed/calculated, measure of saturation at the inlet face of a rock plug based on the amount of fluid expelled from the rock. Numerous methods over the past 50 years have been proposed for

approximating the inlet saturation from centrifuge effluent volumes, but in every case, the model chosen influences the results.

A capillary pressure curve that is determined from the measured oil/water saturation profile under a known pressure gradient as measured from a free-water level would ideally mimic the reservoir. The methodology as proposed herein does provide such positive and negative capillary pressures for both drainage and imbibition. Furthermore, the method appears to be accurate, rapid and robust.

Methodology and Results

The method under development *directly* measures the oil/water saturation distribution in a rock plug which has been established via a known fluid differential pressure by centrifuging. *Direct* measurements of the saturations is possible by a number of different techniques, but for this study, magnetic resonance imaging was used because it provides high spatial resolution. Previously, the authors (Baldwin et al., 1996) had discussed some of the different methods by which magnetic resonance images of the saturations within rock plugs could be measured. All saturations for this work were determined by imaging the liquid water phase while the oil phase was solid and does not image. The saturation profile was established and locked in place, by cooling, while in the centrifuge. The measurement of the complete oil/water saturation profile determined with more than a hundred measurements within a rock plug has an advantage over other typical techniques which measure saturations one point at a time.

An additional advantage is that both the positive and negative portions of the capillary pressure curve can be measured simultaneously by positioning the free water level along the length of the plug as shown in Figure 1. The capillary pressure is zero at the free water level. Drainage or imbibition is achieved by centrifuging the plug under hydrocarbon or water when starting the plug at an appropriate saturation state. The sequence of the centrifuge steps is important because it

determines the direction of fluid flow and possible hysteresis. Capillary pressure as a function of position in the plug and the achievable pressure range is calculated from the speed of the centrifuge, the height above the free water level, the fluid density difference and the sample length.

Water and octadecane which has a melting point of about 27 degrees Celsius were used. Other hydrocarbons which are solid at the ambient temperature in the magnetic resonance imager would also work. When one phase is frozen, the relaxation time in the magnetic resonance imager is so short that it is not imaged. Thus, in this system only the water was imaged. Because the hydrocarbon was frozen in place while centrifuging, redistribution of the water in the plug when handled at normal ambient temperature will not occur. The small volume change created by the contraction of the hydrocarbon during freezing can be easily corrected. One disadvantage is that the water as the wetting phase had a relaxation time that was dependent on the size of the pore spaces it occupied. In chalks with a relatively narrow pore size distribution, this was not a problem. However, sandstones with a broad pore size distribution had relaxation times for the lower water saturations that were significantly shorter than those for high water saturation and consequently affected the image intensity. A correction (Baldwin, et al., 1991) was calculated for this effect in the sandstones by using T1 mapping where the relaxation time was measured on a pixel by pixel basis and extrapolated back to zero relaxation time to minimize the relaxation effect on intensity. This procedure produced a porosity map where intensity was proportional to the water saturation.

Laboratory experiments for this study consisted of preparing both a berea sandstone plug and a reservoir chalk plug. These plugs were selected because they have a great disparity in rock properties (Table 1) and it was intended to evaluate the methodology for both. The reservoir chalk plug was previously cleaned by extraction with mild solvents. No cleaning was necessary for the berea plug.

Each plug was initially saturated with 100% of the water phase. The experimental work with each plug was done separately, but the steps were basically the same. Once placed in their centrifuge

holders, water and octadecane (warmed to slightly above its melting point) was added.. No oil imbibition was expected to occur, nor was it observed, since both samples were water-wet. The final free water level height was adjusted by adding the appropriate amounts of each fluid. This position was expected to change since one fluid will be expelled from the rock during the test while the other will enter. Movement of the free water level was minimized by having the volume of bulk fluids around the plugs significantly greater than the pore volume of the rock plugs as indicated in Figure 1. Centrifuging at a temperature above the melting point of octadecane was conducted for an appropriate amount of time, 1 day intervals for the berea and 3 day intervals for the chalk. At the end of the centrifuging time, but while still centrifuging, the sample was cooled to solidify the oil, but not the water. When the oil phase in the sample was frozen in approximately 4 hours, it was removed from the centrifuge and imaged for saturation. The centrifuge procedure was repeated until the saturation profiles in the plugs were observed to be stabilized. The height of the free water level was locked in place by the frozen oil phase and becomes part of the image. Distances from the free water level for each pixel of the intensity image were determined and local pressures calculated from standard centrifuge equations. Local pressures determine the capillary pressure at any point on the image from the free water level. Capillary pressure curves as measured by this method for primary drainage of berea sandstone and reservoir chalk are shown in Figures 2 and 3. The scatter in capillary pressure data for the berea reflects the less uniform porosity distribution found in the sandstone as compared to the chalk. Note, however, that for these tests, the image represented only a 4 millimeter slice through each plug. Averaging or imaging more of the plug by MRI can further smooth the capillary pressure curves.

Following the determination of the primary drainage capillary pressure curve, the plugs were centrifuged under 100 percent oil phase and inverted as necessary to drive the plugs to a relatively uniform initial water saturation. The plug at initial water saturation was then centrifuged with a free water level near the center of the plug. Again centrifuging of the plugs continued until the saturation profiles were observed to be stable. The resultant primary imbibition capillary pressure

curve are illustrated in Figures 4 and 5 for the berea sandstone plug and the reservoir chalk core plug, respectively.

Centrifuging under 100 percent oil phase can establish a relatively uniform residual oil saturation before the development of the secondary drainage capillary pressure curves. This can be repeated, as well as the imbibition step above, to obtain a set of hysteresis capillary pressure curves. Secondary drainage curves for these plugs will be developed in future papers on this methodology.

The time needed to complete each step of the above test depended on how rapidly the fluids reached their equilibrium saturation in the centrifuge. This was largely determined by the permeability of the rock. This was especially true for low permeability chalk which had to be centrifuged up to 12 days to obtain and verify a stabilized saturation profile compared to up to 2 days for the berea sandstone. The total experimental time to generate equilibrium primary drainage and primary imbibition capillary pressure curves in this study took approximately 1 week for the berea sandstone plug and approximately 1 month for the low permeability chalk plug.

Conclusions

1. Direct measurement of the saturation distribution in centrifuged rock plugs by magnetic resonance imaging or other means eliminates the need for assumed or indirect determination of fluid saturations.
2. Placement of the free water level along the length of rock plugs allows for the simultaneous development of both the positive and negative capillary pressures for drainage and imbibition.
3. Freezing of the oil phase during centrifuging allows for handling and determination of the water saturation in rock plugs without fluid redistribution.
4. The combination of centrifuging for pressure and direct measurement of the resulting saturation distribution can provide a rapid, accurate and robust laboratory method for determining

capillary pressure curves in porous media.

References Cited

1. Baldwin, B. A. and Yananashi, W. S., Sept.-Oct.1991. Capillary-pressure determinations from NMR images of centrifuged core plugs: berea sandstone: The Log Analyst p. 550-556.
2. Baldwin, B. A. and Spinler, E. A. , 1996, A direct method for simultaneously determining positive and negative capillary pressure curves in reservoir rock: 4th International Symposium on Evaluation of Reservoir Wettability and Its Effect on Oil Recovery proceedings.

Figure Captions

Figure 1: Schematic of plug with free water level and large cell volume in centrifuge.

Figure 2: Primary drainage capillary pressure curve for berea plug bc.

Figure 3: Primary drainage capillary pressure curve for chalk plug 10052b.

Figure 4: Imbibition capillary pressure curve for berea plug bc.

Figure 5: Imbibition capillary pressure curve for chalk plug 10052b

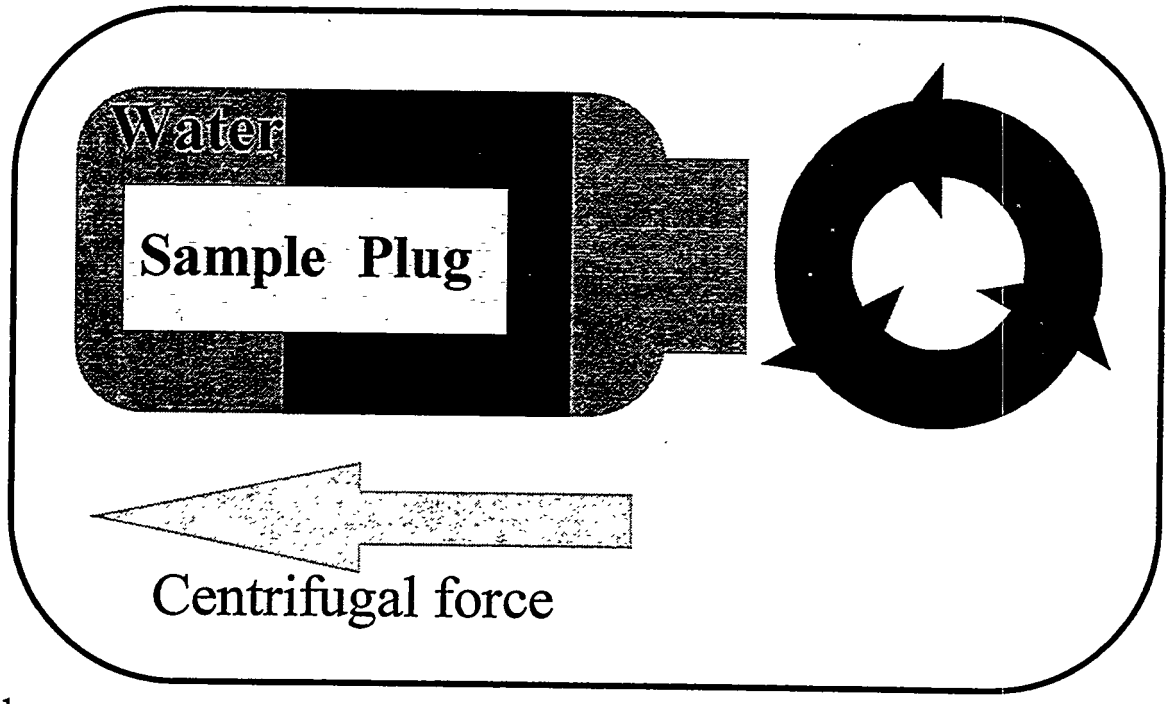

Figure 1.

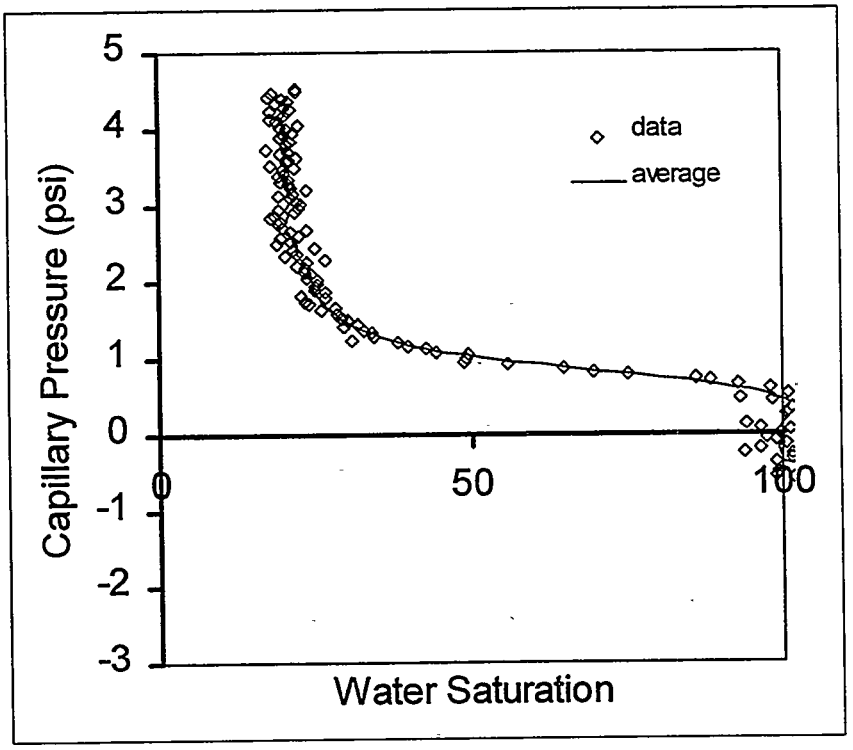

Figure 2.

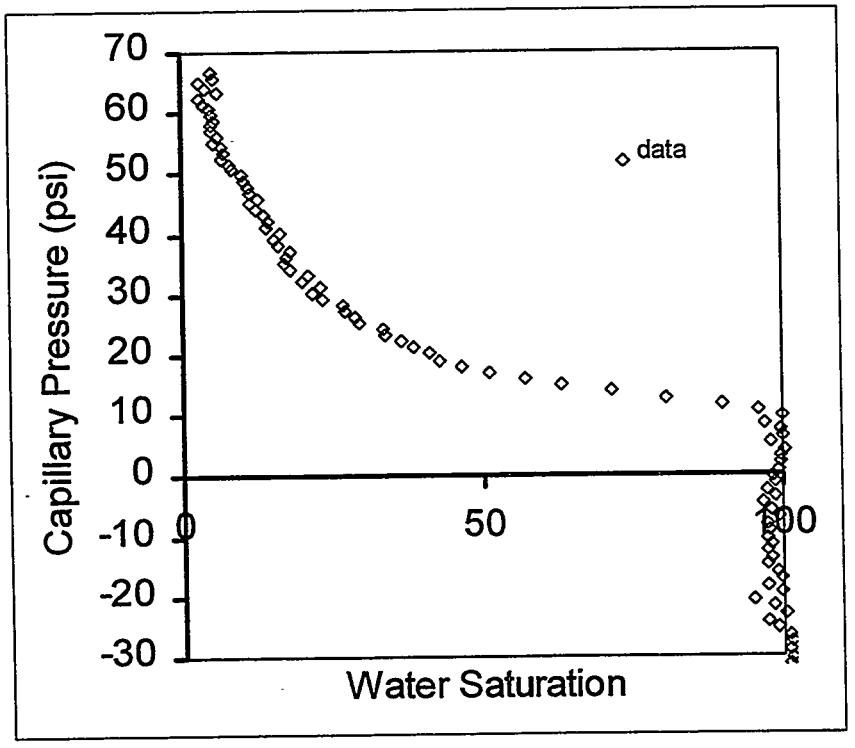

Figure 3.

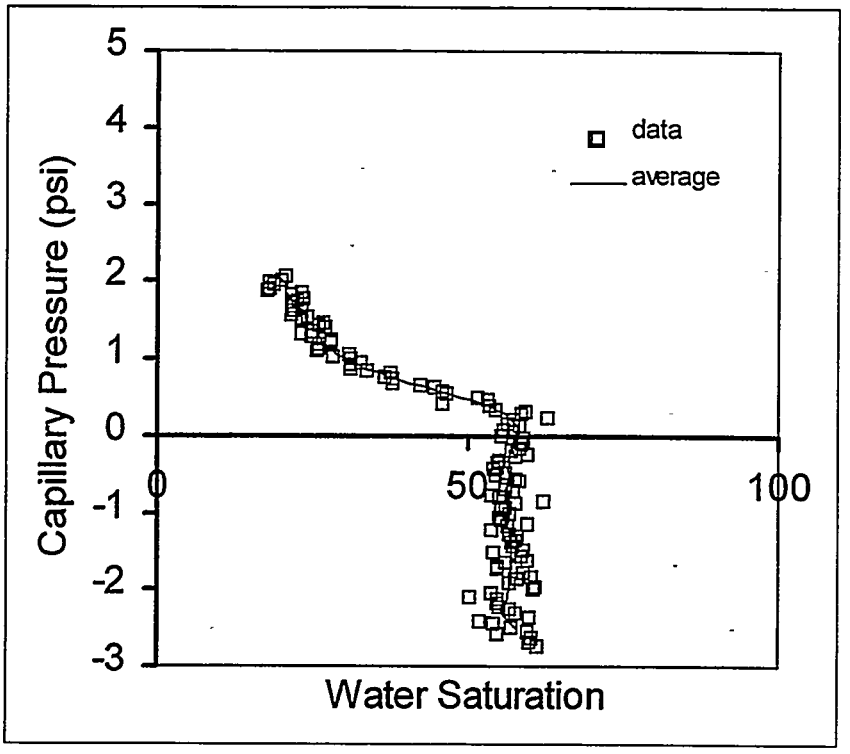

Figure 4.

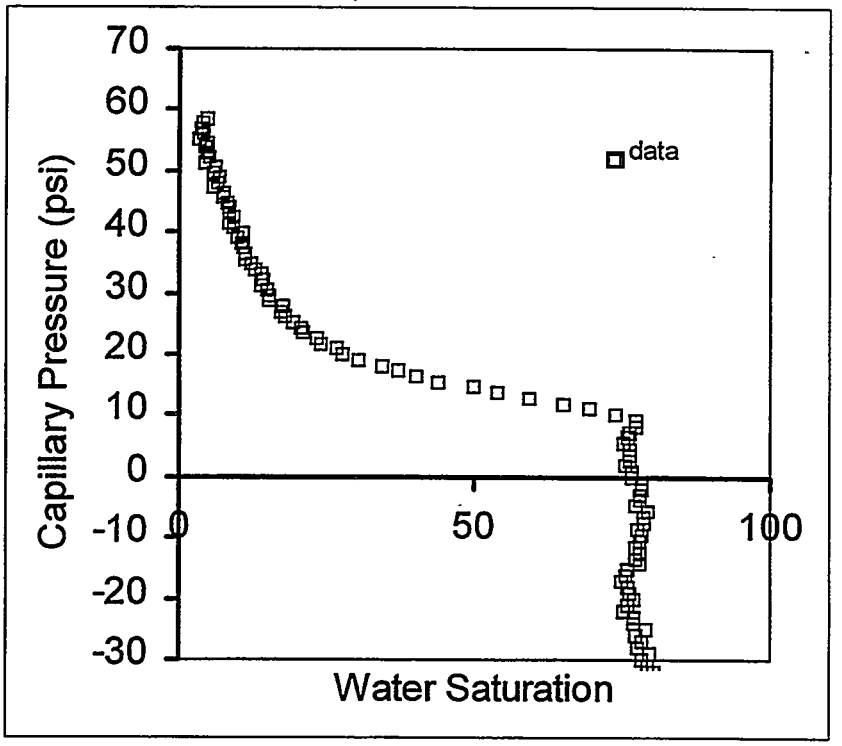

Figure 5.

Table 1 - Petrophysical Properties

Plug #	Type	Length (cm)	Diameter (cm)	Porosity (fraction)	Permeability (md)
bc	berea	4.68	2.54	0.21	~ 600
1052b	chalk	3.94	2.54	0.33	~ 5

RESERVOIR CHARACTERIZATION BASED ON TRACER RESPONSE AND RANK ANALYSIS OF PRODUCTION AND INJECTION RATES

Belkis T. Refunjol
Lagoven, S.A., PDVSA, Venezuela

Larry W. Lake
Center for Petroleum and Geosystems Engineering
The University of Texas at Austin
Austin, TX 78712

ABSTRACT

Quantification of the spatial distribution of properties is important for many reservoir-engineering applications. But, before applying any reservoir-characterization technique, the type of problem to be tackled and the information available should be analyzed. This is important because difficulties arise in reservoirs where production records are the only information for analysis.

This paper presents the results of a practical technique to determine preferential flow trends in a reservoir. The technique is a combination of reservoir geology, tracer data, and Spearman rank correlation coefficient analysis. The Spearman analysis, in particular, will prove to be important because it appears to be insightful and uses injection/production data that are prevalent in circumstances where other data are nonexistent. The technique is applied to the North Buck Draw field, Campbell County, Wyoming.

This work provides guidelines to assess information about reservoir continuity in interwell regions from widely available measurements of production and injection rates at existing wells. The information gained from the application of this technique can contribute to both the daily reservoir management and the future design, control, and interpretation of subsequent projects in the reservoir, without the need for additional data.

INTRODUCTION

Appropriate representation of reservoir heterogeneity is important to successful modeling of past and future production performance. Because of this, description and quantification of reservoir heterogeneity have achieved significant progress in recent years. Among the new developments are depositional and stochastic models of reservoir heterogeneities.

Generating good stochastic or geological models requires a lot of data. Thus, these technologies are difficult, if not impossible, in reservoirs where production records are the only data to be analyzed. Moreover, many models do not acknowledge the fluid processes taking place in the reservoir. The technique proposed here relies entirely on fluid data and uses only production records. We also use tracer data and results of a geologic study to validate the model.

The following sections contain the results from the tracer-response analysis and from the nonparametric statistical analysis of the production and injection rate ranks. The analysis is extended to investigate the effect of lag time on well-to-well correlations. The use of lag time analysis is, as far as we can tell, new to the application of Spearman rank analysis to production data. We conclude with a reservoir description based on rank correlation coefficient and gas tracer analysis.

RESERVOIR OVERVIEW

The study area is the North Buck Draw field, located in Campbell County, Wyoming, approximately 60 miles northeast of Casper (Fig. 1). The field produces from the Lower Cretaceous Fall River Formation in the west-central portion of the Powder River Basin. The limits of the Buck Draw field and the delineation of the Fall River channel are shown on a structural map in Fig. 2.

General Geology - Several studies have been made of the Buck Draw field stratigraphy and depositional patterns (Hawkins and Formhals, 1985; Rasmussen *et al.*, 1985; Sellars and Hawkins, 1992). A recent interpretation (Gardner *et al.*, 1994) based on outcrop studies

revealed a complex valley-fill architecture and reservoir compartmentalization. The valley-fill system is interpreted to be composed of multilateral and vertical channel facies that change in character with geographic and stratigraphic position within a valley.

The main hydrocarbon-trapping mechanism at Buck Draw is the meandering of the channel. The reservoir is more shaley in the northwest portion of the field, with thin, low-permeability sands. This change in lithology is interpreted to form a barrier to hydrocarbon migration in the northwesterly direction. Other barriers are the shaley facies of the Fall River that form the bottom seal and the overlying shale of the lower Skull Creek (Sellars and Hawkins, 1992).

Reservoir Development - North Buck Draw field porosity and permeability are areally and vertically heterogeneous. Both properties appear to be greater along the middle-stream axis of the channel, with expected preferred fluid-flow direction along this axis. Generally, reservoir sand quality declines in a direction normal to the channel axis.

The reservoir fluid is a near-volatile oil; fluid properties fall between those of black and volatile oils. The fluid meets the majority of volatile-oil criteria, including large oil formation volume factors and solution gas-oil ratios (Hawkins, 1987). The bubblepoint pressure is 4,680 psia, and the reservoir fluid is a single-phase, low-viscosity (0.12 cp) fluid above this pressure. There is no free water in the reservoir.

North Buck Draw commercial production began in June 1983. In 1988 a pressure maintenance project was initiated by injecting gas. Radioactive tracers were injected into the reservoir and their occurrence was monitored at the producing wells from February 1989 until March 1993. These tracer data are used in this work as helpful information for the reservoir description.

TRACER BEHAVIOR AND RESERVOIR DESCRIPTION

A total of seven injectors were tagged with one of six gas tracers in a three-stage program. The gas tracers used to distinguish breakthrough from the different injectors at each producer

were tritium (HT), krypton-85 (Kr-85), tritiated methane (CH3T), tritiated ethane (C2H5T), tritiated propane (C3H7T), and sulfur hexafluoride (SF6). The tracer program was carried out over a four-year period, long enough to use the tracer response data to define fluid movement for investigation of reservoir heterogeneity.

During the tracer project, samples to determine tracer concentration were taken from all of the producers in the field. Figure 3 shows the areal distribution of the tracer response in each producer, by displacing the inferred breakthrough times. Injector-producer communication is good for wells on the west side of the channel (injectors 11-18, 12-7, and 14-18). There was apparently no communication in wells to the east, injectors 22-17, 22-20, 23-31, and 23-8.

The arrival at the producers of the tagged gas injected in the west, some at early breakthrough times and some at late breakthrough times, indicated no sealing geological barriers are present. Conversely, the lack of response to tracers injected in wells on the east side of the reservoir indicates no communication or, at least, less communication between these wells and the rest of the reservoir.

The fluid characteristics are ideal for the use of tracer-response curves for calculating gas distribution and swept volumes based on the procedures commonly used in water tracing. The assumptions made were that partitioning into oil would be minimal at reservoir conditions and that, since the majority of tracers used in this project were light components, they would partition exclusively into the gas phase in the field test separators where samples were gathered for analysis.

Calculations were performed for each pair of wells with measured tracer response. The tracer recovery values obtained were extremely small, only 6 to 9% recovery after four years of injection.

Tracer	Injected into Well	Recovery, %
CH3T	11-18	9.0
C2H5T	12-7	8.6
C2H5T	14-18	6.2
Kr-85	23-8	9.2

However, there is a good chance that at least 50% of the wells showing tracer prodcution were sampled after breakthrough had occurred. A large volume of tracer could have been produced before measurement started. The qualitative results of the tracing program were helpful in identifying directional flow trends when analyzed together with the Spearman rank correlation results as follows.

We made no further attempt to identify the causes for the low tracer recovery obtained.

NONPARAMETRIC STATISTICS IN RESERVOIR DESCRIPTION

Parametric statistics involve the calculation of a statistic from a sample and the comparison of this statistic with a population parameter. If the statistic corresponds to a highly unlikely value of the parameter, the sample is assumed not to have come from the population described by the parameter (Volk, 1969). Parametric statistical tests often use the mean and variance of a distribution, which require operations on the original numerical values. Tests not employing these directly are called nonparametric methods; they generally depend on ranking, that is a set of observations arranged in order of size, rather than using their actual numerical values.

Nonparametric statistics do not require conditions on the parameters of the population from which the samples are drawn. They do not involve any assumptions about the distribution of the population; they are parameter-free. Certain assumptions are associated with most nonparametric statistical tests, such as that the observations are independent and that the variable under study has underlying continuity. These assumptions are fewer and less restrictive than those associated with parametric tests (Siegel, 1956). The price for using nonparametric statistics is a loss of strength in statistical tests; nevertheless, some nonparametric tests are highly efficient. For measuring the degree of correlation, correlation coefficients such as the Spearman or the Kendall coefficients are appropriate for ordinal scales.

The Spearman rank correlation coefficient (r_s) is a function of the sum of the squares of the difference of the two rankings for each observation and the number of observations.

$$r_s = 1 - \frac{6}{n(n^2-1)} \sum_{i=1}^{n} d_i^2$$

where r_s = Spearman rank correlation coefficient

d_i = difference between the rankings of the i th observations

n = number of observations

Since r_s is a correlation coefficient, it has the property that $-1 \le r_s \le 1$. If there is perfect positive correlation, all the differences will be zero and r_s = 1. If there is perfect negative correlation, in which the low-ranking observation in one classification corresponds to the high-ranking observation in the other, the term $6\sum d^2$ will be equal to $2n(n^2-1)$, and the correlation coefficient will be equal to -1 (Volk, 1969). If the two ranking sets are independent, r_s will be zero.

If all the assumptions of the parametric statistical model are met in the data, the nonparametric statistical tests are wasteful of data. The degree of wastefulness is expressed by the power-efficiency of the nonparametric test (Siegel, 1956). The efficiency of the Spearman rank correlation when compared with the parametric correlation, the Pearson r, is about 91 percent (Hotelling and Pabst, 1936).

Method Used - Rank correlations are more suitable when data are not normally distributed. Production and injection rates are not likely to be normally distributed, so the significance of parametric statistics cannot be tested. All rates from production and injection histories in the North Buck Draw field show fluctuations about some average value, and it is the relationship between these fluctuations that should reflect reservoir heterogeneities and preferential flow trends. None of the rates at Buck Draw were normally distributed.

The Spearman rank correlation coefficient is a quick, simple, and powerful test of the existence of the association between variables, regardless of the population distribution from which the samples are drawn, that provides a tool for investigating the correlation between production and injection rates in the reservoir. The data used for the analysis were the monthly production and injection rates from wells in the North Buck Draw field. The Spearman rank

correlation coefficient was calculated between flow rates of injector/producer pairs of wells to establish dominant communication trends in the reservoir.

The calculations were based on the total (oil and gas) monthly fluid production and injection rates. The rates were converted to ranks, and the Spearman rank correlation coefficient was calculated for pairs composed of each injection well and all its adjacent production wells. The upper plot in Fig. 4 shows the well rate ranks for two typical wells, injector 11-10 and producer 33-7, in the Buck Draw field as a function of time.

In the Heffer *et al.* (1995) application, all of the correlations were sought at zero time lag, a reasonable assumption since that work was investigating pressure fluctuations carried primarily through the rock. Since we are dealing with fluctuations in fluid rates, the assumption of instantaneous response is inappropriate here, since fluids are more compressible. Consequently, we investigated the effect of nonzero time lags between injector-producer pairs.

We considered the effect of a possible lag time between the response of a producer and an injector in the application of the technique. The argument for doing this is that any response at a producer would occur at some time after the stimulus in the injector. The procedure employed for each pair of wells was first to convert production and injection rates to ranks and then to calculate the rank correlation coefficient at zero lag time. From this, a series of correlation coefficients were calculated by shifting the time for the producers starting at one month up to a shifted time no greater than half the total number of months in the period analyzed. The two lower plots in Fig. 4 show how the well rank histories change with lag time. In the case shown, the maximum rs occurs at a time lag of 13 months. Note how shifting the lag time causes data to be discarded for both the injector and producer.

A extreme coefficient value occurs at the lag time of maximum correlation between producer and injector. This extreme correlation coefficient (r_{smax}) was tested to determine whether it indicated a significant correlation between the production and injection rates for that specific pair of wells. Since the values of r_{smax} could be positive or negative, that is, there is no predicted direction of the coefficient, the test becomes a two-tailed test. The significant limit was established at 0.02, so that for an extreme value to be taken as significant, it had to be

outside the significant limits imposed by the 2%-level statistical tables. From this, a value of maximum rank correlation coefficient (extremal value) at a lag time of maximum correlation was obtained for each possible injection-production pair.

The observed correlation coefficient at each lag time was plotted for every possible adjoining pair of wells in the field. Plots in Fig. 5 present the correlation of the rates from injectors to the rates of surrounding producer wells. The results exhibit some negative r_{smax} values, which were interpreted as negative correlations. These negative correlations, which physically represent a decrease in injection rate with a subsequent increase in the production rate of the nearby well, could be explained by the influence of a third well. More analysis should be done to understand these negative correlations. See Refunjol (1996) for a possible way to account for them.

At first we paired every injector with every producer in the reservoir (96 pairs). This method gave a few well pairs that showed significant r_{smax} at multiple pattern spacing. Like the negative correlations mentioned above, this must be because of multiple well effects; consequently, we limited subsequent study to adjacent well pairs (40 pairs). Heffer *et al.* (1995) also mention such large correlation at a distance.

Preferential Flow Direction Based on r_{smax}. One of the main objectives of this work was to infer preferential flow directions by the information provided from the rank correlation coefficient technique. To do this, the r_{smax} value was analyzed against information about the producer-injector distance in each pair, grouping the pairs based on the spatial orientation of the wells. This is, graphs were constructed for pairs of wells in four different groups: wells oriented N to N30E, N15E to N45E, N30E to N60E, and N45E to N75E. We constructed a histogram based on the orientation of the well pairs with maximum correlation (r_{smax}). Using 30-degree-angle classes, Fig. 6 shows a higher frequency of correlation in pairs with an orientation between N31E and N60E. This is in accordance with the southwest-northeast permeability trend observed from the geologic studies.

Along a given direction, the value of r_{smax} decreases with increasing distance in all the data analyzed, especially in the N30E to N60E direction group (Fig. 7). This figure is actually an autocorrelogram that could be interpreted with conventional models such as the exponential or spherical (Jensen *et al.*, 1996); we show a least-square straight-line fit in Fig. 7. Whatever the model being used, there is clearly very long-range autocorrelation in the N30E to N60E direction, well in excess of 10,000 ft.

Another way to illustrate directional trends is to map r_{smax}. We did this by linearly interpolating along a line from an injector to a producer between the calculated value of r_{smax} and $r_{smax}= 1$. This assumes that perfect correlation, $r_{smax}= 1$, occurs when the injector and producer are coincident. After this interpolation, we contoured the interpolated values around each injector. Figures 8 to 11 display these maps for injectors 11-18, 12-7, 13-18, and 14-18. All four maps exhibit a clear pattern of southwest-northeast preferential flow trend as expected. These wells are located on the west flank of the channel. The four injectors to the east of the channel showed no preferential flow trends (22-20) or even no correlation at all (22-17, 23-8, and 23-31).

Injector 22-20 presented significant rank correlation coefficients when related to the four surrounding wells, but with no clear preferential direction of correlation. In the analysis of each of these four pairs of wells, we observed that the producers were closer to and more influenced by other injectors than to well 22-20, suggesting no reliable information.

SUMMARY OF RESERVOIR DESCRIPTION AND CONCLUSIONS

With this research project, a practical and theoretically based technique was developed to determine preferential flow trends in a reservoir by integrating tracer response, Spearman rank correlation coefficient results, and reservoir geology. Most importantly, the work's basic information is tracer data and the widely available measurements of production and injection rates. This makes the technique suitable for implementation in all types of reservoirs, including ones with scarce information.

The Spearman rank correlation coefficient method appears to be successful, as measured by consistency with tracer breakthrough and geologic inference. The integrated reservoir description is summarized as follows:

- A southwest-northeast preferential flow trend is indicated.
- The middle-stream axis of the channel contains high-quality reservoir sand, with preferential flow direction along this axis.
- Communication is good between injectors on the west flank of the channel with the rest of the reservoir, especially in the southwest-northeast direction. Injectors located to the east flank of the channel are not effectively connected to the rest of the reservoir.

The information gained from the application of this technique can contribute to the daily reservoir management and the future design, control, and interpretation of subsequent projects in the reservoir. No additional data besides the available measurements of production and injection rates are required.

Although we have had some success in the description, significant questions must be answered before we can claim that the Spearman technique, by itself, is a useful characterization technique. These include the role of fluid compressibilities in the correlations, accounting for multiple-well correlation, and explanations for correlations at a distance. However, the Spearman technique uses data that are available in virtually all mature fields, and data that can be acquired with little additional expense. These advantages, plus the encouragement from this work, give ample justification for more research.

ACKNOWLEDGMENTS

The authors acknowledge the data provided by Kerr-McGee, through the Deltas Industrial Affiliate Project at the Bureau of Economic Geology, and the permission to publish this paper. Thanks go to Christopher White for his valuable suggestions and to Drs. Mike King and Kes Heffer for their discussions on applications of the Spearman rank correlation technique. Thanks are also due to Lagoven, S.A. for permission for preparation and publication of this

paper. Larry W. Lake holds the W.A. (Tex) Moncrief Centennial Chair at The University of Texas.

REFERENCES

Gardner, M.H., W. Dharmasamadhi, B.J. Willis, S.P. Dutton, Q. Fang, S. Kattah, J. Yeh, and F. Wang, October 1994, "Reservoir characterization of Buck Draw field," Bureau of Economic Geology Deltas Industrial Associates field trip manual.

Hawkins, C.M., and S. Formhals, 1985, "Geology and engineering aspects of Buck Draw field, Campbell and Converse counties, Wyoming," Wyoming Geological Association 36th Annual Field Conference guidebook, p. 33-45.

Heffer, K.J., R.J. Fox, and C.A. McGill, October 1995, "Novel techniques show links between reservoir flow directionality, earth stress, fault structure and geomechanical changes in mature waterfloods," paper SPE 30711 presented at the Annual Technical Conference and Exhibition of the Society of Petroleum Engineers held in Dallas, TX.

Hotelling, H. and M.R. Pabst, 1936, "Rank correlation and test of significance involving no assumptions of normality," Annual Math. Statist., p. 29-43.

Jensen, J.L., L.W. Lake, P.W.M. Corbett, and D.J. Goggin, 1996, *Statistics for Petroleum Engineers and Geoscientists*, Prentice Hall PTR, Upper Saddle River, New Jersey 07458.

Lake, L.W., 1989, *Enhanced Oil Recovery*, Prentice Hall, Englewood Cliffs, New Jersey.

Mirzadjanzade, A.Kh., I.M. Ametov, A.A. Bokserman, and V.P. Filippov, October 1993, "New perspective trends of research in oil and gas recovery," paper presented at the 7th European IOR Symposium held in Moscow, Russia.

Rasmussen, D.L., C.L. Jump, and K.A. Wallace, 1985, "Deltaic system in the early cretaceous Fall River formation, Southern Powder River basin, Wyoming," Wyoming Geological Association 36th Annual Field Conference guidebook , p. 91-111.

Refunjol, B.T., 1996, "Reservoir characterization of North Buck Draw field based on tracer response and production/injection analysis," M.S. Thesis, The University of Texas at Austin.

Sellars, R., and C.M. Hawkins, 1992, "Geology and stratigraphic aspects of Buck Draw field, Powder River basin, Wyoming," Wyoming Geological Association 43rd Annual Field Conference guidebook, p. 97-110.

Siegel, S., 1956, *Nonparametric Statistics for the Behavioral Sciences*, McGraw-Hill Book Company, New York.

Volk, W., 1969, *Applied Statistics for Engineers*, McGraw-Hill Book Company, New York.

Zemel, B., 1995, *Tracers in the Oil Field*, Elsevier Science B. V., Amsterdam.

LIST OF FIGURES

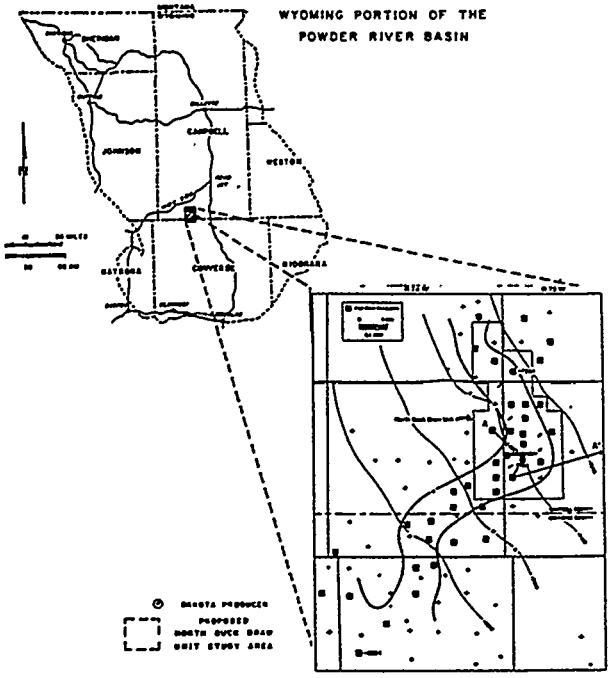

Figure 1. Location map.

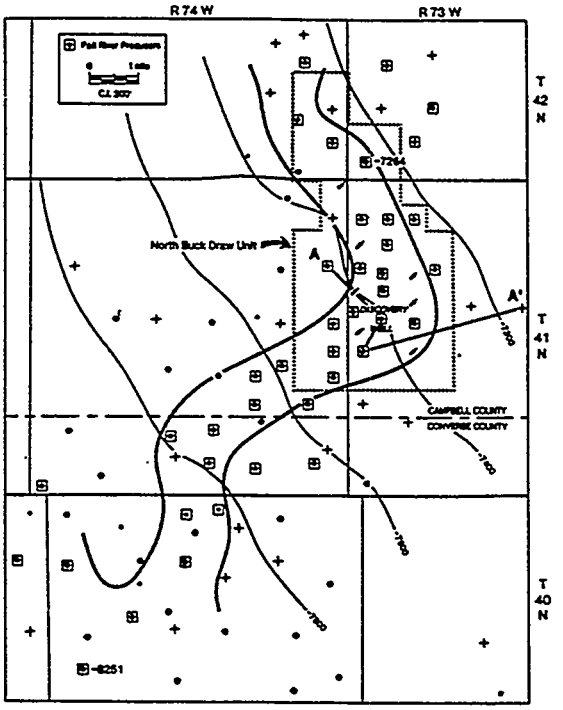

Figure 2. Limits of North Buck Draw field.

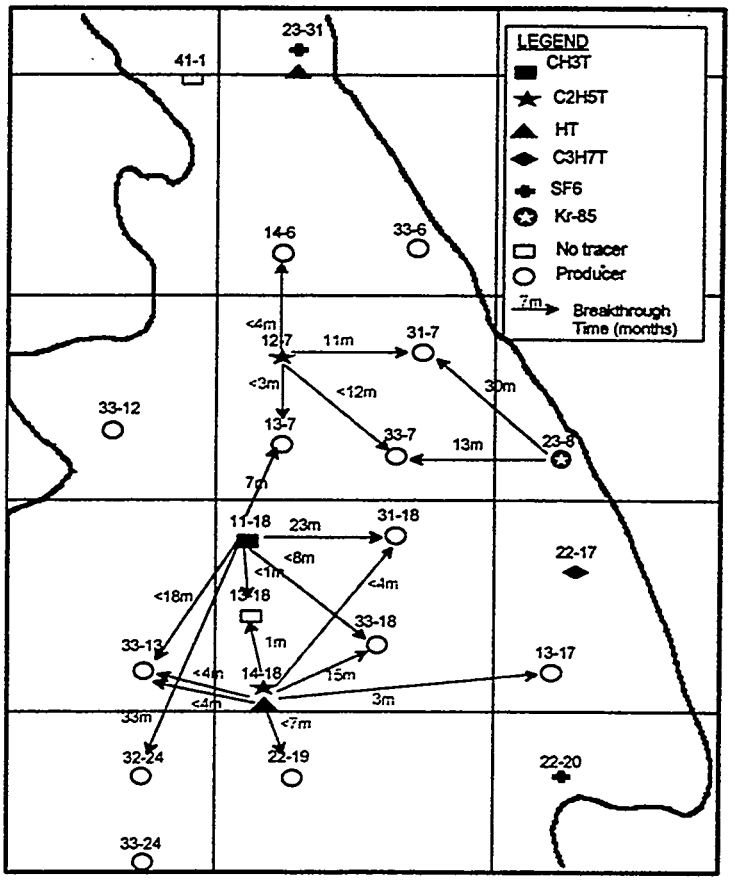

Figure 3. Tracer response pattern map.

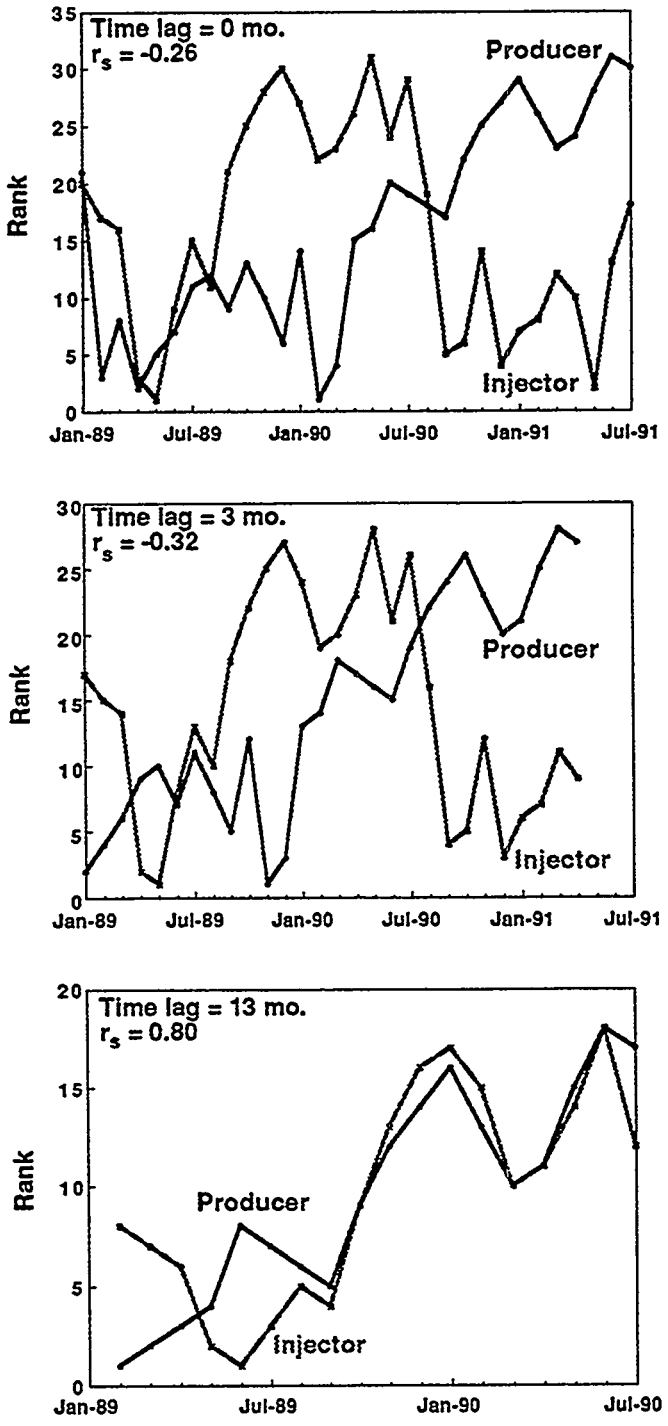

Figure 4. Spearman ranks between producer 33-7 and injector 11-16 vs. time for three time lags.

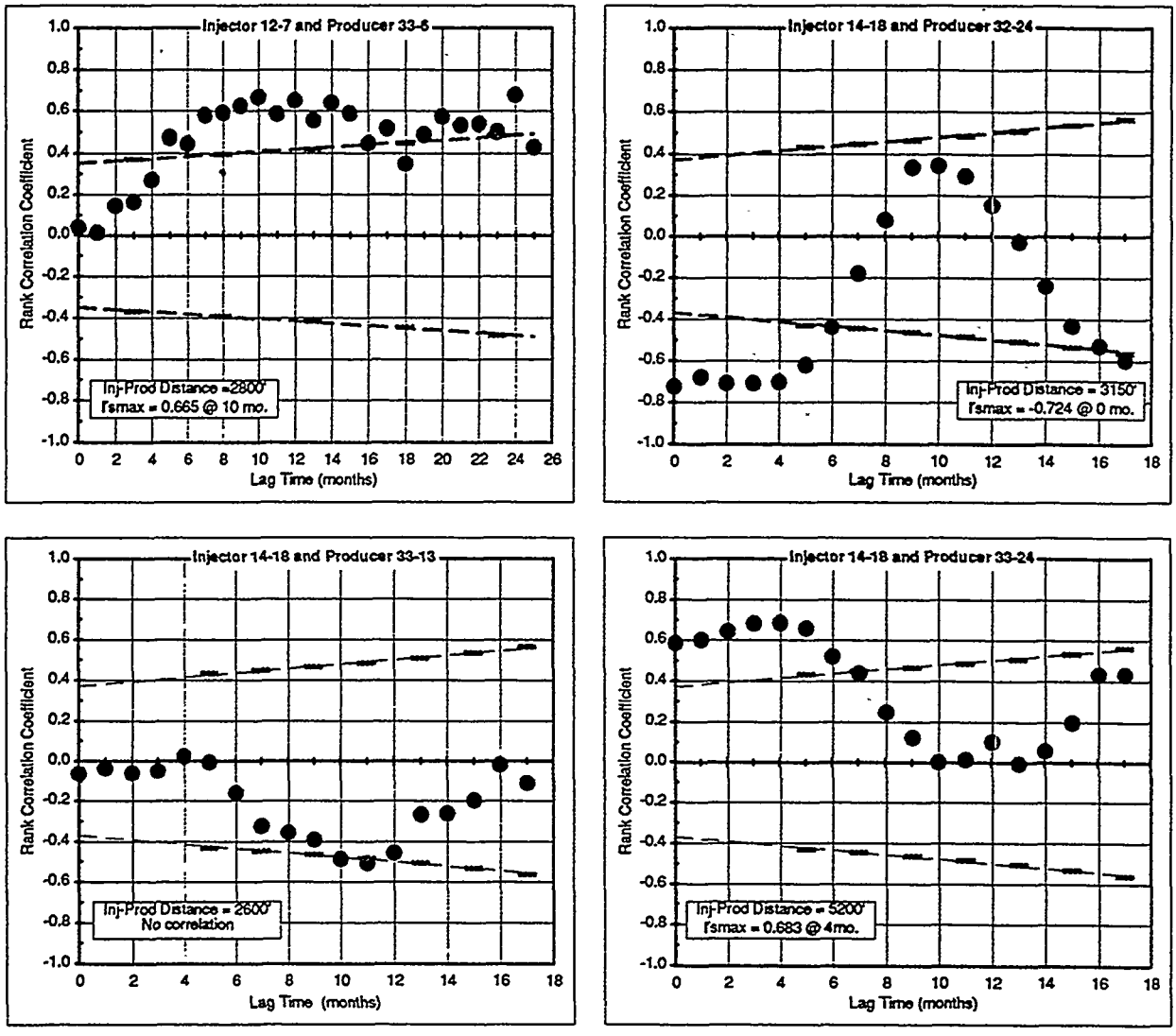

Figure 5. Rank correlation coefficient vs. lag time.

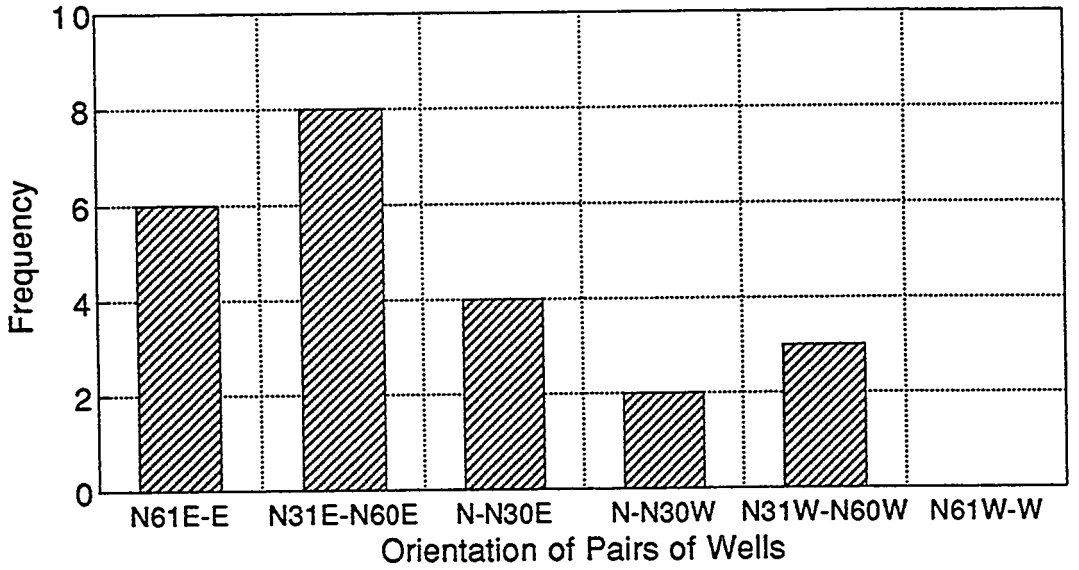

Figure 6. Histogram for preferential direction from maximum rank correlation in all wells.

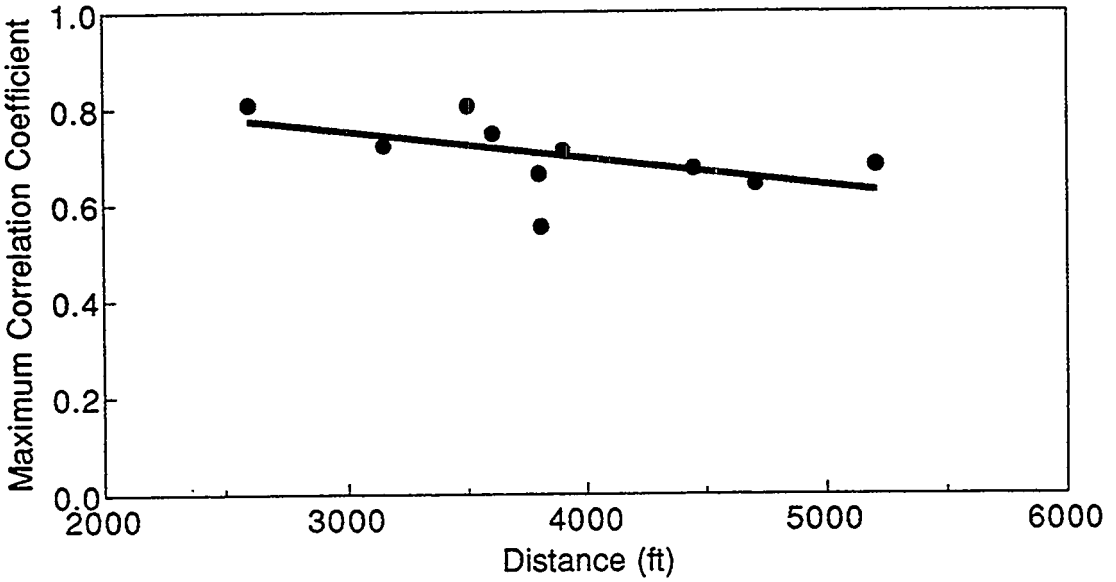

Figure 7. Rank correlation coefficient vs. distance for pairs on the N30E to N60E orientation.

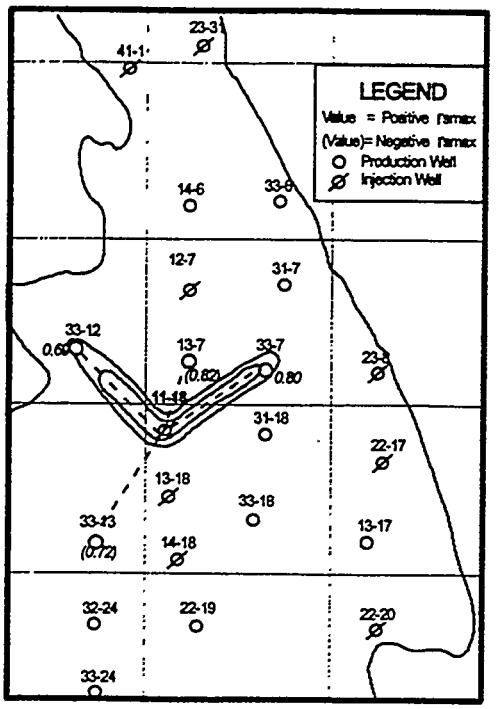

Figure 8. Iso- r_{smax} map for injector 11-18.

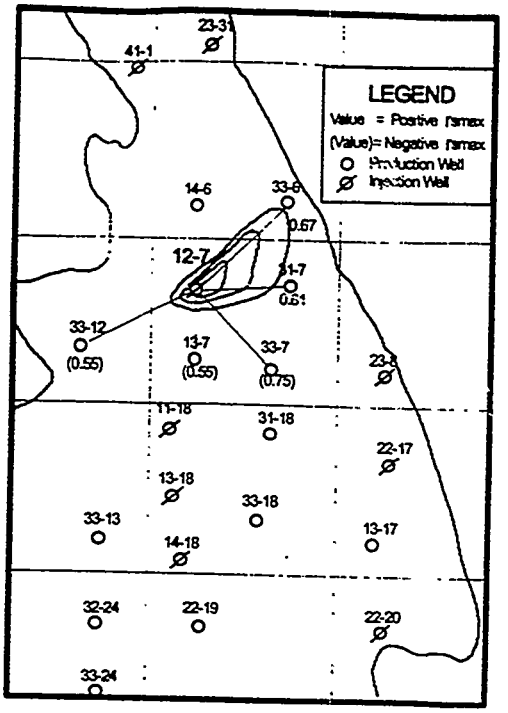

Figure 9. Iso- r_{smax} map for injector 12-7.

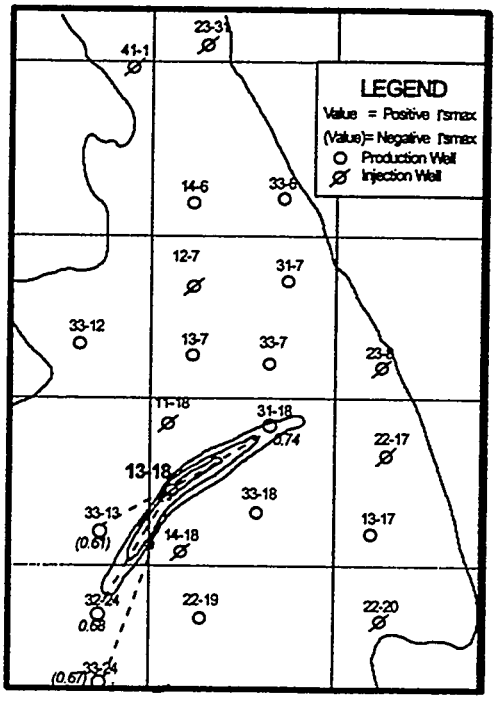

Figure 10. Iso- r_{smax} map for injector 13-18.

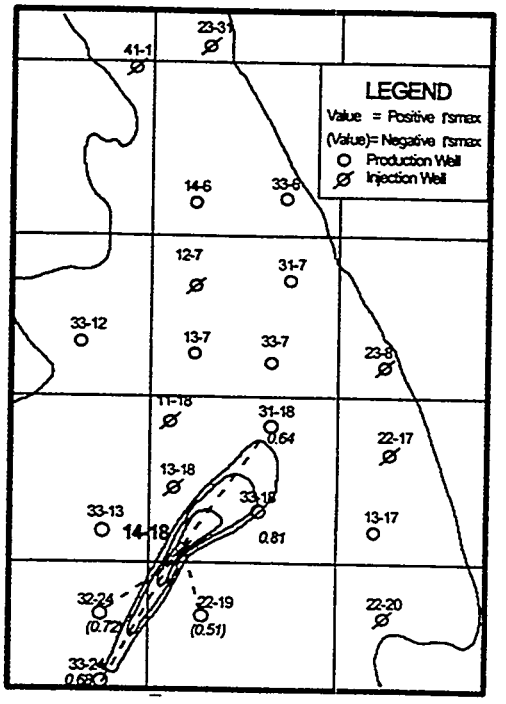

Figure 11. Iso- r_{smax} map for injector 14-18.

Non-parametric Transformations for Data Correlation and Integration: From Theory to Practice

Akhil Datta-Gupta, Guoping Xue, and Sang Heon Lee

Department of Petroleum Engineering

Texas A&M University

College Station, Texas

ABSTRACT

The purpose of this paper is two-fold. First, we introduce the use of non-parametric transformations for correlating petrophysical data during reservoir characterization. Such transformations are completely data driven and do not require *a priori* functional relationship between response and predictor variables which is the case with traditional multiple regression. The transformations are very general, computationally efficient and can easily handle mixed data types for example, continuous variables such as porosity, permeability and categorical variables such as rock type, lithofacies. The power of the non-parametric transformation techniques for data correlation has been illustrated through synthetic and field examples. Second, we utilize these transformations to propose a two-stage approach for data integration during heterogeneity characterization. The principal advantages of our approach over traditional cokriging or cosimulation methods are: (1) it does not require a linear relationship between primary and secondary data, (2) it exploits the secondary information to its fullest potential by maximizing the correlation between the primary and secondary data, (3) it can be easily applied to cases where several types of secondary or soft data are involved, and (4) it significantly reduces variance function calculations and thus, greatly facilitates non-Gaussian cosimulation. We demonstrate the data integration procedure using synthetic and field examples. The field example involves estimation of pore-footage distribution using well data and multiple seismic attributes.

INTRODUCTION

During initial stages of data correlation, often we are interested in pursuing exploratory analysis. Rather than imposing our preconceived notions or models, we want to gain insight into the nature of the data set and if possible, the underlying phenomenon that might have produced the data set. Unfortunately traditional multiple regression techniques for data correlation are limited in this respect since they require *a priori* assumptions of functional forms relating the response (dependent) and predictor (independent) variables. This is a significant drawback for correlating rock or petrophysical properties because of the inexact nature of the underlying relationship. When used as a predictive tool for pertrophysical data, conventional multiple regression suffers from several other limitations as discussed by Jensen and Lake, 1985, Wendt et al., 1986, and Xue et al., 1996(a).

Parametric transformations have been suggested for optimization of regression-based permeability-porosity predictions. Notable amongst these are the power transformations proposed by Jensen and Lake (1985). The underlying theory is that if the joint probability distribution function of two variables is binormal, their relationship will be linear (Hald, 1952). Several methods exist to estimate the exponents for power transformation. One method, described by Emerson and Stoto (1982 and adopted by Jensen and Lake (1985), is based on symmetrizing the probability distribution

function (p.d.f.). Another method is a trial-and-error approach based on a normal probability plot of the data. By power transforming permeability and porosity separately, the authors are able to improve permeability-porosity correlation. However, using a trial-and-error method for selecting exponents for power transformation is time consuming, and symmetrizing the p.d.f. does not necessarily guarantee a binormal distribution of transformed variables. Most importantly, there are no indications as to whether power transformations will work for multivariate cases. This is a severe limitation since we are often interested in correlating permeability with multiple well log responses.

We propose here a more adaptive approach offered by non-parametric transformation and regression methods for correlating petrophysical data (Hastie and Tibshirani, 1990; Xue et al, 1996(a)). Our approach is quite general and can be applied to other types of data such as Pressure-Volume-Temperature (PVT) data. The non-parametric transformation techniques generate regression relations in a flexible data-defined manner through the use of *conditional expectations* or *scatterplot smoothers* and in doing so, let the data itself suggest functional forms or detect inherent non-linearities. Optimal non-parametric transformations can be shown to produce maximum correlation in the transformed space (Breiman and Friedman, 1985). The power of these methods lie in their ability to directly incorporate multiple and mixed variables, both continuous and categorical, into correlation. Moreover, the transformations are computationally efficient, easy to use and can provide significant insight during exploratory data analysis.

Next, we utilize these non-parametric transformations to propose a two-stage approach to integrate seismic or other secondary data into reservoir characterization. First, we calibrate seismic and well data using optimal non-parametric transformations. Stochastic cosimulation is then carried out in the transformed space to generate conditional realizations of reservoir properties. The principal advantage of this approach over traditional cosimulation methods are: (1) it does not require a linear relationship between seismic and well data, (2) it exploits the secondary information to its fullest potential by maximizing the correlation between the primary and secondary data, and (3) it can be easily extended to cases where several types of soft data are involved. Moreover, the use of non-parametric transformations results in a significant reduction in variance function calculations and thus, greatly facilitates non-Gaussian cosimulation through the use of indicator approaches.

The organization of this paper is as follows. First, we briefly review the theory and motivation behind non-parametric transformations and regression. Next, we discuss application of such transformations for data correlation and integration. Finally, we present synthetic and field examples which demonstrate the power and utility of such transformations for correlating petrophysical properties using multiple regression. A field example involving integration of 3-D seismic data is also discussed to illustrate the data integration procedure.

NON-PARAMETRIC TRANSFORMATION AND REGRESSION: THEORY

In general, the regression problem involves a set of predictors, for example, a p-dimensional random vector X and a random variable Y which is called the response variable. The aim of regression analysis is to estimate the conditional expectation, $E(Y \mid X_1, X_2, \ldots, X_p)$. Conventional multiple regression requires a functional form to be presumed *a priori* for the regression surface, thus reducing the problem to that of estimating a set of parameters. Such parametric approach can be successful provided the model assumed is appropriate. When the relationship between the response and predictor variables is unknown or inexact, as is frequently the case for reservoir rock or petrophysical properties, parametric regression can yield erroneous and even misleading results. This is the primary motivation behind non-parametric regression techniques which make only few general assumptions about the regression surface (Friedman and Stuetzle, 1981).

The non-parametric transformations techniques generate regression relations in a flexible data-defined manner through the use of *scatterplot smoothers* and in doing so let the data suggest the functionalities. The most extensively studied non-parametric regression techniques (kernel, nearest neighbor or spline smoothing) are based on some sort of local averaging which take the form:

$$E(Y|x) = \sum_{i=1}^{N} H(x, x_i)\, y_i \qquad (1)$$

where $H(x, x')$ (the kernel function) usually has its maximum at $x' = x$ with its absolute value decreasing as $|x' - x|$ increases. A critical parameter in local averaging is the span $s(x)$ which is the interval, centered at x', over which most of the averaging takes place and thus, controls the bias-variance trade-off. Optimal span selection based on local cross-validation has been discussed by Friedman and Silverman (1989).

More recently, however, non-parametric regression techniques that are based on successive refinements have gained wide popularity in a variety of disciplines ranging from medical sciences to air pollution control (Hastie and Tibshirani, 1990). We will focus here on these non-parametric regression techniques that attempt to define the regression surface in an iterative fashion while remaining 'data-driven' as opposed to 'model-driven'. We can broadly classify them into those which do not transform the response variable (Generalized Additive Models) and those which do (Alternating Conditional Expectations and its variations). A brief discussion of these techniques follows. For further details, the reader is referred to Hastie and Tibshirani (1990), Buja *et al.* (1989) and Xue *et al.* (1996(a)).

Generalized Additive Models (GAM)

An additive regression model has the general form:

$$E(Y|X_1, X_2, \ldots, X_p) = \alpha + \sum_{l=1}^{p} \phi_l(X_l) + \varepsilon \qquad (2)$$

where X_l are the predictors and ϕ_l are functions of predictors. Thus additive models replace the problem of estimating a function of a p-dimensional variable X by one of estimating p separate one-dimensional functions, ϕ_l. Such models are attractive if they fit the data since they are far easier to interpret than a p-dimensional multivariate surface.

The technique for estimating ϕ_l's is called the *local scoring* algorithm and uses scatterplot smoothers for example, a running mean, running median, running least squares line, kernel estimates or a spline (see Buja *et al.*, 1989 for a discussion of smoothing techniques). In order to motivate the algorithm, let us consider the following simple model:

$$E(Y|X_1, X_2) = \phi_1(X_1) + \phi_2(X_2) \qquad (3)$$

Given an intial estimate $\phi_1(X_1)$, one way to estimate $\phi_2(X_2)$ is to smooth the residual $R_1 = Y - \phi_1(X_1)$ on X_2. With this estimate of $\phi_2(X_2)$, we can get an improved estimate $\phi_1(X_1)$ by smoothing $R_1 = Y - \phi_2(X_2)$ on X_1. The resulting iterative smoothing procedure is called *backfitting* (Hastie and Tibshirani, 1990) and forms the core of additive models.

In general, an algorithm for fitting a generalized additive model consists of a hierarchy of three modules: (i) *scatterplot smoothers* which a can be thought of as a general regression tool for fitting functional relationship between response and predictor variables, (ii) a *backfitting* algorithm that cycles through the individual terms in the additive model and iteratively updates each using the Gauss-Siedel method by smoothing suitably defined partial residuals, and (iii) a *local scoring* algorithm that utilizes an iteratively reweighted least squares procedure (Hastie and Tibshirani, 1990) to generate a new additive predictor. A step by step procedure for the Generalized Additive Model can be found in Hastie and Tibshirani (1990).

Response Transformation Models: ACE Algorithm and its Variations

The response transformation models generalize the additive model by allowing for a transformation of the response variable Y. The models have the following general form:

$$\theta(Y)=\alpha+\sum_{l=1}^{p}\phi_l(X_l)+\varepsilon \tag{4}$$

The main motivation behind response transformation is that often a simple additive model may not be appropriate for $E(Y \mid X_1, X_2,..., X_p)$, but may be quite appropriate for $E\{\theta(Y) \mid X_1, X_2,..., X_p\}$. An example of such model is the Alternating Conditional Expectation (ACE) algorithm and its modifications.

The ACE algorithm, originally proposed by Breiman and Friedman (1985), provides a method for estimating optimal transformations for multiple regression that result in a maximum correlation between a dependent (response) random variable and multiple independent (predictor) random variables. Such optimal transformations can be derived by minimizing the variance of a linear relationship between the transformed response variable and the sum of transformed predictor variables. For a given set of response variable Y and predictor variables $X_1,...,X_p$, the ACE algorithm starts out by defining arbitrary measurable mean-zero transformations $\theta(Y)$, $\phi_1(X_1),...,\phi_p(X_p)$. The error ($e^2$) not explained by a regression of the transformed dependent variable on the sum of transformed independent variables is (under the constraint, $E[\theta^2(Y)]=1$)

$$e^2(\theta,\phi_1,...,\phi_p)=E\{[\theta(Y)-\sum_{l=1}^{p}\phi_l(X_l)]\}^2 \tag{5}$$

The minimization of e^2 with respect to $\phi_1(X_1),...,\phi_p(X_p)$ and $\theta(Y)$ is carried out through a series of single-function minimizations, resulting in the following equations

$$\phi_l(X_l)=E[\theta(Y)-\sum_{j\neq l}\phi_j(X_j)\mid X_l]$$

$$\theta(Y)=E[\sum_{l=1}^{p}\phi_l(X_l)\mid Y]/\|E[\sum_{l=1}^{p}\phi_l(X_l)\mid Y]\| \tag{6}$$

Two basic mathematical operations involved in here are conditional expectations and iterative minimization and hence, the name *alternating conditional expectations*. The final $\phi_l(X_l)$, $l=1,...,p$ and $\theta(Y)$ after the minimization are estimates of optimal transformation $\phi^*_l(X_l)$, $l=1,...,p$ and $\theta^*(Y)$. In transformed space, the response and predictor variables will be related as follows

$$\theta^*(Y)=\sum_{l=1}^{p}\phi_l{}^*(X_l)+\xi \tag{7}$$

where ξ is the misfit.

The optimal transformations are derived solely based on the data sets and can be shown to result in a maximum correlation in the transformed space (Breiman and Friedman, 1985). The transformations

do not require *a priori* assumptions of any functional form for the response or predictor variables and thus, provide a powerful tool for exploratory data analysis and correlation.

Although ACE is a potent and versatile approach for building correlations, it suffers from some anomalies when one views it as a regression tool. Such anomalies become particularly prominent in low-correlation settings. A modification of ACE designed primarily for regression problems was proposed by Tibshirani (1988) and differs from ACE in that it chooses $\theta(Y)$ to achieve a special asymptotic variance stabilizing feature. The goal here is to estimate transformations θ and ϕ_l which have the following properties:

$$E\{\theta(Y)|X_1,X_2,...,X_p\}=\sum_{l=1}^{p}\phi_l(X_l)$$

$$\text{Var}\{\theta(Y)|\sum_{l=1}^{p}\phi_l(X_l)\}=\text{constant} \qquad (8)$$

The transformation θ is assumed to be strictly monotone (and thus, invertible) and the conditional expectations are approximated using the scatterplot smoothing algorithm *supersmoother* (Friedman and Stuetzle, 1982). In the examples that follow, we use this modification of the ACE algorithm. A step by step procedure for the ACE model and its modification can be found in Hastie and Tibshirani (1990).

NON-PARAMETRIC TRANSFORMATION: APPLICATION

In this section we discuss how the non-parametric transformation techniques discussed above can be applied for data correlation and integrating diverse data types. We will focus on the response transformation models since they are more general in nature and thus, encompass other non-parametric techniques.

Data Correlations and Estimation

Non-parametric transformations techniques offer a flexible and data-driven approach to building correlation without *a priori* assumptions regarding functional relationship between response and predictor variables. The following equation is used to estimate or predict dependent variable, y_i^{pre} for any given data point $\{x_{1i},...,x_{pi}\}$ involving p- independent variables

$$y_i^{pre}=\theta^{*-1}[\sum_{l=1}^{p}\phi_l^*(x_{li})] \qquad (9)$$

The calculation involves p forward transformations of $\{x_{1i},...,x_{pi}\}$ to $\{\phi_1^*(x_{1i}),...,\phi_p^*(x_{pi})\}$, and a backward transformation, Eq. 9. By restricting the transformation of the response variable to be monotone, we can ensure that θ^* is invertible.

The power of non-parametric transformations as a tool for correlation lies in their ability to handle variables of mixed type. For example, we can easily incorporate categorical variables such as rock types and lithofacies into the correlation and also, handle missing data values without additional complications (Breiman and Friedman, 1985).

Our experience has shown that for most of the applications considered by us (petrophysical and PVT data), the non-parametric transformations $\phi_l(X)$ and $\theta(Y)$ can be fitted by simple functions such as polynomials, power functions or cubic splines (Xue *et al.*, 1996(a) Crogh, 1996). This allows for a rapid and powerful alternative to traditional multiple regression for building correlation for a variety of applications particularly in the presence of several predictor variables.

Data Integration

One critical aspect of integrating different data types during reservoir characterization is the calibration between primary and secondary data, for example, correlating well and seismic data. Cokriging or cosimulation has traditionally been used for data integration in which such calibration is accomplished by modeling cross covariance functions. Given a primary variable (hard data) $y(u_\alpha)$, sampled at n locations, and secondary variables (soft data) $x_1(u_\beta),...,x_p(u_\beta)$, all assumed sampled at the same m locations, the full cokriging estimator of $y(u)$ is

$$y(u) = \sum_{\alpha=1}^{n} \lambda_\alpha y(u_\alpha) + \sum_{\beta=1}^{m} \mu_{1\beta} x_1(u_\beta) + ... + \sum_{\beta=1}^{m} \mu_{p\beta}\ x_p(u_\beta) \qquad (10)$$

where, λ_α's are the weights for the primary variable y, and $\mu_{l\beta}$'s are the weights associated with the secondary variables, x_l (l=1,...,p). However, in practice, several limitations restrict the application of full cokriging for data integration. First, the implementation of Eq.10 requires modeling of $(p+1)^2$ variance functions which include $(p+1)$ covariance functions and $p(p+1)$ cross covariance functions. Modeling of variance functions becomes extremely tedious when several secondary variables are involved, for example multiple seismic attributes. Second, cokriging matrix may become unstable (close to singular) because of the sparse primary and dense secondary data samples (Alameida, 1993). Third, because the cross covariance functions can only capture the linearity between the primary and secondary data samples, the influence of secondary data samples on the cokriging estimator can be reduced significantly in the presence of non-linearity. This is particularly critical for integration of seismic data since in general the link between reservoir and seismic properties can be expected to be non-unique, multivariate and non-linear (Xue and Datta-Gupta, 1996(b)).

We propose here a two-stage approach to integrating seismic or other secondary data into reservoir characterization. First, we use the non-parametric transformational approach to calibrate the seismic and well data to maximize correlation between the two data sets. This leads to a set of transformations $\theta^*, \phi_l^*, l=1, p$. Cokriging or stochastic cosimulation is then carried out in the transformed space to generate conditional realizations of reservoir properties. The cokriging equations now take the following form

$$\theta^*(y(u)) = \sum_{\alpha=1}^{n} \lambda_\alpha' \theta^*(y(u_\alpha)) + \sum_{\beta=1}^{m} \mu_\beta' \phi_s^*(x(u_\beta)) \qquad (11)$$

where ϕ_s^* is the sum of transformed secondary data samples (for example, seismic attributes) as follows

$$\phi_s^*(x(u_\beta)) = \phi_1^*(x_1(u_\beta)) + ... + \phi_p^*(x_p(u_\beta)) \qquad (12)$$

Notice that the new formulation for cokriging estimator with optimal transformations (Eq.11) now contains only two terms compared to $(p+1)$ terms in Eq.10. As a result, it reduces the number of variance functions required by cokriging from $(p+1)^2$ to 4 regardless of the number of secondary variables involved. A further simplification can be made by introducing collocated cokriging

algorithm with Markov hypothesis (Alameida, 1993) into Eq.11 resulting in the following collocated cokriging estimator

$$\theta^*(y(u)) = \sum_{\alpha=1}^{n} \lambda_\alpha' \theta^*(y(u_\alpha)) + \mu' \phi_s^*(x(u)) \qquad (13)$$

The underlying assumption in Eq.13, in addition to Markov screening hypothesis, is that the secondary data samples must be available at every location where primary variable is to be estimated. This is always satisfied for seismic data.

Stochastic cosimulation algorithm provides another important tool for data integration. Such cosimulation generates multiple realizations of random field conditioned to prior information, allowing assessment of model uncertainty. Indicator cosimulation has the capability of integrating soft and hard data without the assumption of a multiGaussian distribution. The limitations of multiGaussian assumptions are well established in the literature (Journel and Alabert, 1990). The use of Markov-Bayes (Zhu and Journel, 1992) algorithm in conjunction with optimal transformation can significantly simplify the modeling of indicator variance function, especially when several type of soft data are involved.

In transformed space, we define hard indicator as

$$I(u_\alpha, \theta_j^*) = \begin{cases} 1, & \text{if } \theta^*[y(u_\alpha)] \le \theta_j^* \\ 0, & \text{otherwise} \end{cases} \qquad (14)$$

where θ_j^* j=1,...,k are cutoffs for transformed hard data. Similarly, we define local soft indicator data, originating from the calibration between transformed hard data and the sum of transformed soft data

$$z(u_\beta, \theta_j^*) = \text{Prob}\{\theta^*[y(u_\beta)] \le \theta_j^* | \phi_s^*(u_\beta)\} \quad \in [0,1] \qquad (15)$$

Having indicator coded the transformed data, we follow the procedure outlined by Zhu and Journel (1992). After simulation, we back transform to the original data space.

RESULTS: SYNTHETIC AND FIELD EXAMPLES

In this section we describe application of the concepts discussed above to synthetic and field examples. The synthetic examples are designed to test the validity of our approach and to compare with the methods currently in practice. The field examples serve to illustrate the versatility to handle field scale applications.

Data Correlation: A Synthetic Example

This synthetic example is designed to demonstrate the ability of non-parametric transformations to identify functional relationship during multiple regression and correlation. Our example involves 300 observations generated using the following model

$$y_i = x_{1i} + x_{2i}^2 + x_{3i}^3 + 0.1\varepsilon_i \qquad (16)$$

where x_{1i}, x_{2i}, and x_{3i} are independently drawn from a uniform distribution $U(-0.5,0.5)$, and ε_i is drawn from a standard normal distribution $N(0,1)$. Fig. 1a through Fig. 1c show plots of y_i versus x_{1i}, x_{2i}, and

x_{3i}, respectively. Except for y_i versus x_{1i}, the functional relationships between the dependent variable y_i and independent variables x_{2i}, and x_{3i} can not be identified from the scatterplots.

The optimal transformations for y_i and x_{1i}, x_{2i}, and x_{3i} derived using ACE are plotted in Fig. 1d through Fig. 1g. The transformations for both y_i and x_{1i} yield essentially straight lines. The transformation for x_{2i} reveals a quadratic function and the transformation for x_{3i} reveals a cubic function. Thus ACE is able to identify the following optimal transformations

$$\theta^*(y_i) \cong y_i$$
$$\phi_1^*(x_{1i}) \cong x_{1i}, \qquad \phi_2^*(x_{2i}) \cong x_{2i}^2, \qquad \phi_3^*(x_{3i}) \cong x_{3i}^3 \tag{17}$$

This is, indeed, remarkable considering that the individual scatterplots hardly reveal any such relationships. A plot of transformed y_i versus the sum of transformed x_{1i}, x_{2i} and x_{3i} is shown in Fig. 1h. The relationship can be fitted approximately by

$$\theta^*(y_i) \cong \phi_1^*(x_{1i}) + \phi_2^*(x_{2i}) + \phi_3^*(x_{3i}) \tag{18}$$

which is exactly optimal.

We also applied generalized additive model (GAM) to the same synthetic example. The results were almost identical to ACE and hence, are not shown here. This is indicated by the bootstrap prediction error obtained with the ACE and GAM models as summarized in Table 1. The bootstrap approach to estimating prediction error involves generating B bootstrap samples, for each sample drawing independently and with replacement from the original data. The correlation model is rebuilt using each sample and then applied to the original as well as bootstrap sample to obtain estimates of apparent error and bias (optimism). The details can be found in Efron and Tibshirani (1993). Because of the similar performance characteristics of ACE and GAM, we have restricted to application of ACE model only in the examples discussed below.

Correlating Petrophysical Data: North Robertson Unit, West Texas

This field example serves to illustrate the versatility of non-parametric transformations to incorporate mixed data types, categorical and continuous, into correlation. The data belongs to the North Robertson Unit (NRU) located in Gaines County, West Texas. This is a mature, highly heterogeneous, shallow shelf carbonate reservoir. The reservoir interval is about 1400 ft in gross thickness with 90% of the interval being dolostone having a complex pore structure. Because of the diagenetic modification of the pore structure, no obvious relationship between porosity and permeability can be established at NRU even when the data are separated based on the depositional environment (Davies and Vessel, 1996). However, definition of rock types based on pore geometry analysis shows good relationship between permeability and porosity within each rock type. This is shown in Figs. 2a through 2c. Figure 2d shows the data for all three rock types combined and as expected, the correlation R^2 is reduced significantly.

Next, we apply non-parametric transformations to the data. Instead of having three separate correlation for the rock types, we can now correlate permeability directly to porosity and rock type. The transformations are shown in Figs. 3a through 3c. The optimal correlation is shown in Fig. 3d with an R^2 of 0.74 as compared to 0.45 as shown in Fig. 2d. On fitting the individual transformations with simple functions, we can derive an equation describing permeability as a function of porosity and rock type:

$$\theta^*(k) = 1.0258\,[\phi_1^*(RT) + \phi_2^*(\phi)] \tag{19a}$$

where the functional form describing $\theta^*(k)$, $\phi_1^*(RT)$ and $\phi_2^*(\phi)$ are shown in Figs. 3a through 3c. Given a porosity and rock type, we use Eq. 19 to compute $\theta^*(k)$. The corresponding permeability can then be obtained from Fig. 3c or using the fitted equation

$$k^{0.5} = 0.077 + 0.559\theta^*(k) + 0.752[\theta^*(k)]^2 \qquad (19b)$$

Table 2 compares bootstrap prediction error associated with permeability estimates using different methods. Three choices have been compared – a single correlation using all rock types, separate correlation for each rock type and the correlation equation developed using the non-parametric approach. As expected, the correlation combining all rock types (Fig. 2d) performs the worst. The correlation based on optimal transformation (Fig. 3d) not only outperforms individual rock type correlation but also collapses them into a single convenient equation.

Data Integration: A Synthetic Example

We simulated a 2-D synthetic case which includes one primary and two secondary variables having the following non-linear relationship

$$y(u) = x_1^{3.5}(u) + x_2(u) + \varepsilon \qquad (20)$$

where u is the location in 2-D space and ε is random Gaussian noise. The simulation grid size is 60 by 40. The secondary variables x_1 and x_2 are generated using the following models

$$\begin{aligned} x_1(u) &= 0.4\,[0.75\,t_1(u) + 0.25\,t_2(u)] + 1.2 \\ x_2(u) &= 2.0\,[0.25\,t_1(u) + 0.75\,t_2(u)] + 6.0 \end{aligned} \qquad (21)$$

In Eq.21, t_1 and t_2 are two mutually orthogonal realizations both with zero mean and unit variance. They are generated by unconditional sequential Gaussian simulations using a spherical semivariogram model. The constants in Eq.21 were selected such that the two secondary variables will have a balanced effect on the primary variable.

Fig. 4a through Fig. 4c show grayscale maps of the simulated x_1, x_2 and y. We use this simulated y as known exhaustive reference. Next, 120 data points (5% of total) are obtained by sampling the exhaustive y data at a regular spacing. These sampled y data, together with the exhaustive secondary data (x_1 and x_2 at 2400 locations) are then used to estimate y values at unsampled locations.

The first step in using our proposed approach for data integration is to derive optimal transformations using the ACE algorithm. In the transformed space, the non linearity between primary and secondary variables is virtually eliminated resulting in a maximal correlation R^2=0.912 as shown in Fig. 5.

The second and third steps are application of optimal transformations to the sampled y data and to all secondary data. Fig. 6 shows a grayscale map of the sum of transformed x_1 and x_2. Notice that because of the strong correlation established between the primary and secondary variables through the optimal transformations, many of the features of the exhaustive y-data is already apparent here.

Next, we perform cokriging using Eq. 13 to estimate the transformed primary values at all locations. The final step is back transformation to the original space. Fig. 7 shows the estimated primary values by cokriging using the optimal transformation approach. The correspondence with the original exhaustive reference (Fig. 4c) is, indeed, very good. For comparison purposes, we also conducted traditional ordinary kriging and cokriging estimation without using any transformations.

Fig. 8a and Fig. 8b show the scatterplots of true y (exhaustive reference) versus estimated y by traditional ordinary kriging and cokriging. Fig. 8c show the scatterplot of true y versus estimated y by cokriging using the optimal transformation approach. The power of the optimal transformation is quite evident from these results. By incorporating optimal transformations, we have improved the

correlation R^2 to 0.86 compared to 0.72 obtained by using traditional cokriging. As expected ordinary kriging performs the worst since the secondary data sets are not used.

The cokriging estimation without transformations is affected by the non-linearity between y and x_1. This is reflected in the concave upward shape in Fig. 8b. Furthermore, in order to use the cokriging estimator (Eq.10), six variance functions are required for this case as opposed to three when optimal transformations are used, both assuming symmetry in cross covariance functions. Table 3 presents a quantitative comparison of the statistics of error distribution. The results clearly indicate the superiority of our proposed approach as evidenced by the small standard deviation of error distribution obtained using the optimal transformations.

We also performed indicator cosimulation using Markov-Bayes algorithm in conjunction with ACE transformations. Five cutoffs, corresponding to 10% 30%, 50% 70% and 90% of the c.d.f of the transformed dependent variable were used in these simulations. Figs. 9a and 9b shows two realizations of y. Both reproduce the features and statistics of the reference y very well. The use of ACE transformations greatly facilitates such indicator cosimulation process by reducing variance function calculations.

Integration of Seismic Data: Stratton Field, South Texas

The Stratton field (Levey *et al.*, 1993) is located on the onshore South Texas Gulf Coast Basin. The Oligocene Frio formation is one of the largest gas productive interval. The middle Frio formation is characterized by a relatively gentle subsurface domal closure. It contains multiple stacked pay sandstones within a series of vertically stacked reservoir sequences referred to as the B-, C-, D-, E-, and F-series.

The available data for this study include 3-D seismic reflections and well log data from a two square-mile area of the Stratton field (Fig. 10). The seismic data consists of 100 inlines and 200 crosslines with a trace spacing of 55 ft in each direction. The well log data are from 21 wells. A zero offset vertical seismic profile (VSP) is available and used for establishing a correlation between the stratigraphic depth and seismic travel time (Fig. 11). The seismic and well log data are utilized to derive an integrated description of reservoir properties in the subject area using the proposed approach.

We selected F11 reservoir (Fig. 11) for our detailed study since it is thick and easy to be traced from seismic reflections in the study area. Our objective is to estimate pore footage ($h^*\phi$) in the study area using the data from well logs as the primary data set and multiple seismic attributes from 3-D seismic reflections as the secondary data set.

The reservoir properties, mainly reservoir thickness and porosity, for various reservoir facies in the middle Frio formations in 21 wells are estimated using SP, neutron porosity, and density log following the approach reported in Levey *et al.* (1993). Time horizons corresponding to reservoir zones are picked from the 3-D seismic data. Three type of seismic attributes, viz. average seismic amplitude A_{AVG}, maximum amplitude A_{MAX}, and root mean square amplitude A_{RMS}, are extracted. Altogether 72 pairs of pore-footage data from middle Frio reservoirs (B to F series) in 21 wells with corresponding nearby seismic attributes are selected for the data calibration. Fig.12a through Fig.12c show the scatterplot of pore footage from wells versus seismic A_{AVG}, A_{MAX}, and A_{RMS}. The highest linear correlation R^2=0.302 is between pore footage and average amplitude. Such a low correlation between pore footage and seismic attributes is not unusual considering the thickness of the sandstone zone, variations in lithology and fluid content, and data noise.

Optimal transformations are derived based on this data set using the ACE algorithm. Fig. 12d is a scatterplot of the transformed pore footage versus the sum of transformed seismic attributes. The correlation R^2 is improved to 0.465 (ρ=0.68) after transformations. This is quite significant in view of the scatter in the original data.

Fig. 13 shows the grayscale map of one of the seismic attributes, A_{AVG} corresponding to reservoir F11. Three such seismic attributes A_{AVG}, A_{MAX}, and A_{RMS}, comprise of our secondary data set whereas the pore footage at the wells are the primary data. We transformed all these seismic attributes and 21 pore-footage data using optimal transformations. Finally, we conducted a collocated

cokriging estimation for transformed $h^*\phi$ at all grid locations. A grayscale map of the estimated $h^*\phi$ by collocated cokriging after back transformation is shown in Fig. 14.

For comparison, we also conducted an ordinary kriging on $h^*\phi$ data from the 21 wells and the results are shown in Fig. 15. Notice the severe smoothing effects of the ordinary kriging and the lack of detail between the wells because of the absence of secondary information.

SUMMARY AND CONCLUSIONS

1. Non-parametric transformation techniques offer a powerful, versatile, and fully automated tool for building correlations for petrological variables. Such transformations, being totally data driven, provide a direct approach to identifying functional relationships between dependent and independent variables during multiple regression.
2. The power of non-parametric techniques lie in its ability to directly incorporate multiple and mixed variables, both continuous and categorical, into correlation. Moreover, the transformations are computationally efficient, easy to use and can provide significant insight during exploratory data analysis.
3. We have presented synthetic and field examples to demonstrate the application of non-parametric transformation techniques for data correlation. A comparison of bootstrap prediction error clearly reveals the superiority of such techniques compared to conventional methods.
4. Cokriging or cosimulation of multiple attributes is considerably simplified when carried out in conjunction with non-parametric transformations. The use of optimal transformations exploits the secondary data to its fullest potential and also allows for non-linearity between reservoir properties and seismic attributes.
5. The proposed data integration method greatly facilitates non-Gaussian cosimulation through the use of indicator approaches, particularly when multiple secondary variables are involved because of a significant reduction in variance function calculations.
6. Synthetic case study clearly shows that cokriging and collocated cokriging using optimal transformation is far superior to ordinary kriging and cokriging in reproducing exhaustive reference data. The field case study demonstrates its capability of integrating multiple seismic attributes with well data for reservoir characterization.

ACKNOWLEDGMENT

We would like to thank Drs. Mohan Kelkar and Xuri Huang at the University of Tulsa for their help in acquiring some of the field data. This work has been partially funded by a grant from the Mathematical Sciences Division of the National Science Foundation.

REFERENCES CITED

Almeida, A., 1993, Joint simulation of multiple variable with a Markov-type coregionalization model: Ph.D Dissertation, Stanford University, Stanford, CA.

Breiman, L. and J. H. Friedman, 1985, Estimating optimal transformations for multiple regression and correlation: Journal of the American Statistical Association, v. 80, No. 391, p.580.

Buja, A., Trevor Hastie, and Robert Tibshirani, 1989, Linear smoothers and additive models: The Annals of Statistics, v. 17, p.453-510.

Crogh, A., 1996, Improved correlations for retrograde gases, MS Thesis, Petroleum Engineering, Texas A&M.

Davies, D. K. and R. K. Vessel, 1996, Flow unit characterization of a shallow shelf carbonate reservoir: North Robertson Unit, West Texas, SPE/DOE 35433 in proceedings of the SPE/DOE 10th Symposium on Improved Oil Recovery.

Efron Bradley and Robert Tibshirani, 1993, An introduction to the Bootstrap: New York, Chapman and Hall, 436 p.

Emerson, J. and M. Stoto, 1982, Exploratory methods for choosing power transformations: Journal of the American Statistical Association, v. 77, No. 377, p. 103-108.

Friedman, J. H. and W. Stuetzle, 1981, Projection pursuit regression, Journal of the American Statistical Association, v. 76, No. 376 , p.817.

Friedman, J.H. and W. Stuetzle, 1982, Smoothing of scatterplots," Technical Report ORION006, Dept. of Statistics, Stanford University, California.

Friedman, J. H. and B. W. Silverman, 1989, Flexible parsimonious smoothing and additive modeling, Technometrics, v. 31, No. 1, p. 3-20.

Hald, A, 1952, Statistical theory with engineering applications, John Wiley and Sons, New York.

Hastie, Trevor and R. Tibshirani, 1990, Generalized Additive Models: London, Chapman and Hall, 335 p.

Jensen, J. L. and L.W. Lake, 1985, Optimization of regression-based porosity-permeability predictions: CWLS 10th Symposium, Calgary, Alberta, Canada, Sep. 29-Oct. 2, 1985.

Journel, A.G. and F. G. Alabert, 1990, New method for reservoir mapping, Jounal of Petroleum Technology (February), p. 212-218.

Levey, R.A., et al., 1993, Secondary natural gas recovery: targeted technology applications for infield reserve growth in fluvial reservoirs, Stratton Field, South Texas: Topical Report, GRI Contract No. 5088-212-1718, Gas Research Institute, Chicago, Illinois, 244 p.

Li, D, 1995, Scaling and upscaling of fluid flow through permeable media: Ph.D Dissertation, University of Texas, Austin, Texas, 302 p.

Tibshirani, R., 1988, Estimating optimal transformations for regression via additivity and variance stabilization, Journal of American Statistical Association, V. 82, p. 559-568.

Venables, W.N. and B. D. Ripley, 1994, Modern Applied Statistics with S-Plus: New York, Springer-Verlag, p. 247-261.

Wendt, W.A., S. Sakurai., and P.H. Nelson, 1986, Permeability prediction from well logs using multiple regression: in Reservoir Characterization, Edited by Lake, L.W. and Carroll, H.B. Jr., Academic Press, Inc. Orlando, Florida, 659 p.

Xue, G., A. Datta-Gupta, P. Valko, and T. Blasingame, 1996(a), Optimal transformations for multiple regression: application for permeability estimation from well logs, SPE/DOE 35412in proceedings of the SPE/DOE 10th Symposium on Improved Oil Recovery.

Xue, G., A. Datta-Gupta, 1996(b), A new approach for seismic data integration using optimal non-parametric transformations, SPE 36500 in proceedings of the 1996 SPE Annual Technical Meeting and Exhibition.

Zhu, H. and A. Journel, 1992, :Formating and integrating soft data: stochastic imaging via the Markov-Bayes algoritm: in Geostatitics Troia'92, edited by A. Soares, Kluwer Academic Publishers, Dordrecht, The Netherlands, p. 1-12.

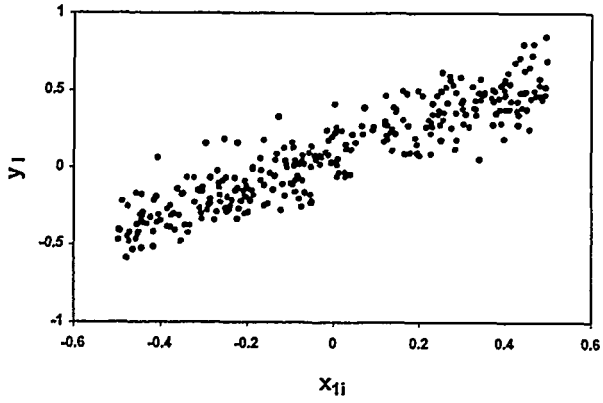

Fig. 1a-Scatterplot of y_i vs. x_{1i} simulated from multivariate model $y_i=x_{1i}+x_{2i}^2+x_{3i}^3+0.1\varepsilon_i$, where x_{1i}, x_{2i}, and x_{3i} are independently drawn from uniform distribution U(-0.5,0.5), and ε_i is independently drawn from standard normal distribution N(0,1).

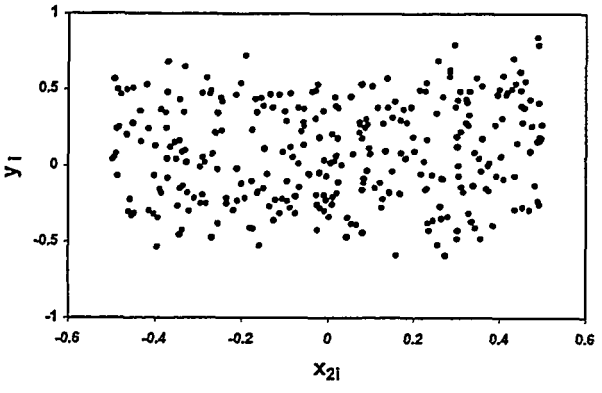

Fig. 1b-Scatterplot of y_i vs. x_{2i} simulated from multivariate model $y_i=x_{1i}+x_{2i}^2+x_{3i}^3+0.1\varepsilon_i$.

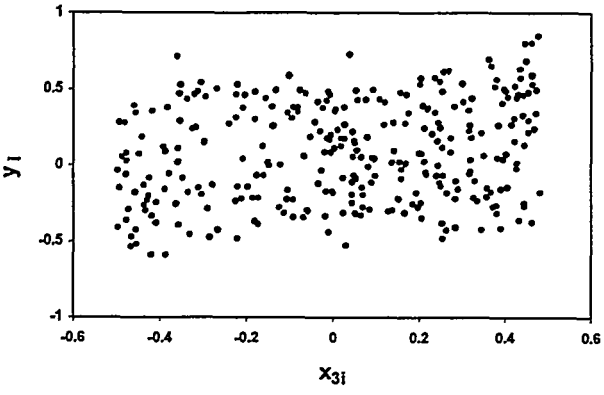

Fig. 1c-Scatterplot of y_i vs. x_{3i} simulated from multivariate model $y_i=x_{1i}+x_{2i}^2+x_{3i}^3+0.1\varepsilon_i$.

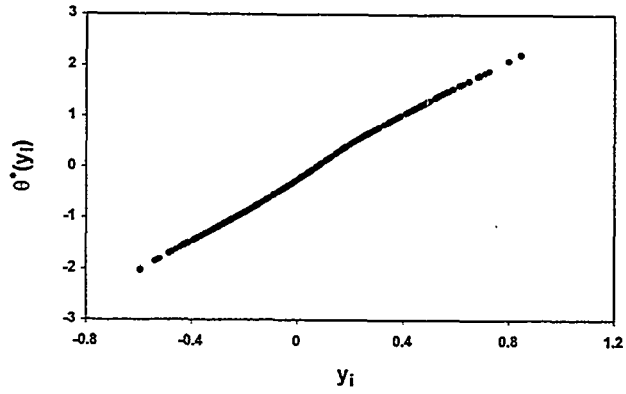

Fig. 1d-Optimal transformation of y_i by ACE.

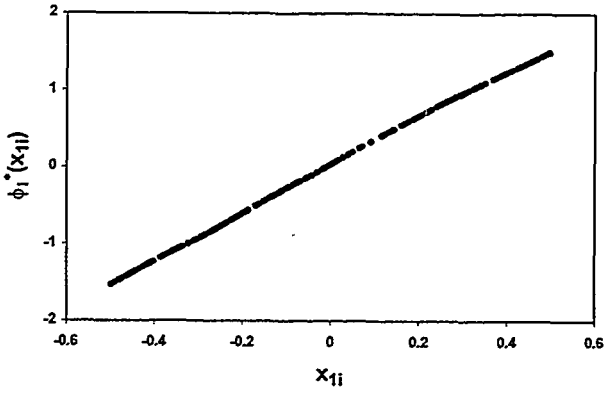

Fig. 1e-Optimal transformation of x_{1i} by ACE.

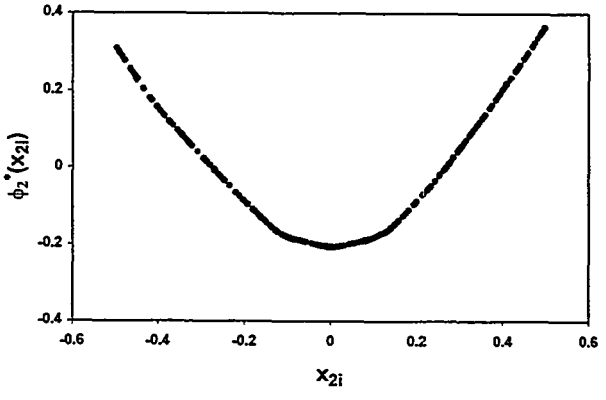

Fig. 1f-Optimal transformation of x_{2i} by ACE.

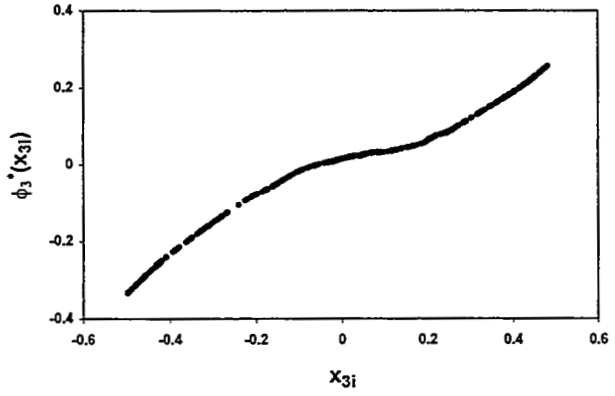

Fig. 1g-Optimal transformation of x_{3i} by ACE.

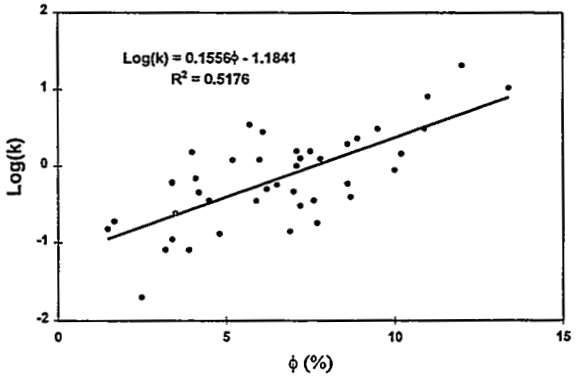

Fig. 2b-Logarithmically transformed permeability vs. core porosity of rock type 2. The solid straight line represents a linear regression of the data.

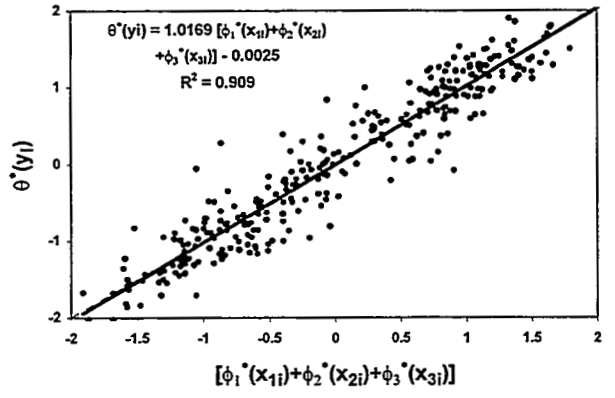

Fig. 1h-Optimal transformation of y_i vs. the sum of optimal transformations of x_{1i}, x_{2i}, and x_{3i}. The solid straight line represents a linear regression of the data.

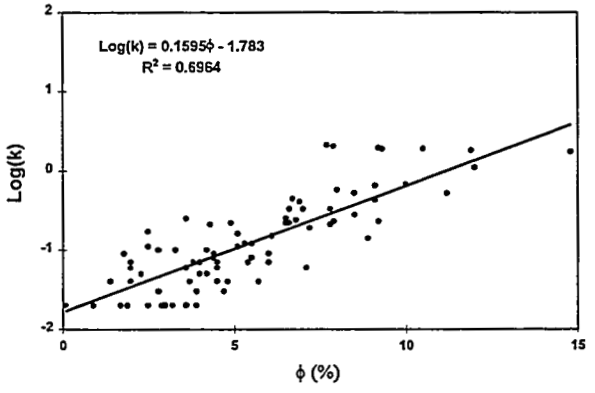

Fig. 2c-Logarithmically transformed permeability vs. core porosity of rock type 3. The solid straight line represents a linear regression of the data.

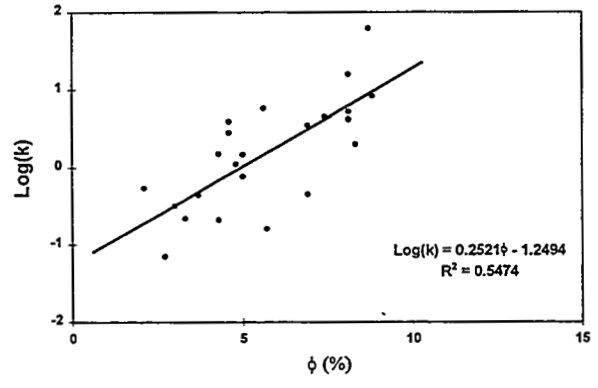

Fig. 2a-Logarithmically transformed permeability vs. core porosity of rock type 1. The solid straight line represents a linear regression of the data.

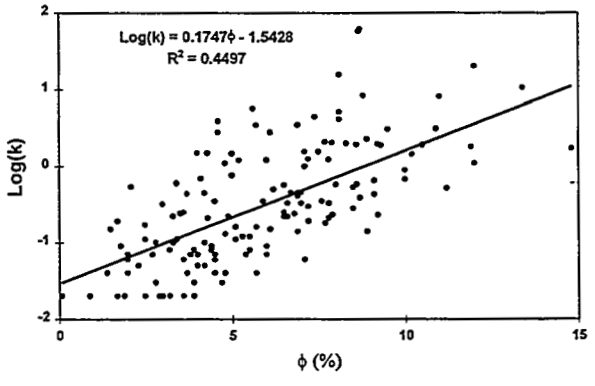

Fig. 2d-Logarithmically transformed permeability vs. core porosity of all rock types (rock type 1,2,&3). The solid straight line represents a linear regression of the data.

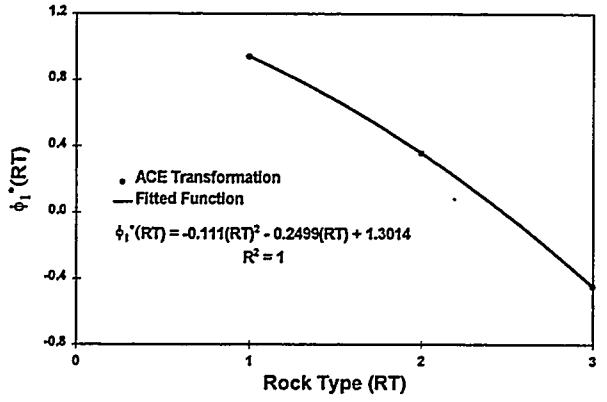

Fig. 3a-Optimal transformation of rock type by ACE . The solid line represents a fitted function.

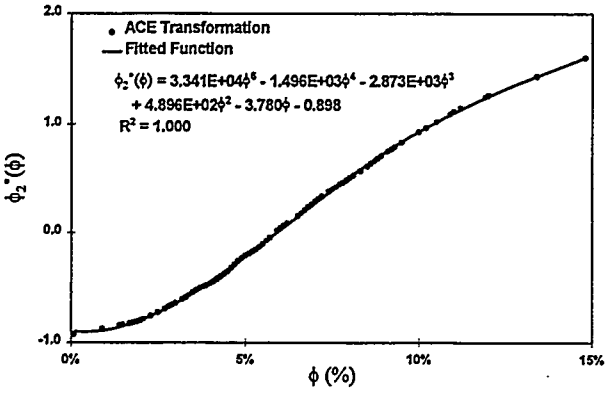

Fig. 3b-Optimal transformation of porosity type by ACE . The solid line represents a fitted function.

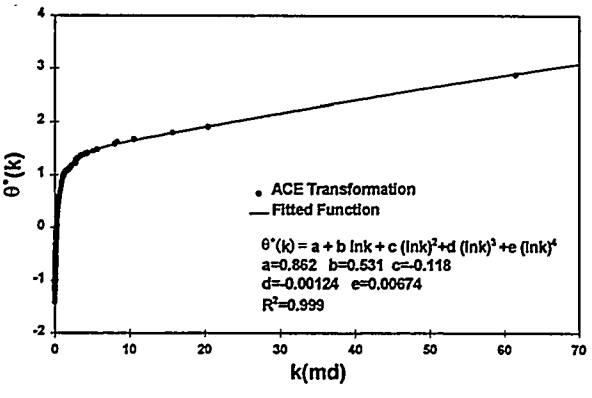

Fig. 3c-Optimal transformation of permeability by ACE . The solid line represents a fitted function.

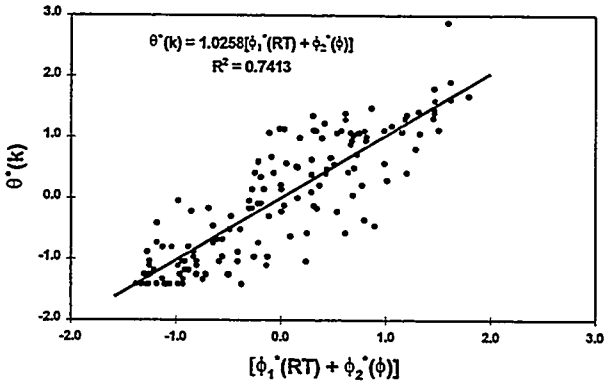

Fig. 3d-Optimal transformation of permeability vs. the sum of optimal transformations of rock type and porosity. The solid line represents a linear regression of the data.

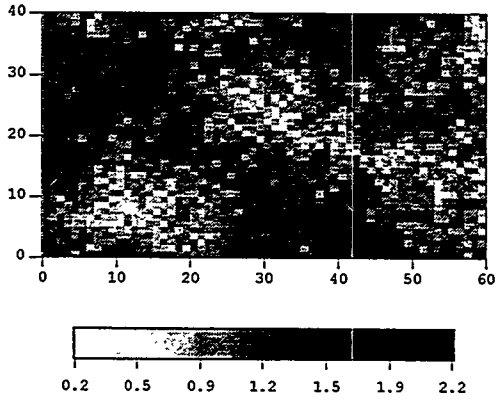

Fig. 4a-Grayscale map of simulated x_1. The simulation grid is 60 by 40.

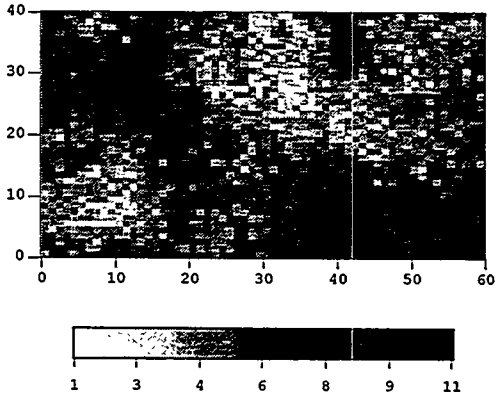

Fig. 4b-Grayscale map of simulated x_2.

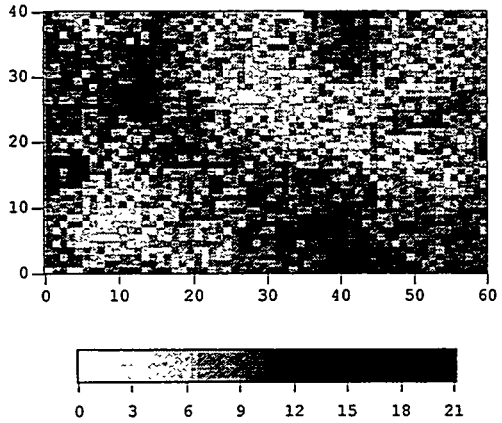

Fig. 4c-Grayscale map of simulated y.

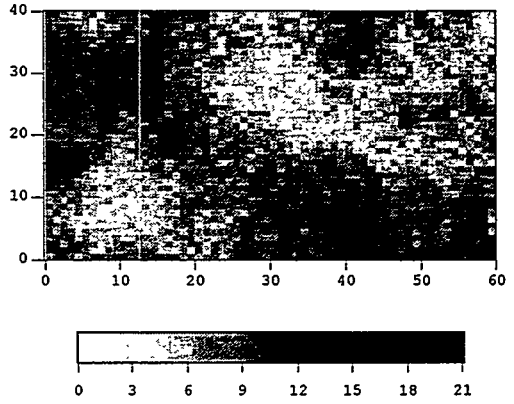

Fig. 7-Grayscale map of the estimated y by collocated cokriging using optimal transformations.

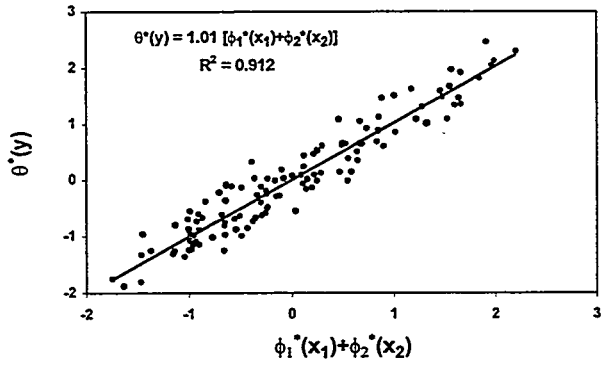

Fig. 5-Optimal correlation between primary (y) and secondary variables (x_1 and x_2) as derived by ACE. The solid line represents a linear regression of the transformed data.

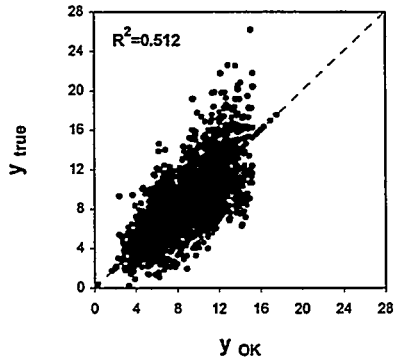

Fig. 8a-True y (reference) vs. the estimated y by ordinary kriging without using transformations. Secondary variables are not used.

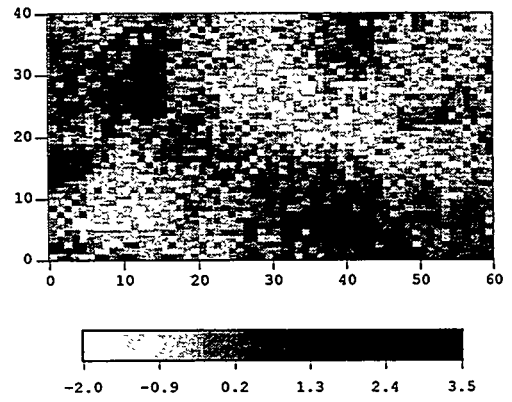

Fig. 6-Grayscale map of the sum of transformed x_1 and x_2.

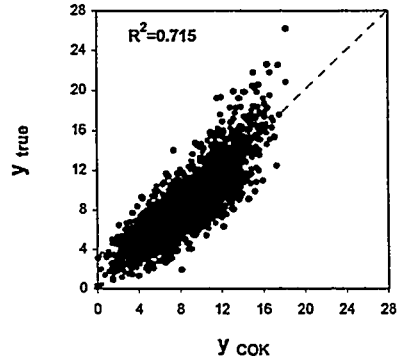

Fig. 8b-True y (reference) vs. the estimated y by cokriging without using transformations.

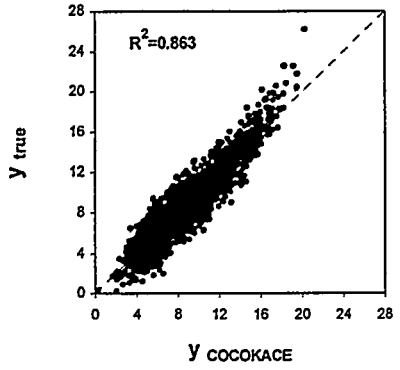

Fig. 8c-True y (reference) vs. the estimated y by collocated cokriging using optimal transformations by ACE.

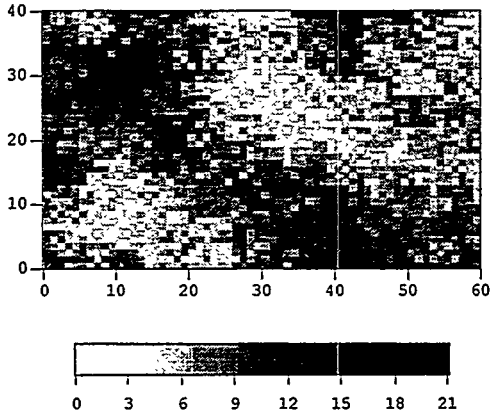

Fig. 9b-Grayscale map of y by indicator cosimulation using Markov-Bayes algorithm in conjunction with ACE. Realization 2.

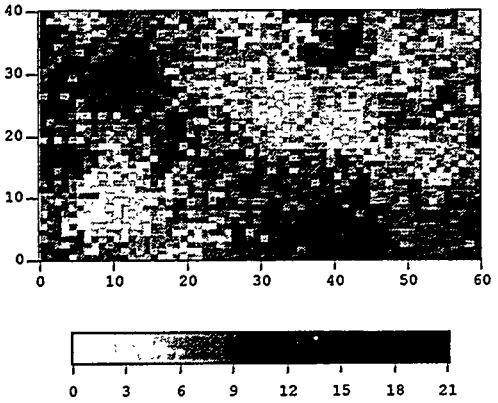

Fig. 9a-Grayscale map of y by indicator cosimulation using Markov-Bayes algorithm in conjunction with ACE. Realization 1

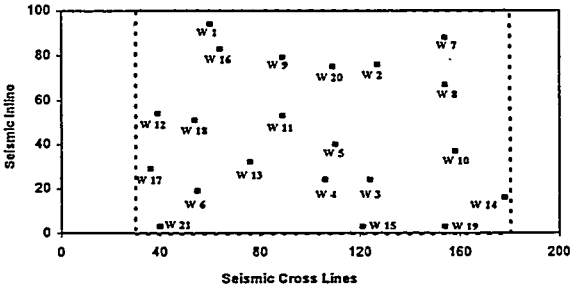

Fig. 10-3-D seismic survey and well location for the study area, Stratton field, South Texas. The dotted framed area is the mapping area.

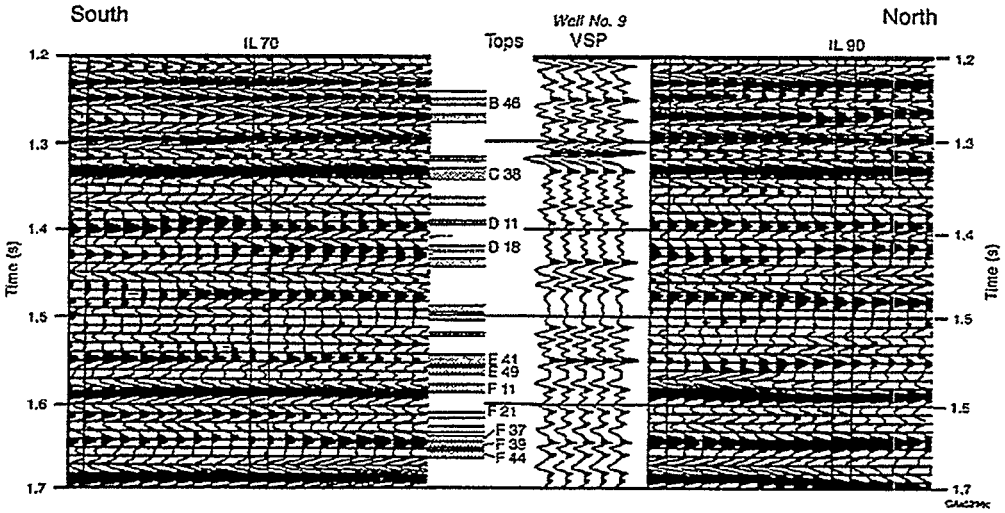

Fig. 11-Calibration of reservoirs using the vertical seismic profiles (VSP) in well 9. Notice the position of F11 reservoir used for the detailed study (Levey, et al., 1993).

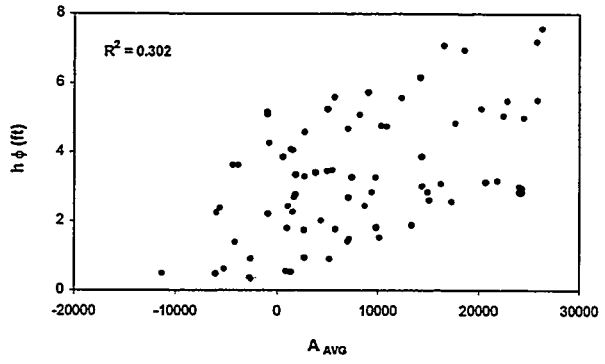

Fig. 12a-Pore footage vs. average seismic amplitude A_{AVG}.

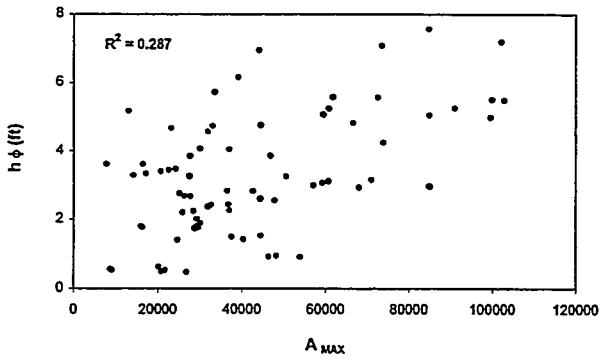

Fig. 12b-Pore footage vs. maximum seismic amplitude A_{MAX}.

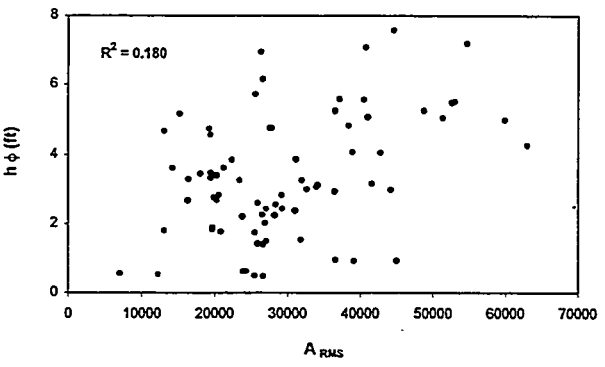

Fig. 12c-Pore footage vs. RMS seismic amplitude A_{RMS}.

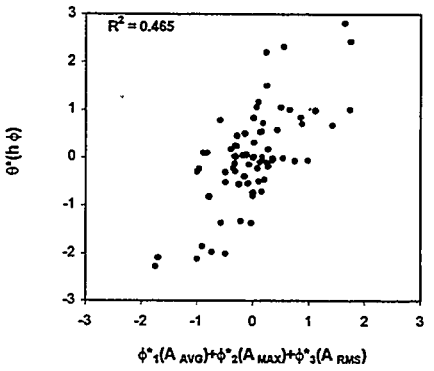

Fig. 12d-Optimal correlation of pore footage vs. seismic attributes as derived by ACE.

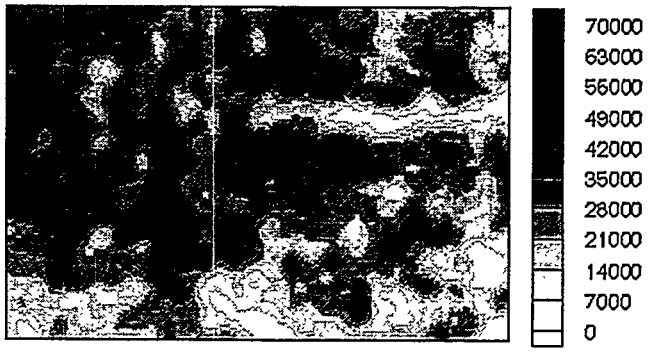

Fig. 13-Grayscale map of the average seismic amplitude A_{AVG} distribution corresponding to F11 reservoir.

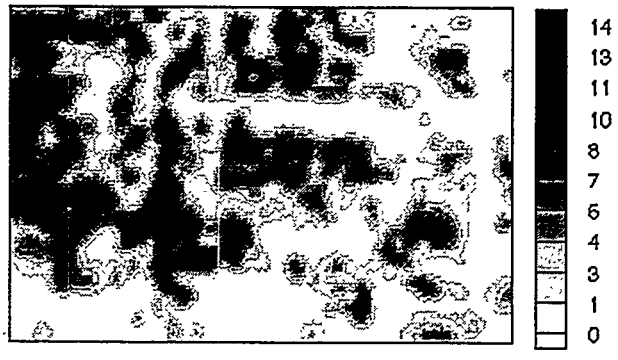

Fig. 14-Grayscale map of the estimated pore footage by collocated cokriging using optimal transformation by ACE.

Fig. 15-Grayscale map of the estimated pore footage by ordinary kriging from well data alone.

Table 3. Summary Statistics for Error Distributions of y Estimated by Various Estimators

$\lvert y_{TRUE}-y_{EST}\rvert$	Ordinary Kriging	Cokriging	Cokriging using ACE
Minimum	0.00	0.00	0.00
Maximum	11.07	7.95	5.91
Mean	1.86	1.44	1.00
Standard Dev.	1.58	1.20	0.80

Table 1. Bootstrap Estimates of Prediction Error (50 Bootstrap Replications) (Synthetic Example: $y_i = x_{1i} + x_{2i} + x_{3i} + 0.1\varepsilon_i$)

Prediction error	ACE	GAM
Apparent error	0.009720	0.009308
Optimism	0.000379	0.000607
Total error	0.010099	0.009915

Table 2. Bootstrap Estimates of Prediction Error (100 Bootstrap Replications) (North Robertson Unit, West Texas)

Prediction error	Logarithmic Model with all Rock Types	Logarithmic Models for Individual Rock Types	ACE with all Rock Types
Apparent	28.9099	22.2025	23.5064
Optimism	0.5808	5.0077	2.3199
Total error	29.4907	27.2102	25.8263

A New Approach to Integrate Seismic and Production Data in Reservoir Models

Ahmed Ouenes, Adwait Chawathé, William Weiss
Petroleum Recovery Research Center, New Mexico Tech
Socorro, New Mexico 87801 USA

Brian Cebull
Nance Petroleum Corporation
Billings, Montana, USA

ACKNOWLEDGMENTS

This research was funded through the Advanced Reservoir Management project at Los Alamos National Laboratory. The authors greatly appreciate the financial support. The Petroleum Recovery Research Center authors would like to thank Nance Petroleum for providing the data and the continous support for the project. The authors would like to thank James R. Ehrets and Beverly Blakeney DeJarnett for sharing their Nisku experience.

ABSTRACT

A great deal of effort is devoted to reducing the uncertainties in reservoir modeling. For example, seismic properties are used to improve the characterization of interwell properties by providing porosity maps constrained to seismic impedance. Another means to reduce uncertainties is to constrain the reservoir model to production data. This paper describes a new approach where the production and seismic data are simultaneously used to reduce the uncertainties. In this new approach, the primary geologic parameter that controls reservoir properties is identified. Next, the geophysical parameter that is sensitive to the dominant geologic parameter is determined. Then the geology and geophysics are linked using analytic correlations. Unfortunatley, the initial guess resulted in a reservoir model that did not match the production history. Since the time required for trial and error matching of production history is exorbitant, an automatic history matching method based on a fast optimization method was used to find the correlating parameters. This new approach was illustrated with an actual field in the Williston Basin. Upscalling problems do not arise since the scale is imposed by the size of the seismic bin (66m, 219 ft) which is the size of the simulator gridblocks.

INTRODUCTION

The wide availability of 3D seismic and the fast development of 4D seismic brings new insights to the reservoir and creates new challenges in reservoir modeling. Since the interpretation of 3D/4D seismic data requires geologic input, and the use of 4D seismic in the modeling process must include a reservoir simulator; it appears that the full integration of geology, geophysics, and reservoir

engineering is becoming an urgent necessity. To respond to this need, there are few tools and methodologies that can be used, at this moment, to create integrated reservoir models that honor geology, geophysics and production history simultaneously. Historically, these three disciplines did not have many opportunities for mixing and cross-linking.

Three distinct stages can be identified from a reservoir modeling perspective. During the first stage (60s and 70s), reservoirs were considered as challenging mathematical inverse problems where the objective was to find a set of reservoir parameters (porosity, and permeability mainly) that matched past production performance. During this stage, the emphasis was on the mathematical optimization algorithms. Geologic and geophysical data was not a concern, and the scale considered was the reservoir simulator scale.

In the second stage (mid 80s to present), geostatistics was introduced in reservoir modeling. As a consequence, geologic constraints are honored in reservoir models and the scale considered becomes very small (log and core scale). This drastic reduction in scale led to reservoir models with a few million gridblocks which could not be simulated on a practical time scale. Hence, the issue of upscaling became crucial. The objective of upscaling algorithms is to derive a model that has a reasonable number of reservoir gridblocks and at the same time maintains the geologic and statistical properties of the original system. The important characteristic of this stage was the total absence of reservoir simulators during the modeling process. Reservoir simulation was used "downstream" where multiple geostatistical realizations were tested to bracket the uncertainties. Unfortunately, the range of production forecasted by the multiple geostatistical realizations could be very wide, therefore not very helpful when it came to identifying a new infill location or an optimal waterflood pattern. As a result, dynamic and seismic data became the primary constraints to be added to the reservoir model in order to reduce the range of the uncertainties.

During the third stage (early 90s to present), various researchers focused on different types of dynamic data to add as a constraint in reservoir modeling. Two approaches were proposed: the near wellbore (Deutsch, 1992, Chu et al., 1995) and the fieldwide approach (Sultan et al., 1993, Hird, 1993, Ouenes et al., 1994a). In the near wellbore approach, various methodologies were proposed to constrain geostatistical realizations with pressure transient data. Unfortunately, this approach improves the reservoir description only around the well providing the pressure data. In the second approach, production data from many wells were considered as a constraint. Both these approaches resuscitate the various optimization and computing problems encountered during the 1960-70s when reservoir modeling was mainly an inverse problem. But many aspects in solving inverse problems have changed in the last two decades. The major difference with the past is that; today, there are more efficient optimization algorithms running on faster computers. Furthermore, the availability of 3D and 4D seismic data brings additional information to solving the inverse problem. In the past, the increase of available data was "cursed" since it was viewed as an additional history matching or optimization constraint.

This paper describes a new approach that views seismic data as a "blessing" since it has been used to: 1) honor the geologic features, 2) reduce the number of optimization parameters considerably,

and 3) provide reservoir models that honor performance history.

BACKGROUND

Until recently, the integration of seismic data in reservoir models was viewed from a geostatistical perspective (Doyen and Guidish 1992, Chambers et al., 1995). The large difference in scales between core (or log) and seismic data makes the integration of 3D seismic data in fine scale geostatistical models a challenging exercise. The question of how to upscale the geostatistical information to the scale of seismic data remains to be answered. Another direct approach to using 3D seismic data is identifying correlations between petrophysical and geophysical reservoir properties. Despite the problem of scale, this approach is commonly used and is available in commercial software. Although there is no doubt that the seismic response depends on reservoir properties, the problem is to find the underlying relationship at the considered scale. Recently, Chawathé et al. (1996) proposed a neural network approach to find the complex relationship that exists between seismic and log data. In contrast to previous work, the problem of scale does not exist since crosswell tomography was used as seismic information to map a reservoir property between two wells. This work indicates that even without the scale problem, the relationship between seismic and log data is very complex. The addition of scale problems worsen the task of relating log or core data to 3D seismic information. Based on these observations, another approach that circumvents the scale problems provides an alternative direction for reservoir modeling.

It is important to realize that the size of bins (few hundred feet) used in seismic surveys are similar to the size of gridblocks used in reservoir simulators. Hence, mathematical reservoir description may be viewed at the reservoir simulation scale which coincidently is also the seismic scale. Furthermore, the availability of seismic data over the entire reservoir volume represents a distinct advantage over the geostatistical approach where the interwell properties are estimated. Based on these observations, it becomes clear that there is a perfect fit between production and seismic data. The problem is to find methodologies that can allow the integration of the two valuable pieces of information. Before describing the existing methodologies and a proposed new one, it is important to identify the main component of such an approach.

The main characteristic of these methodologies is the necessity to include a reservoir simulator and an iterative mechanism when searching for the optimal reservoir model. Although this is not new to reservoir modeling, it has been avoided due to lengthy computation times. However, in our experience using automatic history matching algorithms (Ouenes et al. 1994, Weiss et al. 1995) on actual reservoir studies leads to a considerable reduction in time delivering results and helping oil producers in their reservoir management strategies. The few minutes or hours required to generate a few geostatistical realizations is short compared to reservoir simulation times measured in days. However, when preferably comparing few days of simulation to six months for completing an entire reservoir study (which must include a history match of all the producing wells) simulation times are almost insignificant. Furthermore, by following some general guidelines described in the next sections, the total computation time can be considerably reduced.

Recently Huang and Kelkar (1996) proposed a technique to integrate seismic and production data. In their approach, the porosity map was constrained to seismic impedance. The permeability field, in turn, was derived from the porosity-permeability scatter plot. An iterative process that uses a heuristic optimization method was used to find the best permeability realization which led to the history match of bottom hole pressure at producing wells. As a result, the reservoir model honors seismic (impedance), geology (porosity-permeability correlation), and production data (bottom hole pressures).

PROPOSED METHODOLOGY

The main characteristic of the proposed methodology is the emphasis given to geologic and geophysical interpretation of the data. The reservoir model becomes an integration tool where the geologists' and geophysicists' ideas are confronted by the reality of production history.

The methodology starts by a geologic study of the reservoir. The most plausible depositional environment must be identified. Furthermore the diagenetic factors that control reservoir quality must be isolated. In practice, the geologist proposes one or more primary geologic parameters that control the reservoir quality. This could be the volume of shale, the amount of anhydrite, the degree of dolomitization, or any other diagenetic factor. Since, the available information is often scarce, the initial geologic models may be approximate and incomplete. The proposed approach allows for re-evaluation of geologic interpretations.

After defining the geologic model and the primary geologic parameters, the geophysicist will try to identify the primary geophysical parameter. This is defined as the seismic measurement that is the most sensitive to the primary geologic parameter. Very often the acoustic impedance is used as an indicator of porosity and can be considered as a primary geophysical parameter. The Poissons ratio can be also a good indicator of changes in lithology. Hence, primary geologic parameters tightly related to lithology could benefit more from Poissons ratio if it is considered the primary geophysical parameter. In general, the choice of the primary geophysical parameter will depend on the availability of data and the type of reservoir considered.

The next step in this methodology is to define correlations between the primary geologic, geophysical parameters and the rock properties required in reservoir simulation (porosity, permeability, and initial fluid saturations). The analytical functions used to define the correlations depend on the type of parameters, and the amount of data available to build an initial estimate. The assumed correlations will include unknown coefficients to be estimated during the history matching process. The advantages of using correlations are two fold: first, the relationship between geologic, geophysical and reservoir properties is described quantitatively, and second is the considerable reduction of unknown coefficients in the history matching process. On the other hand, the disadvantage of the correlations is an oversimplification of the complex relationships that exist between primary geologic and geophysical parameters and reservoir properties. The proposed methodology is a trade-off between these advantages and disadvantages. This trade-off is illustrated with an application to a complex carbonate reservoir located in the Williston Basin (Montana).

UNDERSTANDING RESERVOIR GEOLOGY

The considered oil reservoir is located in Northeast Montana and eight wells have been producing since 1979 from the Winnipegosis and Red River formations. Only a single well was completed in the Nisku formation which is about 2000 ft above the Red River. This well produced 125,000 bbl from the Nisku during its first 41 months. Since operating conditions inhibit dual completions and Nisku wells cost almost a million dollars, the need for a Nisku reservoir development plan is apparent. The size of the reservoir and optimum well density are the key unknowns. Recognizing the need for additional Nisku data, a 5000 acre 3-D seismic survey was conducted and processed. In addition to the seismic data, the open hole logs of the eight Red River wells provided reservoir thickness, porosity, and water saturation in the Nisku formation. Pressure data from drill stem tests and transient test were available at four wells at four different time periods. Due to sparse well coverage, and the lack of Nisku producing wells, there was a need to develop a methodology to integrate all the available data into a reservoir model.

The upper Devonian (late Frasnian) Nisku formation is found in Western Canada (Birdbear) and in the Williston Basin. The first fields producing from this formation date back to 1939 in Alberta (Canada). From the mid 1970s to mid 80s, new discoveries were made in the US, mainly in Montana. Although there are some general features common to the Nisku found in Western Canada and Montana, the formation exhibits some specific features in Montana. In eastern Montana, the Nisku produces from platformal buildups (Blakeney and Eby, 1988). The Nisku formation is described as a shallowing-upward carbonate/evaporate sequence with open marine dolomitic wackestones grading up into supratidal laminated dolomites and anhydrites. Nisku carbonates have been completely dolomitized. Ehrets and Kissling (1985) suggested that Mg^{++} enriched brines expelled from overlying evaporites during burial compaction provided the dolomitizing fluids. Therefore, reservoir quality is entirely dependent on the process of dolomitization. Ehrets and Kissling (1985) proposed a dolomitization model that explains reservoir development through paleostructural control (Fig. 1). Recently, Whittaker and Mountjoy (1996) have also suggested a similar model where migration pathways for the dolomitization fluids (dense brines) were influenced by depositional facies and subsurface structures. As a result, Nisku reservoir exhibits some clear characteristics directly related to this dolomitization process. One of these characteristics is the occurrence of the Nisku reservoir around structural noses. However, the thickness and quality of the reservoir varies significantly along the structure. The studied reservoir thins in the updip direction in a similar way to East Kevin field (Blakeney and Eby 1988). Ehrets and Kissling (1985) have indicated that the thick porous intervals are clearly associated with the flanks of the structure where bank deposits are best developed. On the other hand, the structure high, where intertidal conditions prevailed and where bank facies are poorly developed, porosity is less developed. This situation is also found in the studied field. Based on these observations and the model shown in Fig. 1, it appears that the thickness and porosity are the primary geologic parameters. Furthermore, the structural depth seems to be directly related to the thickness and porosity. Thin reservoir and low porosity is found updip, while downdip thickness and porosity improves significantly. Hence, building a reservoir model depends on the knowledge of structure.

LINKING GEOLOGY TO GEOPHYSICS

The eight existing wells in the considered reservoir were all drilled on the structure high. Hence, if a mapping method is used to obtain the Nisku structure it would indicate a flat structure since there is no control data downdip. Fortunately, a 3D seismic survey shows a Nisku structure (Fig. 2) that corroborates the platformal buildup theory. The two-way travel time recorded in the seismic data was converted to depth using the available well control. Unfortunately, the Nisku is thin and less than the 3D seismic vertical resolution. As a result, seismic amplitude or impedance data cannot be considered as primary geophysical parameters. Hence, the only available seismic information that can be considered as primary geophysical parameters is the two-way travel time converted to depth.

The link between geology and geophysics occurs through empirical correlations which include the geologic (porosity and thickness) and geophysical parameters (seismic depth).
Based on the data available at eight wells, we assumed the following correlations:

$$h=a_h \log[\log(d)]+b_h \quad (1)$$

$$\phi=a_\phi \log[\log(d)]+b_\phi \quad (2)$$

where, ϕ, is the reservoir porosity, h, is the Nisku pay thickness and, d, is the subsea depth. The choice of the analytical function *log(log)* is arbitrary. The apparent relationship existing between the geologic and geophysical parameters seems highly non-linear which prompted us to use the log transform twice.

The choice of an analytical expression to describe the complex relationship that exists between geologic and geophysical parameters is a major problem. Unfortunately, there is no evident solution. However it is worth keeping in mind a few remarks when designing these analytical relationships. First, most of rock properties tend to have non-linear relationships with seismic properties. Second, when using very limited data to find these relationships, it is safer to use the functions in the known range of the input variables, and extrapolation may be misleading. For example, when choosing Eq. 2 to describe the relationship between porosity and depth, we verified that the lower depth available in the 3D survey does not lead to porosity higher than 30%, and the relationship is used only for the known range of depth. The limitations of using correlations are balanced by the reduction in the number of unknowns, a and b, in Eqs. 1 and 2. The available data at the existing wells provide an initial estimate of these coefficients and finding their optimal value will require the use of production data.

HONORING PRODUCTION DATA

The correlations defined in Eqs. 1 and 2, combined with the existing data at the eight wells, provides

an estimate for porosity and thickness over the entire reservoir. For a complete and more accurate description of the reservoir, the porosity and thickness maps when used in a black oil reservoir simulator must lead to a production performance that matches the actual production and pressure data. Finding the optimal distribution of porosity and thickness consists of finding the coefficients a and b used in the correlations described in Eqs. 1 and 2 that lead to the match of past performance.

The complete description of the reservoir model used as input in a simulator requires the knowledge of permeability, and initial water saturation. Based on the available data, we defined two more correlations that describe permeability and initial water saturation as a function of the primary geologic parameter, ϕ.

$$S_{wi} = a_S \log[\log(\phi)] + b_S \tag{3}$$

$$k=10^{(a_k\phi - b_k)} \tag{4}$$

Establishing the complete reservoir model consists of determining the eight coefficients a and b used in the four equations depicted in equations (1 to 4) by matching reservoir performance.

HISTORY MATCHING

The history matching process consists of finding the reservoir model that honors the past performance of all the wells, in our case the production history of one well. In the petroleum industry, this time consuming process is usually performed by engineers who change reservoir properties such as permeability manually in the simulator. Sometimes, the final reservoir model may not honor the existing production and pressure history.In this study, history matching is done automatically by a computer and the engineers devote most of their time to analyzing the results. In this case, the history matching problem solved by the computer is the following:

Find the eight unknown parameters used in the four correlations, and the reservoir relative permeability curves, that will match the available production and reservoir pressure.

The computer starts with a set of initial values for all the unknown parameters and creates a reservoir model. This initial reservoir model is fed to a black oil simulator to predict the production and pressure. As expected, the initial reservoir model does not fit the production history. The mismatch between the actual and simulated production and pressure is used to compute the error E:

$$E=\omega_i^{gas} \sum_{j=months} (GR_j^{\,s}-GR_j^{f})^2+\omega_i^{water} \sum_{j=months} (WR_j^{\,s}-WR_j^{f})^2+\omega_i^{pressure} \sum_{j=months} (P_j^{\,s}-P_j^{f})^2 \tag{5}$$

where GR is the monthly gas rate, WR, is the monthly water rate, P is the pressure, and ω are the weighting factors. The superscript s corresponds to simulated values and f corresponds to the field data. At this stage, the computer adjusts and changes the values of some of the unknown parameters. These new values will lead to new maps of porosity, thickness, permeability, and initial water saturation that can be tested with the black oil simulator. After running the simulator for 41 months of available production, a new error E_1 that measures the mismatch between actual and simulated data can be computed for the new reservoir model. This new error E_1 is compared to the previous error obtained with the previous reservoir model. If the new error E_1 shows improvements over the previous error, then the current parameters tested will be considered as the best, and further adjustments are implemented on them. On the other hand, if the new error E_1 is higher that the initial error, the current parameters will be discarded and a new set of parameters will be tested again. This iterative process continues until a good match of the field history is obtained.

The process of adjusting the unknown coefficients automatically depends on the optimization method used. The choice of an optimization algorithm is crucial since it controls the quality of the history match and the time required to reach a good match. The user has the choice between heuristic and deterministic optimization methods. In deterministic methods, the adjustments of the unknown parameters follows a strict rule very often involving the use of gradients. In heuristic method, the new values tested at each iteration involve the use of some random numbers. Both approaches have advantages and disadvantages. Briefly speaking, deterministic methods can be very fast if the search direction for the new values is oriented towards the optimal values. Unfortunately, this situation does not occur at each iteration and causes the algorithm to be trapped in local minima which do not lead to a good match of the production data. On the other hand, heuristic methods do not have privileged search directions and adjust the unknown parameters based on random rules. This approach has the advantage of escaping local minima at the expense of a large number of trials. Based on our experience using simulated annealing in automatic history matching and other reservoir description problems (Ouenes et al., 1994b), we have found that new deterministic optimization methods (Møller, 1993) allow faster convergence and have no local minima problems.

History matching results

Using an automatic history matching algorithm and a black oil simulator, 41 months of production of the first Nisku well was matched. The reservoir model comprised 4060 gridblocks. The producing oil rate was used as a constraint in the simulator and monthly gas (Fig. 3) and water (Fig. 4) rates were matched. The mismatch of water production during the early months is due to the fact that the simulator does not account for completion fluids, but the simulated water rate comprises the actual reservoir water production. In addition to the production history, four pressure data were available and were matched as closely as possible. In addition to the correlations described in Eqs 1-4, the history matching procedure led to the estimation of field relative permeability and capillary pressure curves. These curves are given in the analytic form expressed as:

$$k_{r_w}=0.145\left(\frac{S_w-S_{w_i}}{1-S_{o_r}-S_{w_i}}\right)^{1.8} \quad (6)$$

$$k_{r_o}=0.94\left(\frac{1-S_{o_r}-S_w}{1-S_{o_r}-S_{w_i}}\right)^{2.4} \quad (7)$$

$$P_c=28.0\left(\frac{1-S_{o_r}-S_w}{1-S_{o_r}-S_{w_i}}\right)^{3}-10.0 \quad (8)$$

where, $S_{or} = 0.25$ and $S_{wi} = 0.092$. All the coefficients used in the analytical forms (Eqs. 6-8) were included as estimation parameters for the automatic history matching algorithm. Based on the available production and pressure data, the proposed methodology leads to a reservoir model that honors all the existing data. When new information becomes available (additional wells), this reservoir model could be refined by adding the new production constraints. However, this process will be faster since a reasonable initial guess (current reservoir model) is available. The same approach may be used in 4D seismic, where after each seismic survey a new reservoir model could be derived and used as initial guess for the next model. The resulting reservoir model was used to evaluate reservoir size and oil in place as well as a variety of reservoir management strategies to maximize the oil recovery.

CONCLUSIONS

In this paper, a new approach to integrate seismic and production data in reservoir models was proposed and applied to an actual reservoir. Based on the results presented, the following conclusions can be drawn:

1. The understanding of the depositional environment and diagenetic changes is necessary for finding primary geologic parameters which will be used in reservoir modeling.

2. The identification of primary geophysical parameters, sensitive to changes in the primary geologic parameters, is crucial in finding the best correlations between geologic and

geophysical data.

3. Analytic functions can be used to describe the relationships between geologic and geophysical data.

4. Automatic history matching algorithms may be used to completely define the geology-geophysics relationships and constrain the reservoir model to existing production data.

5. The methodology was illustrated on an actual field and provided a unique opportunity to develop a complete reservoir model with very limited data.

REFERENCES CITED

Blakeney, B., and Eby, D.E., 1988, Upper Devonian Nisku formation at East Kevin field, Sweet grass Arch, Montana: in S. M. Goolsby and M.W. Longman, Occurrence and petrophysical properties of carbonate reservoirs in the Rocky Mountain Region, Rocky Mountain Association of Geologists, Denver, p. 121-128.

Chambers, R.L., Zinger, M.A., and Kelly, M.C., 1995, Constraining geostatistical reservoir descriptions with 3-D seismic data to reduce uncertainty: in J.M. Yarus and R.L. Chambers, Stochastic Modeling and Geostatistics: Principles, Methods, and Case Studies: AAPG Computer Applications in Geology, p. 143-158.

Chawathé, A., Ouenes, A., Weiss, W.W., 1996, Estimation of reservoir properties using fuzzy logic, neural networks and crosswell tomography: PRRC report No. 96-37 and in final report for DOE contract No DE-AC22-93BC14893.

Chu, L., Reynolds, A. C., and Oliver, D. S., 1995, Computation of sensitivity coefficients for conditioning the permeability field to well test pressure data: IN-SITU, 19, May.

Deutsh, C., 1992, Annealing techniques applied to reservoir modeling and the integration of geological and engineering (well test) data, Ph.D. dissertation, Stanford university, CA.

Doyen, P.M., Guidish, T.M., 1992, Seismic discrimination of lithology and porosity, a Monte Carlo approach: in Investigations in Geophysics, London, Society of Explo. Geophy. p. 243-250.

Ehrets, J.R., and Kissling D.L., 1985, Deposition, diagenesis and paleostructural control of Duperow and Birdbear (Nisku) reservoirs, Williston basin: in M.W. Longman et al., Rocky Mountain carbonate reservoirs - A core workshop, SEPM core workshop No 7, Golden, p. 183-216.

Hird, K.B. 1993, A conditional simulation method for reservoir description using geological and well performance constraints: Ph.D. dissertation, University of Tulsa, OK.

Huang, A., Kelkar, M., 1996, Reservoir characterization by integration of seismic and dynamic data: paper SPE/DOE 35415 presented at the tenth symposium on improved oil recovery, Tulsa OK 21-24 April.

Møller, M.F., 1993, A scaled conjugate gradient algorithm for fast supervised learning, Neural Networks, v. 6, p. 525-533.

Ouenes, A., Weiss, W., Richardson, S., Sultan, J., Gum, T., and Brooks, L., 1994a, A new method to characterize fractured reservoirs: application to infill drilling: paper SPE/DOE 27799 presented at the symposium on improved oil recovery, Tulsa, April 17-20.

Ouenes, A., Bhagavan, S., Bunge, P., and Travis, B., 1994b, Application of simulated annealing and other global optimization methods to reservoir description: myths and realities: paper SPE 28415 presented at the SPE annual technical meeting, New Orleans, Sept. 25-28.

Weiss, W., Ouenes, A., and Sultan, J. 1995, Reservoir characterization of a slope/basin reservoir: paper SPE 29597 presented at the joint rocky mountain regional meeting and low permeability reservoirs symposium, Denver, March 20-22.

Sultan J., Ouenes, A., and Weiss, W. 1993, Reservoir description by inverse modeling: application to EVGSAU field: paper SPE 26478 presented at the 1993 SPE annual conference, Houston, Oct. 4-6.

Whittaker, S.G., and Mountjoy E. W., 1996, Diagenesis of an upper devonian carbonate-evaporite sequence: Birdbear formation, Southern interior plains, Canada, Journal of Sedimentary Research, v. 66, No 5, p. 965-975.

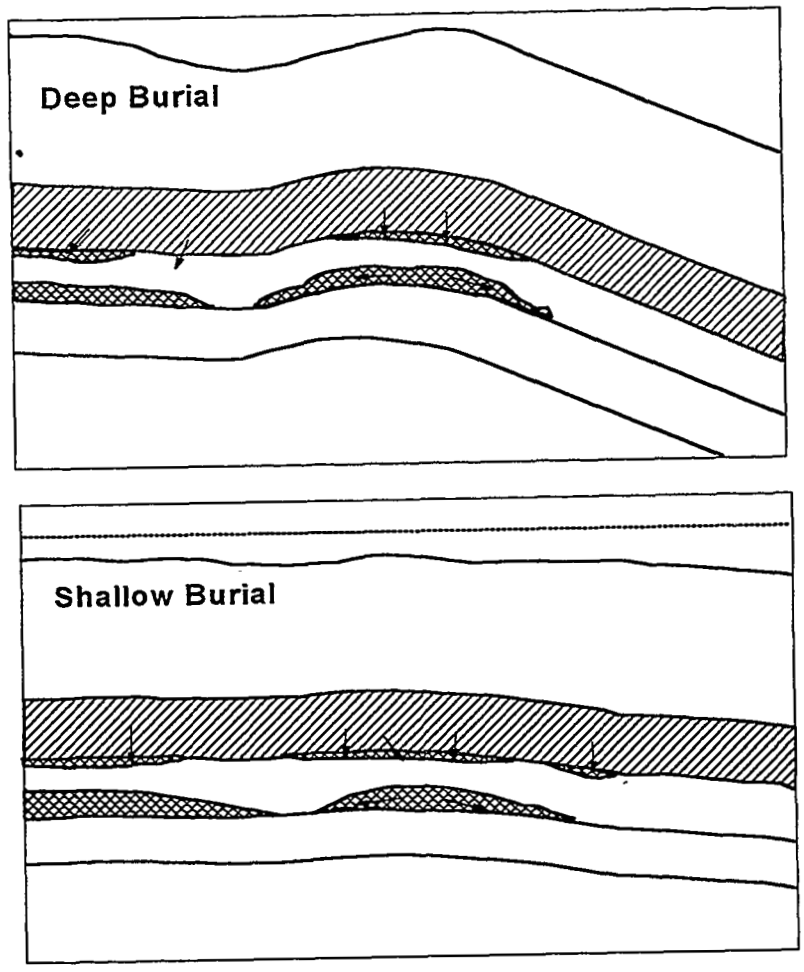

Figure 1: Diagenetic Model for the Nisku formation. The arrows indicate hypothesized flow directions for dolomitizing fluids through skeletal bank deposits during burial stages. (From *Ehrets and Kissling*, 1985)

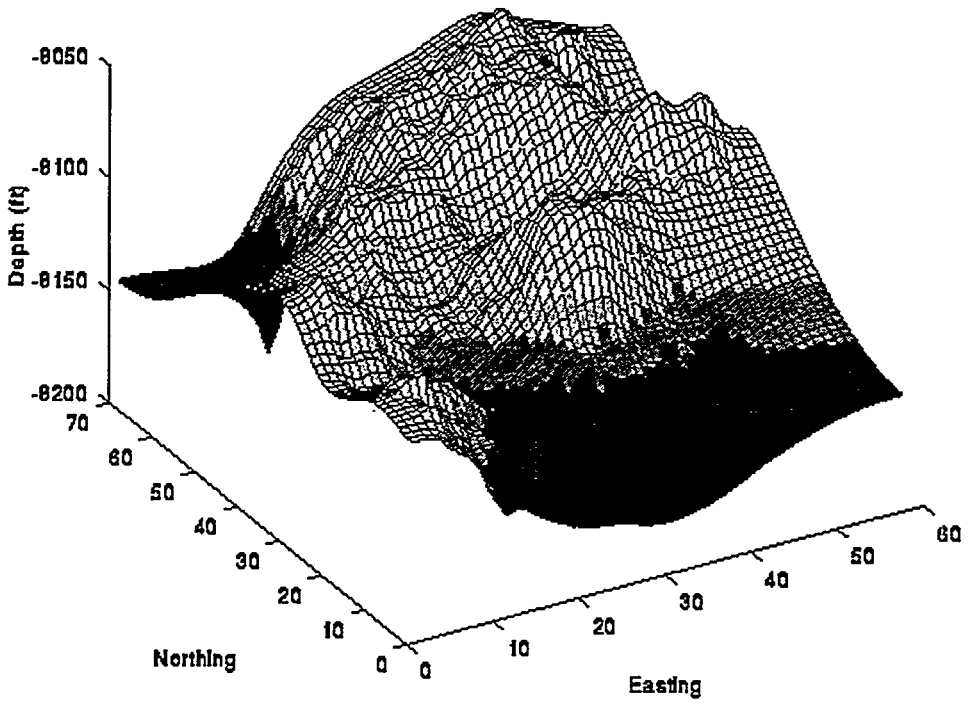

Figure 2: 3D seismic reservoir structure. The bin size is 66 m (219.4 ft) which also is the size of the grid block used in the black oil reservoir simulator.

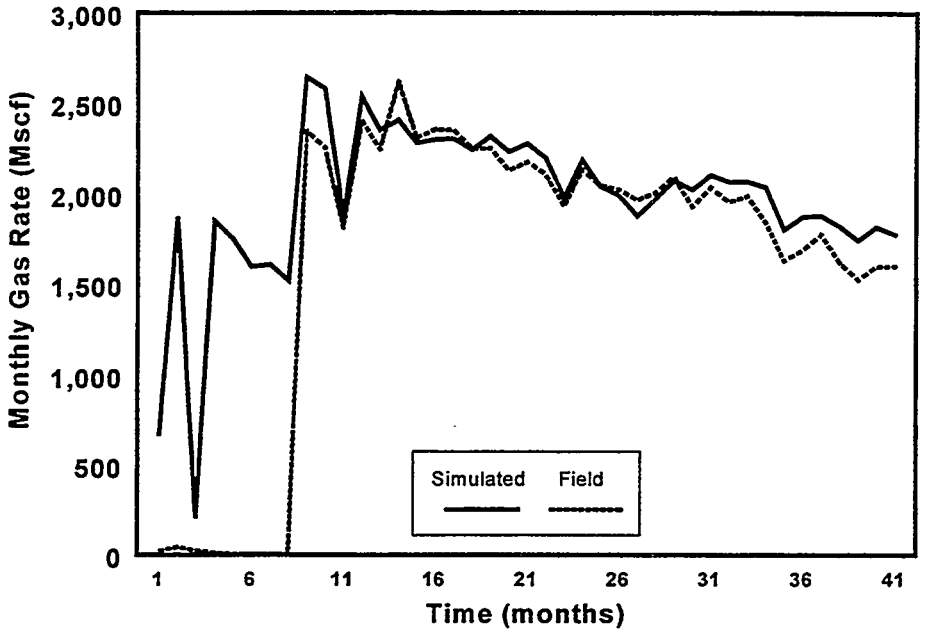

Figure 3: Monthly Gas Production Match.

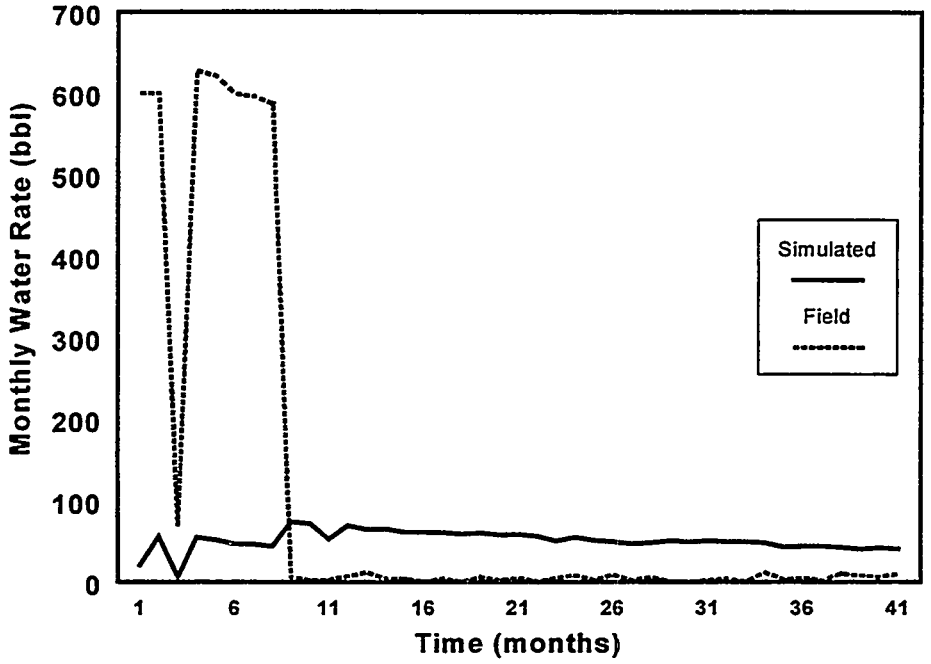

Figure 4: Monthly Water Production Match.

Predicting Interwell Heterogeneity In Fluvial-Deltaic Reservoirs: Outcrop Observations and Applications of Progressive Facies Variation Through a Depositional Cycle

Paul R. Knox and Mark D. Barton
Bureau of Economic Geology, The University of Texas at Austin, Austin, Texas 78713

ACKNOWLEDGMENTS

Studies contributing to this manuscript were partially funded by the U.S. Department of Energy under contract No. DE-FC22-93BC14959 and by the Gas Research Institute under contract No. 5089-260-1902. Mobil Exploration and Producing, U.S., provided subsurface data that made the reservoir characterization study possible. Project supervisors included William Fisher, Noel Tyler, Shirley Dutton, Raymond Levey, and Richard Major of The University of Texas at Austin, Richard Parker, Paul Wescott, and Anthony Garody of GRI, and Edith Allison and Chandra Nautiyal of the U.S. DOE. Assistance was provided by Ted Angle, Douglas Dawson, and Radu Boghici. Technical editing and comments of Steven Seni, Janok Bhattacharya, Brian Willis, Tucker Hentz, and Richard Major significantly improved the manuscript. Discussions with Lee McRae, Michael Gardner, and Tom Ryer also benefited the manuscript. Drafting was done by Randy Hitt, Kerza Prewitt, Joel Lardon, and Michelle Bailey under the direction of Richard Dillon and Joel Lardon. Publication authorized by the Director, Bureau of Economic Geology, The University of Texas at Austin.

ABSTRACT

Nearly 11 billion barrels of mobile oil remain in known domestic fluvial-deltaic reservoirs despite their mature status. A large percentage of this strategic resource is in danger of permanent loss through premature abandonment. Detailed reservoir characterization studies that integrate advanced technologies in geology, geophysics, and engineering are needed to identify remaining resources that can be targeted by near-term recovery methods, resulting in increased production and the postponement of abandonment.

The first and most critical step of advanced characterization studies is the identification of reservoir architecture. However, existing subsurface information, primarily well logs, provides insufficient lateral resolution to identify low-permeability boundaries that exist between wells and compartmentalize the reservoir. Methods to predict lateral variability in fluvial-deltaic reservoirs have been developed on the basis of outcrop studies and incorporate identification of depositional setting and position within a depositional cycle.

The position of a reservoir within the framework of a depositional cycle is critical. Outcrop studies of the Cretaceous Ferron Sandstone of Utah have demonstrated that the architecture and internal heterogeneity of sandstones deposited within a given depositional setting (for example, delta front) vary greatly depending upon whether they were deposited in the early, progradational part of a cycle or the late, retrogradational part of a cycle. Specifically, incised valleys in progradational parts of cycles tend to be narrow, deep, and internally homogeneous, whereas those in retrogradational parts of a cycle tend to be wider, internally heterogeneous, and display lateral channel migration. Additionally, river-dominated deltaic systems are more common in progradational parts of cycles, and wave-dominated deltaic systems are more common in retrogradational parts. Varying accommodation appears to play a significant role in this process, but changes in sediment supply and physiography of the depositional surface also potentially contribute.

Detailed investigations of two fluvial upper delta plain reservoirs in the Oligocene Frio Formation of Tijerina-Canales-Blucher field, South Texas, have documented variability in reservoir architecture and internal heterogeneity that contribute to very different production behavior and different remaining potential. The Whitehill reservoir, deposited early in a depositional cycle, contains several laterally isolated channel belts that are internally homogeneous and can be efficiently drained by wells at a 40-acre spacing. In contrast, the Scott reservoir, deposited late in a depositional cycle, contains a single broad channel belt that is internally heterogeneous, with many depositional low-permeability barriers between 20-acre well locations that have prevented more than 90% of the mobile oil from being recovered. The Scott reservoir

contains significant infill potential, whereas the Whitehill reservoir may contain new pool potential in isolated stratigraphically trapped accumulations away from the structural crest.

The application of techniques similar to those used by this study in other fluvial-deltaic reservoirs will help to estimate the amount and style of remaining potential in mature reservoirs through a quicklook evaluation, allowing operators to focus characterization efforts on reservoirs that have the greatest potential to yield additional resources. These techniques can also be applied to more confidently predict stratigraphy and depositional heterogeneity between wells, allowing more accurate identification of reservoir architecture and compartmentalization. Application of these concepts to mature fluvial-deltaic reservoirs is the first step in locating untapped or incompletely drained compartments that can be targeted by near-term recovery methods to increase production and prevent premature field abandonments.

INTRODUCTION

Unsuspected interwell-scale stratigraphic heterogeneity has contributed to a situation in which more than one-third of the mobile oil in domestic fluvial-deltaic reservoirs remains in place despite many decades of production. According to data from the U.S. Department of Energy TORIS database, 14.4 billion barrels (Bbbl) of oil have been produced from these reservoirs, but 10.8 Bbbl of mobile oil remain, with currently proved reserves equaling less than one-tenth of remaining volumes. The problem of stratigraphic heterogeneity is particularly pronounced in fluvial-deltaic reservoirs because fluvial and shallow marine sandstone bodies may appear laterally continuous but are commonly separated by impermeable abandoned-channel, marginal-marine, and marine mudstones. These long narrow isolated sandstone bodies are ineffectively contacted by conventionally patterned drilling grids and, in some cases, are internally compartmentalized by low-permeability layers that prevent efficient reservoir drainage.

The key to recovering the large volume of remaining mobile oil is to identify those reservoirs that have been poorly drained and apply integrated, advanced characterization methods to locate specific untapped or incompletely drained compartments. The critical first step in the characterization process is to determine the geometry of reservoir sandstones and bounding or

internal low-permeability layers. This process is complicated in fluvial-deltaic reservoirs because geometries may change laterally over distances less than the typical well spacing (Tyler and Finley, 1991), on which most subsurface data such as well logs are based.

Prediction of geometries and heterogeneity at the interwell scale is dependent upon a clear understanding of the depositional setting and the position of the reservoir within a depositional cycle. During the 1960s and 1970s, observations from modern depositional settings helped define major controls on deposition and preservation of sediments in various settings and were used to build facies models that lead to a basic understanding of field-scale reservoir architecture (for example, Coleman, 1982; Selley, 1978; Walker, 1979; Cant, 1982). During this time, models of delta evolution as a consequence of autocyclic lobe-switching were presented to explain cyclic deposition in deltaic settings (for example, Horne et al., 1978). It was recognized that delta style may change from fluvial-dominated to wave-dominated from early to late in a major depositional episode, perhaps as a result of decreased sediment supply (for example, Duncan, 1983). The concepts of sequence stratigraphy developed during the 1970s and 1980s improved the reliability of facies interpretation by more clearly defining the affects of changing relative sea level and sediment supply on depositional cyclicity, facies geometry, and stacking patterns (Vail et al., 1977; Jervey, 1988; Posamentier et al., 1988; Posamentier and Vail, 1988; Galloway, 1989a, b). The recent documentation of high-frequency depositional cycles and a hierarchy of cycle scales has increased the resolution of depositional models (Goldhammer et al., 1990; Mitchum and Van Wagoner, 1991) and underscored the potential of high-frequency eustatic changes to affect stratal geometries.

The advances provided by sequence stratigraphic concepts are being widely applied in order to predict lithology in exploration studies. Only recently, however, has the predictive framework of sequence and cyclic stratigraphy been thoroughly incorporated with facies models to go beyond the prediction of stratal geometries and document progressive changes in facies associations through a high-frequency depositional cycle. Workers in outcrops of carbonate sequences (Sonnenfeld, 1991; Kerans and Fitchen, 1995) and clastic successions (Cross et al., 1993; Gardner, 1993; and

Barton, 1994) recognized that the continually changing balance of depositional controls throughout a depositional cycle also resulted in changes in facies associations and their preservation potential within a depositional system. For example, facies associations in a delta deposited during a fall in relative sea level might correspond to models of river-dominated deltas because of increased fluvial input or decreased wave energy. Preservation of bedforms and facies in the updip area might be low because of pronounced sediment bypass caused by progressively decreasing accommodation. In contrast, deltaic deposits formed during rising relative sea level might correspond to wave- or tide-dominated depositional models because of decreased fluvial input. Preservation potential of these deposits would be increased because of greater accommodation.

This insight into facies associations in a high-frequency stratigraphic framework provides sufficiently detailed information to allow the prediction of reservoir architecture and heterogeneity at the between-well scale. Knox and McRae (1995) provided an early subsurface example demonstrating concomitant changes in reservoir production characteristics.

The primary objectives of this paper are (1) to summarize observations from Ferron Sandstone outcrops that demonstrate changes in facies associations through a depositional cycle and (2) to underscore the potential applications to oil and gas reservoir characterization using examples from mature Oligocene-age reservoirs in the Texas Gulf Coast. The remaining two sections of the Introduction will demonstrate the potential changes in reservoir heterogeneity resulting from differing position within a depositional cycle and summarize cyclic controls on interwell-scale heterogeneity.

A Tale of Two Reservoirs

Characteristics of two vertically adjacent reservoirs in the Oligocene Frio Formation of South Texas illustrate the potential variability in heterogeneity and, consequently, production behavior, that can occur within a single depositional facies. Knox and McRae (1995) interpreted both the Scott and underlying Whitehill reservoirs from the Tijerina-Canales-Blucher field, Jim Wells

County, Texas, as having been deposited in a fluvial upper delta plain environment on the basis of regional setting and blocky to upward-fining log signature.

Although the fluvial upper delta plain depositional setting for these two reservoirs is similar, their production characteristics are very different. The Scott reservoir (dominantly oil-bearing) is nearing abandonment of its ten well completions (at a spacing of less than 40 acres) with more than 90% of the original oil still in place. In contrast, past production in the underdeveloped Whitehill reservoir (dominantly gas-bearing) has demonstrated that the reservoir can be effectively drained by completions at a 40 acre spacing. Knox and McRae (1995) stated that the vastly different drainage areas for completions in these reservoirs are greater than can be accounted for by the difference in mobility of the gas versus oil fluids, and point to differences in internal heterogeneity. Knox and McRae (1995) concluded that these differences in heterogeneity were the result of the different positions within a depositional cycle, with the Whitehill having been deposited during more pronounced progradation (low accommodation leading to scour and removal of fine-grained channel-fill facies, resulting in internal homogeneity) with the Scott being deposited during more pronounced aggradation (high accommodation leading to preservation of fine-grained channel-fill facies, resulting in greater internal heterogeneity).

Cyclic Controls on Interwell-Scale Heterogeneity

The primary controls on clastic sediment deposition (and preservation) and resulting architecture and heterogeneity are accommodation, sediment flux, and antecedent physiography (Jervey, 1988; Posamentier et al., 1988; Van Wagoner et al., 1990, Goldhammer et al., 1990; Swift et al., 1991). Accommodation describes the potential space available for sediment to fill, sediment flux includes the rate and textural mix of sediment input, and antecedent physiography is the three-dimensional shape of the surface on which deposition takes place. These primary controls each have contributory factors that govern their net effects. Accommodation is the net result of subsidence (caused by tectonism, isostatic adjustments to sediment loading, etc., and sediment compaction) and eustasy (high-frequency climate-induced and longer-term geoidal and tectonic

forces). Sediment flux is the net result of tectonism in the source area, climate and changes in climate in the source area, and the changing hydraulic competency of the delivering medium (for example, water flow in a fluvial system or currents in a shelf system). Antecedent depositional topography affects accommodation in that, as relative sea level changes, deposition shifts landward or seaward and total accommodation is determined by both changing relative sea level and the slope of the surface to which deposition has shifted. Antecedent depositional topography affects sediment flux because topography governs wave, tide, and current energies.

Although the controls on sediment deposition are numerous and complex, an overwhelming number of workers have concluded that the sedimentary record (the end result of deposition and preservation) is inherently cyclic, and that this cyclicity occurs at many scales (see Goldhammer et al., 1990, and Mitchum and Van Wagoner, 1991 for more involved discussions). Many previous studies have subdivided depositional cycles into three parts (the highstand, lowstand, and transgressive systems tracts of Posamentier et al. (1988) and Posamentier and Vail (1988)). Various terminology has been applied to describe the hierarchy of scales of depositional cycles, such as parasequences, high-frequency sequences, sequences and composite sequences (Mitchum and Van Wagoner, 1991), and cycles, high-frequency sequences, and composite sequences (Kerans and Fitchen, 1995). Because we recognize marine flooding surfaces as the most useful surfaces in establishing a stratigraphic framework, we consider a generic depositional cycle (independent of scale) to begin at maximum flooding and progress from progradation through aggradation to retrogradation, culminating at a maximum flood. In this sense, the resulting depositional units are akin to genetic depositional sequences as defined by Galloway (1989a). The term 'order' has been used to describe the hierarchy, such as 3rd-, 4th-, and 5th-order (see Goldhammer et al., 1990, and Mitchum and Van Wagoner, 1991), and specific time spans have been assigned to various 'orders.' Unless a cycle is clearly constrained by age dating, we avoid the use of 'order' terminology. Instead, we have applied the generic terms of low-, intermediate-, and high-frequency to describe observed multifold cyclicity.

INTERWELL-SCALE HETEROGENEITY IN OUTCROP

Stratigraphic complexities that result in between-well-scale reservoir heterogeneity are best described in outcrop where rapid lateral changes can be identified and described. The best outcrop sites occur where present landforms and original depositional trends combine to expose long, continuous portions parallel to depositional dip, with sufficient orthogonal exposures to provide information regarding strike-oriented variations. Additionally, stratigraphic units deposited under conditions of high sediment supply and high accommodation provide the best record of high-frequency depositional cyclicity because short-term changes in the balance of depositional controls that result in brief marine flooding events will be recorded by the abundant influx of sediment and preserved by rapid burial and limited ensuing incision.

The conjunction of these factors occurs in exposures of the Upper Cretaceous (Turonian) Ferron Sandstone Member of the Mancos Shale along the Molen Reef and Coal Cliffs fringing the San Rafael Swell of eastern Utah (Figure 1). Cliff faces of greater than 100 m height and 100 km in length expose the entire 250 m of the Ferron, which accumulated during an estimated 0.5 to 2 Ma. Early studies of the Ferron Sandstone Member of the Mancos Shale identified it as major sandstone body composed of two distinct clastic wedges, an early wedge derived from the northwest, typically referred to as the Clawson and Washboard sandstones, and a later wedge derived from the southwest (Hale, 1972), referred to as the Ferron sandstone. Ryer (1981) recognized the upper (Ferron) wedge as being composed of a series of sandstone tongues partially bounded by marine shales. Later studies (Ryer, 1993; Gardner, 1993, Barton, 1994) recognized that each of these tongues is further subdivided by marine shales associated with minor flooding events.

Stratal successions (high-frequency units) bounded by minor flooding surfaces are stacked in a systematic fashion to form five intermediate-frequency (IF) units bounded by major or more regionally extensive flooding surfaces (Figure 2). Within each IF unit, the stacking pattern of high-frequency (HF) units progresses from an initial aggradational-to-progradational set, to a downstepping set, then to an aggradational set, followed in some cases by a retrogradational set

(IF units 3, 4, and 5 in Figure 2).The downstepping set of HF units is interpreted to have been deposited during a fall in relative sea level whereas the aggradational to retrogradational sets are interpreted to have been deposited during a relative rise.

Within each HF unit, a surface characterized by deep fluvial incision and the development of paleosols separates the initial aggradational to progradational set of HF units from subsequent downstepping, aggradational, and retrogradational sets. This surface is interpreted as an unconformity developed during a fall in relative sea level. During a subsequent rise in sea level, incised valleys were filled with fluvial to estuarine deposits and interfluv areas, characterized by paleosols, were onlapped by marginal marine to coastal plain deposits.

Accompanying changes in stacking pattern of IF and HF units are progressive changes in facies associations. Variability of lithofacies geometry and heterogeneity were documented within delta front deposits of IF units by Gardner (1993). Subsequent studies by Barton recognized similar changes in delta-front deposits of HF units (Barton, 1995) as well as within incised valley deposits of IF units. The following discussion summarizes this observed variability and compares it to the position of the deposits within a depositional cycle.

Summary of Outcrop Observations

Detailed observations of lithofacies types, geometry, and permeability were made in many cliff exposures within a 40-km section of Ferron sandstone outcrops (Figure 1) in which the high-frequency genetic stratigraphic framework had been established. These observations make possible a comparison of similar depositional settings at different times in a depositional cycle. Summarized below are comparisons of incised valley fill deposits from a seaward-stepping (low accommodation) IF unit and those from a landward-stepping (high-accommodation) IF unit and comparisons of delta front deposits from two vertically adjacent HF units occupying early and late portions of a lowstand within a seaward-stepping IF unit (see Figure 2).

Incised valley deposits identified by Barton (1995) in cycle 2 exposed along I-70 (Figure 1) are typical of incised valleys observed throughout cycles 2 and 3, which are IF units within the

seaward-stepping portion of the Ferron low-frequency depositional unit. Lithofacies, channelform boundaries, and permeability within this deposit are shown in Figure 3, along with the map view geometry of the valley system. These incised valley deposits tend to be internally relatively homogeneous in both lithology and permeability, with many vertically stacked channel-bar and -fill beds composed nearly exclusively of trough cross stratified sandstones lacking evidence of marine or tidal influence. Channel-on-channel boundaries exhibit thin intervals (0.1 to 1 m) of slightly reduced permeabilities consisting of basal channel lag deposits containing rounded mudclasts and dispersed clay. Valleys are narrow and deep, with width-depth ratios of approximately 7:1.

Valley fill deposits identified by Barton (1995) in cycle 5, a landward-stepping (high-accommodation) IF unit, are typified by outcrops at Muddy Creek (Figure 1). A cross-section of this valley fill, shown in Figure 3, illustrates that in contrast to valleys in cycles 2 and 3, these deposits consist of laterally stacked channelforms containing a heterolithic, upward-fining succession of trough cross strata through rippled strata typical of medium to high-sinuosity rivers. Permeability is somewhat more heterogeneous than in cycle 2 valley fills, with channel lag deposits draping lateral accretion surfaces and exhibiting pronounced reduced permeability arising from a greater volume of mudclasts and dispersed clay. A greater number of stratigraphically equivalent valleys are seen in map view (Figure 3), and each valley tends to have a higher width-depth ratio, approximately 40:1, than those in cycles 2 and 3. Gardner (1993) identified these features as distributary channels and suggested that the difference in morphology was a consequence of low versus high accommodation. Barton (1995) identified these features as incised valleys on the basis of fluvial incision that is several times as deep as a single barform is high. One possible explanation shared by both Gardner (1993) and Barton (1995) is that successive scour in a low accommodation setting removes the upper, fine-grained portion of the channel fill that is normally preserved during periods of higher accommodation, resulting in the marked differences in internal lithologic and petrophysical heterogeneity.

Delta front deposits in two HF units from both early and late lowstand periods in cycle 2 are seen at exposures in Dry Wash (Figure 1). These two units are vertically adjacent but exhibit vastly

different lithofacies and permeability distributions typical of opposing deltaic styles. Delta front deposits of the early lowstand HF unit show characteristics common in fluvial-dominated deltas such as prominent mouth bar facies and growth faulting, and permeability is consequently highly variable. In contrast, delta front deposits of late lowstand HF unit show characteristics common to wave-dominated deltas such as extensive strike-elongate shoreface facies and lagoon/washover facies, with limited lateral variations in permeability. Gardner (1993) documented this style of variability between successive IF units. Several depositional controls could account for the observed changes in depositional style in both IF and HF units. For instance, decreased sediment supply during the late lowstand time could provide more opportunity for mouth bar deposits to be reworked into strike-parallel shoreface facies. Alternatively, higher wave energy may be typical in late lowstand times because of progradation of the delta front into increasingly deeper waters (resulting from rising sea level) resulting in less dissipation of wave energy across the shelf.

Envisioned depositional models for Ferron IF depositional cycles are shown in Figure 4. Deposition progresses from (1) wave-dominated highstand deltas through (2) river-dominated deltas fed by incised valleys during early lowstand, to (3) wave-dominated deltas fed by sinuous fluvial systems in the late lowstand, and culminating with (4) barrier bars, lagoons, and estuaries during transgression. Lowstand deposits are better developed in seaward-stepping IF units and transgressive deposits are thin or absent in these units. The result of this pattern is progressive changes in volume and style of deposits in both the fluvial and deltaic depositional systems throughout intermediate- and low-frequency depositional cycles.

PREDICTING HETEROGENEITY IN THE SUBSURFACE

The above outcrop observations from the Ferron Sandstone provide support to the concept that facies associations change progressively through a depositional cycle. These documented variability in permeability characteristics and facies geometries have significant potential impacts on subsurface reservoir behavior. Low-permeability bounding surfaces identified in outcrop are difficult to resolve in well logs and may have complex distributions between existing wellbores that

significantly impact the ability of the wellbore to communicate with fluids in the reservoir, decreasing per-completion production and leaving large areas of reservoir untapped or incompletely drained. Recognizing which reservoirs might contain such heterogeneities is important because it is those reservoirs that contain significant reserve-growth potential but which will require focused characterization efforts to locate and recover the large volumes of remaining mobile oil.

As outcrop studies of the Ferron indicate, an understanding of the depositional system and stratigraphic position of the reservoir within a larger depositional cycle framework can provide the basis for predicting between-well scale stratigraphic heterogeneity. This concept was applied to the Scott and Whitehill reservoirs mentioned above to evaluate the variability of production characteristics and investigate whether outcrop observations might supply insights into optimization of reservoir production. The Scott and Whitehill reservoirs were deposited in channelized upper delta plain settings and might be subject to the same trends in depositional controls as Ferron incised valleys. For instance, channels deposited during low accommodation might have poorer preservation of fine-grained channel-fill sediments and thus might be more internally homogeneous.

Methodology

The first and most critical step in evaluating any reservoir from the standpoint of position within a depositional cycle is to establish a stratigraphic framework of low- and intermediate-frequency units from subregional information. This gross framework can then be subdivided into HF units within the field using a grid of stratigraphic sections on the basis of throughgoing surfaces that are assumed to correspond to minor flooding surfaces. Net sandstone maps are then prepared for each HF unit of interest and combined with maps of log pattern to interpret the lateral distribution of facies and identify reservoir architecture. Structure and net pay maps are created for each unit, and fluid contacts are determined and annotated. Petrophysical parameters such as porosity and water saturation are determined in order to calculate original hydrocarbons in place and area drained by each completion. Past completions are then mapped and tabulated by HF unit

to document past reservoir drainage and production behavior. This production behavior is a measure of heterogeneity within each architectural unit. Facies architecture and internal heterogeneity are then compared to the facies and position within an IF depositional unit to evaluate any correspondence with outcrop observations.

Subregional Stratigraphic Framework

The Oligocene-age Frio reservoirs of T-C-B field lie within the Norias Deltaic system and Gueydan Fluvial system (Figure 5), as identified by Galloway (1982). The Frio has been divided into the upper, middle, and lower informal members by Galloway (1986). Each member spans 1 to 2 Ma and corresponds to a 3rd-order depositional unit (Mitchum and Van Wagoner, 1991). Further subdivision, down to the 4th-order level, was accomplished by correlating prominent maximum flooding surfaces. Based on their occurrence from 6 to 10 times within a 3rd-order unit, the units bounded by these surfaces are assumed to span approximately 0.1 to 0.6 Ma. These flooding surfaces are correlated from the downdip marine interval, where they can be more easily identified on well logs, into the updip, nonmarine area of T-C-B field. A 100-km-long dip-oriented stratigraphic cross section was constructed with wells spaced approximately every 3-5 km (Figure 6). The Scott and Whitehill reservoirs were found to lie within a single 4th-order unit, with its base being just below the Whitehill and its top being just above the Scott (Figure 6). The Whitehill, then, represents the earliest deposits of sandstone in the T-C-B area during this depositional cycle following maximum flooding, and the Scott represents the last deposits prior to the next maximum flooding.

Architecture of Reservoirs within the Scott/Whitehill Depositional Cycle

The general stratigraphy and architecture of the Scott/Whitehill reservoir interval, a single 4th-order depositional cycle, have been deduced from careful well log correlation. The interval is subdivided into four fifth-order units by laterally continuous surfaces that may correspond to minor marine flooding (Figure 7). Each fifth-order unit ranges in thickness from 6 to 15 m, with each

successive unit generally thickening from the lower Whitehill at the base (6 m) through the upper Scott (15 m) at the top. Assuming equivalent time spans for each unit, this would suggest persistently increasing rates of accommodation.

Sandstones within the Scott/Whitehill interval display symmetrical, blocky, or upward-fining log patterns, range in thickness from 1 m to more than 15 m, and are separated by siltstones and mudstones of similar thickness. Thicker sandstones consist of amalgamated individual channel deposits, each of which reaches a maximum of 6 m in thickness. The dominance of blocky and upward-fining log patterns, the absence of microfauna, and the regional setting all indicate that these sandstones were deposited in an upper delta-plain fluvial setting. Depositional facies identified on the basis of log character include sandy point bar channel deposits, silty to muddy abandoned channel fill, rare sandy splay deposits, silty levee deposits, and fine-grained floodplain mudstones (Figure 7).

The lowermost fifth-order unit, referred to as the lower Whitehill unit, was deposited at the base of the depositional cycle (low accommodation). It is composed entirely of floodplain mudstone throughout the study area. Correlation in the T-C-B area shows no widespread sandstones at this stratigraphic level, but the existence of narrow localized channel deposits has not been ruled out because channel bodies may be narrower than the well spacing used for regional correlation (approximately 2 km apart).

The overlying fifth-order unit, the upper Whitehill unit, in the seaward-stepping to vertically stacked portion of the depositional cycle (low to intermediate accommodation), consists of three relatively narrow (1.5 km wide) but generally thin fluvial channel-belt deposits (Figure 8) separated by large areas of floodplain mudstone. These channel belts are generally dip-elongate and are typically less than 6 m in thickness. Greater thicknesses are the result of vertical stacking of broader channel belts (1.5 km wide) on top of very narrow channel belts (0.5 km wide) at the base of the interval. The comparatively broader channel belts in the middle and upper portion are interpreted to contain two to three incomplete, vertically amalgamated channel deposits, each

ranging from 1.5 to 3 m in thickness. Abandoned channel mudstones are more common in the uppermost channel deposits.

The next highest fifth-order unit, the lower Scott, in the vertically stacked to landward-stepping portion of the depositional cycle (intermediate to high accommodation), is similar to the upper Whitehill except that channel belts tend to be broader (2.5 km wide). Overall, the lower Scott contains a greater volume of sandstone than the underlying upper Whitehill interval.

The upper Scott fifth-order reservoir, at the top of the fourth-order unit and, thus, in the strongly landward-stepping portion of the depositional cycle (high accommodation), differs markedly from the underlying intervals. It is distinctly thicker and sandier, with a single broad channel belt (5.5 km wide) that covers the entire study area and consists of vertically amalgamated channel deposits (Figure 8). Dip-oriented bodies of sandstone having thicknesses in excess of 6 m are the result of two or three vertically amalgamated channel deposits. The geometry of individual channels within the channel belt is not resolvable with well logs, probably because the width of channels is less than the typical well spacing. The uppermost portion of the upper Scott unit is dominated by siltstones and mudstones of abandoned channel, levee, and floodplain deposits (Figure 7).

In summary, from the lower Whitehill fifth-order unit at the base of the fourth-order depositional cycle (lower accommodation) to the upper Scott unit at the top (highest accommodation), there is a progressive change in channel architecture. Individual fifth-order units become thicker upward, and net sandstone percentage increases. Channel belts become wider in each stratigraphically higher unit, and volumes of fine-grained channel-fill deposits, such as upper point bar and abandoned channel fill, increase upward. These features closely correspond to observed architecture in progradational and aggradational channel-fill facies in the outcropping Ferron incised valley channel deposits.

Scott/Whitehill Internal Heterogeneity

Whereas the gross architecture of the reservoir compartments (channel belts) can be identified with reasonable accuracy from well log control, intracompartment heterogeneity cannot. This is because boundaries between individual channelforms potentially occur between wells. In a subsurface setting, the most reliable measure of internal heterogeneity is production performance. The relative size of areas drained in a series of reservoirs is a measure of the internal complexity of the reservoirs, assuming similar drive mechanisms and fluid viscosities.

Reservoir compartment maps have been produced for the upper Whitehill and upper Scott intervals (Figure 8), documenting compartment boundaries and past completions. Structural closure in both cases occurs in areas of subtle highs on a gradually plunging anticlinal nose. The following discussion summarizes the production history of the two reservoirs and estimates drainage areas for successful completions.

The upper Whitehill has produced from two wells, one on the northern structural crest and another on the north flank (Figure 8c), in which perforations were structurally below the documented gas/water contact on the structural crest. Resistivity measurements indicate moderate gas saturations in the southern structure (Figure 8c), but no tests of this potential accumulation have been made. Mapping of channel belts and evidence of tightly carbonate cemented sandstone in one well (Figure 8c) suggest that the northernmost of the two completions is stratigraphically isolated from the structural crest. Volumetric calculations and evidence from wells postdating production indicate that the crestal completion drained approximately 40 acres. At present, insufficient data are available on the other well to document drainage area. Resistivities indicating oil or gas saturation occur in isolated channel belts away from the structural crest, indicating a component of stratigraphic trapping is possible in the upper Whitehill.

Eight wells have produced oil from the upper Scott on the main structural crest (Figure 8d). Cumulative production has ranged from less than 1,000 bbl to more than 54,000 bbl per well. Initial water cuts have varied widely and have been independent of structural position and offset production history, indicating a lack of communication between well locations. Volumetric

analyses suggest that completions have drained areas ranging from less than 1 acre to approximately 5 acres, significantly less than the completion in the Whitehill. Calculations indicate that despite completion at a 20- to 40-acre spacing, and the fact that all current completions are either abandoned, idle, or nearly watered out, less than 10 percent of the original oil in place has been recovered from the Scott.

Although some of the difference in recovery from the Whitehill and the Scott can be attributed to the different mobility ratios of oil and gas, a significant part is attributed to smaller compartment sizes in the Scott zone. This indicates that the upper Scott channel belt (upper portion of depositional cycle, higher accommodation) is much more internally heterogeneous than the upper Whitehill channel belts (lower portion of depositional cycle, lower accommodation).

Scott/Whitehill Summary

As expected from outcrop observations of the Ferron Sandstone, a spectrum of reservoir styles exists within the upper delta-plain deposits of the Frio Formation in T-C-B field (Figure 9). This spectrum is, in part, the result of varying accommodation during deposition of the reservoir sandstones. Reservoirs within 5th-order units range from moderately narrow, internally homogeneous channel belts deposited under conditions of low accommodation in the seaward-stepping portion of a depositional cycle (4th-order unit) to broad internally heterogeneous channel belts laid down under conditions of high accommodation in the landward-stepping phase of a depositional cycle (4th-order unit). These reservoir styles contain varying reserve-growth potential and require very different strategies for optimum development. In general, upper delta-plain fluvial reservoirs in 5th-order units deposited during a landward-stepping period contain the greatest reserve-growth potential and may require the tightest well spacings for optimal reservoir drainage, whereas those deposited during a seaward-stepping period may contain narrow stratigraphically isolated accumulations that are internally homogeneous and present stepout opportunities in mature fields.

Application to Other Reservoir Successions

Our studies of changing reservoir architecture and heterogeneity in an upper delta plain setting provide tremendous insight to production behavior in the T-C-B middle Frio reservoirs. However, other Frio reservoirs will undoubtedly display other vertical trends in characteristics. For example, time-equivalent deposits farther downdip will most likely preserve a greater volume of sandstones within the lower portion of the depositional unit because of greater accommodation, as suggested by Posamentier and Vail (1988). Deposits in the upper part of the downdip depositional unit will likely be mud-dominated as a consequence of decreased sand supply, as sand is preferentially stored in the proximal upper delta plain of the T-C-B area. Thus, specific characteristics of T-C-B reservoirs cannot be used as a model for all Frio fluvial deposits. Instead, studies in other settings must first identify the major flooding surfaces that bound cyclic patterns of deposition and then observe the general trends in sandstone percent and channel belt architecture before predicting between-well heterogeneity.

The above discussion of changing architecture and heterogeneity through a cycle focuses on accommodation trends. However, both the volume and grain size of sediment supplied, as well as physiography, can affect facies variability. The potential control that these factors can exert is recognized, but the relative importance of each has not been defined because of the limited scope of the subsurface study. Additional detailed studies are needed in a variety of settings to document the range of variability within low-frequency systems tracts. Ideally, those investigations will be able to quantify volumes and type of sediment within each high-frequency unit to clarify the changing role of sediment supply throughout a high-frequency depositional cycle. Outcrop investigations, such as those of the Ferron Sandstone, provide critical data that helps constrain reservoir interpretations.

Implications

The model described for the Scott and Whitehill interval only addresses reservoirs deposited in an upper delta-plain fluvial setting. However, it represents a new generation of models for

reservoir characterization. Because rates of accommodation can be demonstrated to control sandstone body architecture and internal heterogeneity, and because these effects are different for each depositional setting but can be documented from outcrop work or implied from careful subsurface study, other models can be developed for reservoirs deposited in a spectrum of depositional settings. Any such models would ideally be based on outcrop observations because continuous lateral exposures are critical for identifying geometries and permeability characteristics of the surfaces that bound potential reservoir compartments. Further understanding of the cyclic nature of the stratigraphic record and the controls on that cyclicity will provide more accurate models and supply more specific guidelines for their application in various depositional settings.

The predictive nature of these new models will improve the accuracy of reservoir characterization studies and increase the use of reservoir characterization by operators of mature fields. The outcome will undoubtedly be increased recovery of oil and gas from reservoirs that otherwise might have been abandoned prematurely. This increased production will thus prevent permanent loss of vital hydrocarbon resources.

CONCLUSIONS

Outcrop observations from the Cretaceous Ferron Sandstone of central Utah demonstrate that facies associations within a given depositional system vary progressively through both intermediate- and high-frequency depositional units. This is exemplified by changes from narrow, internally homogeneous incised valley fills characterized by vertical stacking of channelforms in IF units in the seaward-stepping part of a LF unit to broad, internally heterogeneous incised valley fills exhibiting lateral stacking of channelforms in IF units in the landward-stepping part of a LF unit. HF units vary within single IF units as delta front deposits progress from laterally heterogeneous fluvial-dominated successions in the early lowstand to more homogeneous, strike-oriented wave-dominated successions in the late lowstand.

These systematic changes are also observed in Oligocene Frio Formation reservoirs of the south Texas Gulf Coast. Changes in facies associations in subsurface reservoirs were accompanied

by dramatic changes in production behavior, requiring different reservoir management approaches and presenting varying opportunities for significant reserve growth potential. Upper delta plain fluvial channel belts deposited early in a depositional cycle are narrow, internally homogeneous, and may present reserve-growth opportunities in off-crest, stratigraphically isolated settings. In contrast, channel belts deposited late in the cycle are broad, internally heterogeneous, and are poorly contacted by typical completion spacings, resulting in significant remaining resources following conventional development.

Facies variability in these fluvial-deltaic successions corresponds with the position of a deposit within a depositional cycle that progresses from low accommodation to high accommodation. Although accommodation appears to be a strong controlling factor, changes in sediment supply and physiography may also exert controls on deposition and preservation. Further investigations are required to identify the possible effects of these controls and to document changes in a broader spectrum of depositional systems. A more complete understanding of facies variability within a depositional cycle will provide an important new technology that will allow the prediction of between-well architecture and heterogeneity in mature reservoirs, ultimately resulting in the improved identification and recovery of tremendous volumes of remaining resources.

REFERENCES CITED

Barton, M. D.., 1994, Outcrop characterization of architecture and permeability structure in fluvial-deltaic sandstones, Cretaceous Ferron Sandstone, Utah: University of Texas at Austin, Ph.D. dissertation, 259 p.

Barton, M. D., 1995, Sequence stratigraphy, facies architecture, and permeability structure of fluvial-deltaic reservoir analogs: Cretaceous Ferron Sandstone, Central Utah (Ferron GRI Fieldtrip Guidebook), Bureau of Economic Geology, The University of Texas at Austin, Austin, Texas, 139 p.

Cant, D. J., 1982, Fluvial facies models and their application, *in* P. A. Scholle and D. Spearing, Sandstone depositional environments, The American Association of Petroleum Geologists, Tulsa, Oklahoma, p. 115–138.

Coleman, J. M., 1982, Deltas: Processes of deposition and models for exploration, International Human Resources Development Corporation, Boston, 124 p.

Cross, T. A., et al, 1993, Applications of high-resolution sequence stratigraphy to reservoir analysis, *in* R. Eschard, B. Doligez, eds., Subsurface reservoir characterization from outcrop observations, Editions Technip, Paris, p. 11–33.

Duncan, E. A, 1983, Delineation of delta types: Norias delta system, Frio Formation, South Texas, Gulf Coast Association of Geological Societies Transactions, v. 33, p. 269–273.

Galloway, W. E., 1982, Depositional architecture of Cenozoic Gulf Coastal Plain fluvial systems, *in* Ethridge, F. G., and Flores, R. M., eds., Recent and ancient nonmarine depositional environments: models for exploration: Society of Economic Paleontologists and Mineralogists, Special Publication 31, p. 127–155.

_____.1986, Depositional and structural framework of the distal Frio Formation, Texas coastal zone and shelf: The University of Texas at Austin, Bureau of Economic Geology Geological Circular 86-8, 16 p.

_____ 1989a, Genetic stratigraphic sequences in basin analysis I: architecture and genesis of flooding-surface bounded depositional units: American Association of Petroleum Geologists Bulletin, v. 73, p. 125–142.

_____ 1989b, Genetic stratigraphic sequences in basin analysis II: application to northwest Gulf of Mexico Cenozoic Basin: American Association of Petroleum Geologists Bulletin, v. 73, no. 2, p. 143–154.

Gardner, M. N.., 1993, Sequence stratigraphy and facies architecture of the Upper Cretaceous Ferron Sandstone Member of the Mancos Shale, East-Central Utah: Colorado School of Mines, Ph.D. dissertation, 528 p.

Goldhammer, R. K., Dunn, P. A., and Hardie, L. A., 1990, Depositional cycles, composite sea-level changes, cycle stacking patterns, and the hierarchy of stratigraphic forcing: Examples from Alpine Triassic platform carbonates, Geological Society of America Bull., v. 102, p. 535–562.

Hale, L. A.., 1972, Depositional history of the Ferron Formation, central Utah, in plateau basin and range transition zone: Utah Geological Association, p. 115-138.

Horne, J. C., et al., 1978, Depositional models in coal exploration and mine planning in Appalachian region, American Association of Petroleum Geologists Bulletin, v. 62, no. 12, p. 2379–2411.

Jervey, M. T.., 1988, Quantitative geological modeling of siliciclastic rock sequences and their seismic expression, *in* C. K. Wilgus, B. S. Hastings, C. G. St. C. Kendall, H. W. Posamentier, C. A. Ross, and J. C. Van Wagoner, eds., Sea-level changes: an integrated approach: Society of Petroleum Engineers Special Publication No. 42, p. 47-69.

Kerans, C., and Fitchen, W. M., 1995, Sequence hierarchy and facies architecture of a carbonate-ramp system: San Andres Formation of Algerita Escarpment and Western Guadalupe Mountains, West Texas and New Mexico: The University of Texas at Austin, Bureau of Economic Geology Report of Investigations No. 235, 86 p.

Knox, P. R., and McRae, L. E., 1995, Application of sequence stratigraphy to the prioritization of incremental growth opportunities in mature fields: an example from Frio fluvial-deltaic sandstones, TCB field, South Texas: Gulf Coast Association of Geological Societies Transactions, v. 45, p. 341–359.

Mitchum, R. M., and Van Wagoner, J. C., 1991, High-frequency sequences and their stacking patterns: sequence-stratigraphic evidence of high-frequency eustatic cycles: Sedimentary Geology, v. 70, p. 131-160.

Posamentier, H. W., Jervey, M. T., and Vail, P. R., 1988, Eustatic controls on clastic deposition Iconceptual framework, *in* C. K. Wilgus, B. S. Hastings, C. G. St. C. Kendall, H. W. Posamentier, C. A. Ross, and J. C. Van Wagoner, eds., Sea-level changes: an integrated approach: Society of Economic Paleontologists and Mineralogists Special Publication No. 42, p. 109-124.

Posamentier, H. W., and Vail, P. R., 1988, Eustatic controls on clastic deposition II sequence and systems tract models, *in* C. K. Wilgus, B. S. Hastings, C. G. St. C. Kendall, H. W. Posamentier, C. A. Ross, and J. C. Van Wagoner, eds., Sea-level changes: an integrated approach: Society of Economic Paleontologists and Mineralogists Special Publication No. 42, p. 125-154.

Ryer, T. A.., 1981, Deltaic coals of the Ferron Sandstone Member of the Mancos Shale: Predictive model for Cretaceous coal-bearing strata of the Western Interior: American Association of Petroleum Geologists Bulletin, v. 65, no. 11, p. 2323-2340.

Ryer T. A.., 1993, The autochthonous component of cyclicity in shoreline deposits of the Upper Cretaceous Ferron Sandstone, central Utah. American Association of Petroleum Geologists Bulletin (Abstr.), v. 77, p. 175.

Selley, R. C., 1978, Ancient sedimentary environments, Second Edition, Cornell University Press, Ithaca, New York, 287 p.

Sonnenfeld, M. D., 1991, High-frequency cyclicity within shelf-margin and slope strata of the upper San Andres sequence, Last Chance Canyon, *in* S. Meader-Roberts, M. P. Candelaria, and G. E. Moore, eds., Sequence stratigraphy, facies, and reservoir geometries of the San Andres, Grayburg, and Queen Formations, Guadalupe Mountains, New Mexico and Texas: Permian Basin Section, Society of Economic Paleontologists and Mineralogists Publication 91-32, p. 11–51.

Swift, D. J. P., Oertal, G. F., Tillman, R. W., and Thorne, J. A., 1991, Shelf sand and sandstone bodies: Geometries, facies, and sequence stratigraphy, International Association of Sedimentologists Special Publication No. 14, 532 p.

Tyler, Noel, and Finley, R. J., 1991, Architectural controls on the recovery of hydrocarbons from sandstone reservoirs, *in* Miall, A. D., and Tyler, Noel, eds., The three-dimensional facies architecture of terrigenous clastic sediments and its implications for hydrocarbon discovery and recovery: Society of Economic Paleontologists and Mineralogists, Concepts in Sedimentology and Paleontology, v. 3, p. 1–5.

Vail, P. R., Mitchum, R. M., Todd, R. G., Widmier, J. M., Thompson, S. III, Sangree, J. B., Bubb, J. N., and Hatlelid, W. G., 1977, Seismic stratigraphy and global changes of sea-level, *in* C. W. Payton, ed., Seismic stratigraphic applications to hydrocarbon exploration: AAPG Memoir No. 26, p. 49–212.

Van Wagoner, J. C., Mitchum, R.C., Campion, K. M., and Rahmanian, V. D., 1990, Siliciclastic sequence stratigraphy: American Association of Petroleum Geologists Methods in Exploration Series, No. 7, p. 55.

Walker, R. G., 1979, Facies models, First Edition, Geoscience Canada Reprint Series, 1, Toronto, Ontario, 317 p.

FIGURE CAPTIONS

Figure 1. Location of Ferron Sandstone outcrops along the northwest flank of the San Rafael Swell in central Utah. Observations at indicated localities are discussed in the text.

Figure 2. Schematic cross-section depicting stratigraphic relationships within the five intermediate-frequency cycles of the Ferron sandstone.

Figure 3. Map view and cross-sections of incised valleys in the Ferron Sandstone from a low-accommodation (cycle 2) setting at the I-70 outcrop (a) and a high-accommodation (cycle 5) setting at the Muddy Creek outcrop (b).

Figure 4. Model showing evolution of Ferron depositional system during an intermediate-frequency relative sea level cycle in the Ferron sandstone. Wave-dominated shoreline systems develop during increases in relative sea level, whereas fluvial incision and river-dominated shoreline systems develop during falling relative sea level. Intermediate-frequency genetic units in seaward-stepping portions of the Ferron lack substantial transgressive deposits.

Figure 5. Location of the Tijerina-Canales-Blucher (T-C-B) field within the Frio Fluvial-Deltaic Sandstone (Vicksburg Fault Zone) Play in south Texas. Also shown are the major depositional systems active during Frio deposition, as defined by Galloway (1982). Cross section A-A' is shown in Figure 6.

Figure 6. Dip-oriented stratigraphic cross section A-A' through the Frio Formation from updip of T-C-B field down to the present coastline. The Frio consists of three 3rd-order genetic units, each containing many 4th-order units (not all of which are shown). See Figure 5 for cross-section location.

Figure 7. Dip-oriented cross section B-B' showing the Scott/Whitehill 4th-order genetic unit, which contains at least four 5th-order genetic units. These are, from top down, the upper and lower Scott and the upper and lower Whitehill reservoir intervals. Cross-section location is given in Figure 8.

Figure 8. Net sandstone maps for the upper Whitehill (a) and upper Scott (b) reservoirs and compartment maps of the upper Whitehill (c) and upper Scott (d) reservoirs. Narrow, stratigraphically isolated channel belts of the upper Whitehill interval were deposited in the proximal upper delta plain during the early part of a depositional cycle, whereas the broad, internally complex channel belt of the upper Scott interval was deposited during the latest portion of a depositional cycle.

Figure 9. Spectrum of upper delta plain fluvial reservoir architecture, internal heterogeneity, production characteristics, and reserve-growth potential in the Scott/Whitehill interval.

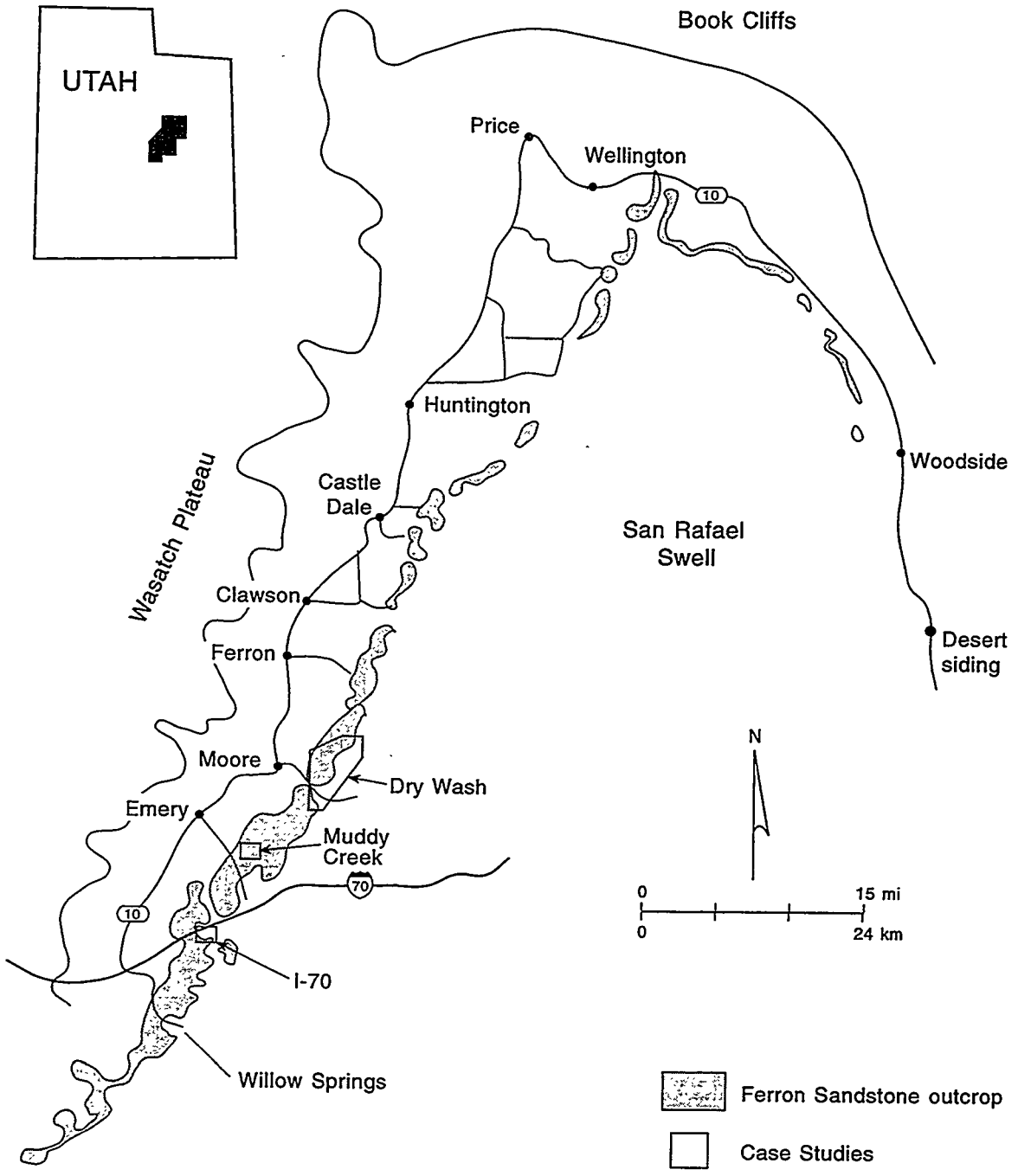
UTAH
Book Cliffs
Price
Wellington
10
Huntington
Woodside
Castle
Dale
Wasatch Plateau
San Rafael
Swell
Clawson
Ferron
Desert
siding
N
Moore
Dry Wash
Emery
Muddy
Creek
70
10
0
15 mi
0
24 km
I-70
Willow Springs
Ferron Sandstone outcrop
Case Studies

Figure 1

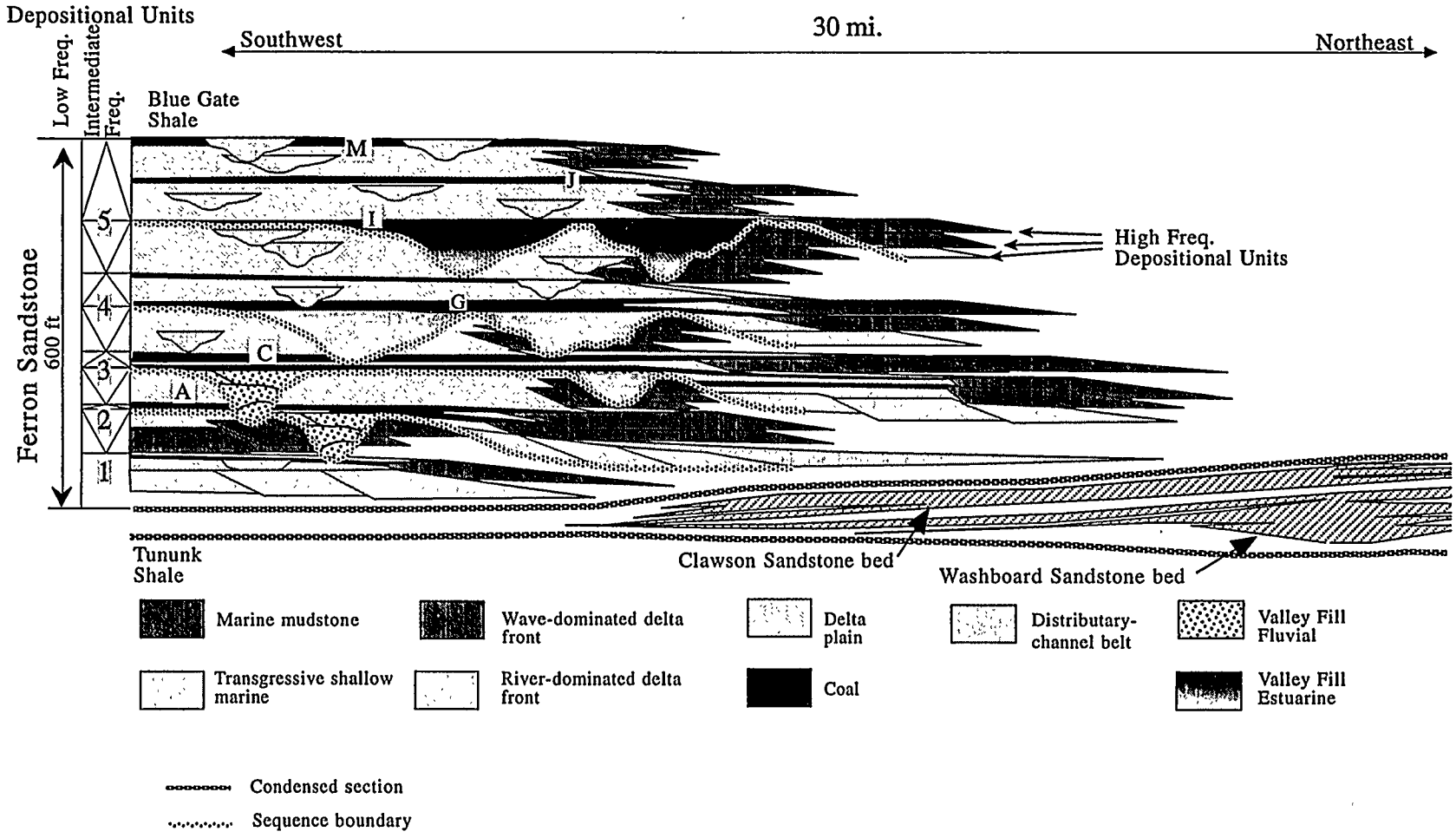

Figure 2. Schematic cross-section depicting stratigraphic relationships of Ferron Sandstone in central Utah.

Figure 2

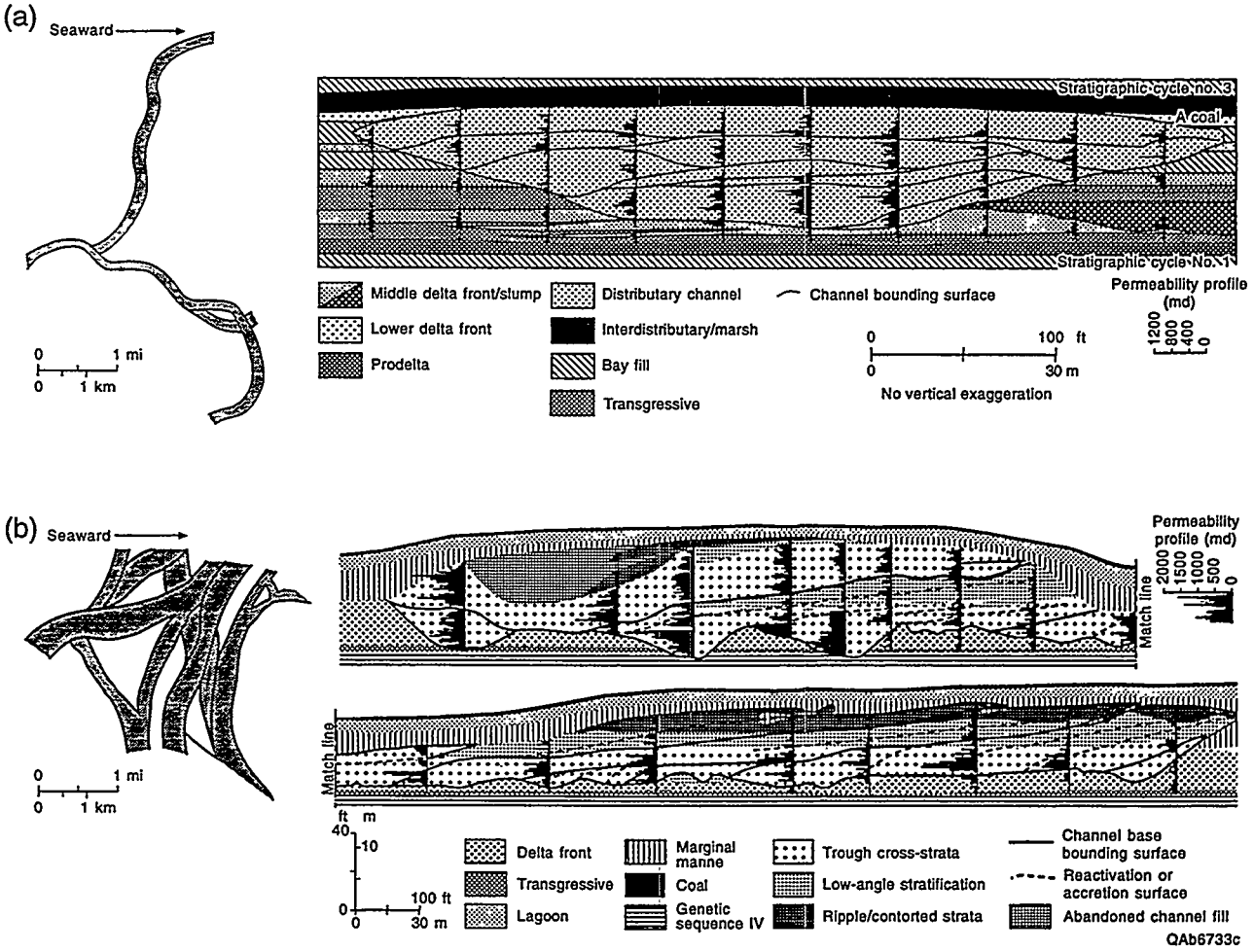
(a)
Seaward
0 1 mi
0 1 km
Stratigraphic cycle no. 3
A coal
Stratigraphic cycle No. 1
Permeability profile (md)
1200
800
400
0
Middle delta front/slump
Lower delta front
Prodelta
Distributary channel
Interdistributary/marsh
Bay fill
Transgressive
Channel bounding surface
0 100 ft
0 30 m
No vertical exaggeration
(b)
Seaward
0 1 mi
0 1 km
Permeability profile (md)
2000
1500
1000
500
0
Match line
Match line
ft m
40
10
0
100 ft
0 30 m
Delta front
Transgressive
Lagoon
Marginal manne
Coal
Genetic sequence IV
Trough cross-strata
Low-angle stratification
Ripple/contorted strata
Channel base bounding surface
Reactivation or accretion surface
Abandoned channel fill
QAb6733c

Figure 3

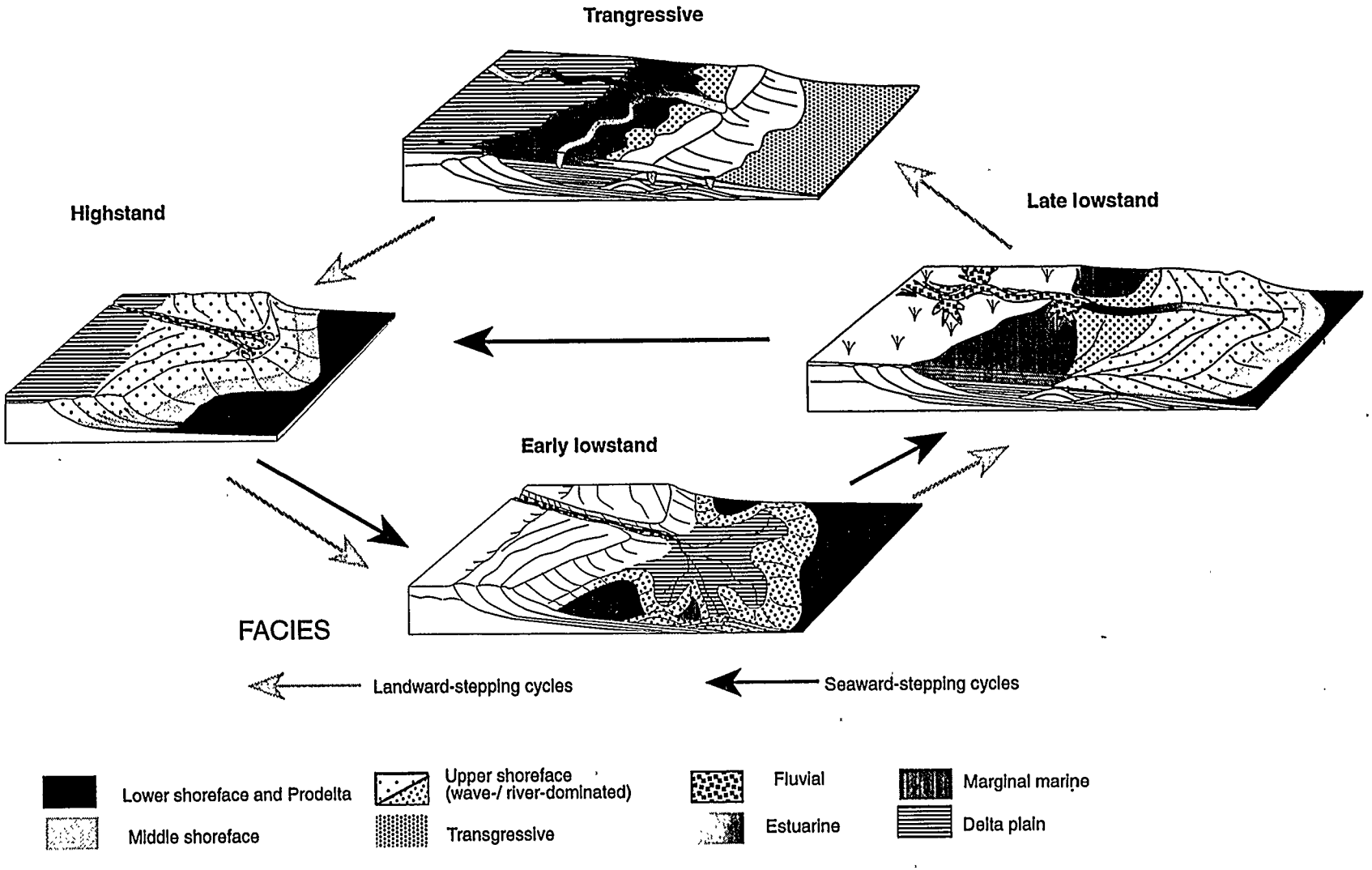
Trangressive
Late lowstand
Highstand
Early lowstand
FACIES
Landward-stepping cycles
Seaward-stepping cycles
Lower shoreface and Prodelta
Middle shoreface
Upper shoreface (wave-/ river-dominated)
Transgressive
Fluvial
Estuarine
Marginal marine
Delta plain

Figure 4

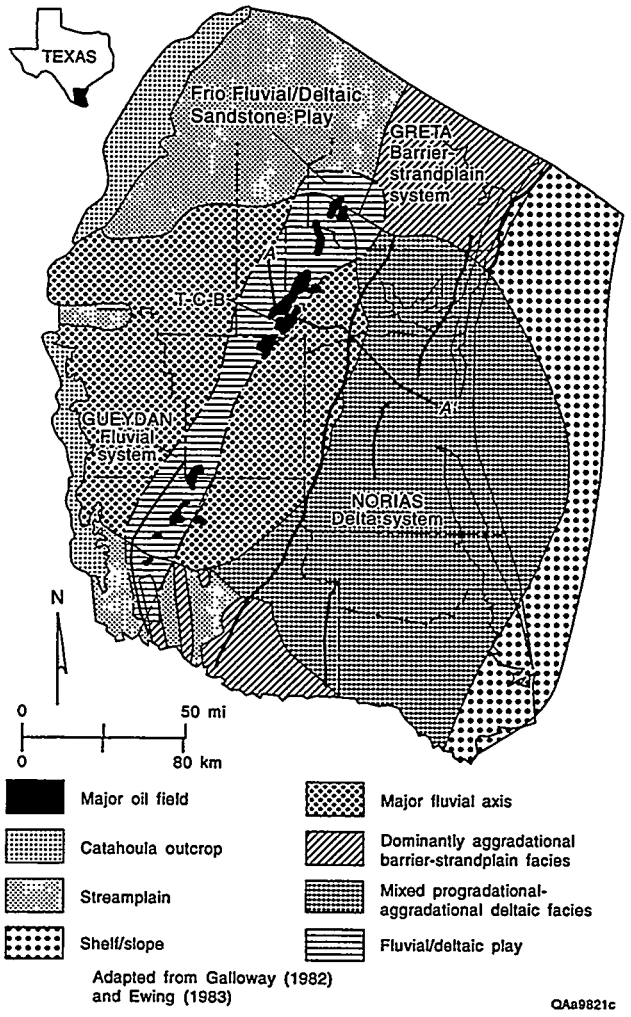
TEXAS
Frio Fluvial/Deltaic Sandstone Play
GRETA Barrier-strandplain system
T-C-B
GUEYDAN Fluvial system
NORIAS Deltaic system
A
A'
N
0
50 mi
0
80 km
Major oil field
Catahoula outcrop
Streamplain
Shelf/slope
Major fluvial axis
Dominantly aggradational barrier-strandplain facies
Mixed progradational-aggradational deltaic facies
Fluvial/deltaic play
Adapted from Galloway (1982) and Ewing (1983)
QAa9821c

Figure 5

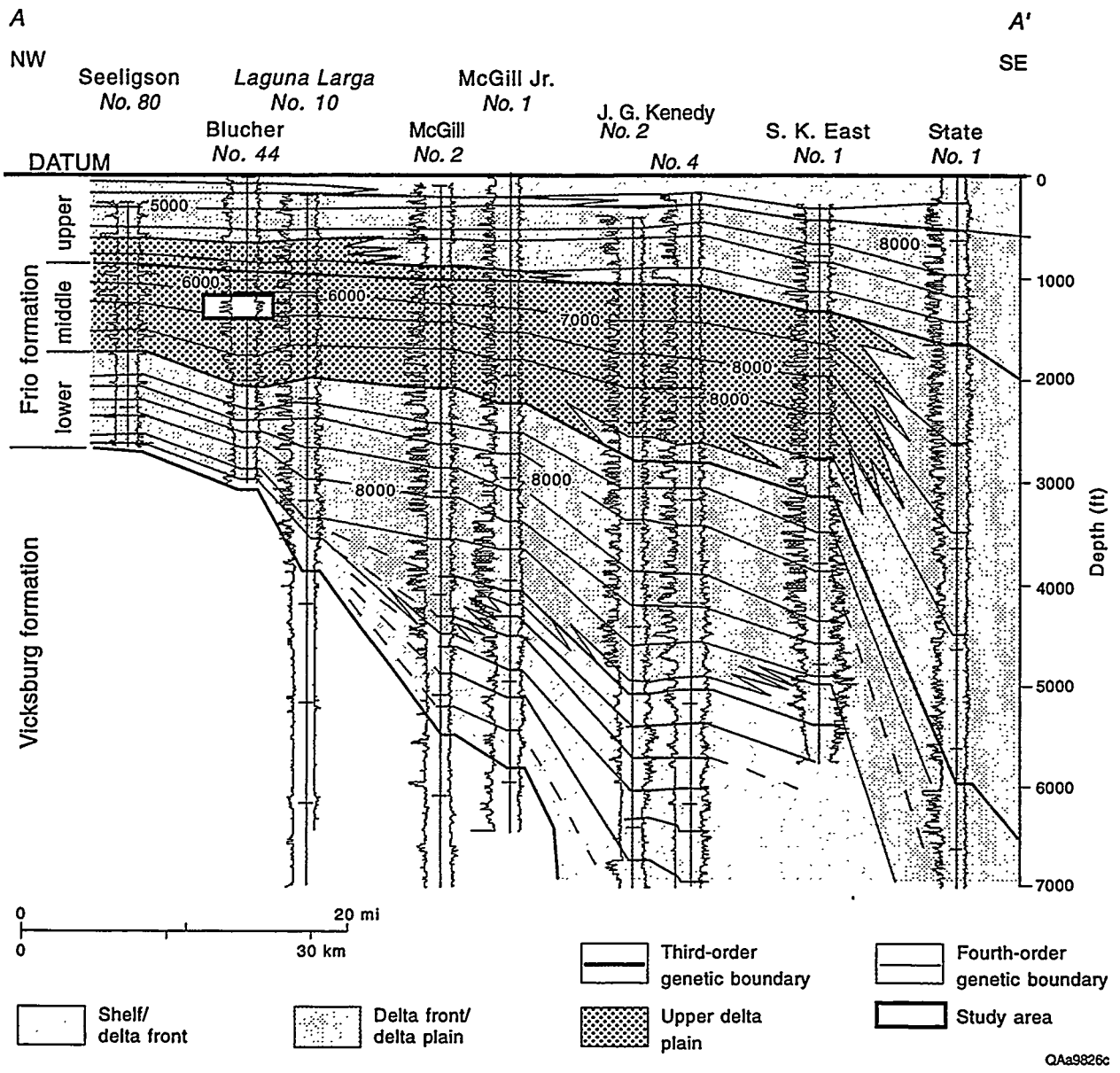
A
NW
A'
SE
Seeligson No. 80
Laguna Larga No. 10
McGill Jr. No. 1
Blucher No. 44
McGill No. 2
J. G. Kenedy No. 2
No. 4
S. K. East No. 1
State No. 1
DATUM
upper
middle
lower
Frio formation
Vicksburg formation
5000
6000
7000
8000
Depth (ft)
0
1000
2000
3000
4000
5000
6000
7000
0
20 mi
0
30 km
Third-order genetic boundary
Fourth-order genetic boundary
Shelf/ delta front
Delta front/ delta plain
Upper delta plain
Study area
QAa9826c

Figure 6

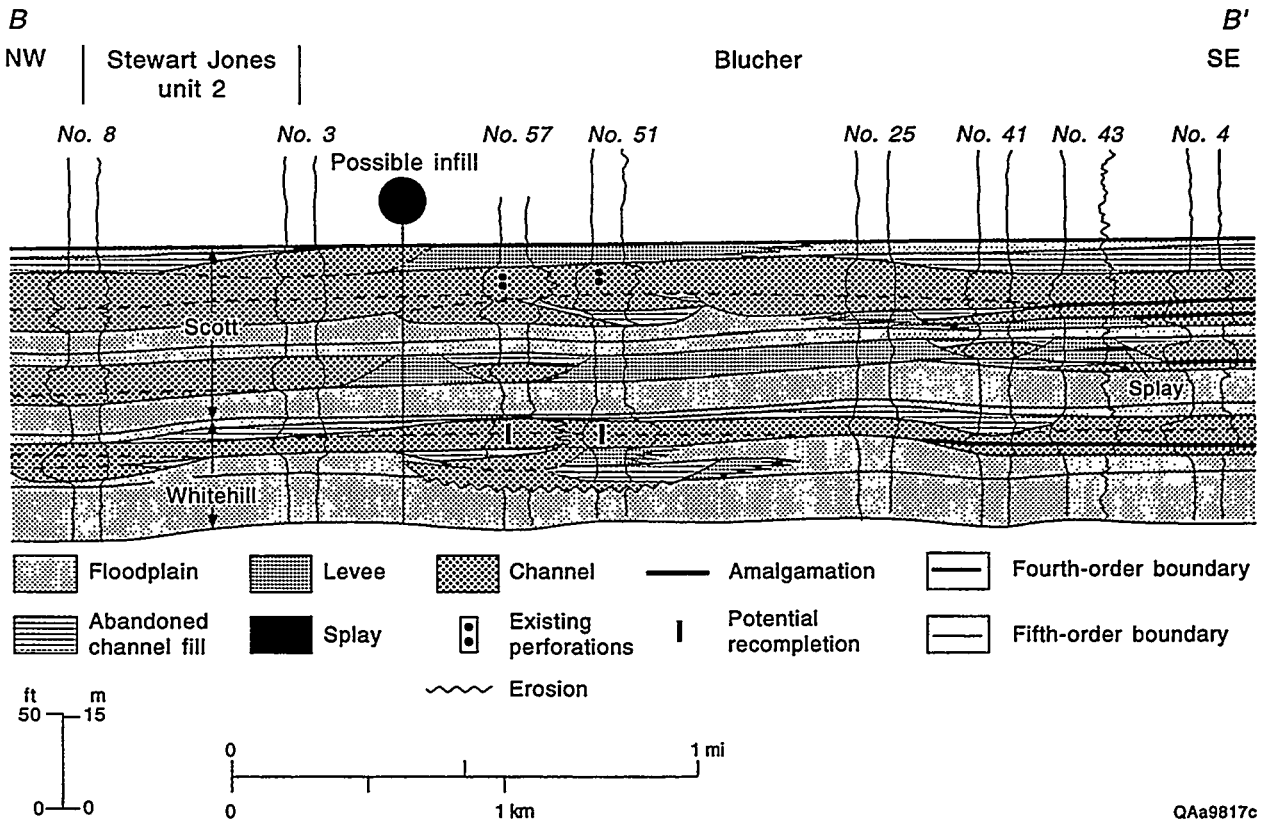
B
B'
NW
Stewart Jones unit 2
Blucher
SE
No. 8
No. 3
No. 57
No. 51
No. 25
No. 41
No. 43
No. 4
Possible infill
Scott
Splay
Whitehill
Floodplain
Levee
Channel
Amalgamation
Fourth-order boundary
Abandoned channel fill
Splay
Existing perforations
Potential recompletion
Fifth-order boundary
Erosion
ft
m
50
15
0
0
0
1 mi
0
1 km
QAa9817c

Figure 7

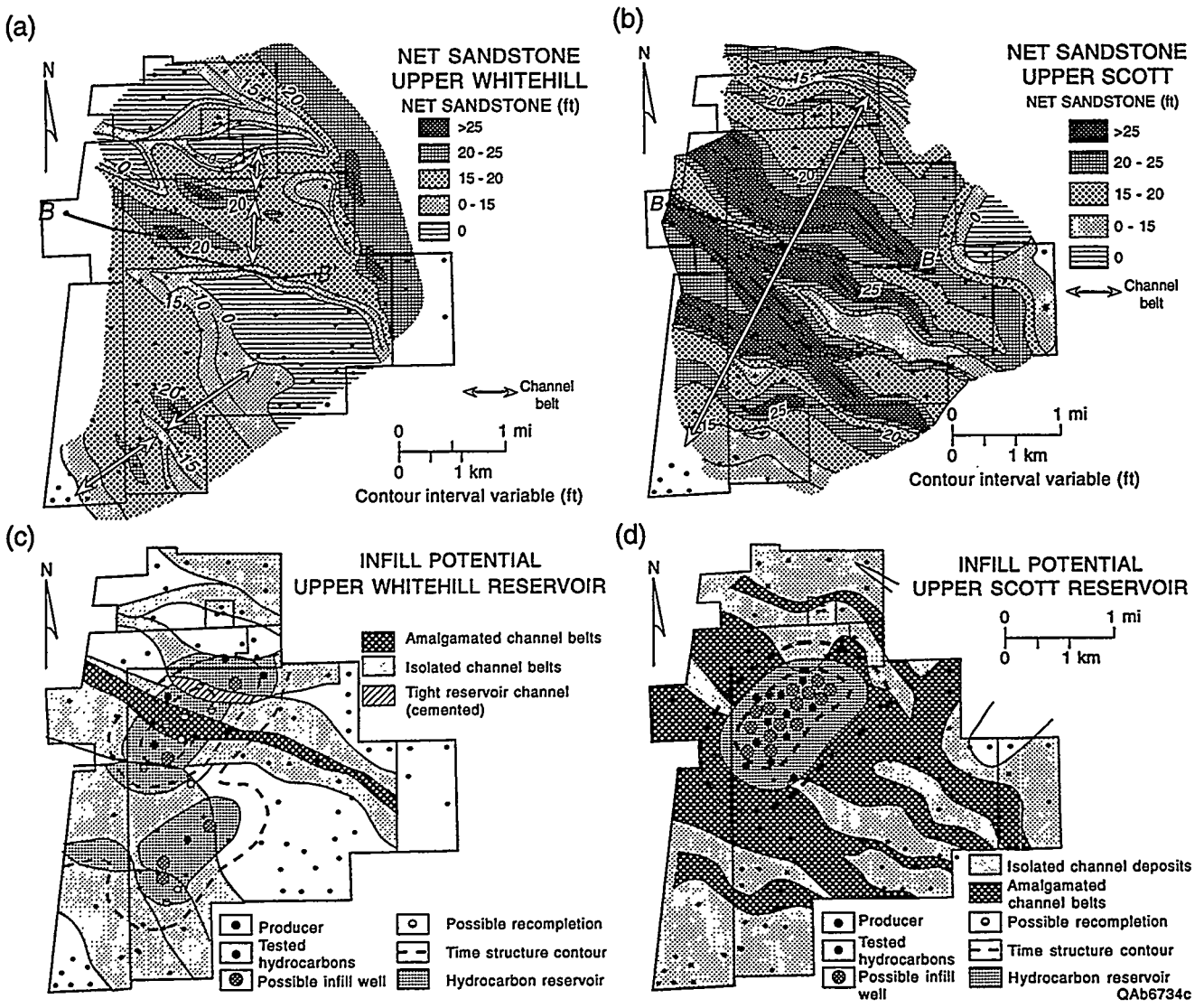
(a)
NET SANDSTONE
UPPER WHITEHILL
NET SANDSTONE (ft)
>25
20 - 25
15 - 20
0 - 15
0
Channel belt
0 1 mi
0 1 km
Contour interval variable (ft)
(b)
NET SANDSTONE
UPPER SCOTT
NET SANDSTONE (ft)
>25
20 - 25
15 - 20
0 - 15
0
Channel belt
0 1 mi
0 1 km
Contour interval variable (ft)
(c)
INFILL POTENTIAL
UPPER WHITEHILL RESERVOIR
Amalgamated channel belts
Isolated channel belts
Tight reservoir channel (cemented)
Producer
Tested hydrocarbons
Possible infill well
Possible recompletion
Time structure contour
Hydrocarbon reservoir
(d)
INFILL POTENTIAL
UPPER SCOTT RESERVOIR
0 1 mi
0 1 km
Isolated channel deposits
Amalgamated channel belts
Producer
Tested hydrocarbons
Possible infill well
Possible recompletion
Time structure contour
Hydrocarbon reservoir
QAb6734c

Figure 8

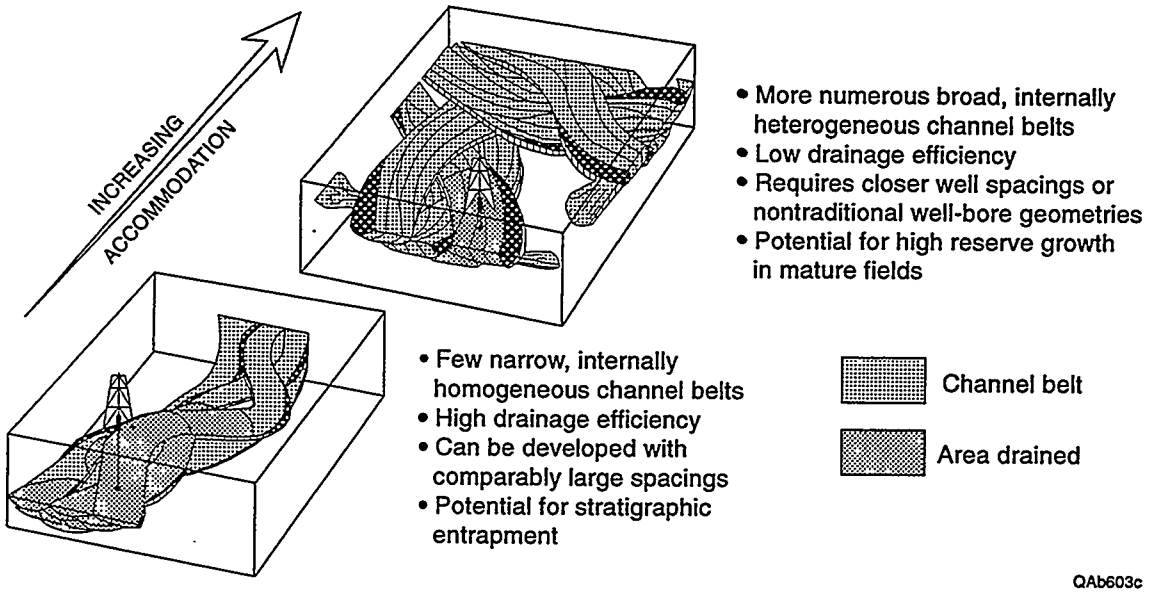
INCREASING ACCOMMODATION
• More numerous broad, internally heterogeneous channel belts
• Low drainage efficiency
• Requires closer well spacings or nontraditional well-bore geometries
• Potential for high reserve growth in mature fields
• Few narrow, internally homogeneous channel belts
• High drainage efficiency
• Can be developed with comparably large spacings
• Potential for stratigraphic entrapment
Channel belt
Area drained
QAb603c

Figure 9

Reducing Uncertainty in Geostatistical Description With Well Testing Pressure Data

Albert C. Reynolds[1], Nanqun He[1] and Dean S. Oliver[2]

1 Department of Petroleum Engineering, University of Tulsa, Tulsa, OK 74104

2 Chevron Petroleum Technology Company, P. O. Box 446, La Habra, CA 90633

ABSTRACT

Geostatistics has proven to be an effective tool for generating realizations of reservoir properties conditioned to static data, e.g., core and log data and geologic knowledge. Due to the lack of closely spaced data in the lateral directions, there will be significant variability in reservoir descriptions generated by geostatistical simulation, i.e., significant uncertainty in the reservoir descriptions. In past work, we have presented procedures based on inverse problem theory for generating reservoir descriptions (rock property fields) conditioned to pressure data and geostatistical information represented as prior means for log-permeability and porosity and variograms. Although we have shown that the incorporation of pressure data reduces the uncertainty below the level contained in the geostatistical model based only on static information (the prior model), our previous results assumed did not explicitly account for uncertainties in the prior means and the parameters defining the variogram model.

In this work, we investigate how pressure data can help detect errors in the prior means. If errors in the prior means are large and are not taken into account, realizations conditioned to pressure data represent incorrect samples of the a posteriori probability density function for the rock property fields, whereas, if the uncertainty in the prior mean is incorporated properly into the model, one obtains realistic realizations of the rock property fields.

ACKNOWLEDGEMENTS

This work was supported by a grant from the Strategic Research Department of Chevron Petroleum Technology Company and the member companies of Tulsa University Petroleum Reservoir Exploitation Projects (TUPREP). This support is gratefully acknowledged. Yafes Abacioglu, who also has implemented the techniques presented here, reviewed the manuscript and offered constructive comments.

INTRODUCTION

Our objective is to generate realizations of three-dimensional rock property fields (simulator gridblock values of log-permeability and porosity) conditioned to a prior model and well-test pressure data. The prior model is based on a multivariate Gaussian distribution with known covariance matrix and uncertain prior means. As in previous related work (e.g., Oliver, 1994; Chu et al., 1995a; Reynolds et al., 1995; He et al., 1996), the prior covariance matrix can be derived from given variograms for the log-permeability and porosity fields and the associated cross-variograms.

Unlike the past work mentioned above, we specifically account for uncertainty in the prior means by introducing a partially doubly stochastic prior model using basic ideas described in Tjelmeland et al. (1994). Our basic procedure for generating realizations of the rock property fields relies on generating the joint probability density function (pdf) for the rock property fields and the errors in the prior means conditioned to pressure data, and then sampling this pdf to obtain realizations. Although we do not have permission to publish the actual data here, this work was actually motivated by a field study in which we found that the prior mean for permeability was significantly overestimated in the geostatistical model and resulted in unrealistic descriptions of the permeability field if the realizations of the permeability field were conditioned to pressure data without accounting for the uncertainty in the prior mean.

An efficient procedure for sampling the pdf is obtained by adapting ideas and techniques presented in Oliver (1996) and Oliver et al. (1996a) to the problem considered here. A procedure for generating the maximum a posteriori estimates of the rock property fields and prior means is also presented. Specific realizations and maximum a posteriori estimates are generated by minimizing an appropriate objective function using the Gauss-Newton method. Sensitivity coefficients are computed using the procedure presented by He et al. (1996).

It is important to note that our objective in generating realizations of rock property fields is to obtain a set of realizations which represent a correct sampling of the probability density function for the rock property fields. By making a performance prediction with each realization, one can then evaluate the uncertainty in the predicted parameters, e.g., break through time or cumulative oil production. If one simply generates a set of realizations that honor all the data, but the set does not provide a correct sampling of the probability density function, we know of no feasible procedure for evaluating the uncertainty in performance predictions.

RESERVOIR MODEL

The reservoir is assumed to be a rectangular parallelepiped of uniform thickness h. Reservoir boundaries are assumed to be no-flow boundaries. Three-dimensional single-phase flow in a Cartesian coordinate system is considered. The reservoir can contain any number of complete-penetration or restricted-entry vertical wells. Each well is produced at a specified rate where the rate may vary with time; pressure buildup at a well is simulated by setting the rate to zero subsequent to a producing period. Interference or observation wells are simulated by setting the rate to zero at all times. Fluid properties are assumed to be known. We assume a slightly compressible fluid of constant compressibility and viscosity. In all results, the values of the following parameters are fixed: $c_t = 10^{-5}$ psi^{-1}, $\mu = 0.8$ cp. and $r_w = 0.3$ ft at all wells.

The permeability and porosity fields are assumed to be heterogeneous. Permeability may be either isotropic or anisotropic, but we assume that the principal axes of permeability coincide with the directions of the x-y-z coordinate system, i.e., the only permeabilities involved are k_x, k_y and k_z. The variogram for each permeability field may be anisotropic. The variogram for porosity may also be anisotropic. Permeability attributes (k_x, k_y and k_z) are assumed to have

log-normal distributions with variances given by $\sigma^2_{k_x}$, $\sigma^2_{k_y}$ $\sigma^2_{k_z}$. Porosity is assumed to be normal with variance given by σ^2_ϕ. Each rock property attribute is modeled as a stationary Gaussian random function so that the covariance functions are directly related to the variograms (Journal and Huijbregts, 1978). The correlation coefficients between the various attributes are assumed to be known, but may be zero. As discussed in more detail later, prior estimates of the means of the attributes are assumed to be uncertain.

As indicated in the preceding paragraph, our model is quite general, however, the specific examples presented here pertain to a case where $k_x = k_y = k$ and $k_z = 0.1k$ at all gridblocks. Thus, in generating realizations of the rock property fields, realizations of porosity and $\ln(k)$ are generated and the corresponding realizations for the vertical permeability field is determined explicitly via the relation $k_z = 0.1k$ which is applied at each gridblock. As in Chu et al. (1995), the cross variogram between porosity and log-permeability is generated using the screening hypothesis of Xu et al. (1992). This eliminates the necessity of specific modeling of the cross variogram.

For given rock property fields, pressure responses are obtained by a standard purely-implicit, seven-point finite-difference simulator, where wellbore pressure is related to the well's gridblock pressures by Peaceman's method (1983); see Chu et al. (1995a) and He et al. (1996). To test the procedures used to resolve rock property fields, a simulator is used to generate synthetic multiwell pressure data, which is then assumed to represent measured wellbore pressure data.

Prior and A Posteriori Probability Density Functions

N denotes the number of simulator gridblocks. For the specific problems considered here, the rock property model, or vector of rock property model parameters, is given by

$$m = \begin{bmatrix} m_\phi \\ m_k \end{bmatrix}, \tag{1}$$

where m_ϕ is the N-dimensional column vector of gridblock porosities, m_k is the N-dimensional column vector of gridblock values of $\ln(k)$. Note the dimension of m is $N_p = 2N$. To use standard notation from probability theory, we let M denote the random vector of rock property model parameters, with specific realizations denoted by m given in Eq. 1. For a fully anisotropic permeability field, the model m must be modified so that it includes components for $\ln(k_x)$, $\ln(k_y)$, $\ln(k_z)$ and porosity and the covariance matrix given by Eq. 2 below must also be modified; see He et al. (1996).

As in our past work (Oliver, 1994; He et al., 1996; Oliver et al., 1996a), the prior model is assumed to have a multivariate Gaussian probability density function with prior covariance matrix, C_M. For the specific examples given here, C_M is given by

$$C_M = \begin{bmatrix} C_\phi & C_{\phi k} \\ C_{\phi k} & C_k \end{bmatrix}, \tag{2}$$

where C_ϕ is the covariance matrix for gridblock porosities derived from the porosity variogram, C_k is the covariance matrix for gridblock $\ln(k)$'s derived from the variogram for $\ln(k)$, $C_{\phi k}$ is the cross covariance matrix between porosity and $\ln(k)$ at the set of gridblocks.

Throughout, m_{prior} is the vector containing the prior means of the model parameters, i.e,

$$m_{prior} = \begin{bmatrix} m_{prior,\phi} \\ m_{prior,k} \end{bmatrix}. \tag{3}$$

Since $\ln(k)$ and porosity are modeled as stationary random functions in the prior model, $m_{prior,\phi}$ and $m_{prior,k}$ are treated as constant vectors although the general formulation presented allows each entry of m_{prior} to be different. The random vector Θ represents the error in or correction to m_{prior} with θ denoting specific realizations of Θ. Introduction of Θ allows for the incorporation of uncertainty in the vector of prior means, whereas, in our past work, (Oliver, 1994; He et al., 1996; Oliver et al., 1996), we assumed no error in m_{prior}. The pdf for Θ is assumed to be Gaussian and is given by

$$p_\Theta(\theta) = a \exp\Big(-\frac{1}{2}(\theta - \theta_0)^T C_\Theta^{-1}(\theta - \theta_0)\Big), \tag{4}$$

where θ_0 is the mean or expectation of the random vector Θ and C_Θ is the associated covariance matrix. In this work, we assume that errors in the prior means are independent so C_Θ is a diagonal matrix. Although it is appropriate to choose $\theta_0 = 0$, the derivation is done for any value of θ_0. The conditional distribution (pdf) of M given $\Theta = \theta$ is given by

$$p_{M|\Theta}(m|\theta) = a \exp\Big(-\frac{1}{2}(m - m_{prior} - \theta)^T C_M^{-1}(m - m_{prior} - \theta)\Big). \tag{5}$$

so the joint pdf for M and Θ is given by

$$p_{\hat{M}}(\hat{m}) = p_{\hat{M}}(m, \theta) = p_{M|\Theta}(m|\theta) p_\Theta(\theta) =$$

$$a \exp\Big(-\frac{1}{2}(m - m_{prior} - \theta)^T C_M^{-1}(m - m_{prior} - \theta) - \frac{1}{2}(\theta - \theta_0)^T C_\Theta^{-1}(\theta - \theta_0)\Big), \tag{6}$$

where

$$\hat{M} = \begin{bmatrix} M \\ \Theta \end{bmatrix}. \tag{7}$$

For simplicity, a realization $\hat{m}$ of $\hat{M}$ is sometimes written as (m, θ) instead of $(m^T, \theta^T)^T$. Throughout, the superscript T is used to denote the transpose of a matrix or vector. For convenience, we refer to m_{prior} as the prior mean, however, one should note that Eq. 5 indicates that the conditional expectation of M is given by $E[M|\Theta = \theta] = m_{prior} + \theta$.

All measured well-test pressure data that will be used as conditioning data is incorporated in the N_d-dimensional column vector d_{obs}. Note N_d is the total number of observed or measured pressure data used as conditioning data. As is standard, d represents the corresponding vector

of pressures that will be calculated for a given realization m of the rock property fields and the relationship between the data and m is represented by

$$d = g(m). \tag{8}$$

Given a specific m, Eq. 8 represents the operation of calculating wellbore pressures by running the reservoir simulator.

As in our earlier work (Oliver, 1994; He et al., 1996; Oliver et al., 1996a), we assume that the random vector ϵ which represents measurement errors consists of independent identically distributed random variables with zero mean and variance σ_d^2 so that the data covariance matrix C_D is a diagonal matrix with all diagonal entries equal to σ_d^2. Given m, the observed pressure data may be regarded as a realization of the random vector $D = g(m) + \epsilon$. Thus, the a posteriori pdf for $\hat{M}$ conditional to the observed pressure data, d_{obs}, can be derived as in Tjelmeland et al. (1994) by a standard applications of Bayes theorem and is given by

$$\pi(m,\theta) = p_{\hat{M}|D}(\hat{m}|d_{obs}) = a \exp\Big(-\frac{1}{2}(g(m)-d_{obs})^T C_D^{-1}(g(m)-d_{obs})$$

$$-\frac{1}{2}(m-m_{prior}-\theta)^T C_M^{-1}(m-m_{prior}-\theta) - \frac{1}{2}(\theta-\theta_0)^T C_\Theta^{-1}(\theta-\theta_0)\Big), \tag{9}$$

where the first equality of Eq. 9 simply defines notation. Eq. 9 gives the pdf we wish to sample to generate realizations (m,θ) of $\hat{M}$. To generate the most probable model (maximum a posteriori estimate) for $\hat{M}$, we need to minimize the objective function $O(\hat{m})$ given by

$$O(\hat{m}) = \frac{1}{2}(g(m)-d_{obs})^T C_D^{-1}(g(m)-d_{obs}) +$$

$$+\frac{1}{2}(m-m_{prior}-\theta)^T C_M^{-1}(m-m_{prior}-\theta) + \frac{1}{2}(\theta-\theta_0)^T C_\Theta^{-1}(\theta-\theta_0)\Big) \tag{10}$$

At this point, the dimension of θ is the same as the dimension of m, i.e., N_p.

NEWTON ITERATION

It is convenient to partition the gradient as

$$\nabla O(\hat{m}) = \begin{bmatrix} \nabla_m O(\hat{m}) \\ \nabla_\theta O(\hat{m}) \end{bmatrix}. \tag{11}$$

where ∇_m represents the gradient operator with respect to m and ∇_θ represents the gradient operator with respect to θ. Using basic vector calculus, it follows that

$$\nabla_\theta O(\hat{m}) = -C_M^{-1}(m-m_{prior}-\theta) + C_\Theta^{-1}(\theta-\theta_0). \tag{12}$$

Similarly,

$$\nabla_m O(\hat{m}) = G^T C_D^{-1}(g(m)-d_{obs}) + C_M^{-1}(m-m_{prior}-\theta), \tag{13}$$

where G^T is the transpose of the $N_d \times N_p$ sensitivity coefficient matrix G which is defined as

$$G = \nabla_m [g(m)^T]. \tag{14}$$

Using Eqs. 12 and 13 in Eq. 11 gives the total gradient of the objective function. Again using basic vector calculus, the Hessian matrix for the Gauss-Newton iteration is given by

$$H = \begin{bmatrix} G^T C_D^{-1} G + C_M^{-1} & -C_M^{-1} \\ -C_M^{-1} & C_M^{-1} + C_\Theta^{-1} \end{bmatrix}. \tag{15}$$

The Hessian is guaranteed to be positive semidefinite. It is well known (Fletcher, 1987) that if the Hessian is modified, the Gauss-Newton method will still converge to the same maximum a posteriori estimate provided the modified Hessian is positive definite. Thus, in order to obtain a simpler computational scheme, we replace the Hessian H by $\hat{H}$ where

$$\hat{H} = \begin{bmatrix} G^T C_D^{-1} G + C_M^{-1} & O \\ O & C_M^{-1} + C_\Theta^{-1} \end{bmatrix}. \tag{16}$$

Since C_D, C_M and C_Θ are all positive definite matrices, it is clear that $\hat{H}$ is positive definite.

When $\hat{H}$ is used as the modified Hessian in the Newton iteration procedure, the overall iteration can be decomposed as follows:

$$(G_l^T C_D^{-1} G_l + C_M^{-1}) \delta m^{l+1} = -G_l^T C_D^{-1} (g(m^l) - d_{obs}) - C_M^{-1} (m^l - m_{prior} - \theta^l) \tag{17}$$

$$(C_M^{-1} + C_\Theta^{-1}) \delta\theta^{l+1} = C_M^{-1} (m^l - m_{prior} - \theta^l) - C_\Theta^{-1} (\theta^l - \theta_0), \tag{18}$$

$$m^{l+1} = m^l + \mu_l \delta m^{l+1}, \tag{19}$$

$$\theta^{l+1} = \theta^l + \mu_l \delta\theta^{l+1} \tag{20}$$

where l refers to the iteration index and μ_l is the step size determined by the restricted step method (Fletcher, 1987). Note in the spirit of the restricted step, it is important to use the same value of μ_l in both Eqs. 19 and 20, otherwise we effectively change the search direction. Note by replacing H by $\hat{H}$, we avoid inversion of H, i.e., we have "decoupled" the iteration on the model (m) from the iteration on the correction (θ) to the prior mean.

The prior mean given by Eq. 2 can be written as

$$m_{prior} = \begin{bmatrix} m_{prior,\phi}\ e \\ m_{prior,k}\ e \end{bmatrix}, \tag{21}$$

where e is the N-dimensional column vector with all entries equal to unity. More generally, we let e represents a column vector of dimension N_e with all components equal to unity, i.e.,

$$e = [1, 1, ..., 1]^T, \tag{22}$$

and assume that m_{prior} has the form

$$m_{prior} = \begin{bmatrix} m_{prior,1}\, e \\ m_{prior,2}\, e \\ \vdots \\ m_{prior,N_a}\, e \end{bmatrix}. \tag{23}$$

In this case, it is reasonable to require that the correction to the prior mean have the same structure as m_{prior}, i.e., we require that

$$\theta = \begin{bmatrix} \alpha_1\, e \\ \alpha_2\, e \\ \vdots \\ \alpha_{N_a}\, e \end{bmatrix} = \begin{bmatrix} \theta_1\, e \\ \theta_2\, e \\ \vdots \\ \theta_{N_a}\, e \end{bmatrix}, \tag{24}$$

for some constants, α_j, $j = 1, 2, ..., N_a$. Since m_{prior} and θ are both N_p-dimensional column vectors, $N_a N_e = N_p$. For the case where all attributes are modeled as stationary random functions, N_a is equal to the number of attributes, e.g., $N_a = 2$ if Eq. 3 applies. However, if the mean of each attribute varies from gridblock to gridblock, then $N_a = N_p$ (the dimension of the model m). In this case, e is one dimensional and Eq. 24 does not place any restrictions on the components of θ. When Eq. 24 applies, C_Θ is defined as a block diagonal matrix with the jth diagonal block given by $\sigma^2_{\theta,j} I$ for $j = 1, 2, ..., N_a$ where I is the $N_e \times N_e$ identity matrix.

The $(N_a N_e) \times N_a = N_p \times N_a$ matrix E is defined by

$$E = \begin{bmatrix} e & O & \dots & O \\ O & e & \dots & O \\ \vdots & \vdots & \ddots & \vdots \\ O & O & \dots & e \end{bmatrix}, \tag{25}$$

so the transpose of E is given by

$$E^T = \begin{bmatrix} e^T & O & \dots & O \\ O & e^T & \dots & O \\ \vdots & \vdots & \ddots & \vdots \\ O & O & \dots & e^T \end{bmatrix}, \tag{26}$$

If $N_a = N_p$ ($N_e = 1$), then E is the $N_p \times N_p$ identity matrix. Defining the N_a dimensional column vector α by

$$\alpha = [\alpha_1, \alpha_2, \dots, \alpha_{N_a}]^T, \tag{27}$$

Eq. 24 can be written as $\theta = E\alpha$.

Partial Subspace Procedure

Reynolds et al. (1995) have implemented subspace methods (Kennett and Williamson, 1988; Oldenberg et al., 1993; Oldenberg and Li, 1994) to significantly enhance the computational efficiency of the Gauss-Newton method. Here, we consider only a partial subspace procedure where $\delta\theta^{l+1}$ in Eq. 18 is expanded as

$$\delta\theta^{l+1} = E\delta\alpha^{l+1} \tag{28}$$

at all Newton iterations. Using Eq. 28 in Eq. 18 and multiplying the resulting equation by $E^T C_M$ gives

$$E^T(I + C_M C_\Theta^{-1})E\delta\alpha^{l+1} = E^T(m^l - m_{prior} - \theta^l) - E^T C_M C_\Theta^{-1}(\theta^l - \theta_0). \tag{29}$$

Eq. 28 indicates that $\delta\theta^{l+1}$ is a linear combination of the columns of E, i.e., the columns of E represent the associated subspace vectors. If the initial guess for θ, $\theta^0 = \theta_0$, is also a linear combination of these subspace vectors, then by mathematical induction, it follows that for all l, θ^l is a linear combination of these subspace vectors. This result is apparent because if θ^l is a linear combination of these subspace vectors, i.e., $\theta^l = E\alpha^l$, it follows from Eqs. 20 and 28 that

$$\theta^{l+1} = E\alpha^l + \mu_l E\delta\alpha^{l+1} = E(\alpha^l + \mu_l\delta\alpha^{l+1}). \tag{30}$$

It now follows that when Eq. 18 is replaced by Eq. 29, Eq. 20 can be replaced by

$$\alpha^{l+1} = \alpha^l + \mu_l\delta\alpha^{l+1}, \tag{31}$$

and

$$\theta^{l+1} = E\alpha^{l+1}. \tag{32}$$

With this modification, the overall computational scheme for estimating the maximum a posteriori estimate (Eqs. 17 through 20) can now be written as

$$\delta m^{l+1} = m_{prior} + \theta^l - m^l - C_M G_l^T\left(C_D + G_l C_M G_l^T\right)^{-1}$$

$$\times[g(m^l) - d_{obs} - G_l(m^l - m_{prior} - \theta^l)]. \tag{33}$$

$$\left[E^T(I + C_M C_\Theta^{-1})E\right]\delta\alpha^{l+1} = E^T(m^l - m_{prior} - \theta^l) - E^T C_M C_\Theta^{-1}(\theta^l - \theta_0), \tag{34}$$

$$m^{l+1} = m^l + \mu_l\delta m^{l+1}, \tag{35}$$

and Eqs. 31 and 32. Eq. 33 was obtained from Eq. 17 by using basic matrix inversion lemmas (Tarantola, 1987; Chu et al., 1995a). The preceding subspace implementation of the Gauss-Newton iteration will converge to the so-called maximum a posteriori estimate $(m_\infty, \theta_\infty)$, which is commonly referred to as the most probable model. However, as noted previously, our

objective is not to simply generate the most probable estimate of $\hat{m}$, but to generate a suite of realizations which represent a correct sampling of the pdf of Eq. 9. The sampling procedure we use is presented in the following section.

SAMPLING THE A POSTERIORI DISTRIBUTION

Markov chain Monte Carlo (MCMC) methods provide theoretical techniques which are guaranteed to produce a correct sampling of a given pdf if a sufficiently large number of states are generated. However, current implementations (Oliver et al., 1996b; Cunha et al., 1996) are too computationally intensive for practical applications when the goal is to generate realizations conditioned to production data and the generation of each state in the Markov chain requires a run of a reservoir simulator. Procedures based on approximating the a posteriori pdf by a Gaussian centered at the maximum a posteriori estimate require computing either the Cholesky decomposition or the square root of the a posteriori covariance matrix and do not always generate a correct sampling of the pdf (Oliver et al., 1996b; Cunha et al., 1996). Thus, we pursue a computationally efficient alternative. For the case where uncertainty in the prior mean is ignored, the basic procedure has been discussed by Oliver et al. (1996a) and relies on underlying theory developed by Oliver (1996). The basic procedure is technically correct only for the case where the data is linearly related to the model, however, Oliver et al. (1996a) have presented arguments which suggest that the procedure should give an approximately correct sampling in the nonlinear case.

Linear Case

Here, we extend the results of Oliver (1996) and Oliver et al. (1996a) to the case where we incorporate uncertainty in the prior mean. We consider the case where the data is linearly related to the model, so Eq. 8 can be written as

$$d = Gm, \tag{36}$$

where G is an $N_d \times N_p$ matrix. For this case, the maximum a posteriori estimate can be obtained by solving the following two equations: $\nabla_\theta O(\hat{m}) = 0$ and $\nabla_m O(\hat{m}) = 0$ (see Eqs. 12 and 13) to obtain m_∞ and θ_∞. It is easy to show that this solution satisfies

$$\begin{bmatrix} G^T C_D^{-1} G + C_M^{-1} & -C_M^{-1} \\ -C_M^{-1} & C_M^{-1} + C_\Theta^{-1} \end{bmatrix} \begin{bmatrix} m_\infty \\ \theta_\infty \end{bmatrix} = \begin{bmatrix} C_M^{-1} m_{prior} + G^T C_D^{-1} d_{obs} \\ -C_M^{-1} m_{prior} + C_\Theta^{-1} \theta_0 \end{bmatrix}. \tag{37}$$

Note that the coefficient matrix on the left side of Eq. 37 is the Hessian matrix defined in Eq. 15. Moreover, when Eq. 36 applies it is easy to show that the a posteriori pdf for $\hat{M}$ (Eq. 9) is Gaussian with covariance matrix given by H^{-1} and expectation given by $(m_\infty, \theta_\infty)$ (Tarantola, 1987).

Next, we present a procedure for sampling $\pi(m, \theta)$ which does not require the generation and Cholesky or square root decomposition of H^{-1}. To construct a realization, we generate an unconditional simulation of m, which is denoted by m_{uc} and is given by

$$m_{uc} = m_{prior} + C_M^{1/2} Z, \tag{38}$$

where the components of the N_p-dimensional column vector Z are independent standard random normal deviates. Similarly, unconditional simulations of the data and the correction to the prior mean, respectively, are generated by

$$d_{uc} = d_{obs} + C_D^{1/2} Z_D, \tag{39}$$

and

$$\theta_{uc} = \theta_0 + C_\theta^{1/2} Z_\theta, \tag{40}$$

where again the components of Z_D and Z_θ are independent standard random normal deviates. The $1/2$ superscript on the matrices in the preceding three equations represent the square root of the matrix, but the square roots could also be replaced by the lower triangular matrix arising from the LL^T decomposition of the matrix. However, C_D and C_Θ are diagonal matrices, thus, it is trivial to compute their square root. Because we wish to avoid explicit factorization of C_M, in our computer implementation, we actually use sequential Gaussian cosimulation (e.g., Gomez-Hernandez and Journel, 1993) in place of Eq. 38 to generate m_{uc}. If we replace, m_{prior} by m_{uc}, d_{obs} by d_{uc} and θ_0 by θ_{uc} in Eqs. 12 and 13, set both equations to zero and solve to obtain the solution denoted by (m_s, θ_s), then similar to Eq. 37, we find that

$$\begin{bmatrix} G^T C_D^{-1} G + C_M^{-1} & -C_M^{-1} \\ -C_M^{-1} & C_M^{-1} + C_\Theta^{-1} \end{bmatrix} \begin{bmatrix} m_s \\ \theta_s \end{bmatrix} =$$

$$\begin{bmatrix} C_M^{-1}\left(m_{prior} + C_M^{1/2} Z\right) + G^T C_D^{-1}\left(d_{obs} + C_D^{1/2} Z_D\right) \\ -C_M^{-1}\left(m_{prior} + C_M^{1/2} Z\right) + C_\Theta^{-1}\left(\theta_0 + C_\Theta^{1/2} Z_\theta\right) \end{bmatrix}. \tag{41}$$

Subtracting Eq. 37 from 41, we see that the conditional simulations, m_s and θ_s satisfy

$$\begin{bmatrix} G^T C_D^{-1} G + C_M^{-1} & -C_M^{-1} \\ -C_M^{-1} & C_M^{-1} + C_\Theta^{-1} \end{bmatrix} \begin{bmatrix} m_s - m_\infty \\ \theta_s - \theta_\infty \end{bmatrix} = \begin{bmatrix} C_M^{-1} C_M^{1/2} Z + G^T C_D^{-1} C_D^{1/2} Z_D \\ -C_M^{-1} C_M^{1/2} Z + C_\Theta^{-1} C_\Theta^{1/2} Z_\theta \end{bmatrix} = B, \tag{42}$$

where the last equality of Eq. 42 serves to define B. The random vector $\hat{M}_s$ is defined by

$$\hat{M}_s = [m_s^T, \theta_s^T]^T. \tag{43}$$

Since the expected values of Z, Z_D and Z_θ are all zero, it is clear that the expected values of $\hat{M}_s$ is given by

$$E[\hat{M}_s] = \begin{bmatrix} m_\infty \\ \theta_\infty \end{bmatrix}, \tag{44}$$

i.e., $E[m_s] = m_\infty$ and $E[\theta_s] = \theta_\infty$. The covariance of the random vector $\hat{M}_s$ is given by

$$E\left[\left(\hat{M}_s - E[\hat{M}_s]\right)\left(\hat{M}_s - E[M_s]\right)^T\right] = H^{-1}E[BB^T]H^{-1}, \tag{45}$$

where B is defined by the last equality of Eq. 42. Using the fact that Z, Z_D and Z_θ are independent vectors, with components of each vector representing independent standard random normal deviates, it is straightforward to show that $E[BB^T] = H$ and thus, Eq. 43 reduces to

$$E\left[\left(\hat{M}_s - E[\hat{M}_s]\right)\left(\hat{M}_s - E[M_s]\right)^T\right] = H^{-1}. \tag{46}$$

Thus, we have shown that the covariance and expectations of $\hat{M}$ and $\hat{M}_s$ are the same. Since both random vectors satisfy Gaussian distributions when Eq. 36 applies, we can generate a sampling of $\hat{M}$ by sampling the distribution for $\hat{M}_s$. Samples of $\hat{M}_s$ can be generating by solving Eq. 41 for m_s and θ_s for a set of independent unconditional simulations, m_{uc}, d_{uc} and θ_{uc}.

Basic Sampling Procedure, Nonlinear Case

For the nonlinear case of interest, the same type of procedure is applied except we restrict θ by introducing a subspace method, i.e, samples are generated by the computational algorithm of Eqs. 33, 34, 35, 31 and 32 with m_{prior} replaced by m_{uc}, d_{obs} replaced by d_{uc} and θ_0 replaced by θ_{uc}. Note this simulation procedure represents automatic history matching of the pressure data with prior information used as a regularization term.

In this process, θ_{uc} must be generated so it lies in the appropriate subspace. To do this, recall that C_Θ is a block diagonal matrix where the jth diagonal block is given by $\sigma^2_{\theta,j}I$ and introduce the associated covariance matrix C_α, which is related to C_Θ by

$$C_\alpha^{-1} = E^T C_\Theta^{-1} E. \tag{47}$$

C_α is an $N_a \times N_a$ diagonal matrix with jth diagonal entry denoted by $\sigma^2_{\alpha,j}$. We compute

$$\alpha_{uc} = \alpha_0 + C_\alpha^{1/2} Z_\alpha, \tag{48}$$

where the components of the N_a dimensional column vector are independent standard random normal deviates and set

$$\theta_{uc} = E\alpha_{uc}. \tag{49}$$

COMPUTATIONAL EXAMPLE

The example considered pertains to a reservoir containing nine completely-penetrating wells. A simulation grid with 25 gridblocks in the x and y directions and 10 gridblocks in the z direction is used, i.e., 6,250 gridblocks are used. Since we wish to generate realizations of the

log-permeability and porosity fields, there are 12,500 model parameters. The areal grid is 400 ft by 400 ft and all gridblocks in the z directions are of thickness (height) 10 feet. Fig. 1 shows the areal grid and well locations.

The reservoir is areally isotropic $k_x = k_y = k$ and we require that $k_z = 0.1k$. Thus, determination of a distribution for k automatically determines the vertical permeability at each gridblock. An anisotropic spherical variogram for $\ln(k)$ is used with the range in the x-direction equal to 3,200 ft, the range in the y-direction equal to 1,600 ft and the range in the z-direction equal to 30 feet. The variance of $\ln(k)$ (sill of the variogram) is specified as $\sigma_k^2 = 0.5$. The anisotropic variogram for porosity is identical to the one for $\ln(k)$ except the variance for porosity is specified as $\sigma_\phi^2 = 0.002$. The correlation coefficient between log-permeability and porosity is specified as $\rho_{k,\phi} = 0.7$.

The true log-permeability is shown in Fig. 2. This truth case was obtained by unconditional simulation (Eq. 38) using $m_{prior,k} = 4.0$ and $m_{prior,\phi} = 0.20$. This unconditional simulation also yields the true porosity field. For convenience, we refer to $m_{prior,k} = 4.0$ and $m_{prior,\phi} = 0.20$ as the true prior means. Synthetic well-test pressure data were generated by running the simulator using the true permeability and porosity fields. Well-test pressure data were collected at wells 2, 4, 5, 6 and 8 (see Fig. 1) during a period when the other four wells were produced at a specified rate. At the center well (well 5), a two-day drawdown followed by a one-day buildup test was run. At the other four tested wells (wells 2, 4, 6 and 8) pressure data were measured during three day drawdown tests. This synthetic pressure data is referred to as measured pressure data from this point onward.

In the following, we apply our procedures for sampling the a posteriori pdf (Eq. 9). We consider a case where we use $m_{prior,k} = 5.0$ and $m_{prior,\phi} = 0.25$ (referred to as the incorrect prior means) with and without allowing for uncertainty (errors) in the prior means.

Fig. 3 shows an unconditional simulation of the log-permeability field generated from Gaussian cosimulation using the true prior mean. Fig. 4 shows an unconditional simulation of the log-permeability obtained from Gaussian cosimulation using the incorrect prior means. As expected the gridblock values of log-permeability tend to be much higher when the incorrect mean is used; compare Figs. 3 and 4. Similar results were obtained for the porosity field since the incorrect mean for porosity is higher than its true mean.

Fig. 5 shows a conditional simulation of the log-permeability field obtained by applying the method of Oliver et al. (1996a) using true prior means for $\ln(k)$ and porosity. This is equivalent to our basic procedure with θ set equal to zero at all iterations, i.e., we do not incorporate uncertainty in the prior mean. Fig. 6 shows a conditional simulation obtained by the same procedure except in this case, the incorrect prior means were used. Note that the log-permeability values obtained in Fig. 6 tend to be much higher than those obtained in Fig. 5. This is the expected result because the incorrect prior means are much higher than the true values.

Fig. 7 shows a conditional realization obtained by our basic procedure. In this case, we used the incorrect prior means, but accounted for uncertainty in the prior means, where the 2×2 diagonal covariance matrix C_α (see Eq. 47) has as its two entries $\sigma^2_{\alpha,1} = 0.001$ and $\sigma^2_{\alpha,2} = 0.2$. Note the realization in Fig. 7 is almost identical to the one of Fig. 5 which was generated with the true prior means by assuming no errors in the prior means. Although they are not presented here, similar results were obtained for the porosity field.

The results of Figs. 5 through 7 and the corresponding results for porosity (not shown) illustrate that our procedure for accounting for uncertainty in the prior means is viable and yields reasonable realizations of the rock property fields. The values of θ_s obtained by our basic procedure which gave the results of Fig. 7 indicate that the correction to the prior mean for $\ln(k)$ was -1.041 and the correction to the prior mean for porosity was -0.047. Note these values are very close to the true error in the incorrect prior means.

The permeability values corresponding to the results of Fig. 7 and associated porosity values were input to the simulator to predict pressure data at the five wells tested. Fig. 8 shows that the pressure data predicted at well 5 from this realization is in good agreement with the measured pressure data. Equally good agreement was obtained at the other tested wells. The dashed curve in Fig. 8 represents the pressure data predicted using the corresponding unconditional simulation, m_{uc}, as input in the reservoir simulator. As this m_{uc} was used as the initial guess in the Gauss-Newton method when constructing the conditional simulation by our basic simulation method, the results of Fig. 8 give a qualitative measure of how the incorporation of pressure data changes estimates of rock property fields obtained solely from the prior model.

We also generated 50 conditional simulations of the rock property fields using our basic simulation procedure. As discussed previously, this suite of realizations of the rock property fields represents an approximate sampling of the a posteriori pdf of Eq. 9. For each realization, we simulated reservoir performance for $1,000$ days where each of the nine wells was produced at a specified bottom-hole pressure. Reservoir performance was also predicted from the set of m_{uc} values generated by Gaussian cosimulation. The lower set of curves in Fig. 9 represent the field cumulative oil production predicted from the 50 history-matched realizations, i.e., illustrates the uncertainty in predicted reservoir performance. The curve through the solid dots represents the field cumulative oil production generated using the true permeability and porosity fields as simulator input. The top set of curves in Fig. 9 represent the predictions of cumulative oil production obtained from the set of 50 m_{uc} models which were used as initial guesses in the Gauss-Newton procedure. Note these realizations predict erroneously high values of cumulative oil production since the incorrect prior means are much higher than the true prior means.

A histogram of the cumulative oil production at $1,000$ days and associated cumulative distribution function are shown in Fig. 10. The expected value (mean) is 5.70×10^6 STB, the median is 5.74×10^6 STB, and the standard deviation is 1.68×10^5 STB. Note the bar in the histogram over 5.80×10^6 STB represents the number of outcomes (15) between 5.7×10^6 STB

and 5.80×10^6 STB. The cumulative oil production at 1,000 days predicted using the true rock property fields was 5.68×10^6 STB.

CONCLUSIONS

Errors in the prior means can be properly taken into account by using the partially doubly stochastic model developed here. Based on the model, we have presented an automatic history procedure which can be applied to generate a set of realizations conditioned to pressure data and a prior geostatistical model. This set of realizations represents an approximate sampling of the a posteriori probability density function for the rock property fields. It has been proven rigorously that the basic procedure for sampling the pdf is correct if measured data are linearly related to the model. It has been shown that if estimates of prior means are inaccurate and the errors in the prior means are not accounted for, one can not obtain a correct sampling of the pdf for the rock property fields.

Using our basic procedure for sampling the pdf, one can predict reservoir performance for each realization to evaluate the uncertainty in predicted reservoir performance.

REFERENCES CITED

Chu, L., A. C. Reynolds, and D. S. Oliver, 1995a, Computation of sensitivity coefficients for conditioning the permeability field to well-test pressure data, *In Situ* v. 19, p. 179-223.

Chu, L., A. C. Reynolds, and D. S. Oliver, 1995b, Reservoir description from static and well-test pressure data using efficient gradient methods, paper SPE 29999, presented at the 1995 SPE International Meeting on Petroleum Engineering, Beijing, Nov. 14-17.

Cunha, L. B., D. S. Oliver, R. A. Redner, and A. C. Reynolds, 1996, A hybrid Markov chain Monte Carlo method for generating permeability fields conditioned to multiwell pressure data and prior information, paper SPE 36566, presented at the 1996 SPE Annual Technical Conference and Exhibition, Denver, Oct. 6-9.

Fletcher, R., 1987, *Practical Methods of Optimization*, John Wiley & Sons, Inc., New York.

Gomez-Hernandez, J. J. and A. G. Journel, Joint sequential simulation of multi-Gaussian random variables, 1993, in Soares, A., editor, *Geostatistic Troia 92*, Kluwer, p. 133-144.

He, N., A. C. Reynolds, and D. S. Oliver, 1996, Three-dimensional reservoir description from multiwell pressure data, paper SPE 36509, presented at the 1996 SPE Annual Technical Conference and Exhibition, Denver, Oct. 6-9.

Journel, A. G. and Ch. J. Huijbregts, 1978, *Mining Geostatistics*, Academic Press Limited, London.

Kennett B. L. N. and P. R. Williamson, 1988, Subspace methods for large-scale nonlinear inversion, in *Mathematical Geophysics: A Survey of Recent Developments In Seismology and Geodynamics*, eds. Vlarr, N. J. et al., D. Reidel Publishing Company, Dordrecht, p. 139-154.

Oldenberg, D. W., P. R. McGillivray, and R. G. Ellis, 1993, Generalized subspace methods for large-scale inverse problems, *Geophysics J. Int.*, v. 10, p. 12-20.

Oldenberg, D. W. and Y. Li, 1994, Subspace linear inverse method, *Inverse Problems,* v. 10, p. 915-935.

Oliver, D. S., 1994, Incorporation of transient pressure data into reservoir characterization, *In Situ* v. 18, p. 243-275.

Oliver, D. S., 1996, On conditional simulation to inaccurate data, *Math. Geology,* v. 28, p. 811-817.

Oliver, D. S., N. He, and A. C. Reynolds, 1996a, Conditioning permeability fields to pressure data, Proceedings of at the 5th European Conf. on the Mathematics of Oil Recovery, p. 259-269.

Oliver, D. S., L. B. Cunha, and A. C. Reynolds, 1996b, Markov chain Monte Carlo methods for conditioning a permeability field to pressure data, to appear in *Math. Geology.*

Peaceman, D. W., 1983, Interpretation of well-block pressures in numerical reservoir simulation with non-square grid blocks and anisotropic permeability," *Soc. Pet. Eng. J.*, v. 23, p. 531-543.

Reynolds, A. C., N. He, L. Chu, and D. S. Oliver, 1995, Reparameterization techniques for generating reservoir descriptions conditioned to variograms and well-test pressure data, paper SPE 30588, presented at the 1995 SPE Annual Technical Conference and Exhibition, Dallas, Oct. 22-25, to appear in *Soc. Pet. Eng. J.*

Tarantola, A., 1987, *Inverse Problem Theory, Methods for Data Fitting and Model Parameter Estimation,* Elsevier Science Publishers, Amsterdam.

Tjelmeland, H., H. Omre, and B. J. Hegstad, 1994, Sampling from Bayesian models in reservoir characterization, Technical Report Statistics No. 2, University of Trondheim.

Xu, W., T. T. Tran, R. M. Srivastava, and A. G. Journel, 1992, Integrating seismic data in reservoir modeling: the collocated cokriging approach, paper SPE 24742, presented at the 1992 SPE Annual Technical Conference and Exhibition, Washington D.C., Oct. 4-7.

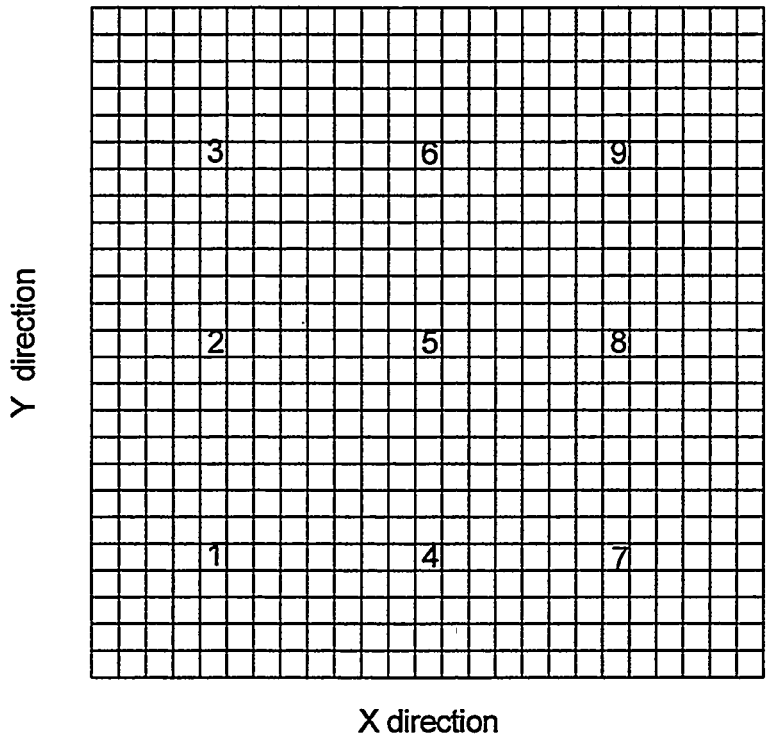

Fig. 1 - Areal grid, well locations and well numbers.

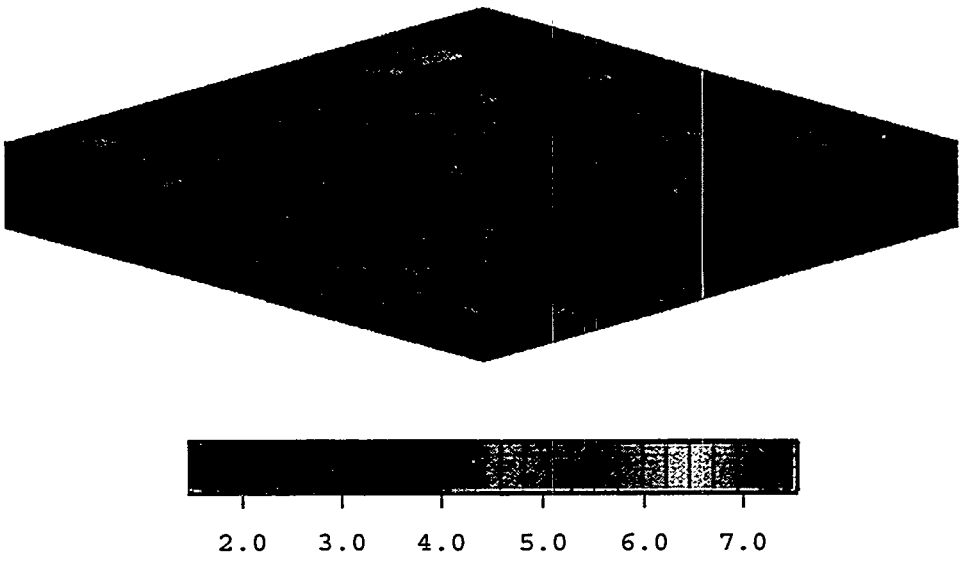

Fig. 2 - True log-permeability field.

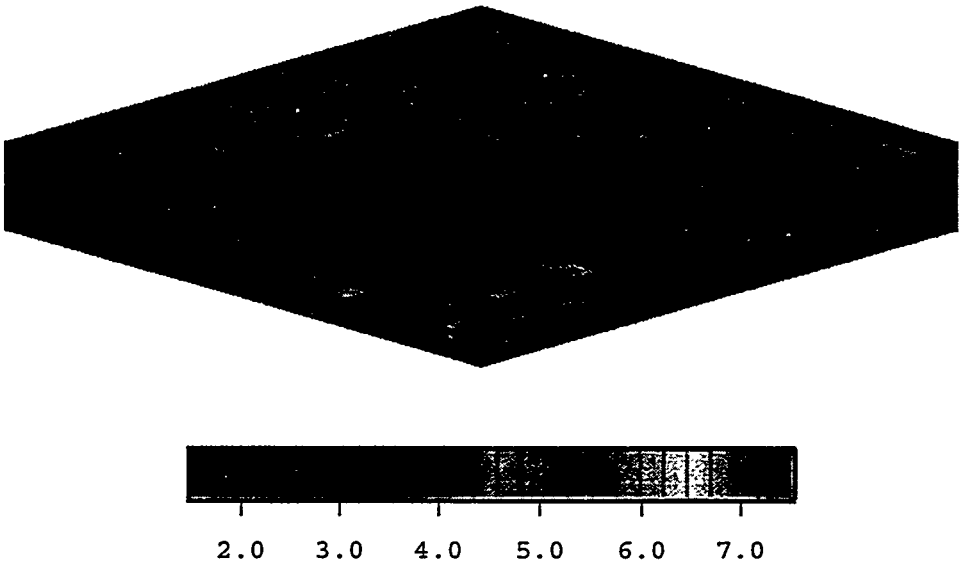

Fig. 3 - Unconditional realization of log-permeability field with true prior means.

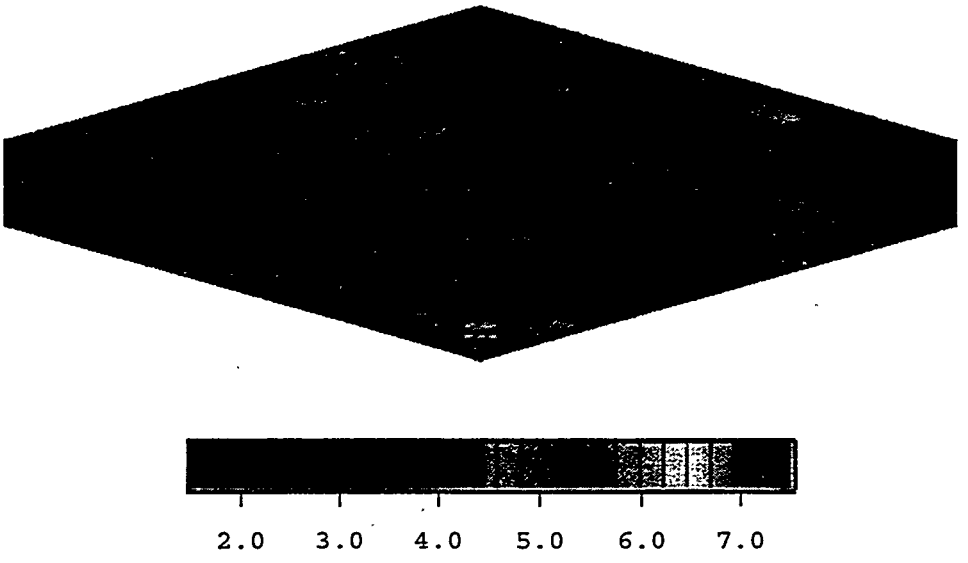

Fig. 4 - Unconditional realization of log-permeability field with incorrect prior means.

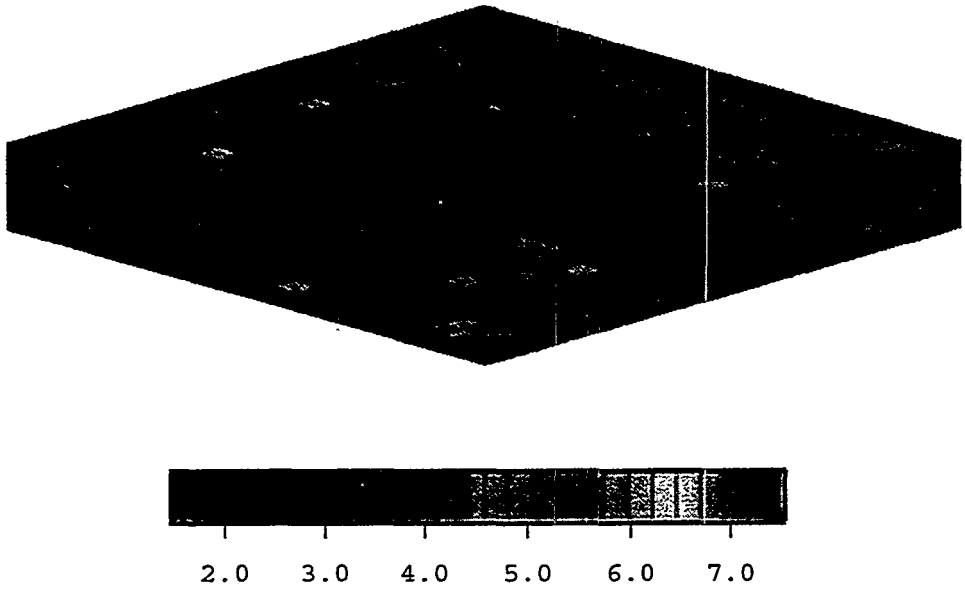

Fig. 5 - Realization of log-permeability field conditioned to pressure data using true prior means.

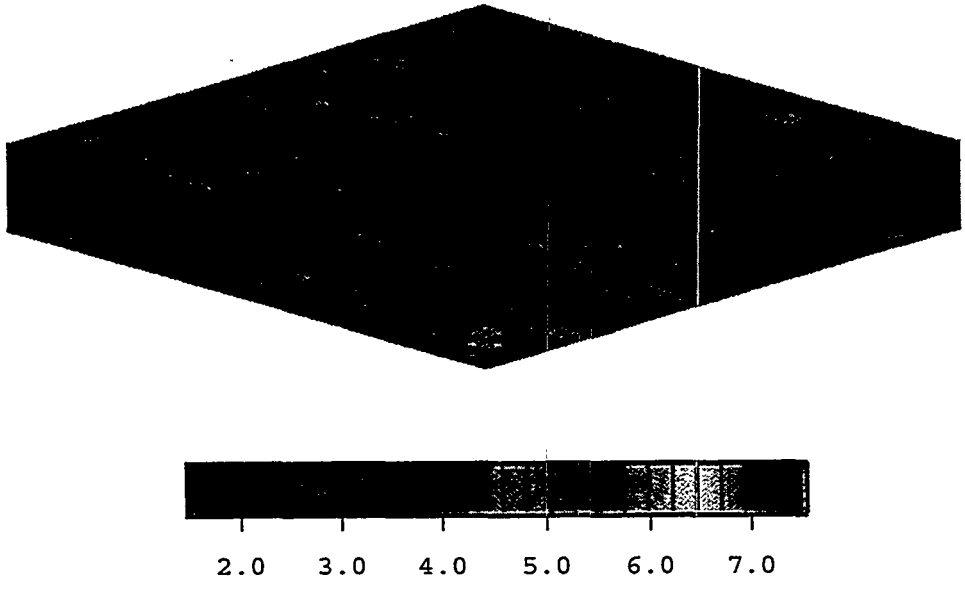

Fig. 6 - Realization of permeability field conditioned to pressure data using incorrect prior means without correction to prior means.

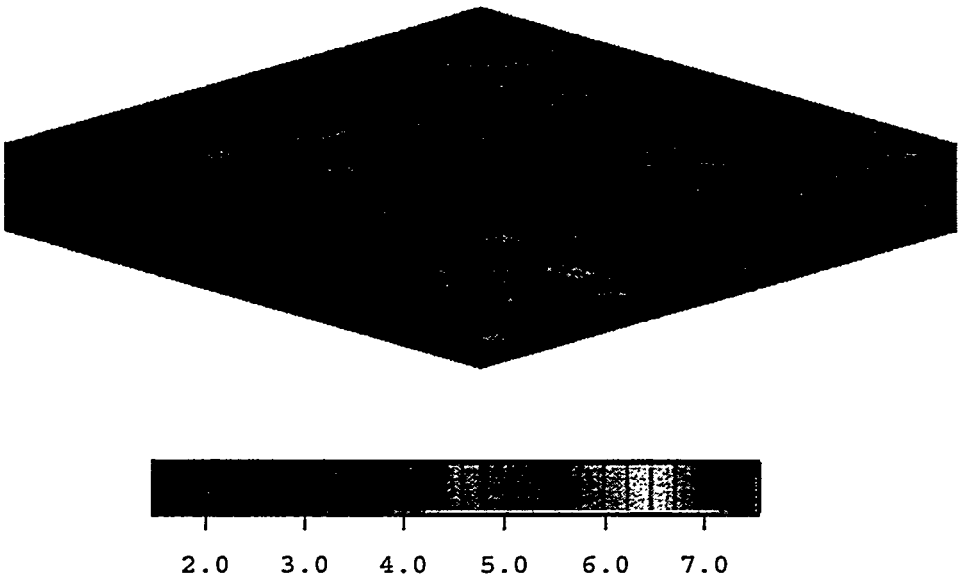

Fig. 7 - Realization of log-permeability field conditioned to pressure data with correction to incorrect prior means.

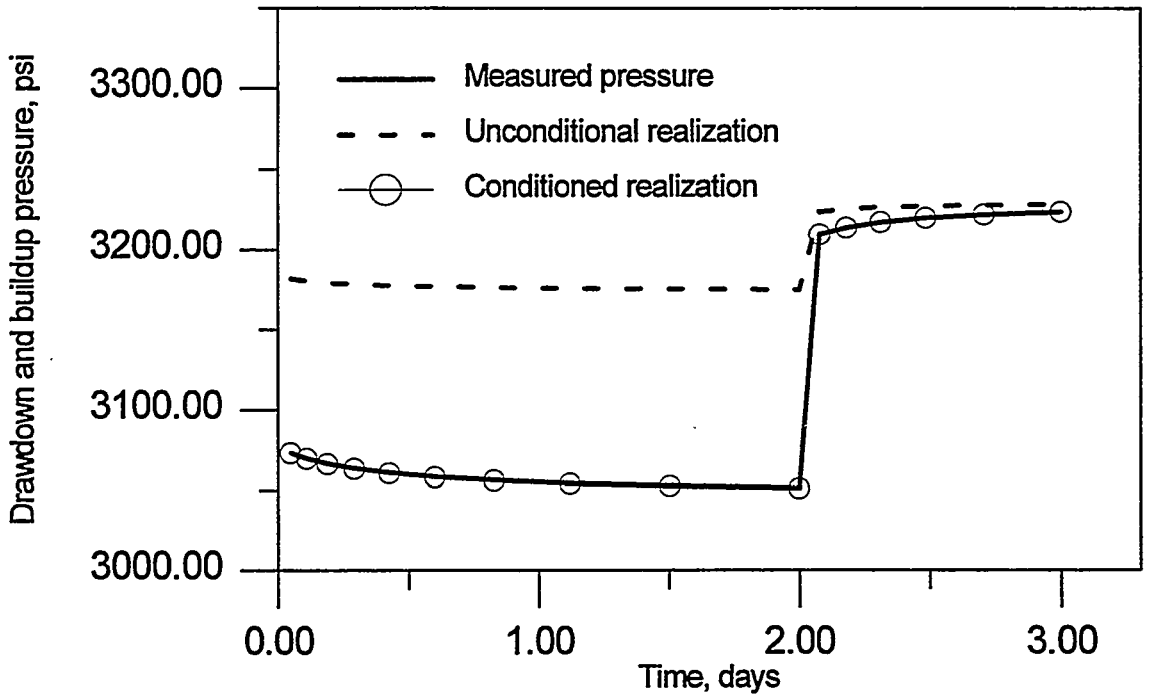

Fig. 8 - Pressure data predicted at well 5 from conditional and unconditional simulations of rock property fields compared to measured pressure data.

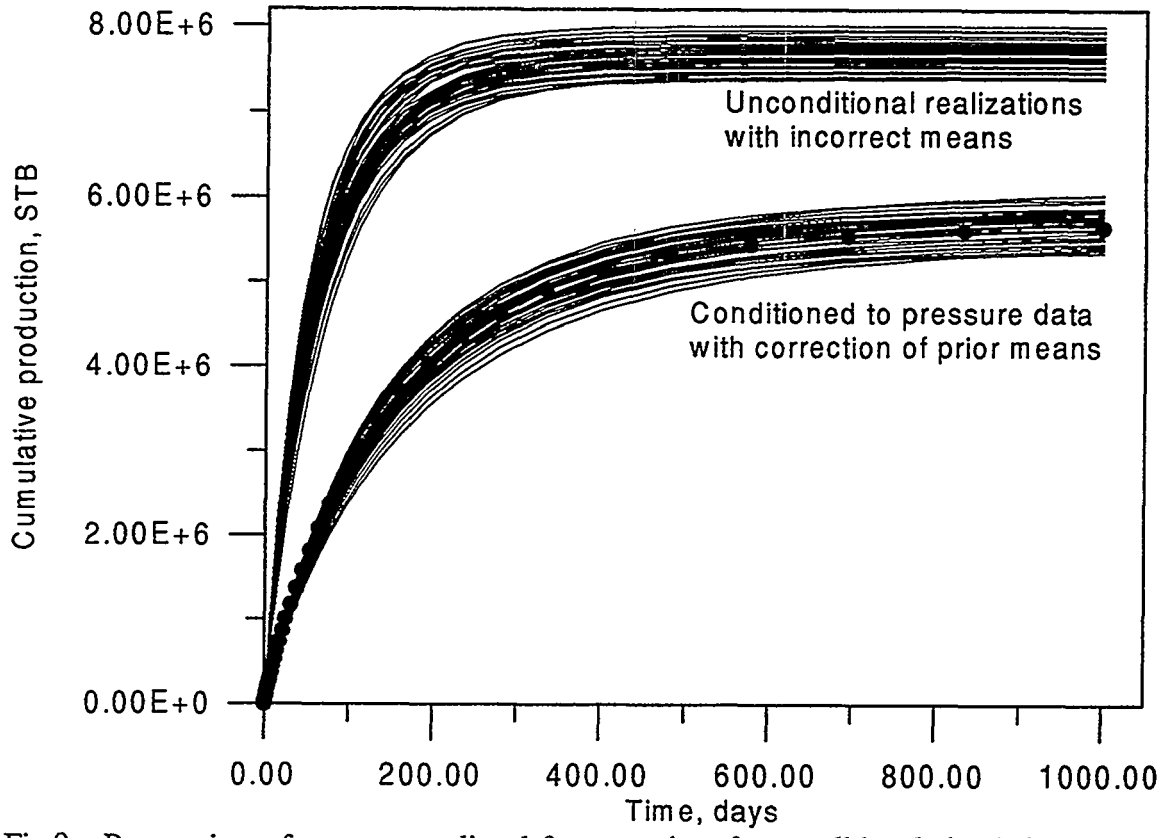

Fig.9 - Reservoir performance predicted from a suite of unconditional simulations and a suite of conditioned simulations.

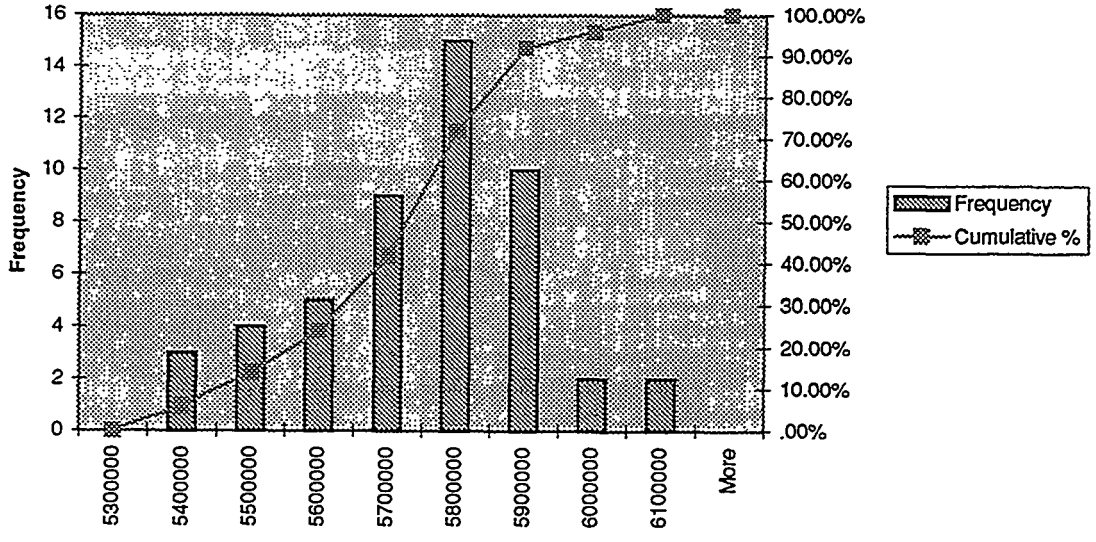

Fig 10 - Histogram and cumulative distribution of cumulative oil production at 1,000 days.

A QUANTITATIVE METHOD FOR MEASURING THE QUALITY OF HISTORY MATCHES

Tom S. Shaw, Kerr-McGee Corporation, Oklahoma City, OK

Roy M. Knapp, University of Oklahoma, Norman, OK

Abstract

History matching can be an efficient tool for reservoir characterization. A "good" history matching job can generate reliable reservoir parameters. However, reservoir engineers are often frustrated when they try to select a "better" match from a series of history matching runs. Without a quantitative measurement, it is always difficult to tell the difference between a "good" and a "better" matches. For this reason, we need a quantitative method for testing the quality of matches. This paper presents a method for such a purpose.

The method uses three statistical indices to (1) test shape conformity, (2) examine bias errors, and (3) measure magnitude of deviation. The shape conformity test insures that the shape of a simulated curve matches that of a historical curve. Examining bias errors assures that model reservoir parameters have been calibrated to that of a real reservoir. Measuring the magnitude of deviation assures that the difference between the model and the real reservoir parameters is minimized.

The method was first tested on a hypothetical model and then applied to published field studies. The results showed that the method can efficiently measure the quality of matches. It also showed that the method can serve as a diagnostic tool for calibrating reservoir parameters during history matching.

1. Introduction

A numerical reservoir model can be envisioned as a sophisticated instrument. The instrument must be properly calibrated before it can give accurate readings. History matching thus can be conceived as a model calibration process. The process involves adjusting the reservoir parameters of a numerical model to produce a *"best"* match between the simulated results and the observed reservoir performance data. The objective of a history matching process is to devise a set of reservoir data to properly describe the reservoir being simulated.

Reservoir simulation assumes that a numerical model which works during history matching mode will also work during the prediction mode. This implies that a model must be valid during history matching to be valid during prediction. The reliability of the predicted reservoir performance thus depends on the quality of the reservoir description data used to build the model. It is thus very important that the reservoir description data used in a model be the one that can best describe the reservoir being simulated.

What is considered the best data that can describe a reservoir? Theoretically, the set of reservoir description data that produces the *"best"* match between the simulated results and the observed reservoir performance data is presumed to be the one that can best describe the reservoir. In practice, however, it is difficult to tell when the best match has been achieved, unless a quantitative measure is provided for comparing the quality of matches. Unfortunately, to date, there is still no efficient quantitative method for measuring the quality of history match. Qualitative description such as "good matches", "excellent matches" or "poor matches" are often used to describe the quality of matches. This paper will present a quantitative method for measuring the quality of history matches.

2. Scope of This Paper

Because history matching is an ill-conditioned problem, different sets of reservoir parameters can result in the same quality of match. Evaluation of the quality of matches thus must include addressing two fundamental questions: (1) the quality of matches between simulated results and observed data; and (2) the uniqueness of the solution. Although knowing whether the estimated reservoir parameters represent the true solution is very important, solution nonuniqueness is an inherent problem to the history matching process that can not be readily resolved. The scope of this paper will focus on examining the quality of matches between simulated results and observed data.

3. Statistical Interpretation of The Quality of History Matches

During the past several decades, much work in reservoir simulation has been devoted to developing history matching algorithms and improving computation efficiency. Associated with these developments, various statistical indices have also been used to test the quality of history matches. Jahns (1966) used the standard deviation to test the reliability of reservoir properties estimated from regression analyses. Slater and Durrer (1971) suggested using the multiple correlation coefficient and the F-test for measuring the quality of matches. Dixon, *et al* (1973) applied the student-t test to express confidence limits on reservoir parameters estimated from history matches. Dogru and Knapp (1975) extended the student-t test to analyze the reliability of reservoir parameters estimated from history matching drawdown test data. Watson, *et al* (1984) used the chi-square test in an analytic study to express the confidence levels of reservoir parameters estimated from history matching.

Although application of the statistical tests described above requires that errors be randomly distributed and uncorrelated, this necessary condition was never addressed. If errors occurred in a certain pattern and were correlated, it indicated that the model reservoir properties had not been calibrated to match the "true" reservoir properties. Watson, *et al* (1989) incorporated residual analyses and the Durbin-Watson (D-W) Test (Draper and Smith, 1981) into the history matching process to examine error distribution and correlation. These two tests insured that the residuals were randomly distributed, a necessary condition for any least-squares minimization algorithm. However, the D-W test is a parametric method that requires the identification of the number of variables used to describe the model. In history matching problems, the number of variable used to model the reservoir system being simulated cannot be readily identified.

Although limited work has specifically been directed to the problems of quantitative measurement of the quality of history matches, there is still no efficient method developed for such a purpose. This can be attributed to the following reasons:

(1) Methods such as the chi-square method and correlation coefficient can only provide a indication of overall fit between simulated and observed values. Overall fit is a necessary but not a sufficient condition for measuring the fit between model calculated and observed values (Draper and Smith, 1981).

(2) Methods such as the F-test and Durbin-Watson test are parametric methods which require knowing the number of variables used to build the model being studied (Chatterjee and Price, 1977). In history matching, the number of variables used to build the numerical model is not readily identifiable. Therefore, parametric methods are not suitable for measuring the quality of history matches.

4. Factors Affecting The Quality of History Matches

There are three types of errors that can affect the quality of reservoir parameters estimated from a history matching process: (1) simulator errors (e_s) arise from the failure of the simulator to properly represent the physics of fluid flow process occurring in the reservoir, and failure to numerically integrate the descriptive equations accurately; (2) measurement errors (e_m) result from incorrect sampling procedures, measurement errors or instrument malfunctions, etc.; and (3) history matching errors (e_h) attributed to assigning incorrect reservoir parameter values to the numerical model representing the reservoir being studied. The total error (e_t) in a history matching run may include all three error types, or

$$e_t = e_s + e_m + e_h \qquad (1)$$

Where $e_s = 0$ since it is generally assumed that: (1) the simulator accurately represents the physics of fluid flow process occurring in the reservoir system being studied and, (2) care has been taken to minimize the effects of truncation errors in the finite difference approximation process that their impact on the simulated results will be small. The e_m term contains only random errors since, in practice, it is generally assumed that all testing instruments function properly and correct sampling and measurement procedures have been taken to avoid adding patterned errors to e_m. The e_h term contains errors resulting from assigning incorrect reservoir parameter values to the numerical model representing the study reservoir system. Assigning incorrect reservoir parameters to a numerical model will cause the simulated reservoir performance to deviate from observed reservoir performance. Under such a condition, the e_h will be biased. With actual data, it is difficult to identify the exact contributions of each

type to the errors in the estimated reservoir parameter values.

5. Statistical Properties of Errors

Let R denote the model representing the system of governing equations plus the boundary and the initial conditions necessary to describe the reservoir system being simulated; y, x, b denote the dependent variables, independent variables and parameters of the model, respectively, then the reservoir model can be written as

$$Model = R(y, x, b) \tag{2}$$

In a simulator where the y terms represent the state variables, e.g., pressure and saturation; the x terms represent the spatial and time variables, e.g., grid block location and time step; and the b terms represent the coefficients of the finite difference equations to be solved, e.g, porosity and permeability. When R has a unique solution, then the postulated model can be expressed by

$$y = f(x, b) \tag{3}$$

If y^o denotes the observed data and y^* denotes the solution calculated from the postulated model, then y^* can be related to y^o by

$$y^*_i = y^o_i + e_i \tag{4}$$

In regression analysis, the e_i are generally referred to as residuals. They contain all the available

information which the model fails to properly explain for the observed variations in the dependent variables. Draper and Smith (1981) stated that the residuals contained two types of errors: random errors, e_{ri}, and bias errors, e_{bi}, that is:

$$e_i = e_{ri} + e_{bi} \tag{5}$$

They stated that: (1) the quantity e_{ri} is a random variable that has zero mean whether the model is correct or not; and (2) the quantity e_{bi} is zero if the model is correct and e_{bi} is not zero, but has a value that depends on the true model if the model is not correct. These statements imply that, when the model is correct, the bias errors are eliminated, i.e.,

$$\sum_{i=1}^{n} e_{bi} = 0 \tag{6}$$

and the sum of residuals is zero since the residuals contain only random errors. Under such a condition, the residuals are randomly distributed. However, if the model is not correct, then the residuals contain random and bias errors, i.e.,

$$\sum_{i=1}^{n} e_i = \sum_{i=1}^{n} e_{ri} + \sum_{i=1}^{n} e_{bi} \tag{7}$$

and the residuals are no longer randomly distributed. Under such a condition, the sum of the residuals equals the bias errors because the sum of random errors is zero whether the model is correct or not. The objectives of a history match process are not only to ensure a good match between the simulated

results and the observed data, but must also include eliminating bias errors in the residuals. If the bias errors can not be eliminated, then the sum of the residuals should be minimized.

6. Procedures for Measuring The Quality of History Matches

The above discussions indicate that measuring the quality of history match requires not only testing the degree of match between the simulated results and the observed reservoir performance data, but also examining of the randomness of the residuals and a measuring of the magnitude of the residuals. Measuring the quality of history matches thus requires the following steps:

(1) **test the goodness of fit** between the simulated results and the observed data to see whether there is a similarity between the shape of the simulated and the observed reservoir performance curves;

(2) **examine the randomness of residuals** to see whether the residuals are randomly distributed and bias errors are eliminated; and

(3) **measure the magnitude of residuals** to see whether bias errors are minimized if a perfect match can not be achieved and the bias errors can not be eliminated.

6.1 Testing The Goodness of Fit

Goodness of fit is used in regression analysis to describe the degree of fit between the results calculated by a model and the observed data. Statistically, a close fit indicates that it is likely that the theoretical outcomes and the observed values have occurred under the same conditions and the shapes of the theoretical and the observed curves will be similar. Reservoir performance curves

represent the records of behavior as a reservoir reacts to fluid production and/or injection. A close similarity between the shape of the simulated and the observed reservoir performance curves indicates there is a similarity between the model and the actual reservoir behavior. A good fit between the simulated and the observed curves thus reflects how close a reservoir model represents the reservoir system being studied. A lack of fit between the simulated and the observed curves indicates that differences exist between the actual reservoir properties and the model input data. Thus testing the goodness of fit to see whether there is a similarity between the shape of the simulated and the observed reservoir performance curves becomes the first step in measuring the quality of history matches.

6.2 Examining Residuals for Bias Errors

Residuals can be considered as the amount of observed values by which a model fails to account for. If the model is correct, there should be no discernible pattern to the distribution of residuals; that is, the residuals do not occur in a systematic way. Any pattern of variation present in the residuals indicates that the model input data have not been calibrated to reflect the "true" reservoir description data. Thus a "good fit" between the simulated and observed reservoir performance curves can be meaningful only insofar as the assumptions concerning the residual terms in the model are satisfied. Consequently, analyzing residuals for randomness to see whether bias errors are eliminated is the second step in measuring the quality of history matches.

6.3 Measuring the Magnitude of Residuals

If a model has been calibrated to reflect the "true reservoir" under study, then there

should be no discernible pattern to the distribution of residuals. Since it is often impossible, if not impractical, to obtain a "perfect" match between the simulated results and observed data, a set of data that provides the "best" match is generally selected to describe the reservoir. However, for an "imperfect match" condition, residuals can contain bias and random errors, i.e., $e_i = e_{r\,i} + e_{b\,i}$. The magnitude of the e_i increases with the increase in $e_{b\,i}$ since the $e_{r\,i}$ are randomly distributed and the sum of $e_{r\,i}$ is zero. The magnitude of the residuals represents the bias errors and measuring the magnitude of residuals becomes another necessary task in evaluating the quality of history matches.

7. Three Indicators for Measuring the Quality of Matches

As discussed in Section 3, there is still no efficient quantitative method for measuring the quality of history match. Today, qualitative phrases are often used to describe the quality of history matches. This is because methods proposed in the past were either inefficient or cumbersome to use. To avoid these shortcomings, the following non-parametric indicators were selected for measuring the goodness of fit, the randomness of residuals and the magnitude of residuals:

7.1 Kolmogorov-Smirnov (K-S) Statistic

The K-S statistic involves comparing the cumulative frequencies of a theoretical distribution, E(X), with the observed cumulative frequency distribution, O(X), of N random samples and possible score X. The point at which the two distributions show the maximum divergence determines how close the observed values fit the theoretical distribution. The maximum divergence, MD, is defined as:

$$MD = maximum \mid O(X) - E(X) \mid \qquad (8)$$

The goodness of fit is measured by the significance level (α) of the K-S statistic associated with the calculated MD value (Smirov, 1948). Approximate values of α of the K-S statistic can be calculated by the following equation given by Birnbaum (June, 1952):

$$\alpha = \exp (- 2 . N . MD) \qquad (9)$$

Since O(X) and E(X) are dimensionless, this property makes the K-S statistic suitable for testing the goodness of fit for history matching problems because the matches can be done on any unit or scale without distorting the test results.

7.2 The Runs Test

The randomness of the sequence in which the residuals occur can be examined by the Runs Test. A run is defined as a succession of identical symbols which are preceded or followed by different symbols. The test examines the order of the symbols to determine the number of runs that a sample exhibits. The total number of runs in the sample gives the indication of whether the sample occurs in random sequence. If very few or a great many runs occur, it may suggest that a trend due to lack of independence exists in the residuals. A good approximation to the sampling distribution of r is the normal distribution, with mean

$$u = \frac{2\, n_1\, n_2}{n_1 + n_2} + 1 \tag{10}$$

and standard deviation

$$s = \sqrt{\frac{2\, n_1\, n_2\, (2\, n_1\, n_2 - n_1 - n_2)}{(n_1 + n_2)^2\, (n_1 + n_2 - 1)}} \tag{11}$$

and the probability of a normal distribution with u and s

$$z = \frac{r - u + 0.5}{s} \tag{12}$$

where 0.5 is the usual continuity correction factor to compensate for the fact that a continuous distribution is being used to approximate a discrete distribution (Draper and Smith, 1981). The computed z value is compared to the normal distribution table to determine whether the residuals are randomly distributed. The significance level at which the computed z value equals the tabulated value indicates the degree of randomness in the sequence in which the residuals occur.

If the runs test reveals a lack of randomness in the residuals sequence, graphic procedures can be used to analyze the residuals for patterns of errors. Draper and Smith (1981) believed that more information could be obtained from an informal examination of a residual plot than from a formal test of statistical significance of some limited null-hypothesis. They suggested that a detailed examination of a residual plot could generally reveal error patterns which could be used as the

basis for correcting model deficiencies. However, interpreting residual plots requires insight and skill. Consequently, interpretation can be very subjective and formal statistical tests are still needed for quantitatively measuring residuals randomness.

7.3 Mean Absolute Error

The mean percentage error, MAE, which is defined as:

$$MAE = \frac{1}{n} \sum_{i=1}^{n} \left| \frac{e_i}{y_i^o} \right| \tag{13}$$

where the absolute values of e_i / y^o_i are used to avoid cancellation between positive and the negative residuals. The magnitude of each e_i is still compared to its corresponding value of y^o_i to show the importance of the deviation at that time step. Since the residuals contain bias and random errors, therefore

$$MAE = \frac{1}{n} \sum_{i=1}^{n} \left| \frac{e_{bi}}{y_i^o} \right| + \frac{1}{n} \sum_{i=1}^{n} \left| \frac{e_{ri}}{y_i^o} \right| \tag{14}$$

The mean absolute error approaches infinity when any y^o_i approaches zero. The following procedures are used to correct this problem:

(1) When both the simulated and the observed values at any time step are zero, then the residual at that time step will be treated as zero.

(2) When any observed value is zero, for instance, $y^{o}_{j} = 0$, but the corresponding model value, y^{*}_{j} is not zero, then an $y^{o}_{j+0.25}$ and an $y^{*}_{j+0.25}$ are interpolated for $t_j + 0.25(t_{j+1} - t_j)$ to substitute for y^{o}_{j} and y^{*}_{j}, respectively. A new $e_{j+0.25}$ is calculated as a substitute for e_j. The constant 0.25 is an arbitrary number used to account for the fact that the $y^{o}_{j+0.25}$ is interpolated as a substitute for y^{o}_{j} rather than y^{o}_{j+1}. The interpolation process can also be carried backward to point t_{j-1} if preferred. If $y^{o}_{j+1} = 0$, then the interpolation is carried on to the time step until where the observed value is greater than 0.

The interpolation process is justified because when there is a good fit between the simulated and the observed curves, y^{o}_{j} will be close to y^{*}_{j} and the interpolated values will also be close to each other. Therefore, the error introduced by the interpolation process will be small. If there is not a good fit, then there is no need to worry about the magnitude of residuals, since the match will have been rejected.

8. Evaluation of The Efficiency of The Method

A hypothetical reservoir model was used to generate "observed" data. Six sets of simulated results were generated by setting porosity and permeability values 5%, 10% and 20% above and below the true values. All other reservoir and well control parameters were unchanged. The simulated BHP, GOR and WOR data were compared with the "observed" data. The K-S statistic, the runs test and the mean absolute error were used to evaluate the quality of the six sets of simulated results. The results, given in Figure 1, show that the three statistical indicators are effective for measuring the quality of matches:

(1) The match quality improved with decreases of errors in the porosity and permeability. This shows that the proposed method can effectively detect the changes in the quality

of reservoir description data.

(2) The best fit, the highest randomness of residual and the lowest magnitude of residuals of the matches occurred for the cases with the smallest errors in the porosity and permeability. This further confirms that the K-S statistic, the runs test and the mean absolute error are effective methods to measure the quality of history matches.

(3) Generally, when the K-S statistic showed a good fit and the mean absolute error showed a small magnitude of residuals, the runs test still showed a low level of residuals randomness. This indicates that the runs test is highly sensitive to bias errors in the residuals.

9. Application of The Method

The three statistical indicators were applied to analyze the quality of 44 reported history matches from seven published field studies. The data were obtained from digitizing the published graphs (Ader and Stein, 1982; Kuo, et al, 1990; Grantz, 1980; Hopkins and Lancaster, 1991; Moltz, 1991; Kansas Corporation Commission Docket C-164, 1985), except one that was supplied by the author (Young and Paul, 1993). The results indicate that a good fit only indicates a close conformity between the shapes of the simulated and the observed curves. It does not guarantee that bias errors, as indicated by the randomness of residuals, do not exist in the residuals. Figure 2 compares the goodness of fit, the randomness of residuals and the magnitude of residuals of the 44 matches analyzed. Note that the matches are arranged according to the goodness of fit values in an ascending order. The figure shows most of the matches that had a low residual randomness also had a low goodness of fit. Only eight of the 22 matches tested with greater than 5% residual randomness

occurred to the matches that had a better than 90% goodness of fit. This shows that residuals can contain bias errors even when the simulated performance curve appears to closely conform to the observed curve. The distribution of the magnitude of residuals for the 44 matches shows a distinct trend when compared to the goodness of fit values, only in inverted order. Most of the matches tested with lower than 90% goodness of fit had a 10% or higher in residual magnitude. This indicates that conformity in the shapes of the simulated and the observed curves generally reduced the magnitude of residuals, although this may not be true in every match. However, these two indicators together do not guarantee a good match quality. For instance, two curves having a close similarity in shapes may show a high goodness of fit with small residual magnitude, yet the runs test may still show a low level of residual randomness.

10. Conclusions

Application of the method to test the quality of history matches for published field studies confirms that the K-S statistic, the runs test and the mean absolute error are efficient indicators for measuring the quality of history matches. It is concluded that:

(1) Quantitative measurement of the quality of history matches requires all three quality indicators: the goodness of fit, the randomness of residuals and the magnitude of residuals; no single indicator can be ignored.

(2) The K-S statistic, the runs test and the mean absolute error are efficient indicators for testing the goodness of fit, examining randomness of residuals and measuring the magnitude of residuals, respectively.

(3) An efficient history matching strategy should first be devoted to increasing the

goodness of fit and the randomness of residuals, then to minimizing the magnitude of residuals.

(4) Residuals plots are effective tools for detecting and analyzing bias errors present in the residuals.

ACKNOWLEDGEMENT

The authors would like to thank Advanced Resources International, Inc. of Lakewood, Colorado for providing a portion of the data used in this study.

REFERENCES CITED

Ader, J. C. and Stein, M. H., 1982: Slaughter Estate Unit CO_2 Pilot Reservoir Description via a Black Oil Model Waterflood History Match, SPE #10727, Proceedings of the 3rd SPE/DOE Joint Symposium on Enhanced Oil Recovery, Tulsa, Oklahoma, April 4-7, 1982, pp. 817-838.

Birnbaum, Z. W., June, 1952: Distribution-Free Tests of Fit for Continuous Distribution Functions, Preprint of the Meeting of the Inst. of Mathematical Statistics in Eugene, Ore., June 21, 1952, pp. 1-8.

Birnbaum, Z. W., September, 1952: Numerical Tabulation of the Distribution of Kolmogorov's Statistic for Finite Sample Size, American Statistical Association Jour., September 1952, pp. 425-441.

Chatterjee, S. and Price, B., 1977: Regression Analysis by Examples, John Wiley & Sons, N.Y., 1977.

Dixon, T. N., Seinfeld, J. H, Startzman, R. A. and Chen, W. H., 1973: Reliability of Reservoir Parameters from History Matched Drill Stem Tests, SPE #4282, Proceedings of the 3rd SPE Numerical Simulation of Reservoir Performance Symposium, Houston, Tx, January 10-12, 1973.

Dogru, A. H. and Knapp, R. M., 1975: The Reliability of the Predicted Performance of Natural Gas Reservoirs using Reservoir Parameters from Well Test Data Containing Errors, Preprint of the Rocky Mountain Regional Meeting of SPE, Denver, Co., April 7-9, 1975.

Draper, N.R. and Smith, H., 1981: Applied Regression Analysis, 2nd ed., John Wiley & Sons, N.Y., 1981.

Grantz, R. E., 1980: Waterflood History Match Study of the Torchlight Tensleep Micellar Pilot, SPE #9046, Preprint of the SPE Rocky Mountain Regional Meeting, Casper, Wyoming, May 14-16, 1980.

Hopkins, C. W. and Lancaster, D. E., 1991: History Match Analysis of Production and Well Test Data from Mitchell Energy Corporation's Stella Young 4 Well, Topical Report on Reservoir Engineering and Treatment Design Technology, GRI Contract #5086-213-1446, November 1991.

Jahns, H. O., 1966: A Rapid Method for Obtaining a Two-Dimensional Reservoir Description from Well Pressure Response Data, SPEJ, December 1966, pp. 315-327.

Kansas Corporation Commission Docket C-164, 1985: Direct Opening Testimony and Rebuttal Testimony Exhibits: Application of Cities Service Oil and Gas Company for an Order Amending the Basic Proration Order for the Kansas Hugoton Field before the State of Kansas, February - April, 1985.

Kuo, M. C. T. and Dulaney, J. P., Deer, M. W. and Evans, B. S., 1990: Optimization of Waterflood Performance and CO_2-Flood Design Using a Modeling Approach, Mallet Unit, Slaughter Field, Proceeding of the 65th Annual Technical Conference & Exhibition of SPE, New Orleans, La., September 23-26, 1990, pp. 609-620.

Slater, G. E. and Durrer, E. J., October, 1971: A Statistical Method for Judging the Adequacy of a Numerical Reservoir Simulation, SPE #3182, Preprint of the 46th SPE Annual Fall Meeting, New Orlean, La., October 3-6, 1971.

Watson, A. T., Gavalas, G. R. and Seinfeld, J. H., 1984: Identifiability of Estimates of Two-Phase Reservoir Properties in History Matching, SPEJ, December. 1984, pp. 697-706.

Watson, A. T., Gatens, J. M, III, Lee, W. J. and Rahim, Z., 1989: An Analytical Model for History Matching Naturally Fractured Reservoir Production Data, Proceeding of the SPE Production Operations Symposium, Oklahoma City, OK, March 13-14, 1989, pp. 295-305.

Young, G.R.C. and Paul, G.W., 1993: Reservoir Characterization of Mary Lee and Black Creek Coals at the Rock Creek Field Laboratory, Black Warrior Basin, GRI Topical Report, Contract #5091-214-2316, August 1993.

Figure 1. Quality of Matches vs. Errors in Porosity and Permeability.

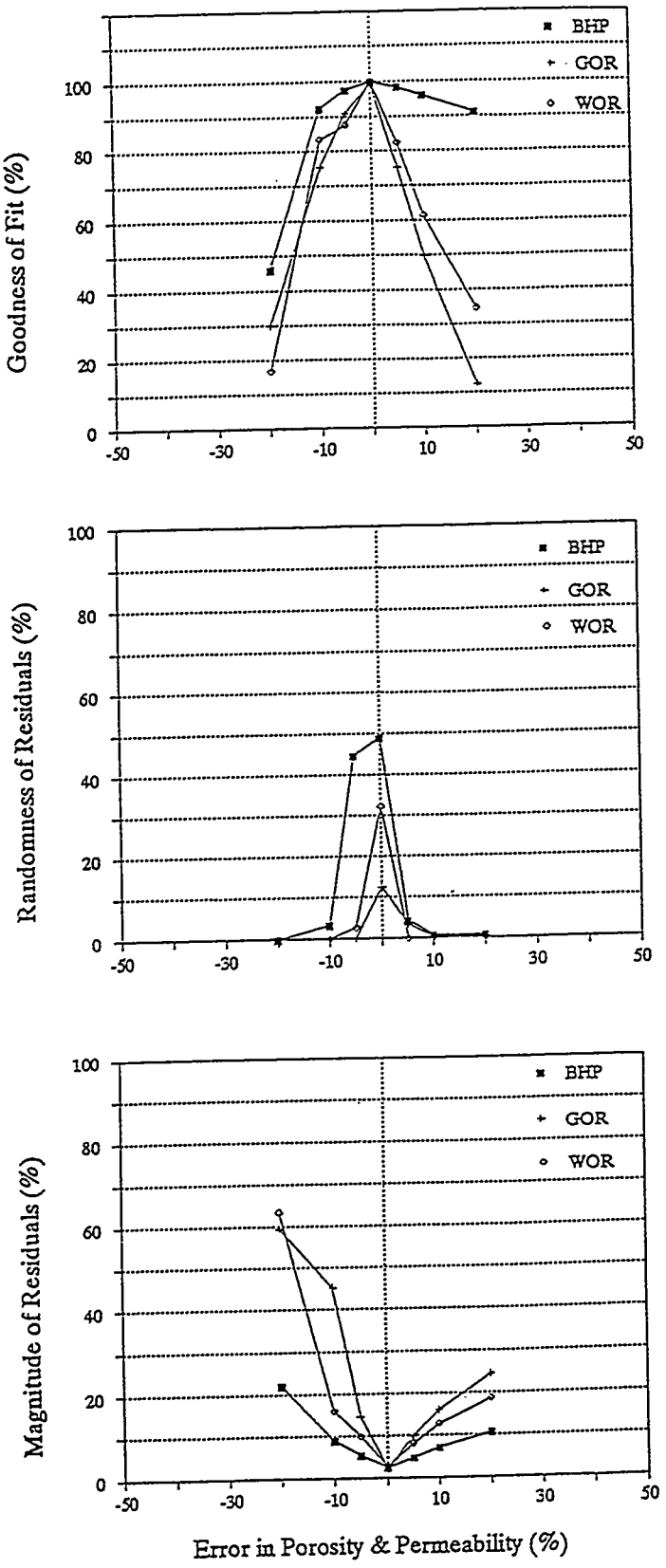

Figure 2. Quality of Matches on Published Studies.

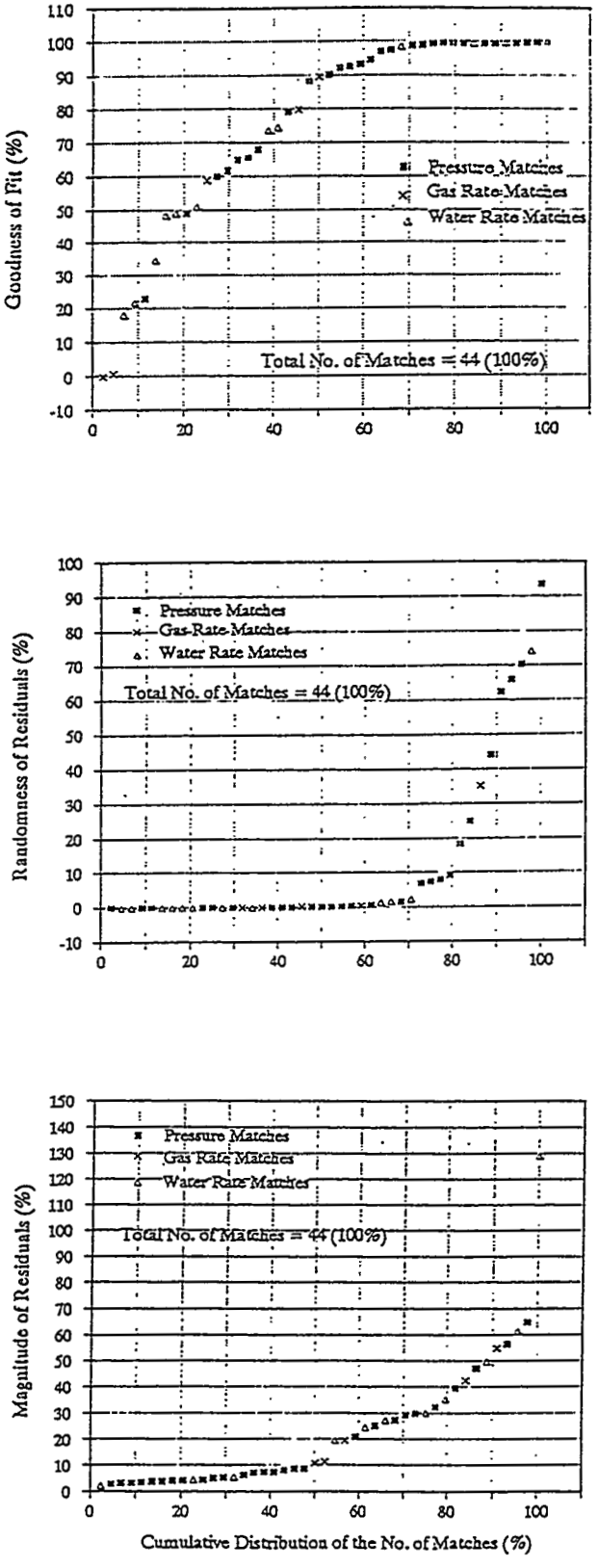

Study on Fine Geological Modelling of the Fluvial Sandstone Reservoir in Daqing Oilfield

Zhoa Han-Qing
Daqing Research Institute
of Exploration and Development
Ranghulu, Daqing
Helongjiang 163712 P.R. China

ABSTRACT

These paper aims at developing a method for fine reservoir description in maturing oilfields by using close spaced well logging data.

The main productive reservoirs in Daqing oilfield is a set of large fluvial-deltaic deposits in the Songliao Lake Basin, characterized by multi-layers and serious heterogeneities. Various fluvial channel sandstone reservoirs cover a fairly important proportion of reserves. After a long period of water flooding, most of them have turned into high water cut layers, but there are considerable residual reserves within them, which are difficult to find and tap. Making fine reservoir description and developing sound a geological model is essential for tapping residual oil and enhancing oil recovery.

The principal reason for relative lower precision of predicting model developed by using geostatistics is incomplete recognition of complex distribution of fluvial reservoirs and their internal architecture's. Tasking advantage of limited outcrop data from other regions (suppose no outcrop data available in oilfield) can only provide the knowledge of subtle changing of reservoir parameters and internal architecture. For the specific geometry distribution and internal architecture of subsurface reservoirs (such as in produced regions) can be gained only from continuous infilling logging well data available from studied areas. For developing a geological model, we think the first important thing is to characterize sandbodies geometries and their general architecture's, which are the framework of models, and then the slight changing of interwell parameters and internal architecture's, which are the contents and cells of the model. An excellent model should posses both of them, but the geometry is the key to model, because it controls the

contents and cells distribution within a model. Inaccurate framework geometry results in complete failure of modelling, but inaccurate contents and cells can only bring about partial error.

Relying on sedimentological knowledge of modern deposits, using close spaced well logging curves which are available in large areas, we have succeeded in seeking out a new method for fine and accurate description of the framework and geometry of fluvial reservoirs. According to sedimentary rules which are unique in the various channels and the sedimentary facies preserved in the sandbodies, we studied the sandbody geometries, internal architecture and heterogeneities at different levels, in order to finally develop fluvial reservoir sedimentation models, to describe the reservoir heterogeneity. By largely applying this thought to subsurface study, we have got a great success.

The first step is according to close spaced well curves, subdividing the sedimentary units of fluvial reservoir into single channel sedimentary units (single fluvial cycle) and then drawing the unit microfacies map based on the accurate recognition of sedimentary microfacies.

The second is recognizing the single channel sandbody from complex channel sandbody extending widely in lateral, and judging the genetic type of each channel, and finally predicting boundary positions between wells, describing geometry, scale and associated pattern.

In the third step, the thickness distribution pattern of each single channel sandbody is finally described. The results can be further used to reveal the thickness distribution pattern, geometry, scale orientation and Marco-architecture of the river bar and the filling body. Then such kind of structure model is used to direct the modelling study of permeability distribution of channel sandbodies in different horizons. As to more detailed reservoir hetrogeneities, such as the lateral accretion bodies of point bar and the lateral accretion baffles between them should be predicted with the help of outcrop knowledge and modern sedimentation study.

Utilizing this method, four types of fluvial channel sedimentation models in Daqing oilfield, such as sandy braided channel, high sinuosity distributary channel, low sinuosity distributary channel, and straight distributary channel have been developed. Those models systematically represent the main hetrogeneous characteristics including the sedimentary associated

features of various channel sandbodies, geometry internal architecture, permeability distribution rule, even the baffles distribution pattern of each single sandbody.

Credible accuracy and wide adaptability of these models have been proved by infilling well data and production performance. These models are particularly applied to oilfields like Daqing which have taken the technique of selective production of multizones in a single well. Meanwhile, they also provide framework models for the predicting of interwell reservoir parameters by using geostatistic and developing high resolution reservoir predicting models.

A Combination of Streamtube and Geostatical Simulation Methodologies for the Study of Large Oil Reservoirs

Dr. Avi Chakravarty; A. S. Emanuel; J. A. Bernath
Chevron Petroleum Technology Company
1300 Beach Boulevard
LaHabra, CA 90631

ABSTRACT

The application of streamtube models for reservoir simulation has an extensive history in the oil industry. Although these models are strictly applicable only to fields under voidage balance, they have proved to be useful in a large number of fields provided that there is no solution gas evolution and production. These models combine the benefit of very fast computational time with the practical ability to model a large reservoir over the course of its history. These models do not, however, directly incorporate the detailed geological information that recent experience has taught is important.

This paper presents a technique for mapping the saturation information contained in a history matched streamtube model onto a detailed geostatistically derived finite difference grid. With this technique, the saturation information in a streamtube model, data that is actually statistical in nature, can be identified with actual physical locations in a field and a picture of the remaining oil saturation can be determined. Alternatively, the streamtube model can be used to simulate the early development history of a field and the saturation data then used to initialize detailed late time finite difference models.

The proposed method is presented through an example application to the Ninian reservoir. This reservoir, located in the North Sea (UK), is a heterogeneous sandstone characterized by a line drive waterflood, with about 160 wells, and a 16 year history. The reservoir was satisfactorily history matched and mapped for remaining oil saturation. A comparison to 3-D seismic survey and recently drilled wells have provided preliminary verification.

The Ardross Reservoir Gridblock Analogue: Sedimentology, Statistical Representivity, and Flow Upscaling.

Philip Ringrose, Gillian Pickup, Jerry Jensen, and Margaret Forrester
Dept. Petroleum Engineering, Heriot-Watt University,
Edinburgh, EH14 4AS, UK.

Acknowledgements: This work has been funded by sponsors of the Reservoir Heterogeneity Project: Amerada Hess, British Gas, Chevron, Conoco, Deminex, UK Dept. of Trade and Industry, Elf, Esso, Fina, Mobil, Pan Canadian, Petrobras, Phillips, Shell, Statoil, Talisman. We thank our colleagues in the Reservoir Description Group for advice and discussion, especially Patrick Corbett, Ken Sorbie. Yaduo Huang kindly provided the lab-sample permeability data.

Abstract

We have used a reservoir gridblock-sized outcrop (10m by 100m) of fluvio-deltaic sandstones to evaluate the importance of internal heterogeneity for a hypothetical waterflood displacement process. Using a dataset based on probe permeameter measurements taken from two vertical transects representing "wells" (5cm sampling) and one "core" sample (exhaustive 1mm-spaced sampling), we evaluate the permeability variability at different lengthscales, the correlation characteristics (structure of the variogram function), and larger-scale trends. We then relate these statistical measures to the sedimentology.

We show how the sediment architecture influences the effective tensor permeability at the lamina and bed scale, and then calculate the effective relative permeability functions for a waterflood. We compare the degree of oil recovery from the formation: (a) using averaged borehole data and no geological structure, and (b) modelling the sediment architecture of the interwell volume using mixed stochastic/deterministic methods.

We find that the sediment architecture has an important effect on flow performance, mainly due to bed-scale capillary trapping and a consequent reduction in the effective oil mobility. The predicted oil recovery differs by 18% when these small-scale effects are included in the model. Traditional reservoir engineering methods, using averages permeability values, only prove acceptable in high-permeability and low-heterogeneity zones. The main outstanding challenge, represented by this illustration of sub-gridblock scale heterogeneity, is how to capture the relevant geological structure along with the inherent geo-statistical variability. An approach to this problem is proposed.

Introduction

The effects of sedimentary architecture on flow in petroleum reservoirs have been widely studied (e.g., Weber, 1982; van de Graaff & Ealey, 1989; Corbett et al., 1992; Jones et al., 1993; Kjønsvik et al., 1994; Saad et al. 1995). In most of these studies, the importance of considering the sedimentary architecture at a lengthscale relevant to the fluid flow problem (e.g., connectivity between wells versus sweep efficiency within flow units) has been stressed. But very often, the uncertainties associated with permeability estimation, inter-well variability, and relevance to effective flow behaviour at different lengthscales are un-differentiated. Thus, a general flow estimation problem, with large uncertainties, emerges. In this paper, we illustrate how sedimentary variability at different scales can be separated out into lithology-dependent components, to provide a better means of accurately judging effective flow properties of a reservoir unit. We base the illustration on a study of an outcrop the size of a typical reservoir gridblock.

The Ardross Cliff, an outcrop of Lower Carboniferous deltaic and fluvial sandstones, lies on the south coast of Fife, in eastern Scotland. This outcrop was chosen because it contains a variety of sediment architecture types which illustrate the heterogeneity which typically occurs at the sub-gridblock scale within reservoir simulation models. The main exposure is a 10 x 100m cliff, comprising two sandstone units - the Upper and Lower Ardross Castle Sand Units - separated by a prominent coal stratum (Figures 1 and 2). The lower unit is underlain by heterolithic sand and shale units, and the upper unit is overlain by a Limestone bed; both are assumed to be no-flow boundaries. The lower unit is characterised by ripple lamination, manifested in parts by well-preserved climbing ripple sets, and related to the building out of a delta front. The upper unit contains abundant trough crossbedding formed within a fluvio-deltaic channel.

Analysis of permeability measurements

Two types of probe permeameter measurements have been taken in the Ardross units. Firstly, two vertical transects of 5cm-spaced measurements were taken in the field using a steady-state field permeameter calibrated against known samples. The two transects are 70m apart and represent "wells" at either end of the "gridblock" analogue. The probe tip used had a 4mm inner radius and a 24mm outer radius (implying a hemispheric volume of investigation of about 2cm diameter). Surface preparation comprised chipping rock edges to expose a fresh surface 1 to 2cm beneath the natural surface. This avoided most of the effects of the weathered crust, although no systematic study of surface effects was conducted. Secondly, measurements were made in the laboratory, using a pressure-decay permeameter on a block sampled from the logged section, representing a "whole core" sample for determination of relative permeability and capillary pressure curves. Exhaustive 1mm-spaced

permeability profiles were aquired from a slab cut from this sample. The probe tip used had 3mm inner radius and a 6mm outer radius (implying a hemispheric volume of investigation of about 1.5cm diameter). These data thus represent higher resolution and more accurate measurements (as the pressure decay device has a higher dynamic range). The calibration established for the field permeameter appears to give a consistent dataset, with no major systematic error.

The two probe-measurement transects taken in the field are shown in Figure 2. The upper sand unit has high permeabilities, average 566md, whereas the lower unit is less permeable, average 266md. The main features of permeability variation in the two wells (e.g. high permeability layer at 2.0m below datum) can be correlated between wells.

Figure 3 shows permeability histograms for the two sand units and the lab sample. The whole formation has an approximately log-normal distribution spanning over 3 orders of magnitude (1mD to 1.4D) with a mode at 100mD. The arithmetic averages for the two units are statistically different at the 95% level. Furthermore, the high-end tail to the permeability distribution for the Lower Sand Unit can be associated with a thin cross-bedded unit (at around -2.0m on well 1 and at -2.3m on well 2, Figure 2), and the lower values in the Upper Sand Unit can be associated with ripple bedding at the base (between 0.0 and 1.0m, Figure 2). Thus, the field permeability data can be separated into two distinct groups on the basis of lithology.

At the core-scale, one can resolve the sedimentological components (lamina and beds), whose effects are aggregated in the larger-scale dataset. Figure 4 shows two of five permeability profiles collected on the core sample and a histogram of all the data. The profiles show a marked oscillatory pattern as the sand-rich and mica-rich laminae alternate, and these laminae are clearly seen on the core surface. The lamina spacing is around 2cm. Despite a drift in the precise location and permeability of these laminae as successive permeability profiles are acquired, the lamina-scale fabric is persistent and evident in the bi-modal permeability histogram (Figure 4). The permeability contrast between sand-rich and mica-rich laminae varies between about 2:1 and 5:1. In a similar manner, the upper crossbedded sand unit reveals lamina and bed-scale patterns in permeability. These patterns are used for bed-scale permeability models for each lithofacies in the following section.

Semi-variogram analysis (Jensen et al., 1996) of the 5cm-spaced well data (Figure 5) reveals the presence of holes at lags of around 0.3m, 0.9m and 1.2m. By inspection of the outcrop, we relate this evidence of cyclicity to bed-scale repetitions in the ripple-bedded lithofacies. The large nugget reflects the undersampling of lamina-scale heterogeneity by the 5cm-spaced data. The Upper Sand Unit does not display strong vertical cyclicity, but an average crossbed thickness can be identified. These lengthscales of cyclicity are used as a guide to defining the bed-scale grid dimensions used in the flow

modelling. They also define the volume scale at which the observed variability in bedscale permeability is captured as an effective flow property.

Single-phase permeability estimation

Using the field and lab permeability data, we constructed lamina-scale permeability models for the ripple-laminated Lower Sand Unit and the crossbedded Upper Sand Unit. These deterministic templates were designed to portray the characteristic permeability structure of each bed type (i.e. permeability contrast, lamina spacing, lamina shape, lamina continuity and internal grading). Variations in these characteristics, such as drift of the average between the two wells and vertical variations within the same facies, were treated by imposing stochastic variations and interwell trends on these templates. The models are illustrated in Figure 6. Two end-member cases were considered for the ripple model by allocating higher or lower permeability values for the bottomset to reflect observed variations. These end-members also represent well-connected and poorly connected extremes as far as flow is concerned. The lamina-scale ripple models were then scaled-up and assembled into stochastic bed-scale templates to capture the range of variability observed in the the wells.

A comparison of model statistics with well data is given in Table 1. A reasonable match of model to data is achieved. This could be improved on by detailed adjustment of the model values; however, our aim has been to honour the sedimentary architecture (especially lamina permeability contrasts) as much as the measured well data, so this match is quite acceptable given the uncertainties inherent in sampling.

The tensor effective permeabilities for the models were determined (Pickup et al., 1995; Pickup & Sorbie, 1996), using the Periodic Boundary Condition method, and these are shown in Table 2. The ripple lamina-scale models and the crossbed model have off-diagonal terms that are about 4% of the diagonal term, due to their cross-laminated architecture. The bed-scale ripple model, however, has negligible off-diagonal terms. This is because, at this scale, the effects of smaller-scale cross-lamination are masked by the effects of the approximately layered bed-scale architecture. The tensor permeability values also differ significantly from the arithmetic (k_a) and harmonic averages (k_h), which one might have used to estimate effective permeability. The crossbed model has $k_{xx} = 0.92\ k_a$. The actual size of the off-diagonal term depends on the crossbed geometry and lamina permeability contrast. For example, an idealised crossbed unit with layers of 10:1 permeability contrast, an angle of 26.565 (arctan 0.5) and no bottomset would have $k_{xx} = 0.866\ k_a$ (a reduction of about 13%). Thus, the lithofacies model geometries impose a small but significant control on the effective single-phase

permeability, with small but appreciable off-diagonal terms. However, the geometrical control is much more important in determining the multiphase flow behaviour.

Waterflood scale-up of the Lower Ardross Sand Unit

The lithofacies models of the Ardross Cliff have been evaluated in terms of their likely impact on a waterflood displacement, using the geopseudo method (Corbett et al., 1992, Ringrose et al., 1993, Pickup et al., 1994). This approach attempts to capture the impact of small-scale permeability architecture on multiphase flow, using some form of pseudofunction numerical scheme. For this illustration we use the Kyte & Berry (1975) method. We have evaluated the potential errors implicit to the pseudofunction scheme by comparison with other methods (e.g. Pc-equilibrium steady state). The differences can be significant but do not alter the overall conclusion, which is more influenced by the choice of rock and fluid properties than by the numerical scheme.

In the case of the crossbed model, one scale-up step is sufficient to define pseudo relative permeability functions for the gridblock model (0.3m high gridcells). However, in the case of the ripple-bedded model, pseudofunctions were first defined at the laminaset scale (3cm high model) for the high bottomset and low bottomset models. These pseudos were then applied to the stochastic bed-scale model (Figure 6) to define pseudofunctions for the gridblock model (0.3m high gridcells). Simulations at all scales are done at a flow rate of 0.2m/day, and assume a water-wet system with an endpoint mobility ratio of 1.76 (details of modelling assumptions are given in Ringrose et al., 1993). All models are 2D vertical sections.

Results for these models are given in Table 3. As a measure of the significance of these calculated recovery factors, the lithofacies-based model of the Lower Ardross Sand Unit has been compared with a model using 30cm layers defined using 30cm averages of the permeability data from Well 2. This case represents a common approach of only upscaling the permeability data (usually by averaging) and assuming the core scale relative permeability functions apply directly to the upscaled gridcell. The difference in recovery is 18%. This appreciable difference can be attributed mainly to the process of capillary oil retention within the small-scale cross-lamina and cross-bed architecture of the two lithofacies present in this section. In other work, Huang et al. (1995) and Honarpour et al. (1995) have conducted core-scale laboratory waterfloods to demonstrate that these small-scale capillary trapping phenomena do indeed occur. We are therefore confident that this degree of systematic difference in recovery (c. 20%) between models which capture and ignore the effects of lamina architecture is reasonable.

Figure 7 compares the oil production and watercut for the geopseudo model of the Lower Ardross Sand Unit with the 30cm average model. Not only is the recovery much poorer for the geopseudo model, but the watercut has earlier breakthrough and a steeper rise. Clearly, the effects of sediment architecture in this formation could have important economic significance if this formation were an oil reservoir. A cross-sectional model based on 30cm averages (1 foot spacing) would over-estimate recovery and field performance considerably. In practice, averaging as a basis for upscaling is often done at a much larger scale (c. 10m) and so the errors may be even larger.

Discussion

This study of the sedimentary architecture, permeability data, and flow property calculation serves to illustrate the potential effects of internal rock structure and variability on flow at the scale of a single reservoir model gridcell. Other studies have evaluated the impact of sedimentary architecture on waterflood over a wider range of scales (e.g. Corbett et al., 1992; Jones et al., 1993; Kjønsvik et al.,1994; Ciammetti et al., 1995; Saad et al., 1995). The general conclusion that can be drawn from these integrated studies is that small-scale heterogeneity can be important for multiphase flow, but exactly how much depends on the specific details of the sedimentary and reservoir architecture, and the displacement process being considered. One must consider the problem on a case-by-case basis. We have, however, developed some simple guidelines for assessing the potential influence of small-scale sedimentary structure on a waterflood. These are:

1) Are immiscible fluids flowing (rates <1m/day)?

2). Are significant small-scale heterogeneities present? Specifically:

Small-scale heterogeneity questions	Criterion
Is the permeability contrast	greater than 5:1 ?
Is the layer thickness pertaining to this contrast	less than 20cm ?
Is the mean permeability	less than 500md ?

If these criteria are all satisfied, then capillary/heterogneity effects should be evaluated.

A further criterion, involves the relative importance of small-scale and large-scale reservoir architecture. Even if the small-scale structure is important, it may be that the large-scale reservoir connectivity issues are still the dominant uncertainty. Using the simple classification of reserovir heterogeneity proposed by Weber and van Guens (1990), we infer the following guidelines on this aspect of the problem:

- Layer cake reservoirs - small-scale structure will usually have primary importance.
- Jig-saw puzzle reservoir - small-scale structure may be important.
- Labyrinth reservoir - small-scale structure will usually be of secondary importance.

Once the potential importance of small-scale heterogeneities have been considered and a decision to proceed with a detailed evaluation has been made, we are then faced with detailed questions about how to go about the study. We have attempted to demonstrate an approach for doing this with the gridblock analogue described here. Figure 8 summarises the procedure we have used. The underlying problem is how to handle the uncertainties inherent in an incomplete dataset (the sampling and estimation problem) along with the scale-dependent flow-structure interactions. We advocate the importance of referring both the parameter estimation problem and the flow upscaling problem to the sedimentological lengthscales inherent in the reservoir system. The procedures for doing this include:

1) Considering the sample sufficiency of the well data. An important guide is the permeability C_v (Jensen et al., 1997, pp.150-153).
2) Evaluate the scales at which permeability variability is expressed. In this example, we compared an exhaustive permeability dataset acquired from one core sample with the well data to establish the degree of small-scale variability and importantly the typical lamina permeability contrasts. Wireline microscanner measurements could help to assess the permeability contrasts and small-scale sedimentary architecture.
3) Use correlation measures (e.g. semivariogram of well data) to identify inherent sedimentary lengthscales. In this example, we identified bed-cyclicity at the 30cm lengthscale and used this to guide the definition of the small-scale gridcells.
4) Apply a knowledge of sedimentology to define likely bed-scale architectural patterns. In this example, the ripple and crossbed architectures were found to have a significant effect on remaining oil. Where aspects of the architecture are uncertain, stochastic approaches can be used.
5) Use a flow upscaling framework based on the sedimentary hierarchy of lengthscales. In this example, we used two different schemes to define upscaled flow models for the two lithofacies present in the analogue (i.e. ripple bedding and cross-bedding).

This approach has been applied to a 3D reservoir study of a fluvio-aeolian system (Sylvester et al., 1996). This study shows that the approach is practicable within a realistic field development programme and has a significant impact on field performance predictions (in the case the geologically-based upscaling led to a 29% difference in recovery). However, more automated methods are needed in order to perform this type of study on a more routine basis.

The difficulties in actually detecting and modelling geological structure in the subsurface should not be under-estimated (Jensen et al., 1996). However, a greater emphasis on the smaller scale aspects of reservoir architecture is warranted in view of their potentially significant impact on flow. Conventional geostatistical approaches (modelling the reservoir at a single scale using correlation functions) may fail to account for the reservoir architecture that actually affects flow.

Finally, there is considerable uncertainty about the choice of multiphase flow function to use as input to the scale-up procedure. We have not considered this problem here, but have argued elsewhere (Ringrose et al., 1996) that the lithofacies control is also vital when considering the choice of special core analysis sample, the laboratory method, and the procedure for applying it to the simulator model. We have also tested our upscaling approach against a whole core experiment to lend support to our choice of multiphase flow functions for input at the lamina scale (Huang et al., 1995).

Summary

The Ardross analogue provides an illustration of flow-heterogeneity interactions at the reservoir gridblock scale. Although the analogue is a specific example from a deltaic sequence, the sediment structures involved (ripple and crossbed lamination) occur quite widely in many other sediment environments. Our studies of effective single-phase permeability and two-phase waterflood of the cliff have demonstrated some very significant effects of sediment structure:

1. The tensor effective permeability k_{xx} term can be 10% less than the arithmetic average.
2. Waterflood oil recovery could be 20% lower than that estimated from arithmetic averages of 30cm (1 ft) intervals.

The architectural characteristics of any particular reservoir unit can be established using well data, provided that the data sufficiency is evaluated and the true lengthscales and patterns of permeability variability are identified. The basic tools for doing this involve the comparison of data from different lengthscales, different sedimentological models and use of correlation measures. We have shown how spatial and scale-dependent variability can be captured using mixed deterministic/stochastic models which incorporate the sediment structure as well as known spatial variability. This small-scale sedimentary architecture is particularly important when assessing waterflood behaviour.

References

Ciammetti, G., Ringrose, P.S., Good, T. R., Lewis, J. M. L., and Sorbie, K. S., 1995. Waterflood recovery and fluid flow upscaling in a shallow marine and fluvial sandstone sequence. SPE 30783, presented at the SPE Annual Technical Conference and Exhibition, Dallas, USA, 22-25 Oct., 1995.

Corbett, P. W. M., Ringrose, P. S., Jensen, J. L., and Sorbie, K. S., 1992. Laminated clastic reservoirs - the interplay of capillary pressure and sedimentary architecture. SPE Paper 24699, presented at the SPE Annual Technical Conference, Washington, 4-7 October, 1992.

Honarpour, M.M. Cullick, A.S., Saad, N. and Humphreys, N.V., 1995. Effect of rock heterogeneity on relative permeability: implications for scale-up. Journal of Petroleum Technology, November 1995, p.980-986.

Huang, Y., Ringrose, P. S., & Sorbie, K. S., 1995. Capillary Trapping Mechanisms in Water-wet Laminated Rock. SPE Reservoir Engineering, November 1995, p.287-292.

Jones, A., Doyle, J., Jacobsen, T., and Kjønsvik, D., 1993. Which Sub-seismic heterogeneities influence waterflood performance? A case study of a low net-to-gross fluvial reservoir. Proceedings of the 7th European IOR Symposium, Moscow, Russia, 27-29 October, 1993.

Jensen, J. L., Corbett, P. W. M., Pickup, G. E. and Ringrose, P. S., 1992. Permeability semivariograms, geological structure and flow performance. Mathematical Geology, 28(4), p. 419-435.

Jensen, J. L., Lake, L., Corbett, P. W. M., and Goggin, D. J., 1997. Statistics for Petroleum Engineers and Geoscientists. Prentice Hall PTR, New Jersey.

Kjønsvik, D., Doyle, J., Jacobsen, T., and Jones, A., 1994. The effects of sedimentary heterogeneities on production from a shallow marine reservoir - What really matters? SPE paper 28445, presented at the European Petroleum Conference, London, 25-27 October, 1994.

Kyte, J. R. and Berry, D. W., 1975. New Pseudo Functions to Control Numerical Dispersion. Soc. Pet. Eng. J., August, 1975, 269-275.

Pickup, G. E., Ringrose, P. S., Forrester, M. M., Jensen, J. L., & Sorbie, K. S., 1994. The Geopseudo Atlas: Geologically-Based Upscaling of Multiphase Flow. SPE Paper 27565 given at the SPE European Petroleum Conf., Aberdeen, 15-17 March 1994, p.277-289.

Pickup, G. E., Ringrose, P. S., Corbett, P.W.M., Jensen, J. L., & Sorbie, K. S., 1995. Geology, geometry and effective flow. Petroleum Geoscience, 1(1), p.37-42.

Pickup, G. E. and Sorbie, K. S., 1996. The Scaleup of Two-Phase Flow in Porous Media Using Phase Permeability Tensors. Society of Petroleum Engineers Journal, December 1996, in press.

Ringrose, P. S., Sorbie, K. S., Corbett, P. W. M., and Jensen, J. L., 1993. Immiscible flow behaviour in laminated and cross-bedded sandstones. Journal of Petroleum Science and Engineering, 9, p.103-124.

Ringrose, P. S., Jensen, J. L. and Sorbie, K. S., 1996. Use of geology in the interpretation of core-scale relative permeability data. SPE Formation Evaluation, Sept. 1996, p.171-176.

Saad, N., Cullick, A.S. and Honarpour, M.M., 1995. Effective relative permeability in scaleup and simulation. Paper SPE 29592, presented at the 1995 SPE Joint Rocky Mountain Regional/Low-Permeability Reservoirs Symposium, Denver, CO., March 20-22.

Sylvester, I. F., Carruthers, D., Ringrose, P. S., Bratvold, R. B., and Lia, O., 1996. Gas/water flow upscaling in a mixed fluvio-aeolian reservoir simulation model. SPE Paper 35492, presented at the European 3D modelling Conference, Stavanger, 16-17 April, 1996.

van de Graff, W. J. E. and Ealey, P. J., 1989. Geological modelling for simulation studies. American Association of Petroleum Geologists Bulletin, 73(11), p.1436-1444.

Weber, K. J., 1982. Influence of common sedimentary structures on fluid flow in reservoir models. Journal of Petroleum Technology, March 1982, p.665-672.

Weber, K. J., and van Geuns, L. C.,1990. Framework for constructing clastic reservoir simulation models. Journal of Petroleum Technology, October 1990, p.1248-1297.

Figure Captions

Figure 1. Photograph of part of the Ardross outcrop showing the nature of the two main sand units.

Figure 2. Stratigraphic logs and permeability data for the two wells sampled at either end of the outcrop. (The coefficient of variation, Cv, is defined as the standard deviation divided by the arithmetic mean).

Figure 3. Permeability histograms.

Figure 4. Permeability profiles from the core data revealing the presence of the alternating sand-rich and mica-rich laminae within the ripple-bedded facies.

Figure 5. Semivariogram of well data from well 1.

Figure 6. Flow model templates for (A) lamina-scale ripple model (3cm high by 15cm long), (B) bed-scale ripple model (0.3m high by 1.5m long), (C) bed-scale crossbed model (0.3m high by 1.5m long). Darker tones indicate lower permeabilities.

Figure 7. Simulated oil production and watercut for a cross-sectional model of the Lower Ardross Sand Unit: (A) using geopseudo upscaling (B) using pseudos of 30-cm averaged well data.

Figure 8. Illustration of the integrated approach to flow upscaling, accounting for sedimentology and statistical representivity.

Lithofacies model	Arithmetic average (standard deviation) of model	Arithmetic average (st. dev.) of corresponding well data
Crossbed model (for both wells)	664 (356)	566 (308)
Ripple model Well 1 high-k bottomset	308 (211)	329 (153)
Ripple model Well 1 low-k bottomset	213 (158)	
Ripple model Well 2 high-k bottomset	154 (106)	153 (97)
Ripple model Well 2 low-k bottomset	107 (79)	

Table 1. Comparison of permeability statistics for lithofacies models and well data.

Lamina-scale ripple model (low-k bottomset)

192	0	-9
0	213	0
-9	0	124

Lamina-scale ripple model (high-k bottomset)

289	0	-11
0	308	0
-11	0	162

Bed-scale ripple model

234	0	0.08
0	259	0
0.08	0	139

Bed-scale crossbed model

612	0	-20
0	664	0
-20	0	311

Key to tensor permeability terms

k_{xx}	k_{xy}	k_{xz}
k_{yx}	k_{yy}	k_{yz}
k_{zx}	k_{zy}	k_{zz}

Table 2. Permeability tensors for the ripple and crossbed lithofacies models (well 1).

	Small-scale (3cm high)	bed-scale (30cm high)	Field-scale
Upper Ardross Sand Unit			
Curved graded crossbed model		50.19	54.34
Lower Ardross Sand Unit			
Ripples: Low k bottomset	38.00		
Ripples: High k bottomset	44.54		
Ripple bed-scale model with stochastically distributed high and low bottomsets		41.36	44.29
Model using 30cm average peremability data in place of lithofacies models			52.52
Difference in recovery if small-scale sedimentary architecture is ignored (Lower Sand Unit)			+18.6%

Table 3. Waterflood recovery (percent of original oil in place) after injection of 1 pore volume for different models of the Ardross Cliff.

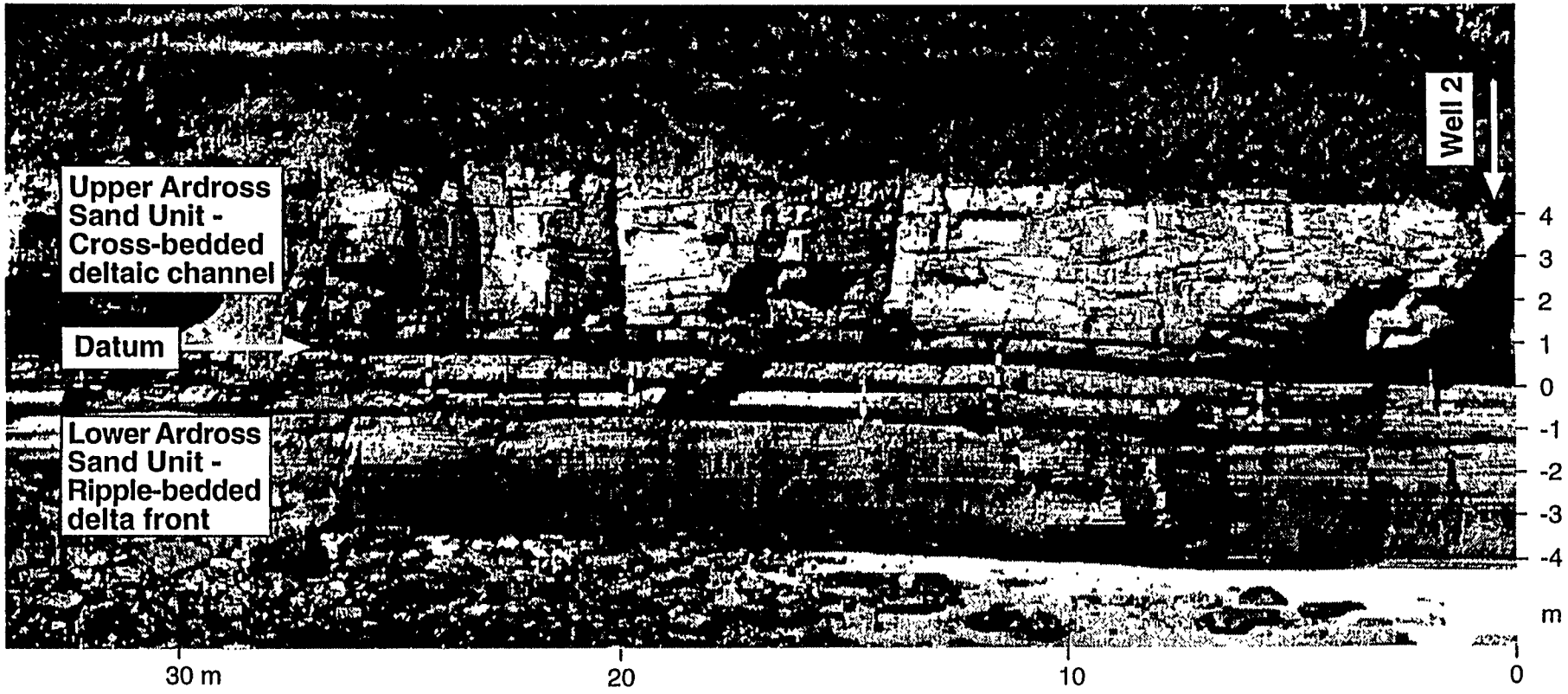
Upper Ardross Sand Unit - Cross-bedded deltaic channel
Datum
Lower Ardross Sand Unit - Ripple-bedded delta front
Well 2
4
3
2
1
0
-1
-2
-3
-4
m
30 m
20
10
0

Figure 1

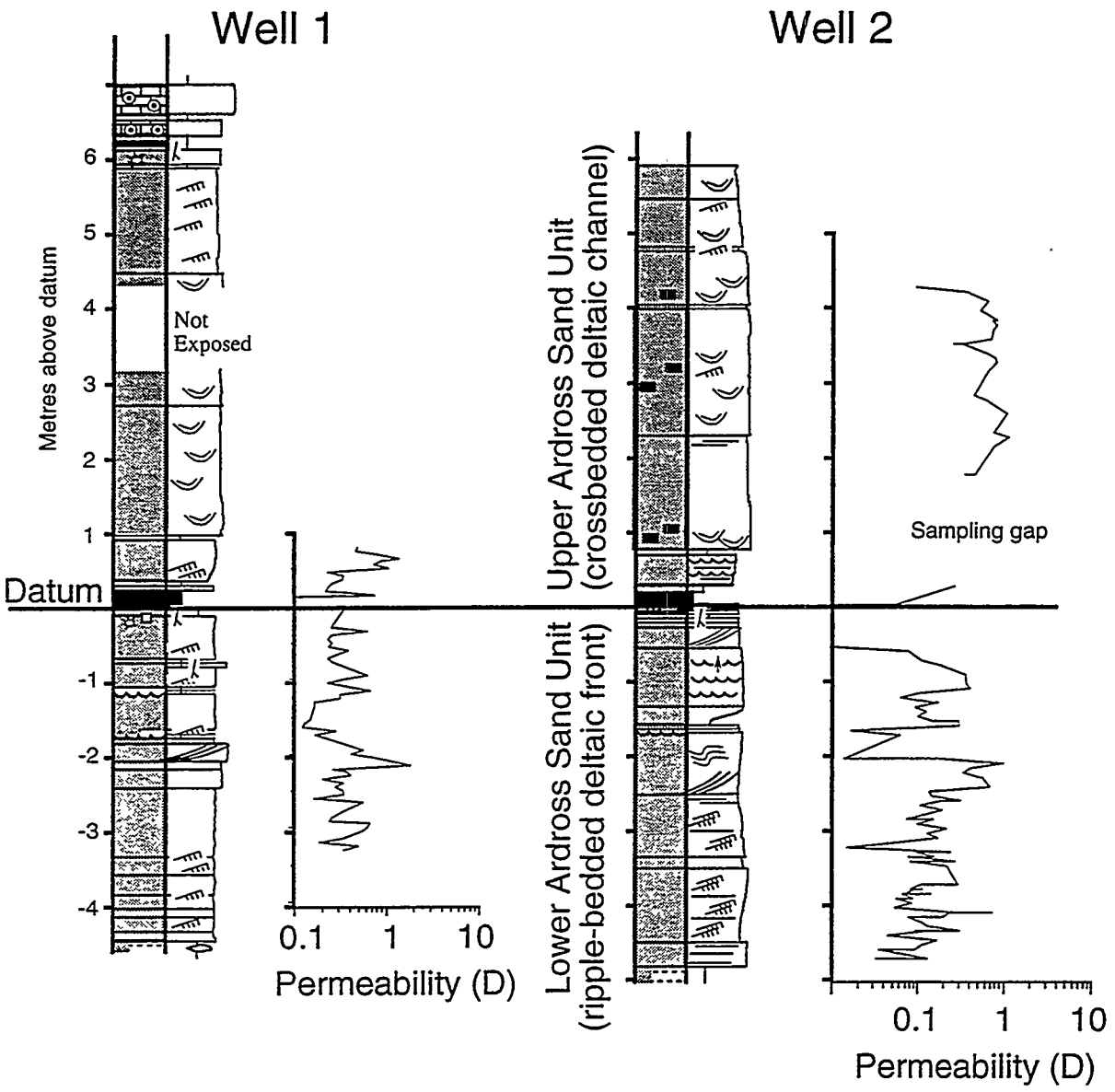

	Both Units	Lower Unit	Upper Unit
Well 1	N = 57	N = 43	N = 14
Arith Av	433.41	391.19	571.35
St. Dev.	313.40	290.98	353.64
Cv	0.72	0.74	0.62
Well 2	N = 115		N = 30
Arith Av	290.15	194.68	563.84
St. Dev.	272.08	189.82	288.84
Cv	0.94	0.97	0.51
Both Wells	N = 172		N = 44
Arith Av	341.09	266.01	566.34
St. Dev.	294.71	249.36	307.89
Cv	0.86	0.94	0.54

Figure 2

A) Histogram of field probe data from both wells separated into Lower and Upper Sand Units

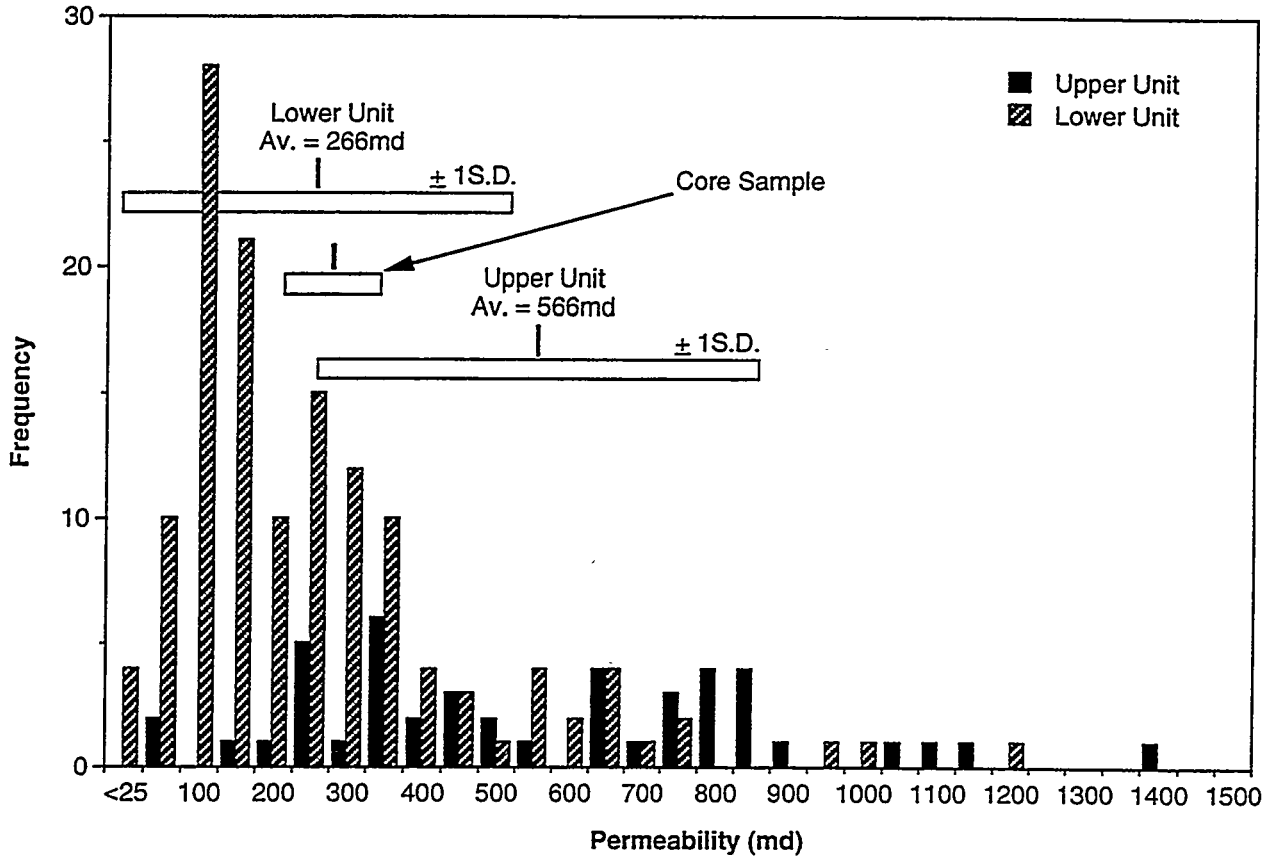

B) Histogram of (exhaustive) lab probe data from one core sample from the Lower (ripple-bedded) Sand Unit

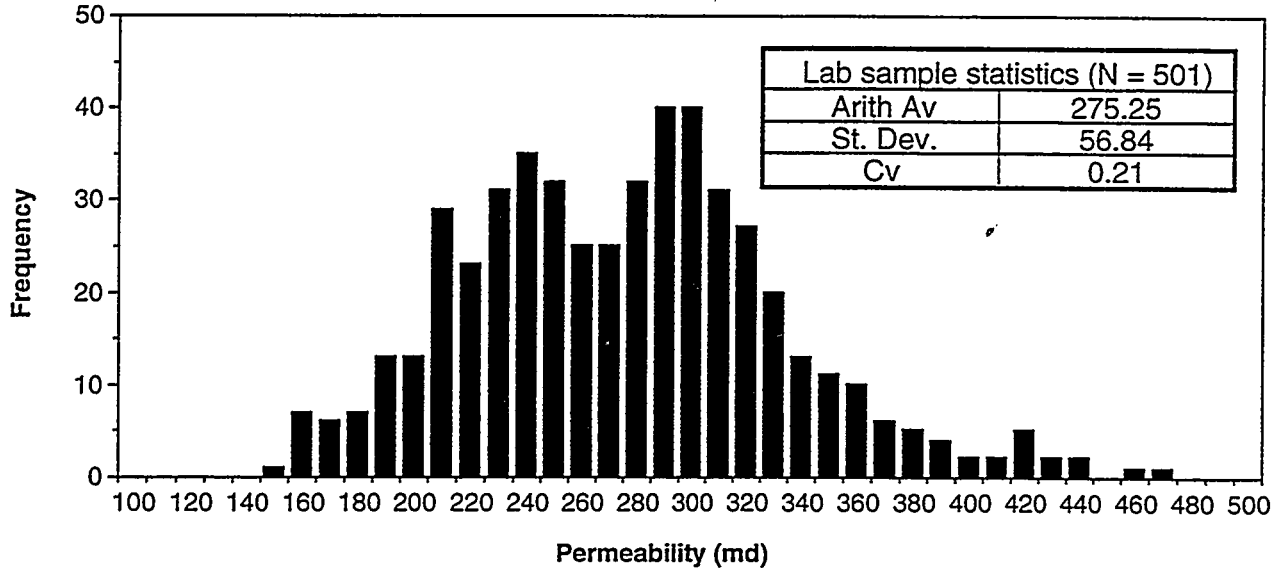

Figure 3

Permeability (md)
Frequency (All five profiles)
Permeability profiles
Distance (cm)
1st profile
5th profile
Mica-rich laminae
Sand-rich laminae

Figure 4

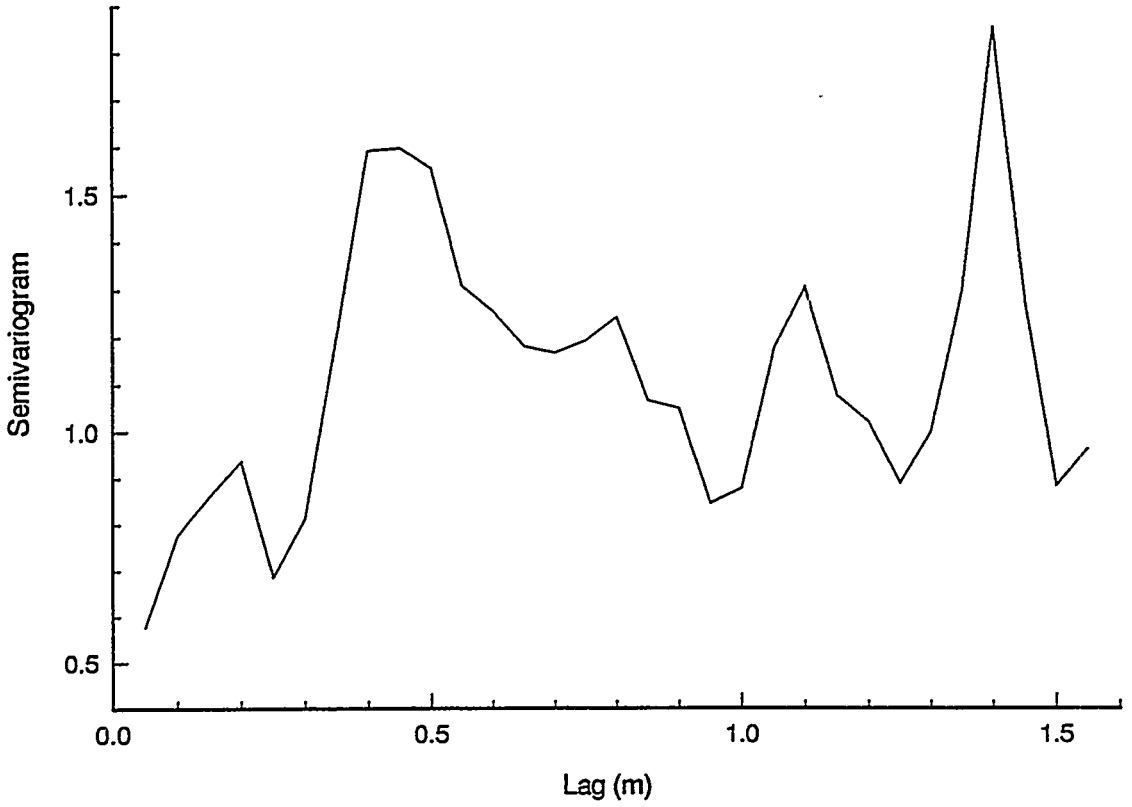

Figure 5

A

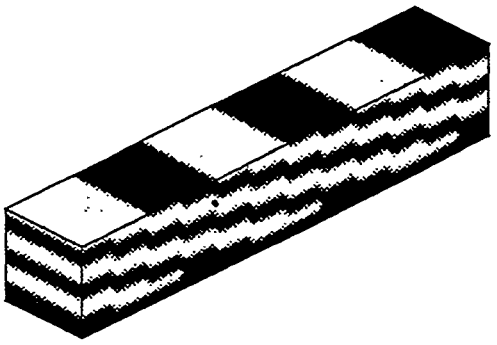

B

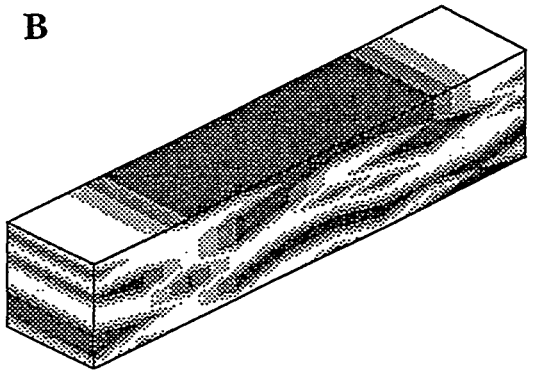

C

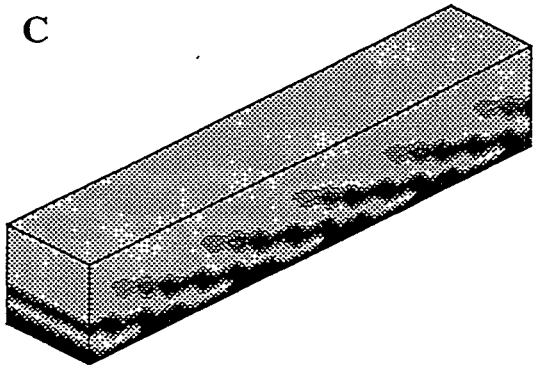

Figure 6

A) With geopseudos

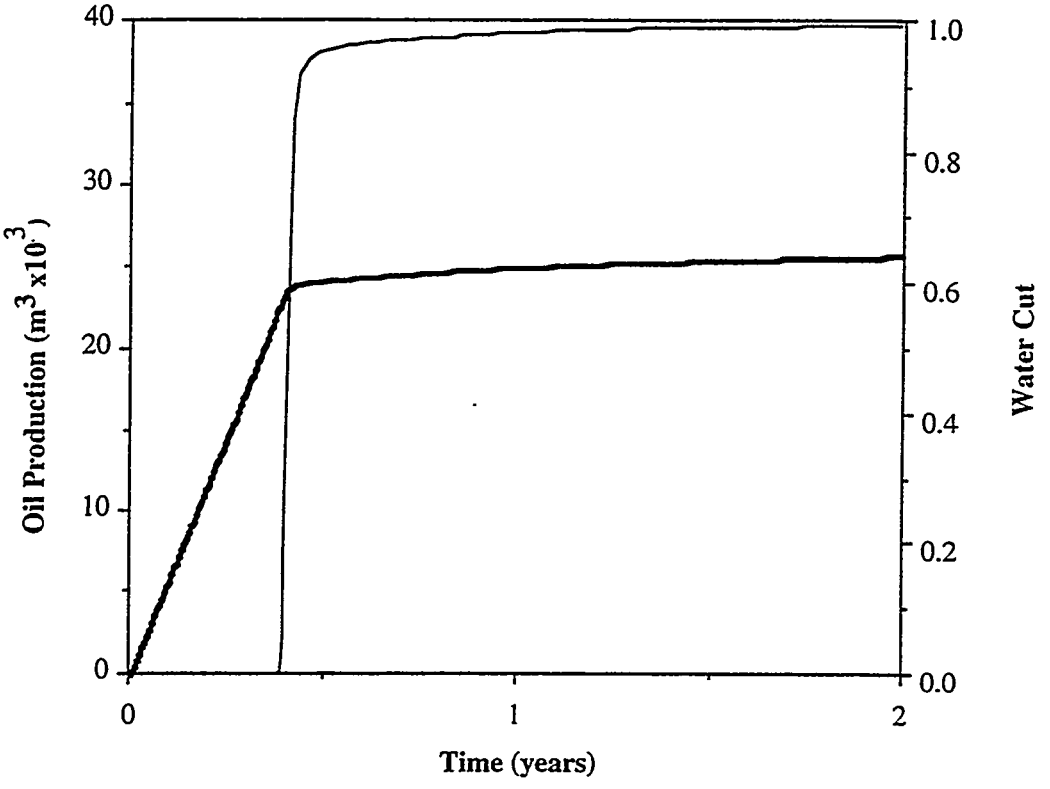

B) With 30cm average pseudos

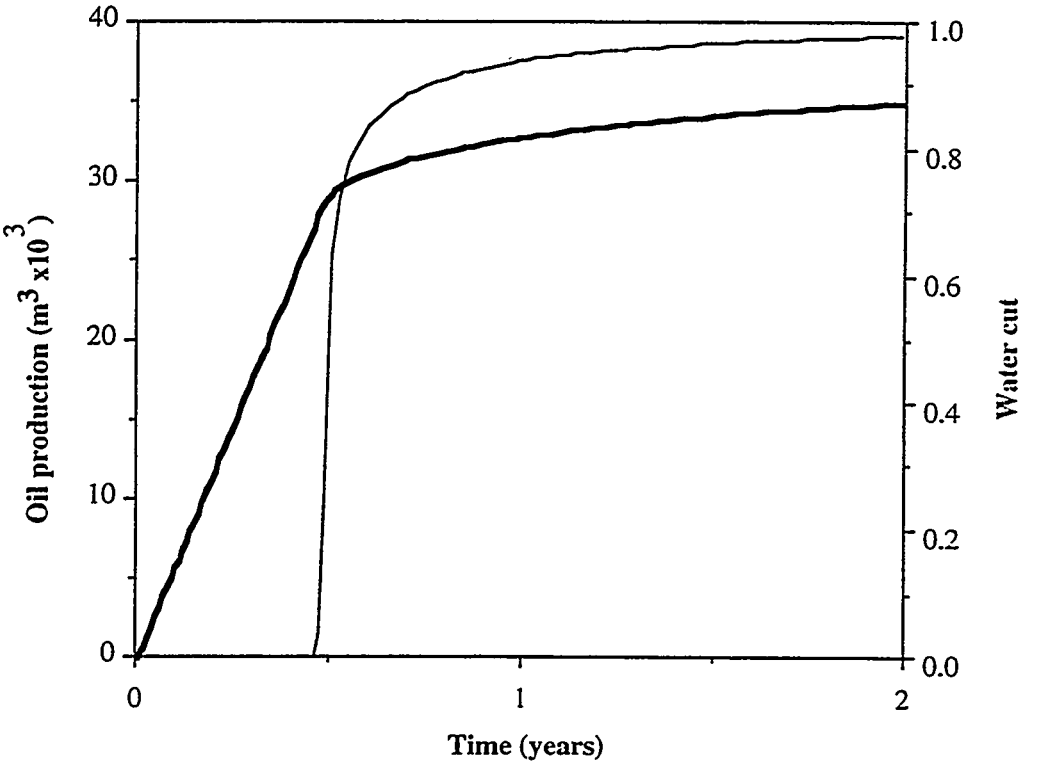

Figure 7

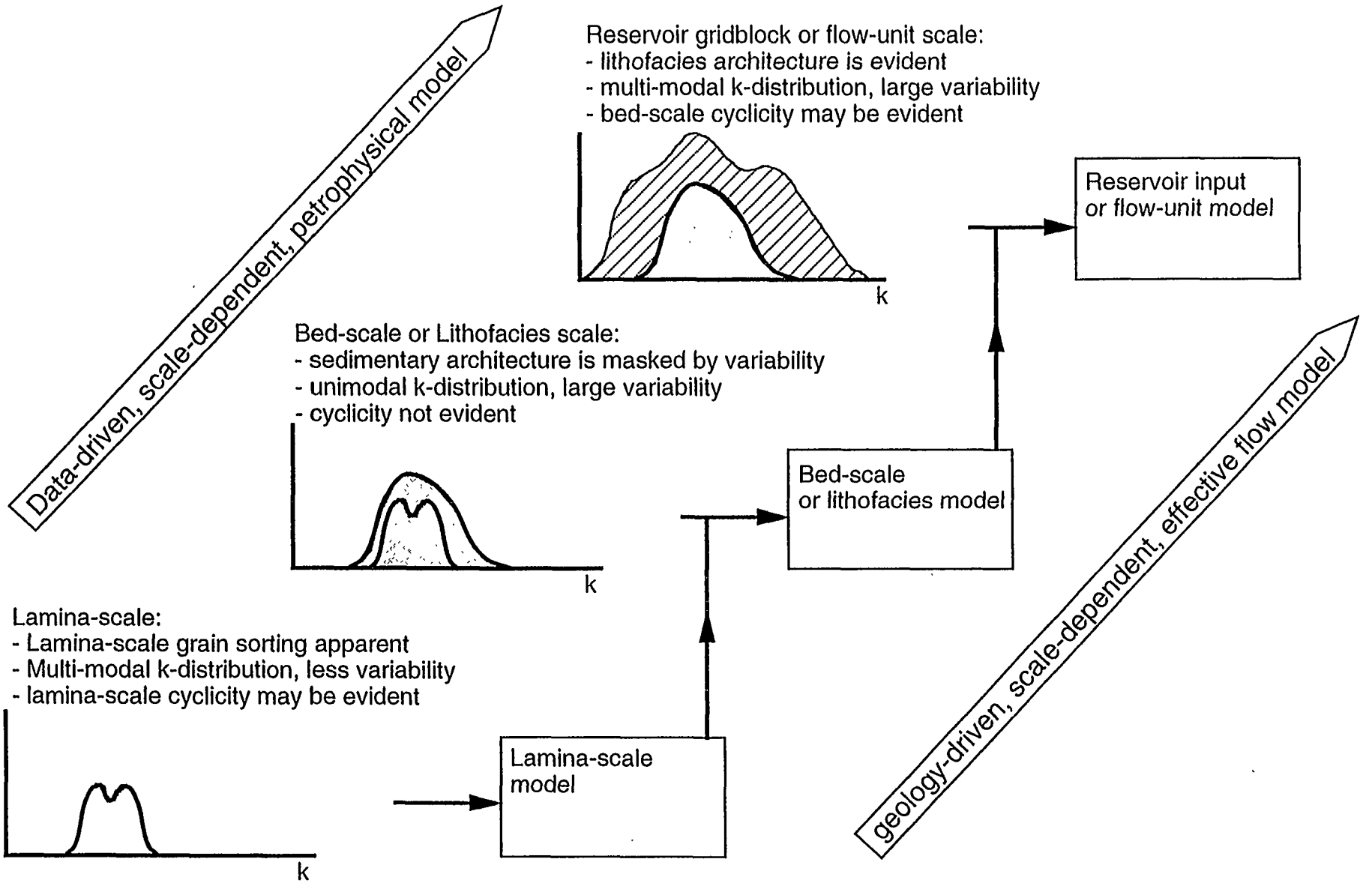
Data-driven, scale-dependent, petrophysical model
Reservoir gridblock or flow-unit scale:
- lithofacies architecture is evident
- multi-modal k-distribution, large variability
- bed-scale cyclicity may be evident
k
Reservoir input
or flow-unit model
Bed-scale or Lithofacies scale:
- sedimentary architecture is masked by variability
- unimodal k-distribution, large variability
- cyclicity not evident
k
Bed-scale
or lithofacies model
Lamina-scale:
- Lamina-scale grain sorting apparent
- Multi-modal k-distribution, less variability
- lamina-scale cyclicity may be evident
k
Lamina-scale
model
geology-driven, scale-dependent, effective flow model

Figure 8

Title: Use of Element Model to Evaluate Transmissibility Reduction Due to Barriers.

Authors: Tarald Svanes, Deborah South, Ole Magnar Drønen,

Statoil, 5020 Bergen, NORWAY.

ABSTRACT

Water breakthrough has been observed a year earlier than expected in the productive Oseberg Formation in the Veslefrikk Field. Production data revealed extensive water override, whereas the opposite situation was expected based on a homogeneous and coarse flow simulation model.

A new model was developed to include geological heterogeneities using a simple upscaling method. The Oseberg Fm. consists of an upper homogeneous unit (zone 2) and a lower unit containing thin barriers of shale and calcite cemented sandstone (zone 1). The barrier content varies laterally. When barriers are distributed in a complex 3D pattern, they reduce the upscaled horizontal transmissibility more than what is obtained by multiplying the sand permeability by the net-to-gross ratio (N/G). However, the transmissibility reduction strongly depends on the spatial distribution of barriers and their geometry. Therefore, a fine scale element model was used to derive the average transmissibility reduction as a function of N/G for alternative geological descriptions of the barriers. A geo-statistical method called General Marked Point Process was used to generate the fine scale descriptions.

This work has resulted in a simple upscaling routine for horizontal transmissibility, which represents an effective bridge between geological evaluation of uncertainties and fluid flow simulation. The method combines geo-statistical and deterministic modelling in an elegant manner, recognising that most often these methods complement one another.

INTRODUCTION

Nature is often more complex than the petroleum engineers account for, especially in the North Sea where the well spacing is large (more than 1 km) and the reservoirs are heterogeneous. Predictions of production and spatial reservoir drainage, are often based on full field flow simulation models. The uncertainties regarding small scale heterogeneities and inter-well reservoir description, and the fact that full field models are to coarse to be able to incorporate the effect of such features, may result in poor predictions. For practical reasons, such as computing time, the full field models have to be coarse, and fine scale 3D models generated by geo-statistical techniques must be scaled up. Element models have a large potential in deriving suitable upscaling procedures applicable on the full field model, and in detailed studies of small scale heterogeneities (ref 1). The same idea has been widely used in flow simulation, for instance when generating pseudo relative permeability curves in order to incorporate effects related to the change in model resolution.

The Veslefrikk field (see figure 1) is situated in the Norwegian sector of the North Sea. The field is defined as a local horst block on the northwestern flank of the Horda platform. The most important reservoir is the Middle Jurassic deltaic Brent Group. Other reservoirs are the Early Jurassic Intra Dunlin Sand (equivalent to the Cook Fm.) and the Statfjord Fm. (ref 8). The Brent Group is subdivided into the Oseberg, Rannoch, Etive, Ness and Tarbert Formations. This study concentrates on the Oseberg Fm.

In this study, the barriers in zone 1 of the Oseberg Fm. have been of main focus as these are the most important sedimentological heterogeneities influencing fluid flow in the Oseberg Fm.. The barriers in this zone include both calcite cementations and shales. These heterogeneities in zone 1 are referred to as small scale. Zone 2 is described as homogeneous even though numerous smaller scale heterogeneities (e.g. laminations on centimetre scale) are present (see figure 2). Significant barriers to flow are lacking in zone 2.

References and illustrations at end of paper

OSEBERG GEOLOGY

The Oseberg Fm. has been interpreted as being deposited as a sandy fan-delta prograding in a westerly direction during Middle Jurassic (ref 5). The main components of zone 1 and 2 are subaqueous, dipping fan-delta foresets comprising slump and grain flow deposits. Calcite layers are concentrated in zone 1, i.e. in the marine foreset deposits of the fan-delta.

A study done on the origin and extent of the calcite cemented intervals in the Oseberg Fm. (ref 11) showed that the geometry of the calcite cemented intervals reflected the original geometry of the distribution of calcareous bioclastic material. The calcite cemented intervals are classified into two main groups:

1. Cross bedded or massive cemented zones probably with an extent of less than a few hundred metres. These zones are not associated with laterally extensive surfaces of erosion or non-deposition, but are sourced either from evenly dispersed or isolated pockets of carbonate fossils. They occur as scattered concretions, continuous or discontinuous layers of concretions.

2. Intensely bioturbated zones probably with a lateral extent of upto a few kilometres. These layers may be correlatable between wells and represent surfaces of bioclastic concentrations as a result of prolonged non-deposition of siliciclastic material.

The calcite cemented layers occur in the lower part of the Oseberg Fm., often in direct association with fine-grained, shale rich layers. On the basis of this observation, a decision was made to model the barriers as a combination of both shale rich and calcite cemented layers, as both shale and calcite may act as a barrier alone or in combination.

OVERRIDE IN OSEBERG - OBSERVATIONS

The fact that the uppermost part (zone 2) of Oseberg has been water flooded much sooner than the lower part, was revealed by a saturation log in A-1 and a production log in A-3. After this logging, A-17A was drilled, and open hole logs indicated that both zone 1 and zone 2 was flooded at this location (see figure 2). Water injector, A-10 (further to the north, see figure 1), supports the Oseberg producer A-3.

Formation pressure measurements indicate that none of the barriers in zone 1 act as field wide pressure seals. In addition to the contrast in barrier content between zone 1 and 2, there is a difference in quality of the sandy intervals. For instance, the average permeability in zone 2 is approximately 700 mD compared to 300 mD in zone 1.

WHAT MAY CAUSE THE OVERRIDE?

The observed override in A-1 and A-3 may have alternative explanations:

1. A complex 3D pattern of small scale barriers in zone 1 may slow the water flooding compared to in the homogeneous zone 2 (see figure 6).

2. If the barriers dip downwards towards the injector (A-10), the water will be forced up into zone 2 (figure 6).

3. If most of the water is injected into zone 2 and there is an extensive barrier between zone 1 and 2, zone 2 will be flooded more efficiently. Due to the completion design in the injector A-10 the injection split in Oseberg cannot be measured.

Combinations of the 3 alternatives listed above may also cause override.

MODELLING BARRIERS IN OSEBERG

The goal of the modelling was to include and evaluate the effect of the alternative geological explanations listed in the previous section. The geological uncertainty range is large and covered by generating numerous models. By flow simulation the range was restricted as not all models reproduced the observed override.

Why Geo-Statistical Modelling?

Geo-statistical modelling involves computer based algorithms distributing heterogeneities in 3D (ref 4). The following advantages were crucial in this project:

1. These algorithms contain statistical correlation structures, controlled by user given input parameters, enabling heterogeneities smaller than the well spacing scale to be distributed - heterogeneities that ordinary mathematical interpolation routines are not able to generate. Hence the models become

more realistic.

2. Heterogeneity patterns could be hand-contoured by geologists. It is, however, time consuming to cover the geological uncertainty by generating alternative models - all conditioned to well observations and other input data. By varying the input parameters to geo-statistical routines, rapid generation of alternative models is possible, all consistent with input data.

3. The most commonly used geo-statistical routines are stochastic processes, which means that each run gives different outcomes (realizations) even though all input parameters are kept constant. This represents an additional level of variation in the uncertainty modelling, impossible to incorporate by any other method.

A geo-statistical modelling tool called General Marked Point Process was used to generate the fine scale barrier descriptions (ref 3). This routine is designed to model barrier structures with a large degree of flexibility.

Why Element Model?

The main reasons for performing element instead of full field modelling are as follows:

1. The lateral extent of the barriers inducing the override (particularly the calcites) are believed to be of the same order of magnitude as the average grid cell size in the full field flow simulation model. Hence, the spatial distribution of these small scale barriers would not influence the behaviour of the upscaled full field model. On the other hand, the intensity and geometry of the barriers is extremely decisive regarding flow behaviour. Therefore, it is not necessary to distribute barriers in the full field, but the effect may be incorporated by using N/G to control the barrier intensity and alternative 3D element models to evaluate the geometrical aspect.

2. Evaluating alternative geological element models is much faster than working with detailed full field models. Both the model size and complexity are more practical as long as no conditioning data and structural maps are needed.

3. An important parameter in matching the Oseberg production from wells where the override is not observed, has been the communication across the faults. As figure 3 illustrates, it would be time consuming to generate alternative full field models matching the history by tuning the fault communication differently for each model. This is one of the reasons why N/G was chosen as the correlative parameter when upscaling permeability for alternative geological cases to the full field model, see next section for more details.

Method: N/G Scaling of Permeability

The rationale for this method is that when relatively small barriers are distributed in a complex 3D pattern, they reduce the upscaled horizontal transmissibility more than what is obtained by multiplying the averaged permeability in sand by the averaged N/G (which was used in the original flow simulation model which did not predict override). Figure 6 clearly illustrates this phenomenon, and also emphasizes that the amount of transmissibility reduction strongly depends on the spatial distribution of barriers and their geometry. Therefore, a fine scale element model was used to derive the average transmissibility reduction as a function of N/G for alternative geological descriptions of the barriers in zone 1, and the process is described step by step in the next section.

Model Description

The following process is performed for each alternative geological case as defined by the geologists (see figure 4):

1. A fine scale realization is generated without conditioning to any well observations.
2. The realization is validated by geologists using 3D visualization.
3. The fine scale model is water flooded after assigning permeability (500 mD) and porosity (20%) to the non-barrier. The injection and production rates are given such that the pressure development is comparable with the full field model.
4. The fine scale model is upscaled into a coarse element model by using a Darcy based technique deriving the permeability vector, and arithmetic averaging deriving porosity and N/G.
5. The upscaled element model is water flooded using

the same well control as for the fine scale model, and pseudorized relative permeability curves to avoid numerical dispersion.

6. The two element simulations are compared focusing on water production, and if the match is poor, the upscaling is re-run using alternative methods until a satisfactory match is obtained (i.e. re-do step 4 to 6).
7. The upscaled permeability in X and Y direction for each coarse cell is plotted against the corresponding N/G, i.e. adding 15 points (number of coarse cells) to the plot.

   Step 1 to 7 is re-run using the same geological model parameter setup, but varying the target volume fraction of barriers and the seed to the random number generator (i.e. generating many realizations), until the whole N/G range is covered and a clear trend is recognizable.

When using automatic routines to perform all the steps, each geological case is modelled and analysed in approximately 30 minutes.

Results

Some of the geological alternatives for barrier distribution are illustrated in figure 5 with derived N/G plots. The "base case" was initially assumed to represent the most probable barrier distribution within zone 1. In each N/G plot a straight line is drawn from (N/G=0,Permeability=0) to (NG=1,Permeability=500) representing how the upscaled N/G acts on permeability in the original model (see figure 6). Most of the alternative geological models represent a significant deviation from this straight line, except for the case Wide, since the barriers there are much larger than the coarse cell. For all anisotropic cases (i.e. when a direction is specified, e.g. the Dip and Ellips), the N/G plot is different for Kx and Ky. This was important to recognize when applying the results on the full field N/G matrix, as described in next section.

IMPLEMENTATION IN THE FULL FIELD MODEL

The idea behind the element model described so far was to establish a simple upscaling routine for horizontal transmissibility taking into account the effect of small scale barriers (not correlatable between wells), and to evaluate the geological uncertainty in their influence. However, there are other more extensive barriers present in the Oseberg Fm., most often related to zone boundaries since they are correlatable between wells. These barriers in combination with the smaller ones will reduce the vertical transmissibility, and to evaluate this an extended element model was established consisting of 3 homogeneous zone 2 layers overlying the heterogeneous zone 1 from alternative geological models already generated (see figure 7). This extended model proved to be useful concerning some additional aspects: It helped to eliminate those geological cases not reproducing the observed override, and it was used to optimize the strategy to drain the unswept oil in zone 1 (e.g. by horizontal producers).

The geo-statistical element modelling helped the geologists to evaluate their understanding of the reservoir by varying the input parameters and via 3D visualization. Based on this, and further evaluation in the extended element model, the case containing dipping barriers (Dip3) with some vertical transmissibility reduction between zone 1 and zone 2, seemed to be the most probable one. This element model was transferred into the full field model via the following steps:

1. The full field N/G matrix was updated based on a seismic lithology study which derived N/G maps from a correlation between seismic attributes and the concentration of calcite cemented barriers.
2. The field was divided into segments, and a barrier dip direction was assigned to each segment. Then the N/G plot from figure 5 (Dip3) was used to change the permeability matrix, both Kx and Ky.
3. Finally the vertical transmissibility between zone 1 and zone 2 was revised by the geologists based on well interpretations and the extended element model.

Figure 8 illustrates the difference between the new and the old permeability distribution in zone 1, and the resulting water-flood is shown in a vertical cross section. In addition, the improved history match is plotted both for the field production and the A-3 producer.

DISCUSSION

The idea behind this study was to implement the geological uncertainty regarding small scale barriers, however there are other uncertain features not included, such as faults beyond seismic resolution. In addition, there are uncertainties regarding the validity and resolution of the input data used, e.g. the shale and permeability log curves, the saturation logs and the sedimentological analogues. Finally, the lack of data (e.g. the injection log in A-10) complicates the overall uncertainty picture. Hence, the conclusion that Dip3 (dipping small scale barriers) is the most probable one, is preliminary, and further analysis and data acquisition will be performed - particularly concerning the nature of the more lateral extensive barriers. In addition, the work on optimizing the strategy for draining reserves trapped by small scale heterogeneities using the extended element model, will continue, since these barriers are not explicitly included in the coarse model.

CONCLUSION

A simple upscaling routine for horizontal transmissibility has been developed and tested. The method represents an effective bridge between geological evaluation of uncertainties and flow simulation. Geo-statistical modelling helps the geologists in evaluating their impression of the reservoir via 3D visualization of the models and by the generation of new models simply by modifying input parameters. Geological uncertainty is implemented by deriving transmissibility reduction functions for alternative barrier models in zone 1.

The extended element model was used to eliminate those geological cases not reproducing the observed override, and to evaluate the effect of various strategies, e.g. a horizontal well in zone 1 to produce the remaining reserves. When applying the transmissibility reduction function on the full field N/G matrix, an improved history match was obtained.

Transmissibility reduction as a function of N/G may very well be derived for other depositional environments and heterogeneity styles (if the heterogeneities are small compared to the cell size in the flow simulation model) and further improve the Veslefrikk model. The method combines geo-statistical and deterministic modelling approaches in an elegant manner, recognising that most often they complement one another.

Acknowledgments

The authors thank Statoil and the Veslefrikk partners for permission to publish this paper. We also thank our colleagues for contributing with ideas and input.

NOMENCLATURE

Φ	=	Porosity
Kas	=	arithmetic averaged permeability in sand
Kcell	=	permeability in grid cell
Kx	=	Permeability in X-direction
mD	=	milli Darcy
N/G	=	Net/Gross ratio (sometimes NTG is used)
S-log	=	Saturation log
std	=	standard deviation
SWI	=	Initial water saturation
Sw	=	Water saturation
Q	=	Production rate
3D	=	3 dimensional

REFERENCES

1. Begg, S.H., Kay, A., Gustason, E.R., and Angert, P.F. (1996): "Characterization of a Complex Fluvial-Deltaic Reservoir for Simulation", SPE Formation Evaluation, Sept. 1996

2. Bjørkum, P.A. and Walderhaug, O. (1990): "Geometrical arrangement of calcite cementation within shallow marine sandstones". Earth Science Reviews, 29, P145-161

3. Bratvold, R.B., Holden, L., Svanes, T. and Tyler, K.J (1994).: "STORM: Integrated 3D Stochastic Reservoir Modelling Tool for Geologists and Reservoir Engineers", paper

SPE 27563 presented at SPE 1994 European Petroleum Conference.

4. Damsleth, E. and Holden, L. (1994): "Mixed Reservoir Characterization Methods", paper SPE 27969 presented at the 1994 University of Tulsa Centennial Petroleum Engineering Symposium, Tulsa, Aug.

5. Graue, E., Helland-Hansen, W., Johnsen, J., Lømo, L., Nøttvedt, A., Rønning, K., Ryseth, A., and Steel, R. (1987): "Advance and retreat of the Brent delta system, Norwegian North Sea". Petroleum Geology of Northwest Europe, P915-937

6. Kjønsvik, D., Doyle, J., Jacobsen, T., and Jones, A. (1994): "The Effects of Sedimentary Heterogeneities on Production from a Shallow Marine Reservoir", paper SPE 28445 presented at the 1994 SPE European Petroleum Conference, London Oct.

7. Lia, O. et al (1995): "The Great Reservoir Uncertainty Study - GRUS", PROFIT Project Summary Reports, Norwegian Petroleum Directorate, Stavanger, P191-204.

8. Pedersen, P.Å., Hauge, R. and Berg, E. (1994): "The Veslefrikk Field", North Sea Oil and Gas Reservoirs - III, P51-73

9. Tyler, K.J., Svanes, T., Omdal, S. (1993): "Faster History Matching and Uncertainty in Predicted Production Profiles with Stochastic Modelling", paper 26420 presented at the Annual Technical Conference and Exhibition, Houston, Oct.

10. Walderhaug, O., Bjørkum, P.A. and Nordgård Bols, H.M. (1989): "Correlation of calcite cemented layers in shallow marine sandstones of the Fensfjord Formation in the Brage field". In: Correlation in hydrocarbon exploration (Ed. J. D. Collinson), Graham and Trotman, London, P367-375

11. Walderhaug, O. and Bjørkum, P.A. (1992): "Effect of meteoric water flow on calcite cementation in the Middle Jurassic Oseberg Formation, well 30/3-2, Veslefrikk field, Norwegian North Sea", Marine and Petroleum Geology, 9, P308-318.

FIGURES

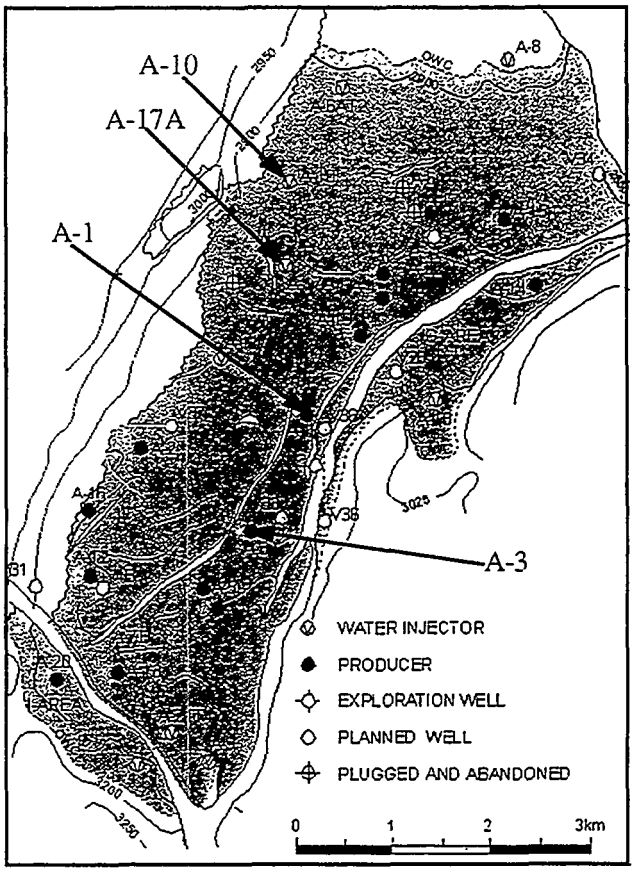

FIGURE 1 Field map with wells, top Etive Fm.

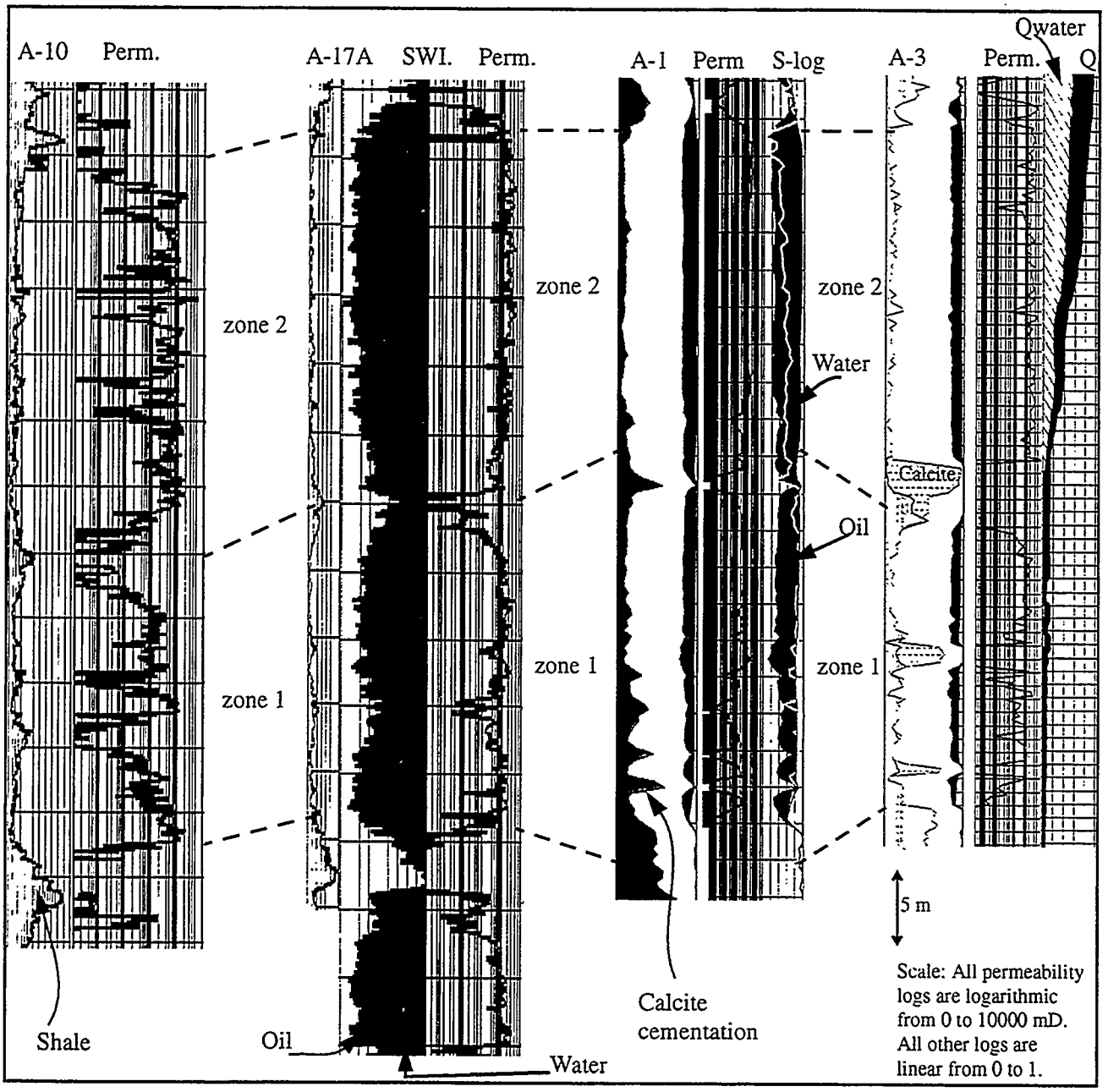

FIGURE 2 Observations: A-10, open-hole log in A-17A, saturation log in A-1, production log in A-3

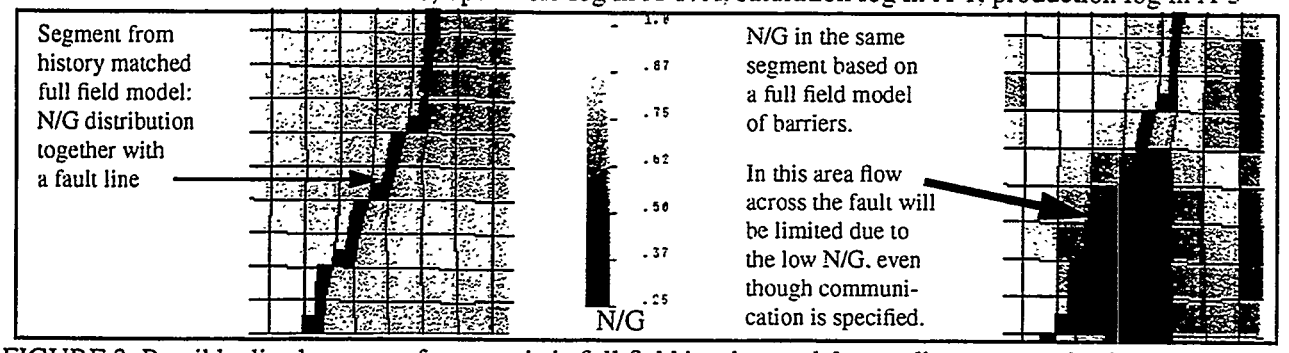

FIGURE 3 Possible disadvantage of geo-statistic full field barrier model regarding communication across faults.

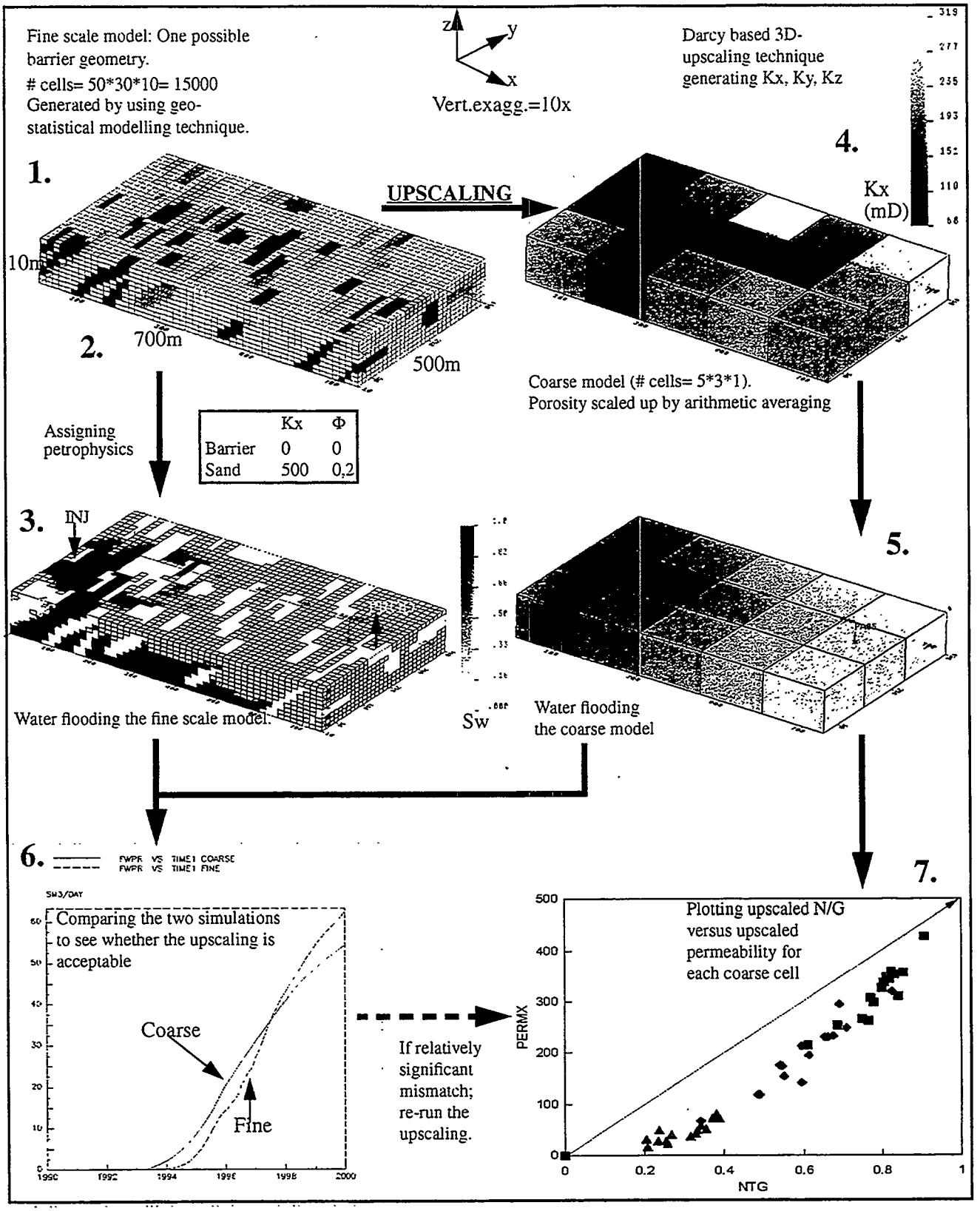

FIGURE 4 Method used to derive the relationship between N/G and permeability.

Model (brief description)	3D visualization (one example)	Resulting N/G-plot
Base case: Width=100m, std= 25m, thickness= 2m, no dip, circles, invers correlation between width and thickness	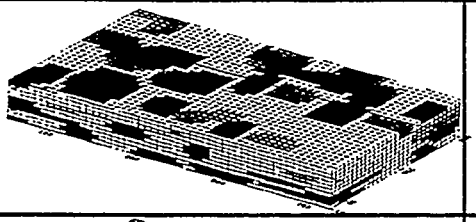	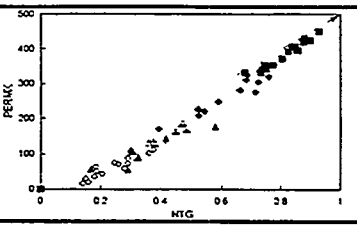
Thick: As base case but with thickness= 4m	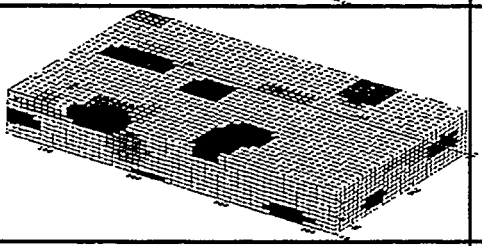	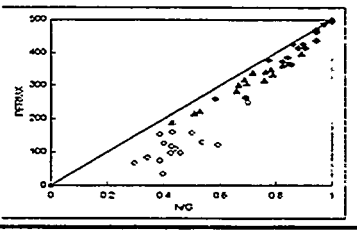
Narrow: As base case but with width= 30m (std=15m)	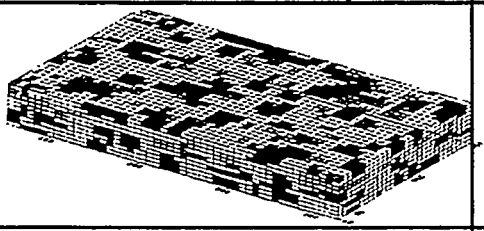	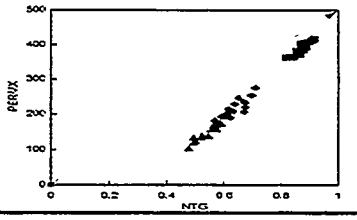
Wide: As base case but with width= 450m (std=100m)	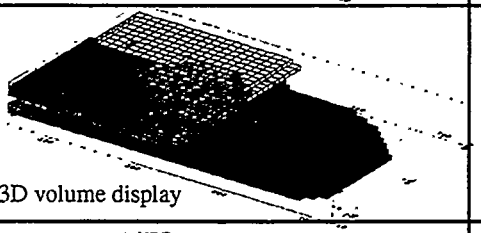 3D volume display	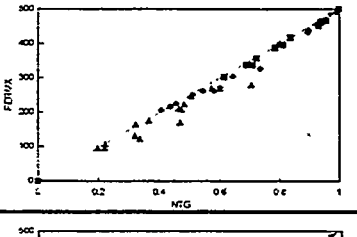
Dip3: As base case but with dip angle= 3 deg. (std=1.5m)	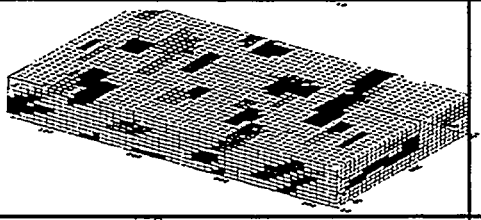	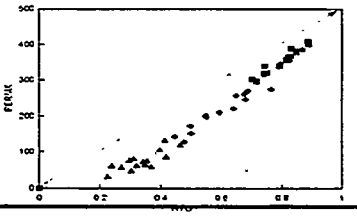
Dip6: As base case but with dip angle= 6 deg. (std=2)	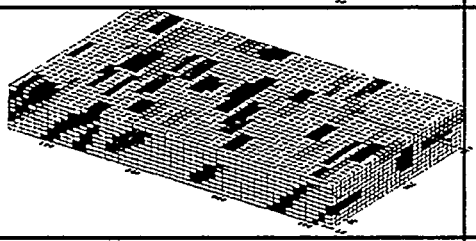	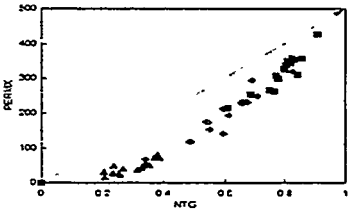
Ellips: As base case but with elliptical barriers, width= 50m and length= 175m	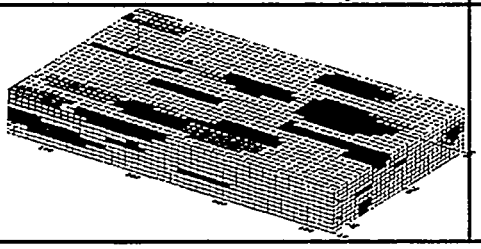	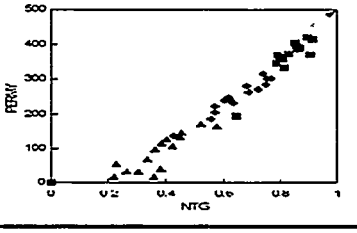

FIGURE 5 Some alternative barrier models with corresponding N/G-PERM-relationship plots.

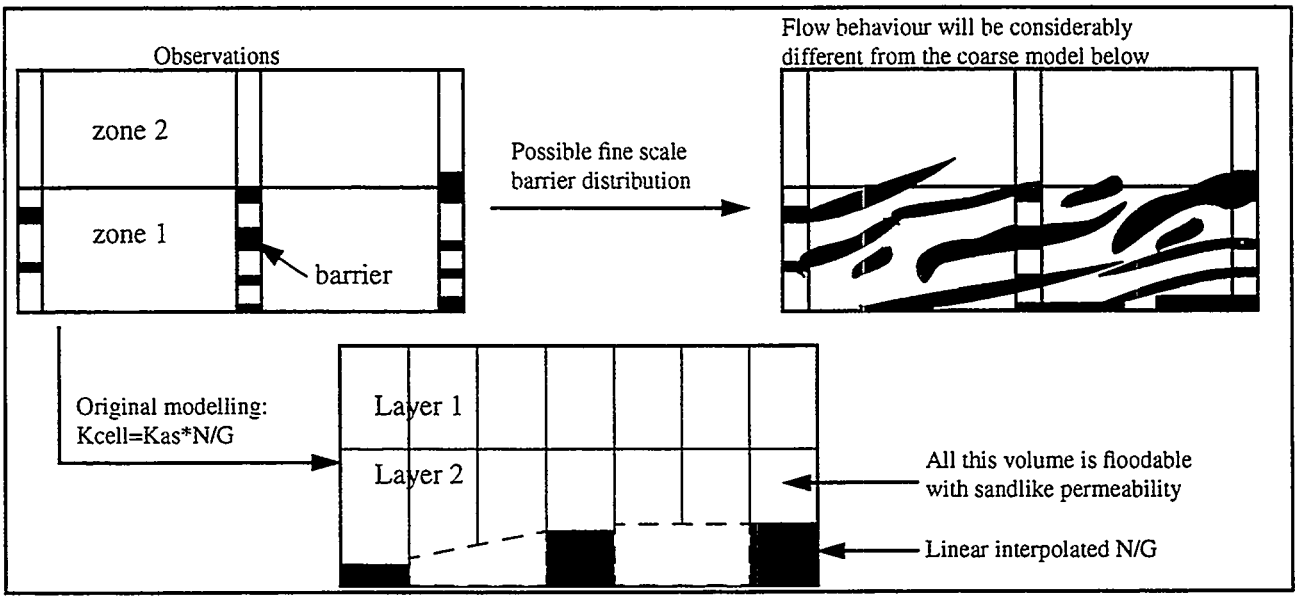

FIGURE 6 Comparison between original scaling of permeability and the effect of fine scale barriers.

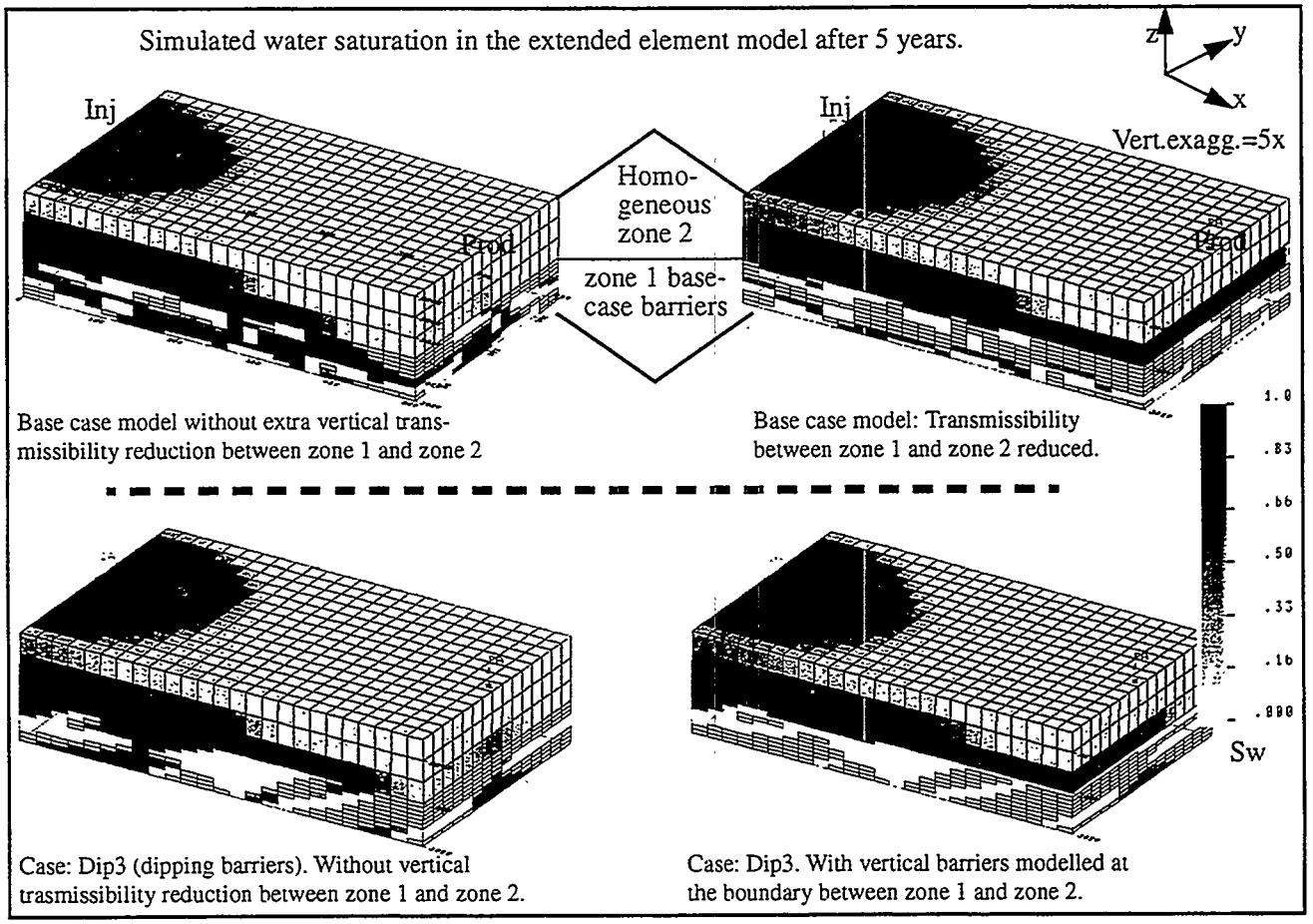

FIGURE 7 Flow simulations of the extended model: Two geological cases with varying vertical communication.

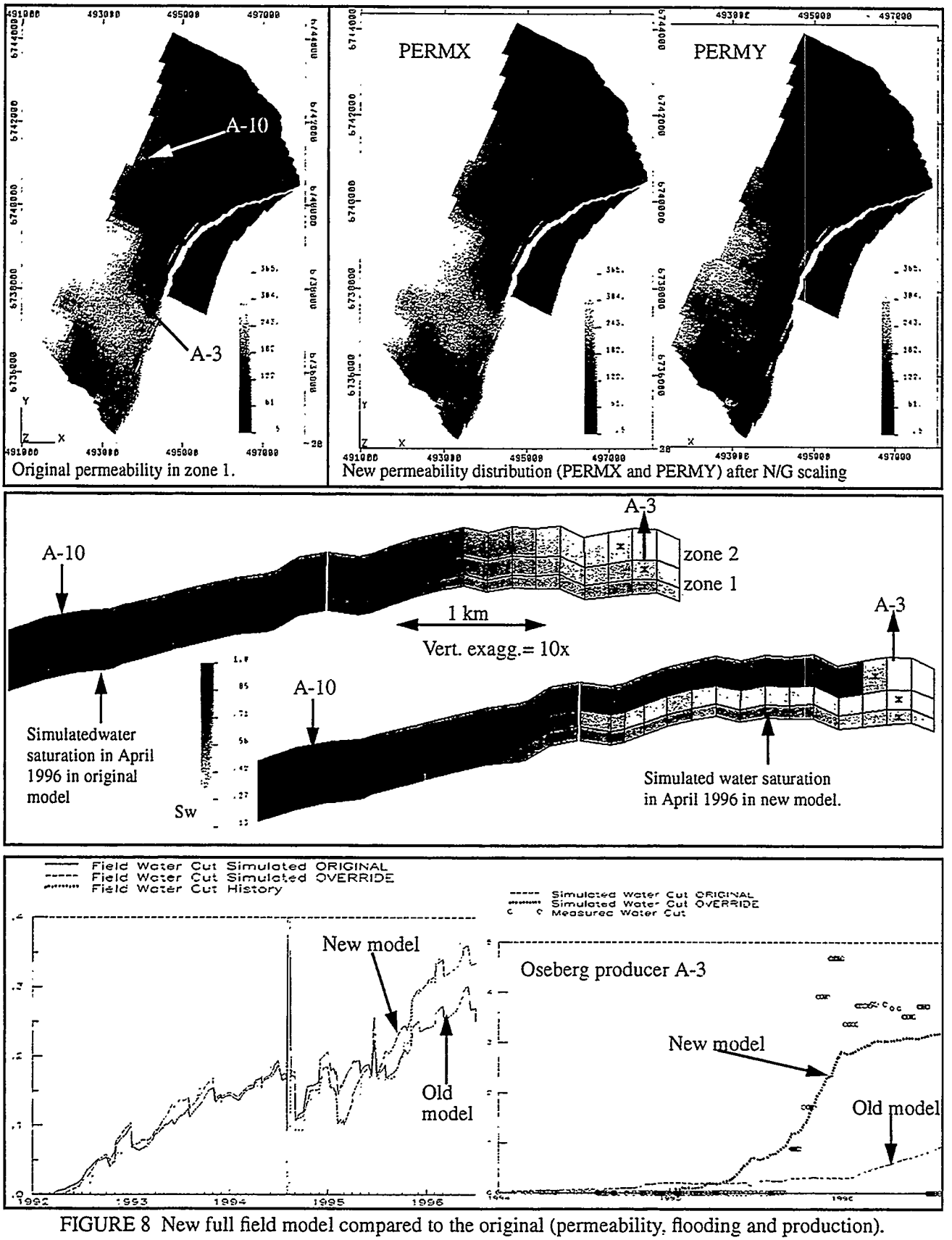

FIGURE 8 New full field model compared to the original (permeability, flooding and production).

QUICK EVALUATION OF MULTIPLE GEOSTATISTICAL MODELS USING UPSCALING WITH COARSE GRIDS: A PRACTICAL STUDY.

P. LEMOUZY

INSTITUT FRANÇAIS DU PÉTROLE AND ELF/IFP HELIOS GROUP

PAU, FRANCE

ACKNOWLEDGEMENTS

The author would like to thank the managements of the Institut Français du Pétrole and Elf for permission to publish this work performed within the Elf/IFP Helios Joint Research Group.

ABSTRACT

In field delineation phase, uncertainty in hydrocarbon reservoir descriptions is large. To quickly examine the impact of this uncertainty on production performance, it is necessary to evaluate a large number of descriptions in relation to possible production methods (well spacing, injection rate, etc.). The method of using coarse upscaled models was first proposed by Ballin (1993). Unlike other methods (connectivity analysis, tracer simulations), it considers parameters such as PVT, well management, etc., .

After a detailed review of upscaling issues, applications to water-injection cases (either with balance or imbalance of production, with or without aquifer) and to depletion of an oil reservoir with aquifer coning are presented.

Much more important than the method of permeability upscaling far from wells, the need of correct upscaling of numerical well representation is pointed out Methods are proposed to accurately represent fluids volumes in coarse models. Simple methods to upscale relative permeabilities, and methods to efficiently correct numerical dispersion are proposed.

Good results are obtained for water injection. The coarse upscaling method allows the performance of sensitivity analyses on model parameters at a much lower CPU cost than comprehensive simulations. Models representing extreme behaviors can be easily distinguished.

For depletion of an oil reservoir showing aquifer coning, however, the method did not work properly. It is our opinion that further research is required for upscaling close to wells.

We therefore recommend this method for practical use in the case of water injection.

INTRODUCTION

Need for fast evaluation of multiple geostatistical realizations

At delineation time, when only a few wells have been drilled, there remains a lot of uncertainty in the reservoir description:

- In the geometry of the reservoir, leading to uncertainty in the volume of hydrocarbon in place.
- In the amount of reservoir facies (which can be expressed as net/gross (N/G) ratio), leading also to uncertainty in the hydrocarbon in place volume.
- In the dimensions of geological bodies (i.e., channels, lobes) and of their internal heterogeneities, which control the connectivity of reservoir bodies, and thus the recovery.
- In the petrophysical characterization of the facies.

The major problem is to estimate the expected oil in place, the expected production profiles, and the attached uncertainties. If the value of expected production is below the economic standard of the operator, the decision will be to cancel any further development. When uncertainty is too large, additional data will be required (seismic, drilling) until a reasonable degree of certainty is reached, allowing the launching of a development. Determining the uncertainty is more critical offshore than onshore.

To estimate the uncertainty, two approaches are possible:

- One can determine scenarios (e.g., minimum, mode, maximum, or proven, probable, possible, etc.) for each factor participating in oil in place or in production profile computations (e.g., reservoir top depth map, porosity, N/G ratio), and combine them to obtain scenarios for the studied value. This approach can go from simple products of scenario values to more sophisticated Monte-Carlo computations, but it neglects possible interaction between factors.
- From a few wells, geological analysis can provide very realistic reservoir geological models. This knowledge can be expressed in terms of geostatistical parameters, used to build up very detailed reservoir models in lithofacies and/or petrophysics. The overall uncertainty is determined by the examination of the production behavior of a large number of realizations, letting uncertainty play for petrophysics, geometry, etc. The issue studied in the present paper is, therefore, the evaluation of the production behavior of a large number of realizations.

Previous works

Guérillot et al. (1992) proposed a simplified flow simulator to sort several realizations. They used a single pressure field calculated once, and they computed the saturation evolution. This method is limited to cases when pressure has a limited impact on flow, e.g., for waterflood at a pressure above oil saturation pressure. It is exact for unit mobility ratio and negligible gravity and capillary effects, and inexact otherwise. Nevertheless it yields a satisfactory ranking of geostatistical realizations with respect to some production parameters (e.g., water breakthrough time) in its domain of validity.

Ballin et al. (1992) used tracer simulations to rank realizations. Similar to the previous method, it requires only a single calculation of the pressure field. Both methods have the same limitations. Saad and al (1996) confirmed that both methods are nearly equivalent with respect to cumulative oil production or water breakthrough time ranks.

Ballin et al. (1993) investigated how using the results of coarse upscaled model simulations can achieve a good ranking of multiple realizations. They proposed a methodology to approximate the cumulative distribution function (cdf) of production data which would be obtained through extensive simulations of fine models. Deutsch (1996) investigated statistical criteria and the use of coarse upscaled models, and concluded that the latter method is a valuable one.

The emergence of streamline-based computations (e.g., Thiele, 1996) is noteworthy. The method is similar to Guérillot's, as it uses a pressure field calculated once or a limited number of times. But it propagates 1D flow solutions along streamlines, making it faster and more general. Simplified simulations or streamline computations should present the same limitations concerning gravity and capillary effects, or strongly pressure dependent effects (e.g., gas liberation from oil).

The coarse upscaling approach is appealing because it is not restricted to a limited physical domain, as are the previous methods. It can handle cases with strong effects of pressure (three-phases flow, compositional). Moreover, sophisticated management of wells and reservoirs can be reproduced thanks to the possibilities of commercial simulators (e.g., a control of well flow-rate to limit the GOR can be handled automatically, a workover to plug a water-producing layer can be simulated).

UPSCALING METHODS

General

Upscaling must be performed considering the actual function of a reservoir simulator. First it processes data describing the reservoir (such as geometrical, petrophysical, PVT data), given as grid-block properties. The output of this pre-processing or initialization phase is a network composed of nodes (to which are attributed some grid-block data such as pore volume, pressure and saturation) and links (to which are attributed a transmissivity and a depth difference allowing to calculate gravitational potential differences). Flow equation are then solved for this network. This is not unfamiliar for people who worked with analog models made of resistors before the emergence of numerical models.

When upscaling flow models, it is better to define directly the components of the upscaled network, rather than the whole set of upscaled grid-block properties, which would be changed in the pre-processing phase. The coarser the model, the more critical it is to determine directly the network components, as the geometric approximations of pre-processing become inaccurate.

Another point to emphasize is that the upscaling problem in question is a pseudoization (calculation of properties depending on local conditions, as flow pattern and boundary conditions) rather than a homogenization (calculation of effective characteristics of an equivalent homogeneous medium).

Permeability

As previously seen, we determined directly upscaled transmissivity, rather than upscaling block permeability and computing the transmissivity afterwards. This was proposed by Gomez-Hernandez (1990), who upscaled inter-block permeabilities. As the geometry of their model was regular, the geometric term within transmissivity (the ratio S/L, S being the surface of the interface between two blocks, and L the distance between block centers) was constant, therefore upscaling either inter-block permeability or transmissivity was equivalent.

An explanation of the interest of direct upscaling of transmissivities may be found in Romeu et al. (1995). The authors investigated how numerical simulation gives the equivalent permeability of a block made of several sub-blocks with permeabilities obeying a spatially correlated distribution. They showed that the accuracy of numerical determination depends on the ratio of the size of the sub-block to the variogram range, and on the numerical method (finite difference (FD) underestimates equivalent permeability, while finite element (FE) overestimates it). The larger the sub-block size, the larger the error in the equivalent numerical permeability. They demonstrated that a special FD method, termed "direct", consisting in using permeability directly within the transmissivity term in place of the harmonic average of adjacent block permeabilities, yields equivalent numerical permeability closer to the value which would be obtained with an exact numerical method.

Attributing directly upscaled transmissivity is an application of this "direct" method. Upscaling implies that the ratio of block size to variogram range will be much larger in the coarse model, leading to large errors when using FD or FE methods. Using transmissivities directly allows for less error.

The upscaled transmissivities are computed by solving numerically for each coarse block small steady-state single-phase flow problems on fine scale models composed of the coarse block itself and of the existing neighboring blocks (up to 27 coarse blocks). Constant potential conditions are applied on two opposite faces of the model, and no-flow conditions on the remaining faces. One problem must be solved for each principal directions X, Y and Z. Processing the results of the flow models (potential and flowrate) gives the interface transmissivities T. We have to sum up the flowrates q_i across each fine block interface composing a coarse block interface, and to calculate the average potential Φ for each block separated by the interface.

$$Q = \sum q_i \qquad T_{IJ} = \frac{\mu Q}{\bar{\Phi}_J - \bar{\Phi}_I} \tag{1}$$

The potentials are averaged by considering an arithmetic average of fine block potentials weighted by porous volume (V ϕ). This is obtained assuming that total compressibility is constant over fine blocks. Detailed derivation and discussion are presented in Appendix A.

$$\bar{\Phi} = \frac{\sum V_i \phi_i \Phi_i}{\sum V_i \phi_i} \tag{2}$$

Initialization

Initialization of flow models consists in computing, for each block, its initial saturation and pressure, and attributing functions of pressure (PVT) or saturation (Kr-Pc). It requires the knowledge of the gravity center depths of blocks. In current use of FD numerical simulators, this gravity center depth is calculated from the geometrical description of the block, assuming the block is homogeneous. Thus the gravity center coincides with the geometric center of the block. When the coarse block is made of sub-blocks of different properties, these two points are not identical. When density of fluid is constant, the calculation detailed in appendix B leads to:

$$\bar{Z} \sum V_i \phi_i = \sum V_i \phi_i Z_i \tag{3}$$

Porous volume is also needed for the simulation. It is computed from fine scale models with equations A3 and A4.

Initial pressure is determined in the same way for coarse and fine blocks: given the initial reservoir pressure known at datum, PVT, and block depth, it is computed during the pre-processing phase of simulations. The same PVT is assumed to apply to the two scales. The question of whether to perform some kind of upscaling for PVT may be raised, as shown by the next equation expressing equivalence of oil in place volume at standard conditions for fine and coarse models:

$$\frac{\overline{\phi V So}}{\overline{Bo(P)}} = \sum \frac{\phi_i V_i So_i}{Bo(P_i)} \tag{4}$$

At initial equilibrium, pressure depends only on depth, and it is reasonable to keep the same PVT for coarse and fine blocks, as long as the dimensions of the coarse blocks are not too large.

To compute initial saturations, flow simulators consider the gravity-capillarity equilibrium, assuming that during migration, hydrocarbon displaced water by a drainage process. The saturation computation requires the definition of drainage capillary pressure (Pc) curves, and of fluid contacts, which define the null Pc depth. Two methods have been tested:

- Upscaled drainage Pc curves may be determined, as explained in Appendix C. Using these curves for the coarse model initialization ensures that gravity-capillarity equilibrium is honored.
- Average saturations of coarse blocks resulting from the initialization of the fine model (equation C4) can be directly entered into the coarse model. In that case, if upscaled Pc curves are not provided to the coarse model, gravity-capillarity equilibrium will not be respected.

Well representation

Wells are represented in numerical models by special nodes and links of the numerical network:

- A new node where well pressure is computed is added for each perforated reservoir block.
- The link between this node and the reservoir node representing the perforated block is characterized by a production index (PI) and by relative permeability functions, often those of the perforated block for a producing well.

When upscaling flow models, it is of prime importance to correctly upscale the characteristics of well functions (PI and Kr). The bottom hole pressure (BHP) is the most frequent pressure data available

(directly or from well head pressure through a friction loss equation), and it must be represented accurately. Moreover, the production operations (pumping, injecting, gas-lift) provide constraints for BHP and well flowrate. Their impact on the reservoir behavior can only be assessed if well functions are carefully computed. The radial flow pattern near wells is different from the nearly linear behavior far away from wells: therefore upscaling near wells is not the same as far from wells.

Classically, numerical PI is computed with the Peaceman (1978) equation. This equation has been established for centered vertical wells in a regular grid and homogeneous reservoir, far from reservoir limits and from other wells. Recently, Ding (1994) has proposed to process the results of a fine-scale simulation of steady-state single-phase flow around wells to compute upscaled PI, and upscaled transmissivities of interfaces of the perforated coarse blocks. This method takes into account, with the accuracy of the fine scale simulation, the following points:

- The true position of the well in the coarse block (not always centered).
- The deviation of the well from the vertical.
- Partial perforation of the coarse block.
- The effect of reservoir limits close to the well.
- Interference with another well (provided their flowrates keep the same ratio during simulation).
- The heterogeneity of reservoirs close to the well.

Practically, the steady-state single-phase simulation is performed on a fine scale model including the studied well and neighboring wells. In that model, the Peaceman equation is used. Well flowrates are set according to realistic values. Steady-state regime may be established when producing and injecting wells are present. For depletion, a pseudo steady-state may be simulated. From simulation results, the well flowrates q_i of perforated fine blocks composing a perforated coarse block are summed up to provide its flowrate Q. Average potentials of the perforated coarse block Φ_b, and of surrounding blocks are obtained by a porous volume weighted average (Equation 2). Upscaled transmissivities near wells are calculated with equation 1. Finally, the upscaled PI is simply obtained from well potential Φ_w:

$$\overline{PI} = \frac{\mu Q}{\Phi_b - \Phi_w} \qquad (5)$$

Kr is needed to calculate the phase productions into the well. Due to the radial flow around the well, it is clear that saturation within fine blocks close to the well influences very much the overall mobility between the block and the well. That saturation detail is lost in the coarse block, where only average saturation is considered. Therefore, specific well Kr should be built-up. Furthermore, PVT must not be forgotten: one can imagine a case where only a few fine blocks around well have pressures below oil saturation pressure. The presence of gas close to the well has an impact on Kr, and thus on phase flows. But no gas appears in the coarse block if its average pressure is above saturation pressure: therefore significant differences between fine and coarse model results should occur. These PVT and Kr points have not been tackled in the present work, but we think they deserve further work.

Relative Permeability

Relative permeability (Kr) may be upscaled in two steps:

- First, a physical upscaling gives the coarse scale Kr.
- Then, a correction of numerical dispersion is applied

Physical upscaling

Upscaled Kr depends on relative magnitude of gravitational, capillary and viscous forces. When one force prevails, upscaling may be performed rather quickly, as the saturation distribution at fine scale may be obtained without any flood simulation. Then applying permeability upscaling techniques to the phase permeabilities provides upscaled Kr. Otherwise, the current practice is to use fine scale flow simulations and to process their results (e.g., Kyte & Berry, 1975). This is obviously impractical when evaluating multiple realizations at the lowest computer time possible.

This is why we used an approximate but fast method. Kr curves are split into two sets of data:
- The set of end points (saturation and Kr).
- The set of Kr shapes, obtained by normalizing these curves in the [0, 1] range for both saturation and Kr axes with linear transformations.

Kr may be preserved through scales for some physical situations, and their preservation has been established in some practical cases by Kossak (1990). We only upscaled end points, and we kept the fine scale Kr shapes at the coarse scale. This choice is obviously erroneous in general cases, but we do hope that ranking capability of upscaled models will not be affected.

One issue is to select an average Kr shape when lithotypes show different shapes. In this case, we privileged the Kr shape of the most permeable lithotype, as it will dominate the flow capacity.

For saturation end points, we recalculated effective residual saturation, considering the initial saturation status in the fine model. When aquifer crosses a coarse block, the fine blocks below contact show a null oil saturation. Thus residual oil saturation for these blocks is set to zero. Once corrected, end point saturations are upscaled by a pore volume weighted average (equation C4).

For Kr end points, we considered permeability upscaling methods applied to phase permeability (K Kr). Algebraic methods are preferable, being faster than numerical ones. Among them, the power average method is useful, provided the exponent ω characteristic of the reservoir is known. The upscaled Kr is obtained knowing the proportions of lithotypes x_i:

$$\overline{K_r} = \frac{\left[\sum x_i \left(K_i K_r^i\right)^{\omega}\right]^{\frac{1}{\omega}}}{\left[\sum x_i K_i{}^{\omega}\right]^{\frac{1}{\omega}}} \qquad (6)$$

The determination of ω requires a calibration step. As we did not perform this step, we assumed $\omega = 1$. This exponent corresponds to a layered reservoir, that is obviously often far from the actual configuration. Moreover, when a lithotype permeability is much larger than others, the end point Kr of this lithotype is recovered. Thus, we also tested the use of a proportion weighted average of Kr which gives a lower Kr:

$$\overline{K_r} = \sum x_i K_r^i \qquad (7)$$

Correction of numerical dispersion

Once the physical upscaling is done, one must tackle the problem of numerical dispersion. Use of coarse grids spreads displacing fluid fronts with usual FD methods. The analysis of this artefact is well known in 1D displacements (Lantz, 1971). To correct numerical dispersion in 1D, we can compute pseudo Kr from pressures and flowrates of a fine scale 1D flood simulation. They can be obtained for different aggregation ratios of fine blocks into coarse blocks. They depend on several factors: viscosity ratio, distance to injection block, capillary number. Nevertheless, a single Kr pseudo computed at half the mean distance between injector and producer, for the viscosity, capillary and velocity mean conditions prevailing in the reservoir, enables a reasonable reproduction of fluid rates at the producer.

It is thus attractive to use pseudo Kr computed in 1D to correct the numerical dispersion in 2D or 3D cases. As vertical velocity is usually low in reservoirs, we assume that correction of dispersion in 3D can be achieved by a 2D correction considering an areal flow.

The aggregation ratio to apply to 1D flow results must be chosen. To do this, we compared 2D areal flood simulations for a flood direction parallel or diagonal to the grid, and for favorable and unfavorable mobility ratios. We also calculated pseudo Kr in 1D for different aggregation ratios, and looked at the best choice of this ratio to reproduce the results of fine 2D simulations on coarse 2D grids.

From these simulations, the following conclusions may be drawn:

- When the mobility ratio is unfavorable, flood results of fine and coarse grids are identical. As the flood is unstable, no front is developed, and consequently no spreading of front occurs.

- When the mobility ratio is favorable, floods parallel to the grid direction show higher dispersion than floods along the diagonal direction of the grid.

- The best aggregation ratio for floods parallel to the grid is the actual aggregation ratio: e.g., if fine blocks are grouped into 5 x 5 to give a coarse block, a satisfactory pseudo Kr is obtained from 1D flow with an aggregation ratio of 5:1.

- The best aggregation ratio for floods along the diagonal direction of the grid is half the actual aggregation ratio. For a 4 x 4 grouping of fine blocks, a pseudo Kr from 1D flow with an aggregation ratio of 2:1 is efficient to recover results of the fine grid on the coarse grid.

PRESENTATION OF CASE STUDIES

First case: waterflooding a reservoir without active aquifer

This case, C1, deals with a turbiditic reservoir with two drilled wells. The study was aimed at determining the impact on production forecasts of the uncertainty on geostatistical parameters. Four lithotypes were described:

- Two types of channels (facies 1 and 2), of different petrophysical characteristics.
- A less permeable lithotype (facies 3), corresponding to levees.
- A shaly lithotype (facies 4), filling the remaining volume of the valley in which the turbiditic system was deposited.

A portion of this reservoir was represented by a rectangular box, elongated along the principal axis of the system. Geological uncertainty was thought to be important for two factors:

- The proportions of the facies. These data were simplified, considering the relations between the proportions of different facies, and reduced to a single factor, the proportion of channel 1.
- The dimensions of the reservoir bodies (facies 1 to 3). These dimensions are indirectly modeled thanks to variogram ranges (spherical model). As for proportions, the variogram range of channels 1 in the X direction perpendicular to the principal direction of the system (Y) is the single factor considered.

The possible value ranges of these factors was determined by a geologist. Applying experimental design techniques, five sets of geostatistical data (table 3) were compiled:

- The first set S_0 corresponded to what the geologist thought was the most probable. It is the central point of the experimental plan, used to validate the model derived from the others sets.
- The four others sets S_1 to S_4 were build according to a complete factorial plan, each factor being fixed at one of the two limits of its range.

The parameter sets were used as input of the SISIMPDF routine of GSLIB (Deutsch, 1992) to obtain several facies simulations for each set. The chosen grid is shown in table 1. The block dimensions were 25 m in X, 60 m in Y and 1 m in Z. Each facies was given constant petrophysical data (table 2). Kr end points and shapes were different for each lithotype. Aquifer being far from this reservoir part, Pc was neglected (Pc = 0 during simulations) and initial water saturation was at its irreducible value.

A waterflood with the two existing vertical wells and two new wells was simulated (Fig. 1). A perforation method for new wells was determined: the blocks of channel facies were systematically perforated. To maximize the impact of varying geostatistical parameters, high liquid production rates were imposed at producing wells. Injection rates were set to balance the total production, as long as injection pressure did not reach an upper limit. This led to an unbalanced waterflood, as the producing rate was not always able to balance production. Thus, depletion below bubble point pressure occurred near producing wells, making the GOR increase. The GOR was controlled by decreasing the liquid rate when an upper GOR limit was reached. Results were recorded at two different times: at 500 days,

shortly after water breakthrough, and at 2000 days, at which time the water-cut reached values close to 80 %.

Second case: depleting or waterflooding a reservoir with active aquifer

The reservoir was an anticline structure, with a thickness of 40 m, an oil leg of about 60 m above an active aquifer. Two wells were drilled, and the study was aimed at determining the uncertainty of production either under balanced waterflood, or under depletion. Forty-nine geostatistical simulations of horizontal permeability conditioned to the two existing wells were performed in a grid presented in table 4. The block dimensions were 50 m by 50 m by 2 m. Porosity was attributed through a correlation between logarithm of horizontal permeability and porosity. A vertical to horizontal permeability ratio was assigned according to the level of horizontal permeability. The same Kr curves applied on all blocks.

For the waterflood case, two producing wells (P1 and P2) and four injecting wells (I1 to I4) were considered (Fig 2). P1 and I4 were the drilled wells, and they were perforated in the same way for all realizations. The other wells were perforated according to depth and permeability criteria. Liquid rates were fixed at producing wells. The sum of injection rates compensated the total fluid production of producers. As the total rate was moderate, no imbalance occurred during simulations, and reservoir pressure was above saturation pressure. The production results were recorded at two times: first when reservoir water-cut was at 5 %, and secondly at the end of production (20 years).

For the depletion case, seven producing wells (P1 to P7) were implemented in the oil zone (Fig. 3). P1 and P2 were the two drilled wells. The other wells were perforated according to depth and permeability criteria.

The production results are presented at end of production (20 years).

ANALYSIS OF COMPARISON TESTS BETWEEN FINE AND COARSE SIMULATIONS.

General

To test the value of upscaling to rank multiple realizations, a comparison between simulated productions results (termed X) of fine and upscaled models is performed. This yields the error δX:

$$\delta X = X_f - X_u$$

δX is composed of two parts: its mean is the systematic error of using upscaled models, and is meaningless with respect to ranking. The important part of δX is its standard deviation, which gives the magnitude of random-like fluctuations around the mean: in the event of this standard deviation being null, one would obtain a perfect ranking of X, even if δX is far from being null. As the value of δX in itself is not sufficient to compare the ranking capability for different production results X^i, we propose to look at:

$$\varepsilon_1^i = \frac{\sigma(\delta X^i)}{\mu(X_f^i)} \text{ and } \varepsilon_2^i = \frac{\sigma(\delta X^i)}{\sigma(X_f^i)}$$

ε_1 represents the normalized accuracy of the "random" part of the error. ε_2 represents the ranking capability: the smaller this figure, the better the ranking. A good ranking capability can be obtained either with small upscaling "random" errors, or because of a large variability of X. Conversely, if X has a small variability, ranking will be difficult, but in this case, uncertainty is not much of concern.

Another way to analyze ranking capability is to compute linear correlation coefficients. Exact scaling-up methods would provide a perfect linear correlation: $X_u = X_f$. As upscaling is not exact, one should expect a departure from this linear behavior, reasonably approximated by a linear correlation. Correlation coefficients between fine and upscaled simulation results will thus be calculated for both production parameters (ρ_X) and their ranks (ρ_r).

The simulated production data examined are of two types:

- Cumulative data: produced volumes of oil (Np), gas (Gp), water (Wp), and oil recovery factor. These data are smooth functions of time. Volumes produced are crucial for economic calculations (e.g., net present value). Normalized data such as recovery factor are important from a technical point of view to compare performances of different reservoirs.
- Instantaneous rates or rate ratios: oil flow-rate (Qo), gas-oil ratio (GOR), water-cut (Fw). These data may vary a lot versus time and are the most difficult to recover through upscaled models.

Tests of case C1

The tests (w1 to w5) differ according to the following options (see table 7):

- Coarse grid used.
- Method to upscale well functions:
  - 1: A simple method is used to compute upscaled PI. The Peaceman equation is applied to perforated coarse blocks, attributing a permeability which is the arithmetic average of the perforated fine blocks. No correction of transmissivities close to wells is done.
  - 2: Only PI is upscaled (equation 5), without any correction of transmissivities close to wells.
  - 3: PI and near well transmissivities are upscaled from fine scale well steady-state simulations.
- Aggregation ratio for computing corrected Kr shapes.
- Processing of end points:
  - 1: with equation 6 ($\omega = 1$).
  - 2: with equation 7.

Tests of case C2, waterflood

The tests (w1 to w6) differ according to the following options (see table 8):

- Coarse grid used.
- Aggregation ratio for computing corrected Kr shapes.
- Initialization of saturation:
  - 1: With a transfer of saturation from fine scale model initialization, and no Pc considered during waterflood.
  - 2: By using upscaled drainage Pc curves, used also during the imbibition phase.
- Using a correction of gravity term close to producing wells. As these wells are perforated close to aquifer, water coning or cusping occurs during production. To accurately describe the potential variation in the oil phase close to the well, a fine grid is necessary. When the grid is coarse, the driving potential difference that builds up the water cone is underestimated. This can be tackled in our numerical simulator by increasing the driving gravity term ($g(\rho_w - \rho_o)$) applied in the blocks close to the well. A constant multiplying factor has been used in all realizations for all producing wells.

Tests of case C2, depletion

The tests (d1 to d3) differ according to the following options (see table 9):

- Method to upscale well functions:
  - 1: Only PI is upscaled (equation 5), without any correction of transmissivities close to wells.
  - 2: PI and near well transmissivities are upscaled from fine scale well steady-state simulations.
- Using a correction of gravity term close to producing wells, as for the waterflood case.

The finest coarse grid was always used.

Influence of correction of numerical dispersion

This influence is shown when comparing the following waterflood tests of case 2 (table 5):

- w1: Kr curves are not corrected for numerical dispersion.

• w2: Kr curves are corrected with an aggregation ratio 5:1.
• w4: Kr curves are corrected with an aggregation ratio 2:1.

Test w4 exhibits the best ranking performance for both intermediate and final production data. This observation confirms the conclusion of the 2D numerical dispersion investigation. The aggregation factor for computing corrected Kr curve (2:1) is close to half the 1D block aggregation factor (5:1).

Influence of Kr physical upscaling

It is shown when looking at tests w3 and w5 of case 1 (table 10). The option to compute Kr end point in w5 gives better overall results for intermediate and final times. This shows that upscaling Kr is important to improve ranking. Methods used here are simplistic, and better ones should be developed. Li et al. (1995) recently proposed a promising method which seems accurate though not CPU expensive.

Influence of upscaling well parameters

This influence is shown when comparing the following depletion tests of case 2 (table 6):
• d2: Only PI is upscaled.
• d1: PI and near well transmissivities are upscaled.

The results of test d2 are clearly worse than those of test d1,and the necessity of accurately computing near well transmissivities is clear.

Influence of saturation initialization

This influence is shown when comparing the following waterflood tests of case 2 (table 5)
• w3: coarse models are initialized with upscaled Pc drainage curves.
• w4: coarse models are initialized with initial saturation computed on the fine scale models.

These tests do not show significant differences whether in correlation (ρ), or accuracy (ε) coefficients. Thus, the simplest method is preferable in practical cases.

Influence of grid size

This influence is shown when comparing:
- Tests w3 and w4 of case 1 (table 10).
- Tests w4 and w5 of case 2 (table 5).

Correlation coefficients are improved at final times for finest grids. They are also improved near breakthrough for case C1. For case C2 near BT, the accuracy (ε_1) is improved, though the correlation coefficient is not.

Coning

Coning is present in case C2, especially for depletion. It can be better represented either with a finer grid (test w4), or by the trick on gravity coefficient (test w5, d3). The results show effectively an improvement of correlation coefficients when these options are chosen. This emphasizes the importance of correctly upscaling near wells.

The depletion case is demonstrative: if aquifer was not active, the depletion would be completely controlled by porous volume and well PI, which are well represented by the methods used in this study. Coning, which occurs in the vicinity of wells, deteriorates dramatically the results of upscaled models. Our present methods of Kr upscaling have to be improved and extended. We feel that the well PVT and Kr issues touched on in the discussion about upscaling methods are critical.

Additional results

The upscaling method appears to be effective for waterflood cases, either when aquifer is present or not, or when injection balances production or not. It is possible to pick up realizations exhibiting extreme behaviors (Fig. 4, 6, 8, 9). Cumulative data appear easier to recover through upscaled models.

Oil recovery is not so well recovered (Fig. 10): as shown by error analysis, this comes from the small variability of this parameter, although recovery is obtained with the same precision as cumulative oil production. Instantaneous data (flowrates or rate ratios) are less easily captured. But yearly flowrates used in NPV calculations can be satisfactorily derived from cumulative data.

Depletion in the presence of an active aquifer cannot be accurately simulated with the present upscaling methods (Fig. 11), making this approach ineffective.

Fig. 5 represents the mean final oil production computed for each geostatistical set of case1. The mean values of fine scale models are satisfactorily approximated by upscaled models. In the preliminary phase of a sensitivity study, when the most important factors are not known, it is interesting to use upscaled models to investigate the relative importance of factors, and then to use fine models in a second phase focused on the controlling factors.

Fig. 7 depicts how the variation coefficients of several simulated productions parameters are approximated with upscaled models: their relative magnitude is preserved, thereby allowing the focus to be on the uncertainty of the most variable ones.

COMPARISON OF COMPUTATIONAL COSTS

The mean performances for the case C1, compared to a mean computer time of 100 for the comprehensive simulation, are as follows:

Task	Computer time
Computation of pore volume, depth, saturation	0.24
Computation of transmissivities	1.19
Well model for PI computation	0.40
Upscaled flow simulation	0.79
Total	2.62
Ratio Upscaled Model / Fine Model	1: 38

Under some conditions (moderate permeability anisotropy and variance of the permeability field), the numerical solutions used for transmissivities and for well representations could be replaced by algebraic solutions, leading to smaller ratios of total time for upscaled simulation to fine scale simulation time. With the present options, smaller ratios would also be obtained for larger fine scale models.

CONCLUSIONS

- We have successfully used upscaling to rank multiple geostatistical realizations, for waterflood cases. Upscaling with a large aggregation ratio is thus a practical method, which dramatically speeds up sensitivity studies, which would otherwise be precluded by business constraints.
- When depletion is controlled by aquifer coning, the upscaling techniques we used failed to provide a correct ranking of the realizations. Upscaling close to the well appears to be a critical point. A practical recommendation is to use fine grid-blocks around wells when upscaling from a geological model to a flow model.
- Upscaling of relative permeability is also a critical point. We recognize that we used over-simplified Kr upscaling methods for the sake of rapidity, and that further progress is necessary.
- When working with a regular coarse grid, correction of numerical dispersion seems necessary. A practical method consisting of computing a correction for 1D flow and applying it in 3D worked well. This correction depends on the respective directions of flow and of grid.

Nomenclature

c^t	=	total compressibility, $m^{-1}Lt^2$, $m^3/m^3/Pa$
K	=	permeability, L^2, m^2
Kr	=	relative permeability
$n_1:n_2$	=	aggregation ratio, n_1 fine blocks grouped into n_2 coarse blocks
P	=	pressure, $mL^{-1}t^{-2}$, Pa
Pc	=	capillary pressure, $mL^{-1}t^{-2}$, Pa
q	=	flowrate, L^3t^{-1}, m^3/s
S	=	saturation, L^3/L^3
t	=	time, t, s
$\underline{V}$	=	volume, L^3, m^2
$\overline{X}$	=	upscaled or averaged property X
x	=	proportion, adimensional
Z	=	depth, L, m
ϕ	=	porosity, L^3/L^3
Φ	=	potential, $mL^{-1}t^{-2}$, Pa
μ	=	viscosity, $mL^{-1}t^{-1}$, Pa.s
$\mu(X)$	=	mean of X
$\sigma(X)$	=	standard deviation of X

Subscripts

f	=	fine
i	=	index
o	=	oil
u	=	upscaled
w	=	water

APPENDIX

A. Computation of average potential

In transient regime, the discretized equation of conservation of volume (assuming that density of fluid is constant), is written as follows for either fine or coarse blocks:

$$\frac{V\phi c^t(\Phi^{n+1}-\Phi^n)}{\Delta t}=\sum_{i\in I} q_i \quad , I = \text{set of interfaces of the block} \qquad (A1)$$

As the sum of all flowrates across interfaces of fine blocks is equal to the sum of flowrates across interfaces of the coarse block, we have:

$$\frac{\overline{V\phi}\,\overline{c^t}(\overline{\Phi}^{n+1}-\overline{\Phi}^n)}{\Delta t}=\sum_{i\in B}\frac{V_i\phi_i c_i^t(\Phi_i^{n+1}-\Phi_i^n)}{\Delta t} \quad , B = \text{set of fine blocks} \qquad (A2)$$

Total volume and porous volume of the coarse block are computed thanks to simple equivalence equations:

$$\overline{V}=\sum_{i\in B} V_i \quad \text{and} \quad \overline{V\phi}=\sum_{i\in B} V_i\phi_i \qquad (A3, A4)$$

Equation A2 shows that averaging of compressibility and potential are not independent. One possibility is to compute average potential with porous volume weighting.

$$\overline{V\phi\Phi} = \sum_{i\in B} V_i\phi_i\Phi_i \quad (A5)$$

It follows that average compressibility is computed according to:

$$\overline{c^t}\sum_{i\in B} V_i\phi_i\Delta\Phi_i = \sum_{i\in B} V_i\phi_i c_i^t\Delta\Phi_i \quad (A6)$$

Equation A6 means that average compressibility varies with time, as boundary conditions on the coarse block evolve in transient regime.

A second possibility is to compute the average compressibility as follows:

$$\overline{V\phi c^t} = \sum_{i\in B} V_i\phi_i c_i^t \quad (A7)$$

The average potential resulting from the choice of compressibility averaging is given by the following equation:

$$\overline{V\phi c^t\Phi} = \sum_{i\in B} V_i\phi_i c_i^t\Phi_i \quad (A8)$$

In the special case where total compressibility is constant, the average compressibility is equal to the small-scale compressibility for both choices, and the potential is simply averaged with porous volume weighting. This occurs when the total compressibility is composed of a negligible rock term, and a prominent constant fluid term. For cases where small-scale compressibility varies, further work is needed to determine which formulation is the best.

B. Computation of gravity center depth

From the equivalence of gravitational potential between fine and coarse scale we obtain the following equation:

$$\overline{\rho V\phi gZ} = \sum \rho_i V_i\phi_i gZ_i \quad (B1)$$

From equivalence of mass we have:

$$\overline{\rho V\phi} = \sum \rho_i V_i\phi_i \quad (B2)$$

And finally:

$$\overline{Z} = \frac{\sum \rho_i V_i\phi_i Z_i}{\sum \rho_i V_i\phi_i} \quad (B3)$$

When the specific gravity ρ is constant, it is a porous volume weighted average of block center depths:

$$\overline{Z} = \frac{\sum V_i\phi_i Z_i}{\sum V_i\phi_i} \quad (B4)$$

C. Computation of upscaled drainage capillary pressure curve

This is going to be done for a water-oil case. Before production starts, the reservoir is in equilibrium between capillary and gravity forces, resulting in a saturation vertical profile honoring the drainage Pc curve. The Pc in a fine block i may be expressed versus the small-scale Pc at the gravity center of the coarse block:

$Pc_i = Pc(\overline{Z}) + \varepsilon g(\rho_w - \rho_o)(\overline{Z} - Z_i)$, $\varepsilon = \pm 1$ depending on vertical axis orientation (C1)

The average Pc in the coarse block is obtained thanks to a volume average:

$$\overline{Pc} = \frac{\sum Pc_i \phi_i V_i}{\sum \phi_i V_i} = Pc(\bar{Z}) + \varepsilon g(\rho_w - \rho_o) \frac{\sum \phi_i V_i (\bar{Z} - Z_i)}{\sum \phi_i V_i} \qquad (C2)$$

From equation B4, it follows that

$$\overline{Pc} = Pc(\bar{Z}) \qquad (C3)$$

The appropriate choice of the gravity center of the coarse block leads to that simple relation, allowing to build up an upscaled drainage curve for a coarse block:

i) Choose a value for $\overline{Pc} = Pc(\bar{Z})$

ii) Compute Pc_i for each fine block (C1), and the corresponding water saturation S_w^i from the drainage Pc curve.

iii) Average water saturation for the coarse block:

$$\overline{S_w} = \frac{\sum V_i \phi_i S_w^i}{\sum V_i \phi_i} \qquad (C4)$$

iv) Join the new point $(\overline{S_w}, \overline{Pc})$ to the upscaled drainage Pc curve, and iterate the sequence.

The fine-scale Pc curve is characterized by a maximum S_w, for which $Pc = Pc_{min}$, and a minimum S_w for which $Pc = Pc_{max}$. This curve has to be extended outside this Pc range as follows:

$$Pc > Pc_{max} \Rightarrow S_w = S_{wmin} \; ; \; Pc < Pc_{min} \Rightarrow S_w = S_{wmax}$$

To completely define the upscaled Pc curve, the value picked up in step i must vary in the range between $Pc_{min} - \varepsilon g(\rho_w - \rho_o)(Z - z_{top})$ and $Pc_{max} - \varepsilon g(\rho_w - \rho_o)(Z - z_{bot})$, where z_{top} and z_{bot} are the depths of the uppermost and lowermost fine blocks inside the coarse one. This results in an upscaled drainage Pc curve with a range of negative Pc values.

This method may be applied to homogeneous blocks, to initialize their saturation according to the capillary vertical profile, and to cases of pure gravity segregation when the capillary transition zone has a negligible thickness (the drainage Pc curve is then defined by: $Pc \geq 0 \Rightarrow S_w = S_{wmin}$; $Pc < 0 \Rightarrow S_w = S_{wmax}$).

REFERENCES

BALLIN, P. R., JOURNEL, A. G., AZIZ, K.,1992, Prediction of uncertainty in reservoir performance forecast: Journal of Canadian Petroleum Technology, Vol. 31, No. 4, p 52-62, April 1992.

BALLIN, P. R., AZIZ, K., JOURNEL, A. G., 1993, Quantifying the impact of geological uncertainty on reservoir performing forecasts, Paper SPE 25238 in Proceedings of the 12th SPE Symposium on Reservoir Simulation held in New Orleans, LA, USA, February 28-March 3, 1993.

DEUTSCH, C. V., JOURNEL A. G., 1992, GSLIB, Geostatistical Software Library and User's Guide, Oxford University Press editor, p 167-170.

DEUTSCH, C., SRINIVASAN S., 1996, Ranking stochastic reservoir models, Paper SPE/DOE 35411: in Proceedings of 10th Symposium on Improved Oil Recovery, Tulsa, OK, USA, April 21-24, 1996.

DING Y., 1995, Scaling-up in the vicinity of wells in heterogeneous fields: paper SPE 29137, in Proceedings of 13 th SPE Symposium on Reservoir Simulation, San Antonio, Feb. 1995.

GOMEZ-HERNANDEZ, J. J., JOURNEL, A. G., 1990, Stochastic characterization of grid-block permeabilities: from point values to block tensors, in D. Guérillot and O. Guillon editors, Second European Conference on the Mathematics of Oil Recovery, Paris, Editions Technip, p83-90.

GUÉRILLOT, D. R., MORELON, I. F., 1992, Sorting Equiprobable geostatistical images by simplified flow calculations, Paper SPE 24891: Proceedings of the 67th Annual Technical Conference and Exhibition of the SPE held in Washington, DC, USA, October 4-7, 1992.

KYTE, J.R., and BERRY, D.W., 1975, New Pseudo Functions to Control Numerical Dispersion, in SPE Journal (Aug. 1975), p 269-275.

LANTZ, R. B., 1971, Quantitative evaluation of numerical diffusion (Truncation error): SPE Journal, Sept. 1971, p315-320.

LI, D., CULLICK, A.S., LAKE, L. W. , 1995, Scale-up of reservoir models relative permeability using a global method: paper SPE 29872 in Proceedings of 9th Middle East Oil Show and Conference, Bahrain, March 1995.

PEACEMAN, D. W., 1978, Interpretation of well-block pressures in numerical reservoir simulation: in Transactions of AIME, 1978, p253.

ROMEU R.K., NŒTINGER B., 1995, Calculation of internodal transmissibilities in finite-difference models of flow in heterogeneous media: Paper 94WR02422, in Water Resources Research, Vol. 31, n°4, April 1995, p943-959.

SAAD, N., MAROONGROGE V., KALKOMEY, C. T., 1996, Ranking geostatistical models using tracer production data: Paper SPE 35494, Proceedings of European 3D Reservoir Modelling Conference, p 131-142, Stavanger, Norway, April 16-17, 1996.

THIELE, M. R., BATICKY, R. P., BLUNT, M. J., ORR, F. M., 1996, Simulating flow in heterogeneous systems using streamtubes and streamlines: SPE Reservoir Engineering, Volume11, No. 1, p5-12, February 1996.

FIGURES

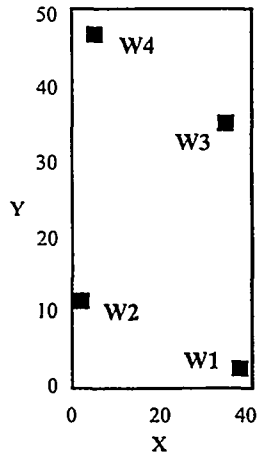

Fig. 1: Well implementation, case C1.

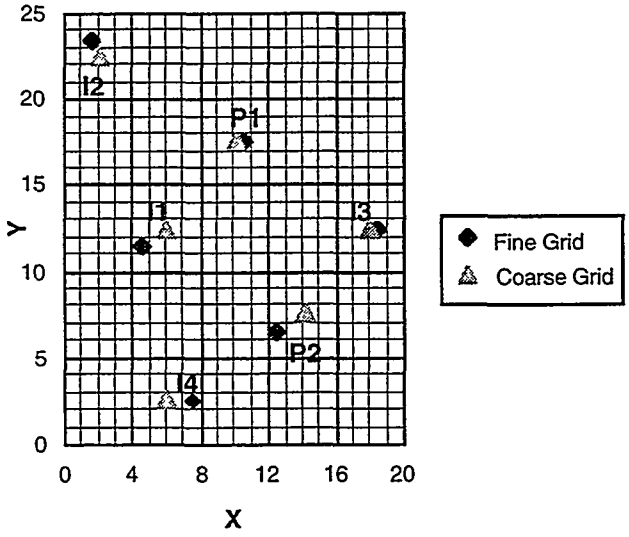

Fig. 2: Well implementation and grids, case C2 waterflood.

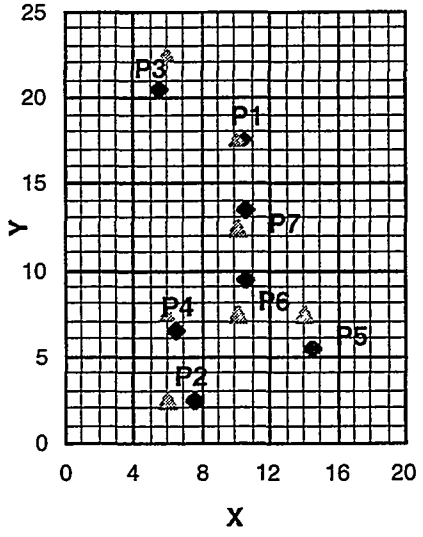

Fig. 3: Well implementation and grids, case C2 depletion.

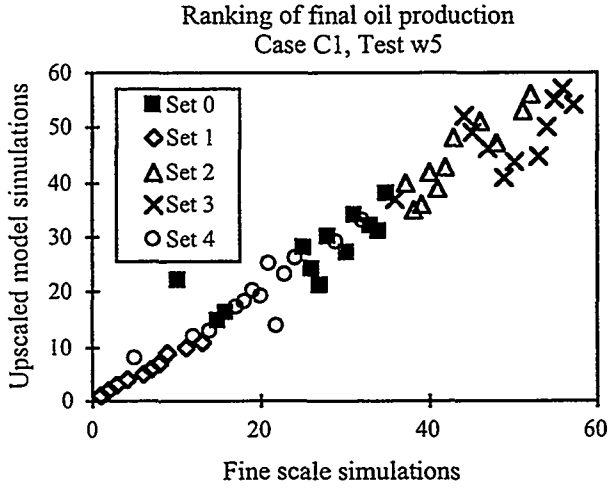

Fig. 4: Ranking of final oil production case C1, test w5.

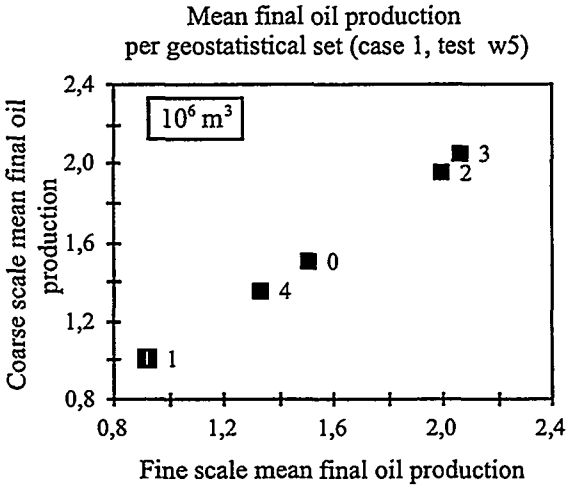

Fig. 5: Comparison of experimental planning results on fine and coarse models.

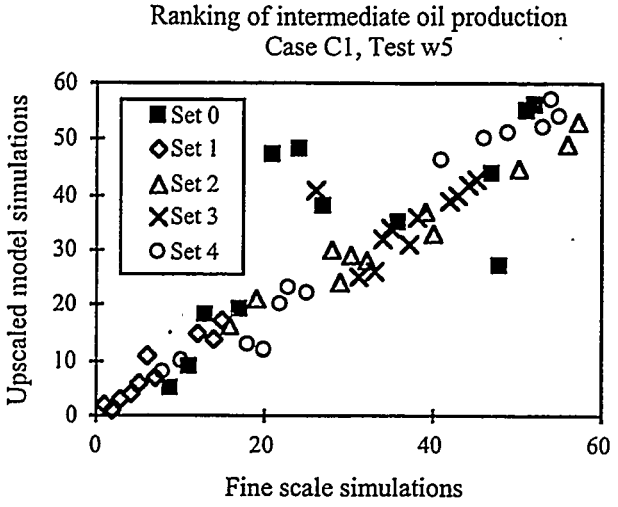

Fig. 6: Ranking of intermediate oil production case C1, test w5.

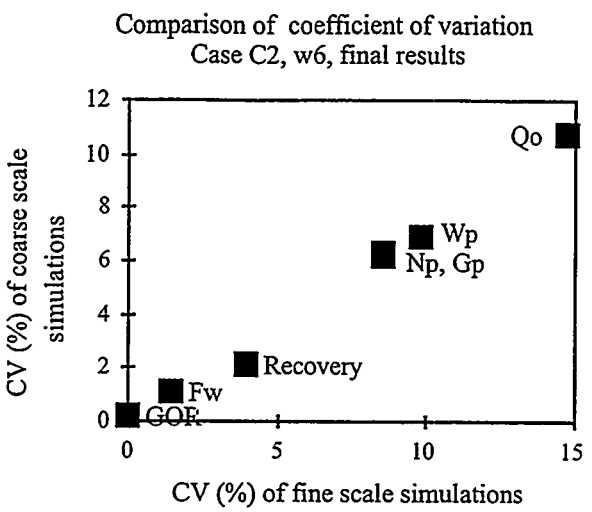

Fig. 7: Comparison of coefficients of variation for fine and coarse models.

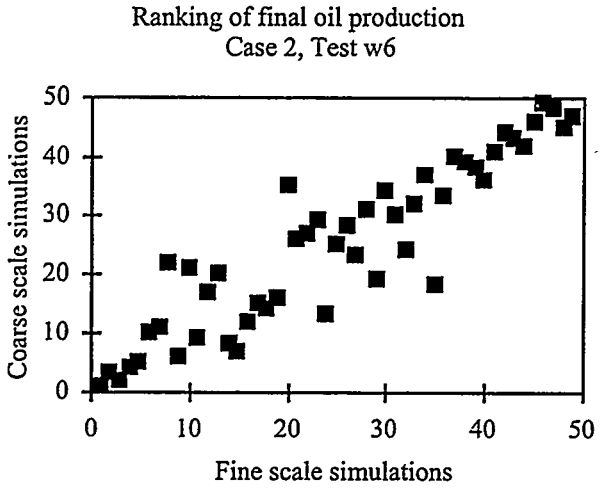

Fig. 8: Ranking of final oil production, case C2, test w6.

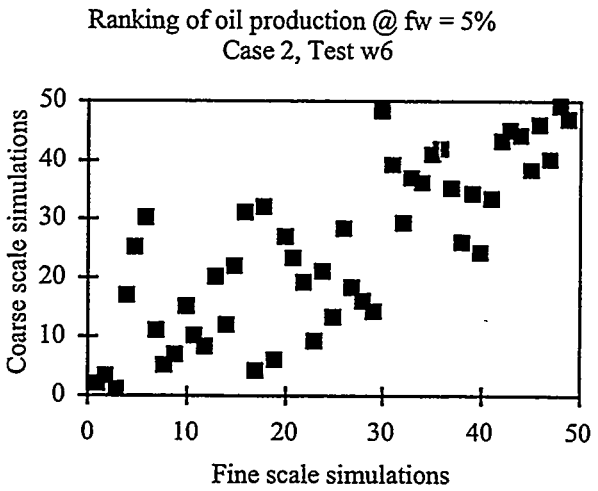

Fig. 9: Ranking of intermediate oil production, case C2, test w6.

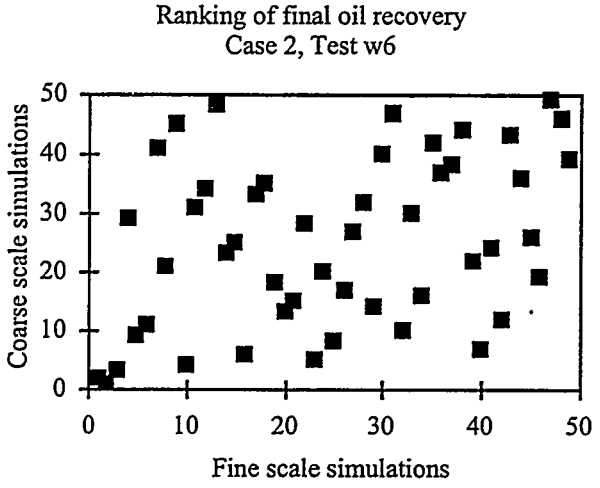

Fig. 10: Ranking of final oil recovery, case C2, test w6.

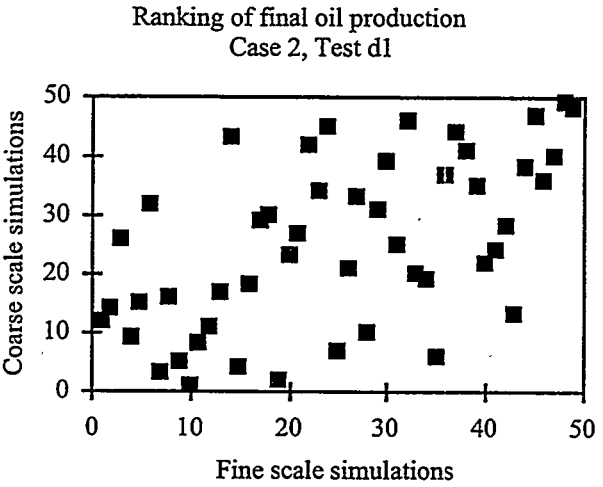

Fig. 11: Ranking of final oil production, case C2, test d1.

TABLES

Table 1: Grid description case C1.

Grid	Block number / Aggregation ratio			
	X	Y	Z	Total
Fine	41	51	20	41820
Coarse 1	8 / ~5:1	10 / ~5:1	4 / ~5:1	320 / ~130:1
Coarse 2	10 / ~4:1	13 / ~4:1	5 / ~4:1	650 / ~64:1

Table 2: Grid description case C2.

Grid	Block number / Aggregation ratio			
	X	Y	Z	Total
Fine	20	25	20	10000
Coarse 1	5 / 4:1	5 / 5:1	2 / 10:1	50 / 200:1
Coarse 2	5 / 4:1	5 / 5:1	4 / 5:1	100 / 100:1

Table 3: Petrophysical characteristics of facies, case C1.

Facies	Permeability		Porosity	Swi	Sor	Krwmax
	Horizontal (mD)	Kv/Kh				
1	3000	0.1	0.30	0.15	0.20	0.40
2	300	0.01	0.26	0.30	0.17	0.20
3	25	0.001	0.06	0.35	0.18	0.15
4	1	0.00001	0.022	0.45	0.15	0.11

Table 4: Definition of geostatistical sets, case C1.

Set	Proportions	Variogram range (m)
S_0	0,15	100
S_1	0,10	50
S_2	0,20	50
S_3	0,20	200
S_4	0,10	200

Table 5: Case C2 - Waterflood Production Results

		End of production (20 years)						fw = 5%						
	Data	w1	w2	w3	w4	w5	w6	w1	w2	w3	w4	w5	w6	mean
ρ_x	Np	0.93	0.96	0.95	0.95	0.94	0.95	0.63	0.63	0.65	0.64	0.76	0.71	0.81
	Qo	0.45	0.42	0.47	0.47	0.58	0.51	0.05	0.09	0.02	0.01	0.04	0.11	0.27
	Gp	0.93	0.96	0.95	0.95	0.93	0.95	0.64	0.63	0.65	0.64	0.76	0.71	0.81
	Wp	0.93	0.94	0.95	0.95	0.94	0.95	0.23	0.27	0.15	0.20	0.08	0.02	0.55
	Fw	0.45	0.19	0.48	0.28	0.57	0.50	0.08	0.04	0.10	0.06	0.08	0.07	0.24
	Recov.	0.55	0.59	0.57	0.58	0.74	0.55	0.51	0.49	0.52	0.51	0.69	0.61	0.58
	mean	0.71	0.68	0.73	0.70	0.78	0.74	0.36	0.36	0.35	0.34	0.40	0.37	
ρ_r	Np	0.87	0.93	0.91	0.90	0.90	0.92	0.76	0.78	0.77	0.79	0.71	0.79	0.84
	Qo	0.41	0.45	0.46	0.45	0.53	0.49	0.12	0.03	0.22	0.24	0.00	0.07	0.29
	Gp	0.87	0.93	0.91	0.90	0.91	0.92	0.76	0.78	0.77	0.79	0.71	0.80	0.84
	Wp	0.87	0.94	0.91	0.93	0.90	0.92	0.09	0.07	0.11	0.02	0.05	0.02	0.49
	Fw	0.43	0.41	0.51	0.40	0.57	0.50	0.11	0.05	0.20	0.10	0.05	0.17	0.29
	Recov.	0.31	0.35	0.33	0.32	0.63	0.37	0.64	0.64	0.65	0.67	0.64	0.70	0.52
	mean	0.63	0.67	0.67	0.65	0.74	0.68	0.41	0.39	0.45	0.43	0.36	0.42	
ε_1 %	Np	5.3	3.4	3.9	2.5	2.7	3.1	12.8	36.5	18.0	23.3	15.1	18.9	12.1
	Qo	13.5	20.0	13.7	11.8	12.8	10.5	746	0.3	0.4	0.3	0.3	0.5	69.1
	Gp	4.2	4.8	3.9	2.6	2.3	2.6	13.1	38.4	18.0	24.5	15.7	18.9	12.4
	Wp	6.1	4.1	4.5	2.7	3.1	3.6	16.8	40.8	62.3	35.3	39.4	48.6	22.3
	Fw	1.4	2.1	1.4	1.3	1.3	1.1	51.3	5.8	6.2	5.7	5.9	9.8	7.8
	Recov.	5.3	3.5	3.9	2.5	2.7	3.1	15.3	37.1	18.2	23.8	15.3	19.6	12.5
	mean	6.0	6.3	5.2	3.9	4.1	4.0	143	26.5	20.5	18.8	15.3	19.4	
ε_2 %	Np	33.8	29.7	28.0	22.5	24.7	24.2	46.2	70.8	42.1	67.9	49.6	72.3	42.6
	Qo	63.2	81.6	66.3	63.7	64.3	54.2	2460	106	226	189	109	186	306
	Gp	30.0	31.9	28.0	25.6	21.9	21.7	47.3	70.5	42.1	68.8	51.2	72.3	42.6
	Wp	33.9	32.8	28.0	22.1	24.6	24.2	84.9	88.7	80.6	60.8	75.1	114	55.8
	Fw	62.7	93.7	65.1	78.8	68.4	54.7	235	84.3	186	157	90.9	168	112
	Recov.	69.2	70.2	57.5	50.8	55.2	50.9	53.6	83.4	48.2	79.2	56.2	83.6	63.2
	mean	48.8	56.7	45.5	43.9	43.2	38.3	488	83.9	104	104	72.1	116	

Table 6: Case C2 - Depletion Production Results

		End of production (20 years)			
	Data	d1	d2	d3	mean
ρ_x	Np	0.57	0.22	0.57	0.45
	Qo	0.10	0.00	0.28	0.13
	Gp	0.63	0.29	0.63	0.52
	GOR	0.09	0.00	0.12	0.07
	Wp	0.54	0.19	0.47	0.40
	Fw	0.04	0.00	0.13	0.06
	Recov.	0.37	0.02	0.36	0.25
	mean	0.33	0.10	0.37	
ρ_r	Np	0.56	0.23	0.55	0.45
	Qo	0.26	0.20	0.15	0.20
	Gp	0.61	0.26	0.65	0.51
	GOR	0.23	0.40	0.20	0.27
	Wp	0.49	0.13	0.51	0.38
	Fw	0.13	0.27	0.13	0.18
	Recov.	0.38	0.09	0.34	0.27
	mean	0.38	0.23	0.36	
ε_1 %	Np	36.3	77.8	29.5	47.9
	Qo	86.0	100	83.3	89.8
	Gp	9.0	72.3	8.6	30.0
	GOR	60.3	100	64.5	74.9
	Wp	34.5	94.2	34.0	54.2
	Fw	129	100	171	133
	Recov.	36.1	77.8	29.4	47.8
	mean	55.8	88.9	60.1	
ε_2 %	Np	103	97.5	102	101
	Qo	98.5	100	82.5	93.7
	Gp	70.7	95.8	70.5	79.0
	GOR	97.5	100	96.6	98.0
	Wp	75.4	99.6	68.2	81.1
	Fw	103	100	113	106
	Recov.	115	102	114	110
	mean	94.9	99.2	92.4	

Table 7: Test specifications case C1

			Correction of Kr	
Test	Grid	Wells	Shape	E. P.
w1	CG1	1	1:1	1
w2	CG1	2	5:1	1
w3	CG1	3	5:1	1
w4	CG2	3	5:1	1
w5	CG1	3	5:1	2

Table 8: Test specification case C2 waterflood

Test	Grid	Wells	Kr shape	Saturation initializ.	Gravity correction
w1	CG1	1	1:1	1	No
w2	CG1	1	5:1	1	No
w3	CG1	1	2:1	2	No
w4	CG1	1	2:1	1	No
w5	CG2	1	2:1	1	No
w6	CG1	1	2:1	1	Yes

Table 9: Test specification case C2 depletion

Test	Grid	Wells	Gravity correction
d1	CG2	1	No
d2	CG2	2	No
d3	CG2	1	Yes

Table 10: Case C1 - Waterflood Production Results

		2000 days					500 days					
	Data	w1	w2	w3	w4	w5	w1	w2	w3	w4	w5	mean
ρ_X	Np	0.98	0.99	0.98	0.98	0.98	0.93	0.95	0.92	0.93	0.95	0.96
	Qo	0.28	0.07	0.44	0.25	0.75	0.97	0.96	0.95	0.95	0.96	0.66
	Gp	0.96	0.96	0.93	0.96	0.96	0.80	0.90	0.82	0.84	0.87	0.90
	GOR	0.28	0.65	0.17	0.31	0.67	0.91	0.94	0.92	0.90	0.92	0.67
	Wp	0.68	0.74	0.66	0.84	0.88	0.73	0.24	0.17	0.50	0.16	0.56
	Fw	0.50	0.49	0.24	0.49	0.90	0.44	0.11	0.37	0.61	0.08	0.42
	Recov.	0.56	0.76	0.60	0.65	0.79	0.74	0.89	0.82	0.83	0.86	0.75
	mean	0.61	0.67	0.57	0.64	0.85	0.79	0.71	0.71	0.80	0.68	
ρ_r	Np	0.97	0.98	0.97	0.97	0.98	0.85	0.90	0.84	0.87	0.91	0.92
	Qo	0.38	0.38	0.55	0.36	0.77	0.86	0.85	0.79	0.81	0.88	0.66
	Gp	0.94	0.95	0.92	0.94	0.96	0.73	0.80	0.76	0.74	0.80	0.85
	GOR	0.41	0.64	0.38	0.42	0.70	0.89	0.90	0.82	0.86	0.87	0.69
	Wp	0.77	0.78	0.75	0.86	0.90	0.77	0.57	0.49	0.60	0.46	0.70
	Fw	0.72	0.70	0.62	0.72	0.87	0.84	0.63	0.60	0.71	0.60	0.70
	Recov.	0.61	0.70	0.59	0.61	0.79	0.70	0.89	0.83	0.83	0.85	0.74
	mean	0.69	0.73	0.68	0.70	0.85	0.81	0.79	0.73	0.77	0.77	
ε_1 %	Np	9.2	5.0	6.2	6.1	4.2	7.6	5.1	6.9	6.3	6.2	6.3
	Qo	33.5	37.6	41.6	37.4	23.1	6.3	6.4	8.5	7.2	6.7	20.8
	Gp	8.4	5.9	7.7	6.0	5.8	10.7	6.8	8.9	8.1	8.1	7.7
	GOR	27.3	20.9	30.1	24.5	18.9	7.8	5.0	5.8	6.0	6.8	15.3
	Wp	64.7	43.1	55.0	43.9	23.9	157	87.6	89.3	71.1	89.4	72.5
	Fw	38.0	31.6	38.4	30.6	15.4	102	97.3	88.4	74.5	93.4	61.0
	Recov.	9.3	5.1	6.4	6.3	4.5	9.9	6.2	8.5	7.7	7.5	7.1
	mean	27.2	21.3	26.5	22.1	13.7	43.0	30.6	30.9	25.8	31.1	
ε_2 %	Np	19.4	12.5	15.6	16.1	13.0	40.2	32.1	41.7	39.4	36.1	26.6
	Qo	82.4	100	80.8	85.5	49.0	23.5	24.9	27.9	26.1	23.8	52.4
	Gp	24.8	19.3	26.9	21.6	19.0	56.3	38.3	48.4	47.9	44.9	34.7
	GOR	91.8	74.2	128	95.6	62.8	41.4	29.5	31.9	37.5	35.0	62.7
	Wp	56.0	55.8	58.2	45.1	39.0	139	92.4	94.5	80.0	94.6	75.4
	Fw	73.8	75.7	88.8	76.8	38.7	120	99.9	94.5	76.2	99.3	84.4
	Recov.	47.7	38.0	47.7	46.3	41.3	69.4	45.3	62.3	55.7	52.1	50.6
	mean	56.6	53.6	63.7	55.3	37.5	69.9	51.8	57.3	51.8	55.1	

FIGURES CAPTIONS

Effect of Wettability on Scale-up of Multiphase Flow from Core-Scale to Reservoir Fine-Grid-Scale

Y. C. Chang, V. Mani & K. K. Mohanty
Department of Chemical Engineering
University of Houston
Houston, TX 77204-4792

ABSTRACT

Typical field simulation grid-blocks are internally heterogeneous. The objective of this work is to study how the wettability of the rock affects its scale-up of multiphase flow properties from core-scale to fine-grid reservoir simulation scale (~10'x10'x5'). Reservoir models need another level of upscaling to coarse-grid simulation scale, which is not addressed here. Heterogeneity is modeled here as a correlated random field parameterized in terms of its variance and two-point variogram. Variogram models of both finite (spherical) and infinite (fractal) correlation length are included as special cases. Local core-scale porosity, permeability, capillary pressure function, relative permeability functions, and initial water saturation are assumed to be correlated. Water injection is simulated and effective flow properties and flow equations are calculated. For strongly water-wet media, capillarity has a stabilizing/homogenizing effect on multiphase flow. For small variance in permeability, and for small correlation length, effective relative permeability can be described by capillary equilibrium models. At higher variance and moderate correlation length, the average flow can be described by a dynamic relative permeability. As the oil wettability increases, the capillary stabilizing effect decreases and the deviation from this average flow increases. For fractal fields with large variance in permeability, effective relative permeability is not adequate in describing the flow.

INTRODUCTION

Heterogeneities exist at several length scales in naturally-occurring porous media. Variations in properties such as permeability and porosity can occur in core scale, stratum scale, bedding scale, well-log scale, and interwell scale (Worthington, 1991). Reservoir heterogeneity at different scales has different impacts on ultimate oil recovery in displacement processes. In the last decade, much progress has been accomplished on the characterization of detailed heterogeneities in oil reservoirs and the integration of these heterogeneities into the flow calculations (Wolcott and Chopra, 1993). Geostatistical techniques have been developed for estimation of the heterogeneities (Journel, 1990). Emerging parallel computers and new numerical techniques are increasing the power of reservoir simulation (Thiele et al., 1994; Bhogeswara and Killough, 1993). However,

typical reservoir-scale simulation models still do not have the resolution to incorporate fine-scale heterogeneities directly and rely on the use of effective properties to represent the effect of small-scale heterogeneities in large-scale numerical grids (Edwards and Christie, 1993).

Upscaling techniques have been developed to estimate effective flow properties in heterogeneous media (Warren, J. E. and Price, 1961; Gelhar, 1984; King, 1989; Durlofsky, L. J. et al., 1995; Glimm et al., 1993). The techniques developed for single phase flow are accurate and range from simple statistical estimates to detailed numerical simulations. The upscaling of multiphase flow has proven to be difficult. Multiphase flow in porous media is governed by functions such as relative permeability (k_r) and capillary pressure (P_c). Barker and Thiebau (1996) have reviewed the pseudo relative permeability method and point out its lack of generality. Capillary-equilibrium method has been professed by many (Smith et al. 1989), but is applicable in water-wet rocks at small scales (e.g. laboratory-scale) at low flow rates. The homogenization method proposed by Quintard et al. (1996) and others is valid for small correlation lengths. The stochastic method proposed by Butts (1991) and Gelhar (1984) is valid for small permeability variations. The effective relative permeability approach has been proposed by many (Muggeridge et al., 1991; Hewett and Behrens,1991) to take into account the dynamic effects of flow. It can be calculated by many methods: fine-grid simulation (Muggeridge et al., 1991), space renormalization (King et al., 1993) or heuristic methods (Li et al., 1996).

The applicability of the effective relative permeability approach for core-to-numerical grid (in typical pattern simulations) scaleup was tested for water-wet media by Chang and Mohanty (1997). This issue involves two questions. First, can the flow at a larger scale be adequately described by the multiphase Darcy's law involving an effective relative permeability (and an effective capillary pressure)? Second, if the Darcy's law is adequate, what is the effective permeability (and is effective capillary pressure) as a function of intrinsic relative permeability and heterogeneity? Chang and Mohanty (1997) found that in water-wet rocks the average flow can be described by an effective relative permeability if the permeability variance and correlation lengths are not very large. Such a formulation is not valid if the permeability variance is large and the spatial correlation is fractal. Water-wet capillary pressure plays an important role in stabilizing the waterflood displacement fronts.

Many reservoirs are not water-wet. The objective of this work is to study how the wettability of the rock affects its scale-up of multiphase flow properties from core-scale (~2") to pattern simulation grid-scale (~10'). Reservoir models need another level of upscaling to coarse-grid simulation scale (Li et al., 1996; Barker & Thibeau, 1996), which is not addressed here. Two key simplifying assumptions are used in this paper: effects of gravity are neglected and two-dimensional flow regions are considered. The scale-up of flow in only the horizontal direction is considered in several permeability fields. The anisotropic nature of the scaled-up relative

permeability is outside the scope of this paper. Also, the scale-up of the capillary pressure is not considered here. In the following section, the methodology used to represent reservoir wettability, heterogeneity and flow is summarized. The results are described in the following section.

METHODOLOGY

Heterogeneity is modeled here by a spatially correlated random permeability field parameterized in terms of its variance and two point variogram, similar to our earlier work (Chang & Mohanty, 1997). Local porosity, permeability, capillary pressure, relative permeability and initial water saturation are assumed to be correlated to one another. High resolution reservoir simulation of water/oil displacement is conducted to understand the effect of heterogeneity on detailed multiphase flow. The saturation fronts and pressure drops were monitored and the JBN method (Johnson et al., 1959) is used to compute the effective relative permeabilities from these simulation data.

The computional flow field is taken to be 16 ft by 8 ft, about the size of a typical grid block in a reservoir pattern simulator. This system is modeled by a 100x50 grid of uniform size. The individual grid blocks are 0.16 ft by 0.16 ft, about the size of typical laboratory systems on which relative permeability and capillary pressure functions are measured. Each grid block is assumed to be homogeneous with prescribed intrinsic multiphase flow functions. Darcy's law for multiphase flow and capillary pressure-saturation relations are presumed to be valid at each grid block scale.

The permeability heterogeneity is specified by its probability distribution function and its two-point variogram. The probability distribution function for permeability is assumed to be log-normal with the average of 100 md and a standard deviation of σ_{logk}. σ_{logk} is varied from 0.2 to 0.8. Both spherical variograms with correlation lengths of 0.05 to 0.2 the system length and fractal variograms with Hurst dimension 0.87 are considered. The correlation length in the horizontal direction is considered to be twice the correlation length in the vertical direction. Thus the flow field is anisotropic, but only the overall flow in the horizontal direction is calculated in this work. The porosity was correlated to the permeability by the equation,

$$K = a \cdot 10^{b\phi} \tag{1}$$

where a and b are set to 0.001 and 25, respectively (Beier and Hardy, 1993).

Water-Wet System

The water-wet media were modeled similar to our earlier work (Chang & Mohanty, 1997). Model parameters are listed in Table 1. The intrinsic relative permeability function is given by the Corey model (Honarpour et al., 1982) as

$$k_{ro} = k_{ro}^{0} \left(\frac{S_o - S_{or}}{1 - S_{or} - S_{wr}} \right)^{n_o} \tag{2}$$

$$k_{rw} = k_{rw}^{0}\left(\frac{S_w - S_{wr}}{1 - S_{or} - S_{wr}}\right)^{n_w}. \quad (3)$$

The residual oil saturation (S_{or}) and initial oil saturation (S_{oi}) are related by the correlation (Land, 1968)

$$S_{or} = \frac{S_{oi}}{1 + c \cdot S_{oi}}. \quad (4)$$

The irreducible water saturation S_{WI} is assumed to be a constant for all grid points and equal to 0.2. The initial oil saturation (S_{oi}) depends on the initial capillary pressure of the system. The permeability, the porosity, and the primary drainage capillary pressure functions are correlated by the use of the J-function (Lake, 1989). Since the J-function depends on only the effective saturation, the capillary pressure function can be expressed in terms of permeability, porosity, and effective saturation and is given by

$$P_c^{Dr}(S) = \Gamma\sigma(K/\phi)^{1/2} S^{-1/\beta} \quad (5)$$

where Γ and β are constants and S is given by

$$S = \frac{S_w - S_{wr}}{1 - S_{wr}}. \quad (6)$$

The imbibition capillary pressure, P_c^{Im}, is given by an equation similar to Eq. 5 but with a different constants Γ and β and the effective saturation S is defined as

$$S = \frac{S_w - S_{wr}}{1 - S_{or} - S_{wr}}. \quad (7)$$

Capillary pressure hysteresis and relative permeability hysteresis are assumed to follow the model developed by Killough (1976).

Mixed-Wet System

For mixed-wet media, the wettability is heterogeneous and strongly depends on initial water saturation. Jadhunandan and Morrow (1995) have studied the initial water saturation effect on wettability and the effect of wettability on oil recovery for oil/brine/rock system. They found that the initial water saturation increases as the wettability changes from oil-wet to water-wet. The wettability index I_{w-o} obtained from Amott tests is linearly related to initial water saturation. The relation can be described by

$$I_{w-o} = S_{wi} \cdot m + I_{w-o}^{*} \quad (8)$$

The slope (m) and the intercept (I_{w-o}^{*}) depend on brine composition and crude oil. They also demonstrated that the residual oil saturation decreases as the wettability changes from strongly water-wet to a neutral wettability, then it increases as wettability changes to strongly oil-wet. Residual oil saturation, S_{or} and wettability index, I_{w-o} can be expressed by

$$S_{or} = a\left(\left|I_{w-o} - I_{w-o}^{min}\right|\right)^{b} + S_{or}^{min} \quad (9)$$

By substituting Eq. 9 into Eq. 10, the initial water saturation and residual oil saturation can be

explicitly related by

$$S_{or} = a\left(\left|S_{wi}\cdot m + I^{*}_{w-o} - I^{min}_{w-o}\right|\right)^{b} + S^{min}_{or} \tag{10}$$

The model parameters are listed in Table 1. Depending on the initial water saturation, we classify the grid blocks into three categories: strongly water-wet ($S_{wi} \geq 0.4$); mixed-wet ($0.2 < S_{wi} < 0.4$); strongly oil-wet ($S_{wi} \leq 0.2$). For strongly water-wet system, S_{or} and S_{wi} can be related by Land's correlation. Figure 1 shows the relation between S_{wi} and S_{or} in such mixed-wet systems.

The relative permeability is also given by the Corey model (Eqs. 2 &3), but the parameters, k^0_{rw}, k^0_{ro}, n_w, n_o are assumed to depend on the wettability (which depends on the initial water saturation). For mixed-wet media, the parameters are interpolated between the values of strong water-wettability and strong oil-wettability, according to the initial water saturation. Table 2 shows the parameters for relative permeability model in grids of different wettability. Figure 2 shows the relative permeability curves at different initial water saturations.

Imbibition capillary pressure function also depends on wettability. For water-wet grids ($S_{wi} \geq 0.4$), capillary pressure is positive at all saturations, while capillary pressure is negative at all saturations for oil-wet grids ($S_{wi} \leq 0.2$). For mixed-wet grids ($0.2 < S_{wi} < 0.4$), capillary pressure is positive at low water saturation and negative at higher saturation. The imbibition capillary pressure for mixed-wet grids is described by

$$P_c = P_c^{ww} - F_{mw}\left(P_c^{ww} - P_c^{ow}\right), \tag{11}$$

where

$$F_{mw} = \begin{cases} 1, & \text{for } S_{wi} \leq S^{ow}_{wi}, \\ \dfrac{\dfrac{1}{\left(S_w - S_{wi}\right)\cdot\left(S^{ww}_{wi} - S_{wi}\right) + \varepsilon} - \dfrac{1}{\varepsilon}}{\dfrac{1}{\left(S^{ww}_{wi} - S^{ow}_{wi}\right)\cdot\left(S_w - S^{ow}_{wi}\right) + \varepsilon} - \dfrac{1}{\varepsilon}}, & \text{for } S^{ow}_{wi} < S_{wi} < S^{ww}_{wi}, \\ 0, & \text{for } S_{wi} \geq S^{ww}_{wi}, \end{cases} \tag{12}$$

and S^{ww}_{wi}, the critical initial water saturation for water-wet media, is set to 0.4; S^{ow}_{wi}, the critical initial water saturation for oil-wet media, is equal to 0.2; ε is a given parameter. Here water-wet capillary pressure, P_c^{ww} and oil-wet capillary pressure, P_c^{ow} are given by

$$P_c^{ww} = P_c^{init}\cdot\left(\frac{S_w - S_{wcp}}{S_{wi} - S_{wcp}}\right)^{-1/\lambda_p} \tag{13}$$

and

$$P_c^{ow} = -\Gamma\cdot\left(\frac{S_o - S_{ocm}}{1 - S_{ocm} - S_{wcm}}\right)^{-1/\lambda_m}, \tag{14}$$

where P_c^{init} is the equilibrium capillary pressure at S_{wi}; λ_p, λ_m, S_{wcp}, S_{wcm}, S_{ocm} and Γ are given parameters. Figure 3 shows the capillary pressure at different initial water saturation.

Oil-Wet System

The intrinsic relative permeability and capillary pressure of the oil-wet system are represented by functions similar to those of the water-wet system. The relative permeabilities are described be Eqs. 2 and 3, but with parameters listed in Table 1. Capillary pressure is denoted by

$$P_c(S) = \Gamma\sigma(K/\phi)^{1/2} S^{-1/\beta} \tag{15}$$

where Γ and β are constants and S is given by

$$S = \frac{S_o - S_{oc}}{1 - S_{oc} - S_{wc}} \tag{16}$$

For simplicity, no hysteresis in relative permeability and capillary pressure was assumed for oil-wet media.

Waterflood Simulation

Two-dimensional fine grid simulations of waterflood were conducted to investigate the impact of heterogeneity on two-phase flow. A two-phase, immiscible, third-order, finite difference simulator with flux limiters was used. The numerical scheme is implicit in pressure and explicit in saturation. Water was injected at the left boundary at a specified total rate. The pressure at the right boundary was specified. The top and bottom were no-flow boundaries. Gravitational effects were neglected. The following parameters affect waterflood, but were kept constant in this study at the values listed. $\Delta\rho = 0$, $\mu_o = 10$ cp, $\mu_w = 1$ cp, velocity = 0.49×10^{-2} cm/s, $N_{gv} = 0$, $N_{cv} \sim 3$, $R_l = 2$. The effect of these parameters is discussed elsewhere (Li & Lake, 1993; Chang & Mohanty 1997).

From computed 2-D saturation distributions, cross-sectionally averaged 1-D saturation fronts are calculated and monitored. The objective in scale-up is to relate the flux of a certain phase to its average saturation around any location and thus predict approximate 1D saturation distributions at any time. In this work, we determine whether the relative permeability formulations can be used to estimate these average saturations and the effective relative permeabilities. For homogeneous media and 1-D flow, Darcy's law leads to the traditional fractional flow theory (Lake, 1989). When the capillary pressure term is negligible, fractional flow theory dictates that each saturation, S_w, has its own constant characteristic velocity given by df_w/dS_w. Even when the capillary pressure term is not negligible, the characteristic velocity of each saturation depends only slightly on time. If a heterogeneous system can be averaged to a 1-D homogeneous system, the plot of S_w vs its characteristic velocity (x/t) must be independent of time. Only then, can the Darcy's law with relative permeability be used to describe multiphase flow in a large scale heterogeneous system and appropriate effective relative permeability functions be identified. We will call such systems "k_r-formulation adequate". If, however, the characteristic velocity of each

saturation depends on time strongly, i.e. the plots of S_w vs velocity (x/t) do not fall on one line, the system will be identified as "k_r-formulation inadequate". These systems cannot be described by a traditional relative permeability at the large scale. New flow equations need to be developed for effective multiphase flow of these systems.

Effective relative permeabilities were calculated by the JBN method (Johnson et al., 1959) by monitoring the effluent fractional flow and pressure drop during waterflood simulations. This method is commonly used to determine relative permeabilities from coreflood experiments.

RESULTS

Three typical heterogeneous permeability fields are illustrated in Figure 4. Figure 4(a) shows the permeability distribution for the case of a small standard deviation and a small correlation length, e.g. σ_{logk}=0.2 and λ=0.05. Figure 4(b) shows the permeability distribution for the case of a large standard deviation and a large correlation length, e.g. σ_{logk}=0.8 and λ=0.2. Figure 4(c) shows the permeability distribution for the case of the fractal model with a large standard deviation, e.g. σ_{logk}=0.8 and H=0.87. As discussed earlier, three kinds of wettability scenarios are studied: completely water-wet, mixed-wet and oil-wet. In the mixed-wet scenario, the grids with S_{wi}>0.4 (black in Figure 4 (d-f)) are water-wet, those with 0.2<S_{wi}<0.4 are mixed-wet, and those with S_{wi}<0.2 are oil-wet. The distribution of the water-wet region depends on the correlation length of the permeability field.

The results for strongly water-wet media has been presented elsewhere (Chang & Mohanty, 1997). We have conducted numerical simulations for mixed-wet media and oil-wet media in this work. For the mixed-wet media, the wettability is heterogeneous and capillary pressure and relative permeability depend on initial water saturation as described earlier. Figures 5(a)-(b) shows saturation-velocity profiles for mixed-wet systems at σ_{logk} = 0.2 with λ=0.05 and λ=0.20. As discussed earlier, these profiles were obtained by averaging the simulated 2-D saturation profile in the vertical direction and plotting them against the ratio of the distance over time. The shock fronts are more dispersive and the fluctuations of characteristic velocity are larger than those for water-wet media with similar heterogeneity. This is due to wettability heterogeneity and more oil-wet characteristics. Saturation-velocity curves at large times fall on top each other, so k_r-formulation is adequate for small standard deviation and finite correlation length cases. For the fractal field as shown in Figure 5(c), the saturation-velocity curves do no follow together, so k_r-formulation is inadequate for this case.

Figures 6(a)-(c) shows saturation profiles for mixed-wet systems at σ_{logk} = 0.8 with different λ. The saturation-velocity profiles are similar to those for water-wet system, except that the fluctuations are larger. For λ=0.05 and 0.20, the average characteristic velocity is a function of saturation alone, thus k_r-formulation is adequate at large σ_{logk}. For the fractal field, the saturation

velocity profile does not fluctuate around an average. The average characteristic velocity is not a function of saturation alone, thus k_r-formulation is not adequate at for fractal fields at large σ_{logk}.

Figure 7 illustrates the effective relative permeabilities at σ_{logk}=0.2. The effective relative permeabilities at small permeability deviation with λ=0.05 and λ=0.2 are almost identical, while the effective relative permeabilities for the fBm fractal field are a little lower than those for small correlation ones. Since the relative permeability depends on initial water saturation, the intrinsic relative permeability chosen was based on the initial average saturation of the whole medium. All the effective relative permeabilities at this small permeability heterogeneity are comparable to intrinsic relative permeability. As permeability variance increases, the deviation between effective relative permeability and intrinsic relative permeability increases as shown in Figure 8, especially for water relative permeability. All effective relative permeabilities to water at large σ_{logk} are higher than the intrinsic one.

Figure 9 shows the saturation-velocity profiles for oil-wet systems at σ_{logk}=0.8. The saturation-velocity profiles for oil-wet systems at σ_{logk}=0.2 are very similar to those of the mixed-wet systems. The fluctuations of saturation-velocity at large σ_{logk} and finite λ are much larger than those for mixed-wet and water-wet systems. However, the characteristic velocities after break through for the fBm fractal field are more smooth and close to each other at large times compared to those for mixed-wet and water-wet media. This is due to the constant initial water saturation assumed in this oil-wet system. The situation is similar to stratified layer system with constant initial water saturation and the saturation fronts move at the same velocity at each layer. Therefore, the 1D cross-sectionally averaged saturations are more smooth than those of nonuniform initial water saturations. Figure 10 shows the effective relative permeabilities at σ_{logk}=0.2. The effective relative permeabilities at small permeability variance are close to intrinsic relative permeability. However, at large permeability variance, the effective relative permeabilities for various correlation lengths are quite different, as illustrated in Figure 11. Intrinsic oil relative permeability overestimates all the oil effective relative permeabilities while intrinsic water relative permeability underestimates the water effective relative permeabilities at low water saturation. The water effective relative permeability at σ_{logk}=0.8 and λ=0.2 is higher than the other two with distinct λ, while oil effective relative permeability is lower than the other two. The flow in this large permeability variance and large correlation length media has the earliest breakthrough. The effect of correlation length of permeability field on effective relative permeability increases as the medium become more oil-wet.

From the above simulation results, we realize that permeability variance has more significant impacts on the fluctuation of saturations-velocity than correlation length for permeability fields with finite length autocorrelation model. To quantify the effect of the permeability variance on the fluctuation of saturation velocity, the average saturation velocity was first determined based

on the saturation-velocity profiles after breakthrough using a weighted least square method, then the deviation between average saturation velocity and saturation velocity was calculated. Figure 12 shows the relation between the standard deviation of fluctuation of saturation-velocity, $\sigma_{f(Sw)}$ and standard deviation of permeability field, σ_{logk} at λ=0.05. The variance of fluctuations of saturation velocity for both water-wet and oil-wet systems increase almost linearly with the permeability variance. The velocity fluctuation is larger for oil-wet systems than for water-wet systems at the same intensity of heterogeneity. Therefore, the heterogeneity region for which the k_r-formulation is adequate is larger for the water-wet media than for the oil-wet media.

In-situ water saturations provide insights to understand the effect of wettability on multiphase flow in heterogeneous media. Figure 13 compares the in-situ water saturations at σ_{logk}=0.8 and λ=0.2 for water-wet and oil-wet media. The constant initial water saturation is assumed in the oil-wet media. The right hand side of the figure is the flow distributions at different injected pore volumes for the oil-wet medium. As water flows through the oil-wet medium, water first move to high permeability grids as illustrated in the figure at 0.05 PV, 0.1 PV and 0.2 PV. Capillary pressure in the oil-wet medium resists the water to flow through low permeability grids. Water can move through the low permeability grids only when the viscous force overcomes the capillary force. Even at 1.0 PV, a lot of low permeability regions are still bypassed. The capillary pressure term in the oil-wet medium tends to destabilize front movement. In water-wet media, capillary pressure helps imbibe water into low permeability grids while viscous pressure drop tends to move water into high permeability grids. As shown on the left hand side of the figure at 0.05 PV, 0.1 PV and 0.2 PV, the saturation fronts in the water-wet medium are more uniform than those of oil-wet case. The medium is almost completely swept at 1.0 PV. The capillary pressure term in the water-wet medium will help to stabilize front movement.

Conclusions

This study has looked at upscaling of relative permeability from the laboratory scale (several centimeters) to fine grid field scale (several meters). The effect of various wettability, permeability variation and correlation length scale are studied. Only the flow in the horizontal direction is considered. Gravitational effects and three-dimensional flow are neglected.

- For strongly water-wet media, capillarity has a stabilizing/homogenizing effect on multiphase flow. As the oil wettability increases, the capillary stabilizing effect decreases and the deviation from this average flow increases.
- For small variance in permeability, and for small correlation length, effective relative permeability can be described by intrinsic relative permeability models. At higher variance and moderate correlation length, the average flow can be described by a dynamic relative permeability. The deviation from this average increases with increasing oil wettability.

• For fractal fields with large variance in permeability, effective relative permeability is not adequate in describing the flow.

ACKNOWLEDGEMENTS

This work was partially funded by the Energy Lab, ARCO, Chevron and Mobil.

REFERENCES CITED

Barker, J. W. & Thibeau, S.: "A Critical Review of the Use of Pseudo Relative Permeabilities for Upscaling," SPE 35491, presented at the European 3D Reservoir Modelling Conf., Stavanger, Norway, April 16-17, 1996.

Beier, R. A. and Hardy, H. H.: "Comparison of 2D and 3D Fractal Distribution in Reservoir Simulation," SPE 25236, SPE 12th Symposium on Reservoir Simulation, New Orleans, LA, Feb. 28-March 3, 1993.

Bhogeswara, R. and Killough, J. E.: "Parallel Linear Solvers for Reservoir Simulation: A Generic Approach for Existing and Emerging Computer Architectures," SPE 25240, SPE 12th Symposium on Reservoir Simulation, New Orleans, LA, Feb. 28-March 3, 1993.

Butts, M.B.: "A Stochastic Model for Two-phase Flow in Heterogeneous Porous Media," Prog. Rep. 73, Inst. Hydrodyn. and Hydraulic Eng., Tech. Univ. Denmark, (1991) 31-54.

Chang, Y.C. & Mohanty, K. K.: "Scale-up of Two-Phase Flow in Heterogeneous Porous Media," to be published in J. Petrol. Sci. & Eng. (1997).

Durlofsky, L. J. et al.: "Scale-up of Heterogeneous Three Dimensional Reservoir Descriptions," SPE 30709, ATCE of SPE, Dallas, TX, Oct. 22-25, 1995.

Edwards, M. and Christie, M. A.: "Dynamically Adaptive Gudonov Schemes with Renormalization in Reservoir Simulation," SPE 25268, SPE 12th Symposium on Reservoir Simulation, New Orleans, LA, Feb. 28-March 3, 1993.

Gelhar, L. W.: "Stochastic Analysis of Flow in Heterogeneous Media," Fundamentals of Transport Phenomena in Porous Media, J. Bear and M. Y. Corapcioglu (eds.), Martinus Nijhoff Publishers, Boston, 1984, 673-718.

Glimm, J., Lindquist, W. B., Pereira, F. and Zhang, Q.: "A Theory of Macrodispersion for the Scale-Up Problem," Transport in Porous Media, 13, 97-122, 1993.

Hewett, T. and Behrens, R.: "Scaling Laws in Reservoir Simulation and Their Use in a Hybrid Finite Difference / Streamtube Approach to Simulating the Effects of Permeability Heterogeneity," *Reservoir Characterization II*, edited by Lake et al., Academic Press, 1991, 402-441.

Honarpour, M., Koederitz, L. F., and Harvey, H. A.: "Empirical Equations for Estimating Two-Phase Relative Permeability in Consolidated Rock," *J. Petrol. Tech.* (1982) 34, 2905-2908.

Jadhunandan, P. P. & Morrow, N. R.: "Effect of Wettability on Waterflood Recovery for Crude-Oil/Brine/Rock Systems," SPERE, 40-48, 1995.

Johnson, E.F., Bossler, D.P. and Naumann, V.O.: "Calculation of Relative Permeability from Displacement Experiments," Transactions of the AIME, (1959) 216, 370-372.

Journel, A. G.: "Geostatistics for Reservoir Characterization," SPE 20750, 65th ATCE of SPE, New Orleans, LA, Sep. 23-26, 1990.

Killough, J. E.: "Reservoir Simulation with History-Dependent Saturation Function," *SPE J.* (1976) 16, 37-48.

King, P. R.: "The Use of Renormalization for Calculating Effective Permeability," Transport in Porous Media, 4, 37-58, 1989.

King, P.R., Muggeridge, A. H. and W. G. Price.: "Renormalization Calculation of Immiscible Flow," *Transport in Porous Media* (1993) 12, 237-260.

Kossack C. A., Aasen, J. O. and Opdal S.T.: "Scaling up Heterogeneities with Pseudofunctions," SPEFE, 226-232, Sept. 1990.

Lake, L. W.: *Enhanced Oil Recovery*, Prentice Hall (1989).

Land, C. S.: "The Optimum Gas Saturation for Maximum Oil Recovery from Displacement by Water," SPE 2216, 43rd ATCE of SPE, Houston, TX, Sep.29-Oct.2, 1968.

Li, D., Cullick, A.S., Lake, L. W.: "Scale-up of Reservoir Model Relative Permeability With a Global Method," SPERE, 149-157, 1996.

Muggeridge, A. H.: "Generation of Effective Relative Permeabilities from Detailed Simulation of Flow in Heterogeneous Porous Media," *Reservoir Characterization II*, edited by Lake et al., Academic Press, 1991, 197-225.

Quintard, M. and Whitaker, S.: "Two-Phase Flow in Heterogeneous Porous Media I: The Influence of Large Spatial and Temporal Gradients," *Transport in Porous Media* (1990) 5, 341-379.

Smith, E. H.: "The Influence of Small-Scale Heterogeneity on Average Relative Permeability," *Reservoir Characterization II*, edited by Lake et al., Academic Press, 1991, 52-76.

Thiele, M. R., Blunt, M. J., and Orr, F. M.: "A New Technique for Predicting Flow in Heterogeneous Systems Using Streamtubes," SPE/DOE 27834, SPE/DOE 9th Symposium on Improved Oil Recovery, Tulsa, OK April 17-20, 1994.

Warren, J. E. and Price, H. S.: "Flow in Heterogeneous Porous Media," JPT, Sept. 1961, 153-169.

Wolcott, D. S. and Chopra, A. K.: "Incorporating Reservoir Heterogeneity with Geostatistics to Investigate Waterflood Recoveries," SPEFE, March 1993, 26-32.

Worthington, P. F.: "Reservoir Characterization at the Mesoscopic Scale," *Reservoir Characterization II*, edited by Lake et al., Academic Press, 1991, 123-165.

Table 1 Model Parameters

Water-Wet System

Parameter	Value	Equation	Parameter	Value	Equation
k_{ro}^o	1	2	k_{rw}^o	0.16	3
n_o	2	2	n_w	3	3
c	1.5	4	σ	30	5
Γ (Drainage)	1.537	5	Γ (Imbibition)	0.461	5
β (Drainage)	2	5	β (Imbibition)	2.76	5
S_{wr}	0.2	2,3,6,7			

Mixed-Wet System

Parameter	Value	Equation	Parameter	Value	Equation
m	7.5	8	I^*_{w-o}	2	8
a	0.3	9	b	2	9
I^{min}_{w-o}	0.25	10	S^{min}_{or}	0.15	10
ε	0.05	12	P_c^{init}	13 psi	13
S_{wcp}	0.1	13	λ_p	0.5	13
S_{ocm}	0	14	λ_m	0.5	14
S_{wcm}	0.2	14	Γ	3	14

Oil-Wet System

Parameter	Value	Equation	Parameter	Value	Equation
k_{ro}^o	1	2	k_{rw}^o	0.5	3
n_o	4	2	n_w	2	3
σ	30	15	Γ	0.745	15
β	0.7	15	S_{oc}	0	16
S_{wc}	0.2	16			

Table 2 Parameters of relative permeability model for mixed-wet media

	Oil-Wet Grid	Mixed-Wet Grid	Water-Wet Grid
S_{wi}	≤ 0.2	0.2~0.4	≥ 0.4
S_{or}	Eq. 4	Eq. 10	Eq. 4
k_{rw}^0	0.5	Interpolation	0.1
k_{ro}^0	1.0	1.0	1.0
n_w	2.0	Interpolation	4.0
n_o	4.0	Interpolation	2.0

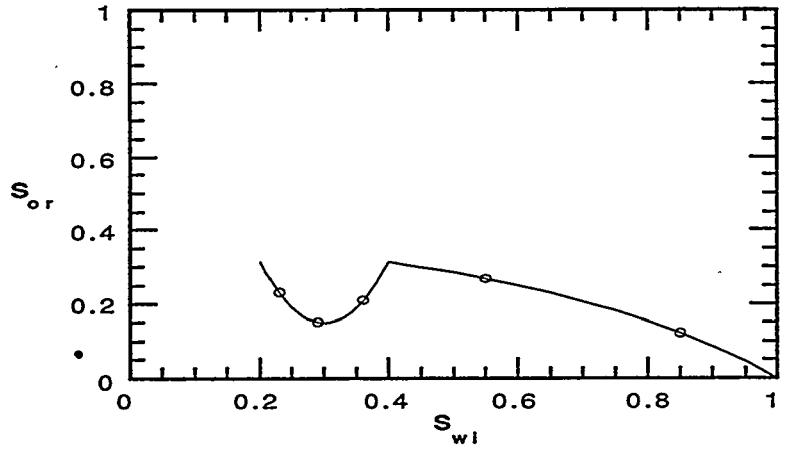

Figure 1 Relation between S_{oi} and S_{or} in mixed-wet system.

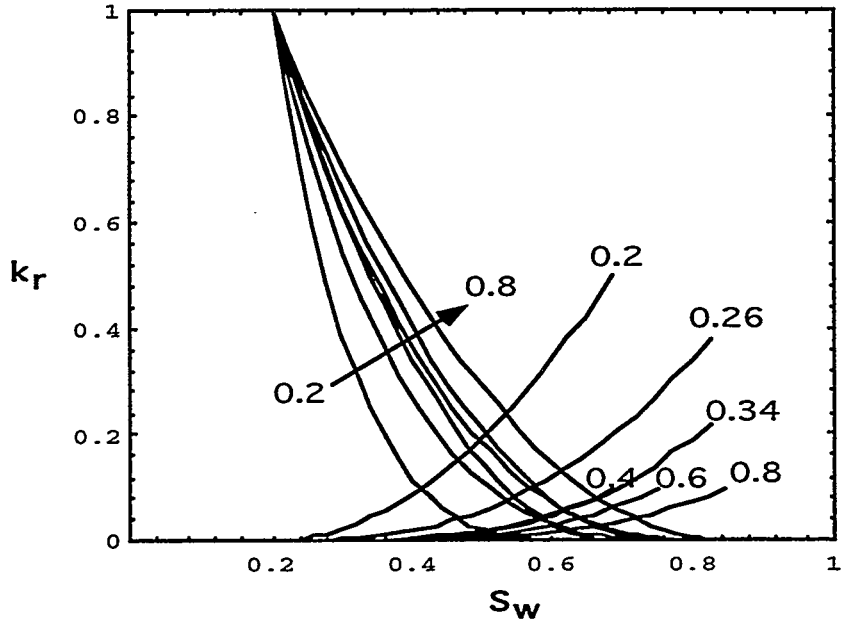

Figure 2 Relative permeability at different initial water saturation in mixed-wet system.

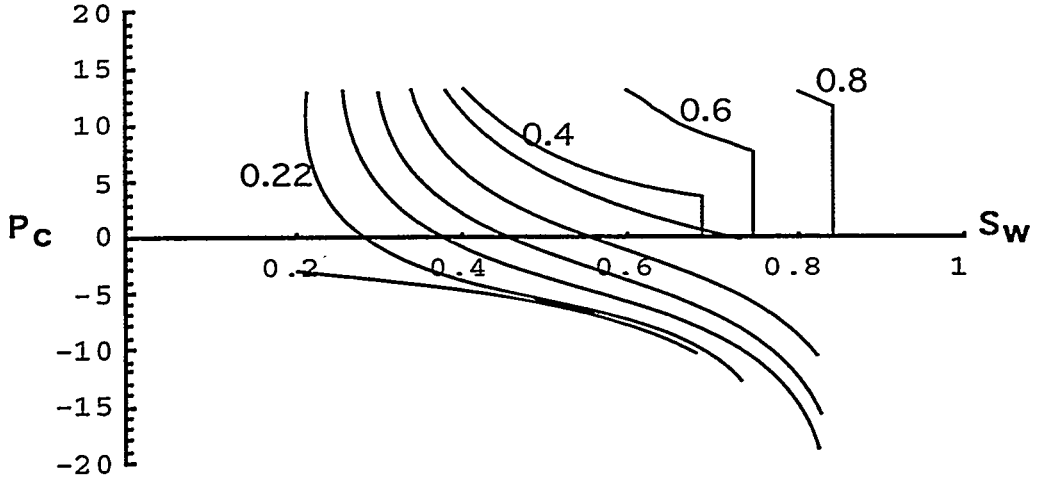

Figure 3 Capillary pressure at different initial water saturation in mixed-wet system.

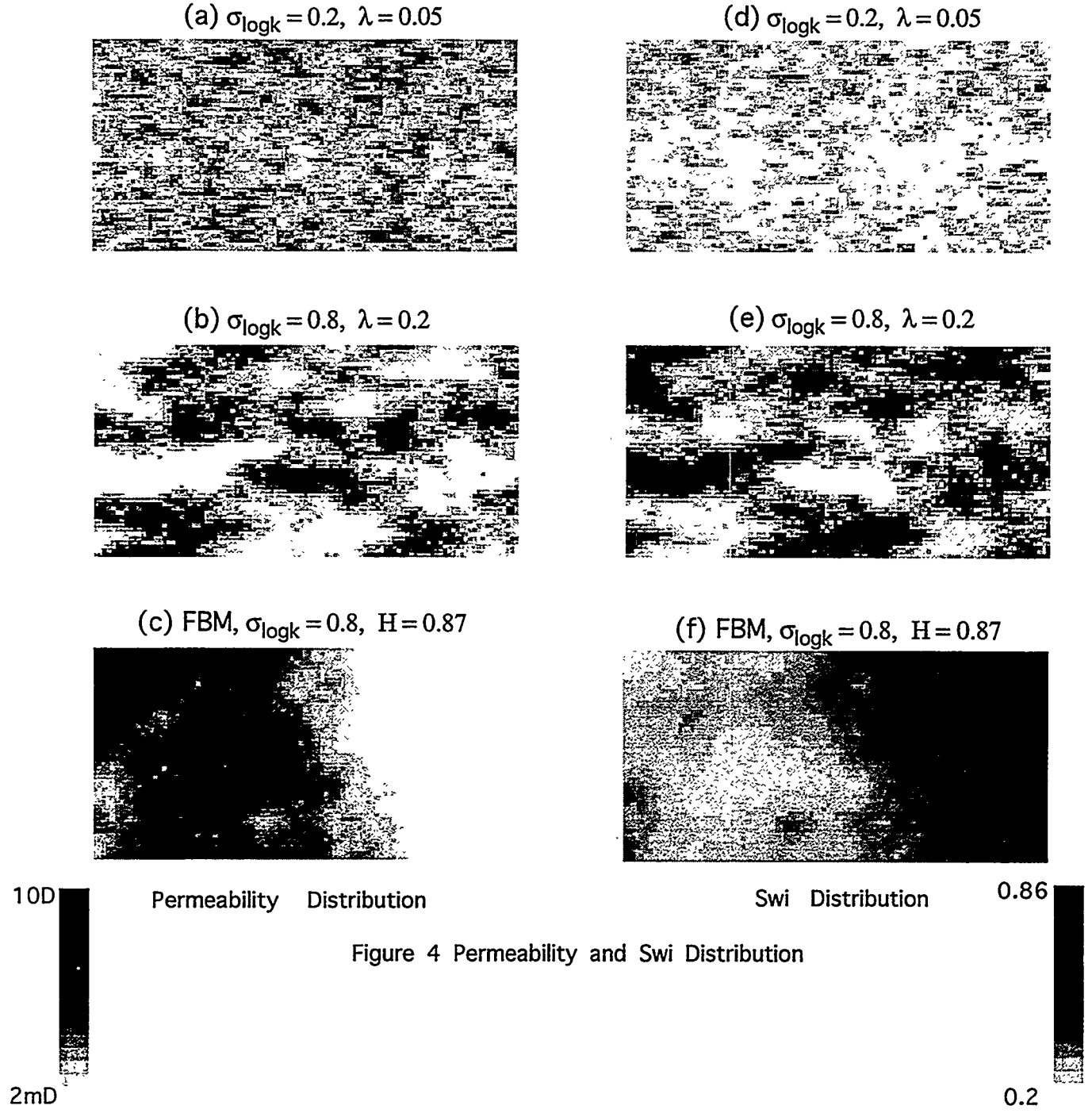

Figure 4 Permeability and Swi Distribution

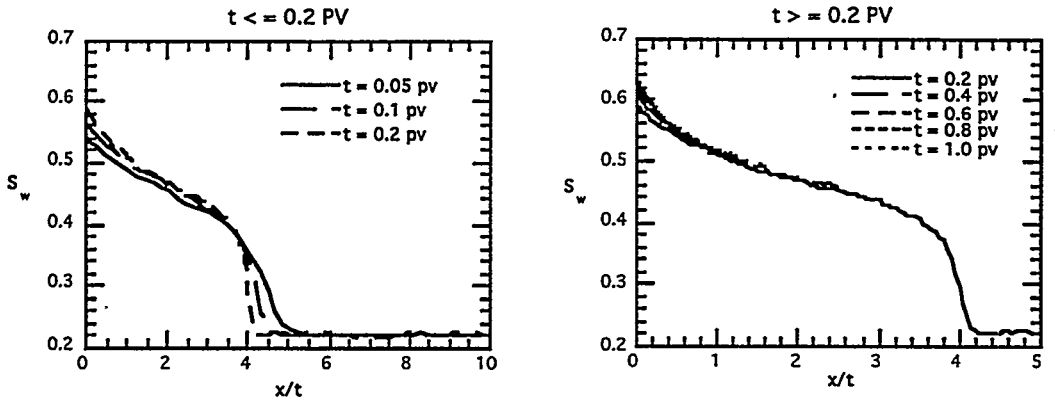

(a) σ_{logk}=0.2 and λ=0.05

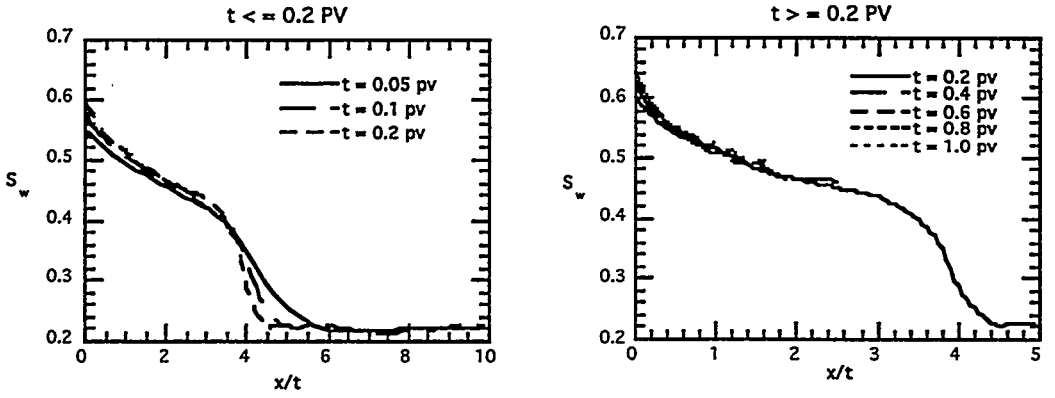

(b) σ_{logk}=0.2 and λ=0.20

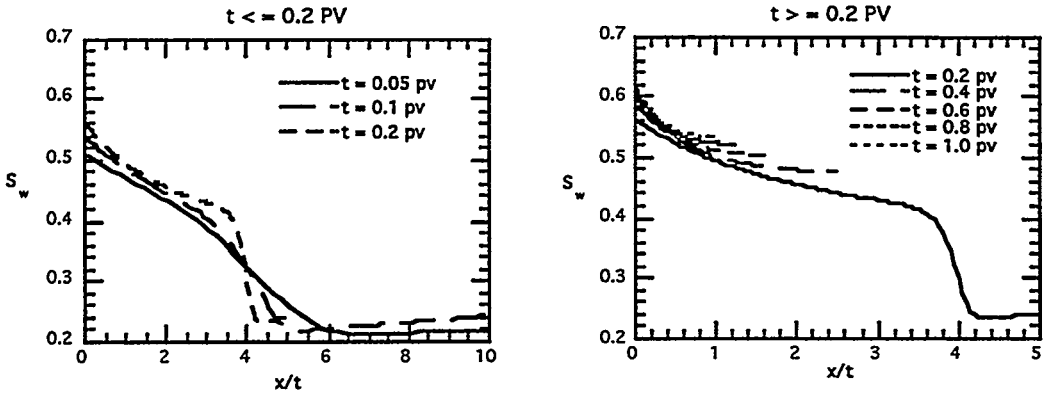

(c) FBM, σ_{logk}=0.2, H=0.87

Figure 5 Saturation-velocity profiles at σ_{logk}=0.2 for mixed-wet system.

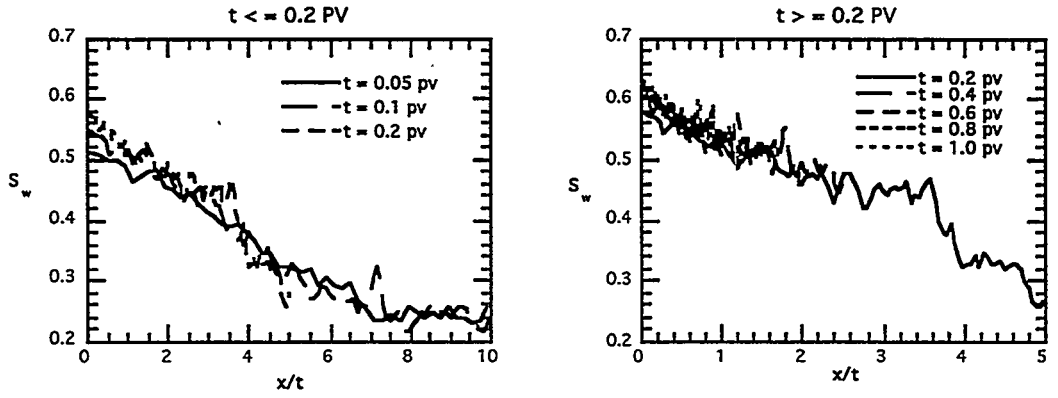

(a) σ_{logk}=0.8 and λ=0.05

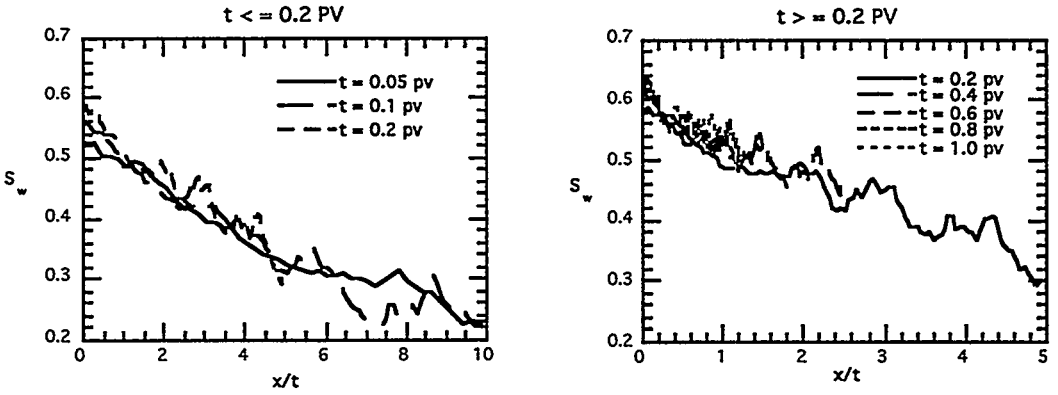

(b) σ_{logk}=0.8 and λ=0.20

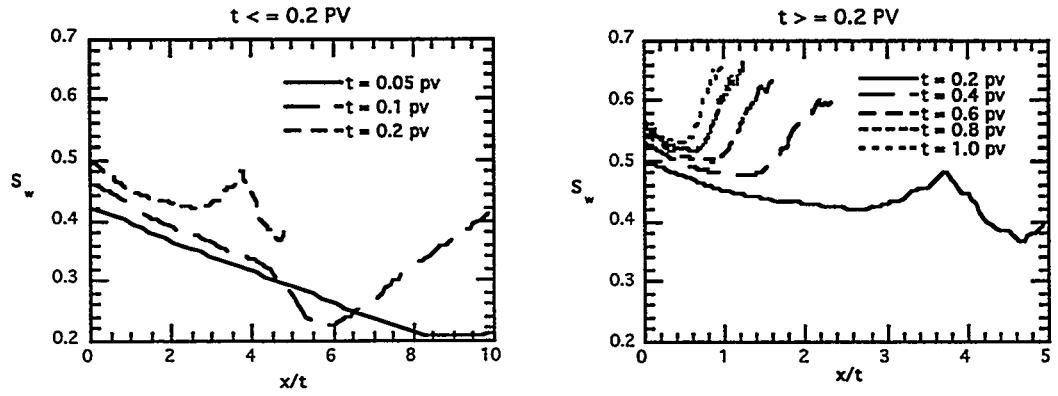

(c) FBM, σ_{logk}=0.8, H=0.87

Figure 6 Saturation-velocity profiles at σ_{logk}=0.8 for mixed-wet system.

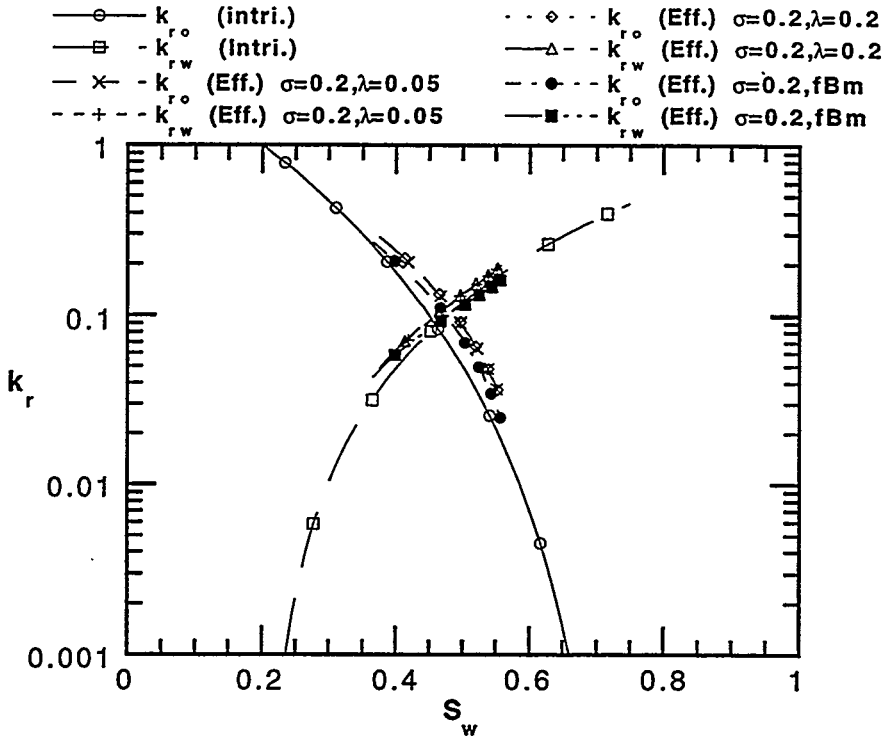

Figure 7 Relative permeability at σ_{logk}=0.2 for mixed-wet system.

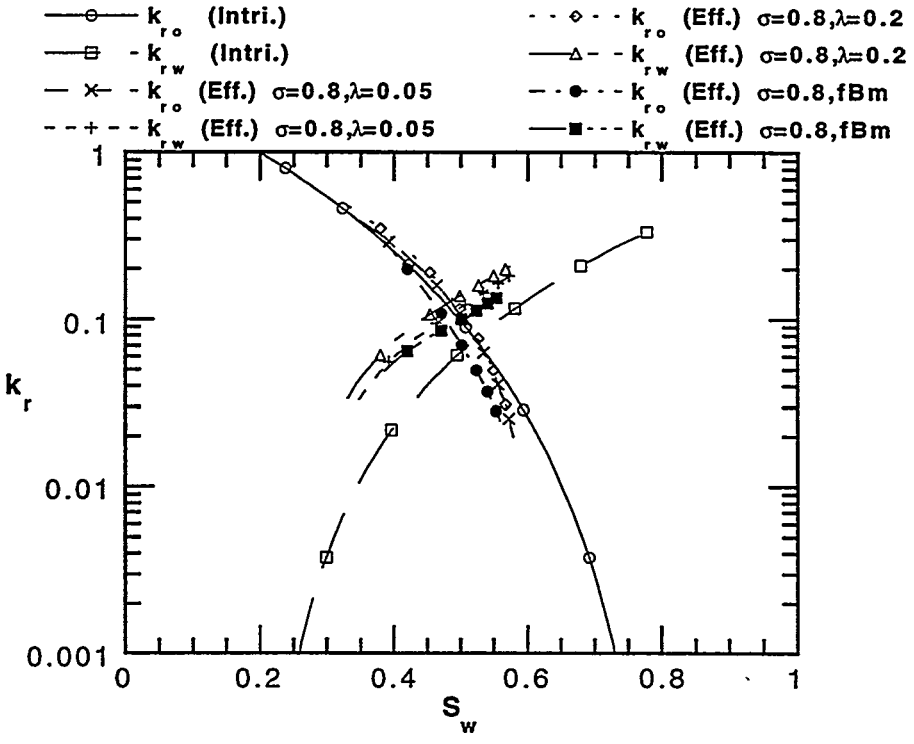

Figure 8 Relative permeability at σ_{logk}=0.8 for mixed-wet system.

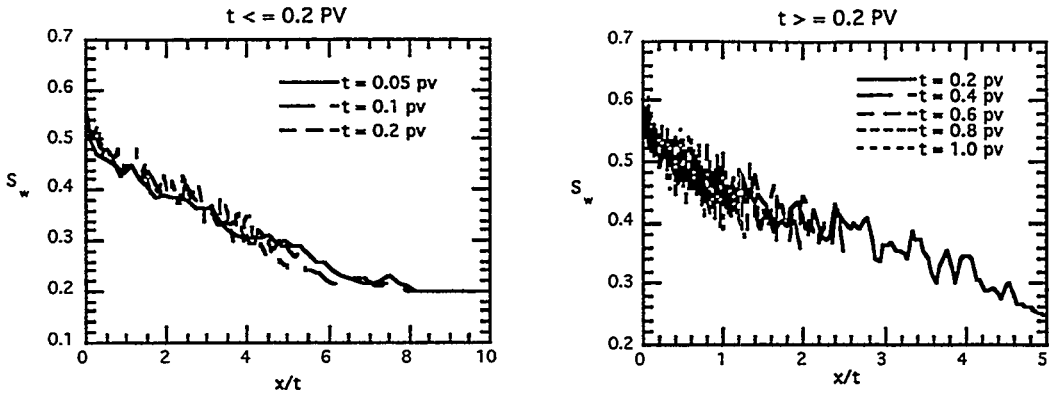

(a) σ_{logk}=0.8 and λ=0.05

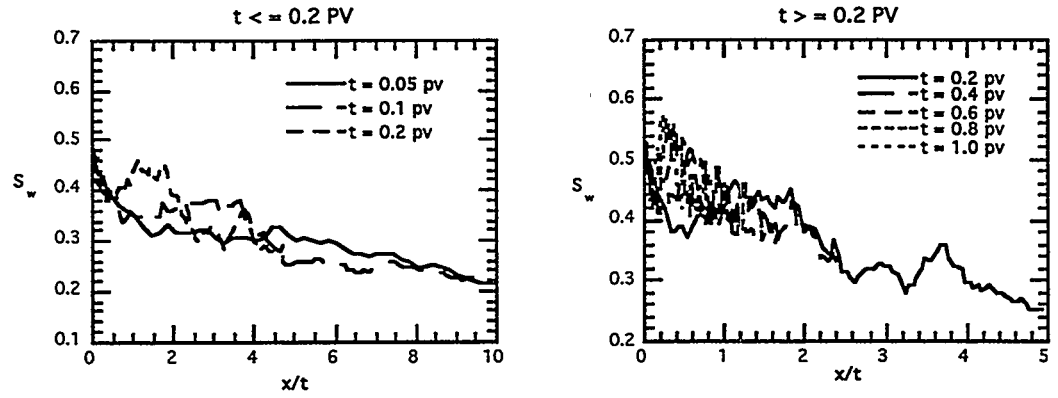

(b) σ_{logk}=0.8 and λ=0.20

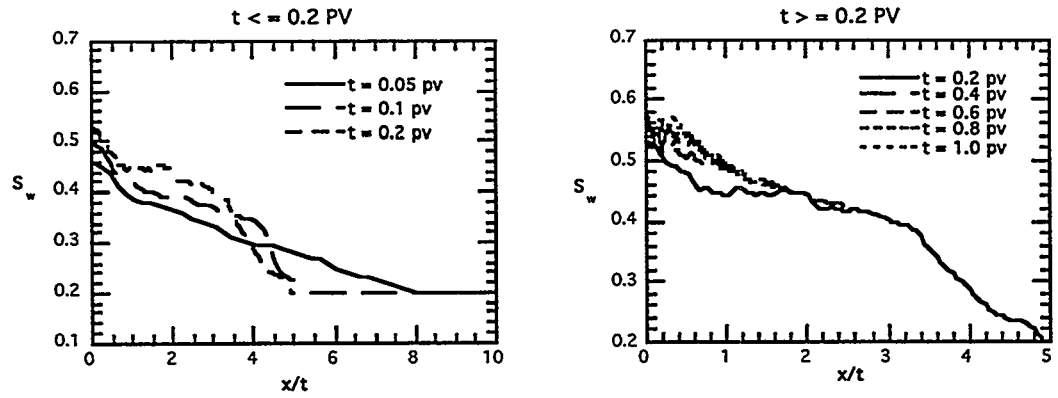

(c) FBM, σ_{logk}=0.8, H=0.87

Figure 9 Saturation-velocity profiles at σ_{logk}=0.8 for oil-wet system.

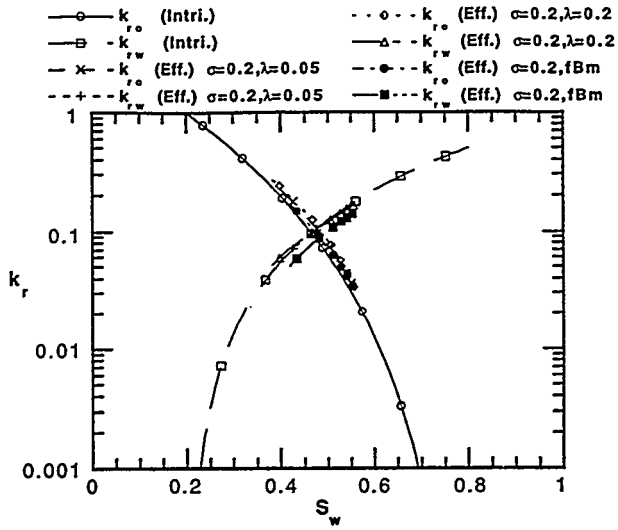

Figure 10 Relative permeability at σ_{logk}=0.2 for oil-wet system.

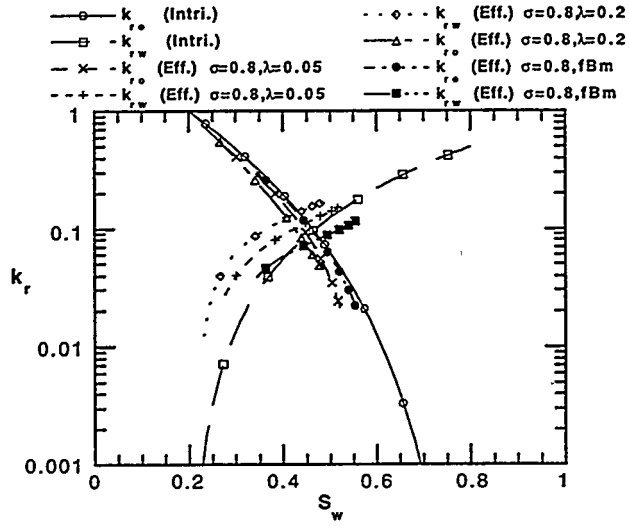

Figure 11 Relative permeability at σ_{logk}=0.8 for oil-wet system.

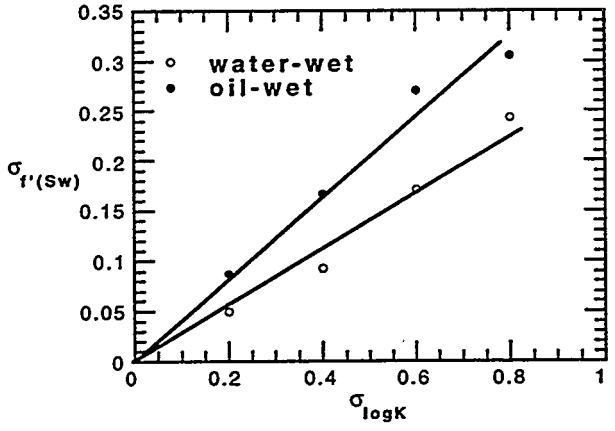

Figure 12 The effect of standard deviation of permeability on the fluctuation of saturaion-velocity for λ=0.05.

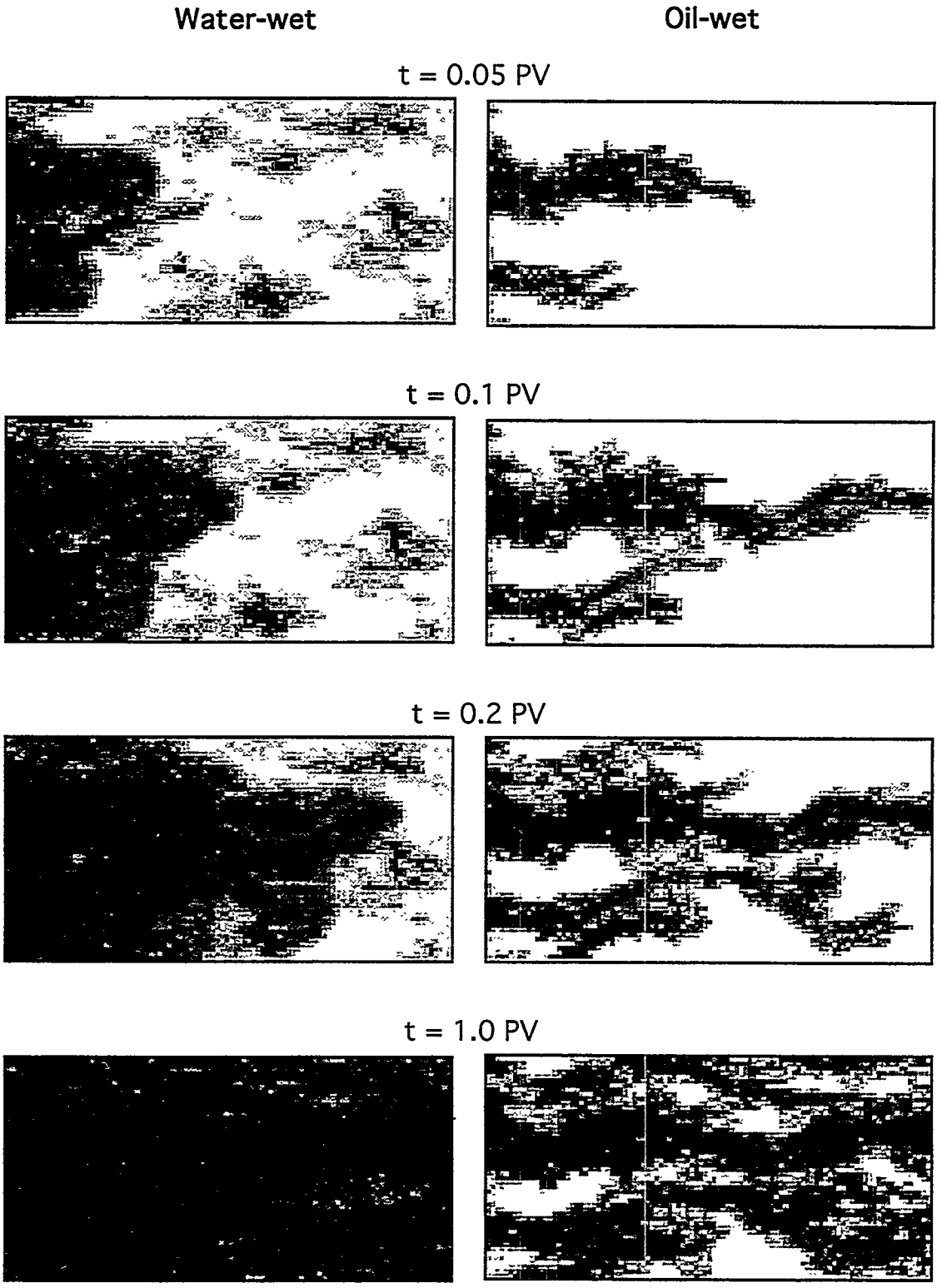

Figure 13 In-situ water saturations for water-wet and oil-wet media at σ_{logk}=0.8, λ=0.2.

Adaptive Upscaling with the Dual Mesh Method

Dominique Guérillot[1]
Sophie Verdière[1,2]

1: Institut Français du Pétrole
2: Université de Pau et des Pays de l'Adour

ABSTRACT

The objective of this paper is to demonstrate that upscaling should be calculated during the flow simulation instead of trying to enhance the a priori upscaling methods. Hence, counter-examples are given to motivate our approach, the so-called Dual Mesh Method. The main steps of this numerical algorithm are recalled. Applications illustrate the necessity to consider different average relative permeability values depending on the direction in space. Moreover, these values could be different for the same average saturation. This proves that an a priori upscaling cannot be the answer even in homogeneous cases because of the "dynamical heterogeneity" created by the saturation profile. Other examples show the efficiency of the Dual Mesh Method applied to heterogeneous medium and to an actual field case in South America.

I Motivations

Darcy's equations give a simple relation between the speed $\vec{Q}_\varphi$ of a phase φ and the pressure gradient P_φ in this phase. When only one phase is present, this relation is fully determined by the introduction of the absolute permeability tensor $\overline{\overline{k}}$, the viscosity μ, the density ρ of the fluid and the height z, i.e.:

$$\vec{Q} = -\frac{\overline{\overline{k}}}{\mu}\vec{\text{grad}}(P - \rho g z).$$

When several phases are considered, the relative permeability curves $k_{r\varphi}$ allow to consider the same type of equation for each phase:

$$\vec{Q}_\varphi = -\frac{\overline{\overline{k}}}{\mu} k_{r\varphi} \vec{\text{grad}}\left(P_\varphi - \rho_\varphi g z\right).$$

These relative permeability curves are very convenient because they incorporate different phenomena in one single curve depending only on one parameter: the saturation S_φ of the phase φ. The capillary pressure curves are considered also to depend only on the saturation.

The following remarks showt why we propose to calculate the upscaled relative permeability during the flow simulation.

At the laboratory scale, the above equations allow to explain the observations and relative permeability curves can be obtained by different methods ("Pen State", "Hassler", etc... ; see for instance [Marle, 1972]). Relative permeabilities, and capillary pressures, depend obviously on the phase distribution at the pore level. There are several distributions of phases for the same saturation. Hence, several relative permeabilities may correspond to these different cases.

For three-phase sytems, (see for instance [Kalaydjian, 1993]) current research is focused on the impact of the phase distribution on the relative permeability and capillary values.

In reservoir simulations, the flow behaviour is also modelized by this concept of relative permeability equations and the reservoir is described by a set of cells.

usually, the main question is: *"what curve should be used at the scale of one cell to reproduce properly the behaviour of the flow in the reservoir ?"*.

One approach is to find out situations where assumptions can be made to consider that an average saturation is sufficient. This is the case for instance when in the reservoir the saturation profile along the vertical is nearly always the same, i.e. when there is an equilibrium between gravity and capillary forces. "Vertical Equilibrium" pseudos can be calculated by the method of [Coats et al, 1971].
However in many reservoirs, the saturation distribution depends on the production history, i.e. on the location of the wells and their perforations, their flow rates and pressures (boundary conditions). Hence the relative permeabilities and capillary pressures will depend on this history. This is why "dynamic pseudo relative permeabilities" are currently considered in practice (see the critical review: [Barker & Thibeau, 1996]). The principle is to calculate these curves by running

flow simulations with a detailed description of the porous media and with the relative permeability and the capillary pressure curves obtained at the laboratory scale. The principle is very similar to the one used at the laboratory scale. Instead of measurements, a fluid flow simulator is used to "calculate" the flow rate of the different phases coming out from one or a group of cells submitted to different boundary conditions. Our point of view is that approach may be very heavy in cases when this distribution may vary widely depending on the location in space (distance from the wells for instance) and the boundary conditions.

So unstead on trying to uncouple the saturation distribution calculation and the averaging process, we propose to upscale during the fluid flow simulation.

II Difficulties of the "a priori" methods

The following example illustrate some major difficulties of the "*a priori*" methods or "dynamic relative permeabilities" with two counter-examples for a two phase system $(\varphi = w, o)$.

The total mobility m(s) is defined as:

$$m(s) = \frac{k_{rw}}{\mu_w} + \frac{k_{ro}}{\mu_o}$$

II.1 First Counter-example

With an IMPES scheme (see for instance [Aziz & Setari, 1979]), the average value of the product of absolute permeability by the total mobility ($\overline{\overline{k}m(s)}$) is needed for the pressure equation. With the "*a priori*" approaches, the averages $\overline{\overline{k}}$ and $\overline{m}(\bar{s})$ are calculated separately, where $\bar{s}$ is for instance the average water saturation.
One difficulty is that the following inequality may occur:

$$\overline{\overline{km(s)}} \neq \overline{\overline{k}}\,\overline{m}(\bar{s})$$

For instance, in a 1D example (cf. Figure 1).

$$\begin{cases} k_{rw}(s) = s & (s = s_w) \\ k_{ro}(s) = 1 - s \\ S_{wi} = S_{or} = 0 \end{cases}$$

The aim is to determine $\overline{\overline{k}\,m(s)}$ and $\overline{\overline{k}}\,\overline{m}(\bar{s})$ over the homogeneized cell containing the cells 1 and 2. Cell 1 (resp. cell 2) is supposed to have a saturation equal to $1 - S_{or}$ (resp. S_{wi}) and an absolute permeability k_1 (resp. k_2).

$$\overline{\overline{k\,m(s)}} = \frac{2k_1 m(s_1) k_2 m(s_2)}{k_1 m(s_1) + k_2 m(s_2)} = \frac{2k_1 k_2}{\mu_o k_1 + \mu_w k_2}$$

$$\overline{\overline{k}}\,\overline{m}(\bar{s}) = \frac{2k_1 k_2}{k_1 + k_2} * m\left(\frac{S_{wi} + 1 - S_{or}}{2}\right) = \frac{k_1 k_2}{k_1 + k_2} * \left(\frac{1}{\mu_w} + \frac{1}{\mu_o}\right)$$

These 2 values are often different. So, even if an homogeneous case is considered ($k = k_1 = k_2$), we have, for $\mu_o = 10\,\mu_w$:

$$\overline{\overline{k\,m(s)}} = \frac{2k}{11\mu_w} \neq \frac{11k}{20\mu_w} = \overline{\overline{k}}\,\overline{m}(\bar{s}), \text{ it means } \frac{\overline{\overline{k\,m(s)}}}{\overline{\overline{k}}\,\overline{m}(\bar{s})} \cong \frac{1}{3}$$

The difference increases with the contrast of permeability between the two cells.

II.2 Second Counter-example in 2D (xy)

Let us now consider a 2 D example (cf. Figure 9). An homogeneous absolute permeability is also supposed. Even if the average saturation of the cells (1,5) and (5,1) are the same, these one should not have the same directional total mobilities to the extent that the directions of the flow of each cell are completly different and influence the calculation of the pseudo function.

II.3 Solutions

Considering more parameters to caracterise the flow behaviour. For instance, one way of thinking is to consider the distribution of the saturation in the cell.

One can consider other equations to modelize the flow, with the MHD method for instance [Lenormand, 1996].

It is also possible to keep a level of detail in the saturation such that the permeability and the capillary curves are valid and to transfer the problem of upscaling on the numerical scheme side.

It is the latest option that has been considered. In fact, even if the other options may give good answers, they will be very difficult to implement on a practical way.

III Dual Mesh Method

III.1 General Remarks

The Dual Mesh Method, early proposed by the authors (cf. [Guérillot and Verdière, 1995]) allows to adapt in time and space the discretization for each unknown. So, for a typical two phase problem, the saturation equation will be solved over the geological mesh, and the pressure equation over a lower resolution grid, like in a classical simulator (which correponds to the upscaled flow model).

This method enables to make "adaptive upscaling". Indeed, it is possible to upscale the parameters necessary to the pressure equation by taking into account the evolution of the saturation during time. So, there is no more problem due to:

- boundary conditions over each lower resolution grid,
- the opening and closing of a well, during the simulation, which would require new calculation of pseudos functions.

III.2 Description of the Algorithm

Let us briefly summarize the principle of the Dual Mesh Method. For that, 2 different grids are introduced: a Low Resolution Grid (called LR Grid) and a High Resolution Grid (called HR Grid). A time step is associated to each grid [Verdière et al, 1996]. We consider the update of the unknowns (pressure and saturation) for a LR time step:

Step 1 - Calculation of the LR time step,

Step 2 - Calculation of the parameters necessary to solve the pressure equation by using an adaptive homogeneization from the HR to the LR grid,

Step 3 - Calculation of the pressure over the LR Grid, with the LR time step,

Step 4 - Reconstruction of the flow-rate over the HR grid at each HR time step by using the pressure over the LR grid,

Step 5 - Resolution of the saturation equation over the HR grid for each HR time step.

IV Numerical Results

IV.1 Description of the Test Cases

A quarter of five spot is considered (cf. Figure 4). The HR and a LR grids are different according to the simulations. For each test-case, the HR grid is considered as the reference.
In order to avoid differences between numerical results due to Productivity Indices (PI) problems, boundary conditions have been considered rather than well conditions (cf. Figure 3).

Three different types of permeability maps are generated:

- the first case is an homogeneous case with K=100 mD (over a 90x90 grid);
- the second case (called **heter. case 1**) is an heterogeneous porous medium with a lognormal distribution (see Figure 4). With these choices, an algebric estimator [Guérillot, 1988] is used to estimate averaged permeability maps over lower resolution grids (10x10, 30x30 and 90x90);
- the third case (called **heter. case 2**) comes from a field case study in South America. The reservoir (Albian/Cenomanian) deposited in an overall trangressive context, produces from turbidite sandstones and is composed of massive sandstones, classical Bouma turbidites, marls and shales. The lithofacies map (cf. Figure 5) was generated in a sequential statigraphic context. It corresponds to an horizontal cross section. The lithofacies 1, 2, 3, 4 are respectively very porous sandstone (1), sandstone (2), thin bedded turbidite sandstone (3) and carbonate rock (4). For each lithofacies, the permeability are measured on plugs (k_1=2779 mD, k_2=177 mD, k_3=14 mD, k_4 =1 mD).

The relative permeabilities used are of the Corey type [Brooks & Corey,1966] as follows:

$$k_{rw}(S) = k_{wm} S^{*n_w} \text{ and } k_{ro}(S) = k_{om}\left(1 - S^*\right)^{n_o}$$

$$\text{with } S^* = \frac{S - S_{wi}}{1 - S_{wi} - S_{or}}$$

The fractional flow is noted f_w .

The tests are built with three mobility cases:

- a linear case (cf. Figure 6);
- an unfavourable case; the mobility ratio is equal to 2 (cf. Figure 7);
- a favourable case; the mobility ratio is equal to 0.16 (cf. Figure 8).

IV.2 Importance of Saturation Profile for the Upscaling

An homogeneous case with the favourable mobility ratio is simulated (M=0.16, see Figure 8). The LR grid is 10x10 and the HR grid is 90x90 (cf. Figure 9)

For each time step, and for each lower cell, the algebric method of upscaling allows to calculate the product of the absolute permeability and the total mobility, for each direction of the flow, called kmx and kmy. This product corresponds to the coefficients of the pressure equation (see II).

By considering in particular the cells (1,5), (2,2) and (9,9) (Figure 9), kmx and kmy are plotted, function of the average saturation calculated with the average saturation obtained over the HR Grid. The "fine km" of the Figure 9 corresponds to the analytical function of km with the Corey's law, supposed to be over the HR Grid.

The different saturation profiles for each cell give different averaged total mobility.

The cells (2,2) and (9,9) give similarly the same pseudo function to the extent that boundary conditions are the same. Besides, kmx=kmy because of the symmetry of the problem.

On the other hand, we find different curves for kmx and kmy in the cell (1,5). If we consider a 1D problem along the west boundary, kmy should be equal to a harmonic mean of km over the HR Grid. This result is approximately found for kmy of the cell 1,5, which is close to a 1D flow.

So, we can say that the Dual Mesh Method allows really to make adaptive upscaling. The real boundary conditions, and also the real saturation profile over the geological model are used to dynamically upscale the needed coefficients for the pressure equation

IV.3 Quality of the Results and Efficiency of the Dual Mesh Method

The heteregeneous case 1 (Figure 4) with the unfavourable mobility ratio (M=2, see Figure 7) is simulated. Three different grids are considered: 10x10, 30x30 and 90x90.

The comparison of watercut (Figure 15) for each simulation reveals that the result obtained with a fully HR grid simulation are similar to the one obtained with the Dual Mesh Method with a resolution of the pressure equation over the 10x10 grid and a resolution of the saturation equation over the finer grid (30x30 or 90x90 according to the case).

The Table 1 shows the Cpu-Time of the different simulations. Computing cost using DMMs is of the same order as the LR method, even if it is more important (about three times), while the HR grid method requires a very long simulation.

IV.4 Field Case Study

The heteregeneous case 2 (Figure 5) in constant total mobility (M=1, see Figure 6) is simulated. Two different grids are considered: 16x16 and 256x256.

The different saturation maps (Figures 11 to 14) show qualitatively the capability of the Dual Mesh Method to integrate the fine (256x256) grid petrophysical information, eventhough the pressure equation is solved over a LR grid (16x16). More details of this field will be described elsewhere.

V Conclusion

This paper demonstrates it is possible to upscale the relative permeability curves during the flow simulation for a two phase flow problem.

The efficiency of the Dual Mesh Method is proven for an oil field case produced by water injection. It is straightforward to add gravity and capillary forces for this two phase problem. Current resarch focus on the ability to consider phase exchanges, to apply this approach to basin modeling and to integrate the capacity of parallel computers.

Acknowledgements

The authors thank the "Institut Français du Pétrole" for permission to publish this work.

They also thank Eric Delamaide, Patrick Lemonnier for their useful comments.

Références

Aziz, K., Setari, A.: "Petroleum Reservoir Simulation", Applied Science Publisher LTD, 1979

Barker, J., Thibeau, S., "A Critical Review of the Use of Pseudo Relative Permeabilities for Upscaling", European 3-D Reservoir Modelling Conference, Stavanger, April 16-17 1996

Brooks, R.H., Corey, A.T., "Properties of Porous Media Affecting Fluid Flow", Journal of the Irrigation and Drainage Division, Proceedings of ASCE (1966), Vol. 92, NO IR2

Coat, K.H., Dempsey, J.R., Henderson, J.H.: "the Use of Vertical Equilibrum in Two-Dimensional Simulation of Three -Dimensional Reservoir Performance", SPEJ, March 1971, pp. 63-71

Guérillot, D., Rudkiewicz, J.L., Ravenne, C., Renard G., : "An Integrated Model for Computer Aided Reservoir Description from Outcrop Study to Fluid Flow Simulation", 5th European Symposium on Improved Oil Recovery, Budapest, April 25-27 1989, Rev IFP, Vol 45-1, 71-77

Guérillot, D., Verdière, S.: "Different Pressure Grids for Reservoir Simulation in Heterogeneous Porous Media", Proceedings of 13th SPE Symposium on Reservoir Simulation, SPE 29148, San Antonio, Fév. 1995

Kalaydjian, F., Moulu, J.-C., Vizika, O., Munkerund, P.K., "Three-Phase Flow in Water-Wet Porous Media: Determination of Gas/Oil Relative Permeabilities Under Various Spreading Conditions", SPE 26671, presented at the 68th Annual Technical Conference and Exhibition of the SPE, Houston, Texas, 3-6 Oct. 1993, to appear in the Journal Science and Engineering 554 (1996)

Marle, C.-M., "Les écoulements polyphasiques en milieux poreux", Editions Technip, 1972

Ramé, M., Killough, J., "A New Approach to the Simulation of Flows in Highly Heterogeneous Porous Media", 11th SPE Symposium on Reservoir Simulation, Anaheim, February, 1991

Verdière, S., Guérillot, D.,Thomas, J.M. : "Dual Mesh Methods in Heterogeneous Porous Media", "Proceedings of the 5th European Conference on the Mathematics of Oil Recovery", Leoben, Sept 1996

Figure Captions

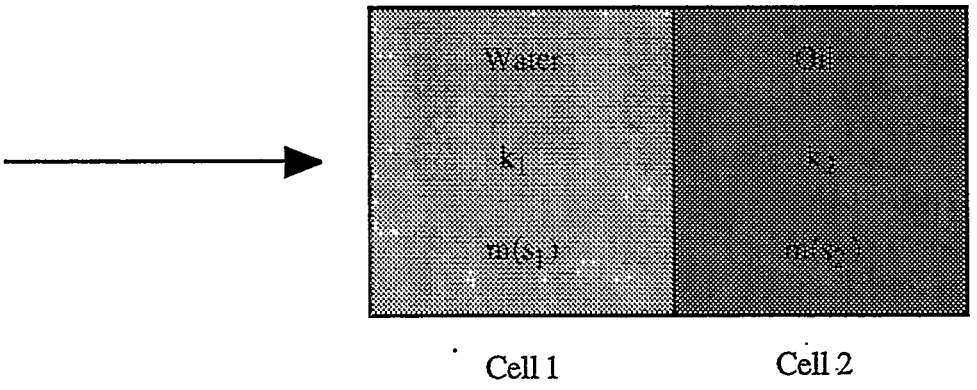

Figure 1: 1D Counter-Example

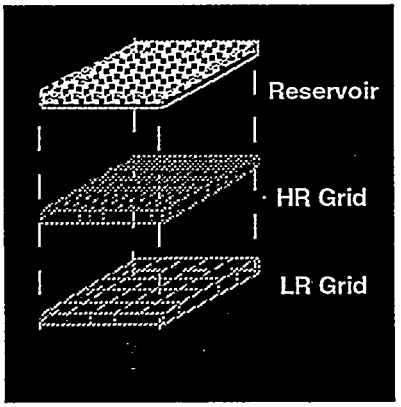

Figure 2: Dual Mesh Representation

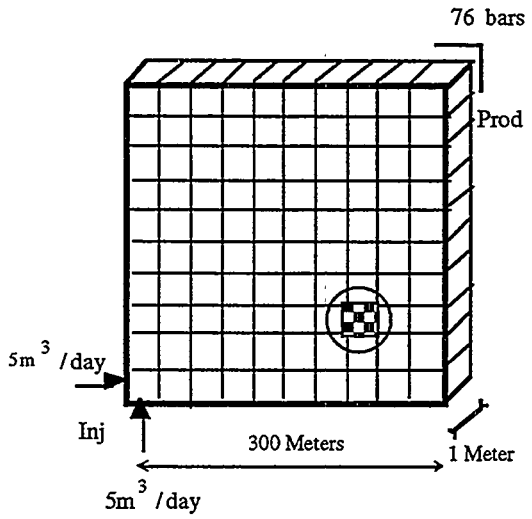

Figure 3: Geometrical Characteristics of the Test-Cases

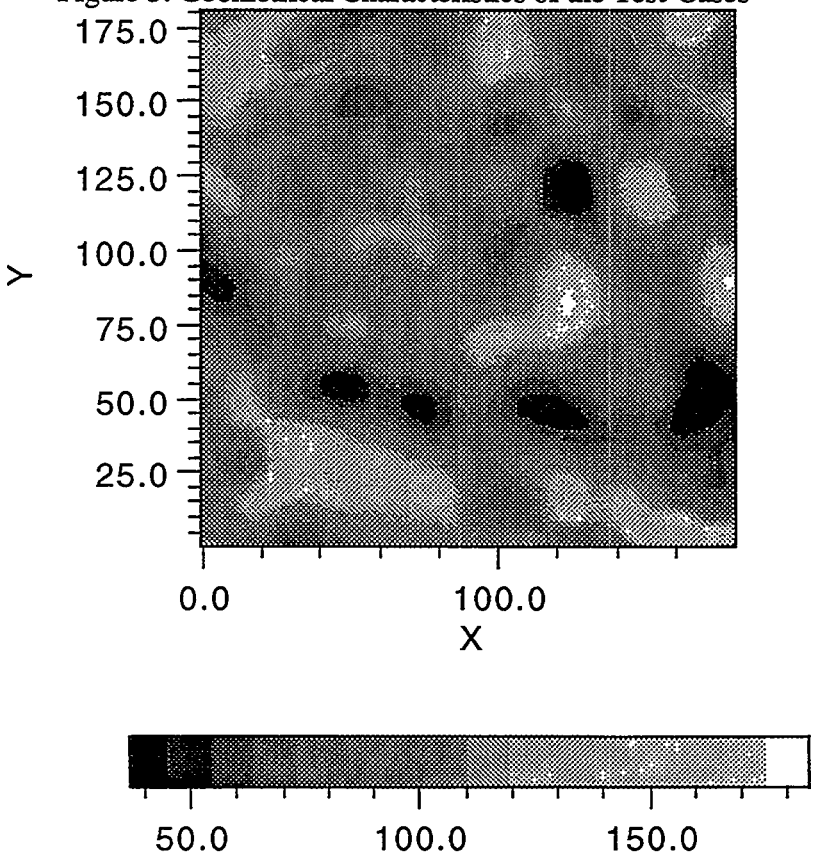

Figure 4: Permeability Map - Heter. Case 1

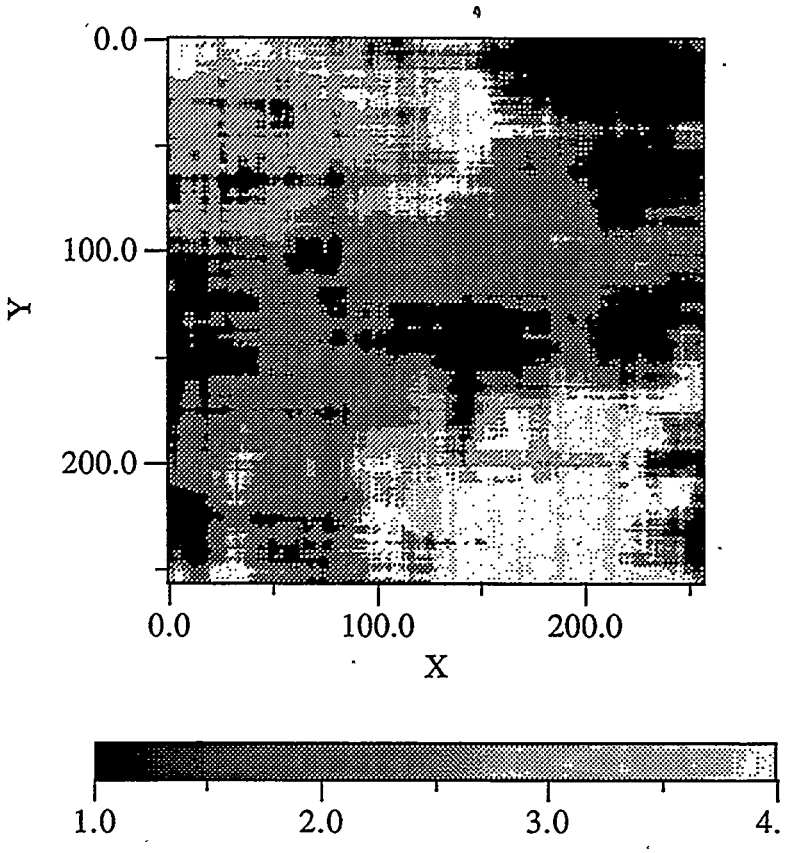

Figure 5: Lithofacies Map - Heter. Case 2

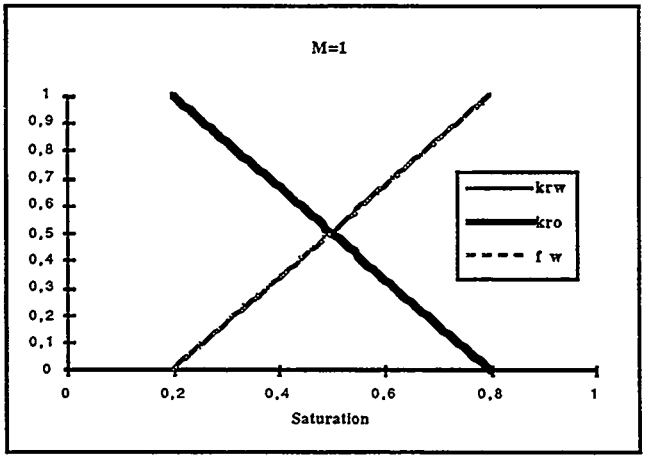

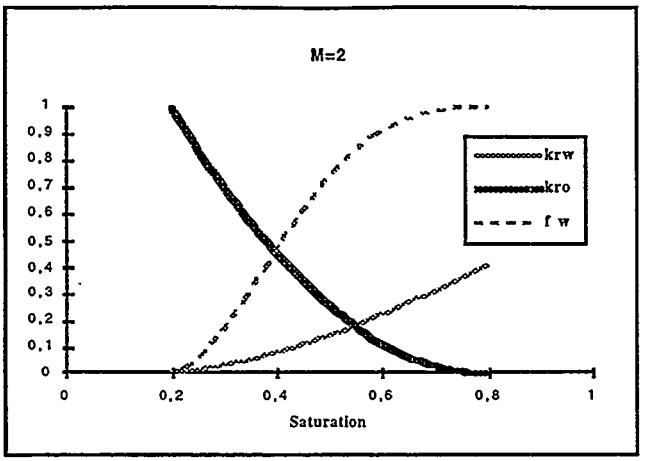

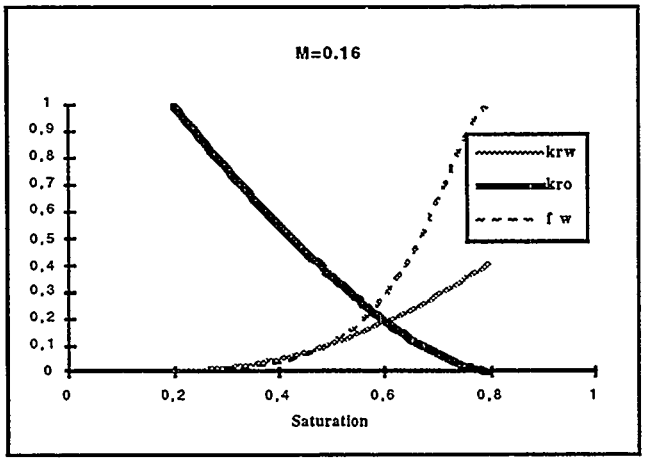

Figures 6, 7 and 8: Fluid Properties for the Different Mobility Ratios

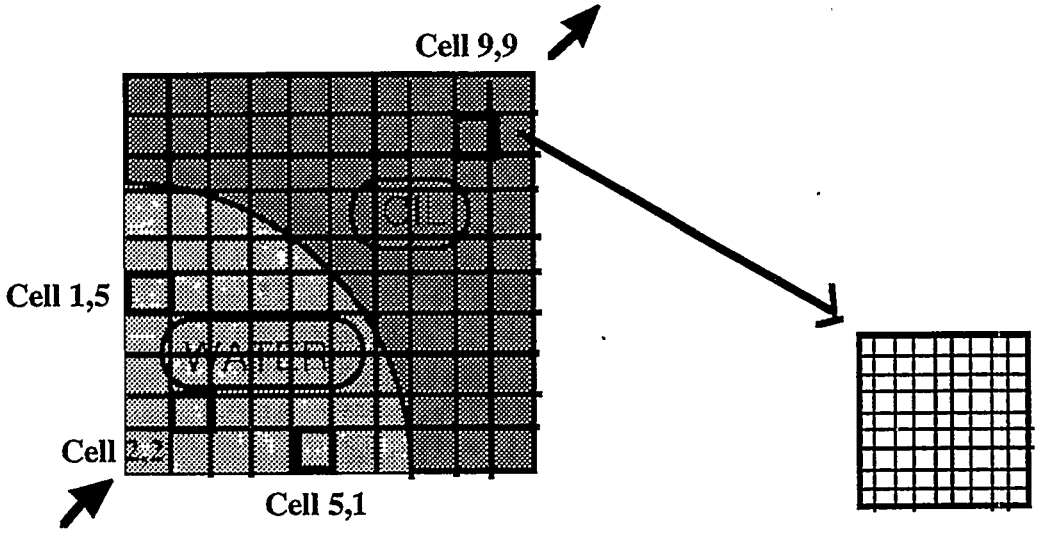

Figure 9: 2D Counter-Example

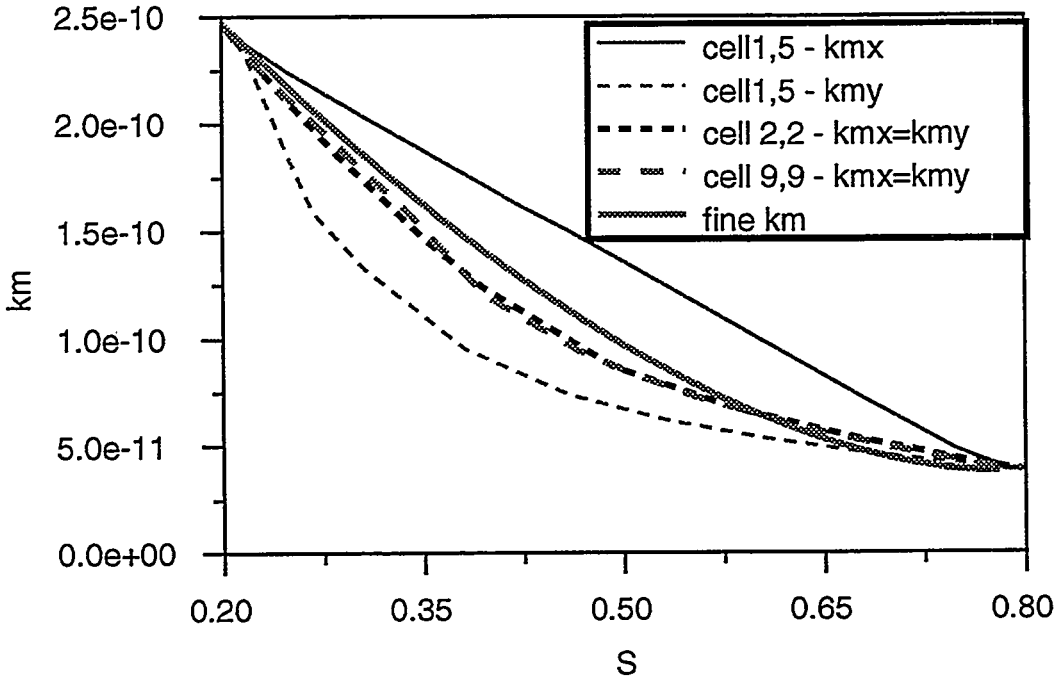

Figure 10: Comparison of Averaged Total Mobilities

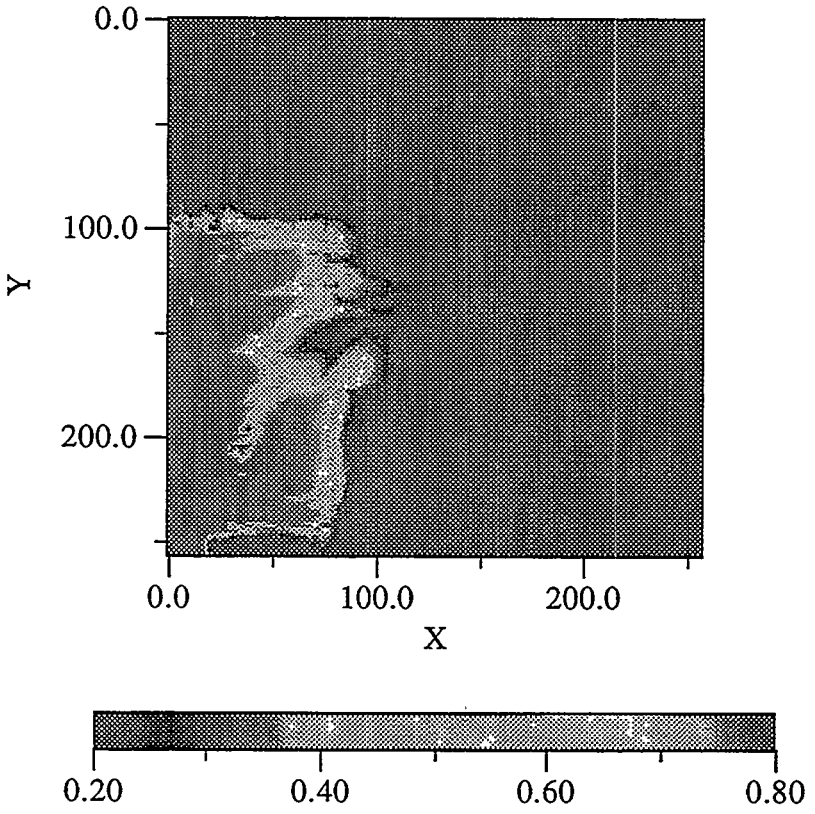

Figure 11: Saturation Map - Heter. Case 2 - M=1 - Time = 200 days

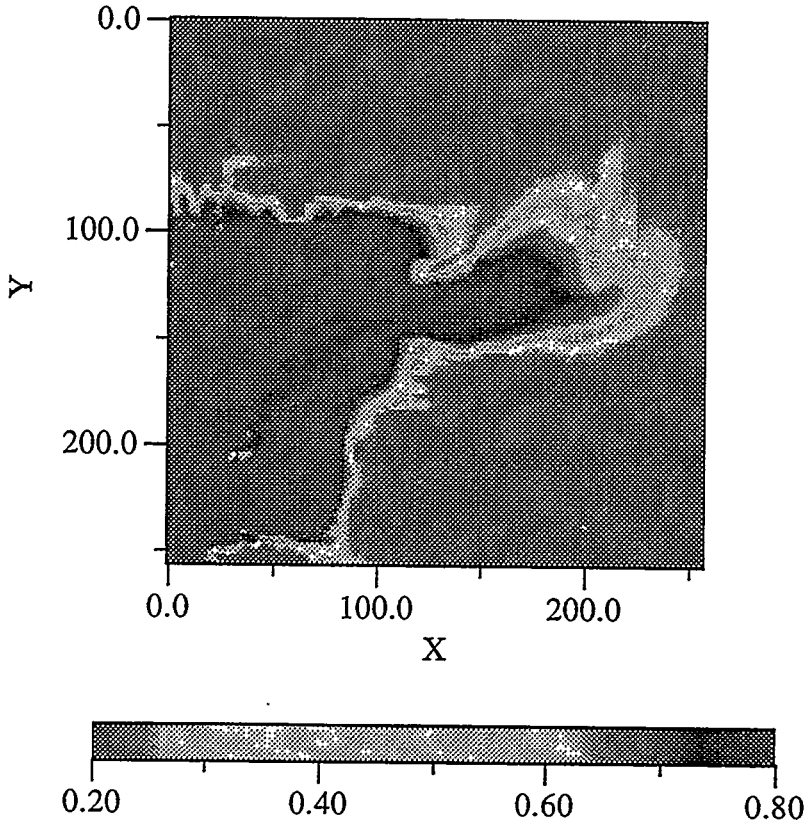

Figure 12: Saturation Maps - Heter. Case 2 - M=1 - Time = 400 Days

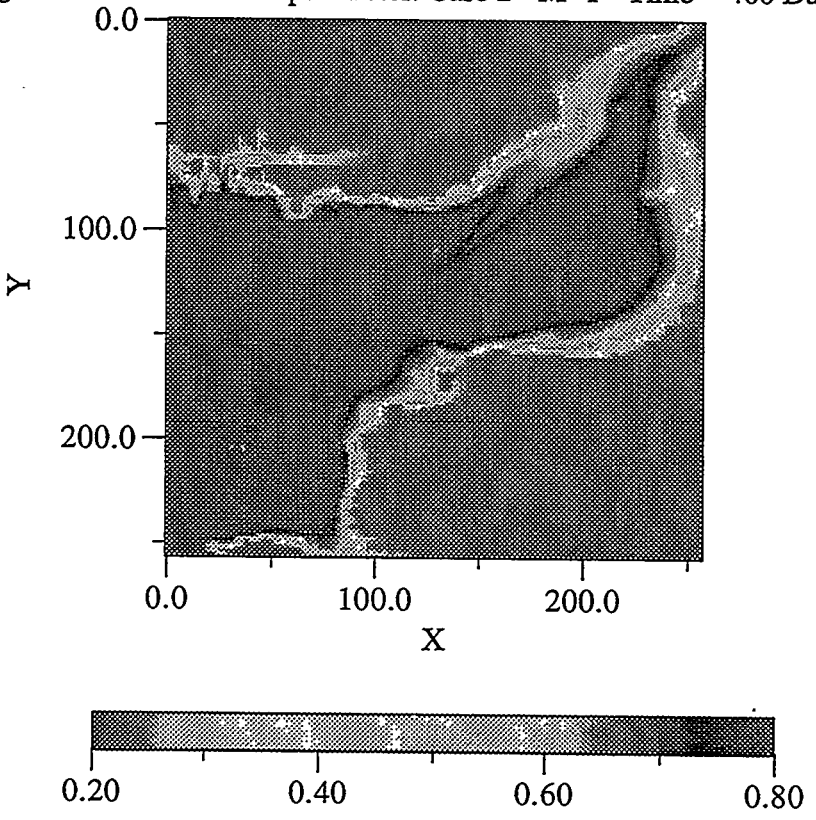

Figure 13: Saturation Map - Heter. Case 2 - M=1 - Time = 600 Days

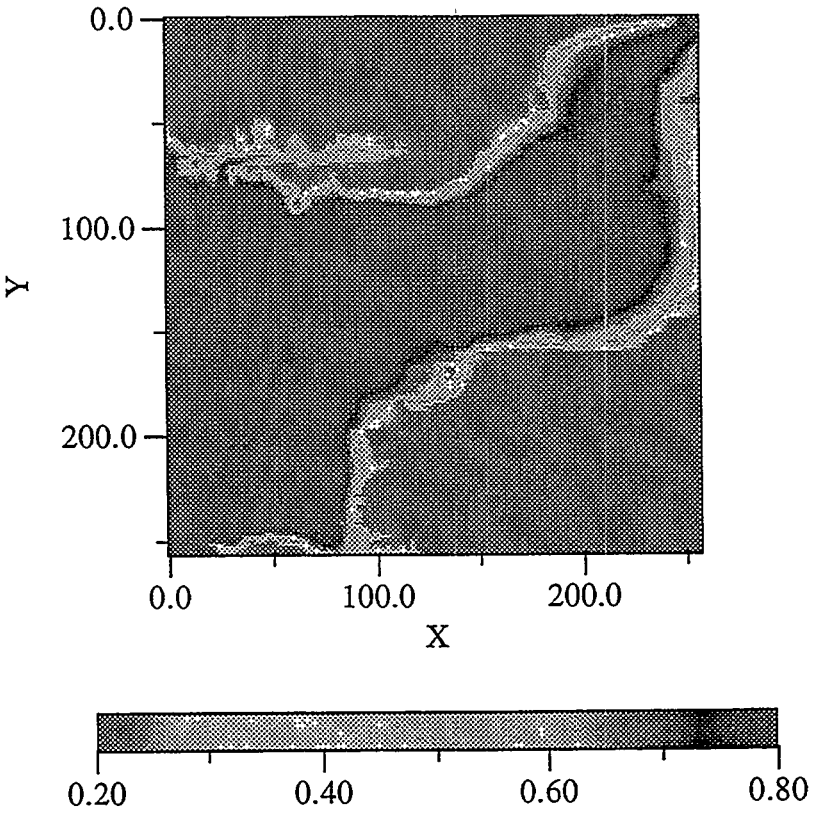

Figure 14: Saturation Map - Heter. Case 2 - M=1 - Time = 800 Days

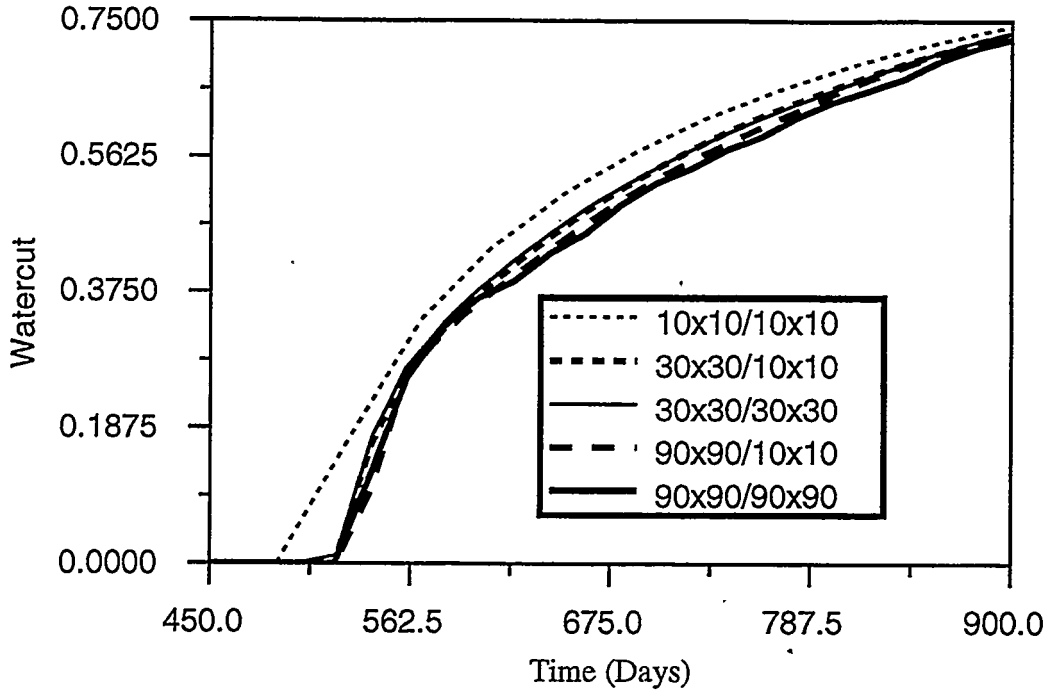

Figure 15: Comparison of Watercut - Heter. Case 1 - M=2

Pressure Grid → Saturation Grid ↓	10x10	30x30	90x90
10x10	11	XXXX	XXXX
30x30	52	293	XXXX
90x90	797	1350	18052

Table 1: Comparison of the Cpu-Time (s) - Heter. Case - M=2

UPSCALING VERTICAL PERMEABILITY WITHIN A FLUVIO-AEOLIAN RESERVOIR

S.D. Thomas, P.W.M. Corbett and J.L. Jensen
Department of Petroleum Engineering, Heriot-Watt University,
Edinburgh, Scotland. EH14 4AS

Abstract

Vertical permeability (k_v) is a crucial factor in many reservoir engineering issues. To date there has been little work undertaken to understand the wide variation of k_v values measured at different scales in the reservoir. This paper presents the results of a study in which we have modelled the results of a downhole well tester using a statistical model and high resolution permeability data. The work has demonstrates and quantifies a wide variation in k_v at smaller, near wellbore scales and has implications for k_v modelling at larger scales.

Introduction

Vertical permeability has been identified as a critical factor in the reservoir engineering concerns of the Morecambe Gas Fields (Wannell et al, 1992,1993). These concerns include maximising low saturation gas recovery from beneath gas-water contacts, producing from high angle deviated wells in thin high permeability aeolian sands and maximising small satellite field production with strong aquifer support.

The low saturation gas beneath the gas-water contact of the North Morecambe Field constitutes reserves in excess of 300bcf in-place. Simulation has indicated that a vertical permeability (k_v) of 0.02mD would allow 50% of this gas to migrate upwards into the main gas cap for recovery (McCulloch, 1994). However, a k_v of 0.002mD would allow just 6% to migrate to the gas cap. The small satellite gas fields identified surrounding the

Morecambe Fields amount to 500bcf of total gas-in-place with individual fields of 15-150bcf. The presence of a strong aquifer beneath these reservoirs means that both high and low extremes in k_v will have detrimental effects on gas recovery. k_v must be high enough to allow this gas to migrate upwards from unperforated intervals while also being low enough to prevent the encroaching water front from trapping gas behind it. Simulation indicates that gas recovery is maximised where the vertical - to - horizontal permeability ratio (k_v/k_h) is approximately 0.004 (Wannell, 1993). Although k_v is commonly estimated from production data, there is clearly a good case for its early prediction in order to estimate the financial viability and facility size of a field before production data become available.

Field k_v/k_h measurements derived from 1" core plugs reveal k_v/k_h values of approximately 0.3-0.5 while larger scale estimates derived from wireline test tools indicate values of around 0.01. The range of vertical resolution for these tools is from 1-10ft (Wannell et al, 1993). Production and vertical pressure profiles indicate a further reduction in anisotropy for the reservoir scale to ~0.002. While these measurements provide accurate anisotropy estimates for their respective scales of investigation, they do not necessarily offer any indication as to the geological controls on its variability (Figure 1).

Numerical methods provide ways of quantifying the reservoir k_v/k_h variation at all scales by calculation of effective permeabilities (k_{eff}) from reservoir models. However, these methods require a thorough understanding of the reservoir architecture and the permeability distribution within it. Although these numerical techniques are well documented, they are commonly misinterpreted for k_v and k_v/k_h estimation due to the quality of the data used in them (Bourdarot et al, 1989). The need for high resolution data is essential for numerical modelling of k_{eff} (Hurst, 1993; Corbett et al, 1992, 1993; Pickup et al 1995; Thomas et al, 1996; Jensen et al, 1997).

This paper describes how k_{eff} estimates derived from the simplest of these numerical methods are improved through use of sufficiently high resolution data. This model is used to determine upscaled permeability anisotropy for comparison with k_v/k_h estimates derived from the wireline tester. This paper also demonstrates how this model is able to quantify the permeability structure and assess the geological controls on the relationship between k_v and scale in Figure 1. Guidelines are also established for the larger k_v/k_h variation and suitable grid-block thicknesses for reservoir simulation.

Numerical Permeability Upscaling

For a simple layered reservoir model, harmonic and arithmetic averages of the layer permeabilities (Figure 2) maybe used to estimate layer normal (k_v) and layer parallel (k_h) flow respectively (Muskat, 1937 p. 403-404). In this case, each layer within the model are assumed to be isotropic. Numerical estimates of k_v and k_h derived from this method are supported by the results of simulation.

Data input to these models are commonly derived from core plug measurements, made at 1ft intervals, or from well log predictions of permeability, at 0.5ft interval but with substantial volumes of investigation. It is an unfortunate result that these measurements frequently undersample the reservoir and this undersampling may lead to over-estimation of vertical permeability (Bourdarot, 1989, Corbett & Jensen, 1992) for three reasons. Firstly, because thin low permeability reservoir intervals, such as fluvial channel clay drapes or aeolian toe-sets, are commonly missed by the sampling program. These intervals, while not greatly affecting horizontal fluid flow, do affect vertical fluid flow. Since these intervals are not included in the model, vertical permeability will be over-estimated. Secondly, the population means are only approximated by the respective averages. These sample averages require sufficient sampling to ensure that they lie within acceptable limits of the true means. The method employed to ensure sample sufficiency is the so-called No

technique (Hurst & Rosvoll, 1991; Corbett & Jensen, 1992; Jensen et al., 1997). This method defines the number of samples required to estimate the arithmetic and harmonic means within ±20% for 95% of cases and is defined as:

$$N_0 = (10C_v)^2$$

$$\text{where } C_v = \frac{\text{Standard Deviation}}{\text{Arithmetic Average}}$$

Therefore the more heterogeneous the reservoir, the larger is the C_V and the more samples which are required. As demonstrated later, routine core plugging and well logging may undersample the reservoir heterogeneity (e.g., Ball et al., 1994). Both core plugs and well logs have the added problem that they are both upscaled measurements in themselves and represent average reservoir properties, for a particular set of boundary conditions, at the scale of their measurement (Corbett et al, 1996). Finally, in contrast to the arithmetic average, the harmonic average has a positive statistical bias associated with it. This results in overestimation of the harmonic mean, especially within heterogeneous or undersampled intervals. This bias has been quantified and may be corrected (Jensen et al, 1997):

$$\overline{X}_h^* = \overline{X}_h\left(1+\frac{C_v^2}{n}\right)$$

$\overline{X}_h^*$ = Bias Corrected Harmonic Average
$\overline{X}_h$ = Harmonic Average &
n = Sample Number

The advent of fine-scale reservoir measurement techniques, notably the probe permeameter (Robertson & McPhee, 1990; Corbett & Jensen, 1992,1993; Goggin 1993; Halvorsen, 1990; Sutherland et al, 1993) and micro-scanner tools (Bourke, 1992, 1993; Ekstrom et al, 1987; Hackbarth et al, 1988; Lovell et al, 1991; Safinya et al, 1991; Troullier et al, 1989; Thomas et al, 1996) now enable the collection and prediction of extensive, small-scale permeability datasets which reduce the problems brought about by undersampling and

outlined above. The following case study uses probe permeability data to successfully upscale both k_v and k_h for cross-scaling with a wireline measurement of anisotropy over the same interval.

Case Study Location & Dataset

The location of the study well, 110/8a-5, is shown in Figure 3. It lies within the East Irish Sea Basin off the west coast of the UK and south of the South Morecambe Gas Field. The reservoir interval in this area is the Sherwood Sandstone Group (Stuart & Cowan, 1991; Cowan, 1993) which comprises mixed fluvio-aeolian facies associations. These associations are dominated by seven major facies types: wet sabkha, dry sabkha sandsheet, ephemeral channel/ sheetflood, stacked fluvial channel, channel abandonment, playa/playa margin and aeolian dune/dune remnant.

Along with core plug permeability and probe permeability, both resistivity micro-scanner and wireline tester data were also available for this well. Four wireline tester measurements were obtained, all located within an interval of stacked fluvial channel deposits and set between major channel abandonments. Their aim was to establish the lateral abandonments as local no-flow barriers and to determine the permeability anisotropy in the fluvial channel sand between them. The responses of these measurements are all remarkably consistent with an average k_v/k_h of 0.02 (Figure 4). Only one test was taken within a cored interval, WT4. Its position alongside the core plug and probe permeability data is shown in Figure 5. The plug data were taken at 1ft intervals and the probe data at 0.05ft intervals. The permeability data statistics are summarised in Table 1.

Modelling Wireline Tester Scale Estimates of k_v/k_h

The large lateral continuities of the fluvial channel facies types, a product of their environment of deposition, allows for the assumption of a simple layered model of the near wellbore region. Harmonic and arithmetic averages of the model's layer permeabilities is therefore appropriate for estimation of k_v and k_h respectively. Recent numerical simulation of the wireline tester behaviour (Atherton, 1993; Hollinshead, 1994) has demonstrated that its response is most sensitive to the formation permeability directly between the pressure probes of the tool. Numerical models of k_v/k_h were therefore constrained to thicknesses of approximately 7ft, the separation of the probes.

The permeability anisotropy estimates derived using both plug and probe data in these numerical models are shown in Figure 6 with the k_v/k_h estimate from WT4. Both numerical estimates have been corrected for harmonic average bias. Using probe data, the numerical model closely matches the tester k_v/k_h of 0.008. Using plug data, the model overestimates permeability anisotropy by a factor of 50. This overestimation is the result of insufficient sampling by the plug dataset (Table 1) and the failure of plugs to capture the low permeability clay drape at 4242ft (Figure 5).

The success of this simple numerical model allows us to assess the near wellbore k_v/k_h variability throughout the fluvial section (Figure 7). For this calculation, the 7ft window was retained and k_v/k_h was modelled over the interval of fluvial deposits between the channel abandonments at 4235 and 4255ft (Figure 5). Figure 7 demonstrates the wide range of k_v/k_h estimates for this scale of measurement even over this relatively thin reservoir interval. The estimates of k_v/k_h have a range of nearly three orders magnitude with probe data model variability clustering into two groups; one of $k_v/k_h \approx 0.3$ and the other of $k_v/k_h \approx 0.01$. The small group with relatively high k_v/k_h represents those

estimates made within the channel sand units with relatively little internal heterogeneity (e.g.' 4250ft), while the much larger and more variable cluster of k_v/k_h estimates represents those intervals affected by low permeability clays and silts (e.g., 4242ft). The presence of clustering is a reflection of geological structure in the interval which controls the observed variation of k_v/k_h with scale. This also suggests that the 7ft probe spacing of the wireline test is not estimating k_v/k_h at a representative scale for this fluvial channel facies type. As we will shortly explain, the 7ft probe spacing may not give a reliable indication of the permeability anisotropy for the sand located between the major channel abandonments. This has important implications for upscaling k_v/k_h away from the near wellbore region.

Structural Analysis and Representative Scales

The understanding and capture of reservoir permeability structure in our models is crucial since it often plays a fundamental role in the control of fluid flow during production e.g., fining upwards sequences, distributions of shales, or the presence of high permeability streaks. Structural analysis of log and permeability data has traditionally been undertaken using the semivariogram (Hohn, 1988). This method analyses the average difference between data separated by increasing distances or lag (Figure 8). Simple theoretical models which maybe fitted to the semivariogram include the linear, spherical, exponential, gaussian and 'holed'. Each of these types models the phenomenon of decreasing data correlation with increasing separation. The 'holed' model (Figure 8) attempts to capture the increasing degree of correlation at certain lag distances within structured data. However, the semivariogram has a number of limitations. Firstly, semivariograms are sensitive to the distribution of the data and problems occur with highly skewed data, a problem which may be overcome by data transformation prior to the calculation of the semivariogram. Secondly, the experimental semivariogram commonly requires 'nested' or multiple models to achieve a fit, a process prone to ambiguous results. Finally, the method gives no

quantification of the permeability within the structure other than its similarity/variability at certain separations.

Another method for analysing data structure is the Representative Elementary Area/Volume (REA/V) method (Bear, 1972; Haldorsen, 1986; Norris & Lewis, 1991). This method simply calculates or measures reservoir properties at increasing scales over intervals of the reservoir, thus allowing the property variability to be assessed at different scales (Figure 8). A representative scale within a reservoir is one at which the sample variability is reduced to a local minimum. In a structureless, random reservoir model a representative scale would be purely defined as a function of the variability of the data. Therefore the more variable and/or skewed the data in the model, the larger the scale of representivity will be. The determination of representative scales is made more complex in the presence of sedimentary structure, especially in heterogeneous reservoirs such as those at Morecambe. In many cases there may be multiple representative scales.

Figures 9-11 display the range of upscaled k_v and k_h (and therefore k_v/k_h) over a range of scales from 0.5 - 20ft within the stacked fluvial channel section of 110/8a-5. The envelopes shown in Figures 9 and 10 define the behaviour of the same permeability data randomly distributed throughout the interval. Actual permeability estimates become less variable at approximately 12ft due to the presence of thick, low permeability channel abandonment deposits occuring at this length scale. Beyond this scale, permeability estimates vary by less than an order of magnitude, k_h between 10 - 80mD, k_v between 0.1 - 1mD and k_v/k_h between 0.003 - 0.02. Below this scale, k_h estimate variability steadily increases with only a minor reduction in at 3ft (Figure 9). However variability in the estimates of k_v rapidly increases (Figure 10), not uniformly but by clustering into intervals where $k_v \approx 30$mD and those where $k_v \approx 0.3$mD . Similarly, k_v/k_h estimates cluster between 3ft - 12ft into intervals where $k_v/k_h \approx 0.3$, 0.02 and 0.002 (Figure 11). Analysis

of core and image data shown in Figure 5 reveals that these clusters are due to distinct intervals of clean sand, sand containing intrachannel clay drapes and those with channel abandonment features.

The semivariograms of these data indicate 'nested' structure (Figure 12). The semivariogram of the raw data contains a large nugget effect and appears to indicate structure at approximately 3ft, while the semivariogram of the log transformed data has a smaller nugget and structure identified at approximately 10ft. The strength of the representative volume method, as compared with the semivariogram of this dataset, is its ability to identify that structure which influences horizontal and vertical fluid flow. For example, Figures 9-10 clearly show that, while the structure at 12ft controls k_h it is the structures at approximately 3-12ft which are controlling k_v. This method also quickly quantifies the permeability variability present at these scales for incorporation in larger scale models. For example, at the scale of the wireline tester, 7ft, the range in k_v/k_h is between 0.002 and 0.2. This degree of variability clearly shows that this tool is not measuring a representative volume. Therefore, when constructing a larger scale model for permeability upscaling, this must be taken into consideration and these higher k_v/k_h intervals included.

Figure 13 demonstrates the estimation of k_v using the same technique applied to an interval of aeolian deposits from within 110/8a-5. The high resolution permeability data were derived from micro-resistivity image data (Thomas et al, 1996). The patterns of permeability variability and clustering occurring in these data differ in scale and magnitude from the previous fluvial example. Permeability anisotropy is far greater in this setting due to the interbeddeding of high permeability aeolian dune sands with clay rich and evaporitic sabkha deposits. This behaviour contrasts with the usual assumption that fluvial deposits are more heterogeneous than aeolian sediments This permeability dataset shows estimate variability reduction at approximately 15ft with clustering occuring between 4ft and 15ft.

This clustering represents those intervals containing thin evaporite cemented laminae and those intervals of aeolian dune where no evaporitic cement exists.

These results also suggest that, when developing a reservoir scale numerical model, the gridding should differ between the aeolian and fluvial regions. Grid blocks should be approximately 10ft thick in the fluvial regions, with two element types. The first with $k_v \approx$ 0.3mD and allowed to vary for a history match by no more than one order of magnitude, and the second with $k_v \approx$ 30mD and with little or no variation. For the aeolian region, two element types are also necessary, one where $k_v \approx$ 0.009mD with one and a half orders of magnitude variation and the other where $k_v \approx$ 30mD and with a permitted variation of one order of magnitude. Lateral extent of these elements would be derived from outcrop analogue studies.

Summary and Conclusions

In this work we have demonstrated that, with adequate sampling, simple averages of probe permeability data may be used to model the vertical and horizontal permeability of the near wellbore region. The work has also shown that care must be taken when applying the permeability estimates of wireline testers to larger scale models since they may not be giving a reliable estimate for that scale. This work has also shown that the use of representative elementary units is a useful tool when defining structure within complex, heterogeneous reservoir intervals. Finally we have demonstrated that, while kv vs. scale plots reflect geological and petrophysical architecture, semivariograms help elucidate the controlling structure.

Acknowledgements

The authors would like to thank British Gas for their data and support of this work.

References Cited

Atherton, G.M., (1993). An investigation into the use of the MDT* tool for layer permeability identification. Unpublished MEng. Thesis, Heriot-Watt University, Edinburgh.

Ball L.D, P.W.M. Corbett, J.L. Jensen and J.J.M. Lewis, (1994) The Role of Geology in the Behaviour and Choice of Permeability Predictors, SPE 28447, Presented at: 69th SPE Annual Technical Conference, New Orleans, September 25-28, p. 867-879.

Bear, J., (1972). Dynamic of fluids in porous media: New York, Elsevier Publishing Company.

Bourdarot, G. and F. Daviau, (1989). Vertical Permeability: Field Cases: SPE 19777 presented at: 64th SPE Annual Technical Conference, San Antonio, October 8-11, p. 53-68.

Bourke L.T., (1992). Sedimentological borehole image analysis in clastic rocks: a systematic approach to interpretation. In: A. Hurst , C.M. Griffiths and P.F. Worthington , Geological applications of wireline logs II Geological Society Special Publication, 65, 31-42.

Bourke L.T. (1993). Core Permeability Imaging: Its Relevance to Conventional Core Characterisation and Potential Application to Wireline Measurement, Marine and Petroleum Geology, August, 1993, 318-324.

Corbett P.W.M. and J.L. Jensen, (1992). Estimating mean permeability: How many measurements do you need?. First Break, v. 10, p. 89-94.

Corbett, P.W.M. and J.L. Jensen, (1993). Quantification of variability in laminated sediments: A role for the probe permeameter in improved reservoir characterisation, in C.P. North and D.J. Prosser. Characterisation of Fluvial and Aeolian Reservoirs, Geological Society Special Publication, v. 73, p. 433-442.

Corbett, P.W.M., J.L. Jensen and K.S. Sorbie, (1996). Up-scaling and cross-scaling of core and log data for interpretation and prediction, presented at Geological Society/London Petrophysical Society "Core-log Integration" Meeting, September 17-18.

Cowan, G., (1993). Identification and significance of aeolian deposits within the dominantly fluvial Sherwood Sandstone Group of the East Irish Sea Basin UK. In : C.P. North and D.J. Prosser, Characterisation of Aeolian and Fluvial Reservoirs, Geological Society Special Publication, v. 73, p. 231-245.

Ekstrom M.P., C.A. Dahan, M.Y. Chen, P.M. Lloyd and D.J. Rossi, (1987). Formation Imaging with Microelectrical Scanning Arrays. The Log Analyst, v. 28(3), p. 294-306.

Goggin, D.J., (1993). Probe permeametry: Is it worth the effort? Marine and Petroleum Geology, v. 10, p. 299-308.

Hackbarth, C.J. and B.J. Tepper., (1988). Examination of BHTV, FMS and SHDT images in very thinnly bedded sands and shales. SPE 18118 presented at: 63rd SPE Annual Technical Conference, Houston, October 2-5, p. 119-127.

Haldorsen, H.H., (1986). The problem of scale in reservoir engineering, in L.W. Lake and H.B. Carroll., Reservoir Characterisation, Orlando, Academic Press.

Halvorsen, C. and A. Hurst., (1990). Principles, practice and applications of laboratory permeametry, in P.F. Worthington. Advances in core evaluation, accuracy and precision in reserves estimation. Amsterdam, Gordon and Breach, p. 521-549.

Hohn, M.E. (1988)., Geostatstics and Petroleum Geology. New York, Van Nostrand Reinhold, 264 p.

Hollinshead, M., (1995). A comparison between probe permeability and MDT* detremined Anisotropy. Unpublished MEng. Thesis, Heriot-Watt University, Edinburgh.

Hurst, A. (1993)., Sedimentary flow units in hydrocarbon reservoirs: some shortcomings and a case for high-resolution permeability data, in S. Flint and I. D. Bryant. Quantitative description and modelling of clastic hydrocarbon reservoirs and outcrop analogues: International Association of Sedimentologists Special Publication. v. 15. p. 191-204.

Hurst, A. and K. Rosvoll., (1991). Permeability variations in sandstones and their relationship to sedimentary structures, in L.W. Lake, H.B. Carroll. Jr. and T.C Wesson, Reservoir Characterisation II: San Diego, Academic Press, p. 166-196.

Jensen, J.L., S. D. Thomas and P.W.M. Corbett., (1997). On the bias and sampling variation of the harmonic average. Mathematical Geology, v. 29, no. 2 (in press).

Lovell, M.A. and P.D. Jackson., (1991). Electrical flow in rocks: The application of high resolution electrical core measurements. Presented at the Societ of Professional Well Log Analysts 32nd Annual Logging Symposium, June 16-19.

McCulloch, N., (1994). Unlocking North Morecambe's Trapped Gas: Prediction and enhancement of recovery. Unpublished MEng. Thesis, Heriot-Watt University, Edinburgh.

Muskat, M., 1937, Flow of homogeneous fluids: New York, McGraw-Hill, 763 p.

Norris, R, J, and J.J.M. Lewis., (1991). The geological modelling of effective permeability in complex heterolithic facies: SPE 22692 presented at: 66th Annual Technical Conference and Exhibition, Dallas, October 6-9, p. 359-374.

Pickup, G.E., P.S. Ringrose, P.W.M. Corbett, J.L. Jensen and K.S. Sorbie., (1995). Geology, geometry and effective flow. Petroleum Geoscience, v. 1, p. 37-42.

Robertson, G.M. and C.A. McPhee., (1990). High resolution probe permeametry: an aid to reservoir description. In P.F. Worthington, Advances in Core Evaluation: Accuracy and Precision in Reserves Estimation, London, Gordon and Breach, p. 495-520.

Stuart I.A. and G. Cowan, (1991)., The South Morecambe Field, Blocks 110/2a, 110/3a, 110/8a, UK East Irish Sea. In I.L. Abbotts, 25 Years Commemorative Volume, Geological Society Memoir, v. 14, p. 527-541.

Sutherland, W.J., C. Halvorsen, A. Hurst, C.A. McPhee, G. Robertson, P.R. Whattler and P.F. Worthington. Recommended practice for probe permeametry. Marine and Petroleum Geology, v. 10, p. 309-318.

Safinya K.A., P. Le Lan, M. Villegas, and P.S. Cheung., (1991). Improved formation imaging with extended microelectrical arrays. SPE 22726 presented at 66th ATC, Dallas, October 6-9, p. 653-664.

Thomas, S.D., P.W.M. Corbett and J.L. Jensen., (1996). Characterisation of Permeability and Permeability Anisotropy Characterisation in the Near Wellbore: A Numerical Model using the Probe Permeameter and Micro-Resistivity Image Data. Presented at the Societ of Professional Well Log Analysts 37th Annual Logging Symposium, June 19-22.

Trouiller, J-C, and J-P. Delhomme., (1989). Thin-bed reservoir analysis from borehole electrical images: SPE 19578 presented at: 64th Annual Technical Conference and Exhibition, San Antonio, October 8-11, p. 217-228.

Wannell, M, J, and E.C. Ezekwe., (1992). The use of Observation Wells in reservoir management: SPE 24671 presented at: 67th Annual Technical Conference and Exhibition, Washington DC, October 4-7, p. 89-100.

Wannell, M, J, and N.M. Colley., (1993). The use of a new technique to determine Permeability Anisotropy: SPE 26801 presented at: Offshore European Conference, Aberdeen, September 7-10, p. 489-495.

Figure Captions

Figure 1. k_v/k_h decrease with increasing scale observed from different measurement types.

Figure 2. Simple numerical model for estimation of k_v & k_h using harmonic and arithmetic averages respectively.

Figure 3. Location of the study well, 110/8a-5.

Figure 4. Similar values for vertical and horizontal mobility given by the wireline tool within the fluvial channel facies association of 110/8a-5.

Figure 5. Permeability data collected with core plugs and the probe permeameter over the ~50ft interval from around WT4 in 110/8a-5. Note the improvement in resolution given by the probe permeability data over the plug data (left), the reflection of this permeability heterogeneity in the electrical images (middle) and the position at which WT4 was set.

Figure 6. Estimates of k_v/k_h from core plug and probe datasets at location of WT4.

Figure 7. Estimates of k_v/k_h for core plug and probe datasets over 7ft windows within a fluvial channel sand unit, 4235-4255ft.

Figure 8. Methods for structural analysis: the Representative Elementary Volume and Semivariogram.

Figures 9 - 11. Numerical estimates of k_h, k_v and k_v/k_h determined using probe permeameter dataset from the stacked fluvial channel core. The envelope in these figures indicates the expected reduction in upscaled permeability for a ramdomly distributed permeability field.

Figure 12. Semivariograms of raw and log transformed probe permeability data from fluvial channel core.

Figure 13. Numerical estimates of k_v determined using predicted permeability dataset from aeolian deposits within 110/8a-5.

	Plug Data	Probe Data
Cv	1.9	2.0
Samples	38	435
No	379	403
Do (=No/Samples)	0.1	1.1
Arithmetic Avg. (mD)	64.7	46.2
Harmonic Avg. (mD) (Bias Corrected)	0.426 (0.467)	0.218 (0.220)
Anisotropy (Bias Corrected)	0.007 (0.007)	0.005 (0.005)

Table 1.

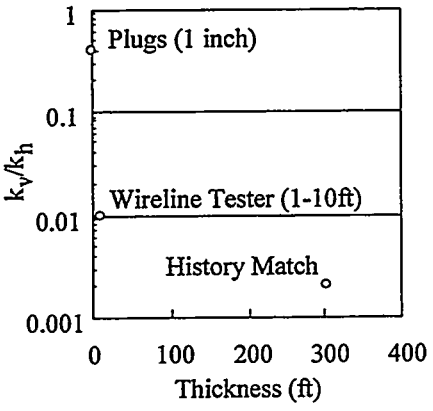

Figure 1.

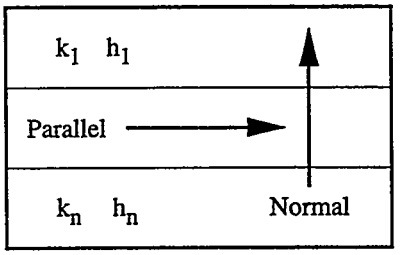

$$k_{parallel} = \frac{\sum_{i=1}^{n} k_i h_i}{\sum_{i=1}^{n} h_i} \approx k_h \qquad k_{normal} = \left(\frac{\sum_{i=1}^{n} h_i}{\sum_{i=1}^{n} k_i} \right) \approx k_v$$

Figure 2.

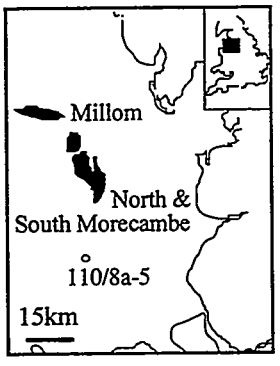

Figure 3.

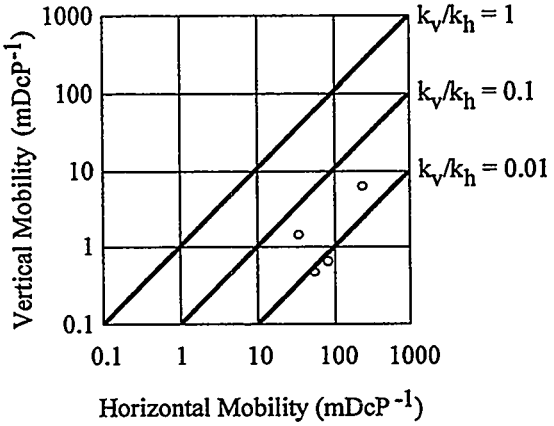

Figure 4.

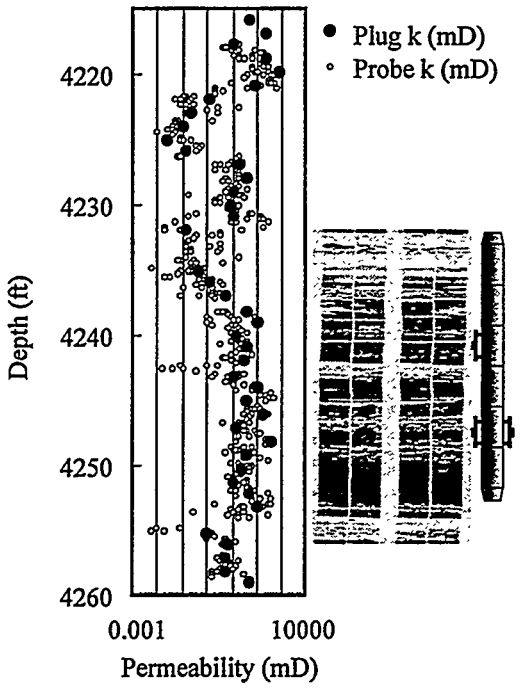

Figure 5.

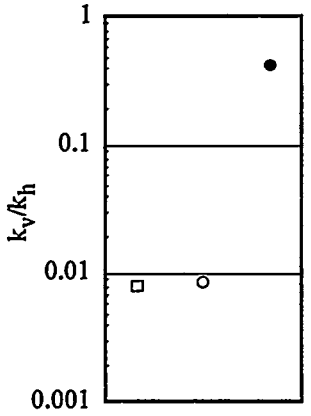

Figure 6.

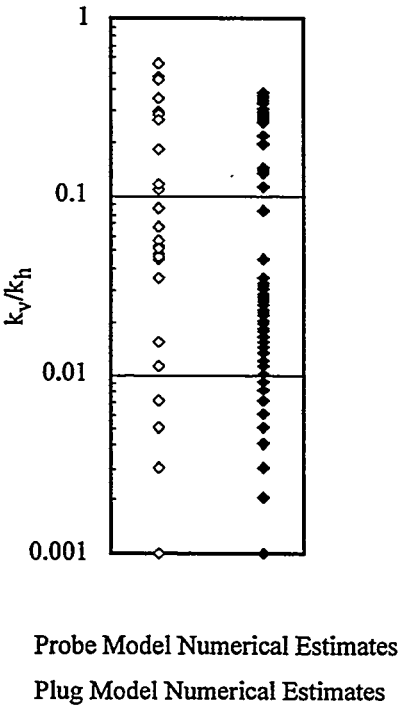

Figure 7.

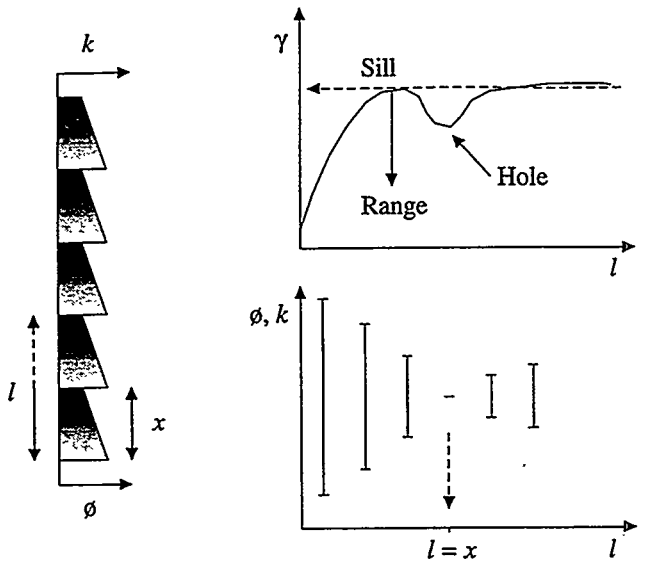

SEMIVARIOGRAM METHOD

γ= semivariogram of reservoir property with units of ϕ^2 or k^2

l = lag distance

RET METHOD

x = the length scale of permeability/ sedimentary structure

l = the length scale of the calculated/ measured reservoir property

ϕ, k = calculated/measured reservoir property

Figure 8.

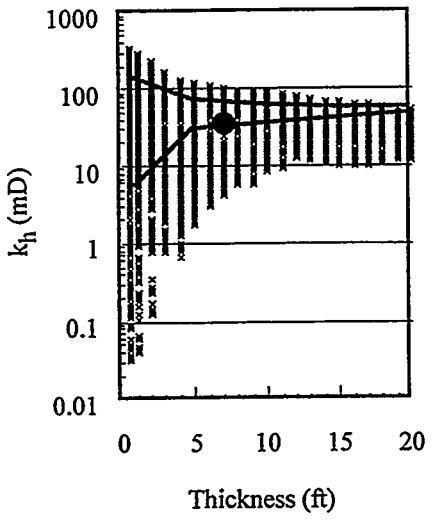

Figure 9.

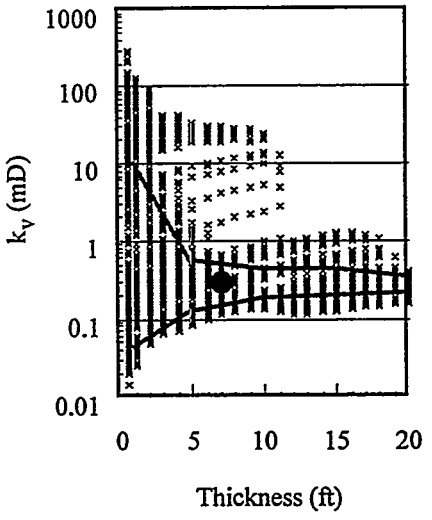

Figure 10.

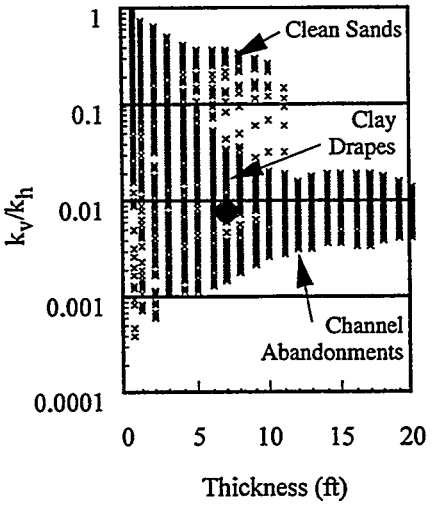

Figure 11.

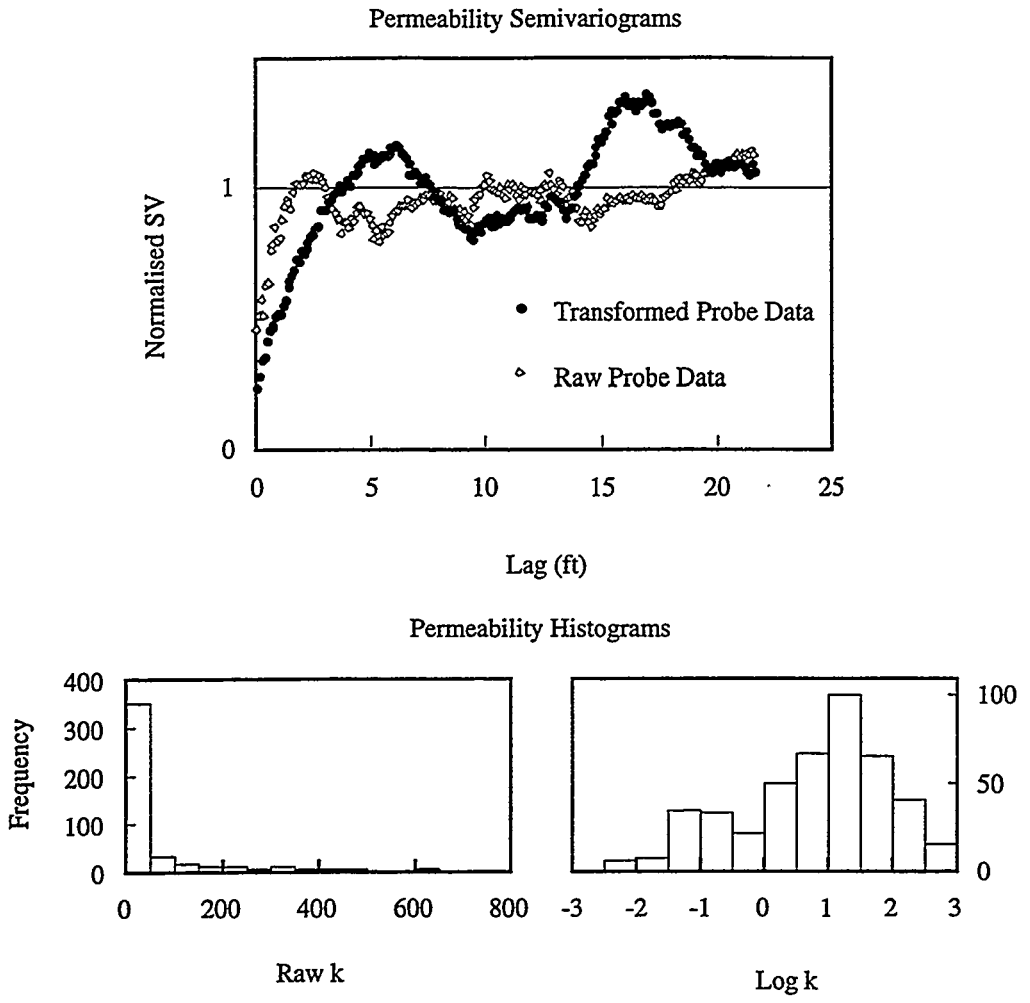

Figure 12.

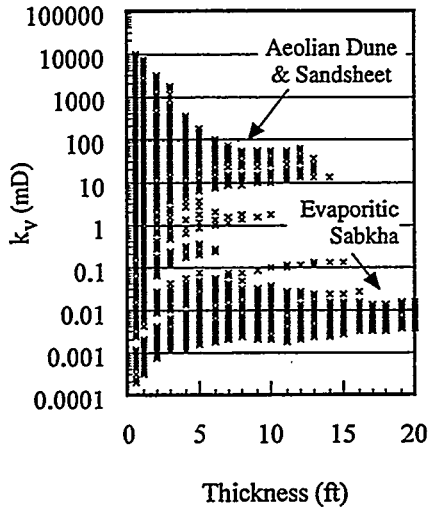

Figure 13.

Use of Geostatistic Techniques to Describe a Reservoir to be Submitted into a Secondary Recovery Process Field Case: "Eocene B-Inferior/VLG-3659, Ceuta, Venezuela"

Thamera Hernandez; Walter Poquioma
Maraven, S.A.
LaEstancia Avenue Chuao
Caracas, Venezuela

ABSTRACT

This study presents the results of an integrated reservoir study of the Eocene B-Inferior/VLG-3659, Area 7, Ceuta filed. This field located in the Maracaibo Lake in the western side of Venezuela. The objective was to evaluating the feasibility to implement a secondary recovery project by means of water flooding. Core information was used for this study (194 ft), PVT analysis, RFT, build-up and statistic's pressure analysis, modern logs and production history data.

Using geostatistical techniques (Kriging) it was defined a low uncertainty geological model that was validated by means of a black oil simulator (Eclipse). The results showed a good comparison of historical pressure of the reservoir against those obtained from the model, without the need of "history matching". It means without modifying neither the initial rock properties nor reservoir fluids. The results of this study recommended drilling in two new locations, also the reactivation of four producing wells and water flooding under peripherical array by means of four injection wells, with the recovery of an additional 30.2 MMSTB. The economical evaluation shows an internal return rate of 31.4%.

How Incorporating More Data Reduces Uncertainty in Recovery Predictions

Fernando P. Campozana*

Larry W. Lake*

Kamy Sepehrnoori*

* Center for Petroleum and Geosystems Engineering

The University of Texas at Austin

ABSTRACT

From the discovery to the abandonment of a petroleum reservoir, there are many decisions that involve economic risks because of uncertainty in the production forecast. This uncertainty may be quantified by performing stochastic reservoir modeling (SRM); however, it is not practical to apply SRM every time the model is updated to account for new data.

This paper suggests a novel procedure to estimate reservoir uncertainty (and its reduction) as a function of the amount and type of data used in the reservoir modeling. Two types of data are analyzed: conditioning data and well-test data. However, the same procedure can be applied to any other data type. Three performance parameters are suggested to quantify uncertainty.

SRM is performed for the following typical stages: discovery, primary production, secondary production, and infill drilling. From those results, a set of curves is generated that can be used to estimate (1) the uncertainty for any other situation and (2) the uncertainty reduction caused by the introduction of new wells (with and without well-test data) into the description.

INTRODUCTION

Reservoir uncertainty is the result of a lack of information. Sample data taken at well locations (cores and well logs) are too scarce to allow a detailed description. Other types of information such as (1) seismic data, (2) geological interpretation, (3) outcrop analogs, and (4) tracer, well-test, and production data can reduce, but not eliminate, uncertainty in reservoir description. As a result, multiple, equiprobable models of the same reservoir can be generated, all of them honoring the available information. This process, called stochastic reservoir modeling (SRM), allows one to (1) quantify reservoir uncertainty (2) verify fluctuations in the cash flow of projects (3) find where unswept areas of the reservoir are probably located, and (4) better manage improved oil recovery projects or infill drilling.

To stochastically simulate reservoir performance, one generally needs to build a probability density function (pdf) for each of the reservoir simulation parameters. Assuming independence among all parameters, this can be achieved by performing the following steps[1]:

- define a reference or most probable reservoir model;
- generate multiple realizations of each reservoir parameter of the reservoir model;
- perform repeated flow simulations varying only one reservoir parameter, keeping unchanged the others from the reference model parameters; and
- define a performance parameter such as oil recovery at a given time, water cut, or breakthrough time to build the pdf of the parameters.

The procedure outlined above provides an estimate of how reservoir performance varies with each parameter. This information is useful to determine the degree of accuracy necessary for each reservoir parameter. After estimating the pdfs of the reservoir parameters, multiple reservoir models can be obtained by applying the Monte-

Carlo method, as shown in Fig. 1. Each reservoir model is defined by randomly selecting the reservoir parameters from their pdfs. Reservoir uncertainty is then quantified by using each reservoir model as input to a numerical flow simulator. Based on performance parameters obtained from the simulation results, a pdf can be built similarly to what was done for each individual reservoir parameter.

Stochastic reservoir modeling can be time-consuming and sometimes computationally prohibitive. Since no satisfactory numerical simulator based on stochastic differential equations has yet been developed, each reservoir model must be input one at a time. To overcome this limitation, a number of techniques have been suggested. First, the sampling process can be minimized without losing information by using either the Stratified Sampling Method or Latin HyperCube Sampling[2]; second, subjective pdfs (like triangular distributions) can be considered for those parameters that practical experience or previous sensitivity analysis have shown not to be critical[3]; and, finally, one can perform simplified numerical simulations to rank each reservoir description and then select those that correspond to the most important quantiles to run full numerical simulations[4]. The fast, simplified numerical simulations are usually done by using a coarse grid simulation, a tracer simulator, or a simplified flow model such as a streamline simulator.

It must be pointed out that, usually, reservoir parameters exhibit multivariate dependence and application of multivariate statistics is necessary. The calculated variance of production profiles, assuming independence among the variables, can be very different from that calculated considering multidependence. However, a complete study on the dependence of all variables is rarely feasible because it requires information that is not available. Bivariate statistics considering, for example, dependence between porosity and permeability, is strongly suggested.

Applying SRM every time new information is added to the reservoir description is not viable, even with the sampling techniques described above. In this work, a

procedure is suggested that allows one to infer uncertainty in production performance for any data configuration, as well as the uncertainty reduction caused by the incorporation of new data into the model, with a reasonable computational effort.

THE APPROACH

The more data are considered in a description, the better a model should represent reality. Reservoir uncertainty should decrease. To quantify reservoir uncertainty as a function of the amount and type of data used in the model without applying SRM after every model update the following procedure is suggested:

- generate a reference model that accounts for as much data as possible and and use it as input of a numerical simulator to obtain a production forecast;
- perform some samplings from the reference model (say, four) to mimic a typical sequence of data acquisition obtained from equally spaced wells (as in the example shown in Fig. 2);
- perform SRM for each data configuration assuming the only information known about the reference model is that provided by the samples;
- choose one or more performance parameter(s) to rank the realizations and quantify the uncertainty in the recovery for each data configuration; and
- plot the performance parameter versus the number and type of data.

The uncertainty related to the reference model is bounded by two extremes: when no data are available it is a maximum and when all block values of the reference model are known it is zero. With this information, plus the points obtained using the procedure above, a curve that describes reservoir uncertainty versus number of wells can be generated. Interpolation may be used to estimate uncertainty for any number of wells.

Many performance parameters have been suggested in the literature[5]; most of them require the use of numerical flow simulation. An interesting parameter that does not rely on numerical simulation is the visual likeness factor[6]. It is defined as

$$\Gamma = \frac{\sum_i (Z_i - \bar{Z})(Y_i - \bar{Y})}{\sqrt{\sum_i (Z_i - \bar{Z})^2 \sum_i (Y_i - \bar{Y})^2}} \qquad (1)$$

where Z_i and Y_i are, respectively, the values of the variable at the ith block of the simulated image and the reference or base case. $\bar{Z}$ and $\bar{Y}$ are the average values. A perfect match gives $\Gamma = 1$, while $\Gamma = 0$ means that there is no correlation between the base case and the generated image. The visual likeness factor is very similar to the well-known correlation coefficient, the difference being that Γ considers the spatial location of the samples. This is why Γ is sometimes called spatial correlation coefficient.

Given a set of simulations, the uncertainty in the recovery prediction (*URP*) can be expressed as

$$URP_i^j = \left(RF_{opt} - RF_{pess}\right)_i^j \Big/ RF_{base}. \qquad (2)$$

where the subscript i refers to the number of conditioning wells, the superscript j refers to the algorithm used to generate the set of images, and RF_{opt}, RF_{pess}, and RF_{base} are, respectively, the most optimistic, the most pessimistic and the base-case recovery factors after a given time of production. If the reference model is updated, this parameter can be adjusted accordingly.

Analyzing the boundaries, $URP = 0$ if all i realizations match the reference case perfectly since both RF_{opt} and RF_{pess} coincide with RF_{base}. The upper bound of *URP* is obtained from Eq.2 for the set of realizations that gives the largest or maximum recovery

range: $URP_{\max} = \left(RF_{opt} - RF_{pess}\right)^{j}_{i\ \max} \Big/ RF_{base}$. Generally, this set is the one that accounts for less data. A set of unconditional simulations could be used for this purpose. An alternative expression, URP^{*}, is independent of the base-case recovery and varies between 0 and 1:

$$URP^{*j}_{i} = URP^{j}_{i} \frac{RF_{base}}{(RF_{opt} - RF_{pess})_{\max}} = \frac{(RF_{opt} - RF_{pess})}{(RF_{opt} - RF_{pess})_{\max}} \qquad (3)$$

A plot of URP versus the number of wells gives an estimate of the recovery range one would obtain for a generic configuration of wells, provided that they are approximately equally spaced. Obviously, if the wells are clustered, they will not reduce uncertainty as much as if they were equally spaced.

A third parameter measures the reduction of the uncertainty in the recovery prediction ($RURP$) as more data are added to the description:

$$RURP^{j}_{i} = \left(URP_{\max} - URP\right) \Big/ URP_{\max} = 1 - URP^{*j}_{i} \qquad (4)$$

A plot of $RURP$ versus the number of wells quantifies the impact of new data on reservoir uncertainty.

AN EXAMPLE APPLICATION

A hypothetical reservoir submitted to waterflooding is stochastically modeled to observe how reservoir uncertainty decreases as more conditioning data and well-test information are added to the description. For the sake of simplicity, only absolute permeability is allowed to vary. All other reservoir parameters are assumed to be perfectly known. A synthetic base case is generated and used as input to the commercial ECLIPSE 100 numerical simulator[7] to obtain dynamic data (well-test permeability and

oil recovery). The results are compared to those obtained using several sets of geostatistical realizations that honor different amounts of conditioning and well-test data.

The Base Case

A two-dimensional permeability field was generated using the matrix decomposition method (MDM)[8,9]. The hypothetical reservoir is a square of 4500'x4500' divided into 45x45 square gridblocks of 100'x100' each. For purposes of numerical simulation, nine equally spaced wells are active in the field: four are water injectors and five are oil producers. Their location and rates are shown in Fig. 3. The grayscale map of the base-case permeability field is shown in Fig. 4. The semivariogram model is isotropic, spherical, with no nugget, and has a range of 2,250' (half of the side length of the reservoir). The reservoir properties are given in Table 1.

The base case was then used as input to ECLIPSE 100. Two types of flow simulation were performed: a production forecast and well tests. The radius of investigation of the well-test simulations is equal to 1500'. These synthetic data are considered as reference or the *truth* case.

Stochastic Modeling

Three geostatistical algorithms were used to generate realizations conditioned to different types of data: turning bands method[10] (TBM), simulated annealing[11-13] (SA), and MTWELL[14]. The TBM algorithm was used to generate a set of unconditional simulations that was constrained only by the semivariogram. The SA algorithm was used to generate four sets of realizations conditioned to different numbers of wells (1, 5, 9, and 25) and to the semivariogram. Finally, the MTWELL algorithm was used to obtain four more sets of realizations conditioned to the semivariogram, to the same wells used in the SA realizations, and their respective well-test permeabilities derived from

pressure-transient analysis. Each set is composed of 30 two-dimensional, 45x45 permeability realizations.

The configurations of the conditioning data used in the SA and MTWELL realizations are shown in Fig. 2. These configurations can be associated with the discovery, primary production, secondary production, and infill drilling phases of the reservoir. Each well is representative of the block in which it is located. The semivariogram used in all realizations is identical to that of the base case. Therefore, uncertainty in the semivariogram model is not being considered in this application.

A statistical procedure was followed to verify if 30 realizations were enough to give meaninful results[14]. All sets of realizations were submitted to several samplings without replacement and the recovery range $\left(OR_{opt} - OR_{pess}\right)$ was calculated for each sample. Figures 5 and 6 show how the recovery range varies with the number of SA and MTWELL realizations, respectively. Stable values are reached after 25 realizations for all sets, meaning that 30 realizations are enough for the present example.

Figures 7 to 11 show one TBM, two SA, and two MTWELL realizations randomly taken from their sets. Comparing these images with the base case (Fig. 4), there is improvement as (1) the number of conditioning data increases and (2) well-test data are incorporated into the description. This improvement will be quantified in the next sections.

The Visual Likeness Factor

The visual likeness factor (see Eq. 1) was calculated for all realizations, as well as the mean value $\bar{\Gamma}$ of each set. In the limiting case where all block values (2,025) are known, $\bar{\Gamma} = 1$ for both the SA and MTWELL cases, since all realizations are identical to the base case. A plot of $\bar{\Gamma}$ versus the number of wells (N_W) is shown in Fig. 12. The visual likeness increases as N_W increases, but the impact of additional wells on $\bar{\Gamma}$ becomes smaller as N_W increases. The sets of realizations conditioned to the well-test

data (MTWELL) have a greater $\bar{\Gamma}$ than those conditioned only to the data points (SA). The TBM set had the lowest value of $\bar{\Gamma}$.

For the cases run, the data points are close to a straight line on a semilog plot, and $\bar{\Gamma}$ can be reasonably well predicted for any number of equally spaced wells by using the equation $\bar{\Gamma} = 0.258 \log N_w + 0.145$ for the SA realizations and the equation $\bar{\Gamma} = 0.219 \log N_w + 0.281$ · for the MTWELL realizations. Analyzing the difference between the two curves, one can see the improvement in $\bar{\Gamma}$ caused by the incorporation of well-test information into the description. Although accounting for well-test data always improves the description, its contribution diminishes as the number of conditioning wells increases.

Uncertainty in the Recovery Prediction

Numerical simulation was used to transfer uncertainty in the reservoir models to a production forecast. The nine sets of 30 permeability realizations described in the previous section were used as input to the commercial simulator ECLIPSE 100. All other reservoir properties were kept identical to those of the base case. Although the number of conditioning data varied from zero to 25, the number of active wells (injectors and producers) was kept unchanged during the numerical simulation (see Fig. 3).

The uncertainty in the recovery prediction (*URP*) was calculated for all sets of realizations (see Eq. 2). Figure 13 shows that, like the behavior of $\bar{\Gamma}$, *URP* decreases as N_W increases, but the impact of additional wells on *URP* decreases as N_W increases. Notice also the reduction in *URP* caused by the inclusion of well-test data into the description, especially for small values of N_W. If all 2,025 permeability block values are known, *URP* must be zero, since all realizations would be identical to the base case. Unlike $\bar{\Gamma}$, *URP* is not linearly related to the logarithm of N_W.

The reduction of the uncertainty in the recovery prediction (*RURP*) can now be analyzed in detail. Since the TBM realizations had the largest recovery range of all sets, Eq. 4 can be rewritten as

$$RURP = (URP_{TBM} - URP)/URP_{TBM}. \quad (5)$$

The results obtained using Eq. 5 are shown in Table 2 and plotted in Fig. 14. For N_W = 1, the *RURP* of the MTWELL set is 47 %, while that of the SA set is only 14 %. On the other hand, to get the same *RURP* of 47 % without considering well-test data, one needs five conditioning wells. Therefore, in this situation, testing the single well is as valuable as adding four wells to the description. However, for N_W = 25, the *RURP* of the MTWELL and SA realizations are not too different (89 % and 83 %, respectively).

CONCLUSIONS

A method based on stochastic reservoir modeling has been proposed to estimate the reservoir uncertainty and its reduction as a function of the amount and type of data used in the description. This method allows one to assess (1) reservoir uncertainty for any data configuration and (2) the impact of new data on reservoir uncertainty. Three performance parameters are suggested to quantify geostatistical realizations. An application example shows how uncertainty decreases as more conditioning data and well-test data are incorporated into the model. The impact on reservoir uncertainty of adding well-test information to the description is larger in the early stages of a field development, when only a few wells are available.

AKNOWLEDGEMENTS

We acknowledge the Enhanced Oil Recovery Research Program of the Center for Petroleum and Geosystems Engineering at The University of Texas at Austin for partial support of this work. We thank Geoquest for providing the ECLIPSE-100 simulator and the Deltas Industrial Affiliates Program of the Bureau of Economic Geology of The Unniversity of Texas for the computer time. Fernando Campozana thanks Petrobras for his financial support. Larry W. Lake holds the W. A. (Tex) Moncrief Centennial Chair.

NOMENCLATURE

N_W	= number of wells
pdf	= probability density function
RF	= recovery factor (fraction)
$RURP$	= reduction of the uncertainty in the recovery prediction
SRM	= stochastic reservoir modeling
URP	= uncertainty in the recovery prediction
Y_i	= value of the stochastic variable at the i^{th} block for a generalized realization
$\bar{Y}$	= mean value of the variable Y_i
Z_i	= value of the stochastic variable at the i^{th} block for the the base case realization
$\bar{Z}$	= mean value of the variable Z_i
Γ	= visual likeness factor
$\bar{\Gamma}$	= mean value of the visual likeness factor
Superscripts	
j	= refers to the algorithm used to generate the realizations
*	= normalized

Subscripts

base	= base case
i	= refers to the number of conditioning data used in the realizations
max	= maximum
opt	= optimistic
pess	= pessimistic
TBM	= turning bands method

REFERENCES

1. Haldorsen, H.H. and Damsleth, E.: "Stochastic Modeling," J. Pet. Tech. (Apr. 1990), 404-412.

2. Ding, L.Y., Mehra, R.K., and Donnelly, J.K.: "Stochastic Modeling in Reservoir Simulation," paper SPE 18431, Proceedings of the 10th SPE Symposium on Reservoir Simulation, Houston, TX, Feb. 1989.

3. Øvreberg, O., Damsleth, E., and Haldorsen, H.H.: "Putting Error-bars on Reservoir Engineering Forecasts," paper SPE 20512, Proceedings of the 65th Annual Tech. Conf. and Exhib. of the SPE, New Orleans, LA, Sept. 1990.

4. Ballin, P.R.: "Approximation of Flow Simulation for Uncertainty Assessment," Ph.D. dissertation, Stanford University, CA (June 1992).

5. Ballin, P.R., Aziz, K., Journel, A.G., and Zuccolo, L.: "Quatifying the Impact of Geological Uncertainty on Reservoir Performing Forecasts," paper SPE 25238, Proceedings of the 12th SPE Symposium on Reservoir Simulation, New Orleans, LA, Feb. 1993.

6. Ouenes, A., and Saad, N.: "A New, Fast Parallel Simulated Annealing Algorithm for Reservoir Characterization," paper SPE 26419, Proceedings of the 68th Annual Tech. Conf. and Exhib. of the SPE, Houston, TX, Oct. 1993.

7. ECLIPSE-100, Exploration Consultants Ltd. - Highlands Farm, Oxfordshire (RG9-4PS), England.

8. Fogg, G.E. and Lucia, F.J.: "Stochastic Simulation of Interwell-Scale Heterogeneity for Improved Prediction of Sweep Efficiency in a Carbonate Reservoir," Proceedings of the NIPER/DOE Second International Reservoir Characterization Technical Conference, Dallas, TX, June 1989.

9. Young, A.P.: "Stochastic Heterogeneity and Dispersion," Ph.D. dissertation, the University of Texas, Austin, TX (1990).

10. Journel, A.G. and Huijbregts, C.J.: *Mining Geostatistics*, Academic Press, London, 1978.

11. Kirpatrick, S., Gelatt, C.D., Jr., and Vecchi, M.P.: "Optimization by Simulated Annealing," Science (1983), 220, 671-680.

12. Farmer, C.L.: "The Mathematical Generation of Reservoir Geology," Proceedings of the Joint IMA/SPE European Conf. on the Math. Oil Recovery, Robinson College, Cambridge University, July 1989.

13. Otten, R. and Van Ginneken, L.: *The Annealing Algorithm,* Kluwer Academic Publishers, Dordrech 1989.

14. Campozana, F.P., Lake, L.W., and Sepehrnoori, K.: "Reservoir Modeling Constrained to Multiple Well-Test Permeabilities," paper SPE 36569, Proceedings of the 71th Annual Tech. Conf. and Exhib. of the SPE, Denver, CO, Oct. 1996.

LIST OF FIGURES

spherical semivariogram. There is no nugget effect and the range of correlation is one-half of the reservoir horizontal length.

5. Variation of the recovery range with the number of SA realizations. The samplings are made in increments of 5.

6. Variation of the recovery range with the number of MTWELL realizations. The samplings are made in increments of 5.

7. Single realization randomly taken from the TBM set (unconditional).

8. Single realization randomly taken from the SA set conditioned to one well.

9. Single realization randomly taken from the SA set conditioned to five wells.

10. Single realization randomly taken from the SA set conditioned to nine wells.

11. Single realization randomly taken from the SA set conditioned to 25 wells.

12. Single realization randomly taken from the MTWELL set conditioned to one well plus its well-test permeability.

13. Single realization randomly taken from the MTWELL set conditioned to five wells plus their well-test permeabilities.

14. Single realization randomly taken from the MTWELL set conditioned to nine wells plus their well-test permeabilities.

15. Single realization randomly taken from the MTWELL set conditioned to 25 wells plus their well-test permeabilities.

16. Variation of the visual likeness factor with the number of conditioning wells and type of data.

17. Variation of the URP factor with the number of conditioning wells and type of data.

18. Variation of the RURP factor with the number of conditioning wells and type of data.

Table 1 - Reservoir Properties	
Reservoir dimensions, ft	4500 x 4500
Number of gridblocks (n_x, n_y,n_z)	45 x 45 x 1
Block dimensions (Δx, Δy, Δz)	100 x 100 x 20
Porosity, fraction	0.2
Wellbore radius, ft	0.25
Total compressibility, 1/psi	4.7×10^{-7}
Initial water saturation	0.22
Oil formation volume factor, bbl/STB (at initial pressure, 2200 psia)	1.15
Oil viscosity at 2200 psia, cp	0.8
Initial pressure, psia	2200

Table 2 - Numerical simulation results.				
Algorithm	N_w	***RF range****	***URP***	***RURP***
TBM	0	0.133	0.284	0
SA	1	0.115	0.245	0.135
SA	5	0.07	0.149	0.474
SA	9	0.044	0.094	0.669
SA	25	0.022	0.047	0.835
MTWELL	1	0.071	0.151	0.466
MTWELL	5	0.04	0.085	0.699
MTWELL	9	0.022	0.047	0.835
MTWELL	25	0.014	0.030	0.895
-	2025**	0	0	1

* Range of the recovery factor (RF_{opt} - RF_{pess}).

** Extrapolation.

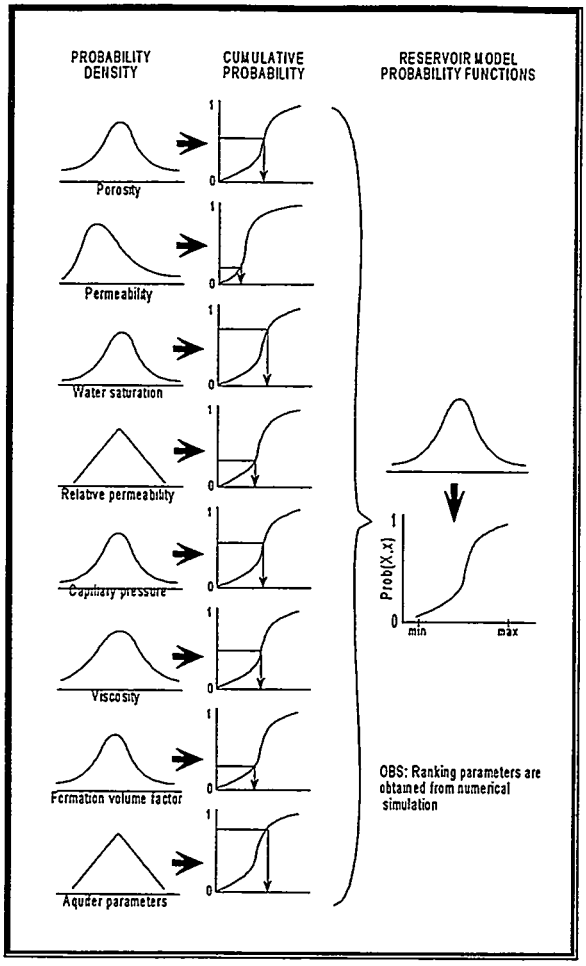

Figure 1. Monte-Carlo approach to reservoir stochastic modeling.

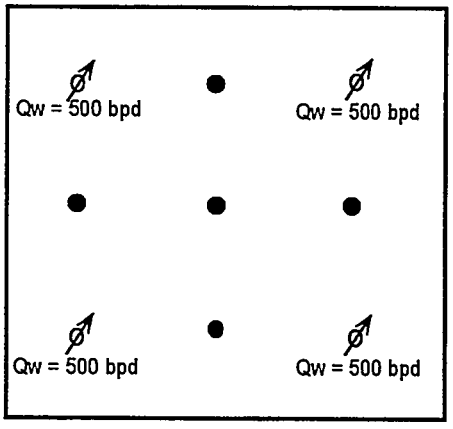

Figure 3. Well locations and water injection rates for all numerical simulations.

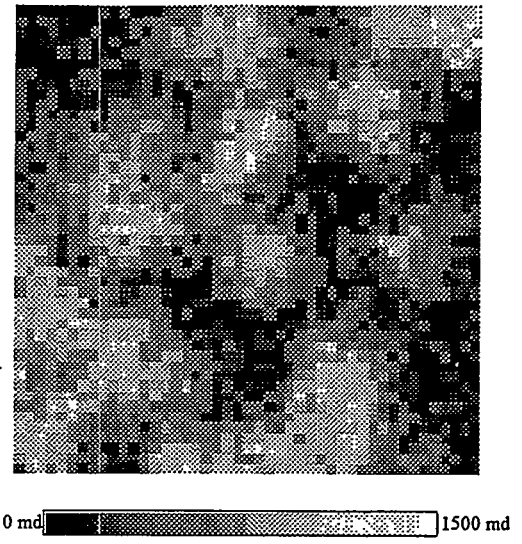

Figure 4. Base-case permeability distribution generated using sequential Gaussian simulation (SGS). The image is conditioned to the permeabilities at the nine wells in fig. 3 and to a spherical semivariogram. There is no nugget effect and the range of correlation is one-half of the reservoir horizontal length.

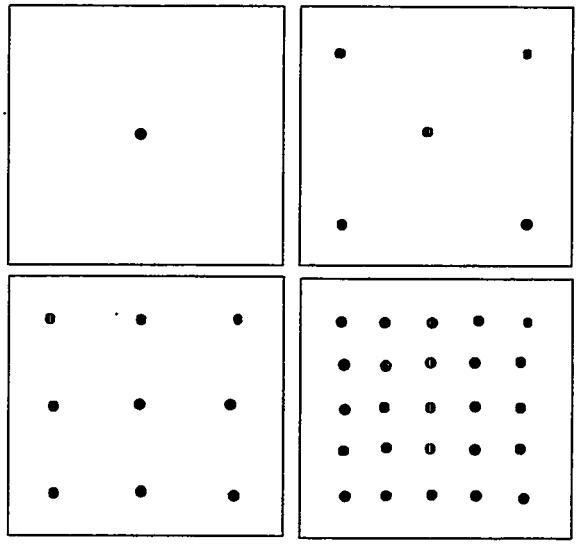

Figure 2. Four configurations of the conditioning data. From top to bottom and left to right: field discovery, primary production, secondary production, and infill drilling.

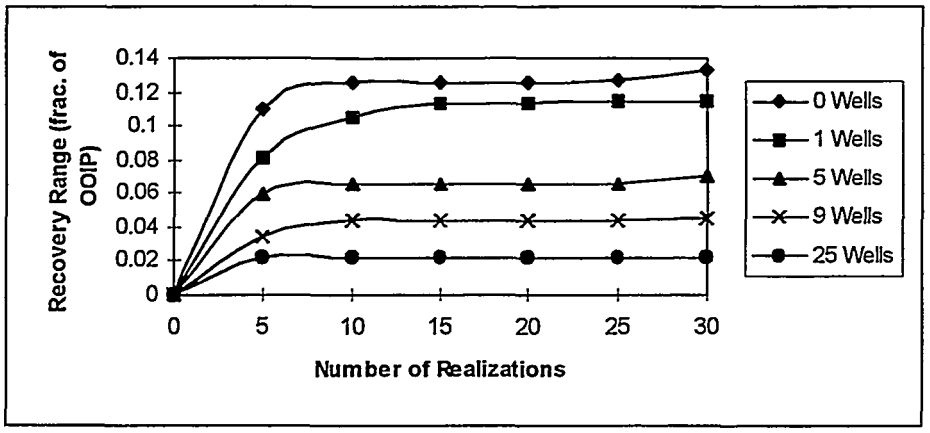

Figure 5. Variation of the recovery range with the number of SA realizations. The samplings are made in increments of 5.

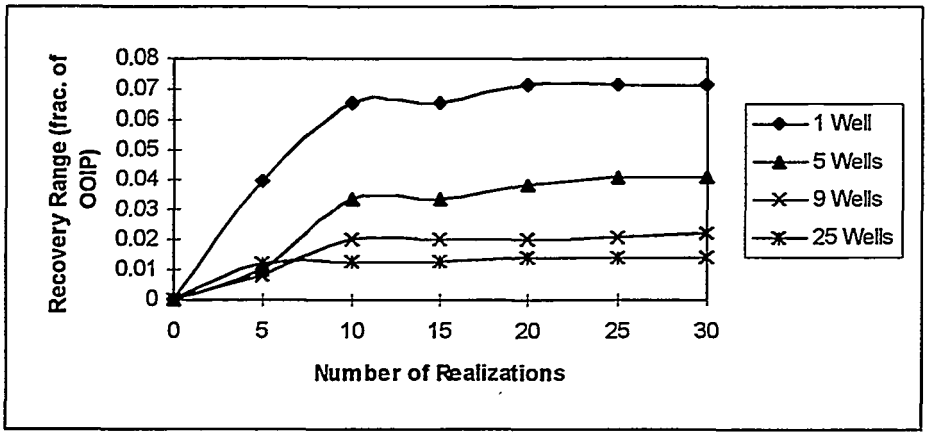

Figure 6. Variation of the recovery range with the number of MTWELL realizations. The samplings are made in increments of 5 without replacement.

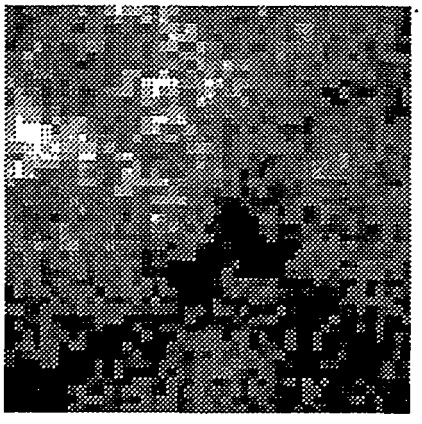

Figure 7. One realization randomly taken from the TBM set (unconditional).

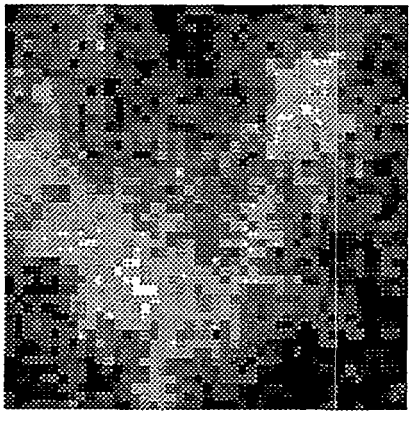

Figure 8. One realization randomly taken from the SA set conditioned to one well.

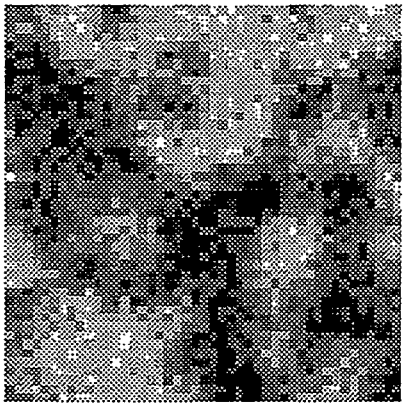

Figure 9. One realization randomly taken from the SA set conditioned to 25 wells.

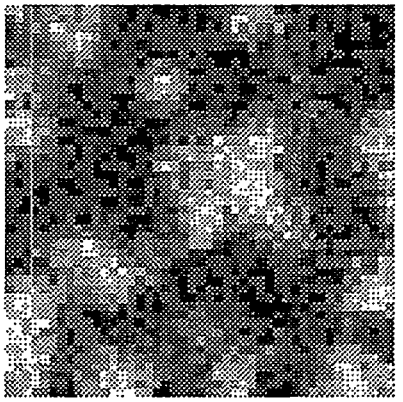

Figure 10. One realization randomly taken from the MTWELL set conditioned to one well plus its well-test permeability.

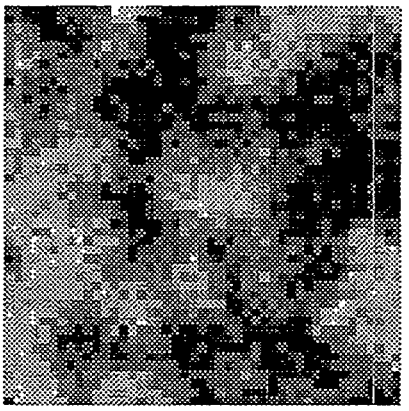

Figure 11. One realization randomly taken from the MTWELL set conditioned to 25 wells plus their well-test permeabilities.

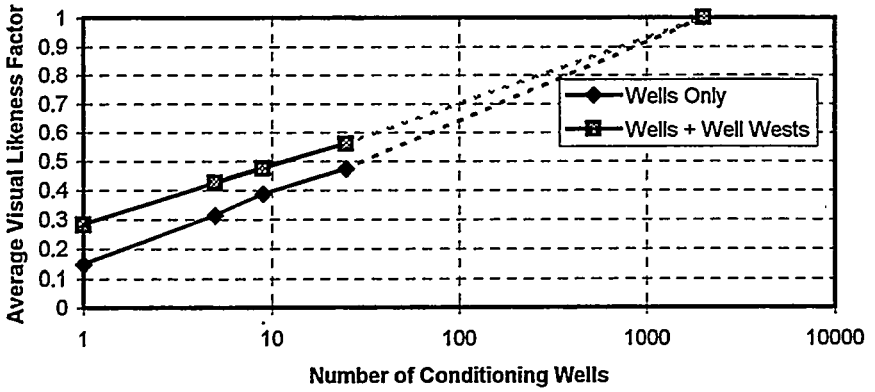

Figure 12. Variation of the visual likeness factor with the number of conditioning wells and type of data. The dotted lines are extrapolations.

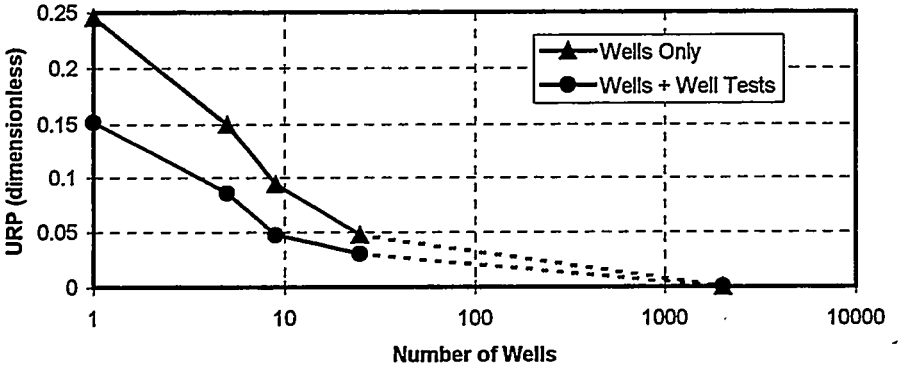

Figure 13. Variation of the uncertainty in the recovery prediction (*URP*) with the number of conditioning wells and type of data. The dotted lines are extrapolations.

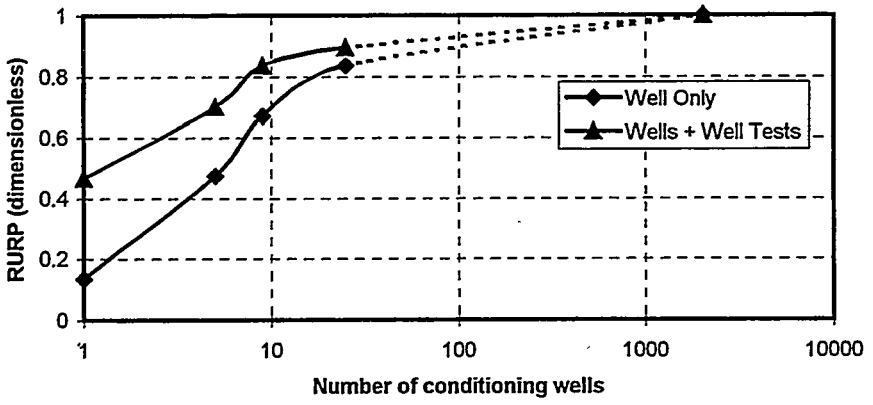

Figure 14. Reduction of the uncertainty in the recovery prediction (*RURP*) with the number of conditioning wells and type of data. The dotted lines are extrapolations.

Evaluation of Field Development Plans Using 3-D Reservoir Modelling

D. Seifert[1], J.D.H. Newbery[2,3], C. Ramsey[2,4] and J.J.M. Lewis[1,5]

[1]Heriot-Watt University, Edinburgh, Scotland
[2]Conoco (UK) Ltd, Aberdeen, Scotland
[3]Present Address: Enterprise Oil Ltd, London, England
[4]Present Address: LASMO North Sea Plc, London, England
[5]Present Address: Landmark, Austin, Texas

Abstract

Three-dimensional reservoir modelling has become an accepted tool in reservoir description and is used for various purposes, such as reservoir performance prediction or integration and visualisation of data. In this case study, a small Northern North Sea turbiditic reservoir was to be developed with a line drive strategy utilising a series of horizontal producer and injector pairs, oriented north-south. This development plan was to be evaluated and the expected outcome of the wells was to be assessed and risked.

Detailed analyses of core, well log and analogue data has led to the development of two geological "end member" scenarios. Both scenarios have been stochastically modelled using the Sequential Indicator Simulation method. The resulting equiprobable realisations have been subjected to detailed statistical well placement optimisation techniques. Based upon bivariate statistical evaluation of more than 1000 numerical well trajectories for each of the two scenarios, it was found that the wells inclinations and lengths had a great impact on the wells success, whereas the azimuth was found to have only a minor impact. After integration of the above results, the actual well paths were redesigned to meet external drilling constraints, resulting in substantial reductions in drilling time and costs.

Introduction

Journel and Alabert (1990) stated that "the goal of detailed reservoir description is to provide a numerical model of the reservoir attributes for input into various flow simulators". Today, reservoir (flow) simulations form the basis of almost all economic decisions for a field development strategy (including IOR and EOR), and reservoir management (Haldorsen and van Golf-Racht, 1992). Even though flow simulation is probably still the most important application of numerical reservoir models, there are by now other very important applications, such as well

placement optimisation studies, the provision of a common database (forcing quantification and integration of data) and the three-dimensional visualisation of data.

This study is an example of one of these applications. Based on two-layer, single-phase flow simulation, a development plan was devised for this reservoir, utilising a series of horizontal injector and producer pairs, oriented north-south. The objective of this study was to develop a stochastic model of the reservoir, evaluate the planned drilling programme and transfer the technology to the operating environment.

To ensure the latter, the company seconded the development geologist to Heriot-Watt University for the duration of the entire study so he would gain "hands on" experience with every step within the study-process. The study-process was building on earlier work (Hern et al., 1996; Seifert et al., 1996) and involved quantitative sedimentological analysis, stochastic reservoir modelling and statistical well placement optimisation.

In this statistical well placement optimisation technique, a number of static measurements are used to identify the optimum trajectory for development wells. Based on these data, actual drilling trajectories are designed by developing "drilling diagrams" which envelope the potential range of drilling targets (Solomon et al., 1993). During the drilling process, newly developed LWD tools are able to provide new data every hour which may be quickly integrated into a deterministic framework of the models to help steer the drill bit in-between the "target boundaries" (Bryant and Baygün, 1996).

Geological Overview and Initial Development Plan

The field under study is a small turbidite sandstone reservoir of late Palaeocene age located in the Northern North Sea. It comprises four way dipped closed structure which is relatively flat but has steep flanks along the channel margins. Prior to development, the field was delineated by four wells, all of which were comprehensively logged and cored.

A wide variety of facies has been identified in the core. These range from massively stacked channel sands representing high density turbidite flows to thinly interbedded very fine sands and shales that represent channel margin deposits. Relatively thick hemipelagic shales have also been identified in the core. Over parts of the field, some of the sediments have moved due to post-depositional liquefaction. This movement has caused load structures, sand injection features and where body shear has occurred, significant slumping.

The initial (Phase 1) development plan has been designed to access a proven, minimum reserves case. Three horizontal production wells have been targeted at areas where the likelihood of

encountering stacked submarine channel sands is highest, close to the existing appraisal wells. These areas also coincide with those parts of the field with the highest structural relief, and hence have the potential to achieve highest deliverability. Added together, the Phase 1 development areas are estimated to contain over half of the oil-in-place for the field.

In order to pursue a strategy which confirms the minimum reserves case while providing the potential to access additional economic reserves, the original development plan included a range of up to nine high angle/horizontal wells, comprising four producers and five injectors. The three producers drilled as Phase 1 prior to first oil, were to be followed by at least one further producer and up to five injectors comprising Phase 2.

The biggest concern regarding recovery efficiency, and the eventual Phase 2 well count, is pressure maintenance. Even in the Phase 1 development area where sand connectivity is assumed to be good, basal aquifer support has been considered to be a major uncertainty. As a result, the base case development strategy assumes that following an initial period of primary depletion during which formation pressure data will be obtained, a line drive waterflood may need to be implemented to maintain reservoir pressure above the bubble point and to improve sweep efficiency. This second phase of drilling is planned to commence once sufficient production data have been acquired to define the most appropriate water injection strategy.

Data Acquisition and Analysis (Reservoir and Analogue)

To perform any modelling work it is necessary to delineate the modelling elements and gain quantitative data on their form and spatial distribution. To acquire the appropriate data for the modelling process a multi-step approach has been employed which involves (i) identification of the lithofacies, (ii) definition of the genetic units, (iii) derivation of spatial statistics of the genetic units (proportion, geometry, size, orientation) and (iv) construction of a conceptual model.

Identification of Lithofacies. The sedimentological logs, probe-permeametry data, petrophysical data and core photographs were analysed with each probe-permeametry point being given a lithofacies indicator label. The probe-permeametry data gives significant control on this identification process (Hurst and Goggin, 1995). It appeared that a significant number of the sandstone "flow units" have an upward increasing permeability profile. Similar profiles have been identified in the Tabernas Basin (Kleverlaan, 1994) where it may be associated with dewatering structures. On identification of each lithofacies unit in the cored section, a full core viewing was held to calibrate the results.

On completion of the lithofacies identification from the core, petrophysical descriptors were applied to each type. These descriptors, or signatures, were then applied to the remainder of the reservoir zone in the uncored sections. In practise, this was difficult to do as the log characteristics did not allow for detailed facies identification. However, the hemipelagic shales could be identified from their "hot" gamma ray responses.

Definition of the Genetic Units (GU's). A genetic unit is defined as a body of rock that is distinct from other bodies on the basis of geometrical, petrophysical and spatial properties (Dreyer, 1993). This definition can be expanded to "...a genetic unit is an association of facies which are related by the same depositional process and which are distinct from other genetic units..." (Hern and Good, 1996, personal communication). Consequently, a genetic unit may contain several lithofacies types if it is believed they were deposited at the same time and have the same or similar spatial properties.

From core data, a total of seven genetic units were interpreted (Table 1). These relate to the depositional processes involved and the grain size of the resulting deposits.

Derivation of Spatial Statistics. The genetic units represent the basic building blocks of the reservoir model. It is therefore important to characterise the relevant GU's in terms of shape, size and orientation within the reservoir. Of fundamental importance is the proportion of a given GU at a given location within the reservoir. Some of these data can be derived from core and well data, such as proportions and thicknesses of the relevant GU's. Regional orientations on the reservoir scale will be most likely derived from regional geological interpretations, including data from nearby fields. Dipmeter data, however, may provide an indication of (local) orientation of, for example, fluvial GU's.

Other data, such as width and approximate length of GU's can only be deduced from outcrop analogue data. It is, of course, very difficult to find a "true" analogue for any reservoir (unless the very formation crops out in the "neighbourhood"). However, certain measures can be used to assess the similarity of the outcrop with the reservoir at hand (Hern and Good, 1996, personal communication). For example, thicknesses, aspect ratios and proportions of individual GU's can be compared, as well as the size of the entire depositional system.

For this study, the Eocene Ainsa II channel complex in the south-central Pyrenées was chosen as an analogue (Clark and Pickering, 1996). The Ainsa II is not a "true" analogue to the field under study. However, there are similarities between them in terms of turbidite system dimensions, channels and flow units. Integrating the quantitative sedimentological and petrophysical data from

the Ainsa II and published ancient and modern data, the key genetic units could be delineated. Data gathered included average thicknesses and proportions (from wells), and aspect ratios and estimated lengths (from outcrop) of the key GU's.

Conceptual Reservoir Model. Before any stochastic modelling is undertaken, it is essential that a conceptual geological model be developed. In this case, it was important to understand the stacking and channel fill patterns of the channels and flow units. Clark and Pickering (1996) have shown that in a typical upper fan channel fill, different stacking and channel fill patterns are to be expected. To capture this degree of complexity stochastically within one model is very difficult and it was therefore decided to model the two endpoints of the sedimentation process separately; "scour & fill" and "lateral accretion". The "scour & fill" model assumed the flow units to be horizontal, whilst the "lateral accretion" model had the units dipping at a low angle.

Reservoir Modelling Procedures

Modelling Technique. The sequential indicator simulation (SIS) method (pixel-based stochastic simulation technique) was chosen over a boolean method (object-based simulation technique). The main advantage of this modelling method is its capability to reproduce very complex heterogeneity patterns, allowing for different orientations, aspect ratios and frequencies for each modelling category (discrete or continuous). This method also allows for reproduction of geological trends and facies associations through spatial cross-correlation between indicator variables. The flexibility comes from the use of one indicator variogram for each indicator variable to be modelled. Detailed discussions of the SIS technique have been provided by Deutsch and Journel (1992) and Alabert and Modot (1992). Numerous case studies have shown that SIS proves to be effective in modelling reservoir heterogeneities (Journel and Gómez-Hernández, 1989; Alabert and Massonnat, 1990; Journel and Alabert, 1990; Massonnat et al., 1992).

Model Setup. The aim of this study was not to produce a full field three-dimensional model for reservoir simulation purposes, but to model the reservoir heterogeneity as accurately as possible to understand its impact on well placement. As a result, stochastic modelling was only applied to model discrete variables, i.e. the key genetic units.

Geological uncertainty exists at two scales. Firstly, on a large scale, the possibility exists that there are two channel systems present within the reservoir, instead of only the one that has been found by Well A (Figure 1). To reduce this uncertainty, it was decided to focus on the northern part of the field where two of the three Phase 1 wells would be drilled. However, this model could also serve as a generic model for the southern channel system, if present. Secondly, on a smaller scale, uncertainty exists whether the sands within the channel system(s) are laterally accreted or represent

a "scour & fill" scenario (Figure 2). In order to account for this uncertainty, both possibilities, representing two sedimentological end members, have been modelled and subsequently analysed separately.

In addition, three general assumptions were made for the modelling:

a) all structure has been removed, resulting in an orthogonal reservoir model;
b) no faulting is present within the modelled area; and
c) the thickness of the reservoir model was set to 80 ft even though the proven oil column is about 150 ft.

Assumptions (a) and (b) allow the model and subsequent well placement optimisation results to be adapted quickly to fit any geophysical interpretation. This was deemed important as this reservoir is currently in its earliest stage of development and the seismic interpretation is likely to be revised after more well data becomes available. Assumption (c) was made because (i) the top 20 ft of the reservoir was classed as non-pay to avoid potential poorly connected sand bodies which included sand injection features or thin, isolated turbidite flows, (ii) the uncertainty on the geophysical top structure map was about ± 20 ft and (iii) based on flow simulation studies it was decided that no producing well should go within 50 ft of the oil-water contact, to avoid water coning.

As a result the modelled area covered a volume of 4,600 x 4,300 x 80 ft. The size of the smallest genetic unit that needed to be modelled, the "slumped" GU, determined the cell size, resulting in a total model of 632,960 cells, each of which 50 x 50 x 1 ft in size.

Sensitivity Testing. Extensive sensitivity testing is an essential first step within the reservoir modelling procedure. In sensitivity testing, it is the aim to establish the proper parameters for both, technique specific (e.g. variogram type, search ellipsoid) and geological (e.g. lateral trends, correlation lengths) parameters. Up to thirty binary, ternary and four-component models were created for both depositional end members, using models that have a reduced total thickness of only 25 ft (to save computation time), but full lateral dimensions.

It was not possible to model all seven genetic units stochastically (Table 1) because each simulation run would take too long to complete. It was therefore necessary to group several GU's together appropriately into modelling categories. Therefore, after establishing the proper variogram parameters for each GU (e.g. variogram type, correlation lengths, anisotropies) and search neighbourhood (i.e. ellipsoid), it was investigated how well the heterogeneity would be represented using models with two, three and four modelling categories.

For the binary model, pay was modelled versus non-pay. Effectively, the clean sands were modelled versus the mixed sands and shales (Figure 3). For the ternary model, three different groupings were investigated. The most appropriate grouping modelled the shale GU versus the slumped GU versus the clean sand GU (Figure 4). For the four-component model, two different groupings were investigated. The most appropriate grouping modelled the shale GU versus the slumped GU versus the clean sand GU versus the sands with loaded structures GU (Figure 5).

By comparing Figures 4 and 5, it can be seen that the four-component model improved the level of heterogeneity by splitting the pay up into two different sand genetic units (white and light grey). If flow simulation had been the end product of this study, the four-component representation would have allowed for different effective properties within the pay sands and therefore yielded a more accurate description of the heterogeneity. This was, however, considered unnecessary, since only the intersection of sands with the wells was of interest, not their type. The binary model was not believed to be appropriate because it forced an amalgamation of the slumped GU and the shale GU into one modelling category. Because both have significantly different shapes and sizes, it would not have been possible to represent their presence appropriately within the channel sands. Their appropriate representation, however, is most crucial in this high N/G reservoir, as these govern the potential compartmentalisation of the channel sandbodies. Therefore, the approach taken in the ternary model (Figure 4, Table 1) was chosen as the optimum way to proceed.

A further complication was introduced when trying to reproduce the lateral deterministic trends as expected within this reservoir. The model was to extend beyond the main channel system to the north and south (Figure 1). Both edges are expected to have much lower N/G ratios than the channelised centre. Secondly, both edges would have different proportions of each GU, because the northern edge would represent the end of the turbidite system, exhibiting a very low proportion of hemipelagic shales but a fairly high proportion of slumped material, whereas the southern edge would represent a barrier or transition zone between two possible channel systems, therefore resulting in mixed proportions of hemipelagic shales and slumped materials. Finally, all deposits are expected to be flat lying within the edge volumes, even for the case that the channelised centre would be inclined to represent the lateral accretion system. As a result, these "edge" volumes would have had to be modelled differently from the main channelised section.

The stationarity principle in stochastic modelling ensures that a certain set of parameters, represented by indicator variograms and proportion statistics for the SIS method, will be applied and "honoured" throughout the entire model. Therefore, lateral non-stationarity could only be modelled by splitting up the model into three sections along the Y-axis, with a centre of 3000 ft, and a northern and southern edge of 650 ft each (Figure 6). Appropriate sets of statistical

parameters were defined for each section based on well data and geological assumptions with reference to the respective depositional end member to be modelled. The sections were then modelled sequentially, conditioning each section to the adjacent face of the neighbouring section.

This sequential process turned out to be complex. It became important in which order the sections were modelled. In the case of modelling the edges before the centre section, results looked much different from the case where the centre was modelled before the edges (Figure 7). This is an effect of the conditioning process using the adjacent face of the neighbouring section. When modelling the edges first, all GU's would be distributed "evenly" throughout the edge sections. This would result in a significant amount of slumped and shale GU's at the border to the centre section. These would then have to be honoured by the subsequently modelled centre section, drawing a lot of these GU's to the edge of the centre model, leaving much fewer of these behind within the centre of the centre section. The result was a sharp drop in N/G across the section boundaries (Figure 7a). When modelling the centre section first, all GU's would get distributed "evenly" and only a low proportion of the slumped and shale GU's would be placed at the border to the edges. These would then be honoured by the edge statistics, drawing a lot of the channel sands within these sections towards the centre section. The result was a transition zone of medium high N/G between the high N/G of the centre section and the lower N/G of the outer edges (Figure 7b). With respect to the geological model, the second approach was deemed more appropriate, because it resulted in a smooth transition across the boundaries of the sections. This illustrates how dependent the end result can be on the modelling approach. Hence, it is of crucial importance to check the results of each modelling step with respect to the geological model of the reservoir under study.

Modelling and Model Descriptions. Analysis of the geological data and the sensitivity testing, resulted in two different geological scenarios, representing the "scour & fill" and the "lateral accretion" end members. Each scenario was modelled by subdivision into three sections, the first section to be simulated (Section 1) being constrained by Well A, Sections 2 and 3 being conditioned to the adjacent faces of Section 1. For each scenario, a total of 15 equiprobable realisations were obtained.

Figure 8 shows a vertical cross-section through the "scour & fill" model. The centre has a very high proportion of channel sands (light grey) and very low proportions of slumped deposits (dark grey) and hemipelagic shale (black). It is obvious, that size and geometry information for the sand GU are of minor effect to this model. The slumped sands and shales are of much smaller size than the hemipelagic shales. The northern edge of the model (Section 2) representing the edge of the turbidite system where the channels are getting thinner and other deposits increase in proportion, is characterised by a medium N/G ratio, a slightly lower proportion of slumped deposits and a

relatively low proportion of hemipelagic shale. The ratio between the slumped and the hemipelagic shale is approximately 2:1. The southern edge of the model (Section 3), representing the area between two potential channel systems, is characterised by a medium N/G ratio and lower proportions of slumped deposits and hemipelagic shales (ratio of 1:1). Within the edge sections, the channel sands are generally situated near to the centre model, resulting in a gradual reduction of the sand proportions.

Figure 9, shows a vertical cross-section through the "lateral accretion" model. Notice the approximately 5° inclination (strong vertical exaggeration) of all genetic units in the centre model. The genetic units in the edges, however, have been modelled horizontally, as this was found more appropriate for the northern edge and southern transition zone.

To complete the visual representation of this reservoir, Figures 10 and 11 are showing areal cross-sections through both end member models. Notice the different proportions of the GU's in the northern and southern sections and the much narrower shales (black) in Figure 11, representing the thickness of the inclined shales. Further, in Figure 11, the boundaries for the sections and the well trajectories (below) have been superimposed.

Assessment of Potential Object-based Modelling. For the channel genetic unit, excellent geometry and size data was available from outcrop analogue. This would destine this genetic unit to be best modelled using an object-based approach. However, these geometries and sizes have lost importance due to the extremely high N/G ratio within the centre portion of the reservoir. Geometry and size data for the slumped and shale GU's are much more important as they govern the inter-connectivity of the sands. Since their sizes and geometries are only poorly known, they are likely to be modelled best using a pixel-based approach. In conclusion, this particular reservoir is likely to be modelled optimally with a pixel-based approach such as SIS. Object-based modelling would introduce geometrical artefacts based on assumed geometries that are not known. However, in cases where N/G ratios are significantly lower, a good knowledge of the channel geometries may elevate an object-based or combined modelling approach to be the method of choice.

Well Placement Optimisation Procedures

The resulting 15 realisations per geological end member have been subsequently, but independently subjected to detailed statistical well placement optimisation techniques (Seifert et al., 1996). In essence, originating from eleven cluster locations (Figure 11), a variety of linear wells have been drilled at every 15° azimuth with varying well lengths (ranging from 1000 to 2250 ft) and inclinations (ranging from 0° to 5°). A total of 1,004 numerical wells were drilled through each of

the 30 realisations. Along each well trajectory, the amount of channel sand penetrated (SGUP's - "Sand GU Proportions") and the number of sand bodies intersected (SBI's) were extracted and analysed. The following bivariate statistical evaluation of these data resulted in a statistical database of 60,240 datapoints.

Analysis of Results

Bivariate statistical analysis (SGUP's and SBI's) of the 2 x 15 realisations results in minimum, mean and maximum outcome values which need to be evaluated. The mean value represents the likely outcome and the difference between the minimum and the maximum values represents the range of the possible outcomes. The range of SGUP's and SBI's for each well trajectory can be quantified in terms of:

- location within the reservoir model;
- azimuth angles;
- angles of inclination; and
- well success versus well lengths.

Because this paper intends to show the procedure rather than actual results, the presentation of the analysis will focus on the results from Cluster 4 (located in the western centre of the centre section) and the 15 realisations with respect to the "scour & fill" scenario.

Location within the Reservoir Model. It is aimed to keep all development wells in the area of highest N/G which corresponds to the centre section of the model. Therefore, eight of the clusters have been placed all across the centre section, making sure that the wells do not extend beyond the edges (Figure 11). By analysing these clusters only, the outcomes evaluated will refer to the most likely case. However, in order to assess the impact on the wells success in the case that the actual wells will extend beyond the first channel system into the transition zone to the south, two clusters have been placed there, for analysis. Similarly, one cluster was placed in the very north to provide an outcome assessment for the case that the wells would reach the reservoir depth prematurely and drill through the edge of the turbidite system. These clusters could be analysed all together or separately, taking their locations into account.

Azimuth Angle. For each well cluster, 12 azimuth angles were analysed which covered the whole 360 degree spectrum on a 15 degree incremental basis. Figure 12 plots the sand genetic unit proportions (SGUP's) versus azimuth, for Cluster 4. All wells have the same inclination and length. As can be seen, the mean value remains almost the same throughout the dataset and the range of possible values displays only little variation. It is therefore obvious that azimuth (i.e. drilling across or along channel) will have a minor impact on the success of the wells. The reason

is that because of the very high N/G, channel bodies tend to lie next to each other and are not often separated by slumped material or hemipelagic shales. This is a very important result, particularly when considering that the drilling platform location is one of the external constraints on the drilling programme. Therefore, the azimuth of 15 degrees was considered optimum because it allowed to minimise the well length prior to entering the reservoir at target depth and azimuth.

Angle of Inclination. By changing the inclination angles from 0 degrees (horizontal) to 5 degrees (sub-horizontal) in 1 degree increments, it is apparent in Figure 13 (for optimum azimuth) that even though the mean value doesn't change much, the range of outcome values reduces significantly, as the inclination angle increases to about 3 degrees. For example, the minimum value for the 3 degree well is more than 20% greater than for the 1 degree well, therefore reducing the risk of drilling a poor well.

With increasing the inclination, one can also observe that the amount of bodies intersected increases (Figure 14). Compared to the horizontal well of 0 degrees inclination, the 3 degree inclined well almost triples the average (mean) number of sand bodies intersected, therefore significantly increasing the connected pay-volume. Upon further inclination, the average (mean) values remain very similar, only the range increases significantly. However, because of the very high N/G ratio in this reservoir, this indicator is of minor importance, especially when considering that the intervening shales may not act as barriers, therefore, not isolating one "sandbody" from another.

It has been concluded, that inclination of 3 degrees is the optimum drilling angle, because it allows a penetration of the target zone of up to 1500 ft. Upon further inclining the well, well length would have to be reduced in order to not extend into the 50 ft envelope of the oil-water contact. The outcome of such a well, however, would be similar to the 3 degree inclined well.

Well Success as a Function of Well Length. From reservoir simulation studies, it had been concluded that a certain amount of net pay intersected by each of the development wells was required for well deliverability. Therefore, six different well lengths have been investigated in this study. Figure 15 plots the cumulative pay intersected as a function of well length, for the optimum azimuth with respect to the location of the drilling platform. There appears to be a linear relationship between cumulative pay and well length. Using the slope of the lines connecting the values, one can identify what well length is likely to be needed to ascertain a minimum penetration of net pay.

It is further of importance for the drilling crew, how much shale (proportion and number of bodies) are likely to be encountered for a given well. Figure 16 gives an example of the likely proportions of each genetic unit to be encountered during drilling.

General Comments. It is important to note that the results of the well placement optimisation have to be analysed taking into account geometrical considerations when setting up the model and the well trajectories as well as the geological assumptions that led to the stochastic models. For example, the optimum inclination of 3 degrees is based on the assumption, that a linear well entering the target zone 20 ft below top structure is not to come within 50 ft of the oil-water contact in a 150 ft thick reservoir section. A well inclined at a greater angle would yield similar outcomes but violate the geometrical constraints of the reservoir model and is, therefore, considered only sub-optimum.

Secondly, this analysis is based upon only two static parameters, the amount (or proportion) and number of bodies of net pay intersected. Because of the high N/G, the second parameter is of minor importance. In order to make these interpretation results more robust, one should engage into multivariate statistical evaluations, taking dynamic parameters into account as well. This could be done, for example, by modelling the inflow performance of the best well trajectories and relating this to different well lengths. For example, using tensors for the dynamic properties, derived from lamina scale models of the genetic units, the azimuth at which the channel bodies are being intersected for drainage may become important.

Finally, taking such multivariate evaluations into account, wells could be ranked again and by assigning confidence intervals to the results, risk and uncertainty could be assessed more accurately.

Impact of Results on Drilling Plan

The results from the above analysis showed that azimuth would have a minor impact on the success of the well. Because the drilling platform location is one of the given constraints, a target azimuth of 15 degrees was considered optimum as it reduces the well length prior to entering the reservoir at target depth (Figure 17), while keeping the well in the across-channel orientation. For the drilling process, this not only resulted in time savings per well but further reduced the amount of material used (i.e. pipe, drill-bit), ultimately resulting in reductions in drilling costs.

To date, three development wells (Phase 1) were drilled following the recommendations as closely as practical. The wells showed very high sand proportions as predicted. However, the wells also showed that some of the geological assumptions made prior to the modelling process are invalid.

For example, the edge of the sand prone part of the system is very abrupt whereas it was modelled as a smooth transition across the boundaries of the sections.

This proves that there is a need for much improved understanding of the sedimentological processes that generate turbidite reservoirs. Furthermore, detailed quantitative sedimentological data for a wide range of submarine channel systems is needed. Such data can be used in the modelling process to investigate sedimentological uncertainties and will result in greater geological control during the modelling process and in greater confidence in the stochastic end product.

Summary and Conclusions

This paper describes the hybrid deterministic-stochastic modelling of genetic unit distributions within a deep marine clastic (turbidite) reservoir. Using Sequential Indicator Simulation (SIS), two end member scenarios have been modelled in a part of the reservoir in order to account for uncertainties associated with the geological model. Extensive sensitivity tests were run, in 2-D and 3-D, in order to derive the appropriate modelling parameters. A pixel-based modelling technique is believed to be best suited for modelling this particular reservoir, because of the lack of good geometry data on the most important elements of this reservoir, the slumped sands and the hemipelagic shales.

The objective of this study was to evaluate the existing development drilling plan, which consisted of pairs of horizontal injectors and producers, oriented parallel to the north. The resulting set of realisations for both end members, were subjected to detailed well placement optimisation and analysis techniques. The optimum wells were defined in terms of azimuth, inclination angle and well length. These results had to be put into context of the structural and bedding dip as well as existing external constraints in order to derive the optimum drilling trajectories for the reservoir. As a result, the existing drilling programme was revised, saving significant amounts of drilling time, materials and ultimately costs.

It is acknowledged that there still exists uncertainty within several elements of this study. This includes uncertainty as to the stacking and fill pattern of the channels, the identification of petrophysical GU-descriptors applied to the uncored sections of the wells, the stochastical modelling procedure and the static bivariate statistical analysis of the data. However, it is believed that these uncertainties have been dealt with appropriately considering the time constraints and objectives of the study.

Today, after drilling of three development wells, it can be concluded that azimuth, inclination and well length have a relatively minor impact on the wells which is largely due to the high N/G ratio

of the reservoir. The outcomes of the (successful) wells, however, raise questions about the validity of the stochastic model which is based on geological assumptions which in turn were derived from much fewer well data. It is evident that a better quantitative sedimentological understanding of this reservoir would have resulted in a more reliable reservoir model. Thus, this study should be seen as a stepping stone in the development process. The new wells provide quantitative data in lateral dimensions which incorporated into a new modelling study would yield a reservoir model which is much better constrained geologically, as this study could have been.

In summary, a thorough understanding of the sedimentology as well as the uncertainties associated with the stochastic modelling process are necessary prerequisites for developing appropriate stochastic reservoir models.

Acknowledgements

The authors wish to thank C. Hern, J. Clark, K. Pickering, P. Sherwood and D. Macklon for their helpful comments during the duration of the project. Their expertise helped ensure that the data was obtained and interpreted in a way that could readily benefit the development of the field. Furthermore, the authors wish to thank John Warrender who critically reviewed the manuscript. Thanks are also due to the managements of Conoco (UK) Ltd and LASMO North Sea Plc for permission to publish this study. Finally, the authors are grateful to Landmark Graphics Ltd for the donation of their SGM software.

References Cited

Alabert, F.G. and Massonnat, G.J., 1990, "Heterogeneity in a Complex Turbiditic Reservoir: Stochastic Modelling of Facies and Petrophysical Variability", paper SPE 20604 presented at the 1990 SPE Annual Technical Conference & Exhibition, New Orleans, LA, Sept. 23-26, p. 775-790

Alabert, F.G. and Modot, V., 1992, "Stochastic Models of Reservoir Heterogeneity: Impact on Connectivity and Average Permeabilities", paper SPE 24893 presented at the 1992 SPE Annual Technical Conference & Exhibition, Washington, DC, Oct.4-7, p. 355-370

Bryant, I.D. and Baygün, B., 1996, Reservoir Description for Optimal Placement of Horizontal Wells, paper SPE 35521 presented at the 1996 SPE/NPF European 3-D Reservoir Modelling Conference, Stavanger, Norway, April 16-17, p. 301-305

Clark, J.D. and Pickering, K.T., 1996, *Submarine Channels: Processes and Architecture*, Vallis Press, London, 231 p.

Deutsch, C.V. and Journel, A.G, 1992, *GSLIB - Geostatistical Software Library and User's Guide*, Oxford, Oxford University Press, 340 p.

Dreyer, T., 1993, "Quantified Fluvial Architecture in Ephemeral Stream Deposits of the Esplugafreda Formation (Palaeocene), Tremp-Gaus Basin, Northern Spain" *Alluvial Sedimentation*, IAS Special Publication No.17, p. 337-362

Haldorsen, H.H. and van Golf-Racht, T., 1992, "Reservoir Management into the Next Century", SEG Investigations in Geophysics No.7, *Reservoir Geophysics*, R.E. Sheriff (ed.), Society of Exploration Geophysics, Tulsa, p. 12-24

Hern, C.Y., Lewis, J.J.M., Seifert, D. and Steel, N.C.T., 1996, "Geological Aspects of Model Construction For Well Placement Optimization in a Mixed Fluvio-Aeolian Reservoir", presented at the 1996 AAPG Annual Meeting, San Diego, CA, May 19-22, Annual Convention Program (abs.), p. A64

Hern, C.Y. and Good, T., 1996, personal communication

Hurst A. and Goggin, D., 1995, "Probe permeametry: An overview and bibliography", *AAPG Bulletin*, Vol.79, No.3 (March), p. 463-473.

Journel, A.G. and Gómez-Hernández, J.J., 1989, "Stochastic Imaging of the Wilmington Clastic Sequence", paper SPE 19857 presented at the 1989 SPE Annual Technical Conference & Exhibition, San Antonio, TX, Oct.8-11, p. 591-606

Journel, A.G. and Alabert, F.G., 1990, "New Method for Reservoir Mapping, *Journal of Petroleum Technology*, Feb., p. 212-218

Kleverlaan, K., 1994, "Architecture of a Sand-Rich Fan From The Tabernas Submarine Fan Complex, SE Spain", presented at the SEPM Gulf Coast Section 15th Annual Research Conference, Houston, TX, Dec.4-7, p. 209-216

Massonnat, G.J., Alabert, F.G. and Giudicelli, C.B., 1992, "Anguille Marine, a Deepsea-Fan Reservoir Offshore Gabon: From Geology to Stochastic Modelling", paper SPE 24709 presented at the 1992 SPE Annual Technical Conference & Exhibition, Washington, DC, Oct.4-7, p. 477-492

Seifert, D., Lewis, J.J.M., Hern, C.Y. and Steel, N.C.T., 1996, "Well Placement Optimisation and Risking using 3-D Stochastic Reservoir Modelling Techniques" paper SPE 35520 presented at the 1996 SPE/NPF European 3-D Reservoir Modelling Conference, Stavanger, Norway, April 16-17, p. 289-300

Solomon, S.T., Ross, K.C., Burton, R.C. and Wellborn, J.E., 1993, "A Multi-Disciplined Approach to Designing Targets for Horizontal Wells", paper SPE 25506 presented at the 1993 SPE Production Operations Symposium, Oklahoma City, OK, March 21-23, p. 53-67

Category	Genetic Unit Description	Interpretation
channel sand	clean sandstones, often stacked	high density turbidites
	argillaceous sandstones, often stacked	low density turbidites
	clean sandstones, with mixed sandstones and shales at tops	high density turbidites topped by "load" structures and slumped materials
	clean sandstones, with mixed sandstones and shales at base	high density turbidites with "loaded" shales and sandstones at base
slumped	mixed sandstones and shales, often containing clastic injections	slump deposits and sandstone injections
	mixed sandstones and shales, often containing clastic injections	slump deposits and sandstone injections
shale	bioturbated mudstone	hemipelagic shales

Table 1: Modelling categories, GU description and interpretation.

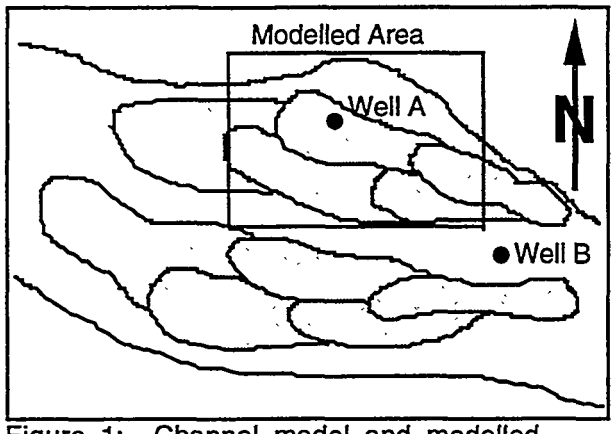

Figure 1: Channel model and modelled area.

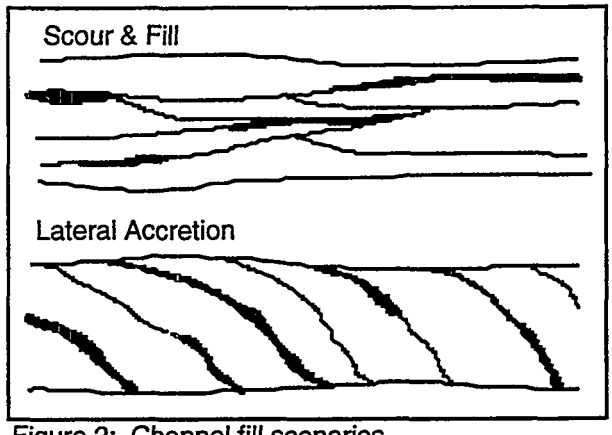

Figure 2: Channel fill scenarios.

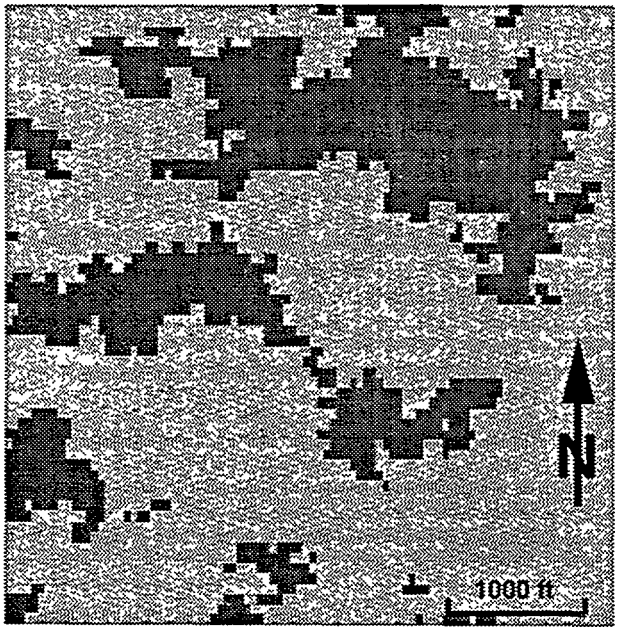

Figure 3: Binary model (areal cross-section). Sand (light) vs. non-pay (dark).

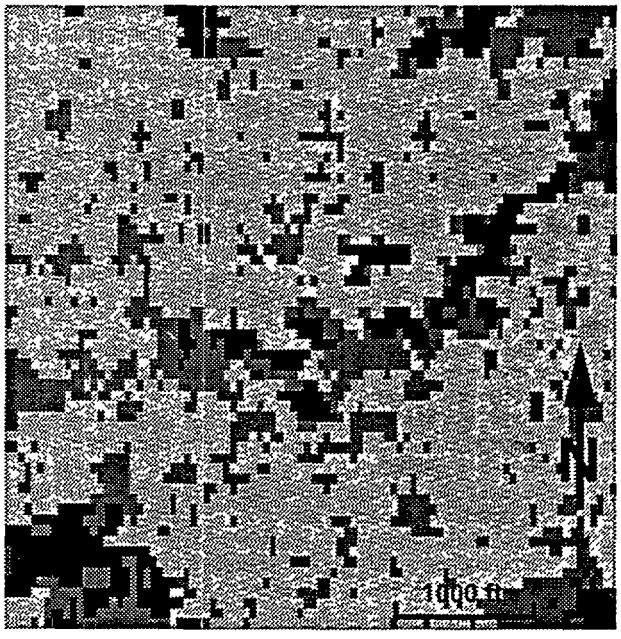

Figure 4: Ternary model (areal cross-section). Sand (light) vs. slumped (dark) vs. shale (black).

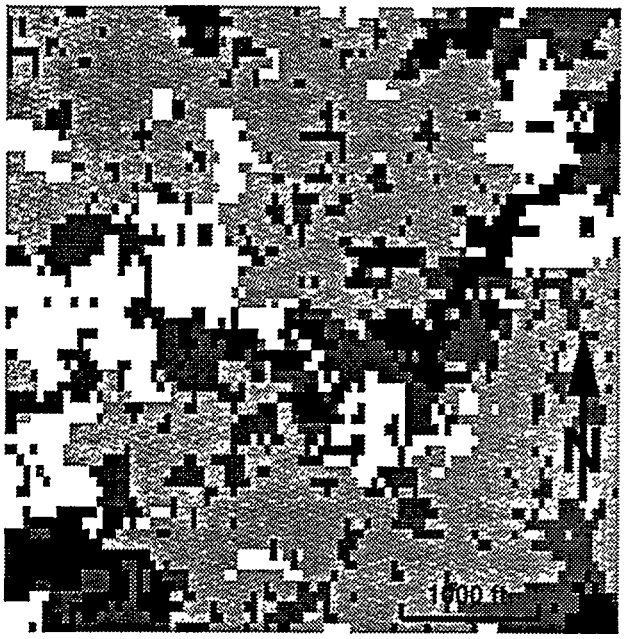

Figure 5: Four-component model (areal cross-section). Sand A (white) vs. sand B (light) vs. slumped (dark) vs. shale (black).

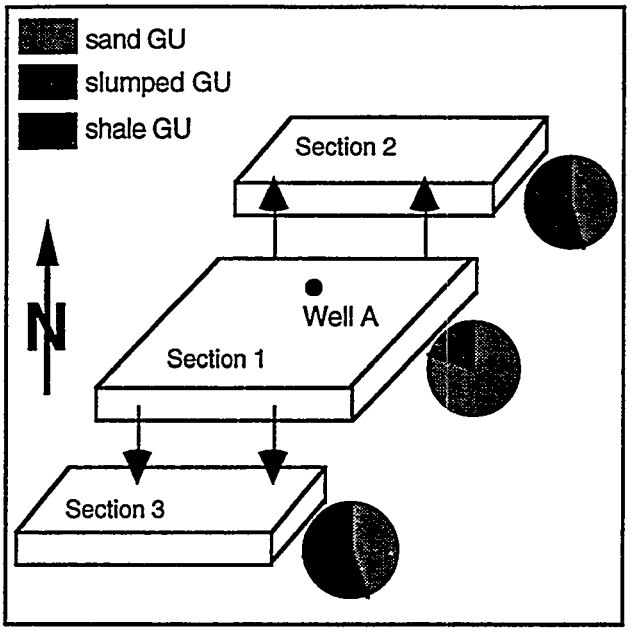

Figure 6: Sub-division of model. Pie diagrams show proportions of GU's present within sections.

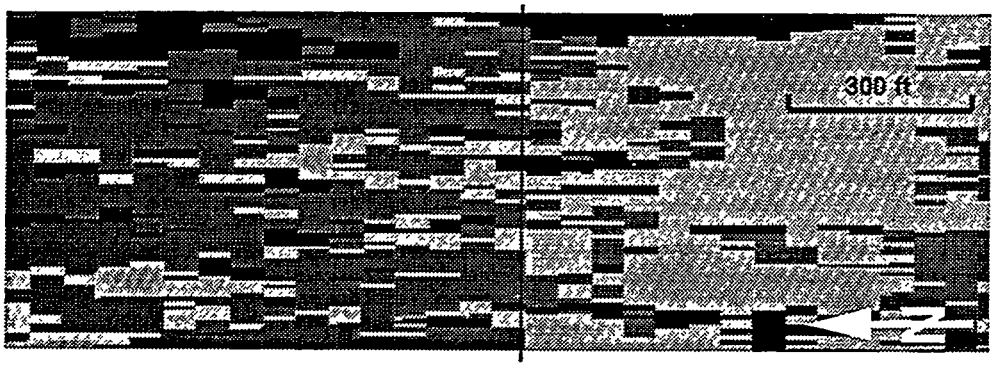

Figure 7a: Vertical cross-section (80 ft). Modelling the edge first (left) results in a sharp contrast across the boundary of the sections.

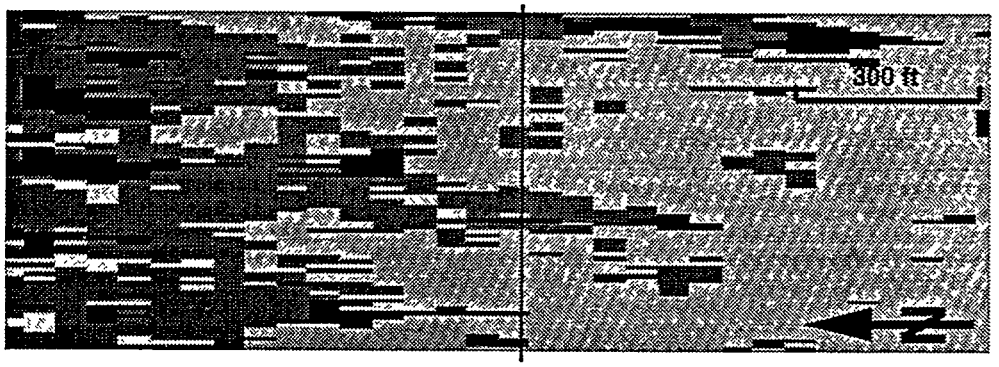

Figure 7b: Vertical cross-section (80 ft). Modelling the centre first (right) results in a smooth transition across the boundary of the sections.

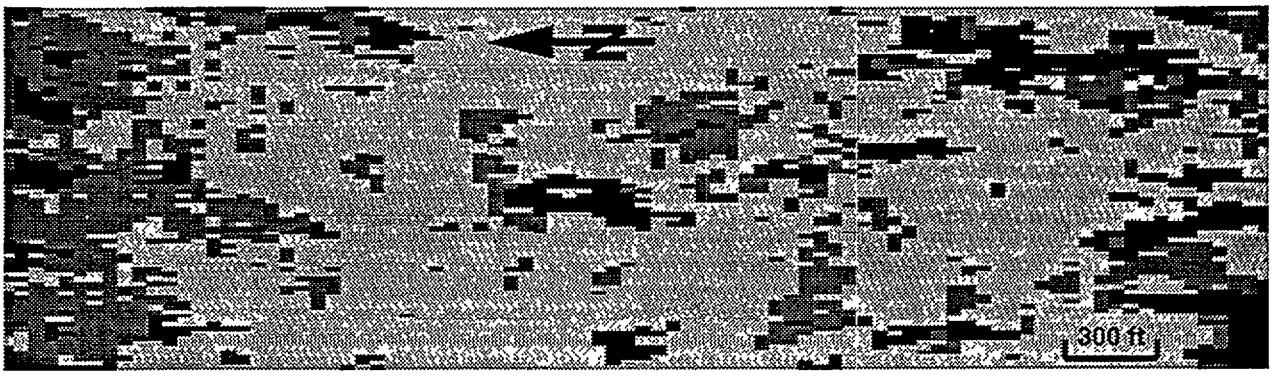

Figure 8: Vertical cross-section (80 ft) of the "scour & fill" scenario.

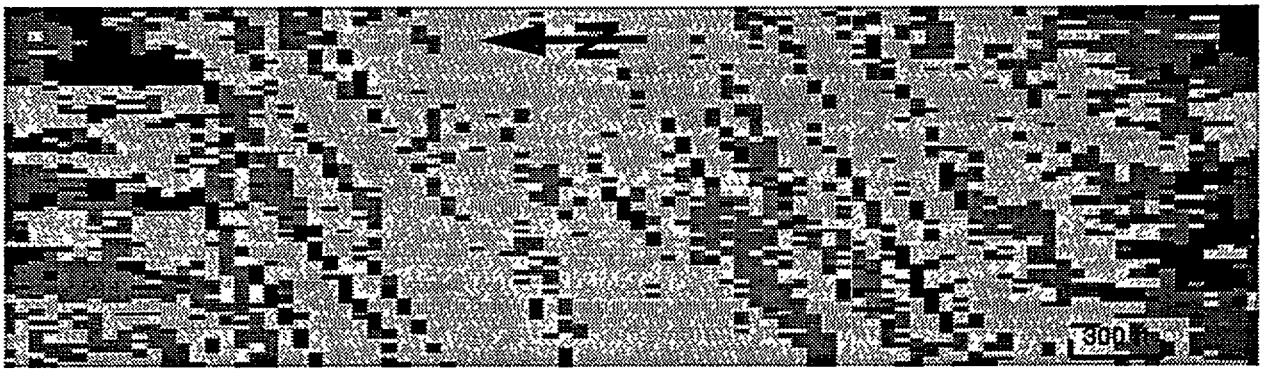

Figure 9: Vertical cross-section (80 ft) of the "lateral accretion" scenario.

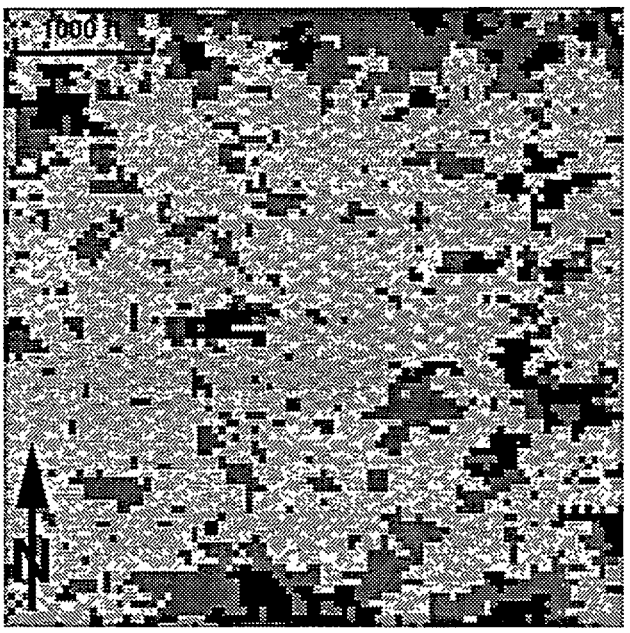

Figure 10: Areal cross-section of the "scour & fill" scenario.

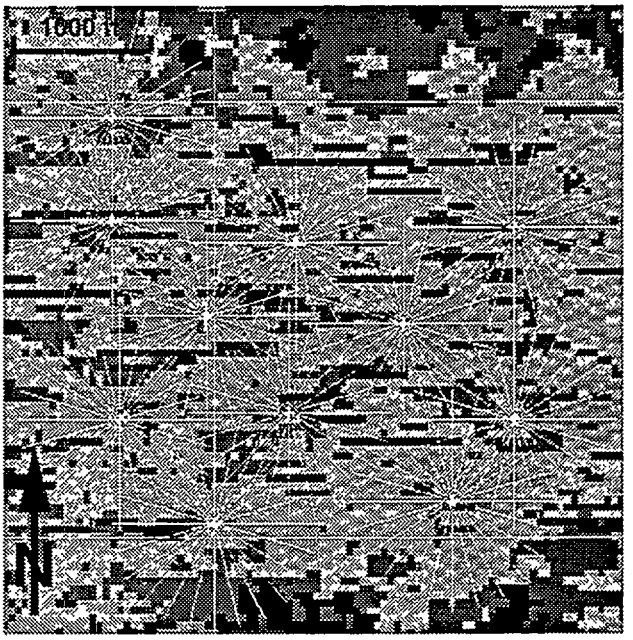

Figure 11: Areal cross-section of the "lateral accretion" scenario. Well trajectories and boundaries of sections are superimposed.

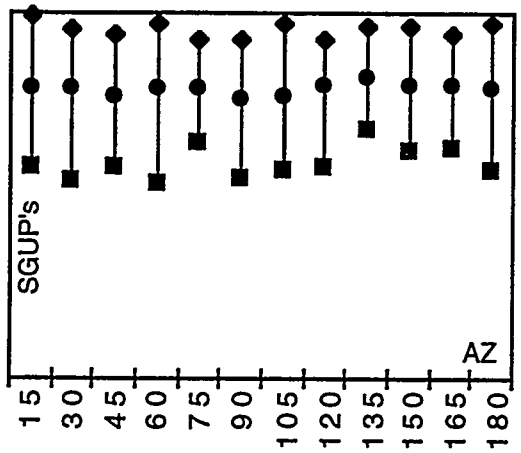

Figure 12: Cluster 4, "scour & fill" model, INC=3°; well length=1500 ft. Sand proportions vs. azimuth.

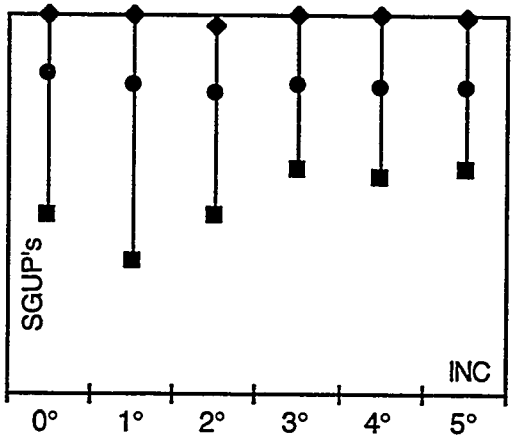

Figure 13: Cluster 4, "scour & fill" model, well length=1500 ft. Sand proportions vs. inclination.

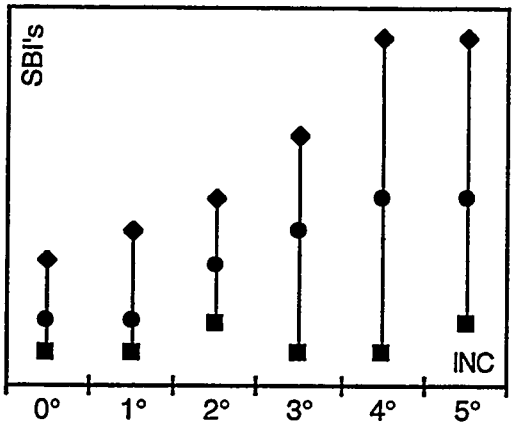

Figure 14: Cluster 4, "scour & fill" model, well length=1500 ft. Sand bodies intersected vs. inclination.

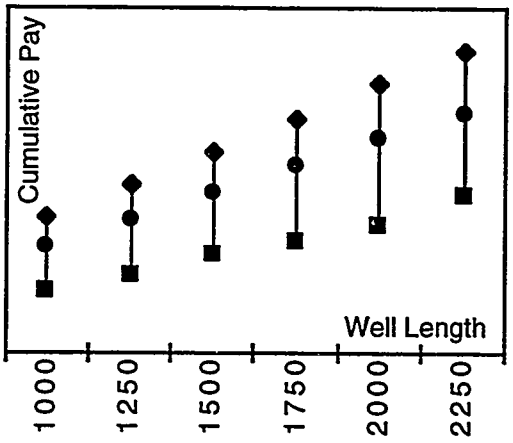

Figure 15: Cluster 4, "scour & fill" model. Cumulative pay vs. well lengths for optimum azimuth.

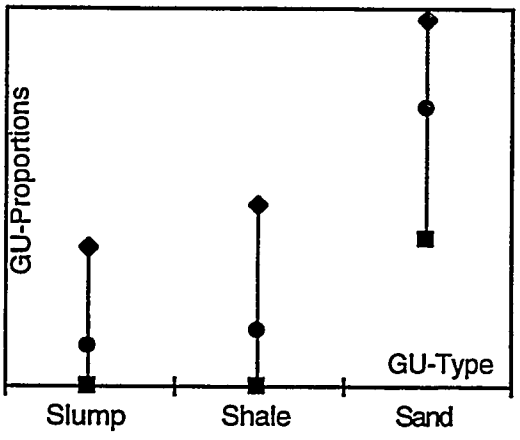

Figure 16: Cluster 4, "scour & fill" model, INC=3°, well length=1500 ft, AZ=30°. Genetic unit proportions by genetic unit type.

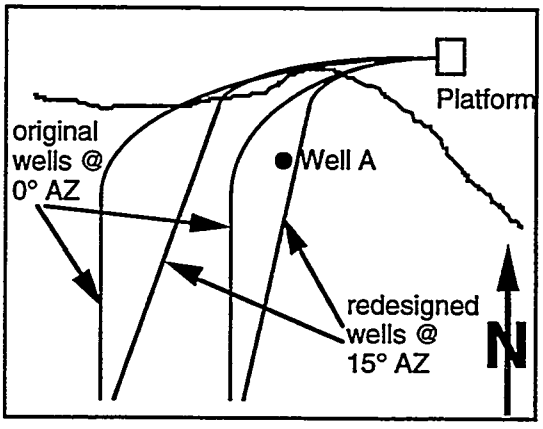

Figure 17: Original and revised drilling plan (schematic).

Improved Characterization Of Reservoir Behavior By Integration Of Reservoir Performance Data And Rock Type Distributions

David K. Davies,[1] Richard K. Vessell,[1]
Louis E. Doublet,[2] and Thomas A. Blasingame[2]

ABSTRACT

An integrated geological/petrophysical and reservoir engineering study was performed for a large, mature waterflood project (>250 wells, ~80% water cut) at the North Robertson (Clear Fork) Unit, Gaines County, Texas. The primary goal of the study was to develop an integrated reservoir description for "targeted" (economic) 10-acre (4-hectare) infill drilling and future recovery operations in a low permeability, carbonate (dolomite) reservoir. Integration of the results from geological/petrophysical studies and reservoir performance analyses provide a rapid and effective method for developing a comprehensive reservoir description.

This reservoir description can be used for reservoir flow simulation, performance prediction, infill targeting, waterflood management, and for optimizing well developments (patterns, completions, and stimulations). The following analyses were performed as part of this study:

- Geological/petrophysical analyses: (core and well log data)
  - "Rock typing" based on qualitative and quantitative visualization of pore-scale features.
  - Reservoir layering based on "rock typing" and hydraulic flow units.
  - Development of a "core-log" model to estimate permeability using porosity and other properties derived from well logs. The core-log model is based on "rock types."
- Engineering analyses: (production and injection history, well tests)
  - Material balance decline type curve analyses to estimate total reservoir volume, formation flow characteristics (flow capacity, skin factor, and fracture half-length), and indications of well/boundary interference.
  - Estimated ultimate recovery analyses to yield movable oil (or injectable water) volumes, as well as indications of well and boundary interference.
  - Well tests to provide estimates of flow capacity, indications of formation damage or stimulation, and estimates of drainage (or injection) volume pressures.

Maps of historical production characteristics (contacted oil-in-place, estimated ultimate recovery, and reservoir pressure) have been compared to maps generated from the geologic studies (rock type, permeability-thickness, hydrocarbon pore volume) to identify the areas of the unit to be targeted for infill drilling. Our results indicate that a close relationship exists between the rock type distribution and reservoir performance characteristics throughout the unit.

The reservoir performance data also suggest that this reservoir depletes and recharges almost exclusively according to the rock type distribution. This integration of "rock" data and the reservoir performance attributes uses existing data and can eliminate the need for "evaluation" wells, as well as avoiding the loss of production that occurs when wells are shut-in for testing purposes.

In short, a comprehensive analysis, interpretation, and prediction of well and field performance can be completed quickly, at a minimal cost. This analysis can be used to directly improve our understanding of reservoir structure and performance behavior in complex formations.

[1] David K. Davies & Associates, Inc., Kingwood, Texas

[2] Texas A&M University, College Station, Texas

INTRODUCTION

This study was funded in part by the U.S. Department of Energy as part of the Class II Oil Program for improving development and exploitation of shallow-shelf carbonate reservoirs. According to the DOE, shallow-shelf carbonate (SSC) reservoirs in the USA originally contained >68 billion bbls of oil (10.81×10^9 m^3)--or about one-seventh of all the oil discovered in the Lower 48 States. Recovery efficiency in such reservoirs is low, as only 20 billion bbls of oil have been produced, and current technology may only yield an additional 4 billion bbls (Pande, 1995).

The typical low recovery efficiency in SSC reservoirs is not restricted to the USA--it is a worldwide phenomenon. SSC reservoirs such as the North Robertson (Clear Fork) Unit (NRU) share a number of common characteristics (Pande, 1995), including:

- A high degree of areal and vertical heterogeneity, relatively low porosity and low permeability,
- Reservoir compartmentalization, resulting in poor vertical and lateral continuity of the reservoir flow units and poor sweep efficiency,
- Poor balancing of injection and production rates, and early water breakthrough in certain areas of the reservoir. This indicates poor pressure and fluid communication and limited repressuring in the reservoir, and
- Porosity and saturation (as determined from analysis of wireline logs) do not accurately reflect reservoir quality and performance.

Production at the NRU is from the Lower Permian Glorieta and Clear Fork Carbonates. The reservoir interval is thick, with a gross interval of approximately 1,400 ft (427 m), and more than 90% of the interval has uniform lithology (dolostone). Unfortunately, the interval is characterized by a complex pore structure that results in extensive vertical layering. The reservoir is characterized by discontinuous pay intervals and high residual oil saturations (35% to 60%, based on steady-state measurements of relative permeability). The most important, immediate problem in the field is that porosity and saturation determined from logs do not accurately reflect reservoir quality and performance.

Given these reservoir characteristics, the ability to accurately target infill well opportunities is critical because blanket infill drilling will be uneconomic in most cases. For this particular study, the cost-effective, and readily available reservoir characterization tools outlined in this work allowed us to optimally target specific well locations. After implementing a targeted infill drilling program, the total production at the NRU increased over 30 percent, while the total well count increased by only 7 percent.

HISTORICAL BACKGROUND

The NRU is located in Gaines County, west Texas, on the northeastern margin of the Central Basin Platform (Figure 1). The hydrocarbon-bearing interval extends from the base of the Glorieta to the base of the Lower Clear Fork, between correlative depths of approximately 6,160-7,200 ft (1,877-2,195 m). The unit includes 5,633 surface acres (2253 hectares, 22.8 km^2) containing a total of 270 wells (November, 1996). This includes 156 active producing wells, 113 active injection wells, and 1 fresh water supply well.

Development and Production History

Production from the North Robertson field area began in the early 1950s with 40-acre (16-hectare) primary well development. This 40-acre primary development resulted in 141 producing wells by 1965. The NRU was formed effective March, 1987 for the purpose of implementing waterflood and infill drilling operations and nominal well spacing was reduced from 40 acres to 20 acres (8 hectares). Secondary recovery operations were initiated after unitization and in conjunction with infill drilling. Most of the 20-acre infill drilling was completed between unitization and the end of 1991.

The contacted original oil-in-place from material balance decline type curve analysis is estimated to be 262 million bbls (41.66×10^6 m^3), with an estimated ultimate recovery factor of approximately 15% (primary and secondary) based on the current production and workover schedule. Figure 2 presents the production and injection history of the unit from development in 1956 through November 1996.

The total oil and water volumes produced and injected since field development are tabulated below:

Time Frame	Oil Produced (mil.bbls)	Water Produced (mil. bbls)	Water Injected (mil. bbls)
As of 1987 (primary)	17.5	8.2	0.0
1987-1996 (secondary)	9.3	28.3	64.2

Prior to 10-acre (4-hectare) infill drilling, the total unit production rates were approximately 2,740 STBO/D (436 m^3/day), 1,130 MSCF/D gas (32,000 m^3/day), and 12,230 BW/D (1,945 m^3/day). Water injection prior to the infill program was approximately 19,000 BWI/D (3,021 m^3/day), with injection water comprised of produced water, and fresh water from the Ogallala aquifer obtained from a water supply well within the unit.

The eighteen (14 producers, 4 injectors) 10-acre infill wells that were drilled during the second and third quarters of 1996 have increased unit production rates to 3,600 STBO/D, 1,700 MSCF/D gas, and 13,500 BW/D. Current injection at the unit is approximately 19,600 BWI/D.

The well configuration at the NRU is an East-West line drive pattern (staggered five-spot) as shown in Figure 3, and was developed for optimum injectivity and pressure support. Sweep efficiency is difficult to quantify due to differences in depositional environments throughout the unit. Fortunately, these differences are easily identified on the basis of reservoir rock type.

GEOLOGIC STUDY

This geological/petrophysical reservoir characterization of the NRU involved the following methodologies:

- Development of a depositional and diagenetic model of the reservoir,
- Definition of "rock types" based on pore geometry and development of the rock-log model,
- Rock type extension to non-cored wells using the rock-log model,
- Definition of flow units and cross-flow barriers, and
- Mapping of reservoir parameters (thickness, ϕh, kh, and hydrocarbon pore volume) and rock type for each flow unit.

The purpose of the geological/petrophysical portion of this study was to identify and map individual hydraulic flow units (HFU's) to evaluate the potential for continued development drilling. Flow units had to be readily identified using wireline logs because core data are sparse (8 wells). Thus, the fundamental reservoir description is well log-based. However, because values of porosity and saturation derived from routine well log analysis do not accurately identify productive rock in most shallow-shelf carbonates, it is necessary to develop a core- and rock-log model that allows for the prediction of another producibility parameter--in this case formation permeability.

A geologic model is developed for the reservoir, based fundamentally on the measurement of pore geometrical parameters. Pore-level reservoir modeling allows for improved accuracy in the identification and prediction of rock types, permeability, and the identification of flow units. Pore geometry attributes were integrated with well log data to allow for log-based identification of intervals of rock with different capillary characteristics, as well as the prediction of permeability throughout the unit.

No new wells were drilled to aid the reservoir description. The existing database consisted of conventional cores from eight wells, and relatively complete log suites in 120 wells consisting of:

- Gamma ray, GR
- Photoelectric capture cross-section, PE
- Compensated neutron porosity, ϕ_N
- Compensated formation bulk density, ρ_b
- Dual laterolog (LLD and LLS--deep/shallow resistivities)
- Borehole caliper

Pore Geometry Modeling

At the NRU, no strong relationship exists among core derived values of porosity, permeability, and depositional environment, as indicated by the wide scatter of data points shown in Figures 4 and 5. Different environments exhibit similar ranges of

porosity and permeability which is not surprising as the carbonates have undergone significant diagenetic alteration of pore geometry after deposition. Thus, there is no fundamental relationship between depositional environment and permeability. This is a common problem in many diagenetically-altered reservoirs (sandstones and carbonates).

Analysis of 3D pore geometry data allows reservoir characterization efforts to be pore system oriented. The resulting reservoir models are based on characteristics of the pore system. Analysis of pore geometry involves identification of individual pore types and rock types.

Quantitative analysis of pore geometry is used to develop the vertical reservoir layering profile of the reservoir (*i.e.*, to identify vertical compartmentalization) at the NRU. Integration of pore scale observations with depositional and diagenetic data allows for the determination of the areal compartmentalization and permeability distributions within the reservoir.

Pore Types: The determination of pore types in a reservoir requires the use of rock samples (conventional core, rotary sidewall cores, and cuttings samples in favorable circumstances). In this study, analyses were based on the end-trims of 1 inch plugs removed from conventional cores. Individual pore types were classified in terms of the following parameters:

Pore Body Size and Shape: Determined using scanning electron microscope (SEM) image analysis of the pore system (Clelland and Fens, 1991).

Pore Throat Size: Determined through capillary pressure analysis and SEM analysis of pore casts (Wardlaw, 1976).

Aspect Ratio: The ratio of pore body to pore throat size. This is a fundamental control on hydrocarbon displacement (Wardlaw, 1980; Li and Wardlaw, 1986).

Coordination Number: The number of pore throats that intersect each pore (Wardlaw and Cassan, 1978).

Pore Arrangement: The detailed distribution of pores within a sample (Wardlaw and Cassan, 1978).

These parameters are combined to yield a classification of the various pore types in these rocks (Table 1). Pore types were identified in each core sample (350 samples in this study). Commonly, each sample contained several different pore types. It was therefore necessary to group pore types into rock types.

For each sample, the volumetric proportion of each pore type was determined using SEM-based image analysis (Clelland and Fens, 1991). Because the pore throat size is known for each pore type, it is possible to develop a pseudo-capillary pressure curve for each sample using the well known relation (Thomeer, 1983):

$$p_c = \frac{214}{d} \quad \text{.....(1)}$$

for which p_c is mercury-air capillary pressure in psia and d is pore throat diameter in microns (10^{-6} m).

The validity of the geologically-determined rock types was evaluated using mercury capillary pressure analysis of selected samples. Our results reveal differences between the rock types in terms of the measured capillary characteristics (Figure 6 and Table 2). Such cross-checks allow for independent validation of the pore geometrical classification of rock types. Mercury capillary pressure data are also used to aid in the determination of pore throat sizes.

Rock Types: A "rock type" is an interval of rock characterized by a unique pore structure (Archer and Wall, 1986), but not necessarily a unique pore type. In this study, eight rock types were identified, based on the relative volumetric abundance of each pore type (Figure 7). Each rock type is characterized by a particular assemblage (suite) of pore types (Ehrlich and Davies, 1989). For example, Rock Type 1 is dominated by Pore Type A, while Rock Type 2 contains few pores of Type A and is dominated by Pore Types B and C (Figure 7). Identification of rock types is fundamentally important because porosity and permeability are related within a specific pore structure (Calhoun, 1960).

Porosity-Permeability Relationship

At the NRU, the basic relationship between porosity and permeability exhibits a considerable degree of scatter (up to 4 orders of magnitude variation in permeability for a given value of porosity). In contrast, the porosity and permeability are closely related for each rock type (Figure 8).

Permeability calculations on the basis of rock type have an error range of less than one-half decade for most samples. Regression equations for permeability as a function of porosity were developed for each rock type to quantitatively define each relationship (using log-log plots to avoid zero porosity intercepts). These equations were used in the field-wide prediction of permeability using well logs (permeability being a function of porosity and rock type).

Average values of porosity and permeability are given for each rock type in Table 3. We immediately note that the highest porosity rocks at the NRU do not exhibit the highest permeability. The principal pay rock at the NRU is Rock Type 1. Rock Type 1 has significantly lower values of porosity than Rock Type 4 (flow barrier). This characteristic has important implications in terms of selecting zones to perforate. Given our observations, the zones with the highest porosity should not always be the principal targets in this field.

Rock-Log Model

Analysis of pore geometries reveal that eight rock types occur in the NRU. Six of the rock types are dolostone, one is limestone (non-pay--structurally low and water-bearing in this field), and one is shale (Table 3). Individual rock types can be recognized using specific "cut-off" values based on analysis of environmentally corrected and normalized well log responses and using the comparison of core-based determination of rock type.

The well log responses used to isolate the eight different rock types for the NRU study were:

- ρ_{maa} versus U_{maa} with gamma ray (Figure 9)
  - This data plot allows the discrimination of dolostone, limestone, anhydritic dolostone, siltstone, and shale
  - Can be used to identify "pay" vs. "non-pay" reservoir rock
- Shallow and deep laterolog resistivities and porosity (Figure 10)
  - Provides discrimination of "pay" Rock Types 1-3.

The rock-log model was first developed using data from only 5 cored wells. Subsequently the model was extended to include the 3 remaining cored wells. Evaluation of cored intervals reveals successful discrimination (>80%) of each of the principal rock types (Rock Types 1-3) despite the fact that wells were logged by different companies at different times. Misidentification of Rock Type 1 results in identification of Rock Type 2, while misidentification of Rock Type 2 results in identification of Rock Type 1. Thus, there is no significant misidentification of the dominant rock types by logs over the cored intervals. The model has been extended to all wells with sufficient log suites in the field (120 wells in the NRU). Specific algorithms allow for rock type identification on a foot-by-foot basis in each well.

As we showed previously (Figure 8), permeability is a function of both rock type and porosity. We have established that rock type and porosity can be determined from well log responses alone. Therefore, permeability can, in principle, be predicted using only well log data. This gives us the ability to develop a vertical layering profile based on rock type and permeability in cored and non-cored wells.

Hydraulic Flow Units

Individual HFU's were identified based on the integration of the data for the distribution of rock types, petrophysical properties (in particular, permeability and fluid content) and depositional facies. Evaluation of this data for 120 wells revealed that rock types are not randomly distributed, rather the principal reservoir rocks (Rock Types 1, 2, and 3) generally occur in close association, and typically alternate with lower quality rocks (*e.g.*, Rock Types 4, 6, 7 and 8). Correlation of rock types between wells reveals an obvious layering profile in which 12 distinct layers, or HFU's, are distinguishable at the NRU (Figure 11). Correlation of these layers is aided by a knowledge of the distribution of depositional environments as there is a weak relationship between depositional environment and rock type. Better quality rocks (> 1 md permeability, > 10% porosity,) occur most commonly in the shoal deposits (Figure 4). Consequently, Rock Types 1 and 2 are more common in the high energy deposits (shoals). Rock Types 3 and 4 are more common in low energy deposits (supratidal, tidal flat, lagoon).

Maps were prepared for each of the HFU's to illustrate the distribution of important petrophysical parameters (Figure 12). The distribution of the principal rock types for each HFU is also mapped (Figure 13). This allows for rapid identification of areas of the field dominated by either high or low quality reservoir rock.

There is a general tendency at the NRU for the higher quality rocks (Rock Types 1 and 2) to occur in discrete trends on the NE (high energy) edge of the unit while relatively lower quality rocks (Rock Types 3 and 4) occur in SW (low energy) portions of the unit. Within these general trends, variations exist in the distributions of permeability. These variations are important as they result in compartmentalization of the reservoir. There are no faults in the NRU--compartmentalization is entirely stratigraphic and is the result of areal variations in the distributions of individual rock types within the reservoir.

ENGINEERING STUDY

In order to verify the results of the rock-log modeling, long-term production and injection data were analyzed using material balance decline type curves, and the results were mapped for comparison to the petrophysical parameter and rock type maps generated from the work summarized above. In addition, the results of pressure transient tests (average reservoir pressure and flow characteristics) were also incorporated to help correlate the reservoir rock type and historical performance.

Other applications for the decline curve results are:

- Reservoir delineation, recovery and rate forecasting,
- Maps of reservoir performance potential,
- Estimating efficiency of reservoir drive mechanism(s),
- Analogy with offset properties, and
- Calibrating reservoir simulation models.

Material Balance Decline Type Curve Analysis

An initial study of the 40- and 20-acre producing wells, and 20-acre water injection wells was performed using rigorous material balance decline type curve methods (Doublet et al., 1994; Doublet and Blasingame, 1996). The goals of these analyses were:

- To analyze long-term production data as well as injection rate and pressure data to evaluate reservoir performance.
- To provide the same flow characteristics associated with the acquisition of field data and without well "downtime."

The results of these analyses include the following:

- In-place fluid volumes:
  - Contacted original oil-in-place,
  - Movable oil or injectable water at current conditions, and
  - Reservoir drainage or injection area.
- Reservoir properties (based on performance):
  - Skin factor for near-well damage or stimulation, *s*, and
  - Formation flow capacity based on production performance, *kh*.

Examples of the decline type curves for both unfractured and hydraulically-fractured wells are shown in Figures 14 and 15.

The results of the analyses performed on the 40-acre and 20-acre producing wells are presented in this work. We focused on using data that operators acquire as part of normal field operations (*e.g.*, production rates from sales tickets and pressures obtained from permanent surface and/or bottomhole gauges). In most cases, these will be the only data available in any significant quantity, especially for older wells and marginally economic wells, where both the quantity and quality of any types of data are limited.

This approach of using production and injection data eliminates the loss of production that occurs when wells are shut in for pressure transient tests, and provides analysis and interpretation of well and field performance at little or no cost to the operator. This technique allows us to evaluate reservoir properties quickly and easily, and provides us with an additional method for locating the most productive areas of the reservoir.

The results of the decline type curve analyses were used to generate reservoir quality maps of contacted original oil-in-place (OOIP), permeability-thickness (*kh*), and estimated ultimate

recovery (EUR) for both the original 40-acre (primary), and 20-acre (secondary) producing wells as shown in Figures 16-19.

Pressure Transient Analysis

A unit-wide pressure transient data acquisition program was initiated prior to 10-acre infill drilling. The purpose of this study was to:

- Obtain sufficient data for a representative comparison with tests recorded prior to the initiation of water injection,
- Provide additional data for simulation history matching,
- Estimate completion/stimulation efficiency,
- Identify the best areas of the reservoir with regard to pressure support, and
- Identify any other major problems related to waterflood sweep efficiency.

Our data acquisition program consisted of taking 10 pressure buildup tests (on producing wells) and 13 pressure falloff tests (on injection wells). The locations for these tests were well distributed throughout the unit in order to obtain a representative, unbiased sampling.

The estimated formation flow characteristics (permeability, skin factor, fracture half-length) compare very well with the results from the pre-waterflood transient tests. The major difference we noted was the relative change in average reservoir pressure throughout the unit after eight years of continuous water injection. Reservoir pressure maps for the 1988 and 1995 tests (from pressure buildup and falloff tests) are shown in Figures 20 and 21.

COMPARING GEOLOGICAL AND PETROPHYSICAL PROPERTIES WITH HISTORICAL PERFORMANCE

If the pore modeling and rock typing exercises are performed properly, the resulting rock type and permeability distributions associated with the reservoir should mirror the historical production performance. The petrophysical parameter and rock type maps resulting from our geological/petrophysical study were compared to the performance maps derived from the results of decline type curve analyses and pressure transient tests. This provided us with a rapid, cost-effective, and accurate method for targeting infill well locations at the NRU. The results of these comparisons are outlined in the section below.

From Figure 12, we note that the thickest reservoir intervals in HFU #12 (Lower Clear Fork) lie in a NW-SE trend along the northern edge of the unit which correlates to the region in which high energy deposits (shoals, sand flat, forebank) dominated. Porosity is also well developed along this same trend (Figure 12B). There is moderate porosity development in discrete locations within the interior of the unit, primarily to the southwest where low energy deposits (supratidal, tidal flat, lagoon) dominate.

Looking at permeability development within this layer, we note a relatively low concentration of good permeability rock in the lower energy deposits, but very good permeability characteristics along the NW-SE trend in which the higher energy deposits dominate. Hydrocarbon pore volume (HPV) is most pronounced in the same area, however, there are also some fairly good accumulations within the unit's interior that correspond to porosity development.

It is worth noting that the primary reservoir rock types (Rock Types 1 and 2) are most prevalent along the same NW-SE trend on the northern edge of the NRU. Rock Type 3 is dominant in the southern interior of the unit along a roughly E-W trend, in an area of relatively poorer porosity and permeability characteristics (Figure 13).

Examining the reservoir performance maps generated from decline curve analyses (Figures 16-19), we note that the highest accumulation of contacted oil-in-place and the best regions with regard to ultimate recovery are in the same regions as those possessing good permeability and porosity characteristics and large volumes of Rock Types 1 and 2.

The producing mechanisms in the southwestern section of the unit in which Rock Type 3 is dominant are much more complex. We note from Figures 16-17 that there is a considerable volume of producible oil within this region although it is not as prolific as the trend along the northern edge of the unit. The flow capacity, $(k_o h)$, estimated from decline curve analysis of the 40-acre primary producing wells indicates a fairly continuous, moderate permeability trend across the southern part

part of the unit. The waterflood response in this area could have been predicted before water injection was initiated, based on the type of rock-log modeling used in this study. As can be seen in Figure 19, the ultimate recovery in the 20-acre producing wells due to water injection will be very good. We note from Figures 12B,D and Figures 16-17 that there were hydrocarbons initially in place, and Rock Type 3 does have sufficient permeability and porosity to contribute significantly to total production.

Producing wells in areas of the unit in which Rock Types 1 and 2 are prevalent usually produce at high total fluid rates with fairly high water cuts (60-90%). Producing wells in areas in which Rock Type 3 is dominant usually produce at fairly low total fluid rates with very low water cuts (20-40%). Based on this information, we are of the opinion that the producing characteristics of individual wells are also a direct function of the local rock type distribution.

Comparing the rock type maps made as part of the geologic study (Figure 13) with the average reservoir pressure maps, we note that the reservoir depleted (Figure 20) and recharged (Figure 21) along the same geologic trends noted above. The regions of the reservoir with the highest quality rock are at a relatively low pressure due to increased fluid production as a result of greater continuity and higher permeability. The converse is true in the areas of lower reservoir quality within the central regions of the unit where the reservoir was never really depleted due to a lack of continuity and overall reservoir quality. Therefore, we believe that the reservoir has depleted and recharged in accordance with its rock type distribution (*i.e.*, reservoir quality).

Optimizing Well Completions and Stimulations At The NRU

Another benefit of the specific type of geologic analyses performed on the new and existing whole core was the more accurate targeting of discrete producing intervals within the 1,400 ft Glorieta/ Clear Fork section. For the most part these intervals coincide with zones containing a predominance of Rock Type 1 (that this is the main pay rock type). These are zones of relatively high permeability and porosity, which are separated by larger intervals of lower permeability and porosity rock that act as barriers or source beds for the higher quality reservoir sections. At North Robertson, these discrete productive intervals include:

- Lower Clear Fork: ±7,000-7,180 ft
- Middle Clear Fork: ±6,350-6,500 ft
  ±6,770-6,900 ft
- Upper Clear Fork: ±6,160-6,250 ft

Since all wells at the North Robertson Unit are hydraulically-fractured before they are placed on production or injection, knowledge concerning the distribution of porosity and permeability is of paramount importance. If the vertical extent of the completion interval can be reduced, then the completion efficiency can be increased and completion costs can be decreased.

The result of these improved completion techniques is shown in Figure 22. For the 18 10-acre infill wells drilled during 1996, total unit production has increased over 30 percent, while the total well count was increased by only 7 percent. The average three-month initial potential (IP's) for these new infill wells are two to three times greater than the IP's from the previous drilling and completion programs at the NRU.

CONCLUSIONS

One of the principal objectives of this study is to identify useful and cost-effective methods for the exploitation of the shallow-shelf carbonate (SSC) reservoirs. The techniques presented herein for the formulation of an integrated reservoir description, can be applied in all oil and gas reservoirs. However, these techniques have proven particularly useful in the NRU, a heterogeneous, low permeability carbonate reservoir. Based on the results of this study, we conclude that:

1. Measurement of pore geometry parameters allows for the improved prediction of permeability and permeability distribution from wireline logs in partially cored intervals, and in adjacent uncored wells. This approach improves the prediction of reservoir quality in non-cored intervals and results in improved well completions and EOR decisions.

2. Detailed pore geometry attributes allow for better definition of hydraulic flow units. These attributes can be related to well log responses, which allows for the development of a field-wide, log-based reservoir model.
3. The material balance decline type curve techniques summarized in this work provide very good estimates of reservoir volumes (total and movable), and reasonable estimates of formation flow characteristics. Using this approach to analyze and interpret long-term production and injection data is relatively straightforward and can provide the same information as conventional pressure transient tests, without the associated costs of data acquisition, or loss of production.
4. Comparison of geological and petrophysical parameters with historical production performance data, reveals that the producing characteristics of individual wells are a direct function of the local rock type distribution. The reservoir depletes and re-pressures as a function of reservoir quality (rock type), throughout all areas of the unit.
5. We identified regions in the unit with additional reserves potential (accelerated or incremental), as well as those areas in which infill drilling is not likely to be economic.
6. Uniform infill drilling is neither prudent, nor warranted, given the stratigraphic compartmentalization and irregular permeability distributions in this, and similar reservoirs. Infill drilling should be restricted to:
   a) Areas of the field that exhibit Rock Types 1, 2, and 3 as dominant, with good permeability and hydrocarbon pore volume (HPV) characteristics, high primary and secondary recovery, and
   b) Areas of poor reservoir continuity with acceptable porosity and permeability values, with a significant abundance of Rock Types 1, 2, or 3, and good primary, yet poor secondary recovery characteristics.
7. If the productive intervals within the reservoir can be better defined based on core and well log analyses, then completion efficiency (initial potential and reserves recovery) can be increased and completion costs can be decreased.

REFERENCES CITED

Archer, J.S. and Wall, C.G.: Petroleum Engineering Principles and Practice, Graham and Trotman, Ltd. (1986) 362.

Calhoun, J.C.: Fundamentals of Reservoir Engineering, Univ. Oklahoma Press, Norman, Oklahoma (1960) 426.

Clelland, W.D. and Fens, T.W.: "Automated rock characterization with SEM/Image analysis techniques", SPE Formation Evaluation (1991) v. 6, No. 4, 437-443.

Doublet, L.E., Pande, P.K., McCollum, T.J. and Blasingame, T.A.: "Decline curve analysis using type curves--analysis of oil well production data using material balance time: application to field cases," SPE Petroleum Conference and Exhibition of Mexico, Veracruz, Mexico, Paper 28688 (1994).

Doublet, L.E. and Blasingame, T.A.: "Evaluation of injection well performance using decline type curves," SPE Permian Basin Oil and Gas Recovery Conference, Midland, Texas, Paper 35205 (1996).

Ehrlich, R. and Davies, D.K.: "Image analysis of pore geometry: relationship to reservoir engineering and modeling", Proc. SPE Gas Technology Symposium, Dallas, Texas, Paper 19054 (1989) 15-30.

Li, Y. and Wardlaw, N.C.: "The influence of wettability and critical pore-throat size ratio on snap-off", J. Colloid and Interface Sci. (1986) v. 109, 461-472.

Pande, P.K.: "The NRU-DOE prospectus", Fina Oil and Chemical Co., Midland, Texas (1995).

Thomeer, J.H.: "Air permeability as a function of three pore-network parameters," Journal of Petroleum Technology (1983) v. 35, 809-814.

Wardlaw, N.C.: "Pore geometry of carbonate rocks as revealed by pore casts and capillary pressure", AAPG Bull. (1976) v. 60, 245-257.

Wardlaw, N.C. and Cassan, J.P.: "Estimation of recovery efficiency by visual observation of pore systems in reservoir rocks", Bull, Can. Pet. Geol. (1978) v. 26, 572-585.

Wardlaw, N.C.: "The effects of pore structure on displacement efficiency in reservoir rocks and in glass micro models", SPE Paper 8843, First Joint SPE/DOE Symposium on Enhanced Oil Recovery, Tulsa, Oklahoma (1980) 345-352.

Table 1 - Pore Type And Classification At The NRU

Pore Type	Size, μm	Shape	Coordination Number	Aspect Ratio	Pore Arrangement	Geologic Description
A	30-100	Triangular	3-6	50-100:1	Interconnected	Primary interparticle
B	60-120	Irregular	<3	200:1	Isolated	Shell molds and vugs
C	30-60	Irregular	<3	100:1	Isolated	Shell molds and vugs
D	15-30	Polyhedral	~6	<50:1	Interconnected	Intercrystalline
E	5-15	Polyhedral	~6	<30:1	Interconnected	Intercrystalline
F	3-5	Tetrahedral	~6	<20:1	Interconnected	Intercrystalline
G	<3	Sheet/slot	1	1:1	Interconnected	Interboundary sheet and intercrystalline pores

Table 2 - Capillary Characteristics By Rock Type Based On Mercury Injection

Rock Type	Entry Pore Throat Radius, μm	Displacement Pressure, psia	Ineffective Porosity (porosity invaded by Hg at p_c > 500 psia), %
1	7.6-53.3	2-10	8.2-29.6
2	2.7-3.6	30-40	23.1-49.5
3	0.4-1.3	80-300	61.6-72.3
4*	1.8	60	88
5	1.1-1.8	60-150	21.7-57.2
6*	0.1	800	100

* - Only one (1) measurement

Table 3 - Porosity, Permeability, And Lithology By Rock Type

Rock Type	Median Porosity, %	Median Permeability, md	Lithology	Reservoir Quality	Cross-flow Barrier Quality
1	4.0	0.70	Dolostone	Excellent	Poor
2	5.6	0.15	Dolostone	Good	Poor
3	3.5	0.39	Dolostone	Moderate	Moderate
4	7.5	0.01	Dolostone	Poor	Moderate
5*	5.8	0.40	Limestone	Good (water-bearing)	Poor
6	1.0	<0.01	Anhydritic Dolostone	None	Good
7	2.3	<0.01	Silty Dolostone	None	Good
8	--	--	Shale and argillaceous dolostone	None	Good

* - Structurally low and wet at the NRU

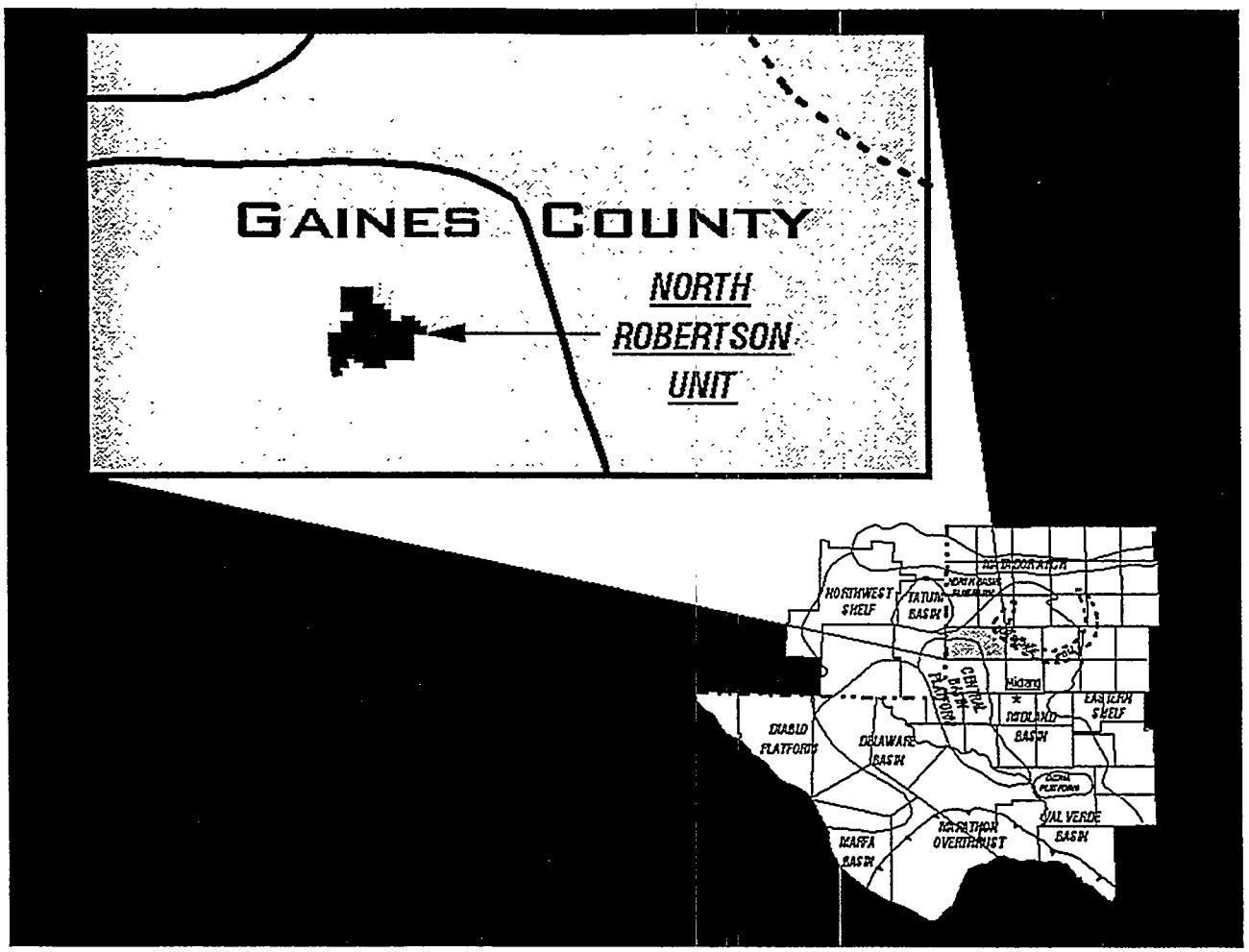

Figure 1 - Regional map showing location of the North Robertson (Clear Fork) Unit.

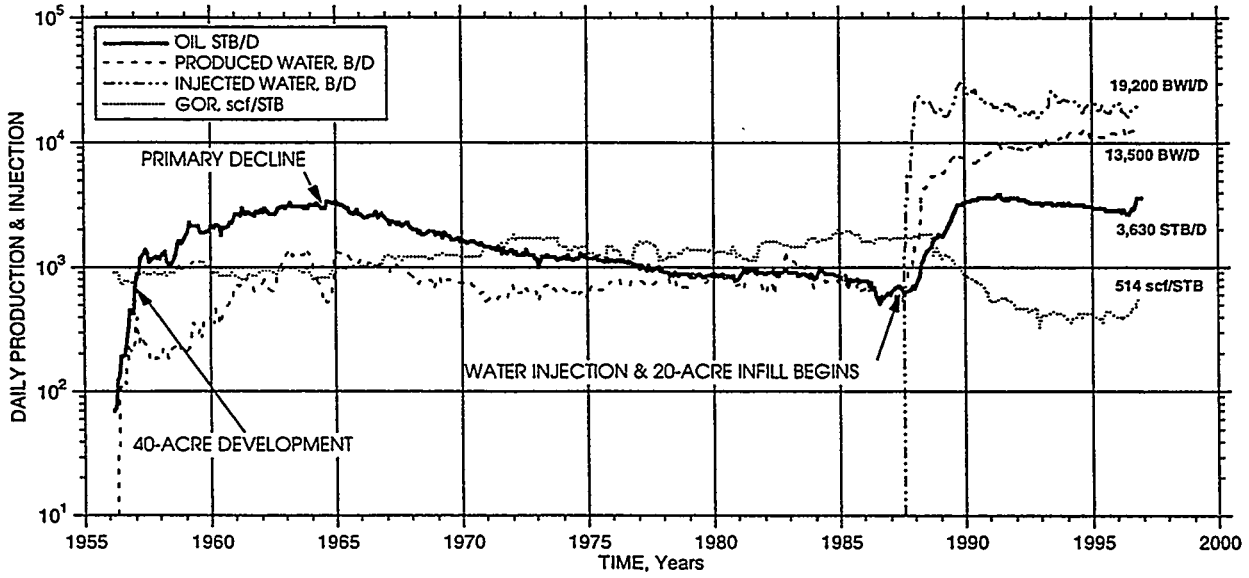

Figure 2 - NRU production and injection history.

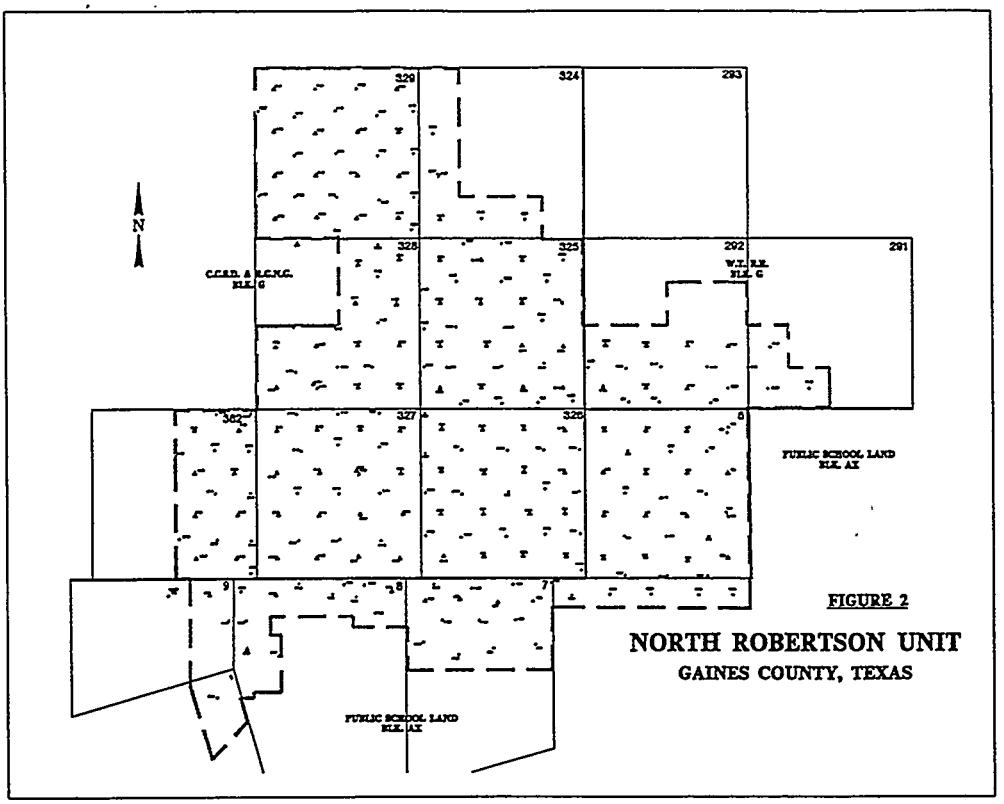

Figure 3 - North Robertson Unit - well configuration.

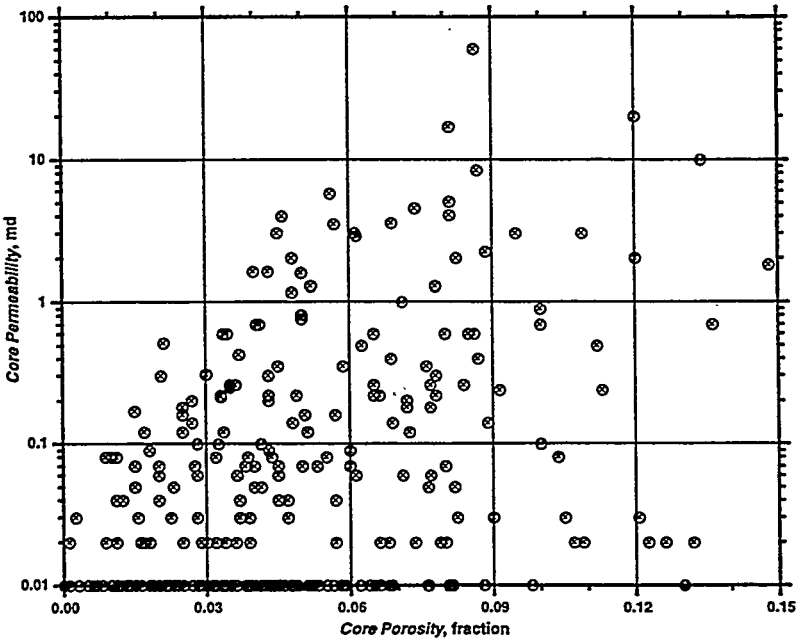

Figure 4 - Porosity-permeability relationships - all core data.

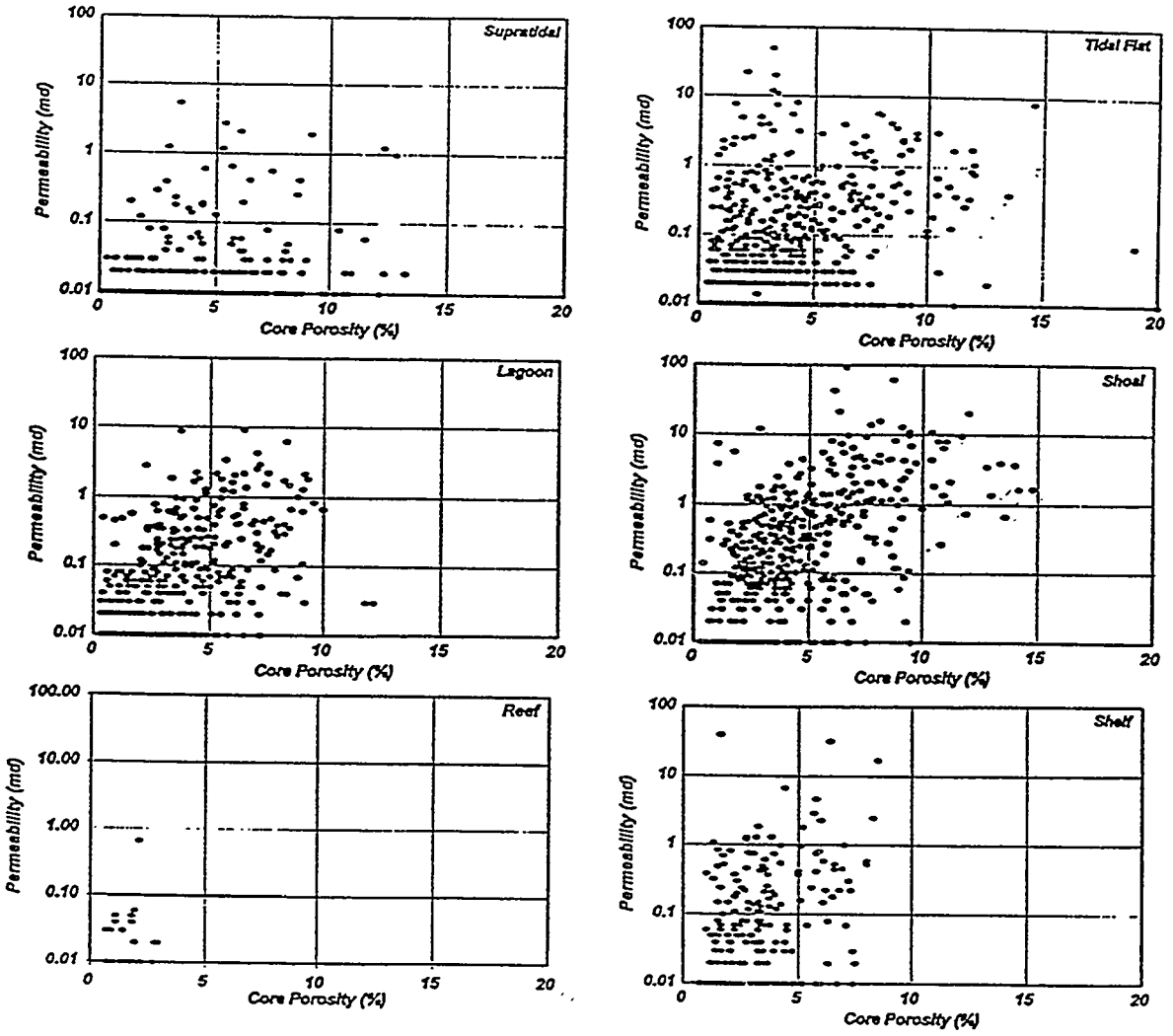

Figure 5 - Porosity and permeability for principal depositional environments.

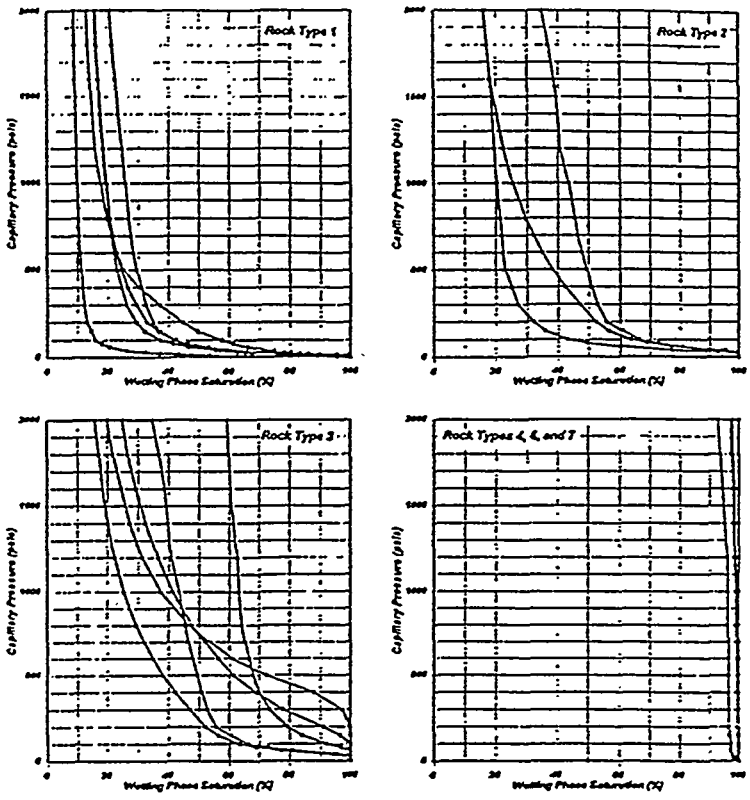

Figure 6 - Capillary pressure curves by rock type.

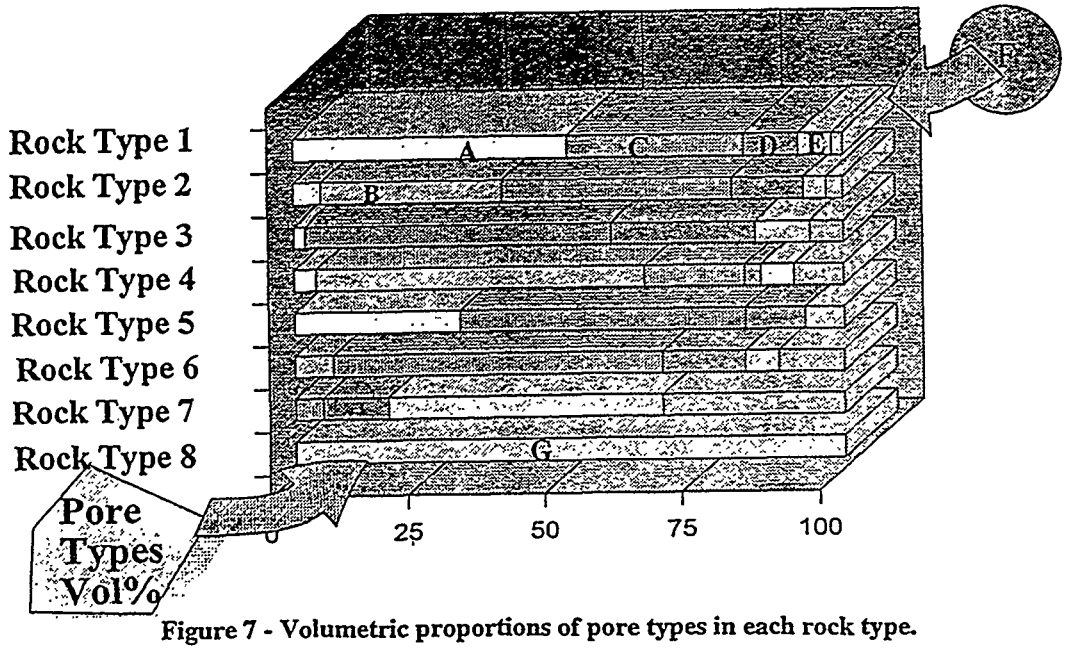

Figure 7 - Volumetric proportions of pore types in each rock type.

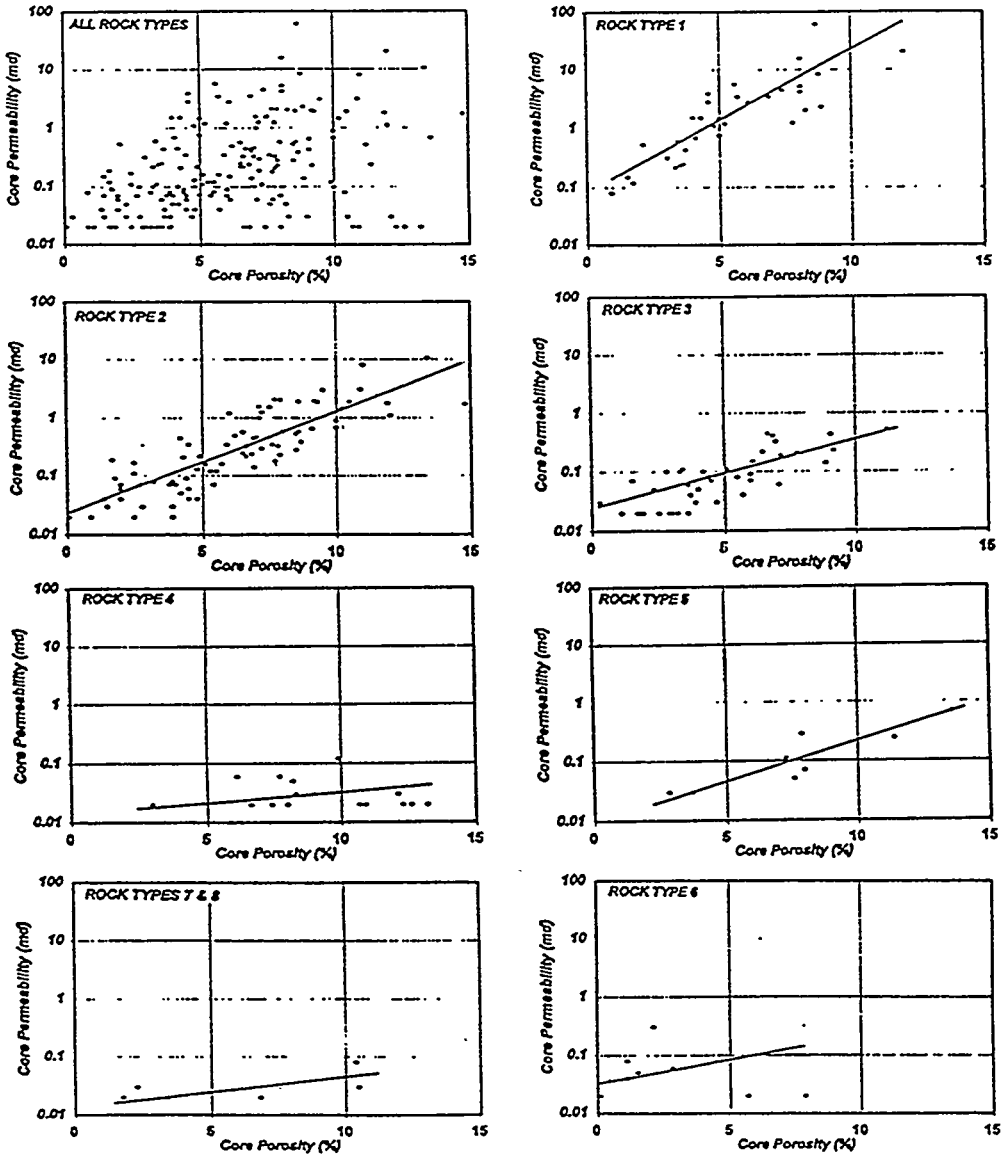

Figure 8 - Porosity and permeability by rock type

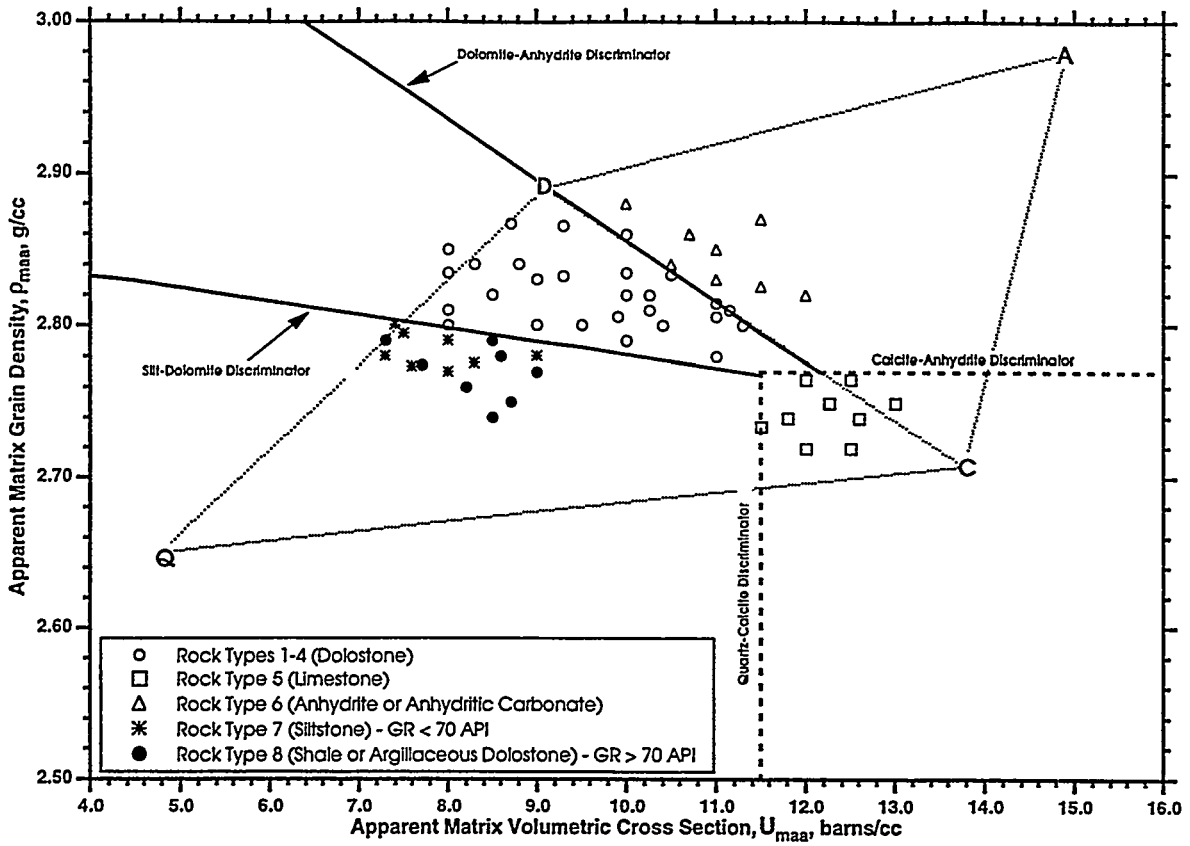

Figure 9 - Differentiating "pay" from "non-pay" reservoir rock.

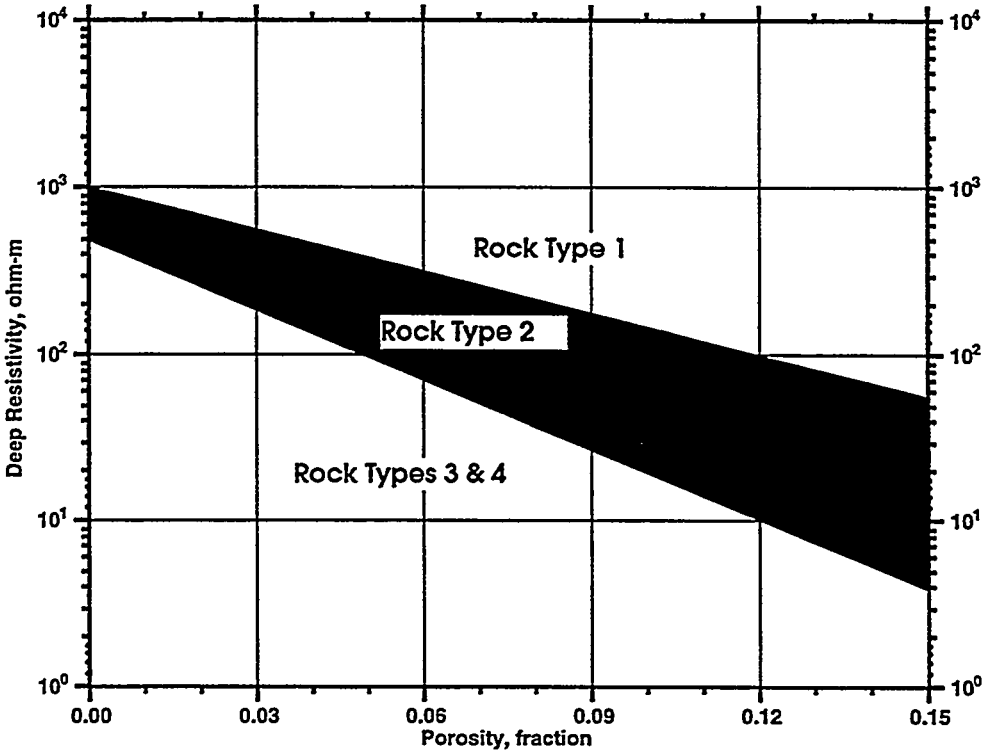

Figure 10 - Differentiating between "pay" rock types 1-3.

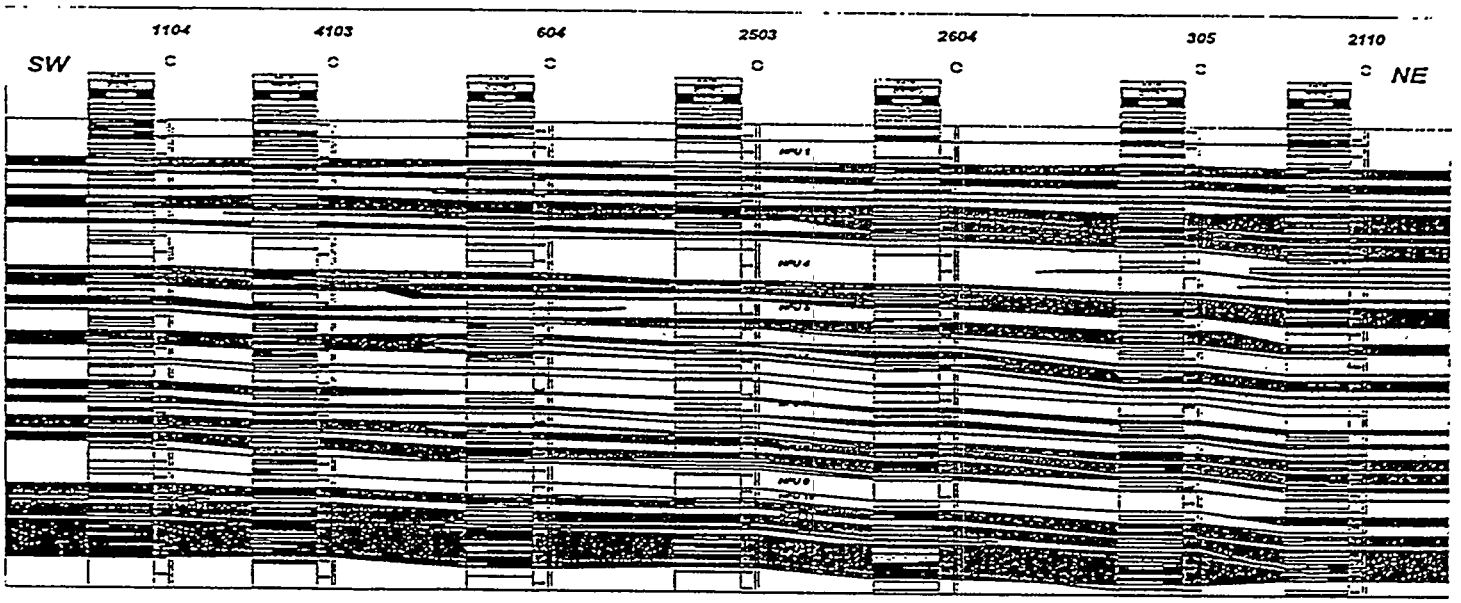

Figure 11 - Cross-section of NRU showing distribution of HFU's. Dark zones are Rock Types 1 and 2. Light zones are Rock Types 3, 4, 6, 7, and 8.

Figure 12 - Contour map of HFU #12 showing distribution of: (A) thickness, (B) ϕh, (C) kh, and (D) HPV.

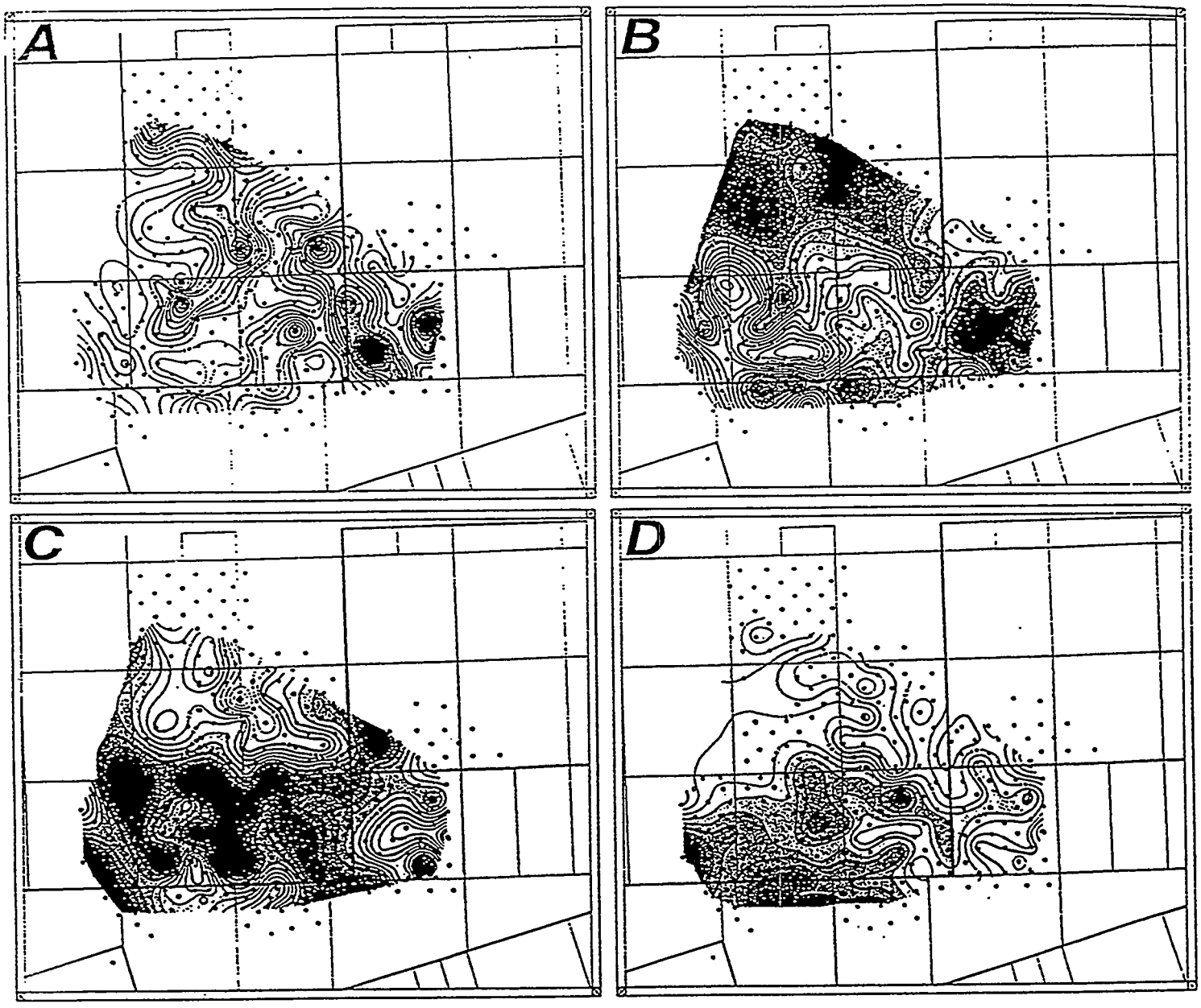

Figure 13 - Contour map of HFU #12 showing distribution of Rock Types 1-4. Note: Darker areas have higher values than lighter areas.

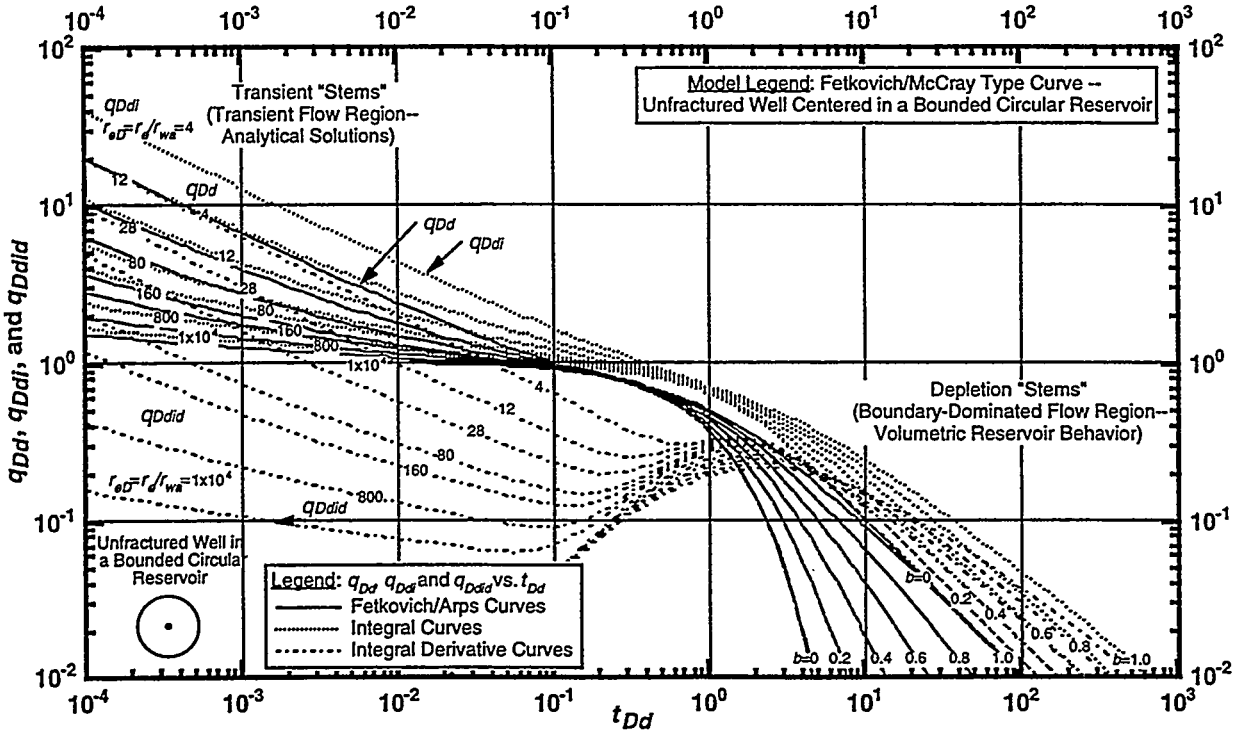

Figure 14 - **Fetkovich/McCray decline type curve for an unfractured well (q_{Dd}, q_{Ddi}, and q_{Ddid} versus t_{Dd} solutions).**

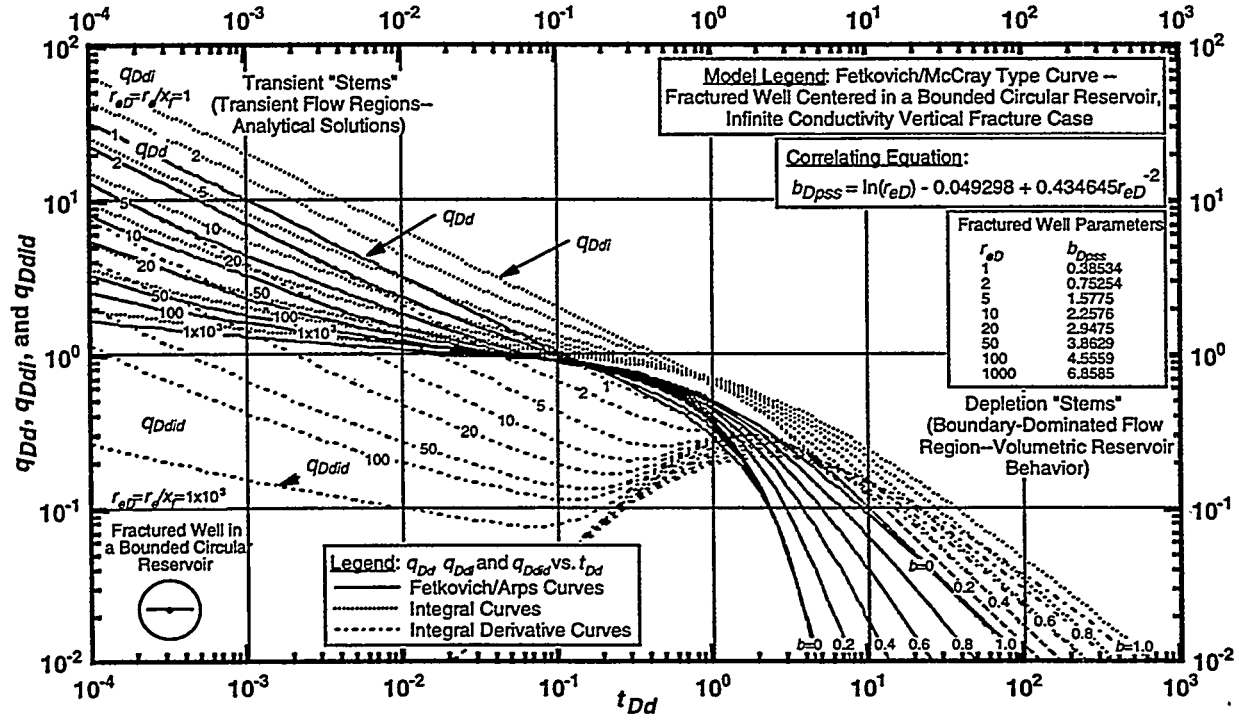

Figure 15 - **Fetkovich/McCray decline type curve for a well with an infinite conductivity vertical fracture (q_{Dd}, q_{Ddi}, and q_{Ddid} versus t_{Dd} solutions).**

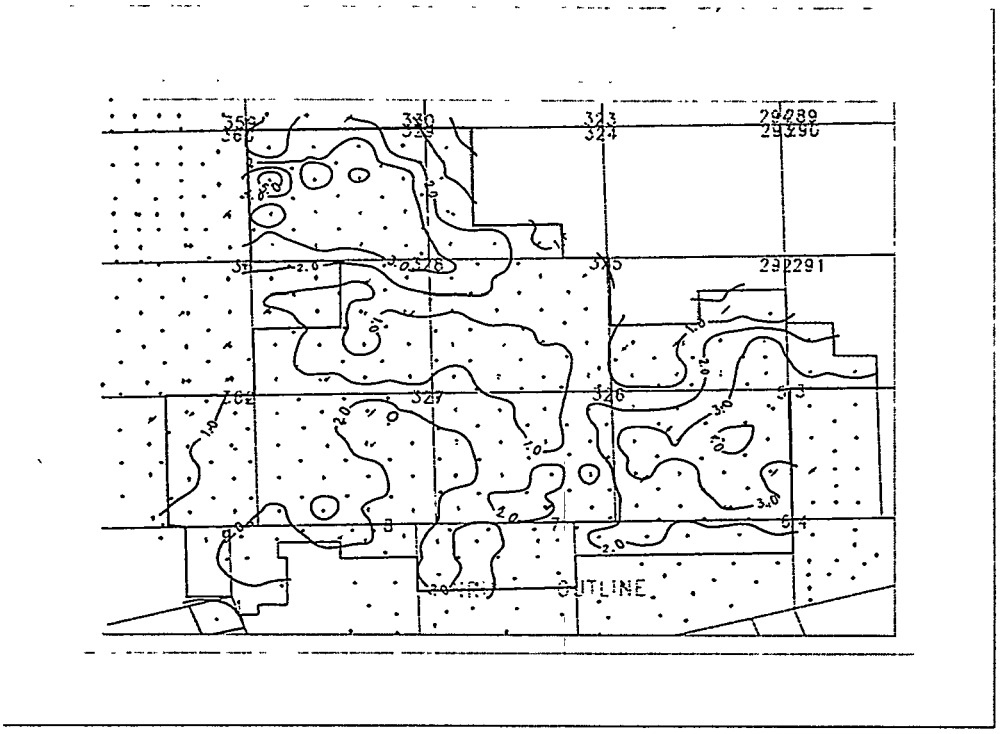

Figure 16 - Map of forty-acre well contacted oil-in-place (OOIP) from decline curve analysis (CI = 1.0 mil. bbls).

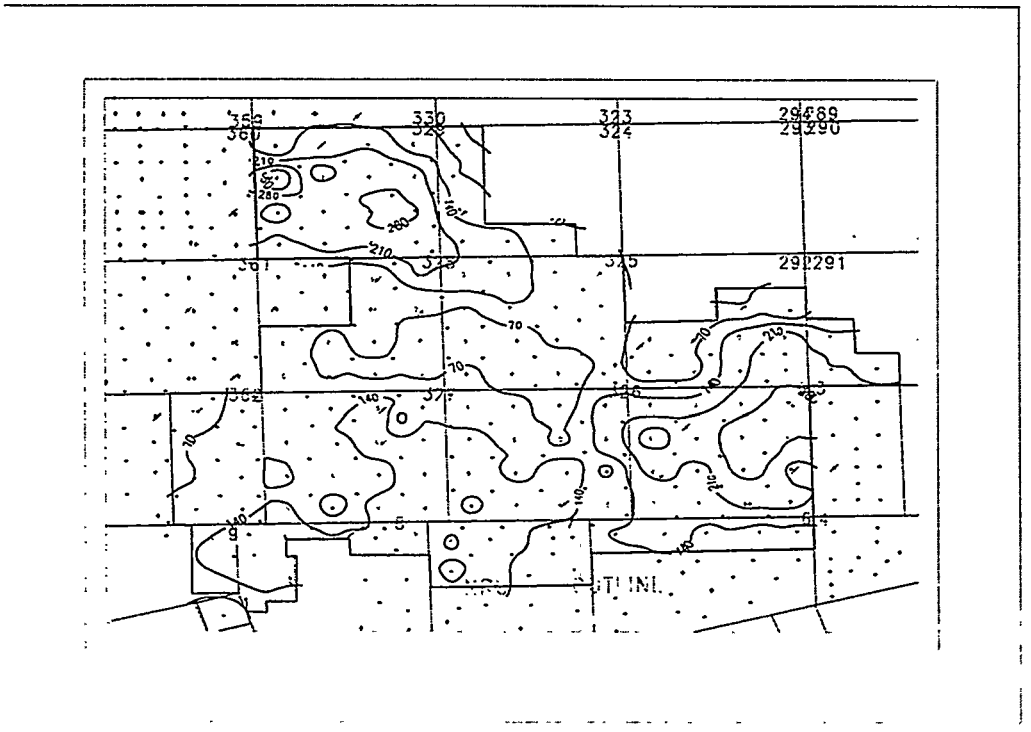

Figure 17 - Map of forty-acre well estimated ultimate recovery (EUR) from decline curve analysis (CI = 70x10^3 bbls).

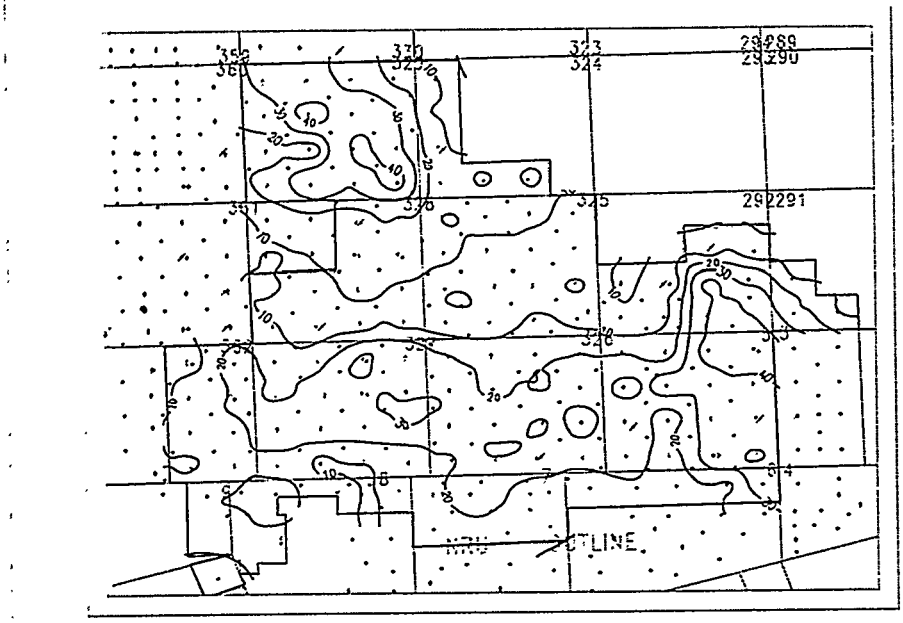

Figure 18 - Map of forty-acre well flow capacity ($k_e h$) from decline curve analysis (CI = 10md-ft).

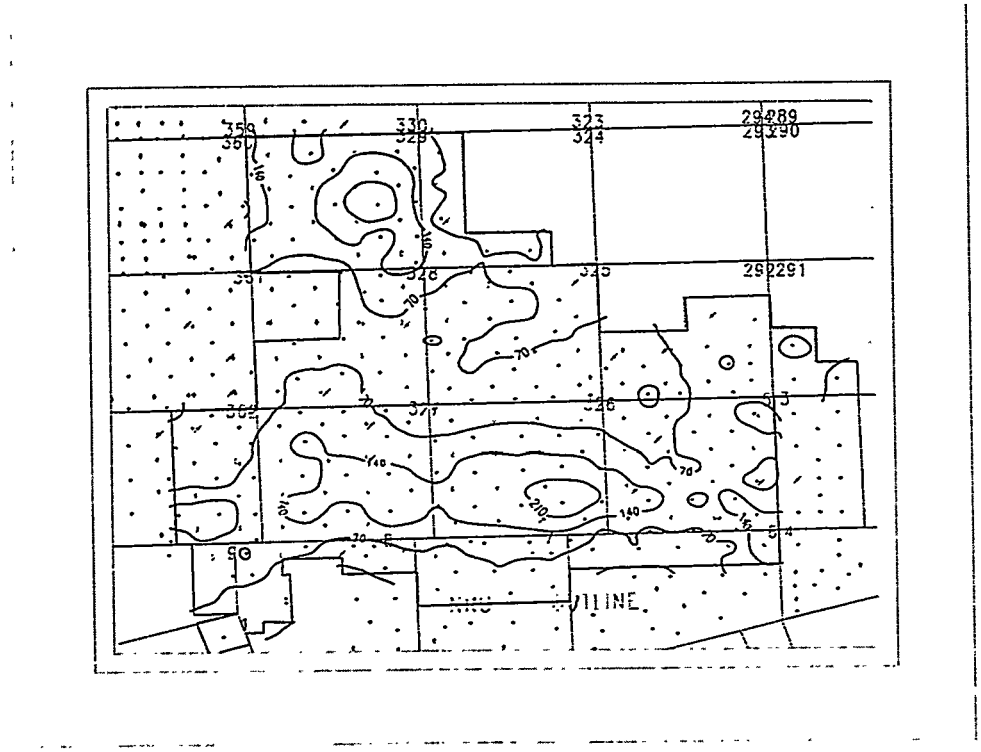

Figure 19 - Map of twenty-acre well est. ultimate recovery (EUR) from decline curve analysis (CI = 70x10^3 bbls).

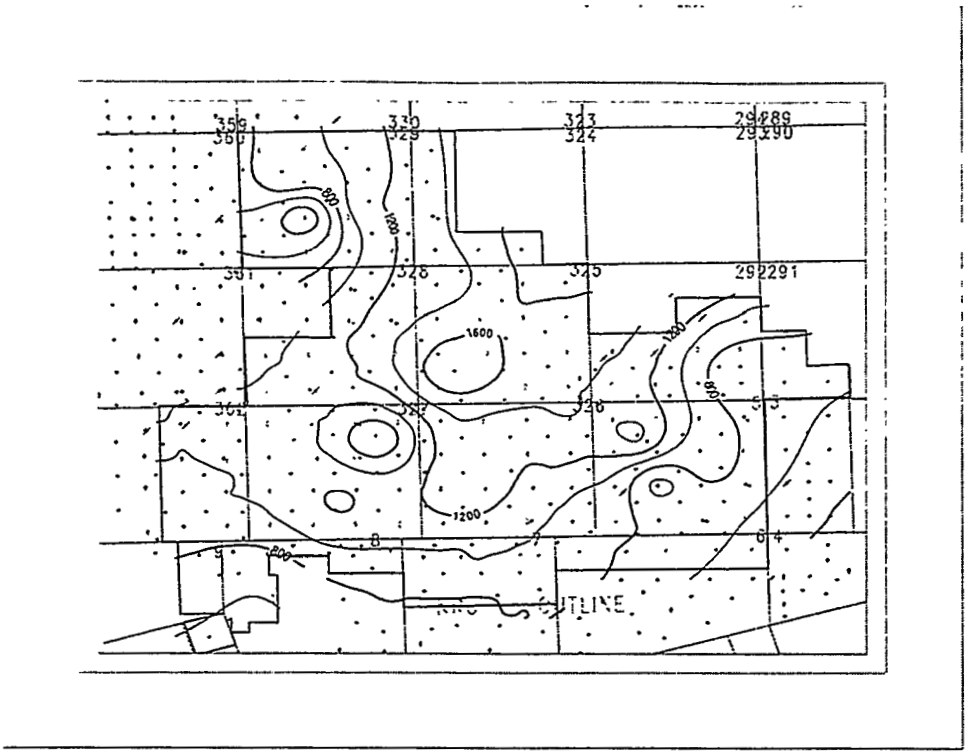

Figure 20- Map of 1988 average reservoir pressure from pressure transient tests (CI = 200 psia).

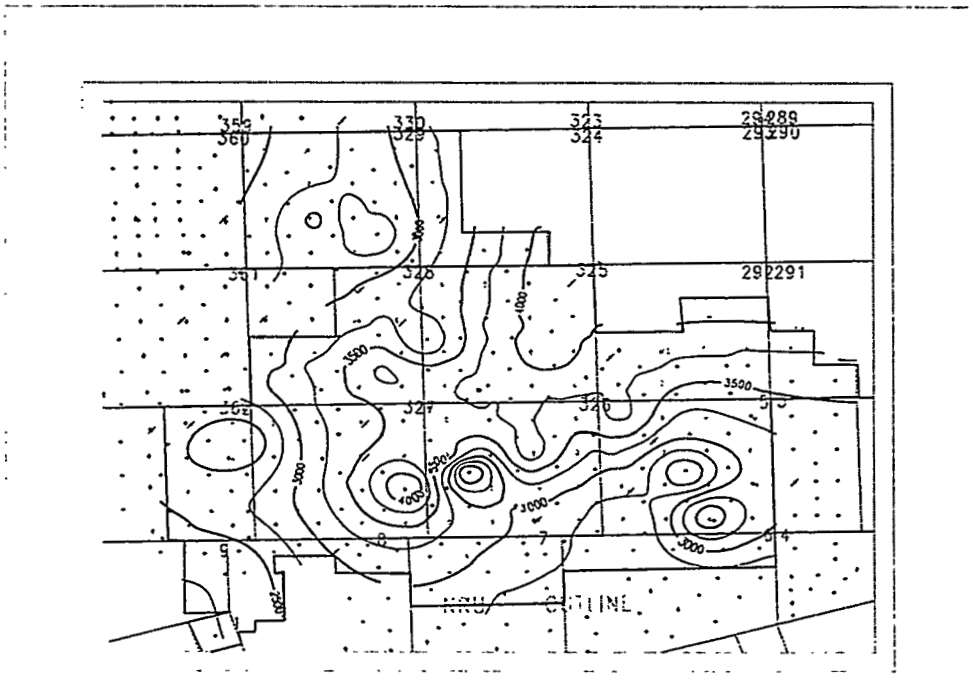

Figure 21- Map of 1995 average reservoir pressure from pressure transient tests (CI = 250 psia).

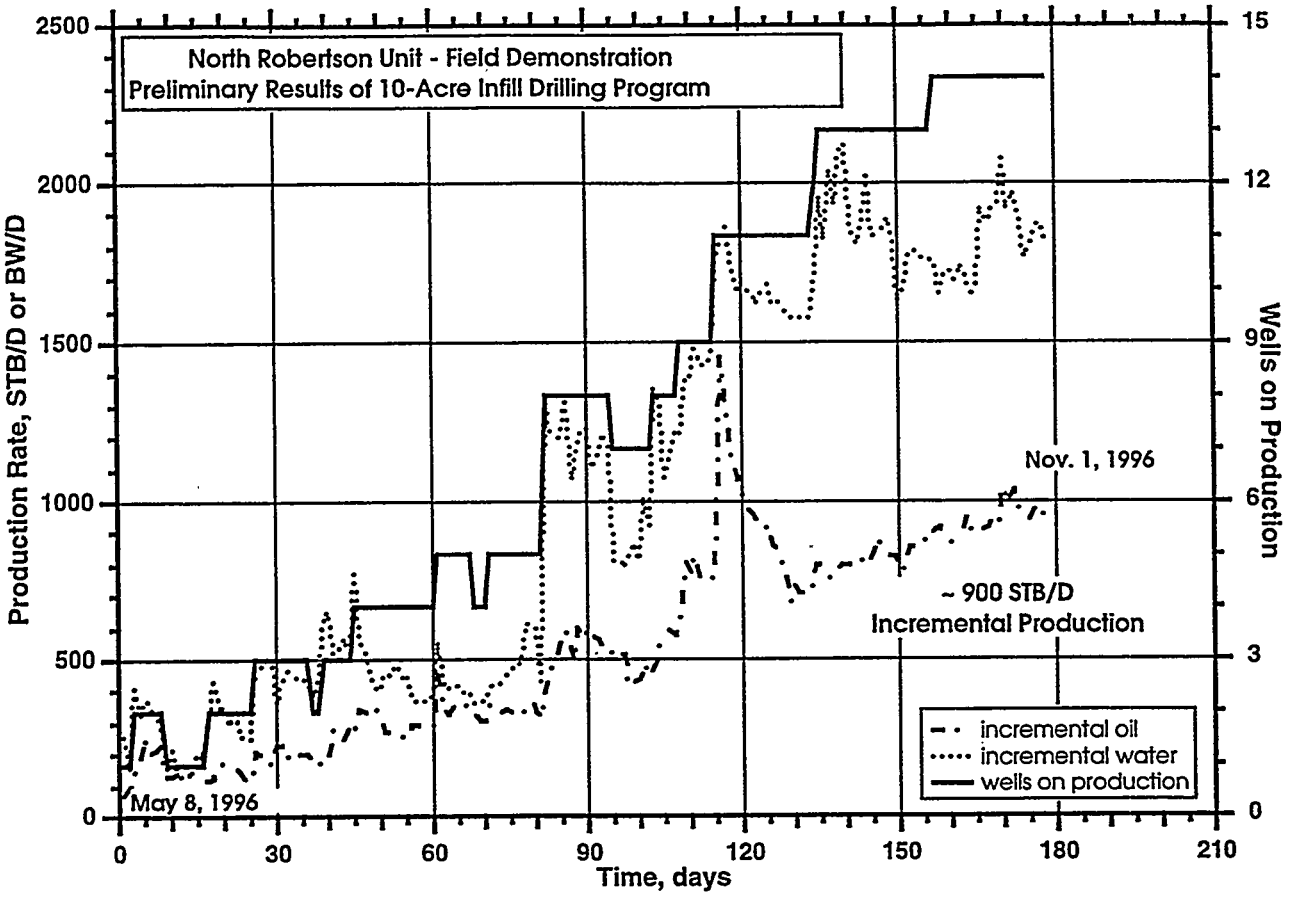

Figure 22 - Preliminary Ten-Acre Infill Well Results (November 1996).

The Role of Reservoir Characterization in the Reservoir Management Process (as Reflected in the Department of Energy's Reservoir Management Demonstration Program)

Michael L. Fowler, BDM-Petroleum Technologies, P.O. Box 2543, Bartlesville, Oklahoma, 74005
Mark A. Young, Michael P. Madden, BDM-Oklahoma, P.O. Box 2565, Bartlesville, Oklahoma, 74005
E. Lance Cole, Petroleum Technology Transfer Council, P.O. Box 246, Sand Springs, Oklahoma, 74063

ABSTRACT

Optimum reservoir recovery and profitability result from guidance of reservoir practices provided by an effective reservoir management plan. Success in developing the best, most appropriate reservoir management plan requires knowledge and consideration of (1) the reservoir system including rocks, fluids, and rock-fluid interactions (i.e., a characterization of the reservoir) as well as wellbores and associated equipment and surface facilities; (2) the technologies available to describe, analyze, and exploit the reservoir; and (3) the business environment under which the plan will be developed and implemented.

Reservoir characterization is the essential to gain needed knowledge of the reservoir for reservoir management plan building. Reservoir characterization efforts can be appropriately scaled by considering the reservoir management context under which the plan is being built. Reservoir management plans de-optimize with time as technology and the business environment change or as new reservoir information indicates the reservoir characterization models on which the current plan is based are inadequate.

BDM-Oklahoma and the Department of Energy have implemented a program of reservoir management demonstrations to encourage operators with limited resources and experience to learn, implement, and disperse sound reservoir management techniques through cooperative research and development projects whose objectives are to develop reservoir management plans. In each of the three projects currently underway, careful attention to reservoir management context assures a reservoir characterization approach that is sufficient, but not in excess of what is necessary, to devise and implement an effective reservoir management plan.

INTRODUCTION

In discussing the definition of reservoir characterization at the first meeting of the organizing committee for the first International Reservoir Characterization Technical Conference in Dallas, Texas in 1985, the attendees, who represented a wide spectrum of technical backgrounds, decided on the following definition: "Reservoir characterization is a process for quantitatively assigning reservoir properties, recognizing geologic information and uncertainties in spatial variability." (Lake and Carroll, 1986). Traditionally, reservoir characterization has aimed at the quantitative transfer of information on reservoir property distribution with a sufficient level of detail and accuracy to a numerical simulator so that fluid flow simulation predictions would match reservoir performance. Through simulation, an appropriately detailed and accurate model of reservoir property distribution will allow the operator to avoid the deleterious effects of heterogeneities and/or exploit them to best economic advantage. To the extent that the information supplied to the simulator is incomplete, inaccurate, or at an inappropriate scale, the ability to predict reservoir performance and maximize economic returns will be lessened.

Reservoir characterization, when appropriately done, is recognized as a valuable tool to avoid costly errors in reservoir decision making. Powerful reservoir characterization tools and techniques have evolved since that first conference in 1985, and new tools and techniques continue to be developed, tested, and refined, but efficient and cost-effective reservoir characterization is still more commonly viewed as an art rather than as a science. Operators have often found it difficult to prescribe and construct at an acceptable cost an appropriate reservoir characterization model in terms of its degree of detail (resolution) and its associated degree of uncertainty.

Characteristics of the reservoir characterization model are a function of the purpose of the model, which in turn depends strongly on the reservoir management context in which the model is to be applied. A proper understanding of reservoir management is therefore fundamental to performing appropriate reservoir characterization. The primary goal of this paper will be to identify the role of reservoir characterization in reservoir management and to elucidate the factors that determine the type of reservoir characterization model necessary for a given reservoir management situation.

The relationship between reservoir characterization and reservoir management has been explored by the authors under the auspices of the Department of Energy's Reservoir Management Demonstration Program by review of extensive literature on reservoir management and by participation in program projects with a variety of small independent operators. Two of these projects will be used as examples to show appropriate scaling of reservoir characterization efforts in reservoir management. Much was also learned about the relationship between reservoir

characterization and reservoir management from observation and study of field demonstration projects being carried out under the Department of Energy's Reservoir Class Program and from the authors' experience in industry reservoir management and reservoir characterization projects performed in the context of major and independent oil companies.

RESERVOIR MANAGEMENT, PERCEPTIONS VS REALITIES

Misconceptions about reservoir management abound. Some operators think of reservoir management as something done only to large reservoirs where large improved recovery targets can justify the large investments in time and dollars they see as necessary. Others think of reservoir management as the day-to-day reservoir problem solving activities of reservoir engineers. Yet others, usually those with limited familiarity with new technologies, view reservoir management as a strictly "high-tech" venture involving the application of state-of-the-art new techniques and technologies. And, of course, there are numerous operators of marginally profitable mature reservoirs who think only of reservoir management as an unaffordable expenditure. Fortunately, not all reservoir operators can be categorized with the above examples, but a general atmosphere of conservatism and reluctance prevails, and, as a consequence, the full potential of effective reservoir management has not been realized.

Definition of Reservoir Management

Just as there are many publications on the subject, so are there many definitions of reservoir management to accompany them. Thakur (1991) defined reservoir management as the "judicious use of available resources to maximize economic recovery" Cole et al. (1993) went on to specify that "resources" in the above definition include people, equipment, technology, and money. Other definitions, such as that offered by Wiggins and Startzman (1990), that reservoir management is "application of state-of-the-art technology to a known reservoir system within a given management environment," take a slightly different view. Most definitions, however, focus on identification of the components of reservoir management much as if we were to define an automobile as consisting of engine, wheels, steering mechanism, etc.

Nearly all discussions of reservoir management agree on the following as general characteristics:

- It requires and makes use of resources.
- It is continuous and long-term, over the life of a reservoir.
- It concentrates on economic optimization.

From this, we can surmise that the main activity of reservoir management is a sequence of resource-deployment decisions made to maintain optimum economic recovery of petroleum.

The Plan as a Central Concept

Definitions are valuable in that they serve to enlighten us to the important considerations that are critical to reservoir management activities, but taking a slightly different perspective may help us grasp the concept more completely. Let us assume that every reservoir being operated today, like every business being operated today, is being managed. Some are managed well, and some are without question poorly managed. We can think of well and poorly managed reservoirs and businesses as those that are and are not realizing their maximum potential to their operators, respectively. Every reservoir operator is taking some kind of approach, that is, has some kind of philosophy, guidelines, or strategy that is used to guide his interaction with the reservoir. Formulating these guidelines or plans and following them is the real essence of reservoir management (Cole et al., 1994).

The spectrum of possible approaches, strategies, or plans that might be employed in reservoir management is extremely wide. Some plans may be very simply conceived or literally just assumed. Such a simple and straightforward approach could amount to a stark "produce the reservoir until the total cost of production becomes greater than the revenue obtained, then quit," where "quit" implies either selling the property to an organization with lower overhead costs that can continue to operate the reservoir at a profit or simply abandoning the reservoir. The opposite extreme might be a case in which all the latest improved oil recovery technologies are periodically screened and selected technologies are carefully applied in the context of a complete and detailed 3-D description of the physical and chemical aspects of the subsurface reservoir in an attempt to retrieve substantial dollar amounts of oil in return. Intermediate between the extremes are plans that consist of informal guidelines that may or may not be regularly reviewed for appropriateness. Reservoir management can be thought of as the decision-making process that matches the approach or plan to the reservoir and its operator in such a way as to maximize the profitability of the reservoir to the operator.

Consequences of Plan Mismatch

If close attention is not paid to developing reservoir management plans or guidelines, it is possible to get a poor match between the approach implemented and the reservoir's and/or operator's needs. The most likely consequence of a poor match is a less-than-optimum economic performance. Some common scenarios include:

- *Gambler's ruin* - A company invests capital it cannot afford to lose in a reservoir management project. Not only does the project fail to make a return, but the investment is

lost also.

- *Partial failure* - A moderately profitable reservoir management project is carried out. Returns, however, are not as good as predicted, and other investments available would have done better.
- *Partial success* - A reservoir management project makes a return as good or better than predicted. The reservoir, now depleted to its economic limit, is sold to another operator who makes a windfall from enhanced production.
- *Unrecognized failure* - A reservoir performs as expected under an implemented plan to the projected economic limit. It is then sold to a smaller operator with lower overhead who continues under the same approach. Only the reservoir knows about the millions of dollars of additional revenues that could have been obtained under a different approach.

Because a generally conservative attitude has prevailed toward reservoir management in the past, there is potential for increasing profitability in a large number of petroleum reservoirs. In a majority of cases, this increased profitability could be accompanied by increased recovery as well. Recognizing these facts and in keeping with its mission to increase profitability and recovery from domestic reservoirs to prevent or forestall their abandonment, the Department of Energy is funding a program of reservoir management demonstration projects. The program was initiated in 1995 with the primary objective of improving reservoir management understanding through demonstration and technology transfer. Program projects encourage operators, especially small independent operators, to learn, apply, and disseminate sound reservoir management techniques. Projects are now underway to develop reservoir management plans for a variety of reservoirs managed by small operators. Technology transfer plays a vital role in each of these projects.

CONSTRUCTING AN OPTIMUM RESERVOIR MANAGEMENT PLAN

How can we match the vast number of possible reservoir management approaches to appropriate reservoir situations? The answer is "it is a matter of how well we know (1) the business environment, both internal and external to our company, under which the reservoir management plan will be constructed and implemented, (2) the availability and use of proven and developing technologies, and (3) the reservoir and its facilities (i.e., the reservoir system)" (Fowler et al., 1996). Of particular note is the concept that knowing the context under which reservoir management is to be performed is important as well as knowing about the reservoir itself. The importance of this contextual information will carry over to reservoir characterization planning as well.

Knowledge of the Reservoir Management Business Environment

Reservoir management business environment factors fall into one of two categories: those that are external to the operator's organization (i.e., those that affect all operators equally), and those that are internal and perhaps unique to the operator's organization. No plan can be optimized without paying close attention to both types of factors, and some reservoir management projects fail due to oversights in this area. Furthermore, any of these factors is subject to change at any time, either during the formulation of a reservoir management plan or after it has been implemented. Maintaining an awareness of the consequences of such changes enables plans to be revised to maintain optimum performance.

Examples of external factors that need to be considered include market economics, taxes, operational laws and regulations, safety and environmental laws and regulations, and less tangible items such as public opinions. Internal factors include the organization's ability to raise and/or commit capital and a number of items related to the "corporate culture" of the organization. The latter include factors such as how the company measures value (i.e., is the objective to increase reserves?, to obtain a certain rate of return on investment?, or to achieve some other measure of success?). Other factors might include the organization's attitude toward risk, its organizational structure, and its ability to commit to long term plans (Cole et al., 1993; Wiggins and Startzman, 1990). Some of an organization's internal factors may be pliable and capable of being changed to accommodate the best interests of a reservoir management plan, but some factors may be difficult or impossible to alter. The structure of the reservoir management plan has to acknowledge those factors which cannot be altered.

A Further Note on Organizational and Team Structure

The larger structure of the organization may have a minimal direct impact on reservoir management activities, but there is a general consensus that successful reservoir management requires a team approach. Ideally the team will include all persons who have anything to do with the reservoir (Satter et al., 1992). An organizational structure that encourages the formation of multidisciplinary teams will be much more conducive to creation of optimal reservoir management plans than one that effectively dictates that plans be created by geologists, engineers, and others working sequentially and independently. Satter and Thakur (1994) present an excellent discussion on the structure and function of reservoir management teams.

At project inception, all members should share in developing common project goals and objectives and aid in developing and assigning project responsibilities for each team member. A team leader with the multidisciplinary insight and management skills to encourage cooperative participation in these and subsequent project activities is a necessity.

The dynamic interaction of the group comprising the reservoir management team is a strong contributor to the success of the effort. The team leader must be aware that the members of the team may have varying degrees of technical skill and experience in their own disciplines and may have varying experience in working closely with people from other disciplines. The leader must monitor and nurture the daily interaction of team members. To do so the team leader must be aware of individual personality traits and differences in rank, must be aware that certain team members may have commitments to other projects that may compete for their time and dedication at inconsistent and often inconvenient intervals (though management should do everything possible to minimize conflicts in priorities!), and must realize that occasional disruptions such as loss or addition of team members may inevitably occur.

Knowledge of Available Technologies

A second contextual consideration necessary for creating optimal reservoir management strategies is a familiarity with existing and newly developing technologies that are available to improve hydrocarbon recovery, increase operational efficiencies, and characterize reservoirs. Maintaining an awareness of appropriate technologies in such diverse areas as recovery, wellbore and facilities, and reservoir characterization is a difficult task, especially for smaller organizations. The difficulty of the task is compounded by the rapid evolution of technology in almost every area. Membership and participation in professional societies, attendance at their meetings, and review of their publications may help, but it is not realistic to assume that any organization will have (or should have!) the necessary knowledge and experience in all areas that may be required. A realistic goal would be to obtain enough of a general or screening-level knowledge of available technologies to know when an expert should be consulted for in-depth evaluation. Professional societies and organizations like the regional offices of the Petroleum Technology Transfer Council can often provide contact with the appropriate consulting expertise.

Improved Recovery Technologies

It is important to be aware of routine applications techniques as well as new techniques and technologies associated with improved recovery. Secondary recovery techniques include injection of water or gas (immiscible) for pressure maintenance or displacement of hydrocarbons. Advanced secondary recovery techniques include those aimed at improving contact with mobile oil such as conformance and recompletion considerations, infill drilling using vertical, deviated, and horizontal wells, and employing polymers for profile modification and mobility control. Enhanced oil recovery techniques include application of processes to recover immobile oil such

as microbial, alkaline and alkaline-surfactant-polymer, surfactant, steam, in situ combustion, and miscible and immiscible gas-injection processes. A moderately comprehensive review of technologies associated with advanced secondary and enhanced recovery is presented by Cole et al. (1994).

Wellbore and Facilities Technologies

Familiarity with existing and evolving techniques and technologies associated with wellbore equipment and surface facilities can also bear on formulating an appropriate reservoir management plan. The ability of the mechanical equipment both within wells and on the surface to handle changes in fluid types, volumes, and relative volumes under different pressures and temperatures due to possible changes brought about by a reservoir management project can be critical to its success. New or different technologies and/or techniques may be required to accommodate such changes. In some instances, the focus of a reservoir management plan may be to incorporate new technologies or approaches just to improve performance of facilities and equipment.

Reservoir Characterization Technologies

Successful reservoir management is also dependent on a familiarity with existing and newly developing technologies that are available to characterize reservoirs. Technological knowledge related to the building of reservoir models from both analog and deterministic sources is appropriate, but it is becoming increasingly important to include technologies involved with the collection, handling, integration, and analysis of the large volumes of data that have become associated with reservoir characterization. This does not imply that a high-tech approach is necessarily the appropriate one to take. It is important to be aware of the wide range of both traditional and newly developing technologies available and to have some familiarity with economics involved in assessing and implementing those technologies.

Knowledge of the Reservoir System

The third consideration for reservoir management plan building is a knowledge of the reservoir system. The reservoir system is composed of subsurface reservoir rock, the reservoir's contained fluids, all its wellbores and downhole equipment, and its surface equipment and facilities. Man's activities may have affected any of the components of the reservoir system and should be considered also.

The Physical Reservoir

In the past, the terms "reservoir description" and "reservoir characterization" have been used almost interchangeably. Reservoir description perhaps more aptly connotes collection of descriptive or deterministic data from the reservoir itself. Reservoir characterization, on the other hand, might be thought of as a more comprehensive undertaking employing other information sources such as analog reservoirs, outcrops, and modern environments as well as directly measured data from the subsurface reservoir. The end result of reservoir characterization is a complete conceptual picture or model of the reservoir.

A reservoir characterization model is a representation or estimate of reservoir reality. It represents not only the three-dimensional extent or bounds of the reservoir, but the qualitative (presence or absence) and quantitative (magnitude) values of rock, fluid, and other reservoir parameters affecting fluid flow at every location in the volume of the reservoir. The degree of uncertainty associated with placement and magnitude of fluid-flow properties is an important facet of this model.

An important objective of reservoir characterization model construction is to accurately represent and minimize, as far as economically feasible, the uncertainty in our knowledge of reservoir parameters. In the past, the aim of reservoir characterization generally was to create a single "most probable" representation of the reservoir to be used as input to subsequent decision making, but the need for a small number of more extreme yet reasonably probable representations should be recognized as a useful if not critical addition. This approach allows bracketing the range of reasonably expected recovery and economic outcomes. We can think of the goal of reservoir characterization as the construction of a model or small number of models that will aid in predicting by simulation or other means the outcome or probable range of outcomes of potential reservoir management plans (i.e., projects, processes, or operating plans and procedures) in order to evaluate their relative economic merits.

Deterministic reservoir characterization data (i.e., data derived by actual measurement of reservoir properties rather than derived by analogy from similar reservoirs or deposits) can come from a wide variety of technologies and cover a wide range of scales. Although data are taken directly from the reservoir, uncertainties in many types of information gathered are inherent due to the resolving power of the tool used and the inability of many tools to measure desired properties directly. However, the degree of uncertainty associated with the deterministic, quantitative measurement of reservoir properties is often less than that associated with properties assigned by a model of conceptual or analog origin. Figure 1 schematically depicts the scale of measurement and associated resolving power associated with several common deterministic tools.

A number of geological and engineering tools are commonly available to gather deterministic information from which to formulate a reservoir model. Samples of reservoir rocks and fluids collected early in a reservoir's development history may be the best source of information available to predict fluid-flow patterns that may be critical when the reservoir reaches maturity. Reservoir production and injection data are often-overlooked and inexpensive sources of information on larger scale reservoir architecture and heterogeneities. A wide variety of geophysical wireline logging tools, in addition to having great utility in establishing structural and stratigraphic frameworks, are available to make direct measurements of reservoir properties such as rock composition, porosity, and fluid content. Single- or multiple-well pressure transient tests may be run for the purpose of qualitatively or quantitatively discerning variations in the properties of the reservoir's pore system. Tracer testing, i.e., the addition of small quantities of an easily detectable (often radioactive) material to an injected fluid and the subsequent monitoring of its temporal and/or volumetric appearance in the same or adjacent wells, results in direct measurements of critical well-to-well flow characteristics or estimates of residual oil saturation.

Among existing direct measurement techniques, approaches based on seismic methods perhaps have the greatest potential to provide reliable information on reservoir property variations in the interwell region. Recent advances in several areas of seismic technology are making this possible. The accuracy, resolution, and utility of 3-D seismic are being realized thanks to continuing improvements in data acquisition instrumentation, field procedures, data processing software, and 3-D data visualization techniques. Development of procedures for extracting useful information from attributes of the seismic signal such as amplitude, phase, and frequency facilitate the delineation of stratigraphic traps and other subtle geological features and make it possible to determine the distribution of porosity and fluid content in reservoir rocks. Developments in downhole seismic surveys like cross-well tomography and vertical seismic profiling are adding to resolution capabilities in the interwell area.

The deterministic tools discussed above do not constitute an all inclusive list by any means. Other tools and techniques include electromagnetic mapping, remote sensing, surface geochemical sampling surveys, and any of numerous other approaches that have potential to add to our knowledge of the distribution and movement or potential movement of fluids in the reservoir.

Because a single reservoir characterization model or a small number of such representations is the desired result, and because the necessary data are of both engineering and geological origin, the need for close cooperation between geoscientists, engineers, and other professionals (i.e., the members of the reservoir management team) in formulating such models is paramount. Data from various individual technological sources often suggest a number of nonunique interpretations of reservoir reality. It is the duty of the reservoir management team to

understand and use the various technological data types in complementary and supplementary fashions to arrive at the most probable range of possible reservoir realities upon which to base future reservoir performance predictions. Model construction is not a trivial task, and its successful completion requires continual cooperation and interchange of information and ideas among team members. The task cannot be efficiently accomplished (indeed it may not be accomplishable at all!) if geologists and engineers work on the task sequentially and independently.

Reservoir Infrastructure and History

An additional important aspect of reservoir knowledge is familiarity with the production/injection infrastructure. Natural processes in the subsurface can interact with wellbore equipment resulting in problems such as corrosion, scaling, paraffin deposition, etc. Surface processes, such as erosion or flooding can affect wells and facilities. Knowledge of the history of drilling, completion, recompletion, and workover practices employed in field development as well as familiarity with current surface and wellbore facilities is also necessary. Equally important is a knowledge of past production and injection practices.

Human development activities may certainly affect surface facilities and the use of wellbores. It is also important, however, to know of alterations in the natural properties of the reservoir that have resulted from past human activities. Human activities in development and depletion of a reservoir can have a profound influence on its basic characteristics and thus on its performance. In some cases, human activities are equivalent to introduction of whole new and often extreme episodes of diagenesis, tectonics, and/or fluid exchange. The nature of these changes is unexpected in many instances and can result in decreased reservoir performance and permanent reservoir damage if not considered. Examples might include situations where stimulation practices have led to communication between reservoir units behind pipe, or where long periods of water injection above formation parting pressure have led to channeling between injection and production wells.

Steps in Reservoir Management Plan Construction

One of the key objectives in the Reservoir Management Demonstration Program being sponsored by the Department of Energy has been to resolve the sequence of considerations that goes into the development of an effective reservoir management plan. At this time, only the broadest categories have been identified, but it is hoped that subsequent work on a variety of reservoir management projects under different contexts will enable the procedures to be defined in greater detail with time.

As currently recognized, the primary steps in plan construction are:

Defining the target size

Locating the target

Identifying appropriate technologies

Optimizing technology implementation

Optimizing operational procedures and technologies

An ideal plan will also specify its own limitations based on the conditions and assumptions that were incorporated into its development. The plan may project expected performance by simulation or by other means of all aspects of reservoir performance over the plan's duration (e.g., reservoir wellbore injection and production performance, facilities and equipment usage, environmental and other regulatory compliance, etc.). The plan may specify surveillance and monitoring activities, including data types, collection protocol, database construction, data processing and analysis, and performance variance to be tolerated. The plan may also specify or recommend future plan revisions based on specific criteria such as timing or volume performance of reservoir fluid production or injection. In any event, the plan should be developed so that it is not so rigid as to be inflexible to potential modifications.

These steps are very general and should be applicable whether or not improved recovery is being considered as a reservoir management option. In each step careful attention must be paid to the complete context of reservoir management, i.e., the reservoir system, available technologies, and the business environment. Specific objectives of any plan will depend on the context in which the plan is developed as discussed above, including consideration of the current stage of reservoir development and the type and scale of the decisions required (e.g., evaluation of a potential new process implementation, local production and injection optimization, new facilities or equipment technologies, etc.). A comprehensive reservoir management plan initiated at the time of reservoir discovery will assure early collection of native-state reservoir data vital to implementation of advanced recovery processes many years in the reservoir's future. On the other hand, reservoirs in which data collection has been neglected and reservoirs acquired without adequate accompanying data require a reservoir management plan designed to correct or alleviate the effects of information deficiencies. Ideally, a reservoir management plan or series of plans will provide guidelines over the life of the reservoir.

Target Definition

Defining the target size, whether that target may be the recovery of additional petroleum resources or merely saving dollars associated with addressing chronic production problems or spent on inefficient operating procedures, will help to determine the scale and scope of the plan

being developed as well as help scale the effort expended in constructing the plan. Multiple targets of the same or different types may be addressed by the same reservoir management plan. In fact, this approach should lead to a plan that will optimize the profitability of the reservoir to the operator on several fronts. Often the target or targets can be defined adequately with existing data, but there are instances in which additional information may have to be collected to reduce uncertainty about the target size to an acceptable level. If the target (or one of the targets) is additional recovery, reservoir characterization at least at some general level, will be needed to estimate the quantity of petroleum that might potentially be present unless this information is already available and reliable from previous work.

Target Location

In some cases, the focus of the reservoir management plan will include the entire field, but more often, certain zones or areas of the field will present the best development of the target situation. Additional data may have to gathered on a field-wide scale to locate the target or targets accurately. If additional recovery is the target, questions such as whether the oil is mobile or immobile may also have to be addressed. Reservoir characterization required to answer the questions posed at this stage in plan development will probably be more detailed than that required to estimate the size of the recovery target in the previous step.

Technology Selection

Identifying appropriate technologies to achieve the target may involve gathering yet more information in order to evaluate not only the technical appropriateness of potential technologies, but to arrive at an economic prioritization of potentially acceptable technologies as well. For example, when the target is improved recovery, this step will include a first-pass screening evaluation of a wide variety of technologies followed by an in-depth evaluation of the appropriateness of the resulting top-ranking recovery technologies.

Technology Optimization

Optimizing an implementation scheme for selected technologies can require major data collection and analysis efforts, especially if recovery technologies are a focus. Reservoir characterization in particular may need to be done in great detail to allow development of models to predict recovery and economic results with a sufficiently low degree of uncertainty. Well placement and completion configurations will be strongly dependent on the results of this

modeling optimization.

Operational Optimization

Implementation of new technologies in a reservoir is likely to mean that operational procedures and associated technologies will need to be adjusted for best reservoir performance.

SCALING THE RESERVOIR CHARACTERIZATION EFFORT

If additional recovery is an objective, reservoir characterization plays a major role in four of the five major steps in plan development. In the development of any given reservoir management plan, four separate reservoir characterizations may not have to be performed, however. If estimates of the size of the recovery target are highly uncertain (i.e., are uncertain to the point of being unable to define whether an economic target is present), basic reservoir characterization data should be collected to reduce that uncertainty before proceeding. This approach avoids the expenditure of large amounts of effort and money to build a highly detailed reservoir characterization model for a reservoir that turns out to have an unjustifiably small target.

Initial estimation of the location of a recovery target and post-screening selection of appropriate recovery method or process may require more accurate and more detailed information about the reservoir than that needed for rough target size estimation. Optimizing the implementation of a selected methodology, however, will require a degree of detail and uncertainty dictated by the method selected. In many instances, especially when recovery processes involving large investments in chemicals are involved, this will require a level of detail much greater and uncertainty much lower than that for initial process selection. This step might be thought of as an extremely detailed refinement of the initial target location step.

Steps in Constructing an Appropriate Reservoir Characterization Model

The general methodology involved in constructing a reservoir characterization model to fit any stage of reservoir management plan preparation may be summarized in a small number of sequential steps. In practical application, the steps may need to be followed through several iterations to achieve an acceptable product. A flowchart summarizing typical activities in these steps is presented in Figure 2.

Specify Appropriate Resolution and Uncertainty Characteristics

This step consists of making an initial estimate of the of detail and degree of uncertainty necessary to perform the evaluation. This will be a function of the stage of reservoir management plan development under which the reservoir characterization is being performed. The required level of model detail may vary from place to place within the reservoir or the model may be entirely focused on a segment of the reservoir.

Incorporate Existing (or New) Information

Information that goes into the building of a reservoir characterization model originates in: (1) data collected from different sources (e.g., rock and fluid samples, wireline logs, seismic, well tests, production data, etc.), (2) data collected at different resolution, and (3) data collected with inherently different degrees of uncertainty (including both deterministic and conceptual or analog information). A reservoir characterization model must provide information throughout the 3-D volume of that portion of the reservoir that is of interest, but this does not mean that each deterministic data type needs to be collected throughout the entire volume of interest. Instead, information derived from various data sources is incorporated by interpolation, extrapolation, or correlation with other data of deterministic or conceptual/analog origin. This diverse information is incorporated in mutual support of a single reservoir characterization model or a small number of models that express the probable range of variation. Information derived from geoscience, reservoir engineering, and other data is continually compared and contrasted to test various details of the emerging reservoir characterization model(s) until indications from all existing sources are in agreement. Inconsistent information or conflicting information derived from different sources, scales, or uncertainty models may have to be addressed with additional data collection before full confidence is achieved.

Test the Model Against Known Reservoir Performance

Models from the previous step are tested either qualitatively or quantitatively using simulation or simpler approaches to measure their ability to serve as a basis for predictions of reservoir pressure and production. Failure of the reservoir characterization models to support a reasonable match with actual reservoir past performance indicates that the models need correction through incorporation of new information. If models perform well, they are ready for use in predicting future performance of the reservoir under the plan being formulated.

Identify, Collect, and Incorporate New Information

Our knowledge of the reservoir will never be perfect, but collection of additional information can be viewed as an attempt to reduce model uncertainty and, ultimately, risk when the reservoir management plan is implemented. Several guidelines govern judicious collection of information. The primary objective is to obtain the maximum information affordable, in terms of proposed reservoir management project economics, to reduce uncertainty in prediction of project outcome. If the cost of reducing uncertainty to an acceptable level is found to be too high, the reservoir management plan may have to be redesigned. Information from all potential sources should be evaluated in terms of possible contribution to reducing model uncertainty. Potential contributors of low-cost information such as conceptual models from the published literature should not be overlooked. After a reservoir characterization model has been revised or refined by incorporation of new information, it should be retested.

Use the Model to Predict Future Reservoir Performance

Production performance predictions obtained by simulation or other means from reservoir characterization models will form the basis for economic analysis of various possible scenarios for inclusion in the reservoir management plan. This step enables plan optimization through selection of the best economically performing activities, processes, process implementation strategies, operational strategies, etc. If economic analysis indicates that results will be unacceptable or if the range of probable outcomes includes unacceptable economic performance, the plan may need to be redesigned.

THE RESERVOIR MANAGEMENT PROCESS

The world of reservoir management is dynamic rather than stable. Technologies are evolving rapidly on numerous fronts, and the petroleum business environment is ever changing. Changing business and technological contexts de-optimize previously existing reservoir management plans. The formulation, implementation, and revision of reservoir management plans can therefore be considered to be a fundamental reservoir management process. It is by necessity an iterative process (see Figure 3) requiring regular if not continuous attention or monitoring for every reservoir being managed.

The reservoir management process consists of first formulating an appropriate reservoir management plan in the context of reservoir knowledge, knowledge of technologies, and a knowledge of the business environment as has been discussed in previous sections of this

paper. The plan is then implemented as specified. Once the plan has been implemented, monitoring of both the performance of the reservoir and of the current status of knowledge of the reservoir, technologies and the business environment should begin immediately.

Events Triggering Reservoir Management Plan Revision

The reservoir management plan itself may specify a condition or set of conditions that, when met, indicate the plan should be reevaluated. These criteria may include such items as cumulative volume, relative volume, or rate of production or injection of a specified fluid, passage of a specific period of time, or attaining a particular stage of reservoir development.

At any time, however, reservoir performance anomalies of any kind (e.g., production or injection volumes, facilities usage, or regulatory compliance) with respect to plan expectations or predictions may indicate immediate need for plan revision. Ideally, the plan should specify guidelines for tolerance in variation from plan prediction in all critical performance areas. When these tolerances are exceeded, the plan should be reviewed and revised.

New information may also be just cause for plan revision at any time. New information may take various forms. It may be new reservoir information, perhaps extracted from data collected under specifications of the current plan, that indicates a conflict with the assumptions that went into formulating the plan. It may be in the form of the introduction of new technologies, ideas, or procedures not available or known at the time the plan was formulated. The critical new information may even be in the form of performance anomalies arising in analogous reservoirs.

Unexpected or unpredicted changes in circumstances or opportunities related to the general or operator-specific business environment may also present cause to reevaluate the reservoir management plan. Examples of factors that may be significant include market economics, new laws and regulations, changes in key personnel, and decisions to buy, sell, or trade reservoirs.

Influence of the Reservoir Management Process on Reservoir Characterization

From the preceding discussion we have seen that reservoir characterization is a multidisciplinary endeavor that plays an important role in developing a knowledge of the reservoir system and it is, in turn, critical to development of a reservoir management plan. We have also seen that implemented reservoir management plans are likely to become less than optimum as changes in technology and the business environment take place or as reservoir performance anomalies are recognized. The resulting periodic requirement for development of revised reservoir management plans means that revised reservoir characterization models may need to be

built to properly fit new plans to the revised reservoir management contexts. Reservoir characterization, therefore, becomes a consideration that must be addressed numerous times throughout the life of a reservoir.

CASE STUDY EXAMPLES FROM THE DEPARTMENT OF ENERGY'S RESERVOIR MANAGEMENT DEMONSTRATION PROGRAM

Projects supported by the Department of Energy under the Reservoir Management Demonstration Program are limited to oil reservoirs operated by small business organizations. Multiple operators must be involved in proposed projects, although participation by research organizations, state government agencies, service companies, consultants, etc. is encouraged. Projects must address resources significant to the region in which they occur and/or must address a major technological need. Projects are performed under a Cooperative Research and Development Agreement (CRADA) at a total level of funding up to about $500,000, at least 50% of which must be cost-shared by industry partners. DOE's contribution is mainly in the form of professional labor supplied through BDM-Oklahoma, but data acquisition and analysis, additional consulting expertise etc. may also be included in DOE's contribution. Projects are intended to be short, of 12 to 18 months maximum duration, and technology transfer is a major focus of each. All projects have a common goal to develop a comprehensive reservoir management strategy to improve the operational economics and optimize the oil recovery from the target field.

As initially conceived, the Reservoir Management Demonstration Program will include 15 projects, one in each of the ten Petroleum Technology Transfer Council (PTTC) Regions (see Figure 4), three projects involving Native American reservoirs, and two offshore projects. At the present time, three projects have been initiated under the program. One project, begun in early 1995 in the East Randolph field in Ohio, is nearing completion. This project in the Appalachian PTTC Region deals with a small recently discovered oil reservoir in a newly developing play in an area of mostly mature production. A second project, begun in late 1995 in the Citronelle field in Alabama, is a little more than half completed. This project, being performed in the Eastern Gulf PTTC Region, involves developing a strategy for a mature domestic giant reservoir (160 MMBO cumulative production). A third project has just been launched in late 1996 in the Bainville North field in Montana. This project in the Rocky Mountain PTTC Region will deal with the unique problems and opportunities related to optimizing a strategy for and optimization of multiple producing horizons within a field.

Summary of the Plan-Building Process for the East Randolph Field

Since 1992, PEP Drilling Company and Belden & Blake Corporation have developed this unique but significant oil reservoir in the Cambrian Rose Run Formation in Portage County, Ohio (see Figure 5). One of only a few fields to produce oil from the Rose Run, the East Randolph field covers about 1,500 acres, lies at a depth of about 7,200 ft, and contains an average of about 15 ft of pay in the upper three of five marginal marine sand zones typically present. The field contains just over 30 wells and had produced about 450,000 bbl of 42^{0} API oil and 1.2 BCFG as of June 1996. Two items of context associated with the East Randolph field had an especially important bearing on the development of the reservoir management plan for the reservoir. First, the field has been and continues to be developed by small independent operators. Second, the field has been entirely developed in the 1990s. In fact, rapid development is still going on as efforts continue to define the limits of the field.

In the proposal submitted by the operators, they outlined a list of potential targets or opportunities to pursue as reservoir management goals for the plan to address. The list included:

Optimum development and infill well locations

Optimum selection and implementation of secondary recovery method

Optimum hydraulic fracturing techniques

Address paraffin buildup problem in producing wells

In the proposal, the operators also suggested a list of project tasks and teaming arrangements that might be used to best address those tasks.

A kickoff meeting of all project participants was held at the project outset to further prioritize targets and to assign specific plan development tasks to teams and subteams. It was expected that the plan development process would be flexible and capable of changing to accommodate the course suggested by new information obtained.

Role of Reservoir Characterization

Reservoir characterization played a major role in arriving at the reservoir management plan for this project, particularly in pursuit of the targets selected as highest priority, i.e., defining development and infill well locations and selecting an optimum secondary recovery method. A series of incremental and sometimes iterative steps was performed in arriving at the final reservoir characterization model employed (Salamy et al., 1996). The steps involved analysis of existing data, identifying data insufficiencies, obtaining and incorporating new information into the emerging model, and testing the predictive limits of the model.

At the project outset, field limits were not yet accurately defined; pre-project estimates of OOIP were in the neighborhood of 4.4 MMBO. Although the three productive sand intervals in the Rose Run were recognized as such, the high GOR observed for most wells (1,500 to 2,000 SCF/STB) was attributed to conditions in all three sand zones.

Initial geologic work with neutron and density logs digitized in the project suggested that the uppermost sand zone had a much higher gas saturation. Analysis of production data showed a correlation between high initial GORs and occurrence of a well-developed upper sand zone, further suggesting a possible gas cap. Field-wide work based on digital logs and previously existing sidewall core analysis data determined structural heterogeneities (faults), vertical layering of rock properties, and horizontal variations in rock properties (Thomas and Safley, 1996). Zone mapping and volumetric analysis based on this geologic model yielded an OOIP figure of approximately 11 MMBO. This discrepancy in OOIP estimates was considered to be important to resolve considering its potential impact on continued development and future recovery.

In parallel with the initial geological work, and as an initial and potentially cost effective check on reservoir parameters, a single-well reservoir model was developed on one of the highest GOR wells in the field. PVT parameters input to this model were derived using published correlation techniques from initial reservoir parameters. Relative permeability and capillary pressure data input to the model were taken from analogous fields nearby. Model results were unstable in predicting production and indicated the need for more representative values for PVT and relative permeability parameters, additional field pressure data, and field volumetric information. As a result, a pressure buildup was run and surface-recombined fluid samples were obtained from an existing field well.

The new PVT data (which indicated only 485 SCF/STB), new pressure data, and production data were then used in a material balance calculation. A sensitivity analysis done on gas/oil volume ratios indicated that gas/oil volume ratios in the range of .16 to .2 would yield OOIP in the observed range 13 to 11 MMBO, respectively). Using a gas/oil volume ratio of .17 and OOIP of 12 MMBO yielded a reasonable match with observed field pressure history. This analysis confirmed that the field's high GOR was not a result of gas coming out of solution.

A second single-well simulation was run using a 3-layer (1 gas layer, 2 oil layers) model, the new PVT data, and, again, relative permeability data from analogous fields. This modeling confirmed the upper zone as predominantly a gas zone and accurately predicted reservoir pressure encountered by a subsequently drilled well at the edge of the modeling area. Predictions, however, were still found to be sensitive to relative permeability data and the recommendation was made that this new information be obtained.

An infill well was drilled and cored, and relative permeability and capillary pressure data were obtained on samples from the core. A CMR log was run to better define water saturation

distribution, and an FMI log was run to investigate distribution and orientation of natural fractures. Cleaning the samples for special core analysis also gave insight into the nature of the paraffin deposition problem and anomalously low measured permeabilities from routine core analysis samples.

As a final step, a full-field simulation was undertaken using all the newly collected information. The simulation study was completed in two steps. The first step, history matching of field production and pressure data, was done holding constant all known field and experimental data. Results of this first step showed a good match with oil and gas production and field pressure data, thus validating the basic model. The second step used the model to predict waterflood and gas injection results as potential secondary recovery methods for the field. Simulation results indicated that a high producing water/oil ratio coupled with low oil recovery makes waterflooding a less favorable option than gas injection for secondary recovery. The base case simulation indicates that ultimate primary recovery is 8% of OOIP. Waterflooding only adds an additional 0.5% recovery, while gas injection results in an additional 7.8% recovery of OOIP.

Discussion

The fact that the field is operated by small independents governed not only the nature of the implementations recommended by the plan, but the expenditure of effort and capital in collecting and analyzing data to arrive at the plan. Collection of new information had to be adequately justified. Although mutually supportive evidence from different reliable and cost-effective sources was sought, highly redundant confirmations were avoided as unnecessary and unjustifiable. Continued rapid development of the field while the plan was being formulated meant that new information had to be considered and incorporated on a continual basis and that rapid development of a plan was necessary to optimize field development and definition activities.

The incremental approach to reservoir description for plan development employed in this project results in an efficiency in data collection. Existing data were analyzed at each step with the objective of determining whether the uncertainty associated with the predictive power of the models based on those data was acceptable. If not, the type and quantity of new data needed to constrain the modeling efforts were identified and obtained after first considering the potential cost-effectiveness of the new information. This approach avoids the collection of unnecessary data and fits very well with the typical independent operator's economic constraints in reservoir characterization

Summary of the Plan-Building Process for the Citronelle Field

Citronelle field, in Mobile County, Alabama (see Figure 6), has been producing since its discovery in 1955 from fluvial sandstones of the Cretaceous Rodessa Formation at a depth of greater than 10,000 ft. The field, located over a deep-seated salt intrusion, was developed and essentially remains today on 40-acre spacing, covering a surface area of 16,400 acres with 468 wells. An 800-ft-thick gross pay interval contains at least 42 productive sand zones that form over 300 separate reservoirs, each with highly variable permeability characteristic of fluvial deposition. Field pressure declined relatively rapidly, leading to the inception of waterflooding in 1961. By early 1995, approximately 15,000 bbl of water were being injected each day into 50 injection wells to produce about 3,600 bbl of oil from about 175 producers. Cumulative recovery is about 160 MMBO, 120 MMBW, and 1.2 BCFG. Items of context associated with this field that had important influence on plan construction include the fact that both major and independent companies have conducted studies and collected voluminous data (several versions of some parameters) from the field over the course of its 40-year history and the fact that the field is currently being managed in its mature waterflood stage by small operators for the most part.

In the proposal submitted, the operators identified several possible targets for improving the economic performance of the field. These included:

Create a computerized field database for future analyses

Identify untapped, incompletely drained, and new pool targets

Optimize the waterflood strategy

Investigate alternate recovery methods

Evaluate drilling and completion techniques

Investigate casing leak prevention and repair

Investigate production problems related to paraffin, chlorite, scaling, etc.

Investigate improvement of downhole hydraulic pump life

The operators also suggested a list of tasks to address the targets listed above and made tentative assignment of team members to the tasks. In addition to appropriate personnel from BDM-Oklahoma, the reservoir management team for this project included geoscience, engineering, management, and other professionals representing operators of the 341 Tract, East, Southeast, and Northwest Units of the Citronelle field; operators of geologically analogous reservoirs in the area; the Alabama Geological Survey; the State Oil and Gas Board of Alabama; and the University of Alabama. The team also included a private engineering consultant with a long history of association with the Citronelle field.

Several major reservoir management decisions were made by the team very early in the project, even before a detailed blueprint was arrived at for constructing the reservoir management

strategy. All recognized that, under current operations, the economic limit for the field was approaching within a few years. There was also a general agreement that, based on the what was already known about the field and its performance, a substantial oil target remains in the Citronelle field that justifies a reservoir management effort for its recovery. Discussions focused on the necessity of achieving a cost-effective approach through careful matching of the limited resources available for investment by the operators to the probability of improving production and or profitability. The resulting circumscribing of reservoir management activities was, in reality, the beginning of reservoir management plan development.

It was further agreed that, rather than considering the entire field, the most economically reasonable approach would be to concentrate, initially at least, on geographic areas where certain significant problems or opportunities were prevalent. Solutions developed in these areas should have the most significant impact on profitability per dollar expended.

Although the operators had done a considerable amount of work in identifying potential opportunities for improving profitability, a kickoff workshop with the full reservoir management team in attendance was held at project inception to further identify and delineate problems and opportunities to be addressed. Specifically the kickoff workshop addressed:

Identifying and prioritizing opportunities to be pursued

Identifying and prioritizing geographic areas in the field where opportunities are best developed or most prominent

Reviewing the data available to address opportunities in the areas identified

Identifying additional data requirements

Developing a detailed procedure and schedule to govern plan building activities based on the results of the steps above

Assigning team personnel responsible for execution of the tasks delineated in the previous step

Identifying possible opportunities for technology transfer

The highest priority opportunity identified at the kickoff workshop was that of waterflood optimization. Boundary areas (see Figure 7) between the Citronelle 341 Tract Unit and the East and Southeast Units were identified as areas where the current waterflood has been least efficient in recovering oil reserves because no unified effort has been made in those areas in the past to optimize injection or production strategies.

Role of Reservoir Characterization

The long history of the Citronelle field has included numerous field-wide geological and engineering studies performed at various times. These studies, which were based on a strong foundation of core and wireline log data, include most of the current wells in the field. Computerized databases were originally associated with some of these studies, while others were based on work done strictly by hand. Remaining data from all these earlier studies was available only in hardcopy form at project inception, however. The quality of much of the work done in the past was judged to be sufficient to justify using it as a basis for the reservoir characterization needs of the current study.

A decision was made early in the project to pursue two parallel approaches to reservoir characterization for the Citronelle project. The first approach would involve using interpreted sand geometries and associated volumetric parameters derived from past studies along with past pay determinations and preliminary estimates of permeabilities, porosities, and water saturations from past engineering studies to perform preliminary characterization of the reservoir in the areas of interest along the Unit boundaries. A second and simultaneous approach involved entering gross and net pay data along with gradually refined estimates of permeabilities, porosities, and water saturations into a field-wide database that could be used with modern mapping tools to create minimally biased volumetric and other estimates in the late stages of the current study and in future studies beyond the scope of the current work. Production data were obtained from the state of Alabama and cumulative values a various points in time were entered into this database also.

As a first step in determining the best areas and approaches for obtaining additional waterflood recovery, cross sections in the areas of interest defined along the unit boundaries were used to define potential flow units as isolatable targets for improved recovery. These flow units were defined by combining into one package sands that are likely to be in vertical and horizontal communication with each other across the area of interest, but at the same time separated from adjoining sands or packages by substantial shale barriers. Due to past hydraulic fracturing practices in the field, a 30-ft minimum thickness was used to define effective shale barriers separating sand packages. As a next step toward identifying potential recovery targets, floodable OOIP volumetrics were calculated for each of the approximately 20 sand packages or flow units identified.

Flow units do not occur in isolation, however. Several flow units are commonly present in a single well, as well as numerous sands not identified as belonging to discrete flow units. The next step involved looking at groups of wells characterized by presence of multiple flow units in common. These wells form logical groups to consider for production optimization through

alteration of injection/production strategies. Identifying these groups of wells and prioritizing them on the basis of their OOIP volumetrics is now nearing completion.

The anticipated next step is to review the completion, production, and injection histories of the associated wells for the top priority groups to determine the size of the remaining potential recovery target. The final step will be to evaluate and strategize recompletions and injection/production geometries to maximize recovery for all sand packages and flow units involved in the groups.

Discussion

The series of steps involving progressive prioritization first on the basis of OOIP and then on the basis of remaining or recovery potential is meant to assist in assuring that areas with the best recovery economics can be addressed first. In its refined form, this general methodology can then be applied throughout the field to maximize economic recovery from other sand packages. Such an approach would allow the untapped profitability potential of the field to be developed in small incremental steps that are more financially feasible for small operators than if the entire field were examined in detail at once.

Summary of the Plan Building Process for the Bainville North Field

The Bainville North field was discovered in 1979 in the Williston Basin in Roosevelt County, Montana (see Figure 8), with establishment of production from the Devonian Winnepegosis Formation at a depth of 11,500 ft. Production has since been added from four additional zones between the Mississippian Ratcliffe Formation at 8,500 ft and the Ordovician Red River Formation at 12,500 ft. Fifteen wells currently produce in the field whose cumulative production is 2.8 MMBO, 2.8 BCFG, and 1.4 MMBW through early 1996.

In the 1990s, Nance Petroleum Corporation has substantially increased production from the Red River Formation through use of 3-D seismic and other advanced rock, fluid, and high-resolution wireline log data to locate infill wells. Although only seven wells are currently producing from the Red River interval, through early 1996 cumulative production from the interval was 1.0 MMBO and 762 MMCFG.

In the operators' proposal, reservoir characterization of the highly heterogeneous dolomitic Red River reservoir for purposes of improved recovery implementation was presented as a top priority. The reservoir management strategy developed in the project will also address the design and implementation of improved recovery processes within the context of the field's multiple productive horizons. This will include considerations of well spacing and utilization,

artificial lift optimization, and facilities requirements. Additional problems to be addressed may include paraffin deposition, scaling, corrosion, and casing collapse.

Role of Reservoir Characterization

Reservoir characterization is expected to proceed by integration of existing core data, fluid data, wireline log data, pressure data, 3-D seismic data, and any additional data deemed necessary into reservoir models for use in simulation. Historical performance of the field will be simulated and predictions made for the implementation of improved recovery techniques. From these results, a reservoir management strategy will be formulated.

Discussion

This project is just beginning, but it has potential for significant impact on Williston Basin petroleum development. Because of the geologic similarities between the various producing horizons in the basin, and because very few advanced recovery projects have been implemented in the basin, the reservoir management strategies developed to address the opportunities at Bainville North will be applicable to most reservoirs in the region.

CONCLUSIONS

Reservoir management is not optional; anyone who is responsible for a reservoir is managing it. Reservoir management is not a luxury reserved for large recently discovered reservoirs or for major oil companies. Reservoir management does not necessarily imply a "high-tech" approach.

A plan or strategy that guides the operator's interaction with the reservoir is the heart of reservoir management. Efficient reservoir management is the creation of a plan that maximizes the profitability of a reservoir to a specific operator. An appropriate reservoir management plan can not be "bought off-the-shelf" or transported from one reservoir to another or from operator to operator; it must be custom built. To accomplish this requires a knowledge of the business environment, a knowledge of technologies available to describe, analyze, and exploit the reservoir, and a knowledge of the reservoir system including its rocks, fluids, wellbores, and surface facilities.

Reservoir characterization is an important technique to gain needed knowledge of the reservoir for reservoir management plan building. Reservoir characterization approaches can be appropriately scaled by considering the reservoir management context, both the context within

the reservoir management plan-building process and the context of the business environment and the status of technology.

Reservoir management is a dynamic process. Reservoir management plans de-optimize as technology and business environment change or as new reservoir information indicates the reservoir characterization models on which the current plan is based are inadequate. Continual monitoring will allow identification of reservoir management plans that are no longer optimum. De-optimized plans should be revised to maintain maximum profitability and recovery. Revision of plans commonly calls for a revised reservoir characterization model or models as well.

The generally risk-averse approach to reservoir management, especially of domestic reservoirs, taken by industry means that many reservoirs are operated under less-than-optimum reservoir management plans. The potential to increase profitability and recovery from domestic reservoirs is therefore great. The Department of Energy's Reservoir Management Demonstration Program focuses on this concept. The program is seeking to improve domestic reservoir recovery and profitability and delay abandonment through encouraging operators to develop, apply, and disseminate efficient reservoir management techniques.

Work accomplished in two program projects demonstrates the scaling of reservoir characterization efforts in developing reservoir management plans for reservoirs under widely contrasting contexts. Both projects were cognizant that small operators have limited capital resources to invest in extensive reservoir characterization efforts. Reservoir characterization in the East Randolph field project took an incremental approach to defining critical reservoir parameters while this small newly discovered field was still under active development and definition. In the Citronelle project, the focus is on developing an improved recovery approach or methodology for small areas of high potential in this already mature waterflood. The methodology developed can then be repeated by the operators for remaining improved recovery targets in this large field.

ACKNOWLEDGMENTS

The authors and other researchers participating in the Department of Energy's program of reservoir management demonstrations are appreciative of the Department's foresight in supporting methodological research and demonstration in the critical areas of reservoir management and reservoir characterization. Neither would this product have been possible without the dedication and support received from all members of the East Randolph, Citronelle, and Bainville North field reservoir management teams. We are also grateful to the BDM-Oklahoma Information Services Department for their support.

REFERENCES

Cole, E.L., R.S. Sawin, and W.J. Weatherbie, 1993, Reservoir Management Demonstration Project, The University of Kansas, Energy research Center, Technology Transfer Series 93-5.

Cole, E.L., M.L. Fowler, S.P. Salamy, P.S. Sarathi, and M.A. Young, 1994, Research Needs for Strandplain/Barrier Island Reservoirs in the United States, report DE95000118, United States Department of Energy, Bartlesville, Oklahoma, 186p.

Fowler, M.L., M.A. Young, E.L. Cole, and M.P. Madden, 1996, Some practical aspects of reservoir management, SPE Paper 37333 presented at the Eastern Regional Meeting in Columbus, Ohio, October 23-25.

Jackson, S.R., and L. Tomutsa, 1991, Reservoir characterization---state-of-the-art review: in Research Needs to Maximize Economic Producibility of the Domestic Oil Resource, Part I - literature review and areas of recommended research, Department of Energy Report NIPER-527, p. 143-172.

Lake, L.W., and H.B. Carroll, Jr., 1986, Preface, in L.W. Lake and H.B. Carroll, Jr., eds., Reservoir Characterization, Academic Press, Orlando, Florida, 659pp.

Riley, R.A., and M.T. Baranoski, 1992, Reservoir heterogeneity of the Rose Run Sandstone and adjacent units in Ohio and Pennsylvania, presented at the Ohio Oil and Gas Association Winter Meeting, Canton, Ohio, October 20.

Salamy, S.P., M.A. Young, L.E. Safley, J.L. Wing, and J.B. Thomas, 1996, Application of reservoir management techniques to the East Randolph field, Portage County, Ohio: Reservoir engineering study, SPE Paper 37334 presented at the Eastern Regional Meeting in Columbus, Ohio, October 23-25.

Satter, A., and G.C. Thakur, 1994, Integrated Petroleum Reservoir Management - A Team Approach, Pennwell Publishing Co., Tulsa, OK, 335p.

Satter, A., J.E. Varnon, and M.T. Hoang, 1992, Reservoir management: technical perspective, SPE Paper 22350, presented at the International Meeting on Petroleum Engineering in Beijing, China, March 24-27.

Thakur, G.C., 1991, Waterflood surveillance techniques - a reservoir management approach, Journal of Petroleum Technology, v. 43, no. 10, p. 1180-1188.

Thomas, J.B., and L.E. Safley, 1996, Improved reservoir characterization of the Rose Run Sandstone in East Randolph field, Portage County, Ohio, presented at the Fourth Annual Technical Canton Symposium, Canton, Ohio, October 8-9.

Wiggins, M.L., and R.A. Startzman, 1990, An approach to reservoir management, SPE Paper 20747, reservoir management panel discussion, 65th Annual Technical Conference and Exhibition, New Orleans, Louisiana, September 23-26.

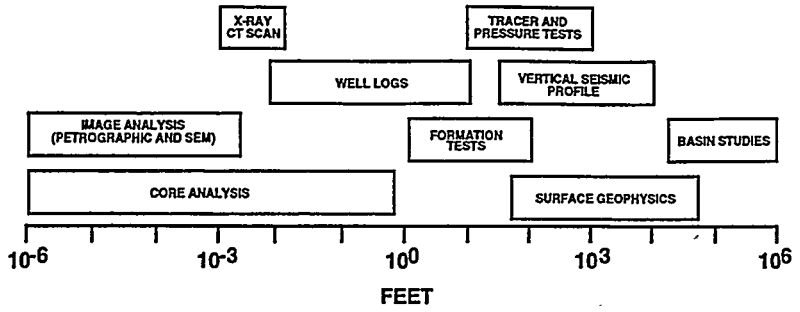

Figure 1—Scales of measurement and relative resolution of some common deterministic reservoir charaterization tools (modified from: Jackson and Tomutsa, 1991).

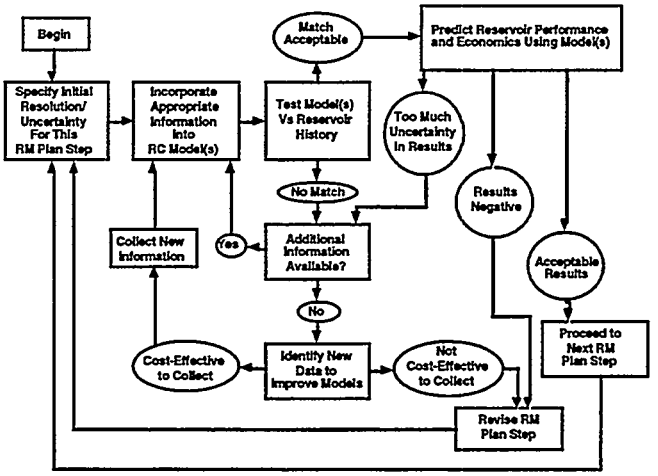

Figure 2—Construction of appropriate reservoir characterization (RC) models is an interactive procedure strongly controlled by reservoir management (RM) context and the cost-effective availability of information.

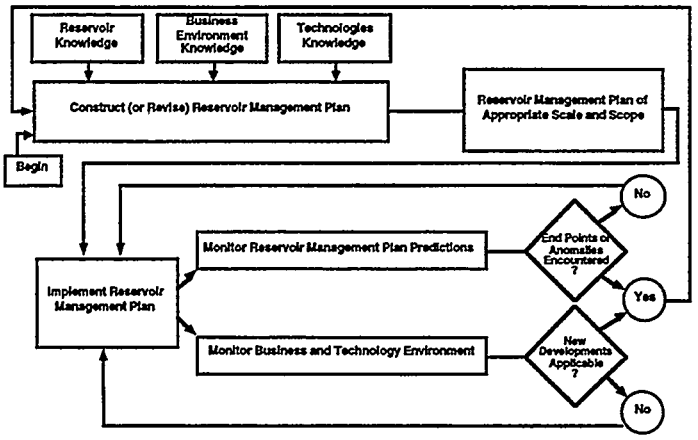

Figure 3—The reservoir management process is an interactive procedure involving plan construction (or revision), plan implementation, and monitoring of reservoir performance, technological advancements, and the reservoir management business environment (from Fowler et. al., 1996).

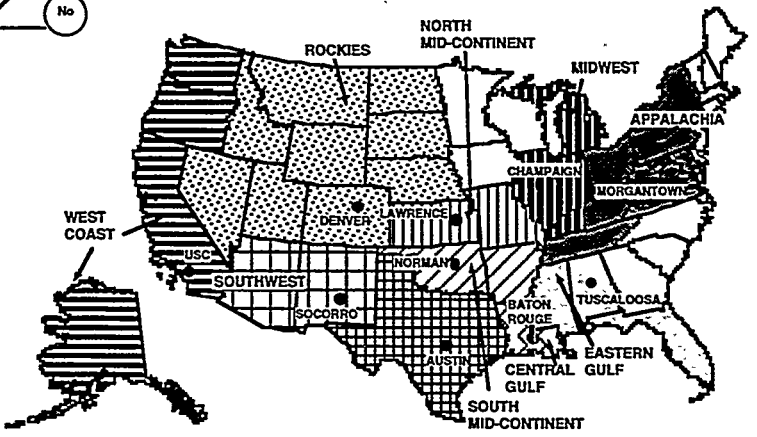

Figure 4—The ten Petroleum Technology Transfer Council regions and the cities in which their Regional Lead Organizations are located.

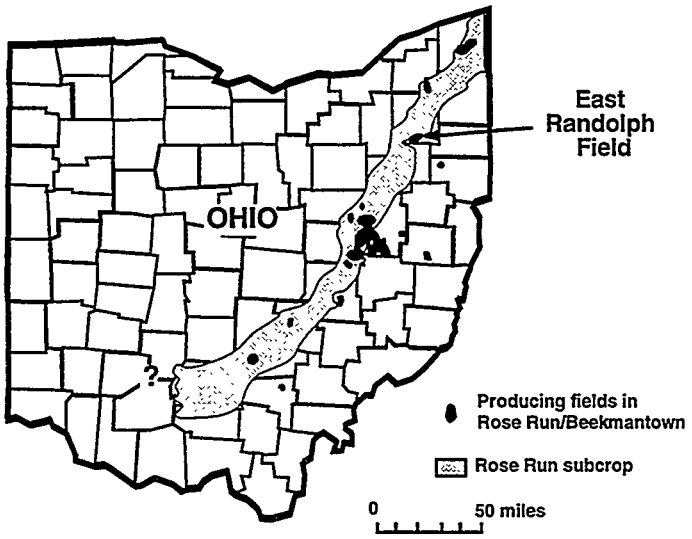

Figure 5—The East Randolph field is loacted in eastern Ohio in a northeast-southwest trend of reservoirs producing mostly gas from the Rose Run (from Fowler et al., 1996; Riley and Baranoski, 1992).

Figure 6—The Citronelle field is located on the eastern edge of the Mississippi Interior Salt Basin in Mobile County, Alabama (from Fowler et al., 1996).

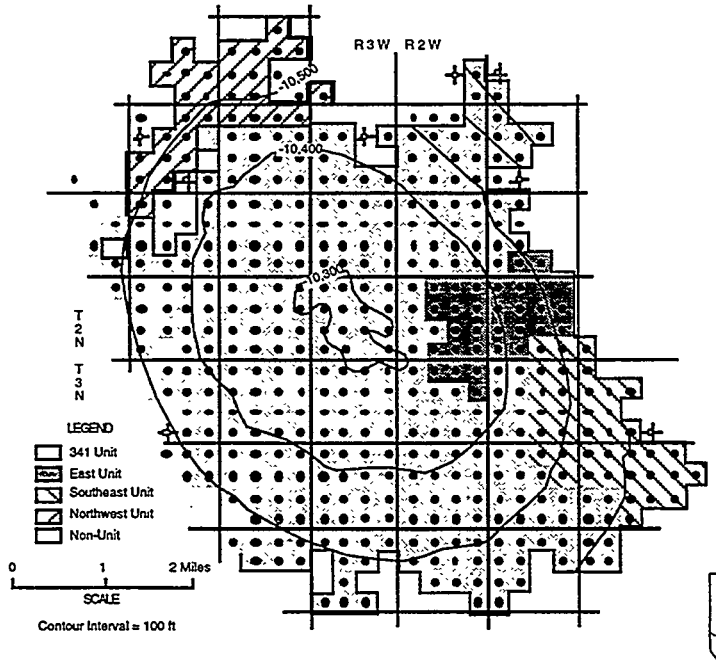

Figure 7—The boundary areas between the units in the Citronelle field are the primary focus of the current reservoir management study. Structural countours are on the base of the Ferry Lake Anhydrite immediately overlying the Citronelle reservoir (from Fowler et. al., 1996).

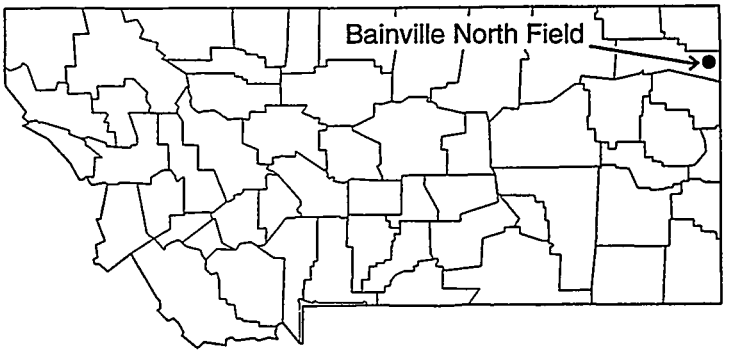

Figure 8—The Bainville North field is located in Roosevelt County, Montana in the Williston Basin.

ADVANCED RESERVOIR CHARACTERIZATION FOR IMPROVED OIL RECOVERY IN A NEW MEXICO DELAWARE BASIN PROJECT

Authors:

F. David Martin
Richard P. Kendall
Earl M. Whitney
Dave Martin and Associates, Inc.
917 Belmont Drive
Socorro, New Mexico 87801

Dr. Bob A. Hardage
The University of Texas at Austin
Bureau of Economic Geology
University Station, Box X
Austin, Texas 78713-7508

Bruce A. Stubbs
Pecos Petroleum Engineering, Inc.
P.O. Box 2885
Roswell, New Mexico 88202

Bruce Uszynski
Territorial Resources, Inc.
P.O. Box 1521
Roswell, New Mexico 88202

William W. Weiss
New Mexico Petroleum Recovery Research Center
801 Leroy Place
Socorro, New Mexico 87801

Acknowledgment:

Mr. Mark B. Murphy
Strata Production Company
P.O. Box 1030
Roswell, New Mexico 88202

ABSTRACT

The Nash Draw Brushy Canyon Pool in Eddy County, New Mexico is a field demonstration site in the Department of Energy Class III program. The basic problem at the Nash Draw Pool is the low recovery typically observed in similar Delaware fields. By comparing a control area using standard infill drilling techniques to a pilot area developed using advanced reservoir characterization methods, the goal of the project is to demonstrate that advanced technology can significantly improve oil recovery.

During the first year of the project, four new producing wells were drilled, serving as data acquisition wells. Vertical seismic profiles and a 3-D seismic survey were acquired to assist in interwell correlations and facies prediction.

Limited surface access at the Nash Draw Pool, caused by proximity of underground potash mining and surface playa lakes, limits development with conventional drilling. Combinations of vertical and horizontal wells combined with selective completions are being evaluated to optimize production performance.

Based on the production response of similar Delaware fields, pressure maintenance is a likely requirement at the Nash Draw Pool. A detailed reservoir model of pilot area was developed, and enhanced recovery options, including waterflooding, lean gas, and carbon dioxide injection, are being evaluated.

INTRODUCTION

The Nash Draw Brushy Canyon Pool, operated by Strata Production Company (Strata), is located in Sections 12-, 13-, and 14-T23S-R29E, and Section 18-T23S-R30E, in Eddy County, NM. General characteristics of this Slope Basin Clastic reservoir are listed in Table 1. Production at Nash Draw Pool (NDP) is from the basal Brushy Canyon zones of the Delaware Mountain Group of Permian, Guadalupian age.

The primary concerns at the NDP are: (1) the low primary oil recovery of approximately 10%, (2)

a steep oil production decline rate, and (3) rapidly increasing gas-oil ratios. This low recovery is caused by low reservoir energy, and less than optimum permeabilities and porosities. Initial reservoir pressure is just above the bubble-point pressure and declines to below the bubble point after a few months of production. With the solution gas drive reservoir, oil production declines approximately 50% in the first year, and gas/oil ratios increase dramatically. These concerns point out the importance of considering various reservoir management strategies to maximize the economic recovery of oil at the NDP. Based on the production characteristics that have been observed in similar Delaware fields, pressure maintenance is a likely requirement at the NDP.

Early in the NDP development, Strata identified three basic constraints: (1) limited areal and interwell geologic knowledge, (2) lack of an engineering tool to evaluate the various producing strategies, and (3) limited surface access that will prohibit development with conventional drilling. The limited surface access at the NDP is caused by the proximity of underground potash mining and surface playa lakes (see **Fig. 1**). Based on the risk involved in developing advanced technologies to address these constraints, Strata submitted a proposal under the DOE Class III solicitation. The project was approved by the DOE and began in September 1995. The objectives of the project are: (1) to demonstrate that a development drilling program and pressure maintenance program, based on advanced reservoir management methods, can significantly improve oil recovery compared with existing technology applications, and (2) to transfer the advanced methodologies to oil and gas producers, especially in the Permian Basin.

Typical of small independent producers, Strata lacked the in-house expertise to address all of the needs of the Class III project, and, therefore assembled a diverse team of experts to manage and analyze the NDP. Strata is responsible for the management and day-to-day operations of the NDP; the Petroleum Recovery Research Center (PRRC) provides technical support and technology transfer functions; Dave Martin and Associates, Inc., with Drs. Richard Kendall, Earl Whitney, and John Killough, provides reservoir characterization and simulation services; Dr. Bob Hardage of the Bureau of Economic Geology (BEG) at

the University of Texas at Austin provides seismic and geophysical expertise; Territorial Resources, Inc. provides geological expertise; and Pecos Petroleum Engineering, Inc. provides reservoir, production, and drilling engineering services. One challenge to this type of organization is providing communication and coordination between the team members located in a diverse geographic area. Reporting and coordinating of five subcontractors uses advanced technologies to communicate and coordinate efforts. The use of E-mail, the Internet, and high capacity data transfer are used successfully to exchange data and conclusions between each group.

RESULTS AND DISCUSSION

A number of planning sessions of the "virtual project team" were held during the early stages of the NDP project. As a result of these meetings, a project plan was developed for the first phase of the project. This paper will highlight results of the first year of the NDP project; detailed results are contained in the first annual report **(Murphy 1996)** submitted to the DOE.

Data Acquisition

The data acquisition portion of the project included compiling existing reservoir and engineering data as well as acquiring new data. As part of the project, four new wells have been drilled to date for data acquisition, and the NDP now consists of 15 producing wells and one salt water disposal well (see **Fig. 1**). Multiple sidewall cores were obtained for analysis when each new well was drilled, and, when Well No. 23 was drilled, 66.6 m (203 ft) of full core was cut for laboratory analysis. Normal suites of logs were obtained in all of the wells, and a magnetic resonance tool was run in Well No. 23 for comparison to the core analysis. Two vertical seismic profiles (VSPs) and a 3-D seismic survey were recorded in Well No. 25 to aid the characterization of the NDP reservoir.

Production, transmissibility, capillary pressure data, and geological interpretations were combined to arrive at reservoir maps which honor the available data. It was necessary to perform a detailed correlation of the sands in the basal Brushy Canyon sands in order to better understand the lateral and vertical

distribution of the reservoirs. Detailed correlations also facilitate a more accurate geological model for use in the reservoir simulation phase of the study. The data were compiled into a spreadsheet for ease of use between all members for the project team. Well data were compiled for each of the wells within and directly adjacent to the Nash Draw Pool for the purposes of constructing the maps for the initial structural and stratigraphic model.

Geology of the NDP

The structure trend at the NDP is N-S to NE-SW, and there were at least three depositional events. The sandstone reservoirs of the basal Brushy Canyon sequence lie above the Bone Spring Formation **(Fig. 2)**. The top of the Bone Spring is marked by a regionally persistent limestone varying from 16.4 to 32.8 m (50 to 100 ft) in thickness that provides an excellent regional mapping horizon. Regional dip is to the east-southeast in the area of the NDP. The structural dip resulted from an overprint of post-depositional tilting that is reflected in reservoir rocks of the Delaware Formation and impacts the trapping mechanism in the sands.

The reservoir consists of complex sands - a series of stacked micro-sands, vertical permeability is extremely low, and horizontal permeability is poor to good. The main producing intervals of the Brushy Canyon formation, the "K" and "L" sands, have multiple lobes, and both sands can be divided in four sub-units. Mineralogy of the "K" and "L" sands are similar. Both zones contain some clays - illite and chlorite. The "K" sand has up to 2% more chlorite that occludes permeabilties and may have influenced higher initial water saturation in the "K" sand. Overall, the "K" sand has a higher water saturation than the "L" sand.

Comparison of NDP Data to Other Nearby Delaware Fields

Log and core data were obtained from wells in the E. Loving Delaware Pool and the Texaco wells southeast of the NDP. These data were analyzed to determine if the zone characteristics were uniform over this general area. Results indicate that the core data are in good agreement, especially in the "L" Zone. Data from wells in these fields and from Maralo wells offsetting the NDP were obtained and analyzed. Structure

maps and cumulative oil, gas, and water production for the E. Loving Pool, and data from all three fields were analyzed and compared to data from the NDP. Core data correlate very well in the "L" zone, but there is less agreement in the data from the "K" and "K-2" zones.

Sixteen wells in the E. Loving Pool in Section 14, T23S-R28E were selected as an analogy to the NDP. These wells represent varying structural positions and corresponding production characteristics. Logs have been obtained from each well, structure maps have been constructed, and available core data have been obtained for the wells in the study area. A series of preliminary structure and isopach maps have been developed in the analog area using the same criteria that were used in the NDP area. It appears that the rock characteristics in the analog area are similar enough to those in the NDP to allow accurate comparisons of the production data and characteristics of the two areas.

Petrophysical Data

Sidewall core data from each well in the NDP were compiled, and porosity/permeability (ϕ/k) relationships were determined. These relationships were compared to the whole core data and found to be in good correlation.

The whole core obtained from Well No. 23 was cut from the "J" zone through the "L" zone. Basic core data including porosity, permeability, oil and water saturations, grain density, show description, and lithology description, were measured for each foot of core. The core data were used to prepare a transform to correct the log cross-plot porosity to yield a true porosity based on the whole core porosity. The relationship between cross-plot log porosity (logs run on a limestone matrix) and core porosity was determined to be:

$$\phi_{CORR} = (\phi_{x\text{-}plot} - 3.7685)/.848294 \qquad (1)$$

Permeability was plotted against porosity, and a regression analysis was performed to generate equations to fit the data. These relationships were used to predict the permeability of each zone based on corrected log

porosities. Permeability/porosity distributions were prepared for each zone as presented in **Fig. 3.**

Generally, the rock is fine to very fine-grained, massive to very thinly laminated. There is some evidence of turbulence as exhibited by sets of low to medium angle cross bedding within some of the sand units. Evidence of bioturbation occurs in some of the shaley and silty zones. There is also carbonate clastic debris present in some intervals within the core. Examination of the core under ultraviolet light shows the discontinuous character of the hydrocarbon distribution throughout the reservoir. This correlates with the erratic vertical distribution of calculated oil and water saturations seen in the log analysis.

These data were used to calibrate the logs and determine pay distribution in each zone. By performing a detailed core calibrated log analysis of Sxo, Sw and porosity, a detailed analysis was applied to the digitized logs to determine the productive and water zones in each interval. The application of porosity/permeability transforms and relative permeability data to each zone yielded flow capacity data for each interval. These data were summed for each layer to be input into the reservoir simulator.

Permeability (k_a)/ Porosity Relationships for Each Interval

Porosity/permeability relationships were developed from the sidewall cores and full core analyses. The flow unit variables *a* and *b* are given in Table 2 for the power function:

$$k = 10^{a\phi - b} \qquad (2)$$

A data file was prepared for each well that included digitized log files, perforations, cement programs, tracer logs, completion information, and frac treatments. These data were used to allocate production, estimate drainage areas, determine productivity, estimate saturations for each interval, and prepare data files for reservoir simulation.

Using core and log data, each well was calibrated to match production, net pay, and transmissibility. By calculating a kh/μ value for each interval, production rates and cumulative production was allocated to each interval. The transmissibility for each layer will be used as input into reservoir simulation model along

with saturation data to determine the producing characteristics of each layer. **Figure 4** shows the transmissibility values used to establish production from the various zones for 14 of the 15 wells in the NDP.

Reservoir Model of the NDP

The structure and isopach maps were loaded into Landmark's Stratamodel® program, and a preliminary 3-D geological layer model was developed. Surface intersections in the multi-layered model were eliminated by fine tuning the relationships of the structural surfaces using isopach maps. The model was constructed from the bottom up using the Bone Spring surface as the basal surface (see **Fig. 5**).

An initial ten-layer geological model has been developed for the basal Brushy Canyon sands in order to develop a more detailed reservoir model for simulation. The "K" and "L" sands were divided into four sub-units. The sands were correlated laterally from well to well in the NDP. Gross isopach, net porosity isopach and log-derived net pay maps were constructed for each of the sub-units of the "K" and "L" sands as well as the "K-2" and "J" sands. The maps were contoured to conform to the overall gross interval isopach maps for the respective pay zones that were used to construct the geological model. Reservoir attributes such as porosity, relative permeability, and oil and water saturations will be distributed vertically and laterally throughout the layers in the simulation model.

To date, two "generations" of models have been developed. Both of these are based solely on petrophysical measurements, that is, they exclude any geophysical input. In the first instance, a full NDP model was developed from the initially-available geological interpretation based on logs and cores. The second generation model was based on this data plus newly-interpreted pressure transient data. The integration of the log, core and pressure transient data led to an interpretation of the NDP with three non-communicating lobes of oil. The pilot area is confined to one of these lobes. It is anticipated that the inclusion of geophysical data like seismic amplitude will lead to further refinement of the present model--a third generation model.

Digitized maps of the interpreted horizons ("J", "K" with four subzones, "K-2," "L" with four subzones,

and the top of the Bone Spring formation) were imported into SGM® to create a stratigraphic framework model of the eastern half of the NDP (which contains the oil lobe supporting the pilot). Since the producing zones and subzones are relatively thin, great care had to be exercised to prevent intersections of the horizons. It is also critical that the surfaces tie to the well picks of the lithological markers in the well traces. In general, the most successful approach to this problem was based on the use of gross isopach thickness interpretations building from the structural top of the Bone Springs formation to the structural top of the "J" sand.

The next major step was the development of a well attribute model. This activity was supported by the Lotus engineering database. For each of the 15 NDP wells, the following attributes were imported into the well model: neutron porosity and gamma ray, interpreted porosity and permeability, perforated interval and fractured interval, net pay, and water saturation. In some instances, these attributes were available on a foot-by-foot basis for one or more of the producing zones. Not all of the attributes were available for each well. For reservoir simulation, the most important reservoir attributes are fluid conductivity and rock matrix storage capacity. The distribution of these properties throughout the NDP have been based on the well attribute model. Within SGM, these distributions are interpolated deterministically, that is, weighted by the reciprocal of the square of the distance between the location of interest and nearby wells in the reservoir model. The distribution of net pay, porosity, and water saturation are shown in **Figs. 7, 8, and 9**, respectively. Techniques like kriging (and co-kriging) may be used to distribute these attributes in the third generation model.

Reservoir Simulation

Having completed the supporting geological model, attention focused on the generation of a reservoir simulation model for the pilot area. It is envisioned that a single well in the pilot area will be converted to injector status to test the efficacy of injecting water, lean gas (immiscible), and/or CO_2 (immiscible or miscible) to improve oil recovery at the NDP. The following tasks are required to complete the pilot simulation phase: possible scale-up of lithological units, interpolation of geological attributes on the

simulation grid, validation of pilot simulation model, and design and execution of prediction cases.

3-D Seismic

The VSP calibration data acquired in Well No. 25 established the top of the Bone Spring as a robust reflection peak, the "L" sequence was associated with the first reflection trough immediately above the Bone Spring and the "K" sequence began just above the first reflection peak above the Bone Spring. The 3-D seismic survey generated amplitude maps that show the producing trends and high amplitude areas. Well productivity appears to be directly correlatable to the amplitude of the dominant "K" reflection peak and "L" reflection trough. Future wells will be drilled to confirm this analogy and evaluate targeted drilling of the seismic anomalies.

Conclusion

The reservoir characterization, geological modeling, seismic interpretation, and simulation studies should yield a detailed model of the Brushy Canyon zones. This model will be used to predict the success of different reservoir management scenarios and to aid in determining the most favorable combination of targeted drilling, pressure maintenance, stimulation, and well spacing to optimize recovery from the Nash Draw Pool.

REFERENCE CITED

Murphy, M.B., B.A. Stubbs, B.J. Uszynski, F.D. Martin, R.P. Kendall, E.M. Whitney, B.A. Hardage, and W.W. Weiss: "Advanced Oil Recovery Technologies for Improved Recovery from Slope Basin Clastic Reservoirs, Nash Draw Brushy Canyon Pool, Eddy County, N.M.," First Annual Report to the U.S. Department of Energy, DOE Cooperative Agreement No. DE-FC-95BC14941 (October 1996).

Figures

Figures

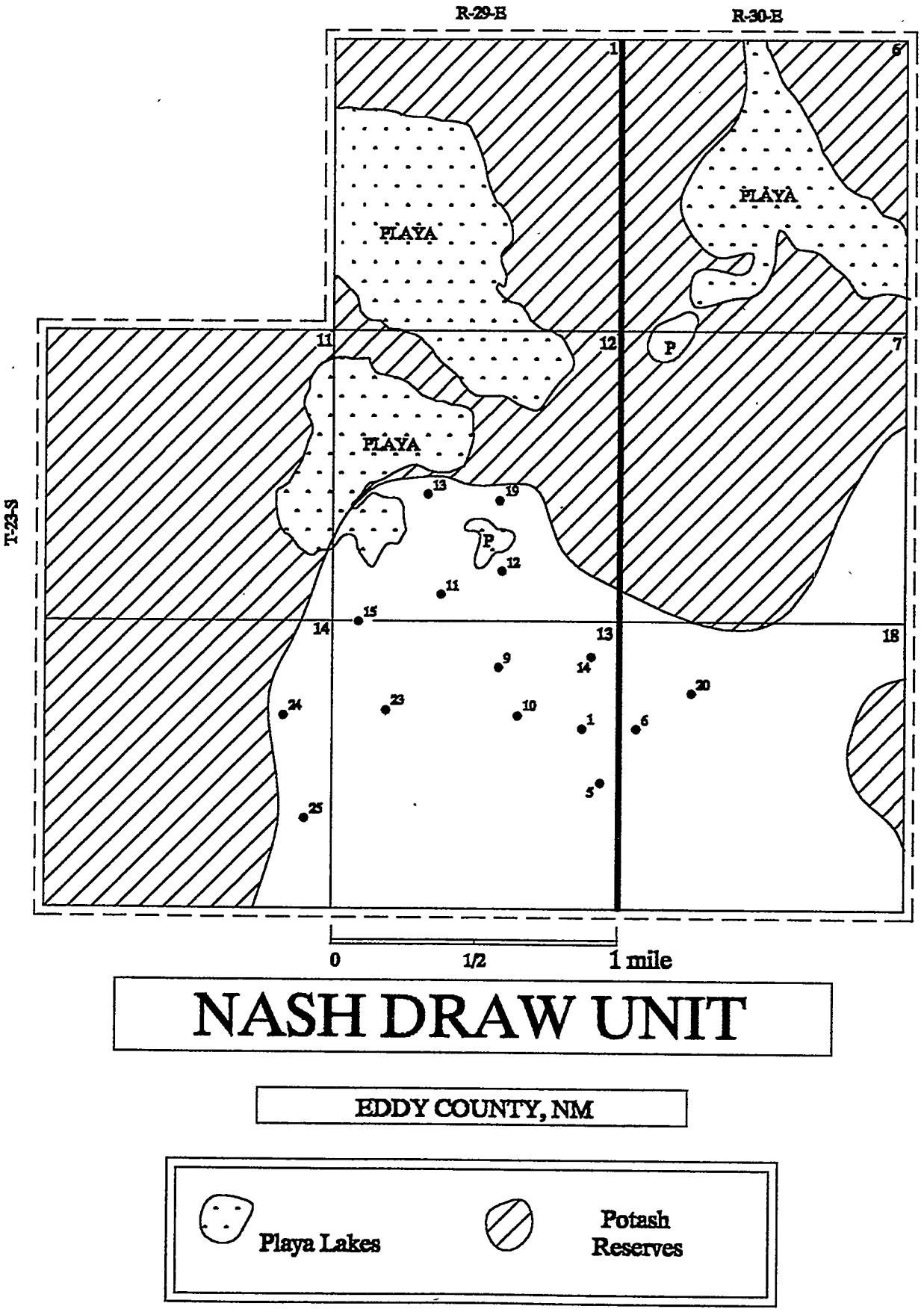

Fig. 1 Map of the Nash Draw Unit area.

TYPE LOG

STRATA PRODUCTION COMPANY

NASH UNIT #15

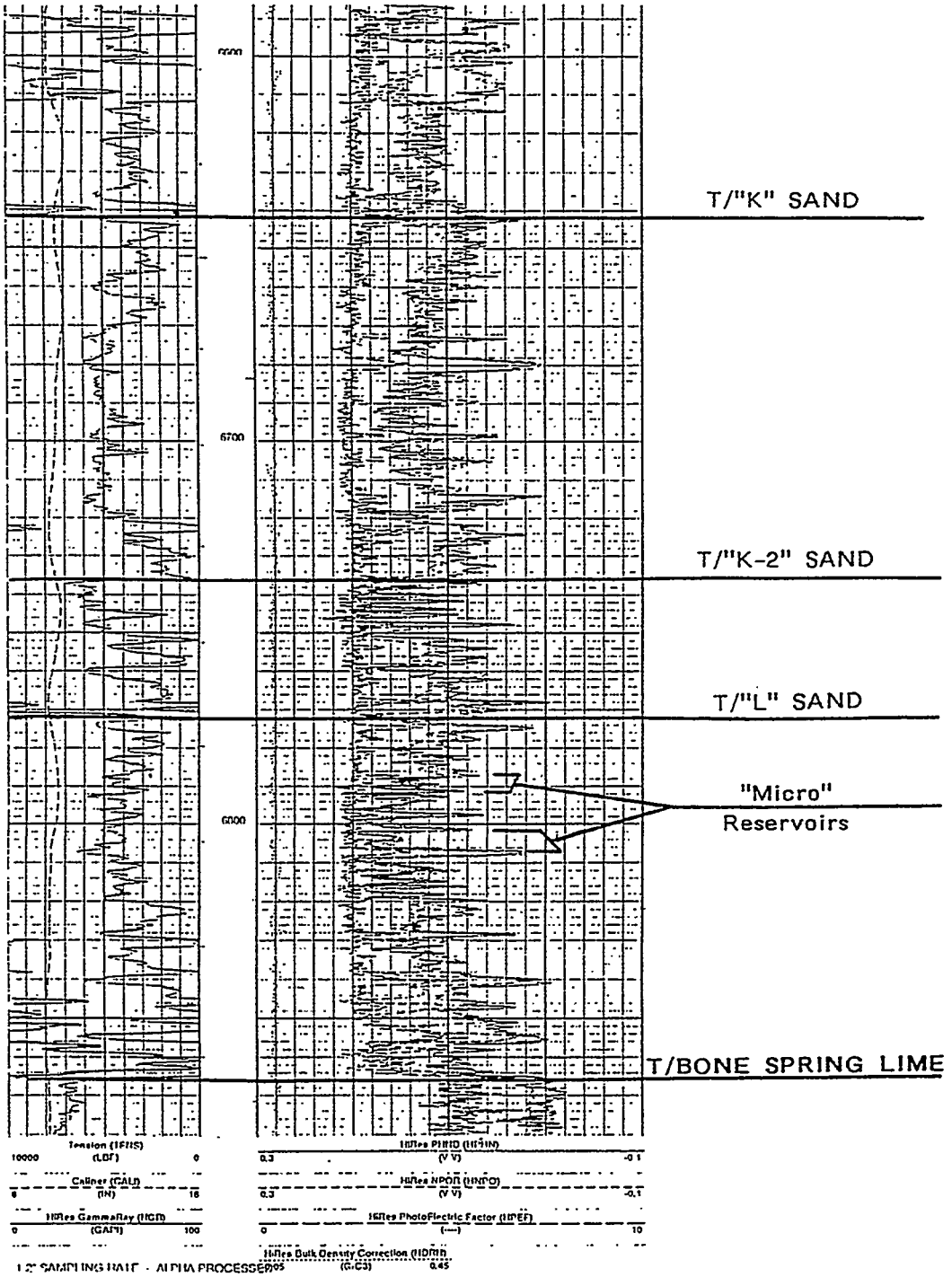

Basal Brushy Canyon Sands Showing Stacking of Thin, Multiple Reservoir Packages. Each Sand is Composed of Stacked "Micro" Reservoirs with Vertical Permiability Barriers.

Fig. 2 Type log.

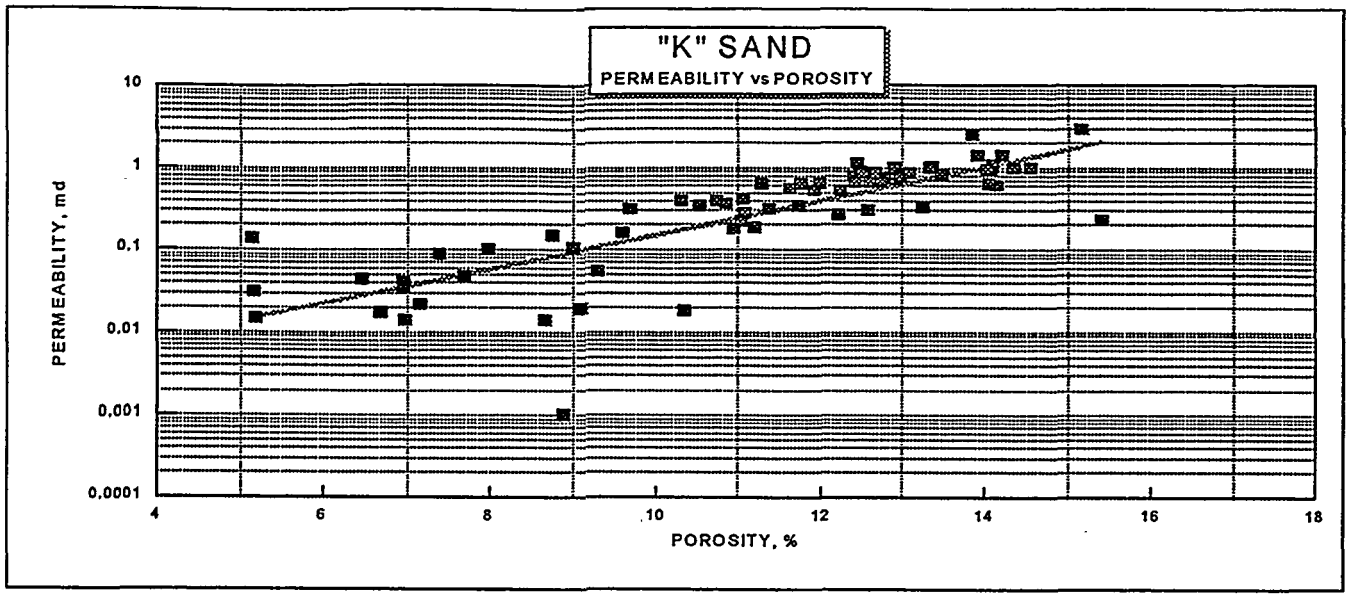

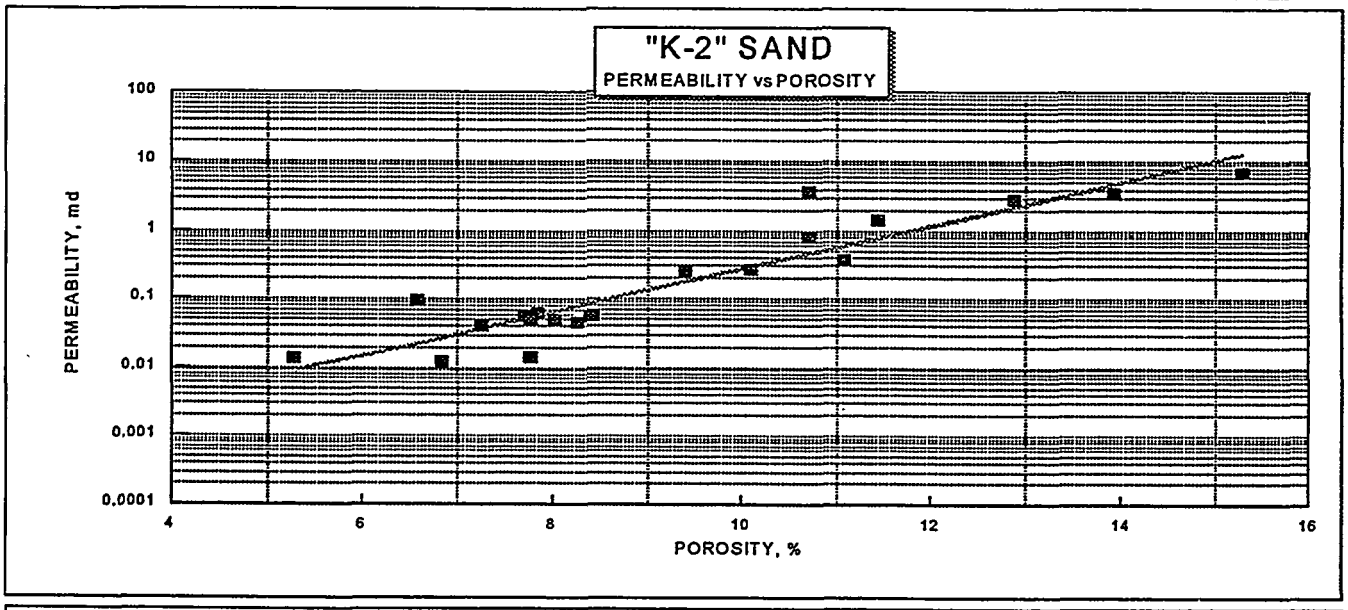

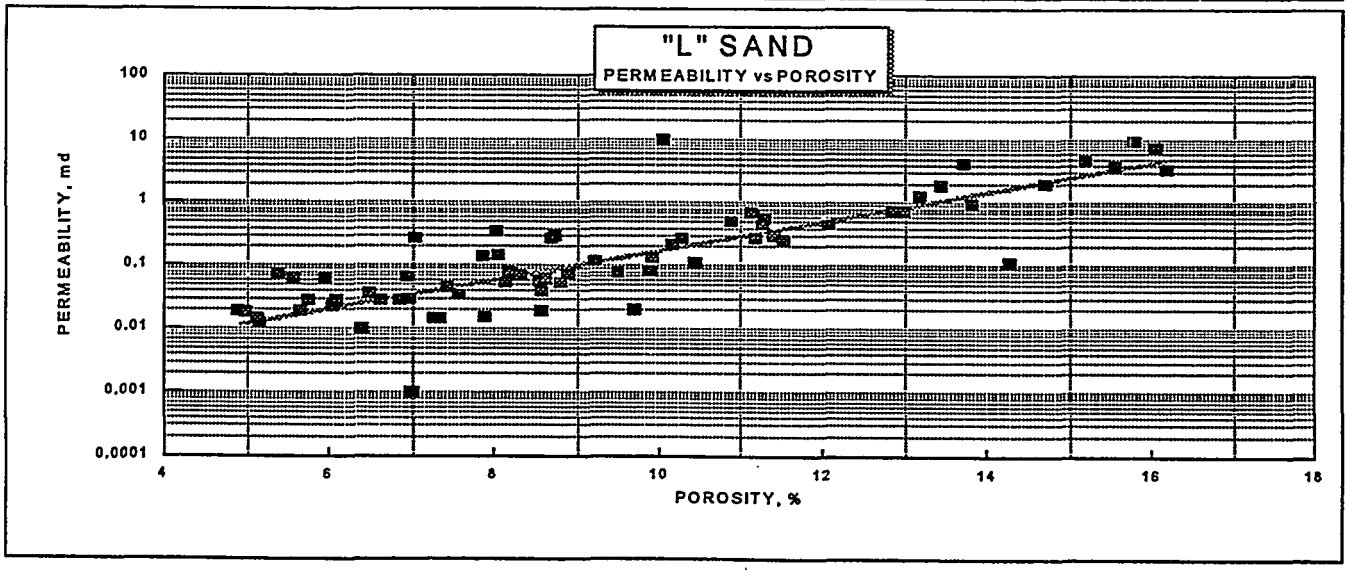

Fig. 3. Permeability versus porosity.

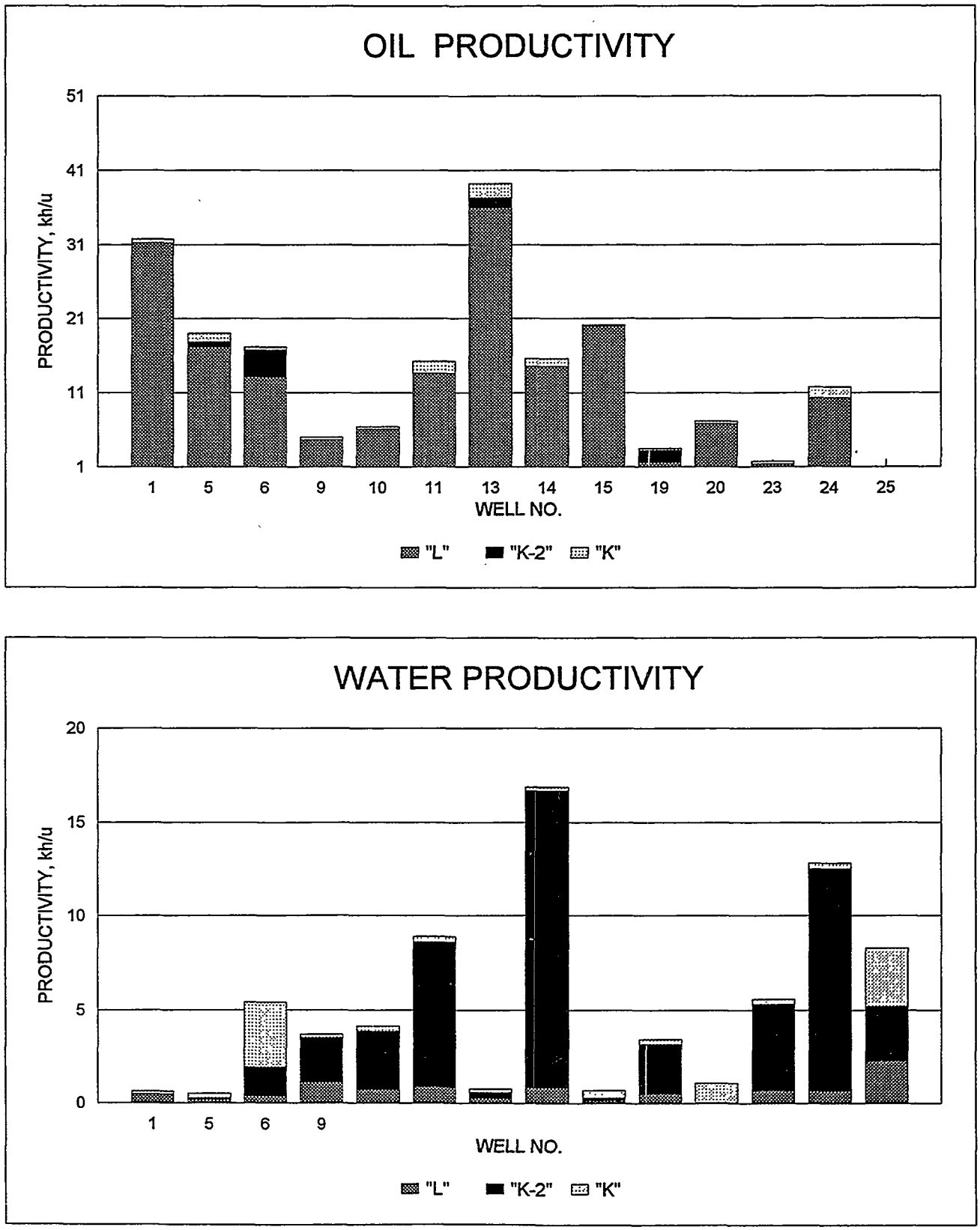

Fig. 4 Productivity values used for production allocations.

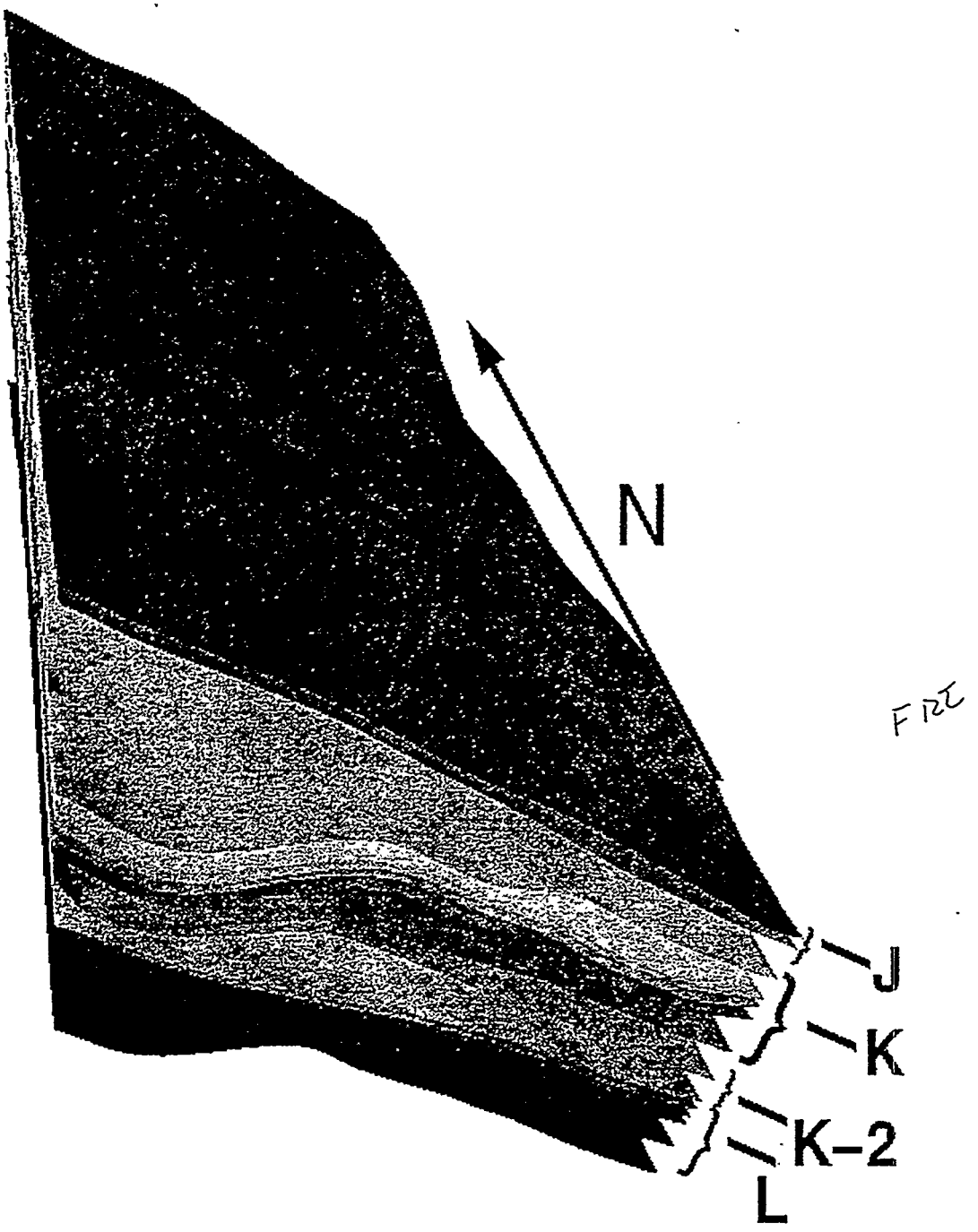

Fig. 5 Stratigraphic framework model.

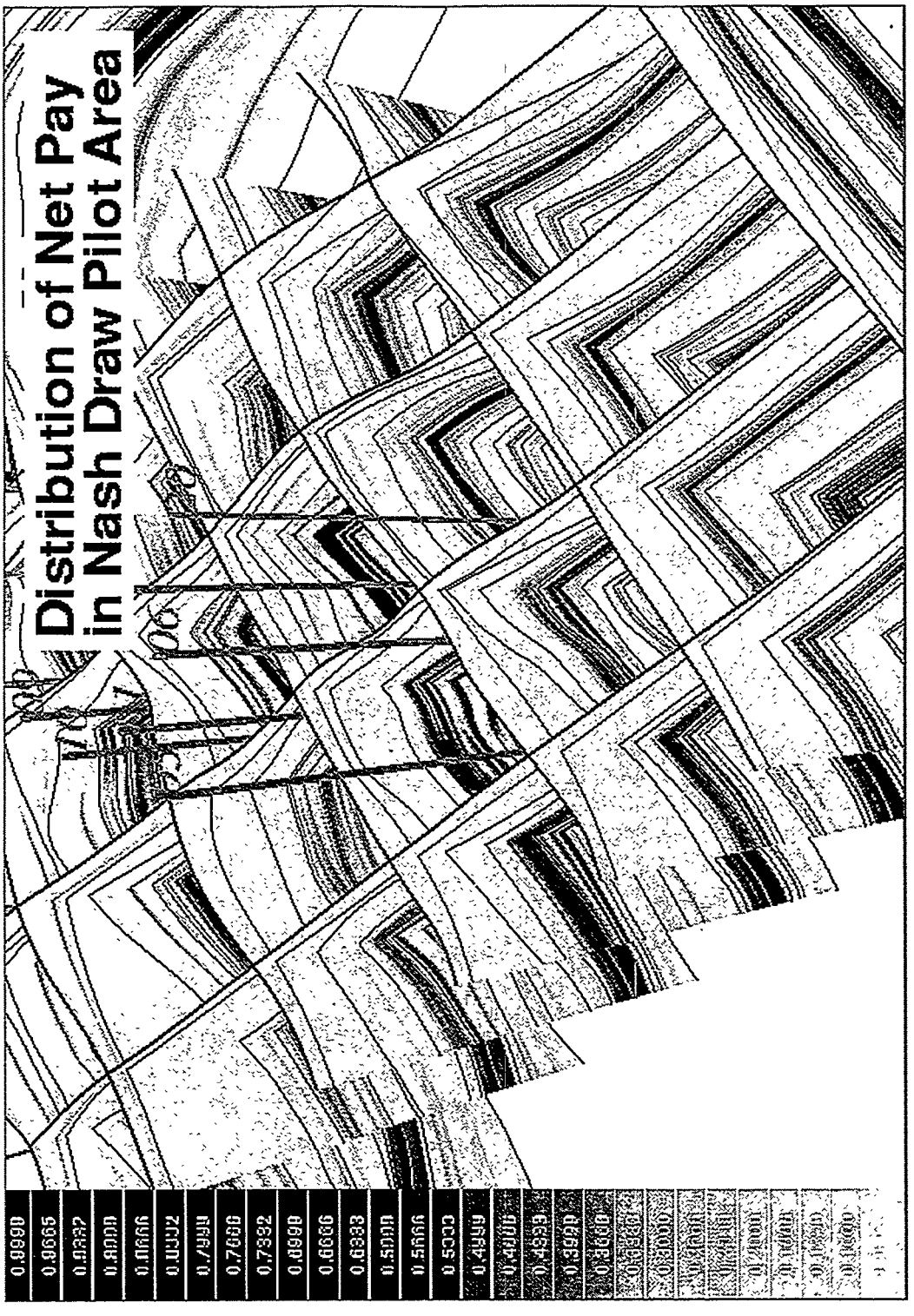

Fig. 6 Net pay distribution.

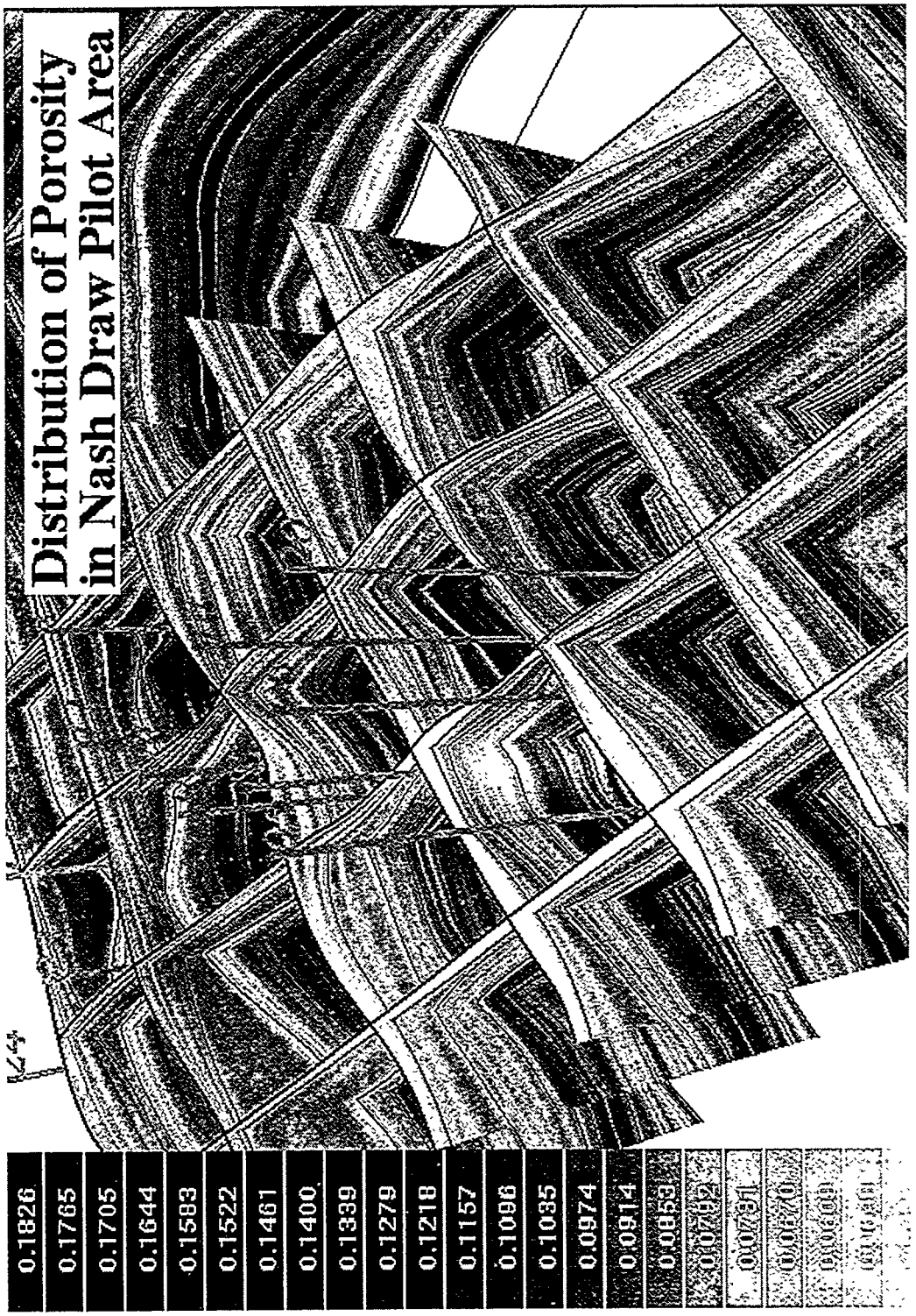

Fig. 7 Porosity distribution.

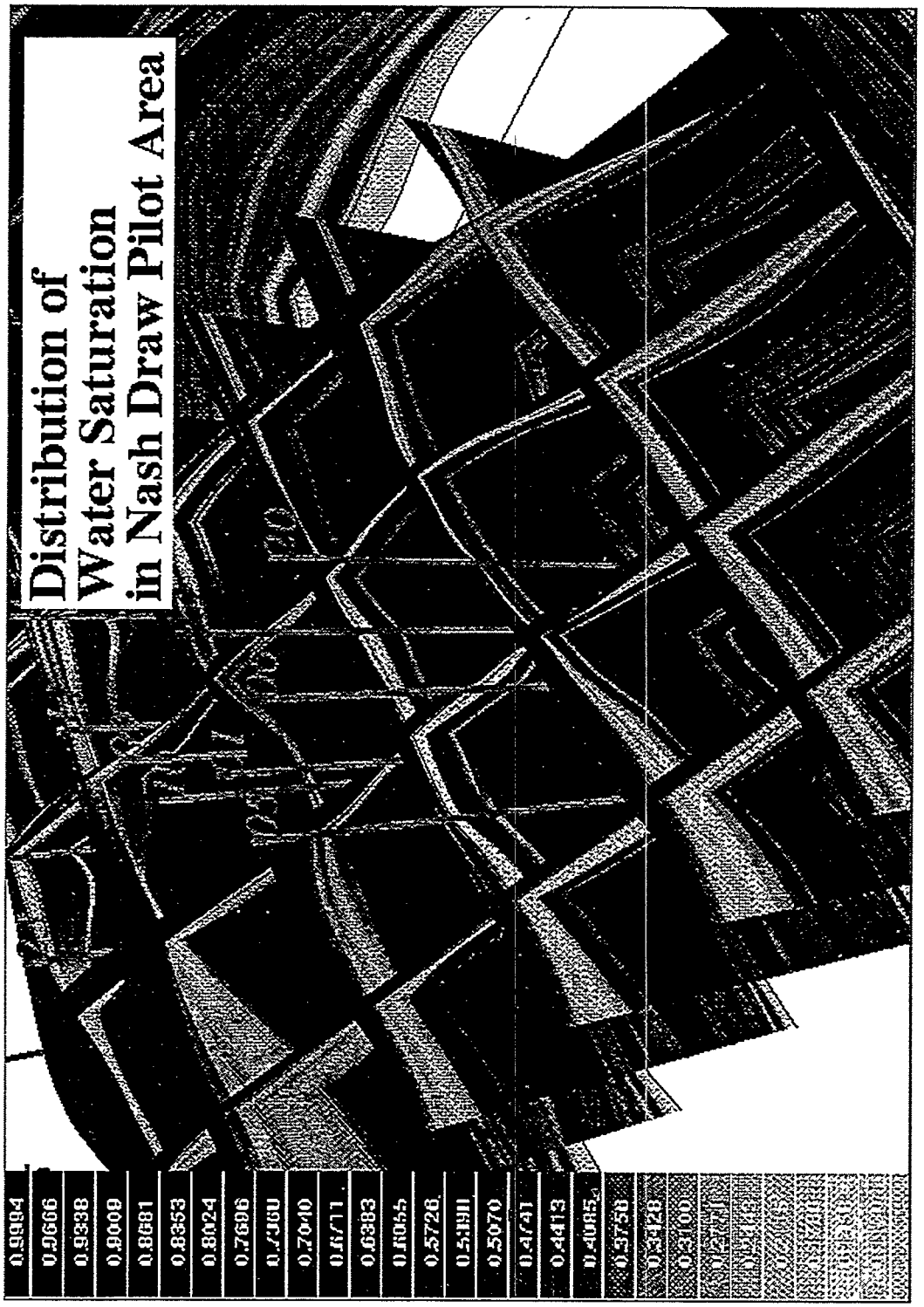

Fig. 8 Water saturation distribution.

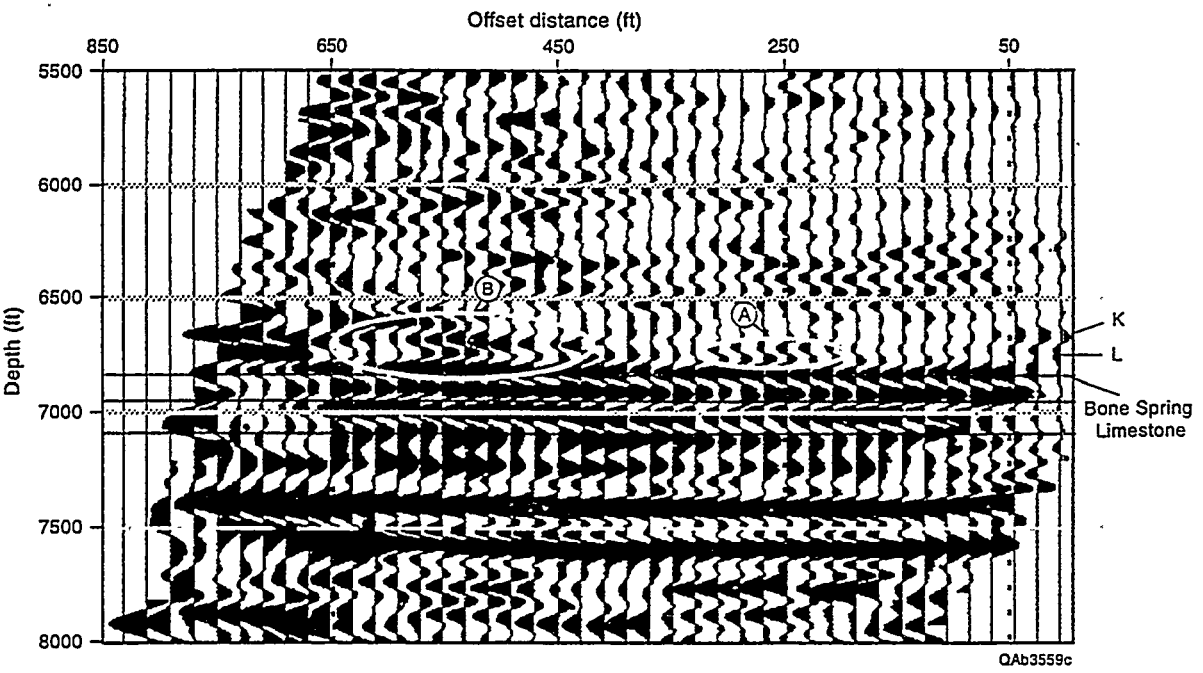

Fig. 9 VSP image.

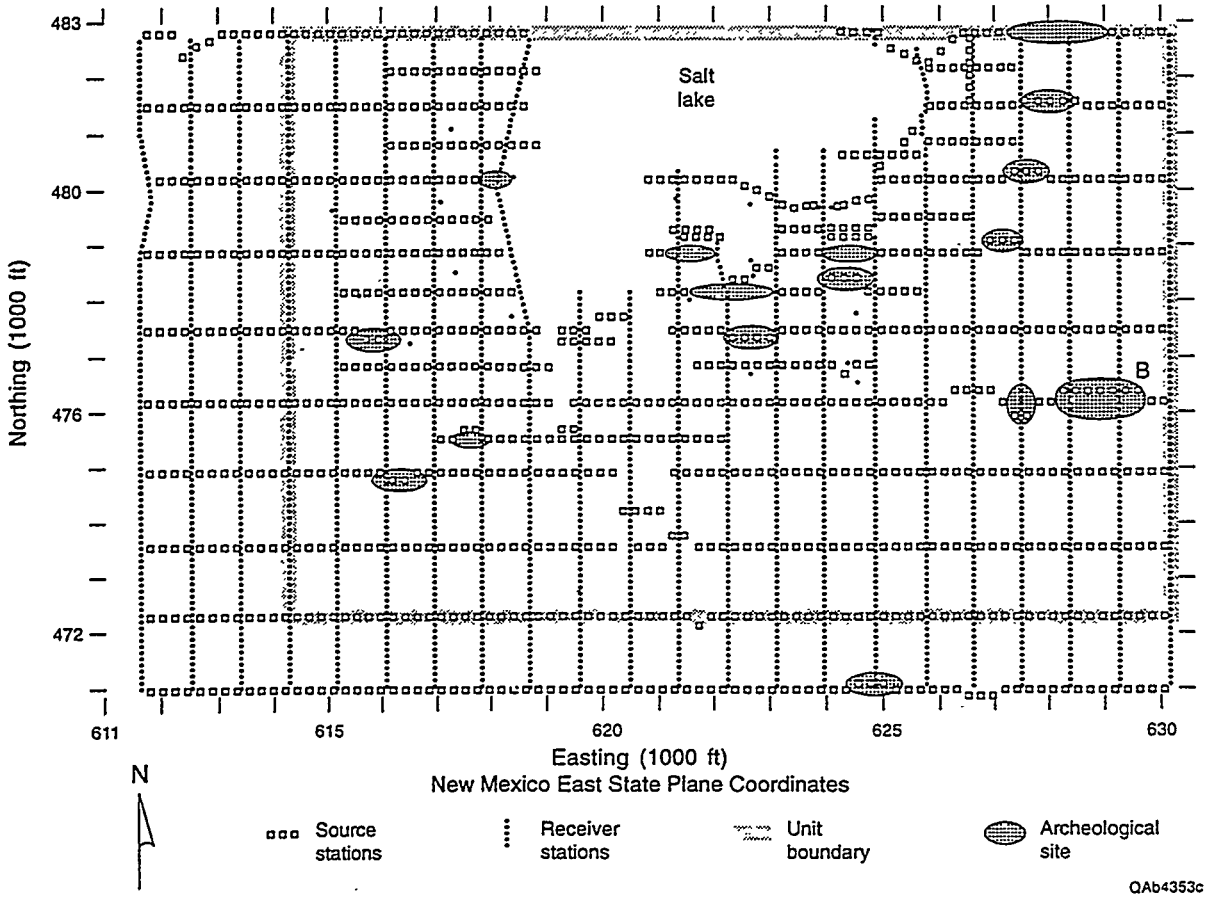

Fig. 10 Seismic grid.

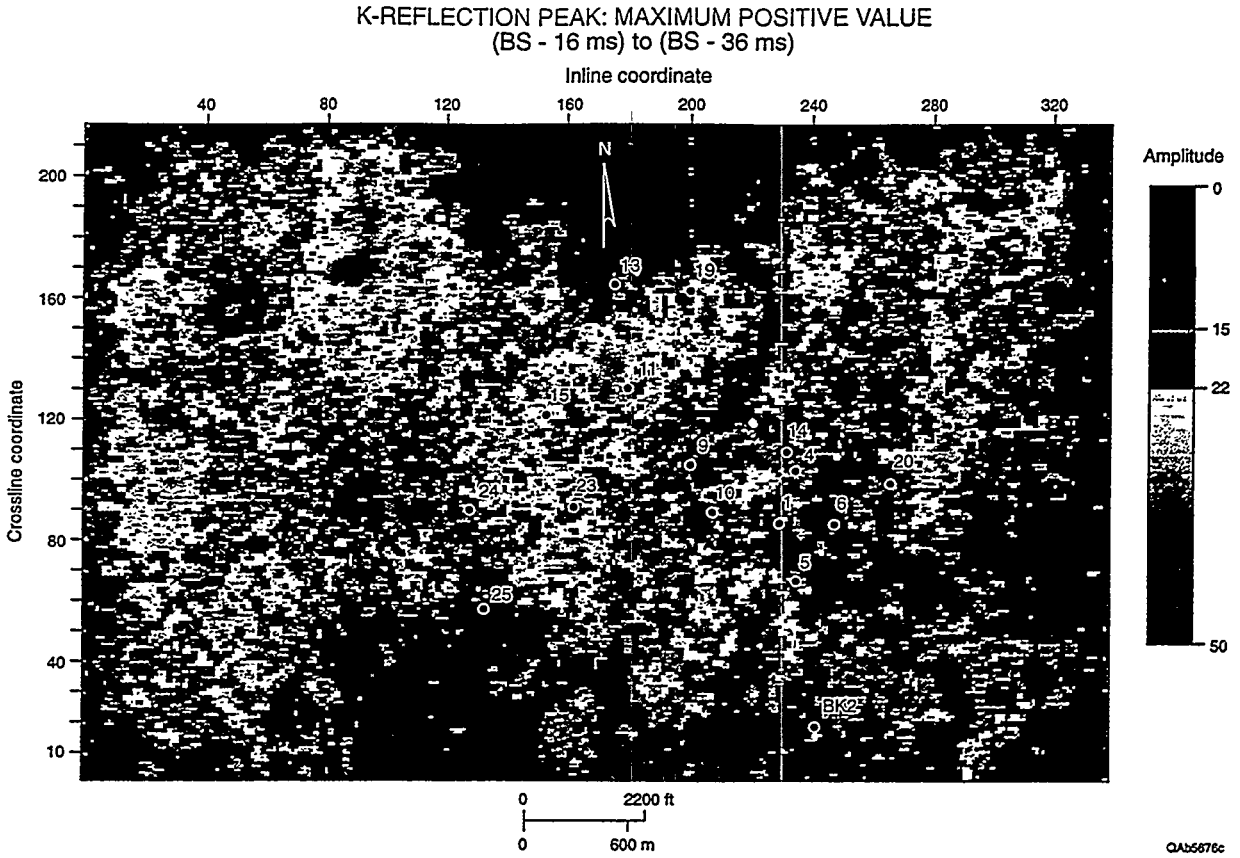

Fig. 11 "K" zone amplitude map.

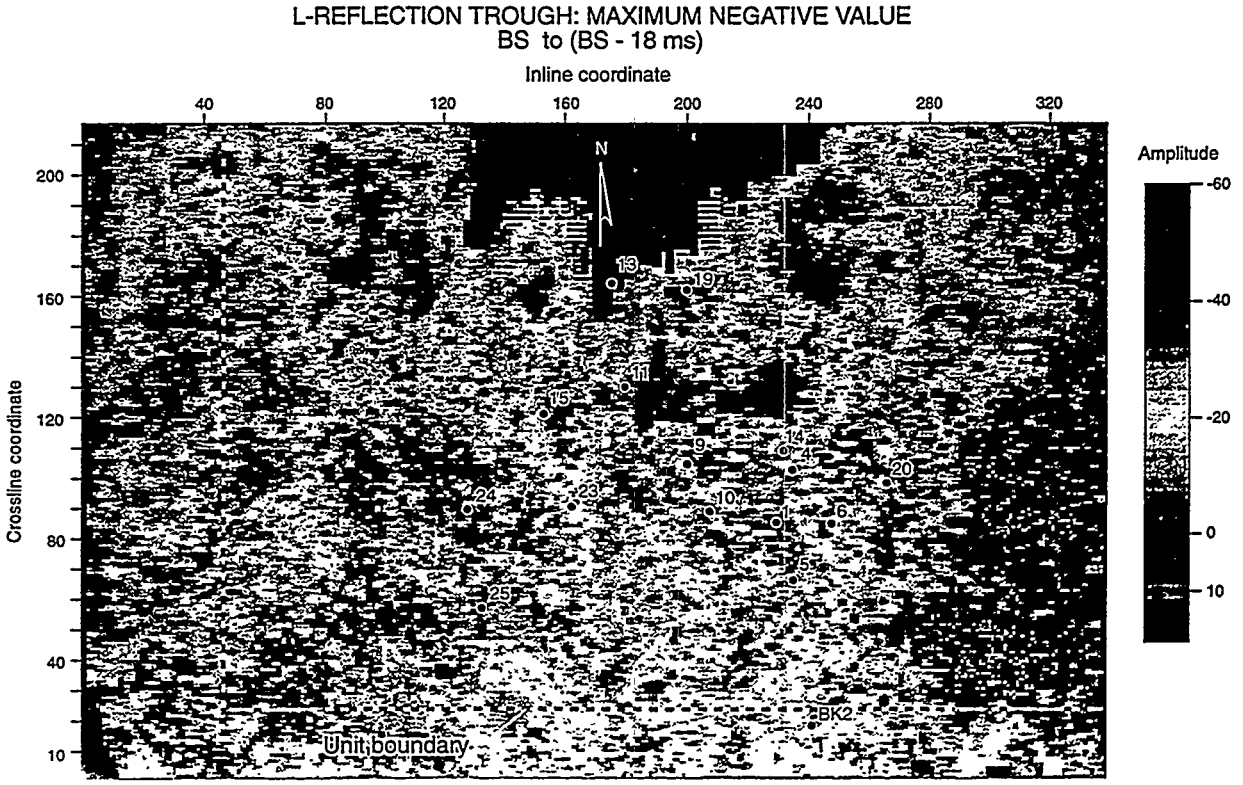

Fig. 12 "L" zone amplitude map.

Table 1. General Characteristics of the Nash Draw Delaware Field, Eddy County, New Mexico.

Discovery Date	1992
Trapping Mechanism	Stratigraphic Trap
Current Number of Wells	15
Current Production	490 BOPD + 2.4 MMCFGPD + 500 BWPD
Reservoir Depth	6600 to 7000 ft
Pay Thickness—K & L Sandstones	20 to 50 ft
Reservoir Porosity	12 to 20%
Reservoir Permeability	0.2 to 6 md
Initial Reservoir Pressure	2963 psi
Bubble Point Pressure	2677 psi
Drive Mechanism	Solution Gas Drive
Oil Gravity	42.4□ API
Primary Recovery Factor	10 to 15% oil in place
Estimated Oil in Place	25 to 50 MMbbl
Reserves, Primary Recovery	2.5 to 5 MMbbl

Table 2. Permeability/Porosity Correlations.

Flow Unit	Sidewall	Core	Full	Core
Variable	a	b	a	b
"K"	0.164915	2.25338	0.207675	2.8858
"K-2"	0.186535	2.06872	0.315038	3.69966
"L"	0.179787	2.45666	0.231250	3.06330

Table 1. General Characteristics of the Nash Draw Delaware Field, Eddy County, New Mexico.

Discovery Date	1992
Trapping Mechanism	Stratigraphic Trap
Current Number of Wells	15
Current Production	490 BOPD + 2.4 MMCFGPD + 500 BWPD
Reservoir Depth	6600 to 7000 ft
Pay Thickness—K & L Sandstones	20 to 50 ft
Reservoir Porosity	12 to 20%
Reservoir Permeability	0.2 to 6 md
Initial Reservoir Pressure	2963 psi
Bubble Point Pressure	2677 psi
Drive Mechanism	Solution Gas Drive
Oil Gravity	42.4° API
Primary Recovery Factor	10 to 15% oil in place
Estimated Oil in Place	25 to 50 MMbbl
Reserves, Primary Recovery	2.5 to 5 MMbbl

Table 2. Permeability/Porosity Correlations.

Flow Unit	**Sidewall**	**Core**	**Full**	**Core**
Variable	a	b	a	b
"K"	0.164915	2.25338	0.207675	2.8858
"K-2"	0.186535	2.06872	0.315038	3.69966
"L"	0.179787	2.45666	0.231250	3.06330